Xiaoming Tao
Editor

Handbook of Smart Textiles

Springer Reference

Handbook of Smart Textiles

Xiaoming Tao
Editor

Handbook of Smart Textiles

With 565 Figures and 66 Tables

Springer Reference

Editor
Xiaoming Tao
Institute of Textiles and Clothing
The Hong Kong Polytechnic University
Hung Hom, Hong Kong SAR

ISBN 978-981-4451-44-4 ISBN 978-981-4451-45-1 (eBook)
ISBN 978-981-4451-46-8 (print and electronic bundle)
DOI 10.1007/978-981-4451-45-1

Library of Congress Control Number: 2015943787

Springer Singapore Heidelberg New York Dordrecht London
© Springer Science+Business Media Singapore 2015
This work is subject to copyright. All rights are reserved by the Publisher, whether the whole or part of the material is concerned, specifically the rights of translation, reprinting, reuse of illustrations, recitation, broadcasting, reproduction on microfilms or in any other physical way, and transmission or information storage and retrieval, electronic adaptation, computer software, or by similar or dissimilar methodology now known or hereafter developed.
The use of general descriptive names, registered names, trademarks, service marks, etc. in this publication does not imply, even in the absence of a specific statement, that such names are exempt from the relevant protective laws and regulations and therefore free for general use.
The publisher, the authors and the editors are safe to assume that the advice and information in this book are believed to be true and accurate at the date of publication. Neither the publisher nor the authors or the editors give a warranty, express or implied, with respect to the material contained herein or for any errors or omissions that may have been made.

Printed on acid-free paper

Springer Science+Business Media Singapore Pte Ltd. is part of Springer Science+Business Media (www.springer.com)

Preface

"Smart Textiles" is an emerging transformative research area which deals with the creation and studies of new generations of fiber assemblies and apparel systems that can sense, react with, and adapt to external conditions or stimuli in a manual or programmed manner. The rapid development of nano-scaled science and technologies as well as miniaturization of devices make it possible to impart novel functions like electronic and photonic functions on the surface of or inside fibers and their assemblies. Fiber-based electronic and photonic devices and systems have outstanding flexibility and wearing comfort, superior fatigue resistance in long-term repeated large deformation, and excellent ubiquitousness, perfectly suited for wearable applications. Their fabrication normally involves low-cost and environment-friendly processes by using conventional facilities at low temperature, often in ambient conditions. Such man-made fiber-based devices and systems hoist many new scientific and technological challenges that have never been encountered before.

It has been almost 15 years since the first book on this topic, *Smart Fibers, Fabrics and Clothing*, was published in 2001, when the field of smart textiles and clothing was only at its beginning. Then, I was encouraged to look freely into the unknown future, with the only guidance then being the scientific principles, based upon which to dream about things possible. Now looking back, during this period of time, many exciting developments have occurred as wished.

In 2001, only a handful number of research groups around the world were working on this topic. Now almost all major universities have research activities and publications. The topic of smart textiles has attracted many researchers of other fields to make contributions, at the same time helping traditional textile science and technology in its transition to work at multidisciplinary research frontiers. Having a synergic effect with the rapid developments of related areas, e.g., nanoscience and technology, smart materials and structures, microelectronics, Internet, and wireless communication, smart textiles has become a fertile field of research leading to many technological breakthroughs and excitements.

As a result, *Handbook of Smart Textile* has expanded to four volumes as compared to the single-volume book of 2001. They cover the following topics:

The first section, "**Smart Fibers and Fibrous Assembly Structures**," deals with multiscaled design and material synthesis of a range of metallic, inorganic,

organic, polymeric, and hybrid smart materials for imparting single- or multifunctional intelligence to fibers and fibrous assemblies and their structures, performance, and characterization techniques.

The second section, "**Interactive Textile Devices**," describes structures, functions, mechanisms, and characterization technologies for sensing, communicating, memorizing, actuating, and energy harvesting by single-fiber or textile-based interactive devices and multiscale computational engineering techniques for designing and engineering intelligent fibrous products to achieve specific or multifunctions.

"**Product Integration and Evaluation Technology**" gives concise account to the principles, processes, equipment, and operation of a range of technologies to fabricate and evaluate the intelligent multifunctional textiles and apparel products.

The last section, "**Applications of Smart Textiles**," provides a globe view of the development and industrial applications with case studies, system design, product standards, analysis of the supply chain, challenges, and opportunities.

I wish readers to find the Handbook informative and useful in their endeavors.

June 2015 Xiaoming Tao
Hong Kong

Contents

Part I Smart Fibers and Fibrous Assembly Structures **1**
Jinlian Hu and Xiaoming Tao

1 Electric Functions of Textile Polymers 3
Toshihiro Hirai and Hong Xia

2 Conducting Polymer Fibers 31
Javad Foroughi, Geoffrey M. Spinks, and Gordon G. Wallace

3 Conductive Polymer Fibers for Sensor Devices 63
Mutsumi Kimura

4 Optical Fibers 79
Anne Schwarz-Pfeiffer, Viktorija Mecnika, Markus Beckers, Thomas Gries, and Stefan Jockenhoevel

5 Polymer Optical Fiber for Smart Textiles 109
Wei Zeng

6 Fibers with the Tunable Structure Colors Based on the Ordered and Amorphous Structures 127
Wei Yuan, Chaojie Wu, Ning Zhou, and Ke-Qin Zhang

7 Photochromic Fibers and Fabrics 155
Marzieh Parhizkar, Yan Zhao, and Tong Lin

8 Shape Memory Fibers 183
Jinlian Hu and Jing Lu

9 Silk Fibers as Smart Materials Toward Medical Textiles 209
Yasushi Tamada and Katsura Kojima

10 Phase Change Fibers and Assemblies 225
Qinghao Meng, Guoqiang Li, and Jinlian Hu

Part II Interactive Textile Devices **253**
Xiaoming Tao

11 Fiber-Based Wearable Electronic Circuits and Systems 255
Shu Lin

12 Flexible Fabric Strain Sensors 293
Weijing Yi

13 Soft Tactile Sensors for Human-Machine Interaction 317
Fei Wang

14 Textile Sensors 357
Hatice A. K. Toprakci and Tushar K. Ghosh

15 Flexible Actuators 381
Wei Chen and Zicai Zhu

16 Development of Nanogenerators in Wearable Electronics 411
Chen Song, Xiaoming Tao, and Songming Shang

17 Textile Antenna Systems: Design, Fabrication, and Characterization 433
Hendrik Rogier

18 Energy-Harvesting Fabric Antenna 459
Alessandra Costanzo and Diego Masotti

19 Mechanisms for Fiber-based Nanogenerators 487
Wei Zeng

20 Functional Nanofibers for Energy Storage 513
Yao Lu, Chen Chen, and Xiangwu Zhang

21 Fabric Substrates and Interconnectors for Three-Dimensional Surfaces 549
Qiao Li and Xiaoming Tao

22 Photonic Fabric Devices for Phototherapy 577
Shen Jing

23 Polymer Optical Fiber Bragg Grating 597
Zhang Zhifeng

Part III Product Integration and Evaluation Technologies **615**
Vladan Koncar and Xiaoming Tao

24 Applications of Electrospun Nanofibers for Electronic Devices 617
Jian Fang, Hao Shao, Haitao Niu, and Tong Lin

25 Printed Textile-Based Electronic Devices 653
R. Torah, Y. Wei, Y. Li, K. Yang, S. Beeby, and J. Tudor

26 Thermal Regulation of Electrically Conducting Fabrics 689
Jiahui Tong and Li Li

27 Relationship Between Electromechanical Properties and Fabric Structures Made from Intrinsically Conductive Fibers 719
Zhang Hui

28 Fabrication of Organic Materials for Electronic Textiles 739
Tae Hwan Lim, Seong Hun Kim, and Kyung Wha Oh

29 Evaluation Methods and Instruments of Dry Biopotential Electrodes 775
Liu Hao and Xiaoming Tao

30 Applications of Terahertz Wave Technology in Smart Textiles 809
Dongxiao Yang

31 Standards for Smart Textiles 843
Carla Hertleer and Lieva Van Langenhove

Part IV Applications of Smart Textiles 857
Vladan Koncar, Jinlian Hu, and Xiaoming Tao

32 Color-Changing Textiles and Electrochromism 859
Fern M. Kelly and Cédric Cochrane

33 Smart Nanofibrous Membranes with Controllable Porous Structure and Surface Wettability for High Efficient Separation Materials 891
Yang Si, Xiaomin Tang, Jianyong Yu, and Bin Ding

34 Thermo-responsive Textiles 919
Jiping Wang, Qi Zhong, Jindan Wu, and Tao Chen

35 Novel Synthesis Pathways for PNIPAAm-Based Hydrogels and Their Application in Thermosensitive Textiles 953
Petar Jovancic, S. Petrusic, and R. Molina

36 Textile-Based Body Sensor Networks and Biomedical Computing for Healthcare Applications 985
Yong Kim and Honggang Wang

37 Photonic Fabrics for Fashion and Interior 1005
Jeanne Tan

38 Smart Textiles: Past, Present, and Future 1035
Lieva Van Langenhove

Index 1059

About the Editor

Xiaoming Tao Institute of Textiles and Clothing, The Hong Kong Polytechnic University, Hung Hom, Hong Kong SAR

Prof. Xiaoming Tao has a B.Eng. in textile engineering from ECITST and a Ph.D. in textile physics from UNSW. She has been Chair Professor of Textile Technology at The Hong Kong Polytechnic University since 2002. She is an affiliate faculty member of the Interdisciplinary Division of Biomedical Engineering. Prof. Tao is the past World President of the Textile Institute, Fellow of the American Society of Mechanical Engineers and Fellow of the Royal Society of Arts, Design and Commercial Applications, UK.

Prof. Tao's expertise is materials science and textile engineering. She is known for her leading research on smart fibrous materials, textile-based electronic and photonic technology, textile manufacturing, and textile composites. With more than 200 international journal papers and 6 research monographs, her work has been cited extensively with an h-index of 46. Over 10 invented technologies in the areas of textile manufacturing and smart textiles have been licensed worldwide for industrial production. She was the recipient of the Honorary Fellowship of the Textile Institute in 2011 and Founder's Award by Fiber Society of USA in 2013, top individual awards offered by these two international professional organizations.

Section Editors

Xiaoming Tao Institute of Textiles and Clothing, The Hong Kong Polytechnic University, Hung Hom, Hong Kong SAR

Jinlian Hu Institute of Textiles and Clothing, The Hong Kong Polytechnic University, Hung Hom, Hong Kong

Vladan Koncar GEMTEX Laboratory, Roubaix, France

Contributors

Markus Beckers RWTH Aachen University, Aachen, Germany

S. Beeby Electronics and Computer Science, University of Southampton, Southampton, UK

Chen Chen Fiber and Polymer Science Program, Department of Textiles Engineering, Chemistry and Science, North Carolina State University, Raleigh, NC, USA

Tao Chen Key Laboratory of Advanced Textile Materials & Manufacturing Technology, Ministry of Education, National Base for International Science and Technology Cooperation in Textiles and Consumer-Goods Chemistry, Zhejiang Sci-Tech University, Hangzhou, China

Wei Chen Suzhou Institute of Nano-Tech and Nano-Bionics (SINANO), Chinese Academy of Sciences, Suzhou, Jiangsu, China

Cédric Cochrane ENSAIT, GEMTEX, Roubaix, France

University of Lille Nord de France, Lille, France

Alessandra Costanzo DEI, University of Bologna, Cesena, Italy

Bin Ding State Key Laboratory for Modification of Chemical Fibers and Polymer Materials, College of Materials Science and Engineering, Donghua University, Shanghai, China

Nanomaterials Research Center, Modern Textile Institute, Donghua University, Shanghai, China

Jian Fang Institute for Frontier Materials, Deakin University, Geelong, VIC, Australia

Javad Foroughi ARC Centre of Excellence for Electromaterials Science, Intelligent Polymer Research Institute, University of Wollongong, Wollongong, NSW, Australia

Tushar K. Ghosh North Carolina State University, Raleigh, USA

Thomas Gries RWTH Aachen University, Aachen, Germany

Liu Hao School of Textiles, Tianjin Polytechnic University, Tianjin, China

Carla Hertleer Department of Textiles, Ghent University, Zwijnaarde, Belgium

Toshihiro Hirai Fiber Innovation Incubator, Faculty of Textile Science Technology, Shinshu University, Ueda-shi, Nagano-ken, Japan

Jinlian Hu Institute of Textiles and Clothing, The Hong Kong Polytechnic University, Hung Hom, Hong Kong

Zhang Hui School of Textiles, Zhejiang Fashion Institute of Technology, Jiangbei District, Ningbo, Zhejiang Province, China

Shen Jing National Engineering Research Center for Ophthalmic Equipments, Beijing Institute of Ophthalmology, Beijing Province, China

Stefan Jockenhoevel RWTH Aachen University, Aachen, Germany

Petar Jovancic Textile Engineering Department, Faculty of Technology and Metallurgy, University of Belgrade, Belgrade, Serbia

Fern M. Kelly ENSAIT, GEMTEX, Roubaix, France

Seong Hun Kim Department of Organic and Nano Engineering, Hanyang University, Sungdong-gu, Seoul, South Korea

Yong Kim Department of Bioengineering, University of Massachusetts Dartmouth, North Dartmouth, MA, USA

Mutsumi Kimura Division of Chemistry and Materials, Faculty of Textile Science and Technology, Shinshu University, Ueda, Nagano, Japan

Katsura Kojima National Institute of Agrobiological Sciences, Tsukuba, Ibaraki, Japan

Guoqiang Li Department of Mechanical and Industrial Engineering, Louisiana State University, Baton Rouge, LA, USA

Li Li The Hong Kong Polytechnic University, Hong Kong, China

Qiao Li Institute of Textiles and Clothing, The Hong Kong Polytechnic University, Kowloon, Hong Kong SAR, China

Y. Li Electronics and Computer Science, University of Southampton, Southampton, UK

Tae Hwan Lim Technical Textile and Materials R&BD Group, Korea Institute of Industrial Technology, Ansan-si, Gyeonggi-do, South Korea

Department of Organic and Nano Engineering, Hanyang University, Sungdong-gu, Seoul, South Korea

Shu Lin Institute of Textiles and Clothing, The Hong Kong Polytechnic University, Hung Hom, Hong Kong

Tong Lin Institute for Frontier Materials, Deakin University, Geelong, VIC, Australia

Jing Lu Institute of Textiles and Clothing, The Hong Kong Polytechnic University, Hung Hom, Hong Kong

Yao Lu Fiber and Polymer Science Program, Department of Textiles Engineering, Chemistry and Science, North Carolina State University, Raleigh, NC, USA

Diego Masotti DEI, University of Bologna, Bologna, Italy

Viktorija Mecnika RWTH Aachen University, Aachen, Germany

Qinghao Meng Mechanical Department, Southern University, Baton Rouge, LA, USA

R. Molina Plasma Chemistry Group, Department of Chemical and Surfactants Technology, Institute of Advanced Chemistry of Catalonia, Consejo Superior de Investigaciones Científicas, IQAC-CSIC, Barcelona, Spain

Haitao Niu Institute for Frontier Materials, Deakin University, Geelong, VIC, Australia

Kyung Wha Oh Department of Fashion Design, Chung-Ang University, Anseong-si, Gyeonggi-do, South Korea

Marzieh Parhizkar Australian Future Fibers Research and Innovation Centre, Institute for Frontier Materials, Deakin University, Geelong, VIC, Australia

S. Petrusic Ecole Nationale Supérieure des Arts et Industries Textiles, ENSAIT, GEMTEX, Roubaix, France

Université Lille Nord de France, Lille, France

Hendrik Rogier Department of Information Technology, iMinds/Ghent University, Ghent, Belgium

Anne Schwarz-Pfeiffer Niederrhein University of Applied Sciences, Mönchengladbach, Germany

Songming Shang Institute of Textiles and Clothing, The Hong Kong Polytechnic University, Kowloon, Hong Kong, SAR, China

Hao Shao Institute for Frontier Materials, Deakin University, Geelong, VIC, Australia

Yang Si State Key Laboratory for Modification of Chemical Fibers and Polymer Materials, College of Materials Science and Engineering, Donghua University, Shanghai, China

Nanomaterials Research Center, Modern Textile Institute, Donghua University, Shanghai, China

Chen Song Institute of Textiles and Clothing, The Hong Kong Polytechnic University, Kowloon, Hong Kong, SAR, China

Geoffrey M. Spinks ARC Centre of Excellence for Electromaterials Science, Intelligent Polymer Research Institute, University of Wollongong, Wollongong, NSW, Australia

Yasushi Tamada Division of Applied Biology, Faculty of Textile Science and Technology, Shinshu University, Ueda City, Nagano, Japan

Jeanne Tan Institute of Textiles and Clothing, The Hong Kong Polytechnic University, Hung Hom, Hong Kong

Xiaomin Tang State Key Laboratory for Modification of Chemical Fibers and Polymer Materials, College of Materials Science and Engineering, Donghua University, Shanghai, China

Nanomaterials Research Center, Modern Textile Institute, Donghua University, Shanghai, China

Xiaoming Tao Institute of Textiles and Clothing, The Hong Kong Polytechnic University, Hung Hom, Hong Kong SAR

Jiahui Tong The Hong Kong Polytechnic University, Hong Kong, China

Hatice A. K. Toprakci Faculty of Engineering, Polymer Engineering Department, Yalova University, Yalova, Turkey

R. Torah Electronics and Computer Science, University of Southampton, Southampton, UK

J. Tudor Electronics and Computer Science, University of Southampton, Southampton, UK

Lieva Van Langenhove Department of Textiles, Ghent University, Ghent, Belgium

Gordon G. Wallace ARC Centre of Excellence for Electromaterials Science, Intelligent Polymer Research Institute, University of Wollongong, Wollongong, NSW, Australia

Fei Wang Institute of Textiles and Clothing, The Hong Kong Polytechnic University, Kowloon, Hong Kong, China

Honggang Wang Department of Electrical and Computer Engineering, University of Massachusetts Dartmouth, North Dartmouth, MA, USA

Jiping Wang Key Laboratory of Advanced Textile Materials & Manufacturing Technology, Ministry of Education, National Base for International Science and Technology Cooperation in Textiles and Consumer-Goods Chemistry, Zhejiang Sci-Tech University, Hangzhou, China

Y. Wei Electronics and Computer Science, University of Southampton, Southampton, UK

Chaojie Wu National Engineering Laboratory for Modern Silk, College of Textile and Clothing Engineering, Soochow University, Suzhou, China

Jindan Wu Key Laboratory of Advanced Textile Materials & Manufacturing Technology, Ministry of Education, National Base for International Science and Technology Cooperation in Textiles and Consumer-Goods Chemistry, Zhejiang Sci-Tech University, Hangzhou, China

Hong Xia Institute of Carbon Science and Technology, Shinshu University, Nagano, Japan

Dongxiao Yang Department of Information Science & Electronic Engineering, Zhejiang University, Hangzhou, China

K. Yang Electronics and Computer Science, University of Southampton, Southampton, UK

Weijing Yi Beijing Institute of Fashion Technology, Beijing, China

Jianyong Yu State Key Laboratory for Modification of Chemical Fibers and Polymer Materials, College of Materials Science and Engineering, Donghua University, Shanghai, China

Nanomaterials Research Center, Modern Textile Institute, Donghua University, Shanghai, China

Wei Yuan National Engineering Laboratory for Modern Silk, College of Textile and Clothing Engineering, Soochow University, Suzhou, China

Ke-Qin Zhang National Engineering Laboratory for Modern Silk, College of Textile and Clothing Engineering, Soochow University, Suzhou, China

Xiangwu Zhang Fiber and Polymer Science Program, Department of Textiles Engineering, Chemistry and Science, North Carolina State University, Raleigh, NC, USA

Yan Zhao Australian Future Fibers Research and Innovation Centre, Institute for Frontier Materials, Deakin University, Geelong, VIC, Australia

Wei Zeng Hong Kong Polytechnic University, Kowloon, Hong Kong, China

Qi Zhong Key Laboratory of Advanced Textile Materials & Manufacturing Technology, Ministry of Education, National Base for International Science and Technology Cooperation in Textiles and Consumer-Goods Chemistry, Zhejiang Sci-Tech University, Hangzhou, China

Ning Zhou National Engineering Laboratory for Modern Silk, College of Textile and Clothing Engineering, Soochow University, Suzhou, China

Zhang Zhifeng The Hong Kong Polytechnic University, Hong Kong, China

Zicai Zhu Suzhou Institute of Nano-Tech and Nano-Bionics (SINANO), Chinese Academy of Sciences, Suzhou, Jiangsu, China

Part I

Smart Fibers and Fibrous Assembly Structures

Jinlian Hu and Xiaoming Tao

Electric Functions of Textile Polymers

1

Toshihiro Hirai and Hong Xia

Contents

Introduction 4
Textile Polymers and Their Electric Characteristics 5
Dielectric Polymer Gel 6
Dielectric Elastomers 8
Dielectric Plasticized Polymers 10
  Electrically Induced Creep Deformation 11
  Creep Induced Bending of PVC Gel 11
  Application for Gripper 12
  Contractile Deformation 13
  Creep-Induced Crawler 16
  Tacking Force and Dielectric Constant 17
  Electrooptical Function 22
  Mechanoelectric Function 22
New Weaving Technology 23
  Vibration of PET Film by Applying a dc Electric Field 23
  Flattering of PVC Gel by Applying a dc Electric Field 25
  Weaving Micro- and Nano- Fiber 25
Summary 26
References 27

T. Hirai (✉)
Fiber Innovation Incubator, Faculty of Textile Science Technology, Shinshu University, Ueda-shi, Nagano-ken, Japan
e-mail: toshihirohirai@me.com; tohirai@shinshu-u.ac.jp

H. Xia
Institute of Carbon Science and Technology, Shinshu University, Nagano, Japan
e-mail: hxia@shinshu-u.ac.jp

© Springer Science+Business Media Singapore 2015

X. Tao (ed.), *Handbook of Smart Textiles*,
DOI 10.1007/978-981-4451-45-1_8

Abstract

Conventional textile materials are made of polymer materials. Many of the textile polymers are mostly dielectric materials. Dielectric polymers with low dielectric constant have been considered inactive to an electric field. However, they turned out to be electrically active. Textile polymers or their gels and elastomers are shown how they can be electrically active. The actions observed are electromechanical, mechanoelectrical, and electrooptical. Even the electromechanical functions have varieties of contractile, bending (or folding), crawling, vibration, and creeping deformation. Some of these polymers exhibit colossal dielectric constant at certain conditions. The characteristics suggest large power generation and novel functions. The electromechanical motility was applied for new type weaving technique that can be applicable for micro- and nano-fiber. Some of the materials for the textile polymers, such as poly (vinyl alcohol) and poly (vinyl chloride), show remarkable electrooptical functions, which can modulate refractive index by dc field application. These polymers can also imply effective piezoelectric function, too, suggesting these might be applied for energy-harvesting materials. These properties might suggest the possibility of conventional textile polymers in novel-type smart fiber and textiles.

Keywords

Textile polymer • Electromechanical function • Electrooptical function • Dielectric constant • Dielectric polymers • Microfiber • Nano-fiber • Actuator • Artificial muscle • Energy conversion • Impact sensor

Introduction

Conventional synthetic fibers are crystalline polymers and usually electrically inactive. However, they turned out to be electrically active in highly swollen gel and were utilized as electrically active materials, particularly as actuators [1]. Optimization of chemical structure might lead to totally new functional material, but even at the present stage, the conventional polymers still stay as the material with fancy functions with enough potential. In this chapter, the authors show the potential of conventional textile polymers as electrically active materials. The mechanism are provided on poly(vinyl alcohol) (PVA) [2, 3], poly(vinyl chloride) (PVC) [4, 5], polyurethane (PU) [6], tri-block poly(methyl methacrylate-co-butyl acrylate-co-methacrylate)(p(MMA-BA-MMA)) [7, 8], and poly(ethylene telephthalate) (PET) [9], etc.

Physical state of the materials treated covers highly swollen polymer gels, elastomers, solid polymer films, and fibers.

Functions treated are electromechanical functions, which include bending, crawling, contraction, creeping, and oscillation. Electrooptical function and

piezoelectric function are also found on these polymers in remarkable manner. All of these functions can be induced in the polymers listed above.

Textile polymers are usually dielectric, and that is the reason why they are inactive. In this sense, the phenomena, introduced in this chapter, are peculiar from common sense for dielectric polymers. However, it will be turned out that they are not peculiar and might be quite common phenomena and that the conventional dielectric polymers can be converted into electrically active materials in simple but various ways. Major reason of these functions can be attributed to the colossal dielectric constant emerged in these conventional polymers, which had not been mentioned for a long time [10]. The authors wish this chapter can be a guide to the novel functionalization of textile polymers.

Textile Polymers and Their Electric Characteristics

Dielectric properties of some polymers are summarized in Table 1. Many of them are conventionally used not only as textile materials but also in many other fields. As can be found, all polymers listed show dielectric constant (ε) below 10 and mostly below 5 in the measuring range of frequency. Usually, the frequency range below 10 Hz is for the ionic charge separation and not for the discussion on the dielectric characteristics. However, even in this low frequency range, it is possible to discuss the dielectric properties of the materials in which the relaxation of long polymer chain with the structure of higher-order hierarchy. Hirai has been investigated the effect of dc field on the polymer materials, mainly on soft polymer materials, with low value of ε. The dielectric behavior in low frequency range is important for the mechanical response of soft polymer materials, since the deformation of these materials has been known to be slow when the deformation accompanies the long-range migration of polymer chains, that is, a large strain, such as 1,000 %, concerns. In the Table 1, ε's are listed for other low-molecular-weight compounds; those are used as plasticizers or solvents. Their values are usually around 3 and less than 10 at most in the measurement range from 1 kHz to 0.01 Hz. These properties contribute to the novel-type deformation function as discussed in the latter section.

Table 1 Dielectric properties of polymers, solvents and plasticizers (typical values are shown. Measurement conditions are not the same, but useful for qualitative comparison)

Material	Relative dielectric constant*
Benzene	2.28
Chloroform	4.9
Nitrobenzene	34.8
Poly(vinyl chloride)	4–8
Poly(vinyl alcohol)	9
Nylon 6	3.5–5.0
Poly(ethylene telephthalate)	3.1–2.35

*Cited from Electrostatics Handbook, Edited by the Institute of Electrostatics Japan, Ohmsha Ltd., ISBN 9784274035104 (1998).

Dielectric Polymer Gel

PVA forms a good fiber; the tough structure is originated by hydrogen bonds among the polymer chains [11]. PVA itself is soluble in water and is usually treated with hydrophilicity control agents. On the other hand, it shows a very excellent property to form hydrogels. The PVA hydrogels can be formed only by physical bonding, that is, PVA polymer chains are connected with hydrogen bonds to form crystallites which work as cross-linking points to result in high water-content gel without chemical cross-links, although thermal stability is poor [12]. By controlling the hydrogen bond and chemical cross-link, the gel exhibits excellent shape memory property, too [13–15].

For the use as electro-active polymer, some researches were carried out on the polyelectrolyte hydrogels by mixing PVA with polyelectrolyte, such as poly(acrylic acid), which can respond to the electric field [16, 17]. These gels are categorized in electrolyte-type actuator and can be actuated by low voltage of dc field. The deformation of the polyelectrolyte hydrogel accompanies swelling and deswelling with water or salt aqueous solution, although it can be actuated by low voltage such as 1–10 V (current accompanied are at least mA level), and presence of water is usually inevitable. Electrolysis or electrochemical consumption is also unavoidable. Responding rate is also slow and usually a couple of seconds are required even in the quickest case.

By the way, PVA can be solubilized in dimethyl sulfoxide (DMSO), which is a dielectric solvent with $\varepsilon = 40$ as shown in Table 1, and can be modified into gel by employing chemical cross-links with glutaraldehyde, in addition to the physical cross-links [18, 19]. As thus obtained, PVA-DMSO gel is the dielectric polymer gel and was first exposed under the dc electric field.

Electrically induced strain (γ) is primarily expected by Maxwell force between the electrodes and can be expressed by the equation, $\gamma = \sigma/\eta = (\varepsilon/\eta)E^2$, where σ is the stress induced by the electric field E, and η is the modulus of the gel. The strain is proportional to the stress as far as the modulus of the gel stays constant. The strain dependence on E was investigated on the PVA-DMSO gel. The relationship $\gamma = (\varepsilon/\eta)E^2$ is held, elucidating the contractile deformation of the gel can be controlled by conventional Maxwell force (Fig. 1) [2]. Reaction time is far much swifter than swelling-deswelling-type actuation, and the electric leak current is depressed to A micro ampere, a range which shows that the energy dissipation is far much less than that of the polyelectrolyte gel.

In addition, the deformation was found not only the contraction in the direction to the electric field, but also accompanied bending deformation. This was elucidated by employing very thin gold films as electrodes [20]. The gel is bent swiftly to the cathode without accompanying any leak of solvent. It suggests the expansion on cathode side and shrinkage on anode side. The mechanism is explained by the asymmetric pressure distribution, which is originated from the ion drag of DMSO from anode to cathode in the gel (Fig. 2). Not only the ion drag, but also charge-holding property of PVA plays a critical

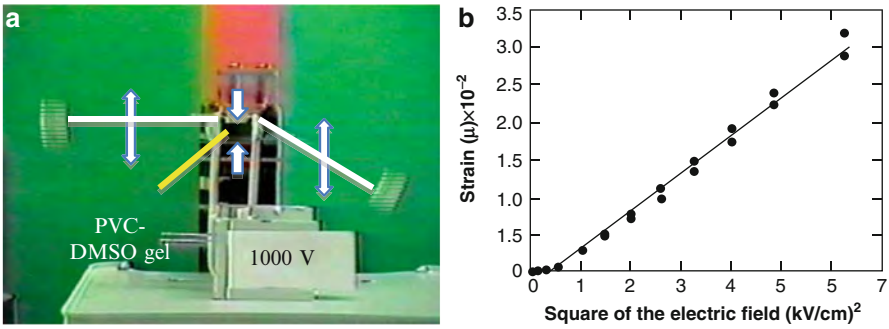

Fig. 1 Contractile deformation (**a**) of PVA-DMSO gel follows conventional Maxwell force (**b**). The motion completed within 100 ms, and a fluttering motion with 20 Hz is possible [2]

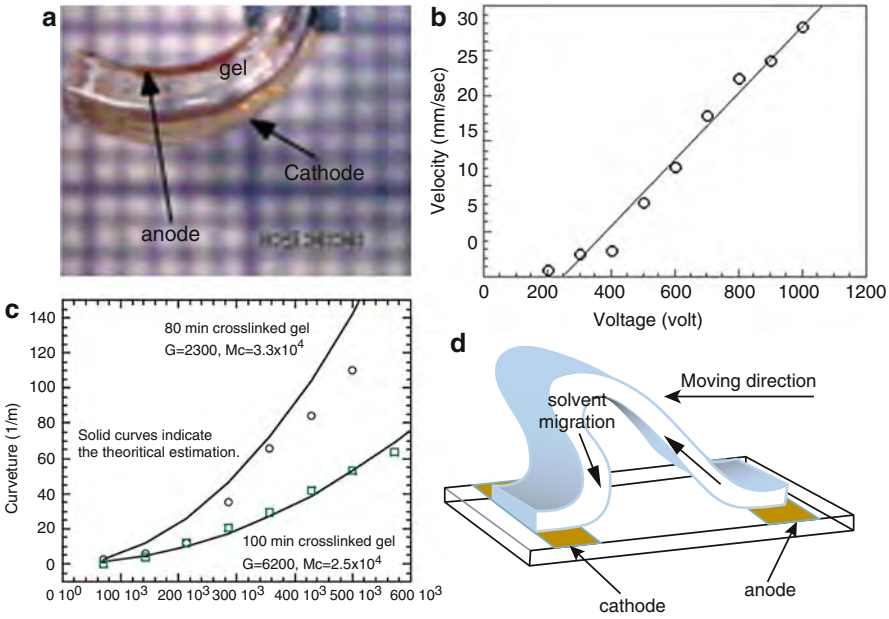

Fig. 2 Ion drag of DMSO from anode to cathode in PVA-DMSO gel caused the bending deformation (**a**). (**b**) Ion-drag induced in DMSO, and the solvent flow can be controlled by applying a dc electric field. (**c**) Bending degree of the depends on the crosslinking time. Higher the crosslinking time, the smaller the bending deformation. DMSO content of the gel is very high (>95 % by weight). The crawling deformation (**c**) can be estimate by assuming ion-drag. (**d**) Crawling deformation can be induced, when the gel was placed on an electrode array [20]

role in the bending deformation. Anyway, 90° bending is attained within 40 ms with the negligible energy dissipation [21, 22].

The finding of very efficient electrical motility of PVA-DMSO gel suggests that "touching to the electrode" is enough for actuation. Actually, the gel on an electrode

array crawled like a worm [21]. These finding implies that various ways of actuation method can be applied for the gel.

However, further increase of ε of solvent is not easy, since the higher the ε value, the easier contamination of the gel by water or humidity in air. The contaminated gel allows the increase of electric leak current in the actuation in air and accompanies the large energy dissipation. In other words, durability in air cannot be long enough for practical use.

Dielectric Elastomers

Although the highly swollen dielectric polymer gels can be a very efficient actuator, the gels are still fragile and the durability of them cannot be high enough. One of the reasons of the defects is originated from the presence of large amount of solvent and large current (although, the value remains in μ micro). Therefore, one way to overcome the defects is to exclude the solvent from the gel without losing high motility of polymer-chain network. So elastomer was employed as a possible candidate of dielectric actuator that does not need the presence of solvent for attaining the polymer-chain motility or the deformability.

First example is PU which is prepared by prepolymer method [6, 23–25]. This method enables the control of the chemical structures such as molecular-weight, functional group, and segment chain length. The longer the chain length between the cross-linking points, the larger the electrically induced strain and the slower the response time [26, 27]. The strain turned out to be controlled by the space charge distribution [28]. When the chemical structure of the soft segment is composed of $–NO_2$ group, negative charge accumulation is observed in the vicinity of anode [29]. When it is composed of –NH group, positive charge accumulation is observed in the vicinity of cathode on the contrary (Fig. 3) [30]. The PU also showed memory effect explicitly on the bending direction as was shown in the Fig. 4. Once it remembered the bending direction, it tended to bend in the same direction irrespective of the polarity of the applied electric field. The memory effect was erased or inverted by applying the inverted field for long time enough (Fig. 4). The memory effect or hysteresis is commonly observed in all dielectric materials [31]. This memory effective is convenient for repetitive operation, since it memorizes the bending direction once it bends much quickly in the successive operation. Although PU can be a good elastomer and good candidate as an actuator, fine chemical structure has various complexity and is difficult to analyze or control in a strict sense.

Anionic polymerization can provide, on the other hand, strictly controlled polymer chains even in the multicomponent copolymers. Block copolymer of methyl methacrylate (MMA) and butyl acrylate (BA) can be a good elastomer. BA chain is much softer than MMA chain, and both chains are not miscible. In the case of tri-block copolymer, p(MMA-BA-MMA), as illustrated, the phase separation of each component in nanoscale leads drastic change in the physical properties of the elastomers (Fig. 5) [7]. The characteristics is used to the control of electrical

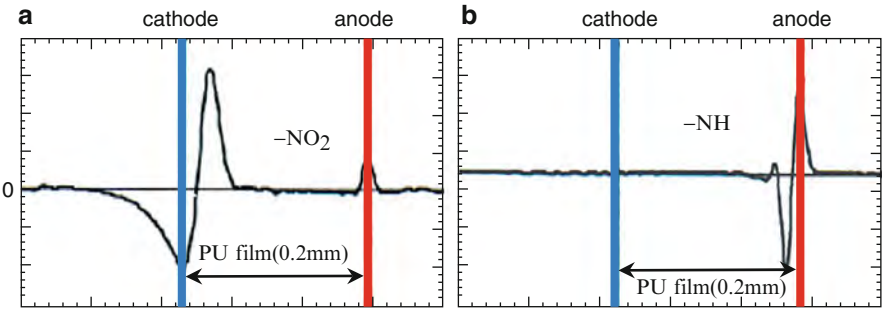

Fig. 3 Chemical structure in the soft-segment changes the bending direction of PU elastomer. (**a**) Positive charge accumulation by –NH group lead the elastomer extension on cathode side, resulting bending to anode. (**b**) Negative charge accumulation by –NO2 group on anode side result the elastomer bending toward cathode

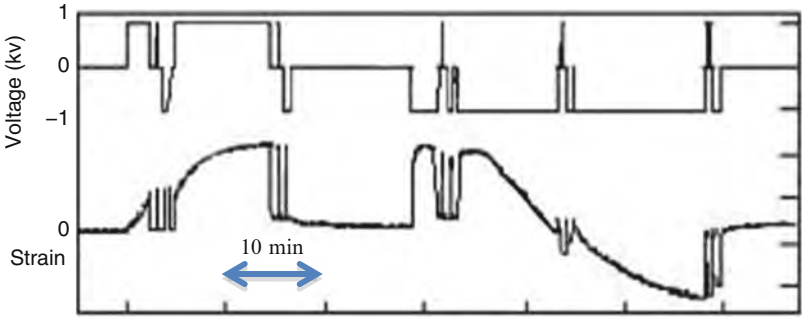

Fig. 4 Memory effect of PU elastomer on bending direction. Once the strain induced by a dc electric field, the PU remembers the direction of the bending, and the PU remembers the direction and magnitude of the strain even after the inversion of the polarity. But it can reset the direction after a long duration of the inverted polarity of the applied field, and behaves as expected. The tendency can be modified by controlling additives

function of the elastomer, that is, the inversion the continuous phase is possible by only controlling the composition of casting solvent. When the electrically active component formed continuous phase, the elastomer can be electrically active. But in the other way, it can be an electrically inactive elastomer. Thus, the same chemical component polymer shows totally different behavior to the electric field. The observed strain is usually small in these cases, as the small dielectric constant suggests. But the deformation such as bending can be large, since the small difference in the strain can be displayed in large bending deformation when the thickness of the sample film is thin enough. This result suggests that the elastomers in the form of fiber and thin film should be a good candidate of electrical actuator.

Elastomer actuator has been intensively investigated from a different viewpoint by the group of SRI [32, 33]. They have been elucidated to be an efficient actuator with large strain, but need higher voltage than gels. Elastomers can save the voltage

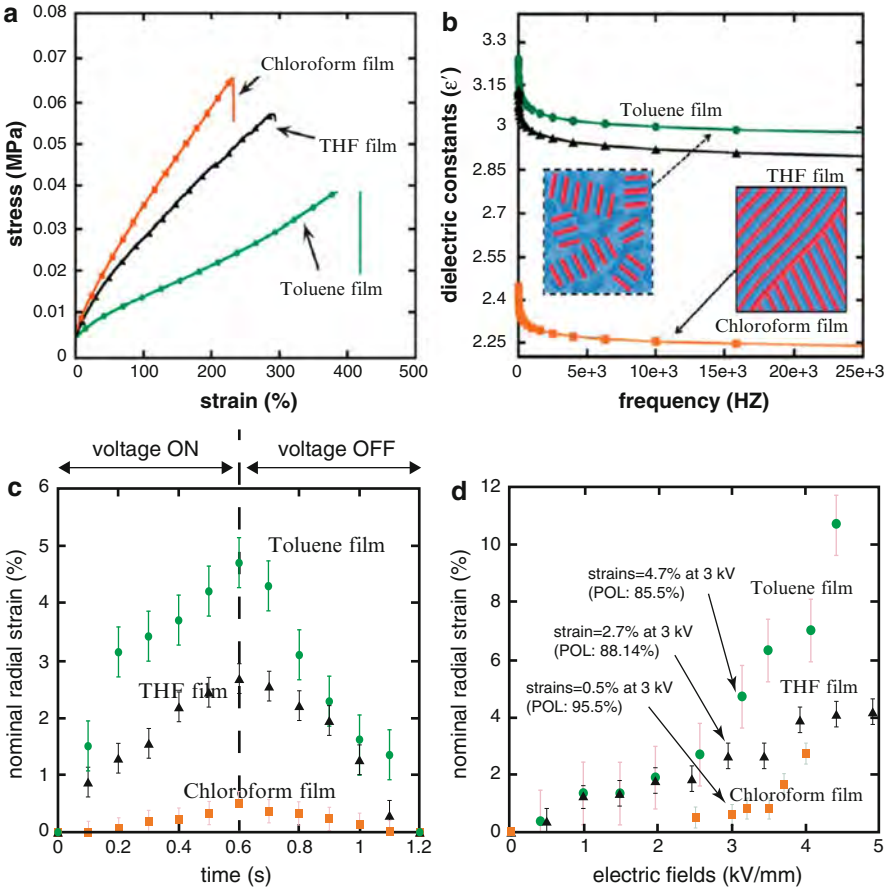

Fig. 5 Nanostructure control of continuous phase in tri-block copolymer, PMMA-PnBA-PMMA, changes electrical property. (**a**) Effect of casting solvent on the elasticity, (**b**) dielectric constant of the elastomers, (**c**) time course of the electrically induced deformation at 3 kV/mm, (**d**) effect of electric field on the strain [7]

some amount, but still need high voltage when they need large strain. High-voltage application shortens the life-span of the actuator. The other type is well-known poly (vinylidene fluoride-co-trifluoroethylene), which is not classified in elastomer, has giant dielectric constant and be actuated with fairly low voltage [34, 35].

Dielectric Plasticized Polymers

Plasticized polymers are other candidates of actuators. The difference of plasticizer from solvent is important. Usually, plasticizers are used as additives to polymers and are miscible but not a good solvent. Polymers are solubilized in solvents and

form solutions, while plasticizers cannot solubilize polymers without the presence of solvents. Usually, the mixtures of PVC and plasticizers are mixed and melted to get a homogeneous material. The plasticized PVC has a long history as plasticized plastics [36]. In this chapter, the plasticized PVC is denoted as PVC gel since PVC plasticized with a wide range of plasticizer content will be discussed.

Electrically Induced Creep Deformation

PVC and plasticizers have low dielectric constant as shown in Table 1, and therefore, expected electrostriction is also small in the direction of the electric field, and actually scarce strain was observed [37]. However, a slight but clear deformation was found microscopically in the gel near the vicinity of anode surface. By increasing the applied voltage, the gel crept out onto the anode and restored the strain by turning off the field [5]. These phenomena are confirmed on various plasticizers. The deformation is named "amoeba-like pseudopodial" deformation (Fig. 6) [38]. Creep deformation is observed in the PVC gel whose plasticizer content is high enough, such as 1:3–1:5 in the weight ratio of PVC: plasticizer. When the plasticizer content is too high, the gel cannot hold its gel form anymore. Structure of the PVC gels had been investigated by small-angle X-ray scattering and was clarified that the gel network had been maintained even at high content of plasticizer such as 70 wt% through the hydrogen bond among the polymer chains [38]. The maximum content of plasticizer depends on the degree of polymerization (DP) or molecular weight of PVC. The higher the DP, the higher the maximum content of plasticizer is.

As PVC gel is transparent, and can be set up as in Fig. 7, the deformation is applied as a focus-controllable lens. The creep deformation can be reproducibly induced by applying a dc electric field. Continuous operation is adequate for swift response, as the strain shows memory effect or hysteresis as suggested in elastomer in above section (Fig. 8).

Creep Induced Bending of PVC Gel

When the setup was employed as shown in Fig. 9, the gel bent to anode [5]. The deformation is actually folding deformation on the tip of anode. The phenomenon indicates that the strain is localized at the tip of the anode. The gel creeps out onto the other side (or outer surface) of the anode surface and bends down to the outer surface of anode. Thus, the gel shows the folding-like bending as Fig. 9. Current observed in this deformation is 100 nA level, and the space charge distribution analysis revealed that only negative charge accumulation was observed in the vicinity of anode (Fig. 10). No charge accumulation is observed in cathode vicinity. By covering either surface of anode or cathode with insulator film such as thin polyethylene film, deformation is not observed. When the anode surface is partly covered by the insulator film, the acceleration of bending speed at most 20 times

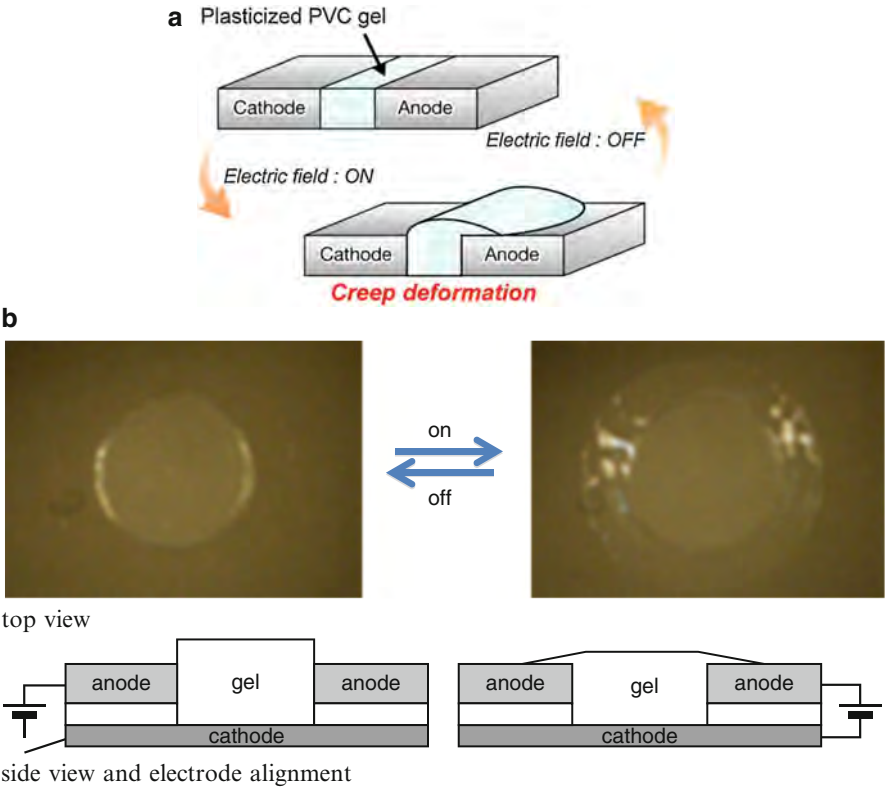

Fig. 6 Amoeba-like pseudopodial creep deformation of PVC gels (**a**). Gel creep out onto the anode surface by applying a dc electric field. When layered electrode alignment is employed, the gel spread out onto the anode surface (**b**)

faster was observed (Fig. 11). The mechanism of the deformation was suggested as following: (1) charge injection from cathode, (2) discharging is disturbed by PVC (as is observed in PVA-DMSO gel), (3) negative charge accumulation causes tacking to the anode, (4) repulsion among the negative charges in the gels leads expansion onto the anode surface, and (5) thus the gel tends to creep out onto the anode and leads to the folding-like bending deformation.

Application for Gripper

The PVC gel can bend very efficiently when it is partly pinched between asymmetric electrodes as in Fig. 9 [5]. Small-contact anode area can lead concentrated charge accumulation and result in the strong tacking or attractive force to the anode. Gel sheet covered with a large cathode plate and two anode rods was aligned as shown in Fig. 12. When an electric field was applied, the gel showed very swift

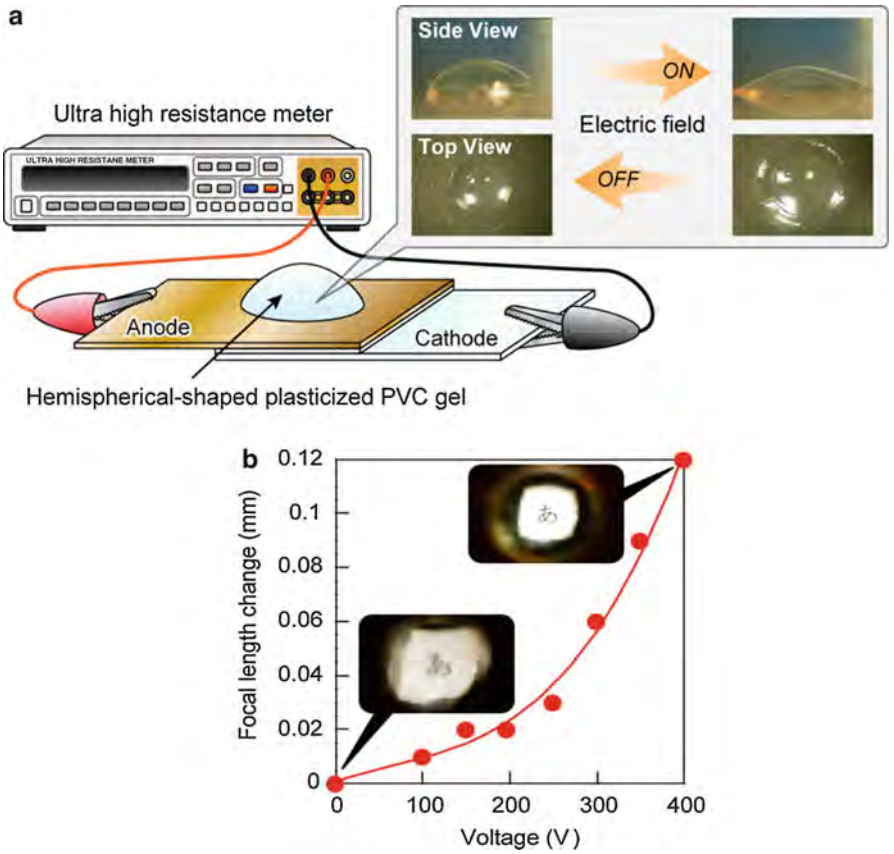

Fig. 7 Set up for PVC gel lens (**a**), and focus control of PVC gel-lens controlled by dc electric field (**b**)

gripping motion [39]. Although the gel itself is very soft and difficult to grip the object strongly, by arranging the surface, thickness, and width of the gel and improving the shape of the electrode, the gripper for micro device is developed that demonstrates good durability in consecutive operation(s) of over 200,000 times. Electrical energy dissipation is almost negligible, since the current is nano ampere range. This gripper has a very simple structure and is adequate for micro-fabrication.

Contractile Deformation

Electrically induced strong tacking force of PVC gel can also be converted into contractive motion by employing the shape and alignment of the electrodes as illustrated in Fig. 13 [40]. One case is shown in Fig. 13(1), in this case, a gel which

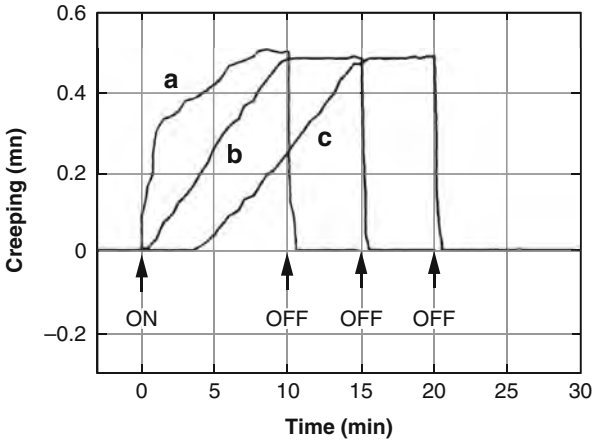

Fig. 8 Memory effect observed in PVC gel. In this Figure, PVC gel plasticized with DBP was shown. When the electric field was applied first time, gel creep out onto the anode and reached at steady state after a moment (*b*). When the field of inverted polarity was applied induction period was appeared, and then the creep deformation occurred (*c*). The successive application of the electric field of the inverted polarity induced swift creep deformation (*a*). Induction period in (*c*) and swift creep on the repetition (*a*) are the results of memory effect

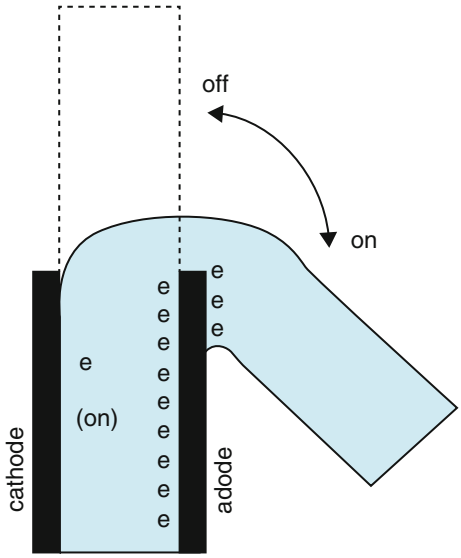

Fig. 9 Bending (or Folding) deformation was shown with the plausible charge distribution in the bending [5]

behaves like a semiliquid and can be dragged into the space between the electrodes when the electric field is on. The experimental result showed reasonable results in the case of dielectric solvent such as DMSO [20]. The expected deformation is just like myosin filament dragged into the space between two acting filaments in biological muscle. It can be possible if PVC gel has a huge-enough dielectric constant and

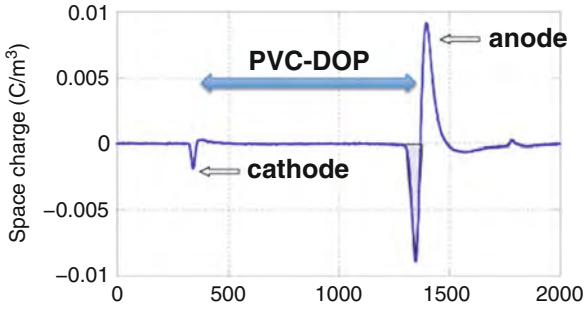

Fig. 10 Space charge distribution in PVC-DOP gel under the electric field. Remarkable negative charge is accumulated in the vicinity of anode surface in the gel (*Blue arrow* is in the gel)

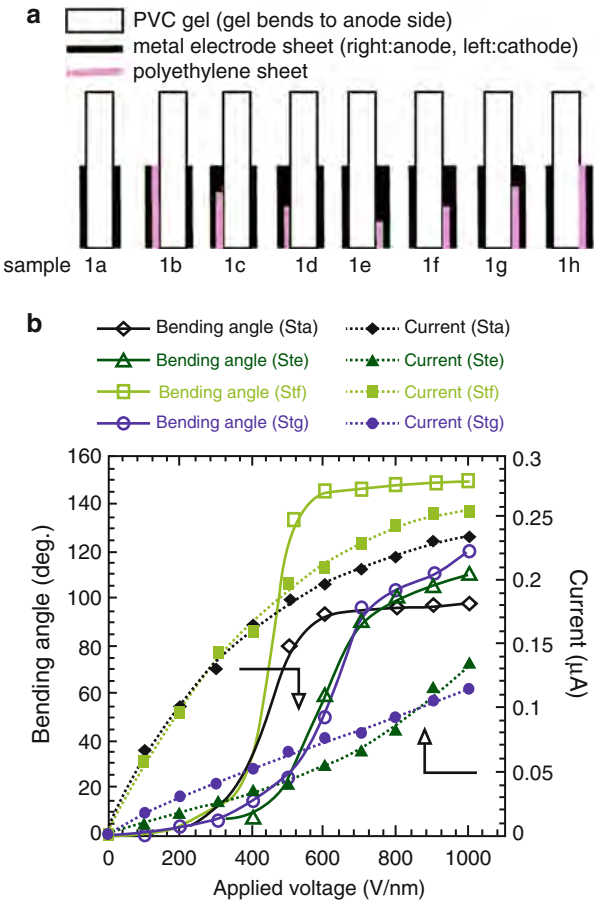

Fig. 11 Effect of electrode alignment on the bending deformation of PVC gel. (**a**) Effective electrode area was controlled by shielding with polyethylene sheet. (**b**) Electrode area can control bending or folding deformation rate. Current increase also reflects bending speed. In this case, about 20 times acceleration of bending velocity was observed

low-enough friction to the electrodes. However, very small deformation was detected in this case so far on PVC gel, because of the high friction to the anode.

The other way to attain a contractile actuator is by applying the tacking force and creep deformation of the PVC gel shown in Fig. 13(2) [41]. In this case, actual

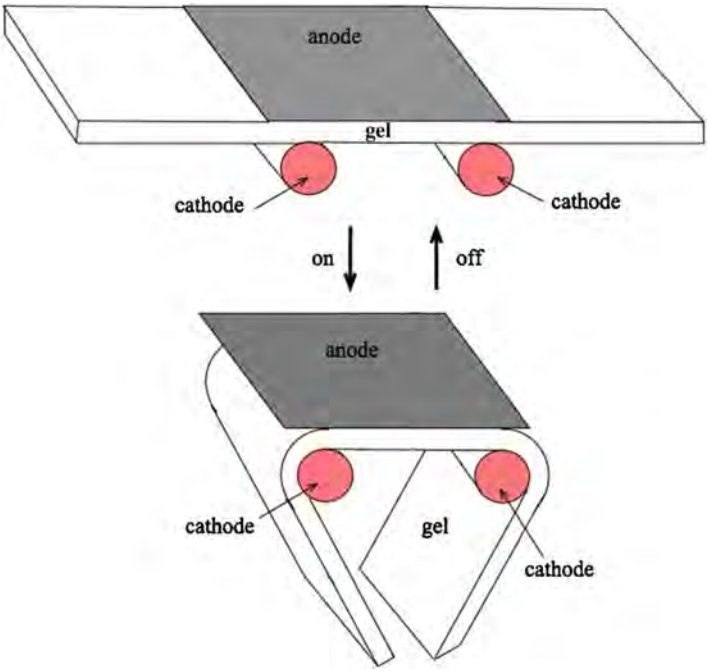

Fig. 12 Gripper finger of PVC gel. By applying dc field, PVC gel attaches to anode inducing folding deformation of the gel, thus the gel can be used as a gripper. The continuous operation of folding and unfolding motion can exceed over 200,000 times

material deformation is not contractile, but motion of the electrodes is similar to Maxwell contractile deformation as the distance between the electrodes narrows by turning on the field and widens by turning off. However, this is not the Maxwell-type deformation, since PVC gel does not deform or show negligibly small contractile deformation in the direction of the electric field [5]. The deformation is basically induced by tacking and creep onto the anode that accompanies thinning of the gel thickness and results in the contractile motion in the electrode-electrode distance as illustrated in Fig. 13(2). In this alignment, by integrating the layer, large contractive deformation can be realized [42]. As will be explained in the following section, this actuator can be utilized for a fairly large force and large strain generation with a far smaller voltage (around 50 V/unit layer) than the conventional voltage (1 kV/unit layer).

Creep-Induced Crawler

The creep deformation can also be applied for a crawler. As PVC gel crawls out onto the anode; the gel that has a certain rod diameter can roll up and down on an

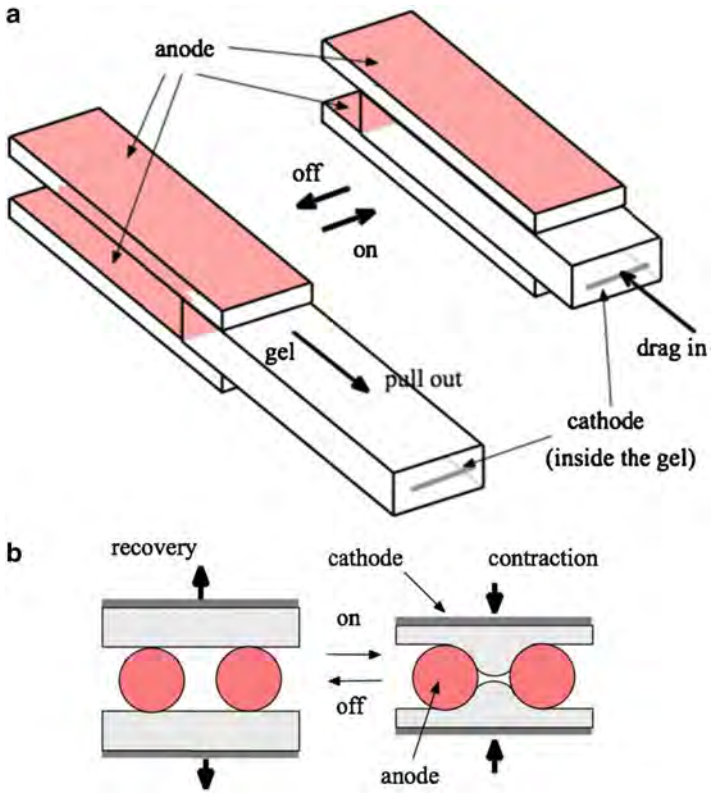

Fig. 13 Contractile deformation induced by tacking and creep deformation of PVC gel. (**a**) Gel is pulled in between the couple of anode, but need pulling out to restore. (**b**) Same time of deformation in Fig. 12 can be applied for stacking type contractile deformation, in this case actuator restores is original position by removing electric field, and long duration of continuous operation is possible by turning on-and-off the electric field

electrode array by shifting the anode position. This motion can be applied for a specific locomotion (Fig. 14).

The plasticized PVC gels have durability in the air for more than 2 years, depending on the composition of the gel.

Tacking Force and Dielectric Constant

In the above section, PVC gel was pointed out to possess the electrically induced tacking force and showed various possibilities of application. But explanation or the origin of the tacking force is not clarified enough. Here the dielectric properties of the gel are discussed.

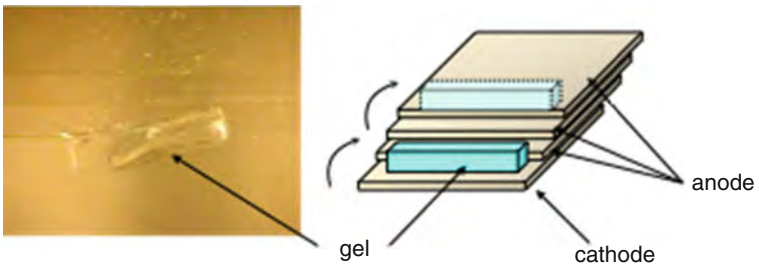

Fig. 14 Tacking and creeping deformation can induce crawling locomotion of PVC gels. By shifting the position of anode and cathode, the gel crawls to the anode by shifting tacking position. Crawler can be prepared

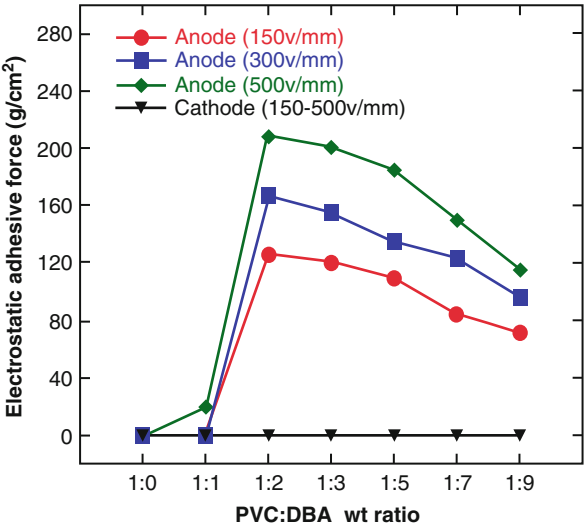

Fig. 15 Dependence of tacking force on plasticizer content (Modified from Ali et al. [10])

The dependence of tacking force on the plasticizer content at the specific voltage was shown in the case of dibutyl adipate (DBA) in Fig. 15. When the DBA content in the weight ratio of PVC: DBA is raised from 1:2 to 1:3, the tacking force to the anode jumps up, and further increase of DBA leads gradual decrease of the force [10, 43]. This tremendous increase of the tacking force in the particular range of plasticizer content suggests a big change of the phase structure of the gel. According to Yamaguchi's analysis by small-angle X-ray scattering (SAXS), the distance among the scattering species in the gel spreads out into a larger value with a small expansion of the intra-particle size of the scattering species over the 1:1 ratio of PVC: dioctyl phthalate (DOP) [38]. This result suggests loosening of the inter-particle interaction results in the high mobility of polymer chain and in the smooth migration of plasticizer, although the gel still sustains good-enough elasticity for practical use. Even at the DOP content of 70 wt%, the inter-particle correlation remains clearly.

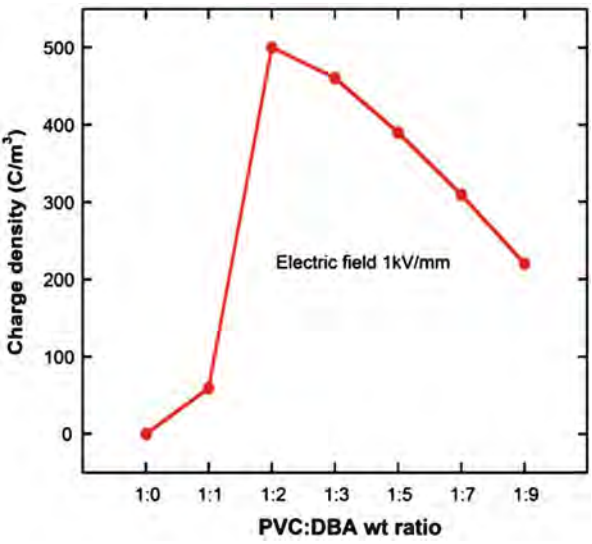

Fig. 16 Space charge dependence on plasticizer content. Tendency is the same in that of Fig. 15, suggesting space charge accumulation on anode is the origin of tacking force (Modified from Ali et al. [10])

Analysis of space charge distribution in the PVC gel clarifies that the negative charge accumulates in the vicinity of the anode but the positive charge does not accumulate in the vicinity of the cathode. The amount of accumulated charge in the vicinity of anode increases with the amount of plasticizer and after it reaches maximum at around 1:3 (in weight ratio of PVC:DBA) (Fig. 16). This tendency is very similar to those on the adhesive force or tacking force to the anode in Fig. 15 [10]. The results imply the tacking force to the anode is originated from the accumulated charge in the gel in the vicinity of the anode.

Taking SAXS analysis into account, the sharp increases of accumulated charge and adhesive force (or tacking force) at around 1:2 (in PVC: DBA by wt ratio) in Figs. 15 and 16 imply the drastic structure change in the composition range. The structure change might be a kind phase transition such as the spinodal decomposition. In the composition range, both PVC phase and plasticizer phase can percolate through the gel. In such a structure, injection and accumulation of electrical charge is much easier than in solid PVC phase. Further increase of plasticizer leads to the acceleration of discharging rate on the anode and result into a decline of space charge accumulation. For further detail, dynamic analysis on the gel structure should be carried out.

Effect of dielectric constant ε' of the gel on the plasticizer content was shown in Fig. 17. The ε' increases with DBA content up to 1:5 in the weight ratio of PVC to DBA. Further increase of DBA content caused the decrease of ε' as shown in Fig. 17. It is interesting that the peak of ε' is observed at 1:2 in Fig. 16 instead of 1:5 in Fig. 17. Charge accumulation in the vicinity of the anode surface was discussed in Figs. 15 and 16, but the total charge capacitance of the gel reached maximum at 1:5 (in weight ratio of PVC: DBA) as in Fig. 17, suggesting that the value of ε' reflects a much loser structure or a higher mobility of each component in

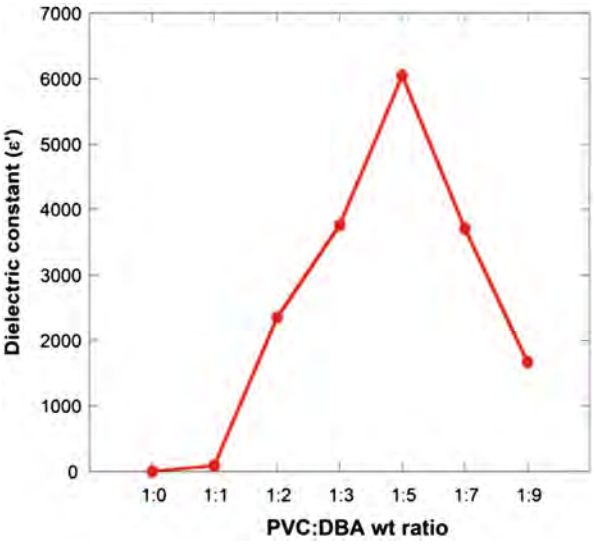

Fig. 17 Dielectric constant dependence on plasticizer content. Dielectric constant depends on the plasticizer content in remarkable manner, and it reaches the maximum value of 6,000 at the ratio of 1:5 (PVC:DBA by weight). Colossal value can explain electrically induced huge strain of the gel [10]

the gel. After reaching maximum ε' value, further increase of plasticizer caused sharp decline of ε'. It means that ε' value goes closer to the value of the plasticizer itself naturally at the very high content of the plasticizer. But in the other words, the gel structure with the high ε' value can be sustained up to the high plasticizer content such as 1:5 compositions.

Mention has to be paid to the value of ε', since the value increased remarkably over 1,000 times larger than those of the components of the gel. ε's of PVC and DBA are around 5 and 10 at 1 Hz. The ε' values of each component are far less from that of the gels. It clearly shows that the colossal value is originated from cooperative interaction between PVC and DBA.

For the comparison between PVA gel and PVC gel, the dielectric constant was investigated on PVA-DMSO gel. The dependence of ε' on the frequency was shown in Fig. 18. The ε' value of PVA-DMSO gel cannot exceed the maximum value of ε' of DMSO in Fig. 18. This result suggests that the high ε' value of PVA-DMSO gel is originated from that of DMSO itself, and not because of the cooperative phenomena as in the extreme case of PVC-DBA. Presence of PVA has the function to pull slightly the high ε' zone to higher frequency range [44]. This is the usual case expected in the mixture.

The interaction between PVC and DEA is a peculiar one in which both values of ε' are strongly enhanced to each other to build up cooperatively the value of the colossal dielectric constant. In PVC gels, in other words, both ε' value and its expansion to the high frequency range are attained. The value can be the origin of the characteristic behavior of the PVC gels. The same phenomena are also observed in other plasticizers such as various adipates, phthalates, etc., but the efficacy of the cooperativity depends on their chemical structure [45] (Fig. 19).

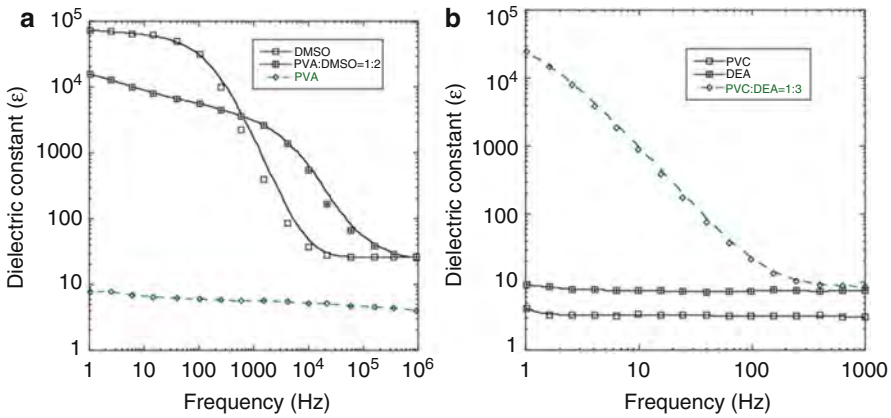

Fig. 18 Frequency dependence of dielectric constant of PVA-DMSO gel and PVC-DEA gel. (**a**) The high ε value of PVA-DMSO gel was originated from that of DMSO itself. Presence of PVA caused an expansion of the high ε range [43]. (**b**) The high value of ε of PVC-DEA gel was attained by the cooperative interaction between PVC and DEA. The extreme interaction between PVC and DEA is the origin of this phenomenon. Similar function was also observed on other plasticizers [44]. The colossal dielectric constant can be the origin of the characteristics behavior of the PVC gels

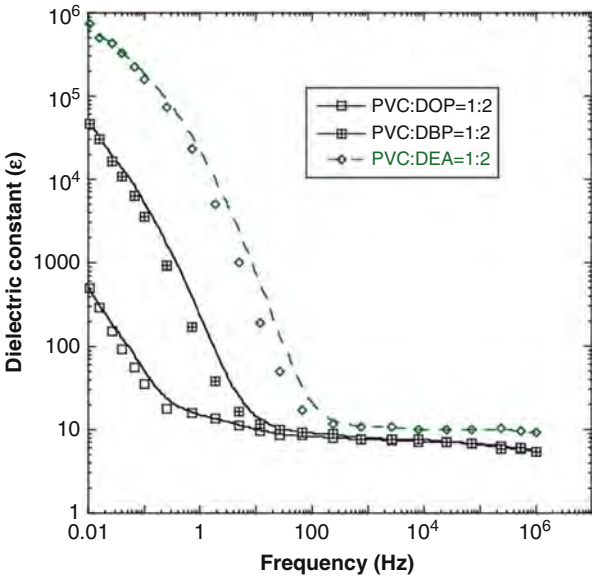

Fig. 19 Effect plasticizer on the colossal dielectric constant cooperatively induced in plasticized PVC

The cooperative phenomenon in Fig. 19 is the characteristic properties of the PVC gel and can be the origin of various functions. When the characteristic colossal dielectric constant of the gel is mentioned, further functions can also be expected as described in the next section.

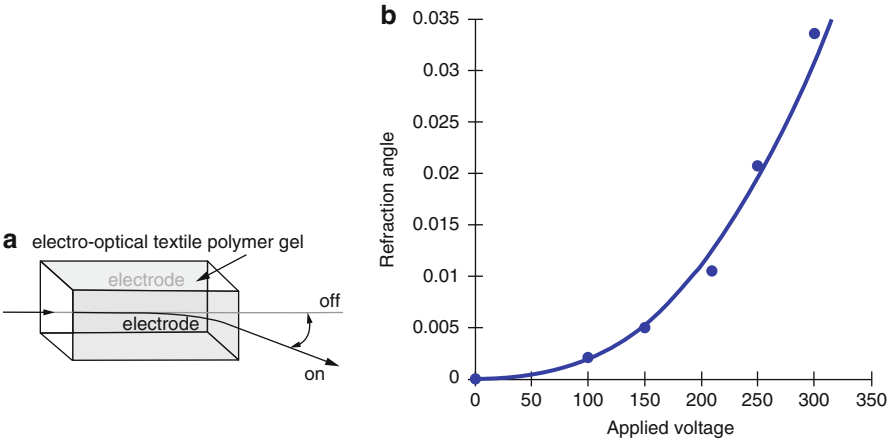

Fig. 20 Electrooptical function of PVC gel. (**a**) Light path can be controlled by the electric field. (**b**) Refraction angle depends on the applied voltage. In this case, it is proportional to the square of the electric field [46]. Pockets effect is not depicted. Figure must be rearranged

Electrooptical Function

The colossal dielectric constant suggests the possibility of electrooptical function, too, since refractive index of a matter is expressed by the following equation:

$$n = \sqrt{\frac{\varepsilon}{\varepsilon_0}}$$

$$n = n_0 + aE + bE^2$$

where n_0 is the refractive index of the matter at $E = 0$, a is Pockels effect, and b is Kerr effect. Since n is the function of ε, large change of ε can be expected to be useful in optical function [46].

As was shown in Fig. 20, PVC gel can bend the light path effectively, and the bending angle is proportional to the square of the electric field. The effect depends on the plasticizer and its content, too. As the material is soft and contains a large portion of plasticizer, the function is very peculiar.

The similar function is also found in PVA gel, too. But the dependency is not quadratic but linear, which suggests that the gels have electrooptical functions with Pockets effect [47]. The structure formation in the PVA gel under the applied electric field plays critical role.

Mechanoelectric Function

When mechanical impact was applied to the PVC gel, it responded instantly with a generation of electric field of 1–2 V/cm^2 (Fig. 21) [48]. This function is also an

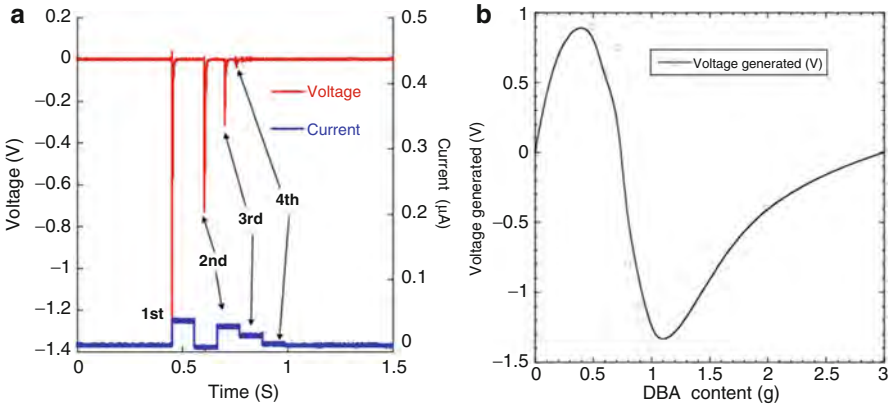

Fig. 21 Falling ball on the PVC gel sheet can induce electric field. (**a**) Impact can induce voltage and current. (**b**) The polarity of the voltage can be controlled by plasticizer content [48]

interesting phenomena, since the material is very soft and is believed amorphous or homogeneous. The generated voltage depends on the plasticizer content very much, and it shows a peculiar characteristic in Fig. 21. The generated voltage depends on the plasticizer content very much, and shows a peculiar characteristic such as the polarity inversion at a certain content of plasticizer.

This phenomenon suggests that the electric field generation by a physical impact is originated from the asymmetric friction on the electrode or the displacement between the polymer and plasticizer. Further analysis is necessary for detail understanding.

New Weaving Technology

Textile polymers were revealed to possess excellent electrical functions, such as actuators, refractive index modulator, and impact sensor. As can be expected from these results, the electrical motility of the fiber should also be investigated for novel-type weaving, since motility of fiber is easily induced even in the polymer of crystalline state, too. As has been already pointed out, even a very small strain in the polymer could be enhanced into huge deformation in thin fibers and thin films when adequately treated.

Vibration of PET Film by Applying a dc Electric Field

First example is a solid PET. The PET film can also be actuated by applying a dc electric field. As the strain induced in PET as in PU is really too small to be utilized practically, different viewpoint has to be applied for designing actuation. Electrostatic interaction is the one, but surface modification is required to facilitate the mobility of the electrostatic charge on the PET. When the surfaces are modified

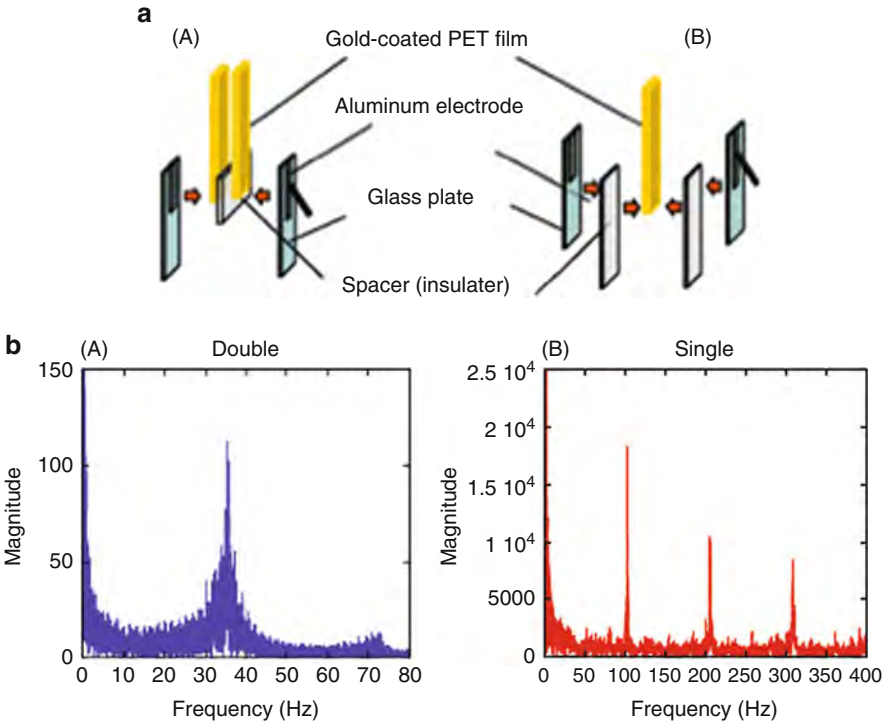

Fig. 22 DC electric field applied to the PET film can induce oscillation. (**a**) Lay-out of film and electrodes, (*A*) for the double film flapping actuator, and (*B*) for the single film vibrator. (**b**) A example for each vibrating system, and frequency can be controlled by electric field

only one side with gold thin film and set as shown in Fig. 22, the two films gathered together by turning on the dc field, and detached by turning off. While both sides of the film surfaces are covered with a thin gold (electrically conductive) layer, the two films start oscillatory flattering motion by applying a dc electric field. These are electrostatic actuation of the solid film [49]. The mechanism are explained by the following steps: by turning on the dc electric field, (1) the films are oppositely polarized and attracted to attach each other; (2) right after attaching, the charges are neutralized and filled with the electrode charge polarity and the two films of the same polarity detached swiftly by repulsive force; and (3) repeating the tow processes (1) and (2) results in the oscillation of touching and detaching. The oscillation can also be induced in single film system. In the single film case, caution on the alignment of the film is required, that is, both sides of the film must be coated with electrically conductive layer and both sides of the film have to be separated from electrodes with thin and small insulator film. In the two films system, the frequency of oscillation can only be controlled by the oscillator film dimension. In the single film case, the frequency of oscillation can be controlled by the dc voltage applied, not only by the film dimension [39].

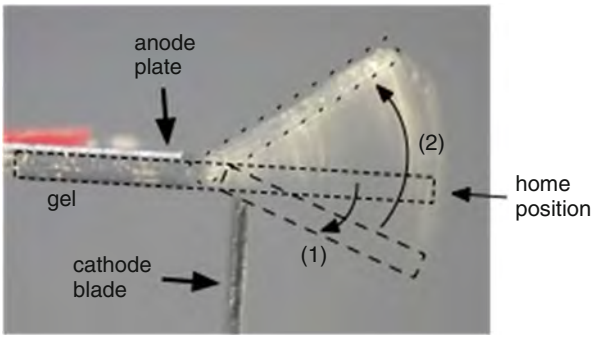

Fig. 23 Flattering motion of PVC-DEA gel (PVC:DEA = 1:9, thickness = 0.59 mm) at 1 kV. By applying an electric field, (*1*) the gel was attracted to anode blade, and *right* after touching to anode blade, (*2*) the gel was discharged and swing back to anode by the bending force to anode and goes back to home position. Flattering motion was resulted by repeating (*1*) and (*2*)

Flattering of PVC Gel by Applying a dc Electric Field

PVC gel can also flatter by applying a dc electric field. But the mechanism is a little different from that of PET film. In the case of PVC gel, tacking and creep deformation of the gel plays an important role [9]. In the alignment in Fig. 23, the gel is attached to anode, and cathode is perpendicularly set to the gel apart from the gel in detached position. When the electric field is on, and the cathode blade comes close to the gel, gel is attracted electrostatically bends to cathode. Once the gel touches to the cathode blade, negative charges flow into gel, and the attractive force disappears. When the attractive force disappeares, the gel instantly detaches from cathode blade and swings back to anode. Then again the gels charges positively and attracted to cathode blade, and thus, repeat swings back and forth. Controlling factors are plasticizer and its content together with PVC molecular weight, but a modification of the gel surface is not necessary.

Weaving Micro- and Nano- Fiber

The vibration in the above section "Vibration of PET Film by Applying a dc Electric Field" is the case of the thin PET films of which surfaces are modified by gold thin layer as electrodes. But without any modification, many fibers are electrically manipulated. Electrostatic charges do not easily disappear once it attached on the surface. Through the experience of dielectric polymer actuator, the electrical function can be controlled in a certain range. One is by addition of additives such as solvent, plasticizers, and ionic species [50].

Micro- and nano- fibers have been considered to be difficult to manipulate in monofilament state, because they are very thin and usually easily broken by mechanical machines or tools. But if the motility of the fibers can be controlled,

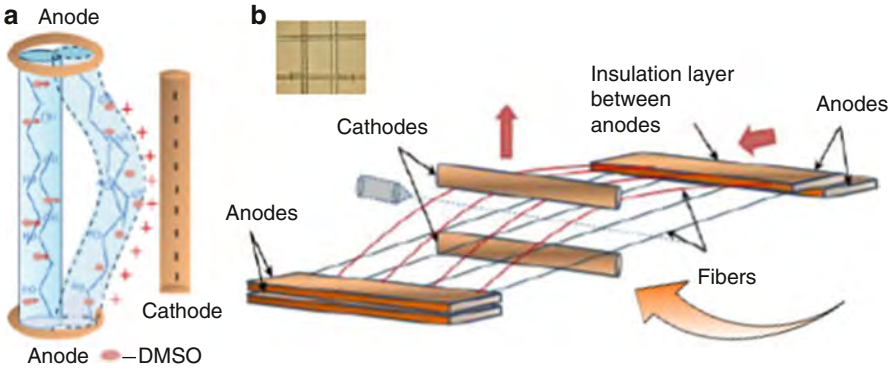

Fig. 24 Micro- and nano- PVA fiber can be manipulated by electric field (**a**), and electrically induced shedding motion (**b**), inserted *up-left* figure shows an example [50, 51]

and they can be autonomically arranged in the textile form by themselves, that may provide new efficient weaving method. The possibility was investigated on some of the conventional fibers. It turned out that it is possible to weave the microfibers by electrically manipulating them, although the technique is at very primitive stage at this moment (Fig. 24) [51]. In a device shown in Fig. 23, shedding motion of microfiber could be induced. This could be done by using electrostatic property of the fiber of PVA, which has been known to possess a fairly large dielectric constant among the conventional fibers. Other fibers with some additives will be the possible candidates. However the efficacy of the device is pre-matured at this stage, and need to be improved. When this technology becomes practical, totally new textile application will be realized in such as photonic function with flexible textiles [52].

Summary

Dielectric polymers conventionally used in textile industry were investigated from electrically active materials. They can be very attractive actuators, sensors, and optical devices. The functionality can also be applied to the novel nano-web which might be a photonic device in future, too.

One of the important finding in these investigations is the colossal dielectric constant induced from the interaction between the polymer and solvent, plasticizers or additives. Although only limited cases were introduced in this chapter, there are many other possible attractive phenomena on the conventional polymers or speciality polymers used in textile industries.

The authors wish young scientists and engineers are involved in the field of fiber and textile engineering, and open the new frontier of emerging fiber industries that can provide fundamental textile material technologies for sustainable world.

References

1. Hirai T et al (2001) Electrically active polymer materials – application of non-ionic polymer gel and elastomers for artificial muscles. In: Tao X (ed) Smart fibres, fabrics and clothing. Woodhead, Cambridge, pp 7–33
2. Hirai T et al (1993) Actuation of poly(vinyl alcohol) gel by electric field. J Intell Mater Syst Struct 4:277–279
3. Hirai T (1999) Polymer gel generating bending and crawling motion. WW-EAP Newsl 1(1):4–5
4. Hirai T, Watanabe M, Yamaguchi M (1999) PVC gel deforms like a tongue by applying an electric field. WW-EAP Newsl 1(2):7–8
5. Uddin MZ et al (2001) Electrically induced creeping and bending deformation of plasticized poly(vinyl chloride). Chem Lett 2001:360–361; Uddin MZ, Watanabe M, Shirai H, Hirai T (2002) Creeping and novel huge bending of plasticized PVC. J Rob Mechatronics 14:118–123
6. Hirai T et al (1996) Polyurethane elastomer actuator. Angew Makromol Chem 240:221–229
7. Jang Y, Hirai T (2011) A control method for triblock copolymer actuators by nano-lamellar pattern. Soft Matter 7(22):10818–10823
8. Jang Y, Hirai T (2011) Solvent-induced phase-inversion and electrical actuation of dielectric copolymer films. Mater Sci Appl 2(3):187–195
9. Tsurumi D, Hirai T (2013) Electrically induced oscillatory motion of dielectric soft polymer materials. In: 62nd SPSJ symposium on macromolecules, polymer preprints, vol 3637. The Society of Polymer Science, Kanazawa, p 2ESB12
10. Ali M et al (2011) Influence of plasticizer content on the transition of electromechanical behavior of PVC gel actuator. Langmuir 27(12):7902–7908
11. Finch CA (1973) Polyvinyl alcohol; properties and applications. Wiley, New York
12. Peppas NA, Wright SL (1998) Drug diffusion and binding in ionizable interpenetrating networks from poly(vinyl alcohol) and poly(acrylic acid). Eur J Pharm Biopharm 46(1):15–29
13. Hirai T (1991) Shape memory of PVA [poly(vinyl alcohol)] hydrogel prepared by freezing-and-thawing. Kobunshi 40(8):524–527
14. Hirai T, Hayashi S (1991) Function and use poly(vinyl alcohol) hydrogel. Kobunshi Kako 40(5):225–230
15. Hirai T et al (1992) Effect of chemical crosslinking under elongation on shape restoring of poly (vinyl alcohol) hydrogel. J Appl Polym Sci 46(8):1449–1451
16. Suzuki M (1991) Amphoteric polyvinyl alcohol hydrogel and electrohydrodynamic control method for artificial muscles. In: DeRossi D et al (eds) Polymer gels. Plenum Press, New York, pp 221–236
17. Shiga T et al (1989) Bending of high-strength polymer gel in an electric field. Kobunshi Ronbunshu 46(11):709–713
18. Hirai T et al (1991) Actuation of PVA gel by electric field. Polym Prepr Jpn 40(7):2116–2118
19. Hirai T et al (1991) Fluttering wings – first step for flying up-above into the sky? In: Preprints of second symposium on polymer gels, Tsukuba, 10–11 Dec 1991, p 129
20. Hirai T, Zheng J, Watanabe M (1999) Solvent-drag bending motion of polymer gel induced by an electric field. In: Proceedings of SPIE-the international society for optical engineering (Electroactive polymer actuators and devices), SanDiego, vol 3669. pp 209–217
21. Hirai T, Zheng J, Watanabe M, Shirai H, Yamaguchi M (2000) Electroactive nonionic polymer gel – swift bending and crawling motion. In: Furukawa T, Zhang QM, Bar-Cohen Y, Sheinbeim J (eds) Electroactive polymers (EAP). Materiasl Research Society, Pennsylvania, Boston, pp 267–272
22. Zheng J et al (2000) Electrically induced rapid deformation of nonionic gel. Chem Lett 5:500–501
23. Amachi Y et al (2000) Polyurethane-PVA hydrogel film for artificial skin, etc., and its manufacture. In: Japan Kokai Tokkyo Koho. Nitta K.K., Japan. Jp., 4 pp

24. Amaike Y et al (2000) Polyurethane actuator. In: Japan Kokai Tokkyo Koho. Nitta K.K., Japan. Jp., 7 pp
25. Hirai T, Sugino T, Kasazaki T (1994) High-speed-response polyurethane gel activator. In: Japan Kokai Tokkyo Koho. Nitta K.K., Hirai Toshihiro. Jp., 5 pp
26. Watanabe M et al (1999) Effects of polymer networks on the bending electrostriction of polyurethanes. In: Stokke BT, Elgsaeter A (eds) Synthetic versus biological networks, vol 2, Wiley polymer networks group review series. Wiley, Chichester, pp 213–221
27. Watanabe M et al (1997) Bending deformation of monolayer polyurethane film induced by an electric field. Chem Lett 1997:773–774
28. Su J, Zhang QM, Ting RY (1997) Space-charge-enhanced electromechanical response in thin-film polyurethane elastomers. Appl Phys Lett 71(3):386 (3 pages)
29. Watanabe M, Shirai H, Hirai T (2001) Ionic polarization in bending-electrostrictive response of polyurethane films. J Appl Phys 90(12):6316–6320
30. Watanabe M et al (2003) Bending electrostriction and space-charge distribution in polyurethane films. J Appl Phys 94(4):2494–2497
31. Watanabe M et al (2001) Hysteresis in bending electrostriction of polyurethane films. J Appl Polym Sci 79(6):1121–1126
32. Kornbluh R et al (2000) Ultra-high strain response of elastomeric polymer dielectrics. In: Materials Research Society symposium proceedings (Electroactive polymers (EAP)), Boston, vol 600. pp 119–130
33. Pelrine R et al (2001) Applications of dielectric elastomer actuators. In: Proceedings of SPIE-the international society for optical engineering (Electroactive polymer actuators and devices), San Diego, vol 4329. pp 335–349
34. Meijer K, Rosenthal MS, Full RJ (2001) Muscle-like actuators? A comparison between three electroactive polymers. In: Proceedings of SPIE-the international society for optical engineering (Electroactive polymer actuators and devices), San Diego, vol 4329. pp 7–15
35. Zhang QM et al (2002) An all-organic composite actuator material with a high dielectric constant. Nature 419(6904):284–287
36. Wilkes CE et al (2005) PVC handbook. Hanser, Munich
37. Hirai T, Hirai M (2000) Electrically induced strain in polymer gels swollen with non-ionic organic solvents. In: Osada Y, DeRossi DE (eds) Polymer sensors and actuators. Springer, Berlin, pp 245–258
38. Hirai T et al (2004) Bending induced by creeping of plasticized poly(vinyl chloride) gel. In: Bar-Cohen Y (ed) Electroactive polymer actuators and devices (EAPAD), SPIE proceedings (Smart structures and materials), vol 5385. pp 433–441; Masaki Y (2000) Electrical actuation of plasticized PVC. Master thesis, Shinshu University
39. Hirai T et al (2013) Characteristic electrical actuation of plasticized poly(vinyl chloride): various electrical functions in relation with the dielectric plasticizers. In: Vincenzini P, Skaarup S (eds) Electroactive polymers: advances in materials and devices. Trans Tech Publications, Durnten-Zurich, pp 1–6
40. Ogawa N et al (2009) Characteristics evaluation of PVC gel actuators. In: The 2009 IEEE/RSJ international conference on intelligent robots and systems (IROS 2009), St. Louis, 2009
41. Xia H, Hirai T (2010) Electric-field-induced local layer structure in plasticized PVC actuator. J Phys Chem B 114(33):10756–10762
42. Yamano M et al (2009) A contraction type soft actuator using poly vinyl chloride gel. In: Proceedings of the 2008 I.E. international conference on robotics and biomimetics (ROBIO 2008), Bangkok, 2009
43. Ali M, Hirai T (2011) Characteristics of the creep-induced bending deformation of a PVC gel actuator by an electric field. J Mater Sci 46(24):7681–7688
44. Hashimoto N (2010) Dielectric property of PVA swollen with DMSO. Graduation thesis, Hirai Laboratory, Shinshu University
45. Hirai T, Ali M, Xia H, Sato H, Ueki T (2012) Plasticized poly(vinyl chloride) gel as super paraelectric actuator. In: IUMRS-international conference on electronic materials

(IUMRS-ICEM 2012) (The Materials Research Society of Japan (MRS-J), Pacifico Yokohama, Yokohama, 23–28 Sept 2012
46. Satou H, Hirai T (2013) Electromechanical and electro-optical functions of plasticized PVC with colossal dielectric constant. In: SPIE proceedings (Electroactive polymer actuators and devices (EAPAD) 2013), San Diego, vol 8687. p 868728-1-7
47. Sato H, Gotoh Y, Hirai T (2013) The electro-optic effect of PVA gel and PVC gel. In: 62nd SPSJ symposium on macromolecules, polymer preprints, vol 3639. The Society of Polymer Science, Kanazawa University, Kanazawa, p 2ESB13
48. Tanaka Y, Hirai T (2013) Mechano-electric function of plasticized poly(vinyl chloride) for impact sensor and energy harvesting. In: Polymer preprints Japan. Polymer Society Japan, Kanazawa University
49. Kataoka N (2009) Fabrication of lectrostatic actuator of PET film. In: Department of Materials Chemistry. Hirai Laboratory, Faculty of Textile Science and Technology, Shinshu University
50. Xia H, Hashimoto Y, Hirai T (2012) Electric-field-induced actuation of poly(vinyl alcohol) microfibers. J Phys Chem C 116:23236–23242
51. Xia H, Hirai T (2013) New shedding motion, based on electroactuation force, for micro- and nanoweaving. Adv Eng Mater Commun 15:962–965
52. Abouraddy AF, Bayindir M, Benoit G, Hart SD, Kuriki K, Orf N, Shapira O, Sorin F, Temelkuran B, Fink Y (2007) Towards multimaterial multifunctional fibers that see, hear, sense and communicate. Nat Mater 6(5):336–347

Conducting Polymer Fibers

2

Javad Foroughi, Geoffrey M. Spinks, and Gordon G. Wallace

Contents

Introduction 32
Polyaniline 34
Polypyrrole 36
Polythiophene 38
Chemical Polymerization 40
Vapor Phase Polymerization 40
Fiber Spinning of Conducting Polymer 40
Spinning of Polyaniline Fibers 41
Spinning of Polypyrrole Fibers 47
Spinning of PEDOT Fibers 52
Applications of Conducting Polymer Fibers 57
Summary 58
References 60

Abstract

Organic fibers that can function as electronic components such as batteries, sensors, and actuators are exciting prospects for new textile technologies known as "smart fabrics" or "e-textiles." Conducting polymer materials are ideal candidates for such fibers as a result of their good electronic conductivity and mechanical properties and their electrochemical activity. The latter allows the polymer to act as a battery or supercapacitor electrode, to respond to its chemical surroundings as a sensor and to change properties (e.g., color, conductivity, and stiffness) and size when oxidized or reduced. Developing these useful materials into fiber forms has involved wet spinning of soluble forms of polyaniline, polypyrrole, and polythiophene. Both structural modification to

J. Foroughi (✉) • G.M. Spinks • G.G. Wallace
ARC Centre of Excellence for Electromaterials Science, Intelligent Polymer Research Institute, University of Wollongong, Wollongong, NSW, Australia
e-mail: foroughi@uow.edu.au; gspinks@uow.edu.au; gwallace@uow.edu.au

© Springer Science+Business Media Singapore 2015

X. Tao (ed.), *Handbook of Smart Textiles*,
DOI 10.1007/978-981-4451-45-1_14

the base monomer and the use of solubilizing dopants have been used to render the polymer soluble. In some cases, the addition of carbon nanotubes to the spinning solution has been used to produce composite fibers with improved mechanical and electrical properties. These fibers have been evaluated for applications including biomechanical sensors and artificial muscles. The main current limitation in the further development of conducting polymer fibers for textiles processing is their low toughness.

Keywords
Conducting polymer • Fiber spinning • Electrical conductivity • Mechanical property • Carbon nanotubes • Wet spinning

Introduction

Smart materials are one of the exciting new frontier technologies in engineering and manufacturing. A smart material is capable of recognizing appropriate environmental stimuli, processing the information arising from the stimuli, and responding to it in an appropriate manner and time frame. It is well known that inherently conducting polymers (ICPs) provide some interesting possibilities in this regard. ICPs are polymers capable of conducting electricity and have the ability to sense and actuate, leading many researchers to envisage *"intelligent polymer systems"* based on ICPs [1].

Most organic polymers are electrically insulating. In contrast, inherently conducting polymers (ICPs) are materials that exhibit electrical conductivity approaching that of metals. Their discovery in 1977 by Shirakawa, MacDiarmid, and Heeger and their subsequent development led to the Nobel Prize in Chemistry for these pioneers in the year 2000 [2–4]. They first discovered that upon exposure to halogen vapors, polyacetylene films increased in electrical conductivity (σ) by 10^9 times to as high as 10^5 S cm^{-1}. Such conductivities are higher than that of mercury (~1.04×10^4 S cm^{-1}) and comparable to that of copper (~5.65×10^5 S cm^{-1}). Following this discovery, many ICPs (with a common π-conjugated structure) have been discovered, including polypyrrole (PPy), polyaniline (PAni), and polythiophene (PTh) (Fig. 1) [5].

Due to their unique electrical, chemical, and physical properties, ICPs have found many applications in different areas, including chemical sensors, composite membranes for gas separations, rechargeable batteries, electrochromic displays, light-emitting devices, electrocatalysts, electromagnetic interference shielding, mechanical actuators, and controlled drug release. As a result of their metal-like conductivity or semiconductivity and other fascinating properties, conducting polymers now play important roles in specialized industrial applications. Electrical conduction in ICPs is achieved through a unique oxidized π-conjugated system in which mobile charge carriers are created. These charge carriers are radical cations, called polarons, that are partially delocalized across ~3–4 monomer units. When sufficient electrons are removed, the polaron concentration is sufficient to

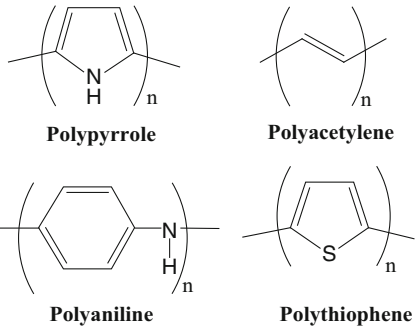

Fig. 1 Chemical structures of selected π-conjugated inherently conducting polymers in their neutral undoped form

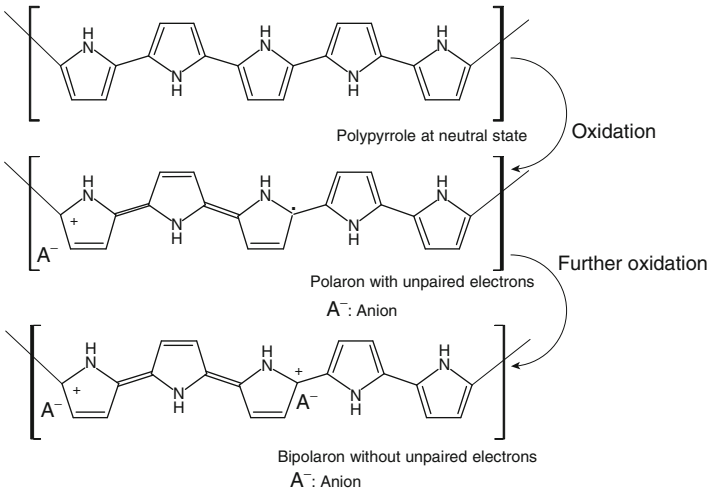

Fig. 2 Schematic showing the formation of polaron and bipolaron states in PPy

result in the formation of dications, commonly called bipolarons. Bipolarons are energetically more favorable than the separated polaronic states, as shown in Fig. 2 (taking PPy as an example). Polarons and bipolarons are mobile in an electric field and are responsible for the electrical conduction properties of ICPs.

The positive charges in the polaron and bipolaron states are stabilized by negatively charged dopant counterions, incorporated in close vicinity. In this unusual charge transport structure, all charged dopants are spatially removed from the quasi-one-dimensional conduction pathway, so that the resistive backscattering of electrons is reduced and this leads to a theoretical conductivity of up to 2×10^7 S cm^{-1}, which is far higher than the conductivity of metals such as copper. However, in real situations, individual polymer chain lengths of 100– 1,000 monomer units would be too short to allow electrical conduction over appreciable distances. Furthermore, the electrical conductivity of ICPs is proportional to the product of the concentration of charge carriers and their mobility. Even though the

concentration of charge carriers in fully doped conducting polymers, including PPy, is in the range of 10^{21}–10^{23}/cm^3, which is four to five orders of magnitude higher than that of inorganic semiconductors, the electrical conductivities of most conducting polymers are in fact in the same range as those of inorganic semiconductors. This reduced conductivity indicates the relatively low mobility of carriers in conducting polymers, which results from the low degree of crystallinity and many other defects. Therefore, if higher electrical conductivities are to be achieved in conducting polymers, the mobility of charge carriers must be improved. The overall mobility of charge carriers in conducting polymers depends on two components: intrachain mobility, which corresponds to charge transfer along the polymer chain, and interchain mobility, which involves the hopping or tunneling of the charge from one chain to a neighboring chain. When an electric field is applied to conducting polymers, the charge carriers necessarily begin to move along the polymer chain by the rearrangement of double and single bonds in the polymer backbone, since the interchain charge transport requires considerably more energy than intrachain conduction. In addition, almost all ICPs prepared either chemically or electrochemically inevitably have defects that lead to the loss of conjugation. When the charge carriers reach any defect point in the chain or the end of the polymer chain itself, the carriers have to hop to a neighboring chain. Therefore, an interchain charge hopping mechanism has been proposed to explain the discontinuous charge transport in ICPs. In this mechanism, the electrical conduction between two terminated chains is achieved by the hopping of mobile charge carriers (e.g., polarons, bipolarons) from one polymer chain onto adjacent chains. Chain defects reduce the electrical conductivity of ICPs to generally less than 1,000 S cm^{-1}. The interchain charge hopping mechanism also explains why the electrical conductivity of ICPs generally increases with temperature, which is opposite to the behavior observed for metals. Therefore, the total conductivity of a conducting polymer is dominated by the combination of intrachain and interchain components [5].

Polyaniline

Polyaniline (PAni) has been the most extensively studied ICP over the past decade, due to its reversible redox and pH-switching properties, ease of synthesis, and wide range of potential applications [1]. Its polymeric structure is different from the other ICPs, such as polypyrrole and polythiophene, and leads to three readily accessible oxidation states, each with its own distinctive color. The fully reduced leucoemeraldine base (LEB) form is very pale yellow, the protonated emeraldine salt (ES) form is bright green, and the fully oxidized pernigraniline base (PGB) form is dark blue. In addition, its solubility in a number of solvents and other properties has made it one of the most promising organic conducting polymers for commercialization. PAni can be synthesized via either chemical or electrochemical oxidation of aniline. Electrochemical polymerization to the emeraldine salt (ES) form is routinely carried out in an acidic aqueous solution of aniline under an applied potential between 0.80 and 1.10 V (versus Ag/AgCl). Chemical

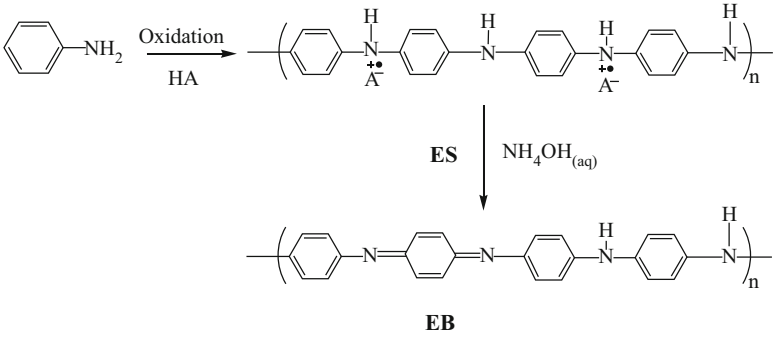

Fig. 3 A general scheme for polymerization of aniline and two common forms of polyaniline emeraldine salt (*ES*) and emeraldine base (*EB*)

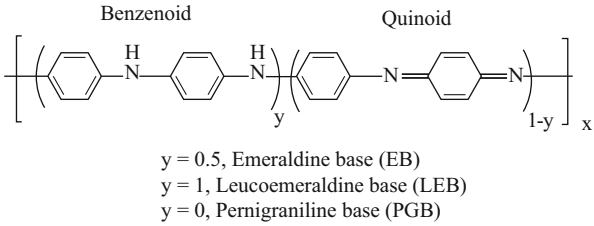

Fig. 4 Different states of oxidation in the base form of PAni (y = 0.5, emeraldine base (*EB*); y = 1, leucoemeraldine base (*LEB*); y = 0, pernigraniline base (*PGB*))

polymerization is usually carried out in an acidic aqueous solution of aniline and an oxidant such as ammonium persulfate (APS). The chemical and electrochemical polymerization of aniline is depicted in Fig. 3. In order to produce the emeraldine base (EB) form of PAni, the above polymerization is followed by dedoping of the green ES form using a basic compound (e.g., $NH_4OH_{(aq)}$) (Fig. 3).

The structure of each tetramer repeating unit of PAni contains benzenoid diamine and/or quinoid diimine segments which are present based on the extent of reduction or oxidation. The extent of reduction of the repeating unit of PAni is represented by the value of y indicated in the chemical structure in Fig. 4, where x is the degree of polymerization. y varies between y = 1 for leucoemeraldine base (LEB) to y = 0 for pernigraniline base (PGB), while y = 0.5 corresponds to emeraldine base (EB).

The conductivity of PAni depends both on the oxidation state of the polymer and the degree of protonation, which is characterized by the proton doping level. The maximum conductivity occurs when PAni is protonated at a doping level of 50 %. Numerous methods have been reported to dissolve PAni in the doped (ES) or undoped (EB, LEB) states without changing the molecular structure. It was reported that the emeraldine base form of PAni can be dissolved in *N*-methyl-2-pyrrolidone (NMP) or *N*, *N*′-dimethyl propylene urea (DMPU) [6–9]. NMP and DMPU are both polar solvents with a high dielectric constant and are classified as polar aprotic (dissolving power without hydrogen attached to oxygen or nitrogen)

as well as Lewis base solvents. Furthermore, PAni (EB) can also be processed from solution by doping with a functionalized sulfonic acid such as camphorsulfonic acid, which renders the resulting PAni.HCSA emeraldine salt (ES) complex soluble in organic acids [10, 11].

Polypyrrole

Among the conducting polymers, polypyrrole is attractive since it has relatively high electrical conductivity and good environmental stability. PPy is stable in air and electroactive in both organic and aqueous electrolyte solutions [12]. It can be switched between its oxidized and reduced states allowing dynamic control of electrical, chemical, and mechanical properties (Fig. 5). Generally, small anionic species are incorporated into the PPy chains in the oxidized state and expelled in the reduced state in order to maintain charge neutrality (Eq. 1). However, in the case of bulky and immobile dopants, charge neutrality is achieved via the incorporation of cations from the electrolyte upon reduction (Eq. 2). With subsequent oxidation, the expulsion of cations or addition of anions would occur. In most cases, a combination of both processes occurs. The dominant process depends on how firmly the anions are trapped in the polymer and how easily the cations can enter the polymer. Incorporation of a wide range of dopant anions is possible giving rise to polymers with varying properties. In particular, PPy has been identified as a nontoxic, potentially biocompatible material for the immobilization of biologically active molecules, such as enzymes, antibodies, receptors, or even whole living cells [12–14]. Microrobots using PPy–Au bilayer actuators have been used to move and position other microcomponents [15–17]. Strain gauges and pressure sensors using PPy for biomedical applications have been constructed. The use of PPy as a model ion gate membrane for controlled drug delivery has also been demonstrated [18, 19].

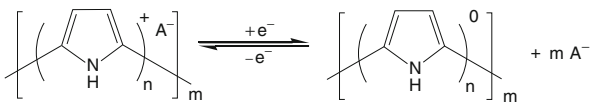

Equation: 1

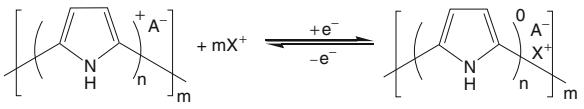

Equation: 2

Fig. 5 Redox switching of polypyrrole, where A^- is the dopant anion incorporated into the PPy during synthesis, X^- represents a cation from the electrolyte, n is the number of pyrrole units for each A^- incorporated, and m is the number of PPy repeat units that determine the molecular weight of the polymer

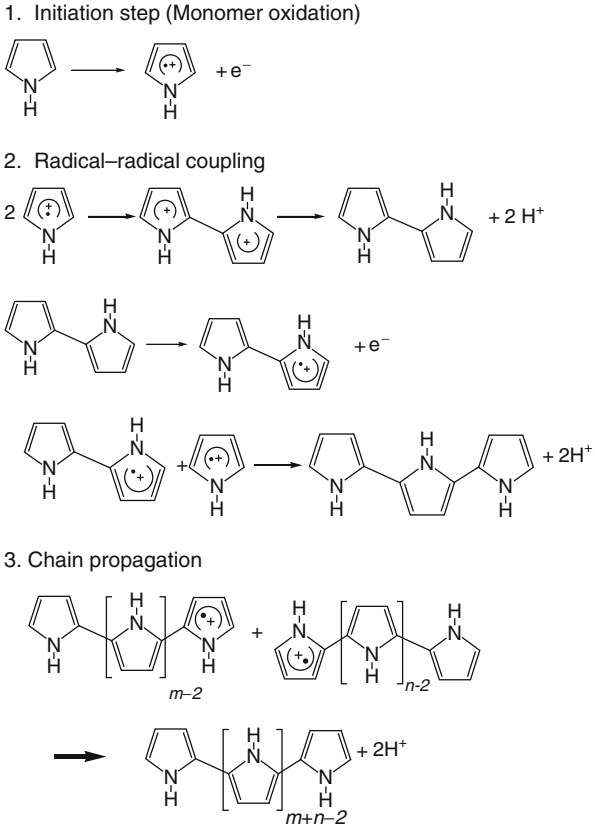

Fig. 6 Polymerization mechanism for pyrrole through the coupling of two radical cations [5]

PPy can be synthesized by chemical or electrochemical oxidative polymerization of pyrrole monomer in solution. Both processes involve the incorporation of anionic dopant species into the oxidized polymer. Chemical polymerization generally involves mixing the pyrrole monomer with chemical oxidant in a suitable solvent. Alternatively, a two-step procedure is sometimes used: a substrate is coated in the oxidant then exposed to pyrrole vapor. On the other hand, electrochemical polymerization is carried out by oxidizing pyrrole monomer in a supporting electrolyte at a suitable anode. As mentioned earlier, PPy may be prepared by either chemical or electrochemical oxidation of pyrrole monomer. The most widely accepted polymerization mechanism for PPy is the coupling between radical cations, as shown in Fig. 6 [5]. Generally, the first step is an oxidation of the monomer to form a delocalized radical cation. The next step is dimerization of the monomer radicals, which occurs via radical-radial coupling at α position, accompanied by the expulsion of two H^+ ions to produce the neutral dimer. Chain propagation then proceeds via facile chemical or electrochemical oxidation of the neutral dimer to form the dimer radical cation, since the neutral dimer and higher molecular weight oligomers oxidize more easily than the neutral monomer.

The radical dimer can combine chemically with other monomeric, dimeric, or oligomeric radical cations to extend the chain. Chain growth is generally terminated when the radical cation of the growing chain becomes too unreactive or more likely when the reactive end of the chain becomes sterically hindered from further reaction. Once the chain length of the oligomers exceeds the solubility limit in the solvent, precipitation of PPy occurs. The termination step has not been fully elucidated but is presumed to involve nucleophilic attack on the polymer chain [5]. On the other hand, an alternative mechanism has been proposed, in which a radical cation attacks a neutral pyrrole monomer as in common chain polymerization, but this explanation is not generally accepted.

Polythiophene

Polythiophenes (Fig. 7) have much in common with polypyrroles. They are formed from a cyclopentadiene molecule but which has an S heteroatom. Thiophene is oxidized to form a conducting electroactive polymer with the greatest conductivity obtained from α–α linkages. Polythiophene can be synthesized either electrochemically or chemically using a simple oxidation process according to figure 7:

As with polypyrrole, *n* is usually between 2 and 4; A^- is a counterion incorporated into the polymer during growth to balance the charge on the polymer backbone, and m is a parameter proportional to the molecular weight. As with polypyrroles, the mechanism of polymerization involves formation of radical cations that react with each other or the starting monomer to develop the polymeric structure (Fig. 7). The reaction of the radical cation with the thiophene monomer has been elegantly demonstrated in recent studies where small amounts of bi- or terthiophene are added to reduce the polymerization potential [1]. Even after the additive was consumed, polymerization continued at lower potentials. This is particularly important because the development of systems utilizing thiophene have been thwarted by the "polythiophene paradox." It has been clearly shown that at potentials required to oxidize the thiophene monomer, the polymer itself becomes overoxidized. This overoxidation process proceeds according to Fig. 8 and results in deterioration in the chemical and physical properties of the polymer. Using constant current or constant potential polymerization, the product obtained is, therefore, a mixture of polythiophene and overoxidized polythiophene.

A range of alkoxy groups (**1**, **2**, **3**) has also been added to the bithiophene starting material in order to reduce the oxidation potential even further. Attachment of the

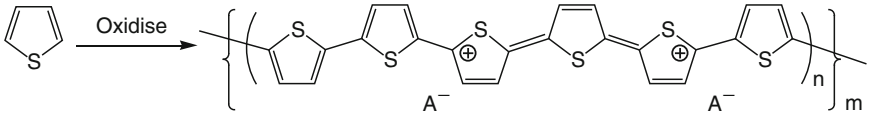

A⁻ molecular dopant, n determines degree of doping, m determines molecular weight

Fig. 7 Polymerization mechanism for thiophene

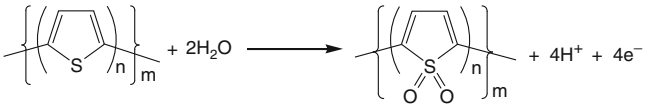

Fig. 8 Overoxidation process of polythiophene

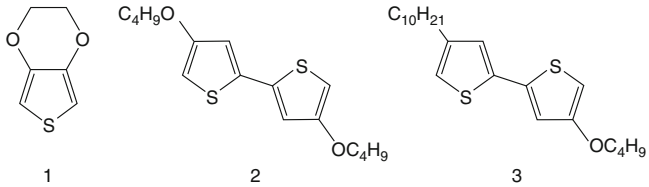

Fig. 9 Three alkoxy groups

alkyl group (**3**) also facilitates the solubility of the polymer in nonpolar organic solvents (Fig. 9).

A range of copolymers involving functional thiophene have also been formed electrochemically. For example, Sato and co-workers formed a copolymer containing 3-dodecyl-thiophene and 3-methylthiophene [20]. The material had a solubility of 75 (w/w) % in chloroform and a conductivity of 220 S cm^{-1}.

Polythiophenes are normally produced from nonaqueous media since the monomer is more soluble in these solvents. Also, a wider electrochemical potential window is available, and this is required since polythiophene is more difficult to oxidize than pyrrole. The influence of water on the polymerization process for thiophene and on the redox-switching properties has been studied. The presence of water as low as 1 % causes mislinkages and a subsequent deterioration in polymer properties [1]. Other authors have claimed that optimal polymers are produced from propylene carbonate. These same workers also point out that the minimum thiophene concentration required to enable polymerization is solvent dependent [1]. The required minimal solvent concentration decreases for solvents with a large dielectric constant. They claim that solvents with a high dielectric constant (having an electron-withdrawing substituent) influence the reactivity of the cation radical intermediate and, therefore, play an important role in the polymerization process.

The counterion employed can also affect the rate of polymerization at a fixed potential. The effect of the counterion's chemical nature on the oxidation of 3-methylthiophene was found to be potential dependent [1]. At low anodic potentials (+1.25 V to +1.34 V), the initial rate of reaction was found to be quickest when the ClO^{-}_{4} anion was used as dopant [1]. The next quickest rate was with the BF^{-}_{4} ion, closely followed by PF^{-}_{6}. This trend was similar to the oxidation potentials measured by cyclic voltammetry. At higher anodic potentials (+1.40 V to +1.5 V), the ClO^{-}_{4} ion showed the slowest reaction rate. At even higher potentials ($>$ +1.50 V), the reaction involving ClO^{-}_{4} was severely inhibited with currents

dropping to low values. The perchlorate ion is known to undergo oxidation at these potentials to form ClO_4. This species may well have reacted with the intermediate monomer radicals to inhibit the polymerization process.

Chemical Polymerization

As with polypyrrole, polythiophene can be produced using a chemical oxidant. However, due to the limited solubility of thiophene, this reaction must be carried out in nonaqueous media. Copper (II) perchlorate has been used as an oxidizing agent in acetonitrile to yield a simultaneous polymerization/doping process [1]. This process results in polymer materials with conductivities of approximately 8 S cm^{-1}. Alternatively, a Grignard reaction can be used to produce polythiophene which is the first time conventional synthesis techniques have been used [1].

Vapor Phase Polymerization

Vapor phase polymerization (VPP) has also been employed in a few cases to prepare polythiophene-based films. This approach was first successfully used by de Leeuw and co-workers in 1994 to prepare smooth films of poly (3,4-ethylenedioxythiophene) (PEDOT) using ferric *p*-toluenesulfonate as the oxidant [1]. Imidazole was added as inhibitor to suppress the polymerization of the EDOT monomer until the solvent was evaporated. Fe (III) sulfonates do not have sufficient oxidizing power in VPP to produce coherent and conducting polythiophenes from thiophene monomer itself. However, Winther-Jensen and co-workers have recently prepared polybithiophene (PBTh) and polyterthiophene (PTTh) via the vapor phase polymerization of the more readily oxidized bithiophene and terthiophene using Fe (III) tosylate as oxidant [1]. Both polymers were formed in their blue, oxidized state but spontaneously reduced to their neutral, yellow-orange state upon washing in ethanol.

Fiber Spinning of Conducting Polymer

Since the nineteenth century, revolutionary changes have been occurring at an unprecedented rate in many fields of science and technology, which have profound impacts on every human being. The last century also brought tremendous advances in the textile industry, which has a history of many thousands of years. Solid foundations of scientific understanding have been laid to guide the improved usage and processing technology of natural fibers and the manufacturing of synthetic fibers. Consequently, spinning techniques have been widely developed and employed to fabricate new materials such as conducting polymers. Although polymers dominate the general fiber and textile industries, they have had little impact on applications that require electrical conduction or electronic properties. Conducting

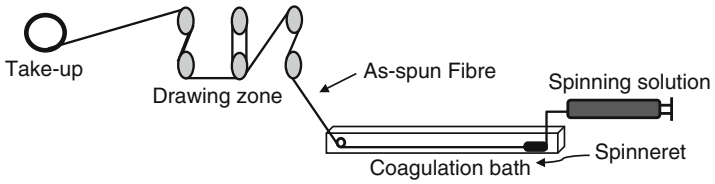

Fig. 10 Schematic showing the setup used for wet spinning of fibers [33]

polymer fibers are likely to be important for electronic textile applications as they allow the possibility to incorporate desirable features such as chemical sensing or actuation that are not feasible with metallic fibers. However, the production of continuous conducting polymer fibers has proved difficult as their common forms are not soluble and cannot be processed by melt techniques like extrusion. Basically, spinning of polymers can be divided into methods involving either melt spinning or solution spinning. Melt spinning is inappropriate for conducting polymers. Therefore, solution spinning is the only method used to spin conducting polymers. Wet spinning involves the extrusion of polymer solution into a liquid bath containing low molecular weight substances miscible with the solvent but that do not dissolve the polymer and using a setup such as shown in Fig. 10. In the coagulation bath, the polymer is precipitated from the solution, and a solid gel fiber containing considerable amounts of solvent and possibly coagulation agent is formed. Solidification occurs because of the exchange of solvent and non-solvent. The solvent diffuses out of the extrudate into the bath, and a non-solvent diffuses from the bath into the extrudate. The polymer precipitates as a gel initially at the extrudate–coagulant interface but progressively throughout the extrudate. The final structure of the fiber arises through counterdiffusion processes involving solvent and non-solvent occurring during formation. The coagulated fiber passes over a guide toward driven rollers. The steps after coagulation vary according to the product but typically include washing, stretching, and drying.

Spinning of Polyaniline Fibers

PAni fibers have been produced using either a two-step or one-step wet-spinning process. The doping of PAni before fiber formation should result in fibers with more ideal properties. It was reported that employing concentrated sulfuric acid allowed the production of conductive PAni fiber from protonated PAni solution. The PAni fibers obtained from these acidic processing systems exhibited very poor mechanical properties and moderate electrical conductivity [21]. It has also been reported that processing of PAni (ES) is possible using sulfonic acids as dopant [11]. Using a functionalized sulfonic acid such as camphorsulfonic acid (HCSA), the emeraldine base (EB) form of PAni was converted to the doped PAni–HCSA emeraldine salt. This material was in solvents such as *m*-cresol and suitable for wet spinning. The as-spun fiber obtained from anisotropic liquid crystalline PAni/CSA/*m*-cresol

Table 1 The mechanical and electrical properties of neat PAni fiber produced by the two-step process wet spinning followed by acid doping [22]

Fiber process	Breaking stress (MPa)	Modulus (GPa)	Strain at break (%)	Dopant	Conductivity (S cm^{-1})
LEB/ DMPU [23]	308	7.8	15	HCl	150
LEB/ DMPU [24]	127	2.97	13	MSA[a]	350
EB/NMP [24]	63	1.85	6	BPA[b] – HCl	10

[a]Methane sulfonic acid
[b]Benzene phosphinic acid

solution had a brittle structure and weak mechanical properties but good electrical conductivity. In the two-step process, concentrated PAni solutions in the form of EB or LEB have been prepared by using gel inhibitors such as 2-methyl aziridine (2-MA), 4-methyl piperidine (4-MP), and pyrrolidine or reducing agents such as phenylhydrazine in N-methylpyrrolidone (NMP) or dimethyl propylene urea (DMPU), respectively [22]. Fibers have subsequently been spun from these solutions. The fibers were successively doped with acid to render them conductive. The best results reported in the literature are represented in Table 1. These data reveals the following facts that can be used in the optimization of processes: the increase in mechanical strength of the fibers processed from LEB/DMPU is accompanied with a decrease in conductivity, and electrical conductivities for the LEB/DMPU fibers after oxidation and doping gave values of 150 S cm^{-1} which is lower than that observed for EB/DMPU fibers (350 S cm^{-1}).

The two-step process for preparing conducting PAni fibers involves the adverse influence of the acid doping process on mechanical properties. Nonhomogeneous doping and the possibility of dedoping through diffusion of small anions from the skin of the fibers cause heterogeneities in the fiber structure. Doping of polyaniline in solution, however, results in more homogeneous doping and a more uniform material after casting. Doping of polyaniline with sulfonic acids results in an extended coil conformation and a high level of crystallinity resulting in high electronic conductivity [22]. In this regard, a number of studies involving the processing of polyaniline solution blended with sulfonic acids in a suitable solvent have been conducted. The production of an electronically conductive emeraldine salt (ES) form of polyaniline fiber using 2-acrylamido-2-methyl-1-propane sulfonic acid (AMPSA) (in dichloroacetic acid) as the dopant has recently been reported. The ultimate tensile strength, elastic modulus, and electrical conductivity reported were 97 MPa, 2 GPa, and 600 S cm^{-1}, respectively, after annealing of fibers that had been drawn to 5× their original length. This inverse relationship is due to the presence of microvoids in the fibers with the density of the LEB/DMPU fiber being twice that of the EB/DMPU materials. It has been claimed that the presence of microvoids in EB fibers causes weaker mechanical properties and facilitates diffusion of dopants resulting in higher conductivities [22]. Fewer voids generate lower

conductivity for LEB fiber and higher mechanical properties. It is worth noting that the dopants that have been used for the two samples were different. However, the role of dopant has been ignored and the higher conductivity was attributed solely to microvoids. Microvoids also cause facile dedoping through the removing of volatile dopant. It was also reported that benzene phosphinic acid (BPA) is a more efficient dopant than HCl and achieves higher conductivity due to reduced volatility. In addition, results of other studies emphasized that doping the fiber with inorganic acids (HCl) embrittles the fiber as a result of reduced cohesion force between polymer chains [22]. In contrast, doping with organic acid (acetic acid, benzene phosphinic acid, $MeSO_3H$) may produce better mechanical and electrical properties. Acid doping raises conductivity but is detrimental to mechanical properties. The tensile strength of both LEB/DMPU and EB/DMPU fibers decreased more than 50 % after acid doping [22]. The processing of PAni fibers from EB/NMP/2-MA significantly decreases the conductivity compared with fibers produced from EB/DMPU without any gel inhibitor present. By contrast, the conductivity of PAni fiber doped with HCl processed from EB/NMP without gel inhibitor shows a conductivity in the range of 20 S cm^{-1}. Therefore, the low conductivity obtained in the presence of the gel inhibitor can be attributed to a decrease in the degree of delocalization along the polymer backbone. The main problem in the fiber spinning process involves post-doping. If the doping acid can diffuse into the fiber, to be effective as a dopant, then it is also possible for it to diffuse out again during storage or use. Secondly, in most cases, a higher mechanical strength is associated with a denser fiber, so that only doping of the fiber skin is achieved and dedoping readily occurs. In spite of these problems with the two-step process, it has some advantages. These include the high stability of the spinning solution and ease of processing.

The doping of PAni before fiber formation (i.e., in solution form) should result in fibers with more ideal properties. The concentrated sulfuric acid was used to produce conductive PAni fiber from protonated PAni solution. The PAni fibers obtained from these acidic processing systems exhibited very poor mechanical properties and moderate electrical conductivity (about 50 S cm^{-1}). Another alternative was borrowed from the discovery by processing of PAni (ES) using sulfonic acids. Using functionalized sulfonic acids such as CSA, PAni rendered the doped PAni soluble in many new solvents such as m-cresol. It has been shown previously that the use of functionalized sulfonic acids gives rise to high levels of crystallinity in the PAni [22], which directly correlates to a metallic electrical conductivity contribution in the material. The as-spun fiber obtained from anisotropic liquid crystalline PAni/CSA/m-cresol solution has a brittle structure and weak mechanical properties but good electrical conductivity. PAni fibers have also been fabricated directly in the emeraldine salt (ES) conductive form using dichloroacetic acid (DCAA) as solvent and 2-acrylamido-2-methyl-1-propane sulfonic acid (AMPSA) as dopant. Table 2 summarizes the results obtained from mechanical and electrical conductivity tests. The as-spun fiber obtained from anisotropic liquid crystalline PAni/CSA/m-cresol solution shows weak mechanical properties and brittle structure but good electrical conductivity. However, the DCAA–AMPSA

Table 2 The mechanical and electrical properties of PAni fiber processed from one-step method [22]

Fiber process	Breaking stress (MPa)	Modulus (GPa)	Strain at break (%)	Conductivity (S cm^{-1})
PAni/CSA/m-cresol [25]	17	0.65	8.4	200
PAni/AMPSA/DCAA [26]	20–80	0.04	n/a	100
As above and 5× drawn [26]	83	1.4	n/a	600

is a desirable dopant/solvent alternative compared to the CSA/m-cresol system with both lower toxicity and greater processability. It has been observed that the as-spun fiber of PAni/AMPSA/DCAA is highly flexible and can be drawn five times versus its initial length due to the plasticizing effect of AMPSA. The high draw enables high orientation of the polymeric chain to obtain conductivity in the range of metallic material in the stretched form. These values are higher than can be obtained with the PAni/CSA/m-cresol formulation. It has been shown that the ultimate tensile strength and elastic modulus of 5× drawn fibers of PAni/AMPSA/DCAA fiber can be improved, respectively, to 97 MPa and 2 GPa by thermomechanical stretching [22].

Despite having excellent conductivity, fibers spun from the PAni/AMPSA/DCAA have mechanical properties that are inferior to fibers obtained from EB/DMPU and LEB/DMPU fibers. Moreover, the mechanical properties of all these PAni fibers are inferior to natural or synthetic fibers applicable in the textile industry. In this regard, several studies have been conducted to produce composite fibers of PAni and common thermoplastic polymers such as poly–ω-aminoundecanoyle (nylon-11) and poly-phenylene terephthalamide (Kevlar) using wet-spinning process [25, 27–30]. In both groups of studies, concentrated H_2SO_4 has been used as both solvent and dopant; however, the former requires post-doping using dilute HCl to be conductive. The tensile strength and modulus of the PAni/Kevlar composite fiber are very high due to the presence of Kevlar, with highly oriented polymer chains, compared to PAni/nylon-11, with low compatibility of PAni as host polymer. These fibers may have promising applications in electrostatic charge dissipation or EMI shielding. However the conductivity is lower than that required for different applications in electronic devices (Table 3).

There is a need to introduce a reinforcing filler that enhances the mechanical properties of PAni fibers while having a positive impact on their electronic properties. In this regard, the use of carbon nanotubes as a conductive reinforcement for PAni has been investigated. Both single-walled carbon nanotube (SWNT) and multi-walled carbon nanotube (MWNT) have been investigated. The examples for reinforcement of mechanical and electrical property of matrices using carbon nanotubes comprise PMMA/SWNT, PVA/SWNT, and epoxy/SWNT composites as a film or PBO/SWNT and PAN/SWNT as fiber. The superposition of electrical, electrochemical, and mechanical properties of neat PAni and SWNT potentially

Table 3 The electrical and mechanical properties of composite of PAni and thermoplastic polymer [22]

Fiber process	Breaking stress (MPa)	Modulus (GPa)	Strain at break (%)	Conductivity (S cm^{-1})
PAni (30 %)/Kevlar [29]	3,130	56	5.9	0.1
PAni (20 %)/nylon-11 [28]	238	n/a	n/a	0.1

introduces this composite as multifunctional material for diverse applications. The synthesis and characterization of PAni–SWNT composites has also been investigated previously [22]. Direct dissolution of pristine nanotubes (without chemical functionalization) in aniline can occur via formation of a donor/acceptor charge complex. Using this approach, SWNT/PAni composite films have been produced by chemical or electrochemical polymerization of aniline containing dispersed SWNTs. Alternatively, the SWNTs have been blended with preformed polyaniline in solvents such as *N*-methylpyrrolidone (NMP) [22]. The enhanced electroactivity and conductivity of SWNT/PAni composite films has been attributed to the strong molecular level interactions that occur between SWNTs and PAni [31]. Many challenges are inherent in the wet spinning of carbon nanotube/PAni fibers, particularly the preparation of highly dispersed CNTs in the PAni solution and control of the nature of the CNT/PAni interface to ensure both charge transport and the transfer of mechanical load. The electrical conductivity tests show a 150 % increase in tensile stress (229 MPa) and a 110 % increase in Young's modulus (5.2 GPa) as well as a 30 times enhancement in electrical conductivity (from 1.2 to 32 S cm^{-1}) with the addition of 2 % CNTs [22]. SEM studies confirm the lower porosity of the composite fiber due to a higher viscosity of the composite spinning solution. In addition, it was also reported that the addition of carbon nanotubes to PAni–AMPSA fibers processed from dichloroacetic acid resulted in materials with high conductivity and high mechanical strength and modulus. Conductivities as high as 750 S cm^{-1} were achieved in continuously spun fibers up to 50–100 m in length. Tensile strength of 250–300 MPa and modulus of 7–8 GPa for PAni–SWNT composite fibers were approximately two times higher than for neat PAni fiber. The fibers produced were tough enough to be knotted or twisted. Electroactivity was enhanced by the addition of nanotubes, as shown by cyclic voltammetry. AMPSA in dichloroacetic acid was shown to be a highly effective dispersant for carbon nanotubes. Rheological studies and Raman spectroscopy studies indicated strong interactions between the SWNTs and the PAni. These interactions very likely contributed to the effective transfer of load and charge between the PAni matrix and the SWNT fibers. The unique properties of high strength, robustness, good conductivity, and pronounced electroactivity make these fibers potentially useful in many electronic textile applications. The use of dichloroacetic acid (DCAA) containing 2-acrylamido-2-methyl-1-propane sulfonic acid (AMPSA) has been shown to act as an excellent dispersing medium for carbon nanotubes and for

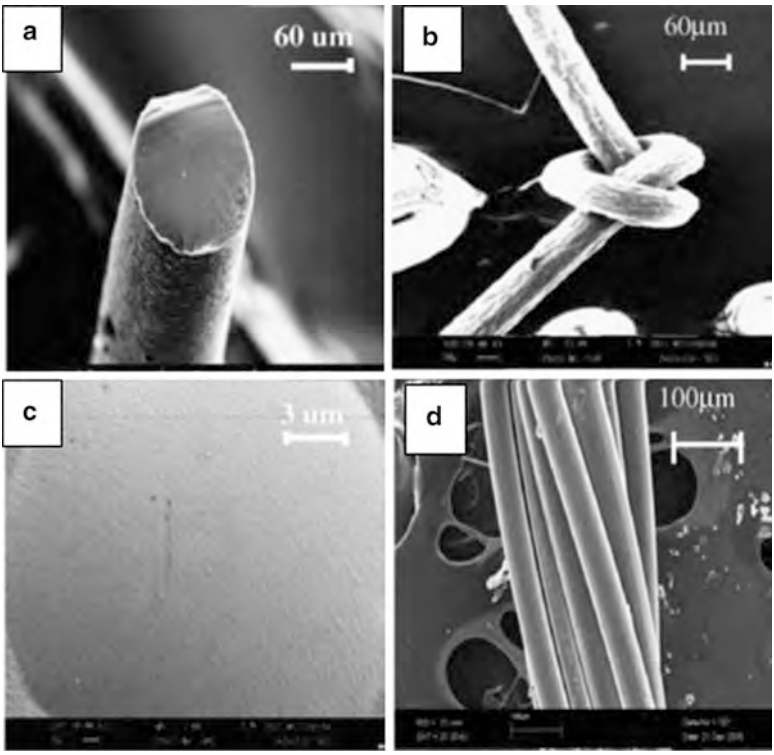

Fig. 11 SEMs of (**a**) PAni–AMPSA and (**b**) knotted PAni–AMPSA–SWNT (0.76 % (w/w) SWNTs), (**c**) cross section of as-spun fiber, and (**d**) 16-ply twisted fiber of PAni–AMPSA–SWNT (0.76 % w/w). (Reprinted from [31] with permission from Elsevier)

dissolution of polyaniline [31]. The viscosity of DCAA–AMPSA solution undergoes a transition from Newtonian to non-Newtonian viscoelastic behavior upon addition of carbon nanotubes. The ultimate tensile strength and elastic modulus of PAni–AMPSA fibers were increased by 50–120 %, respectively, upon addition of 0.76 % (w/w) carbon nanotubes. The elongation at break decreased from 11 to 4 % upon addition of carbon nanotubes; however, reasonable flexibility was retained. An electronic conductivity percolation threshold of 0.3 % (w/w) carbon nanotubes was determined with fibers possessing electronic conductivity up to 750 S cm^{-1}. SEMs of the cross sections of fibers containing 0.76 %(w/w) SWNTs are illustrated in Figs. 11b. Although the strain at break decreases considerably with increasing carbon nanotube content, knots formed in PAni–AMPSA fibers with SWNTs showed high degrees of flexibility, as demonstrated in the SEMs in Fig. 11a–c. The fiber containing nanotubes also shows high level of twistability (i.e., 36 twists per inch (TPI)) which is essential to enable the fiber to form a strong thread to be as warp or weft in textile matrix (Fig. 11c) [31, 32].

Spinning of Polypyrrole Fibers

Several studies have focused on the development of new soluble or fusible PPy suitable for fiber spinning. A major breakthrough came with the modification of the chemical structure of PPy by adding solubilizing substituents onto the pyrrole monomer unit [5]. PPy derivatives containing alkyl or alkoxy substituents at the 1-, 3-, or 4-positions of pyrrole were synthesized and found to be soluble in chloroform, tetrahydrofuran, and *o*-dichlorobenzene [33]. Since the bulky side groups reduce the molecular interactions between main chains and increase chain entropy, the substituted conducting polymers can be processed from solution. However, as the addition of substituents induces steric interference along the chains, the planarity of the polymer structure is significantly reduced to the detriment of the conductivity by the reduction of the degree of π-orbital overlap. It was reported that the electrical conductivity of poly(3-alkylpyrrole) decreased with the size of alkyl chain [5]. Water-soluble PPy has also been synthesized via the grafting of pyrrole onto the *p*-aminodiphenylamine moieties of a water-soluble copolymer [5]. Pyrrole was chemically polymerized using APS as oxidant and self-doped PPy copolymer was produced. It was observed that the film obtained by casting from a PPy copolymer solution was homogeneous, while that obtained from a suspension was heterogeneous because of the two distinct polymers involved. After drying in vacuum, the PPy copolymer film had a conductivity of 1.96 S cm^{-1}. It was also reported that the conductive copolymer exhibited a maximum conductivity of 3.4 S cm^{-1} when [pyrrole monomer]/[copolymer] ratio was 1:1 [5].

Foroughi and co-workers [34] have developed continuous polypyrrole fibers for the first time using a wet-spinning process. The process is enabled by the formation of highly soluble non-functionalized PPy by the incorporation of the di (2-ethylhexyl) sulfosuccinate (DEHS) dopant anion which renders the polymer soluble in various organic solvents. The solutions were amenable to a wet-spinning process that produced continuous doped polypyrrole fibers. Polypyrrole $[(Py_3)^+(DEHS)^-]_x$ powder was chemically synthesized then PPy–DEHS was added to DCAA (dichloroacetic acid) as solvent to prepare the spinning solution. The coagulation bath contained 40 % (v/v) DMF (dimethylformamide) in water at 20 °C. The mechanical and electrical properties of as-spun PPy fiber have shown that the ultimate tensile strength, elastic modulus, and elongation at break were 25 MPa, 1.5 GPa, and 2 %, respectively, with an electronic conductivity of ~3 S cm^{-1}. Cyclic voltammetry demonstrated the electroactivity of the polypyrrole fibers. Following the first PPy fiber fabrication, Foroughi and co-workers also reported a new method to produce high-performance PPy fiber with reasonable mechanical, electrical, and electrochemical properties by optimizing of the synthesis conditions and spinning processes (Fig. 12) [35]. These properties are achieved through the increase in PPy molecular weight allowing the drawing of the fibers. These new high molecular weight doped polypyrroles were synthesized, and the intrinsic viscosity of PPy solutions showed that the molecular weight of PPy is very sensitive to the polymerization temperature. A significant increase in molecular

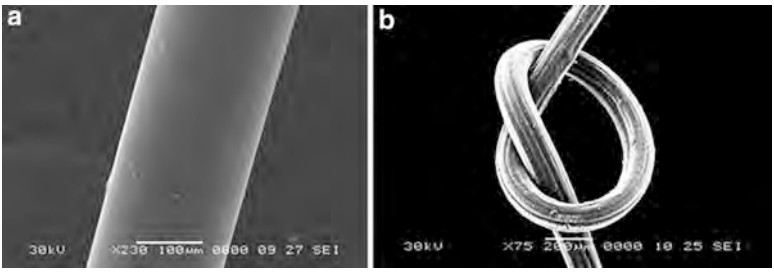

Fig. 12 SEM micrographs of as-spun PPy fiber (Reprinted from Ref. [35] with permission from Elsevier)

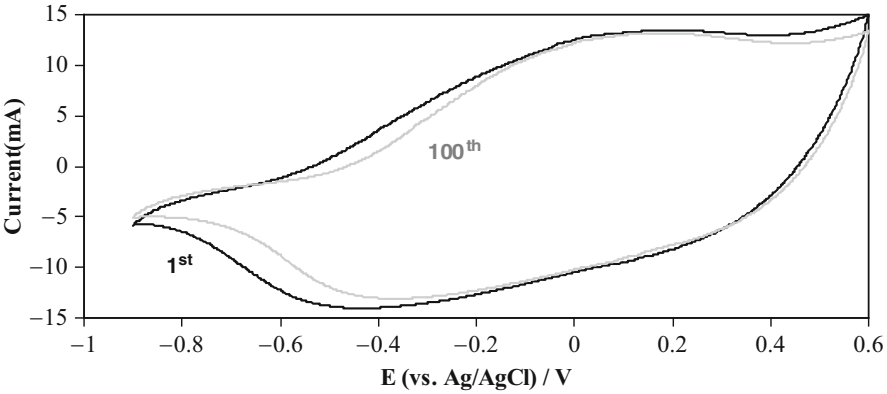

Fig. 13 Cyclic voltammogram of PPy fiber potential was scanned between −0.9 V to +0.6 V (versus Ag/AgCl) in 0.1 M DEHS in acetonitrile/water (1:1) at 100 m Vs^{-1} (Reprinted from Ref. [35] with permission from Elsevier)

weight was achieved by reducing the polymerization temperature from 0 °C to −15 °C. The resultant solutions were amenable to a wet-spinning process that produced continuous, doped high-performance polypyrrole fibers. The mechanical properties of as-spun PPy fibers have shown that as-spun PPy fibers had a significant increase in ductility of the latter. The ultimate tensile strength, elastic modulus, and elongation at break of the higher molecular weight fibers were 136 MPa, 4.2 GPa, and 5 %, respectively. These values were 500 %, 250 %, and 280 % higher than obtained from the lower molecular weight fibers. The higher molecular weight produced by the low-temperature polymerization reduces the brittleness and allows a higher ductility than occurs in the early PPy fibers.

Cyclic voltammetry for the PPy fiber in electrolyte is shown in Fig. 13 [35]. Reasonable electroactivity was observed in the PPy fibers as evidenced by oxidation and reduction peaks at ~0 and −0.5 V (Ag/AgCl reference), respectively. The redox activity was reasonably stable for up to 100 cycles. The electroactivity and electrical conductivity observed in these fibers suggests that the fibers may be useful for sensors, actuators, and batteries.

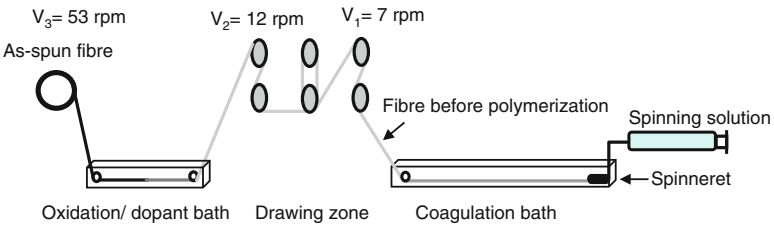

Fig. 14 Continuous wet spinning and polymerization line [36] (Reproduced by permission of The Royal Society of Chemistry http://pubs.rsc.org/en/content/articlehtml/2011/jm/c0jm04406g)

Drawing of PPy fibers to 40 % strain at 100 °C increased the electrical conductivity to 30 S cm^{-1}. Similar increases in conductivity have been reported upon drawing of PPy–DEHS cast films [34]. The elongated coil structure formed during drawing likely increases the overlap of pi orbitals and thereby increases intrachain conductivity. Recently, a novel approach to produce bicomponent PPy fiber has been developed [36]. Electrically conducting robust fibers comprised of both an alginate (Alg) biopolymer and a polypyrrole component have been produced using reactive wet spinning. Using this approach, polypyrrole-biopolymer fibers were also produced with single-walled carbon nanotubes (CNTs), added to provide additional strength and conductivity. Fiber spinning was carried out using a continuous in situ wet-spinning and polymerization process (Fig. 14). The coagulation bath contained a 5 % w/v solution of $CaCl_2$ in a mixture of methanol/water solvent (70/30). The as-spun fibers were drawn to 7.5 times during wet spinning and continuously passed through an oxidant/dopant bath. The pyrrole monomer retained in the coagulated fiber is polymerized in this second bath. In the case of PPy-alginate fiber, the color changed from white to black/green after a few minutes, demonstrating the formation of PPy.

SEM images of the PPy–Alg composite fibers clearly show the tubular multifilament form of the alginate fiber impregnated with PPy nanoparticles (Fig. 15a and c). The rough surface of PPy–Alg fibers can be clearly seen at higher magnification in Fig. 15c. CNTs are clearly observed on the cross-sectional micrograph of PPy–Alg–CNT fibers (Fig. 15d) while the CNTs cannot be observed on the surface. The fibers produced containing CNTs show a 78 % increase in ultimate stress and 25 % increase in elongation to break compared to PPy–alginate fiber. The Young's modulus obtained for the PPy–Alg–CNT fibers showed a 30 % increase compared to the PPy–alginate fiber.

The mechanical properties of Alg, PPy–Alg fibers, and PPy–Alg–CNT nanocomposite fiber have shown that ultimate stresses of ~307 ± 10 MPa, ~140 ± 6 MPa, and ~250 ± 5 MPa with ~12 ± 2 % strain, ~8 ± 1.5 % strain, and ~10 ± 1.3 % strain were obtained for the alginate, PPy–Alg, and PPy–Alg–CNT fibers, respectively. Similarly, the Young's moduli were found to be 13 ± 2, 7 ± 1, and 10 ± 0.5 GPa for the alginate, PPy–Alg, and PPy–Alg–CNT fibers, respectively. These results confirm the reinforcing role played by CNTs in the PPy–Alg fibers. However, the decrease in mechanical properties of the alginate

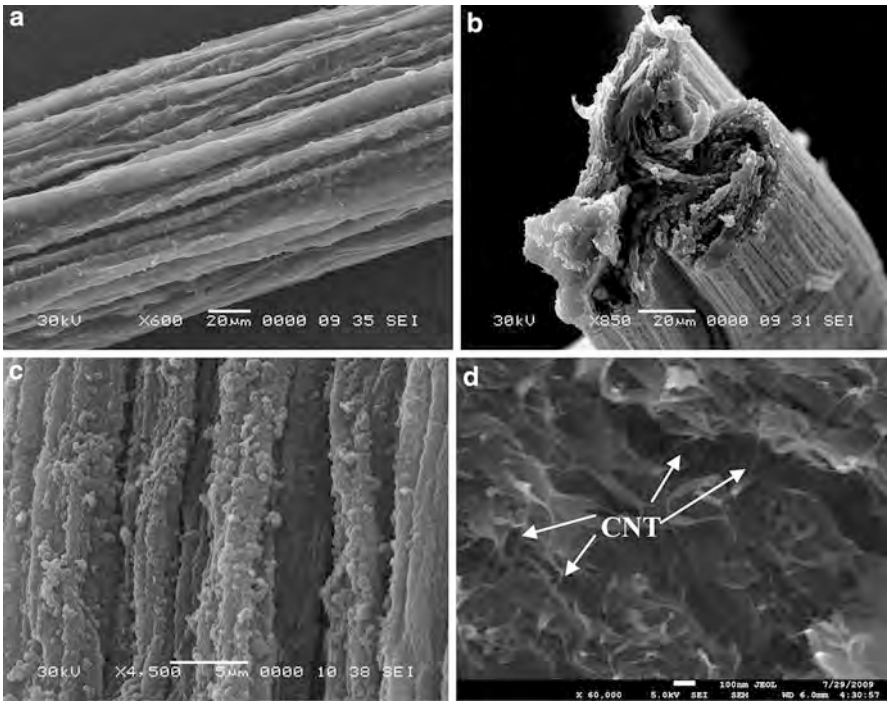

Fig. 15 SEM micrographs of the fibers: (**a**) PPy–Alg, (**b**) PPy–Alg cross-sectional, (**c**) higher magnification PPy–Alg, and (**d**) PPy–Alg–CNT fiber [36] (Reproduced by permission of The Royal Society of Chemistry http://pubs.rsc.org/en/content/articlehtml/2011/jm/c0jm04406g)

Table 4 Effect of the oxidant/dopant on electrical conductivity of as-spun fibers (Reproduced by permission of The Royal Society of Chemistry http://pubs.rsc.org/en/content/articlehtml/2011/jm/c0jm04406g)

Material	Conductivity (S cm^{-1})
PPy–Alg (APS/DEHS)	0.5 ± 0.2
PPy–Alg–CNT (APS/DEHS)	3.0 ± 0.5
PPy–Alg–CNT ($FeCl_3$/DEHS)	2.0 ± 0.4
PPy–Alg–CNT (APS/*p*TS)	4.0 ± 0.8
PPy–Alg–CNT ($FeCl_3$/*p*TS)	10.0 ± 1.5

fiber with the addition of PPy (with or without CNTs) was unexpected and may be due to the low compatibility of alginate and PPy. The average electrical conductivity of PPy–Alg fiber was measured to be ~0.5 S cm^{-1} which was increased to 3 S cm^{-1} by addition of CNTs. Use of other oxidant and dopant systems affected the conductivity, with the highest value (10 S cm^{-1}) obtained using $FeCl_3$ and *p*TS (Table 4). All these conductivity values were considerably lower than the electrical conductivity of wet-spun PPy–DEHS, which is likely due to the presence of nonconductive alginate polymer.

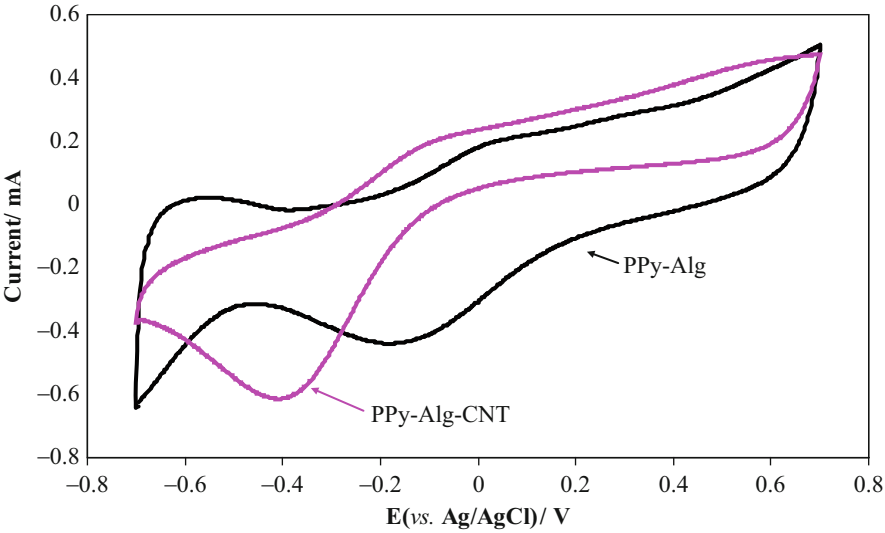

Fig. 16 Cyclic voltammograms of PPy–Alg and PPy–Alg–CNT (APS/DEHS) fibers. Potential was scanned between −0.7 and +0.7 V (versus Ag/AgCl) in 1.0 M $NaNO_3$ at 100 mVs^{-1} [36] (Reproduced by permission of The Royal Society of Chemistry http://pubs.rsc.org/en/content/articlehtml/2011/jm/c0jm04406g)

Cyclic voltammograms for the PPy–Alg and PPy–Alg–CNT fibers in 1.0 M $NaNO_3$ are shown in Fig. 16. Each exhibited reasonable electroactivity, as evidenced by redox peaks at −0.2 to +0.1 V (PPy–Alg fiber) and −0.4 to 0 V (PPy–Alg–CNT fiber) versus Ag/AgCl reference electrode, respectively. The fibers produced were electrochemically active and capable of electromechanical actuation with a strain of 0.7 % produced at a scan rate of 100 mV s^{-1} of the potential [36].

To further develop highly conducting and mechanically robust fibers, conducting polymer carbon nanotube yarn has recently been fabricated [37]. Hybrid polypyrrole–multi-walled carbon nanotube (MWNT) yarns were obtained by chemical and electrochemical polymerization of pyrrole on the yarn surface. Single- and two-ply multi-walled carbon nanotube yarns were used to develop the PPy–CNT yarn. SEM micrographs of the pristine CNT and PPy–CNT yarns were carried out to reveal a core-sheath structure for the electrochemically prepared PPy–CNT yarn (Fig. 17). However, chemically developed PPy–CNT yarn had a heterogeneous morphology consisting of dense regions of PPy-infiltrated CNT and more porous areas having less PPy. The mechanical properties of CNT and PPy–CNT yarn showed a significant difference in mechanical properties. Analysis of the stress–strain curves indicates a stress at break of ~460 MPa with ~5 % strain for the single CNT yarn, compared with ~510 MPa stress with ~2.5 % strain for the chemically prepared single PPy–CNT yarn. The Young's moduli of these yarns were ~12 GPa and ~35 GPa for the CNT yarn and chemically prepared PPy–CNT yarn, respectively. It is expected that PPy in the PPy–CNT yarn reduces the slippage between CNT bundles, thereby increasing the shear resistance and elastic modulus. The effect of the

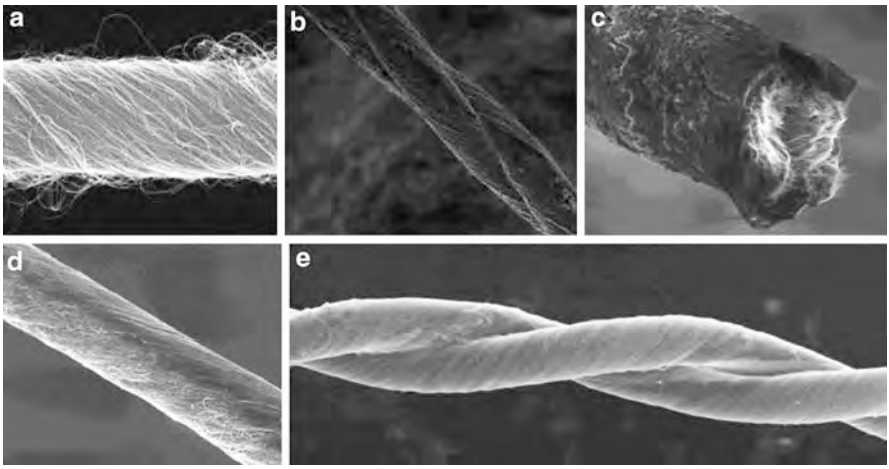

Fig. 17 SEM micrographs of (**a**) pristine CNT yarn, (**b**) electrochemically prepared PPy–CNT yarn showing the surface morphology of a two-ply PPy–CNT, (**c**) cross section of electrochemically prepared PPy–CNT yarn, and (**d–e**) chemically prepared single- and two-ply PPy–CNT yarn [37] (Reproduced by permission of The Royal Society of Chemistry http://pubs.rsc.org.ezproxy.uow.edu.au/en/content/articlehtml/2012/nr/c2nr11580h)

preparation method on mechanical properties of PPy–CNT yarn was investigated using the two-ply twisted yarns. The chemically prepared two-ply PPy–CNT yarn showed significantly higher mechanical properties than the electrochemically prepared composite, with a stress at break of ~740 MPa at ~1.5 % strain compared with ~273 MPa stress at ~4.5 % strain for the electrochemically prepared two-ply PPy–CNT yarn. The Young's moduli of these yarns were ~57 GPa and ~7.6 GPa for the chemically and electrochemically prepared PPy–CNT yarns, respectively. The significant increase in modulus over the pristine CNT yarn is consistent with the PPy forming inside the yarn and acting to bind the MWNT bundles together in the case of the chemically prepared PPy–CNT yarn. In contrast, the electrochemically developed PPy–CNT yarn exhibited a significantly lower modulus than the chemically developed PPy–CNT yarn but similar to the 2-ply pristine CNT yarn. Since the electrochemically prepared PPy has little effect on the CNT yarn modulus, it is likely that little PPy forms within the CNT yarn pores. Electrochemical polymerization appears to occur preferentially on the surface of the yarn. As such, the PPy deposited electrochemically does not alter the internal yarn structure, and the mechanical properties are not significantly affected [37].

Spinning of PEDOT Fibers

Okuzaki and Ishihara reported the first study on fabrication of conducting microfibers of PEDOT doped with poly(4-styrene sulfonate) using a wet-spinning technique [38]. The effects of spinning conditions on changes in the diameter and

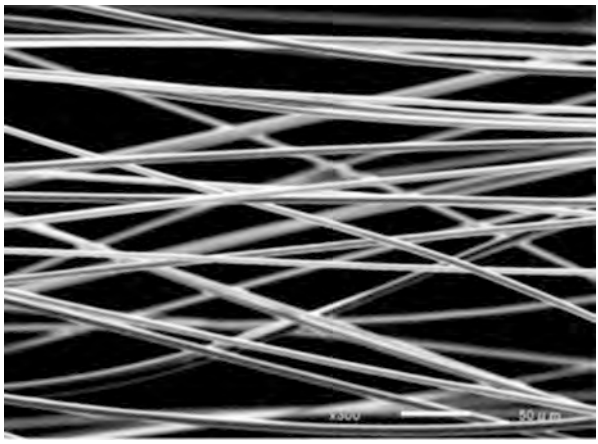

Fig. 18 SEM images of PEDOT–PSS fibers fabricated by wet spinning (Reprinted from Ref. [39] with permission from Elsevier)

electrical conductivity as well as the microstructure and mechanical properties of the resulting fibers have been investigated. The PEDOT–PSS microfibers were fabricated via wet-spinning process where PEDOT–PSS aqueous solution was extruded into an acetone coagulation bath through a single-hole spinneret with different inner diameters of 180, 260, 340, and 410 μm. The resulting microfiber was continuously wound on a winding spool. Young's modulus, tensile strength, and elongation at break for the microfiber were found to be 1.1 GPa, 17.2 MPa, and 4.3 %, respectively. The electrical conductivity of the PEDOT–PSS fiber was 0.1 S cm^{-1}. Later Okuzaki and co-workers [39] also reported the highly conductive microfibers made of PEDOT–PSS were fabricated by wet spinning and subsequent dip treatment in ethylene glycol (Fig. 18). The as-spun fiber conductivity ranged from 11 to 74 S cm^{-1}, depending on the commercial source of the PEDOT–PSS employed. An improvement in electrical conductivity was demonstrated by incorporating a post-spinning treatment, which involved immersing the fiber into an ethylene glycol (EG) bath, followed by annealing at 160 °C for 30 min. This two-step treatment resulted in a 6–17-fold increase in conductivity (from 195 to 467 S cm^{-1}), accompanied by a 25 % increase in tensile strength after drying (from 94 to 130 MPa). The higher conductivity was explained by removal of insulating PSS from the surface of the PEDOT–PSS grains and crystallization of PEDOT, which led to the formation of large numbers of higher conductive grains that enhanced the transport of charge carriers in the microfiber [39].

Recently, Wallace and co-workers [40, 41] have fabricated the wet-spun PEDOT–PSS fiber with and without single-walled carbon nanotube (SWNT). They have developed a simplified wet-spinning process for the production of continuous PEDOT–PSS fibers. They reported that use of isopropanol as a coagulation bath significantly decreases the coagulation rate during spinning, allowing for an improved ordering process for the PEDOT chains during fiber coagulation. Several PEDOT–PSS non-solvents were investigated as a coagulation bath but only acetone and isopropanol (IPA) produced continuous fiber lengths. Acetone and IPA

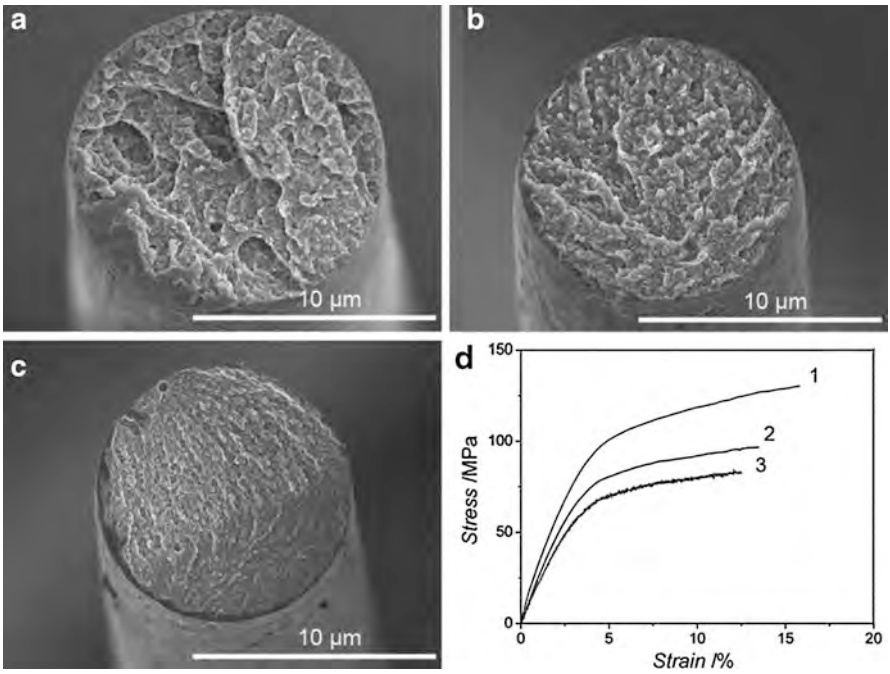

Fig. 19 Representative SEM images of PEDOT–PSS fiber spun into (**a**) acetone, (**b**) isopropanol (IPA), and (**c**) PEDOT–PSS–PEG fiber spun into IPA. (**d**) Representative stress–strain curves for (1) PEDOT–PSS fiber prepared using isopropanol coagulation bath, (2) PEDOT–PSS–PEG fiber spun into IPA, and (3) PEDOT–PSS fiber spun into acetone (Reprinted from Ref. [40] with permission from Wiley)

both acted to dehydrate the PEDOT–PSS spinning formulations at a rate most suited to the vertically oriented fiber spinning setup. In this setup, the spinning solution was extruded from the top and into a vertical glass column containing the coagulation bath. As the spinning solution exited the spinneret, the dehydration process occurred gently after which it continued to solidify and be stretched by gravity. Uniform fibers with circular diameter were obtained from acetone and IPA coagulation baths, but they differed in diameter, even when the same spinning formulation and injection rate were used (Fig. 19a–c). Fibers prepared from acetone bath always resulted in a larger fiber diameter (15 μm) and had bigger internal pores than those prepared from IPA bath (12 μm). The representative stress–strain curves for each PEDOT–PSS fiber clearly show that IPA was the most appropriate coagulation bath (Fig. 19d). PEDOT–PSS fibers prepared with IPA displayed the highest mechanical properties achieving modulus, strength, and breaking strain, of 3.3 GPa, 125 MPa, and 15.8 %, respectively. Conductivity enhancement of PEDOT–PSS fibers up to 223 S cm^{-1} has been obtained when these fibers are exposed to ethylene glycol as a post-synthesis processing step. In a new spinning approach, it is shown that by employing a spinning formulation consisting of an aqueous blend of PEDOT–PSS and poly(ethylene glycol), the need for

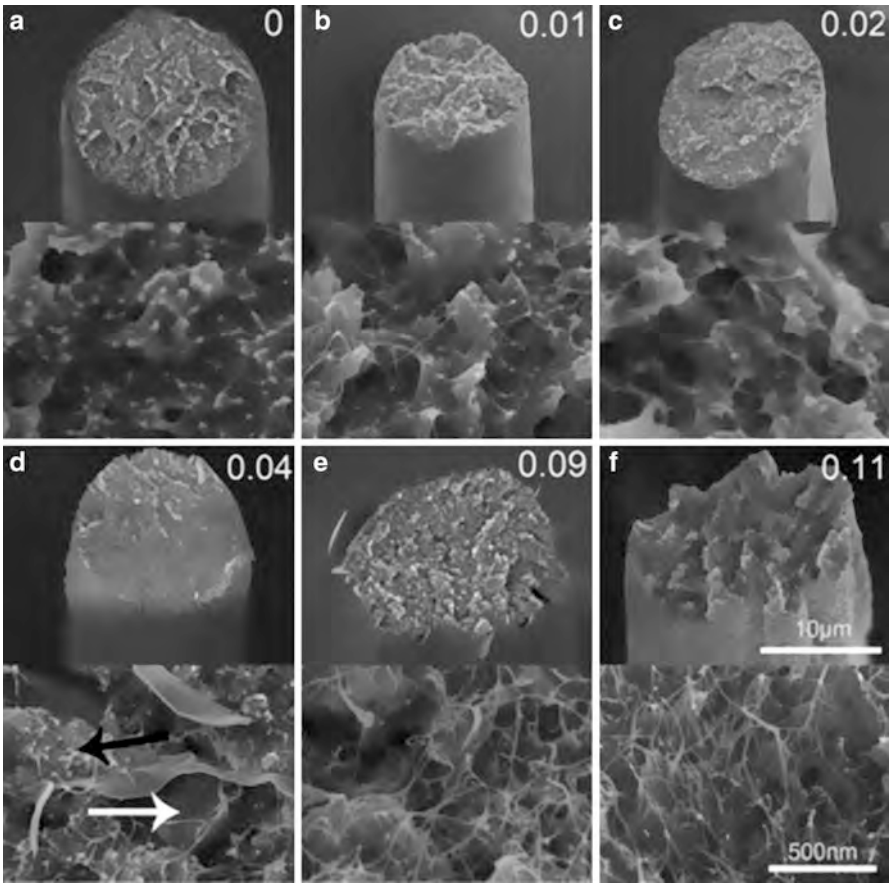

Fig. 20 Cross section of tensile fractured PEDOT–PSS–SWNT composite fibers at low and high magnifications showing transformations of shape and microstructure of PEDOT–PSS composite fiber upon the addition of SWNT at various loadings. Volume fraction of SWNT indicated on each pair of images. *White* and *black arrows* at D show PEDOT–PSS- and SWNT-rich region, respectively. Scale bars are similar for all images in each series [41] (Reproduced by permission of The Royal Society of Chemistry http://pubs.rsc.org.ezproxy.uow.edu.au/en/content/articlehtml/2012/jm/c2jm35148j)

post-spinning treatment with ethylene glycol was eliminated. With this approach, 30-fold conductivity enhancements from 9 to 264 S cm^{-1} were achieved with respect to an untreated fiber. The one-step PEDOT–PSS–PEG fiber approach represents a significant advantage over the post-EG-treated PEDOT–PSS fibers. Fiber posttreatment by EG requires the use of a second EG bath, which weakens the fiber, making it prone to breaking prior to further drying. Wallace and co-workers [41] also have investigated the effects of spinning formulations and processing parameters on the formation and subsequent properties of PEDOT–PSS–SWNT composite fibers (Fig. 20). The method used to obtain the SWNT, the protocol used

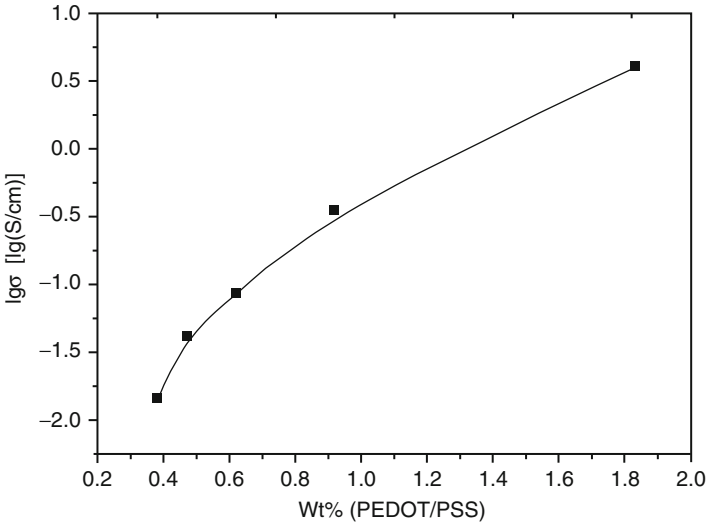

Fig. 21 Relation of the content of PEDOT–PSS and the conductivity (r) of the PEDOT–PSS/PAN composite fibers (Reprinted from Ref. [42] with permission from Wiley)

for addition of SWNT to the PEDOT–PSS, and the loading level employed have been directly correlated to the quality and ease of spinnability of the formulations and to the mechanical and electrical properties of the resultant fibers. They reported that utilizing highly exfoliated SWNT and PEDOT–PSS to obtain wet-spinnable composite formulations at various nanotube volume fractions. The addition of only 0.02 volume fractions of aggregate-free and individually dispersed SWNT resulted in a significant enhancement of modulus, tensile strength, and electrical conductivity of PEDOT–PSS–SWNT composite fibers to 5.2 GPa, 200 MPa, 450 S cm^{-1}, respectively.

Liu and co-workers [42] had developed composite conductive fibers based on poly(3,4-ethylenedioxythiophene)–polystyrene sulfonic acid blended with polyacrylonitrile (PAN) via a conventional wet-spinning process. The influences of the PEDOT–PSS content on the electrical conductivity, thermal stability, and mechanical properties of the composite fibers were investigated. They found that there were no obvious rules between the PEDOT–PSS content and the mechanical performance. For pure PAN, the breaking strength, elongation at break, and initial modulus were 0.60 cN/dtex, 50 %, and 5.06 cN/dtex, respectively. When the content of PEDOT–PSS was 1.83 wt %, the breaking strength, elongation at break, and initial modulus were 0.36 cN/dtex, 36.73 %, and 3.32 cN/dtex, respectively. The relationship of the content of PEDOT–PSS to the conductivity of the PEDOT–PSS/PAN composite fibers is shown in Fig. 21. The electrical conductivity of the PEDOT–PSS/PAN composite fibers increased as the content of PEDOT–PSS increased. The highest value of conductivity was up to 5.0 S cm^{-1} when the PEDOT–PSS content was 1.83 wt%. This could be attributed to the conductive

mechanism of the conductive fibers. As a matter of fact, many factors, including the doped extent of PEDOT, the dispersion and distribution of PEDOT in the polymer matrix, and the measuring technique, influenced the conductivity of the blends. In this case, as the content of PEDOT–PSS increased, the effective conductive paths of the conductive fibers also increased, and this made the conductivity rise. In this method, the content of the PEDOT–PSS in the whole composite fiber was only 1.83 %, but its conductivity was as high as 5.0 S cm^{-1} [42].

Applications of Conducting Polymer Fibers

Conducting polymers are well suited to a range of applications including battery electrodes [43], gas sensors [44], biological sensors [45], ion sieving, corrosion protection [46], microwave shielding [47, 48], e-textiles, and artificial muscles [49, 50]. Certain applications for conducting polymers would benefit from a solution-processable form of the polymers. For example, soluble PPy has been proposed [35] for semitransparent bilayer electrodes, electrically conducting blends with conventional polymers, transparent anode or hole transport layer in polymer LED, and a reflective bistable cholesteric-polymer dispersion display. Conducting polymer fibers are ideally suited and can be readily utilized as electronic textiles. Figures 22 and 23 show some applications for actuating and sensing textiles using conducting polymers. Application of conducting polymer fibers as mechanical actuators ("artificial muscles") has illustrated some of the benefits of the fiber geometry. The first conducting polymer fibers used as artificial muscles were short hollow PPy fibers prepared by electrochemical polymerization on a wire electrode with

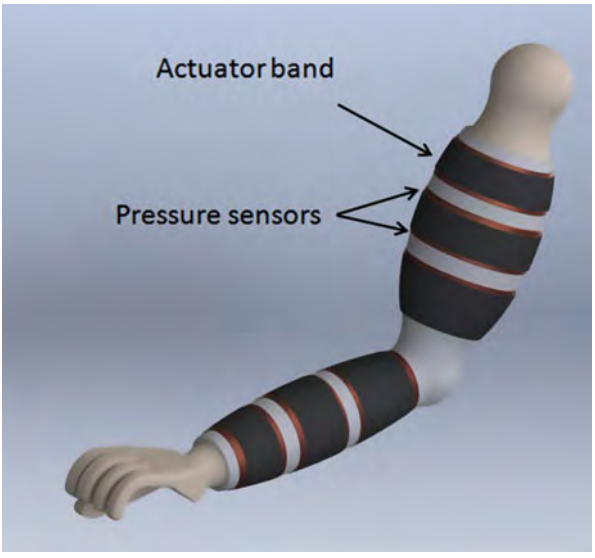

Fig. 22 The Lymph Sleeve will be developed using lightweight actuating fabric that will detect swelling and then respond by "squeezing" the arm to enhance lymph flow [52]

Fig. 23 Conducting textiles as a wearable sensor device for monitoring and manipulating human movement (Reprinted from Ref. [53] with permission from Wiley)

subsequent removal of the inner electrode [51]. It was found that the method also allowed the incorporation of a thin, helically wound platinum wire within the PPy fiber wall. The platinum wire greatly improved the electroactivity of the PPy fiber an increased the actuation strain and strain rate by a factor of 4. Similarly, the inclusion of CNTs (2 % w/w) into PAni fibers increased conductivity and electroactivity resulting in a doubling of actuation strain [22]. Mechanical drawing of the neat and CNT-reinforced PAni fibers further increased conductivity, but with a small decrease in actuation strain due to the highly aligned molecular structure. These fibers, however, were able to operate against very large external stresses, in excess of 100 MPa, or more than three times higher than other conducting polymer artificial muscles [22].

Summary

The development of materials and methods for preparing conducting polymer fibers is an important enabling step in the application of these materials in smart textiles and other applications. Wet spinning has been the preferred method for preparing conducting polymer fibers, although some short fibers have also been fabricated by electrochemical polymerization. Due to the intractable nature of many conducting polymers, the first stage of development has involved methods for preparing conducting polymer solutions. PAni is readily soluble in its emeraldine base and leucoemeraldine base forms and can be directly spun into fibers. However, these fibers were inferior in properties due to the subsequent doping step. Wet spinning of conducting PAni emeraldine salt could be achieved from concentrated sulfuric acid; however, best results were obtained by using large dopant ions that rendered the ES soluble in organic solvents. Fibers prepared from such solutions could be further improved by mechanical drawing and incorporation of carbon nanotubes. Similar techniques have been applied to PPy, with fibers prepared using solubilizing dopants

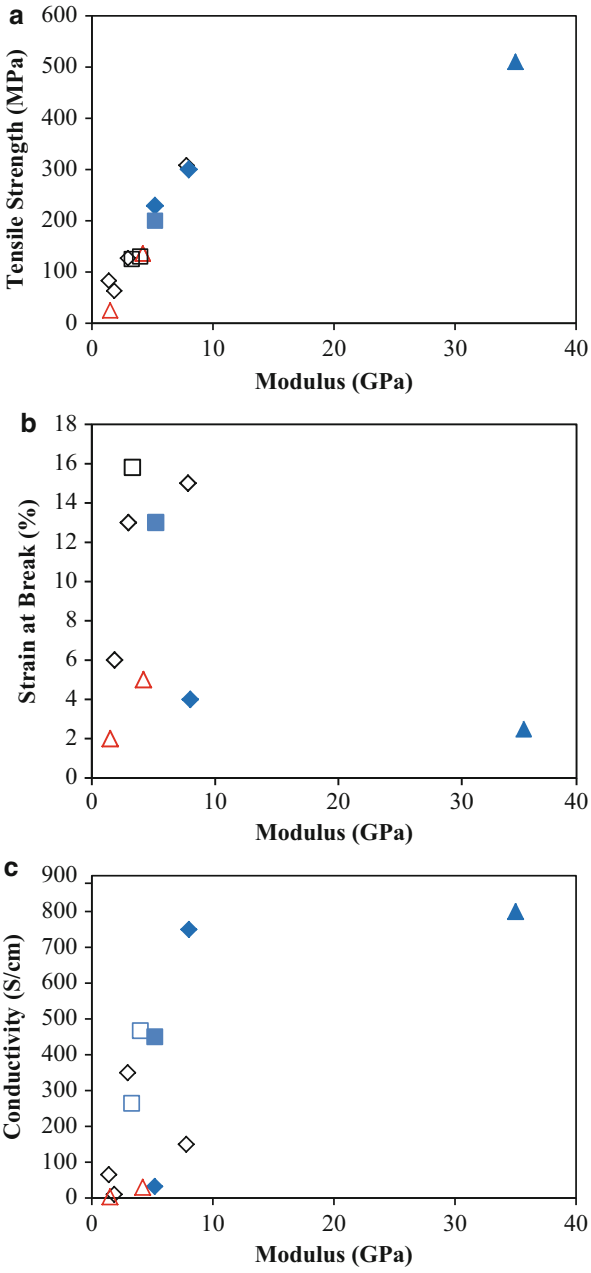

Fig. 24 Mechanical and electrical properties of conducting fibers: (**a**) tensile strength, (**b**) elongation at break, and (**c**) electrical conductivity, all shown with Young's modulus. *Filled symbols* show data for conducting polymer–CNT fibers and unfilled symbols are for neat conducting polymer fibers of PAni (*diamonds*), PPy (*triangles*), and PEDOT (*squares*)

and with or without CNTs. Polythiophene is readily available in a water-soluble form as PEDOT doped with PSS. Again, this polymer could be wet-spun into fibers.

The various material compositions and processing techniques have generated conducting polymer fibers with a wide range of properties. Figure 24a–c charts and

summarizes the key mechanical and electronic properties of conducting polymer fibers as described in this chapter. These charts show that the greatest improvements in tensile strength, Young's modulus, and electrical conductivity have been achieved through the addition of carbon nanotube filler to make composite fibers. However, the addition of CNTs also causes a decrease in elongation at break. In fact, all conducting polymer fibers are quite brittle with elongations less than 20 % at break. This brittleness is in contrast to common textile fibers, such as nylons and polyesters, and improving the toughness of conducting polymer fibers remains as the biggest challenge in their further development.

References

1. Wallace GG et al (2008) Conductive electroactive polymers: intelligent polymer systems, 3rd edn. CRC Press, Boca Raton
2. Chiang CK et al (1978) Synthesis of highly conducting films of derivatives of polyacetylene, (CH)x. J Am Chem Soc 100(3):1013–1015
3. Chiang CK et al (1977) Electrical conductivity in doped polyacetylene. Phys Rev Lett 39(17):1098
4. Shirakawa H et al (1997) Synthesis of electrically conducting organic polymers: halogen derivatives of polyacetylene, (CH)x. J Chem Soc Chem Commun 16:578–580
5. Cho SH, Song KT, Lee JY (2007) In: Skotheim TA, Reynolds JR (eds) Handbook of conducting polymers, 3rd edn, Conjugated polymers theory, synthesis, properties and characterization. CRC press, Boca Raton, pp 8.1–8.87
6. Angelopoulos M et al (1988) Polyaniline: solutions, films and oxidation state. Mol Cryst Liq Cryst 160:151–163
7. Jain R, Gregory RV (1995) Solubility and rheological characterization of polyaniline base in *N*-methyl-2-pyrrolidinone and *N*, *N*'-dimethylpropylene urea. Synth Met 74(3):263–266
8. Pomfret SJ et al (1999) Advances in processing routes for conductive polyaniline fibres. Synth Met 101(1–3):724–725
9. Pomfret SJ et al (2000) Electrical and mechanical properties of polyaniline fibres produced by a one-step wet spinning process. Polymer 41(6):2265–2269
10. Cao Y, Qiu J, Smith P (1995) Effect of solvents and co-solvents on the processability of polyaniline: I. solubility and conductivity studies. Synth Met 69(1–3):187–190
11. Cao Y, Smith P, Heeger AJ (1992) Counter-ion induced processability of conducting polyaniline and of conducting polyblends of polyaniline in bulk polymers. Synth Met 48(1):91–97
12. Wallace GG, Kane-Maguire LAP (2002) Manipulating and monitoring biomolecular interactions with conducting electroactive polymers [Review]. Adv Mater 14(13–14):953
13. Campbell TE, Hodgson AJ, Wallace GG (1999) Incorporation of Erythrocytes into Polypyrrole to Form the Basis of a Biosensor to Screen for Rhesus (D) Blood Groups and Rhesus (D) Antibodies. Electroanal 11(4):215–222
14. Gooding JJ et al (2004) Electrochemical modulation of antigen-antibody binding. Biosens Bioelectron 20(2):260–268
15. Smela E, Ingamas O, Lundstrom I (1995) Controlled folding of micrometer-size structures. Science 268(5218):1735–1738
16. Smela E, Kallenbach M, Holdenried J (1999) Electrochemically driven polypyrrole bilayers for moving and positioning bulk micromachined silicon plates. IEEE J Microelectromech Syst 8(4):373–383
17. Jager EWH et al (2002) The cell clinic: closable microvials for single cell studies. Biomed Microdevices 4(3):177–187

18. Kontturi K, Pentti P, Sundholm G (1998) Polypyrrole as a model membrane for drug delivery. J Electroanal Chem 453(1–2):231–238
19. Kontturi K et al (1998) Preparation and properties of a pyrrole-based ion-gate membrane as studied by the EQCM. Synth Met 92(2):179–185
20. Sato M-A, Tanaka S, Kaeriyama K (1986) Electrochemical preparation of conducting poly (3-methylthiophene): comparison with polythiophene and poly(3-ethylthiophene). Synth Met 14(4):279–288
21. Andreatta A et al (1988) Electrically-conductive fibers of polyaniline spun from solutions in concentrated sulfuric acid. Synth Met 26(4):383–389
22. Mottaghitalab V (2006) Development and characterisation of polyaniline – carbon nanotube conducting composite fibres. University of Wollongong, Wollongong
23. Chacko AP et al (1997) Viscoelastic characterization of concentrated polyaniline solutions: new insights into conductive polymer processing. Synth Met 84(1–3):41–44
24. Gregory RV et al (2012) Synthesis and characterization of high molecular weight polyaniline for organic electronic applications. Polym Eng Sci 52(8):1811
25. Hsu CH, Cohen JD, Tietz RF (1993) Polyaniline spinning solutions and fibers. Synth Met 59 (1):37–41
26. Pomfret SJ et al (1998) Inherently electrically conductive fibers wet spun from a sulfonic acid–doped polyaniline solution. Adv Mater 10(16):1351–1353
27. Hsu CH et al (1999) High tenacity, high modulus conducting polyaniline composite fibers. Synth Met 101(1–3):677–680
28. Hsu C-H, Vaca-Segonds P, Epstein AJ (1991) Polyaniline/PPD-T fibers. Synth Met 41(3):1005–1008
29. Zhang Q et al (2001) Morphology of conductive blend fibers of polyaniline and polyamide-11. Synth Met 123(3):481–485
30. Zhang Q et al (2002) Preparation and properties of conductive polyaniline/poly-omega-aminoundecanoyle fibers. J Appl Polym Sci 85(7):1458–1464
31. Mottaghitalab V, Spinks GM, Wallace GG (2006) The development and characterisation of polyaniline – single walled carbon nanotube composite fibres using 2-acrylamido-2 methyl-1-propane sulfonic acid (AMPSA) through one step wet spinning process. Polymer 47(14):4996–5002
32. Mottaghitalab V, Spinks GM, Wallace GG (2005) The influence of carbon nanotubes on mechanical and electrical properties of polyaniline fibers. Synth Met 152(1–3):77–80
33. Foroughi J, Spinks GM, Wallace GG (2010) Nanotechnology and Conducting Polymer Fibre: Towards the Development of Nano-Structured Conducting Polymers and Nano-Composite Fibres. Lambert Academic Publishing, Saarbrucken, Germany
34. Foroughi J et al (2008) Production of polypyrrole fibres by wet spinning. Synth Met 158(3–4):104–107
35. Foroughi J, Spinks GM, Wallace GG (2009) Effect of synthesis conditions on the properties of wet spun polypyrrole fibres. Synth Met 159(17–18):1837–1843
36. Foroughi J, Spinks GM, Wallace GG (2011) A reactive wet spinning approach to polypyrrole fibres. J Mater Chem 21(17):6421–6426
37. Foroughi J et al (2012) Preparation and characterization of hybrid conducting polymer-carbon nanotube yarn. Nanoscale 4(3):940–945
38. Okuzaki H, Ishihara M (2003) Spinning and characterization of conducting microfibers. Macromol Rapid Commun 24(3):261–264
39. Okuzaki H, Harashina Y, Yan H (2009) Highly conductive PEDOT/PSS microfibers fabricated by wet-spinning and dip-treatment in ethylene glycol. Eur Polym J 45(1):256–261
40. Jalili R et al (2011) One-step wet-spinning process of poly(3,4-ethylenedioxythiophene): poly (styrenesulfonate) fibers and the origin of higher electrical conductivity. Adv Funct Mater 21(17):3363–3370
41. Jalili R, Razal JM, Wallace GG (2012) Exploiting high quality PEDOT:PSS-SWNT composite formulations for wet-spinning multifunctional fibers. J Mater Chem 22(48):25174–25182

42. Liu Y, Li X, Lü JC (2013) Electrically conductive poly(3,4-ethylenedioxythiophene)–polystyrene sulfonic acid/polyacrylonitrile composite fibers prepared by wet spinning. J Appl Polym Sci 130:370–374
43. Kim JH, Sharma AK, Lee YS (2006) Synthesis of polypyrrole and carbon nano-fiber composite for the electrode of electrochemical capacitors. Mater Lett 60(13–14):1697
44. Hacarlioglu P, Toppare L, Yilmaz L (2003) Polycarbonate-polypyrrole mixed matrix gas separation membranes. J Membr Sci 225(1–2):51
45. Walkiewicz S, Michalska A, Maksymiuk K (2005) Sensitivity and selectivity of polypyrrole based AC-amperometric sensors for electroinactive ions – frequency and applied potential influence. Electroanalysis 17(14):1269
46. Han G et al (2005) Electrodeposition of polypyrrole/multiwalled carbon nanotube composite films. Thin Solid Films 474(1–2):64
47. Kim MS et al (2002) PET fabric/polypyrrole composite with high electrical conductivity for EMI shielding. Synth Met 126(2–3):233
48. Yavuz O et al (2005) Polypyrrole composites for shielding applications. Synth Met 151(3):211
49. Spinks GM et al (2009) Conjugated polymer actuators: fundamentals. In: Biomedical applications of electroactive polymer actuators. Wiley, Chichester, pp 193–227
50. Foroughi J, Spinks GM, Wallace GG (2011) High strain electromechanical actuators based on electrodeposited polypyrrole doped with di-(2-ethylhexyl)sulfosuccinate. Sens Actuators B 155(1):278–284
51. Ding J et al (2003) Use of ionic liquids as electrolytes in electromechanical actuator systems based on inherently conducting polymers. Chem Mater 15(12):2392–2398
52. Spinks G (2012) Microdevices muscle up. Australas Sci 19–21, Australia
53. Wallace GG et al (2012) Organic conducting polymers. In: Organic bionics. Wiley-VCH, Weinheim, pp 81–112

Conductive Polymer Fibers for Sensor Devices

3

Mutsumi Kimura

Contents

Conductive Fibers 64
Wet Spinning of PEDOT:PSS/PVA Blended Fibers 66
Fabrication of Textile-Based Sensors for Heartbeat Detection 69
Conductive Nanofibers 70
Continuous Electrospinning of P3HT 72
Electric and Mechanical properties of P3HT Nanofiber Assemblies 73
Tactile Sensor 74
Summary 76
References 76

Abstract

This chapter introduces the sensor applications of conductive fiber assemblies of poly(3,4-ethylenedioxythiophene) doped with poly(4-styrene sulfonate) (PEDOT:PSS) and regioregular poly(3-hexylthiophene) (P3HT). The scalable conductive multifilament of PEDOT:PSS and poly(vinyl alcohol) (PVA) was fabricated by a coagulation of spinning dope solution in cold methanol. The multifilament was composed of uniform circular fibers with an average diameter of 60 ± 5 μm and showed good enough mechanical properties for textile processes while maintaining electronic conductivity. The foldable textiles based on the PEDOT:PSS/PVA blended fibers worked as flexible electrodes to detect human heartbeats. Uniform P3HT nanofibers are obtained through a continuous electrospinning process using a homogeneous solution of high-molecular-weight P3HT. The P3HT nanofibers are oriented by collecting them on a rotating drum collector. Small physical inputs into the self-standing P3HT

M. Kimura (✉)
Division of Chemistry and Materials, Faculty of Textile Science and Technology, Shinshu University, Ueda, Nagano, Japan
e-mail: mkimura@shinshu-u.ac.jp

© Springer Science+Business Media Singapore 2015

X. Tao (ed.), *Handbook of Smart Textiles*,
DOI 10.1007/978-981-4451-45-1_9

nanofiber assemblies give rise to additional contact among neighboring nanofibers, which results in a decreased contact resistance in the directions orthogonal to the nanofiber orientation. The P3HT nanofiber assemblies could detect pressure changes and bending angles by monitoring the resistance changes, and the sensor responses were repeatable. The organic-conductive fibers can be a platform for lightweight wearable electronics.

Keywords
Conductive polymer • PEDOT:PSS • Wet spinning • Textile electrode • Heartbeat • Electrospinning • P3HT • Nanofiber • Doping • Tactile Sensor

Conductive Fibers

When miniaturized electronic devices are embedded on one-dimensional conducting fibers, the fibers will have the ability to sense, react, interact, and move [1–7]. Furthermore, multifunctional wearable systems can be fabricated by assembling each functional fiber component in the textile platform through conventional textile processing techniques including weaving, knitting, crocheting, and knotting (Fig. 1). These textile devices can monitor your health, guard you in case of danger, and generate ambient energy by conversion from light, vibration, and temperature difference.

Many efforts have been devoted to develop conducting fibers including metal plating, deposition of metal layers, and coating of conductive materials as metal nanoparticles and carbon nanotubes [8–11]. The deposition of conductive thin layers onto fiber surface has the disadvantage of being expensive, and the fibers are heavy

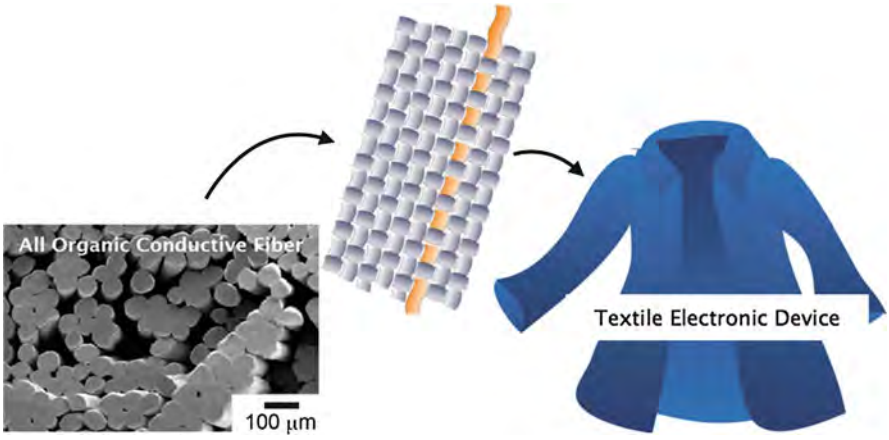

Fig. 1 Smart textile devices made of organic-conductive fibers (© 2014 WILEY-VCH Verlag GmbH & Co. KGaA, Weinheim)

and brittle. Since the discovery of electronic conductivity for organic polymers [12], organic-conductive polymers have been paid special attention as active components for organic solar cells, printed electronic circuits, organic light-emitting diodes, actuators, electrochromism, supercapacitors, and biosensors [13–17].

Conducting fibers made from organic-conductive polymers such as polyaniline and poly(3,4-ethylenedioxythiophene)-poly(styrene sulfonate) (PEDOT:PSS) have been fabricated to realize textile devices without the use of inorganic materials. Polyaniline was the first conducting polymer to be successfully fabricated into conducting fibers. In 1995, Wang et al. reported the fabrication of polyaniline fibers doped with camphor sulfonic acid from the anisotropic liquid-crystalline solutions of *m*-cresol [18]. The polyaniline fiber was also spun from solution of polyaniline doped with 2-acrylamido-2-methyl-1-propanesulfonic acid in dichloroacetic acid by using various coagulation solutions reported by Pomfret et al. [19, 20]. When the as-spun fibers were cold drawn to extensions of >500 %, the electronic conductivity was enhanced from 70–150 to 1,995 S/cm. Bowman and Mattes succeeded a scalable production of polyaniline fibers prepared from a high-molecular-weight and defect-free polyaniline by continuous wet-spinning techniques [21]. The polyaniline filament was marked as Panion^{TM}.

While polyaniline fibers require an acidic environment to keep their conductivity, PEDOT:PSS fibers display good thermal and environmental stability. In 2003, Okuzaki et al. succeeded in fabricating continuous PEDOT:PSS fibers with a diameter of ca. 10 μm by a simple wet-spinning process [22, 23]. The dehydration of aqueous PEDOT:PSS solution into acetone produced the continuous fibers, and the resulted as-spun fibers displayed low electronic conductivities due to the their poor crystallinity. Recently, Razal and Wallace et al. reported the one-step fiber wet-spinning process for PEDOT:PSS fibers by mixing PEDOT:PSS with poly (ethylene oxide)s (PEO) [24]. The PEDOT:PSS fibers prepared from an aqueous blend solution of PEDOT:PSS and PEO exhibited a good electronic conductivity above 200 S/cm without post-spinning treatment with ethylene glycol. With these approaches, aqueous dispersion of PEDOT:PSS colloidal particles were coagulated by the dehydration with acetone or isopropanol. However, we found that the rates of fiber formation/solidification from aqueous dispersion of PEDOT:PSS were very slow, and the resultant PEDOT:PSS fibers showed poor mechanical properties due to the formation of internal pores.

The blending of PEDOT:PSS with other polymers has been investigated to improve the mechanical properties of films. Poly(vinyl alcohol)s (PVAs) have been used as a matrix component for the blended PEDOT:PSS films, and the blended films showed a high tensile strength and good flexibility. Hopkins and Reynolds reported the dependence of electrical conductivity of blended PEDOT:PSS/PVA films on the weight fraction of PEDOT:PSS in the insulating PVA matrix [25]. Chen et al. found that electrical conductivity was enhanced by adding *N*-methyl-2-pyrrolidinone (NMP) to the blended films [26]. Although blending PEDOT:PSS with polymer hosts has been investigated for films, PEDOT:PSS blended fibers have not been reported.

This chapter presents on a continuous wet-spinning process for blend fibers made from PEDOT:PSS and PVA. Uniform PEDOT:PSS/PVA multifilament fibers were fabricated by optimizing the wet-spinning process including a blend ratio between PEDOT:PSS and PVA, molecular weights of PVA, and coagulation bath. The multifilament fibers showed good enough mechanical properties for textile processes while maintaining electronic conductivity. The fabrication of textile sensors for detecting human heartbeats and fibrous actuators by using conductive PEDOT:PSS/PVA fibers were demonstrated.

Wet Spinning of PEDOT:PSS/PVA Blended Fibers

High-tenacity and high-modulus PVA fibers have been produced by the "gelation-spinning" from DMSO solution of PVA and cold methanol coagulation bath [27]. When the DMSO solution of PVA is extruded into cold methanol, the gel of the spinning dope is formed through liquid-liquid phase separation (spinodal decomposition) and the formed microcrystals of PVA act as cross-linking points in the gels. The mechanical properties of PVA fibers are greatly influenced by the concentration of PVA and temperature of the coagulation bath for the gelation-spinning process. The mechanical properties of PEDOT:PSS fibers were expected to be improved through the gelation-spinning process from the blended DMSO solution of PEDOT:PSS and PVA.

PEDOT:PSS was prepared by polymerizing 3,4-ethylenedioxythiophene (EDT) in the presence of poly(styrene sulfonic acid) (PSS). The combination of EDT and PSS resulted in a water-soluble polyelectrolyte system with good film-forming properties. Commercially available PEDOT:PSS is supplied as an aqueous dispersed solution with a low concentration of around 1.3 wt%. Solvent exchange of PEDOT:PSS dispersion from water to DMSO is difficult, and the continuous spinning requires the optimization of solution viscosity. To avoid these limits of PEDOT:PSS formulation, PEDOT:PSS pellets (ORGACON^{TM} Dry) were used for the preparation of the spinning dopes. The PEDOT:PSS pellets were re-dispersed in DMSO by using a high-speed homogenizer, and PVA was dissolved in the DMSO solution of PEDOT:PSS at 80 °C by stirring. The viscosity of a 10.0 wt% dope solution containing 4.0 wt% PEDOT:PSS and 6.0 wt% PVA (DP = 4,000, saponification degree >99.7 %) was 4,400 cps at 80 °C as determined by a rotational viscometer. The concentration of solids in the spinning dope solution varied from 5.0 to 10.0 wt% and found that the viscosity of a 10.0 wt% solution provided the most spinnable formulation for the continuous spinning process.

The solution was spun with a spinneret containing 30 holes into a cold methanol coagulation bath at 0 °C. The end of the spinneret was just submerged in the coagulation solvent, and the extruded polymer solution was solidified to form continuous fibers within the coagulation bath (Fig. 2). The dope solution formed a gel in the cold coagulation solvent, and the extraction process from the gel occurred gently. After washing with two methanol baths, the resultant fibers were dried by hot air and collected by winding on a spool rotated at 10.8 m/min.

Fig. 2 Photographs of custom-built wet-spinning apparatus for PEDOT:PSS/PVA blended multifilament fiber (© 2014 WILEY-VCH Verlag GmbH & Co. KGaA, Weinheim)

The winding speeds in the spinning process were gradually increased to maintain continuous stretching and tensioning of the filament. The 10 wt% blended PEDOT:PSS/PVA dope solution spun continuously until the end of solution supply, and the multifilament PEDOT:PSS/PVA fibers were obtained. Figure 3 shows an SEM image of PEDOT:PSS/PVA fibers. The resulting fibers displayed a uniform circular diameter with an average diameter of 60 ± 5 μm, and the fibers did not contain internal pores. The circular diameter of fibers suggests the homogeneous coagulation without the formation of a skin layer. The linear mass density of multifilament PEDOT:PSS/PVA fibers was determined to be 1,177 dtex/30f (Table 1). While the as-spun PVA fibers could be drawn to about 25 times their initial length, the drawing ratio of the blended fibers was less than 2 times. The tenacity of blended fibers was 0.26 ± 0.2 cN/dtex, which was much lower than that of drawn PVA fibers. The lower tenacity and drawing ratio of blended fibers indicate that the dispersion of PEDOT:PSS in the PVA matrix prevents the crystallization of PVA.

When two electrodes were drawn at both ends of a 15 cm blended fiber with silver paste, the PEDOT:PSS/PVA blended fiber revealed a linear relationship in the current-voltage characteristics and was noted to have a consistent electronic conductivity of 7 ± 1 S/cm. This conductivity of the blended fibers was higher than that of casting films of PEDOT:PSS/PVA blends with the same composition ratio between PEDOT:PSS and PVA reported by Chen et al. [26]. This improvement in conductivity may be attributed to the alignment of PEDOT:PSS polymer chains along with the fiber axis. The fiber morphology and conductivity after standing at 80 °C and 80 % RH for 1 week remained unaltered, suggesting excellent durability for PEDOT:PSS/PVA blended fibers.

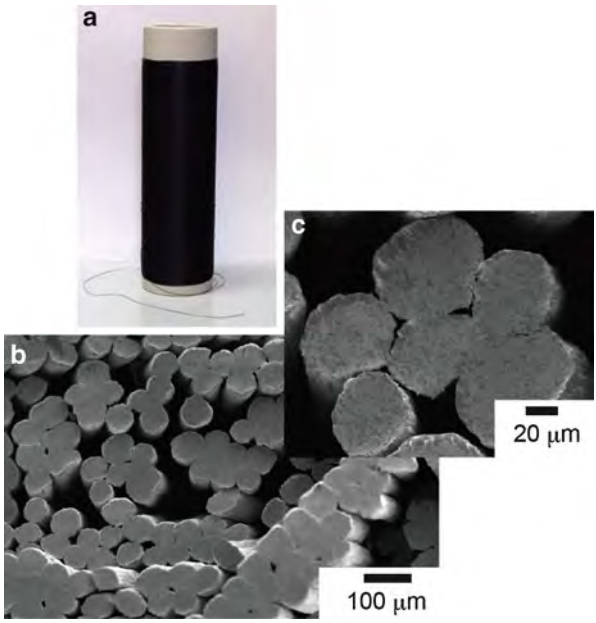

Fig. 3 (**a**) Photograph and (**b**, **c**) SEM images of PEDOT:PSS/PVA blended multifilament fibers (© 2014 WILEY-VCH Verlag GmbH & Co. KGaA, Weinheim)

Table 1 Summary of spinning conditions, mechanical and electrical properties of PEDOT:PSS/PVA blended fibers

1. Spinning dope solution					
Fiber	PEDOT:PSS (wt%)	PVA (wt%)	Viscosity (cps)[a]	Spinneret	Feed rate (ml/min)
1	4.0	6.0	4,400	30[b] (0.2–0.4[c])	11.0
2	4.2	2.8	3,700	10[b] (0.2–0.4[c])	3.0
2. Spinning condition					
Fiber	Coagulation bath	Spinning speed[d] (m/min)	Dry (°C)	Winding speed[e] (m/min)	
1	Methanol (0 °C)	7.6	90	10.8	
2	Methanol (3 °C)	2.6	52	3.1	
3. Mechanical and electrical properties					
Fiber	Linear mass density	Tenacity (cN/dtex)	Strain at break (%)	Conductivity (S cm^{-1})	
1	1,177 dtex/30f	0.26 ± 0.2	134.7 ± 10	7 ± 1	
2	595 dtex/10f	0.16 ± 0.2	261.5 ± 15	20 ± 1	

[a]Determined by rotational viscometer at 80 °C
[b]Hole number
[c]Hole diameter-length of spinneret channel
[d]Spinning speed in coagulation bath
[e]Winding speed at spool

To investigate the dependence of electronic conductivity on the blend ratio, the blended fiber with a higher composition ratio of PEDOT:PSS was prepared. Since the PEDOT:PSS pellets could not disperse into DMSO above 4.2 wt%, the concentration of solids in the spinning dope solution was limited to 7.0 wt% at a 60:40 composition ratio between PEDOT:PSS and PVA. The spinning from the 7.0 wt% dope solution containing 4.2 wt% PEDOT:PSS and 2.8 wt% PVA (DP = 4,000) was unstable due to a poor solution viscosity of 1,400 cps. When a higher-molecular-weight PVA (DP = 7,800) was used, the solution viscosity increased to 3,700 cps. Stable and continuous spinning was achieved by using a dope solution containing high-molecular-weight PVA. The electronic conductivity for the 60:40 blended fibers with 71 ± 5 mm diameter was 20 ± 1 S/cm, indicating that the conductivity increased with increasing composition ratio of blended fibers.

Fabrication of Textile-Based Sensors for Heartbeat Detection

The textile electrodes with 27 cm in width and 14 cm in length were fabricated by using PEDOT:PSS/PVA blended fibers as the weft of fabrics (Fig. 4a). The textile electrode involves two perpendicular sets of yarns, and the conductive PEDOT:PSS/PVA blended fibers were interlaced with nonconductive stretchable polyurethane fibers. The conductive fibers were weaved as the weft of fabrics by using a weaving apparatus (Fig. 5). The weft density in the textile electrode was 38 fibers per 1 cm in length. The conductive fibers were not damaged by friction during weaving and repeated exposure to tensile and bending strains. Furthermore, the conductive fiber in the textile exhibited almost the same electronic resistivity as the parent fiber. Thus, the PEDOT:PSS/PVA blended fibers showed good enough mechanical properties for the weaving process while keeping electronic conductivity.

The contraction and relaxation of cardiac muscles causes blood to flow in and out of the heart. During each cardiac cycle, a group of tissues in the heart generates electrical impulses. These electrical impulses can be detected by placing electrodes in specific points in the human body. The conductive fibers inside the textile were connected to an external circuit board to detect an electrocardiogram (ECG) (Fig. 6) [28–31]. When two pieces of textile electrodes were touched with each hand, an ECG signal was obtained as a voltage change in accordance with the heartbeat (Fig. 4b). R-peaks were clearly detected from the ECG signal. The R-peak shows the ending of atrial contraction and the beginning of ventricular contraction. The heart rate obtained by counting the R-peaks agreed with that determined by a commercial plethysmograph applied to a digit of the hand. The heart rate is one of the most frequently measured parameters of the human body and plays an important role in determining an individual health. The foldable textiles based on PEDOT:PSS/PVA blended fibers can work as flexible electrodes to accurately measure heart rate. When textile electrodes are embedded within clothes and gloves, the textile electrodes touching with the human body allow one to measure heart rate in real time.

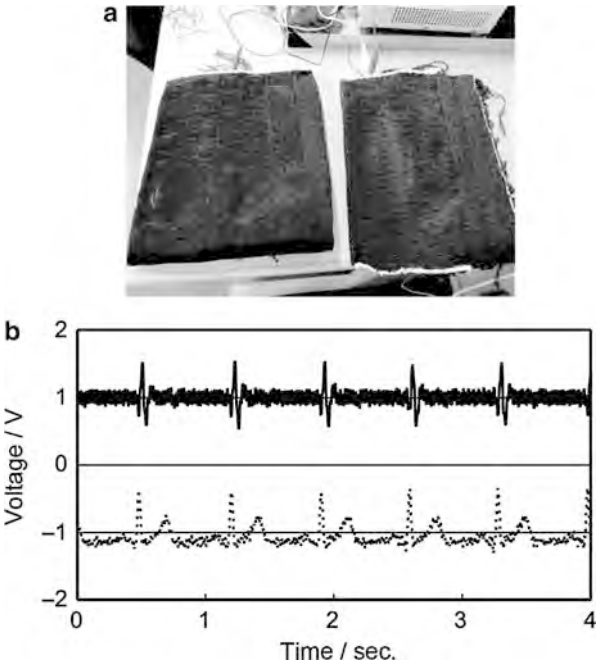

Fig. 4 (**a**) Photograph of two textile electrodes for the detection of ECG. (**b**) ECG spectra detected by textile electrodes (*solid line*) and a commercial plethysmograph applied to a digit of the hand (*dotted line*) (© 2014 WILEY-VCH Verlag GmbH & Co. KGaA, Weinheim)

Fig. 5 Photograph of weaving apparatus for the preparation of textile electrodes using PEDOT:PSS/PVA blended fibers (© 2014 WILEY-VCH Verlag GmbH & Co. KGaA, Weinheim)

Conductive Nanofibers

Biological and artificial materials contain hierarchical structures composed of structural elements possessing different size scales, and the structural hierarchy plays an important role in determining bulk properties [32]. The construction of hierarchical structures based on nano- and microstructures can give rise to

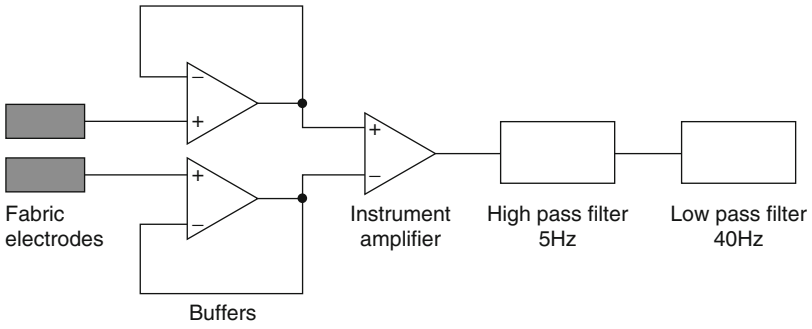

Fig. 6 Block diagram of the circuit for the detection of human heartbeats (© 2014 WILEY-VCH Verlag GmbH & Co. KGaA, Weinheim)

improved or more useful physical properties. Recently, several groups have demonstrated flexible skin-like electronic sensors through the creation of ordered structures on flexible substrates [33–35]. These sensors can detect pressure, strain, and bending changes through the deformation of nano- or microstructures. Assemblies of one-dimensional fibrous structures have also been used as sensing units in the skin-like electronic sensors [36–39]. The assembly of tiny fibers is a useful microstructure for monitoring minute pressure changes.

Regioregular poly(3-alkylthiophene)s (P3HTs) are the most prominent organic semiconductors applied in organic electronics involving organic field-effect transistors and solar cells [40–42]. Nanoscaled P3HT fibers have been fabricating using various techniques, such as self-organization in solutions [43, 44] and electrospinning [45], and their electronic properties have been investigated. Electrospinning is a simple method for producing long and continuous fine fibers with diameters ranging from 10 nm to submicrons. Because of the absence of chain entanglement of rigid rodlike P3HT in a solution, the continuous spinning of uniform P3HT nanofibers requires either mixing with high-molecular-weight insulating polymers or the use of highly concentrated solutions. The mixing of conductive P3HT with nonconductive polymers has resulted in a lower conductivity compared to pure P3HT. To avoid this drawback, core-shell nanofibers embedding P3HT nanofibers have been fabricated by coaxial electrospinning using sacrificial shells [46–49]. To obtain the pure P3HT nanofibers, the shell layers needed to be removed from the core-shell nanofibers, and the residual shell layers around the P3HT nanofibers affected the electronic property. Kotaki et al. fabricated pure P3HT nanofibers by electrospinning from a high-concentrated P3HT solution [50]. They found that the physical entanglement among P3HT backbones in highly concentrated solutions improved the spinnability. However, the resulting P3HT nanofibers possessed nonuniform surface structures, and scalable nanofiber fabrication was impossible due to the instability of the jet initiation process. To overcome these limitations of pure P3HT nanofiber fabrication, a high-molecular-weight regioregular P3HT was used. The molecular weight of this P3HT is about 10 times higher than that of the P3HT used in previous studies. The longer length of

the rigid P3HT backbone would increase the solution viscosity of a low-concentrated solution. This change of solution property may improve the electrospinning stability in the fabrication of pure P3HT nanofibers. An enhancement of the mechanical and electronic properties for high-molecular-weight P3HT nanofibers was also expected. The enhancement is important in terms of developing flexible tactile sensors based on P3HT nanofiber assemblies.

A flexible tactile sensor consisting of aligned P3HT nanofiber assemblies without supporting substrates was developed. Continuous electrospinning of high-molecular-weight P3HT formed self-standing nanofiber assemblies, and the iodine-doped nanofiber assemblies exhibited an anisotropic electronic conductivity along with the fiber axis. The interconnecting of nanofibers within the aligned assemblies caused resistance changes in response to pressure change and bending motion.

Continuous Electrospinning of P3HT

The P3HT nanofiber assemblies were fabricated by the conventional electrospinning process from a homogeneous $CHCl_3$ solution of high-molecular-weight P3HT (Soken Chemical & Engineering; Verazol^{TM} HT-030; $M_w = 300–500$ K g/mol, $M_w/M_n = 2.0–3.5$, regioregularity > 99 %). When low-molecular-weight P3HT (Aldrich; electronic grade, $M_n = 54–75$ K g/mol, $M_w/M_n < 2.5$, regioregularity > 98 %) was dissolved in $CHCl_3$ at 60 °C and then cooled down to room temperature, the color of the solution changed from orange to dark brown, indicating the formation of interpolymer aggregates through strong π-π interaction among rigid P3HT backbones. The formation of self-organized nanofibers in the solution resulted in an unstable electrospinning process. In contrast, the color of the high-molecular-weight P3HT solution remained unaltered after cooling to room temperature. Moreover, the viscosity of this solution at 4.0 w/v % was maintained over 12 h. The P3HT solution at 4.0 w/v% showed a continuous spinning until the end of solution supply at room temperature (8 h at 3.0 ml/h feed rate), and bead-free uniform nanofibers were collected as a nanofiber mats on the target electrode.

Figure 7a shows the SEM images of aligned P3HT nanofiber assemblies as prepared by electrospinning using a rotating drum collector at a fiber take-up velocity of 940 m/min. The resulting P3HT nanofibers displayed a ribbonlike morphology with an average width of 811 ± 115 nm and an average thickness of 61 ± 10 nm. Although substantial misalignment was still observed in the fiber assemblies, the orientation parameter of the nanofiber assemblies estimated by statistical analysis of the direction histogram was found to be 89 %, suggesting that the nanofibers were oriented within ± 20° of the preferred direction. A differential scanning calorimetry (DSC) profile of the P3HT nanofiber showed one endothermic peak at 246 °C, which was attributed to the melting point (Fig. 7b). The observed melting point was slightly lower than that of the powdered sample ($T_m = 257$ °C), and the peak was broader. These differences in DSC seem to indicate the suppression of large-sized crystalline domain formation within the P3HT nanofibers. An X-ray diffraction (XRD) pattern of P3HT nanofibers displayed three diffraction peaks indexed as (100), (200), and (300).

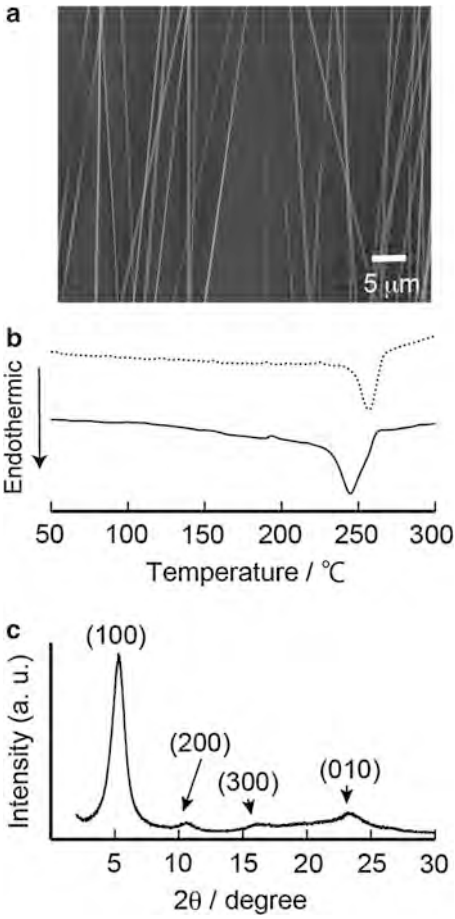

Fig. 7 (**a**) SEM image of aligned electrospun P3HT nanofibers. (**b**) DSC diagrams for the first heating of P3HT nanofibers (*solid line*) and powdered P3HT (*dotted line*). (**c**) XRD pattern of P3HT nanofibers (Copyright © 2012, American Chemical Society)

The positions of the diffraction peaks almost agree with those of the P3HT powder sample, indicating the presence of a crystalline lamellar structure in the P3HT nanofibers. Moreover, a (010) diffraction peak due to the π-π stacking among poly (thiophene) backbones was observed. The dissolved high-molecular-weight P3HT crystallized during the electrospinning process, and the nanofibers then embedded the P3HT microcrystallines.

Electric and Mechanical properties of P3HT Nanofiber Assemblies

Twenty P3HT nanofibers were deposited across a pair of gold electrodes (2.0 cm in length and with a gap width of 1.0 mm) on a glass substrate, and the fibers did not contact with each other (confirmed by optical microscope). The current increased exponentially with increasing voltage, which is a typical semiconductive characteristic. After doping with iodine, a linear relationship in the I-V characteristics was

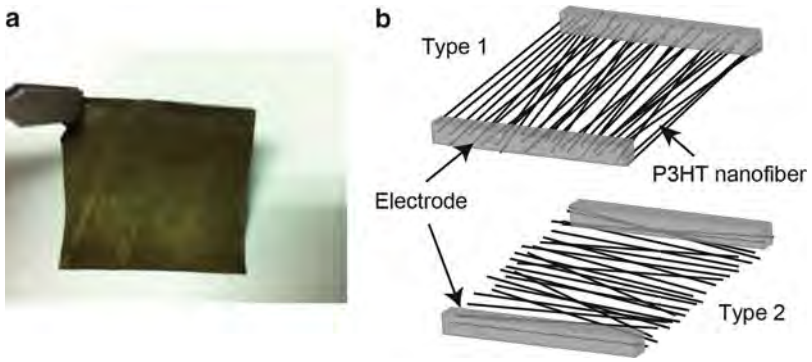

Fig. 8 (**a**) Photograph of aligned P3HT nanofiber assembly (2 × 2 cm). (**b**) Schematic of two arrangements of electrodes (*Type 1* and *Type 2*) on P3HT nanofiber assembly (Copyright © 2012, American Chemical Society)

observed, suggesting that the partial oxidation of P3HT by iodine doping led to the macroscopically observed conductivity of nanofibers. The electronic conductivity of a single P3HT nanofiber was determined to be 122 ± 9 S/cm.

The P3HT nanofibers were collected onto aluminum foil substrate on the rotating disk collector during the continuous electrospinning, and the aligned nanofiber assemblies (thickness: 15 μm) could be peeled off of the aluminum foil (Fig. 8a). The assemblies were not brittle and maintained their shape after removal from the substrates. The tensile strength of the aligned assembly along the nanofiber orientation direction was 4.6 ± 0.2 MPa and the degree of elongation at break was 24.6 ± 2.2 %. The P3HT nanofibers within the freestanding assembly were loosely packed with a density of 0.27 g/cm^3. The nanofiber assemblies were cut into 2 × 2 cm square samples, and two electrodes were drawn at both edges of the sample with silver paste to connect nanofibers (Fig. 8b). The resistance along the nanofiber orientation (type 1) was seven times that in the direction orthogonal to the orientation (type 2), indicating the anisotropic conductivity in aligned nanofiber assemblies. The electron transport in the orthogonal direction requires contact with P3HT nanofibers in order to make pathways in nanofiber assemblies. Thus, the resistance depends on the number of contact positions among the P3HT nanofibers.

Tactile Sensor

The pressure sensing properties of the P3HT nanofiber assemblies were investigated by measuring the current changes in response to different mechanical loads. The I-V measurements of assemblies showed ohmic behavior within a range of 0–5 V, and the currents applied at 1.0 V between two electrodes on the assemblies were monitored. The currents between two electrodes parallel to the nanofiber axis within the assemblies were almost constant with increasing pressure. In contrast, the currents between the orthogonal electrodes increased steeply from 5 Pa and

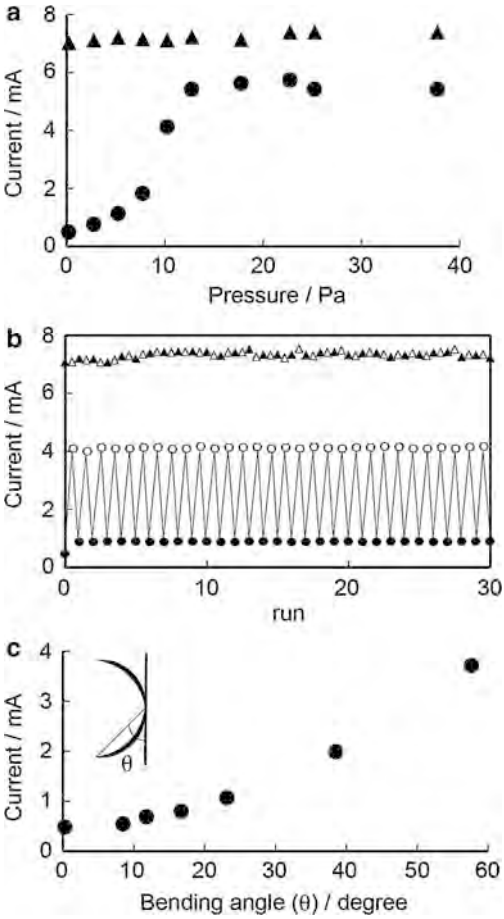

Fig. 9 Electronic characterization of the sensor in response to pressure loads and bending. (**a**) Current changes from P3HT nanofiber assemblies possessing different arrangements of electrodes (▲: *type 1* and ●: *type 2*) as a function of applied pressure. (**b**) Multiple-cycle test (30 cycles) of P3HT nanofiber assemblies (▲, △: *type 1* and ●, ○: *type 2*) with repeated loading (○ and △) or unloading (● and ▲) of pressure at 10 Pa. (**c**) Current changes as a function of bending angle (Copyright © 2012, American Chemical Society)

saturated above 15 Pa (Fig. 9a). Multiple-cycle tests by repeatedly loading and unloading pressure at 10 Pa were performed (Fig. 9b). The output signals in a direction orthogonal to the nanofiber orientation showed a constant value at loading of pressure, and the current returned to the parent value at the unloading. While the current returned to the parent value within 5 s after loading at 10 Pa, the returning needed over 30 min after loading at 30 Pa. When the nanofiber assemblies were compressed by the large loading, the nanofibers in the assemblies would be entangled and the releasing of entanglement requires a long period. The currents along the nanofiber orientation were almost constant, revealing no damage to nanofiber assemblies by applying pressure. When two ends of the nanofiber assembly were stuck to poly(ethylene terephthalate) (PET) film with the silver paste, the assembly could detect the bending angle by changing the currents (Fig. 9c). Small physical inputs gave rise to additional contact among neighboring conductive nanofibers by the compression, which produced a decrease of the contact resistance in a direction orthogonal to the nanofiber orientation.

Summary

This chapter described the fabrications of two sensor devices composed of conductive fiber assemblies. The conductive fibers were fabricated by two different approaches. Continuous organic-conductive fibers were produced by blending PEDOT:PSS with PVA through the gelation-spinning process. The scalable multifilament fibers showed good enough mechanical properties for textile processes while keeping electronic conductivity. The blended fiber exhibited a repeatable contraction motion in air by applying alternating square-wave voltages between 0 and 8 V. The textiles including conductive fibers for the detection of heartbeat were fabricated. The scalable PEDOT:PSS/PVA fiber can be a platform to realize integrated wearable electronics.

A flexible organic tactile sensor based on reversible deformation of high-molecular-weight P3HT nanofibers within the aligned assemblies has been demonstrated. The simple structure composed of aligned electrospun nanofibers can be used to develop tactile sensors for detecting small pressure changes and bending angles. The flexible devices based on simple nanofiber assemblies can be used as ambient sensors to monitor activities by embedding them within clothes and interiors. The sensing range of tactile sensors would depend on the diameter of the nanofibers within the assemblies. Future work will involve the fabrication of fiber devices such as light-emitting diodes, solar cells, and sensors by deposition of functional layers on the organic-conductive fibers. The integration of fiber devices within the textiles will open up a new lifestyle in the future.

References

1. Hamedi M, Forchheimer R, Inganäs O (2007) Towards woven logic from organic electronic fibres. Nat Mater 6:357–362
2. Hamedi M, Herlogsson L, Crispin X, Marcilla R, Berggren M, Inganäs O (2009) Fiber-embedded electrolyte-gated field-effect transistors for e-textiles. Adv Mater 21:573–577
3. Lee MR, Eckert RD, Forberich K, Dennler G, Brabec CJ, Gaudiana RA (2009) Solar power wires based on organic photovoltaic materials. Science 324:232–235
4. Cherenack K, Zysset C, Kinkeldei T, Münzenrieder N, Tröster G (2010) Woven electronic fibers with sensing and display functions for smart textiles. Adv Mater 22:5178–5182
5. Hu B, Li D, Ala O, Manandhar P, Fan Q, Kasilingam D, Calvert PD (2011) Textile-based flexible electroluminescent devices. Adv Funct Mater 21:305–311
6. Gumennik A, Stolyarov AM, Schell BR, Hou C, Lestoquoy G, Sorin F, McDaniel W, Rose A, Joannopoulos JD, Fink Y (2012) All-in-fiber chemical sensing. Adv Mater 24:6005–6009
7. Windmiller JR, Wang J (2013) Wearable electrochemical sensors and biosensors: a review. Electroanalysis 25:29–46
8. Zhu S, So JH, Mays R, Desai S, Barnes WR, Pourdeyhimi B, Dickey MD (2013) Ultrastretchable fibers with metallic conductivity using a liquid metal alloy core. Adv Funct Mater 23:2308–2314
9. Lu W, Zu M, Byun J–H, Kim B–S, Chou T–W (2012) State of the art of carbon nanotube fibers: opportunities and challenges. Adv Mater 24:1805
10. Behabtu N, Young CC, Tsentalovich DE, Kleinerman O, Wang X, Ma AWK, Bengio EA, ter Waarbeek RF, de Jong JJ, Hoogerwerf RE, Fairchild SB, Ferguson JB, Maruyama B, Kono J,

Talmon Y, Cohen Y, Otto MJ, Pasquali M (2013) Strong, light, multifunctional fibers of carbon nanotubes with ultrahigh conductivity. Science 339:182–186
11. Jalili R, Aboutalebi SH, Esrafilzadeh D, Shepherd RL, Chen J, Aminorroaya-Yamini S, Konstantinov K, Minett AI, Razal JM, Wallace GG (2013) Scalable one-step wet-spinning of graphene fibers and yarns from liquid crystalline dispersions of graphene oxide: towards multifunctional textiles. Adv Funct Mater (in press). doi:10.1002/adfm.201300765
12. Shirakawa H, Louis EJ, MacDiarmid AG, Chiang CK, Heeger AJ (1977) Synthesis of electrically conducting organic polymers: halogen derivatives of polyacetylene, $(CH)_x$. J Chem Soc Chem Commun 16:578–580
13. Skothem TA, Reynolds JR (2007) Handbook of conducting polymers, 3rd edn. CRC Press, Boca Raton/London/New York
14. McQuade DT, Pullen AE, Swager TM (2000) Conjugated polymer-based chemical sensors. Chem Rev 100:2537–2574
15. Günes S, Neugebauer H, Sariciftci NS (2007) Conjugated polymer-based organic solar cells. Chem Rev 107:1324–1338
16. Klauk H (2010) Organic thin-film transistors. Chem Soc Rev 39:2643–2666
17. Facchetti A (2011) π-conjugated polymers for organic electronics and photovoltaic cell applications. Chem Mater 23:733–758
18. Wang TZ, Joo J, Hsu CH, Epstein AJ (1995) Charge transport of camphor sulfonic acid-doped polyaniline and poly(*o*-toluidine) fibers: role of processing. Synth Met 68:207–211
19. Pomfret SJ, Adams PN, Comfort NP, Monkman AP (1998) Inherently electrically conductive fibers wet spun from a sulfonic acid-doped polyaniline solution. Adv Mater 10:1351–1353
20. Pomfret SJ, Adams PN, Comfort NP, Monkman AP (2000) Electrical and mechanical properties of polyaniline fibres produced by a one-step wet spinning process. Polymer 41:2265–2269
21. Bowman D, Mattes BR (2005) Conductive fibre prepared from ultra-high molecular weight polyaniline for smart fabric and interactive textile applications. Synth Met 154:29–32
22. Okuzaki H, Ishihara M (2003) Spinning and characterization of conducting microfibers. Macromol Rapid Commun 24:261–264
23. Takahashi T, Ishihara M, Okuzaki H (2005) Poly(3,4-ethylenedioxythiophene)/poly (4-styrenesulfonate) microfibers. Synth Met 152:73–76
24. Jalili R, Razal JM, Innis PC, Wallace GG (2011) One-step wet-spinning of poly(3,4-ethylenedioxythiophene):poly(styrenesulfonate) fibers and the origin of higher electrical conductivity. Adv Funct Mater 21:3363–3370
25. Hopkins AR, Reynolds JR (2000) Crystallization driven formation of conducting polymer networks in polymer blends. Macromolecules 33:5221–5226
26. Chen C, LaRue JC, Nelson RD, Kulinsky L, Madou MJ (2012) Electrical conductivity of polymer blends of poly(3,4-ethylenedioxythiophene): poly(styrenesulfonate):*N*-methyl-2-pyrrolidinone and polyvinyl alcohol. J Appl Polym Sci 125:3134–3141
27. Lewin M (2007) Handbook of fiber chemistry, 3rd edn. CRC Press, Boca Raton/London/New York
28. Ueno A, Akabane Y, Kato T, Hoshino H, Kataoka S, Ishiyama Y (2007) Capacitive sensing of electrocardiographic potential through cloth from the dorsal surface of the body in a supine position: a preliminary study. IEEE Trans Biomed Eng 54:759–766
29. Lim YG, Kim KK, Park KS (2007) ECG recording on a bed during sleep without direct skin contact. IEEE Trans Biomed Eng 54:718–725
30. Lee KM, Lee SM, Park KS (2010) Belt-type wireless and non-contact electrocardiogram monitoring system using flexible active electrode. Int J Bioelectromagn 12:153–157
31. Wartzek T, Eilebrecht B, Lem J, Lindner HJ, Leonhardt S, Water M (2011) EGC on the road: robust and unobtrusive estimation of heart rate. IEEE Trans Biomed Eng 58:3112–3120
32. Lakes R (1993) Materials with structural hierarchy. Nature 361:511–515

33. Someya T, Kato Y, Sekitani T, Iba S, Noguchi Y, Murase Y, Kawaguchi H, Sakurai T (2005) Conformal, flexible, large-area networks of pressure and thermal sensors with organic transistor active matrixes. Proc Natl Acad Sci U S A 102:12321–12325
34. Mannsfeld SCB, Tee BC, Stoltenberg RM, Chen CVH, Barman S, Muir BVO, Sokolov AN, Reese C, Bao Z (2010) Highly sensitive flexible pressure sensors with microstructured rubber dielectric layers. Nat Mater 9:859–864
35. Kim DH, Lu N, Ma R, Kim YS, Kim RH, Wang S, Wu J, Won SM, Tao H, Islam A, Yu KJ, Kim T, Chowdhury R, Ying M, Xu L, Li M, Chung HJ, Keum H, McCormick M, Liu P, Zhang YW, Omenetto FG, Huang Y, Coleman T, Rogers JA (2011) Epidermal electronics. Science 333:838–843
36. Takei K, Takahashi T, Ho JC, Ko H, Gillies AG, Leu PW, Fearing RS, Javey A (2010) Nanowire active-matrix circuitry for low-voltage macroscale artificial skin. Nat Mater 9:821–826
37. Lipomi DJ, Vosgueritchian M, Tee BC, Hellstrom SL, Lee JA, Fox CH, Bao Z (2011) Skin-like pressure and strain sensors based on transparent elastic films of carbon nanotubes. Nat Nanotech 6:788–792
38. Yamada T, Hayamizu Y, Yamamoto Y, Yomogida Y, Izadi-Najafabadi A, Futaba DN, Hata K (2011) A stretchable carbon nanotube strain sensor for human-motion detection. Nat Nanotech 6:296–301
39. Pang C, Lee GY, Kim T, Kim SM, Kim HN, Ahn SH, Suh KY (2012) A flexible and highly sensitive strain-gauge sensor using reversible interlocking of nanofibres. Nat Mater 11:795–801
40. Sirringhaus H, Brown PJ, Friend RH, Nieisen MM, Bechgaard K, Langeveld-Voss BMW, Spiering AJH, Janssen RAJ, Meijer EW, Herwig P, de Leeuw DM (1999) Two-dimensional charge transport in self-organized, high-mobility conjugated polymers. Nature 401:685–688
41. Wang C, Dong H, Hu W, Liu Y, Zhu D (2012) Semiconducting π-conjugated systems in field-effect transistors: a material odyssey of organic electronics. Chem Rev 112:2208–2267
42. Cheng YJ, Yang SH, Hsu CS (2009) Synthesis of conjugated polymers for organic soar cell applications. Chem Rev 109:5868–5923
43. Merlo JA, Frisbie CD (2003) Field effect conductance of conducting polymer nanofibers. J Polym Sci B Polym Phys 41:2674–2680
44. Kim FS, Ren G, Jenekhe SA (2011) One-dimensional nanostructures of p-conjugated molecular systems: assembly, properties and applications from photovoltaics, sensors, and nanophotonics to nanoelectronics. Chem Mater 23:682–732
45. Laforgue A, Robitaille L (2008) Fabrication of poly-3-hexylthiophene/polyethylene oxide nanofibers using electrospinning. Synth Met 158:577–584
46. Kim T, Im JH, Choi HS, Yang SJ, Kim SW, Park CR (2011) Preparation and photoluminescence (PL) performance of a nanoweb of P3HT nanofibers with diameters below 100 nm. J Mater Chem 21:14231–14239
47. Babel A, Li D, Xia Y, Jenekhe SA (2005) Electrospun nanofibers of blends of conjugated polymers: morphology, optical properties, and field-effect transistors. Macromolecules 38:4705–4711
48. Lee S, Moon GD, Jeong U (2009) Continuous production of uniform poly(3-hexylthiophene) (P3HT) nanofibers by electrospinning and their electrical properties. J Mater Chem 19:743–748
49. Chen JY, Kuo CC, Lai CS, Chen WC, Chen HL (2011) Manipulation on the morphology and electrical properties of aligned electrospun nanofibers of poly(3-hexylthiophene) for field-effect transistor applications. Macromolecules 44:2883–2892
50. Chan KHK, Yamao T, Kotaki M, Hotta S (2010) Unique structural features and electrical properties of electrospun conjugated polymer poly(3-hexylthiophene) (P3HT) fibers. Synth Met 160:2587–2595

Optical Fibers

4

Anne Schwarz-Pfeiffer, Viktorija Mecnika, Markus Beckers, Thomas Gries, and Stefan Jockenhoevel

Contents

Introduction 80
Optical Glass Fibers 80
Polymer Optical Fibers 81
Light Transmission Mechanisms 82
Light Transmission by Total Reflection 82
Types of Optical Fibers 86
Glass Fibers 86
Polymer Optical Fibers (Properties and Production) 88
Processing Optical Fibers into Textile Structures 92
Application Fields 93
Data Transmission 93
Light Therapy 94
Sensors 95
Sensor for Cardiac Activity Assessment 103
Lightening Effects for Ambient Assisted Living 104
Summary 105
References 106

Abstract

Integrating optical fibers into textiles opens up a wide range of new, fascinating applications – starting from data transmission to sensory abilities, new lightening concepts, and advanced medical therapies.

A. Schwarz-Pfeiffer (✉)
Niederrhein University of Applied Sciences, Mönchengladbach, Germany
e-mail: anne.Schwarz-Pfeiffer@hs-niederrhein.de

V. Mecnika • M. Beckers • T. Gries • S. Jockenhoevel
RWTH Aachen University, Aachen, Germany
e-mail: Viktorija.Mecnika@ita.rwth-aachen.de; Markus.Beckers@ita.rwth-aachen.de; Thomas.Gries@ita.rwth-aachen.de; jockenhoevel@hia.rwth-aachen.de

© Springer Science+Business Media Singapore 2015

X. Tao (ed.), *Handbook of Smart Textiles*,
DOI 10.1007/978-981-4451-45-1_4

This chapter gives first an overview on the working principle and light transmission mechanisms in optical fibers. It discusses different types of optical fiber materials, before it summarizes recent developments in processing these materials into textile structures. Finally different application fields are explored, which leads to highlighting future trends and potentials of optical fibers.

Keywords
Optical fibers • Polymer optical fibers • Glass fibers • Refractive index • Data transmission • Light therapy • Optical fiber sensors • Photonic textiles

Introduction

Developing the laser in 1960, optical communications engineering was suddenly spotlighted in the research and development world. While the propagation of laser light in the atmosphere has been studied, an attempt was made to guide light in cable ducts. However, the line required a frequent refocusing of light and therefore lenses were used. Over the time, optical fibers evolved and were broadly accepted as their installation and operating costs were lower and they could be more bended. Optical fibers can be categorized into two groups: glass fibers and polymer optical fibers. Due to their diverging properties, they are both applied in different application areas. The development and evolution of both optical fiber types is briefly described below [1].

Optical Glass Fibers

Glass fibers were already known in 1960. They were able to lead light through curves. However, the materials, at that time known, were not suitable for signal transmission, due to their high losses. A breakthrough was achieved by K. C. Kao and G. A. Hockham in the UK in 1966. They attributed the strong losses to chemical contaminants and proposed suitable fibers for communication purposes. Kao was awarded the Nobel Prize in physics for his pioneering achievements in the field of light transmission in 2009. Already in 1969, the first glass fibers were presented with losses of less than 100 dB/km. Thus, they were suitable for communication purposes. Losses are usually expressed in decibels per kilometer. The decibel is one-tenth of a bel. The name is attributed to A. G. Bell. A bel is referred to as the ratio of two quantities having the dimension of power. Table 1 shows typical values of losses.

In 1970, a fiber with losses below 20 dB/km was produced. Nowadays, a lower limit of 0.2 dB/km is obtained with quartz glass. The cost of glass fibers amounted to 5 US$ per meter in 1981. Today the price is below 10 cents per meter. The tremendous price reduction was achieved, because the cost of the raw material quartz is low, the costs of labor are reduced through a high degree of automation, and the market volume is high.

Table 1 Losses in the decibel range (source: ITA, RWTH Aachen University)

Decibel (dB)	Factor ≈
3	2
6	4
10	10
20	100

The development of glass fibers as optical fibers and the advances in laser sources made it possible that most of our telecommunications systems are based on optical technologies today. Minor losses within the fiber enable the bridging of long distances without intermediate stations. The benefits are also evident in comparison to copper-based coaxial cables when used for long transmission distances. One gram of glass fibers replaces around 10 kg of copper – a great weight and space reduction. This difference is partly caused by the limited power density of copper, which is in turn attributed to the skin effect. The skin effect means that the current density is inconstant over the entire cross section of a conductor. This leads to an increase in electrical resistance, especially with increasing frequency [1].

Polymer Optical Fibers

The company DuPont presented the first polymer optical fiber (POF) in 1963. The loss was in the range of 1000 dB/km due to material impurities. In the 1970s, the losses could be reduced to 125 dB/km. This value is close to the theoretical limit for this materials group. The theoretical limit is determined by the unavoidable light absorption of the pure material. However, during this time period, there was no market for these fibers: glass fibers were used for long-distance transmission and copper wires were suitable in the short-range transmission. The progress of digitization in the last two decades has led to a growing demand for powerful transmission systems at short range. Thus, polymer optical fibers are now again increasingly in the focus of research works.

The first polymer optical fibers had, like glass, a single step-index profile (SI-POF). This means that a homogeneous core is surrounded by a single optical cladding. Additionally, a protective layer is coated on top, as illustrated in Fig. 1. An important characteristic of an optical fiber is its numerical aperture (NA). This describes the range of angles within which light that is incident on the fiber will be transmitted along it (see section "Light Transmission by Total Reflection"). For SI-POF a numerical aperture (NA) of 0.5 is used as a standard [2].

Various research teams and companies are continuously looking for ways to improve data transmission rates and to decrease possible bending radii. Nowadays, polymer optical fibers with different core-sheath arrangements exist, which are highlighted in section "Polymer Optical Fibers (Properties and Production)." Figure 1 gives an overview on the different fiber structures existing today.

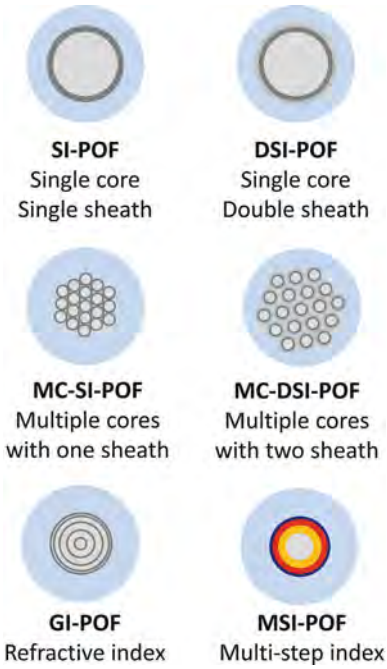

Fig. 1 Overview of different structures of optical fibers [2]

Light Transmission Mechanisms

The propagation of light in optical fibers can be described as geometrical optics. The basic principles, which are described in the following subsections, apply to both glass fibers and polymer fibers.

Light Transmission by Total Reflection

When a light beam passes from one medium to an optically different medium, the light is refracted and reflected at their interface. The refraction depends on the material or medium and a specific material property, which is referred to as refractive index n_{Medium}.

The refractive index is dimensionless and described as the ratio of the speed of light in vacuum c_0 to the speed of propagation of light in the medium c_{Medium}:

$$n_{\text{Medium}} = \frac{c_0}{c_{\text{Medium}}} \tag{1}$$

According to Albert Einstein, the refractive index is greater than one for normal materials.

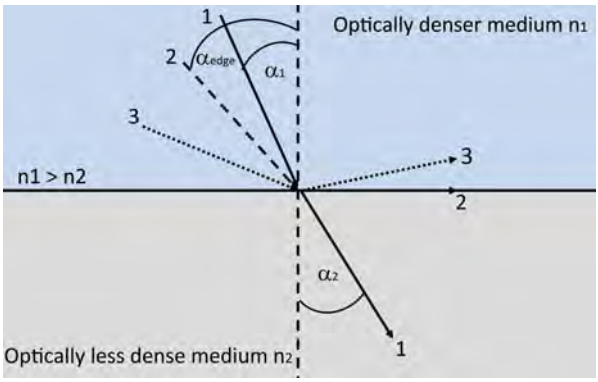

Fig. 2 Refraction of light and total reflectance

The change of direction of a light beam on a surface can be described by the Snell's law:

$$\frac{\sin \alpha_1}{\sin \alpha_2} = \frac{n_2}{n_1} \tag{2}$$

Knowing the refraction indices of the media, the critical angle can be calculated. Above the critical angle, total reflection occurs at the transition of light from an optically denser material into an optically thinner material, i.e., a light beam is reflected into the denser medium without losses at angles greater than the critical angle [1]. Figure 2 illustrates this phenomenon.

Step-Index Fibers

When designing optical fibers, there are two fundamentally different types: step-index fibers and refractive profile. The step-index fiber is mostly used. It has a core-sheath structure with a circular cross section. Most likely the base material used is glass. The core consists of a glass type with a slightly higher refractive index than the cladding. Hence, the light is guided through the core. The surface of the sheath plays only a minor role, and flaw or damage of the sheath is therefore unproblematic. Nonetheless, the fibers are often additionally coated with a protective layer, as illustrated in Fig. 1.

As light guidance, as discussed earlier, occurs only in the core, the coupled light beam needs to stay inside the core. Light rays passing in the sheath are lost for the light conduit. Hence, the light must be totally reflected at the core-sheath interface. The maximum critical angle α_{max} can be calculated when considering Snell's law and the trigonometry of the fiber. A typical value for single-mode fibers is $\alpha_{max} = \pm 7°$:

$$\alpha_{max} = \arcsin\sqrt{n_{Core}^2 - n_{Sheath}^2} \tag{3}$$

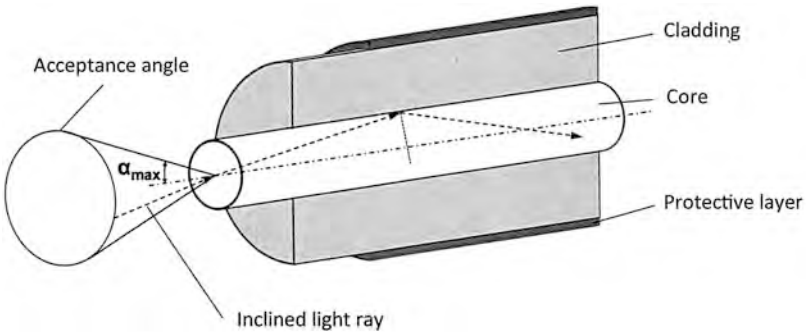

Fig. 3 Principle of aperture and propagation of light in an optical fiber possessing a core-sheath structure

This angle spans that a "cone of acceptance" as within this cone light transmission is possible. The cone is identical when entering the fiber and when exiting due to the irreversibility of the light passing in linear optics. The aperture of light is depicted in Fig. 3.

The argument of arcsin of Eq. 3 is simultaneously a measure of the refractive index difference between core and sheath and is referred to as numerical aperture (NA):

$$\mathrm{NA} = \sqrt{n_{\mathrm{Core}}^2 - n_{\mathrm{Sheath}}^2} \tag{4}$$

A typical value for single-mode fibers is NA = 0.11. Glass multimode optical fibers typically possess values in the range of 0.2. A change of the numerical aperture (NA) affects various fiber properties. An increase of the aperture causes a lower bending sensitivity but an increase in light transmission losses. On top of that, the refraction index difference between core and sheath increases [1, 2].

Modes and Multimode Distortions

For optical fibers, the term mode is often used. There are single- and multimode fibers. Because of its great importance when talking about light transmission, the terms modes and mode dispersion are briefly introduced.

Modes are designated as radiation entering at various angles in the fiber. From Snell's law, it follows that, due to different angles of incidence, other beam paths through the fiber are possible. These may possess different lengths. Figure 4 illustrates this phenomenon.

Since the core has a uniform refractive index, different light paths cause different traveling durations. This results in a transit time jitter for a fed signal. This is also referred to as mode dispersion. As the sub-beams are at an angle to each other, it only leads to an interference pattern over the cross section. If the rays are not inclined to each other, it will come to destructive interference within a few hundred wavelengths due to the path difference. The problem of mode dispersion remains.

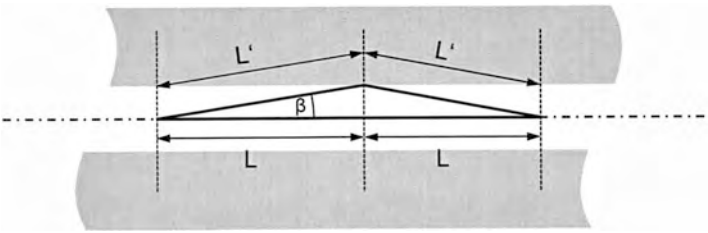

Fig. 4 Mode dispersion: differential mode delay [2]

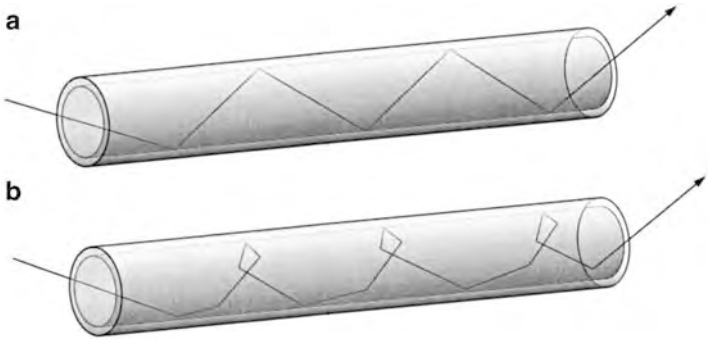

Fig. 5 Propagation of light in the form of a meridional beam (**a**) or helical beam (**b**)

It is even strengthened by a similar effect, which occurs when a coupled beam is inclined in two instead of only one spatial direction. The beam does not spread out as meridional, but propagates as a helical beam on a helix. Figure 5 illustrates these two propagation variations.

These two effects result in a scattering of times. This leads to a broadening of the pulses due to short light pulses and thus to a reduction of the transmission capacity. If the pulses succeed too fast, they cannot be distinguished.

Refractive Index Profile Fibers

Mode dispersion can be minimized or prevented by the use of refractive index profile fibers. This can be achieved by a special refractive index profile as a function of the radius. An optimum can be achieved with a parabolic profile, wherein the profile exponent α equals 2 in Eq. 5:

$$n(r) = \left\{ n_K \sqrt{1 - 2\Delta \left(\frac{r}{R_K} \right)^{\alpha}} ; |r| \leq R_K \right. \tag{5}$$

Equation 5 takes into account the core radius r_{Core} as well as the monic refractive index difference Δ and the refractive indices of the core n_{Core} and the cladding n_{Sheath}.

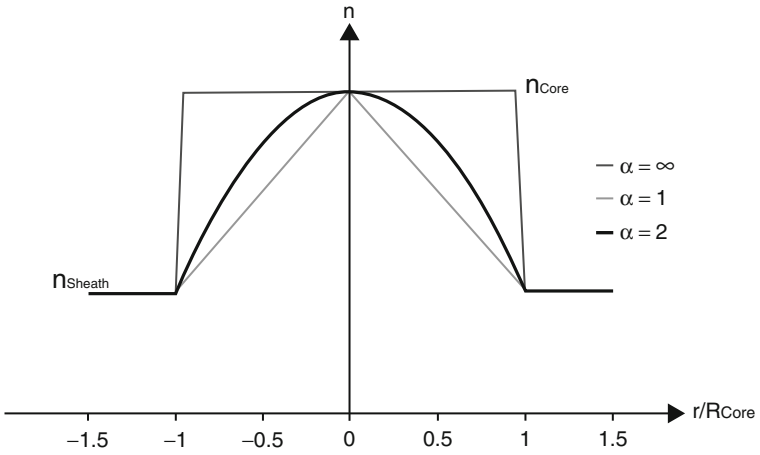

Fig. 6 Three typical index profiles according to [2]

Figure 6 shows three typical index profiles, which result from Equation 5. The y-axis indicates the radius-dependent refractive index. This axis is only partially displayed, since the refractive index difference between core and cladding is very small.

Types of Optical Fibers

Optical fiber types are basically distinguished by their raw materials. They are either based on glass or polymers. For most applications, silica (SiO_2)-based glass fibers are applied. However, polymer fibers have properties that make them attractive for special applications.

While the near-infrared range between 850 and 1,600 nm is particularly well suited for glass fibers, polymer optical fibers are preferred in the visible range from 380 to 780 nm.

Glass Fibers

Glass is the oldest synthetic material. It is used by humans for 7000 years. There are, among other things, evidences of the manufacture of glass from Egypt, Mesopotamia, and China. The modern glass technology has its origin in Germany with Otto Schott (1851–1935), Ernst Abbe (1840–1905), and Carl Zeiss (1816–1888).

The term glass does not describe a special element but a particular spatial arrangement of molecules. Many materials can adopt glassy states. In the optical glass industry, mainly glass made of silica is used.

The irregularity of the glass as compared to the crystal structure causes a local minimum of free energy. The result is a crystallization of the glass. This is known as devitrification [1].

Structure of Glass Fibers

For optical fibers, glassy materials can be used. Crystals are not used because they always contain voids or cross-links, which scatter and reflect the light. This results in larger optical losses. Glass is known as fragile. High flexibility and thus good usability of glass optical fiber result from different effects, e.g., its dimensions. Diameters of optical fibers are in the range of 70–500 μm. Few internal defects may already lead to failure of the fiber in production. The fibers have such a high minimum strength, which has a positive effect on the failure probability.

The main reason for failure of glass is microcracks, which appear when reaching a critical crack length and finally result in total failure of the material. A crack increases as the mechanical energy (caused by residual stress and external stress at the crack tip) is greater than the additional surface energy. Through a minimization of the resistance-reducing microcracks, especially at the glass surface, the flexibility can be increased. In addition, a protective layer can prevent water from entering into the cracks [1].

Production of Glass Fibers

The manufacture of optical fibers can be divided into two steps. In a first step, preform is manufactured typically with a length of about one meter and a diameter of 10–25 mm. The applied methods to manufacture the preform vary among manufacturers and can be outside vapor deposition (OVD), modified chemical vapor deposition (MCVD), Plasma-activated chemical vapour deposition (PACVD), and vapor-phase axial deposition (VAD). When applying the OVD method, glass particles are deposited on a rotating support tube. The glass particles originate from a burner flame, to which gaseous chemicals are added. Subsequently, the resultant glass tube is sintered, the support tube is removed, and the glass tube heats up and collapses. Hence, a massive rod can be produced. The MCVD process is similar to the OVD method: a rotating glass tube is externally heated with a burner flame and gaseous materials are passed through the tube interior. During the PCVD procedure, the tube is electrically heated. The gaseous materials are heated by means of microwave radiation. In this method, the sintering and the rotation of the tube are omitted. The fourth method, the VAD, is different compared to the previously described methods. Here, the glass is formed in a burner flame. The preform is formed in axial direction. A sintering process is required, but the collapsing to a massive rod is eliminated.

During the second step, the preform is molten and stretched to the desired fiber diameter, which is typically 125 or 250 μm. Depending on the drawing ratio, the production speed of the fibers is around 8 m/s. The drawing unit is a major bottleneck during the production. Directly after the cooling down of the pure glass fibers, the fibers are coated with two layers of a protective polymer. The first layer is soft and elastic while the top layer is characterized by rigidness and abrasion resistance. These layers protect the fibers from mechanical and chemical forces [1].

Mechanical Properties

The mechanical strength of glass fibers having a small diameter cannot be compared to glass due to their structure. Glass fibers can be regarded as elastic; the strain is proportional to tension. Elongation can be described by Hooke's law:

$$\frac{\Delta l}{l} = \frac{1}{E} * \frac{F}{A} = \frac{\sigma_{\text{Tensile Strength}}}{E} \tag{6}$$

For optical glass fibers with very small microcracks and a polymer protective layer, the mechanical parameters are in the range of $\Delta l/l_{\text{crit}} = 3\text{–}7\ \%$ for the elongation at break and $\sigma_{\text{Tensile Strength}} = 2{,}000\text{–}5{,}000\ \text{N/mm}^2$ for the tensile strength. During the product life cycle, the strength is decreased by fatigue caused by aging, environmental conditions, and the load history.

The properties of glass fibers lead to very high data rates over long distances. In this area, optical transmission method has displaced the electrical transmission method. Due to their mechanical properties, very small diameters are needed and the minimal possible bending radius is limited. This, in turn, leads to a complex and cost-intensive installation. In particular, the coupling and decoupling of light is complicated due to small diameter sizes. Glass fibers are most likely applied in the area of long-distance communication, as additional costs per unit length are not so high. However, in the area of short-range communication with mostly lower required transmission rates, the fibers have not been successfully applied [1].

Polymer Optical Fibers (Properties and Production)

Polymer optical fibers (POF) have been developed at about the same time as glass fibers. The reason was also the research on optical fibers for optical transmission method according to the development of the laser. First, however, a market for polymeric optical waveguides lacked. Progress in the production of very pure polymer fibers with specific refractive index profiles and the progression of digital development now lead to new market potential for this fiber type. The coupling and decoupling of light in polymer optical fibers having large diameters has become inexpensive and easy. However, the production of the fibers themselves, similar to glass fibers, is associated with high costs. In particular, the generation of a refractive index profile is subjected to an increased difficulty.

Structure of Polymer Optical Fibers

Polymers with linear or branched chains are called thermoplastics. The cohesion of single-molecule chains with each other is solely based on secondary bonding forces. If there are only a few and short branches, the molecular chains will be close to each other. This is called crystallization. Long molecular chains prevent complete crystallization, and such polymers are referred to as semicrystalline thermoplastics. At the boundaries of the crystallites, the light is scattered, which

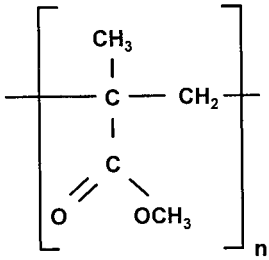

Fig. 7 Chemical formula of PMMA

leads to cloudy or milky optical properties. Plastics with many branches and long side chains are irregular and cannot hold a tight packing. Therefore they have no crystalline areas. The chain molecules are intertwined with each other. They freeze amorphously and are called amorphous thermoplastics. They are optically transparent and crystal clear. Therefore they are also termed synthetic or organic glasses. Typical representatives of amorphous thermoplastics are polymethyl methacrylate (PMMA), polycarbonate (PC), and polyvinyl chloride (PVC) [3].

The thermoplastic PMMA, also known as Plexiglas®, is most commonly used for the production of POF. It is resistant to alkalis, mild acids, gasoline, and mineral and oil of turpentine. The optical transparency is due to the amorphous structure of the macromolecules. The refractive index of PMMA amounts to 1.492. The density is 1.18 g/cm^3 and the region of the glass transition temperature ranges from 95 °C to 125 °C. Each repeat unit of PMMA contains eight CH bonds (Fig. 7).

Many applications require higher operating temperatures. This can be increased when cross-linking PMMA. By means of chemical agents or UV irradiation, the polymer chains are cross-linked to one another. Consequently, the glass transition temperature and thus the operating temperature are increased to 130 °C. Other side effects are deteriorated mechanical properties and an increased scattering. However, the latter offers the possibility to influence the lateral scattering of the fiber.

Another way to increase the operating temperature is the use of polycarbonate. The first PC optical fiber was introduced by Fujitsu in 1986. The operating temperatures are in the range of 130 °C to 147 °C. The disadvantage of this fiber is the high sensitivity to moisture, which leads to a greatly accelerated aging.

Recently, elastomers appear to be suitable as a new family of materials for temperature-resistant POFs. They are also known as elastomeric optical fibers (EOF). The first prototypes have already been realized by some institutions. However, the development of a marketable product is still pending.

Theoretically, cyclic polyolefins can be used as POF material. They can be prepared with a transparent amorphous structure. Their transparency is theoretically better than PMMA, and its glass transition temperature is greater than 150 °C. Currently, however, they are not the subject of research and development projects.

Polystyrene (PS) is also suitable for polymer optical fibers. The first PS-POF was manufactured by Toray in 1972. They can be used in up to 70 °C for use. However, currently they have no significant advantage over PMMA-POF, so they are practically not used at the moment [2].

Production of Polymer Optical Fibers (POF)

Polymer optical fibers can be subdivided into step-index fibers (SI-POF) and index profile fibers (GI-POF). Initially, only step-index fibers were produced. The demand for an increase in the possible data transmission rates has led to the development of index profiles. In the following, different manufacturing processes of two extreme cases are presented: the simplest version of the step-index profile and the most elaborate of the refractive index profile [4].

Production of Step-Index Polymer Optical Fibers (SI-POF)

SI-POFs are produced by continuous processes, such as spinning, extrusion, or drawing from preforms. For the preform methods, first a cylinder is made with a much larger diameter as of the later fiber. The cylinder has a core-sheath structure. The fiber is then drawn out of the cylinder, and the index profile is maintained. Drawing speeds of about 0.2–0.5 m/s can be achieved.

During spinning and extrusion, the core polymer is extruded through a die. The sheath or cladding can be applied directly in a co-extrusion process or thereafter. Some methods make use of an addition cross-linking by UV light, after the polymer has passed through the spinneret. In summary, the spinning and extrusion processes for SI-POF are very similar to conventional melt spinning processes for chemical fibers [2].

Production of Refractive Index Profile Fibers (GI-POF)

The first GI-POFs were presented by Ohtsuka and Hatanaka in 1976. They used a heating drawing method to prepare a fiber composed of a polymer rod. The rod, also called preform, already possessed a gradient profile.

Today, there are five basic manufacturing processes for GI-POF:

- Surface-gel polymerization
- Centrifugation
- Diffusion
- Photochemical reactions
- Extrusion of multilayers (polymerization or coating)

For most methods, a preform is manufactured, which is subsequently thinned to the desired fiber diameter. The preform has a diameter of up to 50 mm.

The surface-gel polymerization technique was developed by Yasuhiro Koike, Keio University, in Japan in the 1990s. In this method, a PMMA tube is filled with two monomers. One monomer has a higher refractive index and large molecules, while the other one is characterized by a small refractive index and small molecules. Subsequently, the tube is rotated at 95 °C for about 24 h. First, the inner wall of the tube is slightly etched. It forms a gel layer which accelerates the polymerization. The smaller monomer can better diffuse into the gel layer. In this way, a concentration gradient forms in the tube. This is fixed with the progressing polymerization of the gel layer. Thus, the desired gradient index can be generated.

The first considerations for the production of GI-POF by centrifugation originate also from the 1990s. The differences in density of different monomers are used as different centrifugal forces lead to a concentration gradient during centrifugation. When the concentration gradient is fixed, a graded index profile can be produced. Fixing is usually caused by an increase in temperature after the desired profile has been formed. One has to take into account process times of 24 h for the formation of the index profile and 12 h for polymerization. So far, this production technology could not be transferred to an industrialized process.

In 2001, a method based on diffusion and rotation was presented. In this method, a cylindrical glass reactor is equipped with two materials: a monomer which surrounds a rod of a material having a higher refractive index. The rod material diffuses slowly in the surrounding monomer at room temperature. The rod and the reactor rotate at different speeds, ranging from 6 to 60 min^{-1}. In this way, process variations can be compensated and a rotationally symmetrical profile is formed. This process takes several hours. Subsequently, the polymerization is initiated by an increase in temperature and the profile is fixed.

Some older methods use photo-copolymerization to shape the index profile. In these cases, a rotating glass tube is filled with a monomer mixture and irradiated with UV light. Due to the higher radiation intensity in the outer regions, the polymerization proceeds rapidly. Thus, a gel forms. If the lower-breaking monomer component has a higher reaction rate, it will accumulate in the outer regions. At higher temperatures, the index profile can be adjusted and finally fixed.

Extrusion of multiple layers is explored for the production of multi-step-index fibers [2, 4].

A more recent development is the polymerization in the centrifuge developed by C. W. Park. The rotation is not used for separation, but to form a rotationally symmetrical index profile. The profile itself is obtained by copolymerizing a polymer blend; its composition is changed stepwise or continuously. The polymerization is initiated by heat or UV radiation. This method results in fibers with a fine layer structure, which leads to an almost ideal parabolic index profile. The process was patented in 1996 [5].

Most of the manufacturing methods of GI-POF use an intermediate step of a preform which is subsequently drawn to the desired fiber diameter. A continuous production for PF-GI-POF has been developed by the company Chromis Fiberoptics (formerly Lucent, OFS). In this method, a SI-POF is first prepared by a co-extrusion. While the core consists of doped CYTOP®, undoped CYTOP® is used for the cladding. Thereafter, a protective layer is applied. The index profile is adjusted by the diffusion of the doping material, which is activated through temperature [2, 4].

Properties of Polymer Optical Fibers

The mechanical properties of polymer optical fibers are characterized by the same effects as for other synthetic fibers. Their properties are optimized, however, particularly in respect to their optical properties. Amorphous thermoplastics are fragile glasses. This means that their viscosity strongly increases with decreasing

temperature. The temperature-dependent change in viscosity can be described by the Vogel-Fulcher law. At higher temperatures, the Arrhenius law applies. Despite the high viscosity, relaxation processes occur in a nonfrozen state of equilibrium in the polymer. These are mainly local rearrangement processes by movement of chain segments and rotations of side groups or parts of them. The relaxation processes are strongly temperature dependent. Long-term storage, for example, leads to embrittling of the polymers just below the glass transition temperature. By a UV irradiation, a similar effect is caused in many polymers. The mechanical strength can be described by Hooke's law in the elastic range. The stretchability during the manufacturing process is temperature dependent. With decreasing temperature, the polymers become more brittle. While drawing, the chain molecules are oriented in fiber direction by the high tensile stresses. If the orientation by local rearrangements cannot take place, crazes are formed. These are elliptical areas in which highly stretched polymer fibrils and microcavities alternate. In the deformation of amorphous polymers, they are visible by white lines in the otherwise transparent material. They can be recognized as white lines in transparent materials during deformation of the polymer fiber. Hence, material defects can strongly affect the optical properties of such a fiber. The transparency of polymer fibers is negatively influenced by microcracks. These are usually caused by inhomogeneities in the material, such as surface defects, foreign bodies, or residual stresses caused by inhomogeneous cooling. In addition, microcracks are often the cause of material failure (break) at too high loads. In this case, the cracks propagate in excess of the critical crack stress. In principle, the fracture properties can be varied by the addition of plasticizers such as methanol. However, plasticizers are often undesirable, because they degrade the optical properties [6].

The mechanical performance properties of polymer optical fibers are better than those of glass fibers. Especially fibers with larger diameter and smaller minimum bending radii can be produced. Depending on the polymer material, the fibers can withstand fatigue bending without loss of optical properties or mechanical failure. However, the absorption properties of the materials lead to a much higher attenuation compared to glass fibers. As a result, polymer optical fibers are often better suited when looking at the performance properties and costs but eliminated due to their high attenuation. Therefore, they play no role in the long-distance communication. The number of required repeaters would be too high. Instead they can be used as sensors, sensor cables, or lighting elements [2].

Processing Optical Fibers into Textile Structures

Optical fibers are challenging when it comes to integrating them into a textile structure. They are sensitive to bending and mechanical stress. The minimum bending radius of a fiber is the smallest possible value of the radius of the arc formed by the fiber as it is bent. If the fiber is bent over this radius, it will break immediately. Usually the bending radius is at least several millimeters. For instance, a typical polymer optical fiber with a diameter of 250 μm has a minimum

bending radius of 1.5 mm [7]. Processing optical fibers into textile products leads to thin and lightweight structure, offering manifold 2D design possibilities. Advantages of optical fiber solutions are multifaceted. Optical fiber textiles enrich the range of illuminating products with their enhanced appearance, flexibility, and even drapability.

The most explored textile technology to process optical fibers into textile structures is weaving. The individual characteristics of different weaving patterns and weft insertion principles offer a variety of optical fiber textile structures. In most applications optical fibers are used as weft yarns to allow a certain flexibility during production since weft yarns can be exchanged easily. When applying them in warp direction, optical fibers are exposed to more process steps and are guided over and through more machine elements, hence, causing friction and tension. Warp yarns are spooled onto a warp beam, guided through weaving frames and bent up and down during shed action. This exposes the warp to more stress than weft yarns, possibly damaging the surface or breaking the fibers [8].

Flexibility and drape, typical characteristics of a textile, are influenced by the arrangement and type of optical fibers used to create a woven optical fiber fabric. Generally, the fiber diameter, the weaving pattern, and the fabric density (number of yarns per cm) influence the flexibility [9]. The selection of the right fiber diameter is crucial, as a thick fiber causes inflexibility and fibers with small diameters result in low shear resistance and loss of light intensity. Furthermore, choosing an open weaving pattern increases the flexibility and bendability of an optical fiber fabric.

Knitting optical fibers is mostly explored by the creative industry to create illuminating interior textiles and installations as knitted structures are able to conform to sophisticated forms. As the bending and friction forces during the loop-forming process tend to be very high, optical fibers may break. A way to integrate optical fibers in a knitted structure is achieved by weft insertion or inlays.

Embroidery is another technology that is explored to apply optical fibers onto a textile substrate. Most likely, tailored fiber placement (TFP), where the optical fiber is attached to the substrate material, fixing it with a sewing yarn in a zigzag manner, is applied. This technique allows freedom in pattern shapes and designs.

Application Fields

Being originally developed for data communication, optical fibers are increasingly explored for illumination and sensing applications nowadays. This section provides an overview on a variety of application fields of optical fibers.

Data Transmission

Modern technologies often address optical fibers as an efficient scope for fast and reliable data transfer. There is a lot of literature available on optics applications

Fig. 8 Wearable Motherboard™ for vital signs monitoring based on optical fiber technology [11]

for these purposes, and optics technology for data transmission is already presented on the market in a great variety of products. Since the first attempts to develop smart clothes and textiles appeared, optical fibers were used for data transmission. Already as a classic example of optical fiber application in smart textiles, the Wearable Motherboard™ (Fig. 8) developed by Georgia Tech can be mentioned [10]. In this study, optical fibers carry multiple functions and ensure both biomonitoring and data transmission. A vast field of research is technical textiles which enable sensorial functions ensured by optics technology. Also herein optical fibers provide continuous data flow to the processing unit, making them advantageous and multifunctional material for smart textile developers.

Light Therapy

Optical fibers have a significant role in biomedical engineering, especially based on laser technologies. Those are crucial compounds in many medical devices for imaging and diagnostics for all medicine spheres. Within new social, technological, and economic trends, optical fibers found applications in wearable technologies and particularly in smart textiles for medicine and healthcare. Optical fiber technology for medicine can be used not only as a sensorial compound but also a mean of healing, i.e., in light or phototherapy. In phototherapy, exposed light of specific wavelengths is applied for therapeutic purposes. For therapeutic applications, a polychromatic polarized light can be used or light generated by LEDs, fluorescent, dichroic lamps, or very bright full-spectrum light. Light therapy finds applications in dermatology, wound healing and treatment of neonatal jaundice, neuropathy, and blood circulation damages and is effective in circadian sleep rhythm disorders. Some have reported that light therapy can be an asset in the treatment of such serious disorders as Parkinson's and Alzheimer diseases. For some applications though, light is not enough as the only instrument treatment. Then treatment results

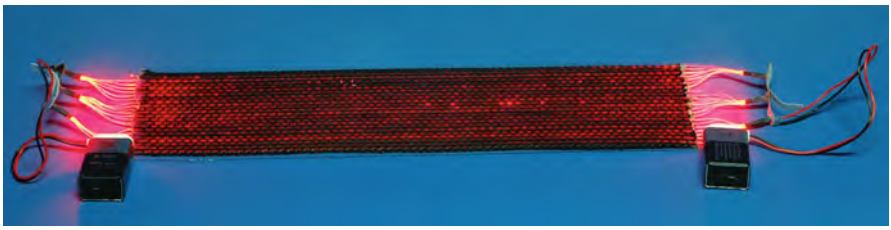

Fig. 9 Woven textile light diffusers

depend on a combination of several parameters that include also drug dose or photosensitizer (PS), drug-light interval, and oxygen and light influence rate [12]. Such light therapy is referred as photodynamic therapy and is important in antitumor immunity. In this case, the PS increases light therapy efficiency by targeting the tumor cells, and light affects exactly the cancer cells.

Initially, research that focuses on textile-based technology for light therapy has addressed light-emitting diodes (LEDs). Some of these solutions are already available on the market, such as the BlueTouch Technology by Philips. In this approach textiles serve as a carrier material and the primary function is brought by LEDs. This approach is a fine solution for applications in which flexibility and drapability are secondary requirements. However, for applications, in which textile properties are crucial, optical fibers may be used. Above that, optical fibers are not influenced by thermoelectrical effects that might cause inconveniences in ready-made clinically tested product manufacturing. Moreover, the integration technology of optical fibers is a continuous processing that can be carried out by such conventional textile manufacturing methods as weaving, knitting, embroidery, and braiding.

Although this sphere of optical fiber use for smart textile development can be regarded as relatively new and challenging in comparison with other applications, there are already a number of studies reported that have started investigations and manufacturing of textile diffusers [13, 14]. To create a textile light diffuser, POFs are appropriate candidates due to their physical properties, while weaving technology encourages design and production of a homogenous flexible light diffuser (Fig. 9). Moreover, this approach has a number of advantages when a large-area light-emitting probe is necessary to be manufactured. On the other side, a single optical fiber can be an asset for miniature concepts and find itself in such applications as wound healing.

Nevertheless, it should be mentioned that single optical fiber phototherapy units are already available for customers online [15].

Sensors

Sensorial functions based on optics are demanded in many technical and medical spheres. Physical and biochemical measurements are required almost in every field of human activity. Smart textile sensors first of all can be referred to as wearable

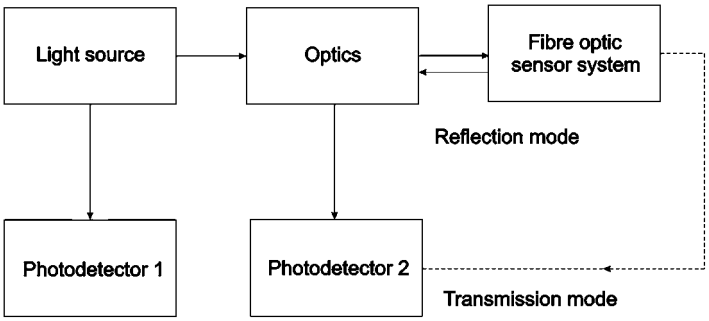

Fig. 10 Block diagram of a generic optical fiber sensor (Adapted from Gupta [16])

and wireless technology. Although the idea of wearables goes down to the 2nd part of the twentieth century, a significant breakthrough was achieved only in the 1990s, and one of the first materials considered for flexible textile-based sensor implementation was optical fibers.

Optical fiber sensors can be defined as fiber-based devices for assessment of physical measurands and concentration of chemical species. The most simple and common scenario to describe the working principle of optical fiber sensors is measuring the changes in the input and output light, i.e., the measurand is characterized by the light loss. Another common approach is time measurements of light distribution over the fiber. In both cases, the light is generated by a light source and then is coupled into the fiber by the appropriate optics in a single fiber or in one or several fiber Bragg gratings. The instrumentation of such sensors varies in their complexity according to specific technical requirements and applications. The working principle of a generic optical fiber sensor is visually introduced in a block diagram pictured in Fig. 10 [16].

Modern fiber-optic sensor technology originally goes down to the breakthrough achieved over five decades ago in the 1960s, when laser technology and low-loss optical fibers were investigated. It aroused the interest was followed by pioneering experimental works focusing on the use of low-loss optical fibers for sensorial applications. It aroused the interest for the sensing and measurement potentials of optical fiber technology in R&D sphere. At present, there are a variety of manufacturing methods to produce optical fibers for sensorial applications that ensure an efficient measuring process [17]. The main advantageous characteristics of optical fiber sensors are their lightweight, compact size, flexibility, immunity to electromagnetic interference (EMI), high sensitivity, large bandwidth, efficient signal transmission, potential of distributed sensing, and relatively low cost.

Optical fiber sensors generally can be divided into physical and chemical or biochemical sensors and have many technical and medical applications competing on the market with electronic measurement devices.

Optical fiber technology can provide appealing solutions to assess such measurands as strain, temperature, pressure, current and voltage, rotation, vibration and acceleration, bending and torsion, positioning, or displacement [18].

This technology is based on physical parameter investigations. It is widely used in structural health monitoring to evaluate stress and strain in buildings and vehicle constructions. Moreover, such lightweight sensor arrays enable remote data transmission.

Above that, optical fibers find applications in the development of biosensors. Those are capable of ensuring qualitative and quantitative assessment of bimolecular interactions and detecting toxic substances and some chemical constituents [19]. Biosensing and biochemical optical sensing is crucial in biotechnology, water and air quality monitoring, and medicine and is used for sensing such parameters as pH, partial pressure of carbon dioxide, glucose, and oxygen.

Optical fiber sensor technology is also an appealing know-how in the sphere of smart and intelligent textiles. The integration process of optical fibers can be fully automated and implemented with such conventional technologies as knitting and weaving. Moreover, these processing techniques ensure dimensional variations and manufacturing of large-scale sensorial areas [20]. Attempts to explore the potentials of optical fiber technology for intelligent textiles started within the first steps toward smart textile development. One of the first successful multifunctional smart clothing prototypes was developed more than 10 years ago. It was mostly based on optics technology using fibers as sensors and data transfer modules. At present, optical fiber is used in manufacturing of biosensing textiles and textile-integrated physical sensors for biomedical and technical applications.

Optical fiber sensor technology is a vast topic involving different manufacturing, processing, and measurement approaches. Hereby, in order to provide summarized information on optical fiber sensors for smart textile applications, those will be grouped and described according to the assessed measurands.

Temperature Sensors

Temperature is a significant factor in manufacturing, physiological, and biological processes. Optical fiber-based temperature sensors have a wide range of measured temperature and can operate at different environmental conditions [21]. Specifically designed and processed optical fiber sensors for temperature estimation have indeed many applications in technical and medical sphere. Temperature sensors based on optical fiber technology are in a great variety available on the market. Nevertheless, in the R&D sphere, those still arouse interest and encourage attempts to improve their performance and properties.

Smart textiles that are in the focus of many applied research projects definitely encourage further investigations and the development of textile-integrated sensors for temperature control. Such textile-integrated sensor or sensor arrays are used for microclimate evaluation and acquisition of body temperature. Especially for medicine and healthcare applications, optical fibers are promising materials to ensure continuous manufacturing and efficient processing of textile sensors based on optic technology.

The fiber Bragg grating (FBG) is the most widespread approach to produce a textile-integrated single sensor or sensor array for temperature assessment that is based on optic technology. FBGs can be defined as intrinsic fiber compounds/elements

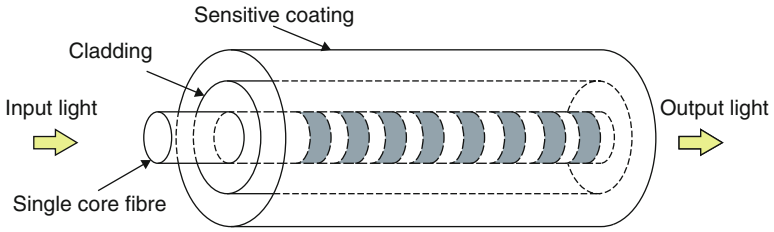

Fig. 11 General scheme of an optical fiber sensor based on FBG

in photosensitive fibers where the index of refraction in the fiber core is periodically modulated by illuminating UV light [22]. According to its processing, the FBG is used to develop a sensor for estimation of a great number of sensors with different applications. Figure 11 displays a generalized scheme of a FBG sensor, which can be applied to describe optical fiber sensors for the assessment of various parameters. Those can be used for evaluation of metal corrosion, bone declaration, humidity, gas, pressure mapping, deformation, and many other phenomena.

There are a number of characteristics that make the FBG an appropriate technologic solution for temperature sensor development in smart textile applications. Namely, FBGs have such advantageous characteristics as versatility for wavelength-encoding applications and simple manufacturing process that ensures regulation of such parameters as period, length, amplitude, apodization, and chirp of the fiber grating. Moreover, such sensors are highly sensible, continuously stable during use, and flexible and have immunity for electromagnetic interference [23]. At present, this topic attracts much interest, and many research projects have explored and continue their scientific work on the topic looking for solutions suitable for smart textile applications. According to specific requirements, the FBG sensor can be manufactured by joining different technologies; particularly such processing is made to increase such properties of the sensor as sensitivity and resolution. A bare FBG usually does not have enough temperature sensitivity (10 pm/°C at 1 550 nm) for physiological applications [24]. Thus, in order to create a durable FBG sensor with efficient performance, such approaches as cladding-etching, polymer packaging, coating, and many others can be applied. Processing that involves temperature-sensitive materials accordingly has a significant effect on the sensor thermal sensitivity [25].

Temperature values are estimated from the dependence of the wavelength and temperature changes. This relationship results in changes of the effective index based on the thermo-optic effect and thermal expansion of the glass material [26].

An example of an optical temperature sensor embedded into textiles is presented by [25]. The research team enhanced the sensing properties of the optical fiber by polymer packaging and achieved both stable structure of the optical sensor and relevant linear relationship between the FBG wavelength and measured temperature. The polymer used for the fiber processing is a copolymerization of unsaturated polyester resin mixtures. The first compound (5.0 wt% methyl ethyl ketone peroxide (MEKP)) was produced by the polycondensation of saturated and

unsaturated dicarboxylic acids with glycols, which ensures highly durable structures and coating. Another polymer compound was 2.0 wt% cobalt naphthenate. Such a processing of the FBG has increased the efficiency of temperature measurements almost 15 times in comparison to the bare FBG. Subsequently, the developed FBG sensor was integrated into a woven fabric. It is crucial to mention that in this case, the sensor is not applied directly to the body, but is separated by an air gap between the skin and clothing. Hereby, the authors offer a mathematical model taking into consideration these particularities of the wearable system. Such a data processing allows acquiring more accurate values to estimate the real body temperature [25].

Besides wearable applications for physiological assessment, this approach has outlooks in structural health monitoring. Braiding technology ensures efficient integration of FBG-based sensors into various composite reinforcement structures. Above that, FBGs can be successfully used to evaluate other crucial parameters for construction quality evaluation, making this optical fiber technology multifunctional and interesting for investigations.

Strain Sensor

One of the most reported application of optical fiber sensors in smart technical and medical textiles is strain or stress measurement. Such sensors assist in monitoring of construction, geotechnics, medicine, and wellness. They give information on mechanical deformations and displacements. Thus, besides structural health monitoring, those have potentials in kinematic analysis. Moreover, optical fiber strain sensors find practical applications as pressure sensors in such fields as industrial process control, dental medicine, ulcer prevention, structural health monitoring in oil wells, and power plants [27, 28].

There are various scenarios for such sensor development resulting in the use of different materials or types of optical fiber sensors and accordingly sensing and data processing techniques. Finally, there are different offered solutions for sensor embedment into a textile structure. Of course, those are chosen accordingly to specific technical requirements and application specifics. Such textiles with integrated optical fiber sensors are already manufactured industriously and are available on the market. Still, in order to improve the technology and expand its applications, this topic is also in the focus of applied research [29]. Due to a great number of sensing techniques and a variety of used materials and approaches to data acquisition, only several most spectacular examples of strain sensors are briefly described further.

Initially, the concept of an optical fiber strain sensor is based on mechanical deformations of the optical fiber polymer coating. Deformation of the polymer structure, in which the optical fiber is embedded, results in modulation of the light passing through the optical fiber core. These changes can be described by physical parameters, and, thus, stress provided by the environment can be calculated.

One of the strain measurement approaches is based on silica fiber distributed sensors. Some years ago, one of the interesting and often used approaches in the variety of strain sensing techniques applied in geotechnical textiles was Brillouin optical fiber time-domain analysis (BOTDA). This approach is based on the

Fig. 12 Optical fiber pressure sensor: plastic optical fiber and two samples of a sensor-woven structure [30]

relationships of the transmitted light, which is sent as a short pulse along the optical fiber, and the backscattered light over the time function. The processed results of this process provide information on the strain applied to the sensor. Such sensor system can operate with a probe distance of 20–30 km but results in low resolution. At present, it is substituted with a more advanced data transmission and processing approach called Brillouin optical fiber frequency-domain analysis (BOFDA). It is based on measurements of a baseband transfer function in frequency domain by a network analyzer. It has a range of advantages such as data processing efficiency and obtained signal quality. Such distributed Brillouin sensor arrays that can be applied for monitoring of long-distance areas are of great interest and potentials for industry. Thus, there are several examples of research projects carried out to encourage further developments of such smart geotextiles [30].

Geotechnical textiles with strain sensor arrays can be developed in various structures, for example, nonwoven, woven, and braided. Especially for geotechnical textiles and those for other technical applications, textile technology offers efficient and low-cost solution in smart monitoring structure development. Figure 12 displays an industriously manufactured geotechnical textile sample [31].

Pressure Sensors

Optical fiber technology finds also applications in pressure sensing and mapping that can be implemented by different approaches. There are many examples of studies based on optics technology using different types of optical fibers. Weaving technology offers vast opportunities in pressure sensor implementation with pattern and structure variation. Some examples of woven pressure sensor design are presented by Swiss company EMPA professionals. They used a flexible silicone fiber to manufacture pressure samples with different patterns (Fig. 13) [30].

Other studies offer pressure sensor implementation addressing interferometry. Moreover, optical fiber sensors based on Fabry-Perot interferometric technology are reported to be able to capture the dynamic pressure transient changes during a blast. Such sensors can assist in the evaluation of a ballistic wave dynamics in military applications [32]. Some studies use also a combined approach of using interferometry technology and FBGs for multiparameter sensor system development [33, 34].

Such sensors find potential applications both in medicine and healthcare and monitoring of structural defects [35].

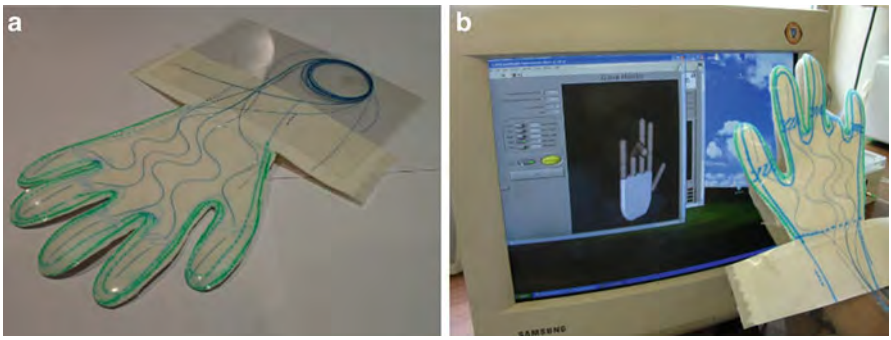

Fig. 13 Smart glove with integrated FBGs for motion visualization (© 2013 Carmo et al., licensee InTech. This is an open access chapter distributed under the terms of the Creative Commons Attribution License (http://creativecommons.org/licenses/by/3.0), which permits unrestricted use, distribution, and reproduction in any medium, provided the original work is properly cited) [38]

Humidity Sensor

Another crucial parameter describing the environment is humidity level. Usually it is associated with relative humidity (%) that traditionally indicates saturation of water vapor in the air. As absolute humidity, the amount of water in a substance is indicted.

Humidity level control is crucial in many technical and medical applications. Optical fiber technology for humidity assessment finds applications in geotechnical and technical textiles for structural monitoring. Moreover, an irrelevant humidity level can injure the construction or encourage bacteria and fungi growth. Above that, it has a great influence on such physiological processes as respiration and cardiac activity.

Since recent years along with the progress in technology, the number of competing techniques and optical fiber solutions for humidity measurements has significantly increased. Optical fiber solutions for humidity estimation include a variety of sensing techniques and involve application of in-fiber grating, evanescent wave techniques, hybrid approaches, and interferometric and absorption methods [36].

Previously described FBG sensors find vast applications also in humidity assessment. Moreover, such sensors are already available on the market, indicating the approach efficiency. Humidity sensing properties of FBG sensors are related to their strain sensitivity. The polymer coats the optical fiber, absorbs the moisture, swells, and expands in volume, thus applying stress on the grating. Such an effect causes the changes in the resonance wavelength, and humidity can be calculated from the strain function.

Kinematic Analysis and Motion Sensor

Kinematic analysis is of a great importance in physiotherapy, rehabilitation, sports medicine, and other spheres of healthcare. It regards gait and posture monitoring, as well as the assessment of dynamics and movements of a particular body part.

One of the urgent problems that encourage the development of such smart textiles is deviations of spinal curvatures and related diseases. Those might be concerned with both physical and social problems of patients of different ages, e.g., discomfort due to pains caused by spinal deformities and contorted posture. Assessments of the spinal cord are commonly realized by radiography, ultrasonography, and other methods that require to be realized by professionals in clinical or laboratory environments. Reduction of spinal deformities and improvement of posture require generally long-lasting therapeutic and physiotherapeutic treatments, e.g., orthotic intervention and therapeutic physical training. Still some extra arrangements might be appropriate during or after therapeutic and physiotherapeutic treatments to control and improve patient's posture in everyday life. One of the options to control patient body position for a long-lasting period is the application of wearable sensor arrays integrated into textiles.

There are a great number of research projects devoted to investigations and exploring possible wearable solutions. Many of them focus on application of inertial sensor systems involving accelerometers and gyroscopes. Nevertheless, textile-integrated systems based on optical fiber technology for these purposes have a range of advantages in comparison with the former due to continuous technological process ensured by such technologies as weaving and tailored fiber placement embroidery.

Initially, optical fiber sensors for motion control and kinematic analysis, as well as some optical fiber sensors for other physiological parameter assessments, are based on the working principle of the strain sensor, which is described in the previous part of the chapter.

Physical and mechanical properties of polymer optical fibers (POFs), as well as simplicity in signal processing, make them attractive both for technical and biomedical applications. Several research projects have introduced textile-integrated POF sensors for health monitoring. For example, an Irish research team has developed a vest with an integrated POF sensor for posture monitoring and control. The POF is integrated to ensure real-time evaluation of the trunk position in the sagittal plain. Strain measurements are caused by mechanical deformations in the fiber sensor that correspond to the wearer's posture [37].

There are also examples of FBG sensor applications for motion monitoring and visualization. One of the described approaches that ensures relatively simple and effective gait monitoring in real time can be implemented by measuring knee movements. This research project suggested the development of a sensing elastic bandage placed around the knee. One of the crucial objectives in such system is accurate measurements during flexion and extension dynamics that characterize movements of a knee joint. FBGs were integrated on a flexible stretchable foil and placed on a hosting polyvinyl chloride (PVC) material [38]. The same approach was applied in the manufacturing of a smart glove with integrated FBGs on a polymeric foil. The obtained data were used to visually reproduce movements of the wearer's hand.

Respiration Rate Monitoring Sensor

Respiration rate is one of the vital parameters that is crucial to be monitored both in preventive and therapeutic purposes. There is already a variety of attempts describing scenarios for smart textile development in order to ensure breath monitoring.

Optics technology offers a technologically simple and efficient solution based on mechanical deformation of the sensors.

One of the most spectacular examples of optical fiber solutions for physiological monitoring is found in the research project OFSETH, which has achieved breakthrough results by developing a respiration rate sensor based on a bare optical fiber fully integrated into textiles. Although other alternatives have already existed before, this development was created particularly for a magnetic resonance imaging (MRI) environment, where conventional medical devices are not compatible or may complicate the examining process. The assessment of respiration rate by optical fiber sensor was ensured by measuring abdominal and thoracic respiratory movements. In the frames of the research project, several scenarios for the wearable sensor were accomplished. Those have addressed different types of optical fibers and implementation technology solutions. Nevertheless, a special focus in the research was made on POF sensor applications as an alternative solution to silica-based fiber due to its biocompatibility [39].

Besides wearable textile sensors, there are possible alternative solutions for respiration monitoring via optical fiber technology. A research team from Japan has reported about the application of an optical fiber pressure sensor as a system for continuous real-time respiration monitoring in a radiation therapy environment. The system was developed on a commercially available pressure sheet that consisted of optical fibers and "Kinotex" tactile sensors embedded in urethane cellular foam. The working principle of the sheet is based on evaluation of changes in light scatter intensity caused by applied pressure. Synchronization and calibration of the acquired data according to a reference medical spirometer ensured the opportunity to display the respiratory wave profile [40].

Another research project carried out in Slovenia has proposed the estimation of respiration rate and heartbeat by a technique based on optical interferometer and wavelet transform. The working principle of interferometry sensors is based on measurements of optical fiber elongation. According to the reviewed literature, such sensors are reported to be of high sensitivity and capable of reacting to micrometric changes in optical fiber length. These characteristics of the described approach bring new potentials for biomonitoring smart textile developers. In this case, the interferometer of the experimental setup was a twisted optical fiber placed under persons' body. Physiological information about respiration and heartbeat was estimated by processing the distorted interferometric signals caused by the mechanical motions during breathing and cardiac activity [41].

Sensor for Cardiac Activity Assessment

Cardiac activity can be characterized by heartbeat and electrocardiography (ECG). Monitoring of cardiac activity was initially a challenging task for smart textile developers, and at present, there are a variety of solutions using different approaches. Optical fibers for cardiac assessment primarily have potentials in clinical applications during MRI.

Heart frequency can be estimated from cardiopulmonary components registered by optical fiber sensors, and this parameter can be obtained by processing physiological data acquired by respiratory optical fiber sensor. This approach is suitable for compact and wearable solutions.

More complicated objectives appear in a sensorial system development for electrocardiographic signal estimation. There are already several studies that have investigated and reported about the applications of optical fiber-based sensors in biopotential activity estimation [42]. One of the scenarios to implement an optical fiber-based bioelectric acquisition system is the application of an interferometer module as the sensing compound. For example, Fernandes at el. proposed a wearable solution based on the electro-optic technology. It uses a photonic setup, which consists of a photodiode, dual-drive lithium niobate ($LiNbO_3$) and Mach-Zehnder interferometer (MZI) modulator, and electronic circuitry for signal processing [43].

Biochemical Sensors

Besides physical measurements, optical fiber-based technology is often chosen for manufacturing biochemical sensors. This is a challenging and promising research field that finds applications for different purposes and environments. Those can be gas sensors where a significant compound of the optical sensor is its coating. In this case, this coating acts as a "smart skin" reacting with specific chemicals in the environment [44].

Hereby, the studies that are looking for new solutions for gas sensing primarily focus on fiber coating technologies, their chemical sensing properties, and durability of the coating. Optical fiber sensors are used as indicators for such chemical compounds as ethanol, methanol and formaldehyde vapor, ammonia gas, etc. [45, 46]. Sensitivity and durability of a gas sensor can be increased by using a multilayer coating approach [47].

Textile-integrated optical sensors for biochemical analysis find application first of all in medicine and healthcare. For example, the BIOTEX research project presents a study that demonstrated a pH sensor for sweat analysis. The sensor was implemented by joining technology and was based on colorimetry [48]. Researchers from Switzerland offered a smart solution for pulse oximetry. They have used weaving and embroidery for sensor manufacturing with polymethyl methacrylate polymer optical fiber (PMMA-POF). The patterns were designed to reproduce light-emitting and light detectors using optical fibers in order to assess human tissue probe [32].

Lightening Effects for Ambient Assisted Living

Social and demographical changes have caused a necessity for new solutions to ensure a safe and comfortable environment of such part of the population as the elderly and those who need professional, social, and medical assistance. Accompanied by technology progress, this situation has triggered the growth of interest and rapid development of the research sphere associated with Ambient Assisted Living (AAL) [49].

The main goals of AAL systems are to enable a networking of the environmental system compounds, provide specific situation-oriented solutions, and be an asset in individual activities. Moreover, the idea of AAL proposes an autonomic recognition of the necessities and flexible adjustment of the system.

The AAL environment incorporates tools for purposes, such as safety insurance of the user, communication, monitoring of his vital signs and behavioral patterns, and navigational assistance. The provided solutions require a multidisciplinary approach and are supported by communication and information technology, engineering, and design. Smart textiles are often a convenient scope to bring additional functionality to the surrounding environment and keep it friendly and aesthetic. Those find applications almost in every AAL tool development and can carry sensor and actuator functions in interactive interface, communication or data transfer, and behavioral and physiological monitoring.

Optical fibers can be an alternative option in some applications of conductive textiles and traditionally are used for data transfer. Moreover, optical fiber technology brings vast opportunities in lightening effect creation. Lightening effects for AAL can be characterized by a fusion of functionality and design. Topographical disorientation can be a serious problem that needs solutions in navigational assistance [50]. Single fibers and textile diffusers are a perfect tool to ensure lightening track and assist the user in coordination and movement in the home environment. Moreover, those can carry the function of a light indicator in a textile interface or give a user a stimulus for specific actions or decisions, for example, assist as a reminder or coordinator. Finally, textile diffusers or compounds based on optical fiber technology can be an asset in light therapy incorporated with interior design.

Summary

Optical fibers are lightweight, flexible, and compatible with textile yarns. One distinguishes mainly two sorts of optical fibers: glass fibers and polymer optical fibers. Having diameters varying between 125 and 1000 μm, they carry signals in the form of pulses of light over distances of up to 50 km without the need for repeaters. These signals may code voice communications or computer data.

Generally, optical fibers have a cylindrical cross-sectional shape. They possess a central core, in which the light is guided, embedded in an outer cladding of slightly lower refractive index. Light rays incident on the core-cladding boundary at angles greater than the critical angle undergo total internal reflection and are guided through the core without refraction. Rays of greater inclination to the fiber axis lose part of their power into the cladding at each reflection and are not guided.

There are three main kinds of fiber optics, the most simple being the “step index” where the light is bounced along the length of the fiber from one side to the other. Two materials with different densities are needed, the less dense being used as coating. In this method, the light travels in zigzag motion and thus transmission of information can take some time. Another way of producing fiber optics involves the “graded index” fiber which also relies on materials with different densities.

The variation occurs in the center of the fiber causing the light to bounce but in a smoother and more gradual curve. The sharpest and most direct transmission of light traveling in a straight line is achieved by applying a synthetic fiber possessing a very narrow inner core, almost the width of the actual path of light.

Interest in the use of light as a carrier for information grew in the 1960s with the advent of laser as a source of coherent light. Initially, the transmission distances were very short, but as manufacturing techniques for very pure glass arrived in 1970, it became feasible to use optical fibers as a practical transmission medium. At the same time, developments in semiconductor light sources and detectors meant that by 1980, worldwide installation of fiber-optic communication systems had been achieved. The Japanese company Mitsubishi Rayon was one of the first companies that were active in developing plastic fiber optics for illumination in the 1990s. Nowadays, optical fibers are applied in versatile areas, ranging from pressure and chemical sensors, illuminating textiles, to light therapy.

References

1. Mitschke F (2005) Fibre optics: physics and technology. Elsevier, Munich
2. Ziemann O, Krauser J, Zamzow P, Daum W (2008) POF handbook: optical short range transmission systems. Springer, Berlin
3. Michaeli W (2006) Einführung in die Kunststoffverarbeitung. Hanser, Munich
4. Nalwa HS (2004) Polymer optical fibres. American Scientific Publishers, Stevenson Ranch
5. Katoot MW (1999) Polymer optical fibres and process for manufacture thereof. US patent 5861129A
6. Hackenberg MR (2001) Untersuchungen zu Versagemechanismen von Kunststofflichtwellenleitern unter thermischer und mechanischer Last. Dissertation, Ulm
7. Oscarsson L, Jacobsen Heimdal E, Lundell T, Peterson J (2009) Flat knitting of a light emitting textile with optical fibres. Autex ResJ 9:61–65
8. Eichhoff J, Hehl A, Jockenhoevel S, Gries T (2013) Textile fabrication technologies for embedding electronic functions into fibres, yarns and fabrics. In: Multidisciplinary know-how for smart-textiles developers. Woodhead Publishing, Oxford
9. Selm B, Gürel E, Rothmaier M, Rossi R, Scherer L (2010) Polymeric optical fiber fabrics for illumination and sensorial applications in textiles. J Intell Mater Syst Struct 21:1061–1071
10. Park S, Jayaraman S (2001) Adaptive and responsive textile structures (ARTS). In: Smart Fibers, fabrics and clothing. Woodhead Publishing, Cambridge
11. Gopalsamy C, Park S, Rajamanickam R, Jayaraman S (1999) The Wearable Motherboard™: the first generation of adaptive and responsive textile structures (ARTS) for medical applications. Virtual Reality 4(3):152–168
12. Cochrane C, Mordon SR, Lesage JC, Koncar V (2013) New design of textile light diffusers for photodynamic therapy. Mater Sci Eng C 33:1170–1175
13. Khan T, Unternaehrer M, Buchholz J (2006) Performance of a contact textile-based light diffuser for photodynamic therapy. Photodiagnosis Photodyn Ther 3:51–60
14. Mordon S, Cochrane C, Lesage JC, Koncar V (2011) Innovative engineering design of a textile light diffuser for photodynamic therapy. Photodiagnosis Photodyn Ther 8:142–143
15. Medwow (2013) http://www.medwow.com. Accessed 30 Nov 2013
16. Gupta BD (2006) Fiber optic sensors - principles and applications. Jai Bharat Printing Press, New Delhi
17. Grattan KT, Sun T (2000) Fibre optic sensor technology: an overview. Sensors Actuators 82:40–61

18. Lee B (2003) Review of the present status of optic fibre sensors. Opt Fibre Technol 9:57–79
19. Chou C, Wu HT, Yu CJ (2007) Fibre-optic biosensors for antigen/antibody kinetic assays. SPIE Newsroom: Biomedical Optics and Medical Imaging
20. El-Sherif M (2005) Integration of fibre optic sensors and sensing networks into textile structures. In: Wearable electronics and photonics. Woodhead Publishing, Cambridge
21. Zhang B, Kahrizi M (2007) High-temperature resistance fiber Bragg Grating temperature sensor fabrication. IEEE Sensors J 7:586–591
22. Mishra V, Singh N, Tiwari U, Kapur P (2011) Fiber grating sensors in medicine: current and emerging applications. Sensors Actuators A 167:279–290
23. Lee CH, Lee J, Kim MK, Kim KT (2011) Characteristics of a fibre Bragg Grating temperature sensor using the thermal strain of an external tube. J Korean Phy Soc 59:3188–3191
24. Li Q, Yang H, Li E, Liu Z, Wie K (2012) Wearable sensors in intelligent clothing for measuring human body temperature based on optical fiber Bragg Grating. Opt Express 20:11740–11752
25. Kim KT, Kim IS, Lee CH, Lee J (2012) A temperature-insensitive cladding-etched fiber Bragg Grating using a liquid mixture with a negative thermo-optic coefficient. Sensors 12:7886–7892
26. Khan I, Ahmed I (2012) Sensing principle analysis of FBG sensors. J Electric Electron Eng 1:1–6
27. Zhan Q, Liu N, Fink T (2012) Fiber-optic pressure sensor based on π-phase-shifted Fiber Bragg Grating on side-hole fiber. Photon Technol Lett 24:1519–1523
28. Sakai K, Nakagami G, Matsui N (2008) Validation and determination of the sensing area of the Kinotex sensor as part of development of a new matress with an interface pressure-sensing system. Bio Sci trends 2:36–43
29. Krebber K (2013) Smart technical textiles based on optical fiber technology. In: Current developments in optical fiber technology. InTech, Rijeka, pp 319–344
30. Rothmaier N, Luong MP, Clemens F (2008) Textile pressure sensor made flexible plastic optical fibers. Sensors 8:4318–4329
31. Liehr S et al (2008) Distributed strain measurement with polymer optical fibers integrated into multifunctional geotextiles. In: Photonics Europe. International Society for Optics and Photonics, pp 700302-700302–15
32. Zou X, Wu N, Tian Y (2013) Rapid miniature fiber optic pressure sensors for blast wave measurements. Opt Lasors Eng 51:134–139
33. Wang W, Jiang X, Yu Q (2012) Temperature self-compensation fiber pressure sensor based on fiber Bragg Grating and Fabry-Perot interference multiplexing. Optics Commun 285:3466–3470
34. Bremer K, Lewis E, Leen G (2011) Fabrication of an all-glass fibre optic pressure and temperature sensor. Proc Eurosensors 25:503–506
35. Pandey NK, Yadav BC (2007) Fiber optic pressure sensor and monitoring of structural defects. Optica Appl 27:57–63
36. Alwis L, Sun T, Grattan KTV (2013) Optical fibre-based sensor technology for humidity and moisture measurement: review of recent progress. Measurement 46:4052–4074
37. Dunne L, Walsh P, Caulfield B (2007) A system for wearable monitoring of seated posture in computer users. In: 4th international workshop on wearable and implantable body sensor networks proceedings, Aachen/Germany, vol 13, pp 203–207
38. Fereira da Silva A, Rocha RP, Carmo JP, Correia JH (2013) Photonic sensors based on flexible materials with FBGs for use on biomedical applications. In: Current developments in optical fiber technology. InTech, Rijeka, pp 105–132
39. Grillet A (2007) Optical fibre sensors embedded into technical textile for healthcare. Tutorial on SFIT, 4th international workshop on wearable and implantable body sensor networks (BSN'07), Aachen
40. Yokokawa M, Miyahara Y, Ikeda S (2010) Evaluation and application of optical fiber pressure sensor as a new real time respiration monitoring system for radiation therapy. In: Proceedings of the 52nd annual ASTRO meeting, San Diego, vol 78. p S673

41. Šprager S, Zazula D (2013) Detection of Heartbeat and Respiration from optical Interferometric signal by using wavelet transform. Comput Methods Programs Biomed 111:41–51
42. Kingsley SA, Sriram S, Pollick A (2004) Photrodes (TM) for physiological sensing. In: Optical fibers and sensors for medical applications, In Biomedical Optics 2004. International Society for Optics and Photonics, Bellingham, vol IV, pp 158–166
43. Fernandes MS, Correia JH, Mendes PM (2013) Electro-optic acquisition system for ECG sensor applications. Sens Actuators A Phy 203:316–323
44. Pasche S, Schyrr B, Wenger B (2013) Smart textiles with biosensing capabilities. Adv Sci Technol 80:129–135
45. Renganathan B, Sastikumar D, Raj S, Ganesan AR (2014) Fiber optic gas sensors with vanadium oxide and Tungsten Nanoparticle coated cladding. Optics Commun 315:74–78
46. Kudo H, Wang X, Suzuki Y (2012) Fiber-optic biochemical gas sensor (Bio-Sniffer) for sub-Ppb monitoring of formaldehyde vapor. Sens Actuators B 1:486–492
47. Jiang H, Yang R, Tang X (2013) Multilayer fiber optic sensor for In Situ gas monitoring in harsh environments. Sens Actuators B 177:205–212
48. Coyle S., Moriss D, Lau K (2009) Textile sensors to measure sweat pH and sweat-rate during exercise. In: Proceedings of 3rd international conference on pervasive computing technologies for healthcare, London
49. Neuhaeuser J, Wilkening M, Diehl-Schmidt J (2012) Different sADL day patterns recorded by an interaction-system based on radio modules. In: Ambient assisted living, Advanced technologies and societal change. Springer, Berlin, pp 95–105
50. Torres-Solis J, Falk TH, Cahu T (2010) A review of indoor localization technologies: towards navigational assistance for topographical disorientation. In: Ambient intelligence. In-Tech, Rijeka, pp 51–84

Polymer Optical Fiber for Smart Textiles

5

Wei Zeng

Contents

Introduction 110
Basics of POF 110
Structure of POF 110
Materials of POF 111
Mechanical Property of POF 113
Operating Principle and Classification of POF Sensor 113
Micro-bending POF Sensor 114
Macro-bending POF Sensor 115
Coupling Fiber POF Sensor 115
Evanescent Field POF Sensor 116
Application of POF Sensors and POF Fabrics 117
Single POFs Used as Fiber Sensor 117
Applications of POFs Integrated into Textiles 117
Summary 122
References 123

Abstract

Polymer optical fiber has significant advantages, including flexibility, durability, lightweight, biocompatibility, and electromagnetic interference immunity. It can not only be used as a single sensor probe but also be integrated into fabric as smart textiles. This chapter presents a review on structures, types, materials, and physical properties of POF; current technologies applied in POF sensors; applications of POF sensor; and POF in textiles. Finally, the current issues in this area are discussed.

W. Zeng (✉)
Hong Kong Polytechnic University, Kowloon, Hong Kong, China
e-mail: wei.zheng@connect.polyu.hk

© Springer Science+Business Media Singapore 2015

X. Tao (ed.), *Handbook of Smart Textiles*,
DOI 10.1007/978-981-4451-45-1_23

Keyword
POF sensor • Light intensity • POF fabric • Smart textile

Introduction

Smart textiles have been exploited for many applications, such as monitoring gesture, heart rate, temperature, or respiration of human, and have great potentials on the textile and apparel market. At present, most of the smart textiles are based on electrical fabric or fibers to form the sensing unit. But the functions of smart textiles integrated with electrical fabric or fibers can be affected by electromagnetic interference.

On the other hand, the optical fiber can be integrated into the fabric as smart textiles for the following reasons:

- Lightweight, small size, durability
- Immunity to electromagnetic interference
- Easy handling, simple connections, biocompatibility
- Light transmission or emission on part or whole fabric surface

In comparison with the traditional silica optical fiber, the polymer optical fiber (POF) displays an eminent pliability, low Young's modulus of several GPas, and large breaking strain of ~6 %. Furthermore, the POFs are more flexible and bio-friendly than their glass-based counterparts and less risky for injuries on human's skin or eyes.

Now, POFs have a wide range of applications especially for networks in buildings, automobiles, railways, and aviation or in industrial plants. In this chapter, the structure, material, physical properties, and working principle of POF sensor are reviewed, particularly on the light intensity-based POF sensors. Finally, the application of single POF sensors and fabric being integrated with POFs are summarized, especially in illumination and biomedical areas.

Basics of POF

Structure of POF

POF is an optical fiber which is made out of polymers that have been developed over 40 years since the first PMMA core step index POF was produced by Dupont in 1968 [1]. POF is normally composed of two parts. The inner part, termed the core, has a refractive index of n_1; the outer part, termed the cladding or clad, has a refractive index of $n_2 < n_1$. The incident rays reaching the core–cladding interface at angles $\theta > \theta_c$ ($\sin\theta_c = n_2/n_1$) are guided inside the core by total reflection at the core–cladding interface, as shown in Fig. 1.

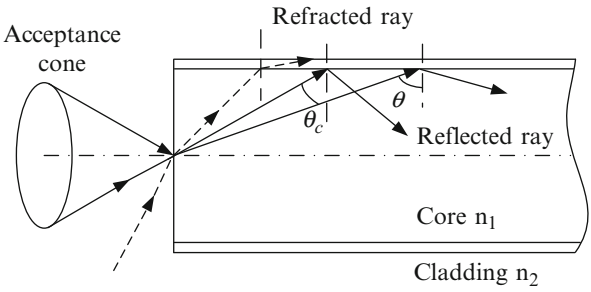

Fig. 1 Light guiding in a multimode POF

There are a few classification methods of POFs. According to the guide mode, they can be divided into two groups as single mode and multimode. Based on the profile of refractive index, they are classified as step index (SI) and gradient index (GI). There is a constant index profile over the whole core cross section in SI fibers. By contrast, in GI fibers, there is a nonlinear, rotationally symmetric index profile, which falls off from the center of the fiber outwards. There are three types of POFs: multimode GI fiber, single-mode SI fiber, and multimode SI fiber. In recent years, microstructured optical fibers (MOFs), known as "photonic crystal fibers" (PCF), are also manufactured by polymers like PMMA and named as microstructured polymer optical fibers (mPOFs). There are many variations of mPOFs' microstructures, and the guiding mechanism is similar to PCF. The patterns of microscopic air holes run down the entire length of the fiber for guiding of light [2].

Materials of POF

PMMA (polymethyl methacrylate), PS (polystyrene), PC (polycarbonate), COC (cyclic olefin copolymers, made by TOPAS Advanced Polymers Co., Ltd), CYTOP (cyclic transparent optical polymer, produced by Asahi Glass Co., Ltd), and silicone are currently used as polymer materials for POFs. The molecular structures of these polymers are shown in Fig. 2. And the properties of them are listed in Table 1.

PMMA is the most commonly used polymer for POFs. It is the polymer from the methacrylate family, which is well known to exhibit high transparency. PMMA has building blocks of monomer methyl methacrylate (MMA), which is produced from acetone. PMMA is manufactured by free radical polymerization using bulk or suspension technique.

PS has no distinct advantage over PMMA. While the PMMA and PS are developed as typical SI POFs' core for the normal conditional use, PC core POF is developed specially for high-temperature applications (Tg $\approx$ 150 °C of PC is higher than that of PMMA and PS). However, the disadvantage of these POFs is that attenuation during transmission is higher than the silica fiber, especially of PC- and PS-based fibers. The attenuation is caused by the electron transition absorption in phenyl groups of PC and PS.

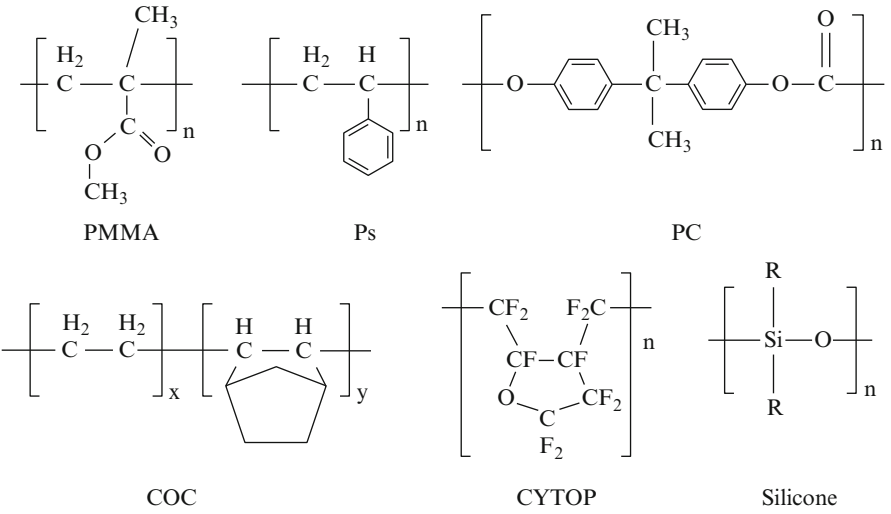

Fig. 2 Molecular structures of polymer materials as POFs (Copyright 2014, The Hong Kong Polytechnic University)

Table 1 Properties of polymer materials for POFs

	PMMA	PS	PC	TOPAS COC	CYTOP [3]	Silicone [4]
Refractive index	1.49 [5] (632.8 nm)	1.59 [5] (632.8 nm)	1.58 [5] (632.8 nm)	1.53 [6] (633 nm)	1.34 (633 nm)	1.41
Radius of fiber (μm)	250–1,000	500–1,000	500–1,000	135	125–150	~500
Optical attenuation (dB/m)	0.055 (538 nm)	0.33 (570 nm)	0.6 (670 nm)	50 (820 nm)	0.016 (1,310 nm)	5.5 (652 nm)
Tg (°C)	105	100	150	178	108	–
Stress-optic constant (10^{-6} mm^2/N)	−4.5 to −4.8	4–7	66–70	−2 to −7	–	–
Water absorption (%)	0.3	0.1	0.2	0.01	<0.01	0

Copyright 2014, The Hong Kong Polytechnic University

COC, CYTOP, and silicone are new developed materials for POFs. Bragg grating has been recorded in microstructured POFs from TOPAS cyclic olefin copolymer for temperature sensing application. And this type of polymer has a promising application in SI/GI POF fabrication. CYTOP is an amorphous, soluble perfluoropolymer having the outstanding properties of highly fluorinated polymers including water and oil repellency, chemical and temperature resistance, and injection formability. The disadvantage is that the fluoride may not be safe for

human health especially during manufacturing and combustion. Silicone can be fabricated as waveguides or optical fibers [4] due to its excellent thermal and chemical stability; high transparency in the ultraviolet, visible, and selected bands of the near-IR spectra; low moisture absorption; and wide range of use temperature. More importantly, it is much softer than those traditional optical polymers like PMMA, PS, or PC. Some silicone elastomers can be easily stretched by 100 % or more and recover its original shape immediately after the strain is released due to its rubber nature. But the high optical attenuation limits its application in sensing area rather than long-distance communication.

Mechanical Property of POF

POF should be flexible and ductile during fabrication into textiles. The physical and optical properties should be varied a little after the textile manufacture. It is necessary to investigate the mechanical property of POFs for understanding the performance of textile sensors based on POF.

Several authors have studied the mechanical properties of POFs. The measured tensile properties for single-mode PMMA POF were summarized by Peters et al. [7]. Young's modulus of these fibers changed from 1.6 to 5.0 GPa, and the break elongations were varied from 6 % to 38 %; cyclic tensile elongation tests were also conducted on the POF. The average residual strain of single-mode POF was 0.045 % in the 10 times cyclic elongation [8], and the power loss of a commercial SI POF reached as high as 18.3 % after 100 cyclic loadings [9].

The mechanical strength of POF depends on many parameters:

1. Drawing tension on preform: A doped PMMA graded index (GI) POF with high tensile strength (~100 MPa), high elongation at break (>50 %), and low length shrinkage (<1 %) was obtained by the optimum tension (~0.8 N) on the preform and followed 70 °C aging [10].
2. Annealing process: Annealing the POF right below the glass transition temperature reduces the degree of chain alignment. The annealed POFs, which were annealed at 95 °C for several days, had higher ductility but lower strength than the unannealed one [11], as shown in Fig. 3.
3. Strain rate: When the applied strain rate was varied from 0.01 to 3.05 min^{-1}, the break elongations of the POF were about 30 % for most of the samples. But the yield strain increased with the applied strain rate [12].

Operating Principle and Classification of POF Sensor

Like silica optical fibers, the basic elements of POF sensing system are shown in Fig. 4. The system includes four parts: several types of light sources under consideration are light-emitting diode (LED), laser diode (LD), vertical cavity surface-emitting laser (VCSEL) diode, etc.; POF can be used as sensing or modulator

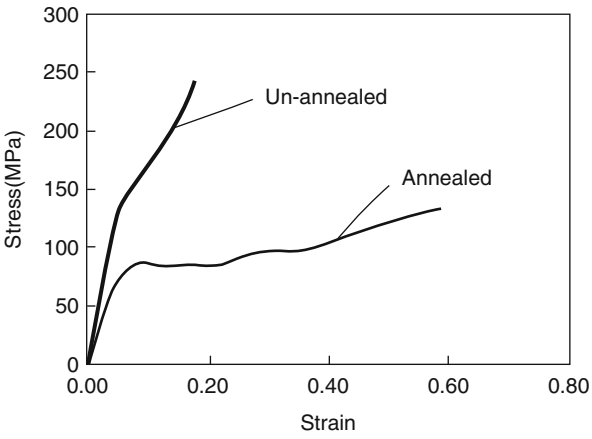

Fig. 3 Effect of annealing on the mechanical behavior of POFs (Copyright 2002, IEEE, License Number: 3544111354880)

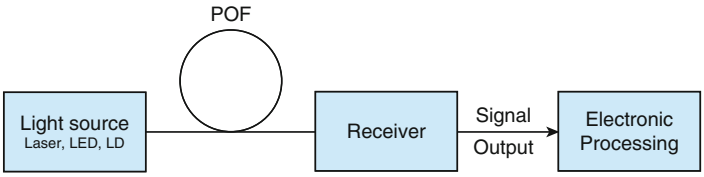

Fig. 4 Basic elements of POF sensing system

element; an optical detector can be used for signal measurement; processing electronics can be used for amplification, signal processing, and data display.

According to the operating principle of modulation and demodulation process, POF sensor technologies include FBG (fiber Bragg grating), interference, OTDR (optical time-domain reflectometry), LPG (long-period fiber grating) and intensity, and so on. The first four technologies have very high sensitivity. Some measurements need complex compensation techniques to reduce the effect of temperature fluctuation in the process of measurement. The advantages of light-intensity POF sensors are low cost, easy coupling, and simplicity in equipment. This type of sensor can be integrated into textile for numerous wearable applications such as display and illumination, fashion design, medical care, and sensing area. Depending on the mechanism of intensity modulation, the working principles of four types of intensity-based sensors are discussed below.

Micro-bending POF Sensor

The typical structure of micro-bending POF sensors is shown in Fig. 5. The light is lost from the optical fiber due to the periodic micro-bend that is induced along the fiber axis and the change in the light intensity can be measured. Hence, by monitoring the decrease in guided optical power in the core as a function of the

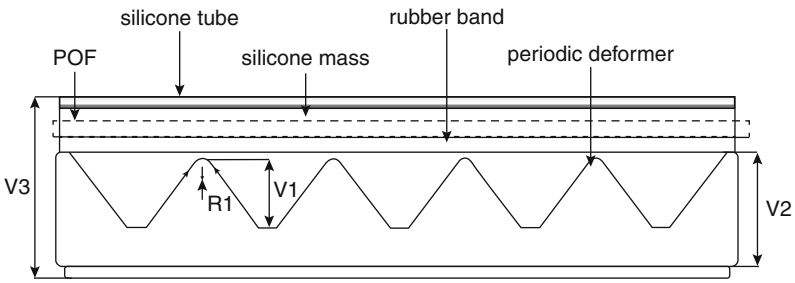

Fig. 5 Schematic diagram of a micro-bending POF anti-squeeze sensor (Copyright 2007, IEEE, License Number: 3554170939219)

amplitude of micro-bending induced on the fiber, pressure sensors can be fabricated [13]. Sensors based on the micro-bending POF sensors have been explored for their good sensitivities but the measurement ranges are very limited.

Macro-bending POF Sensor

Macro-bending losses generally occur when an optical fiber is bent to a radius of several centimeters. Large bending loss is always observed at and below a critical bending of radius, r_c, given by

$$r_c = 3n_1^2\lambda / \left(4\pi\left(n_1^2 - n_2^2\right)^{3/2}\right) \tag{1}$$

where n_1 and n_2 are the refractive indexes of the core and cladding, respectively, and λ is the wavelength of the light. Hence, macro-bending POF sensors are very similar to micro-bending sensors. The difference is the sensor dimension and bending range. In macro-bending, light guided into the cladding is caused by a variation in the angle of incidence. Variation in the light intensity can be detected. For instance, macro-bent POFs glued to a beam were used as an inexpensive sensor to monitor the force on the beam [14]. Sensors based on the macro-bending technique have a wide measurement range, but the resolution is very low in this range. And excess bending has to be prevented with macro-bending sensors to prevent a fiber breakage.

Coupling Fiber POF Sensor

This kind of POF sensor includes the configurations where the light is extracted from a fiber, interacts with the measurand, and is coupled in another or in the same fiber. Reflecting into the same fiber can be achieved by Fresnel reflection or frustrated total internal reflection in the fiber end. Coupling two fibers can be for transmission [15] or for reflection [16], as shown on Fig. 6. But the working range,

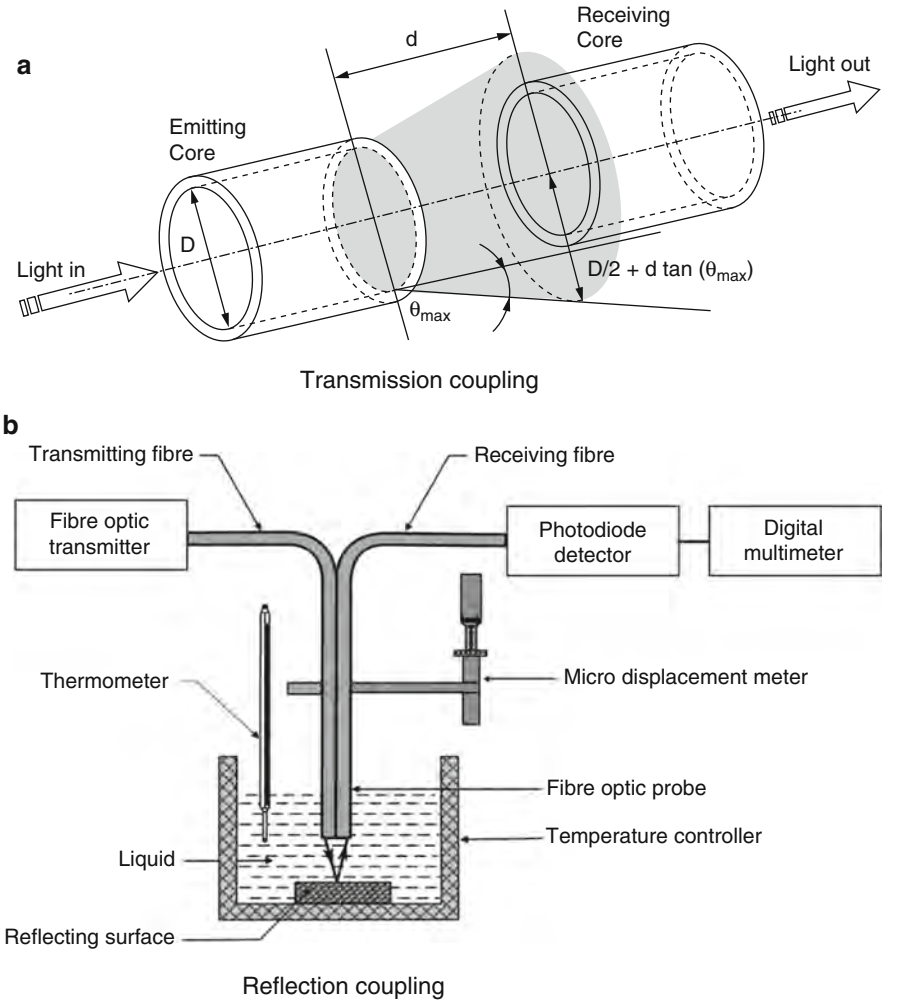

Fig. 6 Schematic drawing of two fibers coupled as POF sensor (a) Transmission coupling (Copyright 2004, IOP,) (b) Reflection coupling (Copyright 2009, Elsevier, License Number: 3554180488468)

the sensitivity, and the linear regions of operation are limited by the configurations of this type of sensor.

Evanescent Field POF Sensor

A weak electromagnetic field tunnels from the high-refractive index medium into the low-refractive index medium when light travels in an optical fiber. This part of the electromagnetic field is called evanescent field and its particularity is to

exponentially decrease. The evanescent field POF sensor is based on the electromagnetic field launched around the fiber core absorbed and/or scattered by the external medium; thus, loss of the light occurs. Hence, it is necessary to come as close as possible to the core to obtain enough sensitivity. In order to increase the sensitivity of the POF curvature sensor, part of the core and cladding are removed from a side of the fiber. Chemical etching, side polishing, and CO_2 laser ablation have been used to remove the cladding or make grooves on the fiber. The main fabrication methods and structures for evanescent field POF sensors are listed in Table 2. The benefits of evanescent field technology include: low-cost manufacturing, fabrication on any configurations, complete matching to fiber system, sensitivity simply and accurately controlled by microstructures on the POF, un-cladding parts of fiber, and structure of the fiber.

In summary, the advantages of light-intensity-based POF sensors are the ease of implementation, low cost, simplicity in signal processing, and possession of adequate sensitivity for a large number of applications. The drawbacks are false reading may be caused by relative measurements and variations in the intensity of the light source, but a referencing system can be used to solve this problem [27].

Application of POF Sensors and POF Fabrics

Single POFs Used as Fiber Sensor

Single POFs in different configuration and structure or imperfection/coating on the surface can be used as sensor elements directly. Table 3 summarizes the main applications of single POF sensors. They are widely used in physical, chemical, and biomedical areas. Most of single POF sensors are based on PMMA; hence, the life of sensor may be affected by thermal, UV, or chemical degradation of PMMA.

Applications of POFs Integrated into Textiles

Integration of Polymer Optical Fiber and Textiles

The most intuitive way to integrate polymer optical fibers into textile or fabric is considering the POFs as a textile fiber or a yarn. Integration could be conducted in a variety of fabric manufacturing processes. Weaving, knitting, and embroidery can be used to integrate POF into fabrics.

Woven fabrics are composed by interlacing two sets of yarns at right angles to each other. The lengthwise yarns are named as warp yarns, while the widthwise yarns are called weft yarns. Weaving is the most common fabric manufacturing method for POF fabrics. POF can be integrated into any woven structure in the warp or weft directions, and the size and mechanical properties of POF should be compatible with the warp or weft yarns. In this structure, the macro-bending loss for the POF is low. To increase surface light emission of woven POFs, mechanical or chemical damage can be used for textile surface treatment. Woven structure POF

Table 2 Fabrication methods and structures of evanescent field POF sensors

POF specification	Microstructures on the POF/structure of sensor	Reference
POF (ESKA CK 10 by Mitsubishi Rayon Co., Ltd) embedded in glass fiber/epoxy composites for strain test	Single transverse crack on the POF surface	[17]
Bent POF (diameter, 1 mm; length, 0.7 m; $n_{core} = 1.49$) as displacement sensor	Imperfection created by abrasive arm with different angle, location angle, displacement, and depth	[18]
Step index POF (ESKA CK 40 by Mitsubishi Rayon Co., Ltd) for monitoring the dynamic response of fiber composite beams	Cladding layer of POF was removed over a length of approximately 70 mm by abrading method	[19]
Step index POF (SH-4001 by Mitsubishi Rayon Co., Ltd) for direct elongation	The grooves with different depths were manufactured on POFs	[20]
POF (ESKA CK 20 by Mitsubishi Rayon Co., Ltd) with a diameter of 0.5 mm and the numerical aperture of 0.5 for curvature measurement	Multiple V-grooves on the surface of POF	[21]
PMMA optical fiber (Industrial Fiber Optics, Inc.) with 0.75 mm core and 0.01 mm cladding used as fluorescence sensor	Micro-channel fabricated on the PMMA fibers by CO_2 laser	[22]
Step index POF with 0.98 mm core and 0.01 mm cladding for fluorescent sensor application	The tapered fiber was fabricated, removing part of the cladding via solvent immersion, and then deposited with fluorophore	[23]
CYTOP graded index POF for absorbance and fluorescence measurements	The cladding was removed by chloroform etch and then the taped structure was formed by heat-pull method	[24]
Two types of POFs, SI fiber (1 mm outer diameter with 0.98 mm core) and GI fiber (1 mm outer diameter with 0.90 mm core), used for deformation sensing	The configuration of POF was multiple loops with grooves deep to the core made by abrading method. This type of sensor was based on both micro-bending and evanescent field technologies	[25]
POF with 1 mm outer diameter and 0.98mm core was used as sensor on pH and concentration response	The 0.02 mm cladding was removed by chemical etch; then, the diameter of fiber was reduced by heat-pull method. After that, the thin fiber was twisted in coiled structure	[26]

Copyright 2014, The Hong Kong Polytechnic University

can be used for luminescent costume fabrication [41]. The details of design and manufacture of a flexible optical fiber display are studied elsewhere [42].

Both knitting and embroidery are techniques for fabricating two-dimensional fabric made from yarns and POFs. The light emissions are achieved by

Table 3 Applications of single POFs sensors

Measurand	Description	Reference
Strain	POF with FBG structure was observed with up to 6.5 % tensile strain with a strain sensitivity of 0.916 pm/$\mu\varepsilon$	[28]
Temperature	The temperature sensitivity of the single-mode POF Bragg grating is found to be 149 pm/°C	[29]
Humidity	Coating the HEC/PVDF on the POF core for real-time humidity sensing	[30]
Temperature and oxygen	Temperature sensing, the side-polished POF surface coated by epoxy glue; oxygen sensing, the POF end coated by a fluorinated xerogel doped with platinum tetrakis pentrafluoropheny porphine	[31]
Liquid refractive index	Side-polished POF for indexing the RI of liquid with the range of 1.30–1.59	[32]
Liquid level	Multipoint liquid-level measurement sensor based on the attenuation caused by bent and polished POFs	[33]
pH	By using a liquid-phase coating method, a pH-sensitive dye-doped CA-film-modified mPOF probe was fabricated with response range from pH 1.5 to 4.5	[34]
Oxygen	A locally tapered optical fiber with a ruthenium complex doping used as sensing element	[35]
DNA and antibodies	The transducer is 3-hole mPOF manufactured by PMMA	[36]
Partial oxygen pressure	Two strands of plastic optical fiber ending in a section of tube, based on fluorescence quenching principle	[37]
Cardiac nerve growth factor (NGF) levels in blood	This sensor utilizes a fiber-optic, immuno-biosensing system which performs a fluorophore-mediated sandwich immunoassay on the surface of an optical fiber	[38]
Blood pressure	A sensor with two static optical fibers and a cantilever. Optical fibers for both illuminating the cantilever surface and receiving the reflected light	[39]
Breath	The refractive index of the media next to the POF tip will determine the amount of light scattered out and the light reflected back into the fiber	[40]

Copyright 2014, The Hong Kong Polytechnic University

macro-bending of POFs, as a result of POFs exposed to severe bends at very small radius of curvature. The drawback is that the POF cannot transmit optical signal in long distance.

Besides the above three technologies, POF could be simply stitched, laminated, or glued into ready fabrics or garment instead of integrating it into the fabric. This structure can be used as macro-bending or micro-bending sensors.

Applications of Textiles Integrated with POFs

The distinguished advantages of textiles integrated with POF are value-added comfort, reliability, and safety. Their applications in engineering and biomedical areas become increasingly popular.

POFs with FBG structure were bonded to a woven textile specimen as strain sensor. The thermoplastic and elastic silicone POF has been reported as woven pressure sensor [4]. Besides, POFs can be integrated into different geotextiles to monitor soil deformation inside dikes and dams and distributed into a garment to locate the exact position of a bullet's impact. But the most significant application of textile integrated with POF is for medical care.

For example, the woven POF illumination pad can be used as a part of a fetal visual stimulation system for fetal and neonatal magnetoencephalography [43] or a part of the Bili-Blanket® system for the treatment of neonatal jaundice [44]. Recently, POFs and traditional yarns are woven as a luminescent fabric layer and integrated into a textile wrapper for jaundice phototherapy as shown in Fig. 7, which can provide comfort, large area, and breathable treatment for the infant [45].

Textiles with POF also can be used as sensor to monitor many vitally important physiological parameters of professionals, patients, and elderly persons. For instance, it can be integrated into fabrics as smart textile to monitor pulse, arterial oxygen saturation in human blood, seated spinal posture, human gait, and heart rate.

Compared with other sensors, the remarkable advantages of POF sensor are flexibility and immunity to electromagnetic interference. In magnetic resonance imaging (MRI) condition, either metallic parts or electrical conductive wires of the monitoring equipment can cause interference of the MRI result and even burn patients' skin. However, POF sensor has immunity to electromagnetic interference, and the optical fiber cable can send a signal detected by sensors to the monitoring instruments and computers outside the MRI field.

An increasing number of respiratory monitors based on the use of optical fibers have recently been developed.

Fig. 7 Phototherapy textile wrapper for treatment of neonatal jaundice

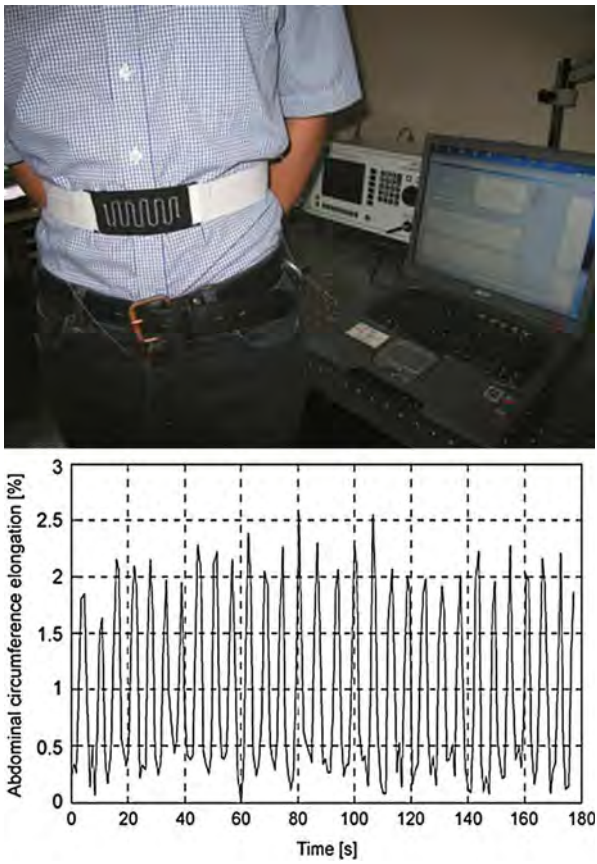

Fig. 8 Abdominal respiratory of an adult monitored and recorded by POF OTDR (Copyright 2002, IEEE, License Number: 3554190358248)

A POF micro-bending sensor was integrated into a mat for breathing rate/breathing pattern monitoring [46]. The sensor was fixed on the back of the person without direct skin contact. The advantages of this type of sensor are high sensitivity, simply design, and inexpensive fabrication costs, but the signal may be affected by the surrounding noises and the measurement range was limited.

Another type of POF sensor was based on OTDR technology [47]. Sensors were embedded into textile fabrics to monitor the respiratory movements in MRI environment (Fig. 8). This technique is very high in sensitivity, but expensive and complex measurement equipment is required.

A new type of four-loop fabric POF sensor is investigated to monitor human respiration [48], as shown in Fig. 9. The loop-structured POF adhered on a flexible and elastic fabric can enlarge the strain range up to 21 %. The POF loops were notched by a CO_2 laser to increase the strain sensitivity. The respiration curves measured by the breath belt and clinic monitor were highly correlated. But the reproducibility of this type of sensors should be improved.

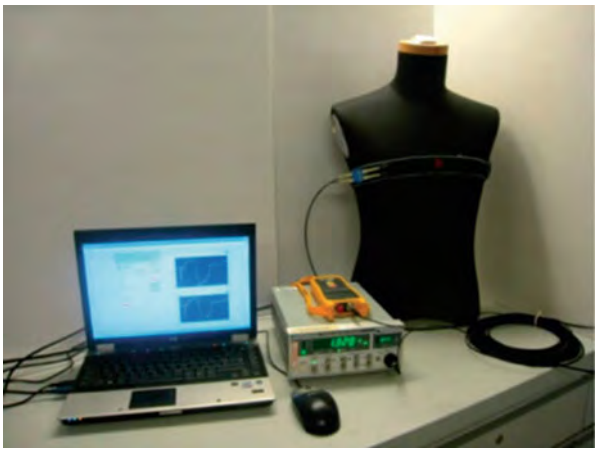

Fig. 9 Human respiration monitoring system based on four-loop fabric POF sensor [48] (Copyright 2014, SAGE)

Some researchers tried combining optical fiber sensor technology to monitor human respiratory. For instance, both the thoracic movements and the abdominal movements of patients were monitored by macro-bending and FBG optical fiber sensors during MRI examination [49]. The respiratory signals were acquired by these two technologies, but both types of sensors were made by silica optical fibers, which were easy to be broken and may hurt the skin or eyes of the patients.

Two different optical fiber sensor technologies are also used to measure respiratory signals during MRI [50]. One was a nasal-cavity-attached sensor that can measure the temperature variation of airflow using a thermochromic pigment. The other sensor was composed of PMMA tubes, a protected aluminum mirror, a spring, and a plastic optical fiber. The distance between the mirror and the end of the POF was changed with the abdominal movement; therefore, the intensity of light reflected by the mirror was changed and detected by optical detector. But the room temperature variation will affect the test results and the PMMA tube was uncomfortable for patients.

Summary

In this review, POFs were described as effective and promising materials integrated into textiles for illumination and sensing application.

Six polymers for POFs were compared, and PMMA is the most common material, which has been commercialized. Hence, commercial PMMA optical fiber has been selected as illumination and sensing element with different modifications and configurations. Mechanical property is a significant physical property of optical fibers. Young's modulus of PMMA optical fibers was in the order of several GPas, and the breaking strain of them was around 6 %, which satisfied the requirement of weaving, knitting, and other textile manufacture technologies.

The advantage of FBG, OTDR, and interference techniques for POF sensors is high sensitivity, which also needs complex and expensive measurement techniques and instruments. Light intensity-based POF sensors have attracted a considerable amount of interests due to their low cost and simple equipment requirement, which has various applications in the engineering area.

Some typical applications of single POF sensor, POF illumination fabrics, and POF sensors in textile were summarized. This review focused on the wearable health monitoring devices based on POF sensor or POF fabrics. Because both POF and fabrics are immune to electromagnetic interference, this type of sensor has potential applications to monitor human breath in MRI condition.

The current issues are the optical materials for POF need to be more flexible, durable, and less light attenuating; the weaving or knitting technologies for POF textiles and relevant optical components should be standardized to push photonic textiles into commercialization; the structure and system for POF sensors should be simplified for wearable application and has higher sensitivity. It is believed that applications of POF sensor and POF in textiles will draw more attention and more products will be commercialized in the future.

References

1. Bartlett RJ, Chandy RP, Eldridge P, Merchant DF, Morgan R, Scully PJ (2000) Plastic optical fibre sensors and devices. Trans Inst Meas Control 22:431–457
2. van Eijkelenborg MA, Argyros A, Bachmann A, Barton G, Large MCJ, Henry G, Issa NA, Klein KF, Poisel H, Pok W, Poladian L, Manos S, Zagari J (2004) Bandwidth and loss measurements of graded-index microstructured polymer optical fibre. Electron Lett 40:592–593
3. http://www.agc.com/english/chemicals/shinsei/cytop/about.html
4. Rothmaier M, Luong M, Clemens F (2008) Textile pressure sensor made of flexible plastic optical fibers. Sensors 8:4318–4329
5. Nikolov ID, Ivanov CD (2000) Optical plastic refractive measurements in the visible and the near-infrared regions. Appl Optics 39:2067–2070
6. Khanarian G, Celanese H (2001) Optical properties of cyclic olefin copolymers. Opt Eng 40:1024–1029
7. Peters K (2011) Polymer optical fiber sensors – a review. Smart Mater Struct 20:013002
8. Yang DX, Yu J, Tao X, Tam H (2004) Structural and mechanical properties of polymeric optical fiber. Mater Sci Eng A 364:256–259
9. Chen YC, Chen LW, Lu WH (2011) Power loss characteristics of a sensing element based on a polymer optical fiber under cyclic tensile elongation. Sensors 11:8741–8750
10. Ishigure T, Hirai M, Sato M, Koike Y (2004) Graded-index plastic optical fiber with high mechanical properties enabling easy network installations – I. J Appl Polym Sci 91:404–409
11. Jiang C, Kuzyk MG, Ding J-L, Johns WE, Welker DJ (2002) Fabrication and mechanical behavior of dye-doped polymer optical fiber. J Appl Phys 92:4–12
12. Kiesel S, Peters K, Hassan T, Kowalsky M (2007) Behaviour of intrinsic polymer optical fibre sensor for large-strain applications. Meas Sci Technol 18:3144–3154
13. Linec M, Donlagic D (2007) A plastic optical fiber microbend sensor used as a low-cost anti-squeeze detector. IEEE Sensors J 7:1262–1267
14. Vijayan A, Gawli S, Kulkarni A, Karekar RN, Aiyer RC (2008) An optical fiber weighing sensor based on bending. Meas Sci Technol 19:105302

15. Kuang KSC, Quek ST, Maalej M (2004) Assessment of an extrinsic polymer-based optical fibre sensor for structural health monitoring. Meas Sci Technol 15:2133–2141
16. Binu S, Mahadevan Pillai VP, Pradeepkumar V, Padhy BB, Joseph CS, Chandrasekaran N (2009) Fibre optic glucose sensor. Mater Sci Eng C 29:183–186
17. Nobuo T (2002) Characterization of microscopic damage in composite laminates and real-time monitoring by embedded optical fiber sensors. Int J Fatigue 24:281–289
18. Babchenko A, Maryles J (2007) A sensing element based on 3D imperfected polymer optical fibre. J Opt A Pure Appl Opt 9:1–5
19. Kuang KSC, Cantwell WJ (2003) The use of plastic optical fibre sensors for monitoring the dynamic response of fibre composite beams. Meas Sci Technol 14:736–745
20. Chen YC, Xie WF, Ke YL, Chen LW (2008) Power loss characteristics of a sensing element based on a grooved polymer optical fiber under elongation. Meas Sci Technol 19:105203
21. Fu Y, Di H, Liu R (2010) Light intensity modulation fiber-optic sensor for curvature measurement. Optics Laser Technol 42:594–599
22. Irawan R, Chuan TS, Meng TC, Ming TK (2008) Rapid constructions of microstructures for optical fiber sensors using a commercial CO_2 laser system. Open Biomed Eng J 2:28–35
23. Pulido C, Esteban Ó (2010) Improved fluorescence signal with tapered polymer optical fibers under side-illumination. Sens Actuators B 146:190–194
24. Gravina R, Testa G, Bernini R (2009) Perfluorinated plastic optical fiber tapers for evanescent wave sensing. Sensors 9:10423–10433
25. Babchenko A, Maryles J (2007) Graded-index plastic optical fiber for deformation sensing. Opt Lasers Eng 45:757–760
26. Armin A, Soltanolkotabi M, Feizollah P (2011) On the pH and concentration response of an evanescent field absorption sensor using a coiled-shape plastic optical fiber. Sens Actuators A 165:181–184
27. Binu S, George J (2013) Displacement sensing with polymer fibre optic probe. Front Sens 1:49–53
28. Zhi Feng Z, Chi Z, Xiao-Ming T, Guang-Feng W, Gang-Ding P (2010) Inscription of polymer optical fiber bragg grating at 962 nm and its potential in strain sensing. IEEE Photon Technol Lett 22:1562–1564
29. Cheng X, Qiu W, Wu W, Luo Y, Tian X, Zhang Q, Zhu B (2011) High-sensitivity temperature sensor based on Bragg grating in BDK-doped photosensitive polymer optical fiber. Chin Opt Lett 9:020602
30. Muto S, Suzuki O, Amano T, Morisawa M (2003) A plastic optical fibre sensor for real-time humidity monitoring. Meas Sci Technol 14:746
31. Chu C-S, Lo Y-L (2008) A plastic optical fiber sensor for the dual sensing of temperature and oxygen. IEEE Photon Technol Lett 20:63–65
32. Zubia J, Garitaonaindia G, Arrúe J (2000) Passive device based on plastic optical fibers to determine the indices of refraction of liquids. Appl Optics 39:941–946
33. Lomer M, Arrue J, Jauregui C, Aiestaran P, Zubia J, López-Higuera J (2007) Lateral polishing of bends in plastic optical fibres applied to a multipoint liquid-level measurement sensor. Sens Actuators A 137:68–73
34. Yang XH, Wang LL (2007) Fluorescence pH probe based on microstructured polymer optical fiber. Opt Express 15:16478–16483
35. Esteban Ó, Pulido C (2013) Simple oxygen gas sensor based on side-illuminated polymer optical fiber. In: Proceedings of SPIE 8794, fifth European workshop on optical fibre sensors, p 879410. http://proceedings.spiedigitallibrary.org/mobile/proceeding.aspx?articleid=1690526
36. Jensen JB, Emiliyanov G, Bang O, Hoiby PE, Pedersen LH, Hansen TP, Nielsen K, Bjarklev A (2006) Microstructured polymer optical fiber biosensors for detection of DNA and antibodies. In: Optical fiber sensors, Cancun, OSA technical digest, p ThA2. http://www.opticsinfobase.org/abstract.cfm?uri=ofs-2006-tha2

37. Jiang J, Gao L, Zhong W, Meng S, Yong B, Song Y, Wang X, Bai C (2008) Development of fiber optic fluorescence oxygen sensor in both in vitro and in vivo systems. Respir Physiol Neurobiol 161:160–166
38. Tang L, Cha Y, Li H, Chen P, Lin S (2006) Fiber-optic immuno-biosensor for rapid and accurate detection of nerve growth factor in human blood. In: Engineering in Medicine and Biology Society, EMBS '06. 28th annual international conference of the IEEE, vol 1, pp 811–814. http://www.ncbi.nlm.nih.gov/pubmed/17946002
39. Myllylä TS, Elseoud AA, Sorvoja HS, Myllylä RA, Harja JM, Nikkinen J, Tervonen O, Kiviniemi V (2011) Fibre optic sensor for non-invasive monitoring of blood pressure during MRI scanning. J Biophotonics 4:98–107
40. Vegfors M, Lindberg L-G, Pettersson H, Öberg PA (1994) Presentation and evaluation of a new optical sensor for respiratory rate monitoring. Int J Clin Monit Comput 11:151–156
41. Cheng X, Liu L, Tam WK., Tao X, Wong WW, Yu J (2007) Photonic fabric display with controlled pattern, color, luminescence intensity, scattering intensity and light self-amplification. USA Patent No.: US 7,466,896, B2
42. Tao X (2005) Wearable electronics and photonics. Woodhead Publishing, Cambridge
43. Wilson JD, Adams AJ, Murphy P, Eswaran H, Preissl H (2009) Design of a light stimulator for fetal and neonatal magnetoencephalography. Physiol Meas 30:N1
44. www.lumitex.com
45. Tao X, Zheng W, Zhang Z, Lau H, Lee L (2014) Phototherapy textile wrapper. USA Patent application No.: 14/534,153
46. Zhihao C, Teng TJ, Huat NS, Xiufeng Y (2012) Plastic optical fiber microbend sensor used as breathing sensor. In: Sensors, 2012 IEEE, Taipei, pp 1–4. http://ieeexplore.ieee.org/xpl/login.jsp?tp=&arnumber=6411048&url=http%3A%2F%2Fieeexplore.ieee.org%2Fxpls%2Fabs_all.jsp%3Farnumber%3D6411048
47. Grillet A, Kinet D, Witt J, Schukar M, Krebber K, Pirotte F, Depré A (2008) Optical fiber sensors embedded into medical textiles for healthcare monitoring. IEEE Sensors J 8:1215–1222
48. Zheng W, Tao X, Zhu B, Wang G, Hui C (2014) Fabrication and evaluation of a notched polymer optical fiber fabric strain sensor and its application in human respiration monitoring. Tex Res J 84:1791–1802
49. Jonckheere JD, Narbonneau F, Jeanne M, Kinet D, Witt J, Krebber K, Paquet B, Depré A, Logier R (2009) OFSETH: smart medical textile for continuous monitoring of respiratory motions under magnetic resonance imaging. In: 31st annual international conference of the IEEE, Minneapolis, pp 1473–1476. http://ieeexplore.ieee.org/xpl/login.jsp?tp=&arnumber=5332432&url=http%3A%2F%2Fieeexplore.ieee.org%2Fxpls%2Fabs_all.jsp%3Farnumber%3D5332432
50. Yoo WJ, Jang KW, Seo JK, Heo JY, Moon JS, Park JY, Lee BS (2010) Development of respiration sensors using plastic optical fiber for respiratory monitoring inside MRI system. J Opt Soc Korea 14:235–239

Fibers with the Tunable Structure Colors Based on the Ordered and Amorphous Structures

6

Wei Yuan, Chaojie Wu, Ning Zhou, and Ke-Qin Zhang

Contents

Introduction 128
The Pollutions of the Dying Process in the Textile Industry 128
The Colors in Nature 129
Colorful Fibers Based on the Photonic Crystals 131
Description on the Photonic Crystal Structures 131
Methods to Prepare the Fibers with the Photonic Structures 132
Colorful Fibers Based on the Amorphous Structure 141
Amorphous Structures in Nature 141
Creation of Amorphous Structures 143
Fabrication of Colorful Fibers Through the Polymeric Phase Separation 144
Applications of the Structurally Colored Materials in the Fields of Sensing and Monitoring 145
Vapor and Solvent Sensors 147
Temperature Sensors 148
Ion and pH Sensors 149
Biological Sensors 150
Summary 151
References 152

Abstract

Dyeing is a process that is critical in the coloring of fibers or fabrics in the textile industry. The waste water discarded from the dyeing process gives rise to the severe pollution to the environment. In this chapter, a novel coloration strategy was presented, which uses structural colors by incorporating ordered photonic and amorphous structure onto fibers. This coloration strategy originates from

W. Yuan • C. Wu • N. Zhou • K.-Q. Zhang (✉)
National Engineering Laboratory for Modern Silk, College of Textile and Clothing Engineering, Soochow University, Suzhou, China
e-mail: yuanwei_147258@163.com; chaojiewu@163.com; superman1104@live.cn; kqzhang@suda.edu.cn

© Springer Science+Business Media Singapore 2015

X. Tao (ed.), *Handbook of Smart Textiles*,
DOI 10.1007/978-981-4451-45-1_6

color structures found in nature, such as butterfly wings and parrot feathers. Furthermore, recent results on the preparation, and mechanical and optical properties of these structurally colored fibers that mimic natural color structures, are discussed in detail. It is believed that structural coloration of fibers has potential as the environment-friendly, non-fading, and economic solution demanded by the current textile industry.

Keywords
Colorful fibers • Structural color • Photonic crystal • Amorphous structures

Introduction

The Pollutions of the Dying Process in the Textile Industry

In the clothing industry, color is the most distinctive trait that is prominent in determining an article of clothing's first impression to customers. Thus, color is a major concern for workers in the textile and clothing industry, who endlessly pursue the creation of fascinating garments and textile products for consumers. Textile products achieve various colors through the coloration processes, which often utilize dyes or pigments. Dyes can diffuse into fibers and have inherent affinity on the fiber materials. Pigments, which can only adhere to the surface of fiber materials through other chemical agents, have no inherent affinity on the fibers. Most manufacturers use synthetic pigments and dyes instead of natural extracts; which are difficult and even impossible to naturally degrade.

The dyeing process involves the transfer dyes from the dyebath onto the fiber. During the dyeing process, dye molecules transfer from the dyebath into the fiber, and other dye molecules desorb from the fiber to reenter the dyebath. When the rates of dye molecules entering and leaving the fiber are equal, the amount of dye in the fiber does not change with additional dyeing time; an equilibrium condition has been established. Exhaustion is expressed as the percentage of amount dye originally added to the dyebath, to the percentage that transfers to the fiber. For example, if 4/5 of the dye originally in the dyebath transfers to the fiber, the exhaustion is 80 %. The most ideal and environmentally friendly scenario is 100 % exhaustion, where no dye is wasted in the bath. However, this ideal condition is not a reality in industry manufacturing. Dye transfers to fiber gradually as dyeing time passes, but exhaustion increase is usually diminished as time increases. The additional time and costs required to produce higher exhaustion may be more expensive than the savings achieved in dye and waste treatment costs [1]. Nearly 10 % of the input dyes are lost during the textile coloration process. Furthermore, auxiliary chemicals are often added to the dyebath to improve dyeing results, and some of them are also lost in the bath. Thus, the complex wastewater from dyeing processes contains unreacted dyestuffs (color), suspended solid, high amount of dissolved solids, and the auxiliary chemicals used in the various stages of dyeing and processing [2].

The unnatural colors of the wastewater are aesthetically unpleasant and easily bring to mind an association with contamination. The wastewater should be controlled and disposed before discharge.

Currently, most common methods of wastewater treatment consist of physical and/or chemical processes. The conventional coagulation process creates a problem of sludge disposal. Biological treatments, such as using of cells or enzymes, show low degradation efficiency. Some new techniques, such as ozonation, electrochemical destruction, treatment using Fenton's regent, and photocatalytic oxidation, usually involve complicated procedures or are economically unfeasible [3]. Many researchers are searching for better methods of wastewater treatment. Experts in the industry often wonder if there are any good solutions to handle the wastewater problem. Some experts are even turning to the dye process itself, exploring the possibility for coloration strategies to replace the dyeing process. The answer may be found in nature.

The Colors in Nature

The world is full of light. Visible light is made of seven wavelength groups. Color is a result of human visual perception to the wavelengths that correspond to red, green, blue, and other distinguishable visible wavelengths. Color derives from the spectrum of light interacting in the eye with the spectral sensitivities of the light receptors. Color categories and physical specifications of color are also associated with objects, materials, light sources, and so on; these categories are based on physical properties such as light absorption, reflection, or emission spectra.

Countless colors can be found in nature, including green leaves, red flowers, and blue sky, as shown in Fig. 1. These colors, which be seen on plants and animals, are produced in two quite distinct ways. One of the methods occurs when light is absorbed in material; this is usually the case for ordinary coloration mechanisms [4] in colored materials such as pigments and dyes. The other method of color production arises when the light is reflected, scattered, and deflected, not reaching the eyes under the presence of a specific nanostructure. The coloration in the second case operates based on purely physical properties. Thus, in nature, there are two types of color: pigmentary color (chemical color) and structural color (physical color).

Pigmentary Color

Pigments change the color of reflected or transmitted light as a result of wavelength-selective absorption. Many materials selectively absorb certain wavelengths of light. For example, the green chlorophyll contained in leaves enables the plants to use sunlight as an energy source for assimilation, allowing for synthesis of sugar, starch, and cellulose from water and CO_2. Chlorophyll can absorb short-wavelength (blue) and long-wavelength (red) light, while medium wavelengths (green or yellow-green) are remitted, making the leaves appear green [5].

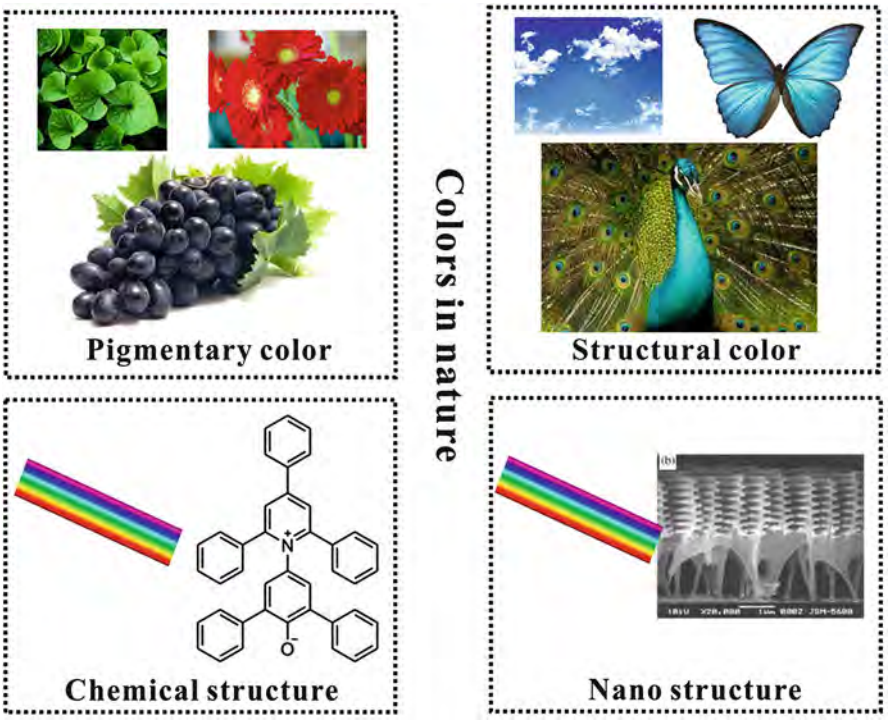

Fig. 1 Two types of coloration mechanism for natural colors. The *left panels* show the pigmentary color through interaction between the light and natural pigments. The *right panels* illustrate the structural colors originating from the periodic nano-sized structures

Structural Color

Besides pigmentary color, the colors due to the interference of light from microstructures composed of different refractive index materials that are comparable to the visible wavelength of light could be observed; such coloration is called structural color [6]. Because structural color is fadeless and no energy is lost from the color mechanism, structurally colored materials have attracted great attention in a wide variety of research fields.

The study of structural colors has long history originating from observations of the complex interactions between light and the sophisticated nanostructures generated in the natural world. The physical mechanisms of natural structural color have been explored intensively [7–10]. One of the main mechanisms is ascribed to the photonic bandgap effects of regular photonic structures, which mostly appears in the feathers of birds and the skins of beetles [11–13]. The incident light is coherently scattered by the periodic structure of photonic crystals (PCs), which results in a part of light with certain frequencies strongly reflected. The final color of the structure is determined by the frequency of the constructively reflected light. The observed color of PCs depends on the angle of the incident light, which is usually

called iridescent phenomena. Light scattering is another coloring mechanism for objects found in nature [14–18], such as the blue appearance of the sky due to the scattering of clouds. The incident light is dispersed by a single scatter, which results with certain frequencies of light being strongly scattered. The frequency of the scattered light always corresponds to certain electromagnetic multipolar modes supported by the polarization of the molecular dipoles in scatters. In such case, the light scatters are randomly packed in space, significantly different from the structure in its periodic arrangements. The incoherent isotropic scattering from such structure occurs, and eventually, this results in the noniridescent color phenomena.

Because the technology of dyeing and finishing in textile industry has some drawbacks, such as high pollution, high energy consumption, and low resource utilization rates, an idea that colors fibers based on physical methods has been put forth, without the assistance of chemical dyes. In this chapter, the methods of structurally colored fiber fabrication will be reviewed, based on the two coloring mechanisms described above: light reflecting of photonic crystals and scattering of amorphous structures.

Colorful Fibers Based on the Photonic Crystals

Description on the Photonic Crystal Structures

Photonic crystals (PCs) [19, 20] are one type of well-known photonic nanomaterials that possess a periodic refractive variance. Due to the periodicity in dielectric, PC materials possess a photonic bandgap (PBG), forbidding certain wavelengths of light located in the PBG from transmission through the material. According to variations in the refractive index and period in space, PCs can be classified as one-dimensional (1D), two-dimensional (2D), and three-dimensional (3D), as shown in Fig. 2a. Because of these distinct functions, PC materials have been utilized in optical fibers, display devices, sensors, and other technology.

Recently, PCs have attracted increasing interest from researchers due to their unique structural color properties [10, 21]. Photonic materials with vivid structural colors exist commonly in nature and are found in species of birds, butterflies, and insects [22, 23]. The colorful appearance of the PC materials can be ascribed to interference and reflection, which can be described by Bragg's law [24] (Fig. 2b). The law is given by

$$\lambda = 2D\left(n_{eff}{}^2 - \sin^2\theta\right)^{1/2} \tag{1}$$

Here, λ is the wavelength of the reflected light, n_{eff} is the average reflective index of the constituent photonic materials, D is the distance of diffracting plane spacing, and θ is the incident angle. Based on the equation, there are several methods for tuning structural color, such as changing the diffracting plane spacing D, the average refractive index n_{eff}, or the incident angle θ.

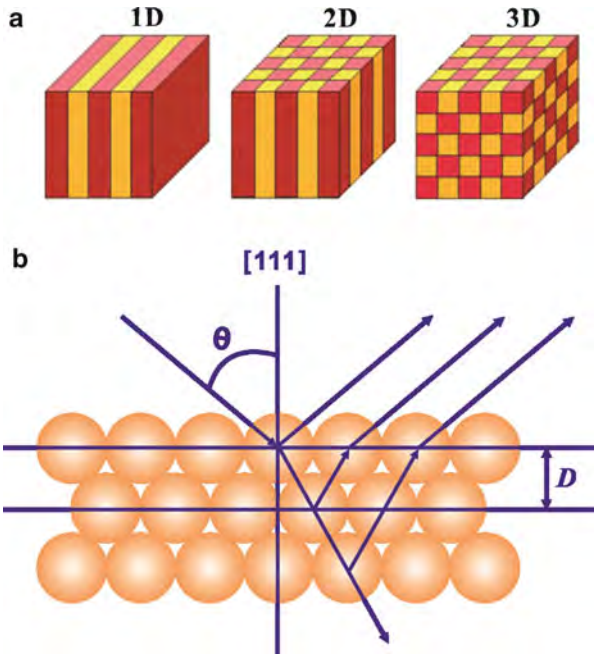

Fig. 2 A schematic diagram of photonic crystal. (**a**) one-, two-, and three-dimensional photonic crystals. (**b**) Incident light with a wavelength predicted by a modified Bragg equation (Eq. 1) undergoes diffraction when propagating through a photonic crystal. The wavelength of light that is coherently scattered is centered on λ and can be estimated by applying Eq. 1 using the incident angle, θ; the effective refractive index of the photonic crystal, n_{eff}; and the periodicity of the structure, D

Methods to Prepare the Fibers with the Photonic Structures

Inspired by the structural colors in nature, structurally colored fibers can be fabricated through two distinct methods. One is multilayer interference (1D photonic crystal) from radial direction of fibers, which widely exists in some insects, fish, and plant leaves. The other is 3D photonic crystal with fibrous sharp. In this section, the methods of structurally colored fibers preparation with multilayer interference and 3D photonic crystal are presented.

Multilayer Interference

Structural colors related to multilayer interference are most commonly found in nature [8, 12]. Metallic reflection from the elytra of beetles is one of the most well-known examples of multilayer interference [8]. Figure 3a shows photographs of the Japanese jewel beetle, *Chrysochroa fulgidissima*. The change in viewing angle from the normal to its tail reveals a remarkable color change from yellowish green to deep blue. The cross section of the elytra was investigated by using a transmission electron microscope. The researchers found that the beetle's frame consisted of epicuticle on the outside and exocuticle on the inside. The epicuticle consists of five alternate layers, as shown in Fig. 3b, which depends on the apparent color of the elytron, and changes from yellowish green to blue.

In the textile world, MORPHOTEX fibers [9] are the world's first non-dyed, nanotechnology-based, structurally colored fibers. The technology marks a significant advance in the history of dyeing based on the use of natural and chemical

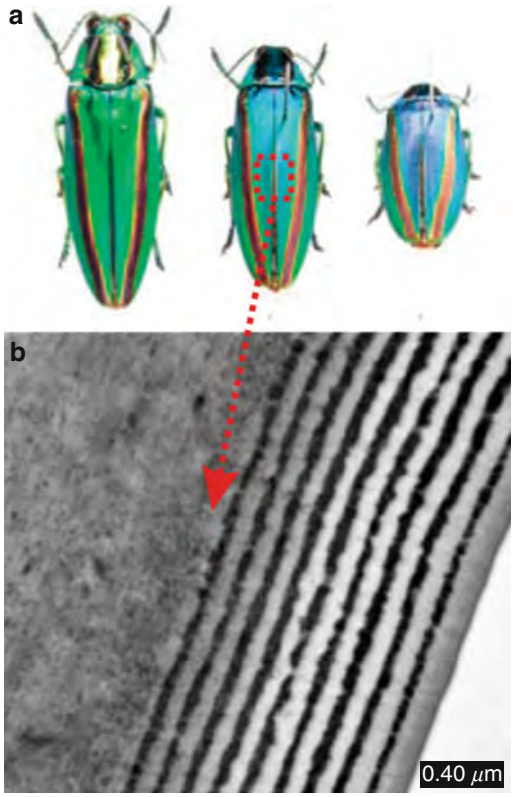

Fig. 3 (**a**) Viewing-angle dependence of the color change in jewel beetles. (**b**) TEM image of the cross section of the elytron (Reprinted with the permission from Ref. [8])

dyes. MORPHOTEX is composed of unstained, structurally colored fibers. This technology is a biomimetic conception based on the microscopic structure of *Morpho* butterfly's wings. No dyes or pigments are used. Energy consumption and industrial waste are reduced because no dye processes are required.

This fiber is made of polyester and has a flattened shape with a thickness of 15–17 μm, within which 61 layers of nylon 6, and polyester with a thickness of 70–90 nm, are incorporated, as shown in Fig. 4a. Because of the multilayer structure, wavelength-selective reflection and change in appearance with viewing angle are obtained. Four types of basic colors, red, green, blue, and violet, can be developed by precisely controlling the layer thickness according to visible wavelength.

Figure 4b demonstrates the weaving of a wedding dress using this fiber. Since the polymer materials constituting the layer have similar refractive indexes ($n = 1.60$ for nylon and $n = 1.55$ for polyester), the reflection bandwidth is limited within a small wavelength region. So the wedding dress seems to be pale blue, and it differs considerably from that of the *Morpho* butterfly. Therefore, some new techniques were prepared for fabrication of structurally colored fibers based on multilayer interference.

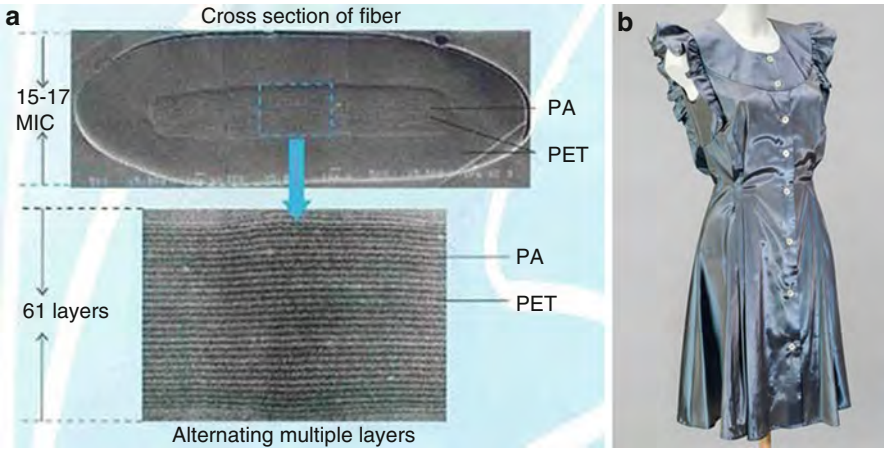

Fig. 4 (**a**) Cross section of the MORPHOTEX fiber (Reprinted with the permission from Ref. [9]). (**b**) The wedding dress fabricated by the MORPHOTEX fibers

Skorobogatiy et al. [25] fabricated solid- and hollow-core PBG Bragg fibers using layer-by-layer deposition of polymer film, as well as co-rolling of commercial and homemade polymer films. The typical solid-core PBG Bragg fiber is presented in Fig. 5a. For fabrication of Bragg fibers, two material combinations were used: polystyrene (PS)/poly (methyl methacrylate) (PMMA) and polycarbonate (PC)/poly(vinylene difluoride) (PVDF), featuring the refractive index contrasts of 1.6/1.48 and 1.58/1.4, respectively.

It was revealed that the hollow-core PBG fiber technology for photonic textiles is advantageous because such fibers can emit guided radiation sideways without the need of any mechanical deformations. Moreover, emission rate and the color of irradiated light can be controlled by varying the number of layers in the reflector and the reflector layer thicknesses, respectively. They also developed all-polymer low refractive index solid-core PBG fibers, which are economical and well suitable for industrial scale-up. The light emitted by the solid-core Bragg fibers appears very uniformly distributed over the fiber length, and no bright spots are typically observed, as shown in Fig. 5b and c. Under white light illumination, emitted color is very stable over time, as it is defined by the fiber geometry rather than by spectral content of the light source.

In order for the color in this type of PBG Bragg fiber to appear, there must be a light source to launch white light into such fiber. The color of the PBG fiber under ambient illumination is nonsignificant. Therefore, such PBG fiber may have potential applications in smart textiles for entertainment.

Kolle et al. [26] revealed a new approach for fabrication of multilayer fibers with structural color. The fibers consist of two elastomeric dielectrics, polydimethylsiloxane (PDMS) and polyisoprene–polystyrene triblock copolymer (PSPI), two inexpensive materials that are commercially available in industrial quantities, and provide a sufficiently high refractive index contrast

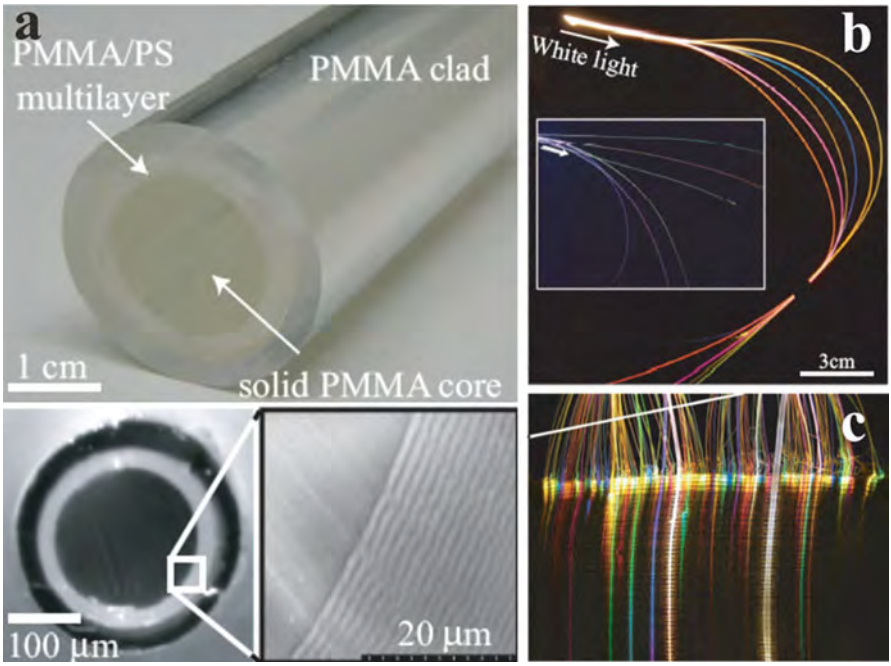

Fig. 5 (**a**) The fundamental structure and cross-section of solid-core plastic Bragg fiber perform (upper) and a resultant fiber (under) with magnified image of PS/PMMA mulitlayers. (**b**) Colorful PBG Bragg fibers by launching white light into the Bragg fibers. (**c**) Launching light into a PBG fiber-based textile (Reprinted with the permission from Ref. [25])

($n_{PDMS} = 1.41 \pm 0.02$, $n_{PSPI} = 1.54 \pm 0.02$, determined by ellipsometry). As shown in Fig. 6a, multilayer fibers were produced by initially forming a bilayer of the two constituent materials, which is subsequently rolled up onto a thin glass fiber with 15 μm to form the multilayer cladding. SEM images of the cross section of the multilayer fiber with 80 periods wrapped around the core glass fiber are shown in Fig. 6b and c. The thickness of the two films in the initial bilayer can be tuned during film deposition. Consequently, the spectral position of the reflection band of the fibers can be freely adjusted. As shown in Fig. 6d, three fibers with high reflectivity in different color ranges and their corresponding complementary colors in transmission are present.

In the process of multilayer fiber fabrication, the glass fiber acts as the substrate for the multilayers in the rolling process; the glass can be removed from the fiber by dissolution in hydrofluoric acid. Once the glass core is removed, the fiber is composed of two elastomers and can now be elastically deformed by stretching it along its axis. An elongation along the fiber axis leads to a compression perpendicular to it, causing a decrease of its overall diameter and a reduction of the thickness of each individual layer. This way, the reflected and transmitted color can be reversibly tuned by axial extension of the fibers, as shown in Fig. 6e.

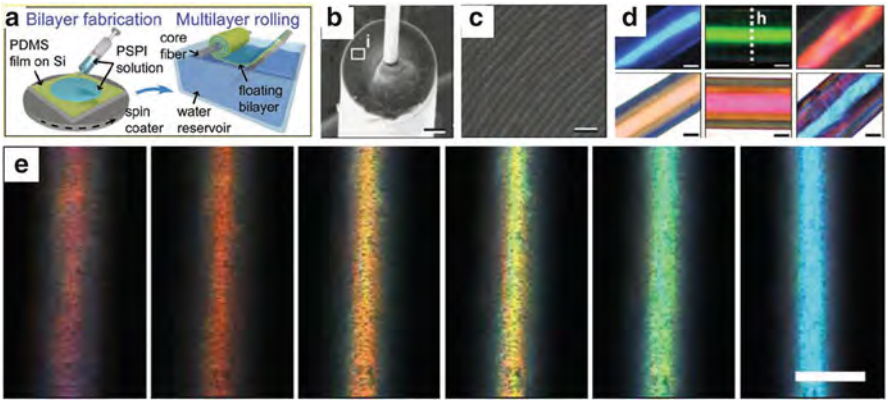

Fig. 6 (**a**) Schematic representation of the manufacturing of artificial photonic fibers. (**b**) The cross-sectional SEM image of the fiber. (**c**) SEM image of the individual layers in the cladding. (**d**) Optical micrographs of three rolled-up multilayer fibers with different layer thicknesses and colors in reflection (*top*) and transmission (*bottom*). (**e**) Color tuning of a fiber with different layer thickness where the glass core was removed by a hydrofluoric acid etch (Reprinted with the permission from Ref. [26])

Cylindrical 3D Photonic Crystal

Fibrous or cylindrical photonic crystals are usually found in some insects and animals in nature. Andrew Parker et al. [11] first discovered photonic crystal structures in the sea mouse (Fig. 7a). The sea mouse is partially covered with long hairs that produce a brilliant iridescence, as shown in Fig. 7b; the sea mouse displays a range of colors that changes with the direction of the incident light and the direction of observation.

The cross-sectional micrograph of a hair, as shown in Fig. 7c, reveals a periodic nanostructured pattern with hexagonal symmetry. Each hair contains thousands of hollow, close-packed, and longitudinally oriented cylinders with a diameter of approximately 230 nm. Bright structural colors are produced when the cylinders collectively diffract light that is incident on the sides of the hair fibers.

Liu et al. [27–29] exploit a method for fabrication of 3D structurally colored fibers based on PCs. Silica colloidal crystals are self-assembled onto a glass fiber by a heating evaporation self-assembly method in micro-space. The colloidal crystal self-assembled onto the fiber endows the fiber with iridescent color. The process of the experiment is shown in Fig. 8a; silica glass capillaries with an inner diameter of 530 μm and a polyimide outer coating were used as the microchannels. Subsequently, a silica optical fiber with 300 μm was put into the microcapillary. Then, the silica suspension was injected into a capillary through a Teflon tube. The capillary was horizontally placed in an oven at 70 °C and dried overnight.

Figure 8b and c show typical SEM images of the fiber self-assembled by colloidal silica. This self-assembly usually results in an ordered lattice structure with a periodic arrangement of silica spheres corresponding to a (111) crystal plane

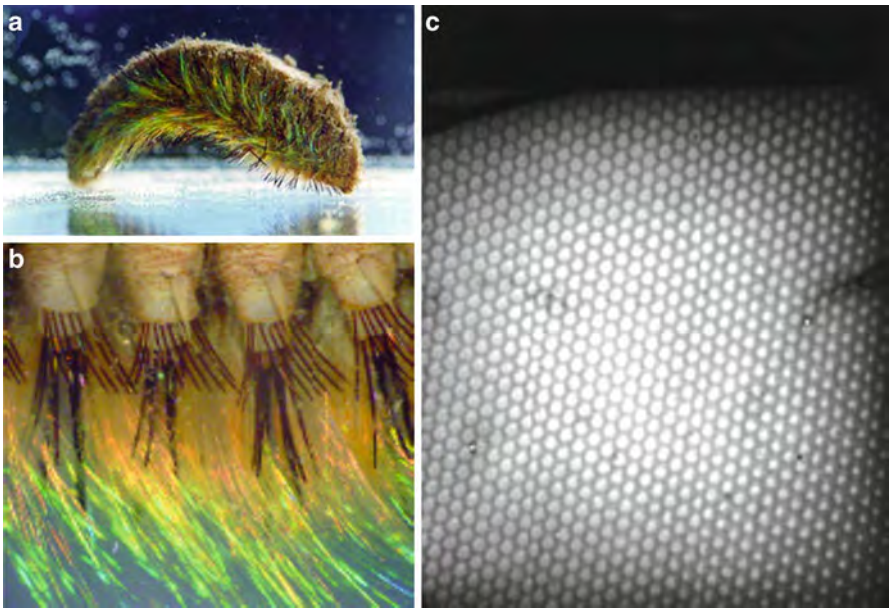

Fig. 7 (**a**) The photography of the sea mouse. (**b**) Its iridescent threads. (**c**) The cross-sectional micrograph of a spine (Reprinted with the permission from Ref. [11])

with an fcc structure. As shown in Fig. 8d and e, different structural colors can be obtained by using different size silica particles at 215 and 240 nm.

There has also been success in fabricating a sort of structurally colored fiber with the assistance of a magnetic field. As shown in Fig. 8f, the Fe_3O_4 colloidal suspension was mixed with a PEGDA resin containing DMPA as a photoinitiator. A plastic fiber was placed in the microcapillary. Then, using a syringe, the Fe_3O_4-PEGDA suspension was injected into a 20 cm long capillary through a Teflon tube. An NdFeB permanent magnet with a center magnetic field strength of 250 mT was used to generate a magnetic field. The capillary was immediately exposed to UV light. Then, the flexible colored fiber was taken out of the microcapillary.

The digital photos of the structurally colored fibers are shown in Fig. 8g–i; it can be clearly seen that, when a magnetic field was applied, a strong structural color was immediately observed. After the color is formed in the micro-space via magnetization, the color is fixed via UV light irradiation, which induces photopolymerization inside the Fe_3O_4-PEGDA suspension. The suspension photopolymerization solidifies the resin into a curving film and maintains the interparticle spacing of the colloidal nanoparticle chains. In this way, the structurally colored fibers are potentially very feasible for mass production.

Zhou et al. [30] exploited a new method for forming structurally colored fibers. As shown in Fig. 9a, the electrophoretic deposition (EPD) technique was adopted to fabricate core–shell colloidal fibers with structural colors. The carbon fiber was

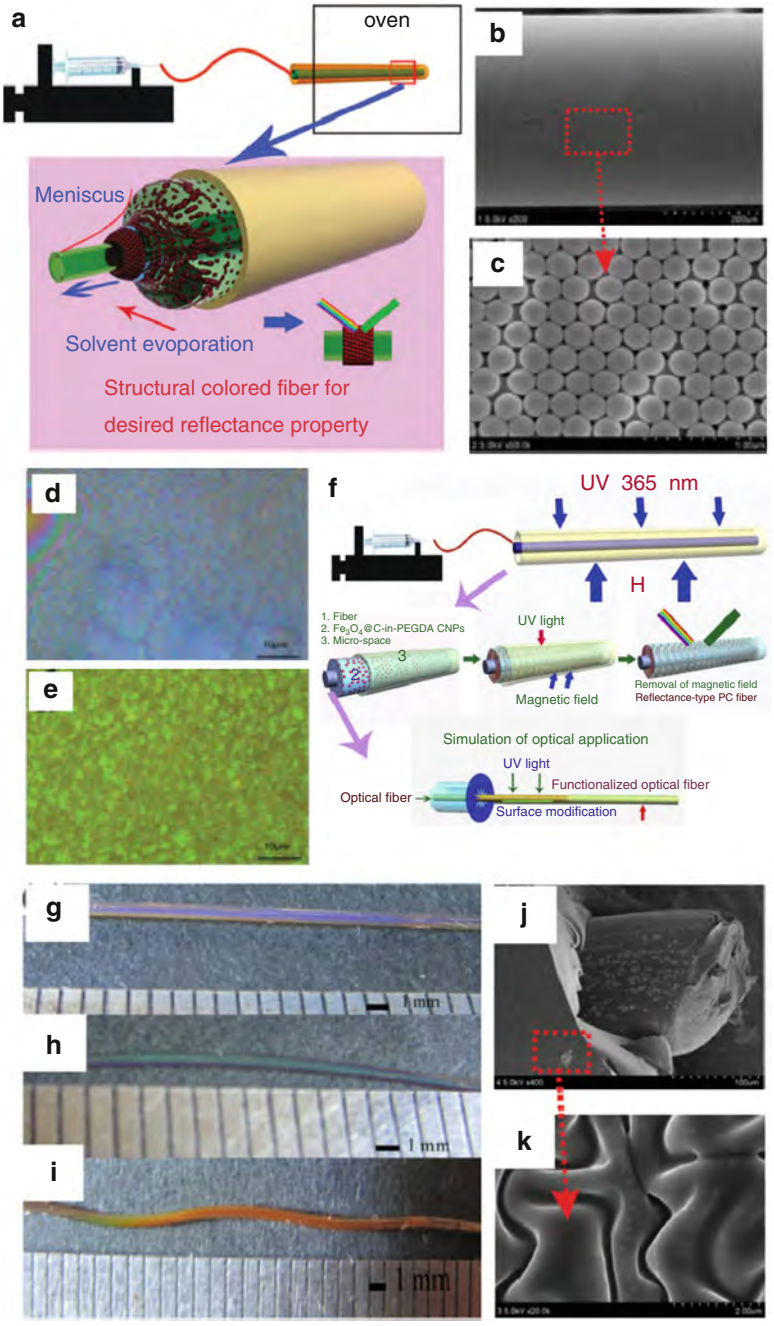

Fig. 8 (**a**) A schematic diagram of the fabrication of a colloid self-assembly opal onto a fiber in micro-space. (**b**) SEM of the obtained fiber surface. (**c**) Magnified zone of (**b**). (**d** and **e**) Optical microscopy images of the corresponding fibers self-assembled with 215 and 240 nm silica

fixed onto the copper plate via conductive silver glue. Subsequently, a voltage was imposed on the electrodes to drive the colloidal spheres to attach, forming cylindrical colloidal assembly on the surface of the carbon fibers. PS nanospheres with diameters of 185, 230, and 290 nm were selected to fabricate colorful core–shell fibers. According to Bragg's law, the photonic crystal assembled by the above PS spheres would present red, green, and blue colors with light normally incident on the (111) plane of the fcc structure. Similar structural colors were expected to appear on the colloidal fibers.

The optical dark-field images of colloidal fibers in red, green, and blue colors, respectively, are shown in Fig. 9b. The reflective spectra were measured by optical spectrometer, as shown in Fig. 9c. The peaks at 635, 525, and 435 nm corresponded to the individual structural color, shown in Fig. 9b. Surface and cross-sectional structures of colloidal fibers consisting of PS nanospheres with diameters of 230 nm are shown in Fig. 9d and e. The arrangement of the colloidal nanospheres deviates from the ideal fcc structure. Ordered domains with the sizes of 10–20 μm^2 are randomly oriented without the long-range order, as clearly observed from the enlarged surface and cross-sectional structures.

Differing from the abovementioned method for fabrication of structurally colored fibers based on self-assemble or electrophoretic deposition, Finlayson et al. [31] reported a new way to produce high-quality polymer opal fiber in an industrially scalable process. First, the core–shell particle precursors were prepared, with the particle consisting of a hard polystyrene (PS) core coated with a thin polymer layer containing allyl methacrylate (ALMA) as a grafting agent and a soft polyethylacrylate (PEA) outer shell, as shown in Fig. 10a. Then, the core–shell particle precursors were loaded into a mini-extruder, which consists of two counterrotating metallic screws with adjustable speed in the range 1–150 rotations per minute (rpm) and adjustable temperatures between 25 °C and 250 °C. In the extruder, the precursors form a melt, homogenized under the extreme shear forces provided by the screws. The overpressure generated then drives the shear-ordered granular material through a stainless steel die, producing thin opal fibers with colors as shown in Fig. 10b–d.

The fibers have sufficient mechanical robustness to demonstrate the anticipated stretch-tunable structural color. They show significant changes in color as they are stretched. Figure 10e and f both visually and spectroscopically shows how the color changes in a 1 mm diameter sample from red through green, blue, and finally a grayish color, as the strain increasing from 0 % to 50 %. These color changes are due to the decreases of the inter-planar distance during stretching, as explained by Bragg diffraction. In the process of stretching the fibers, spheres within each plane

Fig. 8 (continued) (Reprinted with the permission from Ref. [27]). (**f**) Schematic diagram of magnetic field-induced formation of a structural colored fiber in micro-space. Digital photos of the colorful fibers under the same external magnetic field with different sizes of Fe_3O_4 colloidal spheres (**g**) 120 nm, (**h**) 145 nm, (**i**) 180 nm. (**j**) Cross section of the structural colored fiber. (**k**) Visible chain-like structures (Reprinted with the permission from Ref. [29])

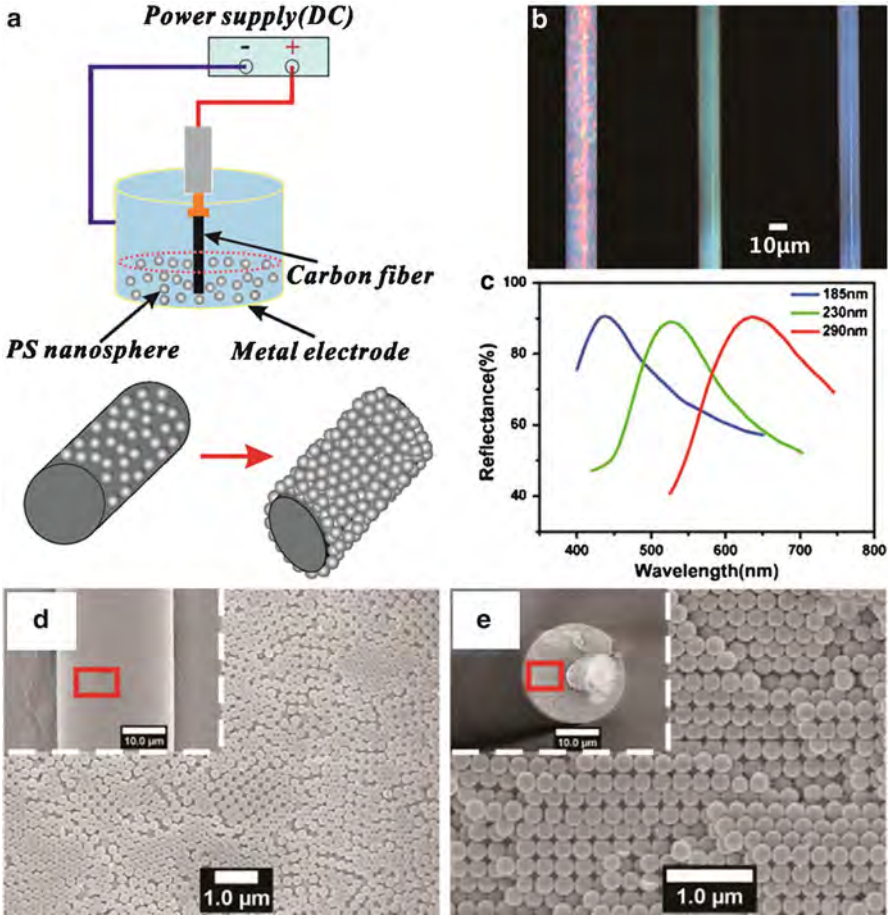

Fig. 9 (**a**) Schematic diagram of the fabrication of the structurally colored fibers. (**b**) *Dark*-field images of *red*-, *green*-, and *blue*-colored fibers under the microscope. (**c**) Reflective spectra. (**d**) Surface and (**e**) cross-sectional SEM images of the colloidal fiber (Reprinted with the permission from Ref. [30])

parallel to the surface move apart, but planes normal to the surface move closer to each other in order to keep the total volume constant, causing the Bragg wavelength to shift to lower values. The dark field reflectance for different strains is shown in Fig. 10f.

These elastomeric polymer opal fibers have many attractive functional features, such as intense structural color, with inherent stretch and bend tunability, in addition to excellent durability and mechanical robustness. These fibers are potential candidates for a novel range of nanomaterials and clothing fabrics, utilizing strong structural color effects as a replacement for toxic and photodegradable dyes.

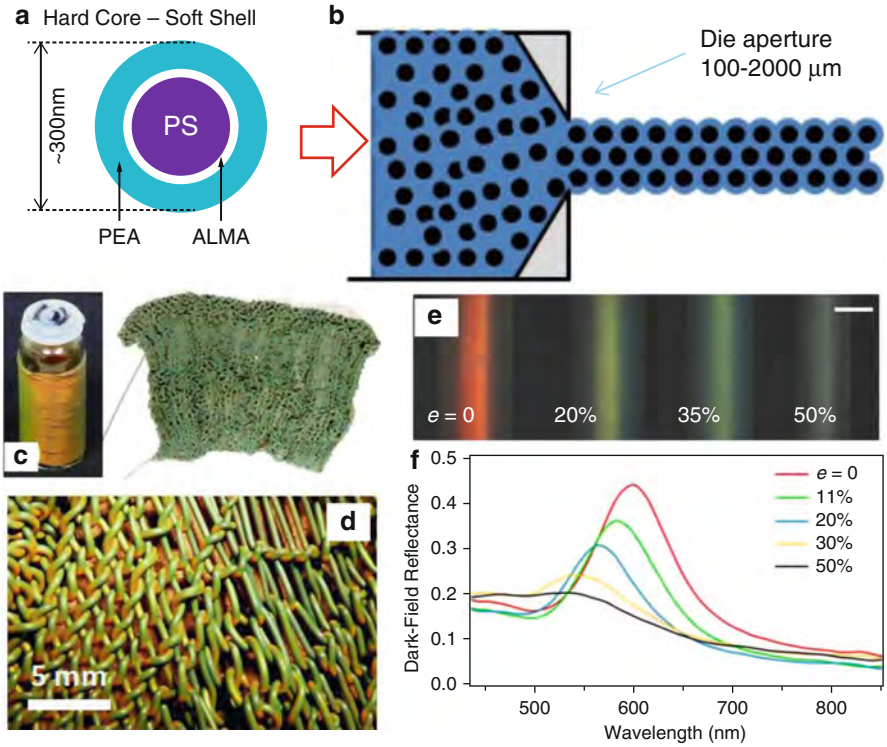

Fig. 10 (**a**) Schematic of core–interlayer–shell system, based on PS-ALMA-PEA. (**b**) Fiber extrusion process. (**c**) Cross-linked fibers may be knitted into fabrics (**d**). (**e**) *Dark*-field images of the opal fiber at strains of 0 %, 20 %, 35 %, and 50 %. (**f**) Corresponding reflectance spectra for different strains (Reprinted with the permission from Ref. [31])

Colorful Fibers Based on the Amorphous Structure

Amorphous Structures in Nature

Living organisms have exploited photonic structures to produce striking structural coloration since the Cambrian period. A variety of ordered photonic structures that produce iridescent colors have been revealed, including thin films, multilayers, diffraction gratings, and PCs, found in birds, insects, sea animals, and even in plants. These iridescent colors depend on the angle of viewing and the incident light. However, such angle dependence presents a barrier for developing displays and sensors using structurally colored materials.

In addition to ordered structures in the biological world, there are amorphous structures that can produce noniridescent structural colors [17, 18, 32–34], as shown in Fig. 11. The caruncles of some birds show noniridescent blue or green colors, which arise from 2D amorphous structures. The SEM image shown in

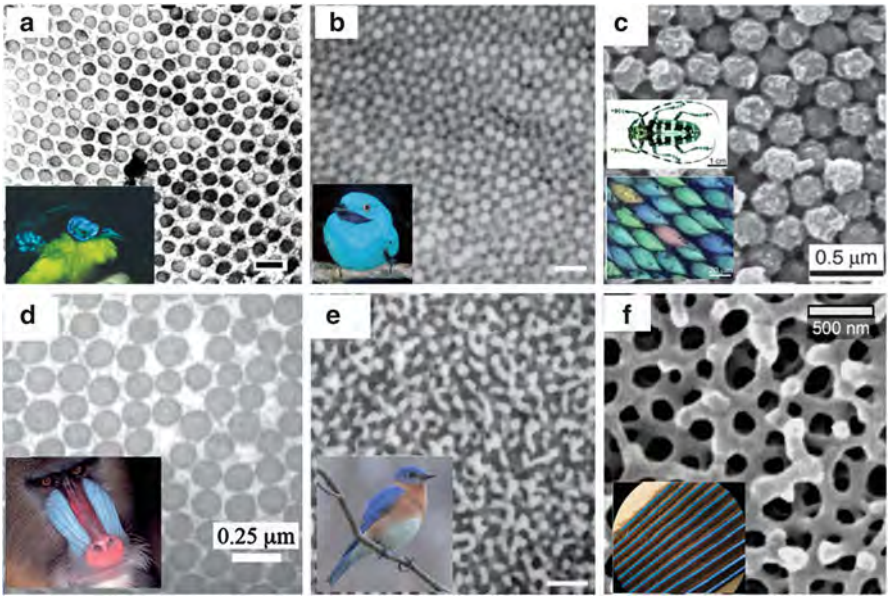

Fig. 11 (**a**) TEM image of collagen arrays in the *light-blue*-colored caruncle of the asity *N. coruscans* (Reprinted with the permission from Ref. [32]). (**b**) TEM of a feather barb of the male plum-throated cotinga (Reprinted with the permission from Ref. [18]). (**c**) SEM of a *green* scale of the longhorn beetle *A. graafi* (Reprinted with the permission from Ref. [33]). (**d**) TEM of the *blue* skin of the mandrill (Reprinted with the permission from Ref. [34]). (**e**) TEM of a feather barb of the male eastern bluebird (Reprinted with the permission from Ref. [18]). (**f**) SEM of a *blue* feather barb of the scarlet macaw (Reprinted with the permission from Ref. [17])

Fig. 11a reveals that the dermis of the caruncles consists of a thick layer of collagen a few hundred microns in thickness, with the parallel collagen fibers forming a quasi-ordered array [32]. A similar 2D amorphous structure is also found in the African mandrill (Fig. 11d) [34], which has noniridescent blue skin under natural sunlight. These colorations are also caused by the constructive interference of parallel dermal collagen fibers with short-range order.

The back feather barbs of the cotinga contain a 3D amorphous structure consisting of nearly random close-packed spherical air cavities that sometimes have small interconnections, as shown in Fig. 11b [18]. This 3D amorphous structure gives rise to a vivid noniridescent blue color. A similar 3D amorphous structure is also found in the scales of the longhorn beetle *Anoplophora graafi*, as shown in Fig. 11c [33]. Overlapping each other in regular order on the beetle elytra, each needlelike scale has a distinct color, and the scale colors vary from blue, green, yellow, to red. Structural characterization revealed that the scales possess a 3D amorphous structure consisting of random close-packed chitin nanoparticle. Different scale colors are due to different nanoparticles and bright greenish-white lateral stripes on the elytra by color mixing.

A spinodal decomposition-like amorphous structure was found in the back feather barbs of the eastern bluebird. The structure leads to a noniridescent blue structural color, as shown in Fig. 11e [18]. Rod-connected amorphous-diamond-structured amorphous photonic crystal offer excellent PBGs. Such amorphous structures already exist in the biological world, found in the blue feather barbs of the scarlet macaw, as shown in Fig. 11f [17].

Noniridescent structural coloration by amorphous structure has fascinated scientists for a long time. The attempts to understand the mechanisms associated with biological materials often lead to the development of new materials exhibiting unique and notable functions.

Creation of Amorphous Structures

To fabricate amorphous structures [16, 35–38], both top-down and bottom-up methods have been used. One of the most commonly used bottom-up methods is the self-assembly of colloids in suspensions. Based on phase-transition behaviors in colloidal systems, amorphous soft glassy colloidal gel with only short-range order was successfully fabricated. Obtained samples show homogeneous and angle-independent structural colors, as illustrated in Fig. 12a [35].

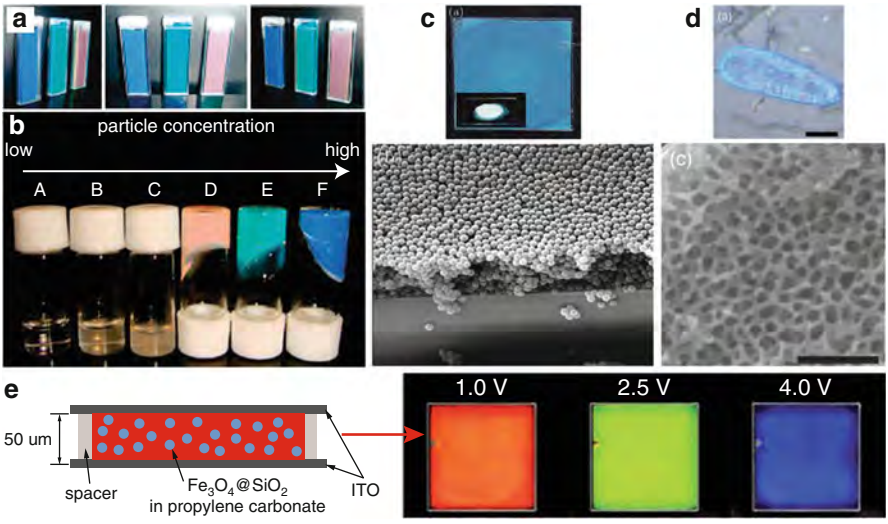

Fig. 12 (**a**) Photographs of gel colloidal suspensions with different polymer contents at different viewing angles (Reprinted with the permission from Ref. [35]). (**b**) Photograph of soft glassy colloidal gel with different colloidal concentrations (Reprinted with the permission from Ref. [36]). (**c**) Photograph and SEM of a dried colloidal amorphous structure film with mixed colloids (Reprinted with the permission from Ref. [37]). (**d**) Microphotograph and SEM of the transverse cross section of a SiO_2 disordered bicontinuous amorphous structure (Reprinted with the permission from Ref. [38]). (**e**) Photographs of electrically tunable structural-color display pixels at different applied voltages (Reprinted with the permission from Ref. [16])

Ueno et al. [36] prepared an amorphous array composed of core–shell particles in an ionic liquid. When the concentration of monodisperse colloids is low in a liquid suspension, the colloids can move freely, forming a fluid-like state, as shown in Fig. 12b (A–C). When the colloidal content increases, the electrostatic interactions among colloids increase, and the suspension forms an equilibrium crystalline state. As the concentration increases further and exceeds a certain critical point, the viscosity of the suspension is so large that the relaxation time for forming crystalline arrangements approaches infinity. At this stage, the system forms a stable glassy state, and the colloidal arrangements possess only short-range order, as shown in Fig. 12b (D–F).

Amorphous structures composed of dried colloids [37] were also successfully fabricated by mixing two sizes of colloids with formation of long-range order during the self-assembly process, as shown in Fig. 12c. The obtained samples of the bidisperse dried colloids show noniridescent structural colors.

Nature provides delicate amorphous structures which serve as templates to model inorganic structures [38]. In the peach-faced lovebird, the blue feather barbs possess a 3D amorphous structure consisting of disordered bicontinuous random network of keratin backbones. By using the feather barbs as hard templates, SiO_2 and TiO_2 3D amorphous structures were replicated with a sol–gel method. As shown in Fig. 12d , inverted SiO_2 amorphous structure displays bright noniridescent structural colors. The SEM image confirmed the faithful replication. Inspired by structural coloration in natural amorphous, electrically tunable full-color display pixels were obtained based on a 3D amorphous structure composed of a Fe_3O_4@SiO_2 core–shell colloidal suspension, [16], as shown in Fig. 12e. Pixel colors can be switched very fast by applying an electrical voltage due to the sensitive electrophoretic responses of the core–shell colloids.

Amorphous structures possess many interesting and unique optical properties such as isotropic PBGs or photonic pseudogaps, and noniridescent structural color productions, which result from their unique structure features such as short-range order. These interesting properties demonstrate that amorphous structures are a new type of optical material and have potential in a variety of important applications such as in photonics, color-related technologies, displays, and solar cells.

Fabrication of Colorful Fibers Through the Polymeric Phase Separation

Phase separation may be used to fabricate amorphous structures [17, 18, 39]. There are two types of phase separation: nucleation and growth, and spinodal decomposition. In an immiscible polymer blend, for example, phase separation via nucleation and growth may give rise to morphology of isolated sphere droplets dispersed in a matrix. In contrast, spinodal decomposition may lead to co-continuous morphology consisting of continuous and interconnected phases.

Nature may have already adopted such phase separations to produce 3D amorphous structures. Based on the morphological similarities, it was conjectured that random close-packed and disordered bicontinuous 3D amorphous structures found in some bird feather barbs may be self-assembled by phase separation [17, 18, 39], driven by the polymerization of keratin from the cellular cytoplasm via nucleation and growth, and spinodal decomposition.

The phase separation may be a feasible way to prepare functional materials of amorphous structure with noniridescent structural colors. However, to the best of our knowledge, there are no existing reports about the fabrication of structurally colored fibers with amorphous structure by phase separation. Meanwhile, in nature, there have some fibrous scales in beetles, which have noniridescent colors owing to amorphous structure.

Dong et al. [39] studied the structural and optical properties of scales in the longhorn beetle *Sphingnotus mirabilis*. As shown in Fig. 13a, the beetle is characterized by long antennae, as long as its body. Its elytra display a noniridescent greenish-blue color marked with bright lateral white stripes. Under optical microscope, the white stripes are composed of fibrous scales. The scales were observed by optical microscopy as shown in Fig. 12b and c. Under the reflection mode, scales show a light blue color, while they display a dim red color under the transmission mode. Colors under reflection and transmission mode are obviously complementary, implying that the scale color is a structural color.

The structural observation as shown in Fig. 13d shows the scales aligned nearly parallel to each other along the longitudinal direction. The cross sections show that the scales are composed of an inner part surrounded by an outer chitin cortex, as shown in Fig. 13e. Obviously, the scale interior is a disordered network of chitin, responsible for the scale color.

The optical properties of scales were characterized experimentally by measuring reflection spectra with the microspectroscopic equipment which consists of a tungsten lamp light source, a microscope with objective 50× and a numerical aperture 0.55, and an optical spectrometer. The measured reflection is given in Fig. 13f. It is characterized by a broad reflection peak positioned at about 560 nm. This reflection peak covers almost all visible wavelengths.

These fibrous scales with amorphous structures in some beetles have noniridescent blue color, which may be a good idea for fabrication of structurally colored fibers with noniridescent color based on phase separation.

Applications of the Structurally Colored Materials in the Fields of Sensing and Monitoring

In nature, many living creatures can reversibly change their structural color in response to external environmental stimuli. Based on the lessons learned from natural photonic structures, some specific examples of photonic crystals

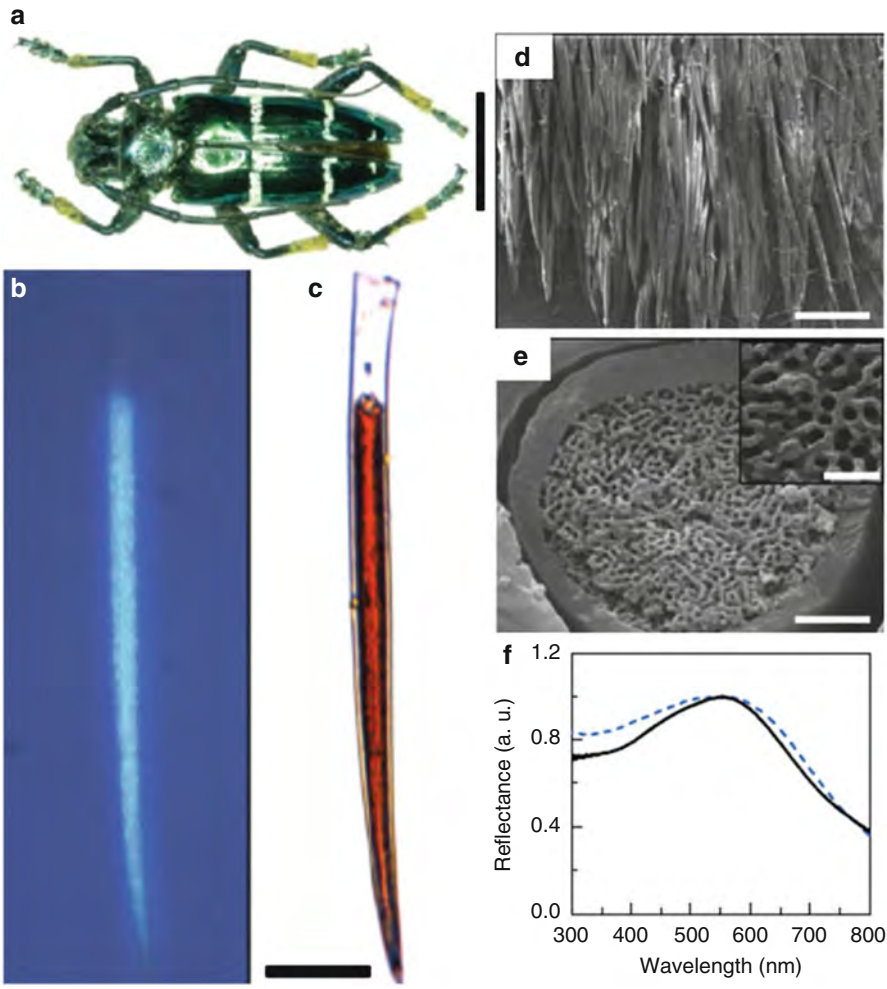

Fig. 13 (**a**) Optical image of the beetle *S. mirabilis*. (**b**, **c**) Reflection and transmission optical microscopic image of a scale, respectively. (**d**) SEM image of the white strip on an elytrum. (**e**) SEM cross-sectional image of a single scale (Reprinted with the permission from Ref. [39])

colorimetric sensors are presented in detail to demonstrate their unprecedented potential in practical applications, such as the detections of temperature, pH, ionic species, solvents, vapor, humidity, pressure, and biomolecules. To use photonic crystals as sensors, diffractions that fall into the visible range are usually preferred, as the optical output can be directly observed by the unaided eye, without the need of complicated and expensive apparatuses to read the signals. Generally, the photonic bandgap of the colorimetric sensors can be reversibly changed in response to external physical or chemical stimuli, which are discussed below.

Vapor and Solvent Sensors

Sensors based on the variation of structural colors analyze vapors and solvents by measuring the reflective peak shift that often occurs during the change of effective refractive index and lattice spacing. Song et al. [40] fabricated a colorful oil-sensitive carbon inverse opal by using poly(St-MMA-AA) colloidal crystals as a template. The peak positions showed a linear relationship with the refractive indices of the oils, by which different oils could be distinguished based on the color of the carbon inverse opal with a pore size of 240 nm. The color shift upon adsorption of oil was reversible, and the response time of the carbon inverse opal was less than 30s. Good oil-sensing stability of carbon inverse opal suggests that it is a promising and economical alternative to traditional oil-sensing materials (Fig. 14). Ozin et al. [41] assembled mesoporous Bragg stacks (MBS) by alternate multiple coatings of meso-TiO_2 and meso-SiO_2. Their optical response is reversibly

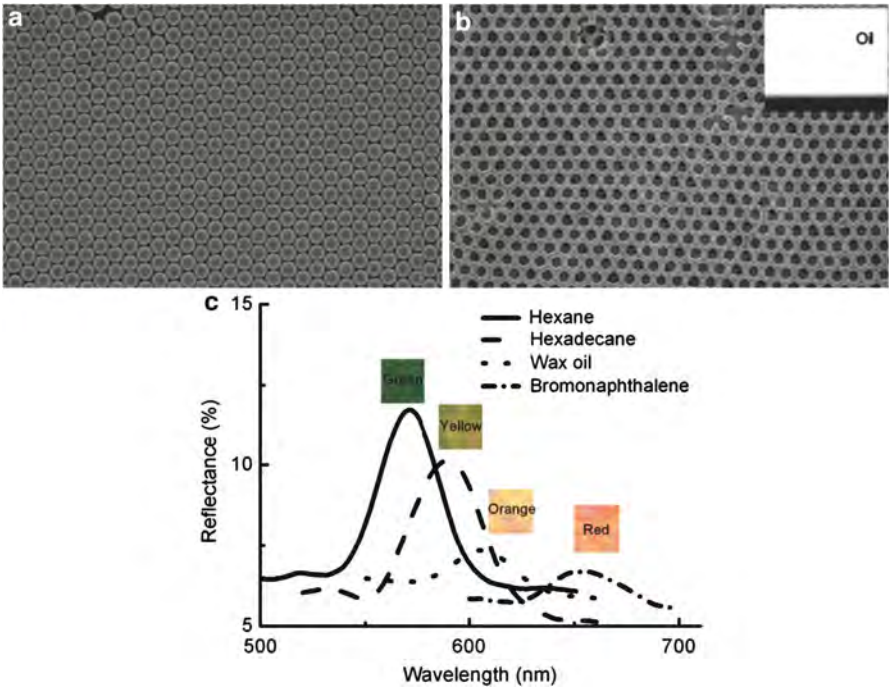

Fig. 14 (**a**) Typical SEM images of the photonic crystal templates with diameters of 228 nm. (**b**) The corresponding carbon inverse opals with diameters of 215 nm. The *inset* shows the spreading of an oil droplet on the carbon inverse opal. (**c**) Reflection spectra of the carbon inverse opal adsorbing four different oils, representing the four different refractive index ranges. The *insets* show the colors of the carbon inverse opal with different oils absorbed (Reprinted with the permission from Ref. [40])

altered by the analyte in their pores, and the optical response of MBS to the infiltration of alcohols and alkanes into its pores reveals better sensitivity and selectivity than conventional Bragg reflectors. Investigation of the response of MBS to a series of alcohols and alkanes revealed that their sensitivity and selectivity are highly dependent on the properties of the mesoporous metal oxide layers constituting the MBS. Yang et al. [42] prepared bioinspired organic/inorganic hybrid one-dimensional photonic crystals (1DPCs) by alternating thin films of titania and poly(2-hydroxyethyl methacrylate-co-glycidyl methacrylate) (PHEMA-co-PGMA) by spin coating. The color of the 1DPCs varies from blue to green, yellow, orange, and red under differing humidities, covering the whole visible range, which successfully combines structural color and water vapor sensitivity. The repeatability of the reversible response of the 1DPCs to water vapor is perfect, and the process can be repeated more than 100 times.

Temperature Sensors

Generally, temperature sensors can be divided into both inorganic and organic sensors. Polymer-based temperature sensors detect temperature change based on fast optical-switching behavior caused by thermally induced reversible swelling and shrinking of the hydrogels. Asher et al. [43] developed a robust nanosecond photonic crystal switching material by using poly(N-isopropylacrylamide) (PNIPAM) nanogel colloidal particles that self-assemble into crystalline colloidal arrays. At a low temperature of 10 °C, these PNIPAM particles are highly swollen with a diameter of 350 nm. As the temperature increases, the particles shrink and expel water, with diameter decreasing to 125 nm at 40 °C. On the other hand, inorganic sensors detect temperature changes based on the change of refractive index. They are good exceptional alternatives for polymer-based sensors in broader application ranges owing to its relatively high stability and wide refractive index range. For example, Sato et al. [44] fabricated composite materials comprised of nematic liquid crystals (LCs) and SiO_2 inverse opal films. The structural color changes when the phases of LC molecules change, as the refractive index of the LCs depends on the phases of LC molecules. The position of reflected peak shifts rapidly as temperature increases, because the temperature affects the LCs phases change from the nematic to isotropic (Fig. 15). Lotsch et al. [45] obtained photonic crystals with textural mesoporosity by bottom-up assembly based on sequential spin-coating suspensions of TiO_2 and SiO_2 nanoparticles on glass substrates. They found that the optical response of the crystals to temperature can be significantly enhanced by varying the relative humidity of the environment. The humidity-enhanced thermal tuning causes shifts of the reflected spectra by up to -1.66 nm K^{-1}. Owing to their high inherent porosities and ease of fabrication, nanoparticle-based photonic crystals offer a great potential for the development of sensitive temperature and humidity sensors.

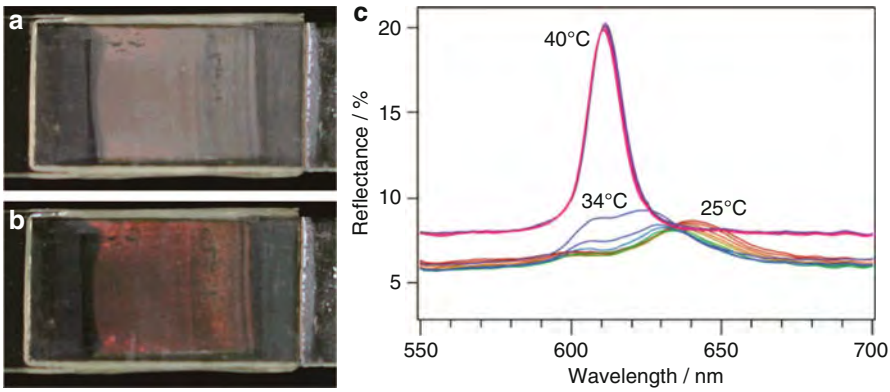

Fig. 15 (**a**) Photographs of sample film below phase transition temperature and (**b**) above phase transition temperature. (**c**) Reflection spectra of nematic liquid crystal 4-pentyl-4-cyanobiphenyl (5CB)-infiltrated inverse opal. The spectra are plotted for temperature increments of 1 °C (Reprinted with the permission from Ref. [44])

Ion and pH Sensors

Quantitative analysis of ions such as Pb^{2+} and K^+ using PC sensors is accomplished by measuring the reflected spectra shift caused by changes of diffracting plane spacing. Takeoka et al. [46] reported the design and synthesis of a novel porous gel with crown ether using a templating technique for capturing K^+ selectively. Such crown ethers swell and shrink reversibly, changing the lattice spacing of the PCs causing the rapid response of color change. Red shifts of diffraction were observed by the naked eye as K^+ concentration increased. However, the structural color was unaffected for sensing Na^+ (Fig. 16). Thomas et al. [47] demonstrated full-color tunability of variously quaternized polystyrene–poly(2-vinyl pyridine) block copolymer films via selection of appropriate anions. The selective swelling of the block copolymer lamellar structure with various ions allows tunability of the film from transparent to blue to red depending on the hydration strength of the ions. The position of the PBG of the photonic gel films can be controlled by choosing hydration characteristics of the counteranions and degree of quaternization for quaternized P2VP microdomains. Recently, the photonic crystals for pH sensors play an important parameter for many water-based reactions and analysis. Wang et al. [48] fabricated a new type of light-diffracting hydrogel composite film for H^+ recognition consisting of nanoparticles and polymer through a combined physical–chemical polymerization process, which significantly reduces the complexity of established methods. The reflected wavelength shift is so obvious that the visible structural color change can be visually identified for the hydrogel.

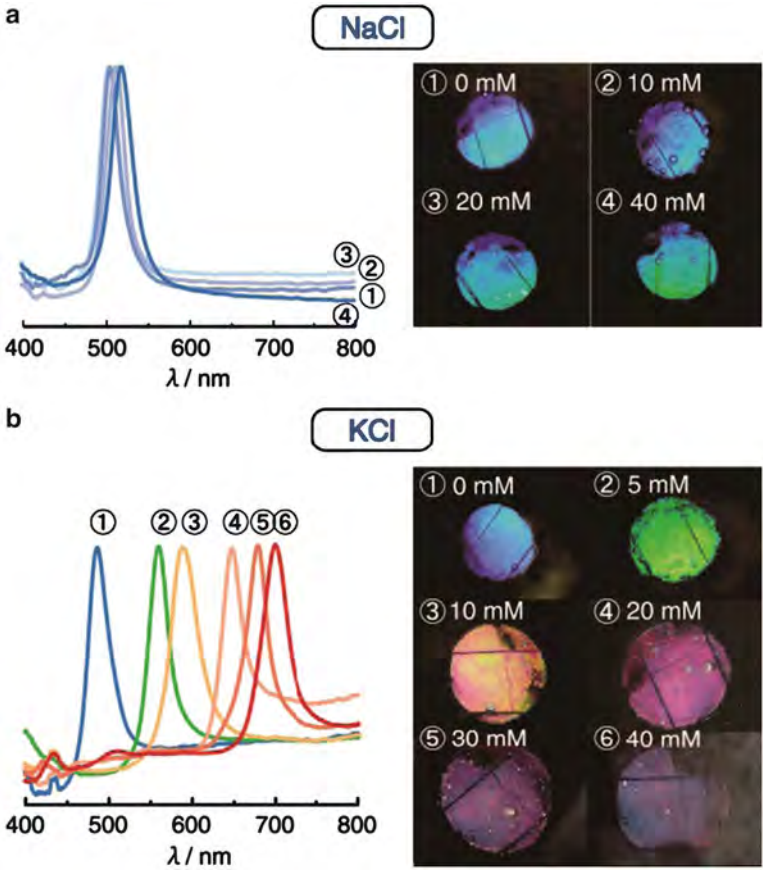

Fig. 16 Reflection spectra and photographs of periodically ordered interconnecting porous gels at 36 °C with different ionic concentrations. (**a**) Na^+. (**b**) K^+ (Reprinted with the permission from Ref. [46])

Biological Sensors

Recently, photonic crystal materials have been employed to design an optical biosensor for bioassays when appropriate physical structures have been attached by recognition groups. Takeoka et al. [49] created a colorimetric glucose sensor that can provide the desired monitoring of glucose levels by the naked eye, which is easier to fabricate and to control than those similar colorimetric systems. Furthermore, the time required for porous gels to reach swelling equilibrium is shorter (Fig. 17). Recently, sensors based on particle plasmon resonance (PPR) have played an important role in biomedical engineering. For example, Zhang et al. [50] reported an optical biosensor based on waveguided metallic photonic crystals (MPCs) for the sensitive testing of biomolecular interactions, which provides practical approaches for the label-free detection of specific bioreactions.

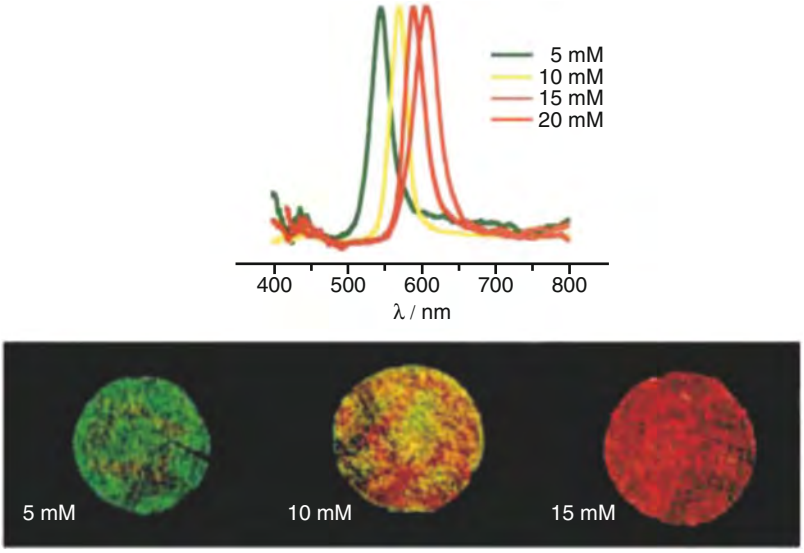

Fig. 17 Reflection spectra and photographs of periodically ordered interconnecting porous poly (NIPA-co-AAPBA) gel in a 2-(cyclohexylamino)-ethanesulfonic acid (CHES) buffer aqueous solution including different concentrations of glucose at 28 °C (Reprinted with the permission from Ref. [49])

The success of this sensor is demonstrated by sensing the specific reaction between the HIV-1 capsid protein (p24) antigen and the monoclonal anti-p24 antibody. The strong and reliable sensor signal evaluated by way of the optical extinction spectra indicates that this kind of sensor device can easily resolve p24 antigens at a concentration lower than 20 ng • ml^{-1}, with a large space for improvement.

Summary

In this chapter, recent progress in the study of structurally colored fibers was reviewed, including their fabrication, optical properties, and applications. Although significant progress has been made in recent years, there are many interesting problems that do not have solutions due to the lack of more in-depth studies. For example, the fabrication of structurally colored fibers with multilayer interference is a feasible way to produce commercial fibers with structural color as MORPHOTEX fibers. However, research has not yet concluded a reliable method of providing the high refractive index contrast of the alternating layers, which may be a barrier for the commercial applications. Owing to the low mechanical properties, the 3D photonic crystal fibers assembled by colloidal nanoparticles may not have practical applications. Amorphous structures can bring moderate noniridescent structural colors, which are more suitable for the visualization. However, the colors may almost appear blue based on amorphous structure.

Dye-free, nanomaterial-based, structurally colored fibers were prepared from various methods. The technology marks a significant advance in the history of dyeing based on the use of natural and chemical dyes, which is a conception based on the biomimetic study of the microscopic structure of some insects or birds. It is believed that this technology will reduce the energy consumption and industrial waste due to its dye-free process.

References

1. Perkins WS (1996) Textile coloration and finishing. Carolina Academic Press, Durham
2. Rajkumar D, Song BJ, Kim JG (2007) Electrochemical degradation of reactive blue 19 in chloride medium for the treatment of textile dyeing wastewater with identification of intermediate compounds. Dyes Pigments 72:1–7. doi:10.1016/j.dyepig.2005.07.015
3. Pearce CI, Lloyd JR, Guthrie JT (2003) The removal of color from textile wastewater using whole bacterial cells: a review. Dyes Pigments 58:179–196. doi:10.1016/S0143-7208(03)00064-0
4. Pauling L (1939) A theory of the color of dyes. Proc Natl Acad Sci U S A 25(11):577
5. Gabrielsen E (1948) Effects of different chlorophyll concentrations on photosynthesis in foliage leaves. Physiol Plant 1(1):5–37. doi:10.1111/j.1399-3054.1948.tb07108.x
6. Ball P (2012) Nature's color tricks. Sci Am 306(5):74–79. doi:10.1038/scientificamerican0512-74
7. Rayleigh L (1930) The iridescent colours of birds and insects. Proc Roy Soc Lond A 128(808):624–641. doi:10.1098/rspa.1930.0136
8. Kinoshita S, Yoshioka S (2005) Structural colors in nature: the role of regularity and irregularity in the structure. Chem Phys Chem 6:1442–1459. doi:10.1002/cphc.200500007
9. Kinoshita S, Yoshioka S, Miyazaki J (2008) Physics of structural colors. Rep Prog Phys 71:076401–076431. doi:10.1088/0034-4885/71/7/076401
10. Zhao Y, Xie Z, Gu H, Zhu C, Gu Z (2012) Bio-inspired variable structural color materials. Chem Soc Rev 41:3297–3317. doi:10.1039/c2cs15267c
11. Parker AR, McPhedran RC, McKenzie DR, Botten LC, Nicorovici NAP (2001) Photonic engineering-aphrodite's iridescence. Nature 409:36–37
12. Kinoshita S, Yoshioka S, Fujii Y, Okamoto N (2002) Photophysics of structural color in the morpho butterflies. FORMA 17(2):103–121
13. Gao X, Yan X, Yao X, Xu L, Zhang K, Zhang J, Yang B, Jiang L (2007) The dry-style antifogging properties of mosquito compound eyes and artificial analogues prepared by soft lithography. Adv Mater 19:2213–2217. doi:10.1002/adma.200601946
14. Mie G (2006) Beitrage zur optik truber medien, speziell kolloidaler metallosungen. Ann Phys 330:377–445. doi:10.1002/andp.19083300302
15. Noh H, Liew SF, Saranathan V, Mochrie SGJ, Prum RO, Dufresne ER, Cao H (2010) How noniridescent colors are generated by quasi-ordered structures of bird feathers. Adv Mater 22:2871–2880. doi:10.1002/adma.200903699
16. Lee I, Kim D, Kal J, Baek H, Kwak D, Go D, Kim E, Kanf C, Chung J, Jang Y, Ji S, Joo J, Kang Y (2010) Quasi-amorphous colloidal structures for electrically tunable full-color photonic pixels with angle-independency. Adv Mater 22(44):4973–4977. doi:10.1002/adma.201001954
17. Yin H, Dong B, Liu X, Zhan T, Shi L, Zi J, Yablonovitch E (2012) Amorphous diamond-structured photonic crystal in the feather barbs of the scarlet macaw. Proc Natl Acad Sci U S A 109:10798–10801. doi:10.1073/pnas.1204383109
18. Dufresne ER, Noh H, Saranathan V, Mochrie SGJ, Cao H, Prum RO (2009) Self-assembly of amorphous biophotonic nanostructures by phase separation. Soft Matter 5:1792–1795. doi:10.1039/b902775k

19. Yablonovitch E (1987) Inhibited spontaneous emission in solid-state physics and electronics. Phys Rev Lett 58:2059–2062. doi:10.1103/physrevlett.58.2059
20. John S (1987) Strong localization of photons in certain disordered dielectric super lattices. Phys Rev Lett 58:2486–2489. doi:10.1103/physrevlett.58.2486
21. Wang H, Zhang KQ (2013) Photonic crystal structures with tunable structure color as colorimetric sensors. Sensors 13:4129–4213. doi:10.3390/s130404192
22. Vignolini S, Raudall PJ, Rowland AV, Reed A, Moyroud E, Faden RB, Baumberg JJ, Glover BJ, Stiner U (2012) Pointillist structural color in Pollia fruit. PANS 109:15712–15715. doi:10.1073/pnas.1210105109
23. Land MF (1966) A multilayer interference reflector in the eye of the scallop, pecten maximus. J Exp Biol 45:433–447
24. Ozin GA, Arsenault AC (2008) P-ink and elast-ink from lab to market. Mater Today 11:44–51
25. Gauvreau B, Guo N, Schicker K, Stoeffler K, Boismenu F, Ajji A, Wingfield R, Dubois C, Skorobogatiy M (2008) Color-changing and color-tunable photonic bandgap fiber textiles. Opt Express 16:15677–15693. doi:10.1364/OE.16.015677
26. Kolle M, Lethbridge A, Kreysing M, Baumberg JJ, Aizenberg J, Vukusic P (2013) Bio-inspired band-gap tunable elastic optical multilayer fibers. Adv Mater 25:2239–2245. doi:10.1002/adma.201203529
27. Liu Z, Zhang Q, Wang H, Li Y (2011) Structural colored fiber fabricated by a facile colloid self-assembly method in micro-space. Chem Commun 47:12801–12803. doi:10.1039/c1cc15588a
28. Liu Z, Zhang Q, Wang H, Li Y (2013) Structurally colored carbon fibers with controlled optical properties prepared by a fast and continuous electrophoretic deposition method. Nanoscale 5:6917–6922. doi:10.1039/c3nr01766d
29. Liu Z, Zhang Q, Wang H, Li Y (2013) Magnetic field induced formation of visually structural colored fiber in micro-space. J Colloid Interface Sci 406:18–23
30. Zhou N, Zhang A, Shi L, Zhang KQ (2012) Fabrication of structurally-colored fibers with axial core − shell structure via electrophoretic deposition and their optical properties. ACS Macro Lett 2:116–120. doi:10.1021/mz300517n
31. Finlayson CE, Goddard C, Papachristodoulou E, Snoswell DRE, Kontogeorgos A, Spahn P, Hellmann GP, Hess O, Baumberg JJ (2011) Ordering in stretch-tunable polymeric opal fibers. Opt Express 19:3144–3154. doi:10.1364/OE.19.003144
32. Prum RO, Torres R, Kovach C, Williamson S, Goodman SM (1999) Coherent light scattering by nanostructured collagen arrays in the caruncles of the malagasy asities (eurylaimidae: aves). J Exp Biol 202:3507–3522
33. Dong BQ, Liu XH, Zhan TR, Jiang LP, Yin HW, Liu F, Zi J (2010) Structural coloration and photonic pseudogap in natural random close-packing photonic structures. Opt Express 18:14430–14438. doi:10.1364/oe.18.014430
34. Prum RO, Torres RH (2004) Structural colouration of mammalian skin: convergent evolution of coherently scattering dermal collagen arrays. J Exp Biol 207:2157–2172. doi:10.1242/jeb.00989
35. Takeoka Y, Honda M, Seki T, Ishii M, Nakamura H (2009) Structural colored liquid membrane without angle dependence. ACS Appl Mater Interfaces 1:982–986. doi:10.1021/am900074v
36. Ueno K, Sano Y, Inaba A, Kondoh M, Watanabe M (2010) Soft glassy colloidal arrays in an ionic liquid: colloidal glass transition, ionic transport, and structural color in relation to microstructure. J Phys Chem B 114:13095–13103. doi:10.1021/jp106872w
37. Forster JD, Noh H, Liew SF, Saranathan V, Schreck CF, Yang L, Park JG, Prum RO, Mochrie SGJ, Hern CSO, Cao H, Dufresne ER (2010) Biomimetic isotropic nanostructures for structural coloration. Adv Mater 22:2939–2944. doi:10.1002/adma.200903693
38. Shi L, Yin H, Zhang R, Liu X, Zi J, Zhao D (2010) Macroporous oxide structures with short-range order and bright structural coloration: a replication from parrot feather barbs. J Mater Chem 20:90–93. doi:10.1039/b915625a

39. Dong BQ, Zhan TR, Liu XH, Jiang LP, Liu F, Hu XH, Zi J (2011) Optical response of a disordered bicontinuous macroporous structure in the longhorn beetle *Sphingnotus mirabilis*. Phys Rev 84:011915. doi:10.1103/PhysRevE.84.011915
40. Li H, Chang L, Wang J, Yang L, Song Y (2008) A colorful oil-sensitive carbon inverse opal. J Mater Chem 18:5098–5103. doi:10.1039/b808675c
41. Choi SY, Mamak M, Freymann GV, Chipra N, Ozin GA (2006) Mesoporous bragg stack color tunable sensors. Nano Lett 6:2456–2461. doi:10.1021/nl061580m
42. Wang Z, Zhang J, Xie J, Li C, Li Y, Liang S, Tian Z, Wang T, Zhang H, Li H, Xu W, Yang B (2010) Bioinspired water-vapor-responsive organic/inorganic hybrid one-dimensional photonic crystals with tunable full-color stop band. Adv Funct Mater 20:3784–3790. doi:10.1002/adfm.201001195
43. Reese CE, Mikhonin AV, Kamenjicki M, Tikhonov A, Asher SA (2004) Nanogel nanosecond photonic crystal optical switching. J Am Chem Soc 126:1493–1496. doi:10.1021/ja037118a
44. Kubo S, Gu ZZ, Takahashi K, Fujishima A, Segawa H, Sato O (2004) Tunable photonic band gap crystals based on a liquid crystal-infiltrated inverse opal structure. J Am Chem Soc 126:8314–8319. doi:10.1021/ja0495056
45. Pavlichenko I, Exner AT, Guehl M, Lugli P, Scarpa G, Lotsch BV (2012) Humidity-enhanced thermally tunable TiO2/SiO2 bragg stacks. J Phys Chem C 116:298–305. doi:10.1021/jp208733t
46. Saito H, Takeoka Y, Watanabe M (2003) Simple and precision design of porous gel as a visible indicator for ionic species and concentration. Chem Commun 7:2126–2127. doi:10.1039/b304306a
47. Lim HS, Lee JH, Walish JJ, Thomas EL (2012) Dynamic swelling of tunable full-color block copolymer photonic gels via counterion exchange. ACS Nano 6:8933–8939. doi:10.1021/nn302949n
48. Gui Q, Wang W, Baohua G, Liang L (2012) A combined physical − chemical polymerization process for fabrication of nanoparticle – hydrogel sensing materials. Macromolecules 45:8382–8386. doi:10.1021/ma301119f
49. Nakayama D, Takeoka Y, Watanabe M, Kataoka K (2003) Simple and precise preparation of a porous gel for a colorimetric glucose sensor by a templating technique. Angew Chem 115:4329–4332. doi:10.1002/ange.200351746
50. Zhang X, Ma X, Dou F, Zhao P, Liu H (2011) A biosensor based on metallic photonic crystals for the detection of specific bioreactions. Adv Funct Mater 21:4219–4227. doi:10.1002/adfm.201101366

Photochromic Fibers and Fabrics

7

Marzieh Parhizkar, Yan Zhao, and Tong Lin

Contents

Introduction 156
Photochromism 156
Definition 156
Brief History 157
Photochromic Compounds and Their Properties 159
Technologies to Prepare Photochromic Fibers/Fabrics 162
Exhaust Dyeing of Fibers and Fabrics 162
Screen Printing 164
Sol–Gel Coating Method 164
Electrospinning 165
Optical Properties of Photochromic Fabrics 169
Photochromic Absorption 169
Coloration–Decoloration Speed 171
Photostability 175
Applications 177
Fashion 177
Security 177
UV Protection 177
UV Sensors 179
Others 179
Outlook and Future Remark 179
Summary 179
References 180

M. Parhizkar • Y. Zhao
Australian Future Fibers Research and Innovation Centre, Institute for Frontier Materials, Deakin University, Geelong, VIC, Australia
e-mail: marzieh.parhizkar@deakin.edu.au; yan.zhao@deakin.edu.au

T. Lin (✉)
Institute for Frontier Materials, Deakin University, Geelong, VIC, Australia
e-mail: tong.lin@deakin.edu.au

© Springer Science+Business Media Singapore 2015

X. Tao (ed.), *Handbook of Smart Textiles*,
DOI 10.1007/978-981-4451-45-1_7

Abstract

Photochromic fibers and fabrics can change color in response to light radiation. They represent a smart textile having attracted much attention recently and showing potential applications in diverse areas. This review chapter gives an overview of the state-of-the-art techniques for the preparation of photochromic fibers and fabrics. The properties and applications of photochromic fabrics are also discussed.

Keywords

Photochromic • Fibers • Smart textile • Color changing • Photostability • Coloration • Decoloration • UV protection • Exhaust dyeing • Sol–gel • Screen printing • Photo-switchable

Introduction

The fascinating color change of photochromic compounds in response to specific light has led to a number of applications in areas including light protection, ophthalmic lenses, security printing, optical data storage, memories, optical switches, sensors, and displays. In recent years, interest has also risen in the development of fibers and textiles with photochromic features mainly for fashion and UV protection purposes. This chapter summarizes recent research progress in photochromic fibers and fabrics and their optical properties and applications. The basic principle of photochromism, the preparation methods of photochromic fibers and fabrics, and the future perspectives of these smart fabrics are also discussed.

Photochromism

Definition

Photochromism is defined in simple terms as a reversible light-induced color change [1]. A more accurate definition would be a reversible transformation between two forms of a chemical compound with different absorption spectra, caused in one or both directions by electromagnetic radiation. The reversibility of the reaction is stressed upon [1–3]. A typical photochromic reaction is given in Fig. 1. Form A, which is the more thermodynamically stable state of the photochromic molecule, is transformed into form B by radiation. This reaction can be reversed thermally or photochemically [1]. If the back reaction occurs thermally, the process is referred to as T-type photochromism, and if driven only by irradiation with light (other wavelengths than UV), it is known as P-type photochromism [1, 4]. Photochromic reactions can also be categorized in another way. The most common photochromic processes are known as *positive*, where form A is colorless and form B colored. In some compounds, however, *negative* photochromism is observed, where form A is colored and form B colorless.

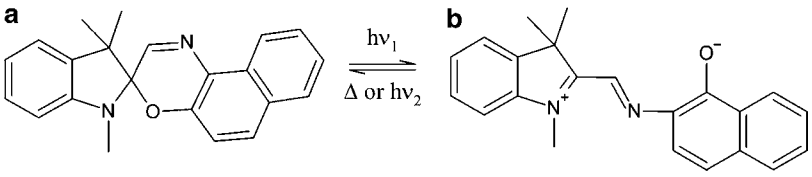

Fig. 1 Structure change of a photochromic compound (spirooxazine): *left*, *closed* colorless form; *right*, *open* colored form [2]

In addition to the color change, the change in the molecular structure of the photochromic compound may lead to changes in its physical properties such as refractive index, electrical conductivity, and solubility [5, 6].

Brief History

Photochromism was first reported in the literature by Fritsche in 1867, who observed a color change in tetracene in the presence of light, and later by *ter* Meer in 1876, who observed this phenomenon in the potassium salt of dinitroethane. Later, Phipson reported that a gate post (covered with a zinc pigment) appeared black in daylight and white at night. Marckwald identified the color change behavior of benzo-1-naphthyridine and tetrachloro-l,2-keto-naphthalenone in the presence of light as a new phenomenon and named it "phototropy." Nowadays, this term is used to describe the behavior of plants towards light. The term "photochromism" was suggested by Hirshberg in 1950. It consists of the Greek words *phos* meaning light and *chroma* meaning color and is a more accurate term for describing a reversible color change.

Before 1921, most studies on photochromism were focused on synthesis and properties of photochromic molecules (e.g., bleaching and fatigue). A decline in the study of this phenomenon occurred in the 1930s. Photochromism came back to attention in the 1940s. This time, however, the focus had shifted towards the mechanism of photochromic processes, the structure of photochromic molecules, and the intermediate species formed in the photochromic reactions. These studies benefited from technological advances, as such characterization tools as nuclear magnetic resonance (NMR) and infrared (IR) spectroscopy became available. The introduction of photochromic sunglasses was a breakthrough in the 1960s. The discovery of time-resolved spectroscopy made it possible to study transient processes and excited states and their lifetime and properties. More recently, some typical photochromic compounds such as fulgides and spiropyrans were thoroughly investigated, and novel photochromic compounds such as spiroindolizines were discovered. In recent years, embedding photochromic molecules in polymeric or other matrices has attracted great interest. Figure 2 shows the rapid growth of the research literature on photochromism since the 1990s. Most of the studies have been conducted in the chemistry area,

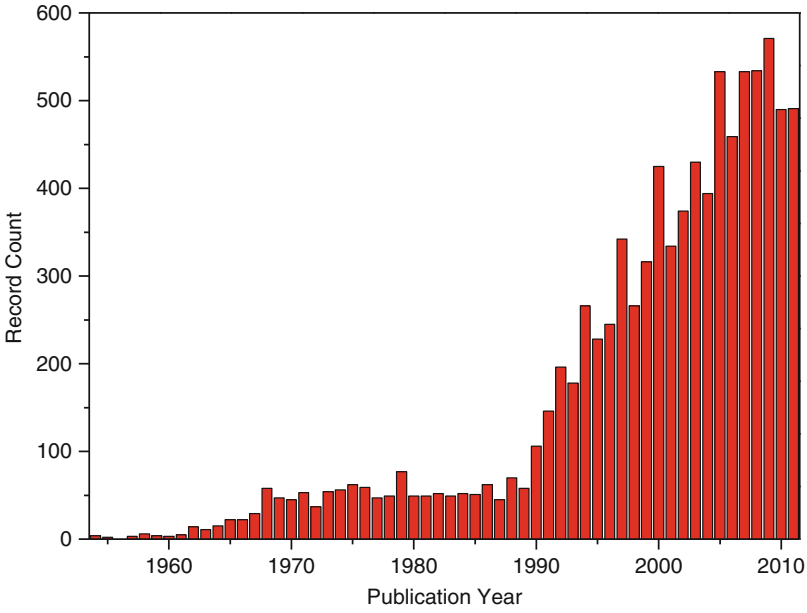

Fig. 2 Publication number versus year of publications on photochromism

Fig. 3 Subject areas where photochromism is studied

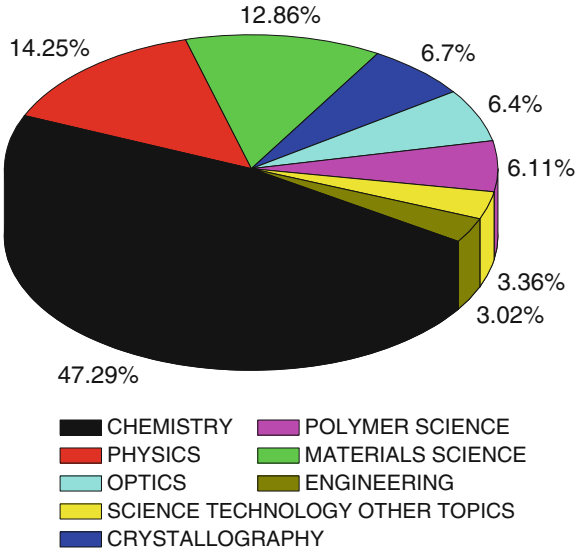

followed by physics and materials science (Fig. 3). Other areas include crystallography, optics, and polymer science. Photochromism is still an inviting field of research, and further investigation could help to develop exciting new applications [1].

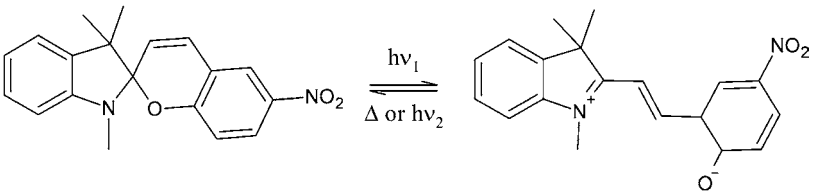

Fig. 4 Photochromism of indolinospiropyrans: *left*, colorless; *right*, colored forms [2]

Photochromic Compounds and Their Properties

Photochromism is observed in organic as well as inorganic or organometallic materials. Examples of inorganic materials exhibiting photochromic properties include metal (e.g., silver) halides, metal oxides, titanium oxides, alkaline earth sulfides, and some natural minerals and transition metal compounds.

Examples of organic photochromic materials include hydrazones, osazones, semicarbazones, anilines, disulfoxides, succinic anhydride, spiro compounds, and derivatives of stilbene, camphor, and *o*-nitrobenzyl. The photochromic processes of organic compounds mostly involve heterolytic cleavage, isomerization, pericyclic reactions, and to a lesser extent redox or electron transfer. Among the photochromic dyes developed, spiropyrans, spirooxazines, naphthopyrans, diarylethenes, fulgides, and azobenzenes are the most widely known classes [2, 3, 6].

Photochromic materials are also categorized as T type or P type based on whether the back reaction occurs thermally (T) or photochemically (P). T-type photochromic compounds include spiropyrans, spirooxazines, naphthopyrans (chromenes), and azobenzenes. P-type photochromic materials include diarylethenes and fulgides [1, 2, 7].

Spiropyrans

Spiropyrans (SPs) are the most widely studied families of photochromic dyes. They are easy to synthesize, exhibit high color depth, and bleach rapidly. Their photochromic reaction involves opening the pyran ring upon UV exposure, leading to a colored form called photomerocyanine (Fig. 4).

The colorless and colored forms of SP are both present at all times and in equilibrium with each other. UV irradiation shifts the reaction in Fig. 4 to the right, that is, towards generation of the merocyanine (MC) species, which produces a deeper color. In the absence of UV irradiation, the reaction is reversed to produce higher concentrations of the colorless species, thus color bleaching. As heat can shift the equilibrium towards the ring-closed, colorless pyran form, elevated temperatures can increase bleaching speeds, reducing the photochromic effect [2].

The shortcoming of the SP family is their relatively low resistance to fatigue. However, they are still used in applications that do not require high photostability, for instance, as probes or controls, in tensile stress sensors, and in photo-switchable magnetic devices [4].

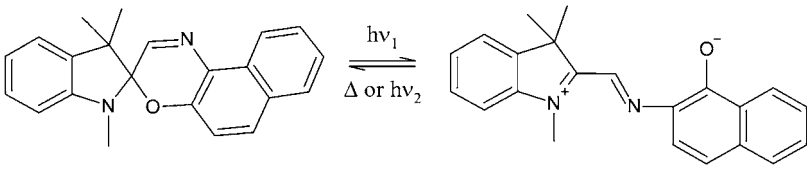

Fig. 5 Chemical structure and photochromism of spirooxazines [2]

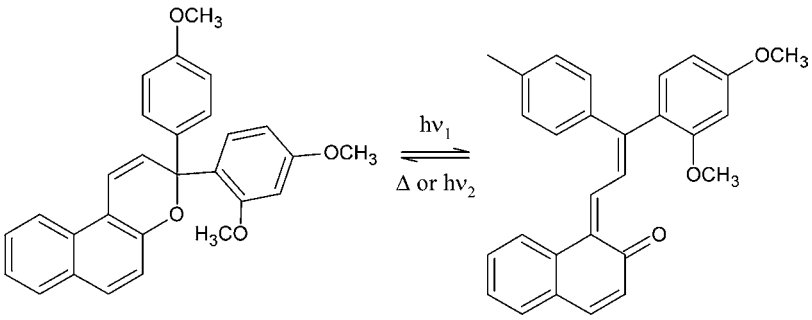

Fig. 6 Photochromism of naphthopyrans [2]

Spirooxazines

This class of photochromic dyes is similar in its structure and photochromism mechanism to spiropyrans. However, it is superior to spiropyrans in terms of photostability. Because of the relatively high fatigue resistance, spirooxazines were used in the first commercial plastic photochromic lenses. Simple spirooxazine compounds have a blue shade in their excited state and bleach relatively quickly. Their shade in the excited state, as well as their photo-coloration/bleaching, can be tailored by introducing suitable functional groups to the molecule [4]. The chemical structure and photochromic reaction of a typical spirooxazine compound is shown in Fig. 5.

Naphthopyrans

This class of photochromic compounds, also known as chromenes, has become the most important in commercial applications. This family of dyes also undergoes a ring-opening transformation when irradiated by UV light (Fig. 6). The chemical structure of naphthopyrans allows the economical incorporation of many types of substituents to tailor photochromic color, kinetics, and stability. The photostability of commercially available naphthopyrans is comparable to other classes of photochromic dyes. Furthermore, they are less heat sensitive compared to spirooxazines. This is why it has been used in the formulation of all marketed plastic photochromic lenses [4, 8].

Diarylethenes

Diarylethenes (with heterocyclic aryl group) belong to P-type photochromic dyes. In other words, their photochromism is thermally irreversible. Furthermore, diarylethenes exhibit high levels of fatigue resistance. They can undergo

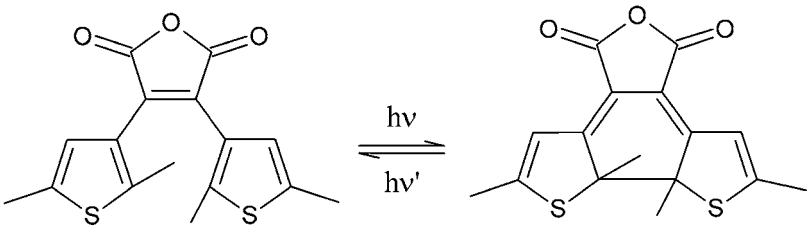

Fig. 7 The ring-closing photochromic process (or photocyclization) of a diarylethene [2]

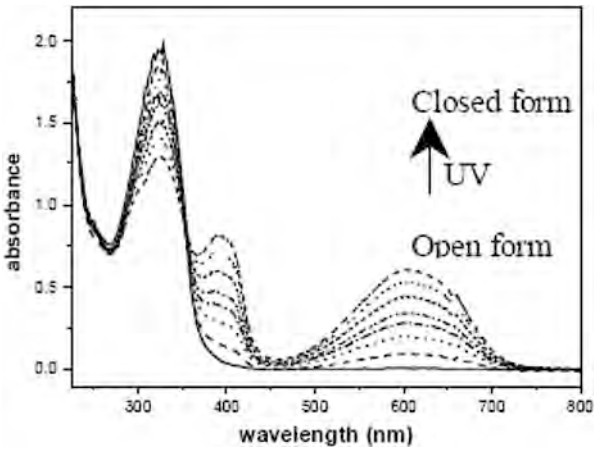

Fig. 8 The spectral changes of a diarylethene derivative during conversion between the open and closed forms (Reprinted from Liu et al. [10] with permission from SPIE)

coloration/bleaching more than 10^4 times, which makes them suitable for applications in optical devices such as memories and switches [9]. Diarylethenes undergo a ring-closing reaction when stimulated by UV light [10]. The open form is thermally stable, while the thermal stability of the closed form depends on the type of aryl group. The ring-closing process of a diarylethene is shown in Fig. 7. Figure 8 shows the spectral changes of a diarylethene compound during conversion between open and closed forms.

Fulgides

Fulgides exhibit photochromism with the same mechanism as diarylethenes, i.e., photocyclization. In other words, UV light triggers a reaction which converts the open colorless form to the closed colored form [11]. The photochromic reaction of a fulgide is shown in Fig. 9. Fulgides belong to P-type photochromic dyes. This means that once activated, fulgides tend to remain in their closed-ring, colored state, unless they are irradiated with visible light. This feature facilitates the application of fulgides in optical memories and switches. Furthermore, unlike spiropyrans and spirooxazines, fulgides can perform photochromic reaction in their solid form [4].

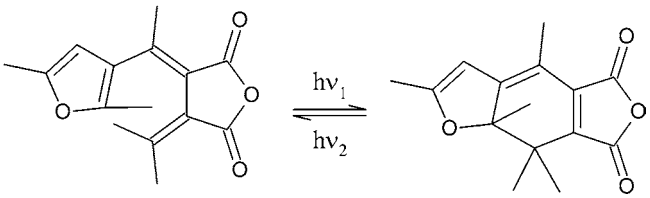

Fig. 9 The photochromic process of a fulgide [2]

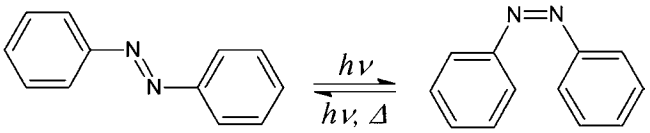

Fig. 10 Isomerization of azobenzenes: E (*trans*) to Z (*cis*) transformation [1]

Azobenzenes

Azobenzenes follow a trans-cis isomerization photochromism (Fig. 10). The *trans* form is commonly referred to as "E" and the *cis* form as "Z." Azobenzenes are thermally reversible, meaning that the Z isomer can transform to the E isomer by means of heat (or visible light). Azobenzene compounds generally have a yellow to red color [1].

Technologies to Prepare Photochromic Fibers/Fabrics

Exhaust Dyeing of Fibers and Fabrics

Exhaust or batch dyeing is a common discontinuous process for dyeing textiles. In this process, the dye slowly transfers or *exhausts* from a relatively large dye bath to the textile. The dye bath is heated where higher temperatures are required. The textiles in any form, including fiber, yarn, fabric, or garment, can be dyed using this method [12].

The way of using dyeing method to prepare photochromic fibers or fabrics is straightforward. Shah et al. [13] dyed nylon, cellulose triacetate, and polyester fibers with mercury (II) dithizonate photochromic compound.

The dyeing solution was prepared by mixing the dye with dispersing agent and wetting agent. The nylon and polyester fibers were treated at a pH of 5–6 at 60 °C for 15 min. Polyester fibers were dyed under high pressure at 120 °C for an hour at a liquor-to-goods ratio of 50:1. Nylon and cellulose triacetate fibers were dyed at 100 °C for 1.5 h. The fibers were then washed with water, a solution containing soap (1 g/L) and sodium carbonate (2 g/L) to remove excess dye, and water again before drying in air.

The fastness of the dyed fibers, including photostability, and wash and abrasion fastness were all measured according to standardized methods [13]. The color of the

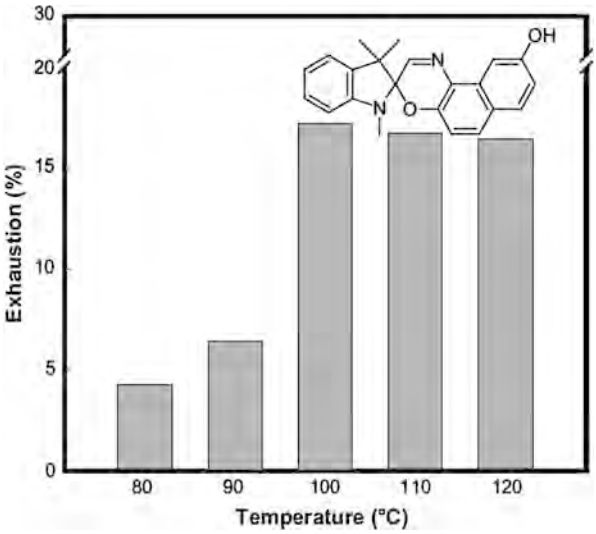

Fig. 11 Effect of temperature on exhaustion of dye onto fabric (Reprinted from Lee et al. [14] with permission from Elsevier)

cellulose triacetate and nylon fibers changed from orange/brown orange to blue gray/violet with exposure to strong sunlight. The decoloration at room temperature took between 30 and 45 min and was fastest in polyester fibers. The decoloration took around 2–3 min at 100 °C. The three fibers displayed excellent photochromism as well as satisfactory photostability and superior wash and abrasion fastness.

Lee et al. [14] incorporated three spirooxazine dyes in polyamide fabrics using an exhaust dyeing process. The fibers were dyed in a dyeing machine at a liquor-to-goods ratio of 50:1 at 40 °C for 10 min and subsequently at a temperature between 80 °C and 120 °C for 1 h. The samples were then rinsed with water and air-dried. The dye exhaustion yield was found to increase with increasing the dyeing temperature (Fig. 11). This was attributed to swelling of the fibers at higher temperatures which facilitates the diffusion of dye molecules into the fibers. It was also attributed to the higher kinetic energy of the dye molecules at elevated temperatures. The dyed polyamide substrates before and after UV irradiation are shown in Fig. 12.

The conventional exhaust dyeing technique was also employed by Billah et al. [15] to prepare photochromic acrylic, nylon, and polyester fabrics. The photochromic fabrics, depending on the dye used, displayed a blue or bluish-purple color under UV irradiation. The nylon fabric showed a deeper color than the acrylic fabric. The dyes were ball milled with a dispersing agent and water, and the resultant dye dispersions were added to the fibers in a dyeing machine. A pH of 5.5 was used in the dying bath for nylon and acrylic and 4.5 for polyester. The liquor-to-goods ratio was 50:1. The starting temperature was 40 °C, which was gradually increased to 90 °C and maintained there for an hour. The temperature was then reduced back to 40 °C and the fabrics were rinsed with water.

They also applied acidic photochromic dyes to wool fabric [16]. Aldib and Christie [17] also applied six photochromic dyes of spironaphthooxazine and naphthopyran types to a polyester fabric by means of exhaust dyeing.

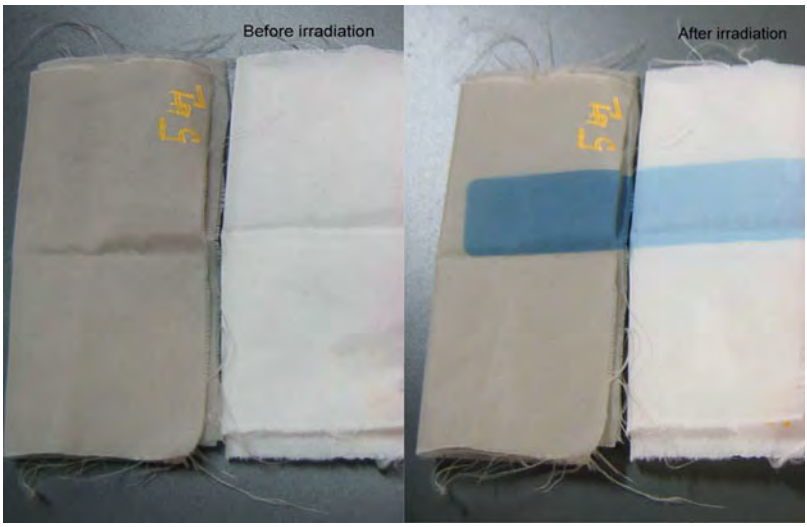

Fig. 12 Polyamide fabrics dyed with spirooxazine dyes, before and after irradiation with UV (Reprinted from Lee et al. [14] with permission from Elsevier)

Screen Printing

Screen printing is a technique where a dyeing paste is passed through a screen using a blade to form a pattern on fabric. Manual, mechanical, and rotary screen printing can be used for treatment of textiles [18]. Little and Christie [19] screen printed commercially available photochromic dyes onto cotton fabric. Feczko et al. [20] also used the screen-printing technique to apply ethyl cellulose–spirooxazine nanoparticles to cotton fabric. To protect the photochromic compounds, microencapsulation was used for incorporating photochromic compounds. Due to the small size of the resultant microcapsules (approximately 3–5 μ), microencapsulated photochromic dyes can be screen printed onto fabrics [21]. The advantage of this technique is that the encapsulating polymer layer offers a protection to the photochromic compounds. However, it reduces the fabric handle properties.

Sol–Gel Coating Method

Sol–gel technology is in general terms a method of producing inorganic materials by way of synthesizing a sol, causing it to gel, and subsequently drying and possibly sintering the gel. This process offers the possibility of fabricating materials with tailored properties in a range of forms including powders, fibers, and films, by selecting suitable precursors and controlling the reaction conditions [22]. Sol–gel process enables the control of pore size and pore arrangement in the inorganic or hybrid matrix [23].

Alkoxides are the most common sol–gel precursors. In the sol–gel process, the alkoxide precursor undergoes hydrolysis in the presence of water:

$$\mathrm{Si(OR)_4 + H_2O \rightarrow HO - Si(OR)_3 + ROH} \quad (1)$$

R represents an alkyl group and •OR an alkoxy ligand. If amounts of water and catalyst are sufficient, the four alkoxy groups are converted to hydroxyl groups, producing $Si(OH)_4$. Otherwise, the hydrolysis reaction stops in an intermediate stage, leading to $Si(OR)_{4-n}(OH)_n$.

Sol–gel process also includes condensation reactions, which occur when partially hydrolyzed metals/metalloids interact. The by-product of the condensation reaction could be water or alcohol, as in Reactions 2 and 3, respectively.

$$\mathrm{(OR)_3Si - OH + HO - Si(OR)_3 \rightarrow (OR)_3Si - O - Si(OR)_3 + H_2O} \quad (2)$$

$$\mathrm{(OR)_3Si - OR + HO - Si(OR)_3 \rightarrow (OR)_3Si - O - Si(OR)_3 + ROH} \quad (3)$$

The condensation reaction polymerizes the monomer into a larger structure.

A gel is formed when a monomer molecule grows into a macroscopic-size polymer covering a large area of the solution. Therefore, a gel can be described as a continuous solid framework within a continuous liquid phase. A sol may be applied onto various substrates to form a uniform coating. Cheng et al. [24–26] used silica sol–gel to encapsulate photochromic spirooxazine dye on wool fabric. The procedure is shown in Fig. 13.

The precursors used as well as the photochromic properties of the coated fabric are shown in Table 1. Figure 14 shows SEM images of the wool fibers before and after sol–gel treatment, abrasion, and wash tests.

The colorless spirooxazine dye turned blue when exposed to UV irradiation. The color change of the photochromic wool fabric with exposure to sunlight is illustrated in Fig. 15 [27].

Cheng et al. [24] reported the absorption maxima of 0.24 and 0.25, coloration half times of 14.75 and 9.30 s, and bleaching half times of 54.25 and 22.75 s for silica coatings from phenyltriethoxysilane (PhTES) and octyltriethoxysilane (OTES), respectively. Furthermore, they reported values of 38.16 % and 37.31 % for the wash fastness of PhTES and OTES sol–gel-coated fabrics, respectively.

Electrospinning

Electrospinning is an efficient method to prepare polymer nanofibers. During electrospinning, a polymer solution is charged by a strong electric field to create a polymer jet that solidifies upon rapid solvent evaporation from the jet during electrospinning. These charged fibers are collected on the counter electrode [28]. When functional chemicals are added to polymer solution for electrospinning,

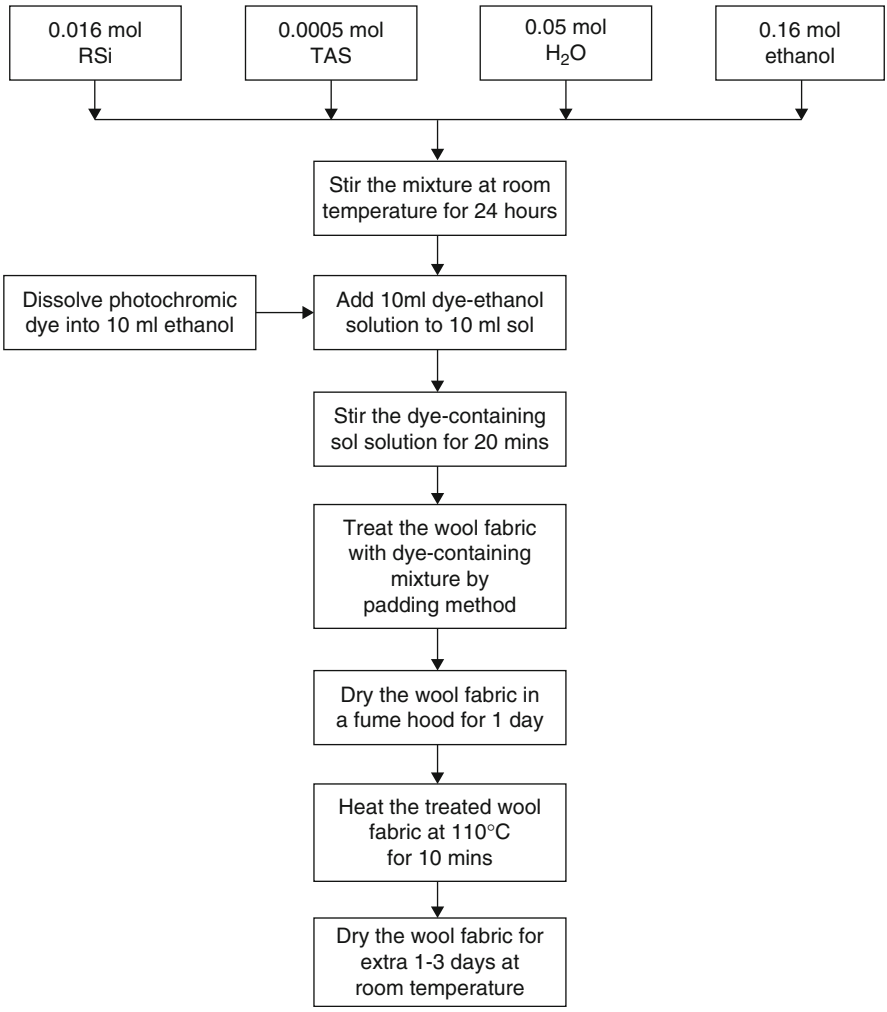

Fig. 13 The process of preparation and application of sol–gel coating to fabric (Reprinted from Cheng [27] with permission from Deakin University)

they are incorporated into fibers and spun easily. In this way, photochromic nanofibers can be produced by adding photochromic dyes to a polymer solution for electrospinning.

De Sousa et al. [29] incorporated a spiropyran–cyclodextrin complex into PMMA nanofibers through electrospinning PMMA solution containing photochromic dyes. Spiropyran was covalently bonded to β-cyclodextrin and the resulting complex was attached to the side chain of PMMA. For comparison, spiropyran alone was also attached to the side chain of PMMA. The hydroxyl groups on the outer surface of cyclodextrin stabilize the merocyanine (colored) form of spiropyran.

Table 1 Sol–gel precursors and photochromic properties of the coated wool fabric (Reprinted from Cheng et al. [26] with permission from Springer Science and Business Media)

	Sample	Percursor structure	ΔA[a]	$t_{1/2}$ (s)	$t_{1/2}$ (s)	Abrasion fastness (%)[b]	Washing fastness (%)	Bending modulus (g/cm^2) Warp	CA Weft	(°)
	MeSi	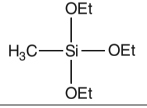	0.22	18	22	50.14	29.75	12.9	2.9	139.5
	PhSi	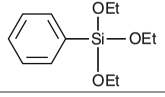	0.24	6	28	57.03	38.16	42.5	8.8	143.7
Silica-coated fabrics	VinSi	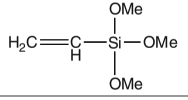	0.17	5	5	55.00	42.86	20.9	2.8	143.8
	CycHSi	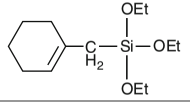	0.20	16	16	63.97	68.27	2.4	0.57	147.9
	OctSi	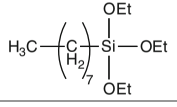	0.24	3	4.5	55.96	37.31	2.0	0.57	145.1
Control	–		0	–	–	–	–	0.41	0.035	126.5

[a]The absorption at 620 nm
[b]The percentage decrease in ΔA after 1,000 abrasion cycles

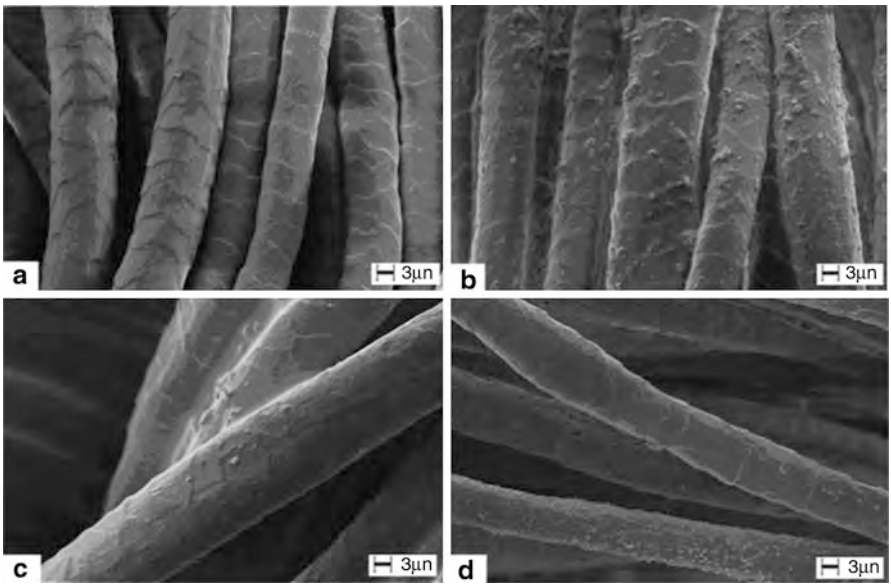

Fig. 14 SEM images of fibers in the wool fabric: (**a**) before and (**b**) after sol–gel treatment, (**c**) after 1,000 abrasion cycles, and **d** after standard wash test (Reprinted from Cheng et al. [25] with permission from Springer Science and Business Media)

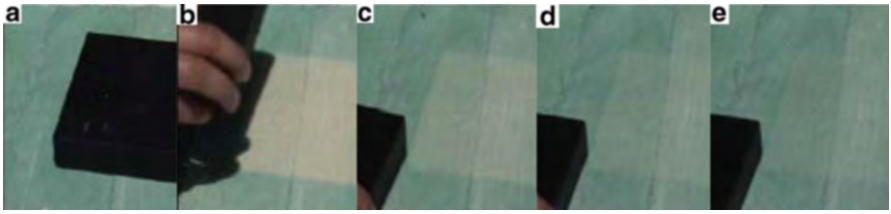

Fig. 15 Still frames taken from a video showing photochromic color change upon exposure of a wool fabric that is treated with spirooxazine dye embedded in a sol–gel-derived silica matrix to sunlight (Reprinted from Cheng [27] with permission from Deakin University)

On the other hand, although PMMA polymer also contains hydroxyl groups, the presence of hydrophobic groups in PMMA as well as limitations on free movement of spiropyran in PMMA matrix causes the stabilization of the colorless form of spiropyran. Therefore, the combination of β-cyclodextrin and PMMA leads to a balanced coloration–decoloration rate.

The electrospun fiber mat was kept at 80 °C for 12 h while subjected to visible irradiation through a mask. Once the mask was removed, the covered area of the mat was light red, which is related to the merocyanine form of the dye, while the area that had been exposed to visible light was white, which is related to the colorless form of spiropyran. Once the mat was exposed to UV irradiation, the color difference between the two areas increased due to the fluorescence of the merocyanine form.

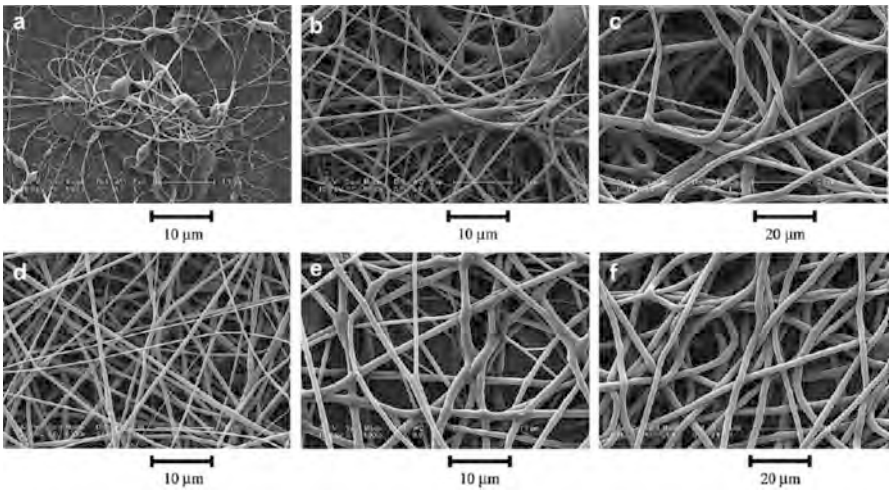

Fig. 16 SEM images of electrospun fibers of polyvinylidene fluoride–hexafluoropropylene copolymer (**a**) 10 wt%, (**b**) 12 wt%, and (**c**) 15 wt%), and electrospun fibers of polyvinylidene fluoride–hexafluoropropylene copolymer containing 1 wt% ester-functionalized nitrospiropyran (**d**) 10 wt%, (**e**) 12 wt%, and (**f**) 15 wt%) (Reprinted from Wang et al. [33] with permission from Elsevier)

Bianco et al. [30] added a diarylethene dye to the solution of polyamide 6 (PA-6) and formic acid for the preparation of electrospun photochromic fibers. They used polarized infrared spectroscopy to study the alignment of the PA-6 polymer chains in the fibers and found that the molecules of the dopant, i.e., photochromic dye, in the fiber were also highly aligned. Kim et al. [31] produced nanofibers by incorporating photochromic pigments into the electrospinning feed solution and fused the nanofibers to produce a photochromic nonwoven fabric. Di Benedetto et al. [32] incorporated a spiropyran into a PMMA polymer matrix to produce photochromic electrospun nanofibers. They observed photo-switchable wettability on the photochromic nanofiber mat. In other words, it changed with the irradiation wavelength. Wang et al. [33] produced photochromic nanofibers by electrospinning the solution of a spiropyran and polyvinylidene fluoride–hexafluoropropylene copolymer (Fig. 16). The color change of the nanofiber mat with exposure to UV and visible light is shown in Fig. 17.

Optical Properties of Photochromic Fabrics

Photochromic Absorption

Figure 18 shows the level of optical absorption of a photochromic textile under UV irradiation. Without UV light, no absorption peak is formed in the wavelength region between 600 and 650 nm for spirooxazine. When the fabric is irradiated by UV light, an absorption peak appears.

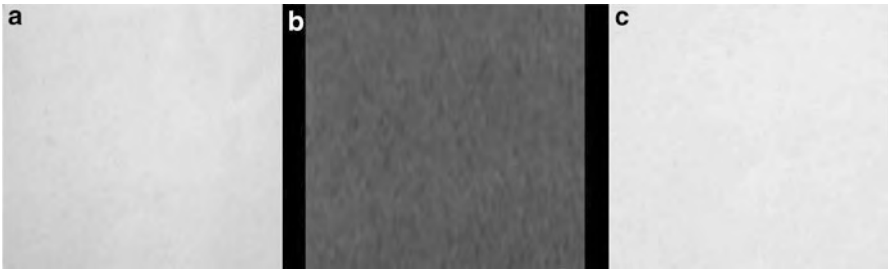

Fig. 17 Photographs of polyvinylidene fluoride–hexafluoropropylene copolymer containing spiropyran: (**a**) before exposure to irradiation, (**b**) after exposure to UV light, and **c** after exposure to visible light (Reprinted from Wang et al. [33] with permission from Elsevier)

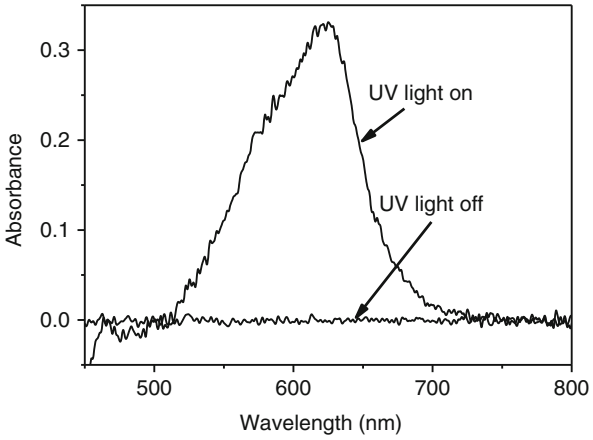

Fig. 18 Optical absorption spectra of a photochromic textile prepared by coating silica sol containing spirooxazine photochromic dye (Reprinted from Parhizkar et al. [35] with permission from Journal of Engineered Fibers and Fabrics)

The absorption intensity reflects the color depth of the fabric; the higher the intensity value, the deeper the color. The depth of color upon UV irradiation is a significant factor in real-life applications of photochromic textiles. Little and Christie [19] found that photochromic spirooxazine dye printed on cotton fabric produced a stronger color with UV irradiation than on polyester. They attributed this to different UV reflection from the surface of the two fabrics. Cotton reflects UV irradiation more than polyester, which results in the printed layer on cotton being exposed to reflected UV light, thus increasing the degree of photo-coloration.

The strength of photochromic color is dependent on dye concentration. Little and Christie [19] observed a stronger color with higher dye concentration up to a maximum level. They explained this as the reduction in dye solubility in the printing paste after a certain point. As the photochromic compound does not display photochromism in its solid form, the degree of photo-coloration is reduced. Dye aggregation was also proposed as a possible explanation, as it hinders the structural transformation of the dye molecules which requires free space. A third explanation offered was that the absorption of UV light by the dye molecules in the upper layers of the print blocks the UV from those in the lower layers.

The dyes studied by Little and Christie [19] showed different degrees of photo-coloration based on the wavelength of UV light. They found that the photochromic color change was mainly initiated by UVA (360–390 nm). UVB (290–320 nm) followed by UVC (220–290 nm) was less influential in the color change of the dyes.

Temperature can also have an impact on the degree of color change or photo-coloration. Increasing the temperature can promote the photochromic back reaction, thereby hindering color change [19].

Additives can also affect the UV absorption of a photochromic fabric. Feczko et al. [20] reported that adding a photo-stabilizer compound, Tinuvin 144, to the screen-printing paste improved the photochromic absorbance of their cotton fabric.

Billah et al. [34] reported that the UV absorption of nylon, polyester, and acrylic photochromic fabrics wetted with water as well as other solvents was significantly higher than that of the dry fabrics. They observed that wetting polyester fabric with acetonitrile, which was the most polar solvent among the five studied, produced the highest UV absorption, while toluene which was the least polar contributed to a smaller UV absorption. They calculated the dipole moments of the photomerocyanine (open form) and closed form of the dye and observed that the photomerocyanine species has higher polarity. Therefore, the more polar solvents stabilized the open form of the dye molecule, thus promoting photo-coloration. However, there was no obvious correlation between polarity and UV absorption for the other three solvents. This was attributed to other possible causes such as hydrogen bonding. They also speculated that the solvents may swell the fibers, thus creating a more favorable environment for photo-conversion of the dye.

The photochromic wool fabric developed by Cheng et al. [24] using a sol–gel-derived silica coating showed an absorption maximum of 0.24 and 0.25 for silica coatings produced from phenyltriethoxysilane (PhTES) and octyltriethoxysilane (OctTES) precursors, respectively (Fig. 19).

Similarly, Parhizkar et al. [35] produced a photochromic fabric by applying a silica coating prepared using sol–gel processing and containing spirooxazine dye. A combination of phenyltriethoxysilane (PhTES) and octyltriethoxysilane (OTES) precursors was used in preparing the coating. The maximum absorption of the fabric was 0.32 ± 0.01.

Coloration–Decoloration Speed

The speed of coloration and decoloration of a photochromic textile or fiber when exposed to UV irradiation is an index of color change speed, which is of importance for practical photochromic effect. The speed of coloration is expressed by the time required for absorption to increase from zero to half of its maximum level upon exposure to UV irradiation. Similarly, the speed of decoloration is expressed by the time taken for absorption to reduce from maximum to half of the maximum [26]. These times are indicated as $t_{1/2}$ and $t'_{1/2}$, respectively, as shown in Fig. 20.

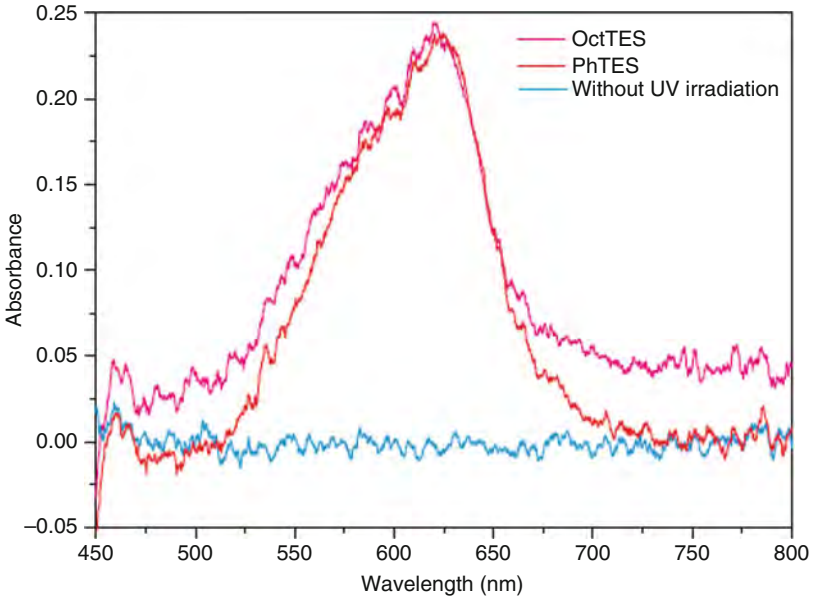

Fig. 19 UV–vis absorption of wool fabric coated with spirooxazine dye embedded in a sol–gel-derived silica matrix with octyl and phenyl functional groups (Reprinted from Cheng et al. [24] with permission from SAGE)

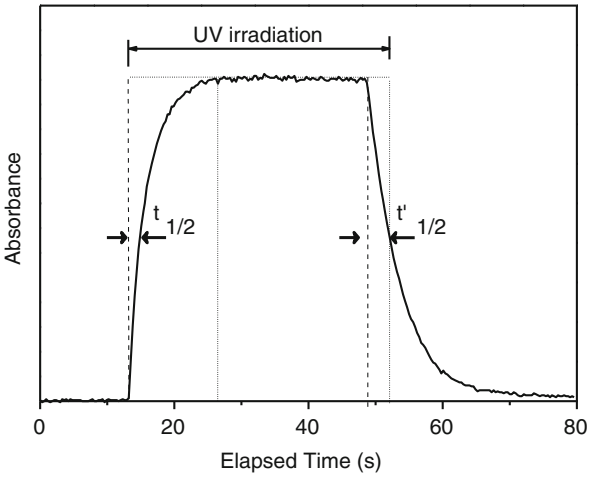

Fig. 20 Coloration–decoloration curve of a photochromic textile: $t_{1/2}$ and $t'_{1/2}$ represent the coloration and decoloration half-lives (Reprinted from Parhizkar et al. [35] with permission from Journal of Engineered Fibers and Fabrics)

The rate of coloration and decoloration largely depends on the matrix in which the photochromic dye is placed. The photochromic molecule requires free space in order for the photo-induced structural transformation and consequently color change to occur. Any steric effects induced by the polymer matrix can affect the

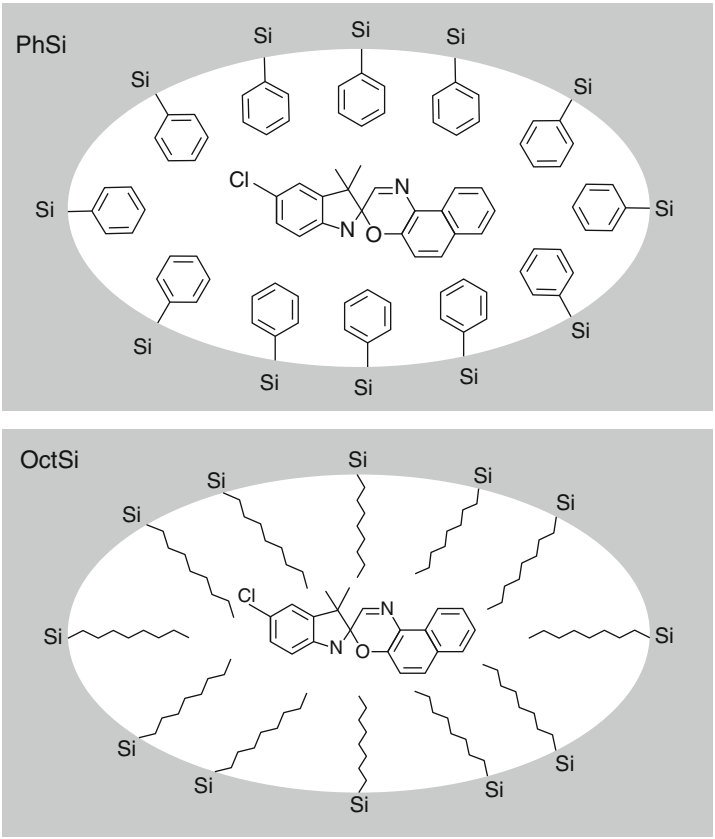

Fig. 21 Schematic of silica matrixes bearing different functional groups encapsulating a spirooxazine dye molecule (Reprinted from Cheng et al. [26] with permission from Springer Science and Business Media)

speed of the dye's transformation. Cheng et al. [26] embedded a spirooxazine dye in five different silica matrixes via the sol–gel method to create photochromic coatings on wool fabric. The coloration times of their coated fabrics varied between 3 and 18 s and the decoloration time between 4.5 and 22 s for coatings prepared from different silica precursors. After comparing the properties of photochromic coatings from silica precursors bearing different organic non-hydrolyzable groups, they concluded that precursors bearing long alkyl chains, such as the octyl group in octyltriethoxysilane, produced better photochromic and handle properties. In another work [25], they compared the properties of coatings from combinations of short- and long-chain alkyl silica with 3-glycidoxypropyltrimethoxysilane (GPTMS) and concluded that the epoxy group of GPTMS improved abrasion and washing durability. Figure 21 illustrates silica matrixes bearing different functional groups with encapsulated spirooxazine dye molecule.

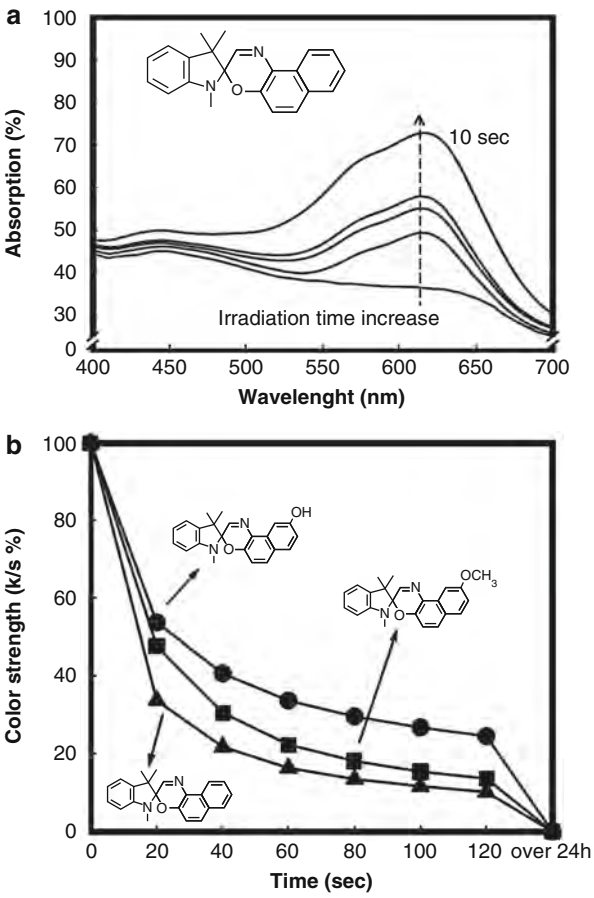

Fig. 22 (**a**) Changes in absorption of photochromic fabric at different wavelengths with UV irradiation time and (**b**) decoloration of three spirooxazine dyes with time (Reprinted from Lee et al. [14] with permission from Elsevier)

Parhizkar et al. [35] also produced a photochromic fabric by applying a coating consisting of spirooxazine embedded in sol–gel-derived silica produced from a combination of PhTES and OTES precursors. The resultant fabric displayed a coloration and decoloration rate of 1.6 ± 0.1 and 3.3 ± 0.1 s, respectively.

In the work of Lee et al. [14], photochromic polyamide fabrics containing spirooxazine dyes exhibited photochromism with UV irradiation at a coloration rate of approximately 10 s (Fig. 22a). The decoloration rate which was expressed as K/S% dropped by 30–50 % within a time frame of 20 s (Fig. 22b).

The coloration and decoloration of a polyester fabric dyed with spirooxazine dye is shown in Fig. 23a, b, respectively [15]. Coloration is presented in the form of spectral changes against wavelength with duration of UV irradiation. It took 10 min for absorbance to reach its peak, and it did not change further with another 5 min of irradiation. Decoloration is shown as the color difference in the fabric between the unexposed and exposed states.

The speed of response to UV irradiation can vary between different classes of photochromic dyes. Little and Christie [19] reported that spirooxazines faded more

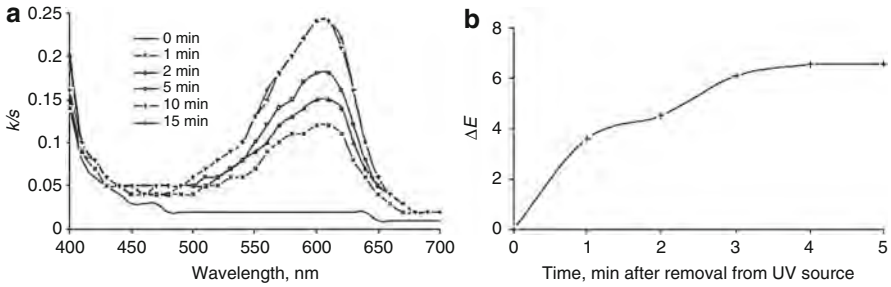

Fig. 23 (**a**) Spectral changes during coloration of photochromic polyester fabric with different exposure times to UV irradiation and (**b**) decoloration with removal of UV light (Reprinted from Billah et al. [15] with permission from John Wiley & Sons)

quickly after removal of the UV source compared with naphthopyrans. Naphthopyrans were reported to display a residual color after decoloration. They observed that different dyes within the same class exhibited similar coloration and fading rates, while these properties differed between two different classes.

Photostability

Photostability or resistance to photodegradation with prolonged UV exposure is another important aspect of a photochromic fabric/fiber for practical applications. Billah et al. [15] reported that a polyester fabric dyed with a spirooxazine dye lost almost all of its photochromic effect after 10 h of exposure to UV irradiation and displayed no color change after 20 h of exposure. However, they reported that after wetting the photochromic fabric which had lost its photochromic effect, it showed color change again with UV irradiation. The photostability of photochromic polyester is shown in Fig. 24.

Aldib and Christie [17] exhaust dyed polyester fabric with spironaphthooxazines and naphthopyrans, applied as disperse dyes. They measured the photostability of the fabric in 20 cycles. In each cycle, the fabric was subjected to UV irradiation for 4 min and subsequently bleached in the dark for 2 h. Furthermore, they measured the stability of the photochromic effect with storage by keeping the fabric in the dark for 170 days. The six studied dyes exhibited different photostability, regardless of their photochromic class, from lower than 50 % retention of the photochromic effect to as high as 100 %. The photochromic fabrics retained between 71 % and 84 % of their functionality after 170 days of storage. The order of the dye storability was not the same as that of their photostability.

Free radicals have been identified as a major cause of degradation of photochromic compounds, as they readily react with the excited form of the chromophore [36]. Oxygen (in free or radical form) has also been linked to the photodegradation of chromophores [37–39]. Different types of UV stabilizers can be used to protect photochromic compounds against photodegradation [40, 41]. These compounds

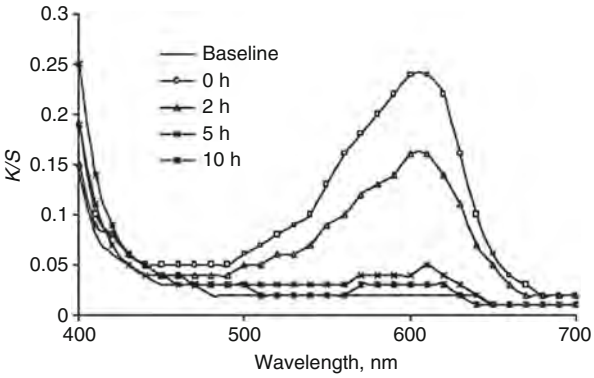

Fig. 24 Loss of photochromic functionality with UV irradiation time (Reprinted from Billah et al. [15] with permission from John Wiley & Sons)

work via different mechanisms including quenching, free radical scavenging, and UV absorbing [39, 42–44]. Little and Christie [45] screen printed some commercial photochromic dyes onto fabrics and reported that the coated fabrics had a relatively low photochromic photostability. The addition of UV absorbers increased the photostability to an extent. For one dye, photostability was increased from 150 min (for loss of half of the photochromic effect with exposure to UV light) to a maximum of 825 min by addition of a UV absorber. However, UV absorbers compete with the photochromic dye in absorbing UV, thus reducing the dye's photo-coloration. On the other hand, the incorporation of hindered amine light stabilizers improved photostability by up to fivefold without significantly affecting photo-coloration.

In the work of Parhizkar et al. [35], the effect of three types of treatment on the photochromic properties, including the photostability of a photochromic fabric, was studied. The photochromic fabric was prepared by coating wool fabric with a silica layer prepared via the sol–gel method and containing spirooxazine dye. The three treatments applied to the fabric included the addition of UV stabilizers to the coating, modification of the hydrophobicity of the coating using a fluorinated silane, and addition of an extra layer of silica to block the pores. The rationale behind the use of UV stabilizers was explained above. Fluorine atoms can help increase hydrophobicity and therefore prevent moisture from accessing the dye in the matrix pores, thus prolonging the life of the photochromic fabric. The additional silica helps block the pores to prevent the diffusion of moisture and other degrading elements into the matrix pores.

The coating solution was prepared by hydrolysis and condensation of a combination of octyltriethoxysilane and phenyltriethoxysilane precursors with acidic catalysis. The dye was then mixed with the sol, which was subsequently applied to the fabric by dip coating. The fabric was then air-dried and cured at 110 °C. The UV stabilizers, which included a UV quencher, two UV absorbers, and a free radical scavenger, were added to the dyeing solution, where required. The fluoroalkyl silane (FAS) was added to the solution at the beginning of synthesis, where applicable. The additional layer of silica, which did not contain dye, was prepared

from 3-aminopropyltriethoxysilane (APS), 3-trimethoxysilylpropylmethacrylate (MPA), or the same silica as the first layer and applied to fabric as described above.

All three treatments improved the photostability of the photochromic fabric, which was measured by irradiating the fabric with a mercury discharge lamp. The photostability of the control fabric was approximately 10 h, which was improved by the incorporation of the UV quencher to approximately 90 h. The UV absorbers and free radical scavenger were considerably less effective than the UV quencher. The incorporation of fluorine atoms also did not enhance photostability significantly. Among the three types of additional silica layer, that prepared from APS was the most effective, increasing photostability to higher than fourfold. This was attributed to the presence of the amino group, which helps protect the dye from photo-bleaching [46]. The other photochromic properties of the fabric, namely, the rate of coloration–decoloration and the absorbance, were not significantly affected by the treatments. The durability of the coated fabric to abrasion was high and the wash fastness was satisfactory.

Applications

Fashion

Photochromic textiles with their fascinating color-changing feature have found applications in fashion [47]. Joshi et al. [48] produced a color-changing umbrella by exhaust dyeing a polyester fabric with thermochromic dyes followed by screen printing of photochromic dyes onto the fabric. Similarly, they applied thermochromic and photochromic dyes to cotton fabric to produce a color-changing curtain, ornamental wall hangings, and color-changing T-shirts. They reported that their photochromic dyes performed equally well on different substrates in terms of depth of color as well as wash fastness.

Security

Minoshima and Osada [49] produced photochromic fibers containing a transition metal acid and a resin binder, which were suitable for application in papers for security purposes. Write [50] produced a security device in the form of a woven material containing photochromic yarns for such applications as product labels and identification cards.

UV Protection

Du and Su [51] prepared a photochromic fabric by depositing a thin film of tungsten oxide on nonwoven polyester fabric by means of magnetron sputtering. Images of their fabric are shown in Fig. 25 and the reflectivity versus wavelength is shown in Fig. 26.

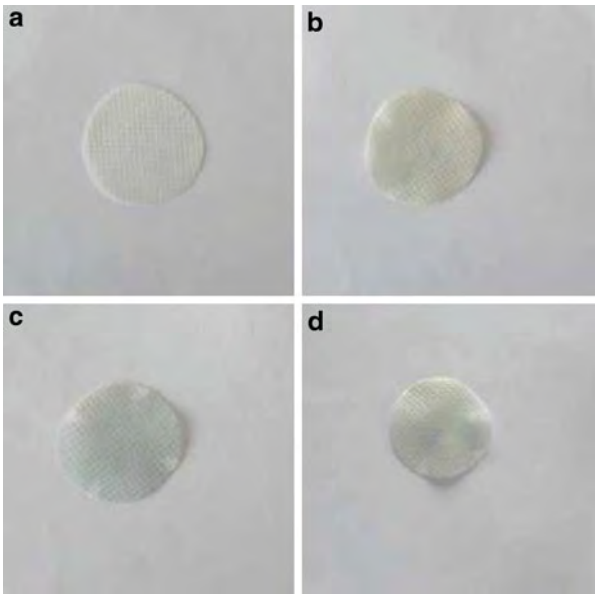

Fig. 25 (**a**) Plain polyester fabric, (**b**) coated fabric under visible light, (**c**) immediately after UV irradiation, and (**d**) 24 h after UV irradiation (Reprinted from Du and Su [51] with permission from Scientific.Net)

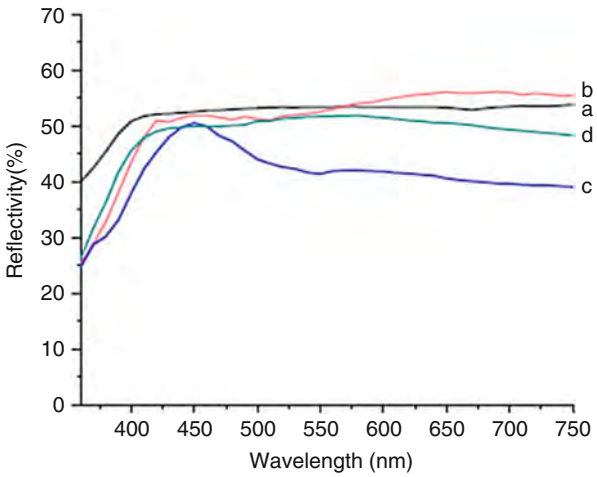

Fig. 26 Reflectivity of the four forms of the fabric (Reprinted from Du and Su [51] with permission from Scientific.Net)

They tested the temperature resistance of their fabric by monitoring the reflectivity of the coated fabric before and after exposure to 0 °C, 25 °C, and 100 °C temperature for 24 h. It was observed that the reflectivity of the sample remained almost unchanged, which demonstrated high-temperature resistance. The ultraviolet protection factor (UPF) of the fabric was also tested. It was found that the UPF of the activated (i.e., exposed to UV light) photochromic fabric was seven times higher than that of the uncoated fabric and twice higher than that of the coated fabric which had not been subjected to UV irradiation. However, the photochromic

fabric in this work did not display a strong color with UV irradiation. Furthermore, the coloration and fading speed were low. The fabric was irradiated for 30 min in a high-pressure mercury lamp to change color and stored in the dark for 24 h to fade back to its original color. However, a residual yellow color remained on the fabric which disappeared after 7 days.

UV Sensors

Vikovα [52] developed a UV sensor based on photochromic textiles. In this work, five different photochromic dyes were applied to PET fabric. The effect of the duration of exposure to UV irradiation on color change was studied. It was also reported that the speed of coloration was higher than decoloration.

Others

Photochromic textiles also have military applications such as aircraft canopies and camouflage [27].

Outlook and Future Remark

Since its discovery, the fascinating phenomenon of photochromism, or color change triggered by UV irradiation, has had many different applications, including in fibers and fabrics. In this chapter, different families of photochromic dyes, methods of applying them to fibers and fabrics, and the properties and applications of photochromic fibers and fabrics were discussed.

As discussed in this chapter, fast-switching color-changing fibers and fabrics have been developed. However, the high production cost and low photostability and wash fastness of photochromic fibers and fabrics have hampered their production on a commercial scale. Although the use of UV stabilizers has helped to improve the lifetime of photochromic materials, the durability properties of photochromic fibers and fabrics still require improvement to enable mass production of these materials. The exciting implications for the clothing and fashion industry can be a great incentive for further research on this topic.

Summary

In this review, photochromism, its history, and recent research development especially in fiber and textile areas have been described. Different photochromic compounds and their properties have also been discussed. The state-of-the-art techniques for applying photochromic compounds to fibers and fabrics and their optical properties and potential applications have been summarized.

References

1. Dürr H, Bouas-Laurent H (2003) Photochromism: molecules and systems. Elsevier: Amsterdam, The Netherlands
2. Crano JC, Guglielmetti RJ (2002) Organic photochromic and thermochromic compounds. Dordrecht: Kluwer Academic Publishers
3. Brown GH (1971) Photochromism. Wiley-Interscience, New York
4. Corns SN, Partington SM, Towns AD (2009) Industrial organic photochromic dyes. Color Technol 125(5):249–261
5. Matsuda K, Irie M (2004) Diarylethene as a photoswitching unit. J Photochem Photobiol C 5(2):169–182
6. Pardo R, Zayat M, Levy D (2011) Photochromic organic-inorganic hybrid materials. Chem Soc Rev 40(2):672–687
7. Patel PD, Mikhailov IA, Masunov AE (2009) Prediction of thermal stability of photochromic materials used for optical switching and data storage applications. In: International conference on computational science, Louisiana
8. Gemert BV, Kumar A, Knowles DB (1997) Naphthopyrans. Structural features and photochromic properties. Mol Cryst Liq Cryst Sci Technol Sect A Mol Cryst Liq Cryst 297(1): 131–138
9. Irie M (2000) Diarylethenes for memories and switches. Chem Rev 100(5):1685–1716
10. Liu X, Pu S, Zhao F, Luo S, Zhang F (2005) Rewritable volume holographic optical storage on pmma film of diarylethene. In Proceedings of SPIE – The International Society for Optical Engineering
11. Yokoyama Y (2000) Fulgides for memories and switches. Chem Rev 100(5):1717–1740
12. Perkins WS (1991) A review of textile dyeing processes. Dyeing Process 23(8):23–27
13. Shah PH, Patel RG, Patel VS (1985) Azodisperse dyes with photochromic mercury(ii)-dithizonate moiety for dyeing polyester, nylon and cellulose triacetate fibres. Indian J Text Res 10(4):179–182
14. Lee S-J, Son Y-A, Suh H-J, Lee D-N, Kim S-H (2006) Preliminary exhaustion studies of spiroxazine dyes on polyamide fibers and their photochromic properties. Dyes Pigments 69(1–2):18–21
15. Billah SMR, Christie RM, Shamey R (2008) Direct coloration of textiles with photochromic dyes. Part 1: application of spiroindolinonaphthoxazines as disperse dyes to polyester, nylon and acrylic fabrics. Color Technol 124(4):223–228
16. Billah SMR, Christie RM, Shamey R (2012) Direct coloration of textiles with photochromic dyes. Part 3: dyeing of wool with photochromic acid dyes. Color Technol 128(6):488–492
17. Aldib M, Christie RM (2011) Textile applications of photochromic dyes. Part 4: application of commercial photochromic dyes as disperse dyes to polyester by exhaust dyeing. Color Technol 127(5):282–287
18. Kozicki M, Sąsiadek E (2012) Uv-assisted screen-printing of flat textiles. Color Technol 128(4):251–260
19. Little AF, Christie RM (2010) Textile applications of photochromic dyes. Part 2: factors affecting the photocoloration of textiles screen-printed with commercial photochromic dyes. Color Technol 126(3):164–170
20. Feczkó T, Samu K, Wenzel K, Neral B, Voncina B (2012) Textiles screen-printed with photochromic ethyl cellulose–spirooxazine composite nanoparticles. Color Technol 129(1): 18–23
21. Unknown (2005) Microencapsulation: for enhanced textile performance. Perform Appar Mark (12): 21
22. Scherer GW (2006) Sol–gel technology. Surfactant science series
23. Dunn B, Zink JI (2007) Sol-gel chemistry and materials. Acc Chem Res 40(9):729–729
24. Cheng T, Lin T, Fang J, Brady R (2007) Photochromic wool fabrics from a hybrid silica coating. Text Res J 77(12):923–928

25. Cheng T, Lin T, Brady R, Wang X (2008) Photochromic fabrics with improved durability and photochromic performance. Fiber Polym 9(5):521–526
26. Cheng T, Lin T, Brady R, Wang X (2008) Fast response photochromic textiles from hybrid silica surface coating. Fiber Polym 9(3):301–306
27. Cheng T (2008) Photochromic wool fabric by sol-gel coating. In Centre for Material and Fibre Innovation of the Institute for Technology Research and Innovation, Deakin University, Geelong, pp 164
28. Doshi J, Reneker DH (1995) Electrospinning process and applications of electrospun fibers. J Electrost 35(2–3):151–160
29. De Sousa FB, Guerreiro JDT, Ma M, Anderson DG, Drum CL, Sinisterra RD, Langer R (2010) Photo-response behavior of electrospun nanofibers based on spiropyran-cyclodextrin modified polymer. J Mater Chem 20(44):9910–9917
30. Bianco A, Iardino G, Manuelli A, Bertarelli C, Zerbi G (2007) Strong orientation of polymer chains and small photochromic molecules in polyamide 6 electrospun fibers. Chem Phys Chem 8(4):510–514
31. Kim C, Yoon UY, Jung YI (2007) Method for manufacturing photochromic nanofiber non-woven fabric, pp 13
32. Di Benedetto F, Mele E, Camposeo A, Athanassiou A, Cingolani R, Pisignano D (2008) Photoswitchable organic nanofibers. Adv Mater 20(2):314–318
33. Wang M, Vail SA, Keirstead AE, Marquez M, Gust D, Garcia AA (2009) Preparation of photochromic poly(vinylidene fluoride-co-hexafluoropropylene) fibers by electrospinning. Polymer 50(16):3974–3980
34. Billah SMR, Christie RM, Morgan KM (2008) Direct coloration of textiles with photochromic dyes. Part 2: the effect of solvents on the colour change of photochromic textiles. Color Technol 124(4):229–233
35. Parhizkar M, Zhao Y, Wang X, Lin T (2014) Photostability and durability properties of photochromic organosilica coating on fabric. J Eng Fibers Fabr 9(3)
36. Malatesta V, Renzi F, Wis ML, Montanari L, Milosa M, Scotti D (1995) Reductive degradation of photochromic spiro-oxazines. Reaction of the merocyanine forms with free radicals. J Org Chem 60:5446–5448, Copyright (C) 2011 American Chemical Society (ACS). All Rights Reserved
37. Malatesta V, Milosa M, Millini R, Lanzini L, Bortolus P, Monti S (1994) Oxidative degradation of organic photochromes. Mol Cryst Liq Cryst Sci Technol Sect A Mol Cryst Liq Cryst 246(1):303–310
38. Guillory JP, Cook CF (1973) Energy transfer processes involving ultraviolet stabilizers. Quenching of excited states of ketones. J Am Chem Soc 95(15):4885–4891
39. Andrei C, Andrei G, Moraru M, Moise G (1999) New metal chelates for the photostabilisation of polyolefins. Polym Degrad Stab 64(1):165–171
40. Misura MS (1997) Photochromic naphthopyran-based compositions with improved light fatigue resistance. pp 45
41. Mennig M, Fries K, Lindenstruth M, Schmidt H (1999) Development of fast switching photochromic coatings on transparent plastics and glass. Thin Solid Films 351(1–2):230–234
42. Ohkatsu Y, Baba R, Watanabe K (2011) Radical scavenging mechanism of distearyl hydroxylamine antioxidant. J Jpn Pet Inst 54(1):15–21
43. Paterson MJ, Robb MA, Blancafort L, DeBellis AD (2004) Theoretical study of benzotriazole uv photostability: ultrafast deactivation through coupled proton and electron transfer triggered by a charge-transfer state. J Am Chem Soc 126(9):2912–2922
44. Baughman BM, Stennett E, Lipner RE, Rudawsky AC, Schmidtke SJ (2009) Structural and spectroscopic studies of the photophysical properties of benzophenone derivatives. J Phys Chem A 113(28):8011–8019
45. Little AF, Christie RM (2011) Textile applications of photochromic dyes. Part 3: factors affecting the technical performance of textiles screen-printed with commercial photochromic dyes. Color Technol 127(5):275–281

46. Guglielmi M, Brusatin G, Giustina GD (2007) Hybrid glass-like films through sol–gel techniques. J Non-Cryst Solids 353:1681–1687
47. Sánchez JC (2005) Intelligent textiles [Textiles de uso tecnico]. Rev Ind Text 432:52–63
48. Joshi HD, Joshi DH, Patel MG (2013) Application of 'smart colorants' to different substrated and study of their colour changing properties. Int Dyer 198(3):39–44
49. Minoshima Y, Osada M (1986) Photochromic fibers for papers. pp 2
50. Wright P (1989) Nonwoven fabrics for security sheets. pp 5
51. Du W, Su Q (2011) Photochromic fabric of wo3 and its anti-uv properties. Adv Mater Res 156–157:1301–1304
52. Vikova M (2003) Textile photochromic sensors for protective textile. Vlanka a textil 10(2): 82–85

Shape Memory Fibers

8

Jinlian Hu and Jing Lu

Contents

Introduction 184
Conventional Shape Memory Fiber 184
Shape Memory Polymers (SMPs), Structure and Synthesis for Fiber Spinning 184
Mechanical Property of Shape Memory Fiber 187
Shape Memory Property and Evaluation 191
Differential Shape Memory Fiber 192
Hollow Shape Memory Fiber 193
Shape Memory Fiber with Nanofillers 194
Liquid Crystal Shape Memory Fibers 197
Nanoscale Shape Memory Fiber 198
Advantages of Nanoscale Shape Memory Fiber 198
Functional Nanoscale Shape Memory Fiber 199
Application of Shape Memory Fiber 200
Textile Application of Shape Memory Fiber 200
Applications in Engineering 203
Summary and Future Trends of Shape Memory Fiber 204
References 205

Abstract

This chapter writes up from the shape memory polymer (SMP) to the conventional shape memory polymer fiber (SMPF) by common spinning method like melt-spun, wet-spun, and dry-spun method. Mechanical properties of the fibers spun by different method will be introduced. Comparisons among shape memory fiber, spandex, and other common fibers will be stressed; then is introduction of shape memory property, stimulus, posttreatment, and evaluation method of shape memory fiber. The application in textiles will include textile processing

J. Hu (✉) • J. Lu
Institute of Textiles and Clothing, The Hong Kong Polytechnic University, Hung Hom, Hong Kong
e-mail: jin-lian.hu@polyu.edu.hk; jing.lu@polyu.edu.hk

© Springer Science+Business Media Singapore 2015

X. Tao (ed.), *Handbook of Smart Textiles*,
DOI 10.1007/978-981-4451-45-1_3

ability of the fiber and how to combine shape memory functions into textiles. In differential shape memory fiber part, hollow fiber and conductive fiber will be introduced and its potential applications. Nanoscale shape memory fiber or nonwoven will be as an independent part for its novel properties of quick response, multifunction, etc. because of the nanoscale.

Keywords

Shape memory fiber • Melt spinning • Wet spinning • Dry spinning • Electronic spinning • Differential shape memory fiber • Mechanical properties • Shape memory fiber for textiles • Self-healing • Biomedical textiles • Posttreatment

Introduction

Shape memory polymers can be processed in fiber form. Several methods, i.e., wet-spun [1], melt-spun [2], dry-spun, reaction [3], and electrospun [4], are employed for their production to fiber form as other synthetic fiber does. In addition, shape memory polymer profile fibers such as hollow fibers were also achieved by melt spinning process [5]. Besides thermal-sensitive fibers, one could also develop electro-responsive shape memory fibers by incorporating CNTs in the structure as reported by Hu et al. [6].

In comparison with other forms of smart polymers, fibers exhibit higher molecular orientation with lower shape fixity, higher shape recovery, and higher recovery stress due to stress-induced orientation during their production. Shape memory polymer fibers (SMPFs) in fibrous form allow one to design and control its mechanical and shape memory properties like elongation, switch temperature, shape fixity, shape recovery, etc. SMPFs with little elongation are suitable to core-spun yarn and used in weaving. SMPFs with large elongation and elasticity have good knitting ability like spandex and can be made to elastic core-spun yarn and cover yarn. SMPFs can be knitted directly or with other common fiber and yarn such as cotton, polyester, and nylon. It is now known that shape fixity and shape recovery can be designed from above 95 % to 20 %. It is also possible to obtain required transition temperature for the specific applications based on various recipes. Because of the easy process ability, soft handle, and better compatibility, the present form of SMPF is most preferred for textile applications and some engineering applications compared to shape memory alloys (SMAs), shape memory foam, and shape memory film.

Conventional Shape Memory Fiber

Shape Memory Polymers (SMPs), Structure and Synthesis for Fiber Spinning

Shape memory behavior is exploited and displayed in various polymer systems with significantly different molecular structure and morphology. The conventional SMP systems include cross-linked PE, PE/nylon6 graft copolymers, trans-polyisoprene (TPI),

cross-linked ethylenevinyl acetate copolymer, styrene-based polymers, acrylate-based polymers, polynorbornene, cross-linked polycyclooctene, epoxy-based polymers, thiol-ene-based polymers, segmented polyurethane (PU), and segmented PU ionomers. Furthermore, some new biopolymers, such as poly (3-hydroxyalkanoate)s (PHAs), copolymers composed of dodecanedioic acid or sebacic acid monomers, and bile acid-based polyester, have been developed to show shape memory effect (SME), but their shape memory or mechanical properties are not highly desirable and need further optimization [7].

SMPs have been reported to be thermal-induced, light-induced, electro-active, water/moisture/solvent induced, pH sensitive, and magnetic sensitive based on their external stimulus. Ratna and Karger-Kocsis [8] and Liu et al. [9] classified SMPs into physically cross-linked and chemically cross-linked SMPs according to the nature of their net points. Even biodegradable SMPs are regarded as a special type of shape memory polymer [8]. SMPs are sometimes subdivided on the basis of their switch type into either Tg-type SMPs with an amorphous phase or Tm-type SMPs with a crystalline phase [8]. However, Behl and Lendlein [10] used actively moving polymers to divide them into shape memory and shape-changing polymers. These classifications may not be uniformly accepted on account of the partial showing of the principle of shape memory polymers.

Shape memory polyurethanes (SMPUs) are a class of SMPs containing urethane groups (-NHCOO-) in the molecules. Although, different SMP networks based on polyolefins, polystyrene, polysiloxanes, and polymethacrylates have been successfully synthesized for many applications, but the most successfully marketed SMPs are based on PUs, i.e., SMPUs. The SMPUs are found to be more suitable for both academic and industrial fields due to following facts: (1) a wide range of raw materials and easily available; (2) easily manufactured in the lab with mild reaction conditions; (3) processed by conventional methods, e.g., molding, casting, melt extrusion, melt injection etc., to obtain different shapes, and also they can be made as thermoplastic or thermoset materials; (4) broad spectrum for structural designs, easy to obtain different varieties of PUs with varying morphologies, structures, and rigidities by selecting different raw materials and molecular weights; (5) excellent physical and chemical properties; (6) flexibility to modify structure by incorporating organic or inorganic units, i.e., silicone, carbon nanotube, acrylate, epoxy components, etc.

The basic requirement for making SMPs is a two-phase heterogeneous structure including hard and soft segments. The SMPUs are basically synthesized from isocyanates, chain extenders, and polyol components by step-growth polymerization. The hard segments contain urethane segments formed by the reaction of diisocyanate with either diols or diamines, while long-chain polyester or polyether glycols behave like soft segments. Both segments differ significantly in molecular polarity and exhibit incompatibility to finally form a two-phase heterogeneous structure and morphology. This micro-phase separation is the essential requirement for the shape memory properties. One can control the micro-phase separation and hence the SMEs of SMPUs by using different raw materials, choosing different molecular weights of monomers, and changing reaction procedures. Because of the

advantages of SMPUs listed above, it has become the main polymer for shape memory polymer fiber development.

SMPUs are produced by commonly used polymerization methods, i.e., solution or bulk. Solution technique uses solvent for the dissolution of raw materials and provides ease in controlling the reaction. However, it is not commercially successful and mostly used for laboratory purposes due to high cost and associated inconvenience and pollution of using solvents [11]. In contrast, bulk polymerization uses solvent free paths and hence is more suitable for industrialization production. Both methods require special attention for the loading sequence of the raw materials which can be specifically categorized as one-step and two-step methods. In one-step method, all of the raw materials including isocyanates, chain extenders, polyols, and other additives are mixed at the same time. One-step method is usually used where the reaction speed is very fast. The most important key to one-step methods is the high efficient mixing since the mixing time is very limited before the reaction begins. The advantage of one-step methods is the convenience and simplicity of the producing process. The disadvantage may be the complicated and unpredictable molecular structure, phase separation, and morphology of the final polyurethane products since the isocyanate reacts with polyols and chain extenders in an "uncontrollable" way. The other synthesis method, i.e., two-step method, is also called prepolymer method and involves two steps for the preparation. In the first step, isocyanate is reacted with polyols in a mole ratio of 2:1 to form isocyanate terminated prepolymer. Then the prepolymer is reacted with chain extenders to form high molecular weight polyurethanes. In some cases, the molar ratio of the isocyanates to polyols exceed 2:1; thus, free isocyanates exist in the prepolymer. In this case, it is also called quasi-prepolymer. In two-step methods, the viscosity of the prepolymer is very critical, since it influences the mixing efficiency with chain extenders, although in solution synthesis, a solvent can be added to dilute the prepolymers.

Shape memory polymer fibers are mainly spun by common SMPUs, but the spin ability of some new emerging SMPUs or SMPU composite are being investigated. Compared to conventional SMPUs, which contain urethane hard segments and polyether/polyester soft segments, those emerging SMPUs have functional components in their structures, such as biodegradable hard segments [12]; inorganic units [13]; β-sheet crystals constitute hard segments, i.e., polyalanine segments [14]; photosensitive units [15]; and supramolecular units [16]. Shape memory polyurethane for wet spinning is usually synthesized using 4,4_-diphenylmethane diisocyanate (MDI) and isophorone diisocyanate (IPDI) as hard segment and poly (ethylene adipate) glycol 600(PEA 600), polycaprolactone diol (PCL)-4000, poly (buthyleneadipate), polycaprolactone diol (PCL)-2000, and poly(tetramethylene adipate) (PTMA, Mw = 2,000). The chain extender is 1,4-butanediol(BDO) as soft segments. Hard-segment contents are designed as 40/50/55/60/66. *N*,*N*_ dimethyl formamide (DMF) and DMAC are frequently used as solvent. The shape memory polyurethane solution with 25–29 % solid content and 380–490 cP viscosity show good wet spinning ability. For melt spinning, PCL-4000 poly(tetramethylene adipate) and PTMA(Mw = 2,000) and isophorone diisocyanate (IPDI) are often

Table 1 Conventional SMPUs with T_{trans}

Hard domain	Soft domain	$T_{s\ witch}$ (°C)	Synthesis method
MDI/1,4-BD	PTMG	$T_g = -13$ to 54	Two-step
MDI/EDA	PTMG	$T_g = 15$ to 25	Bulk polymer
MDI/1,4-BD	PEA	$T_g = 50$ to 60	Two-step/solution and polymer
MDI/1,4-BD	PBA	$T_g = 29$ to 64	Two-step/solution and polymer
MDI/1,4-BD	PCL	$T_m = 43$ to 49	Two-step/solution and polymer
MDI/1,4-BD/BINA	PCL	$T_m = 45$ to 50	Two-step/solution and polymer
Poly(p-dioxanone)	PCL	$T_m = 40$	Solution and polymer
HDI/DHBP	PCL	$T_m = 38$ to 59	Two-step/solution polymer

used as soft segment and hard segment separately. 1,4-Butanediol (BDO) is also as the chain extender. Table 1 lists the range of T_{trans} for some of the conventional SMPUs having different hard and soft segments.

Mechanical Property of Shape Memory Fiber

Compared with other synthetic fibers, particularly elastic fibers, shape memory fibers (SMFs) are unique due to their elastic modulus changing within a specified utilization temperature range and exhibit recovery ability with external stimulus. Shape memory polyurethane can be processed by wet-spun, melt-spun, dry-spun, and electrospun method to fiber form as polyurethane does. The fiber diameter is from millimeter to micrometer and nanometer. Novel structure SMPU fiber like hollow fiber was also developed by melt-spun to give a thermal-sensitive internal diameter. Nowadays, the reported shape memory polyurethane fibers are all thermal-responsive fibers.

Shape memory polyurethane fiber exhibits some distinct properties from polyurethane fiber except shape memory property. The elongation, switch temperature, shape fixity, and shape recovery can be designed and controlled by synthesis. The elongation of shape memory polyurethane ranges from dozens of percentage to above 500 %. Figure 1 exhibits the development process of shape memory polyurethane fibers from small elongation and little elasticity to large elongation and elasticity.

Shape memory fiber has more molecular orientation and hard-segment microdomains than in shape memory polymer. So shape memory fiber exhibits high tenacity. The recovery stresses of shape memory fibers are higher than those of the shape memory polymer. Figure 2 shows the appearances of wet-spun shape memory polyurethane fibers. The cross section of wet-spun SMP fibers is oval and rough along the longitudinal direction because of the solvent diffusion.

Tenacity of wet-spun SMF is a little lower than that of polyurethane elastic fibers, but it also can achieve higher tenacity under high drawing ratio. Figure 2 compares the stress–strain curves of shape memory fibers and other fibers. The elongation at break of the SMF is much lower than that of polyurethane fibers.

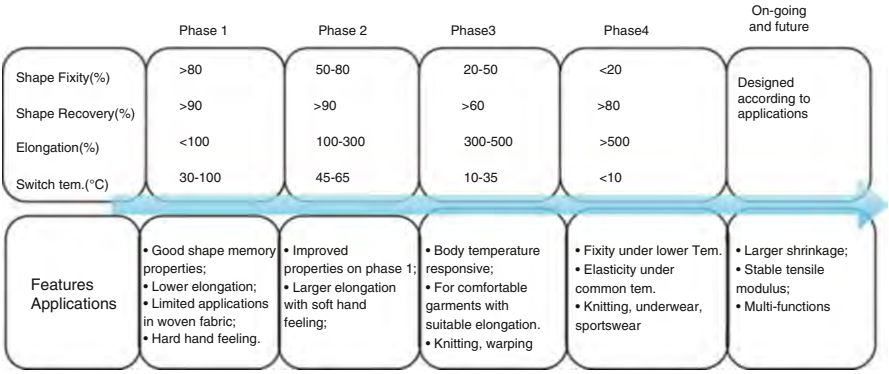

Fig. 1 Development of shape memory polyurethane fibers

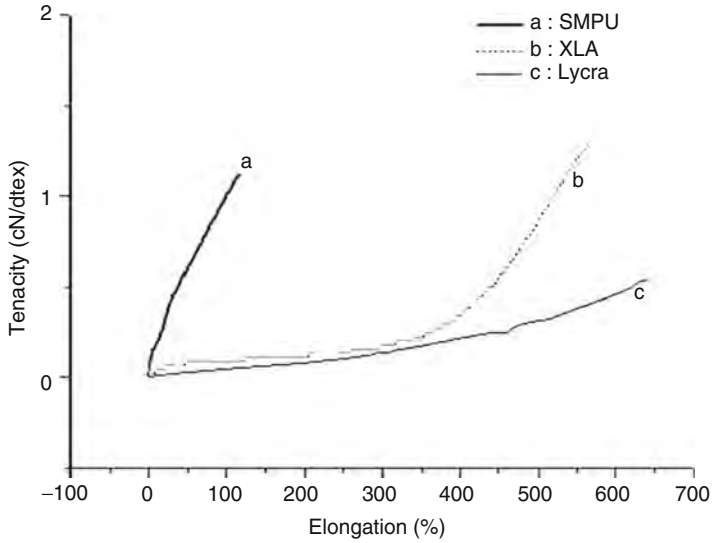

Fig. 2 Stress–strain curves of SMPU fiber, XLA, and Lycra [17]

The difference in mechanical properties between the commercialized elastic fibers and wet-spun shape memory polyurethane fiber has many proposed reasons. Polyurethane elastic fibers have high cohesion energy that enhances both high phase separation and hard-segment stability. The high elongation ratio of polyurethane fibers at break is due to the high molecular weight soft segment phase. The soft segments of the fibers from polyurethane elastic fiber are highly flexible and can be more easily extended to reach their full elongations, whereas the hard segment in the SMF is partially crystallized and more difficult to stretch to reach their full lengths. The elongation of the non-crystallized soft segment phase is restricted by the crystallized soft segment phase. For this reason, wet-spun SMF has lower

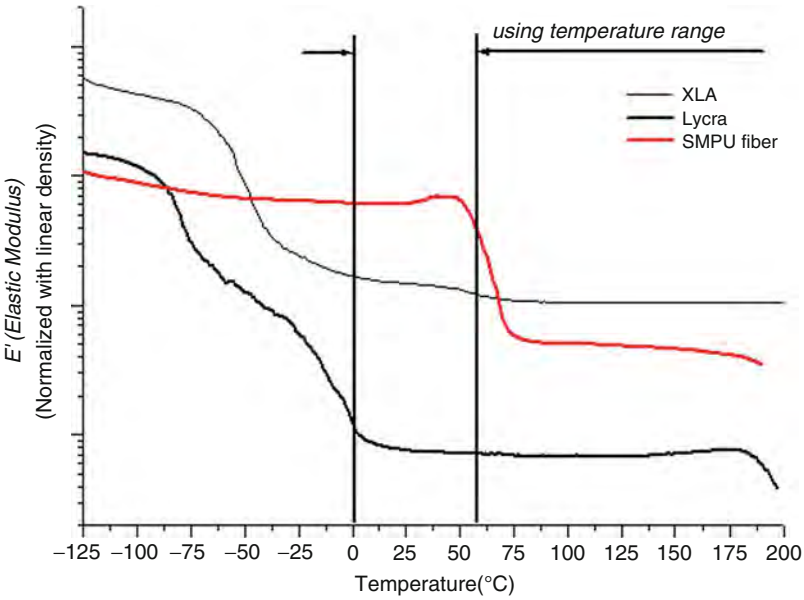

Fig. 3 Dynamic mechanical analysis (DMA) curves of SMPU fiber, XLA, and Lycra [17]

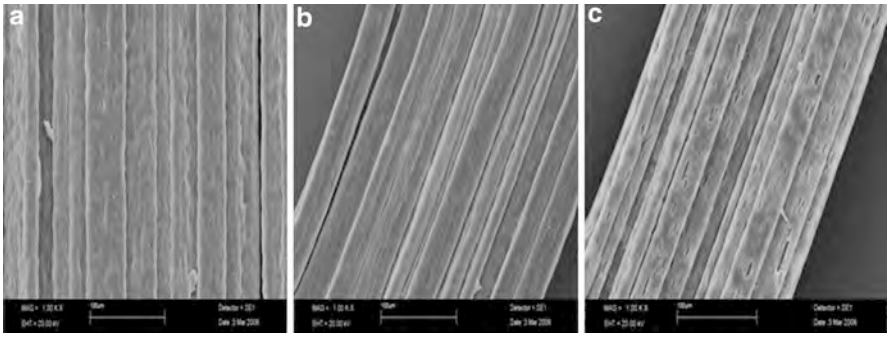

Fig. 4 Scanning electron microscope (SEM) of wet spinning SMPU fibers under. (**a**) Decreasing draw ratio. (**b**) Even draw ratio. (**c**) Increasing draw ratio

elongation ratio at break even though a higher molecular weight soft segment is adopted. Besides, many other important factors may increase the observed difference in mechanical properties between different fibers from different sources.

Figure 3 shows the modulus change with increasing temperature, which exhibits that the shape memory polymer fiber have better temperature response property than spandex, nylon, and XLA (olefinic-based fiber) [17].

The molecular orientation, recovery stress, hard-segment micro-domains, and posttreatments are the main influencing factors to the mechanical properties of wet-spun shape memory polyurethane fiber [17]. Figure 4 compares the

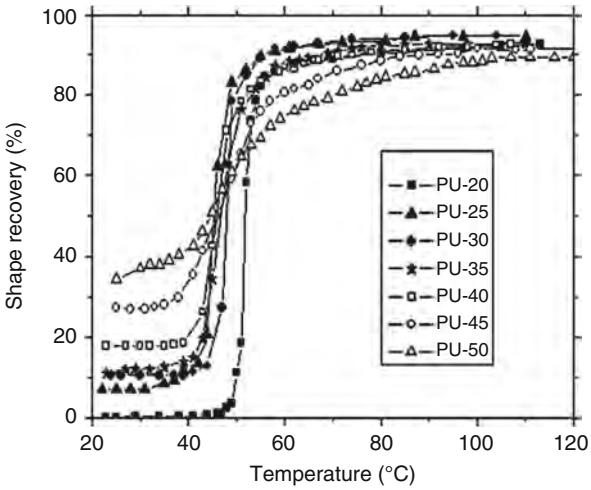

Fig. 5 Shape recovery of different recipes of SMPU [21]

appearances of wet-spun shape memory polyurethane fiber under different drawing distribution. Figure 5 shows the longitudinal views of three samples in wet spinning with various drawing distribution in four drawing zones, but the total drawing ratio is the same. Figure 4a is the fiber under decrease draft ratio distribution. Figure 4b is the fiber under even draft ratio distribution. Fig. 4c is the fiber under increase draft ratio distribution and Fig. 4c displays some cracks on the surface of the fibers. It may result from the overdrawing. Figure 4a shows rough surface because of the heat shrinkage during forming. The fiber under even draft ratio distribution exhibits smooth surface and has a good form.

Posttreatment has large effects on shape memory polyurethane fiber properties. The hard-segment crystallization of SMPU fibers could be induced and the glass transition temperature was lowered, especially for specimens with high hard-segment contents after the high-pressure steaming process. Subsequently, the maximum strain was increased, and the thermal shrinkage could be eliminated significantly with various hard-segment contents steaming. The treated SMPU fibers possess better thermal responsive shape recovery ability with applicable dimensional stability. The SMPU fibers with low hard-segment content acted as the similar elastic recovery behavior to traditional elastic fibers.

For SMF with lower hard segment (55 %), with the increasing of thermal treatment temperature, the modulus ratio of temperatures below and above the transition point is increased significantly and the transition point decreases; for SMP fibers with higher hard segment (66 %), elastic moduli between temperatures below and above the transition point all decrease a little and the transition points are nearly unchanged. The maximum strain increased and the thermal shrinkage could be eliminated significantly with various hard-segment contents steaming [18].

Melt-spun shape memory polyurethane fiber should have high thermal stability and relatively high molecular weight to obtain better mechanical properties than that of wet-spun SMP fibers.

The mechanical properties of melt spinning shape memory polymer fiber can be comparable to that of polyurethane elastic fibers with a tenacity of about 1.0 cN/dtex and breaking strain of 562–660 %. Soft-segment phases of the melt-spun SMP fibers have higher crystallinity, perfect crystallinity, and melting transition temperatures in comparison with those of wet-spun SMFs.

The melting enthalpy of the soft-segment phase of the melt-spun SMP fibers is also large which suggests that more ordered molecular packaging was obtained in the melt-spun SMP fibers. In contrast, the hard segments of wet-spun SMP fibers are mostly dissolved in the soft-segment phases, so the melting transition peaks do not appear in the DSC curves [19].

Melt-spun SMP fibers have a higher degree of phase separation and hard-segment phase stability. During stretch, strong, stable hard phase makes the tenacity of melt-spun SMP fibers higher than that of wet-spun SMP fibers. The high tensile ability is due to the high molecular weight of the soft segment [19]. In the melt-spun SMP fibers, the relatively "pure" soft segments are more readily and heavily stretched during elongation. As a result, the melt-spun SMP fibers have a higher breaking elongation. The melt-spun SMP fibers also have higher recovery ratios and fixity ratios than those of the wet-spun SMFs. The stresses at 100 % strain of the melt-spun SMFs are also a little higher compared to those of the wet-spun SMP fibers.

Shape Memory Property and Evaluation

Depending on different recipes and synthesis route, SMPU fibers show optional shape memory effects from quick shape recovery to progressive recovery as shown in Fig. 5 [20]. In general, the SMPU fiber with good shape fixity and shape recovery effect has shorter breaking elongation and larger modulus than the fiber with less shape fixity. Shape memory fiber has more molecular orientation and hard-segment micro-domains than in shape memory polymer. So shape memory fiber exhibits lower shape fixity and higher shape recovery property than shape memory polymer. The recovery stresses of shape memory fibers are higher than those of the shape memory polymer [21] (Fig. 6).

Besides the chemical structure, the shape memory property of SMP fibers also is affected by spinning methods and posttreatments.

Posttreatment has large effects on the structure of shape memory polyurethane fibers. The hard-segment crystallization of SMPU fibers can be induced and the glass transition temperature reduced, particularly for specimens with high hard-segment contents after the high-pressure steaming process. The treated SMPU fibers possess better thermal responsive shape recovery ability with applicable dimensional stability. The SMPU fibers with low hard-segment content exhibited the similar elastic recovery behavior to traditional elastic fibers. According to the mechanism of shape memory effect for segmented copolymers with *T*m of the soft-segment phase as the switching transition temperature, the high crystallinity of the soft-segment phase and the formation of a stable hard-segment phase are the two prerequisites for good shape memory effects [22].

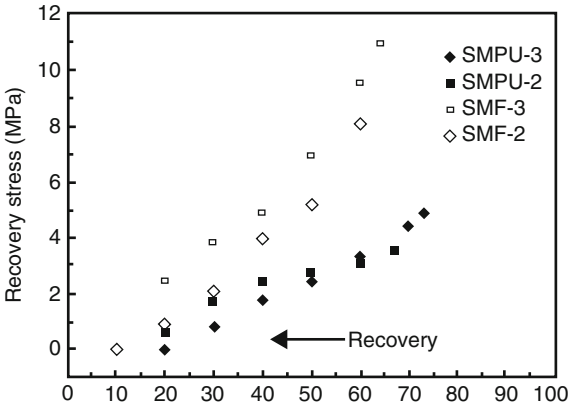

Fig. 6 Comparison of recovery stress of SMPU fiber and SMPU film [21]

With increasing heat-treatment temperature, shape recovery ratios and fixity ratios increase too. In polyurethane bulk systems, soft segment phase is in charge of the shape fixity by freezing polyurethane molecules after being cooled down below switching transition temperature, and the hard-segment phase acting as physical cross-linking takes charges of shape recovery by releasing the stress stored during deformation. But for SMP fibers, which have molecular orientation and internal stress caused by melt spinning, the fiber will shrink on account of the stress released and molecule disorientation. Therefore, after heat treatment, the recovery ratios decrease and fixity ratios increase. With increasing heat-treatment temperature, the soft-segment phase crystallinity and phase separation perfect and increase. The stability of hard-segment phase improved particularly after the heat treatment above 125 °C, and for this reason, the soft segment has more capacity to freeze the polyurethane molecules when the fiber is cooled below the switching transition temperature. In addition, a more stable hydrogen-bonded hard-segment network emerged after heat treatment, so that more deformation energy was stored in the hard-segment phase. Consequently the SMP fiber has more capability to recover to the original shape when heated above the switching transition temperature. As a whole, the shape fixity ratios and recovery ratios increase with increasing heat-treatment temperature (Fig. 7) [22].

Table 2 gives a summary of spinning condition and posttreatment effects on the mechanical properties and shape memory properties of SMPU fibers.

Differential Shape Memory Fiber

Besides the convention fibers, some kinds of versatile shape memory polymer fiber have been developed for multifunction and multi-stimulus. These differential shape memory polymer fibers were obtained by changing the size and structure of fibers,

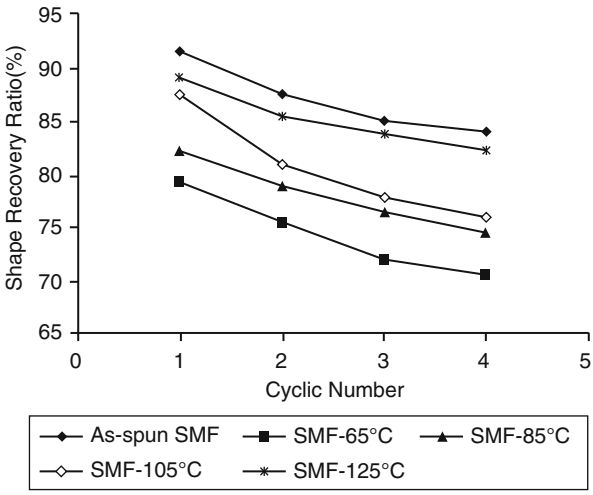

Fig. 7 Heat-treatment effects on shape recovery ratio [22]

Table 2 Spinning condition and posttreatment effects on properties of shape memory fibers

	Drawing ratio		Posttreatment
Properties	High	Low	High temperature or steaming
Appearance (wet-spun)	Cracks and holes	Rough	Rough
Tenacity	√	×	×
Elongation	×	√	√
Recovery stress	√	×	×
Shrinkage	√	×	×
Shape fixity	×	√	√
Shape recovery	√	×	√

Notes: √: Increase; ×: Reduce

adding functional additives or adopting special polymers with two-way shape memory property. The differential shape memory polymer fibers open up new development directions and applications.

Hollow Shape Memory Fiber

Shape memory polymer profiled fibers such as hollow fibers were prepared by melt spinning as shown in Fig. 8 [5]. The internal diameter of the hollow fiber can noticeably change and recover under thermal stimulation as a result of shape memory effect. The hollow fiber had a tenacity of about 1.14 cN/dtex and strain at break of 682 %. The shape fixity ratio was above 80 % and the recovery ratio above 90 %.

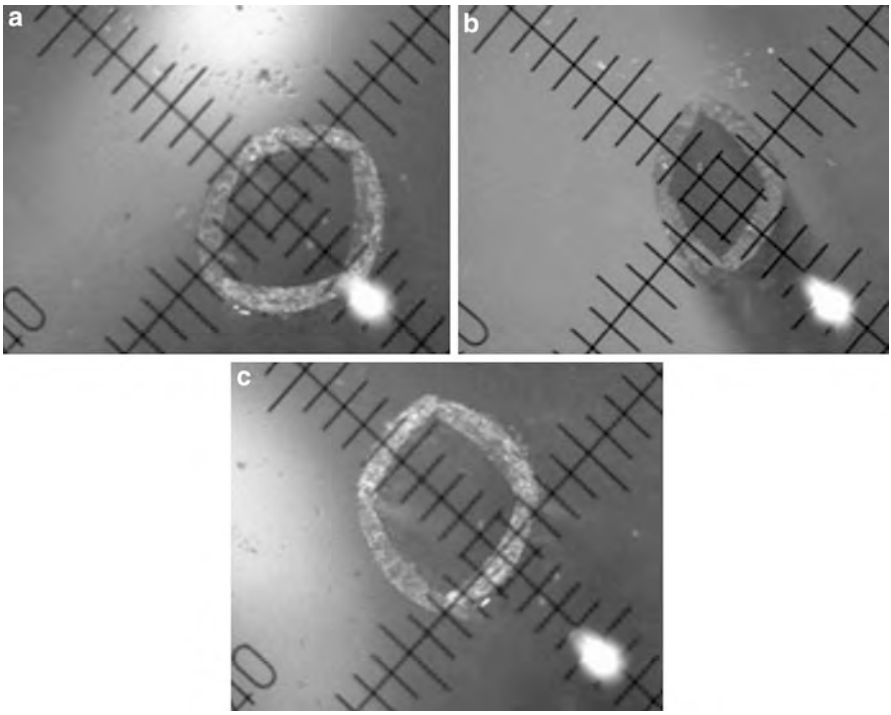

Fig. 8 Thermally adjustable internal holes of the TSHF (deformed by longitude stretching) (**a** original shape, **b** deformed shape, **c** recovered shape) [5]

Because the changes of the internal diameter of hollow fibers can affect the physical properties of textile products, smart SMPU hollow fibers can be used for thermal regulation garments or as stuffing in pillows and mattresses. Furthermore, this kind of hollow fibers has the potential application for smart filtration, drug-controlled release, and liquid transportation.

Shape Memory Fiber with Nanofillers

Carbon nanotube and nanoclay were reported as fillers added into shape memory polymer fibers by melt-spun method to acquire more functions. But adding of the nanofillers affects the performance of spinning, shape memory properties, mechanical properties, and other functions.

Montmorillonite(MMT) nanoclay and multi-walled carbon nanotube (MWNT) are generally used as nanofillers in shape memory polyurethane fibers. The objectives of introducing nanofillers are to improve recovery stress and tenacity. However, the spin ability of SMP–nanofillers decreased significantly with increasing nanofiller content. Because of increasing nanofiller content, the continuity of the polymer matrix is destroyed and the filter screens inside the spinneret are more

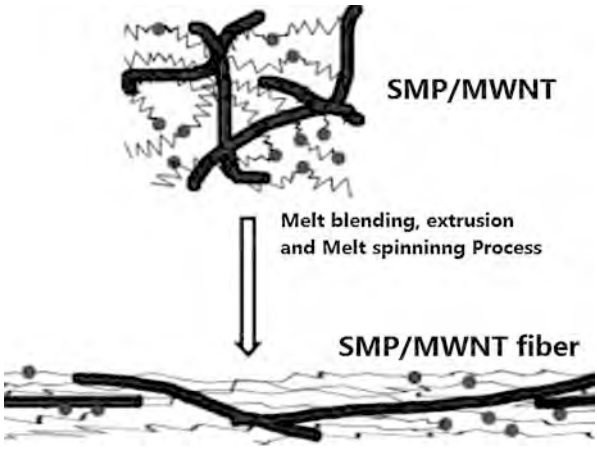

Fig. 9 Schematic representation of the MWNT alignment in SMP fibers after the melt extrusion and spinning process [24]

likely blocked due to nanofiller aggregate under high contents. The melt flow index decrease also reflects the spinning ability deterioration with increasing nanofiller contents. Different kinds of nanofiller exhibit different critical content which destroy the spinning performance and fiber performance. For example, the surface of the SMP–MWNT fiber becomes rough with increasing MWNT content. When the content increased from 3 to 5 wt%, the fiber surface becomes very coarse. When MWNT concentration is up to 5 wt%, MWNT aggregation is exposed on the fiber surface. When the MWNT content is increased to 8 wt%, the rheological property of the composite deteriorates completely. Thus, the fibers cannot be spun [6, 23, 24] (Fig. 9).

A certain amount of nanofillers can increase the tenacity property, melting the temperature because of a small number of nanofillers acting as nucleating agents that will enhance the crystallization process. So the melting temperature of the 1.0 wt% MWNT fiber is higher than that of the pure SMP fibers. The homogeneously distributed and axially aligned nanofiller endowed the fibers with high tenacity and initial modulus at low contents. However, when the content was high, the crystallization was hindered. At high MWNT contents, the aligned MWNTs aggregated and thus degraded the mechanical properties of the fiber.

It is suggested that a fiber having 1.0 wt% MWNT yields more oriented polymer chains and a more well-defined crystal structure. More MWNT contents as fillers become a physical constraint on the SMP molecules and thus lower the soft-segment mobility during crystallization. As a result, the degree of crystallinity and the melting temperature decrease. The tenacity of the SMP fibers with 1.0 wt% MWNT increases, but continuously increasing the MWNT content may degrade the physical properties of the fiber. The tenacity of the fiber has a maximum value at about 1.0 wt% MWNT. The breaking elongation and initial modulus of the SMP fibers exhibit decreasing and increasing trends, respectively, with increasing MWNT content.

The fibers with different MWNT contents have approximately the same shape fixity ratios. But the influence on the shape recovery ratio is great. As discussed

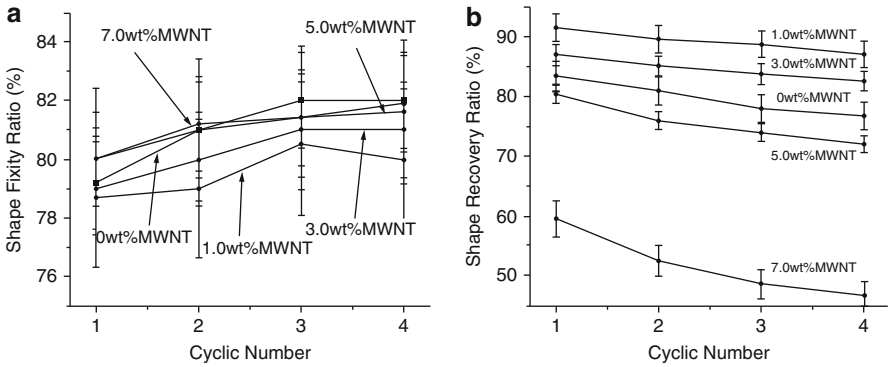

Fig. 10 Shape fixing (**a**) and shape recovery ratio (**b**) of SMP–MWNT fibers with different MWNT contents [6]

above, the recovery stress and recovery rate are mainly controlled by the hard-segment phase. In the SMP–MWNT system, the treated MWNTs, showing better interaction with the hard-segment phase, prevent the chain slippage of the polymer molecular chains. This indicates that the SMP–MWNT fiber is able to withstand higher stress at the same elongation, thus providing higher shape recovery force to the fiber. The recovery ratio of the SMP–MWNT fiber is higher at 1.0 and 3.0 wt% MWNT than that of the pure SMP fiber. However, at 7.0 wt% MWNT, the shape memory ratio is much lower than that of the pure SMF.

That is to say, the nanofillers, having better interactions with the shape memory polyurethane molecules, particularly with the hard-segment regions, help to store the internal stress during stretching and shape fixing. So the shape recovery ratio increases. However, when the nanofiller content is too high, the aggregated degrade the fiber shape recovery effect.

The homogeneously distributed nanofiller helped to improve the shape memory recovery ratio of the SMP fibers. In Meng's research, the MWNTs were distributed homogeneously and aligned axially in the fibers, especially at MWNT fractions below 5.0 wt%, by the in situ polymerization, melt blending, extrusion, and melt spinning and the recovery ratio increased from 83 % (pure SMP fiber) to 91 % (fiber with 1.0 wt% MWNT). The shape memory fixity ratio, on the other hand, was not changed significantly (Fig. 10).

However, even though the shape recovery ratio and the fixing ratio were low, the electro-active shape memory effect was observed in SMP–nanocarbon system.

In the SMP–MMT system, 1.0 wt% content of MMT nanoclay shows a sharp decrease in the enthalpy of melting and crystallization, inducing that the crystallinity of PUs was further reduced by the increased nuclei and limited spaces. The shape memory performance of the SMP–MMT fibers was not enhanced significantly. However, their recovery power was improved significantly up to a strain of approximately 50 % [25].

The dispersion property and contents of nanofillers in shape memory polymer matrix are key issues for the spinning ability, mechanical property, and shape

memory property of this kind of shape memory polymer fibers. For electro-active shape memory polymer fibers, the dispersion status such as continuity will affect the conductivity of the resultant fibers.

Liquid Crystal Shape Memory Fibers

Because of the high cost, low quantity manufacture, and low elongation, liquid crystal shape memory fiber has limited applications in the textile field, but its specific two-way shape memory property attracts more attentions. Their present investigation is limited only to Lab's exploration.

Liquid crystalline elastomers (LCEs) show a first-order phase transition with an endothermic peak on heating curves, which means the material's transition from an anisotropic to an isotropic phase. Currently, the LC phase that serves as the shape memory switch can be either a nematic phase or a smectic phase. Many types of LCEs, including main chain and side chain, have been designed and prepared for use in SMEs by introducing various LC monomers into the elastomers [26].

Main-chain smectic-C LCEs is designed by using 2 distinct mesogenic monomers to control the ratio of the 2 types of monomers. Apart from the thermally induced shape memory effects (SMEs), photo-induced SMEs, like photo-induced contraction or bending, have also been achieved using LCEs. In contrast to the LC monomers of thermally induced SMEs, the LC monomers of photo-induced SMEs usually contain photo-responsive moieties. Although the molecular mechanisms of light-induced LCEs and thermally induced shape memory LCEs are different, both of their SMEs result from the LC phase transition. Notably, most of the LCEs showed two-way SMEs [27, 28]. Moreover, liquid crystal shape memory polymer can be developed to show triple SMEs that memorize more than one shape.

Thermosensitivity two-way liquid crystal effects root in the coupling between the ordered mesogenic moieties and the elastic polymer part. When an LCE film is heated above the anisotropic–isotropic phase-transition temperature, the mesogens become disordered and the film contracts. When the temperature is reduced below the phase-transition temperature, the film will expand back to its original size. However, to observe the unique properties of LCEs on a macroscopic scale, the mesogens must be aligned uniformly over the whole sample to form the monodomain. But the monodomain restricts the application of two-way LCEs as smart materials. However, a glass-forming polydomain nematic network also exhibited quite a large two-way SME comparable with monodomain LCEs. This phenomenon was associated with a polydomain–monodomain transition at relatively low temperatures. Thus, the polydomain LCEs may offer an efficient and simple alternative to their monodomain counterparts because they do not require alignment procedures during processing.

LCEs containing azobenzene units are the most widely investigated photomechanical polymers for two-way light-sensitive SMEs [29, 30] in which the driving force for the deformation arises from the variation in the alignment order. A light-sensitive liquid crystal fiber [31] can repeatedly and precisely bend along any

chosen direction using linearly polarized light. The photoisomerization of azobenzene units at the cross-links has more pronounced effects than at the side chains [32]. A review concluded that LCEs are the most promising materials for constructing artificial muscles driven by light [33]. However, there are still many problems, such as fatigue resistance and the biocompatibility of LCEs, which need further investigation.

Most liquid crystal shape memory fibers are with low elongation. But currently, a maximum spontaneous elongation up to 500 % has been achieved in liquid crystal shape memory polymer fibers by Ahir et al. [34]. Such large elongation occurred because the ordered nematic and the cross-linked telechelic occurred simultaneously, resulting in a high degree of alignment and uniformity during the high shear of fiber drawing.

Moreover, electrospinning method was applied in the main-chain liquid crystal fiber spinning. In the resulting electrospun LCE nanofibers, the nematic phase becomes oriented along the fiber axis during electrospinning, and the nematic director is found to be oriented macroscopically, i.e., a monodomain fiber is formed [35]. These investigations reinforced the understanding of liquid crystal polymer from the film application field to fiber applications in the textile field. However, before liquid crystal fiber can become popular textile products, material scientists are urgently encouraged to modify the synthesis technology, decrease the cost, and improve the quantity of liquid crystal polymer.

Nanoscale Shape Memory Fiber

A porous structure and large surface area to volume ratio endow SMPs with better sensitivity, smart temperature, and moisture control. Although research into this area has just started to attract attention, the outcomes are very inspiring and encouraging. Because of the wide use of SMPs in medical and protective textile materials, such structures could potentially rival existing materials and devices.

Advantages of Nanoscale Shape Memory Fiber

Polymer nanofibers have been attractive materials for a wide range of applications because of their large surface area to volume ratio and the unique nanometer scale architecture built by them. Shape memory polymer nanofibers were successfully electrospun by different people [36–39]. The resulted fibers are with ultrafine diameter in a range of 50 nm to 2 μm. Uniform nanofibers could be prepared by adjusting applied voltage, concentration, and feeding rate, and particularly, the concentration played a key role in controlling its diameters. Good shape memory property of shape memory nanofibers was proofed by cyclic tensile testing with 98 % shape recovery and 80 % shape fixity [36].

Lower shape recovery temperature: The thermal properties of SMPU nanofibrous nonwoven are investigated systematically. Electrospinning process

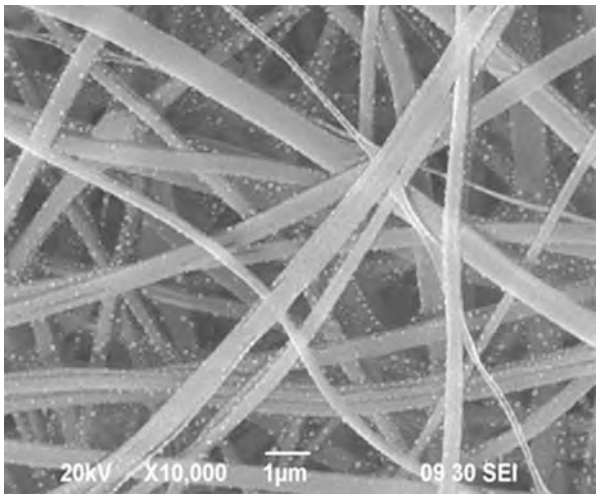

Fig. 11 SEM image of nanofiber nonwoven incorporated with antibacterial agent

has greatly influenced the shape memory polymer fiber property and recrystalline. Temperature-dependent strain recovery curves indicate that the SMPU nanofiber tends to have a lower recovery temperature as compared with the SMPU bulk film due to their ultrafine diameter [37]. Other related work has been reported by Cha et al. [38].

Quicker shape recovery: In many cases such as robotics, the materials should ideally exhibit large property changes in response to small stimuli, generate mechanical stress and strain in fast response to electric signals, and be easy to process. It would be desirable that material properties can be improved by the microstructures to enhance the shape recovery speed of SMPs without changing the chemical composite. Comparing to the bulk SMPU film, microfiber film afforded much quicker and sharper shape recovery when heated in water bath. The shape recovery of the microfiber film only took ~1/4 time of that needed for the bulk film from Rr (shape recovery ratio) = 10 % to Rr = 90 %. The final Rr and Rf (shape fix ratio) of the microfiber film were also enhanced. The quick shape recovery of the microfiber film is considered due to the higher surface area of microfiber film that is favorable for quicker heating/cooling of the sample and quicker diffusion of water. This study offers a possible way to improve the shape recovery speed without changing the chemical composition, which may meet special needs for sensors or actuators of biomedical devices and others (Fig. 11).

Functional Nanoscale Shape Memory Fiber

Functional nanoscale shape memory fibers have been researched in the directions of two-switch, novel structure and functional additives based on the nanoscale of fibers. The combination of multifunction and nanoscale not only enforces the functions but opens up new applications.

A quick response electroactuation fiber is one direction. The electroactuation of polymer microfibers was realized from an ethoxysilane derivative of redox active polyferrocenylmethylvinylsilane (PFMVS). In cases of low cross-link density, resultant fibers rapidly respond (<100 ms) to electrical stimuli applied either via an electrode or by titration with redox active compounds. Large strains occur within 10 ms when fibers are oxidized electrochemically on an electrode surface submerged in a supporting electrolyte. Such structures were predicted potentially rival existing bilayer actuators in strength but maintain rapid response times because of significantly larger surface area to volume ratios and smaller ion diffusion length [40].

The nanofibers with core-shell structure or bead-on-string structure can be electrospun successfully from the core solution of polycaprolactone-based SMPU (CLSMPU) and shell solution of pyridine-containing polyurethane (PySMPU). In addition, the excellent shape memory effect and excellent antibacterial activity against both gram-negative bacteria and gram-positive bacteria are achieved in the CLSMPU-PySMPU core-shell nanofiber. It is proposed that the antibacterial mechanism should result from the PySMPU shell materials containing amido group and the high surface area per unit mass of nanofibers. Thus, the core-shell nanofibers can be used as both shape memory and antibacterial nanomaterials [37].

A twin-switch with improved WVP nonwoven with nanofibers also was published. The SMPU nanofibrous nonwoven was found to have good liquid and water vapor transfer properties. Moreover, the WVP of the nonwoven is sensitive to the change of relative humidity (RH) and temperature (twin-switch). SEM images at a higher temperature suggest that the porous nanofibrous nonwoven structure is the foundation of unique WVP. The web having a high orientation due to an elongation in the process of the electrospinning showed the improved shape recovery and a good moisture and air permeability due to countless nano-sized pores. Therefore, it can be concluded that the SMPU web roved to have potential for intelligent clothing material [39] (Fig. 12).

Application of Shape Memory Fiber

Textile Application of Shape Memory Fiber

SMPU fiber/fabrics have been used for body fit garments [42]; biomedical areas such as wound dressing, orthodontics, scaffold material, etc. [43]; textile aesthetics [44]; and smart fabrics capable to provide unique properties like fire protection, waterproof, etc. [45]. Extensive research works have been done on the characterization and application of different SMPU fibers/fabrics [7]. SMP fibers have been made into yarns by different methods and applied in knitting – weaving for fabrics. Ring and friction spinning techniques have been used to make core-spun yarns. The application base of SMFs in textiles is the shape fixity and recovery along fiber lengthwise accompanied by stress changing.

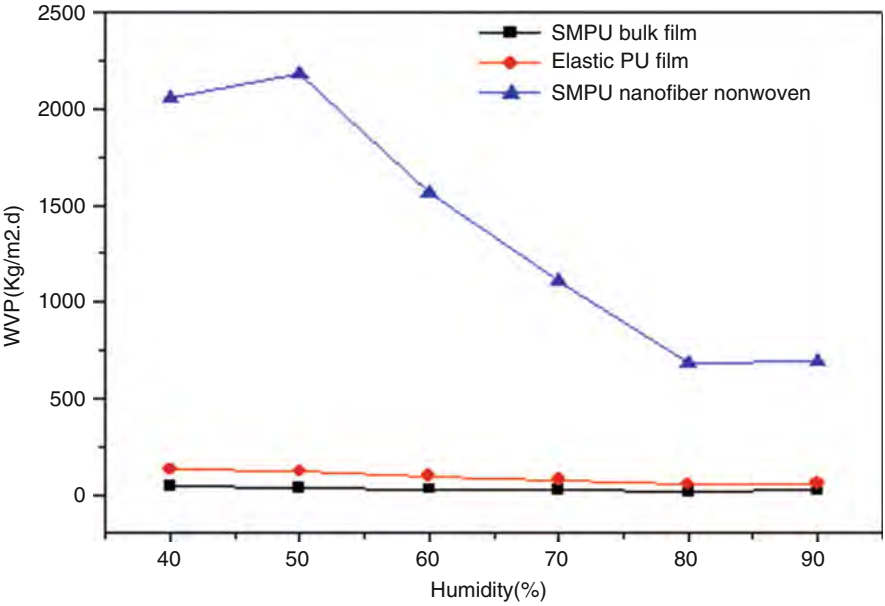

Fig. 12 The dependence of WVP of nanofiber nonwoven on humidity [41]

SMPU fibers via melt spinning have been applied for smart filtration, drug controlled release, and liquid transportation [5]. These SMPU fiber/fabrics showed their future potentiality for the application in biomedical areas such as artificial tendon, artificial cornea, hernia repair, artificial bone joints, orthodontics, scaffold material, and wound dressing [43]. Since the essential properties of protective clothing are high moisture vapor transport, increased fabric breathability, and enhanced toxic chemical resistance, electrospun SMP nanofiber membranes are good candidates for these applications. Moreover, SMPU-profiled fibers, nanoscale fibers such as core-shell nanostructure using coaxial electrospinning, have obtained excellent liquid transfer properties and antibacterial activity against both gram-negative bacteria and gram-positive bacteria [37]. The appearance of SMP nanofibers brings the research of SMPs into the application of nanometer scale. High orientation provides the SMP high mechanical properties and better shape-moving behavior. Large surface area to volume ratio endows the SMPs good sensitivity to heat and moisture.

Table 3 illustrates SMP textile applications. For high-pressure garments or accessories, the SMFs should have lower switch temperature around body temperature and excellent elasticity under using temperature and high shape fixity under lower temperature like in a refrigerator. For comfort garments and accessories, the SMFs should have extensive elongation which can be compatible to spandex but lower stress and shape fixity under body temperature. The products with thermal-wet control function use a particular bicomponent SMFs which can become curl

Table 3 Textile applications of shape memory polymer fiber

Items	Features of shape memory polymer fiber	Applications in common textiles	Applications in biomedical textiles
Comfortable apparels	Shape fixity and shape adjustability	Underwear with lower pressure	
		One size for all	
Comfortable socks and hosiery	Lower stress	Socks for baby	Diabetic socks
Elastic edge with constant pressure	Constant stress during a large strain range	Sock welt	
		Diaper edges	
Easy wear and easy down apparel	Shape fixity at low temperature and shape recovery under body temperature	Pressure sportswear	Varices treatment of socks
			Burn treatment pressure garments
Thermal regulation textiles	Fiber shape change under high and low temperature	Sportswear	–
Multifunctional fabrics	Multi-stimulus (heat or water or moisture or PH) and nanoscale structure	Mask	Antibiosis and cell and hemostasis communication wound dressing
			Artificial skin
			Drug deliver carrier
Other textiles	Good shape memory and shape recovery property	Self-tightening shoelace	Smart conduits for peripheral nerve regeneration
		Reinforce textile for shape memory composite	
		3D fabric design	

and straight with temperature or wet changing. For shape retention textiles, the SMFs should have high recovery stress for flat appearance or wrinkle recovery products and have high shape fixity for crease retention application.

SMFs for fashion design are a kind of special fibers with high shape fixity and shrinkage which could be combined with structure design to achieve obvious style change effect.

The key question of shape memory fabrics and garments is how to use and require the shape memory property and mechanical property of the shape memory fiber. Aiming at different textiles, the designer should raise the different requirements of shape memory fibers such as the fiber with higher or lower shape memory fixity, large or low elongation, modulus, liner density, etc. There still exist enormous challenges and opportunities for the applications of SMPUs, and this demand an extensive research to explore other application areas for the same.

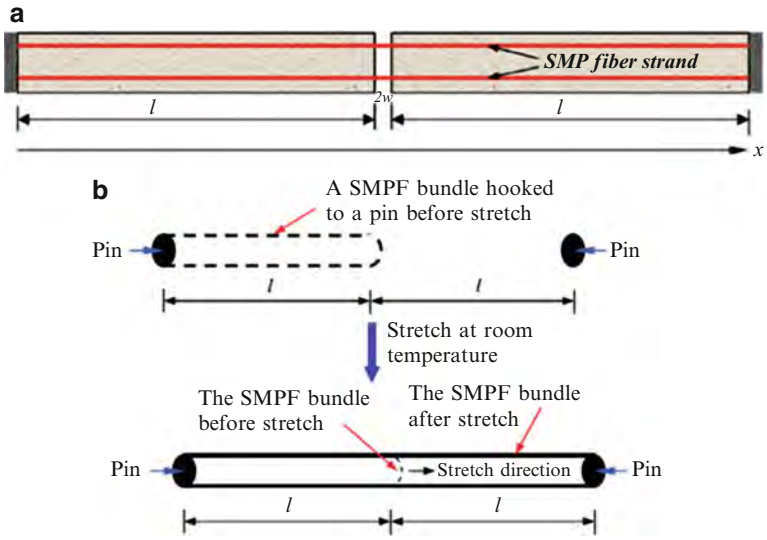

Fig. 13 (**a**) Schematic of a beam specimen with artificial pre-crack during shape recovery (healing) process (the SMPFs are perpendicular to and bridge over the pre-crack) and (**b**) schematic of an SMPF bundle being stretched to 100 % pre-strain [47]

Applications in Engineering

Potential application of SMP fibers as mechanical actuators in smart material systems has been evaluated. It was known that the stress recovery of the SMP fibers provides the required crack closure force. It is found that the polyurethane thermoplastic fibers are strain hardened upon cold-drawing programming, and they can achieve the required recovery stress to close macroscopic cracks [46, 47]. Furthermore, the strain-hardened SMP fibers show excellent mechanical properties, in which a new application field is opened for these fibers to be deployed in SMP fiber-reinforced composite structures. The enhanced mechanical responses of the cold-drawn semicrystalline polyurethane SMP fibers are correlated to the stress-induced crystallization process and the texture updates in the amorphous and crystalline phases. The difficulty in healing structural damage is that most existing methods need external help to bring the fractured surfaces in contact before healing occurs. One self-healing system is constituted from a thermosetting polymer matrix together with dispersed SMP fibers and embedded thermoplastic particles [48, 49] (Figs. 13 and 14).

The ability for the SMP fibers to close a wide opened crack depends on the recovery stress. With the same fiber volume fraction, the higher the recovery stress, the higher the capability to close the crack, and the higher the healing efficiency. The increase in healing efficiency is not directly proportional to the pre-strain level. While the healing efficiency almost doubles with 50 % pre-strained fibers as compared to fibers without pre-strain, further pre-straining to 100 % does not

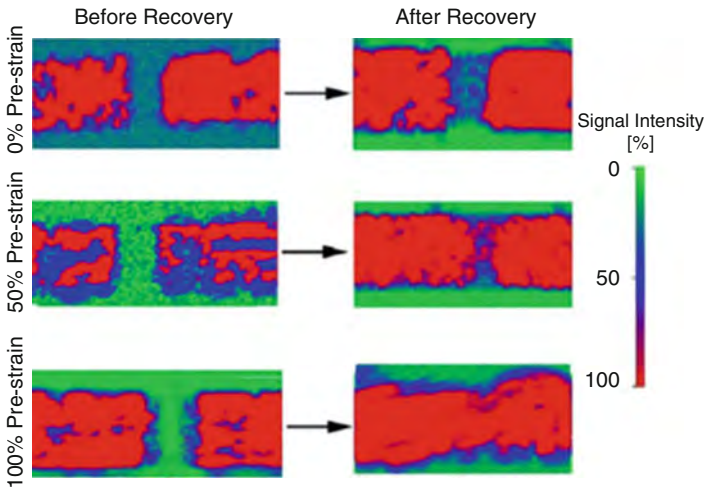

Fig. 14 C-scan images of thermosetting polymer beam specimens embedded with 9.9 % by volume shape memory polymer fibers having pre-tension of 0 %, 50 %, and 100 %: (*left*) pre-crack before recovery and (*right*) crack closure after the first healing [47]

increase the efficiency in the same rate, probably due to the saturated contribution of closing the crack on healing efficiency. It is found that the mechanism for the increase in the constrained recovery stress and enhanced healing efficiency of the cold-drawn SMP fibers is due to the increase in stiffness of the hard-segment domain at the healing temperature. Cold-drawing leads to molecular alignment and formation of some perfect crystals (stress-induced crystallization) in the hard-segment domain.

The strength and stiffness of the programmed fibers have been improved after the cold-drawing process. The increase in Young's modulus of the programmed fibers is almost five times of the nonprogrammed fibers, the yield stress has been improved almost 26 times after the process, and the tensile strength has doubled after the process. After structural relaxation, the programmed SMPU fibers, which are "stress free" or hibernate in a polymer matrix, can still provide some recovery force to close millimeter-scale cracks in the self-healing system when triggered by thermal stimulus.

Summary and Future Trends of Shape Memory Fiber

Although shape memory fibers have been spun by wet spinning, melt spinning, and electrospinning and entered into various textile areas, there is still a lot of scope for them to define new textile products with advanced functional and shape memory property.

Multi-responsive SMP fibers: To date, most of the SMP fibers are based on the thermal-induced shape memory effect. However, the application potential of

multi-responsive SMP fiber which show response to light, heat, electric, and moisture should also be exploited for the smart textile applications. Different stimulus could be used to control the shape memory effects of multi-responsive SMP fibers in textile by incorporating two switches such as water-sensitive and thermal-sensitive switch. This may enhance controllability of shape memory effects and would help to achieve multifunctional textiles. For example, a thermal–water-sensitive shape memory garment could be developed to realize shape memory effects in the presence of both sweat and change in body temperature accordingly to optimize thermal-wet management function.

Multifunctional SMP fibers: Multifunction refers to others like antibacteria and hemostasis except the shape memory function. These can be easily obtained by adding antibacterial and functional particles. SMP fibers with extra functions may be more suitable for health-care products and biomedical textiles which will be more attractive and effective. Shape changing is generally observed in the LC-SMPU and SMPU composites, their high cost and complex manufacture limited their applications greatly. Scientists are inspired continuously to improve the fabrication technology and reduce the cost of SMP fibers.

Strengthen function by shape memory property: SMP fibers will strengthen other functions of textiles, particularly microcapsule releasing system. The present releasing theory of microcapsule mostly is slow release, friction release, and control release by macrospores. SMP capsule may control the releasing speed by temperature, humidity, and water which will further ensure the effective releasing and durability.

Biomimetic SMP fibers: The natural world around us provides excellent examples of functional systems built with a handful of materials. There are numerous examples of functional surfaces, fibrous structures, structural colors, self-healing, thermal insulation, etc., which offer important lessons for the fiber and textile products of the future. The scales of pine cone bend outwards when drying out and reverse when cone wets. SMP fibers may use its shape memory advantage to get the pine cone effect stimulus by heat or water.

References

1. Zhu Y et al (2008) Shape memory fiber spun with segmented polyurethane ionomer. Polym Adv Technol 19(12):1745–1753
2. Kaursoin J, Agrawal AK (2007) Melt spun thermoresponsive shape memory fibers based on polyurethanes: effect of drawing and heat-setting on fiber morphology and properties. J Appl Polym Sci 103(4):2172–2182
3. Hu J, Meng Q, Lu J (2009) Shape memory fibers prepared via wet, reaction, dry, melt and electrospinning. The Hong Kong Polytechnic University
4. Haitao Zhuo H, Hu J, Chen S, Yeung L (2008) Preparation of polyurethane nanofibers by electrospinning. J Appl Polym Sci 109(1):406–411
5. Meng Q, Hu J, Shen L, Hu Y, Han J (2009) A smart hollow filament with thermal sensitive internal diameter. J Appl Polym Sci 113:2440–2449
6. Meng QH, Hu JL (2008) Self-organizing alignment of carbon nanotube in shape memory segmented fiber prepared by in situ polymerization and melt spinning. Compos A Appl Sci Manuf 39(2):314–321

7. Hu J et al (2012) A review of stimuli-responsive polymers for smart textile applications. Smart Mater Struct 21(5):1–23
8. Ratna D, Karger-Kocsis J (2008) Recent advances in shape memory polymers and composites: a review. J Mater Sci 43:254–269
9. Liu C, Qin H, Mather PT (2007) Review of progress in shape-memory polymers. J Mater Chem 17:1543–1558
10. Behl M, Lendlein A (2007) Actively moving polymers. Soft Matter 3:58–67
11. Jinsong Leng, Shanyi Du (year) Shape-memory polymers and multifunctional composites CRC press, England
12. Lendlein A, Langer R (2002) Biodegradable, elastic shape-memory polymers for potential biomedical applications. Science 296(5573):1673–1676
13. Xu JW, Song J (2010) High performance shape memory polymer networks based on rigid nanoparticle cores. Proc Natl Acad Sci U S A 107(17):7652–7657
14. Huang HH, Hu JL, Zhu Y (2013) Shape-memory biopolymers based on beta-sheet structures of polyalanine segments inspired by spider silks. Macromol Biosci 13:161–166
15. Wu LB, Jin CL, Sun XY (2011) Synthesis, properties, and light-induced shape memory effect of multiblock polyesterurethanes containing biodegradable segments and pendant cinnamamide groups. Biomacromolecules 12(1):235–241
16. Zhu Y, Hu JL, Liu YJ (2009) Shape memory effect of thermoplastic segmented polyurethanes with self-complementary quadruple hydrogen bonding in soft segments. Eur Phys J E 28 (1):3–10
17. Zhu Y, Hu JL, Yeung LY, Liu Y, Ji FL, Yeung KW (2006) Development of shape memory polyurethane fiber with complete shape recoverability. Smart Mater Struct 15:1385–1394
18. Zhu Y et al (2007) Effect of steaming on shape memory polyurethane fibers with various hard segment contents. Smart Mater Struct 16(4):969–981
19. Meng QH et al (2007) Morphology, phase separation, thermal and mechanical property differences of shape memory fibres prepared by different spinning methods. Smart Mater Struct 16(4):1192–1197
20. Ji FL, Hu J, Li TC, Wong YW (2007) Morphology and shape memory effect of segmented polyurethanes. Part I: with crystalline reversible phase. Polymer 48:5133–5145
21. Ji FL, Zhu Y, Hu JL, Liu Y, Yeung LY, Ye GD (2006) Smart polymer fibers with shape memory effect. Smart Mater Struct 15(6):1547–1554
22. Meng QH, Hu JL (2008) Influence of heat treatment on the properties of shape memory fibers. I. Crystallinity, hydrogen bonding, and shape memory effect. J Appl Polym Sci 109 (4):2616–2623
23. Meng QH, Hu JL, Zhu Y (2007) Shape-memory polyurethane/multiwalled carbon nanotube fibers. J Appl Polym Sci 106(2):837–848
24. Meng QH, Hu J, Yeung LY (2007) An electro-active shape memory fibre by incorporating multi-walled carbon nanotubes. Smart Mater Struct 16:830–836
25. Hong SJ, Yu WR, Youk JH (2008) Mechanical behavior of shape memory fibers spun from nanoclay-tethered polyurethanes. Macromol Res 16(7):644–650
26. Hiraoka K, Sagano W, Nose T, Finkelmann H (2005) Biaxial shape memory effect exhibited by monodomain chiral smectic C elastomers. Macromolecules 38:7352–7357
27. Yu YL, Ikeda T (2006) Soft actuators based on liquid-crystalline elastomers. Angew Chem Int Ed 45:5416–5418
28. Qin HH, Mather P (2009) Combined one-way and two-way shape memory in a glass-forming nematic network. Macromolecules 42:273–280
29. White TJ, Lee K, Koerner H, Vaia RA, Bunning TJ (2011) Light-activated shape memory of glassy, azobenzene liquid crystalline polymer networks. Soft Matter 7:4318–4324
30. Endo T, Tanaka S, Kim HK, Sudo A, Nishida H (2008) Anisotropic photomechanical response of stretched blend film made of polycaprolactone-polyvinyl ether with azobenzene group as side chain. Macromol Chem Phys 209:2071–2077

31. Yoshino T, Kondo M, Mamiya J, Kinoshita M, Yu YL, Ikeda T (2010) Three-dimensional photomobility of crosslinked azobenzene liquid-crystalline polymer fibers. Adv Mater 22: 1361–1363
32. Ikeda T, Kondo M, Sugimoto M, Yamada M, Naka Y, Mamiya J, Kinoshita M, Shishido A, Yu YL (2010) Effect of concentration of photoactive chromophores on photomechanical properties of crosslinked azobenzene liquid-crystalline polymers. J Mater Chem 20:117–122
33. Ikeda T, Mamiya J, Yu YL (2007) Photomechanics of liquid-crystalline elastomers and other polymers. Angew Chem Int Ed 46:506–528
34. Ahir SV, Tajbakhsh AR, Terentjev EM (2006) Self-assembled shape-memory fibers of triblock liquid-crystal polymers. Adv Funct Mater 16(4):556–560
35. Krause S et al (2007) Photocrosslinkable liquid crystal main-chain polymers: thin films and electrospinning. Macromol Rapid Commun 28(21):2062–2068
36. Zhuo HT, Hu JL, Chen SJ (2008) Electrospun polyurethane nanofibres having shape memory effect. Mater Lett 62(14):2074–2076
37. Zhuo HT, Hu JL, Chen SJ (2011) Coaxial electrospun polyurethane core-shell nanofibers for shape memory and antibacterial nanomaterials. Express Polym Lett 5(2):182–187
38. Cha DI et al (2005) Electrospun nonwovens of shape-memory polyurethane block copolymers. J Appl Polym Sci 96(2):460–465
39. Chung SE et al (2011) Thermoresponsive shape memory characteristics of polyurethane electrospun web. J Appl Polym Sci 120(1):492–500
40. McDowell JJ, Zacharia NS, Puzzo D, Manners I, Ozin GA (2010) Electroactuation of alkoxysilane-functionalized polyferrocenylsilane microfibers. J Am Chem Soc 132(10): 3236–3237
41. Hu J, Shaojun C (2009) A review of actively moving polymers in textile applications. J Mater Chem 20:3346–3355
42. Liu Y, Chung A, Hu JL, Lu J (2007) Shape memory behavior of SMPU knitted fabric. J Zhejiang Univ Sci A 8:830–834
43. Meng Q et al (2009) Biological evaluations of a smart shape memory fabric. Text Res J 79 (16):1522–1533
44. Vili YYFC (2007) Investigating smart textiles based on shape memory materials. Text Res J 77(5):290–300
45. Zhuo H, Hu J, Chen S (2011) Study of water vapor permeability of shape memory polyurethane nanofibrous nonwovens. Text Res J 81(9):883–891
46. Pengfei Zhang GL (2013) Structural relaxation behavior of strain hardened shape memory polymer fibers for self-healing applications. J Polym Sci 51:966–977
47. Li G, Ajisafe O, Meng H (2013) Effect of strain hardening of shape memory polymer fibers on healing efficiency of thermosetting polymer composites. Polymer 54:920–928
48. Shojaei A, Li G, Voyiadjis GZ (2013) Cyclic viscoplastic-viscodamage analysis of shape memory polymers fibers with application to self-healing smart materials. J Appl Mech 80:1–15
49. Li G, Li G (2012) A viscoplastic theory of shape memory polymer fibres with application to self-healing materials. Proc R Soc A 468:2319–2346

Silk Fibers as Smart Materials Toward Medical Textiles

9

Yasushi Tamada and Katsura Kojima

Contents

Introduction 210
Silk Fiber 212
Silk for Medical Applications 213
Creation of a Smart Silk Fiber Using Transgenic Technology 214
Overview 214
PiggyBac-Based Transgenesis 214
How to Alter the Silk Protein by Transgenic Silkworm 216
Modification of Silk Fibroin Protein by Transgenic Technology 217
Cell-Adhesive Silk Fiber 218
Objective of Cell-Adhesive Silk 218
Cell-Adhesive Silk 218
Affinity Silk 219
Definition of "Affinity Silk" 219
Affinity Silk 219
Spider Silk 220
Why Spider Silk in a Silkworm? 220
Silkworm Expressing Spider Silk Proteins 221
Summary 222
References 222

Y. Tamada (✉)
Division of Applied Biology, Faculty of Textile Science and Technology, Shinshu University, Ueda City, Nagano, Japan
e-mail: ytamada@shinshu-u.ac.jp

K. Kojima
National Institute of Agrobiological Sciences, Tsukuba, Ibaraki, Japan
e-mail: kojikei@affrc.go.jp

© Springer Science+Business Media Singapore 2015

X. Tao (ed.), *Handbook of Smart Textiles*,
DOI 10.1007/978-981-4451-45-1_11

Abstract

Silk has been used as a textile fiber for more than 6,000 years. Recently, many applications of silk have been studied for use beyond textiles, especially in medical areas. Silk is reported as a safe material with excellent mechanical properties and biocompatibility. In 2000, a transgenic silkworm technology developed based on the transposon *piggyBac* and microinjection technique, producing transgenic silk fibers having additional new functions to silk, became available. It was expected to expand the application area of silk into medical and other fields. Herein, silk fiber and studies of silk use in medical applications are described, along with an introduction of transgenic silkworm technologies used to produce a smart material based on silk. Cell-adhesive silk fiber with cell-adhesive peptide "RGDS" will be used for cell scaffolds in tissue engineering. "Affinity silk," with a fused single-chain fragment variable (scFv) of IgG protein to silk fibroin protein, will be valuable for affinity purification systems, diagnosis of diseases, detection of pathogenic microorganisms, and development of therapeutic strategies. Spider silk will become an engineering fiber with excellent mechanical strength from a natural origin. Silk fibers are anticipated for use as a smart material in advanced textiles intended for use in medical and various other fields.

Keywords

Silk • Transgenic • Cell adhesion • Antibody • Spider

Introduction

Silk fibers have been used as textile thread for more than 6,000 years because of their physical and physicochemical properties for use as a cloth material. Silk provides mechanical strength and modulus, control of humidity, luster, a smooth texture, and a pleasant feel. Silk is produced by numerous insects and arachnids such as Lepidoptera (butterflies, moths), Hymenoptera (bees, wasps, and sawflies), Orthoptera (crickets), Mantodea (mantids), and orb-weaving spiders [1]. These silks are studied for their amino acid sequences, secondary structures, and physical properties. Their characteristic structures and properties have been reported, but none is applicable for use as a textile fiber today. Spider silk has been investigated in terms of its structure, physical properties, and production process to develop a novel natural fiber with high performance rivaling that of Kevlar because of its impressive mechanical properties [2]. Unfortunately, no dream fiber is used on a commercial basis today. Studies of these silks are anticipated as providing valuable seeds for the development of a new silk fiber. For a long time, the structure, properties, and functions of silkworm (*Bombyx mori*) silk have been studied. Production and modification technology for use as a textile fiber have been developed. Furthermore, many studies of silk fiber and silk proteins have been explored to identify new applications beyond the textile fiber field, especially in medical fields. Silk fiber mainly comprises two proteins: fibroin and sericin (Fig. 1).

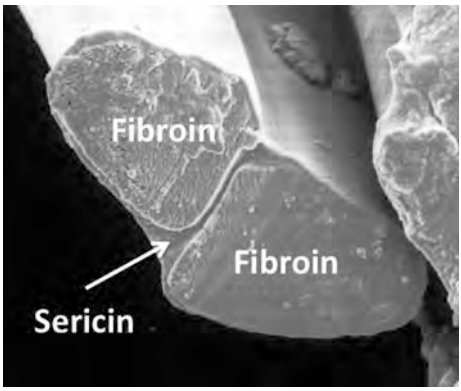

Fig. 1 SEM micrograph of cross section of cocoon silk fiber (Photo by Y. Tamada)

Fig. 2 Various forms of silk fibroin materials (Photos by Y. Tamada)

Fibroin, a structural protein, can form fibers easily from aqueous solution in a cocoon body because of the self-organization property of fibroin molecules. Silk fibroin can be fabricated to various forms such as films, sponges, gels, nanofibers, and resin from the fibroin aqueous solution through water solvent processes [3] (Fig. 2). The various forms of fibroin materials, including those of fibers, have been studied for use as a biomaterial in medical fields such as surgical therapy, drug delivery systems, wound dressing, and tissue engineering because of silk

biocompatibility [4]. Advanced application technologies of fibroin materials aside from medical applications have been reported in electrical and optical fields [5]. In 2000, transgenic silkworm technology was established [6]. The technique has been improved over the last decade. An important use of transgenic silkworms will be the production of recombinant proteins such as growth factors, coagulation factors, serum proteins, and antibodies for therapeutic use, instead of production by microorganisms, cells, and animals [7]. Another valuable utilization of the transgenic silkworm is expected to be modification of silk proteins, resulting in alteration of silk fibers on the mechanical properties and functionality. People will be able to design silk fibers that they want, simply by addition of determined amino acid sequences to silk fibroin protein sequences. This chapter presents a brief summary of silk fiber, application studies of silk materials in medical fields, and modification of silk fiber by a transgenic silkworm to create a smart material for use in medical materials.

Silk Fiber

Silk fibers used mostly worldwide are produced by domestic silkworms (*Bombyx mori*) through the well-established sericultural system that has been improved for a long time. Silk fibers of cocoons consist mainly of two proteins: fibroin and sericin. Usually sericin protein is removed by a degumming process (usually boiling in alkaline solutions) to produce textile fiber. Recently, the presence of many proteins aside from fibroin and sericin was reported from results of proteome analysis [8]. Fibroin, which is synthesized at the posterior silk gland, consists of complexes including 350 kDa heavy chains, 25 kDa light chains, and fibrohexamerin/P25. The synthesized fibroin is moved to the middle silk gland and is stored until spinning. At the middle silk gland, sericin proteins are synthesized surrounding fibroin sol to form a core–shell structure. At the late fifth larval stage, a silkworm starts spinning to produce a cocoon. The silkworm continues spinning for 2 days successively and approximately 1,500 m of silk fiber is spun to make a cocoon. The cocoon is dried by heat to kill the pupa to prevent damage to the silk fiber by hatching. The dried cocoon is boiled (cocoon cooking) in a series of water baths with different temperature to dissolve some sericin and thereby improve the fiber reliability. Raw silk fiber is obtained by a silk-reeling process from the boiled cocoon in a filature factory. Usually 8–10 cocoons' fibers are bunched with twisting to produce a single raw silk fiber. The raw silk fibers are degummed to produce textile silk fiber and fabrics before and after weaving.

The degummed silk fibers can dissolve in several salt aqueous solutions such as LiBr, $CaCl_2$, and LiSCN. Then the salts are removed by dialysis against water, resulting in a fibroin aqueous solution. Once the fibroin aqueous solution is prepared, the fibroin can be fabricated to various forms such as a film, sponge, gel, or nonweaved mat based on the water solvent system [3]. Because almost all as-fabricated fibroin materials are water soluble, the fibroin materials are treated with organic solvents such as methanol and ethanol to render them water insoluble.

Additional water-annealing methods can change the fibroin film and nanofiber from water soluble to water insoluble [9]. The secondary structure of the fibroin molecule changes to a β-sheet from a random coil by these treatments. Several processes used to form fibroin sponge structures were developed based on freeze-drying and post-water-insoluble treatment. A unique process to produce a fibroin sponge is that small amounts of water-soluble solvent such as DMSO and ethanol are added to an aqueous fibroin solution. Then the mixed solution is frozen and thawed [10]. This process requires no freeze-drying or post-water-insoluble treatment. Nonwoven mats from fibroin nanofibers or microfibers formed by electrospinning technique can be fabricated. Electrospinning of silk fibroin is performed from fibroin solution in formic acid, HFA, HFIP, and aqueous solvent. Formic acid, HFA, and HFIP are powerful reagents to solubilize fibroin but are harmful to the human body. Therefore, the use of the organic solvents is inadequate for medical purpose. Although fibroin aqueous solution is better as a spinning dope for electrospinning, high concentration is necessary to achieve continuous electrospun fibroin fiber without defects. To overcome that shortcoming, a mixture of PEO applied to the fibroin aqueous solution as the spinning dope is used to form electrospun fiber [11]. The electrospun fibroin fiber diameter can be controlled by spinning conditions such as the electrical potential, flow rate, distance between the spinneret and target, solvent, and concentration [12].

Silk for Medical Applications

Silk fibers have been used as surgical sutures for a long time. Silk fibers have good handling and good tensile and knot strength for suturing. No severe side effects from the use of silk sutures have been reported, but several experiences related to immune response and inflammation reactions caused by classical silk suture have been described in the literature. These reactions might derive from some impurities existing in the sericin layer of non-degummed classical silk sutures. Recently, it has been demonstrated that carefully purified silk fibers cause no immune or inflammation reaction [13]. Immune and inflammation responses against silk fibroin are confirmed as lower than those to 2-hydroxyethyl methacrylate, collagen, and polylactic acid as a typical biomaterial used in medical applications [14]. Sericins have been recognized as inducing hypersensitivity. Nevertheless, it is difficult to distinguish whether that hypersensitivity results from sericin protein itself or some impurities in the sericin layer. The sericin layer has several impurities such as protein inhibitors, dyes, wax, and seroins, which present the possibility of causing immune and inflammation reactions. Purified fibroin protein (degummed silk fiber) is recognized as a material having good biocompatibility [13].

Sutures are the only practical application of silk fiber in medicine today, but many researchers are attracted to studies of the development of biomaterials and tissue-engineering scaffold based on silk fibroin (fiber). Silk fibroin films, sponges, and nonwoven mats show good cell compatibility such as adhesion and proliferation. Recently, unique cell mobility on fibroin film is found and an advanced nature

of fibroin material in tissue engineering is inferred [15]. Silk fabric is effectively composited with inorganic materials such as apatite, which is the major bone component [16]. Consequently, silk fiber has a good bone-binding property for use in artificial tendons and ligaments with appropriate strength. Artificial vascular graft is constructed by tubular woven silk fiber. One-year patency in a rat abdominal aorta was confirmed [17]. Chemical modification of silk can add new functionality for medical use, such as sulfation of fibroin and sericin to make a silk anticoagulant and an anti-HIV material [18]. 3D porous material (sponge) is probably a suitable form as a cell scaffold for tissue regeneration. Fibroin sponges produced by various processes are studied as scaffolds for tissues and organs such as skin, cartilage, and bone. Nonwoven silk fiber mats formed by electrospinning are also studied for application to tissue engineering for skin, bone, cartilage, and blood vessels. Biocompatible silk fiber is expected to be a smart biomaterial for medical use.

Creation of a Smart Silk Fiber Using Transgenic Technology

Overview

Silk, which is made from fibroin and sericin, can be modified chemically or biologically. One method to modify silk material from its protein composition is transgenic technology. Using transgenic technology, the protein component of silk fiber (fibroin proteins) was modified as intended. Because modified silks might show improved mechanical properties and altered biocompatibility, the silkworm transgenesis is attracting more attention. The silkworm transgenesis technology was first developed by Tamura et al. [6]. To date, the technology has been improved to provide high transgenesis efficiency for new markers, establishment of tissue-specific expression system, and so on. Many studies have been conducted to investigate the gene function by the introduction or knockout/knockdown of the predicted responsible gene using transgenic technology. One aim of silkworm transgenic technology is to express foreign gene products in silk fiber and to alter the physical properties of silk or to add some functions on silk fiber. The transgenic technology presents a powerful tool to create a smart silk fiber for use in various fields including medical applications. A brief outline of silkworm transgenesis is introduced and detailed methods for the modification of silk proteins using transgenic technology are described in this section.

PiggyBac-Based Transgenesis

The transgenic silkworm is generated by the microinjection of transfer vector and helper plasmid into the silkworm eggs. The transfer vector and helper plasmid were constructed from the transposon, *piggyBac*, found from a Noctuidae moth, *Trichoplusia ni*. This transposon works in many eukaryotic cells including those of silkworm, mice, and humans. This transfer vector is widely used for transgenesis.

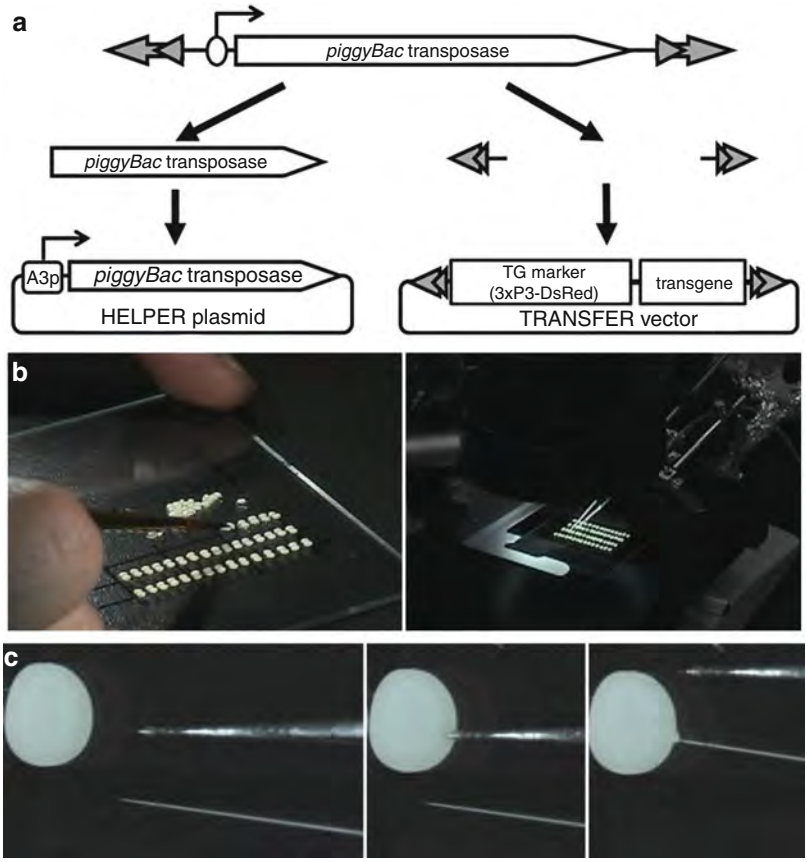

Fig. 3 *PiggyBac* vector and microinjection into the eggs. (**a**) Construction of plasmids. Two plasmids were constructed from piggyBac transposon. The helper plasmid has transposase gene under the control of *Bombyx* actinA3 gene promoter (*left*). The transfer vector includes terminal repeats of piggyBac and the marker gene and the gene cassette of interest (transgene). The sequence between two terminal repeats can be cut out from the transfer vector and inserted into the genome of silkworm. (**b**) Silkworm eggs were aligned on the slideglass (*left*) and put under the microscope with the tungsten needle and glass capillary (*right*). (**c**) Egg, tungsten needle, and glass capillary alignment (*left*). To microinject plasmids into the silkworm egg, first put a hole in the egg shell using a tungsten needle (*middle*). Then plasmids were injected through the hole with a glass capillary (*right*) (Photos and drawing by K. Kojima)

Figure 3a represents the construction of these plasmids. The transfer vector comprises terminal repeats of *piggyBac* and a marker gene (e.g., 3xP3-DsRed2 [19]) and expression gene cassette. The helper plasmid has the expression cassette for *piggyBac* transposase under the control of *Bombyx* actinA3 gene promoter [6]. After microinjection of these plasmids, the transposase, encoded in helper plasmid, is expressed and cuts the sequence between terminal repeats of transfer vector and reinserts the sequence in genomic DNA, resulting in the marker gene and

Fig. 4 Life cycle of silkworm. Silkworm larvae (on the cocoon) were hatched from eggs (14 days) and reared to last instar larvae (20–24 days, *left*). Then they made cocoons. Silk moths were then taken from the cocoon 14 days after cocooning. They mated and oviposited (Photo by K. Kojima)

foreign gene cassette to be inserted in the genomic DNA. Because the insertion of transgene occurs randomly in the genome at the "TTAA" sequence, the gene expression from transgenes might vary among experiments.

The microinjection of transfer vector and helper plasmid into the silkworm eggs is done as follows. First the silk moth is crossed and permitted to lay eggs. The eggs were aligned and fixed on a slide glass and the plasmids were microinjected under the microscope (Fig. 3b). Because the silkworm eggshell is too difficult to microinject using only a glass capillary, it is recommend to put a hole first on the shell using a tungsten needle. Then the DNA solution was injected with the glass capillary through the hole (Fig. 3c).

In these microinjected eggs, transgenes are inserted randomly into the embryo cell genome. Some few embryos have germ cells with the transgene insertion, but other embryos are inserted with the transgene in other cells except germ cells. Every embryo with injected plasmids is reared to an adult moth. Then they are mutually mated and are permitted to lay eggs (Fig. 4). Some eggs from the germ cells having the transgene might become transgenic silkworms, so the eggs are selected by the marker gene expression like fluorescent proteins. Usually, about 5–10 different transgenic silkworm strains are obtainable from 500 to 1,000 microinjected eggs.

How to Alter the Silk Protein by Transgenic Silkworm

Some methods exist to produce foreign proteins in silk by transgenic technology. Silk comprises fibroin fibers and sericin layer covering fibroin fibers. Transgenic technology enabled to express foreign genes into both components using an

appropriate set of promoter and terminator sequences. If the foreign gene was put under one of sericin gene promoters and terminators, the gene product was expressed in the sericin layer. In this case, the foreign protein was expressed as a stand-alone protein and eluted easily from the silk. However, when a foreign gene was bound to fibroin genes with a fibroin promoter and terminator set, the foreign proteins connected with fibroin proteins are expressed as a fusion protein in the fibroin fibers. These two expression methods should be selected according to the objective in use of the transgenic silkworms. In the production of cytokines and antibodies, the sericin layer expression method will be used because the expressed proteins are easily dissolved in the buffers and purified. The modification of silk fiber to design functionality and mechanical properties should be the expression method in fibroin fibers. The modification of silk fibroin proteins by transgenic technology will be promised as a good method for alternating biomaterial based on silk fiber.

Modification of Silk Fibroin Protein by Transgenic Technology

Silk fibroin consists of three proteins: fibroin heavy chain (FibH), fibroin light chain (FibL), and P25/fhx (P25). These proteins are expressed in the posterior part of the silk gland as a high-molecular-weight complex in which the six FibH–FibL heterodimers and one P25 are combined. Because the complex forming and secretion into the lumen of silk gland is strictly regulated [20], foreign protein expression should be designed to fuse the foreign proteins with one of the fibroin proteins expressed in the silk fibroin fiber. The expression of fluorescent proteins fused with these three fibroin proteins in the silk fibroin fiber has been reported [21–23]. The modified silk fibers with fluorescent proteins show fluorescent activities, indicating that the fluorescent proteins fused with fibroin protein can form its natural structure and maintain the function in spun transgenic silk fibroin fiber. It is suggested strongly that other proteins such as cytokines, enzymes, and others might also be expressed as a fusion protein into the silk fibroin and express their functions. Indeed many proteins have been identified and expressed as a fusion protein into the silk fibroin.

Using *piggyBac*-based transgenic technology, one to three copies of transgene on average are inserted constantly and randomly into the genomic DNA of silkworm. Because the transgene is expressed in addition to the native fibroin genes, the transgenic protein expression is competed against those of the native proteins. Therefore the amount of the transgenic proteins results in a low level comparing with the competed native proteins. In the case of the fibroin L-chain fused with a foreign protein expression in silk fibroin, usually 10–30 % (mol / mol) of native fibroin proteins were replaced with the transgenic proteins, which indicates that about 1–3 % (w/w) of silk fibroin weight was the transgenic proteins. This ratio between the transgenic and native proteins almost matches the expression of FibH fusion protein.

Because the expression efficiencies of transgene are insufficient, the great benefit of transgenic silkworms is that the expression efficiency becomes steady through the generation once the transgenic silkworm is established.

Cell-Adhesive Silk Fiber

Objective of Cell-Adhesive Silk

Silk is processable to many shapes, such as a powder, film, solution, and 3D porous structure (Fig. 2). The silk materials are regarded as well adapted for use in regenerative medicine, especially the silk sponge structure. Because silk itself has advanced properties as a cell scaffold in tissue regeneration such as high biocompatibility and high mechanical properties, a silk fibroin sponge will be a suitable material for use as a cell scaffold for load-bearing tissues such as bone and cartilage. Because silk material surfaces fundamentally have cell compatibility, the control of cell adhesion, proliferation, and differentiation presents an important issue for cell scaffolds in tissue regeneration. Among them, the improvement of cell adhesion of a silk material surface will present an adequate strategy to increase cell adhesion to minimize the initial cell number to seed into scaffolds because of a limitation of source cells.

Cell-Adhesive Silk

Cells, including cartilage cells, live in a complex, communicating with surrounding cells and the extracellular matrix (ECM). One such communication is the interaction between integrins on the cell surface and the RGDS motif presented in the fibronectin in ECM. The interaction is specific. Only the 4-amino acid motif is crucially important. Therefore, when the RGDS motif is presented on the silk materials, cells can attach to the silk surface well through biological interaction. Usually, several processes are applied on silk to fabricate silk materials which evoke denaturing protein structures such as degumming and dissolving in 9M LiBr solutions. Therefore simple and short amino acid sequences such as RGDS will be suitable to add functionality to silk fibroin.

Several reports in the relevant literature described the RGDS motif on silk fibroin and investigated improved cell attachment on silk materials. One report has described the construction of a protein with multiple RGDS sequences at the C-terminus of FibL protein [24]. Others have described modified FibL protein fused with 2x“RGDS” sequence at the C-terminus [25–27]. In both cases, transgenic silkworm has produced and the transgenic modified silk presented cell adhesion properties.

A report described that the modified protein, a fusion protein, FibL, and a repeat of a part of collagen type I or a part of fibronectin were expressed under the control of FibL gene promoter and terminator. The expression efficiency was 0.2–3.4 % (w/w) of fibroin. The cell-adhesive activity of the transgenic silk films against fibroblast cells was improved. Another transgenic silkworm silk expressed the FibL–2xRGDS protein in fibroin. The modified protein was 11–23 % (mol/mol) of total FibL proteins. Furthermore, the silk film prepared from a larval silk gland silk solution showed altered initial attachment of fibroblast cells. The cells on the modified silk showed specific pseudopod extension, which was characteristic in the

cells on fibronectin-coated surface but which was not seen in the cells cultured on wild-type silk film. This enhanced cell attachment on silk film was observed also in degummed silk using chondrocytes.

These specific functions observed on the silk structure prepared from degummed cocoon silk indicate its high tolerance to heat, chaotropic ions, and so on. They show its possibility for application as medical materials, for which sterilization is recommended.

Affinity Silk

Definition of "Affinity Silk"

A functional modification of silk fibroin protein is the addition of a biologically specific binding activity such as antigen–antibody, enzyme–ligand, and hormone–receptor to silk fiber. Immunoglobulins work as antibody to protect an organism from the attack of foreign organisms through immune reactions. "Affinity silk" is a genetically modified silk fiber with binding immunoglobulins on it. Consequently, affinity silk can recognize and bind antigens specifically. Some reports describe that the complete IgG is expressed in the silk sericin part and that it can be purified from a cocoon with functionality [28]. However, because the immunoglobulins formed a quite large and complicated protein complex, it is difficult to express immunoglobulins as a part of silk fibroin protein. Recently, "affinity silk" having an antigen recognition property in the silk fiber was developed. And it was fabricated as powder form and its specific antigen-binding capability was confirmed [29]. The "affinity silk" was defined as a silk which has a modified FibL protein fused with a single-chain fragment variable (scFv), instead of the whole IgG protein, at the C-terminus and is expressed as a part of silk fibroin (Fig. 5a).

Affinity Silk

As described in section "Definition of 'Affinity Silk'," affinity silk technology, which provides specific binding ability to the silk fibroin, was established in 2012. The technology was simply realized by the expression of scFv, a modified immunoglobulin protein with only the antigen-binding domains, at the C-terminus of the FibL protein (Fig. 5b). Transgenic silkworm expressing scFv–FibL in the cocoon fibroin in about 25 % (mol/mol) of total FibL protein, which is about 12 % of protein molecules, has the antigen-binding domain. The affinity silk powder can be prepared as follows. Affinity silk fiber with whole cocoon shell protein is dissolved in 9M LiBr solution. It is then dialyzed against water, freeze-dried, and crushed, thereby producing powder with 10–20 μm diameter particles. The affinity silk powder can bind specifically to its antigen protein expressed in *E. coli* and also from the cell extract. The binding activity was confirmed using immunoprecipitation. The binding capacity was almost equal to that of its original monoclonal antibody bound to a protein-G sepharose column.

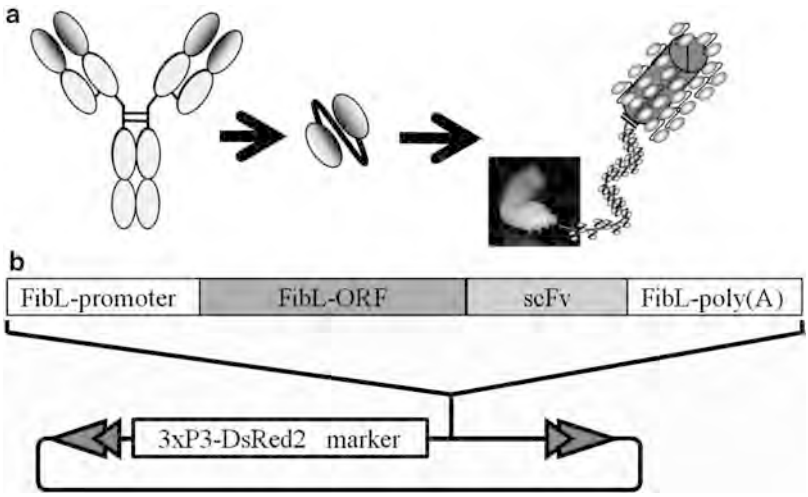

Fig. 5 Construction and expression of affinity silk. (**a**) Schematic representation of affinity silk. Variable domains of IgG were cloned and constructed to be scFv protein. The protein was expressed in silkworm silk fibroin as a fusion protein with fibroin L-chain protein. (**b**) Schematic representation of transfer plasmid used for expression of affinity silk. Modified fibroin L-chain gene (promoter, fusion protein gene, and terminator) was cloned into *piggyBac* transfer vector (Drawing by K. Kojima)

The "affinity silk" is expected to be applicable as a medical textile because of its specific binding activity against antigens. Further improvement of affinity silk technologies is expected to provide novel materials that are highly biocompatible (as well as biodegradable) for the development of an affinity purification system, the diagnosis of diseases, the detection of pathogenic microorganisms, and the development of therapeutic strategies.

These expected applications of "affinity silk" derive from both the characteristics of antibodies which have quite limited target select ability and of silk fiber which has excellent mechanical properties and good biocompatibility. Furthermore, although "affinity silk" can be spun by the transgenic silkworm as a fiber, it can change shapes to various forms depending on the applications through water-based solvent processes. It is expected to be an excellent tool for medical use.

Spider Silk

Why Spider Silk in a Silkworm?

Spider silk, especially dragline silk, is known as an extremely tough fiber. Because of the predatory nature of spiders, it is impossible to cultivate spiders to obtain sufficient amounts of spider silk for commercial use. For almost two decades, many researchers have exerted great efforts to produce spider silk proteins in bacteria,

plants, animal cells, and also in silkworms [30]. However, perfect spider silk fiber has been unobtainable through those attempts because spider silk proteins consist of highly repeated sequences and their cloning and expression has remained difficult. Expressed and purified spider silk proteins from heterologous system are also believed to show inferior physical properties after artificially spun into fiber because the highly repeated large molecular weight nature (>300 kDa) of spider silk proteins is quite difficult to clone in a sufficiently long spider silk protein gene. Moreover, many expression systems cannot even express shorter spider silk proteins in liquid form. Nevertheless, silkworms can express high-molecular-size and highly repeated sequence proteins such as fibroin heavy-chain proteins (ca. 350 kDa and many "GAGAGS/Y" repeats) and produce proteins in quite large amounts (>200–500 mg/larva). This extremely high productivity of silkworm production system is regarded as suitable for spider silk protein production.

Silkworm Expressing Spider Silk Proteins

Production of spider silk protein in transgenic silkworm silk fibroin has succeeded at two laboratories [31, 32]. Spider silk was produced in a silk sericin layer using transgenic silkworm technology [33] and using Baculovirus expression systems [34]. However, the latter two attempts were unable to form fibers. For that reason, the mechanical advantages of spider silk could not be estimated.

In 2007, Kojima et al. [31] established a transgenic silkworm expressing a part of *Araneus ventricosus* dragline silk protein (2.1 kbp of repeated sequence) in silk fibroin protein and demonstrated that the silkworm can express a spider silk protein having large molecular weight (approx. 80 kDa) in a silk fibroin fiber. No influence of the secondary structure of silk fibroin by spider silk expression is confirmed. It will be inferred from the results that silk fibroin of silkworm can accept foreign protein incorporation without changing its natural structure or mechanical properties. In 2012, Teulé et al. also established a transgenic silkworm expressing synthetic spider silk protein that is 2.4 kbp long. The spider silk sequence was constructed artificially with a combination of flagelliform and dragline silk of spider. They reported that the transgenic spider silk fiber has better mechanical properties compared with native silkworm silk fiber, although the expressed protein is artificially constructed, not a native spider silk protein. Surprisingly, one of the developed transgenic spider silks showed superior toughness compared to the native spider dragline silk.

Additionally, a silkworm can spin the transgenic silk containing spider silk proteins as a fine fiber form that can be used directly as a textile. The transgenic silk can also be re-modified into various shapes of materials, as described above, similarly to silk fibroin.

The mechanical properties of the spider silk fiber expressed by transgenic silkworm are not dramatically enhanced today because the expression efficiency is moderately low (approx. 3 %(w/w) of total fibroin) and the molecular length of the expressed protein is too short. If these limitations can be overcome, then the

transgenic spider silk with the highest toughness and strength in the world will certainly be created using transgenic silk technology.

Summary

Silk fiber is a historically important material that has been used as a textile. Many technologies have been developed to improve the production efficiency and quality control of silk fiber in biology, selective breeding, physiology, and pathology of silkworms: chemical engineering, mechanical engineering, factory processing, statics, and material sciences of silk fiber corresponding to the growth of sericulture. It is safe to say that technologies in modern industry could be constructed based on technologies related with the silk industry to a greater or lesser extent. Today, silk should be recognized as different from an old-fashioned material: it is an advanced material because many reports describe varieties of researches about silk material used in various fields such as the medical, tissue engineering, and electrical fields as a naturally occurring material. The number of such reports is increasing every year. Furthermore, as described in this chapter, transgenic technology has been established. It provides a strong tool to modify silk fiber. Silk fiber can be anticipated as a smart material for exploitation as a textile fiber and beyond.

References

1. Sutherland TD, Young JH, Weiseman S, Hayashi C, Meritt D (2010) Insect silk: one name, many materials. Annu Rev of Entomol 55:171–188
2. Vollrath F (2000) Strength and structure of spiders' silks. J Biotechnol 74(2):67–83
3. Rockwood DN, Preda RC, Yucel T, Wang X, Lovett L, Kaplan DL (2011) Materials fabrication from *Bombyx mori* silk fibroin. Nat Protoc 6:1612–1630
4. Vepan C, Kaplan DL (2007) Silk as biomaterial. Prog Polym Sci 32:991–1007
5. Tao H, Kaplan DL, Omenetto FG (2012) Silk materials – a road to sustainable high technology. Adv Mater 24:2824–2837
6. Tamura T, Thibert C, Royer C, Kanda T, Abraham E, Kamba M, Kômoto N, Thomas J-L, Mauchamp B, Chavancy G, Shirk P, Fraser M, Prudhomme J-C, Couble P (2000) Germline transformation of the silkworm *Bombyx mori* L. using a piggyBac transposon-derived vector. Nat Biotechnol 18:81–84
7. Tomita M (2011) Transgenic silkworms that weave recombinant proteins into silk cocoons. Biotechnol Lett 33:645–654
8. Dong Z, Zhao P, Wang C, Zhang Y, Chen X, Wang X, Lin Y, Xia Q (2013) Comparative proteomics reveal diverse functions and dynamic changes of *Bombyx mori* silk proteins spun from different development stages. J Proteome Res 12(11):5213–5222
9. Jin J, Park J, Karageorgiou V, Kim UJ, Valluzzi R, Cebe P, Kaplan DL (2005) Water-stable silk films with reduced β-sheet content. Adv Funct Mater 15:1241–1247
10. Tamada Y (2005) New process to form a silk fibroin porous 3-D structure. Biomacromolecules 60(6):3100–3106
11. Jin HJ, Fridrikh SV, Rutledge GC, Kaplan DL (2002) Electrospinning *Bombyx mori* silk with poly(ethylene oxide). Biomacromolecules 3:1233–1239

12. Sukigara S, Gandhi M, Ayutsede J, Micklus M, Ko F (2003) Regeneration of *Bombyx mori* silk by electrospinning – part 1: processing parameters and geometric properties. Polymer 44:5721–5727
13. Altman GH, Diaz F, Jakuba C, Calabro T, Horan RL, Chen J, Kaplan DL (2003) Silk-based biomaterials. Biomaterials 24(3):401–416
14. Meinel L, Hofmann S, Karageorgios V, Kirer-Head C, McCool J, Gronowicz G, Zichner L, Langer R, Vunjak-Novakovic G, Kaplan DL (2005) The inflammatory responses to silk films in vitro and in vivo. Biomaterials 26:147–155
15. Hashimoto T, Kojima K, Otaka A, Takeda YS, Tomita N, Tamada Y (2013) Quantitative evaluation of fibroblast migration on a silk fibroin surface and TGFBI gene expression. J Biomater Sci Polym Ed 24(2):158–169
16. Tamada Y, Furuzono T, Taguchi T, Kishida A, Akashi M (1999) Ca adsorption and apatite deposition on silk fabrics modified with phosphate polymer chains. J Biomater Sci Polym Ed 10(7):787–793
17. Enomoto S, Sumi M, Kajimoto K, Nakazawa Y, Takahashi R, Takabayashi C, Asakura T, Sata M (2010) Long-term patency of small-diameter vascular graft made from fibroin a silk-based biodegradable material. J Vasc Surg 51:155–164
18. Goto K, Izumi H, Kanamoto H, Tamada Y, Nakajima H (2000) Sulfated fibroin, a novel sulfated peptide derived from silk, inhibits Human Immunodeficiency Virus replication in vitro. Biosci Biotechnol Biochem 64:1664–1670
19. Horn C, Schmid BG, Pogoda FS, Wimmer EA (2002) Fluorescent transformation markers for insect transgenesis. Insect Biochem Mol Biol 32:1221–1235
20. Inoue S, Tanaka K, Arisaka F, Kimura S, Ohtomo K, Mizuno S (2000) Silk fibroin of *Bombyx mori* is secreted, assembling a high molecular mass elementary unit consisting of H-chain, L-chain, and P25, with a 6:6:1 molar ratio. J Biol Chem 275:40517–40528
21. Kojima K, Kuwana Y, Sezutsu H, Kobayashi I, Uchino K, Tamura T, Tamada Y (2007) A new method for the modification of fibroin heavy chain protein in the transgenic silkworm. Biosci Biotechnol Biochem 71:2943–2951
22. Royer C, Jalabert A, Rocha MD, Grenier A-M, Mauchamp B, Couble P, Chavancy G (2005) Biosynthesis and cocoon-export of a recombinant globular protein in transgenic silkworms. Transgenic Res 14:463–472
23. Inoue S, Kanda T, Imamura M, Quan GX, Kojima K, Tanaka H, Tomita M, Hino R, Yoshizato K, Mizuno S, Tamura T (2005) A fibroin secretion-deficient silkworm mutant, Nd-sD, provides an efficient system for producing recombinant proteins. Insect Biochem Mol Biol 35:51–59
24. Yanagisawa S, Zhu Z, Kobayashi I, Uchino K, Tamada Y, Tamura T, Asakura T (2007) Improving cell-adhesive properties of recombinant *Bombyx mori* silk by incorporation of collagen or fibronectin derived peptides produced by transgenic silkworms. Biomacromolecules 8:3487–3492
25. Kambe Y, Takeda Y, Yamamoto K, Kojima K, Tamada Y, Tomita N (2010) Effect of RGDS-expressing fibroin dose on initial adhesive force of a single chondrocyte. Biomed Mater Eng 20:309–316
26. Kambe Y, Yamamoto K, Kojima K, Tamada Y, Tomita N (2010) Effects of RGDS sequence genetically interfused in the silk fibroin light chain protein on chondrocyte adhesion and cartilage synthesis. Biomaterials 31:7503–7511
27. Kojima K (2013) Genetically modified silk as a biomaterial. J Jpn Soc for Biomater 31:72–81
28. Iizuka M, Ogawa S, Takeuchi A, Nakakita S, Kubo Y, Miyawaki Y, Hirabayashi J, Tomita M (2009) Production of a recombinant mouse monoclonal antibody in transgenic silkworm cocoons. FEBS J 276:5806–5820
29. Sato M, Kojima K, Sakuma C, Murakami M, Aratani E, Takenouchi T, Tamada Y, Kitani H (2012) Production of scFv-conjugated affinity silk powder by transgenic silkworm technology. PLoS One 7:e34632

30. Tokareva O, Michalczechen-Lacerda VA, Rech EL, Kaplan DL (2013) Recombinant DNA production of spider silk proteins. J Microbial Biotechnol 6:651–663
31. Kojima K, Kuwana Y, Sezutsu H (2007) Secondary structure analysis of genetically modified silk with spider fiber protein. Koubunshi Ronbunsyu 64:817–819
32. Teule F, Miao YG, Sohn BH, Kim YS, Hull JJ, Fraser MJ Jr, Lewis RV, Jarvis DL (2012) Silkworms transformed with chimeric silkworm/spider silk genes spin composite silk fibers with improved mechanical properties. Proc Natl Acad Sci U S A 109:923–928
33. Wen H, Lan X, Zhang Y, Zhao T, Wang Y, Kajiura Z, Nakagaki M (2010) Transgenic silkworms (*Bombyx mori*) produce recombinant spider dragline silk in cocoons. Mol Biol Rep 37:1815–1821
34. Zhang Y, Hu J, Miao Y, Zhao A, Zhao T, Wu D, Liang L, Miikura A, Shiomi K, Kajiura Z, Nakagaki M (2008) Expression of EGFP-spider dragline silk fusion protein in BmN cells and larvae of silkworm showed the solubility is primary limit for dragline proteins yield. Mol Biol Rep 35:329–335

Phase Change Fibers and Assemblies

10

Qinghao Meng, Guoqiang Li, and Jinlian Hu

Contents

Introduction 226
Phase Change Materials 227
Phase Change Fibers and Assemblies 228
Principles of Phase Change Fibers and Assemblies 228
Phase Change Materials for Temperature-Regulating Fibers and Assemblies 229
Manufacture of Phase Change Fibers and Assemblies 233
Microencapsulation Technology 239
Applications of Phase Change Fibers and Assemblies 240
Outlast Phase Change Fabrics 241
Dive Suites 243
Protective Garments 244
Cooling Vests, Helmets, Cowls, and Neck Collars 245
Medical Products 246
Aerospace Textiles 246
Building Materials 247
Automotive Textiles 248
Development Trend 248
Summary 249
References 249

Q. Meng
Mechanical Department, Southern University, Baton Rouge, LA, USA
e-mail: qinghaomeng@126.com

G. Li
Department of Mechanical and Industrial Engineering, Louisiana State University, Baton Rouge, LA, USA
e-mail: lguoqi1@lsu.edu

J. Hu (✉)
Institute of Textiles and Clothing, The Hong Kong Polytechnic University, Hung Hom, Hong Kong
e-mail: tchujl@inet.polyu.edu.hk

© Springer Science+Business Media Singapore 2015

X. Tao (ed.), *Handbook of Smart Textiles*,
DOI 10.1007/978-981-4451-45-1_2

Abstract

Smart materials respond to environmental changes by actively altering their own properties. Phase change materials, as a type of important smart material, can interactively respond to environmental temperature change and can absorb, store, and release heat without changing their own temperature. The first and immediate application of phase change materials is in clothing. Phase change clothing can store or release heat energy without changing their own temperature; therefore, it can help the human body maintain the natural and comfortable temperature when environment and body temperature fluctuate. Phase change fibers and assemblies have been extensively studied since they were first introduced in the 1980s. They have been applied widely in casual wears, sportswear, protective clothing, diver's coveralls, and space suits and in civil engineering and electrical engineering. This chapter will present an up-to-date review on the various phase change fibers and assemblies in terms of mechanisms, manufacturing methods, performance, and applications. Although much progress has been made, many challenges are still waiting for solutions. The limitations of the various phase change fibers and assemblies are discussed. Future research directions in this field are suggested.

Keywords

Phase Change Textiles • Smart Textiles • Temperature Regulating

Introduction

Smart materials have the capability to respond to environmental changes such as heat, chemical, optical, electrical, humidity, mechanical, and magnetic changes. They change their properties such as color, shape, and mechanical properties to adapt to new environments or for other purposes. Smart materials are common in nature such as in plants and animals, with the human body as the most intelligent system. Because of the wide and promising applications, various synthetic smart materials have been developed, and some of them have been commercialized. Examples of the synthetic smart materials include phase change materials, chameleonic camouflage materials, thermo-active shape memory polymers, electronic electroactive muscles, ionic electroactive muscles, light-active elastomers, magnetic-active gels, and thermo-/pH-active hydrogels.

Phase change materials (PCMs) are a type of important smart materials. They react immediately to environmental temperature and body temperature change by releasing/storing heat without changing their own temperature. Because of this special function, PCMs have been widely used in temperature-regulating textiles, smart housing, waste heat recovery, agricultural greenhouse, solar power plants, spacecraft thermal systems, thermal protection of electronic devices, microprocessor equipment, computer cooling, and biomedical and biological carrying systems [1]. The first and most immediate application of PCMs is in textiles. Phase change textiles can regulate and keep human bodies at a constant and comfortable temperature upon temperature fluctuation by absorbing or releasing heat.

Phase Change Materials

PCMs change from one physical state (solid or liquid or gas) to another physical state without significant change in temperature. During this phase changing process, the PCMs release or store a large amount of heat. In nature, four fundamental phases of matter are commonly observed: solid, liquid, gas, and plasma. Several other states of matter also exist such as Bose–Einstein condensates, neutron-degenerate matter, etc. The states only occur in extreme situation such as ultracold or ultradense matters. Other states of matter are also possible such as quark–gluon plasma which has not been demonstrated experimentally.

Although several phase change states are available, only solid–gas, liquid–gas, solid–liquid, and solid–solid phase change materials have been used. The non-fundamental phase change cannot be used because they only exist in extreme situation. Liquid–gas phase change is not used for PCMs because practically the phase change from liquid to gas causes a big increase in volume. Solid–gas phase change has been used in ceramic fabrication. Figure 1 shows the heat characteristics of a solid–liquid phase change material. Solid–liquid PCMs can repeatedly and reversely convert between solid and liquid states according to the environmental temperature. During this phase change process, the temperature of the solid–liquid PCMs does not change. At temperature above the phase change temperature, the PCM absorbs heat; therefore, it can cause cool feeling. At a temperature below the phase change temperature, the PCM releases heat to the environment by phase change; therefore, it leads to warm feeling [2].

In addition to solid–liquid PCM, solid–solid PCM is another type of PCMs under intense research. Solid–solid PCMs absorb and release heat like solid–liquid PCMs; the difference is that they do not change their states. They merely soften/harden at a narrow temperature range. Compared with solid–liquid PCMs, solid–solid PCMs have advantages of no liquid or gas generation and with only a small volume

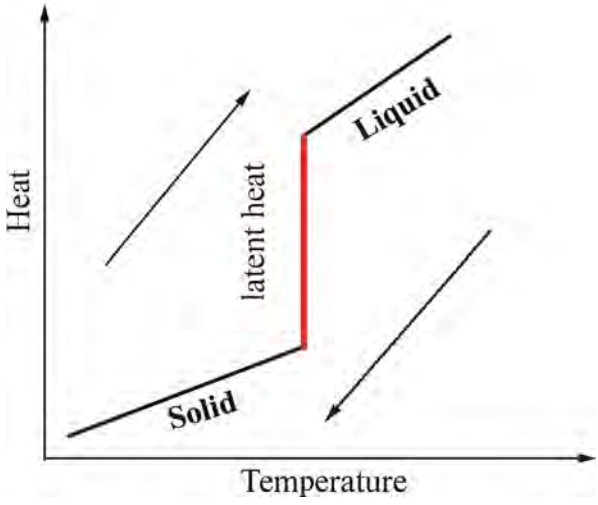

Fig. 1 Phase change of a solid–liquid PCM

change. In addition, most solid–liquid PCMs have to be encapsulated to be used; otherwise, the liquid will be lost during the application cycles. Solid–solid PCMs do not need to be encapsulated because they do not become liquid after the phase change.

The phase change of PCMs is automatic; therefore, the temperature-regulating effect of PCMs is automatic and does not require external intervention. PCMs may also be preheated and used as a heating source to keep other objects warm. Before the temperature starts to drop, a large amount of heat is released by the PCMs to the object as a result of the solidification of the PCMs. PCMs can also be precooled and used as a cooling source to keep other objects cold. Before the temperature rises, the PCMs absorb a large amount of heat to keep the object cold.

Phase Change Fibers and Assemblies

Principles of Phase Change Fibers and Assemblies

The most comfortable skin temperature of the human body is around 33.4 °C with a little fluctuation at different parts of the bodies according to the time of the day. When the temperature of the skin is 3.0 °C above or below this ideal temperature, the human body feels uncomfortable. In addition, the core body temperature of human is around 36.5 °C. A rise or fall of 1.5 °C of the body core temperature can be fatal [2, 3].

The human body has certain thermo-regulating ability at a narrow range by controlling a tight balance between heat loss and gain. This automatic process is controlled by the hypothalamus (in the brain). Physical activity and a high environmental temperature can lead to the increase in core temperature. Hence, heat must be released into the ambient environment to keep the core temperature stable. The hypothalamus can respond to make physiological adjustments such as dilating the blood capillaries and sweating to maintain constant core temperature [4]. In cold situation, several methods are also applied to control human body temperature at the comfort zone. For example, (1) sweat will stop in order to reduce heat loss; (2) the human body constricts the blood capillaries to reduce heat loss; (3) minute muscles beneath the surface of the skin contract. Although the human body has certain temperature-regulating capability, the ability of the human body to keep the temperature at the comfortable zone is limited. Actually, a slight deviation of the temperature from the comfortable zone can lead to significant uncomfortable feeling. Therefore, clothes have to be worn or removed to keep the body temperature stable.

Starting from primitive society, people start to use leaves in place of clothing to keep body warm. Till now, the primary purpose of clothing is still to keep the human body warm. The main functions of clothing have never changed, although clothing in the modern life also has other functions such as reflecting the identity, social status, and adornment. The performance of conventional cold insulation garments depends on the thickness or the amount of air trapped in the clothing

layers. Air is a good thermal insulator in that it consists mostly of empty space. Air molecules do not have much chance to interact or bounce against each other to transfer heat.

To increase the thermal performance of conventional warm clothing, in the late 1980s, two types of active textiles were developed. These two types of active textiles can actively absorb heat from the environment. One such textile is near-infrared textile which can absorb solar ray of near-infrared section to heat up the textile. Another one is far-infrared textile which can absorb the human body's far-infrared irradiation and turn it into heat. On the other hand, if it is hot, people may want to keep their body cold. Therefore, in the 1990s, ultraviolet-absorbing cool-feeling textiles were developed. Ultraviolet-absorbing textiles absorb ultraviolet and reflect near-infrared rays from the sun; therefore, they can produce a cool feeling to the human body [2]. All the near-infrared textiles, far-infrared textiles, and ultraviolet-absorbing textiles have one-way temperature changing effect and are not reversible.

Ideal textiles should have the functions to help regulate human body temperature according to the human body and environmental temperatures. If one feels cold, the textiles can release heat to warm one up; if one feels hot, the textiles can absorb heat to cool one down. PCMs have the function to release/store heat to regulate temperature fluctuations when temperature fluctuates. Being used in textiles, PCMs can regulate human body temperature dynamically, reversibly, and repeatedly. At high temperature, phase change textiles absorb human body heat without increasing their own temperature; therefore, the textiles can keep the wearer's temperature constant. At the same time, the heat can be stored in the textiles. If the wearer is exposed to a cold environment, the textiles can release the stored heat to keep the wearer warm. Numerous studies have shown this interactive/repeatable/reversible temperature-regulating effect of phase change textiles to keep the human body at a comfortable temperature.

Phase Change Materials for Temperature-Regulating Fibers and Assemblies

In nature, all matters such as water, stone, and plants can store heat energy. The most common PCM in nature is H_2O with a solid/liquid phase change temperature at 0 °C and liquid/gas phase change temperature at 100 °C. Although nature has abundant PCMs, most of them cannot be used for textiles because phase change textile applications have strict requirements on the properties of PCMs. PCMs for textile applications should have a phase change temperature in the range of 10–40 °C, high heat storage/release capability, low volume change, no corrosion, no toxicity, high thermal conductivity, no decomposition, and low supercooling.

Solid–Liquid Phase Change Materials

The mostly used PCMs for textile applications are solid–liquid PCMs. Several types of organic and inorganic materials can meet the above basic requirements

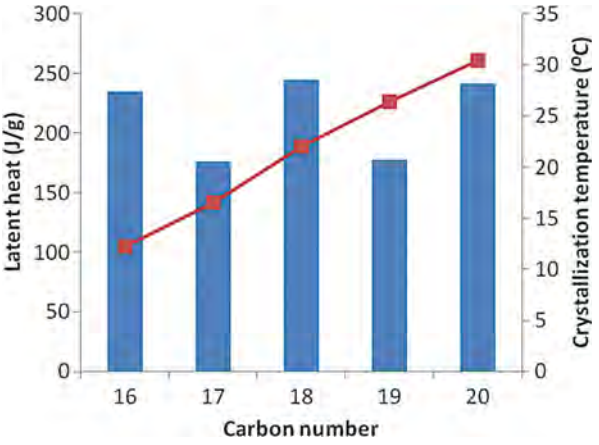

Fig. 2 The latent heat capacity and phase change temperature of paraffin hydrocarbons with different numbers of carbon atoms

for textile applications, such as hydrated inorganic salts, linear crystalline alkyl hydrocarbons (wax), fatty acids and esters, polyethylene glycols (PEG), polytetramethylene glycol (PTMG), and quaternary ammonium clathrates [1–3].

Hydrated inorganic salts are crystal inorganic salts that have varying numbers of water molecules, such as $CaCI_2.6H_2O$, $LiNO_3.3H_2O$, $Na_2SO_4.10H_2O$, and $Na_2SO_4.5H_2O$. These hydrated inorganic salts have a melting temperature at around 30 °C. They have high latent heat capacity with melting enthalpy reaching 300 kJ/kg. In addition, they have high thermal conductivity and low price and are not flammable. Hydrated inorganic salts for phase change textiles have limitations of supercooling and low thermal stability.

Paraffin hydrocarbons (also called linear alkyl hydrocarbons) are by-products of oil refining consisting entirely of hydrogen and carbon. They have a general molecule formula of C_nH_{2n+2}. Paraffinic hydrocarbons are noncorrosive, chemically and thermally stable, and inexpensive, have no supercooling, and have extensive source of raw materials. Crystalline paraffin hydrocarbons are one of the mostly used PCMs in textiles [5]. The phase change temperature of crystalline paraffin hydrocarbons with 16 ~ 21 carbons is in the range of 10 ~ 40 °C. The latent heat capacity and crystallization temperature of linear hydrocarbons with different numbers of carbon atoms are shown in Fig. 2 [5, 6]. Crystalline paraffin hydrocarbons have high latent heat capacity. The crystallization temperature of paraffin hydrocarbons increases with the increase in the molecular length as shown in Fig. 2. In order to obtain a desired phase change temperature, crystalline paraffin hydrocarbons of different carbon numbers may be used together. Although paraffin hydrocarbons have been widely used as the PCMs, for textile applications, they have the problems of flammability, low thermal conductivity, and high changes in volume during phase change. The flammability can be decreased by mixing paraffin hydrocarbons with fire-retardant agents. The thermal conductivity of paraffin hydrocarbons can be improved by filling thermal conductivity enhancers such as metal filler and carbon nanofiber/fiber fillers into paraffin hydrocarbons.

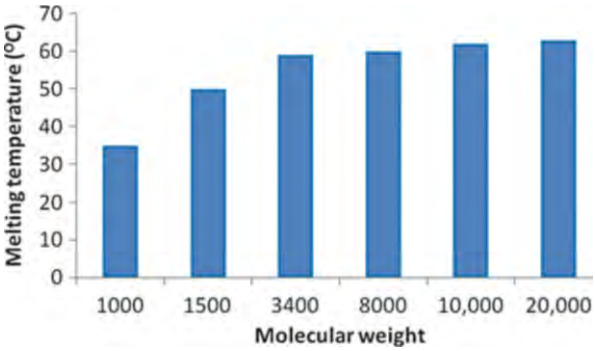

Fig. 3 The melting point of PEG with different molecular weight

Poly(ethylene glycol) (PEG) is another type of mostly used PCMs in textiles which has been intensively studied. PEG is noncorrosive and chemically and thermally stable. In addition, PEG has good biocompatibility because of its intrinsic molecular structure. Depending on the molecular weight, PEG has a melting temperature from around 3.2 °C to 68.7 °C [3, 7]. The melting temperature of PEG increases with increasing molecular weight. Figure 3 [5] shows the melting points of the PEG with different molecular weights. With a molecular structure similar to PEG, poly(tetramethylene glycol) (PTMG) is another kind of polymeric PCM; however, its application is limited because it needs high supercooling for crystallization due to the weak interaction between the molecular chains [3].

Solid–Solid Phase Change Materials

In addition to solid–liquid PCMs, another type of PCMs under intensive study for textile applications is solid–solid PCMs. Solid–solid PCMs do not melt after phase change; instead they soften/harden after the phase transition. Solid–solid PCMs are mostly prepared by incorporating the segment of solid–liquid PCMs into other rigid polymers. The rigid network prevents the segment of solid–liquid PCMs from flowing at a temperature above the phase change temperature. Solid–solid PCMs show several advantages over solid–liquid PCMs such as the no liquid or gas generation, small volume change, and seal/encapsulation. The disadvantages of solid–solid PCMs in comparison with their corresponding solid–liquid PCMs include low latent heat capacity and high supercooling.

With PEG as a phase change ingredient while another "rigid" ingredient as a skeleton, several types of solid–solid PCMs have been developed. Jiang et al. [8] prepared a solid–solid PCM with rigid polymer cellulose diacetate (CDA) serving as a skeleton and PEG as a functional branch chain. More recently, Li and Ding [9] prepared a solid–solid PCM using PEG/MDI (diphenylmethane diisocyanate)/PE (pentaerythritol) cross-linking copolymer via the condensation reaction of PEG with tetrafunctional pentaerythritol isocyanate. In their research PEG10000 was used as the phase change ingredient and tetrafunctional pentaerythritol isocyanate as the multifunctional reactant to form the rigid skeleton. First the tetrafunctional pentaerythritol was end-caped with isocyanate moieties. Then the reaction product

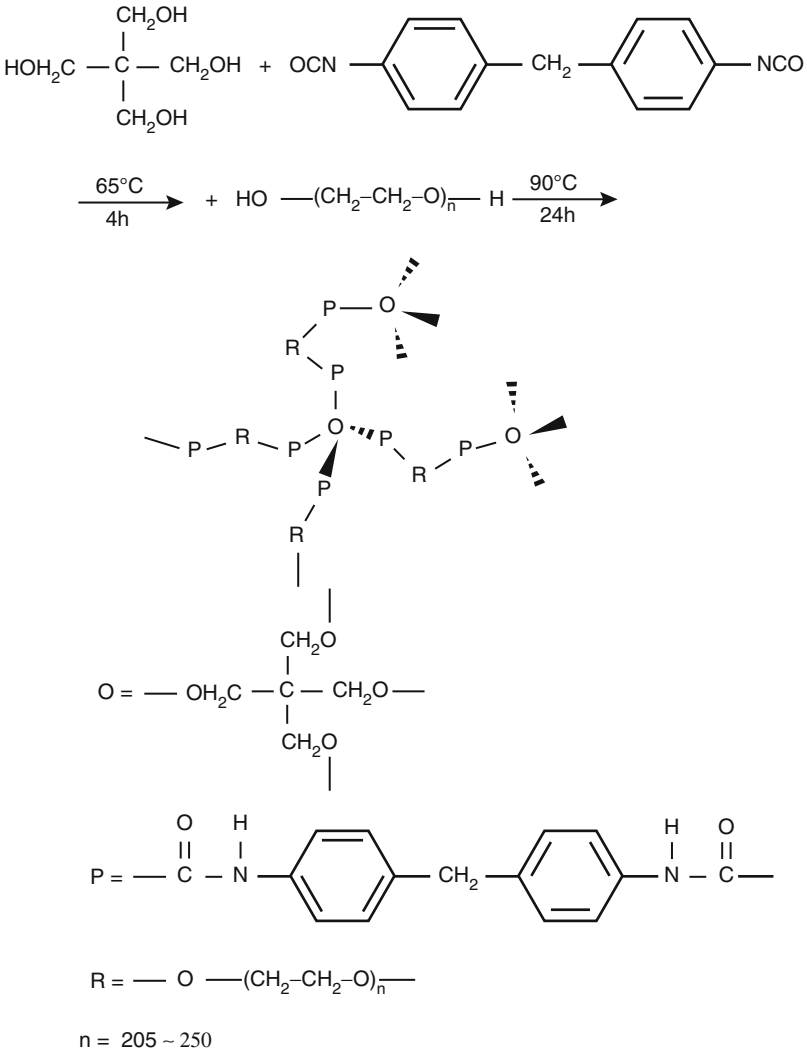

Fig. 4 Reaction mechanism for starlike cross-linking PEG/MDI/PE copolymer (Reprint from Li and Ding [9], Copyright © 2007, with permission from Elsevier)

reacted with PEG to form the starlike copolymer. The reaction of the starlike cross-linking PEG/MDI/PE copolymer is shown in Fig. 4. The phase transition enthalpy of the PEG/MDI (diphenylmethane diisocyanate)/PE (pentaerythritol) cross-linking copolymer was more than 100 J/g with a transition point at 58.68 °C.

The above PEG polymers have chemical cross-linking structure, which significantly affects their melt processability. They cannot be processed using conventional thermoplastic polymer processing technologies because of the chemical cross-linking. To prepare linear solid–solid PCMs, Hu et al. [10] prepared a

solid–solid PCM by copolymerizing PEG as the phase change segment with polyester as the rigid skeleton. The phase change enthalpy of the block copolymer increased to a maximum of 26.85 J/g at 45 wt% PEG proportion. Zhang et al. [11] also prepared a thermoplastic polyester–PEG block copolymer. It was found that the segment of PEG of molecular weight 1,540 at a PEG content of 50 % can form crystalline phase. The melting temperature is 6.86 °C. Increasing the PEG segment length and content can increase the crystallinity and melting temperature. When the PEG molecular weight reaches 4,000 with a PEG content of 50 %, the melting point of the segment polymer reaches 33.05 °C and the melting enthalpy reaches 30.56 J/g. Solid–solid PCMs with shape memory effect were also prepared by employing PEG as soft segment, while isophorone diisocyanate (IPDI) and 1,4-butanediol (BDO) as hard segment. The PCM polyurethanes with PEG as the soft segment show shape memory effect as a result of the phase separation of the micro-phase-segmented polyurethanes. The thermoplastic solid–solid PCMs can be processed into fibers by melt processing. Temperature-regulating fibers have been developed from the above solid–solid PCMs. The disadvantages of the PEG-based block copolymer fibers as a temperature-regulating fiber are that the degree of the supercooling of the fiber is too high and the mechanical properties of the fiber are not satisfactory. In addition, due to the significant melt transition at the low temperature, the PEG-based block copolymers do not have good melt spinnability.

Manufacture of Phase Change Fibers and Assemblies

Currently, the most widely used PCMs in textiles are solid–liquid PCMs because of their high thermal capacity with low volume change. After melting, at the temperature above the phase change temperature, the PCMs become liquid. To prevent the PCM liquid from being lost, several strategies have been used: (1) fill the solid–liquid PCMs into hollow fibers; (2) encapsulate solid–liquid PCMs into microcapsules; (3) graft or cross-link solid–liquid PCMs onto fabric surface; and (4) block copolymerizing solid–liquid PCMs with other rigid polymer structures to fabricate solid–solid phase change textiles.

Hollow Fiber Filling

The first research on PCMs was conducted by Triangle Research and Development Corporation in the early 1980s. At the beginning, solid–liquid PCMs were filled into synthetic hollow fibers. The objective of the research is to develop textiles which can protect astronauts and instruments from extreme temperature change in outer space. Most of the pioneer research was conducted by Vigo and Frost. The research history of this group has been reviewed by Zhang [12]. They filled solid–liquid PCMs into different types of hollow synthetic fibers such as rayon and polypropylene [13]. Solid–liquid PCMs such as $LiNO_3.3H_2O$ and $Zn(NO_3)_2.6H_2O$ were used. Because the solid–liquid PCMs were stored inside hollow fibers, the prepared PCM fibers have good wash resistance and durability.

Unfortunately, the filled fibers did not show good heat storage/release behavior during the heat/cooling cycles because of the poor thermal performance of the inorganic salts.

Later, Vigo and Frost [13] filled solutions of PEG into hollow rayon and polypropylene fibers and prepared temperature-regulating fibers successfully. PEG with average molecular weight of 400, 600, 1,000, and 3,350 were used. The fibers were dried and conditioned after fabrication. The treated fibers could produce heat 1.2–2.5 times greater than untreated hollow polypropylene and 2.2–4.4 times greater than untreated hollow rayon fibers. The heating/cooling capability of the treated hollow fibers could last 50 cycles with no adverse change on their thermal performance.

Fabric Coating

Instead of filling solid–liquid PCMs into hollow fibers, Vigo and Frost [14] first coated PEG and plastic crystal compounds PCM directly on polyester, nylon 66, cotton, and wool fabrics through a conventional fabric finishing process – pad–dry process. The fabrics were dipped into the aqueous solutions of PEG and plastic crystal compounds PCM. Then the fabrics were dried to remove water. Plastic crystal compound was not successfully applied on fabrics because it sublimed during the fabric drying process. The PEG treated fabrics showed heat storage and release capacity of 2–2.5 times greater than those of untreated fabrics. The heat storage/release properties were reproducible for 5 cycles and remained essentially constant for more than 50 cycles. The problem of PEG-coated temperature-regulating fabrics is that laundering or leaching can remove the PEG from the fabric because of PEG's water solubility.

One of the methods to improve the durability of PEG on coated fabric is to chemically graft PEG on the surface of fabrics. Bruno and Vigo [15, 16] used a polyfunctional cross-linking agents DMDHEU (dimethylol dihydroxyethyleneurea) and acid catalysts to bond PEG on fabrics through a pad–dry–cure process. Because of the chemical cross-linking structure formed by DMDHEU, laundry could not remove the PEG from the fabric. The heat release/store properties of the treated fabrics could last for 50 times without significant decrease. The treated fabrics not only had good heat/cooling effect but also showed antistatic properties, water absorbency, resiliency, soil release, pilling and abrasion resistance, moisture regain, and wrinkle recovery. Instead of using DMDHEU, Bruno and Vigo [17] used sulfonic acids and glyoxal to form polyacetals to bond PEG onto fabrics. The durability of the PEG coating on fabrics was also remarkably improved.

The second method to prevent solid–liquid PCMs on fabric surface from being lost is to use PCM microcapsules. The development of PCM microcapsules significantly improved the performance phase change textiles and promoted commercial applications of temperature-regulating textiles. In the first step, microspheres containing PCM solution or emulsion are prepared. The PCMs used for microcapsules are mostly paraffinic hydrocarbons and occasionally PEG. In the second step, PCM microcapsules are attached to textile surfaces by coating. Coating of PCM

microcapsules onto fabric is not difficult to conduct. PCM microcapsules can be coated onto textiles by traditional coating methods such as by knife over roll, knife over air, pad–dry–cure, gravure, dip coating, transfer coating, and screen printing.

Coating methods have remarkable influences on the properties of the fabrics. To study the influence of coating methods on the properties of fabrics, Choi et al. [18] used knife-over-roll and screen printing methods to coat octadecane/melamine–formaldehyde microcapsules onto polyester fabrics. They evaluated the thermal, mechanical, and physical properties of treated fabrics. It was found that the bending and shear rigidities of the fabric coating through knife over roll were higher than those of the fabrics treated through screen printing. The screen printing fabrics had better air permeability and lower hygroscopic properties than knife-over-roll fabrics.

To improve the durability of microcapsules on fabrics, polymers can be used as glue to bind and protect microcapsules on fabrics. Several types of polymer binders have been developed and commercialized such as RESIN CENTER BC® (Color Center Ltd.), PRIMAL E-358 EMULSION® (Rohm and Haas Ltd.), TEXLAKCOLOR SF® (Eurotext), TEXPRINT ECOSOFT N10® (Eurotext), MINERSTAR NEUTRO® (Minerva Color Ltd.), WST SUPERMOR® (Minerva Color Ltd.), and CENTERPRINT ECO® (Color Center Ltd.) [19].

Microcapsules may be first embedded in a coating polymer as binder such as acrylic, polyurethane, and rubber latex, to improve their bonding with fabric surface [5]. Bryant and Colvin [20] first invented the method to integrate paraffinic hydrocarbon microcapsules into fibers and fabrics using tetrafunctional cyclic urea compounds as the binder. They prepared paraffinic hydrocarbon microcapsules of 1.0–10.0 μm in size. The microcapsules were bound on fabrics successfully with improved durability. Shin et al. [21] prepared eicosane/melamine–formaldehyde phase change microcapsules and coated the microcapsules onto fabrics using polyurethane as the binder. The microcapsules were strong enough to be subjected to the coating process including stirring in hot water and high-temperature curing. After five launderings, the treated fabrics maintained 60 % of their heat storage capacity. Further studies are being conducted to improve the laundering durability of PCM microcapsules on fabrics.

Different binders have different performance on binding microcapsules on fabrics. A proper binder has to be selected before application of the phase change microcapsules. Salaun et al. [22] studied the efficiency of different binders on improving the durability of microcapsules coated on fabrics. Several types of binders were investigated, such as ethyl butyl acrylate, polyethyl acrylate, polydimethylsiloxane polyacrylate, polyurethane, ethylene vinyl acetate copolymers, and ethylene vinyl acetate copolymers. They found that the adhesion of microcapsules was closely dependent on the chemical nature and structure of the textile subtract. Therefore, the chemical nature and structure of textile subtracts have to be considered when selecting proper binders to obtain optimal thermal performance.

To further improve the durability of PCM microcapsules on fabrics, Gomes et al. [23] invented microcapsules with reactive groups which can bind the

microcapsules with fabrics using covalent bonding. They used poly(glycidyl methacrylate) on the outer surface of the microcapsules, which directly grafted to the functional groups of fabric fibers followed by thermal fixation. The treated fabric was subjected to physical processes involving frictional forces and domestic and industrial washing, in washing machines or dry cleaning. It was found that the durability of the PCM microcapsules on fabrics was significantly improved.

Polymer binders can improve the durability of phase change microcapsules on fabrics; however, at the same time, the binders can significantly affect the fabric softness, flexibility, breathability, and water vapor permeability. Shin et al. [24] studied the thermal properties, air permeability, moisture vapor permeability, moisture regain, low-stress mechanical properties, and handle of microcapsule-coated polyester knit fabrics with respect to the add-on of microcapsules. The coating was conducted using a pad–dry–cure method with polyurethane as the binding material. They found that the air permeability and moisture vapor permeability of the fabric decreased, whereas the moisture regain increased, with an increase in the add-on. The tensile linearity and geographical roughness increased, whereas the resilience, bending, and shear properties decreased with the increase in the add-on. The fabrics became stiffer, less smooth, and less full as the add-on increased, and thus the total handle value decreased.

Because phase change coating can significantly affect the softness, flexibility, breathability, and water vapor permeability of fabrics, Worley [25] invented a micro-perforations fabric using needling or needle punching which does not affect the above properties. Needles barbed or unbarbed are pushed through the fabric to form micro-perforations or micro-size holes in the fabric. A large number of micro-perforations are produced on the fabric. The micro-perforations on the fabrics significantly improve the softness, flexibility, breathability, and moisture vapor transport properties of fabrics in comparison with those with micro-perforations or micro-size holes on it.

Fiber Spinning

In the early research, PCMs were blended with fiber-forming polymers and were directly made into fibers by melt or wet spinning. By controlling suitable spinning parameters and component contents, researchers have developed several types of temperature-regulating fibers. Zhang et al. [1] blended polypropylene with PEG of 1,000–20,000 molecular weight and a thickening agent. PCM fibers were fabricated from the blend by a melt spinning method. The properties of the prepared fiber were systematically studied. PEG blends with polyester and ethylene vinyl acetate were also made into fibers.

In general, the spinnability of polymer blends from PEG and fiber-forming polymer is not good. In addition, the prepared fibers do not have good laundry durability because the PEG is exposed to air. To solve this problem, Leskovsek et al. [26] used phase change microcapsules in which a PCM was the core. They distributed phase change microcapsules into polypropylene melt using a Brabender mixer. During mixing, the shear forces generated by kneading broke the clusters of microcapsules and distributed the microcapsules in the matrix homogenously.

The cooled melt was granulated into chips. Then phase change fibers were prepared from the composite chips using a melt spinning method. Low viscosity wax was added into the chips to reduce the viscosity of the melt for better spinnability. Zhang et al. [27] prepared poly(acrylonitrile-vinylidene chloride) (PAN/VDC) fibers containing 4–40 wt% of the microcapsules of n-octadecane by wet spinning. It was found that fibers containing less than 30 wt% of microencapsulated n-octadecane could be spun smoothly. The enthalpy of the prepared phase change fiber containing 30 wt% of phase change microcapsules was approximately 30 J/g.

Multicomponent phase change fibers can also be prepared using a PCM as the core and other polymer materials as the sheath. The PCMs may be microencapsulated as the core materials, while other fiber-forming polymers are used as the sheath. Zhang et al. [1] prepared temperature-regulating fibers through a conjugate spinning method using PEG as the core material and polypropylene as the sheath. Magill et al. [28] invented a multicomponent fiber with a PCM as the core and a fiber-forming polymer as the sheath surrounding and protecting the core PCM material. Another advantage of incorporating PCM into the core of multicomponent is that it does not significantly affect the handle, drape, and softness of the fiber.

In comparison with wet spinning, melt spinning is not preferred to prepare phase change fibers because the high temperature during melt spinning may be detrimental to PCMs and their microcapsules. To further protect the PCMs, they may be microcapsulated and mixed with other polymers as the core materials. With the component containing microcapsules as the core, the melt spinnability of conjugate fiber can be improved. Zhang et al. [7] prepared sheath/core composite fibers with 4–24 wt% of microencapsulated n-octadecane by melt spinning with a 24-hole spinneret at 720 m/min. Polyethylene blended with 10–60 wt% n-octadecane microcapsules was used as the core, and polypropylene was employed as the sheath material. In the range of 10–40 wt%, the phase change microcapsules were evenly distributed in the polymer matrix. The enthalpies increased steadily as the content of the phase change microcapsules increased from 10–40 wt%. The enthalpy, tensile strength, and strain of the fiber having 20 wt% microcapsules were 11.0 J/g, 1.8cN/dtex, and 30.2 %, respectively.

Although the above method has significantly improved the spinnability and heat durability of the phase change fiber, the method faces several challenges. First, because microcapsules show the potential to form clusters, they can affect the continuity of the spinning process. Second, because only a small amount of microcapsules can be loaded, the thermal capacity of the prepared phase change fibers is rather low which is about 8–12 J/g [7]. Third, the high temperature during the melt spinning is still a challenge to solid–liquid phase change microcapsules. The high-temperature extrusion and pumping process may damage the microcapsules.

One of the methods to solve these problems is post-spinning in situ microencapsulation of PCMs, which means the microencapsulation process happens after the polymer spinning. PCM and membrane-forming reagents may be added into polymer melts or solutions to form spinning dopes. Then, the PCM fibers are spun by conventional spinning techniques. At or after the final step of the spinning,

through special treatment, PCM microcapsules can be formed in the fiber in situ. With this in mind, Jiang et al. [29] prepared phase change fibers by wet spinning, in which the chemicals can polymerize in situ to form phase change microencapsulation. They prepared the temperature-regulating fiber using polyvinyl alcohol at the polymer matrix while using tetraethyl orthosilicate (TEOS) as the membrane-forming reagent and paraffin as the PCM. After spinning, the fibers were treated to promote the hydrolysis and polycondensation of tetraethyl orthosilicate (TEOS) at the interface between paraffin and polyvinyl alcohol matrix to form microcapsules. Because no microcapsule was added to the spinning dopes before spinning, this method does not affect the spinnability of the material. The phase change polyvinyl alcohol fiber prepared by this method showed a relatively high latent heat value of 23.7 kJ/kg and good thermal stability. This method by in situ microencapsulation has shown promising on developing phase change fibers by wet spinning; its application in melt spinning for phase change fiber production is still under investigation.

Laminating

Microcapsules can also be filled into polymer matrix or foam materials. The polymer film or foam was then laminated with fabric materials to fabricate phase change fabric. The fabric is normally used as the lining of garments [30]. In comparison with fiber spinning methods, this laminating method has two advantages: a high content of PCMs loaded and microencapsulation of PCMs not required.

Pause [31] incorporated PCMs directly into a polymer film, which is then laminated to the nonwoven fabric system. Sarier and Onder [32] incorporated PCM n-hexadecane and n-octadecane directly into the raw chemicals of polyurethane foams. After foaming using methylene chloride and water, the PCMs were distributed in the polyurethane foam. Sandwich structures were made with other fabric materials. The sandwich structures showed good temperature-regulating effect. Bryant and Colvin [33] added phase change microcapsules into the prepolymer mixture of polyurethane and mixed with the mixture to ensure even dispersion. Then, the polymer was foamed according to conventional foaming methods. The foam can be laminated with conventional fabrics and be used for gloves, shoes, outerwear, automotive interiors, and medical products.

During the fabrication of phase change microcapsules, toxic chemicals such as formaldehyde may be used to prepare microcapsule shells. You et al. [34] heat-treated the microcapsules before the microcapsules were used to prepare temperature-regulating polyurethane foam. The microcapsules were heat-treated at 130 °C for 30 min. The heat treatment removed the formaldehyde and water, which is not only helpful for the fabrication of the polyurethane foams but also decreases the toxicity of the fabrics. The fabricated phase change foam absorbed heat energy at approximately 31 °C and released heat energy at approximately 28 °C. The phase change microcapsules have no significant influence on the thermal stability of polyurethane foam.

Shim et al. [35] fabricated body suits made from the laminate fabrics with the temperature-regulating foam. They studied the temperature-regulating effect of the

Table 1 The fabrication methods of phase change microcapsules

Microencapsulation methods	Physical methods	Pan coating
		Air-suspension coating
		Centrifugal extrusion
		Vibrational nozzle
		Spray drying
	Physicochemical methods	Ionotropic gelation
		Coacervation-phase separation
	Chemical methods	Interfacial polycondensation
		Interfacial cross-linking
		In situ polymerization
		Matrix polymerization

garment using a manikin. The results showed that the PCM foams were able to provide small, temporary heating/cooling effect during environmental temperature fluctuation.

Microencapsulation Technology

Microencapsulation technology is a process to encapsulate tiny particles or droplets into wall materials. The IUPAC definition on microcapsule is "hollow microparticle composed of a solid shell surrounding a core-forming space available to entrapped substances. The substances inside can be a drug, pesticide, PCM, dye, etc." The core inside a microcapsule may also be called internal phase or fill. The shell may be called wall, coating, or membrane. Microcapsules usually have walls of less than 2 μm in thickness and 20–40 μm in diameter.

Microcapsules can be prepared through physical methods, physicochemical methods, and chemical methods. The physical methods include pan coating, air-suspension coating, centrifugal extrusion, vibrational nozzle, and spray drying. Physicochemical methods have an ionotropic gelation method and coacervation-phase separation method. Chemical methods consist of interfacial polycondensation method, interfacial cross-linking method, in situ polymerization method, and matrix polymerization method. Table 1 summarizes most of the microencapsulation methods.

Figure 5 shows the schematic structure of a phase change microcapsule with the core material as a solid–liquid PCM. During applications, solid–liquid PCMs need to be encapsulated because at above the phase change temperature the PCM is in a liquid state. When temperature rises, phase change microcapsules absorb heat from the surroundings by melting the PCM in the microcapsules and store energy consequently. When the temperature falls, the microcapsules release the heat by crystallizing the PCM in the microcapsules [36]. Without capsulation, the liquid PCM may be lost. Although solid–liquid PCMs may be filled into hollow fibers, the thermal performance of PCM-filled hollow fibers is not satisfied. The use of phase

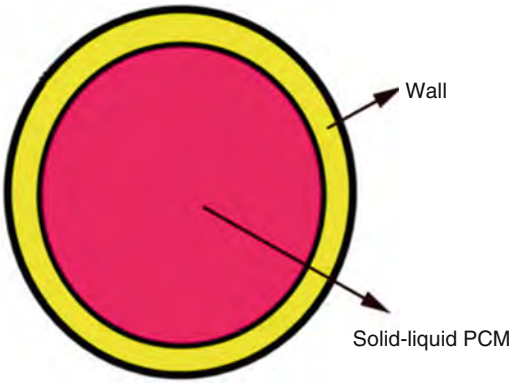

Fig. 5 Schematic structure of phase change microcapsules

change microcapsules can date back to the early 1980s. Bryant and Colvin [20, 37] first encapsulated paraffinic hydrocarbon PCMs such as eicosane or, alternatively, plastic crystals such as 2,2-dimethyl-1,3-propanediol (DMP) and 2-hydroxymethyl-2-methyl-1,3-propanediol (HMP) into small plastic spheres with a diameter of only a few micrometers to prevent dissolution. Improper microencapsulation and improper application of microcapsules can lead to low thermal performance of the final temperature-regulating products.

Phase change microcapsules are mostly prepared through chemical methods. To prepare phase change microcapsules, several types of polymers have been used as the shell materials such as urea–formaldehyde, melamine–formaldehyde resins, N, N-dimethylaminoethyl methacrylate and styrene, poly(butyl acrylate), and Arabic gum. The shell materials should have high toughness and are resistant to abrasion, pressure, friction, heat, and most types of chemicals. Some shell chemicals or residuals can cause environmental and health problems, such as urea–formaldehyde and melamine–formaldehyde resins. Arabic gum and styrene shell as replacement have been developed to replace formaldehyde-based microcapsules. For example, You et al. [38] used styrene–divinylbenzene copolymer as the shell and made microcapsule with n-octadecane as the core. The microcapsules n-octadecane/styrene–divinylbenzene were synthesized by suspension-like polymerization. By using formaldehyde, the microcapsules are healthier to the human body if they are used in garments. In addition, the preparation of styrene–divinylbenzene microcapsules is easy to conduct. Furthermore, it was found that styrene–divinylbenzene microcapsules had better heat performance than those based on melamine–formaldehyde.

Applications of Phase Change Fibers and Assemblies

The temperature-regulating effect of phase change textiles can keep the human body temperature at a constant and comfortable stage. They can bring good benefits to the individual wearer on both physical and physiological aspects. Phase change textiles can be used widely in casual wears, sportswear, protective clothing,

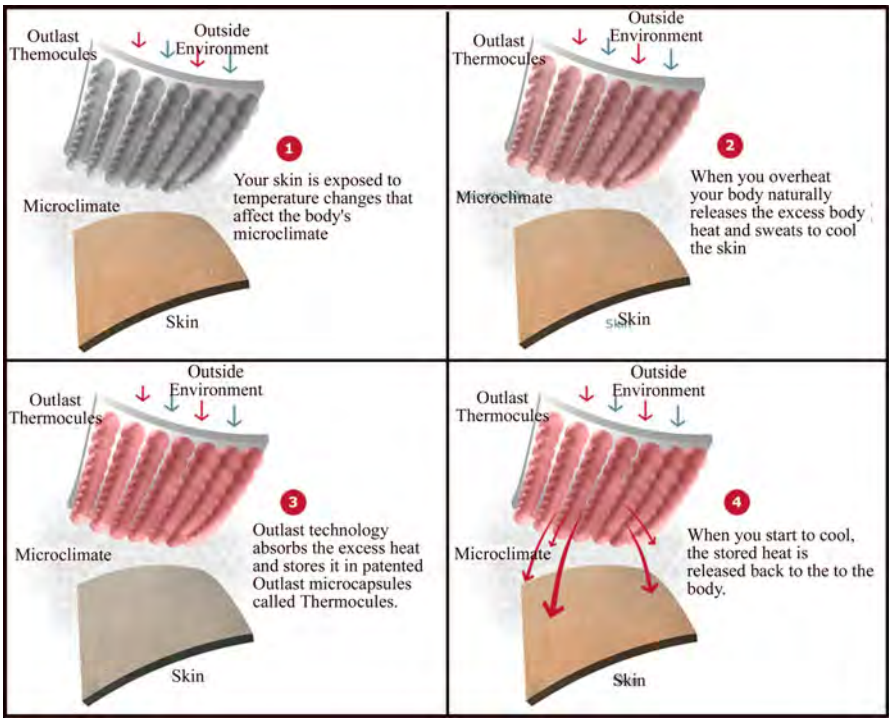

Fig. 6 How Outlast works to regulate wearer's temperature. (Outlast Technologies LLC, http://www.outlast.com/en/. Reprint with permission)

underwear, jackets, firefighter uniforms, skiwear, bulletproof vests, diver's coveralls, space suits, airman suits, field uniforms, sailor suits, curtains, quilts, quilt covers, sleeping bags, special gloves, shoe lining, building materials, automotive interiors, and medical and hygiene applications. Many patents have been filed and granted. This section will not go into details to introduce all the products. Instead, it will mainly introduce briefly typical products in outstanding patents on temperature-regulated textiles.

Outlast Phase Change Fabrics

One of the most successful products of phase change textiles is developed in the mid-1990s in Outlast Technologies LLC (previously Gateway Technologies). Figure 6 shows the working principal of the Outlast temperature-regulating fabric. In the figure, the Outlast Thermocules are phase change microcapsules developed and patented by the company. As shown in the figure (1), both body temperature and environmental temperature changes can affect the individual's comfort feeling; (2) when the human body overheats, the human body releases heat and sweats; (3) the Outlast fabric integrated with Outlast Thermocules absorbs the excess heat

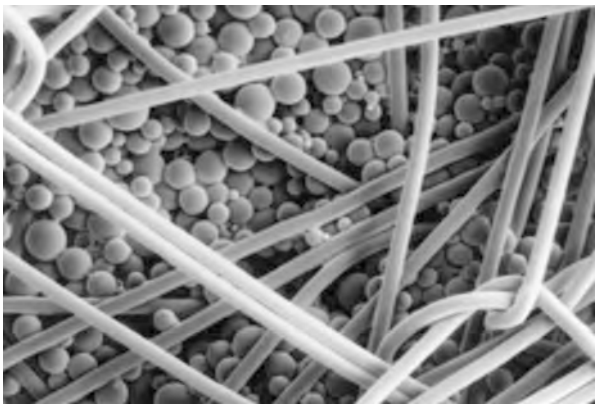

Fig. 7 Fabric coated with phase change microcapsules. (Outlast Technologies LLC, http://www.outlast.com/en/applications/. Reprint with permission)

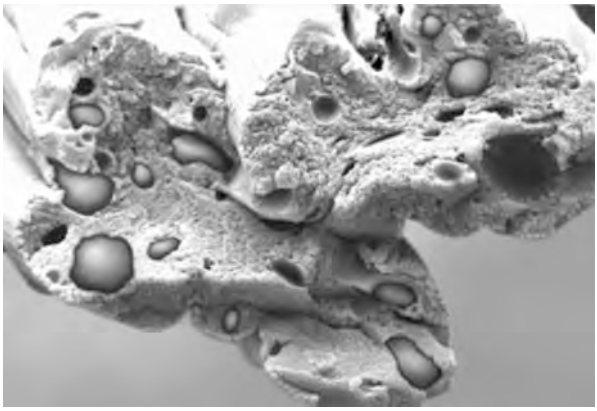

Fig. 8 Fiber embedded with phase change microcapsules. (Outlast Technologies LLC, http://www.outlast.com/en/applications/. Reprint with permission)

and stores it in the Outlast microcapsules; and (4) when the human body starts to cool, the stored heat is released back to the body. This reversible temperature-regulating effect keeps the wearer's body temperature stable without big fluctuation from the comfortable temperature.

Three methods have been used by Outlast Technologies to incorporate the Thermocules microcapsules into fabrics for different applications. The first method is a coating method as shown in Fig. 7, in which a large amount of microcapsules is incorporated. The microcapsules can be coated onto different fabric surfaces such as nonwoven bedding, jacket lining, and mid-layers of multiple-layer fabrics. The coated temperature-regulating fabrics are normally used in products that are not in direct contact with the skin such as outerwear, footwear, bedding, and seating.

The second method is to incorporate microcapsules into fibers as shown in Fig. 8. The microcapsules have been incorporated into acrylic, rayon, and polyester for different applications by different spinning methods such as wet spinning and bicomponent melt spinning. The fabricated fibers are then made into yarns and fabrics. Because the microcapsules are inside the fibers, they do not significantly

Fig. 9 Fabrics coated with phase change materials by printing. (Outlast Technologies LLC, http://www.outlast.com/en/applications/. Reprint with permission)

affect the handle of the fabric. The fabricated fabrics have been used in products next or close to the human skin. The temperature-regulating acrylic fabrics have been used in socks, hats, and sweaters. The temperature-regulating rayon fabrics have been used in underwear, shirts, dresses, sleepwear, work wear, and sportswear. The temperature-regulating polyester fabrics have been used more widely in many clothes, bedspreads, and pillows.

A recently developed method to incorporate microcapsules into fabrics by Outlast Technologies LLC is through printing. After the printing, the microcapsules are infused into the space in between yarns as shown in Fig. 9. The printing method does not affect the handle, wicking, wicking durability, and drape of the fabric. This technology is ideal for brands seeking a larger volume program using novel fabrics. Because the phase change microcapsules are infused into the space in between yarns, the fabrics can be used for products worn next to the skin and are good for casual and sportswear markets.

Outlast Technologies LLC has filed many patents on the phase change textile products. The typical patents are tabulated in Table 2. For detailed information on the specific temperature-regulating products, please refer to the patents.

Dive Suites

The US Navy incorporated PCMs into divers' dry suits to enhance the thermal protection of divers from extremely cold water. Foam materials were used as the thermal insulator, in which phase change microcapsules were incorporated. The thermal performance of the temperature-regulating dry suits was evaluated in comparison with dry suits without phase change microcapsules. Figure 10 shows the assessment of the dry suits. The results indicated that the temperature-regulating dry suit showed improved thermal performance at shallow depths. The thermal performance decreases with increasing diving depth. Nuckols [39] developed an analytical model to predict the thermal performances of the temperature-regulating dry suits in simulated ocean environments. The results showed that the dry suits

Table 2 The typical patents of phase change textiles by Outlast Technologies LLC

Inventor	Title	Patent number
Perry, B. T., Pushaw, R. J., Wyner, D. M., and Zuckerman J. L.	Energy-absorbing fabric coating and manufacturing method	US20020193028
Pushaw, R. J.	Foam article containing energy-absorbing phase change material	US1997006424
Pause, B.	Interactive thermal insulating system having a layer treated with a coating of energy-absorbing phase change material adjacent to a layer of fibers containing energy-absorbing phase change material	US1998015892
Hartmann, M. H., and Worley, J. B.	Cellulosic fibers having enhanced reversible thermal properties and methods of forming thereof	US20130273365
Hartmann, M. H.	Stable phase change materials for use in temperature-regulating synthetic fibers, fabrics, and textiles	US20020054964
Heimbach, J., and Magill, M. C.	Containers and packagings for regulating heat transfer	US20070000484
Gail, D. J., Aharon, E., and Hartmann, M. H	Coated articles formed of microcapsules with reactive functional groups	US20070173154
Hartmann, M. H., Eyal, A., and Raz, C.	Microcapsules and other containment structures for articles incorporating functional polymeric phase change materials	US20090035557
Hartmann, M. H., Roda, G., and Eckert, G.	Articles having reversible thermal properties and moisture wicking properties	US20080233368
Hartmann, M. H., and Henshaw, M.	Fibers and articles having combined fire resistance and enhanced reversible thermal properties	US20110117353
Hartmann, M. H., Roda, G., and Eyal, A.	Thermal-regulating building materials and other construction components containing phase change materials	US8221910
Hartmann, M. H., and Henton, D. E.	Articles containing precisely branched functional polymeric phase change materials	US20120225290

with phase change microcapsules were able to reduce diver heat loss during the initial phase by releasing the stored latent energy in the microcapsules. After a long time of diving, the PCMs in the microcapsule solidify. At that point the dry suit behaves as a conventional suit.

Protective Garments

Nonwoven protective garments can be used widely such as in asbestos abatement, pest control, transportation of hazardous chemical goods, and cleaning chemical

Fig. 10 The thermal protection in cold-water missions of a commercial dry suit system is being assessed (Reprint from Nuckols [39], Copyright © (2013), with permission from Elsevier)

facilities. Nonwoven fabrics can provide high barrier properties against the penetration of dust, liquids, and gas. However, at the same time, nonwoven fabrics limit the transfer of body heat out of the garment. Under strenuous activities, the body temperature may increase to above the comfort level to produce heat stress. The heat stress can lead to discomfort, fatigue, and reduced productivity and, in severe cases, risk the health and safety of the garment's wearer. Pause [40] filled PCMs into nonwoven fabrics and garments. He used the temperature-regulating nonwoven protective garments in pest control and treatment of hazardous waste. The test results indicated that the cooling effect of the PCM can delay the temperature rise and hence limit the moisture rise in the microclimate. As a result, the wearing time of the garment can be extended without the occurrence of heat stress as a serious health risk. The garments can be worn for a long time period without the occurrence of heat stress. In addition to be used as chemical protective suits, the temperature-regulating nonwoven fabrics and garments can be used in surgical gowns, uniforms, and garments to improve thermo-physiological wearing comfort.

Cooling Vests, Helmets, Cowls, and Neck Collars

Colvin and Bryant [41] invented a cooling vest that contains pouches containing PCMs. The covering area of the pouches is less than the surface area of the vest.

In this way, perspiration can evaporate and contribute to the overall comfort of the wearer. Macroencapsulated PCM may be incorporated into the pouch. The diameter of the macrocapsules is in the range of 2–4 mm. The phase change octadecane in the macrocapsules has phase change in the range 26–28 °C. The fabric has honeycomb structure which keeps the macroencapsulated PCMs remaining within designated cells of the honeycombs. The macrocapsules can be recharged without using refrigeration. Other PCMs with different phase change temperatures may also be used. In addition to vest, these cooling effect fabrics can be used in helmet liners, cowls, and neck collars in military and civilian textiles.

Medical Products

PCM-treated fabric and garments can be used in surgical apparel, patient bedding materials, bandages, and other medical and hygiene products such as surgical gauze, nappies, and incontinence products [3]. The temperature-regulating surgical clothing can increase the thermophysical comfort of doctors. As bedding fabrics such as mattress cover, sheets, and blankets, the temperature-regulating textiles can improve the comfort of patients.

Buckley [42] invented a cooling therapeutic blanket for cooling febrile patients. The PCM has a phase change temperature below normal skin temperature. A careful selection of the PCMs with proper phase change temperatures avoided the danger of overcooling the patient. Based on a similar mechanism, heating blankets were developed for gently and controllably reheating hypothermia patients. The second product invented by Buckley [42] is temperature-regulating elastic wraps or orthopedic joint supports. Because of the temperature-regulating effect, these products can provide hot or cold therapy combined with a supporting bandage for joints or muscles. Another product is an artificial skin or wound fabric that can protect of wound from infection while simultaneously applying hot or cold therapy.

Aerospace Textiles

The original research on PCMs was promoted by their potential applications in aerospace as shown in Fig. 11. At the beginning, Johnson Space Center in Texas developed a garment which has running water through small channels in the space suit. The space suit requires large quantity of energy to deliver the water and it needs laborious maintenance. Later, the engineers at Johnson Space Center in collaboration with private industry developed PCMs for space suits and astronaut gloves. These space suits and gloves can self-regulate temperature according to environmental temperature. In the 1980s, they used a lithium chloride PCM for the heat management of instruments used in space. The PCMs were not used in space suit because it is not suitable for garment applications. Later, linear alkyl hydrocarbons and PEG were used as the PCMs in space suit, which can regulate

Fig. 11 Space suits developed by NASA (Outlast Technologies LLC, http://www.outlast.com/en/applications/. Reprint from Nuckols [39], Copyright © (2013), with permission from Elsevier)

astronauts' body temperature by responding to the space suit environment temperature. In addition to space suit, gloves were also developed using similar PCMs.

Building Materials

Phase change textiles can be used in building structures to regulate the temperature change of buildings between daytime and nighttime. Phase change textiles may be applied to roof or ceiling. At night, the temperature is cold; the phase change textile roof embedded in the building can solidify and release heat. At daytime, the temperature is high; the phase change textiles can liquefy and cool down the building. In addition to building structures, PCMs may be used in blinds and curtains for reduction of the heat flux through windows.

Ival O. Salyer [43] invented cementitious hollow core building block having PCMs for increasing the temperature-regulating effect of lightweight construction walls. The PCMs may be in a plastic bag, a metallic pouch, a plastic box, and a glass box, or the PCMs may be simply poured into the hollow core space. The polyolefin is either a cross-linked high-density polyethylene or a high-density polyethylene/ethylene vinyl acetate blend. Neuwald and Kellermann [44] fabricated PCMs in discontinuous portions of a suitable shape, in the form of strips or tiles for building use. The space in between the strips is filled with an intermediary material so as to enable heat conduction to and from the heat accumulating material to the metal front panel and/or between the portions of the heat accumulating material. In another invention, PCM is applied to the entire surface of the backside of the metal front panel. In this way, the thermal capacity of the building component is maximized for a chosen thickness and sort of heat accumulating material. The building materials may be used in the outer wall and/or roof construction, thereby obtaining a slower temperature change of the roof and wall. The inventor reported that because the phase change buildings can reduce the thermal footprint of the building, the delectability of the building can also be reduced for heat-sensitive weapons such as heat-seeking missile [3].

Automotive Textiles

Pause [45] invented a method of using PCM to regulate the temperature and improve the comfort of the interior of an automobile. During summer, the temperature inside a car can be very high. Air-conditioning system is normally used to cool down the interior temperature. However, it requires a large amount of energy. In winter, heater has to been used to increase the temperature inside. Pause's research results showed that phase change microcapsules containing hydrocarbons in headliner and seating materials can regulate the interior temperature by 2–4 °C [45].

Development Trend

Phase change textile products have been used in many applications. The manufacturing and temperature-regulating performance of these phase change textiles have been intensively studied. In addition to temperature regulating, moisture management clothing is another critical aspect of smart clothing. Two types of breathable fabrics which can regulate the passing of air and water molecules have been developed. One type of the breathable fabrics is made of hydrophilic polyether-ester block copolymer (SympaTex from SympaTex Technologies GmbH). Another type of the breathable fabric is made of block polyurethane (DiAPLEX from Mitsubishi Heavy Industries). These fabrics can let air and water vapor pass through at a high temperature. At low temperature, the fabrics can block air and water vapor. Study on both thermal- and moisture-regulating materials may promote the development of new smart clothing that can manage thermal and moisture microclimate simultaneously.

Different application situations of phase change textiles have different requirements on the temperature-regulating effect. Some applications of phase change textiles have high frequency of temperature change, while others do not change temperature so often. If the temperature change is too quick, the heat of phase change textiles may not have enough time to release; therefore, the phase change textiles cannot function properly. The thermal transfer of the phase change textiles is also influenced by many factors such as the phase transformation of the PCMs used, the location of the phase change textiles in the garment, and the layer number and materials of the garment fabric. For optimal performance, various phase change textile products suitable for different applications should be developed.

The content of PCMs incorporated into textiles is low, which has limited the latent heat capacity and durability of phase change textiles for long-term use. Large amount of PCMs loading significantly affects the processability of the textiles such as fiber spinning and fabric coating. Although a larger amount of PCMs can be incorporated into foams as laminating fabrics, the applications of laminating foam fabrics are limited. In addition, PCMs may leach out of phase change textiles, which can significantly affect the handle of the textiles. It is expected that innovation in polymer processing can solve this problem in the future.

To obtain best temperature-regulating effect, more parameters need to be taken into consideration, such as the phase change temperature of PCMs, PCM quantity, coating methods, structure of the garments, temperature profile of the human body, and application environment of the clothing. The phase change temperature range needs to match the application temperature. Thin garments may have high heat conductivity, while thick garment may have low heat conductivity, which may promote or delay the temperature-regulating effect. The temperature at different parts of the human body and during different activities is also different. The heat produced by the human body at different physical activities also varies significantly. To obtain best performance, phase change textiles with different temperature-regulating performance for different activities and different parts of the human body may be developed.

Summary

Traditional fabrics using trapped air for thermal insulation. The functionality is to retain heat as long as possible. Phase change fibers and assemblies have a phase change transition at around human body temperature. They have the capability to keep the human body warm if it is cool; they also have the capability to keep the human body cool if it is hot by regulating the microclimate of the body skin.

PCMs such as linear alkyl hydrocarbons and PEG have been widely used in phase change fibers and assemblies. Thanks to the advancement in microencapsulation technologies in the last several decades, various phase change textile products have been successfully commercialized such as Outlast® from Outlast Technologies LLC, Thermasorb® and ComforTemp® from Frisby Technologies Inc., and schoeller®-PCM™ from Schoeller Textil AG. It is believed that phase change fibers and assemblies will continue to be a popular research area because of their more and more applications.

References

1. Zhang XX, Wang XC, Hu L (1999) Spinning and properties of PP/PEG composite fibers for heat storaging and thermoregulated. J Tianjin Inst Text Sci Technol 18:1–3
2. Tao XM (2001) Smart fibres, fabrics and clothing, vol 3. Woodhead, Cambridge, pp 34–36
3. Mattila HR (2006) Intelligent textiles and clothing, vol 3. Woodhead, Cambridge, pp 98–99
4. Vella CA, Kravitz L (2013) Staying cool when your body is hot. http://www.unm.edu/~lkravitz/Article%20folder/thermoregulation.html. Accessed 30 Oct 2013
5. Mondal S (2008) Phase change materials for smart textiles – an overview. Appl Therm Eng 28:1536–1550
6. Zhang XX et al (2005) Crystallization and prevention of supercooling of microencapsulated N-alkanes. J Colloid Interface Sci 281:299–306
7. Zhang XX et al (2005) Energy storage polymer/microPCMs blended chips and thermoregulated fibers. J Mater Sci 40:3729–3734
8. Jiang Y, Ding E, Li G (2002) Study on transition characteristics of PEG/CDA solid-solid phase change materials. Polymer 43:117–122

9. Li WD, Ding EY (2007) Preparation and characterization of cross-linking PEG/MDI/PE copolymer as solid-solid phase change heat storage material. Sol Energy Mater Sol Cells 91:764–768
10. Hu J et al (2006) Study on phase-change characteristics of PET-PEG copolymers. J Macromol Sci Part B: Phys 45:615–621
11. Zhang XX, Zhang H, Zhang L (1996) Crystallizable and heat-storage properties of PE-PEG block copolymers. Mater Rev 10:63–67
12. Zhang X (2001) Heat-storage and thermo-regulated textiles and clothing in smart fibres, fabrics and clothing edited by Xiaoming Tao. Woodhead, Washington
13. Vigo TL, Frost CM (1983) Temperature adaptable hollow fibers containing polyethylene glycols. J Coat Fabr 12:243–245
14. Vigo TL, Frost CM (1985) Temperature-adaptable fabrics. Text Res J 55:737–743
15. Bruno JS, Vigo TL (1987) Temperature-adaptable fabrics with multifunctional properties. AATCC Int Conf 1987:258–264
16. Vigo TL, Bruno JS (1987) Temperature-adaptable textiles containing durably bound polyethylene glycols. Text Res J 57:427–429
17. Bruno JS, Vigo TL (1994) Thermal properties of insolubilized polyacetals derived from non-formaldehyde crosslinking agents. Thermochim Acta 243:155–159
18. Choi JK et al (2004) Thermal storage/release and mechanical properties of phase change materials on polyester fabrics. Text Res J 74:292–296
19. Sánchez P et al (2010) Development of thermo-regulating textiles using paraffin wax microcapsules. Thermochim Acta 498:16–21
20. Bryant YG, Colvin DP (1988) Fiber with reversible enhanced thermal storage properties and fabrics made therefrom. US Patent 4756985, 1988
21. Shin Y, Yoo D, Son K (2005) Development of thermoregulating textile materials with microencapsulated phase change materials (PCM). II. Preparation and application of PCM microcapsules. J Appl Polym Sci 96:2005–2010
22. Salaun F et al (2009) Application of contact angle measurement to the manufacture of textiles containing microcapsules. Text Res J 79:1202–1212
23. Gomes NR, Vieira MV, Barros PC (2008) Microcapsules with functional reactive groups for binding to fibres and process of application and fixation. US Patent Appl 20080193761, 2008
24. Shin Y, Yoo DI, Son K (2005) Development of thermoregulating textile materials with microencapsulated phase change materials (PCM). IV. Performance properties and hand of fabrics treated with PCM microcapsules. J Appl Polym Sci 97:910–915
25. Worley J (2002) Micro-perforated temperature regulating fabrics, garments and articles having improved softness, flexibility, breathability and moisture vapor transport properties. US Patent 20020132091A1, 2002
26. Leskovsek M, Jedrinovic G, Elesini US (2004) Properties of polypropylene fibres with incorporated microcapsules. Acta Chim Slov 51:699–715
27. Zhang XX et al (2006) Structures, properties of wet spun thermo-regulated polyacrylonitrile-vinylidene chloride fibers. Text Res J 76:351–359
28. Magill MC, Hartmann MH, Haggard JS (2006) Multi-component fibers having enhanced reversible thermal properties and methods of manufacturing thereof. US Patent 6,855,422 B2
29. Jiang M et al (2008) Preparation of PVA/paraffin thermal regulating fiber by in situ microencapsulation. Compos Sci Technol 68:2231–2237
30. Sarier N, Onder E (2012) Organic phase change materials and their textile applications: an overview. Thermochim Acta 540:7–60
31. Pause B (2003) Nonwoven protective garments with thermo-regulating properties. J Ind Text 33:93–99
32. Sarier N, Onder E (2007) Thermal characteristics of polyurethane foams incorporated with phase change materials. Thermochim Acta 454:90–98
33. Bryant YG, Colvin DP (1994) Fabric with reversible enhanced thermal properties. US Patent 5366807, 1994

34. You M et al (2008) Effects of MicroPCMs on the fabrication of MicroPCMs/polyurethane composite foams. Thermochim Acta 472:20–24
35. Shim H, McCullough EA, Jones BW (2001) Using phase change materials in clothing. Text Res J 71:495–502
36. Bayés-García L et al (2010) Phase Change Materials (PCM) microcapsules with different shell compositions: preparation, characterization and thermal stability. Sol Energy Mater Sol Cells 94:1235–1240
37. Nelson G (2001) Microencapsulation in textile finishing. Rev Prog Color Relat Top 32:57–64
38. You M et al (2010) Effects of type and contents of microencapsuled n-alkanes on properties of soft polyurethane foams. Thermochim Acta 500:69–75
39. Nuckols ML (1999) Analytical modeling of a diver dry suit enhanced with microencapsulated phase change material. Ocean Eng 26:547–564
40. Pause BH (2003) Non-woven protective garments with thermo-regulating properties. US Patent 20060024486, 2003
41. Colvin DP, Bryant YG (1995) Microclimate cooling garment. US Patent 5 415 222, 1995
42. Buckley T (2001) Phase change thermal control materials, method and apparatus. US Patent 6 319 599, 2001
43. Salyer IO (1995) Building products incorporating phase change materials and method of making same. US Patent EP0830438 B1, 1995
44. Neuwald J, Kellermann F (2009) Building component based on a phase change material. Us Patent EP2239388 A1, 2009
45. Pause B (2005) Driving more comfortably with phase change materials. Tech Text Int 45:24–28

Part II

Interactive Textile Devices

Xiaoming Tao

Fiber-Based Wearable Electronic Circuits and Systems

11

Shu Lin

Contents

Introduction 256
Fiber Transistors 257
Fiber-Based Circuitry 259
Electronic Interfaces for Fiber-Based Sensor Arrays 261
Fiber-Based System 267
Intelligent Footwear System 267
Smart Cushion Cover 277
Summary 288
References 290

Abstract

Fiber-based wearable electronic circuits and systems are a very promising next-generation technology for human-computer interaction, long-term health monitoring, virtual reality, and other fields. The advancement of nanotechnology has made it feasible to build electronic devices directly on the surface or inside of single fibers, which have typical thickness of several to tens of microns. However, imparting electronic functions to porous, highly deformable, and three-dimensional fiber assemblies and maintaining them during wear represent great challenges from both views of fundamental understanding and practical implementation. This chapter primarily focuses on the elementary electronic devices of fiber-type transistor, as well as fiber-based transistor circuits. As an important tie between the bottom physical layer to the top system layer, the electronic interfaces of fiber-based elements and arrays have been also considered. Lastly, two prototypes of fiber-based wearable system, the intelligent

S. Lin (✉)
Institute of Textiles and Clothing, The Hong Kong Polytechnic University, Hung Hom, Hong Kong
e-mail: shu.lin@polyu.edu.hk; tclshu@polyu.edu.hk

© Springer Science+Business Media Singapore 2015

X. Tao (ed.), *Handbook of Smart Textiles*,
DOI 10.1007/978-981-4451-45-1_24

footwear system and smart cushion cover, are confronted, including the scheme plan, package, testing, and evaluation. Limitations of current materials, fabrication techniques, circuits, and systems concerning manufacturability and performance as well as scientific understanding that must be improved prior to their wide adoption have been also discussed.

Keywords
Wearable electronics • Fiber transistor • Fiber-based circuitry • Sensor array • Textile sensor • Readout approach • Intelligent footwear system • Smart cushion • Planter pressure monitoring • Sitting pressure monitoring

Introduction

There is substantial interest in the wearable electronic technology from the international academic and industry discipline. With the maturation of mobile Internet, technological advances of high-functioning, low-power processing chips, and so forth, close to wearable devices have been already from conceptualization to commercialization. New wearable devices continue to put forth. Google, Apple, Microsoft, Sony, and many other technology companies have also started to explore in depth in this new field. Next generation of wearable electronics demands that the systems directly be worn on soft and curved human body that is covered with highly extensible skins (with an average elongation from 3 % to 55 %). Fiber-based clothing systems are flexible, breathable, durable, and washable, which are the potential platforms of wearable electronics [1]. On the other hand, the rapid growth of nano-science and nanotechnology has accelerated the miniaturization process of electronic components. Electronic functions can be built on or inside a single fiber or fiber assemblies such as yarns and fabrics via well-established textile production processes.

The interdisciplinary development of textile technology and electronic engineering has enabled the combination of the strengths of each technology, the computing speed, and the computing ability of modern electronics, with the flexible, wearable, and continuous nature of fiber assemblies [2]. These fiber assemblies have many characteristics that are suitable to wearable electronics, such as softness and flexibility, that they can be deformed under small external force, large surface areas (about $10^{2–3}$ m^2/kg), porous structure, and structurally defined fiber orientation and packing density. Moreover, they exhibit excellent maintenance of structural integrity during daily wear (several millions of loading cycles) and washing (some 30 washing cycles according to AATCC standard). They show unique mechanical properties of three-dimensional deformation that they can be stretched, twisted, bent, or sheared; unique thermal property that their porous structure and large surface area can work as the insulator of external cold air and also the route of inside hot air and water vapor; and unique breathability especially in long-term wearing around curvilinear human skins. The fiber assembly structure has led to an outstanding fatigue resistance by two factors: the extremely small internal strain

even under a large deformation (the fatigue life is exponentially linked to the internal strain) and the high damage tolerance as catastrophic failure of the structure is prevented by the large number of fibers in the assemblies. Adding on electronic or photonic functions, especially sensing, actuating, communicating, and computing, to fibers or fabrics has been arousing a lot of interests for the potential applications of military garment devices, biomedical and antimicrobial textiles, and personal electronics [3]. Lightweight, flexible, and conformable textile substrates provide a carrier to develop sensors and other devices, integrated into the fabric-based network, to create large-area electronic systems [4]. The most important consideration regarding the realization of fiber-based wearable electronics is the development of sustainable flexible systems with high carrier mobility and excellent electrical performance and mechanical and environmental stability. Some other considerations include the connections among fibers, textiles, and electronics, particularly the electronic interfaces of fiber-based components and their arrays, which is a determinant bridge and an exclusive channel from the bottom physical layer to the top system layer.

This chapter shows the current condition of the fiber-based wearable electronic devices, circuits, and systems. It covers fiber transistors, fabric circuitry, readout interfaces for fiber-based resistive sensors and arrays, and fabric sensor-based smart systems of the intelligent footwear system and smart cushion cover.

Fiber Transistors

At present, the existed fiber transistors can be distinguished into two classes: fiber organic field-effect transistors (OFET) [5] and wire electrochemical transistors (WECT) [6], as seen in Fig. 1.

The former adopts on fiber four-layer cylindrical thin films [7] as insulator, conductor, and semiconductor layers, with insulating materials of inorganic oxides (i.e., SiO_2) or polymer dielectrics (such as poly-4-vinylphenol (PVP) [5] ~10 nF/cm^2) [8] and conductive materials for gates and contacts of metals and conducting polymers (such as aluminum and stainless steel wires, PDOT/PSS) [9]. Highly ordered single polymer fibers [10] were also used in this field. Another type of fiber transistor, named WECT, is fabricated by suspending two PDOT/PSS coated fibers in a cross way and creating an ionic contact by adding an insulating layer/drop of the liquid or gel electrolyte (>10 μF/cm^2) at the junction of fibers [11]. A comparison of the performance between the two types of fiber transistors is given in Table 1.

Some studies have followed up to invent organic electrochemical transistors with a high transconductance for biosensing applications [12] or to use single cotton fiber for sensing liquid electrolyte saline [13]. A fiber-based organic electrolyte-gated thin-film transistor based on poly(3-hexylthiophene) (P3HT) and imidazolium ionic liquids was able to operate in both field-effect and electrochemical operation modes and enabled both delivery of large currents or high speeds (<1 kHz) at low voltages [11]. As the fiber OFET requires precisely positioning and extremely smooth surfaced fibers due to its sensitivity to the gate insulator thickness, the channel length, and the

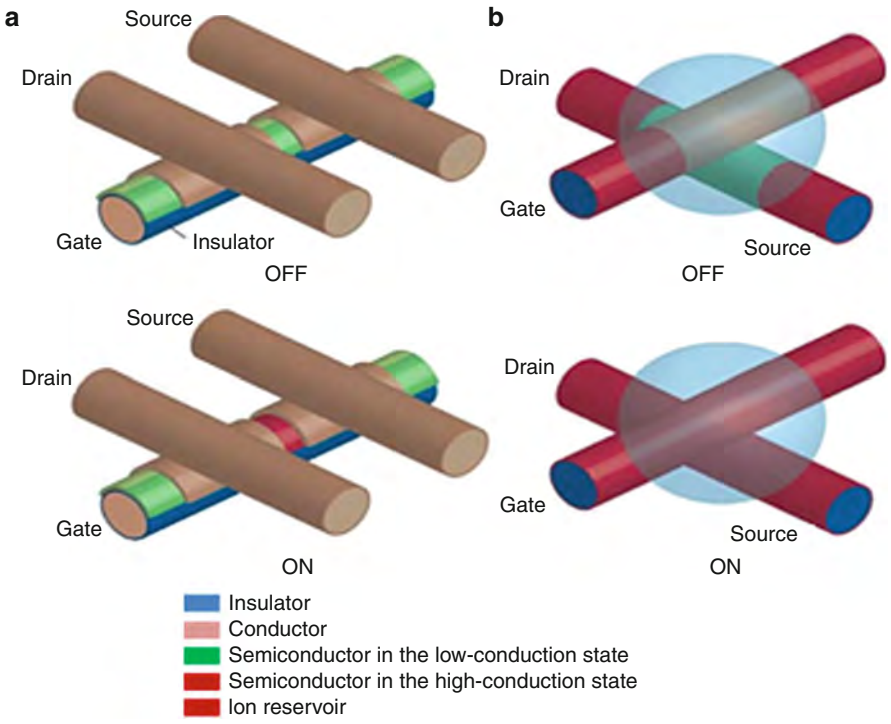

Fig. 1 Fiber transistors [6]: (**a**) fiber organic field-effect transistors (OFETs) and (**b**) wire electrochemical transistors (WECT) (Reproduced with permission [2], Copyright (2014), WILEY-VCH Verlag GmbH & Co. KGaA, Weinheim)

smoothness of the substrate surface for prevention of short circuits, WECT has more practical significance due to its extremely small affections by the local geometry and relative ease of manufacture [14]. The major disadvantage of WECT is the long response time and the consequent low switching frequency resulting from the electrodiffusion of ions within the solid electrolyte where the ionic charge carriers have very low mobility [6]. To overcome the frequency limitation of WECT would be a very important work in the future as the fiber transistors are basic building blocks of more complicated fiber-based electronics that should not be only constricted to quasi-static applications. One possible solution is scaling the dimensional, for example, making the on-fiber PDOT:PSS channel thinner; therefore, de-doping it requires a smaller number of ions [12], as the time characteristics of electrodiffusion processes scale with the inverse square of characteristic lengths [6]. Another improvement way is the synthesis of new materials, especially the conducting polymers with a higher capacity for storing charge, which is also the focus of present research on batteries and electrochemical capacitors, and further studies of the mechanisms of ion transport in conducting polymers. Moreover, ionic liquids and gels enabling higher voltage operations have the potential for higher performances which deserves exploration [12].

Table 1 A comparison of the performance between fiber OFET and WECT

Category	Fiber OFET	WECT
Mobility	>0.5 $cm^2 V^{-1} s^{-1}$[5] Up to 1.4 $cm^2 V^{-1} s^{-1}$	Very low
Operating voltages	About 9–20 V	0–1.5 V
On/off ratio	10^3–10^5	10^2–10^3
Advantages	Good electrical characteristics for many e-textile applications [5]	Very low operating voltages, relatively simple fabrication process, helpful for realization of analog and digital microelectronics directly into textile, and integration of electronic function on new carriers [11]
Disadvantages	High operation voltages, complex manufacturing process, poor stability when fibers are under mechanical stress [7], significant dielectric leakage, and poor reliability [5]	Long switch time (>4–5 s) [8] and long response time. It might limit WECT technology to quasi-static applications with very low frequencies [6]

Reproduced with permission [2], Copyright 2014, WILEY-VCH Verlag GmbH & Co. KGaA, Weinheim

Fiber-Based Circuitry

Printed electronics by inkjets or classical printing methods has great potentials to fabricate fabric circuitry. Another possible technology is weaving of conductive fibers and fiber-based electronic components. Figure 2 shows several reported fiber-based circuitry, including logic circuits based on WECTs [6], textile inverters made by weaving WECTs or fibers with TFT stack on them [8], and fabric-array memory device [15]. Because of the frequency limitations of WECTs, this type of fabric inverters and logic circuits made of Kevlar multifilament with coatings of PEDOT:PSS and BCB35, as well as electrolyte gel [8], exhibited a very long switch time (15–18 seconds), which restricted them for quasi-static applications. The fabric inverters using TFT fibers (SiN_x-coated Kapton fibers with amorphous silicon TFTs fabricated on the surface) [16] have solved this problem, as it uses conventional TFTs on fibers to obtain good performance. The fiber-based memory uses a high tellurium-content chalcogenide glass (GGT and GAST glass fiber), contacted by metallic electrodes internal to the fiber structure to achieve a difference with four orders of magnitudes between its on and off states, although it exhibited a temperature dependence of the threshold voltage [15]. Fabric circuitry has advantages of better integrations within textiles for a wide range of wearable applications. However, its development depends on innovations of fiber-based electronic components especially fiber transistors and relevant methods of integrating electronic-textile or conventional electronic components onto fibers and fabrics.

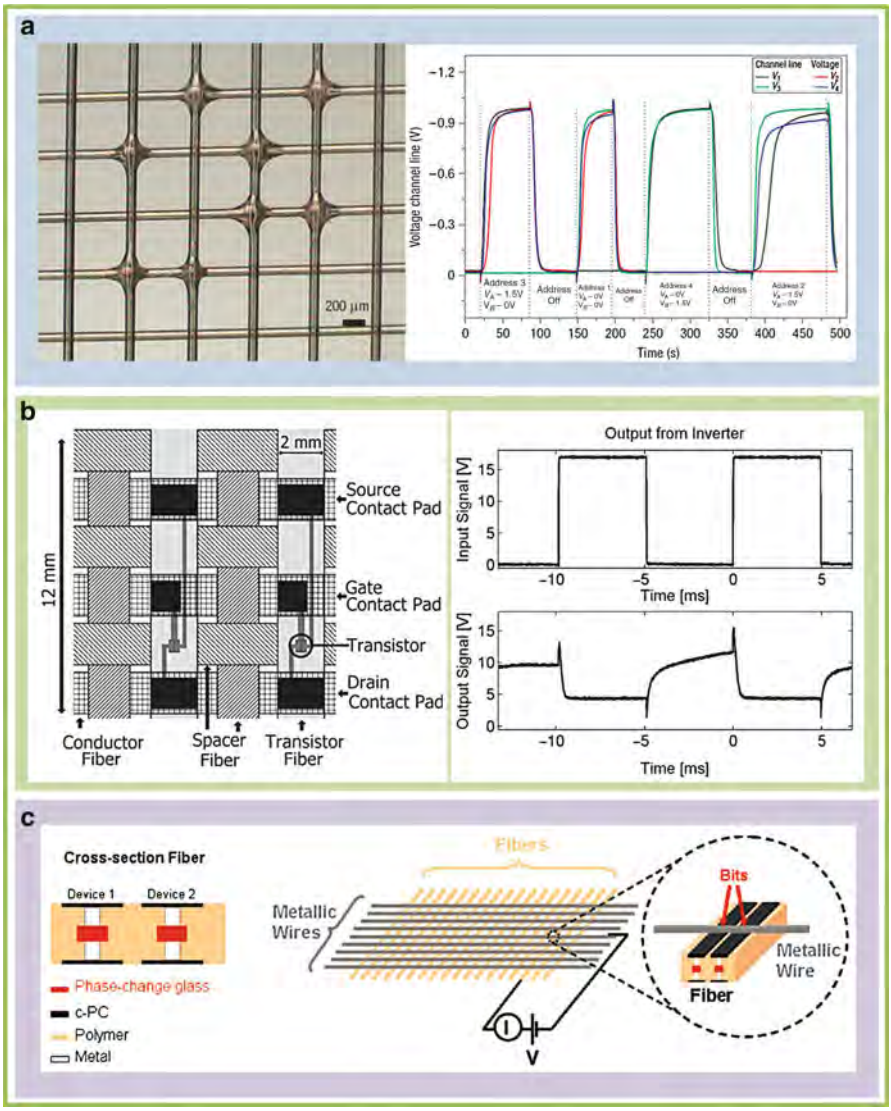

Fig. 2 Fiber circuitry [2]: (**a**) A binary tree multiplexer constructed from WECTs and their dynamic electrical characteristics, (**b**) a woven inverter circuit and its dynamic electrical characteristics, (**c**) fiber-based fabric-array memory device (Reproduced with permission [2], Copyright (2014), WILEY-VCH Verlag GmbH & Co. KGaA, Weinheim)

The major challenge of the fabric circuitry is lack of basic fiber-based electronic element with stable performance and outstanding flexibility due to the following two reasons: (1) The inadequate carrier mobility of present organic materials has limited the development of fiber transistors, which is also the key bottleneck of

organic electronics [14]. Therefore, new fibrous materials with high carrier mobility are worthwhile for search and study. (2) Highly conductive fibers and fabrics with outstanding flexibility and stretchability are still far below the requirements of wearable large-scale circuits, as they are the essential conductive parts of the fabric antenna, wearable electronic connector, and super capacitor for wearable energy storage. The recently developed graphene fibers, PEDOT:PSS fibers, and others may have potentials to address this issue. Another challenge refers to the packaging, integration, and connection of electronic-textile components with other fabric and electronic parts. These packages and connections should be flexible as well as robust, which can sustain the friction, deformation, and environmental variations during the assemblage and daily wearing. However, in many practical applications, failure of these package and connections has been reported as a major problem in this area, like cracking of fiber electronics resulting from poor elongation and bending properties, or connection failure in harsh environments [14]. To go further, the electronic-textile connectors are expected to provide both robust mechanical and electrical connections, hence to enhance the overall robustness of the fiber-based electronics.

Electronic Interfaces for Fiber-Based Sensor Arrays

Fiber-based resistive sensors, due to their good wearability and stability, low cost, and ease to be interfaced by readout circuits, are widely practiced in various fields, e.g., physical or physiological monitoring and biomedical and environmental analysis. Their arrays have been increasingly adopted in a number of applications, like wearable electronics, which have been regarded as a promising approach to monitor patients out of the hospital and to lessen the burden on public healthcare systems in the care of increasing patients with chronic diseases and elderly people. Medium- or large-scale resistive sensor arrays are needed, together with low-complexity readout circuits, which help obtain a good reliability, low-power consumption, small physical dimension and low weight, and in sequence a long service life and an acceptable wearing comfort.

Readout strategies for resistive sensor arrays can be, in general, subdivided into three categories: transistor/diode controlled approach (TDCA) [17], multiplexer- and op-amp-assisted approach (MOAA) [18], and incidence matrix approach (IMA) [19]. Nevertheless, these approaches have contributed to a noticeable complexity in circuits, especially for large-scale arrays, as they require a considerable number of additional electrical components (transistors, diodes, multiplexers, switches, op-amps, current sources, A/D converters (ADCs), etc.). Moreover, measurement errors have not been minimized, due to the presence of cross-talk currents that have not been eradicated and unexpected resistances of additional electrical components.

This part shows a comparison of principles and performances among TDCA, MOAA, IMA, and RMA for 3×3 sensor arrays on a microcontroller-based

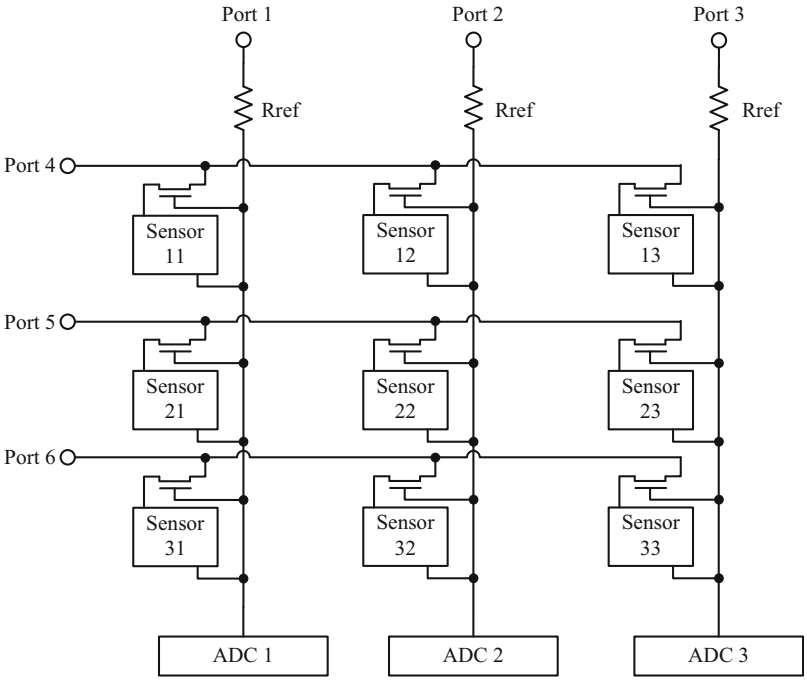

Fig. 3 Schematic of TDCA for readout of a 3 × 3 resistive sensor array on a microcontroller-based platform (Ports 1 ~ 6 are connected to I/O ports of the microcontroller, ADCs 1 ~ 3 are embedded ADCs of the microcontroller. For example, to read sensor 11, ports 1 ~ 6 can be set to 1 0 0 0 1 1 to enable sensor 11 by providing a high level voltage to its corresponding transistor.) (Reproduced with permission [22], Copyright 2014, IEEE)

wearable platform. Figure 3 shows a schematic of the TDCA, where an additional transistor (or a diode) is added in series with each sensor, to guarantee that there are no cross-talk currents flowing across multiple sensors [17]. MOAA requires multiplexers to control scanning and reading of sensors. Figure 4 shows a voltage feedback method of MOAA, where the op-amp and switch form a loop to feedback output voltage on all columns except the enabled one, so that other sensors in the selected row are at the same potential and ideally currents cannot flow across them [20]; hence, the cross-talk currents are eliminated. Another major category of MOAA is the virtual ground technique/zero potential method [18], a popular method for readout of resistive sensor arrays with a high reading rate, which uses virtual ground of op-amps in negative feedback and additional multiplexers to suppress cross-talk currents flowing across one sensor to another. At IMA as shown in Fig. 5, interconnections are placed between adjacent sensors. It estimates the internal resistance distribution based on voltage measurements on its boundary by current injections, which is similar to EIT (electrical impedance

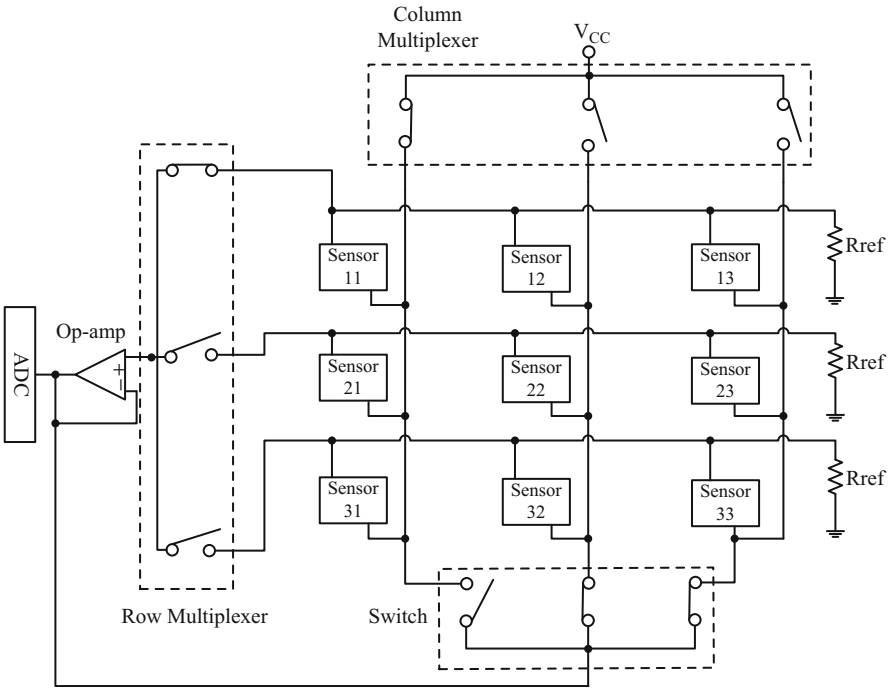

Fig. 4 Schematic of MOAA (a circuit based on the voltage feedback method) for readout of a 3 × 3 resistive sensor array on a microcontroller-based platform (The row and column multiplexers and the switch are connected and controlled by I/O ports of the microcontroller. The ADC is an embedded ADC of the microcontroller. Sensor 11 is selected for readout, and sensors 12 and 13 are disabled without currents.) (Reproduced with permission [22], Copyright 2014, IEEE)

tomography) [21]. Fundamental equations for the circuit in terms of the injecting currents, incidence matrix, sensor resistance, and border voltages can be dealt with by Kirchhoff's and constitutive laws and solved by a symbolic linear reduction to obtain the resistance of each sensor [19]. Figure 6 shows the new approach RMA for readout of resistive sensor arrays, which establishes resistance matrix equations of sensor arrays and identifies sensor resistances by solving the matrix equations [22]. Detailed information of RMA is listed below.

To accomplish a unique solution, that is, a unique set of sensor resistances, a group of standard resistors have been added in the first row; see Fig. 6. Then matrix E becomes $(e_1, \cdots, e_i, \cdots, e_m, e_{m+1})$, and e_i turns to a $(m + 1) \times 1$ vector $(p_1, \cdots, p_i, \cdots, p_m, p_{m+1})^{\mathrm{T}}$. Therefore, $R_{11}, \cdots, R_{1j}, \cdots, R_{1n}$ in fundamental solution (4) are restricted to the unique resistances of $R_1, \cdots, R_j, \cdots, R_n$, and a unique solution representing sensor resistances can be obtained in Eq. 1.

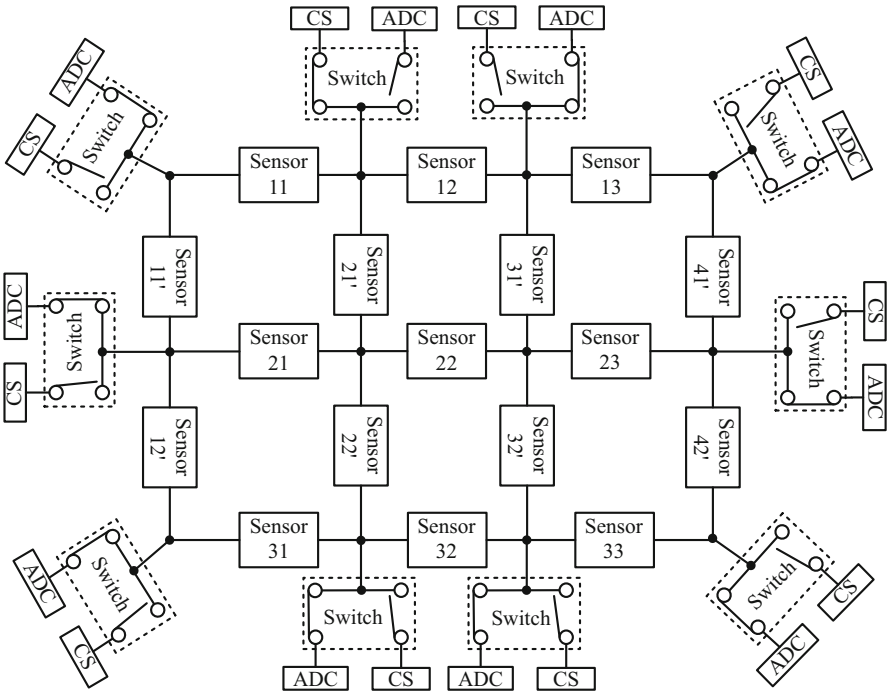

Fig. 5 A distributed sensor array using IMA for conductivity identification on a microcontroller-based platform (These ADCs include embedded ADCs of the microcontroller and external ADCs if needed. The CS components are current sources.) (Reproduced with permission [22], Copyright 2014, IEEE)

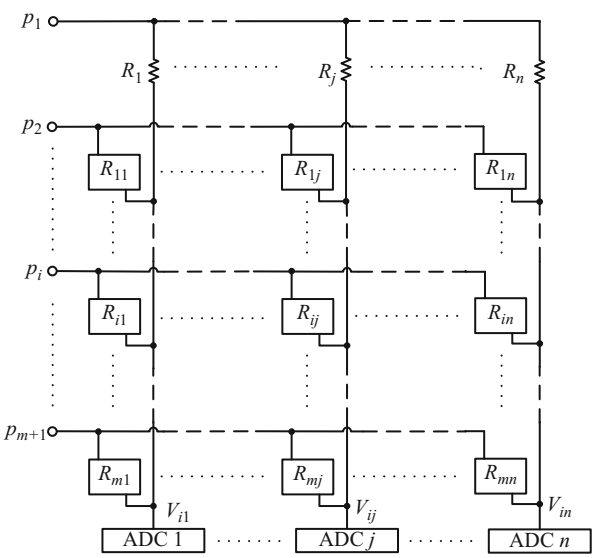

Fig. 6 Schematic of an $m \times n$ sensor array plus n standard resistors on a microcontroller-based platform using RMA method (p_i pins are connected to I/O ports of the microcontroller and ADCs $1 \sim n$ are embedded ADCs of the microcontroller) (Reproduced with permission [22], Copyright 2014, IEEE)

$$\begin{bmatrix} R_{11} & \cdots & R_{1j} & \cdots & R_{1n} \\ \vdots & \ddots & \ddots & \ddots & \vdots \\ R_{i1} & \ddots & R_{ij} & \ddots & R_{in} \\ \vdots & \ddots & \ddots & \ddots & \vdots \\ R_{m1} & \cdots & R_{mj} & \cdots & R_{mn} \end{bmatrix}$$

$$= \begin{bmatrix} \dfrac{\frac{V_{21}}{V_{CC}-V_{21}}+1}{\left(\frac{V_{11}}{V_{CC}-V_{11}}+1\right)}R_1 & \cdots & \dfrac{\frac{V_{2j}}{V_{CC}-V_{2j}}+1}{\left(\frac{V_{1j}}{V_{CC}-V_{1j}}+1\right)}R_j & \cdots & \dfrac{\frac{V_{2n}}{V_{CC}-V_{2n}}+1}{\left(\frac{V_{1n}}{V_{CC}-V_{1n}}+1\right)}R_n \\ \vdots & \ddots & \ddots & \ddots & \vdots \\ \dfrac{\frac{V_{(i+1)1}}{V_{CC}-V_{(i+1)1}}+1}{\left(\frac{V_{11}}{V_{CC}-V_{11}}+1\right)}R_1 & \ddots & \dfrac{\frac{V_{(i+1)j}}{V_{CC}-V_{(i+1)j}}+1}{\left(\frac{V_{1j}}{V_{CC}-V_{1j}}+1\right)}R_j & \ddots & \dfrac{\frac{V_{(i+1)n}}{V_{CC}-V_{(i+1)n}}+1}{\left(\frac{V_{1n}}{V_{CC}-V_{1n}}+1\right)}R_n \\ \vdots & \ddots & \ddots & \ddots & \vdots \\ \dfrac{\frac{V_{(m+1)1}}{V_{CC}-V_{(m+1)1}}+1}{\left(\frac{V_{11}}{V_{CC}-V_{11}}+1\right)}R_1 & \cdots & \dfrac{\frac{V_{(m+1)j}}{V_{CC}-V_{(m+1)j}}+1}{\left(\frac{V_{1j}}{V_{CC}-V_{1j}}+1\right)}R_j & \cdots & \dfrac{\frac{V_{(m+1)n}}{V_{CC}-V_{(m+1)n}}+1}{\left(\frac{V_{1n}}{V_{CC}-V_{1n}}+1\right)}R_n \end{bmatrix} \tag{1}$$

In Eq. 1, R_j is the resistance value of the standard resistor in the jth column and first row and $V_{(i+1)j}$ represents the potential detected by ADC j when the effective voltage combination is e_{i+1} ($p_{i+1} = 0$, others $= 1$), the $(i + 1)$th column of E. By this approach, sensor resistances can be accurately determined in arrays where multiple cross-talk currents are allowed.

Table 2 gives a comparison of circuit complexity among TDCA, MOAA, IMA, and RMA on a microcontroller-based wearable platform. Except the commonly used microcontroller, MOAA needs several multiplexers, switches, op-amps, and resistors, which increase the circuit dimension and weight. IMA also causes an enhanced circuit complexity due to its requirement of a number of diverse electrical components. RMA accomplishes the lowest circuit complexity on a microcontroller-based wearable platform, which needs a microcontroller and n resistors only; therefore, it is more appropriate for wearable electronic applications.

Table 3 gives a comparison of error sources among TDCA, MOAA, IMA, and RMA. The previous two approaches utilize additional transistors or multiplexors and op-amps to eliminate cross-talk currents, and their cross-talk errors can be really small if circuits are optimally configured. Their errors mainly come from extra resistances and currents of those additional electrical chips. In principle, IMA and RMA have minimized cross-talk errors that are caused by cross-talk currents, as they allow and take advantages of cross-talk currents (currents flowing across multiple sensors) in arrays to establish matrix equations to solve sensor resistances.

Table 2 Comparison of circuit complexity among TDCA, MOAA, IMA, and RMA for readout of m × n sensor array on a microcontroller-based wearable platform

Approach	Number of required electrical components							Complexity ranking[a]
	Microcontroller /control circuit	External ADC	Multiplexer/ switch	Op-amp	Transistor	Current source	Resistor	
TDCA	1 (including on-chips resources of embedded ADCs and I/O ports)	0	0	0	$m \times n$	0	n	Medium
MOAA		0	Several[b]	Several	0	0	m	High
IMA		Several[c]	Several[d]	0	0	Several	0	High
RMA		0	0	0	0	0	n	Low

Reproduced with permission [22], Copyright 2014, IEEE

[a]The complexity ranking was estimated by the number and type of required electrical components

[b]Multiplexers and switches connected to V_{CC} and ground can be replaced by I/O ports of the microcontroller. But there are still some multiplexers/switches that cannot be avoided, such as those connected between op-amps and sensors

[c]External ADCs are needed if on-chip ADC resources are inadequate

[d]Multiplexers can be used for multiplexing of limited ADC resources, in which cases the number of external ADCs can be reduced

Table 3 Comparison of error sources among TDCA, MOAA, IMA, and RMA

Approach	Cross-talk error	Error sources
TDCA	Cross-talk currents can be eliminated by transistors. Cross-talk errors are very small	Errors are caused by low precision of ADCs and on-resistance of the transistor/diode, as the measured resistance is a sum of the sensor's resistance and transistor/diode's on-resistance
MOAA	Cross-talk currents are minimized by control of additional chips. Cross-talk errors can be very small under optimal circuit configurations	Errors are caused by nonideality of op-amps, multiplexers' cross-leakage currents and on- resistances of switches and multiplexers, and low precision of ADCs
IMA	Although cross-talk currents are allowed, sensor resistances can be calculated accurately	Errors are caused by low precision of ADCs and current sources and inadequate scanning rate
RMA	Although cross-talk currents are allowed, sensor resistances can be solved accurately	Errors are caused by low precision of ADCs and reference standard resistances and inadequate scanning rate

Reproduced with permission [22], Copyright 2014, IEEE

A detailed evaluation of cross-talk error of RMA is given in part C of Section III. The difference between RMA and IMA includes:

1. Array structure: IMA forms a mesh-like network, while RMA follows a conventional column-row structure.
2. Hardware complexity: IMA needs a large number of ADCs and current sources.
3. Computing complexity: the procedures and methods for establishing and solving the matrix equations are different, where IMA costs a large number of computing cycles while RMA costs less.

Fiber-Based System

Intelligent Footwear System

A family of soft pressure sensors has been recently developed by the authors' group using conductive textile fabric sensing elements. The pressure sensor (Fig. 7) was fabricated by adhering a conductive sensing fabric with conductive yarns and a top and bottom conversion layer, which were prepared by molding of silicon rubbers of varied Young's modulus beforehand. A knitted fabric coated with carbon black-filled silicon was used as the strain sensing element. It has a strain gauge factor of approximately 10 or above and excellent fatigue resistance (>100,000 cycles) for strain up to 40 %. The sensor measurement range is from 10 Pa to 800 kPa, suitable for a wide variety of human-apparel interfaces, such as loosely fit garment, pants for sitting, gloves, sleeping garments, and walking/running shoes. The accuracy is 5 %

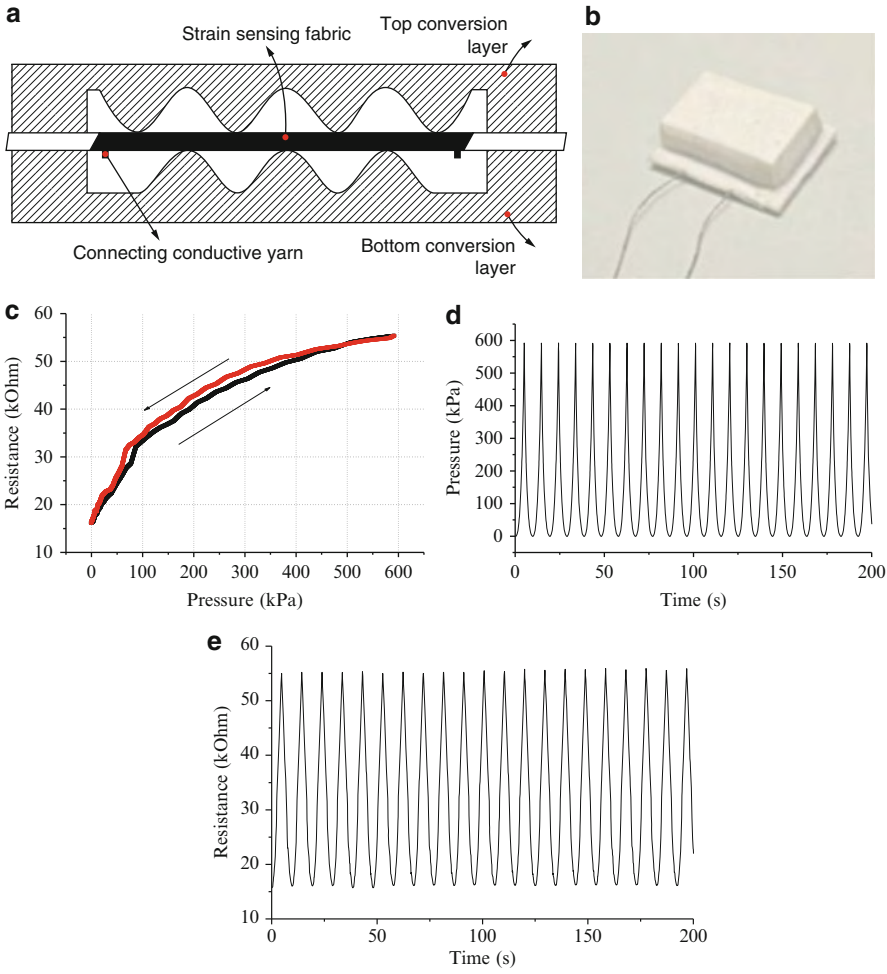

Fig. 7 Textile pressure sensor. (**a**) Schematic diagram of the structure of the pressure sensor (*side view*). (**b**) Package outlook. (**c**) Typical pressure-resistance curve of fabric pressure sensor. (**d**) Pressure against time in a cyclic loading test. (**e**) Resistance against time in a cyclic loading test (Reproduced with permission [27], Copyright 2010, IEEE)

and zero drift less than 5 %. The sensor is packaged by silicon rubber so that moisture and dust will not affect its performance, as shown in Fig. 7b. It is soft, which is essential for comfort consideration in daily activities. The second obvious advantage is its high sensitivity. Figure 7c is a resistance-pressure curve of these textile pressure sensors, which is typically nonlinear but with a reasonable repeatability. A higher sensitivity is helpful for the interface circuits to get a higher accuracy and resolution. The sensing fabric has been tested in a 100,000-cycle loading test, where it shows a long service time, which is very essential for shoes that should be worn for a long period. Figure 7d, e illustrates the responses (pressure

and resistance) of a fabric pressure sensor plotted against time in a cyclic loading test. These textile pressure sensors can be also used in other wearable applications.

Several textile pressure sensors are connected in an "n + 1" line structure to construct a sensor array. One line is connected to each sensor as the "1" ground line of the senor array. Another line of each sensor is the output as the *nth* signal line for the sensor array that contains n sensors. By combination of several textile pressure sensors, the sensor array is able to measure the pressure on a single point region, as well as the distributions. In this prototype, a six-sensor array was used to construct a sensor array in "6 + 1" line structure.

Sensor Position Selection

The sole of foot can be divided into 15 areas, as heel (area 1–3), mid-foot (area 4–5), metatarsal (area 6–10), and toe (area 11–15), as shown in Fig. 8. These areas support most of the body weight and adjust the body balance. The measured force at these positions can be used to derive physiological, structural, and functional information of the lower limbs and whole body. In order to reduce the system complexity, six positions (see Fig. 9) were selected at heel and metatarsal areas in the first prototype shoe, because these areas have a higher pressure during normal activities of children and young and old adults. Exact locations of six sensors were determined by depth shape of the subject's foot in soft model. Bamberg et al. [23] utilized 5 sensors at the positions of the heel, metatarsal, and hallux to achieve a clinical gait analysis. Pappas et al. [24] presented a gait-phase detection system using three sensors underneath the heel and at the metatarsal areas. Six sensors at the heel and metatarsal positions are adequate for such clinical investigation as gait

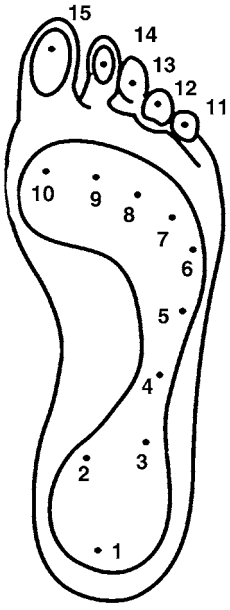

Fig. 8 Foot anatomical areas (Reproduced with permission [27], Copyright 2010, IEEE)

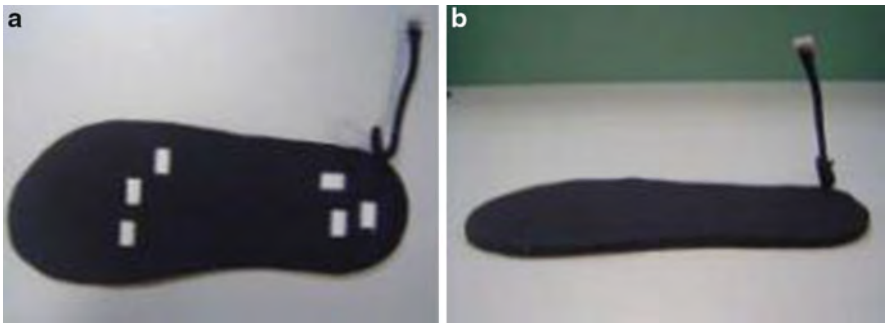

Fig. 9 Insole and its package. (**a**) Textile sensors with bottom layer. (**b**) Insole (Reproduced with permission [27], Copyright 2010, IEEE)

analysis. For sports and fitness, the Nike + iPod Sport Kit used just one sensor in the mid-foot to measure the wearer's pace, distance, and energy consumption during running [25]. The Adidas 1 running shoe uses one sensor at the heel position to provide compression measurement for adjusting to running situation [26]. Hence, six sensors are sufficient for sport or fitness assessments. Ideally adding additional sensors at hallux and mid-foot positions will enlarge the application scopes. As the textile sensor is relatively cheap and has a good fatigue resistance, it is easy to add more sensors in other applications.

Soft Circuit and Insole Package

A polyimide film circuit board was used to fabricate the sensing array in a foot shape. Six block positions, signal paths, ground paths, and connectors are lined out in the soft circuit. Six textile sensors are adhered at the corresponding positions of the soft circuit. Three are put in the forefoot, and the other three are placed in the heel. Conductive yarns from each sensor are mechanically connected and adhered with the soft circuit, which is sandwiched by soft foam layers at the top and bottom. The half and whole integrated insole can be seen in Fig. 9a, b, respectively. A data bus with a proper connector is adhered with the soft circuit and packaged together with the insole.

Temperature and Humidity Effect

The effects of temperature and humidity were measured on the sensing element, that is, the fabric sensor. The resistance change caused by humidity change from 40 % to 90 % is about 2 %, which is very small. Temperature compensation is necessary for an environment with significant temperature variation. However, as the insole temperature was almost constant in this investigation, the compensation was not incorporated.

Data Acquisition and Processing

A wearable, wireless data acquisition system was developed as an electronic interface for the resistive textile sensors. Figure 10 shows the data acquisition

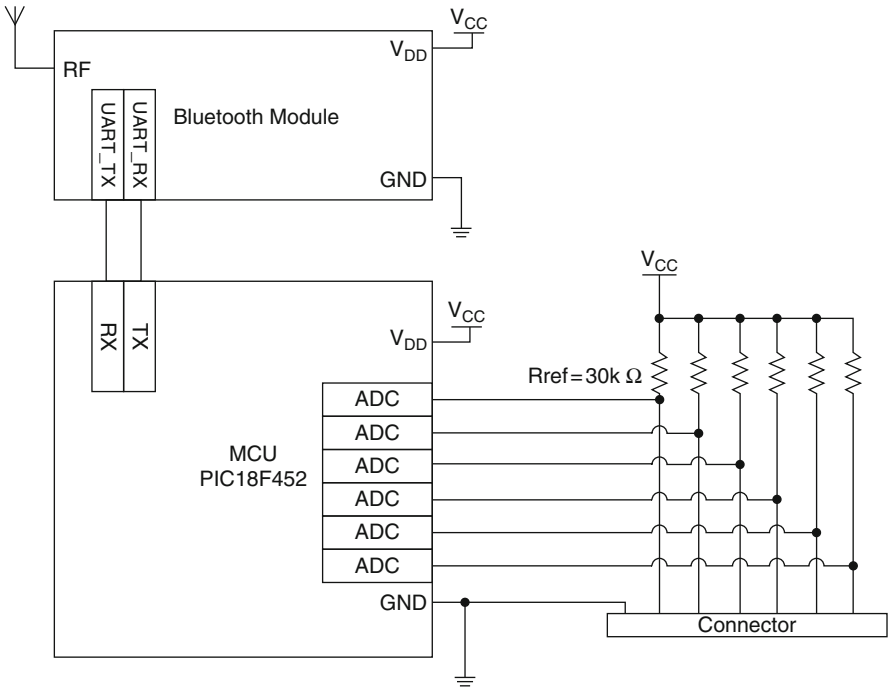

Fig. 10 Data acquisition system diagram (Reproduced with permission [27], Copyright 2010, IEEE)

system diagram. Through the connector, voltage signals on the sensors are extracted from voltage dividers ($R_{ref} = 30$ kΩ) and then sent to the embedded A/D converter channels in the microcontroller PIC18F452. After quantization in the 10 bit A/D converter, the digital voltage values are transformed into resistance values. Through the serial port connection, resistance values arrive at the Bluetooth module. These values finally wirelessly transmitted to a remote receiver by the Bluetooth antenna. A voltage regulator is used to convert 3.7 V from a Li-ion battery to 3.3 V power supply as the system V_{cc}. The data acquisition system has the following advantages:

- Simple structure which leads to a small size and light weight
- Large working range and acceptable accuracy for wearable resistive sensor
- Stable performance to power supply interference
- Removable and rechargeable battery configuration

The six textile pressure sensors in the insole array are connected to the R_{ref} and GND through the connector. Using the voltage division equation, the ADC input analog voltage (A_{input}) can be obtained as

$$A_{input} = \frac{R_{ref}}{R_{ref} + R_{sensor}} \cdot V_{cc} \tag{2}$$

Output digital value (D_{output}) can be obtained as

$$D_{output} = \left[2^m \frac{A_{input}}{V_{ref}} \right] \tag{3}$$

where $[\cdot]$ denotes the integer part of the argument, V_{ref} is the input full-scale voltage, and m is the bit length of D_{output}.

The V_{ref} of embedded A/D converter channels is software selectable to the microcontroller's positive supply voltage V_{cc}. This configuration makes that $V_{ref} = V_{cc}$. Then Eq. 3 can be derived as

$$\begin{aligned} D_{output} = \left[2^m \frac{A_{input}}{V_{ref}} \right] &= \left[2^m \frac{\frac{R_{ref}}{R_{ref} + R_{sensor}} \cdot V_{cc}}{V_{cc}} \right] \\ &= \left[2^m \frac{R_{ref}}{R_{ref} + R_{sensor}} \right] \end{aligned} \tag{4}$$

Equation 4 shows the relationship between digital resistance values from embedded A/D converters and sensor resistances. V_{cc} does not affect the digital outputs. Hence, this data acquisition system can achieve a stable performance even if the power supply is unstable. This feature is especially helpful in wearable applications, because wearable situation in daily activities is likely to attract more noise. Connecting the data acquisition system and the insole, a prototype of the textile sensor-based in-shoe plantar pressure measurement system was fabricated, as seen in Fig. 11.

System Configuration Modes

Bluetooth is utilized as the wireless communication technology in the present system. The wearer is required, in the overlapped radiation range of both Bluetooth modules from the remote receiver and data acquisition system, to ensure a stable and continuous wireless communication path between these two objects. It is a limitation that the wearer is restricted to a short distance range (<10 m) from the remote receiver. But the reason to choose Bluetooth technology lies in its extensive use and easy accessibility in consumer electronics, such as computer, mobile phone, and so on.

Three system configuration modes were provided from the in-shoe plantar pressure measurement system to the remote receiver, distinguished by three types of remote receivers: desktop, laptop, and smartphone. In the first configuration mode, the remote receiver is a desktop computer with a Bluetooth adapter. The wearer is restricted in the range of radiation from Bluetooth adapter. It is suitable for clinical or research laboratories, where the subject is measured within a small activity room. In the second configuration mode, the remote receiver is a laptop with an integrated Bluetooth module. The wearer is still restricted in the radiation

Fig. 11 Prototype of the in-shoe plantar pressure measurement system (Reproduced with permission [27], Copyright 2010, IEEE)

Fig. 12 Configuration mode with smartphone (on the playground) (Reproduced with permission [27], Copyright 2010, IEEE)

range of laptop Bluetooth module. While the laptop can be comfortably taken in outdoor environment, this mode can be used for measurement in small area outdoor activities. The third configuration mode is the most flexible one. The remote receiver is a smartphone with embedded Bluetooth module. A wrist band was designed to fix the smartphone; therefore, it can record the foot pressure of the wearer during the activity without any location restriction. It is suitable for longtime outdoor measurement. Figure 12 demonstrates this configuration mode.

Mode 3 is the most flexible one while it may be defeated by mode 1 and 2 as far as performance of plantar pressure data processing and analysis is concerned. There are obvious hardware performance differences between the three types of remote receivers used in the prototypes. For example, the configuration can be desktop Dell OptiPlex 755(CPU 2.66 GHz, RAM 2 GB, hard disk 160 GB), Laptop Lenovo

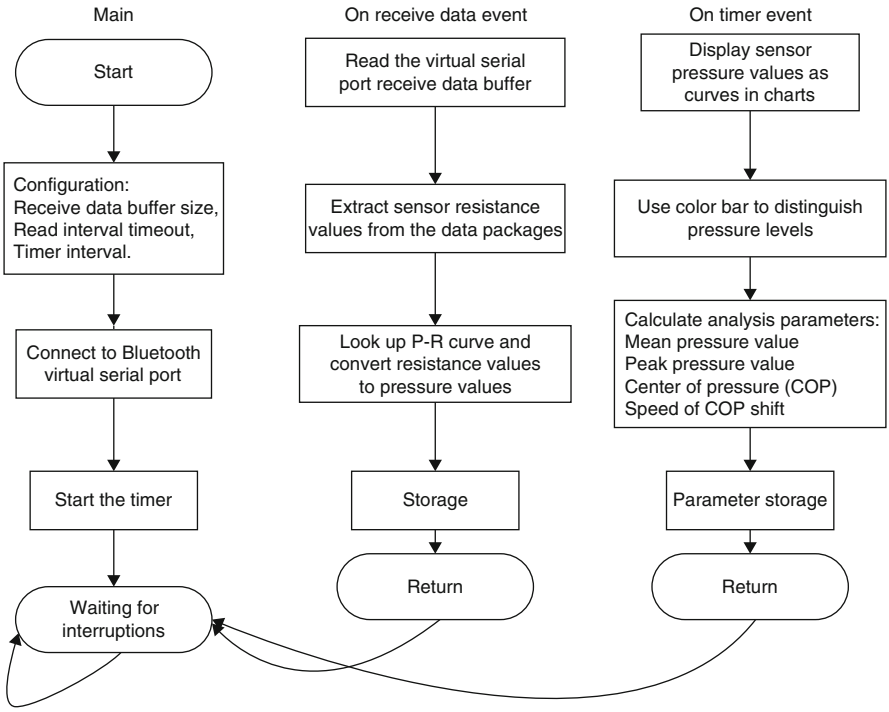

Fig. 13 Flow chart of data processing in the remote receiver (Reproduced with permission [27], Copyright 2010, IEEE)

ThinkPad X61(CPU 2.1 GHz, RAM 2 GB, hard disk 100 GB, battery time about 5 h), and smartphone HTC Touch Cruise (CPU 528 MHz, ROM 512 MB, RAM 256 MB, 8G SD card, battery time about 6–8 h). Because of the hardware technology progress in smartphone, the hardware configuration of smartphone cannot be on par with desktop and laptop. It is mainly to record the plantar pressure data (its battery lifetime is sufficient for a normal outdoor activity record) and simple data processing. The desktop and laptop are able to run complex data processing and analysis.

In the remote receiver, data processing is done as shown in the flowchart of Fig. 13. The data acquisition system is manually connected to the remote receiver through wireless Bluetooth path and is viewed as a Bluetooth virtual serial port. At first, a total configuration, including receiver data buffer size, read interval time-out, and timer interval, is set carefully and concertedly to ensure a following smooth data reception, display, and processing. Then after connected to the Bluetooth virtual serial port, the timer is forced to start with a following waiting status for interruptions. There are two event-driven responses, on receiving data event and on the timer event, corresponding to receiving data and processing data, respectively. On receiving data event, sensor resistance values are extracted from the data packages after reading out of the virtual serial port data buffer and transformed into pressure values according to the pressure-resistance curve of the textile sensor;

see Fig. 7c. After this pressure value data storage, the program will return to the main body. On the timer event, these sensor pressure values are real time displayed as moving curves in charts. Various colors are assigned to each sensor positions basing on a pressure level color bar. Some early analysis parameters, mean pressure, peak pressure, center of pressure (COP), and speed of COP are calculated and stored sequentially. The program will also return to its main body. Parameters are calculated by the following equations:

$$Mean = \frac{1}{n}\sum_{i=1}^{n} P_i \tag{5}$$

$$Peak = Max(P_1, \ldots P_i, \ldots P_n) \tag{6}$$

$$X_{COP} = \frac{\sum_{i=1}^{n} X_i \cdot P_i}{\sum_{i=1}^{n} P_i}, Y_{COP} = \frac{\sum_{i=1}^{n} Y_i \cdot P_i}{\sum_{i=1}^{n} P_i} \tag{7}$$

$$\text{Speed}_{COP} = \frac{u}{\Delta t} \cdot \left(|X_{COP}(t + \Delta t) - X_{COP}(t)|^2 + |Y_{COP}(t + \Delta t) - Y_{COP}(t)|^2 \right)^{1/2} \tag{8}$$

where n denotes the total number of sensors, i denotes a certain sensor, X, Y is the coordinate of the whole foot shape area, u is the unit distance between two neighbor coordinate points, and Δt denotes the time interval.

Two kinds of user interfaces are developed: one is for desktop and laptop users as in Fig. 14a and the other is for smartphone users as in Fig. 14b. The programming tools are Delphi and Lazarus, respectively.

System Features

The technical features of the system are reported as 100Hz maximum sampling rate, synchronous sampling mode, 10–1,000 kPa measurement range, 1 kPa resolution, and ±5 % accuracy. As for the data compression, during data processing, display, and export for further use, the six-sensor pressure values are represented in a user-oriented format. Each sensor contains six bytes including five bytes for integral and one byte blank for separation. One byte LG (line change) and one byte RE (return) are put at the end of a total round data. While in transmission, storage, and import, two bytes of sampled value (SV) are used to represent for each sensor, in order to save transmission time and storage memory. The user should import this data into the software to convert the sampled value to pressure display.

The experimental results presented here were obtained by using the above-described in-shoe plantar pressure measurement and analysis system based on textile sensor array. Figure 15 illustrates a set of measurement results of a standing person (male and 72 kg weight). Figure 15a is the right foot pressure when the wearer stands still with two feet supporting the whole body weight. The pressure readings of the right foot are lower reflecting half of the body weight. Figure 15b

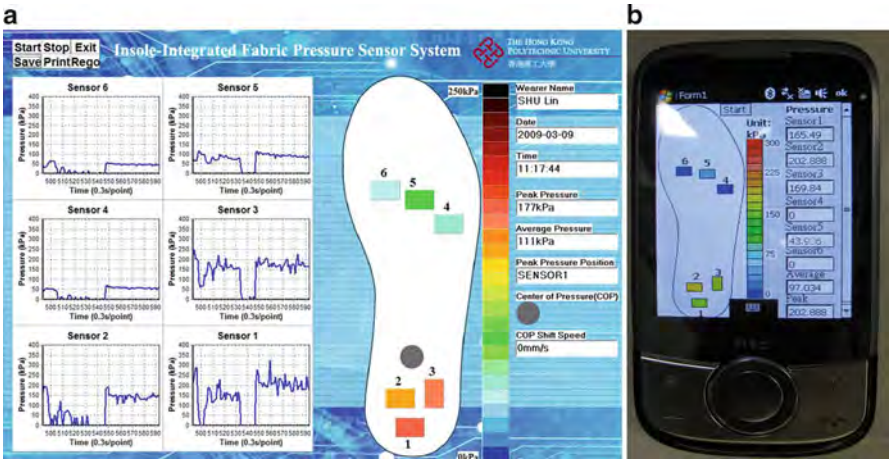

Fig. 14 Plantar pressure data interface (**a**) for desktop and laptop and (**b**) for smartphone (Reproduced with permission [27], Copyright 2010, IEEE)

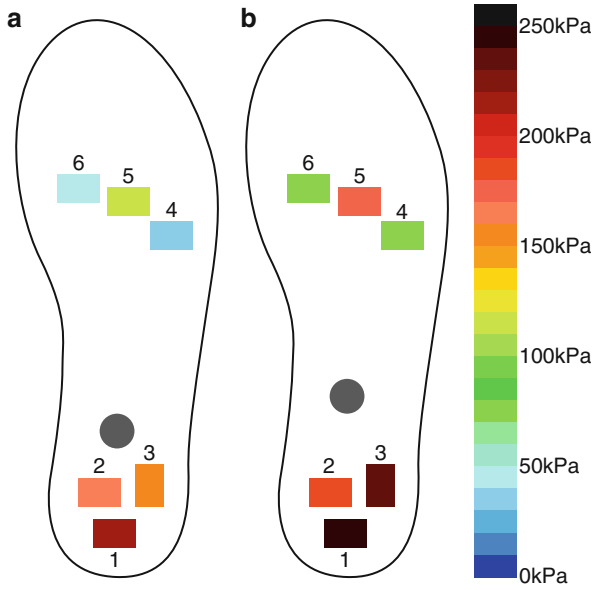

Fig. 15 Plantar pressure data displays: (**a**) two feet on the ground and (**b**) only the right foot on the ground (Reproduced with permission [27], Copyright 2010, IEEE)

shows the pressure readings of the right foot when the wearer stands with his left foot in suspension. With just the right foot supporting the whole body weight, the pressure values of six sensors increase markedly. The black point as COP moves a little to the middle of the foot, which may reflect the wearer's balance control. The dynamic measurements and evaluation were presented where experimental results showed that this system had stable performance in both static and dynamic measurements [27].

Smart Cushion Cover

Implementation on a 10 × 10 Textile Resistive Sensor Array

The RMA was implemented on a prototype of 10 × 10 textile resistive sensor array (sensor size: 10 × 16 × 3 mm), as shown in Fig. 16. One hundred textile pressure sensors with a pressure measurement accuracy of ±5 % (AdvanPro Ltd., HK) [28] were sorted column by column according to their initial resistances from smallest to biggest (from 3 kΩ to 19 kΩ), adhered onto a flexible PET based polymer circuit substrate using silicone glue, and connected to embedded metal wires of the polymer circuit by conductive yarns and adhesives. This sensor array was interfaced by a DAQ (data acquisition) unit via 20 electrical wires of a ribbon cable. The DAQ unit (size: 45 × 33 × 8 mm) utilized a microcontroller MSP430F5418A (Texas Instruments Inc., Dallas, Texas, USA) with embedded 12-bit ADC channels which were on-chip ADC resources for reading potentials, where 11 I/O ports and 10 ADC channels were occupied for this 10 × 10 array. It also used a Bluetooth module for data transmission and a 170 mAh Li-ion battery for power supply. 4.7 and 11.7 kΩ resistors were used as standard reference resistors. Digitized data of potentials measured by the embedded ADCs were wirelessly transmitted via the Bluetooth module to a remote computer, where the matrix equations were established and sensor resistances were solved. The resistance data were then converted to pressure data according to the pressure-resistance characteristic curves of textile pressure sensors provided by the sensor manufacturer. The resistance and pressure data were processed, displayed, analyzed, and stored by the developed smart cushion software in the computer.

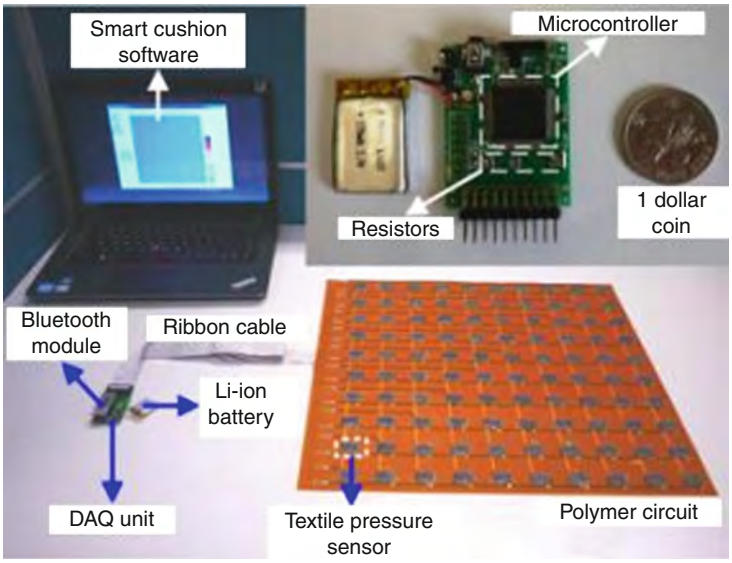

Fig. 16 Prototype of a 10 × 10 textile resistive pressure sensor array and DAQ unit (upper right: an enlarged view of the DAQ unit) (Reproduced with permission [22], Copyright 2014, IEEE)

Thanks to RMA, the DAQ unit used only a microcontroller and several resistors for readout of sensor arrays, which led to a small circuit size; see the enlarged view of DAQ unit in Fig. 16. Actually the dimension could be smaller if a miniaturized connector, power-on button, and battery were adopted.

Accuracy Test of Resistance Measurement by RMA

In the accuracy test of resistance measurement by RMA, the resistances of the 100 sensors were at first measured by a digital multimeter Keithley 2010 with an accuracy of 0.02 % (Keithley Instruments Inc., Cleveland, Ohio, USA) before these sensors were stuck onto the substrate and then measured by the RMA on the implemented array after the adhesion and connection. The relative difference in percentage between these two measurement results was used to present the resistance measurement error: $\text{error}_R(\%) = \text{abs}(R_{RMA} - R_{Keithley})/R_{Keithley}$, where R_{RMA}, $R_{Keithley}$, and abs represented the resistance by RMA, resistance by Keithley, and absolute value, respectively, and the resistance by Keithley was viewed as the standard value. The resistance measurement results and errors of 100 sensors in the array are shown in Fig. 17. The resistance measurement error of 0.61 ± 0.41 % is satisfactory for common wearable applications. This measurement accuracy of RMA could be higher if 16-bit ADCs were used other than 12-bit ADCs. On the other hand, changes of the sensor resistances before and after the adhesion and connection, and deviations of the resistance values of standard resistors from their nominal resistance values, had contributed to the measurement error.

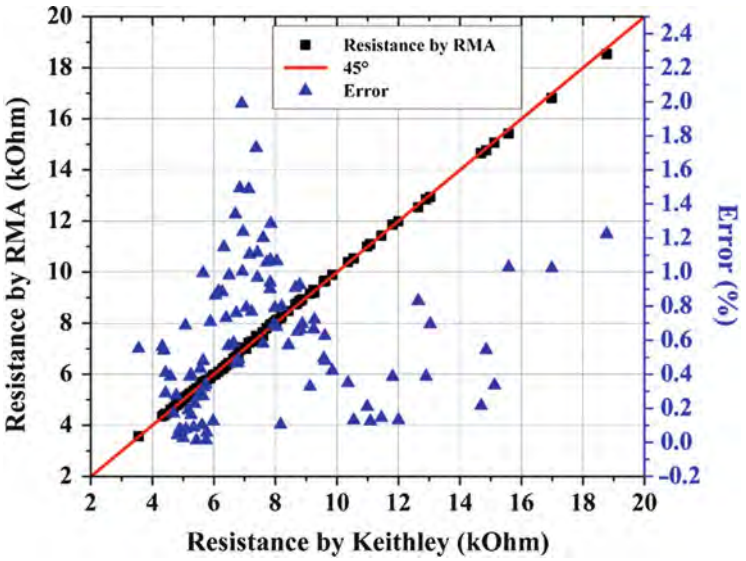

Fig. 17 Measurement results of sensor resistances by RMA compared to those by Keithley and the resistance measurement errors of RMA (Reproduced with permission [22], Copyright 2014, IEEE)

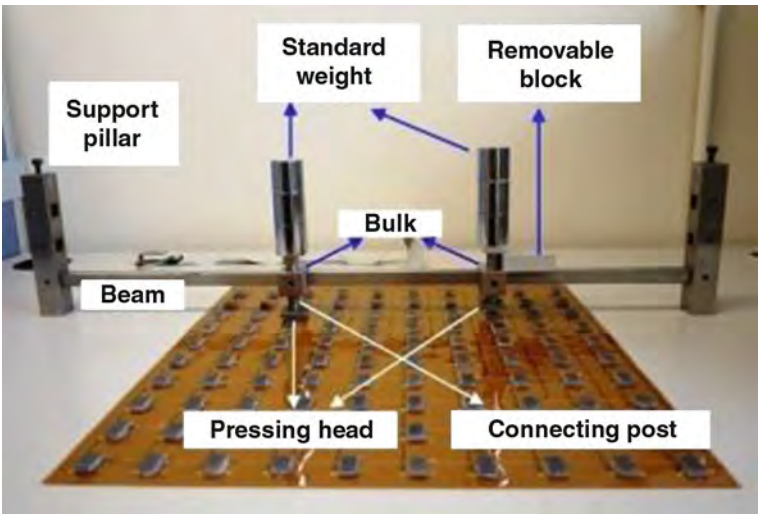

Fig. 18 A loading device for loading sensors in the cross-talk error evaluation tests (Reproduced with permission [22], Copyright 2014, IEEE)

Cross-Talk Error Evaluation

A loading device was designed and fabricated for loading sensors in the cross-talk error evaluation tests, shown in Fig. 18. The bulk had a thru square hole in horizontal direction, which was parallel and coaxial to the beam. Hence, by adjusting the positions of the support pillar, the bulks can be slipped along the beam to the locations of target sensors. It also had a vertical thru circular hole, parallel and coaxial to the connecting post which contacted close to the inner wall of the thru hole and could slide vertically. There was a removable block to control the loading event: once the block was taken out, the post would slide down to deliver the force of gravity of standard weights onto sensors via the pressing head, where the friction force between the post and inner wall of the thru hole was really small to be ignored due to the effects of lubricating oils. The total weight of the standard weight, post, and pressing head was 655 ± 1 g. The contact area between the sensor and pressing head was 10×16 mm. The pressure on the loaded sensor was 40.1 ± 0.1 kPa.

Then the cross-talk errors were evaluated using coefficients of variations of sensor resistances in two cases that one or two sensors were loaded in the array. In the first case of loading one sensor in the array, one sensor randomly selected out of the lot of 100 was loaded by the loading device. Ten tests were conducted; see Table 4. In the second case of loading two sensors, ten tests were conducted, where two standard weights were applied by the loading device onto two sensors randomly selected out of the total 100 sensors; see Table 4. In order to verify whether sensors on the same column or row affect the reading or not and to further quantify the level of cross-talk error, another ten tests of loading two sensors in the same row or column were conducted. No. of row, column, and sensor were randomly

Table 4 Random selection of sensors in loading tests

Testing no.	1	2	3	4	5	6	7	8	9	10
Sensor no.	Loading one sensor in the array									
	R_{1006}	R_{0304}	R_{0701}	R_{0509}	R_{0910}	R_{0807}	R_{0506}	R_{0102}	R_{0903}	R_{0505}
	Loading two sensors in the array									
	R_{0702}	R_{1003}	R_{0208}	R_{1004}	R_{0502}	R_{0106}	R_{0902}	R_{0204}	R_{0210}	R_{0308}
	R_{0810}	R_{0804}	R_{0501}	R_{1002}	R_{0910}	R_{0406}	R_{0101}	R_{0301}	R_{0701}	R_{0210}
	Loading two sensors in the same row or column									
	R_{0709}	R_{0807}	R_{1004}	R_{0806}	R_{0204}	R_{0805}	R_{0609}	R_{0206}	R_{0903}	R_{0407}
	R_{0705}	R_{0809}	R_{1003}	R_{0808}	R_{0202}	R_{1005}	R_{0909}	R_{1006}	R_{0803}	R_{0607}

Reproduced with permission [22], Copyright 2014, IEEE
Note: R_{1006} refers to the sensor in 10th row and 6th column. Others are in the same way

selected; see Table 4. Resistances of 100 sensors were measured by RMA and recorded in the computer in each test.

A total of 30 tests was conducted, with each lasting for 20 s, where the loading occurred in the period of the 11th ~ 13th seconds by removing the block(s) and lasted till the 20th second. Coefficients of variations (CV) of the resistances of each sensor in the periods of 1st ~ 10th seconds and 11th ~ 20th seconds were calculated separately for representing the noise level before and during loading, noted as CV_B and CV_L, respectively. The change of CV (ΔCV) of the resistances of each unloaded sensor was calculated using $\Delta CV = CV_L - CV_B$, which reflected the effects of loaded sensors on the others. Box plots of ΔCV of resistances of 98 or 99 unloaded sensors of each test were given in Fig. 19. ΔCV results show both positive and minus values, implying that the resistance increase of loaded sensors had increased the noise of some unloaded sensors but decreased it in others. Overall, the mean values of ΔCV of resistances in 30 tests were around 0, which proved that loading of one sensor or two sensors had small effects on most of the other sensors. Here the maximum positive value of ΔCV was used to estimate the level of cross-talk error, that is, the level of how much the measured resistance value of one sensor can be affected maximally by the resistance changes of other sensors. Based on the maximum values of ΔCV plotted in Fig. 19, cross-talk errors of loading one sensor in the array, two sensors in the array, and two sensors in the same column and row were estimated as 2.67 ± 0.56 ‰, 2.74 ± 0.74 ‰, and 2.88 ± 0.57 ‰, respectively. The overall cross-talk error of the 30 loading tests was 2.77 ± 0.61 ‰, which was very small. This small cross-talk error of loading two sensors in the same column and row reflected that sensors in the same row or column did not affect each other much. The relative resistance changes of loaded sensors in these 30 tests were 68.88 ± 48.47 % under the pressure of 40.1 ± 0.1 kPa, nearly 248.66 times of the average level of the cross-talk errors.

Application for Sitting Pressure Monitoring

A sensing cushion (size of cushion: $43 \times 43 \times 3$ cm) was fabricated using this 10×10 array sandwiched by two layers of foams and packaged in a cover for

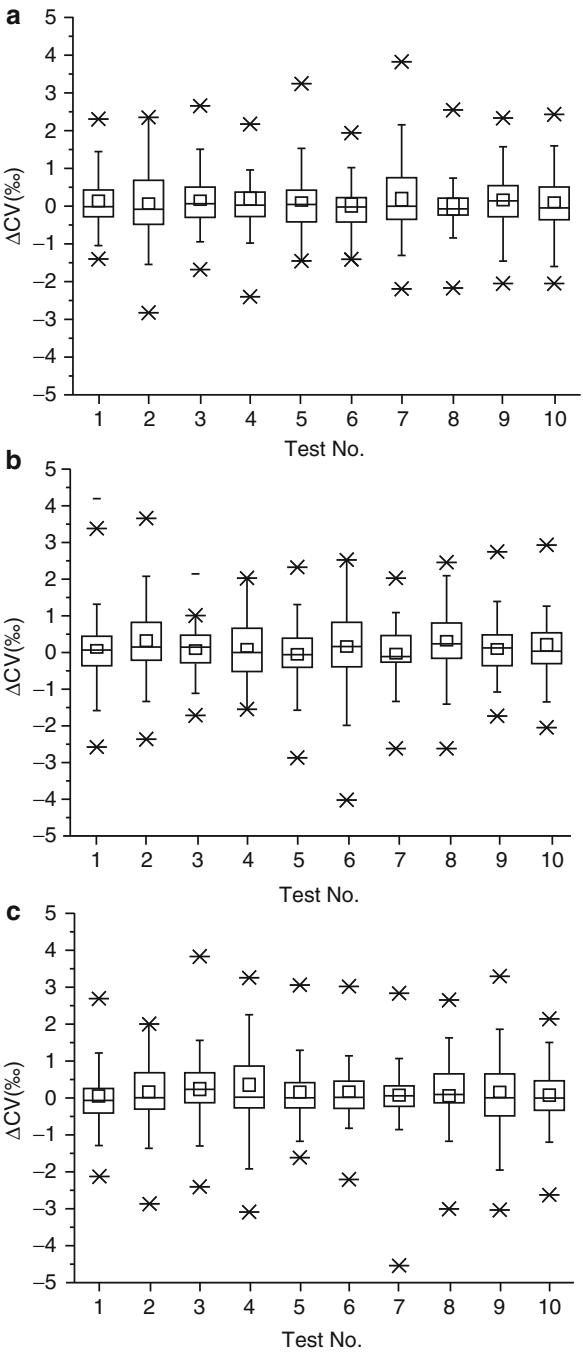

Fig. 19 Change of variations (ΔCV) of sensor resistances in loading tests for cross-talk error evaluation: (**a**) loading one sensor in the array, (**b**) loading two sensors in the array, and (**c**) loading two sensors in the same row or column (box plot configurations: box range – 25–75 %, whisker range – 1.5IQR; meanings of the percentile symbols: '-' refers to the max or min, '×' refers to the 1 % or 99 %, '□' refers to the mean) (Reproduced with permission [22], Copyright 2014, IEEE)

monitoring the sitting pressure of chair-bound people. The upper layer foam, which was softer than the sensors and had the same thickness as the sensors, had 100 holes for mounting the sensors so that the top surface was smooth. Sensors were calibrated by Instron 5944 (Instron Corp., Norwood, MA, US). The sampling rate was set to 10 Hz.

Accuracy Evaluation of the Fabricated Sensing Cushion

The Novel® trublu® calibration device (Novel GmbH, Munich, Germany) including a digital manometer (measurement range: 0 ~ 1 MPa, accuracy:1 kPa), a standard air pressure supply device, was employed for evaluation of accuracy of the fabricated sensing cushion in pressure measurement. Figure 20 shows the experimental setup, where the sensing cushion was inserted into the trublu® device and under the inside air bladder. Compressed air was pumped into the air bladder via the air pipeline and controlled by the on-off switch. Inside standard air pressure value was indicated on the manometer. As the area of sensing cushion was much larger than the trublu® device, only 6 rows of sensors could be evaluated that were away from the seat back where the common sitting area was included. The pressure contact area was about 43 × 26 cm. Seven tests were conducted, where the air

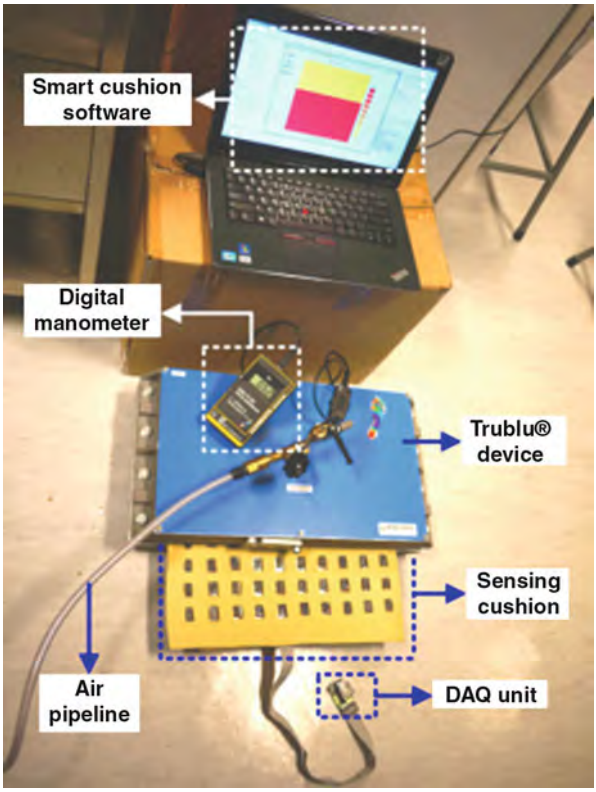

Fig. 20 Experimental setup for the accuracy evaluation of pressure measurement of the fabricated sensing cushion using the Novel® trublu® calibration device (Reproduced with permission [22], Copyright 2014, IEEE)

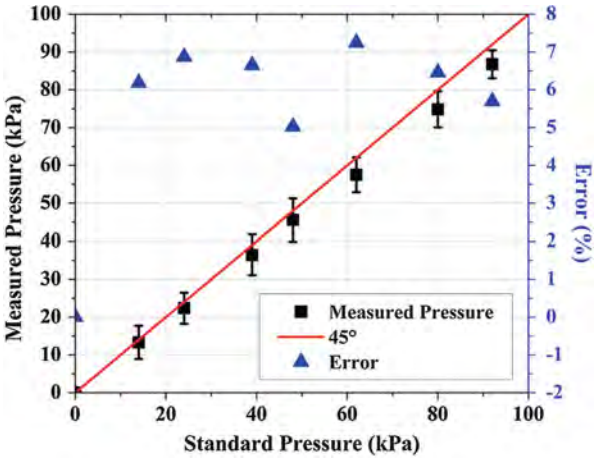

Fig. 21 Accuracy of pressure measurement by the sensing cushion compared to the standard air pressure provided by the Novel® trublu® calibration device (Reproduced with permission [22], Copyright 2014, IEEE)

pressure was increased from 0 to 14, 24, 39, 48, 62, 80, and 92 kPa and held for 30 s at each pressure level. Between each test, the inside compressed air was emptied to keep a zero pressure on the sensors. The mean values of measured pressures by the effective 60 sensors of the sensing cushion, stored by the smart cushion software in the computer, were compared to the recorded standard air pressure values, and their relative differences were computed as the pressure measurement error: $error_p(\%) = abs(P_{cushion} - P_{air})/P_{air}$, where $P_{cushion}$, P_{air}, and abs represented the mean measured pressure by the effective 60 sensors of the sensing cushion, standard air pressure by the trublu® calibration device, and absolute value, respectively. Results are shown in Fig. 21.

The average error of the fabricated sensing cushion in pressure measurement was 6.30 ± 0.75 %, where the textile pressure sensors contributed majorities of measurement errors (about 5 % [28]). This accuracy is acceptable for continuous sitting pressure monitoring. The error bar shows one standard deviation of pressure values sensed by the effective 60 sensors, reflecting obvious variations of sensors in pressure measurement, which might be caused by inconsistent sensor heights due to artificial adhesions. The average measured pressure was some lower than the standard air pressure, which might be caused by the pressure transfer via the covered foam on sensors.

Sitting Pressure Monitoring by the Sensing Cushion

This sensing cushion was further assessed in a trial of continuous sitting pressure monitoring of chair-bound subjects. Subjects were asked to sit on their own chairs covered by the sensing cushion to conduct some typical sitting postures. A 90-min continuous normal work at the office was required for the continuous pressure data record, during which subjects could leave the seat for other activities as usual. Written informed consent was obtained prior to the start of the trial. The trial procedures were approved by the Human Subjects Ethics Subcommittee of the Hong Kong Polytechnic University.

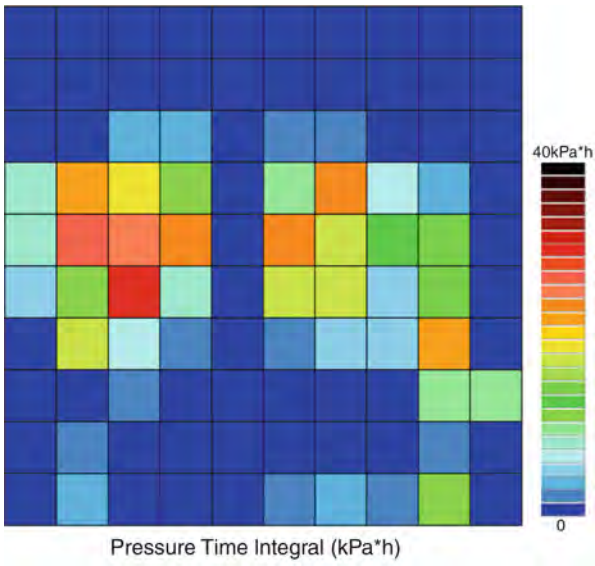

Fig. 22 Pressure time integral result of a subject in a 90-min continuous work at the office measured by the 10 × 10 textile resistive sensor array cushion using RMA (Reproduced with permission [22], Copyright 2014, IEEE)

Figure 22 shows the monitoring results of a subject (male, aged 30 years old, height 174 cm, weight 70 kg, body mass index 23.1 kg/m^2) under three sitting postures of sit-up, backward, and forward, where the areas with high pressure move backward from Fig. 22a, b and move forward from (a) to (c), indicating that the pressure values, contact areas, and positions might reflect characters of those postures. As the cushion type and thickness affect the peak pressure [29], this sitting pressure measurement sensor array is helpful for evaluating cushions and selecting suitable cushions for chair-bound people. Since the cushion will be further applied for monitoring wheel-chair-bound people in the prevention of pressure ulcer, pressure time integral (PTI) was also estimated. Figure 23 shows the PTI result of the same subject in a 90-min continuous work at the office. Here a threshold of around 40kpa·hour (estimated from the graph of "tissue tolerance guideline") was set for signaling the pressure relief for reducing the possibilities of pressure ulcers [30]. This PTI result is useful for reminding wheel-chair-bound people to change postures. It can be also used for analysis of sitting posture preference, for example, Fig. 23 may indicate this subject prefers to sit using his right hip and left thigh for support.

Performances of the Other Prototypes and Products

Some typical prototypes and products for sitting posture and pressure measurement have been found in the literatures. eCushion [31], which had a bigger DAQ unit, utilized MOAA for readout and presented cross-talk effects, especially the mechanical cross talk due to limited spaces between neighbored sensors [32]. The Tekscan CONFORMat® seating and positioning pressure measurement system (Tekscan Inc., Boston, MA, US) based on MOAA [33] presented unavoidable cross-talk errors: when the force applied on an individual sensing cell exceeded 294 mmHg

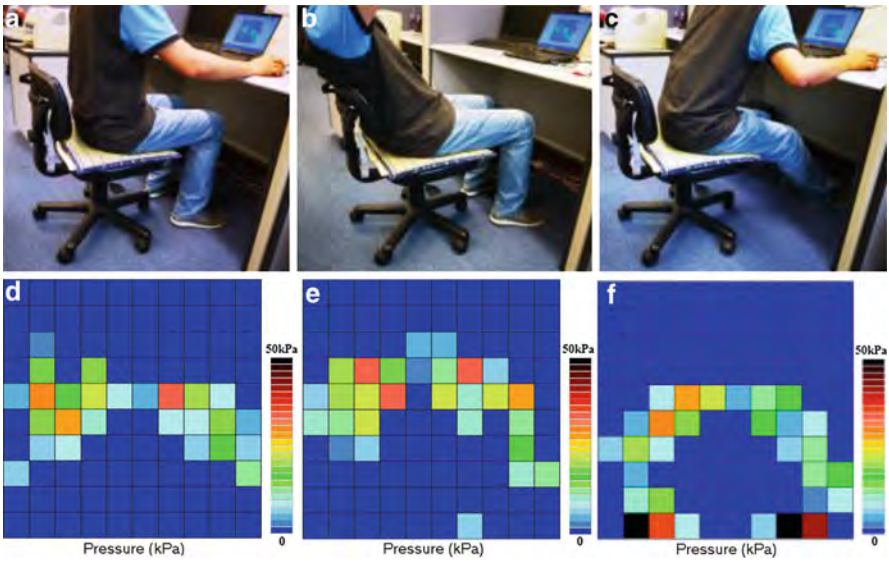

Fig. 23 Pressure mapping results by 10 × 10 textile resistive sensor array (the sensing cushion) using RMA: three sitting postures of (**a**) sit-up, (**b**)backward, and (**c**) forward and the corresponding mapping results shown in (**d**), (**e**), and (**f**), respectively (Reproduced with permission [23], Copyright 2014, IEEE)

(39.2 kPa), another cell in the same column four cells away was also activated to display a pressure value >1 mmHg [34]. In the loading tests, in the smart cushion software, there were no unloaded sensors that displayed a pressure value >0 kPa when one or two sensors were loaded by a pressure >40 kPa. And in accuracy evaluation tests of the fabricated sensing cushion, unloaded sensors had maintained a display of zero pressure also. As for the pressure measurement accuracy, the Tekscan CONFORMat® system exhibited an average measurement error of 20.68 ± 12.14 % in mass loading tests from 1 to 50 kg [34], which was unacceptable and needed further corrections.

Here, some important factors of the RMA are further discussed, including the circuit complexity, sensor capacity, measurement error, array dimension effect, scope of applications, and limitations:

1. Circuit complexity: Table I indicates that RMA has the lowest circuit complexity among the four approaches, if they are compared on a microcontroller-based wearable platform. This complexity ranking is applicable for platforms with processor/controller chips that have adequate on-chip resources of ADCs and I/O ports. On the other platforms, it might not be the same. In the implementation of a 10 × 10 textile pressure sensor array for sitting pressure monitoring, RMA does help for a low-complexity DAQ unit. In a comparison between RMA and the popularly used method (the virtual ground technique), the latter belongs to the category of the conventional method MOAA, which needs a large number

Table 5 Comparison of sensor capacity of TDCA, MOAA, IMA, and RMA on a microcontroller-based wearable platform

Approach	Estimation of sensor capacity	Restrictions: a microcontroller with on-chip 8 embedded ADCs and 20 digital ports, 4–8 multiplexer (4 input pins connecting with I/O ports vs. 8 output pins connecting to 8 rows or columns)
TDCA	Number of ADCs × number of I/O ports	It can connect with 8 × 20 = 160 sensors by the assistance of 160 additional transistors/diodes and 8 ADCs
MOAA	Min (number of ADCs, [number of multiplexers/2]) × (number of rows × number of columns)	It can support min (8, [20/4/2]) × 8 × 8 = 128 sensors, which needs 4 additional multiplexers, 2 op-amps, and 2 switches, but it only takes up 2 ADCs
IMA	(Number of ADCs/4 + 1) × number of ADCs/2	It only sustains (8/4 + 1) × 8/2 = 12 sensors by 8 ADCs
RMA	Number of ADCs × (number of I/O ports – 1)	It supports 8 × (20–1) = 152 sensors by additional 8 standard resistors and 8 ADCs

Reproduced with permission [22], Copyright 2014, IEEE

of op-amps for eliminating cross-talk currents and therefore increases circuit complexity. On the contrary, the RMA allows and takes advantage of cross-talk currents to establish matrix equations and solve them for sensor resistances, which avoids redundant electrical chips that are needed for minimizing cross-talk currents.

2. Sensor capacity: The total numbers of sensors that each approach can sustain in a given restriction of on-chip resources are shown in Table 5. In a given set of restricted numbers of ADCs and I/O ports, IMA has the lowest scalability because of its dependence on the resources of ADCs. MOAA exhibits an unsatisfactory sensor capacity for its reliability on resources of I/O ports. TDCA provides the highest sensor capacity followed by RMA due to their lower dependence on on-chip resources (ADCs and I/O ports).
3. Measurement error: RMA's measurement accuracy is affected by the precision of A/D conversions, deviations of resistance values of the standard resistors from their nominal values, and power supply interferences, as sensor resistances are calculated from the potentials detected by ADCs, standard resistances, and V_{cc} values; see Eq. 4. High-precision ADCs and standard resistors and a stable power supply contribute to a high measurement accuracy. Inaccuracy of the I/O port voltage might also affect the measurements as sensors are driven with voltages provided by I/O ports. The I/O ports of the microcontroller MSP430F5418A by Keithley 2010 were tested. The voltage values of the power supply and the I/O ports (when they were set to 1) were 3.29130 V and 3.29123 ± 0.00001 V, respectively. The low-level voltage output of the I/O ports

when they were set to 0 was very close to 0.00001 V. It showed the error caused by the I/O ports was very small on this platform.

RMA calculates sensor resistances at a time point by utilizing readings of potentials on sequential time points under sequential allocations of P_i pins. A condition must be met that sensor resistances keep the same on those sequential time points. Therefore, measurement errors of RMA are also relevant to a comparison between the potential scanning rate and variation rate of sensor resistances, because calculating $m \times n$ sensor resistances requires $m + 1$ reading cycles of potentials, during which sensor resistances might be altered by external or internal stimulations. Taking a 5×8 sensor array, for example, six potential scanning cycles and several calculation cycles are needed for establishing and solving matrix equations. The variation rate of sensor resistances should be lower than 5 kHz to guarantee a valid measurement by RMA, if those cycles are close to 200 μs. RMA is suitable for monitoring parameters that do not vary rapidly, such as the environmental index (temperature, humidity, gas, etc.) and physical or physiological issues of the human body. However, in cases of monitoring high-speed impacts or rapidly changing objects, high-speed ADCs and microcontrollers should be used for the achievement of an accurate measurement.

4. Array dimension effect: The network dimension effect impacts the measurement performance of RMA especially the error propagation in two ways. One is this effect will enhance the scanning rate effect. With the increase of the dimension of the sensor array, scanning rate decreases. Under such circumstances, the variation rate of sensor resistances has greater possibilities to be higher than the scanning rate, meaning that sensor resistances might change along those sequential time points, which leads to an increase in the measurement errors. The other way is relevant to the accumulated errors from ADCs and reference resistors. RMA's errors are mainly caused by the inaccuracy or low precision of ADCs and standard reference resistors. With the increasing of array dimensions, more ADCs and reference resistors are involved, resulting in a larger accumulated error. To minimize the dimension effect, high-speed and high-precision ADCs, as well as high-precision standard resistors, are extremely helpful. As for the Tekscan CONFORMat® measurement system, the noticeable cross-talk error might be induced by the dimension effect of MOAA as it delivers thousands of sensing cells. With the increasing of array dimensions, more op-amps and multiplexers are needed, and cross-talk currents by nonideality of op-amps and multiplexers' cross-leakage currents increase, which sequentially causes a higher cross-talk error.
5. Scope of applications: As there are no amplifiers for signal amplifications in the RMA circuitry, traditional metal sensors and strain gauges with small sensitivities are not in the scope. Based on these tests, RMA is workable for sensors with a resistance change of 20 % FSO (full-scale output) by a proper configuration of reference standard resistors and works better for sensors with that of 40 % or higher. RMA is extremely suitable for wearable flexible sensors with high sensitivities [35, 36], whose resistance changes could be several tens or hundreds

of percent of their initial resistances. And the applicable resistance range of sensors could be from several kΩ to several hundred kΩ. ADC selection is also important for RMA; 12-bit or higher (16-bit) ADCs are satisfactory. For the used 12-bit ADCs, an actual 10–11 bit resolution was obtained. The lowest 1–2 bit was fluctuated, which reflected the noise level of these embedded ADCs. 10-bit ADC is also acceptable, but the resistance measurement error might be increased. Embedded on-chip ADCs of commonly used microcontrollers are applicable. As for the frame rate and spatial resolution of sensor arrays in seating applications, a minimum requirement was not found in the literatures. There existed some studies using less than 100 sensors, such as the sensor sheet for measuring pressure force by 64 sensors, which achieved an accuracy of 93.9 % in sitting posture classification [37], and the sitting pressure measurement in pressure ulcers risk evaluation with a 5 Hz sampling frequency [38]. So this sensing cushion system with a spatial resolution of 100 sensors and 10 Hz sampling frequency was applicable. The frame rate on this platform was a function of the number of sensors, baud rate (for data transmissions between the microcontroller and Bluetooth module), and Bluetooth transmission durations. If the baud rate was increased from the present 19,200 to 57,600 bit/s, a frame rate around 30 frames/s and a real-time pressure image display can be achieved. On the other hand, RMA is able to realize a high spatial resolution of the sensor array using more ADCs and I/O ports.

6. Limitations and future work: The limitations of this study are that the RMA contributes to a relatively low reading rate and the scanning rate effect on measurement errors might limit this approach to quasi-static applications, which deserve further studies. This chapter concentrates on the presentations of the new approach itself, including its explanation, implementation, evaluation, and application, and a qualitative comparison with other three approaches in terms of the circuit complexity, measurement error sources, and sensor capacity. Ideally, it is better to implement the four readout approaches on a same platform to present a quantitative comparison of the accuracy, cross-talk error, power consumption, and cost. Due to time and effort limitations, this work has not been included in the chapter and will be conducted as another research topic. As for the sensing cushion, the future work refers to a calibration by standard calibrating bladders, measurement of the actual cross-talk error of the COMFORMat® system, analysis and optimization on the frame rate, number of sensors, and spatial resolution.

Summary

In this chapter, a study has been presented on the current state of the art of fiber-based wearable electronic circuits and systems. Several aspects have been covered including the fiber transistors, the fabric circuitry, the interfaces for fiber-based sensor arrays, and the fiber-based electronic systems. The performance

requirements of fiber-based devices and systems are presented in light of the unique characteristics of fiber assemblies. Despite such significant advancements of fiber-based wearable electronics, most of the reported prototypes are a long way from fulfilling their final application. It is of great necessity to address the critical issues and future work for the fiber-based wearable electronics, which places a demand for high performance in terms of electronic functions, structural and functional integrity and stability during use, and deformability together with comfort of the users. Although the developed discrete fiber-based electronics show good performance, they are still far below the requirements of modern, super large-scale integrated circuits, and the roughness of fiber electronics is still too high that it is not suitable for the traditional integrated circuit technology. Compared with conventional silicon-based or thin-film-based electronic devices, however, fiber-based devices are involved with (1) multiple materials with vast difference in properties and (2) multiple scales of three-dimensional structures from nano-, micro-, meso-, and then macroscales. Thus, more critical issues, including electrical, electrochemical, as well as electromechanical performances, are induced from research platform to the commercialization of the fiber-level components and devices. The currently most challengeable issue is the further development of small-sized electronics on microfibers, especially the microfiber-based transistors, and the performance of various components and devices with the marriage of electronics and textiles should be considered. To enable electronics to directly contact soft, elastic, and curved human bodies, it requires the electronics to be porous, flexible, stretchable, reliable, durable, as well as washable.

Other issues include the improving performance of wearable electronic, the creation of truly multifunctional fabrics, the encapsulation of electronic devices on fabric, and the long-term stability of these devices for potential applications. To realize connection of the knitted connectors with conventional electronic components, fabric circuitry, sensors and sensing networks, wearable harvesting devices, and wearable energy storage devices including lithium-ion batteries and SCs is still big a challenge. To date, the areal capacitance is limited due to poor charge transport ability in the electrode; the electrochemical property degrades under charge/discharge cycles due to induced mechanical stress; the bendability, stretchability, as well as durability need to be further enhanced. Thus, the understanding and proper design of fiber hierarchy structures and interfacial properties will play a role to reduce the interface shear stress and occurrence of crack/delamination as well as crack propagation.

In addition, the issues have a common feature of multiple disciplines concerning electronics, materials, solid mechanics, surface chemistry, and thermodynamics. Most reported works have focused on the materials and fabrication of individual novel devices and their potential applications; however, up to date, there has been few systematical fundamental studies in the literature on the highly complex fiber-based electronic devices and systems. Most of the involved mechanisms remain elusive. Design tools for such devices and systems should be developed based on much improved fundamental understandings.

References

1. Tao XM (ed) (2005) Wearable electronics and photonics. Woodhead Publishing, Boca Raton
2. Zeng W, Shu L, Li Q, Chen S, Wang F, Tao XM (2014) Fiber-based wearable electronics: a review of materials, fabrication, devices, applications. Adv Mater 26:5310–5336
3. Reddy AM, ImranáJafri R (2011) Carbon nanocoils for multi-functional energy applications. J Mater Chem 21(40):16103–16107
4. Windmiller JR, Wang J (2013) Wearable electrochemical sensors and biosensors: a review. Electroanalysis 25(1):29–46
5. Lee JB, Subramanian V (2005) Weave patterned organic transistors on fiber for e-textiles. IEEE Trans Electron Devices 52(2):269–275
6. De Rossi D (2007) Electronic textiles: a logical step. Nat Mater 6(5):328–329
7. Hamedi M, Herlogsson L, Crispin X, Marcilla R, Berggren M, Inganäs O (2009) Fiber-embedded electrolyte-gated field-effect transistors for e-textiles. Adv Mater 21(5):573–577
8. Tao X, Koncar V, Dufour C (2011) Geometry pattern for the wire organic electrochemical textile transistor. J Electrochem Soc 158(5):H572–H577
9. Maccioni M, Orgiu E, Cosseddu P, Locci S, Bonfiglio A (2006) Towards the textile transistor: assembly and characterization of an organic field effect transistor with a cylindrical geometry. Appl Phys Lett 89(14):143515
10. Wang S, Kappl M, Liebewirth I, Müller M, Kirchhoff K, Pisula W, Müllen K (2012) Organic field-effect transistors based on highly ordered single polymer fibers. Adv Mater 24(3):417–420
11. Hamedi M, Forchheimer R, Inganäs O (2007) Towards woven logic from organic electronic fibres. Nat Mater 6(5):357–362
12. Khodagholy D, Rivnay J, Sessolo M, Gurfinkel M, Leleux P, Jimison LH, Malliaras GG (2013) High transconductance organic electrochemical transistors. Nat Commun 4:2133
13. Tarabella G, Villani M, Calestani D, Mosca R, Iannotta S, Zappettini A, Coppedè N (2012) A single cotton fiber organic electrochemical transistor for liquid electrolyte saline sensing. J Mater Chem 22(45):23830–23834
14. Zou D, Lv Z, Cai X, Hou S (2012) Macro/microfiber-shaped electronic devices. Nano Energy 1(2):273–281
15. Jalili R, Razal JM, Innis PC, Wallace GG (2011) One-step wet-spinning process of poly (3, 4-ethylenedioxythiophene): poly (styrenesulfonate) fibers and the origin of higher electrical conductivity. Adv Funct Mater 21(17):3363–3370
16. Xu Z, Liu Z, Sun H, Gao C (2013) Highly electrically conductive Ag-doped graphene fibers as stretchable conductors. Adv Mater 25(23):3249–3253
17. Sekitani T, Takamiya M, Noguchi Y, Nakano S, Kato Y, Sakurai T, Someya T (2007) A large-area wireless power-transmission sheet using printed organic transistors and plastic MEMS switches. Nat Mater 6:413–417
18. Sahai Saxena R, Bhan R, Kaur Saini N, Muralidharan R (2011) Virtual ground technique for crosstalk suppression in networked resistive sensors. IEEE Sensors J 11(2):432–433
19. Lorussi F, Rocchia W, Scilingo EP, Tognetti A, De Rossi D (2004) Wearable, redundant fabric-based sensor arrays for reconstruction of body segment posture. IEEE Sensors J 4 (6):807–818
20. Liu H, Zhang YF, Liu YW, Jin MH (2010) Measurement errors in the scanning of resistive sensor arrays. Sensors Actuators A Phys 163(1):198–204
21. Alirezaei H, Nagakubo A, Kuniyoshi Y (2009) A tactile distribution sensor which enables stable measurement under high and dynamic stretch. In: IEEE symposium on 3D user interfaces 3DUI 2009, pp 87–93
22. Shu L, Tao XM, Feng DD (2014) A new approach for readout of resistive sensor arrays for wearable electronic applications. IEEE sensors J 15:442–452
23. Bamberg S, Benbasat AY, Scarborough DM, Krebs DE, Paradiso JA (2008) Gait analysis using a shoe-integrated wireless sensor system. IEEE Trans Inf Technol Biomed 12 (4):413–423

24. Pappas IPI, Keller T, Mangold S, Popovic MR, Dietz V, Morari M (2004) A reliable gyroscope-based gait-phase detection sensor embedded in a shoe insole. IEEE Sensors J 4 (2):268–274
25. Saponas T, Lester J, Hartung C, Kohno T (2006) Devices that tell on you: the nike + ipod sport kit. Department of Computer Science and Engineering, University of Washington. Technical report [Online]. Available: http://www.cs.washington.edu/research/systems/privacy.html. Accessed Nov 2006
26. Eskofier B, Oleson M, DiBenedetto C, Hornegger J (2009) Embedded surface classification in digital sports. Pattern Recogn Lett 30:1448–1456
27. Shu L, Hua T, Wang Y, Li Q, Feng DD, Tao XM (2010) In-shoe plantar pressure measurement and analysis system based on fabric pressure sensing array. IEEE Trans Inf Technol Biomed 14 (3):767–775
28. Wang Y, Hua T, Zhu B, Li Q, Yi W, Tao X (2011) Novel fabric pressure sensors: design, fabrication, and characterization. Smart Mater Struct 20(6):065015
29. Shabshin N, Zoizner G, Herman A, Ougortsin V, Gefen A (2010) Use of weight-bearing MRI for evaluating wheelchair cushions based on internal soft-tissue deformations under ischial tuberosities. J Rehabil Res Dev 47(1):31–42
30. Hagisawa S, Ferguson-Pell M (2008) Evidence supporting the use of two-hourly turning for pressure ulcer prevention. J Tissue Viability 17(3):76–81
31. Xu W, Huang MC, Amini N, He L, Sarrafzadeh M (2013) eCushion: a textile pressure sensor array design and calibration for sitting posture analysis. IEEE Sensors J 13(10):3926–3934
32. Lorussi F, Scilingo EP, Tesconi A, Tognetti A, De Rossi D (2003) Wearable sensing garment for posture detection, rehabilitation and tele-medicine. In: Fourth international IEEE EMBS special topic conference on information technology applications in biomedicine, Birmingham, pp 287–290
33. Data Acquisition Hardware, Tekscan Inc., Boston, MA, US [Online]. Available: http://www.tekscan.com/sensor-technology
34. Wu Y (2010) Development of an approach for interface pressure measurement and analysis for study of sitting. M. Eng. dissertation, Department of Mechanical Engineering, National University of Singapore, Singapore
35. Pang C, Lee GY, Kim TI, Kim SM, Kim HN, Ahn SH et al (2012) A flexible and highly sensitive strain-gauge sensor using reversible interlocking of nanofibres. Nat Mater 11:795–801
36. Mattmann C, Clemens F, Troster G (2008) Sensor for measuring strain in textile. Sensors 8:3719–3732
37. Kamiya K, Kudo M, Nonaka H, Toyama J (2008) Sitting posture analysis by pressure sensors. In: Nineteenth international conference on pattern recognition (ICPR), pp 1–4
38. Tasker LH, Shapcott NG, Watkins AJ, Holland PM (2014) The effect of seat shape on the risk of pressure ulcers using discomfort and interface pressure measurements. Prosthet Orthot Int 38(1):46–53

Flexible Fabric Strain Sensors

12

Weijing Yi

Contents

Introduction 294
Resistive Flexible Fabric Strain Sensors 294
Intrinsically Conductive Polymer-Coated Flexible Fabric Strain Sensors 295
Textile-Based Potential Divider 297
Conductive Yarn Knitted Flexible Fabric Strain Sensors 298
Conductive Nano-Material-Assembled Flexible Strain Sensor 299
Conductive Elastomeric Composite-Based Flexible Fabric Strain Sensor 303
Liquid Metal-Embedded Strain Sensor 307
Comparison of Different Resistive Flexible Fabric Strain Sensors 307
Inductive Flexible Fabric Strain Sensors 307
Polymer Optical Fiber (POF)-Based Flexible Fabric Strain Sensors 311
Summary 311
References 312

Abstract

Sensors that can measure strain of flexible or soft materials especially clothing or skins have attracted increasing attention with the spread of widely accepted concept of wearable electronics, which can be applied in rehabilitation, sports and posture/gesture simulation, etc. To be compatible with the measured substrates, the strain sensors should be flexible and soft for themselves and fulfill some extra properties like low modulus, large working range, and good fatigue to long-term usage besides the necessary sensing performances as a strain sensor, like high accuracy, good linearity, good repeatability, quick responding, etc. Due to the flexibility in all directions and reliable repeatability under extension in elastic range, textile materials have been extensively studied as a

W. Yi (✉)
Beijing Institute of Fashion Technology, Beijing, China
e-mail: ywj1wj@gmail.com; fzyywj@bift.edu.cn

© Springer Science+Business Media Singapore 2015

X. Tao (ed.), *Handbook of Smart Textiles*,
DOI 10.1007/978-981-4451-45-1_22

component or substrate of flexible strain sensors in smart textiles. In this chapter, the previous studies on flexible fabric strain sensors were systematically classified and examined from the point view of sensing mechanism, materials, structures, and performances, and the advantages and disadvantages of them were compared for further optimization and suitable applications.

Keywords
Smart textiles • Fabric strain sensor • Piezoresistive • Polymer optical fiber • Inductive sensor • Sensitivity • Wearable sensor

Introduction

Smart textiles have generated many interest in recent years by endowing generally used fabric or clothing in our daily life with sensing, actuating, and computing functions for wide range of applications in sports, health monitoring, entertainment, and artificial intelligence. As an indispensable part of smart textiles, sensors play a role as a nerve system to detect various environmental conditions or stimuli, like mechanical, thermal, chemical, electrical, magnetic, or other sources [1], and among them, strain gauges/sensors are one of the most frequently used ones for their widely potential applications in deformation measurement, perspiration monitoring, etc.; they can also be transferred to pressure sensor with specific structure design. Strain measurements have been achieved through various materials or methods; however, in smart textiles, the substrates where they were applied, i.e., skins, fabrics, or clothing, are soft, flexible, and easily deformable, so in order to reflect the real deformation of these materials under extension, the strain sensor should also be flexible and soft with modulus smaller than that of substrate materials, which will be able to deform following the human body motion without deteriorating the physical properties of the measured material and feeling any uncomfortable. Furthermore, in most of the daily wearable applications, the strain sensors will endure repeated large deformations, which raised additional requirements for them.

In this chapter, the flexible and soft fabric strain sensors were systematically reviewed and classified according to their sensing mechanism; the most representative samples in each category were demonstrated and their performance was evaluated. By comparison, the group of sensors in which the desired performances can be achieved for special applications was highlighted and their drawbacks was pointed out by considering the materials, structures, fabrication methods, and performances.

Resistive Flexible Fabric Strain Sensors

Measuring the change of resistance caused by deformation is a mainstream to fabricate strain sensors with good sensing performances; for some semiconductor or metals, when mechanical strain was applied, their electrical resistivity will

change accordingly, which is called piezoresistive effect. The sensing behavior of the strain sensor can be demonstrated by the sensitivity, represented by gauge factor (GF), which is defined as the fraction of the electrical resistance increment $\Delta R/R_0$ per unit strain, that is,

$$GF = \frac{\Delta R/R_0}{\varepsilon} \tag{1}$$

where R_0 is initial resistance of the strain gauge, ΔR is the resistance change due to deformation, and ε is the applied strain. The materials of some traditional resistive strain gauges including Cu-Ni, platinum alloys and silicon, etc., and the gauge factor of them are 2.0, 4.0–6.0, and −100 to 150, respectively [2]. The traditional strain gauges made by metal foils usually demonstrate advantages in relatively low resistance, high accuracy, and stable response; however, all of them are rigid and cannot reflect the real strain change of the materials under test; furthermore, their elongation is limited in the range of 0.1–0.5 %, which is hindering their integrate application and accuracy measurement in the field of smart textiles. The working range of silicon-based strain gauges is relatively high and they are more flexible than alloy-based sensors, but compared to textile materials, they are still much more rigid and cannot deform following the substrate materials to measure their accurate strain data under deformation. These performances limited the integrated application of the traditional strain sensors in wearable area.

To facilitate resistive-type strain sensors with performances suitable for wearable application, i.e., endow them with characteristics of low modulus, high working range, good repeatability, high accuracy, etc., different materials, structures, and treatment methods can be used, and one route is to endow inherent conductive polymers or inelastic electrical conductive fibers/yarns with elastic structures through knitting, coating, or pasting methods, whose sensing principles are mainly contributed to the change of contact resistance under deformation. The other route is to use elastic piezoresistive composites prepared by filling conductive particles into an elastic matrix and then integrated with textile materials.

Intrinsically Conductive Polymer-Coated Flexible Fabric Strain Sensors

Electrically conductive polymer composed of macromolecules having fully conjugated sequences of double bonds along the chains, which endow them with inherent conductive property. In the past few years, intrinsically conductive polymers (ICP) such as polypyrrole (PPy), polyaniline (PANI), polythiophenes (PTs), etc., have been extensively studied in many applications like chemical and biosensors, actuators, photovoltaics, rechargeable batteries, separation films, etc.; however, due to the inherent brittle properties and low elasticity of most reported ICPs, like PPy and PANI, they cannot be used as wearable strain sensor with flexibility and large deformation directly but can be combined with flexible substrates to achieve the abovementioned properties.

Since the flexibility and easy deformability of textile materials in all directions, especially their capability of supporting large deformations without deteriorating initial physical properties, they can be made into conductive fibers, yarns, or fabrics by coating PPy or other ICPs on its surface with electrochemical polymerization, in situ polymerization, chemical deposition methods, etc. These conductive materials can be used as potential sensing element for measuring and controlling human movements and activities. In 1997, De Rossi et al. [3] developed a PPy-coated Lycra fabric and examined its strain-sensing behavior for sensing fabric gloves and socks. Under extension, electrical resistance of the conductive fabric decreased about 20 % as tensile strain increased to 1 %, corresponding to a gauge factor of about −13.25, as strains beyond 1 %, the resistance change saturates, and no further sensing behavior can be observed. The conductive fabric also showed relatively good repeatability under cyclic measurement. But unfortunately, it also showed obvious temperature sensitivity (resistance decreased about 60 % when temperature increased from 20 °C to 60 °C), which will affect the measurement accuracy. The low working range also limited their real wearing applications.

PPy was also coated on elastic nylon/spandex and polyester (PET)/spandex fabric by Oh et al. [4] and Kim et al. [5] to study their strain-sensing behavior, electrical resistance of the conductive fabric increased monotonically with strain up to 50 %, and the gauge factor of about −0.7 was achieved for the previous sensor and −3 for the second one, which is due to the uniformly coating of conductive polymer on the single fibers of the fabric; in reference [6] and [7], the same coating method was used to coat PPy on Lycra fabrics, though strain range is limited to 1.2 %, but the gauge factor increased to −12 and −13, respectively. By using screen printing method with chemical vapor deposition under low temperature, the gauge factor of the PPy-coated knitted fabric was significantly increased to 210 at maximum strain of 50 % [8]. With solution-phase chemical polymerization method, the working range of PPy-coated knitted fabric was further increased to 70 % [9]. All the studies demonstrating the feasibility of PPy-coated fabrics can be used as flexible strain sensors for large-strain measurement if the substrate material was optimized. Besides textile materials, rubbers have also been studied as supporting substrates of PPy [10] to fabricate strain sensors in assisting the air-muscle control. Butyl rubber was selected as substrate for the similarity in the mechanical behavior compared to air muscle, while the PPy coating layer denotes the rubber with sensing ability. The gauge factor of the sensor achieved is about 0.65 at strain range of 10 %.

Due to the obvious difference in elasticity between the conductive PPy and textiles/rubbers, after coated on the surface of fabrics, there must be some micro-cracks appeared in the conductive PPy layer as tensile strain beyond a limit, resulting to the unsynchronized mechanical and electrical behavior of PPy-coated sensors at the first and successive extensions, though it can be stabilized by pretreating the sensors with a strain beyond their working range [8]. The change of contact resistance resulted from the opening/closing of cracks at loading/unloading cycles, contributed to the high strain sensitivity of PPy-coated sensors, and was deemed as the sensing mechanism [10–12], which have been demonstrated by the SEM morphology in [11]. As strain increased, some new micro-cracks will

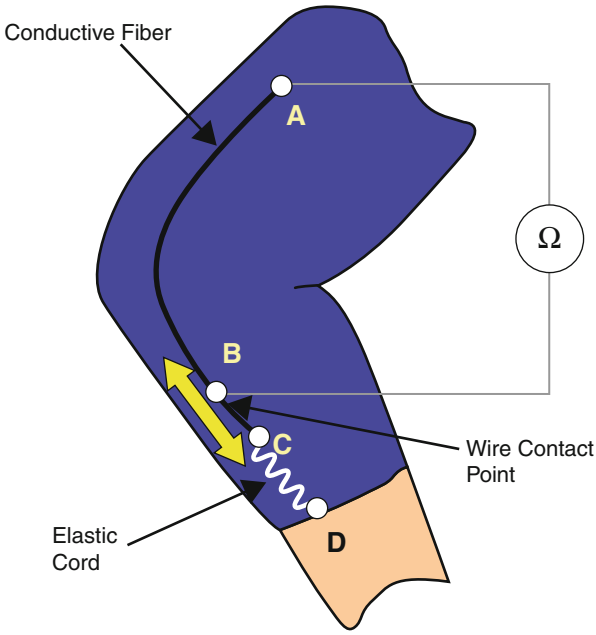

Fig. 1 Schematic of strain-sensing device designed by Gibbs et al. (Reproduced with permission from Ref. [17])

appear; however, after pretreatment with a higher strain than working strain, there will be no new micro-cracks appearing under application and the sensors exhibit stable high sensitivity. Unfortunately, the environmental stability of PPy is not good enough, which is a major problem that hinders the industrial application of this kind of sensors. Considerable efforts have been made to increase the stability of PPy-based strain sensors with chemical-aided process or make it denser to avoid the attack of oxygen [13–15]. However, the efforts of stabilization treatment are partially counteracted by the cracks on the coating layer arising from the sensor pretreatment process. Besides PPy, the potential applications of PANI-based strain sensors were also studied by coating them on PET yarns through absorption of yarns in PANI solution [16], and the similar unsolved problems exist as those for PPy, which need further improvement for industrial applications.

Textile-Based Potential Divider

For a conductive wire with uniform conductivity, the resistance is determined by the length of the wire; based on the principle, Gibbs et al. [17] designed and fabricated a wearable strain-sensing device for continuous monitoring of joint movements, as shown in Fig. 1, which was actually a textile-based potential divider that is using inelastic conductive fiber as sliding track and elastic cord as deformation undertaker, and when there is a motion, the position of the contact point will change, resulting in the corresponding resistance change under deformation, which can be measured by a coupled resistance-measuring device.

Conductive Yarn Knitted Flexible Fabric Strain Sensors

In 1999, Philips Research Laboratories developed a jacket incorporated with flexible strain sensors for upper limb and body movement measurement at the joint positions [18]. The sensor was fabricated by knitting conductive carbon fibers into fabric using plating structure. The electrical resistance of the sensor changed with extension due to the change of contact resistance between loops, and the electrical signal can be transmitted from the sensor to measuring devices by knitted track tape containing conductive wires.

The feasibility of stainless steel multifilament yarn [19–21] and polyacrylonitrile (PAN) oxidized carbon fiber [21, 22] knitted conductive fabric was studied respectively for the desired sensing performances, and the knitted structure can be simulated with a resistance circuit, where the variation of contact resistance between overlapped conductive yarns resulting from the change of fabric structure was considered as the sensing mechanism. The sensitivity of the strain-sensing fabrics expressed by gauge factor was about 5 when maximum strain was set to 20 % for the stainless steel one and higher than 3.0 with maximum strain of 30 % for the carbon fiber one. For the inherent elasticity of knitted structure and excellent heat resistance of the materials, the fabric strain sensors own not only good flexibility and large-strain measuring range but also adjustable sensitivity due to the changeable fabric structures, and most importantly, they can work properly at high temperatures. This kind of fabric strain sensor also have some limitations; the weight penalties as well as rigidity of the stainless steel and high crisp properties of carbon fiber undermined their comfort and reliability under long-term application. Furthermore, the introduction of rigid stainless steel or carbon fibers into textile materials may alter the strain field of textiles significantly [23], which will affect the accuracy of measured results. Silver-coated nylon yarns are usually more flexible than other conductive fibers/yarns, after knitted into fabric strain sensor they are more softer and comfortable for wearable applications [24, 25]. The sensing principle of this kind of fabric strain sensor is relying on the change of contact resistance between loops, while the knitted fabric is easy to deformation, resulting in the unstable initial resistance of the sensor, which will affect the accuracy during strain measurement.

With elastic fiber and polyester as the core, a yarn-based flexible strain sensor was fabricated by wrapping conductive carbon-coated fibers outside [26, 27]. The sensitivity of the sensor can be adjusted from three to nine with strain range of about 25 % when the conductive yarns and their twist levels changed accordingly. Based on the sensor, the elastic belt, band, and even garment can be fabricated for respiration signal monitoring. The configuration of the yarn-based sensor is one dimensional and desired for linear strain measurement, it's easy to knit into textile materials, and, besides, the repeatability of the sensor is also good.

The above mentioned fabric strain sensors made by conductive fibers/yarns are usually very flexible and can even directly be made into clothing. However, the contact resistance change is the main sensing mechanism of this kind of sensor for

the electrical resistance changes of fibers or yarns themselves are negligible, while contact resistance is not stable for the conductive knitted fabric due to their easy deformation properties if there is no other support. The resulting accuracy problem makes this kind of strain sensors suitable for respiration monitoring, but not for accurate strain measurement.

Conductive Nano-Material-Assembled Flexible Strain Sensor

Some conductive nano-materials exhibit excellent mechanical, electrical, and thermal properties, like CNTs, graphene, nanowires, etc.; with different kinds of assembly methods, usually combined with elastic materials, they can be made into flexible strain sensors. Pure CNT fibers or yarns show piezoresistive property, and they have been aligned and transferred onto a polymer substrate [28] to be a strain sensor with gauge factor of about 11.5, but the strain working range of the sensor is less than 1 % for the rigidity of the polymer. To increase the working range of the CNT-based strain sensor, CNT was aligned to a thin layer perpendicular to the strain axis and then adhered to elastic poly(dimethylsiloxane) (PDMS) substrate by strong van der Waals forces; the detailed fabrication process can be found in reference [29]. The strain sensor fabricated by this method demonstrates a very high working range up to 200 % due to opening and closing of gaps between CNTs. It also shows a monotonic resistivity-strain relationship which can be characterized by two linear regions whose gauge factor is 0.82 (0 % to ~40 % strain) and 0.06 (~60 % to 200 %), respectively. The final strain sensor after package showed a better linearity compared to the unpackaged one, good repeatability up to 10,000 cycles in strain range of 150 %, and low resistance creep as well as short response time, which have been used for human motion detection; several prototypes about the application of the sensors in wearable devices and the achieved signals were shown in Fig. 2. The CNT- and PDMS-based sensor showed very good performances except its complicated fabrication process for aligning and transferring the nanotubes and the corresponding high cost needed. Furthermore, the safety of the CNT-based materials also should be carefully considered when they were used near the human skin, for the needlelike CNT is easy to penetrate into the human skin [30].

Graphene nanoplatelets (GNP) have been studied as flexible strain sensors by coating them on different kinds of stretchable yarns layer by layer with controllable thickness [31]. The fabrication process and schematic of the yarn-based sensor is shown in Fig. 3. Three kinds of yarns, rubber, nylon-covered rubber, and wool yarns, were selected as substrates for coating; depending on the yarn structure and thickness of coating, the sensitivity and stretchability of the sensors can be adjusted. For rubber and nylon-covered rubber sensors coated with GNP, the electrical resistance increased with strain, while for wool yarns, the sensing behavior is opposite, which originated from different kinds of deformation behaviors of the yarns during stretching. Similar to PPy-coated elastic yarn, many cracks generated in the GNP coating on rubber during stretching, which contributed to the significant

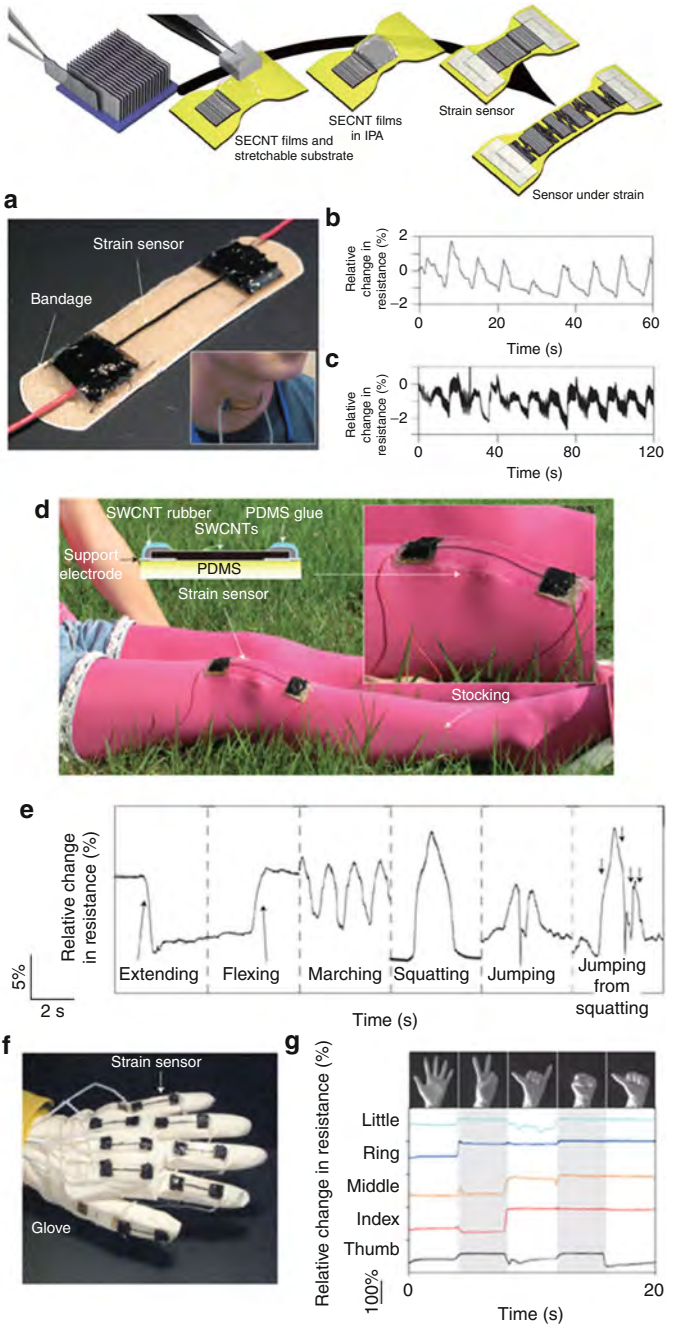

Fig. 2 Wearable devices based on SWCNT strain sensor and their performances (Reproduced with permission from Ref. [29])

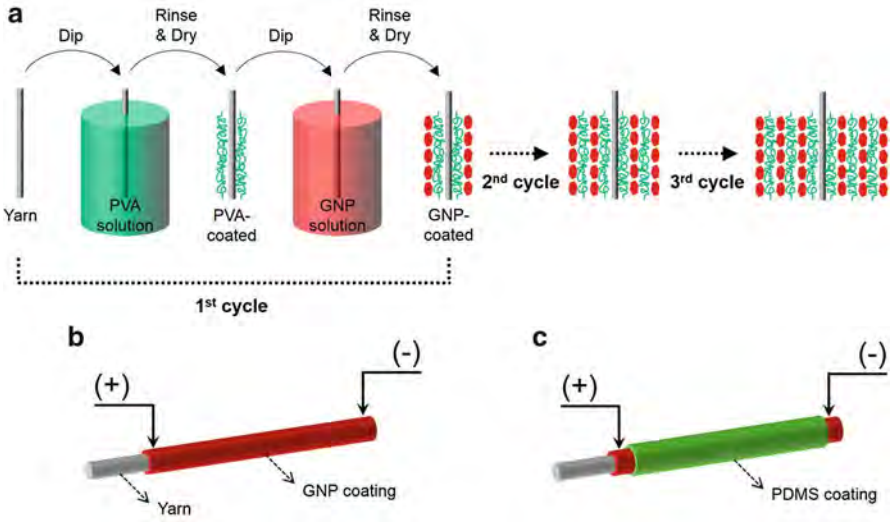

Fig. 3 Fabrication process and schematic of graphene-coated elastic yarn strain sensor (Reproduced with permission from Ref. [31])

increase of resistance under extension. On the other hand, due to the spiral surrounded structure of nylon yarn along the inner rubber, the nylon yarns with GNP were deformed first instead of direct stretch, resulting in much lower sensitivity compared to that of GNP-coated rubber sensor. Wool yarns consist of crimped and twisted fine wool fibers, and they will be aligned and compacted under extension, resulting in better contact resistance between each other, and corresponding a decrease in electrical resistance with the strain, the sensing principle is similar with the abovementioned carbon fiber or stain steel knitted fabric strain sensors. A very high sensitivity for GNP-coated rubber sensor and very high stretchability up to 150 % for nylon-covered rubber yarn sensor can be achieved and they can be used on human body motions like small-scale motions of the throat and the chest and large-scale motion like bending of the arm and hand, depending on the sensor selected.

A layer of conductive silver nanowires (AgNWs) was embedded in two layers of PDMS to be sandwich-structured flexible strain sensors; the fabrication process and prototype were shown in Fig. 4 [32]. The sensor has a better linearity because the piezoresistivity is not due to the fracture or crack propagation of the sensing materials but the change of contact resistance with sliding of AgNWs under extension. It also has tunable GFs in the ranges of 2–14 with a maximum strain up to 70 % depending on the density of AgNWs. But unfortunately, due to the big difference in the modulus between AgNWs and PDMS, the repeatability of the sensor at large strains is not good enough, and the minimum resistance increased 6.25 % when it was stretched to 40 % for 1,000 cycles.

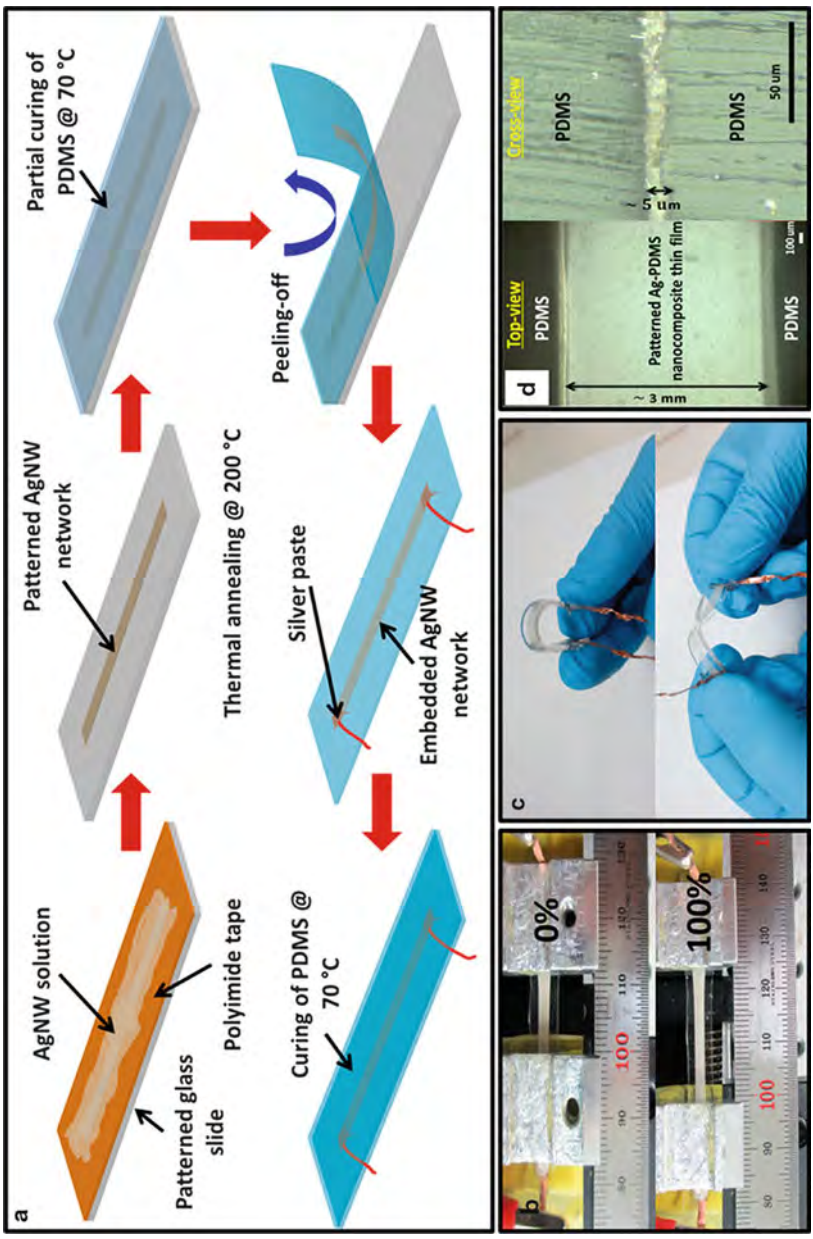

Fig. 4 Fabrication of sandwich-structured flexible strain sensor made by AgNWs thin film embedded between two layers of PDMS (Reproduced with permission from Ref. [32])

Conductive Elastomeric Composite-Based Flexible Fabric Strain Sensor

Most plastics or elastomers are insulating materials, and after filled with conductive fillers, such as metallic particles, carbon black (CB), graphite powder (GP), carbon fiber (CF), carbon nanotubes (CNTs), etc., the electrical resistivity of the composites will decrease. The concentration of conductive fillers is one of the most important parameters affecting electrical properties of the conductive composites. When the filler loading is low, the electrical resistivity of the composites is similar to that of insulating matrix. With the increase of conductive filler, the electrical resistivity decreases and it will significantly decrease by several orders of magnitude when the concentration of conductive filler is beyond a critical value, i.e., percolation threshold. With further increase of the filler loading, the changing in electrical resistivity of the composites is getting moderate.

The obvious change in electrical resistivity for the composites beyond percolation threshold can be achieved not only by the changing of conductive filler loadings but also by applying mechanical forces. The corresponding piezoresistive effect of conductive elastomeric composites can be used as flexible strain sensors to measure large repeated strain or displacement if there is a definite relationship between electrical resistance and mechanical deformation or pressure. Their perceived advantages include excellent flexibility, large deformability, high environmental stability, adjustable conductivity and Young's modulus, as well as relatively low manufacturing cost.

Among the commonly used conductive fillers, metallic materials can supply excellent conductivity, but the composites implanted with metals impose severe weight penalties as well as corrosion and degradation under external environments. GP and CF also have good conductivity and have been studied in conductive composites for sensor applications [33, 34]. However, drawbacks of sliding wear behavior of GP and crisp of CF result in worse repeatability and electromechanical properties under cyclic measurement. CNTs have very high aspect ratio, and when used as conductive filler, a very low loading is needed to reach percolation threshold. It had been added into ethylene propylene diene M-class rubber (EPDM) as sensing element to measure the bending and compressive large beam deflection [35]. Filler loading dependable sensitivity from 5.1 to 1.1 with CNT loading from 10 to 50 wt% was achieved with a relative good linearity between resistance and strain, but its strain measuring range is only 0.4 %. CNT-filled polymethyl methacrylate (PMMA) composites have also been studied with melt processing or solution casting methods for strain-sensing applications, and the results demonstrated that the sensitivity of the conductive films can be tailored by controlling the loadings of the nanotube, degree of nanotube dispersion, and film fabrication process [36], which benefits for developing sensors in different applications. As conductive fillers, carbon nanotubes [37] and graphene [38] can be fabricated into composites for sensing applications with far lower loadings than other conductive fillers. However, up to now, the high price, complex fabricating process, uncertainty of safety effect on humans, small strain measuring range,

as well as difficulty of large-scaled industrial production still limited their further application as flexible, large working range strain sensors in smart textiles.

Compared to CNT and graphene, the price of conductive CB is much lower, and the zero-dimensional structure of CB after good dispersion makes them less constrict on the deformation of matrix materials in composites compared to one-dimensional CNT, which benefits for improving the working range and decreasing Young's modulus of conductive composites. Furthermore, chemical resistance property and low density of CB compared to other conductive fillers make it a more preferred electrically conductive filler in composites for flexible strain sensors with large and repeated strain measuring ability [39].

The electromechanical properties of low-structured CB (Ketjenblack EC)-filled silicone elastomer (SE) composite under axial stretching for single and cyclic loading have been studied [40–42] and demonstrated that under single loading, the relative electrical resistance of the composite increased with tensile strain. Under cyclic measurement, the composite showed irreversible resistance changes between the first and successive cycles as maximum tensile strain was set at 40 %, and with mechanical preconditioning at a higher strain beyond its working range, the irreversible behavior of the composites can be stabilized. The composite also showed maximum strain amplitude and strain-rate dependence behavior, which limited their industrial application.

To compare the effect of CB structure on mechanical and electrical properties of CB-filled elastomers, CBs with low and high structures were filled into ethylene-octene (EO) elastomers, respectively [43]. Under extension, the composite filled with low-structured CB showed an increase in resistivity with strain in the first loading period. While in the following measurement cycles, a similar behavior that composite exhibited irreversible change in both mechanical and electrical properties even at low strains appeared. Different from the low-structured CB-filled composite, the conductive composite with high-structured CB showed a decrease in electrical resistance at low strains (2–4 %) and was then followed by reversible resistance-strain behavior upon cyclic loading to 20 % strain. When the tensile strain was further increased, the decrease in resistivity at low strains (20 %) and the weak increase at intermediate strains (up to about 300 %) can be observed for high-structured CB-filled EO composite [44]. The increase in resistance was believed related to recoverable damage of conductive paths in 100 % strain, while the unrecoverable increase was due to de-percolation of conductive paths at even higher strain. For the requirement of good repeatability, the composite can be potentially used as strain sensor in the strain working range between 0 % and 20 % for its high reversibility. The electrical and mechanical behavior of high-structured CB (HAF N330)-filled natural rubber (NR) and acrylonitrile butadiene rubber (NBR) composites at large tensile strains was also studied [45], and the results showed that the resistance of the composites increased with tensile strain under moderate extensions for unstrained specimen but decreased at higher extension. The increase of resistance followed by tensile strain was ascribed to the breakdown of the CB network, while the decrease of resistance at higher extension was attributed to the alignment of the shaped CB aggregates under large strain.

In the unloading period, the resistivity was significantly higher than that measured in the unstrained elastomer, which may be caused by the destroying of the specimen. When the composites were pressed, the resistance also increased with compressive strain. Xie et al. [46] simulated the electrical behavior of CB-filled NR at large strains based upon an infinite circuit model. Good agreement was achieved between the simulation results and the experimental data from Yamaguchi [76], confirmed the change of electrical resistivity under the strain, and was contributed to the breakdown of CB network and the alignment of CB aggregates.

With acetylene black as conductive filler, conductive composites with different types of insulating matrix such as ethylene-vinyl acetate (EVA), NBR, and ethylene-propylenediene rubber (EPDM) were studied [47, 48]. The electrical behavior of these composites depends on processing parameters like mixing time, rotor speed, mixing temperature, vulcanization time, and other service conditions like the pressure and temperature applied [49]. A very similar percolation behavior was observed for these composites, and the variation of their percolation threshold depended on the polarity and viscosity of matrix. Both the mechanical and electrical behavior of the composites synchronously changed with tensile strain, demonstrating the feasibility of them in the application of flexible strain sensors.

Dependence of CB loadings on reversible piezoresistive effects of CB/polyisoprene composite was studied by Knite et al. [50]. The electrical resistance of the composite increased about 4 orders of magnitude upon 40 % strain when the concentration of conductive filler was at percolation threshold, i.e., about 10 wt% CB loading. Though maximum sensitivity could be achieved at percolation threshold, the higher resistance is usually out of the measurement range of many ordinary instruments. The balance between sensitivity and measured resistance was considered for sensor applications [51], where composites with CB loading well beyond the percolation threshold were selected and a monotone increase in resistance followed by strain was achieved.

The flexible and large deforming properties of CB-filled elastomers are good candidates for strain sensors to measure deformation of textile materials for their low modulus, good elastic properties, and piezoresistive behavior, though the sensing behavior of them is affected by many parameters like CB structures, elastomer types, CB concentrations, fabrication methods, etc. The composites have been studied by being integrated with textile materials. Rubber solution containing micro-disperse phases of carbon on polyester/Lycra jersey fabric has been studied to measure the respiratory rate of human beings [52]. Based on the results, different fabrication routes were further studied.

Conductive fabrics knitted by cotton/Lycra threads with carbon-loaded rubber on the surface [6] and directly smeared CB-loaded elastomer [7, 53] were fabricated, and the gauge factor of 2.5 and 2.8 was achieved for them, respectively. The sensor has negligible capacitive effects up to 100 MHz and diminished long transient time for the latter one; prototypes of upper limb kinesthetic garment and sensing glove fabricated using carbon-filled silicone rubber over Lycra fabric as strain sensor were also studied [54–56].

By comparing the conventional melt-mixing method and solvent-aided method, high-structured CB-filled thermoplastic Evoprene 007 (styrene-butadiene-styrene

copolymer) composites were fabricated using solvent-aided method to produce strain sensor with flexible property [57]. The CB loading of 27.6 vol.%, which is much higher than percolation threshold, was selected to achieve a promise performance between low initial resistance and high sensitivity. Under extension, a nonlinear electrical resistance versus strain curve was observed for the sensor, which can be divided into a nonlinear zone with strain below 15 % and linear zone with strain from 15 % to 45 % with correlation coefficient $R^2 > 0.99$, and a gauge factor about 31 and 80 was calculated for the two ranges, respectively. The exceptionally higher gauge factor of the sensor can be attributed to combination of geometry change of the sensor and variation of percolation network of the system. The effect of climate conditions on the sensor performance was tested and the results showed that with increase of humidity, the electrical resistance of the sensor significantly increased about 40 % when humidity increased from 15 % to 90 % under the fixed temperature of 40 °C, while the effect of temperature is relatively smaller compared to the effect of humidity. Further study showed that the relative resistance of the sensor increased about 42 % at strain of 25 % when strain rate increased from 0.125/min to 12.5/min. The electrical resistivity of the sensor was also tested under cyclic elongation with maximum strain of 4 %; the electrical resistance is stable at maximum strain but slowly increased at minimum strain [58].

A fiber shaped strain sensor fabricated by melt-mixing method that consisting of 50 wt% thermoplastic elastomer (TPE) and 50 wt% CB was also studied for textiles strain measurement, as shown in Fig. 5 [59]. A study on the performance of the sensor showed that the relative resistance increased about 11 % when strain rate increased from 2.5/min to 30/min; the sensitivity expressed by gauge factor was about 20 as resistance relaxed 8.8 % in 2 min with maximum strain of 80 %; the maximum hysteresis error of ±3.5 % (7 %) and the mean hysteresis error over the working range of ±2.25 % (4.5 %) showed its potential industrial applications, and a prototype to measure upper body posters was built with the sensors integrated into textiles.

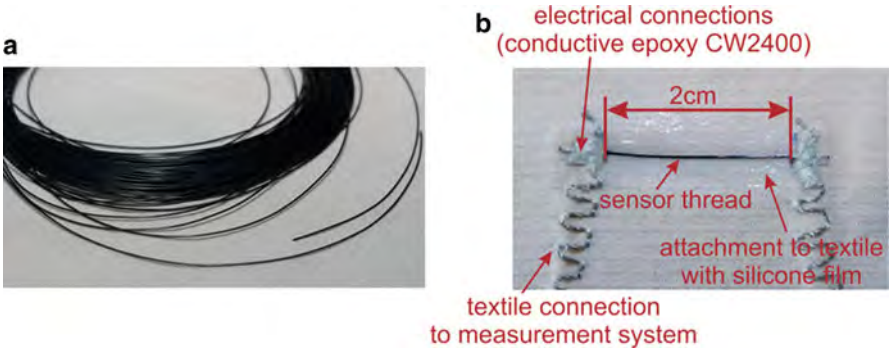

Fig. 5 CB-filled thermoplastic elastomer composite sensor: (**a**) sensor thread after extrusion and (**b**) sensor thread attached to the textile with a silicone film (Reproduced with permission from Ref. [59])

Liquid Metal-Embedded Strain Sensor

Eutectic gallium-indium (EGaIn) alloy is a metal in liquid form when temperature is in room temperature, and it behaves like an elastic material and maintains structural stability until it experiences a critical surface stress, at which point it yields and flows readily. These properties make it suitable to be flexible strain sensor when filled and encapsulated into channels within elastic materials [60]. Due to the Poisson's ratio of the material, when it was stretched, the composite will elongate in the tensile directions and contract in the orthogonal directions, resulting to the similar geometric change of the channel and electrical resistance of the liquid metal increase accordingly, which can be represented as

$$\Delta R = \rho\left[\frac{L+\Delta L}{(w+\Delta w)(h+\Delta h)} - \frac{L}{wh}\right]$$

where ΔR is the change in electrical resistance; ρ is the resistivity of the liquid metal; L, w, and h are the length, width, and height of the channels; and ΔL, Δw, and Δh are the changes in length, width, and height, respectively.

Based on the principle, a flexible strain sensor was developed by filling EGaIn into channels in silicone rubber through layered molding and casting method [61], the sensor could reliably extended to 300 % strain with gauge factor of 3.1 and very low hysteresis and no inflection point, and it was positioned on suit to measure joint angles via applied strains, which could provide a useful tool for physical therapy tasks. This kind of sensor has a very high strain range which is carried on from the elastic silicone rubber. However, besides the high price of the material used, the working temperature of the sensor is limited because the melt point of the liquid metal is usually higher than 15 °C; furthermore, the leakage hazard exists for the sensor when they are cyclically used.

Comparison of Different Resistive Flexible Fabric Strain Sensors

To better understand the development of resistive-type flexible fabric strain sensors and their materials, fabrication methods, and performances, they were categorized and compared in Table 1.

Inductive Flexible Fabric Strain Sensors

Dimensional change of conductive coils will result in variations in their self-inductance, through which strain and sensitivity can be calculated and displacements can be further detected via the change of electromagnetic induction between coils. Based on the sensing mechanism, an inductive flexible fabric strain sensor was fabricated by arranging the electroconductive fibers (polymeric and metallic) with different conductivity levels in helical paths [82], and the sensor was knitted through

Table 1 Summary of resistive flexible strain sensors and their performance

Researcher	Materials and fabrication methods	Performances		Merits and disadvantages	Literature
		Repeated cycles	Strain sensitivity (GF) and range		
Farringdon (Philips Research Laboratories, UK)	Knitted fabric	–	9.5 at 42 % strain	Wide strain working range Nonlinearity and instability	[18, 62, 63]
Tao XM (Hong Kong Polytechnic University, Hong Kong)	Knitted string/fabric with stainless steel filament/ carbon fiber	–	2.2 ~ 5.6 at 10 % strain, maximum strain range about 15 % ~ 32 % according to fabric density 12 ohm to 1 ohm when elongated to 20 % 3.0 with maximum strain of 30 % for carbon tubular fabric 5.6 with strain of 15 % for single warp gauge	Working temperature up to 200 °C Unstable initial status	[19–22, 64–66]
	PPy-coated knitted fabric by screen printing method with chemical vapor deposition under low temperature	–	210 at maximum strain of 50 %	High sensitivity Poor long-term stability	[8, 11, 15, 67, 68]
	9 wt% CNP-filled conductive composite printed on knitted fabric	10^5	4.76 within strain range of 0–40 %	Good repeatability Needs pretreatment	[69, 70]
Troster (ETH Zürich, Switzerland)	50 wt% thermoplastic elastomer (TPE) and 50 wt% CB fabricated by melt-mixing method	3,800	20 with resistance relaxed 8.8 % in 2 min under maximum strain of 80 %	Fiber structure is beneficial for measuring Reliability of connection is not good	[59, 71]

Koncar (Laboratoire de Génie et Matériaux Textiles, ENSAIT, France)	35 wt% CB-filled 65 wt% thermoplastic elastomers by solvent process	–	~31 at strain 0–10 % and ~80 at strain between 15 % and 45 %	High sensitivity and large working range Nonlinear behavior; obviously affected by humidity; resistance increased about 42 % at strain of 25 % when strain rate increased from 0.125/min to 12.5/min	[51, 58, 72]
De Rossi D (University of Pisa, Italy)	PPy-coated Lycra fabric or Lycra/cotton by chemical polymerization	–	~13 at 1.2 % fabric strain	High sensitivity Variation of sensor resistance with time and long response time in several minutes	[6]
	Graphite-loaded rubber coated on cotton/Lycra threads and knitted into fabric Graphite-loaded rubber smearing or screen printed on fabric	–	~2.5 at 10 % fabric strain ~2.8 for strain greater than 40 %	Nonlinearity Obvious resistance relaxation about 30 % at 30 % in 20 s Large hysteresis about 13.6 % at 80 % strain	[6, 52–56, 73–77]
G.G. Wallace (University of Wollongong, Australia)	PPy-coated nylon/Lycra fabric using solution-phase chemical polymerization method	–	~80 at 10–60 % strain	High strain range; pre-strained 20 % to ensure linearity Worse long-term stability	[9]
Wijesiriwardana (University of Manchester, England)	Carbon-filled polymeric fiber laid in the course direction (rows of stitches) of the base structure of knitted fabric	–	~0.5 at 0–80 % strain	Nonlinearity; worse reproducibility	[78]
Chang SH (National Taiwan University, Taiwan)	Twist piezoresistive carbon-coated fibers on elastic core yarn	–	3–9 at 25 % strain	High strain working range, good repeatability Reliability is not good	[26, 27]

(*continued*)

Table 1 (continued)

Researcher	Materials and fabrication methods	Performances		Merits and disadvantages	Literature
		Repeated cycles	Strain sensitivity (GF) and range		
Hata Kenji (National Institute of Advanced Industrial Science and Technology, Japan)	Aligned CNT adheres to PDMS substrate	10,000	0.82 at 0–40 % strain and 0.06 at 60–200 % strain	Large working range; quick responding time Sophisticated fabrication process, low sensitivity	[29]
Seong Hun Kim (Hanyang University, Korea)	PPy-coated PET/spandex	30	−0.5 at 0–50 % strain and 3 at 50 % strain	High strain range Worse long-term stability	[4, 5]
O Ok Park (Korea Advanced Institute of Science and Technology)	Graphene coated on rubber, nylon-covered rubber, and wool yarn, respectively	–	Adjustable GFs according to yarn structure and coating layers, strain range up to 150 % for graphene-coated nylon-covered rubber yarn	Large working range, adjustable sensitivity	[31]
Inkyu Park (Korea Advanced Institute of Science and Technology)	Sandwich-structured PDMS/AgNW/PDMS nanocomposite	1,000	2–14 depending on density of AgNWs with a maximum strain up to 70 %	Large working range, adjustable sensitivity Worse long-term stability	[32]
Ozgur Atalay (University of Manchester, England)	Jersey fabric knitted with silver-coated polymeric yarn and elastomeric yarn	–	3.44 at 0–40 % strain	Large working range Unstable initial resistance	[79]
Ko Frank (University of British Columbia, Canada)	Silver plating fiber knitted fabric	–	About 5 at 10 % strain	Flexible Smaller strain, nonlinearity	[80]
Ehrmann, A (Niederrhein University, Germany)	Knitted fabric containing stainless steel fibers	–	Elongations of 20–60 % cause electric resistance decrease of 90 %	Flexible Nonlinear, unstable	[81]
Conor J. Walsh (Harvard University, USA)	Liquid metal embedded in silicone rubber	–	3.1 at 300 %	Very large working range Obvious temperature effect	[61]

flat bed-knitting technology with three kinds of materials in which conductive fibers with conductivity in the range of the metals were used to form the conductive coils, elastomeric fibers (Lycra) to give the coil required resilience, and nonconductive textured fibers to improve the comfort. This kind of sensors (transducers) is flexible and soft due to the materials and knitted structure adopted and is able to measure large displacement even angular displacement approximately. It has been studied in respiratory measuring systems and motion-capturing systems. However, the accuracy and reliability of the sensor at repeated measurement should be further improved, and their applications are limited due to the circular configuration of the sensor.

Polymer Optical Fiber (POF)-Based Flexible Fabric Strain Sensors

An optical fiber is a tunnel for light waves to transfer along the fiber through internal reflection. It usually consists of a light source, a photodetector, and other electronic equipment. Optical fibers are usually made by glass, which are too rigid and crisp to be employed on textile materials, while polymer-based optical fibers are more flexible; by using Bragg grating, intensity, and interferometric principles [83, 84], they can be embedded in small-sized structures to measure the strain and/or strain distributions for their high accuracy, stability, lightweight, and small size. The inherent tensile range of POF is not large; however, by combing them with elastic materials, especially textile fabrics through interweaving, interlacing, or other types of methods with reasonably structure design, the strain range of the POF sensor will be greatly enlarged. A flexible fabric strain sensor capable of measuring repeated large strain up to 21 % has been reported by integrated looped POF with V-shaped notches of large angle with elastic belt [85, 86]; the sensitivity of the sensor expressed with gauge factor was approximately 3, hysteresis lower than 4 %, and repeatability less than 3 %; and it was little affected by temperature and relative humidity variations.

Marek Krehel et al. [87] developed a POF fabric sensor that can measure the respiratory rate by means of signal intensity changes and be able to distinguish different types of breathing, and it showed good correlation by comparing them with the output of a commercially available device.

Though a complex measuring procedure and relatively expensive accessorial equipment are needed to achieve the data, the most significant advantages of the POF sensors besides mentioned above, immune to the influence of electromagnetic interference (EMI) and computed tomography (CT) and high accuracy, compared to other electrical based sensors, give them wide potential applications in respiration monitoring in hospitals [88–91].

Summary

Smart textiles and clothing have high potential to be applied in fields like rehabilitation, entertainment, sports, etc. Reliable flexible strain sensors that can be easily embedded into textiles with performances of low modulus less than textiles or the

human skin, large-strain measuring range, and good repeatability in cyclic measurement with good fatigue life and good sensing properties are essentially important for market and become the subject of many researches.

The state-of-the-art flexible strain sensors with textile materials as substrates or applied onto textiles for measurement have been systematically reviewed and discussed in this chapter. Strain sensors based on resistive, inductive, and optical changes have been developed using flexible materials to adapt with the wearable applications in which the strain sensors based on resistive change principle are mainstream and many of them own very large working range and high sensitivity. However, some limitations still exist to fulfill the requirements of them in wearing applications, especially in the balance between the wearability, durability, and performances, which need further investigation.

References

1. Tao XM (2001) Smart fibres, fabrics and clothing. Woodhead Publishing, Cambridge
2. Neubert HKP (1975) Instrument transducers: an introduction to their performance and design. Clarendon Press, Oxford
3. De Rossi D, Della Santa A, Mazzoldi A (1997) Dressware: wearable piezo- and thermoresistive fabrics for ergonomics and rehabilitation. Engineering in medicine and biology society. In: Proceedings of the 19th annual international conference of the IEEE, Vol 5. IEEE, Chicago, IL, pp 1880–1883
4. Oh KW, Park HJ, Kim SH (2003) Stretchable conductive fabric for electrotherapy. J Appl Polym Sci 88(5):1225–1229
5. Kim HA, Kim MS, Chun SY, Park YH, Jeon BS, Lee JY, Hong YK, Joo J, Kim SH (2002) Characteristics of electrically conducting polymer-coated textiles. In: 13th Korea-Japan joint forum on organic materials for electronics and photonics, Sendai
6. Tognetti A, Carpi F, Lorussi F, Mazzoldi A, Orsini P, Scilingo EP, Tesconi M, De Rossi D (2003) Wearable sensory-motor orthoses for tele-rehabilitation. In: 25th annual international conference of the IEEE-engineering-in-medicine-and-biology-society, Cancun
7. Lorussi F, Rocchia W, Scilingo EP, Tognetti A, De Rossi D (2004) Wearable, redundant fabric-based sensor arrays for reconstruction of body segment posture. IEEE Sens J 4(6):807–818
8. Tsang J, Leung S, Tao X, Yuen MC, Xue P (2007) Effect of fabrication temperature on strain-sensing capacity of polypyrrole-coated conductive fabrics. Polym Int 56(7):827–833
9. Campbell TE, Munro BJ, Wallace GG, Steele JR (2007) Can fabric sensors monitor breast motion? J Biomech 40(13):3056–3059
10. Tjahyono AP, Aw KC, Travas-Sejdic J, Li KC (2010) Flexible strain sensor for air muscles using Polypyrrole coated rubber. In: BarCohen Y (ed) Electroactive polymer actuators and devices. SPIE, San Diego, California. doi:10.1117/12.847440
11. Xue P, Tao XM, Tsang HY, Leung MY (2006) PPy-coated electrically conducting fabrics with high strain sensitivity. In: Symposium on smart nanotextiles held at the 2006 MRS spring meeting, San Francisco
12. Wang JP, Xue P, Tao XM, Yu TX (2014) Strain sensing behavior and its mechanisms of electrically conductive PPy-coated fabric. Adv Eng Mater 16(5):565–570
13. Kim MS, Kim HK, Byun SW, Jeong SH, Hong YK, Joo JS, Song KT, Kim JK, Lee CJ, Lee JY (2002) PET fabric/polypyrrole composite with high electrical conductivity for EMI shielding. Synth Met 126(2–3):233–239

14. Harlin A, Nousiainen P, Puolakka A, Pelto J, Sarlin J (2005) Development of polyester and polyamide conductive fibre. J Mater Sci 40(20):5365–5371
15. Xue P, Tao XM, Tsang HY (2007) In situ SEM studies on strain sensing mechanisms of PPy-coated electrically conducting fabrics. Appl Surf Sci 253(7):3387–3392
16. Kim B, Koncar V, Dufour C (2006) Polyaniline-coated PET conductive yarns: study of electrical, mechanical, and electro-mechanical properties. J Appl Polym Sci 101(3):1252–1256
17. Gibbs PT, Asada HH (2005) Wearable conductive fiber sensors for multi-axis human joint angle measurements. J NeuroEng Rehabil 2(7). doi:10.1186/1743-0003-2-7
18. Farringdon J, Moore AJ, Tilbury N, Church J, Biemond PD (1999) Wearable sensor badge and sensor jacket for context awareness. In: The 3rd international symposium on wearable computers, San Francisco
19. Yang B, Tao XM, Yu JY (2006) A study on the relation between resistance and strain based on stainless steel fabric. Rare Met Mater Eng 35(1):96–99
20. Zhang H, Tao XM, Wang SY, Yu TX (2005) Electro-mechanical properties of knitted fabric made from conductive multi-filament yarn under unidirectional extension. Textile Res J 75(8):598–606
21. Zhang H, Tao XM, Yu TX, Wang SY (2006) Conductive knitted fabric as large-strain gauge under high temperature. Sens Actuators A 126(1):129–140
22. Zhang H, Tao XM, Yu TX, Wang SY, Cheng XY (2006) A novel sensate 'string' for large-strain measurement at high temperature. Meas Sci Technol 17(2):450–458
23. Xue P, Tao XM, Kwok KWY, Leung MY, Yu TX (2004) Electromechanical behavior of fibers coated with an electrically conductive polymer. Text Res J 74(10):929–936
24. Atalay O, Kennon WR, Demirok E (2015) Weft-knitted strain sensor for monitoring respiratory rate and its electro-mechanical modeling. IEEE Sens J 15(1):110–122
25. Wang F, Zhu B, Shu L, Tao XM (2014) Flexible pressure sensors for smart protective clothing against impact loading. Smart Mater Struct 23:015001. doi:10.1088/0964-1726/23/1/015001
26. Huang CT, Tang CF, Lee MC, Chang SH (2008) Parametric design of yarn-based piezoresistive sensors for smart textiles. Sens Actuators A 148(1):10–15
27. Huang CT, Shen CL, Tang CF, Chang SH (2008) A wearable yarn-based piezo-resistive sensor. Sens Actuators A 141(2):396–403
28. Riekeberg S, Buttner J, Muller J, IEEE (2010) A carbon nanotube based temperature independent strain sensor on a flexible polymer. In: Sensors, 2010 IEEE, Kona, HI, pp 647–651
29. Yamada T, Hayamizu Y, Yamamoto Y, Yomogida Y, Najafabadi AI, Futaba DN, Hata K (2011) A stretchable carbon nanotube strain sensor for human-motion detection. Nat Nanotechnol 6:296–301
30. Zhao HB, Zhang YY, Bradford PD, Zhou QA, Jia QX, Yuan FG, Zhu YT (2010) Carbon nanotube yarn strain sensors. Nanotechnology 21:305502. doi:10.1088/0957-4484/21/30/305502
31. Park JJ, Hyun WJ, Mun SC, Park YT, Park OO (2015) Highly stretchable and wearable graphene strain sensors with controllable sensitivity for human motion monitoring. ACS Appl Mater Interfaces 7(11):6317–6324
32. Amjadi M, Pichitpajongkit A, Lee S, Ryu S, Park I (2014) Highly stretchable and sensitive strain sensor based on silver Nanowire–Elastomer nanocomposite. ACS Nano 8(5):5154–5163
33. Beruto DT, Capurro M, Marro G (2005) Piezoresistance behavior of silicone-graphite composites in the proximity of the electric percolation threshold. Sens Actuators A 117(2):301–308
34. Das NC, Chaki TK, Khastgir D (2002) Carbon fiber-filled conductive composites based on EVA, EPDM and their blends. J Polym Eng 22(2):115–136
35. Kim JH, Kim YJ, Baek WK, Lim KT, Kang I (2010) Flexible strain sensor based on carbon nanotube rubber composites. In: Varadan VK (ed) Nanosensors, biosensors, and info-tech sensors and systems 2010. San Diego, California
36. Pham GT, Park YB, Liang Z, Zhang C, Wang B (2008) Processing and modeling of conductive thermoplastic/carbon nanotube films for strain sensing. Compos Part B Eng 39(1):209–216

37. Hu N, Karube Y, Arai M, Watanabe T, Yan C, Li Y, Liu YL, Fukunaga H (2010) Investigation on sensitivity of a polymer/carbon nanotube composite strain sensor. Carbon 48(3):680–687
38. Yu T, Ni ZH, Du CL, You YM, Wang YY, Shen ZX (2008) Raman mapping investigation of graphene on transparent flexible substrate: the strain effect. J Phys Chem C 112(33):12602–12605
39. Novak I, Krupa I, Janigova I (2005) Hybrid electro-conductive composites with improved toughness, filled by carbon black. Carbon 43(4):841–848
40. Kost J, Narkis M, Foux A (1984) Resistivity behavior of carbon-black-filled silicone-rubber in cyclic loading experiments. J Appl Polym Sci 29(12):3937–3946
41. Kost J, Narkis M, Foux A (1983) Effects of axial stretching on the resistivity of carbon-black filled silicone-rubber. Polym Eng Sci 23(10):567–571
42. Kost J, Foux A, Narkis M (1994) Quantitative model relating electrical-resistance, strain, and time for carbon-black loaded silicone-rubber. Polym Eng Sci 34(21):1628–1634
43. Flandin L, Chang A, Nazarenko S, Hiltner A, Baer E (2000) Effect of strain on the properties of an ethylene-octene elastomer with conductive carbon fillers. J Appl Polym Sci 76(6):894–905
44. Flandin L, Hiltner A, Baer E (2001) Interrelationships between electrical and mechanical properties of a carbon black-filled ethylene-octene elastomer. Polymer 42(2):827–838
45. Yamaguchi K, Busfield JJC, Thomas AG (2003) Electrical and mechanical behavior of filled elastomers. I. The effect of strain. J Polym Sci B 41(17):2079–2089
46. Xie ZM, Yum YJ, Lee CK (2007) Simulation of electrical resistivity of carbon black filled rubber under elongation. J Macromol Sci Part B Phys 46(3):561–567
47. Sau KP, Chaki TK, Khastgir D (1998) The change in conductivity of a rubber carbon black composite subjected to different modes of pre-strain. Compos A Appl Sci Manuf 29(4):363–370
48. Das NC, Chaki TK, Khastgir D (2002) Effect of axial stretching on electrical resistivity of short carbon fibre and carbon black filled conductive rubber composites. Polym Int 51(2):156–163
49. Das NC, Chaki TK, Khastgir D (2002) Effect of processing parameters, applied pressure and temperature on the electrical resistivity of rubber-based conductive composites. Carbon 40(6):807–816
50. Knite M, Teteris V, Kiploka A, Klemenoks I (2004) Reversible tenso-resistance and piezo-resistance effects in conductive polymer-carbon nanocomposites. Adv Eng Mater 6(9):742–746
51. Cochrane C, Koncar V, Lewandowski M, Dufour C (2007) Design and development of a flexible strain sensor for textile structures based on a conductive polymer composite. Sensors 7(4):473–492
52. Scilingo EP, Gemignani A, Paradiso R, Taccini N, Ghelarducci B, De Rossi D. (2003) Performance evaluation of sensing fabrics for monitoring physiological and biomechanical variables. In: International workshop on new generation of smart wearable health systems and applications, Lucca
53. Tognetti A, Lorussi F, Tesconi M, De Rossi D. (2004) Strain sensing fabric characterization. In IEEE sensors 2004 conference, Vienna
54. Tognetti A, Lorussi F, Bartalesi R, Tesconi M, Zupone G, De Rossi D. (2005) Analysis and synthesis of human movements: wearable kinesthetic interfaces. In: IEEE 9th international conference on rehabilitation robotics, Chicago
55. Tognetti A, Carbonaro N, Pone GZ, De Rossi D (2006) Characterization of a novel data glove based on textile integrated sensors. In 28th annual international conference of the IEEE-engineering-in-medicine-and-biology-society, New York
56. Tognetti A, Bartalesi R, Lorussi F, De Rossi D (2007) Body segment position reconstruction and posture classification by smart textiles. Trans Inst Meas Control 29(3–4):215–253
57. Koncar V, Cochrane C, Lewandowski M, Boussu F, Dufour C (2009) Electro-conductive sensors and heating elements based on conductive polymer composites. Int J Cloth Sci Technol 21(2/3):82–92

58. Cochrane C, Lewandowski M, Koncar V (2010) A flexible strain sensor based on a conductive polymer composite for in situ measurement of parachute canopy deformation. Sensors 10(9):8291–8303
59. Mattmann C, Clemens F, Troster G (2008) Sensor for measuring strain in textile. Sensors 8(6):3719–3732
60. Dickey MD, Chiechi RC, Larsen RJ, Weiss EA, Weitz DA, Whitesides GM (2008) Eutectic Gallium-Indium (EGaIn): a liquid metal alloy for the formation of structures in microchannels at room temperature. Adv Funct Mater 18(7):1097–1104
61. Menguc Y, Park YL, Martinez-Villalpando E, Aubin P, Zisook M, Stirling L, Wood RJ, Walsh CJ (2013) In: 2013 IEEE international conference on robotics and automation. IEEE, Karlsruhe, pp 5309–5316
62. Krause A, Siewiorek DP, Smailagic A, Farringdon J (2003) Unsupervised, dynamic identification of physiological and activity context in wearable computing. In: 7th international symposium on wearable computers, White Plains
63. Farringdon J, Nashold S (2005) Continuous body monitoring. In: Cai Y (ed) Ambient intelligence for scientific discovery: foundations, theories, and systems. Springer, Berlin, pp 202–223
64. Yang B, Tao XM, Yu JY (2004) A study on textile structure used as strain sensor made of stainless steel fiber. In: 83rd textile-institute world conference, Shanghai
65. Zhang H, Tao XM, Wang SY (2004) Modeling of elecro-mechanical properties of conductive knitted fabrics under large uniaxial deformation. In: 83rd textile-institute world conference, Shanghai
66. Yang B, Tao XM, Cai JY, Yu TX (2007) Strain sensing behavior of textile structures made of stainless steel continuous filament yarns under uni-axial tensile loading. In: International conference on smart materials and nanotechnology in engineering, Harbin
67. Li Y, Cheng XY, Leung MY, Tsang J, Tao XM, Yuen MCW (2005) A flexible strain sensor from polypyrrole-coated fabrics. Synth Met 155(1):89–94
68. Wang JP, Xue P, Tao XM (2011) Strain sensing behavior of electrically conductive fibers under large deformation. Mater Sci Eng A Struct Mater Prop Microstruct Process 528(6):2863–2869
69. Yi W (2013) Fabric strain sensor integrated with CNPECs for repeated large deformation. Hong Kong Polytechnic University (Hong Kong), Ann Arbor, p 180
70. Yi WJ, Wang YY, Wang GF, Tao XM (2012) Investigation of carbon black/silicone elastomer/dimethylsilicone oil composites for flexible strain sensors. Polym Test 31(5):677–684
71. Mattmann C, Amft O, Harms H, Troster G (2007) Recognizing upper body postures using textile strain sensors. In: 11th international symposium on wearable computers, Boston
72. Koncar V, Cochrane C, Lewandowski M, Boussu F, Dufour C (2007) Electro-conductive sensors and heating elements based on conductive polymer composites. In: 3rd international technical textiles congress, Istanbul
73. Lorussi F, Scilingo EP, Tesconi M, Tognetti A, De Rossi D (2003) Strain sensing fabric for hand posture and gesture monitoring. In: International workshop on new generation of smart wearable health systems and applications, Lucca
74. Bartalesi R, Lorussi F, Tesconi M, Tognetti A, Zupone G, De Rossi D (2005) Wearable kinesthetic system for capturing and classifying upper limb gesture. In: 1st joint eurohaptics conference/symposium on haptic interfaces for virtual environment and teleoperator systems, Pisa
75. Tognetti A, Lorussi F, Tesconi M, Bartalesi R, Zupone G, De Rossi D (2005) Wearable kinesthetic systems for capturing and classifying body posture and gesture. In: 27th annual international conference of the IEEE-Engineering-in-Medicine-and-Biology-Society, Shanghai
76. De Rossi D, Bartalesi R, Lorussi F, Tognetti A, Zupone G (2006) Body gesture and posture classification by smart clothes. In: 1st IEEE RAS-EMBS international conference on biomedical robotics and biomechatronics (BioRob 2006), Pisa

77. Ferro M, Pioggia G, Tognetti A, Carbonaro N, De Rossi D (2009) A sensing seat for human authentication. IEEE Trans Inf Forensics Secur 4(3):451–459
78. Wijesiriwardana R, Dias T, Mukhopadhyay S (2003) Resistive fibre-meshed transducers. In: 7th international symposium on wearable computers, White Plains
79. Atalay O, Kennon WR, Husain MD (2013) Textile-based weft knitted strain sensors: effect of fabric parameters on sensor properties. Sensors 13(8):11114–11127
80. Wang JF, Long HR, Soltanian S, Servati P, Ko F (2014) Electro-mechanical properties of knitted wearable sensors: part 2-Parametric study and experimental verification. Text Res J 84(2):200–213
81. Ehrmann A, Heimlich F, Brucken A, Weber MO, Haug R (2014) Suitability of knitted fabrics as elongation sensors subject to structure, stitch dimension and elongation direction. Text Res J 84(18):2006–2012
82. Wijesiriwardana R (2006) Inductive fiber-meshed strain and displacement transducers for respiratory measuring systems and motion capturing systems. IEEE Sens J 6(3):571–579
83. Fernandez-Valdivielso C, Matias IR, Arregui FJ (2002) Simultaneous measurement of strain and temperature using a fiber Bragg grating and a thermochromic material. Sens Actuators A 101(1–2):107–116
84. Tao XM, Tang LQ, Du WC, Choy CL (2000) Internal strain measurement by fiber Bragg grating sensors in textile composites. Compos Sci Technol 60(5):657–669
85. Ying DQ, Tao XM, Zheng W, Wang GF (2013) Fabric strain sensor integrated with looped polymeric optical fiber with large angled V-shaped notches. Smart Mater Struct 22:015004. doi:10.1088/0964-1726/22/1/015004
86. Zheng W, Tao X, Zhu B, Wang G, Hui C (2014) Fabrication and evaluation of a notched polymer optical fiber fabric strain sensor and its application in human respiration monitoring. Text Res J 84(17):1791–1802
87. Krehel M, Schmid M, Rossi RM, Boesel LF, Bona G-L, Scherer LJ (2014) An optical fibre-based sensor for respiratory monitoring. Sensors 14(7):13088–13101
88. Tang LQ, Tao XM, Du WC, Choy CL (1998) Reliability of fiber Bragg grating sensors embedded in textile composites. In: 7th international conference on composite interfaces (ICCI-VII), Fujisawa
89. Witt J, Schukar M, Krebber K (2008) Medicinal textiles with integrated polymer-optical fibers for respiration monitoring. Tech Mess 75(12):670–677
90. Yang CM, Huang WT, Yang TL, Hsieh MC, Liu CT (2008) Textiles digital sensors for detecting breathing frequency. In: 5th international summer school and symposium on medical devices and biosensors, Hong Kong
91. Yuan SF, Huang R, Rao YJ (2004) Internal strain measurement in 3D braided composites using co-braided optical fiber sensors. J Mater Sci Technol 20(2):199–202

Soft Tactile Sensors for Human-Machine Interaction

13

Fei Wang

Contents

Introduction 318
A Brief Review of the Human Skin 319
Important Characteristics of Soft Tactile Sensors 321
Sensitivity 321
Hysteresis 321
Response Time 322
Spatial Resolution 322
Flexibility 322
Stretchability 322
Soft Tactile Sensors with Various Transduction Techniques 323
Capacitive Tactile Sensors 323
Piezoelectric Tactile Sensors 330
Resistive Tactile Sensors 334
Optical Tactile Sensors 344
Conductive Liquid Tactile Sensors 348
Discussion 351
Current Problems 351
Future Directions 352
Summary 352
References 353

Abstract

With many upcoming aging societies, the demand for automated assembly lines, the need for surgery robots in hospitals, and the growing popularity of personal products with touch interfaces, more advanced and reliable soft tactile sensing techniques are required for human-machine interaction. Soft tactile interface

F. Wang (✉)
Institute of Textiles and Clothing, The Hong Kong Polytechnic University, Kowloon, Hong Kong, China
e-mail: f-e-i.wang@connect.polyu.hk

© Springer Science+Business Media Singapore 2015

X. Tao (ed.), *Handbook of Smart Textiles*,
DOI 10.1007/978-981-4451-45-1_26

will enable new generations of touch-sensitive health-care robots to attend the old and the disabled, pressure-sensing shoes and garment to collect human physiological signals for health monitoring, and many others in various fields including biomedical, agriculture, and food processing.

In the past decade, substantial effort has been made toward soft tactile sensors for smart skin that emulates the human skin, where four different types of touch receptors are embedded in a viscoelastic media, dermis. Current tactile sensing techniques include capacitive, piezoelectric, conductive elastomeric, optical, and conductive liquid types. Although each has its merits and limitations, many extreme tactile sensors have been developed: some can detect a pressure of 13 mPa; some show a sensitivity of 8.4 kPa^{-1} in the low-pressure regime; some tolerate a 300 % stretch; some measure three-dimensional forces; and some remain stable after 100,000 repetitive loadings. Nevertheless, no single sensing technology provides sensors on a par with human skin in all technical aspects, including sensitivity, hysteresis, response time, spatial resolution, flexibility, and stretchability. Fortunately, it is viable to emulate a subgroup of the four human force receptors.

Future directions of soft tactile sensors are task-centered design, nano-material, micro-fabrication and replication techniques, as well as more soft, elastic, and dynamic tactile sensing. Future development of soft tactile sensing solutions for human-machine interface shall reasonably bring more surprises to our life.

Keywords

Tactile sensors • Soft pressure sensors • Human-machine interaction • Flexible pressure sensors • Stretchable pressure sensors • Artificial skin • Electronic skin • Flexible electronics • Stretchable electronics

Introduction

Humans have five types of sensing modalities: sight, hearing, touch, smell, and taste. All the senses collect information from the outside world and transmit them into the brain, for a better understanding of the surrounding environment. To understand the development of the soft tactile sensing technologies, it is necessary to compare the five senses. For the sense of sight or vision, artificial vision devices are extensively used, ranging from medicine (e.g., X-ray images, ultrasound images), industry (machine vision), military (surveillance, missile guidance) to wearable electronics (Google glasses). Sound and audio systems have also found wide applications, with speech analysis and recognition as the hottest research area. At present, the research on the sense of taste and smell is progressing toward devices which can work as a taste stimulator or artificial nose. In general, the five senses in a human body are immensely different in anatomy and physiology. Unlike the other four senses with the organs located at specific areas, the sense of touch covers the entire body, suggesting its importance over the others.

Touch or tactile sensation is the sense by which external objects or forces are perceived through physical contact mainly with the skin [1]. As the most primitive modality of sense, it enables a human to distinguish cold from hot, static from slip, smooth from rough, and soft from hard. Even when the senses of sight and hearing are lost, a man is still able to maneuver and keep himself from harms, or even recognize Braille characters, by touching objects in the immediate environment. By contrast, nobody can lift an egg without the sense of touch.

Human-machine interaction or human-computer interaction involves the study, planning, design, and uses of the interaction between people and machine or computers. Haptic or tactile interface, providing the machine or computer a sense of touch, is a sub-domain of the human-machine interface. As the fields of robotics, biomedicine, and manikins are expanding continuously, soft tactile sensors for human-machine interaction are more desiring than ever before. In robotics, tactile sensing will enable new generations of intelligent robots which can safely interact with humans or perform humanlike, dexterous manipulation tasks in unstructured environment. In biomedicine, it will allow the surgeons to perform minimally invasive surgeries (MIS) or even remote surgery operations. In smart textiles, it will render manikins touch sensitive for garment comfort evaluation and impart shoes or garment the sense of touch to collect human physiological signals for health monitoring. Agriculture and food processing also entail soft tactile techniques.

Over the past decade, substantial progress has been made in the realm of soft tactile sensing technology for human-machine interactions. However, high-performance soft tactile sensors that rival the human skin in terms of sensitivity, pressure measuring range and directions, softness, robustness, and spatial distribution are still unavailable. This chapter, therefore, will review the state of the art of soft tactile sensors, try to give the reasons for the delayed acceptance of tactile sensing technology, and indicate future directions. Since mechanical force detection is the major concern here, the phrases tactile sensors and pressure sensors will be used interchangeably in this chapter.

The chapter is organized as follows: first, the structure and physiology of the human skin is briefly introduced as it sets the benchmark for artificial skins. Second, important characteristics of soft tactile sensors are identified and explained concisely. Third, various tactile sensing techniques are illustrated and compared, with typical examples of tactile sensors that best represent the current state of the art. Forth, current challenges and future trends are proposed, followed by a summary of the chapter.

A Brief Review of the Human Skin

As the largest organ in the human body, the skin covers the entire body and provides different degrees of sensitivity in perceiving touch and temperature. In particular, fingertips, the most sensitive skin in touch, exhibit the shape and agility to feel hardness and texture, as well as to perform dexterous manipulations such as

squeezing, screwing, and unscrewing. The skin is a hybrid system involving the active sensors (the neurons) to detect force and a viscoelastic medium (the dermis) to transmit strain from the epidermis to the neurons. The dermis works like a packaging material to hold the neuron networks and also serves as a transmission media in sensing dynamic forces. Therefore, in order to emulate the tactile system, it is necessary to analyze the skin at a system level rather than considering the sensors only [2].

The human skin consists of an outer layer called the epidermis, 0.06–0.12 mm in thickness, and an inner layer called the dermis, 1–4 mm thick. The dermis harbors many neuron receptors which provide the sense of heat and touch. When the skin is subject to an external force, there will be a strain on the skin. The strain is then transmitted to the neuron receptors, which trigger an electrical signal to the brain [3]. The dermis, composed of a matrix of elastic collagen fibrils, is viscoelastic in nature. Therefore, the mechanical signals (force) can be transmitted into the neurons in terms of both the magnitude of the stress and the rates of change.

A very interesting aspect of the skin is that it has four kinds of force sensors in terms of response speed and the region they are in charge of [3]. In the dermis, there are mainly two classes of touch receptors: the slow-acting (SA) ones which react to sustained strains and the fast-acting (FA) ones in charge of strain rates [3]. The FA and SA receptors can be further divided into two categories according to their working field. The FA I and SA I receptors are closer to the epidermis and respond to highly localized external stress. They are therefore called "near-field" receptors, while the "far-field" receptors SA II and FA II are grown deeper in the dermis and have broader fields of touch sensitivity [3]. Therefore, there are in total four kinds of receptors as listed in Table 1 [2].

The existence of two kinds of polymer networks in the skin: elastic fibers with low modulus and collagen fibers with higher modulus, contributes to the compliance of the skin. Also, the viscoelastic property helps to absorb energy during viscous deformation, thus enabling the detection of reversible mechanical forces/deformations. However, current artificial tactile sensor systems have not successfully emulated the following three aspects of the skin. Firstly, the system is purely digital rendering it more precise, highly sensitive, and noise resistive. Secondly, the variety and characteristics in receptors produce complicated signal generation modes to applied force and strain rate distribution. Both the static and dynamic

Table 1 Response characteristics of the four primary receptors (Reproduced with permissions from Ref. [4]. Copyright 2011, Rights Managed by Nature Publishing Group)

Type of receptors	Response characteristics
Merkel (SA I) (near field with multiple sensitive points; continuous, irregular discharge)	Slow; fine details; 70 units/cm^2; <5 Hz
Meissner (FA I) (near field; on-off discharge)	Slightly faster; grip control; 140 units/cm^2; 5–50 Hz
Ruffini (SA II) (far field; continuous, regular discharge)	Slow speed; stretching; 10 units/cm^2
Pacinian (FA II) (far field; on-off discharge)	Fast vibration; dynamic texture; 20 units/cm^2; 40–400 Hz

distributions of force are measured with one or two sets of receptors [2]. Finally and most importantly, all the components in the human skin are mechanically compliant and stretchable, in other words, soft and robust, which pose considerable challenge to traditional electronic industry based essentially on silicon wafer, a rigid material.

Important Characteristics of Soft Tactile Sensors

In order to properly evaluate the performance of a soft tactile sensor, some mathematical and physical features must be defined to quantify the sensor's characteristics. The features include both the terminologies inherited from the traditional sensor industry and those defined exclusively for soft tactile sensors. The former involves transfer function, sensitivity, linearity, hysteresis, span or dynamic range, repeatability, response time, reliability, etc.; and the latter includes spatial resolution, mechanical compliance or softness, and stretchability. To make it concise, only primary features will be discussed below in greater detail. Others can be easily accessed through a handbook of sensors.

Sensitivity

For mechanical sensors, sensitivity defines the relationship between the measured parameter (e.g., resistance, capacitance) and the mechanical stimuli applied, such as force, pressure, or strain. The sensitivity value is generally the ratio between a small change in the input signal to a small change in the output signal. In the case of soft tactile sensors, the sensitivity is primarily determined by the mechanical properties of the soft materials used. Typically, higher sensitivity can be achieved by using materials with a lower bulk and tensile modulus. Such materials, however, often have a higher hysteresis (refer to section "Hysteresis"), thus affecting the accuracy of the sensors.

Hysteresis

For some sensors, the output value does not return to the initial level following the same path it previously approached. This is more noticeable in a cyclic loading, when the input reaches the same value twice both on its way and on its return. As regards the output signal of a transducer, the hysteresis is the difference between the upscale and downscale approaches to the same point [5]. Hysteresis often arises from the viscoelasticity of the sensor material or from the friction between the sensor and the object. Tactile sensors made purely from soft materials always suffer from a large hysteresis as discussed in the previous section.

Response Time

Response time is the time span between the application of an instantaneous change in the physical input to the sensor and the resulting indication of change in output of the sensor [5]. In other words, the sensor does not react instantly to the stimulus but with a delay. Another terminology for the phenomenon is frequency response. A shorter response time means a higher frequency response, which is obviously a prerequisite for the detection of oscillatory forces. However, since the soft materials deployed for soft pressure sensors are often elastomers, their viscoelasticity shall incur prolonged response time.

Spatial Resolution

For tactile sensors, spatial resolution or sensor density is the number of sensors per unit area. Since the touch receptors in the fingertips can be as high as 150 per cm^2 [4], an ideal artificial skin entails a high spatial resolution of tactile sensors at the same level. Such a high resolution requires an effective militarization of soft tactile sensors. While the microelectromechanical systems (MEMS) provide a solid background for producing micro-sized electrical elements, it is incapable of handling soft materials such as elastomers.

Flexibility

Flexibility or pliability is the degree by which a material or system can be bent easily without breaking. It is the complementary concept of stiffness or rigidity. It is often evaluated by the radius of curvature that the material can conform to. Flexibility is an indispensable property of artificial skin because the human body is curvilinear in shape. Soft materials such as elastomers have a high degree of flexibility; rigid materials such as polyimide or even silicon can also achieve certain level of flexibility when they are thin enough. Obviously, the human skin is flexible because it is composed of elastic materials rather than thin layers of rigid materials. The Young's modulus of the human skin is around 30–70 kPa [6]. In view of bionics, soft tactile sensors can achieve their flexibility by using elastic materials so that they can cover surfaces with any curvatures.

Stretchability

Stretchability refers to how much a material or object can be stretched without breaking. For soft tactile sensors, stretchability is defined within the range of elastic deformation because plastic deformation permanently alters the mechanical and geometrical properties of the sensor. While the flexibility improves the safety of a device, the stretchability will make the sensor nonbreakable and mountable onto

curved surfaces or deformable parts such as joints. The maximum strain of the human skin around the knee joint for a whole squatting and rising (flexion and extension) cycle is up to 44.6 % in every direction [7], which sets the strain standard for soft tactile sensors.

Soft Tactile Sensors with Various Transduction Techniques

During the past decade, large numbers of soft tactile sensors have been developed for human-machine interaction. As a branch of mechanical sensors, soft tactile sensors can be categorized by the methods or techniques deployed for the transduction process. In this way, current soft tactile sensor can be broadly classified into five main categories: capacitive, piezoelectric, conductive elastomeric, optical, and conductive liquid soft tactile sensors. The five categories are discussed in the following sections. A comparison between them can be found in Table 9 at the end of section "Soft Tactile Sensors with Various Transduction Techniques."

Capacitive Tactile Sensors

A capacitive tactile sensor consists of two parallel conductive plates with a dielectric material sandwiched between them. For parallel plate capacitors, capacitance can be expressed as Eq. 1, where A is the area of electrodes, D the distance between them, ε_r is the relative dielectric constant, ε_0 is the permittivity of a vacuum, and C_f is the contribution from edges of the electrodes. When a load is applied to the tactile sensor, D is reduced, and the capacitance increases. Tactile information is registered by measuring the capacitance change. Normally, in the design of tactile sensors, A is much larger than D^2, so C_f is negligible.

$$C = 4\pi\varepsilon_r\varepsilon_0\frac{A}{D} + C_f \tag{1}$$

In general, capacitive tactile sensors merit a high spatial resolution, a good frequency response, and a large measuring range. They are also immune from temperature changes and suitable for large-area applications. This field has well-established design and fabrication techniques. However, they are susceptible to electromagnetic interference. Mesh arrangements would induce cross talk noise, fringing capacitance, and field interactions. Also, they require relatively complicated electronics to decipher the signals as well as to filter out the noises.

Great effort has been made to develop capacitive tactile sensors, either by changing the electrodes or the dielectric layer. Besides, both materials and shapes of the electrodes or dielectric layer can be changed. The capacitive tactile sensors, therefore, have many more variations than the other types of tactile sensors. The common types are described below with typical examples.

Nanotube/Nanowire Electrodes

As an emerging technology, nanotechnology manipulates matters on an atomic or molecular scale and produces new generations of materials such as Ag nanowires (AgNWs) and carbon nanotubes (CNTs). When AgNWs or CNTs are doped into elastomers, elastic conductive composites are formed, enabling stretchable or even transparent electrodes for capacitive tactile sensors.

In 2011, Bao's group [8] developed skin-like pressure and strain sensors based on transparent films of CNTs. As illustrated in Fig. 1, CNTs were spray coated through a stencil mask onto polydimethylsiloxane (PDMS) substrates forming a thin layer of conductive film patterns. After one cycle of stretch and release in the strain-sensing direction, two such PDMS films were laminated together using Ecoflex® silicone elastomer (CNT films face to face and CNT stripes perpendicular to each other). Arrays of capacitors were thus constructed. The stretch and release is necessary to stabilize the morphology of the CNTs. Such sensor arrays can detect normal pressures from 50 to 1 MPa, accommodate to strains up to 50 %, and exhibit a transparency over 68 %. For such sensors, delamination of the CNT layer under repetitive mechanical loadings is a big concern since the CNTs are deposited onto the surface without robust mechanical or chemical bonding. In this regard, Xiaolong et al. [9] in 2013 sprayed single-walled nanotubes (SWNT) onto a fluorinated glass slide, spread liquid PDMS onto the slide, and then cured the PDMS. Conductivity of the elastic conductor showed no significant decline after 100 cycles of 50 % strain tensile tests. Ten tape tests further proved the enhanced

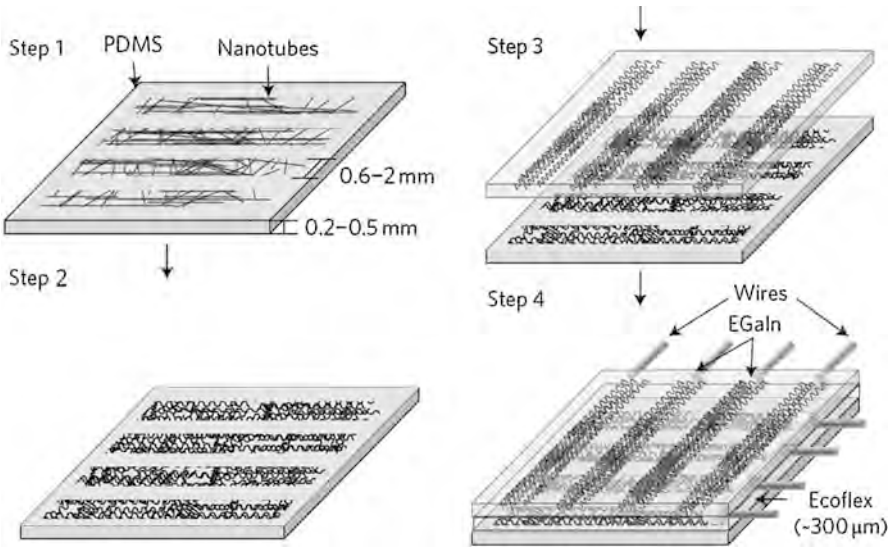

Fig. 1 Processes of fabricating arrays of transparent capacitive pressure sensors. *Step 1*, spray coating of the nanotubes; *Step 2*, pre-stretching along the strain direction; *Step 3*, lamination of the two layers; *Step 4*, wire connection (Reproduced with permissions from Ref. [8]. Copyright 2011, Rights Managed by Nature Publishing Group)

mechanical robustness of this structure. Pressure sensor arrays using such elastic conductors had a gauge factor of 0.59 for pressures from 10 to 124 kPa. Besides, the conductor was able to tolerate strains of up to 300 %. Transparency of the sensors are, however, lower than that of Bao's sensor arrays.

Apart from CNTs, AgNWs were also embedded into soft elastomers to make tactile sensors. Compliant capacitive pressure sensors were fabricated by using electrodes with AgNW networks embedded in the surface layer of polyurethane (PU) [10] and PDMS [11]. They can work both as capacitive pressure sensors and resistive strain sensors.

Here, it is worth noting that, despite the excellent mechanical and electrical properties of CNTs, they pose serious toxic and hazardous issues [12, 13].

Conductive Liquid Electrode

Flexible capacitive pressure sensors that use thin film or other solid electrodes are susceptible to delamination and cracking under repetitive loading or stretching. Liquid metal alloy provides an effective alternative to remove this limitation since sealed liquid flows rather than cracks. In 2012, Ruben et al. [14] fabricated flexible microfluidic normal force sensors that used PDMS layers with microchannels filled with Galinstan. The conductive liquid Galinstan served as both flexible wire connections and robust electrodes. The sensor can detect normal forces from 0 to 2.5 N and tolerate curvatures of 6.289 cm (radius).

Foam Dielectric Layer

Foam is a liquid or solid material containing entrapped air pockets. Solid-state polymer films can improve the compressibility and thermal insulation of pressure sensors [15]. Solid foams are either open cell or closed cell. In open-cell foams, the air pockets connect with each other; while in closed-cell foams, they are isolated from each other by solid materials. The major limitation for foam-based pressure sensors is hysteresis, which becomes serious when the foam is softer.

In 2013, Vandeparre et al. developed extremely robust and conformable capacitive pressure sensors comprising open-cell PU foams and gold-evaporated electrodes [16]. Since all the materials used are highly elastic, the sensors can tolerate crumpling, indentation, and autoclaving without impairing the electromechanical performance (Fig. 2). The sensor detects pressures from 1 to 100 kPa with tunable sensitivities by using different foams.

Microstructured Dielectric Layer

Soft lithography allows easy and low-cost fabrication of PDMS with microstructures of various shapes [17]. The facile replication of highly ordered microstructures of polymers over large areas is of great significance for diverse applications such as biometric adhesive surfaces [18]. Using soft lithography, microstructured elastomer layers can be fabricated easily. Capacitive tactile sensors deploying such microstructured dielectric layers have demonstrated ultrahigh sensitivity for minute pressures.

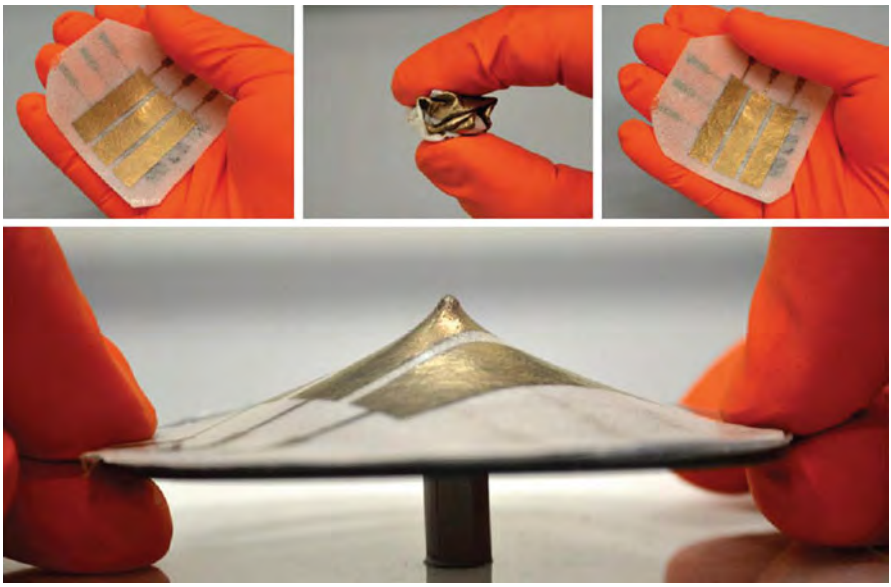

Fig. 2 Picture of the highly compliant and robust foam pressure sensor: original, crumpled, restored, and under indentation (Reproduced with permissions from Ref. [16]. Copyright 2013 AIP Publishing LLC)

In 2010, Bao's group used a thin microstructured PDMS film replicated from a silicon wafer mold as the dielectric layer of capacitive tactile sensors, achieving a high sensitivity of 0.55 kPa^{-1} in the low-pressure regime (<10 kPa) [19]. The structured layers effectively minimized the viscoelasticity of PDMS and offered sensitivity 30 times higher than that of sensors with unstructured dielectric layers. These pressure sensors could detect even a mass of 20 mg, corresponding to a pressure of 3 Pa. The reduced viscoelasticity could allow the detection of a quick series of pressures. Since the structured dielectric layers are highly ordered, they significantly improved the signal-to-noise ratio of the sensors, especially when compared with those with foam dielectric layers. Further in 2013, the same research group deployed the microstructured dielectric layers as the gate dielectric for organic field-effect transistors (OFET) which used a rubrene single crystal as semiconductor as shown in Fig. 3 [20]. The transistors showed a high sensitivity of 8.4 kPa^{-1} and a short response time of <10 ms. With OFET, the capacitance change of the dielectric under compression was significantly amplified in the low-pressure regime (<1 kPa). While highly sensitive, these OFET sensors are complicated in structures and entail quite complex and demanding fabrication processes.

Interestingly in 2012, Wang's group [21] presented a capacitive pressure sensor with almost identical structures to Bao's pressure sensors [19]. The sensor had a low-end detection limit of ~13 mPa. However, this type of pressure sensor is different from Bao's sensors in terms of transduction techniques and power

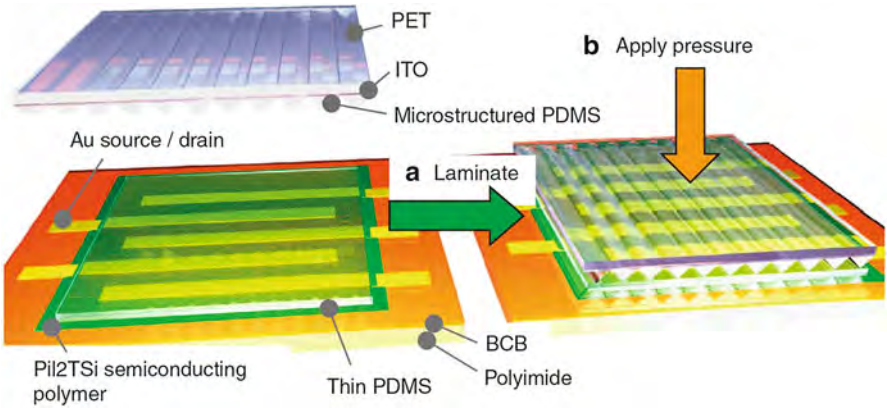

Fig. 3 Schematic of the fabrication steps of the pressure-sensitive resistor. The sensor includes two layers laminated together: one layer contains the *bottom* source-drain electrodes and the semiconducting polymer; and the other contains the gate electrode as well as the microstructured dielectric (Reproduced with permissions from Ref. [20]. Copyright 2013 Macmillan Publishers Limited)

consumption. When there is external forces, electricity can be generated making the sensor a self-powered device. In other words, it is based on power generation rather than measuring the change in capacitance. Since the sensor sends out voltage or current signals only when there are changes in external forces, it is restricted to dynamic pressure measurement, which is similar to piezoelectric pressure sensors in section "Piezoelectric Tactile Sensors."

Breath figure (BF) method provides an effective alternative to fabricate micro- or nanostructured polymer films. It uses the self-assembly of water droplets on the surface of organic polymer solution to achieve honeycomb-structured polymer films. When nano-needle polymer films prepared by breath figure method are used as the dielectric layer of capacitive pressure sensors, the sensitivity can reach 1.76 kPa^{-1} in the low-pressure regime (<1 kPa) [22]. Nevertheless, the aluminum electrodes used in the sensor provide limited flexibility.

Textile-Structured Sensors

Woven fabrics, due to the pliability, conformability, and durability, provide excellent platforms to make pliable and durable pressure sensors. Flexible pressure sensors for sitting posture classification have been made by sandwiching foam spacer between embroidered conductive wire electrodes [23]. The sensor is insufficient in both softness and sensitivity for low pressures. As explained in Fig. 4, large-area capacitive tactile sensors have been developed by measuring the capacitance at the crossing points of conductive warp and weft yarns [24]. The nylon yarns acquire their conductivity via a coating of poly(3,4-ethylenedioxythiophene)/poly(styrenesulfonate) (PEDOT:PSS). There is an outer layer of perfluoropolymer (Cytop), a dielectric polymer, to insulate the conductive yarns at the crossings.

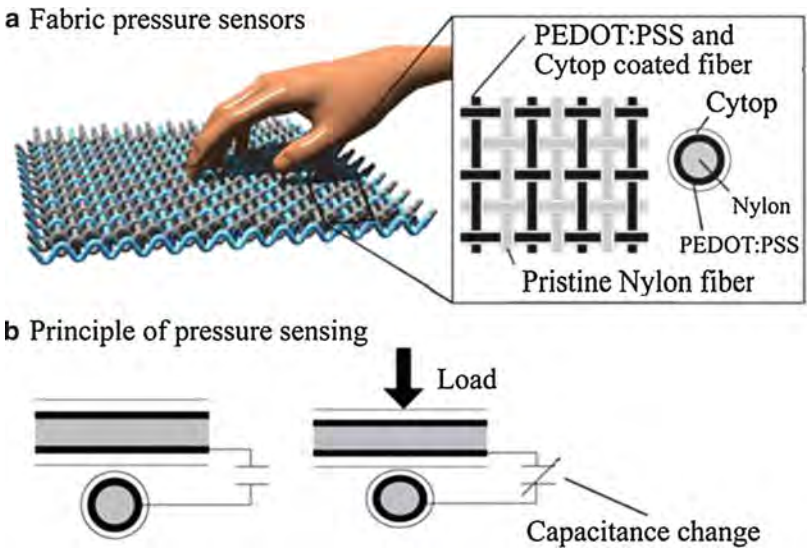

Fig. 4 Schematic of the fabric pressure sensor array. (**a**) The capacitive pressure sensor array is formed by weaving conductive polymer yarns with dielectric film coatings. (**b**) The sensing mechanism (Reproduced with permissions from Ref. [24]. Copyright 2012 Elsevier B.V)

Such sensors can detect pressures from 9.8 to 98 kPa. The main features of the sensors include large-area applicability, simple structure, conformability, and durability.

Three-Axial Pressure Sensors

Despite of the high sensitivity and stretchability, all the capacitive pressure sensors discussed above are incapable of detecting shear stress. By contrast, the skin senses forces in all directions. Capacitive tactile sensors can realize three-axial force detection by using multiple electrodes.

In 2010, Lee et al. developed a three-axial capacitive tactile sensor with four capacitors embedded at each corner of a truncated pyramid-shape PDMS bump [25]. The dielectric layers are air gaps. The average capacitance value of the four capacitors reflects the normal force; and the difference in capacitance values between opposite capacitors indicates shear forces. The sensors detect pressures between 0 and 250 kPa for all three axes even when at a bending radius of 4 mm. One concern of the structure is the use of copper electrodes which has a Young's modulus several orders of magnitudes larger than that of PDMS. The mismatch in rigidity would affect the sensors' durability especially under repetitive loadings.

In 2013, Dobrzynska et al. demonstrated sheet capacitive pressure sensors with finger-shaped electrodes [26]. On a polyimide (PI) substrate, the sensor unit comprises one top electrode over four bottom electrodes with a silicone rubber dielectric layer in between. The finger shape of electrodes could enlarge the change in

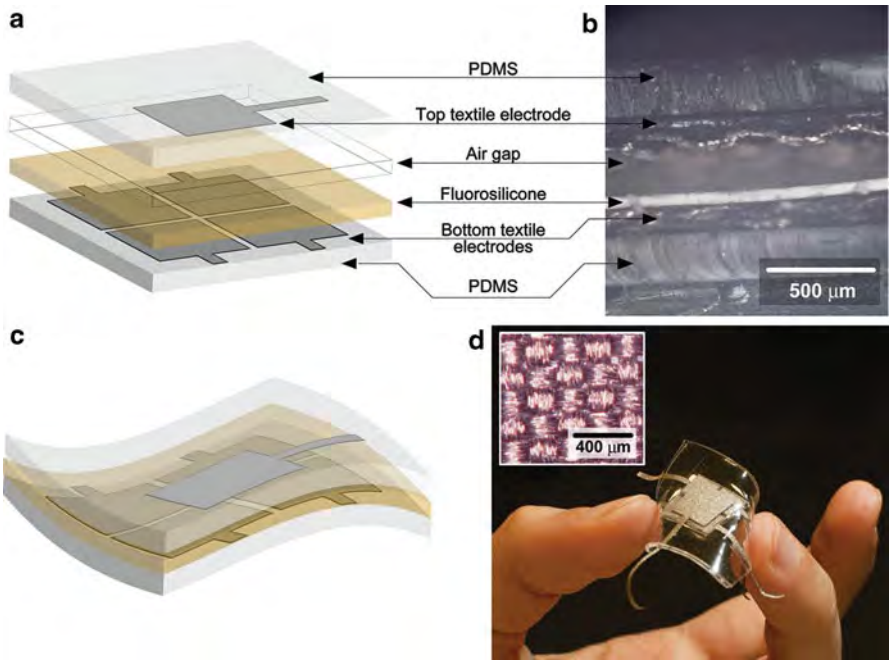

Fig. 5 Schematic of the 3-D fabric pressure sensor. (**a**) Components; (**b**) cross-sectional view; (**c**) schematic of a sensor bent; (**d**) optical picture of an as-made sensor (Reproduced with permissions from Ref. [27]. Copyright 2014 WILEY-VCH Verlag GmbH & Co. KGaA, Weinheim)

capacitance during deformation since they equal to several parallel capacitors. However, in this work, the sensitivity values are only 0.024 kPa^{-1} for normal pressures below 10 kPa and 2.8×10^{-4} kPa^{-1} for shear forces.

By far, the most sensitive capacitive pressure sensor for three-axial force detection was reported in 2014 by Lucie et al. [27], where one top textile electrode was placed above the center of four bottom textile electrodes (Fig. 5). There were fluorosilicone and air gap between electrodes. The whole device was encapsulated using PDMS. The textile electrodes were copper-tin-coated woven fabrics, thus not stretchable. The unique feature of the sensors is that there are three stages in deformation. The first stage is compression of the air gap, which contributes to the high sensitivity in a low-pressure range (<2 kPa, sensitivity 0.91 kPa^{-1}); the second is the deformation of the fluorosilicone layer (2–190 kPa, sensitivity 0.91 kPa^{-1}); and finally the third is the deformation of the fabric electrodes at very large pressures of around 400 kPa (sensitivity 0.0025 kPa^{-1}). For tangential force detection, the reported values were 0.32 ± 0.02 N^{-1} and 0.34 ± 0.02 N^{-1} for 0.5 N and 1 N normal force conditions. This type of pressure sensor is by far the most sensitive capacitive one when considering both normal and shear force measurement. The only limitation is that, due to the use of woven fabric electrodes, the sensor is flexible but not stretchable at all.

For all the capacitive tactile sensors discussed above, technical specifications are summarized in Table 2.

Piezoelectric Tactile Sensors

Piezoelectric materials are insulators that generate a voltage potential gradient when they are mechanically deformed [28]. The electricity either comes from crystal structures, in which the deformation causes the cations and anions to move asymmetrically, resulting in a high polarization, or comes from the alignment of the permanent dipole moment in the molecules of the crystals. Typical piezoelectric tactile sensors involve a configuration similar to capacitive tactile sensors, where the dielectric layer is a piezoelectric thin film of area A and thickness D. When a force F is exerted onto the top plate, there will be a decrease in thickness of the film, and opposite charges will assemble in the two electrodes, leading to a voltage V as given in Eq. 2, where d is the piezoelectric constant of the material; ε_r and ε_0 are the same as in a capacitor. To achieve a high sensitivity, d/ε_r of the piezoelectric material should be as large as possible. In this regard, lead zirconium titanate (PZT) and polyvinylidene fluoride (PVDF) are commonly used for tactile sensing because of their high sensitivity, facile fabrication, and mechanical properties.

$$V = \frac{dD}{4\pi\varepsilon_r\varepsilon_0 A}F \tag{2}$$

When a load is exerted onto piezoelectric materials, the charges generated are highly dependent on the angle between the crystallographic direction and the loading direction. When electrodes are placed along the crystal direction, a voltage is generated with the value in proportion to the force applied. Therefore, highly aligned piezoelectric materials can be used to make very sensitive tactile sensors. In 2013, Rogers' group reported a high-performance piezoelectric tactile device which could sense a pressure of 0.1 Pa [29], because the device deployed highly aligned nanofiber arrays of poly(vinylidenefluoride-co-trifluoroethylene), shorted as P (VDF-TrFE). The high alignment of nanofibers came from electro-spinning process with a collector disk rotating at a speed of 4,000 rpm. However, unlike the capacitive tactile sensors, such piezoelectric sensors are not applicable to static force detection because the piezoelectricity is transient in nature.

Apart from pressure, piezoelectric materials are also sensitive to temperature fluctuations. Therefore, in order to measure pressure in a precise manner, the piezoelectric tactile sensors need additional temperature sensors for compensation. Nonetheless, two piezoelectric materials with disproportional temperature and pressure sensitivities can be combined to detect temperature and pressure simultaneously. For example, when a piezopyroelectric (a mixture of poly(vinylidene-fluoride-co-trifluoroethylene) P(VDF-TrFE) and $BaTiO_3$ nanoparticles) gate dielectric and piezo-thermoresistive (pentacene) organic semiconductor are

Table 2 Specifications of typical capacitive tactile sensors (Reproduced with permissions from Ref. [4]. Copyright 2011, Rights Managed by Nature Publishing Group)

Type	Elements[a]	Pressure measuring range	Sensitivity	Stretchability	Flexibility	Size of unit sensor	References
Nanotube/ nanowire electrodes	Elec: spray-coated CNTs on PDMS Diel: Ecoflex silicone elastomer	50–1,000 kPa	0.23 MPa^{-1}	150 %	Excellent	Width: 0.6–2 mm Thickness: 0.7–1.3 mm	[8]
	Elec: SWNT films in PDMS surface Diel: Ecoflex silicone elastomer	10–124 kPa	0.59 kPa^{-1}	300 %	Excellent	–	[9]
	Elec: AgNW networks in PU Diel: acrylic spacer	0.001–1 MPa	0.51 MPa^{-1}	60 %	Excellent	1.5 × 1.5 mm	[10]
	Elec: AgNW/ PDMS film Diel: Ecoflex silicone elastomer	1.2 MPa	1.62 MPa^{-1} for pressure below 500 kPa; 0.57 MPa^{-1} for pressure above 500 kPa	50 %	Excellent	2 × 2 × 0.9 mm	[11]
Conductive liquid electrodes	Elec: Galinstan Diel: PDMS	0–2.5 N	~0.1 N^{-1}	Good	Excellent	0.5 × 0.5 mm	[14]
Foam dielectric layer	Elec: deposited gold film Diel: PU foam	1–100 kPa	0.015 pF kPa^{-1}	Good	Excellent	1 × 1 cm	[16]
Microstructured dielectric layer	Elec: ITO/PET film Diel: microstructured PDMS layer	0.3–15 kPa	0.55 kPa^{-1}	–	Yes	8 × 8 mm	[19]

(*continued*)

Table 2 (continued)

Type	Elements[a]	Pressure measuring range	Sensitivity	Stretchability	Flexibility	Size of unit sensor	References
	Elec: ITO/PET film Diel: microstructured PDMS layer With OFET	0–60 kPa	8.4 kPa^{-1} for pressures below 8 kPa	–	Yes	–	[20]
	Elec: ITO/PET film Diel: microstructured PDMS layer	As low as 13 mPa	18 V at a current density of 0.13 μA/cm^2	–	Yes	3 × 3 cm	[21]
	Elec: aluminum plate Diel: nano-needle PU film from breath figure method	0–6 kPa	1.76 kPa^{-1} for pressure below 1 kPa	–	Yes	50 mm^2	[22]
Textile structure	Elec: embroidered electrodes made from silver-coated yarns Diel: spacer fabrics or foam	0–120 kPa	–	–	Yes	2 × 2 cm	[23]
	Elec: PEDOT: PSS-coated nylon yarns Diel: Cytop coatings	9.8–98 kPa	Tunable	–	Good	2 × 2 cm	[24]

Three axial	Elec: copper Diel: air gap and PDMS	0–250 kPa for x, y, and z axes	0.013 mN^{-1} 0.012 mN^{-1} 0.012 mN^{-1}	–	Radius of curvature 4 mm	2 × 2 mm	[25]
	Elec: platinum and gold Diel: silicone rubber	Normal: 20 kPa Shear: 220 kPa	0.024 kPa^{-1} for normal pressure below 20 kPa; 2.8×10^{-4} kPa^{-1} for shear force	–	Good	6 ~ 10 × 6 ~ 10 mm	[26]
	Elec: copper-tin-coated woven fabric Diel: air gap and fluorosilicone	Normal: 0–190 kPa Shear: 0.4–1.2 N (normal 0.5 N) 0.8–1.6 N (normal 1 N)	Shear sensitivity: 0.32 ± 0.02 N^{-1} and 0.34 ± 0.02 N^{-1} for the 0.5 N and 1 N normal forces Normal sensitivity: 0.91 kPa^{-1} 0–190 kPa	–	Good	~10 × 10 mm	[27]

[a]For the element column, Elec stands for electrodes; Diel stands for dielectric layer

integrated into field-effect transistor films, real-time bimodal sensing can be realized [30]. Table 3 lists the specifications of typical piezoelectric tactile sensors.

Resistive Tactile Sensors

Many commercial rigid pressure sensors and load cells use metal strain gauges as highly precise sensing elements. There are also many MEMS sensors deploying traditional strain gauges. These MEMS sensors are excluded in this chapter since the metallic or semiconductor (e.g., silicon) strain gauges are rigid, whereas this chapter focuses on soft tactile sensors.

To emulate the softness, compliance, and stretchability of the human skin, elastomers are one of the best candidates, because they have a very low Young's modulus and a high failure strain. They are typically cross-linked rubbery polymers with a random-coil molecular structure. Their exceeding deformability is often referred to as hyper-elasticity in large deformation. Elastomer and rubber are two interchangeably used terms. Although there are many commercially available elastomers with various mechanical properties, the most common type in use by scientific researchers are silicone-based elastomers. Unlike most polymers with their backbones composed of organic constituents (e.g., C, O, N, S, etc.), the backbone of silicones involves organic (O) and inorganic (Si) constituents.

Conductive elastomer composites have found a broad spectrum of applications in the electronic industry. Typically, they are elastomers such as PDMS or PU impregnated with conductive filler particles or fibers including carbon blacks (CB), metal powders, CNTs, etc. Although the elastomer matrix is insulating, the fillers in them can form a conductive network rendering the composite electrically conductive. These pressure sensors are often referred to as pressure-sensitive rubbers (PSR) or force-sensitive resistors (FSR). When a normal force is applied, the resistance of PSR decreases mainly because the filler particles come closer to each other forming more effective conductive networks. Conductive elastomer composites are therefore categorized to piezoresistive materials.

As regards the conductivity of elastomeric composites, one important concept is the percolation threshold. It is a critical value of conductive filler fraction and only when the filler fraction reaches or goes beyond it, the composite becomes electrically conductive. Conductivity of the composite depends on three factors: (i) the conductivity of the filler material, (ii) the geometrical shape of the filler material, and (iii) the volume fraction/ratio of the filler material to the elastomer matrix [31]. The factor volume fraction is often used to adjust the sensitivity of PSR.

The advantages of conductive elastomer composites include corrosion resistance, wide temperature range applicability, low cost, facile fabrication, stretchability, and softness. Besides, the pressure sensitivity of PSR is tunable simply by changing the volume fraction of the conductive fillers. The major limitation is the large hysteresis arising from the viscoelasticity of the elastomers used, which restrict the application of PSR to low-frequency pressure detection.

Table 3 Specifications of typical piezoelectric tactile sensors (Reproduced with permissions from Ref. [4]. Copyright 2011, Rights Managed by Nature Publishing Group)

Type	Key materials	Working range	Sensitivity	Stretchability	Flexibility	Size of unit sensor	References
Piezoelectric pressure sensor	P(VDF-TrFE)	3 Pa–2 kPa	1.1 V kPa^{-1}	–	Excellent	Width: 0.6–2 mm Thickness: 0.7–1.3 mm	[29]
Piezopyroelectric pressure and temperature sensor	P(VDF-TrFE) and BaTiO3 Pentacene	0–0.5 MPa 35–40 °C	–	–	Yes	0.5 × 1 mm	[30]

In recent years, substantial research has been carried out in this field. The most representative soft resistive tactile sensors are discussed below.

PSR Tactile Sensors

Discrete PSR pressure sensors were deployed in multifunctional balloon catheters for cardiac electrophysiological mapping and ablation therapy [32]. Despite the PDMS embedded inside the PSR to enhance the sensitivity, the resistance of such pressure sensors changed by only 4 % at a pressure of 120 kPa.

To take good advantage of the soft and stretchable PSR sheets, OFET has been integrated with PSR into large-area flexible pressure sensor arrays, as demonstrated by Someya's group [33–35]. PSR was placed at the drain-source path and pentacene was used as the semiconducting material. Due to the piezoresistive properties, PSR regulates the current of the transistor according to the pressure applied onto PSR. Sensitivity of the integrated pressure sensors largely depends on the gauge factor of PSR and the field-effect mobility of OFET. In 2004, Someya's group reported a large-area, flexible pressure sensor matrix of this category [33]. One year later, they improved the device in its conformability and integrated thermal sensors as well [34]. In 2013, using an ultra-lightweight design, their device further evolved into an ultrathin active-matrix array with tactile sensors, which was 27-fold lighter than common office paper and could be stretched to twice the original length [35]. Technical specifications of the sensors above can be found in Table 3. Due to the requirement of precise, robust, and monolithic integration, these devices, however, are rather complicated in fabrication processes and highly demanding in the machines deployed.

Besides OFET, nanowire semiconductors have also been employed to make flexible tactile sensor arrays based on PSR. Ali Javey's research group in 2010 reported such 19 $\times$ 18 transistors using germanium/silicon (Ge/Si) inorganic nanowires [36]. Similar to Someya's approach [33], the source electrodes of the transistors were connected to ground through PSR. The transistors were able to monitor distributions of pressure up to 15 kPa at a low operating voltage of below 5 V. The sensors showed no degradation in performance even after bending to small radii of curvature of 2.5 mm for over 2,000 cycles demonstrating excellent mechanical robustness and reliability.

In addition to field-effect transistor matrix, electrical impedance tomography (EIT) provides a unique pathway to realize flexible and stretchable pressure sensors. Based on inverse problem analysis, EIT is a noninvasive imaging technique, in which the internal resistance distribution of an object is inferred simply via electrode measurement on the boundary. EIT is free from complex wires inside the circuit matrix. It transforms a PSR sheet into pressure sensor arrays simply by connecting electrodes on the sheet boundary, which is by far the easiest approach to fabricate large-area stretchable and flexible pressure sensors arrays. In 2007, Hassan and coworkers reported such a highly stretchable tactile distribution sensor for smooth-surfaced humanoids [37].

All the abovementioned PSR use carbon black or graphite as conductive fillers, and there are also composites of metallic fillers and PDMS. In 2013, Debao

et al. reported a skin-like sensor with high stretchability where nickel powder/PDMS composite was used as the piezoresistive elements and AgNW/PDMS composites as stretchable wires [38]. Table 4 presents specifications of the PSR tactile sensors.

Fabric-Based Resistive Pressure Sensors

Most of the above sensors suffer from deterioration in performance after a prolonged period of wearing or repetitive loadings. Knitted fabrics, due to their excellent softness, stretchability, and durability, provide a great substrate to build robust wearable electronic components. Recently, Tao's group has developed a resistive fabric strain sensor (FSS) which is stable (repeatability ±5 % FSO, full-scale output) in measuring strains up to 50 % even after 100,000 loading cycles [39]. These sensors, which have a coating of composite comprising carbon black, silicone elastomer, and silicone oil on a knitted fabric, have been deployed in the development of a family of soft pressure sensors. Two typical types in the family are described below with their specifications listed in Table 5.

In 2011, flexible pressure sensors were reported by sandwiching an FSS between two tooth-structured PDMS layers [39]. The configuration of the sensor is illustrated in Fig. 6. The highly durable FSS and the simple configuration endow the pressure sensors' mechanical robustness, flexibility, and superior fatigue resistance. Two subversions of such sensors were stable even after 100,000 compression cycles. The sensors could measure pressures from 0 to 2 MPa with a sensitivity of 2.98 MPa^{-1}, covering the range of human foot pressure measurement. They are therefore adopted in i-Shoe [40], a foot pressure mapping system registering spatial and temporal plantar pressure distributions in most daily activities.

In 2013, they demonstrated another resistive soft pressure sensor as in Fig. 7. The sensor consisted of two components only: a PDMS cylinder and an FSS. The FSS was mounted on the equator of the cylinder. The FSS can slip freely on the surface of PDMS except for the adhesion part. Due to the large Poisson's ratio of PDMS, the midline perimeter of the cylinder will increase significantly under a normal pressure, leading to a membrane stretch on the sensing element. Such soft pressure sensors can have a large workable pressure range (0–8 MPa), a high sensitivity (1 MPa^{-1}), and a short response time ($\leq$0.1 ms) [41]. The sensitivity of the sensors can be adjusted by using elastomers of different elastic moduli. In addition, different from the previous tooth-structured design, no compressive forces will be directly exerted onto the surface of FSS. Therefore, this type of sensors can be used for impact pressure measurement in martial arts, contact sports, or vehicle collision tests. Smart clothing embedded with such pressure sensor arrays has been developed for in situ pressure distribution measurement of seatbelt in vehicle collision. The smart clothing was examined in simulated vehicle frontal-impact tests. Pressure distributions along the seatbelt in the tests were successfully obtained.

Table 4 Specifications of typical PSR tactile sensors (Reproduced with permissions from Ref. [4]. Copyright 2011, Rights Managed by Nature Publishing Group)

Type	Key materials	Working range	Sensitivity	Stretchability	Flexibility	Size of unit sensor	References
Discrete PSR sensors	PSR, PDMS	120 kPa	~0.003 kPa^{-1}	–	Yes	~0.2 × 0.4 mm	[32]
OFET	PSR, pentacene FET	0–30 kPa	–	–	Yes	2.54 × 2.54 mm	[33]
	PSR, OFET	0–30 kPa	–	25 %	Excellent	4 × 4 mm	[34]
	PSR, OFET	–	–	230 %	Excellent	12 × 12 array in 8 × 8 cm	[35]
Nanowire transistor	PSR, Ge/Si NW-array FET	0–15 kPa	~11.5 μS kPa^{-1}	–	Radii 2.5 mm	19 × 18 array in 7 × 7 cm	[36]
EIT	PSR	Depends on PSR	Depends on PSR	Excellent	Excellent	Tunable	[37]
Nickel powder	Nickel powder, AgNW, PDMS	0–250 kPa	–	30 %	Excellent	4.5 × 6 mm	[38]

Table 5 Specifications of typical fabric tactile sensors (Reproduced with permissions from Ref. [4]. Copyright 2011, Rights Managed by Nature Publishing Group)

Type	Key materials	Working range	Sensitivity	Stretchability	Flexibility	Size of unit sensor	References
Tooth structure	FSS; PDMS	0–2 MPa	2.98 MPa^{-1}	–	Yes	10 × 16 × 4.8 mm	[39]
Cylinder shape	FSS; PDMS	0–8 MPa	1 MPa^{-1}	–	Yes	Ø 11 × 5 mm	[41]

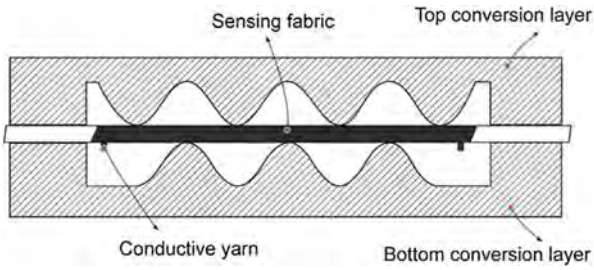

Fig. 6 Schematic illustration of the fabric pressure sensor (Reproduced with permissions from Ref. [39]. Copyright 2011 IOP Publishing Ltd)

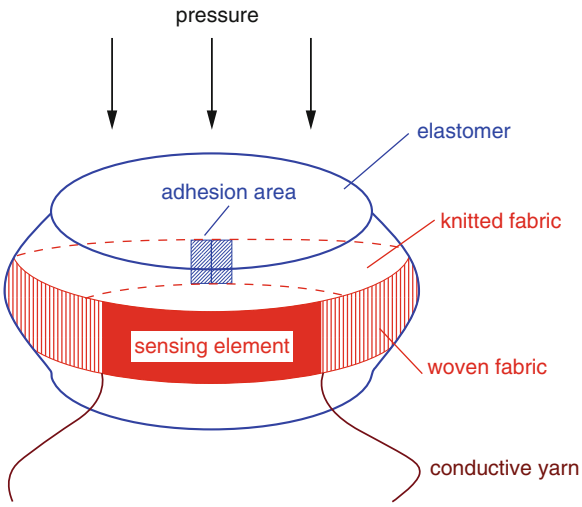

Fig. 7 Schematic illustration of the resistive soft pressure sensor with an FSS (Reproduced with permissions from Ref. [41]. Copyright 2014 IOP Publishing Ltd)

Microstructured Resistive Tactile Sensors

Similar to the microstructured capacitive tactile sensors, resistive sensors can also achieve ultrahigh sensitivity via replicated microstructures. Below are four distinctive sensors in this category reported in 2014. Specifications of the sensors are listed in Table 6.

Pyramid Shape

The first is highly stretchable resistive pressure sensors using a conductive elastomer composite on a micropyramid array (Fig. 8). First, microstructured PDMS layers were replicated from silicon mold. Then PEDOT:PSS/PUD (aqueous polyurethane dispersion) was grafted onto the PDMS layer and covered with a counter electrode made from Au-knitted fabric or other flexible materials [42]. PUD was incorporated to effectively minimize the potential cracks of PEDOT:PSS upon repeated strains. Resistance of the pressure sensor includes three parts: resistance of the counter electrode (Au-knitted fabric), resistance of the piezoresistive electrode (PEDOT:PSS/PUD), and contact resistance between electrodes. Since the surface of PDMS layer was small pyramid in shape, the contact area between the

Table 6 Specifications of typical microstructured tactile sensors (Reproduced with permissions from Ref. [4]. Copyright 2011, Rights Managed by Nature Publishing Group)

Type	Key materials	Working range	Sensitivity	Stretchability	Flexibility	Size of unit sensor	References
Pyramid	PEDOT:PSS/PUD, PDMS, Au-knitted fabric	0–8 kPa	56.8 kPa^{-1} (13–200 Pa) 4.88 kPa^{-1} (0.37–5.9 kPa) 10.3 kPa^{-1} when stretched by 40 %	Over 40 %	Radius 4 mm	Over 8 × μm	[42]
Dome	PDMS, MWNT, platinum electrode	0–60.5 kPa	−15.1 kPa^{-1} (<0.5 kPa)	–	Yes	5 × 5 mm	[43]
Nanohair	PU nanohair, platinum	Pressure: −1.5 kPa Shear: 0–1 N Torsion: 0–0.1 Nm	~11.45 (pressure), ~0.75 (shear), and ~8.53 (torsion)	Yes	Yes	Nanohair is 50 nm in radius	[44]
Silk fabric	PDMS, SWNT ultrathin film	0.6 Pa–1.2 kPa	1.80 kPa^{-1}	Yes	Excellent	Tailorable	[45]

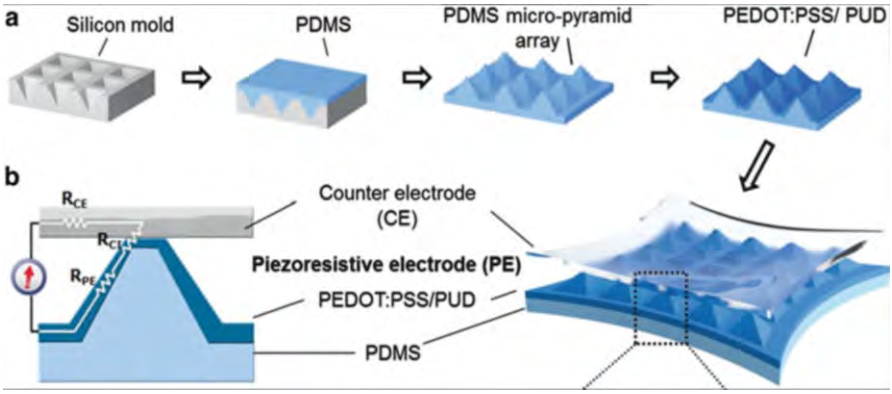

Fig. 8 Schematic illustration of the highly stretchable resistive pressure sensor (Reproduced with permissions from Ref. [42]. Copyright 2014 WILEY-VCH Verlag GmbH & Co. KGaA, Weinheim)

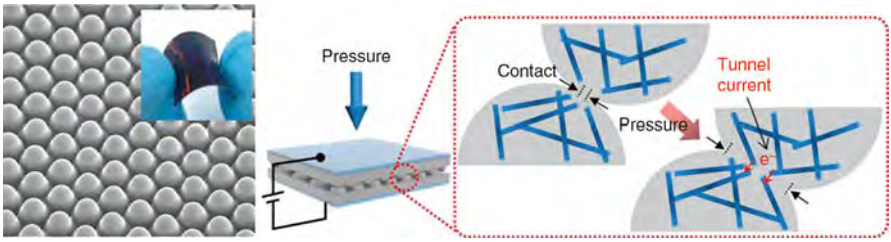

Fig. 9 Schematic illustration of the dome-shaped resistive pressure sensor (Reproduced with permissions from Ref. [43]. Copyright (2014) American Chemical Society)

counter electrode and PDMS layer will increase dramatically under normal pressure, leading to a drop in contact resistance. As all the materials here were soft in nature, the sensitivity of tactile sensor was still as high as 10.3 kPa^{-1} when stretched to 40 %.

Dome Shape

The second example chose dome-shaped microstructures as given in Fig. 9. A composite of multi-walled nanotubes (MWNT) mixed in PDMS (Sylgard 184) was silicon molded into dome features [43]. Two composite films were placed with domes face to face. When there is an external pressure, contact area of the two layers will get larger leading to a decrease in contact resistance. The dome shape is extremely effective in improving the sensitivity. Such sensors were able to detect a pressure as low as 0.2 Pa and the response/relaxation time was around 0.04 s.

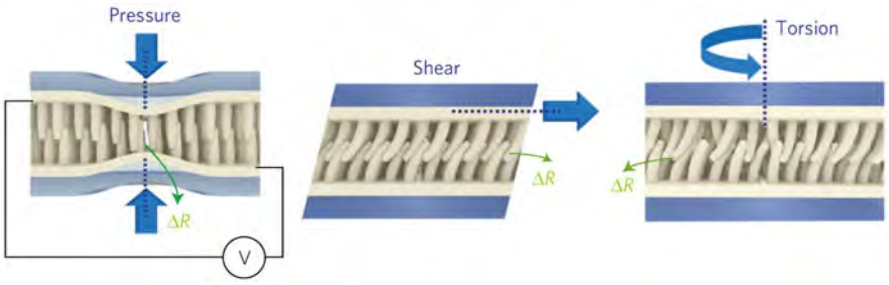

Fig. 10 Schematic illustration of working mode of the multimodal sensor with interlocked Pt nanohairs (Reproduced with permissions from Ref. [44]. Copyright 2012 Macmillan Publishers Limited)

Nanohair Shape

The third representative pressure sensor is based on two interlocked arrays of high-density nanohairs (~1.85 × 109 cm^{-2}) supported on thin PDMS layers [44]. The platinum coatings on nanohairs render the structure electrically conductive. As illustrated in Fig. 10, when there is normal pressure, shear force, or torsion applied, contact resistance between the two interlocked layers will change accordingly with specific and discernable gauge factors. The high-aspect-ratio configuration of nanohairs imparted the device high gauge factors: ~11.45 for pressure, ~0.75 for shear, and ~8.53 for torsion. The minimum detectable pressure was ~5 Pa. Unfortunately, the performance of the sensor was basically stable, only within 8,000 cycles of compression. Besides, stretchability of the device has not been demonstrated.

Silk Fabric

Apart from silicon, silk fabric has also been used to mold PDMS layers [46]. Microstructured PDMS films replicated from silk fabric were laminated with free-standing SWNT ultrathin films (30 nm in thickness) on the patterned surface. Then two such PDMS films were placed face to face into a flexible soft tactile sensor. The sensor demonstrated excellent performance: the sensitivity was high as 1.8 kPa^{-1}, and the minimum detectable pressure was 0.6 Pa; the sharp peaks between layers remained intact even after over 67,500 cycles of compression. It is believed that such excellent sensing capability is attributed to two factors: (i) large numbers of sharp micro/nano-features on the interface of the two SWNTs/PDMS films generate abundant effective contact points, and (ii) the SWNT ultrathin film, which was partially embedded onto the patterned PDMS substrates, imparts the sensor mechanical and electrical stability.

Here, it is worth noting again that, despite the excellent mechanical and electrical properties of carbon nanotubes, they pose serious toxic and hazardous concerns [12, 13]. Such concerns also exist in CNT pressure sensors for normal and shear force detection [47].

Self-Healing Tactile Sensors

One of the fundamental differences between the above artificial touch-sensitive skins and natural skins is the regeneration capability. The human skin, even if severely damaged, may heal itself by forming scar tissue, while the man-made ones do not. In 2012, Bao's group reported for the first time an electrically and mechanically self-healing composite with piezoresistive properties [48]. The composite was composed of a supramolecular organic polymer doped with nickel microparticles. Electrical conductivity could be as high as 40 S cm^{-1}. After rupture, the conductivity restored to 90 % after 15 s healing time; and mechanical properties could fully recover after ~10 min. The great self-healing capability is attributed to the large quantity of weak hydrogen bonds in the supramolecular polymeric hydrogen-bonding network. The hydrogen bonds can break preferentially during a mechanical separation. And they can associate and disassociate at ambient conditions. In addition, the low glass temperature of the composite allows the polymer chains on the broken surface to rearrange, wet, and diffuse, thus healing at room temperatures. The composite is a big step toward self-healing artificial skins. Unfortunately, the sensitivity was so high that it is impractical to use a sensor whose resistance change spans several orders of magnitude. And if the loading percentage of nickel powders increased, the self-healing ability may be severely affected. Much remains to be done toward highly sensitive self-healing tactile sensors.

Optical Tactile Sensors

All the sensors discussed above are based on electricity, and there are also tactile sensors operating on light, a propagation of electromagnetic radiant waves. Light is a very effective form of energy for measuring diverse stimuli, ranging from distance, temperature to chemical composition. Optical tactile sensors normally involve a light source, a transduction medium, and a photodetector (camera or photodiode). They operate on two types of principles: intrinsic and extrinsic. For intrinsic type, the exerted force induces variations in light transmission/reflectance intensity, reflective wavelength, or spectrum, where the light path does not change. For extrinsic type, the light path changes according to exerted force and the sensor usually involves a camera, which inevitably hinders the miniaturization of sensors. Therefore, only intrinsic type of sensors will be discussed in this section.

The major advantages of optical tactile sensors include high spatial resolution and accuracy, intrinsic safety, lightweight, and, most importantly, immunity to external electromagnetic interference. However, since they need both light emitters and receivers, the size is relatively larger than the other sensors. In addition, for sensors working on light intensity, they may suffer from signal alteration or attenuation by bending or misalignment.

Selected typical optical tactile sensors will be discussed below with the specifications listed in Table 7.

Table 7 Specifications of typical optical tactile sensors (Reproduced with permissions from Ref. [4]. Copyright 2011, Rights Managed by Nature Publishing Group)

Type	Key materials	Working range	Sensitivity	Stretchability	Flexibility	Size of unit sensor	References
POF	Cotton yarns, POF, LED, phototransistors	0–30 N	–	–	Excellent	2 × 2 Matrix in 1.5 × 1.5 cm	[49]
FBG	FBG fibers, PDMS	Normal 0–2.4 kPa Shear 0–0.6 kPa	Normal 0.8 pm Pa^{-1} Shear 1.3 pm Pa^{-1}	Yes	Yes	27 × 27 × 25 mm	[50]
Polymer waveguide	PDMS waveguide, (O)LED, (O)PD	0–35 kPa	0.2 kPa^{-1} (<1 kPa)	Yes	Excellent	50 × 50 mm	[51]
	PDMS waveguide, LED, PD	3–160 kPa	1.93 kPa^{-1}	Yes	Yes	Ø 5.5 cm	[52]
	PDMS waveguide, CA, PTBA, PET	0–3 N	0.16 N^{-1}	Yes	Bending radius 1.5 mm	3 × 9 Matrix in 110 × 60 mm	[53]

Plastic Optical Fibers

Polymer optical fibers (POF) are optical fibers made from polymers. Together with cotton yarns, they have been woven into fabrics [49]. Both the warp and weft yarns include POFs, so they periodically interlace with each other. The POFs here are more readily to deform than the cotton yarns. Therefore, for POFs at the crossings, the cross-sectional areas will decrease under compression. By detecting the attenuation in transmitted light intensity, corresponding pressure values can be acquired. The combination with weaving technology enables large-area pressure-sensitive fabrics.

Fiber Bragg Gratings

A fiber Bragg grating (FBG) is a Bragg reflector built in a segment of optical fiber. The Bragg reflector reflects only the light of particular wavelengths and transmits all the others. The core of FBG has a periodic fluctuation in refractive index, forming a wavelength-specific mirror. FBG can therefore transform the strain into variations in wavelength. Soft FBG pressure sensors for precision measurement of shear stress and normal pressure were reported in 2013 [50], where two polymer FBGs (one horizontal and one tilted) were embedded inside a PDMS cuboid. The deformation of PDMS cuboid upon applied pressure leads to strains on the gratings. It is therefore practical to decouple shear and normal forces. The pressure sensitivity for the sensor was 0.8 pm Pa^{-1} within 2.4 kPa and shear sensitivity 1.3 pm Pa^{-1} within 0.6 kPa.

Polymer Waveguide

A polymer waveguide is a polymeric structure that guides light waves inside it. When the shape of the structure changes, the intensity of the light transmitted will change accordingly.

In 2012, Bao's group reported a transparent, optical, pressure-sensitive artificial skin [51]. The structure of the sensor is presented in Fig. 11. This pressure sensor is based on two phenomena: the compression of the waveguide layer under pressure and the out-coupling of the waveguided light at the pressure points. When the PDMS waveguide layer is under compression, the thickness reduced. The photodetector will detect less light. Coupling of the grated in and out light can be calculated by their relationship with the out-coupling angle. This proposed pressure sensor features transparency, stretchability, large-area coverage, and a high sensitivity of 0.2 kPa^{-1}.

In 2013, another soft, transparent skin for distributed and multiple pressure sensing was reported by Alessandro et al. [52], where a similar working principle was deployed to that of Bao's sensors in 2012. When there is a pressure on the sensing area, the light signals reaching the peripheral photodiodes (PDs) experience a loss as a result of the frustrated total internal reflection and deformation of the waveguide. As an extension of Bao's sensor, there were eight light emitters and eight photodiodes evenly distributed on the four edges, namely, a 2×2 sensor array. The sensors were therefore able to detect pressures of multiple points simultaneously.

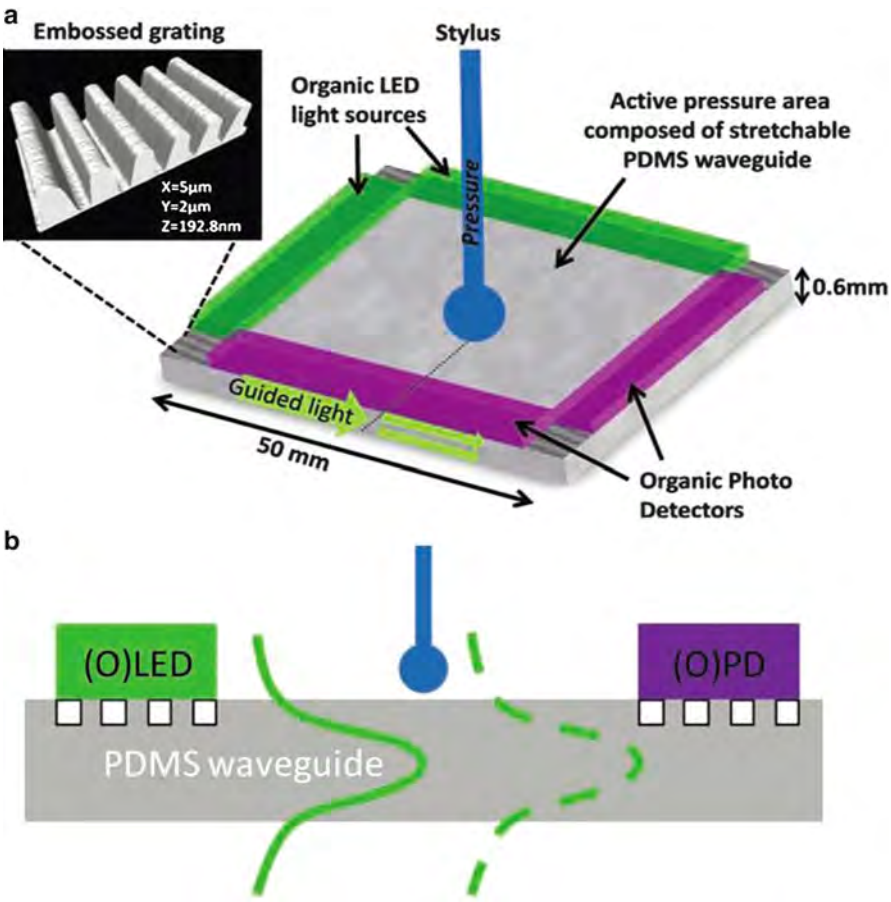

Fig. 11 Schematic of the transparent optical pressure-sensitive skin (Reproduced with permissions from Ref. [51]. Copyright 2012 WILEY-VCH Verlag GmbH & Co. KGaA, Weinheim)

In addition to uniform polymer waveguide with a clad throughout, the waveguide at the sensing area can have a bare core with a touch layer above and without touching it [53]. As explained in Fig. 12, photodetectors at the end of each core provide information on light intensity change. So when there is an external force, the touch layer comes into contact with it, and the light passing through the waveguide will be easily scattered. The amount of light scattered varies with the size of the contacting area which is a direct result of the pressure applied. Three kinds of polymers (cellulose acetate: CA; poly(tert-butylacrylate): PTBA; polyethylene terephthalate: PET) have been used as touch layers. The CA (cellulose acetate) touch layer allowed the force sensor to respond quickly without significant hysteresis to repetitive loadings (ca. 0–3 N). Such pressure sensor arrays can be thin, highly transparent, and highly flexible.

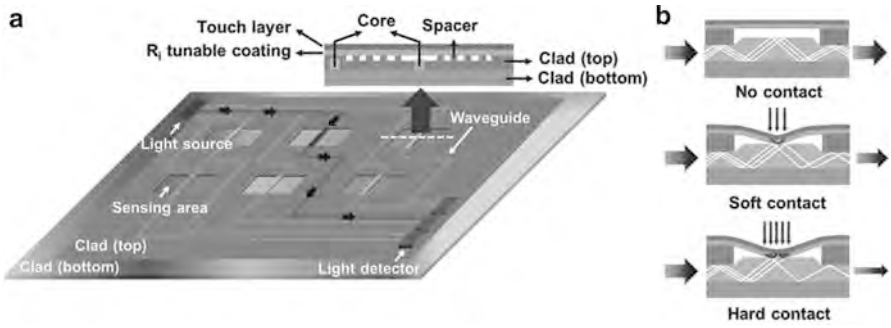

Fig. 12 Schematic of the polymer waveguide flexible tactile sensor array and the working principle (Reproduced with permissions from Ref. [53]. Copyright 2014 WILEY-VCH Verlag GmbH & Co. KGaA, Weinheim)

Conductive Liquid Tactile Sensors

Eutectic gallium-indium (EGaIn), a liquid metal alloy, is ideal for microchannel injection to form stable liquid metal structures. Under a surface stress of 0.5 N/m, it is an elastic material; beyond that, it begins to flow [54]. As a homogeneous conductor, the shape change will induce significant resistance change of EGaIn, hence EGaIn tactile sensors. The key advantage of this kind of sensors is that they can be fully elastomeric and soft: the whole stretchable structure can have a modulus at 63 kPa [55], which is close to that of the human skin around 30–70 kPa [6].

The Park's research team has made much progress in the development of EGaIn pressure sensors (Table 8). In 2012, a three-layer pressure and strain sensor was developed [55]. The first layer is coil shape, responsible for pressure sensing, and the second and third for x and y strain sensing, respectively. It remains functional at a 250 % stretch. The hysteresis is however large due to the viscoelasticity of the elastomer used and the internal flow friction of EGaIn in microchannels. The sensors also suffer from a strong strain rate effect. Later in 2013, they reported a 3D pressure sensor using one force post over three radioactively positioned EGaIn channels [56]. The durability of such a sensor is very doubtful since it consists of moving rigid parts within elastomeric materials. In 2014, soft pressure sensor array for contact force measurement and force localization has been investigated by the coworkers [57]. The array consists of four parallel top channels over two parallel lower channels which are perpendicular to the top ones. Compression at any of the crossings will lead to increment in electrical resistance of corresponding top and lower channels.

As seen from Table 9, each sensing technique has its own merits and limitations. Each was developed for specific applications. There is currently no best universal solution for human-machine interface. Considering that even the human skin, after so many years of evolution, contains four types of mechanical receptors, it is probable to emulate the human skin by combining the abovementioned sensing techniques.

Table 8 Specifications of typical conductive liquid tactile sensors (Reproduced with permissions from Ref. [4]. Copyright 2011, Rights Managed by Nature Publishing Group)

Type	Key materials	Working range	Sensitivity	Stretchability	Flexibility	Size of unit sensor	References
EGaIn (three layers)	EGaIn, PDMS	15–50 kPa	–	250 %	Excellent	25 × 25 mm	[55]
EGaIn (three dimensional)	EGaIn, PDMS, plastic force post	Normal 0–5 N Shear 0–0.45 N	–	Excellent	Excellent	50 × 60 × 7 mm	[56]
EGaIn (force localization)	EGaIn, PDMS	<50 mN	–	Yes	Excellent	200 × 200 μm	[57]

Table 9 Comparison of various sensing techniques, parameter, advantages, and disadvantages (Reproduced with permissions from Ref. [4]. Copyright 2011, Rights Managed by Nature Publishing Group)

Transduction technique	Modulated parameter	Advantages	Disadvantages
Capacitive	Change in capacitance	High sensitivity Temperature independent Large dynamic range Small sizes and high spatial resolutions possible Large-area coverage possible Well-established design and fabrication techniques 3D force sensing possible	Parasitic capacitance Cross talk between sensor units Susceptible to electromagnetic interference Complex circuitry
Piezoelectric	Strain/stress polarization	High sensitivity High frequency response Robust and chemically resistant Mechanically flexible Suitable for dynamic tests	Low spatial resolution Dynamics sensing only Not stretchable
Conductive elastomer composites	Change in resistance (piezoresistivity) or contact resistance	Stretchability Soft material mimics the human skin Simple structures and fabrications Low cost Large-area coverage possible Tailored measurement range High sensitivity with microstructures	Hysteresis of composite material Restricted to pressure sensing Sensitivity to temperature change
Optical	Light intensity/ wavelength/vision	Immune to electromagnetic interference High sensitivity and precision POFs: flexibility and durability LEDs: high spatial resolution LEDs can work as both transmitter and	Signal attenuation due to bending (for polymer waveguides) Low stretchability

(*continued*)

Table 9 (continued)

Transduction technique	Modulated parameter	Advantages	Disadvantages
		detector 3D force sensing possible Transparency	
Conductive liquid	Change in resistance	Superior stretchability Fully elastomeric Soft Simple structure 3D force sensing possible	Strain rate effect Large hysteresis

Discussion

With many upcoming aging societies, the demand for automated assembly lines, the need for surgery robots in hospitals, and the growing popularity of personal products with touch interfaces, more sophisticated, advanced, and reliable tactile sensing techniques are required for human-machine interaction. Substantial effort has been made to exploit various tactile sensing systems, from sensing materials, transduction methods, to matrix circuits and processing algorithms. However, after nearly two decades of research and development, few products can be found in either commercial or industrial markets besides touch-screen devices such as an iPhone (Apple Inc., USA). Here, the author tries to find out current problems in research on soft tactile sensors.

Current Problems

The first problem lies in characterization parameters. To make a critical assessment of a particular kind of sensors, sensor parameters, including sensitivity, repeatability, hysteresis, standard deviation, temperature, and humidity effect, are all essential. However, few of the researchers have covered all the parameters in their publishing. Although in 2003, Eltaib and Hewit [58] investigated design considerations for minimally invasive surgery, definitive standards for tactile sensors are in urgent need to guide further development.

The second reason for delayed acceptance is the cost of tactile sensors, which largely hinders their application in the field of service robot and health care [59]. In this regard, the conductive (especially CB or graphite doped) elastomer composite tactile sensors are probably the most promising candidate.

Another issue is the poor design criteria. To the best of our knowledge, the most effective way in designing tactile sensors should be task-centered design, which

refines the design criteria based on the field of application. For instance, automated production lines require no biocompatible sensors; biomedical devices normally need no pressure sensors with wide dynamic range, while tactile sensors with non-biocompatible materials such as CNTs should not get regulatory approval in biomedical field.

There are also deficiencies in matrix circuits and processing algorithms, which are beyond the scope of this chapter.

Future Directions

The first direction is task-centered design [60]. In recent years, bionics has been attracting increasing interests in the science and research community. As regards tactile sensors, many scientists hope to create artificial skins with tactile sensors that emulate the human skin in structure, physiological and mechanical attributes, and functionalities. While due to the extreme complexity of the human skin, particularly the fingertips, these ambitions are essentially not viable. But artificial tactile sensing for specific applications which emulate the subgroup of the human sense of touch can be practical and attainable. Therefore, task-centered design can help to optimize the sensing system and reduce the cost. More emphasis should be put on the task-based design criteria. Particularly in the low-pressure regimes ($<$10 kPa), it is still challenging to produce all-elastomeric soft tactile sensors for three-dimensional measurement at a low cost.

The second direction is the application of nano-material and micro-fabrication/replication technology. The recent development in material science, nanotechnology, and micro- and nano-fabrication techniques can help to advance the tactile sensing technology in terms of performance, reliability, miniaturization, and other mechanical properties. Detailed discussion can be found in [2].

The third is more elastic, flexible, and dynamic tactile sensing. For example, PDMS has been increasingly used in recent advances of tactile sensing technology, for its biocompatibility and excellent mechanical properties. The adoption of such elastomeric encapsulation materials may effectively improve the sensors' capabilities such as feeling motion and recognizing texture. On the other hand, the tactile sensing element itself has been made from these elastomeric materials (conductive elastomer composites) to achieve soft, flexible, and stretchable sensing arrays. For detailed discussions on elastomeric pressure sensors, please refer to [31].

Besides, challenges in current tactile sensing technique including arrayed sensor design and algorithms, frequency response, spatial resolution, and conformity will guide the direction of research and development of tactile sensing techniques.

Summary

After a brief introduction to the tactile sensing of the human skin and the important characteristics of soft tactile sensors, the transduction techniques and state of the art of the five categories of soft tactile sensors have been reviewed, followed by a

succinct comparison in their sensing parameters, specifications, merits, and limitations. Current problems including characterization standards, cost, and design criteria have been analyzed. Finally, future directions have been pointed out: task-centered design, the application of nano-material technology, and more elastic and dynamic tactile sensing. Particularly in the low-pressure regimes ($<$10 kPa), soft tactile sensors for three-dimensional measurement are still challenging.

The soft tactile sensing technology will aid future advancement in robotics, biomedical devices, sports, automobile, textiles, and many other fields where there are human-machine interfaces. Major successful applications of this technology are consumer electronics like iPhones (Apple Inc., USA) and touch-screen computers. Other successful companies specialized in touch-sensing area such as Tekscan Inc. (Boston, USA) and Pressure Profile Systems Inc. (Los Angeles, USA) further confirm the potential markets for tactile sensing techniques. With many upcoming aging societies, the need for automated assembly lines, the acceptance for biomedical and service robots, and the growing popularity of personal products with touch interfaces, future development of soft tactile sensing solutions for human-machine interface shall reasonably bring more surprises to our life.

References

1. Najarian S, Dargahi J et al (2009) Artificial tactile sensing in biomedical engineering. McGraw-Hill, New York
2. Maheshwari V, Saraf RF (2008) Tactile devices to sense touch on a par with a human finger. Angew Chem Int Edit 47(41):7808–7826
3. Robles-De-La-Torre G, Hayward V (2001) Force can overcome object geometry in the perception of shape through active touch. Nature 412(6845):445–448
4. Johansson RS, Flanagan JR (2009) Coding and use of tactile signals from the fingertips in object manipulation tasks. Nat Rev Neurosci 10(5):345–359
5. Nyce DS (2004) Linear position sensors theory and application. Wiley, Hoboken
6. Groves RB, Coulman SA, Birchall JC, Evans SL (2012) Quantifying the mechanical properties of human skin to optimise future microneedle device design. Comput Method Biomec 15 (1):73–82
7. Wessendorf AM, Newman DJ (2012) Dynamic understanding of human-skin movement and strain-field analysis. IEEE Trans BioMed Eng 59(12):3432–3438
8. Lipomi DJ et al (2011) Skin-like pressure and strain sensors based on transparent elastic films of carbon nanotubes. Nat Nanotechnol 6(12):788–792
9. Wang XL, Li TJ, Adam J, Yang J (2013) Transparent, stretchable, carbon-nanotube-inlaid conductors enabled by standard replication technology for capacitive pressure, strain and touch sensors. J Mater Chem A 1(11):3580–3586
10. Hu WL, Niu XF, Zhao R, Pei QB (2013) Elastomeric transparent capacitive sensors based on an interpenetrating composite of silver nanowires and polyurethane. Appl Phys Lett 102 (8):083303
11. Yao SS, Zhu Y (2014) Wearable multifunctional sensors using printed stretchable conductors made of silver nanowires. Nanoscale 6(4):2345–2352
12. Lam CW, James JT, McCluskey R, Hunter RL (2004) Pulmonary toxicity of single-wall carbon nanotubes in mice 7 and 90 days after intratracheal instillation. Toxicol Sci 77(1):126–134
13. Donaldson K et al (2006) Carbon nanotubes: a review of their properties in relation to pulmonary toxicology and workplace safety. Toxicol Sci 92(1):5–22

14. Wong RDP, Posner JD, Santos VJ (2012) Flexible microfluidic normal force sensor skin for tactile feedback. Sensor Actuat A Phys 179:62–69
15. Eaves D (2004) Handbook of polymer foams. Smithers Rapra Press, Akron
16. Vandeparre H, Watson D, Lacour SP (2013) Extremely robust and conformable capacitive pressure sensors based on flexible polyurethane foams and stretchable metallization. Appl Phys Lett 103(20):204103
17. Xia YN, Whitesides GM (1998) Soft lithography. Angew Chem Int Edit 37(5):551–575
18. Noderer WL et al (2007) Enhanced adhesion and compliance of film-terminated fibrillar surfaces. Proc R Soc A Math Phys 463(2086):2631–2654
19. Mannsfeld SCB et al (2010) Highly sensitive flexible pressure sensors with microstructured rubber dielectric layers. Nat Mater 9(10):859–864
20. Schwartz G et al (2013) Flexible polymer transistors with high pressure sensitivity for application in electronic skin and health monitoring. Nat Commun 4. doi:10.1038/ncomms2832
21. Fan FR et al (2012) Transparent triboelectric nanogenerators and self-powered pressure sensors based on micropatterned plastic films. Nano Lett 12(6):3109–3114
22. Kim J, Ng TN, Kim WS (2012) Highly sensitive tactile sensors integrated with organic transistors. Appl Phys Lett 101(10):103308
23. Meyer J, Arnrich B, Schumm J, Troster G (2010) Design and modeling of a textile pressure sensor for sitting posture classification. IEEE Sens J 10(8):1391–1398
24. Takamatsu S, Kobayashi T, Shibayama N, Miyake K, Itoh T (2012) Fabric pressure sensor array fabricated with die-coating and weaving techniques. Sens Actuat A Phys 184:57–63
25. Lee HK, Chung J, Chang SI, Yoon E (2011) Real-time measurement of the three-axis contact force distribution using a flexible capacitive polymer tactile sensor. J Micromech Microeng 21 (3):035010
26. Dobrzynska JA, Gijs MAM (2013) Polymer-based flexible capacitive sensor for three-axial force measurements. J Micromech Microeng 23(1):105009
27. Viry L et al (2014) Flexible three-axial force sensor for soft and highly sensitive artificial touch. Adv Mater 26(17):2659–2664
28. Cady WF (1946) Piezoelectricity. McGraw-Hill, New York
29. Persano L et al (2013) High performance piezoelectric devices based on aligned arrays of nanofibers of poly(vinylidenefluoride-co-trifluoroethylene). Nat Commun 4:1633
30. Tien NT et al (2014) A flexible bimodal sensor array for simultaneous sensing of pressure and temperature. Adv Mater 26(5):796–804
31. Someya T (2012) Stretchable electronics. Wiley-VCH, Weinheim
32. Kim DH et al (2011) Materials for multifunctional balloon catheters with capabilities in cardiac electrophysiological mapping and ablation therapy. Nat Mater 10(4):316–323
33. Someya T et al (2004) A large-area, flexible pressure sensor matrix with organic field-effect transistors for artificial skin applications. Proc Natl Acad Sci USA 101(27):9966–9970
34. Someya T et al (2005) Conformable, flexible, large-area networks of pressure and thermal sensors with organic transistor active matrixes. Proc Natl Acad Sci USA 102 (35):12321–12325
35. Kaltenbrunner M et al (2013) An ultra-lightweight design for imperceptible plastic electronics. Nature 499(7459):458
36. Takei K et al (2010) Nanowire active-matrix circuitry for low-voltage macroscale artificial skin. Nat Mater 9(10):821–826
37. Alirezaei H, Nagakubo A, Kuniyoshi Y (2007) A highly stretchable tactile distribution sensor for smooth surfaced humanoids. In: Proceedings IEEE-RAS international conference on humanoid robots (ICHR '07), Pittsburgh, pp 167–173
38. Zhou DB, Wang HP (2013) Design and evaluation of a skin-like sensor with high stretchability for contact pressure measurement. Sens Actuat A Phys 204:114–121
39. Wang YY et al (2011) Novel fabric pressure sensors: design, fabrication, and characterization. Smart Mater Struct 20(6):065015

40. Shu L et al (2010) In-shoe plantar pressure measurement and analysis system based on fabric pressure sensing array. IEEE Trans Inf Technol Biomed 14(3):767–775
41. Wang F, Zhu B, Shu L, Tao XM (2014) Flexible pressure sensors for smart protective clothing against impact loading. Smart Mater Struct 23(1):015001
42. Choong CL et al (2014) Highly stretchable resistive pressure sensors using a conductive elastomeric composite on a micropyramid array. Adv Mater 26(21):3451–3458
43. Park J et al (2014) Giant tunneling piezoresistance of composite elastomers with interlocked microdome arrays for ultrasensitive and multimodal electronic skins. ACS Nano 8 (5):4689–4697
44. Pang C et al (2012) A flexible and highly sensitive strain-gauge sensor using reversible interlocking of nanofibres. Nat Mater 11(9):795–801
45. Wang XW, Gu Y, Xiong ZP, Cui Z, Zhang T (2014) Silk-molded flexible, ultrasensitive, and highly stable electronic skin for monitoring human physiological signals. Adv Mater 26 (9):1336–1342
46. Wang XW, Gu Y, Xiong ZP, Cui Z, Zhang T (2014) Silk-molded flexible, ultrasensitive, and highly stable electronic skin for monitoring human physiological signals. Exp Dermatol 23 (3):1336–1342
47. Hu CF, Su WS, Fang WL (2011) Development of patterned carbon nanotubes on a 3D polymer substrate for the flexible tactile sensor application. J Micromech Microeng 21(11):115012
48. Tee BCK, Wang C, Allen R, Bao ZN (2012) An electrically and mechanically self-healing composite with pressure- and flexion-sensitive properties for electronic skin applications. Nat Nanotechnol 7(12):825–832
49. Rothmaier M, Luong MP, Clemens F (2008) Textile pressure sensor made of flexible plastic optical fibers. Sensors Basel 8(7):4318–4329
50. Zhang ZF, Tao XM, Zhang HP, Zhu B (2013) Soft fiber optic sensors for precision measurement of shear stress and pressure. IEEE Sens J 13(5):1478–1482
51. Ramuz M, Tee BCK, Tok JBH, Bao ZN (2012) Transparent, optical, pressure-sensitive artificial skin for large-area stretchable electronics. Adv Mater 24(24):3223–3227
52. Levi A, Piovanelli M, Furlan S, Mazzolai B, Beccai L (2013) Soft, transparent, electronic skin for distributed and multiple pressure sensing. Sensors Basel 13(5):6578–6604
53. Yun S et al (2014) Polymer-waveguide-based flexible tactile sensor array for dynamic response. Adv Mater 26(26):4474–4480
54. Dickey MD et al (2008) Eutectic gallium-indium (EGaIn): a liquid metal alloy for the formation of stable structures in microchannels at room temperature. Adv Funct Mater 18 (7):1097–1104
55. Park YL, Chen BR, Wood RJ (2012) Design and fabrication of soft artificial skin using embedded microchannels and liquid conductors. IEEE Sens J 12(8):2711–2718
56. Vogt DM, Park YL, Wood RJ (2013) Design and characterization of a soft multi-axis force sensor using embedded microfluidic channels. IEEE Sens J 13(10):4056–4064
57. Hammond FL, Kramer RK, Qian W, Howe RD, Wood RJ (2014) Soft tactile sensor arrays for force feedback in micromanipulation. Sens J IEEE 14(5):1443–1452
58. Eltaib MEH, Hewit JR (2003) Tactile sensing technology for minimal access surgery – a review. Mechatronics 13(10):1163–1177
59. Lee MH (2000) Tactile sensing: new directions, new challenges. Int J Robot Res 19 (7):636–643
60. Tiwana MI, Redmond SJ, Lovell NH (2012) A review of tactile sensing technologies with applications in biomedical engineering. Sens Actuat A Phys 179:17–31

Textile Sensors

14

Hatice A. K. Toprakci and Tushar K. Ghosh

Contents

Introduction 358
Capacitive Sensors 359
Inductive Sensors 362
Piezoelectric Sensors 363
Optical Sensors 365
Chemical-Biochemical Sensors 367
Piezoresistive Sensors 369
Conclusions 375
References 375

Abstract

Textiles constitute an ideal choice as platforms for wearable devices, since they are flexible, lightweight, and can be worn everywhere in many forms. This class of textiles with electronic capabilities has been referred to as electronic textiles (e-textiles). Depending on the type and application, e-textiles may be capable of sensing, data processing, actuation, and energy storage or generation. Among all these, textile-based sensing has become an active area of research in the emerging field of e-textiles. Textile based sensors provide an interface between the user and an electronic system by converting physiological or environmental signals into electrical signals. Wearable garments may be capable of monitoring variables such as strain, pressure, temperature, displacement, humidity, etc., and can be used in many applications including medical rehabilitation, health

H.A.K. Toprakci (✉)
Faculty of Engineering, Polymer Engineering Department, Yalova University, Yalova, Turkey
e-mail: aylin.toprakci@yalova.edu.tr

T.K. Ghosh
North Carolina State University, Raleigh, USA
e-mail: tghosh@ncsu.edu

© Springer Science+Business Media Singapore 2015

X. Tao (ed.), *Handbook of Smart Textiles*,
DOI 10.1007/978-981-4451-45-1_37

monitoring, communication, entertainment, sports, security, and surveillance. This review provides an overview about textile based sensors that are capable of sensing fundamental signals related to physiological and mechanical activities, including vital signs of a human body.

Keywords
Textile sensors • E-textiles • Wearable electronics • Piezoresistive textile sensors

Introduction

Unobtrusive sensors deployed in the space close to human body, the so-called "peripersonal" or near space, can provide vital information necessary for tomorrow's adaptive technologies for healthcare, energy conservation, and many others. Obviously, clothing provides the best platform to deploy sensors in the near space and act as an interface between the wearer and an electronic/information system by converting human physiological/environmental or other signals into measurable electrical signals. In the future clothing (and other textiles around us) does not have to be a passive envelope around us. Instrumented garments capable of sensing fundamental signals related to physiological, mechanical, and environmental parameters in and around a human body with no discomfort to the subject are crucial to many applications including biomedicine, rehabilitation, and haptic interfaces. The challenge, however, is to integrate sensors (and other devices) into clothing/textiles in a discreet manner and by preserving the essential "textile" qualities relating to physical and social comfort. Similarly, appropriate sensors could be developed and deployed on textiles used for numerous other applications such as carpets, upholstery, and drapes.

Although research in the field of electronic textiles (e-textiles) started at the end of 1960s, the most important contributions have been made in the last two decades, in parallel with the advances in polymer-based flexible electronics and optics. Development of functional polymers (e.g., conducting) and fibers as well as advanced textile processes have played a significant role in this development [1–10]. Off-the-shelf electronic systems, made of traditional semiconducting materials, are generally not ideal for integration in textiles because of their incompatible properties, such as bulk, rigidity, etc., and associated problems with wearability and lack of durability to washing, perspiration, etc. [1–6]. Although textile-based sensors have many potential advantages over semiconductor-based electronics, the flexibility of the textile substrate and number of other factors related to the application environment bring about a number of challenges. Obviously, placement of a sensor is important for the reliability of the obtained data [2–8]. While sensors to monitor breathing or heart rate are generally placed around the chest [10], sweat sensors are located around the sweating areas [11–16]. Even if sensors are located properly, if the garment is not well fitted, sensory systems might easily move relative to any reference, and the reliability and reproducibility of the data become questionable. Additionally, the sensor materials and systems should be compatible

Fig. 1 Mechanism of sensors

with and stable in the macro- and microenvironment in the near and far space. In addition to all these technical requirements, they should be simple, maintainable, and affordable.

Sensors are transducers that are capable of converting mechanical, chemical, optical, and other forms of stimuli into meaningful electrical signals (see Fig. 1). In other words, sensors are able to measure and convert the "quantity" of physical variable into an electrical signal. Depending on the system, common physical variable or stimulus can be in the form of force, temperature, length, strain, pressure, time, resistance, capacity, frequency, velocity, or acceleration; and output signal can be a measurable voltage or current [17, 18].

Sensors as a part of a system can be located at any place in the system depending on the requirements and accuracy of the signals. Since the outputs of most sensors are relatively weak, and noisy, often it is necessary to amplify, condition, and/or modify the output, through the help of conditioners, processors, filters, amplifiers, etc., in order to generate useful information. Ideally, sensors should be sufficiently sensitive to the input stimulus and should not influence the measurand. May be the most important characteristic of a sensor is its sensitivity – a measure of the change in the sensor's output as a function of change in input and consistency [17, 18].

Sensors can be classified in a number of ways, such as contact/noncontact sensors, depending on the distance to the object; absolute/relative sensors, depending on the chosen reference; and active/passive sensors, depending on the requirement of external power and finally based on the type of measurand (i.e., temperature). However, in a fundamental sense, the most useful classification can be based on the principle of sensing. This would be particularly useful considering that most of the sensor development and application in textiles is still in the early stages. The principles discussed here are not comprehensive by any means, but include the most relevant categories reported in the literature.

Capacitive Sensors

Capacitive sensors are widely used for a large variety of applications including the detection of proximity, position, flow, pressure, and thickness. The working of capacitive sensors is based on the principle of capacitors, wherein a pair of conducting plates is separated by a dielectric medium. Capacitance (C) is the measure of the amount of charge that a capacitor can hold at a given voltage. It is inversely proportional to the distance between the plates (d) and varies proportionally with the area of the plates (A), $C = \varepsilon_0 \varepsilon_r \frac{A}{d}$, where ε_0 and ε_r are the permittivity of the free space and the dielectric constant of the medium, respectively.

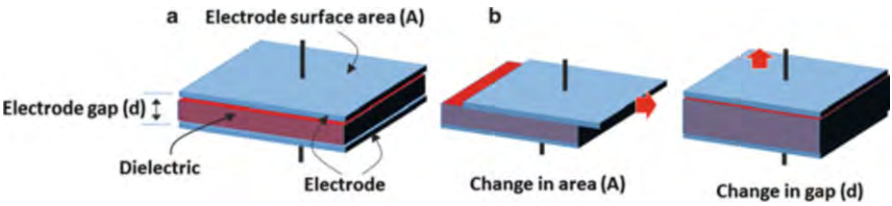

Fig. 2 Schematic diagrams of (**a**) parallel-plate capacitor, (**b**) capacitive sensors based on area and gap variation

Therefore, a capacitive sensor is able to convert a change in any of the three parameters of a capacitor: distance (d), area of capacitive plates (A), and dielectric constant of the medium (ε_r) into an electrical signal [19] (see Fig. 2).

In general, a textile capacitive sensor consists of a polymer dielectric (e.g., 3D fabric spacers [20], foams [21], etc.) with some kind of textile electrodes on the surface [8, 10, 20–22]. Textile-based electrodes can be fabricated in many ways including weaving [23, 24], embroidery [20], and printing [8, 10]. These sensors have been proposed for a variety of sensing including touch [21, 22], proximity, pressure [22], muscle activity and motion [20], and posture [25].

The most reported capacitive sensors in textiles have been for healthcare-related physiological monitoring [8, 10]. The measurands include most physiological parameters that may help in monitoring, diagnosis, or rehabilitation. Examples of capacitive sensors proposed in the literature include a parallel-plate capacitor made of conductive silver ink-printed electrodes to monitor repeated expansion and contraction cycles in breathing. The relative movement of the electrodes along their plane leads to change in active area of the electrodes and capacitance [8]. A similar design in the form of a belt for continuous breath monitoring produced good signal for deep breathing and panting [10].

In an approach similar to that used in content monitoring of sealed packages, a capacitive sensory system in which the human body is used as a dielectric has been used to derive human activity-related information, such as chewing, swallowing, speaking, etc. Electrodes placed on the neck (collar), chest, wrist, and upper legs were used to monitor the changes inside the human body caused by muscle motion and tissue distortion (see Fig. 3). The concept has been shown to be effective in following body posture, arm movement, and head motions as well as monitoring events occurring on a longer time scale, such as having meals and sleeping [25].

One of the recent applications of a textile sensor is sweat-rate determination by capacitive moisture sensors. The sensible change is produced by sweat reaching the dielectric and altering the capacitance of the sensor. Although the system was reported to be useful for the first 30 min of activity, longtime monitoring does not seem to be possible with this system [13].

Capacitive sensing in textiles has also been used to monitor environmental parameters such as temperature and humidity. Polyimide strips (Kapton) containing capacitive gas sensors with planar interdigitated electrodes covered by a dielectric

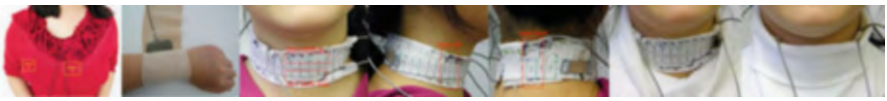

Fig. 3 Sensor placement to determine human activity-related information. Electrodes are placed on the chest, wrist, and neck. For the neck placement, integration in a pullover collar is also shown (Reproduced with permission from Ref. [25])

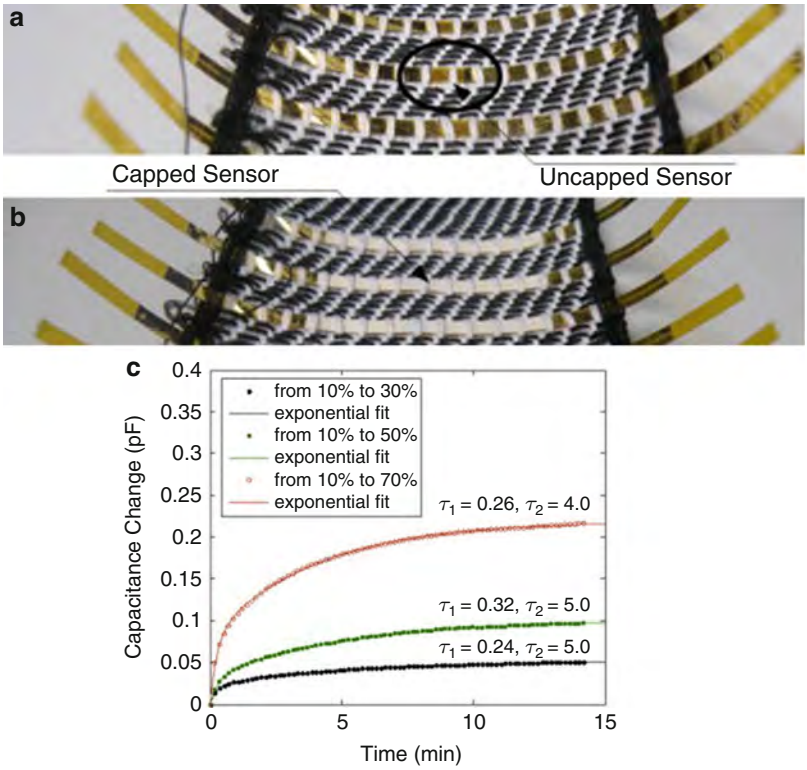

Fig. 4 Woven humidity sensors (**a**) without and (**b**) with the porous capping layer, (**c**) sensor output (capacitance change) as a function of time (Reproduced with permission from Ref. [23])

capable of analyte absorption were woven into fabrics. As shown in Fig. 4, the sensors showed increasing exponential response to relative humidity change and long response time [23, 26].

Flexible and conformable textile tactile (or touch) sensors based on capacitive measurement have been developed and are already incorporated in some commercial products. Electrodes are the key components in these sensors and may pose challenges due to their independent response to stress/strain. Additional complications may come from capacitance changes caused by parasitic deformation, variations in humidity, and temperature [21, 24]. Sergio et al. designed a system for

mapping applied pressure and imaging the shape of the area over which pressure is applied. The sensor is made of conducting fibers arranged in interlaced rows and columns on the opposite sides of thin elastic foam acting as the dielectric. In order to determine the pressure distribution, every row and column is scanned and signals are processed and turned into an image. While the system is advantageous in determining the distribution of pressure, it has the disadvantage of being overly sensitive due to the structure of the foam layer [21]. In a similar approach, a woven fabric sensor constructed from nylon fibers coated with layers of conductive polymer, polymer poly(3,4-ethylenedioxythiophene):poly(styrenesulfonate), and a dielectric, perfluoropolymer (Cytop), has been used to fabricate a tactile sensor array. The sensor fabric was found to be sufficiently sensitive to pressure in the range of human touch [24].

Capacitive sensors are relatively easy to incorporate in textile assemblies because of their multilayered structure. However, these sensors are influenced by dielectric properties of its environment such humidity and require a minimum sensing area to produce measurable change in capacitance.

Inductive Sensors

Inductive sensors are generally used for the determination of position and proximity in order to detect metallic materials in a noncontact mode. They can also be used to detect defects in conducting materials because of their ability to sense the structural changes in the material [17, 18]. An inductor is a passive component designed to resist changes in current. A basic inductive sensor has four components: inductive coil, oscillator, detection circuit, and output circuit (Fig. 5). Inductive sensors emit electromagnetic field generated by the oscillator, if any metallic material approaches to the inductive coil; it affects the amplitude of the field produced by the sensor [17, 18]. By analyzing the change in electromagnetic field and inductance, position and proximity of the target object can be monitored.

Although inductive sensors are widely used in industry, their textile-based derivations are limited [27–29]. Textile-based inductive sensors have been fabricated by forming inductive coils with the help of knitting [28], embroidery [29], stitching, or printing [27, 30], using materials such as copper [28], magnetic wires [27], and conductive print medium [29, 30].

Inductive sensors in textiles have been reported for healthcare-related physiological monitoring including respiration [27–29, 31], heart rate [29, 32], blood pressure [30], and motion [27, 28]. Inductive transducers with copper inductive coils placed into tubular knitted structures were evaluated for respiratory monitoring and motion capture. In some instances these sensors were found superior to resistive transducers made of similar structures [28]. In heart rate measurement, the placement of the inductive coil sensor was found to be crucial [29].

Among the important design parameters of textile inductive sensors are coil configuration and line resistivity. Optimization of these parameters is done to maximize inductive change and electrical stability. Additionally, placement of the

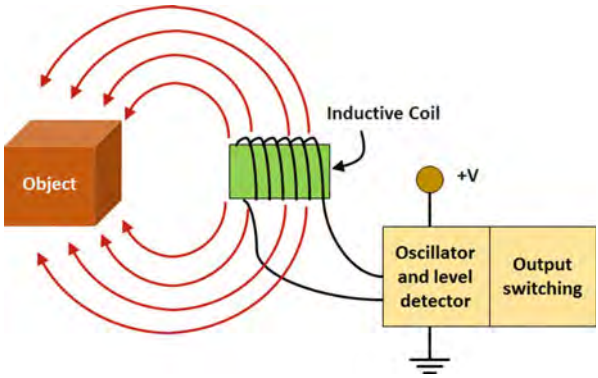

Fig. 5 Schematic of inductive sensor and sensing mechanism

sensor is of importance in terms of sensitivity of the response. Inductive sensors are not affected by the dielectric properties of its environment; however, they are influenced by external magnetic fields.

Piezoelectric Sensors

Piezoelectric materials can generate an electric potential when a mechanical stress is applied, and conversely these materials deform under an applied electric field. Piezoelectric transducers made from these materials have an asymmetrical lattice of molecules that distorts under applied force. The distortion leads to a reorientation of electrical charges within the material, resulting in a polarization of positive and negative charges (see Fig. 6) [17, 18].

The polarization-induced surface charges of opposite polarity can be determined by measuring the difference in voltage between electrodes attached to the opposite surfaces. Traditional piezoelectric sensors are used to determine pressure, acceleration, force, or strain. Piezoelectric sensors have great potential in textiles because of their ability to monitor stress or strain, low cost, and low-power consumption. Although poly(vinylidene fluoride) (PVDF) is the most common material used in the development of piezoelectric textile sensors [33], copolymers such as poly (vinylidene fluoride-trifluoroethylene) (PVDF-TrFE) [34] and its composites [34, 35] have also been used. Piezoelectric sensors are generally used in the film form (between electrodes) and can be integrated into textiles relatively easily [33, 36]. Recently melt-spun fibers with PVDF as the sheath [37] and electrospun fibers of PVDF-TrFE [35] have also been used.

The most reported piezoelectric textile sensors have been for pressure monitoring. A car seat with piezoelectric sensors intended to determine applied pressure was developed with PVDF pressure gauges located between the upholstery fabric and foam (Fig. 7). Changes in phase angle as a function of pressure were monitored for different laminate compositions, and linear sensor output was recorded [33].

Edmission et al. designed an electronic glove to sense the movement of hands with the goal of using it as a functional keyboard. Piezoelectric film sensors were

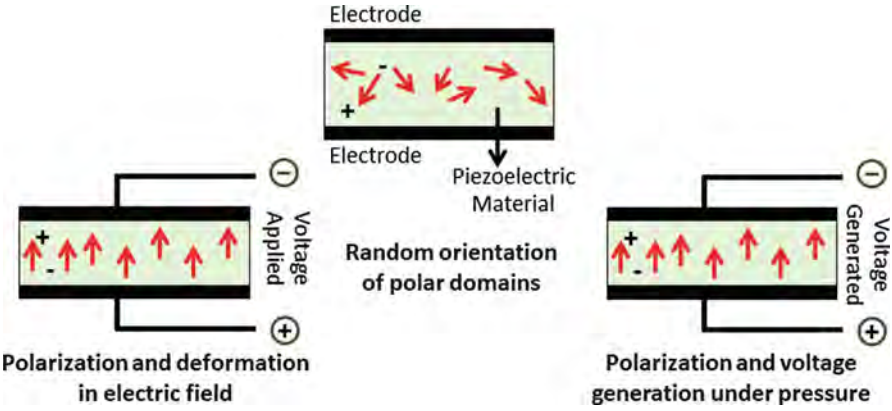

Fig. 6 Mechanism of piezoelectric sensing

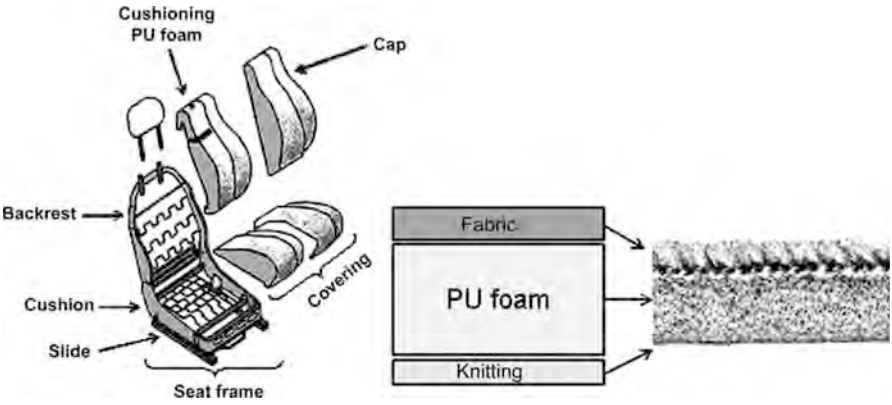

Fig. 7 Car seat structure and cap components (Reproduced with permission from Ref. [33])

placed in key locations of the glove in order to sense flex and tap motions of the hands. Movement of the fingers during flexion and tapping was monitored to determine general design guidelines [36]. Piezoelectric fiber made of melt-extruded PVDF-TrFE in the shape of coaxial filaments with a copper core and vacuum-deposited gold as external electrode has been evaluated as a strain sensor. The fibers were evaluated as part of a woven fabric and were found to be sensitive to applied transverse pressure [34].

Piezoelectric sensing in textiles has also been used to analyze healthcare-related physiological signals including gait stability [38] and cardiorespiratory [36]. A system consisting of two layers of conductive fabrics and a PVDF film sensor embedded in a belt was used to obtain clear cardiorespiratory signals, the heartbeats, and respiratory cycles even better than some commercial sensors (Fig. 8) [39].

An innovative broadband transducer based on PVDF and integrated in a chest belt, reported by Lantana et al., is capable of working as an ultrasound transceiver at

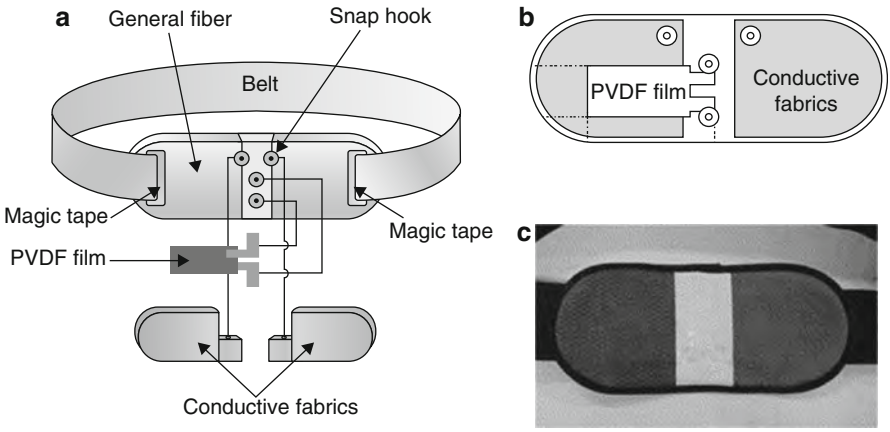

Fig. 8 Schematic of the belt-type sensor (Reproduced with permission from Ref. [39])

high frequencies and as a piezoelectric sensor at low frequencies to monitor heart and respiration-related movements [40].

In a PVDF-TrFE-based design for strain sensor, electrospun fiber webs of PVDF-TrFE and carbon nanotubes were evaluated using a PZT actuator as a strain generator. According to the results, the addition of CNT in the electrospun fibers led to significant enhancement in the strain-sensing capability. The improved performance is attributed to the aligned inclusion of nanotubes as well as the alignment of dipoles in the piezoelectric material in the electrospinning process [35].

Piezoelectric sensors are particularly suitable of textile applications because of their ability to produce measurable signals at small stresses. They respond to almost any type of deformation, including but not limited to compression, tension, torsion, and at almost all magnitudes. Additionally, piezoelectric sensors are capable of having both a positive and negative voltage responses for a given stimulus and are ideally suited for motion sensing. Problems arise in case of static measurements using piezoelectric sensors because of leakage current. Under a constant static load, the output decays to zero.

Optical Sensors

Optical sensors are generally based on measuring a change in intensity, phase, polarization, or wavelength in one or more light beams due to exposure to the measurands (Fig. 9). They have a wide range of applications in the sensing of temperature, pressure, strain, and gas. They are often small, lightweight, and reliable under harsh environmental conditions [17, 18].

Optical sensors offer great potential in textile applications since they are readily available in polymeric fiber form [41–43] and therefore can be easily be incorporated into textiles in different forms including woven [44, 45], knitted [46], and

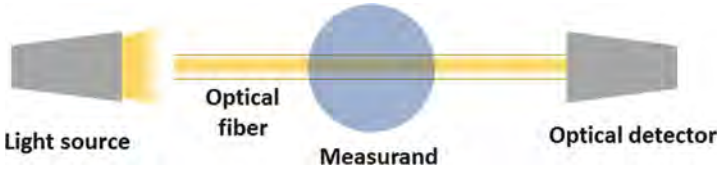

Fig. 9 Principle of operation of optical sensors

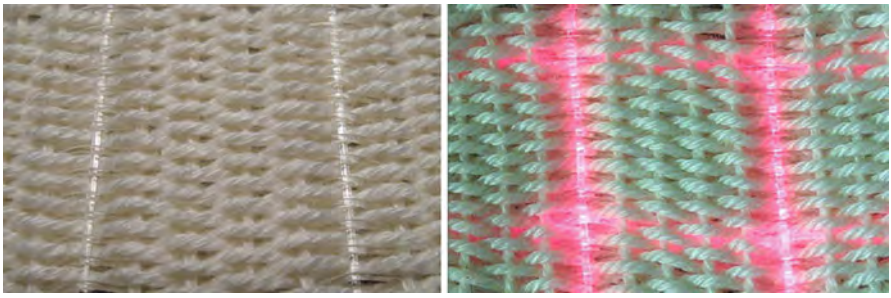

Fig. 10 Woven fabric-based fiber optic sensor (Reproduced with permission from Ref. [44])

nonwoven fabrics [45, 46]. However, in case of glass optical fibers, knitting or weaving processes as well as structures may lead to excessive bending resulting in high curvatures and reduction in the degree of light transmission. In order to minimize these effects, more flexible optical fibers or appropriate fabric structures are preferred for textile applications of optical sensors [44, 46]. Macro-bending [43, 46, 47], Bragg grating [43, 47], and time reflectometry sensors [47] are common textile-based optical sensors reported in the literature. Regardless of type of the optical fiber, they can be used as pressure and strain sensors based on the change in intensity, phase, polarization, wavelength, or spectral distribution of the transferred light after exposure to strain or pressure [43–47].

One of the common applications of optical textile sensors is pressure monitoring. Through the change in transmitted light intensity due to applied pressure, the magnitude of the applied pressure can be determined [46]. Rothmaier et al. developed a textile-based fiber optic sensor by integrating optical fibers into a woven fabric during weaving (Fig. 10). Although the system was found to monitor pressure, it was not effective for the pressure mapping applications [44].

In addition to pressure monitoring, optical textile sensors can be used to analyze bending behavior under strain [46, 47]. Similar to pressure monitoring, response in this instance is obtained as a result of fiber deformation under mechanical effect. Dhawan et al. explored textile-based optical sensors in the form of woven and knitted fabrics by using silica and plastic optical fibers. While woven sensor was found effective in the determination of bending behavior, knitted fabric was reported to measure strain quite effectively [46].

Another application of textile-based optical sensors is in health monitoring. Optical sensors embedded in textiles in the form of a harness have been evaluated for abdominal and thoracic respiratory movement of anesthetized patients during magnetic resonance imaging (MRI). Since metallic materials can affect the quality of the signal during the MRI process, optical fiber sensors are good alternatives for this case [43, 48].

Advantages of optical sensors include excellent transmission properties, multiplexing capability, wide dynamic range, large bandwidth, and lack of sensitivity toward electrical, chemical, and temperature changes [17, 18].

Chemical-Biochemical Sensors

Chemical sensors are capable of interacting with chemical species and generate measurable electrical signals. In general, a chemical sensor consists of two main parts, an active sensing layer and a physical transducer (Fig. 11). The interface between the sensory layer and the transducer can have significant effect on the performance of the sensor. The transduction mechanism can be electrochemical, optical, electrical, mass, or thermal. Chemical sensors generally function with host-guest mechanism, so that they must be specific to the sample. They can work in contact and noncontact modes for various applications including pH, concentration, and color measurement [17, 18].

Chemical sensors on textile substrates have been fabricated using various materials including polyamide/Lycra, polyester/Lycra fabrics with additional layers including pH-sensitive dyes [11, 13], hydrogels, and conductive ink [16]. Although

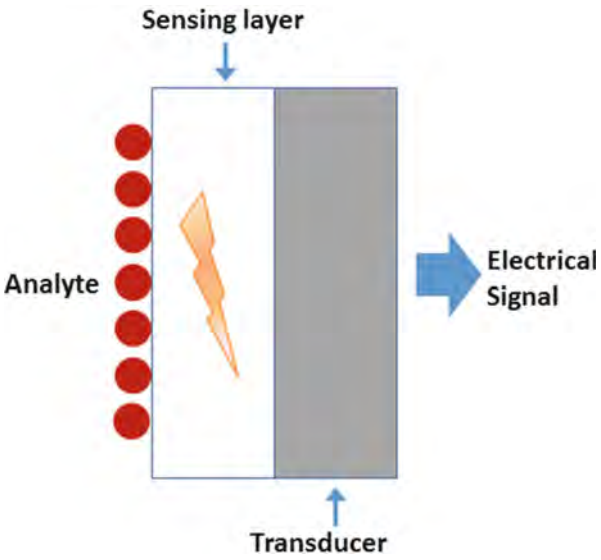

Fig. 11 Principle of operation of chemical sensors

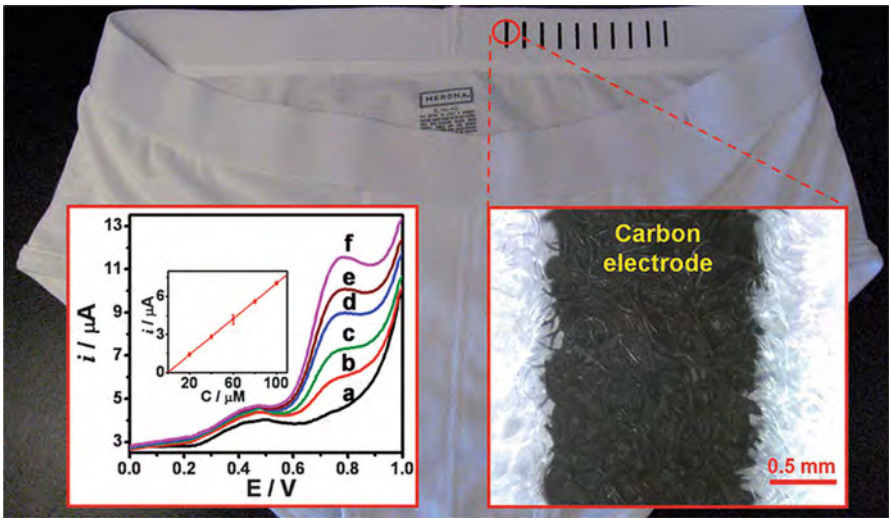

Fig. 12 Image of the screen-printed carbon electrodes on the underwear and linear scan voltammetric response for increasing NADH concentrations over the 0–100 mM range (Reproduced with permission from Ref. [16])

there are different sensing mechanisms for traditional chemical sensors [17, 18], textile-based chemical sensors reported in the literature are mostly based on colorimetric [11, 13–15] and amperometric [16] sensing.

Chemical/biochemical sensors in textiles have been investigated for the determination of body fluids analysis such as sweat composition, rate, and pH. Morris et al. reported an optical detector with pH-sensitive dye to analyze sweat pH and rate [13]. The system consists of a sweat collection system, emitter-detector LEDs, and pH-sensitive dye applied on the fabric sensor. After sweat wicks to the pH-sensitive dye, the color starts to change from yellow to blue and the amount of the absorbed light coming from the LED emitter increases. This leads to decrease in the measured light intensity at the light detector. The same system was used in another study to evaluate the pH and sodium content of sweat during exercise [9]. Along the same vein, potential for direct sweat monitoring using a screen-printed amperometric sensor printed directly on the elastic waist of an underwear has been demonstrated by Yang et al. (Fig. 12) [16].

In addition to monitoring of body fluids, textile-based structures have also been used for detection of blood proteins such as albumin. A proof of concept biosensor, using a highly conductive single-walled carbon nanotube (SWNT)-coated cotton with antialbumin, has been used to detect albumin. When the biosensor interacts with the albumin, removal or rearrangement of antialbumins leads to decrease in the tunneling distance of SWCNTs and increase in conductivity. By monitoring conductivity, the albumin concentration can be monitored even in very low concentrations with high sensitivity and selectivity [49].

Piezoresistive Sensors

Piezoresistive behavior refers to the material property that involves change in its electrical resistance (R) due to applied strain or deformation. This effect provides the basis for a direct transduction mechanism between the mechanical and the electrical domains. It was first reported in 1856 by William Thomson (Lord Kelvin) who observed the resistance change in iron and copper as a result of applied strain [50]. The macroscopic description of the change in resistance (ΔR) of a piezoresistor of length L, under a normal strain (ΔL/L), can be expressed in terms of its resistivity (ρ) and Poisson's ratio (μ) as

$$\frac{\Delta R}{R} = (1 + 2\mu)\frac{\Delta L}{L} + \frac{\Delta \rho}{\rho}$$

Note that the first term represents the change in resistance due to changes in the dimensions as a function of changes in length (ΔL/L) and area (2 μΔL/L) and the second term refers to the change in resistivity (Δρ/ρ) due strain-induced changes in the structure of the material (Fig. 13). In piezoresistive textile strain sensors, both terms can be significant. An important characteristic of sensitivity of piezoresistive sensors is calculated as (G) gauge factor:

$$G = \frac{\Delta R/R}{\Delta L/L}$$

Piezoresistive sensors are commonly used to determine the applied strain or pressure on a material by monitoring change in electrical resistance of the material (see Fig. 14). Generally metal alloys and semiconductors such as germanium and silicon are used for the piezoresistive sensors [17, 18]. However, piezoresistive effect has been also observed for multicomponent systems as conducting composites [51].

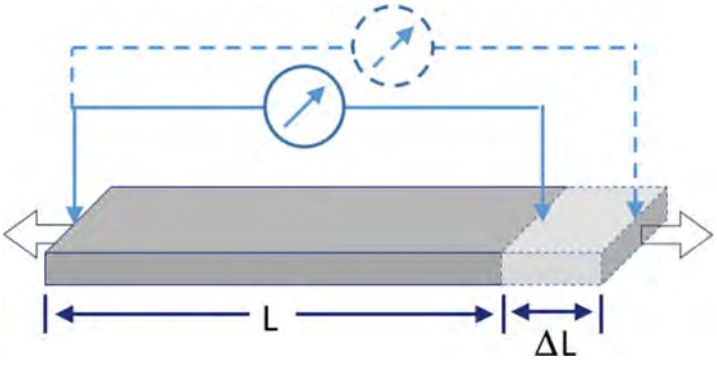

Fig. 13 Mechanism of piezoresistive sensors

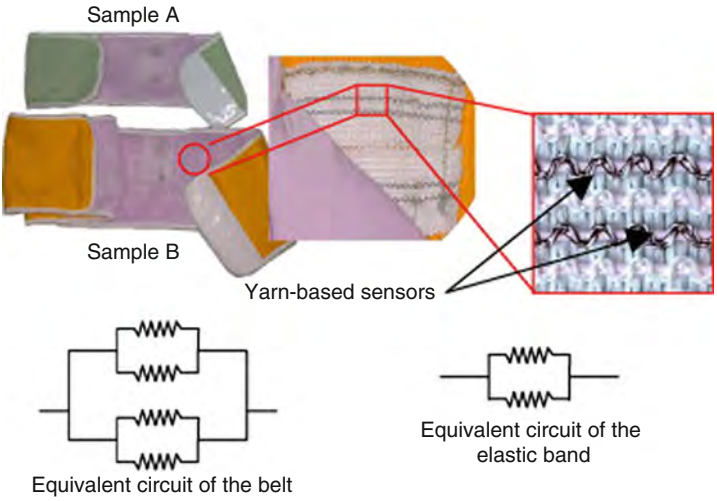

Fig. 14 Instrumented belt for monitoring respiration (Reproduced with permission from Ref. [53])

Development and application of piezoresistive sensors in textiles have been the most extensive of all kinds [1, 2, 4–7, 51–65]. Various materials such as inherently conducting polymers (ICP) [1, 6, 52], conductive elastomeric composites [4, 5, 51], conducting yarns [53], and knitted fabrics [54, 55] have been used as piezoresistive textile sensors. Textiles coated/printed with elastomer composites (EC) containing conducting particles (carbonaceous or metallic) have many advantages over ICPs, including high flexibility, stability, and ease of application. Application of external forces on ECs causes breakdown of the conducting junctions and/or reformation of the new conducting network. Depending on the dominant structural response of the EC, the resistance may increase (positive piezoresistance) or decrease (negative piezoresistance). The response depends on many structural and external factors such as polymer type, filler type, concentration, geometry, filler orientation-dispersion, amplitude, direction, and type of external factor [51].

Piezoresistive textile sensors have been proposed for a wide range of applications including strain monitoring [1, 51, 55], gas sensing [52], temperature sensing [1], stress/pressure sensing [1, 56], health monitoring [53], rehabilitation, and body-posture monitoring with various wearable structures such as gloves [1], knee sleeve [6], leotard [7], shoe insole [56], and bra [57]. For an effective piezoresistive sensor, strain and resistance ranges should be determined carefully in terms of sensitivity and linearity. Piezo-strain sensors can be in different forms such as yarns-filaments [53, 58] and knitted [54, 55], woven [59], and printed/coated fabrics [51, 59]. Piezoresistive sensor yarns of polyester and polyurethane fibers wrapped with one or two carbon-coated nylon fibers showed positive piezoresistive response under strain and used in measuring respiratory signals. The double-wrapped yarn showed superior linear response and lower sensitivity

due to less slippage in the structure [53]. On further analysis of yarn-based sensors, it was reported that soft core yarns resulting from lower twist level produce higher sensitivity with lower linearity [60].

Thermoplastic elastomer (styrene-ethylene-butylene-styrene block copolymer) fibers containing 50 % carbon black powder and attached to textiles with silicone films have been used as sensors to monitor posture. The sensors produced linear response over large strain range (0–100 %), low hysteresis, and low strain-rate dependence [58]. When attached to key positions on a tight-fitting garment, the sensor network achieved sufficient accuracy to distinguish between 27 upper body postures [61].

Knitted fabrics of carbon-coated nylon yarns (Beltron 9R1) used as sensors to monitor abdominal and thoracic respiratory signals have been reported to produce positive and linear piezoresistive behavior in the range of 8–55 % strain [62]. Similarly, tubular weft-knitted and flat warp-knitted fabrics from stainless steel and carbon fibers have been evaluated as strain sensors [54]. Both carbon and steel fabrics showed decreasing resistance with strain resulting from increased level of contact between yarns in the conductive network. The contact resistance is presumed to be a predominant factor in the observed piezoresistive behavior.

In a recent study, Toprakci et al. reported negative piezoresistive behavior at low strains for the first time for printed textile sensors. Nanocomposites composed of a plasticized thermoplastic (poly(vinyl chloride)) or a cross-linked (poly(dimethylsiloxane)) elastomer and carbon nanofibers at concentrations just above the percolation threshold were used as print media. The printed sensors showed negative piezoresistance at small strain levels; beyond a critical strain, however, the resistance reversed and increased with increasing strain, revealing the existence of a negative-to-positive piezoresistivity transition that is fully strain reversible and repeatable upon strain cycling. The mechanism underlying this transition is attributed to the reorientation (rotation and translation) of high-aspect-ratio nanofibers at low strains, followed by separation at high strains [51].

In addition to strain measurement, piezoresistive sensors can be used to monitor pressure. For conductive composites the response depends on the morphology and compressibility of the filler/matrix system under pressure. Shu et al. reported a carbon black-filled silicone-coated fabric pressure sensor for monitoring applied foot pressure during walking [56]. The sensors were positioned between conversion layers such that the sensor fabric experienced mostly in-plane tensile forces under transverse foot pressure, resulting in increasing resistance with applied pressure in the range of 0–600 kPa. A polypyrrole (PPy)-coated polyurethane foam-based pressure sensor has been used in a prototype garment to measure breathing, shoulder movement, neck movement, and scapula pressure [63]. The sensor exhibited increasing and linear resistance pressure response.

Piezoresistive sensors can also be used to monitor gas/vapor. The underlying mechanism involves swelling of the composite due to diffusion of gas/vapor molecules into the structure, resulting in change in dimensions and thereby electrical resistance. Obviously, the piezoresistive response depends on the degree of polymer-vapor interaction. Reversible change in the conductivity of

polypyrrole-coated fabrics was observed due to exposure to different mixture of gases such as NH_3, HCl, and CO_2 [52]. While NH_3/HCl exposure leads to nearly one order of magnitude change in conductivity, the sensor behavior was not found to be repeatable. On the other hand tests carried out with NH_3/CO_2 were found to be more stable with lower change in conductivity.

Monitoring of human body, be it for physiological signals, posture determination, or haptic interaction, has been one of the most investigated areas using piezoresistive principle using textiles. The long-term goal of textile sensors for medical use includes early diagnosis, disease prevention, and treatment. However, most of the published work in this area are focused on health monitoring (e.g., respiration, heart) [53, 64], body-posture determination [5], and rehabilitation [3]. Examples include a fully knitted sensing shirt for simultaneous monitoring of cardiopulmonary vital signals [64]. While the piezoresistive sensor patches, made of nylon yarn with carbonaceous sheath, were used to discriminate between abdominal and thoracic activity, the electrodes, knitted with stainless steel fibers twisted around cotton yarns, were used for electrocardiogram and impedance pneumography. The signal quality of the electrodes was improved using a hydrogel membrane. The quality of signals acquired compared well with commercial systems and were deemed accurate [64].

Huang et al. developed a knitted respiration belt to prevent sudden infant death syndrome [53]. The system consists of sensor yarns made of polyester/elastomeric core, wrapped with one or two carbon-coated conductive yarn(s) (Fig. 14). The conducting yarns spaced in regular intervals in a knit structure were found to be effective for respiration monitoring between 10 and 30 breaths per minute [53].

To improve brassiere design with the goal of limiting excessive breast movement, PPy-coated fabric sensors have been used to measure the amplitude of female breast displacement during exercise (see Fig. 15) [57]. Prestrained (20 %) sensor fabric patches made of PPy-coated nylon/Lycra fabric were found effective in producing accurate signals representing vertical breast movement during exercise. The prestrain was necessary to obtain data in the linear range of the sensor fabric.

Understanding human body kinematics and in particular athletes' motion/body movement is of importance in performance enhancement, injury prevention, and rehabilitation. Munro et al. reported a wearable knee sleeve fitted with prestrained PPy-coated nylon-Lycra fabric sensor to monitor the anterior cruciate ligament movement (Fig. 16) in terms of knee flexion angle. The fabric sensors showed negative piezoresistive behavior with gauge factors ranging between −0.1 and −10.0 within a range of 0–70 % strain. The authors noted that the system is not very efficient for small changes in flexion angle and that consistency in measurement depended on environmental conditions including sweating [6].

Another device to measure knee flexion of patients who are suffering from venous ulcers has been reported by Tesconi et al. [5]. The prototype system included a knee band with four printed sensor patches of conductive elastomeric composite for flexion and extension determination and a shoe with a pressure sensing insole, made of the same materials used in the knee band, to monitor the step signal. The system was able to discriminate the severity level of the diseases

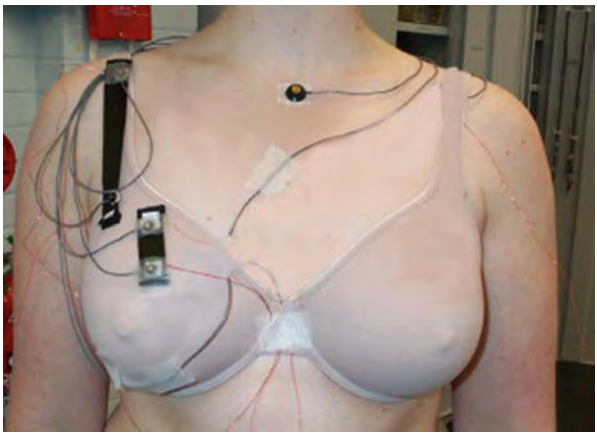

Fig. 15 The strap and brassiere cup fabric sensors attached to the right side of the brassiere (Reproduced with permission from Ref. [57])

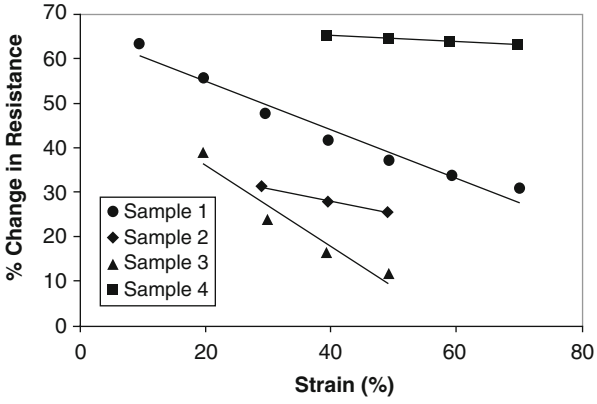

Fig. 16 Knee sleeve design and the electrical calibration curves of four polymer-coated fabric samples displaying their linear dynamic range (Reproduced with permission from Ref. [6])

during normal walking. Tesconi et al. also developed a smart leotard for monitoring movement of lower limbs of an athlete during rowing. The garment consists of an array of printed sensors of graphite/silicone elastomeric composite to monitor knee and hip position during rowing [7]. The sensing garment was compared with a commercial system in measuring the flexion-extension angles during knee movement. The measured change in resistance was interpreted into kinematic output with the help of computational algorithms.

Gibbs et al. developed sensing pants with the ability to determine knee and hip joint movement [65]. The sensing elements in this instance are arrays of conductive textile fibers located around joints. The sensing mechanism has been effective in monitoring joint movement when compared to standard goniometer measurements. An upper body sensing garment to detect the posture and movement with particular focus on stroke rehabilitation has also been reported [4]. The upper limb kinesthetic

Fig. 17 The UKLG prototype and posture recognition trials performed by the user and represented by the avatar (Reproduced with permission from Ref. [4])

garment (ULKG) consists of arrays of electrically conducting elastomer(silicone/graphite) sensor patches applied in a predetermined topology on an elastic garment and can be used for the gesture, posture, and movement monitoring (see Fig. 17). The garment performed at the same accuracy as that obtained from a traditional movement tracking system [4].

Lorussi et al. used a similar approach to develop a sensing glove for acquiring finger movements for use in rehabilitation [3]. The sensing glove is fashioned out of an elastic fabric with coated patches of conductive elastomer(silicone/graphite); while wide patches functioned as sensors, thin patches worked as signal carriers. Although the sensing glove was able to recognize postures well, it showed slow and nonlinear response.

Piezoresistive sensors are currently used extensively in the determination of many parameters including strain, especially in biomedical applications. These sensors can be fabricated using soft polymeric materials and can be relatively easily integrated in textiles. Optimized piezoresistive sensor systems can produce large signals at high rates. However, environmental effects (temperature, humidity), hysteresis, and nonlinearity, particularly at low strains, can be potential problems.

Conclusions

Textile-based sensing has become an active area of research in the emerging field of electronic textiles. Although these sensors cover a wide variety, much of the work has been focused on piezoresistive sensors, primarily because of their simple underlying principle that can be implemented using textile compatible materials and processes, relatively easily. In general, most textile-based sensors discussed in this section offer tremendous potential in many applications. Many textile sensors developed thus far, if optimized, can be easily incorporated into textile structures through traditional processes of fiber formation, spinning/twisting, weaving, knitting, and printing. While comfort (physical and social) and wearability (durability, laundering, etc.) are of paramount importance, functional characteristics required of electronic devices such a power consumption, interconnectivity, reliability, and service life are of concern. Future work should focus on these aspects of textile-based sensors.

References

1. De Rossi D, Della Santa A, Mazzoldi A (1999) Dressware: wearable hardware. Mater Sci Eng C Biomimetic Supramol Syst 7:31–35. doi:10.1016/S0928-4931(98)00069-1
2. Scilingo EP, Gemignani A, Paradiso R, Taccini N, Ghelarducci B, De Rossi D (2005) Performance evaluation of sensing fabrics for monitoring physiological and biomechanical variables. IEEE Trans Info Technol Biomed 9:345–352. doi:10.1109/TITB.2005.854506
3. Lorussi F, Scilingo EP, Tesconi M, Tognetti A, De Rossi D (2005) Strain sensing fabric for hand posture and gesture monitoring. IEEE Trans Info Technol Biomed 9:372–381. doi:10.1109/TITB.2005.854510

4. Tognetti A, Lorussi F, Bartalesi R, Quaglini S, Tesconi M, Zupone G et al (2005) Wearable kinesthetic system for capturing and classifying upper limb gesture in post-stroke rehabilitation. J Neuro Eng Rehab 2:8. doi:10.1186/1743-0003-2-8
5. Tesconi M, Scilingo EP, Barba P, De Rossi D (2006) Wearable kinesthetic system for joint knee flexion- extension monitoring in gait analysis. In: Proceedings of the EMBS '06, IEEE, New York, pp 1497–1500
6. Munro BJ, Campbell TE, Wallace GG, Steele JR (2008) The intelligent knee sleeve: a wearable biofeedback device. Sens Actuator B Chem 131:541–547. doi:10.1016/j.snb.2007.12.041
7. Tesconi M, Tognetti A, Scilingo EP, Zupone G, Carbonaro N, De Rossi D et al (2007) Wearable sensorized system for analyzing the lower limb movement during rowing activity. In: Proceedings of the ISIE 2007, IEEE, New York, pp 2793–2796
8. Kang T, Merritt C, Karaguzel B, Wilson J, Franzon P, Pourdeyhimi B et al (2006) Sensors on textile substrates for home-based healthcare monitoring. In: Proceedings of the 1st transdisciplinary conference on distributed diagnosis and home healthcare, IEEE, Arlington, pp 5–7
9. Morris D, Schazmann B, Wu Y, Coyle S, Brady S, Hayes J et al (2008) Wearable sensors for monitoring sports performance and training. In: Proceedings of the 5th ISSS-MDBS, IEEE, Hong Kong, pp 121–124
10. Merritt CR, Nagle HT, Grant E (2009) Textile-based capacitive sensors for respiration monitoring. IEEE Sens J 9:71–78. doi:10.1109/JSEN.2008.2010356
11. Coyle S, Wu Y, Lau K, Brady S, Wallace G, Diamond D (2007) Bio-sensing textiles – wearable chemical biosensors for health monitoring. In: Proceedings of the 4th international workshop on wearable and implantable body sensor networks, Springer, Aachen, pp 35–39
12. Coyle S, Lau K, Moyna N, O'Gorman D, Diamond D, Di Francesco F et al (2010) BIOTEX-biosensing textiles for personalised healthcare management. IEEE Trans Info Technol Biomed 14:364–370. doi:10.1109/TITB.2009.2038484
13. Morris D, Coyle S, Wu Y, Lau KT, Wallace G, Diamond D (2009) Bio-sensing textile based patch with integrated optical detection system for sweat monitoring. Sens Actuator B Chem 139:231–236. doi:10.1016/j.snb.2009.02.032
14. Coyle S, Benito-Lopez F, Radu T, Lau KT, Diamond D (2010) Fibers and fabrics for chemical and biological sensing. Res J Textile App 14:63–71
15. Curto VF, Fay C, Coyle S, Byrne R, O'Toole C, Barry C, Hughes S, Moyna N, Diamond D, Benito-Lopez F (2012) Real-time sweat pH monitoring based on a wearable chemical barcode micro-fluidic platform incorporating ionic liquids. Sens Actuator B Chem 171–172:1327–1334. doi:10.1016/j.snb.2012.06.048
16. Yang YL, Chuang MC, Lou SL, Wang J (2010) Thick-film textile-based amperometric sensors and biosensors. Analyst 135:1230–1234. doi:10.1039/B926339J
17. Fraden J (2004) Handbook of modern sensors: physics, designs, and applications. Springer, New York
18. Wilson JS (2005) Sensor technology handbook. Newnes/Elsiver, Amsterdam
19. Baxter LK (1997) Capacitive sensors: design and applications. IEEE, New York
20. Meyer J, Lukowicz P, Troester G (2006) Textile pressure sensor for muscle activity and motion detection. In: Proceedings of the 10th IEEE international symposium wearable computers, IEEE, Montreux, pp 69–72
21. Sergio M, Manaresi N, Campi F, Canegallo R, Tartagni M, Guerrieri R (2003) A dynamically reconfigurable monolithic CMOS pressure sensor for smart fabric. IEEE J Solid State Circuits 38:966–975. doi:10.1109/JSSC.2003.811977
22. Wijesiriwardana R, Mitcham K, Hurley W, Dias T (2005) Capacitive fiber-meshed transducers for touch and proximity-sensing applications. IEEE Sensors J 5:989–994. doi:10.1109/JSEN.2005.844327
23. Ataman C, Kinkeldei T, Mattana G, Quintero AV, Molina-Lopez F, Courbat J, Cherenack K, Brianda D, Tröster G, de Rooij NF (2013) A robust platform for textile integrated gas sensors. Sens Actuator B Chem 177:1053–1061. doi:10.1016/j.snb.2012.11.099

24. Takamatsu S, Kobayashi T, Shibayama N, Miyake K, Itoh T (2012) Fabric pressure sensor array fabricated with die-coating and weaving techniques. Sens Actuator A Phys 184:57–63. doi:10.1016/j.sna.2012.06.031
25. Cheng J, Amft O, Lukowicz P (2010) Active capacitive sensing: exploring a new wearable sensing modality for activity recognition. In: Proceedings of the pervasive 2010 8th international conference on pervasive computing, Springer, Helsinki, pp 319–336
26. Mattana G, Kinkeldei T, Leuenberger D, Ataman C, Ruan JJ, Molina-Lopez F, Quintero AV, Nisato G, Tröster G, Briand D, de Rooij NF (2013) Woven temperature and humidity sensors on flexible plastic substrates for e-textile applications. IEEE Sensors J 13:3901–3909. doi:10.1109/JSEN.2013.2257167
27. Kang TH (2006) Textile-embedded sensors for wearable physiological monitoring systems. PhD dissertation, NCSU, Raleigh
28. Wijesiriwardana R (2006) Inductive fiber-meshed strain and displacement transducers for respiratory measuring systems and motion capturing systems. IEEE Sensors J 6:571–579. doi:10.1109/JSEN.2006.874488
29. Koo HR, Lee YJ, Gi S, Khang S, Lee JH, Lee JH, Lim MG, Park HJ, Lee JW (2014) The effect of textile-based inductive coil sensor positions for heart rate monitoring. J Med Syst 38:2. doi:10.1007/s10916-013-0002-0
30. Lee S, Yoo J, Yoo HJ (2009) A wearable ınductor channel design for blood pressure monitoring system in daily life. In: Proceedings of the 3rd international conference on pervasive computing technologies for healthcare, pervasive health, IEEE, London, pp 1–4
31. Teichmann D, Kuhn A, Leonhardt S, Walter M (2014) The MAIN shirt: a textile-ıntegrated magnetic induction sensor array. Sensors 14:1039–1056. doi:10.3390/s140101039
32. Coosemans J, Hermans B, Puers R (2006) Integrating wireless ECG monitoring in textiles. Sens Actuator A Phys 130–131:48–53. doi:10.1016/j.sna.2005.10.052
33. Drean E, Schacher L, Bauer F, Adolphe D (2007) A smart sensor for induced stress measurement in automotive textiles. J Textile Inst 98:523–531. doi:10.1080/00405000701502404
34. Kechiche MB, Bauer F, Harzallah O, Drean JY (2013) Development of piezoelectric coaxial filament sensors P(VDF-TrFE)/copper for textile structure instrumentation. Sens Actuator A Phys 204:122–130. doi:10.1016/j.sna.2013.10.007
35. Laxminarayana K, Jalili N (2005) Functional nanotube-based textiles: pathway to next generation fabrics with enhanced sensing capabilities. Textile Res J 75:670–680. doi:10.1177/0040517505059330
36. Edmison J, Jones M, Nakad Z, Martin T (2002) Using piezoelectric materials for wearable electronic textiles. In: Proceedings of the 6th international symposium on wearable computers, IEEE, Los Alamitos, pp 41–48
37. Nilsson E, Lund A, Jonasson C, Johansson C, Hagström B (2013) Poling and characterization of piezoelectric polymer fibers for use in textile sensors. Sens Actuator A Phys 201:477–486. doi:10.1016/j.sna.2013.08.011
38. Liu J, Lockhart TE, Jones M, Martin T (2008) Local dynamic stability assessment of motion impaired elderly using electronic textile pants. IEEE Trans Autom Sci Eng 5:696–702. doi:10.1109/TASE.2008.923821
39. Choi SJ, Jiang ZW (2006) A novel wearable sensor device with conductive fabric and PVDF film for monitoring cardiorespiratory signals. Sens Actuator A Phys 128:317–326. doi:10.1016/j.sna.2006.02.012
40. Lanata A, Scilingo EP, De Rossi D (2010) A multimodal transducer for cardiopulmonary activity monitoring in emergency. IEEE Trans Info Technol Biomed 14:817–825. doi:10.1109/TITB.2009.2024414
41. El-Sherif MA, Yuan JM, MacDiarmid A (2000) Fiber optic sensors and smart fabrics. J Intell Mater Syst Struct 11:407–414. doi:10.1106/MKNK-E482-GWUG-0HE7
42. El-Sherif M, Fidanboylu K, El-Sherif D, Gafsi R, Yuan J, Richards K et al (2000) A novel fiber optic system for measuring the dynamic structural behavior of parachutes. J Intell Mater Syst Struct 11:351–359. doi:10.1106/JF6U-2FQ9-FQGE-3VXK

43. De Jonckheere J, Narbonneau F, Kinet D, Zinke J, Paquet B, Depre A et al (2008) Optical fibre sensors embedded into technical textile for a continuous monitoring of patients under magnetic resonance imaging. In: Proceedings of the 30th annual international conference of the IEEE engineering in medicine and biology society, IEEE, Vancouver, pp 5266–5269
44. Rothmaier M, Luong MP, Clemens F (2008) Textile pressure sensor made of flexible plastic optical fibers. Sensors 8:4318–4329. doi:10.3390/s8074318
45. Dhawan A, Muth JF, Kekas DJ, Ghosh TK (2006) Optical nano-textile sensors based on the incorporation of semiconducting and metallic nanoparticles into optical fibers. In: Proceedings of the MRS 2006, MRS, 0920-S05-06. doi:10.1557/PROC-0920-S05-06
46. Dhawan A, Ghosh TK, Muth JF (2005) Incorporating optical fiber sensors into fabrics. In: Proceedings of MRS 2005, MRS, 870:H1.6.1-6.6. doi: 10.1557/PROC-870-H1.6
47. Grillet A, Kinet D, Witt J, Schukar M, Krebber K, Pirotte F et al (2008) Optical fiber sensors embedded into medical textiles for healthcare monitoring. IEEE Sensors J 8:1215–1222. doi:10.1109/JSEN.2008.926518
48. Witt J, Narbonneau F, Schukar M, Krebber K, De Jonckheere J, Jeanne M, Kinet D, Paquet B, Depré A, D´Angelo LT, Thiel T, Logier R (2012) Medical textiles with embedded fiber optic sensors for monitoring of respiratory movement. IEEE Sens J 12:246–254. doi:10.1109/JSEN.2011.2158416
49. Shim BS, Chen W, Doty C, Xu C, Kotov NA (2008) Smart electronic yarns and wearable fabrics for human biomonitoring made by carbon nanotube coating with polyelectrolytes. Nano Lett 8:4151–4157. doi:10.1021/nl801495p
50. Thomson W (1856) On the electro-dynamic qualities of metals: effects of magnetization on the electric conductivity of nickel and of iron. Proc R Soc London 8:546–550. doi:10.1098/rspl.1856.0144
51. Toprakci HAK, Kalanadhabhatla SK, Spontak RJ, Ghosh TK (2013) Polymer Nanocomposites containing carbon nanofibers as soft printable sensors exhibiting strain-reversible piezoresistivity. Adv Func Mater 23:5536–5542. doi:10.1002/adfm.201300034
52. Kincal D, Kumar A, Child AD, Reynolds JR (1998) Conductivity switching in polypyrrole-coated textile fabrics as gas sensors. Synth Met 92:53–56. doi:10.1016/S0379-6779(98)80022-2
53. Huang C, Shen C, Tang C, Chang S (2008) A wearable yarn-based piezo-resistive sensor. Sens Actuators A Phys 141:396–403. doi:10.1016/j.sna.2007.10.069
54. Zhang H, Tao XM, Yu TX, Wang SY (2006) Conductive knitted fabric as large-strain gauge under high temperature. Sens Actuators A Phys 126:129–140. doi:10.1016/j.sna.2005.10.026
55. Atalay O, Kennon WR, Husain MD (2013) Textile-based weft knitted strain sensors: effect of fabric parameters on sensor properties. Sensors 13:11114–11127. doi:10.3390/s130811114
56. Shu L, Hua T, Wang Y, Li Q, Feng DD, Tao X (2010) In-shoe plantar pressure measurement and analysis system based on fabric pressure sensing array. IEEE Trans Inf Technol Biomed 14:767–775. doi:10.1109/TITB.2009.2038904
57. Campbell TE, Munro BJ, Wallace GG, Steele JR (2007) Can fabric sensors monitor breast motion? J Biomech 40:3056–3059. doi:10.1016/j.jbiomech.2007.01.020
58. Mattmann C, Clemens F, Troester G (2008) Sensor for measuring strain in textile. Sensors 8:3719–3732. doi:10.3390/s8063719
59. Cochrane C, Koncar V, Lewandowski M, Dufour C (2007) Design and development of a flexible strain sensor for textile structures based on a conductive polymer composite. Sensors 7:473–492
60. Huang C, Tang C, Lee M, Chang S (2008) Parametric design of yarn-based piezoresistive sensors for smart textiles. Sens Actuator A Phys 148:10–15. doi:10.1016/j.sna.2008.06.029
61. Mattmann C, Amft O, Harms H, Troester G (2007) Recognizing upper body postures using textile strain sensors. In: Proceedings of the ISWC 2007, IEEE, Los Alamitos, pp 29–36

62. Pacelli M, Caldani L, Paradiso R. (2006) Textile piezoresistive sensors for biomechanical variables monitoring. In: Proceedings of the 28th IEEE EMBS, IEEE, New York City, pp 5358–5361
63. Dunne L, Brady S, Smyth B, Diamond D (2005) Initial development and testing of a novel foam-based pressure sensor for wearable sensing. J Neuroeng Rehabil 2:4. doi:10.1186/1743-0003-2-4
64. Loriga G, Taccini N, De Rossi D, Paradiso R (2005) Textile sensing interfaces for cardiopulmonary signs monitoring. In: Proceedings of the IEEE conference Engineering in Medicine and Biology Society, IEEE, Shanghai, pp 7349–7352
65. Gibbs P, Asada HH (2005) Wearable conductive fiber sensors for multi-axis human joint angle measurements. J Neuroeng Rehabil 2:7. doi:10.1186/1743-0003-2-7

Flexible Actuators

15

Wei Chen and Zicai Zhu

Contents

Introduction 382
Flexible Actuator Materials 384
Dielectric EAPs 385
Ionic EAPs 389
Other Flexible Actuators 397
Brief Performance Summary 398
Application of Flexible Actuator in Smart Textiles 400
Smart Fashion Design 401
Medicine and Healthcare 402
Human-Machine Interface 406
Summary 408
References 409

Abstract

Flexible actuators exhibit large deformation under external stimulus with advantages of lightweight, softness, and arbitrary shape. Although the technology of flexible actuator used in smart textiles is still at embryonic stage, its shape change and force generation can bring some new fancy functions to smart textiles and advance their intelligence. Flexible actuator is a wide-ranging concept that refers to flexible material (most are based on polymers) that is capable of imparting a force and/or motion. They are divided into three categories, dielectric electroactive polymers (EAP), ionic electroactive polymers, and other flexible actuators. For each category, some typical actuators are introduced including their actuation mechanisms, actuation properties, and possible process integrated

W. Chen (✉) • Z. Zhu
Suzhou Institute of Nano-Tech and Nano-Bionics (SINANO), Chinese Academy of Sciences, Suzhou, Jiangsu, China
e-mail: wchen2006@sinano.ac.cn

© Springer Science+Business Media Singapore 2015

X. Tao (ed.), *Handbook of Smart Textiles*,
DOI 10.1007/978-981-4451-45-1_20

into a textile. Dielectric elastomer and PVDF-based actuators exhibit large strain, high output force, and wide operation frequency but need a relative high driven voltage. Ionic polymer-metal composites (IPMCs) and bucky-gel actuator show large bending deformation under a low voltage but small blocking force and low operation frequency. Thermal-driven actuator and shape-memory polymer often need a heat stimulus. All of them help us to explore their possible applications in smart textiles. Currently, there is rare specific application of flexible actuator technology in smart textiles. However, enormous applications can be envisioned when combining flexible actuators and smart textile. Flexible actuators can produce dynamic shape, generate force or bending moment, and release substance as actuators. They can be used for smart fashion design, assisting people and healthcare in daily life and human-machine interface. In this chapter, some interesting clothing designs are proposed including dynamic decorations, body contouring suit, rehabilitation suit, acupoint massage suit, astronaut suit, drug delivery patch, and force/haptic feedback suit. The field of smart textile is sure to be affected significantly by the application of the flexible actuator technology in the future.

Keywords

Flexible actuators • Electroactive polymer • Dielectric elastomer • PVDF • Electrolyte gel • Ionic polymer-metal composites • Bucky-gel actuator • Shape-memory polymer • Smart fashion • Medicine and healthcare • Human-machine interface • Force/haptic feedback

Introduction

Smart textiles are fabrics that enable electronic components, including miniature power supply, computer for processing and interconnected circuit, and smart materials to be embedded in them. A study on smart textiles can be reduced to smart materials basically, which have the capability to sense external stimulus, if truly smart, to respond to the stimulus and adapts its behavior. From a latest study on smart textiles in Europe, most of researches are still concentrated on sensing to monitor the wearer's health and visual functions in fashion area [1]. Textiles with a sensing function are referred to passive smart textiles, whereas those with an actuation function are described as active smart textiles as they sense a stimulus from the environment and also act to it [2]. The actuators' task in smart textiles is to react to the signal coming from the sensor or data-processing unit, respectively. The type of reaction may be in the form of movement, noise, or substance release. Mechanical functionality is the subject of interesting research for applications in smart textiles. Processing actuators into a textile will make it much smarter.

For the textiles, the key properties are flexibility to conform to the body and comfort to touch, softness, and wearability. Traditional actuation materials such as piezoelectric ceramics, shape-memory alloys, and magnetostrictive materials are often hard and brittle and not easy to be integrated to textiles. Flexible actuators are

emerging as a new class of actuation material that can best be described as soft, flexible materials that are capable of converting electrical energy to mechanical energy and thus imparting a force and/or motion. They are often polymers that respond to external stimulations with a significant size or shape change. Generally, flexible actuators can be classified into two main categories: one is driven by electric field that is named electroactive polymer (EAP) actuator, and the other is driven by other fields such as optical, thermal, and chemical stimulus. They are flexible and light mass; their actuation properties are similar with natural muscle. All of these earn them a name of artificial muscle.

EAP actuators can be divided into two principal classes in general: dielectric and ionic [3]. Dielectric EAPs are materials in which actuation is caused by electrostatic forces between two electrodes which squeeze the polymer. This type of EAP typically requires a large actuation voltage to produce high electric fields (hundreds to thousands of volts), but very low electrical power consumption. Dielectric EAPs require no power to keep the actuator at a given position. Examples are electrostrictive polymers and dielectric elastomers. The former includes ferroelectric macromolecules such as polyvinylidene fluoride (PVDF), poly(vinylidene fluoride-co-trifluoroethylene) (PVDF-TrFE), polyvinyl fluoride (PVF), odd-numbered nylons (with an odd number of carbon atoms between amide groups), and polyurethane. The actuation in ionic EAP is caused by the displacement of ions inside the polymer. Only a few volts are needed for actuation, but the ionic flow implies a higher electrical current compared with dielectric EAPs. Examples of ionic EAPs are polyelectrolyte gels, ionic polymer-metal composites (IPMCs), conductive polymers, and bucky-gel actuator.

The first real breakthrough in EAPs took place in the late 1960s. In 1969 the large piezoelectric effect of PVDF was demonstrated by Kawai. This sparked research interest in developing other polymers systems that would show a similar effect. By the late 1980s, a number of other polymers had been shown to exhibit a piezoelectric effect or were demonstrated to be conductive. In 1994, one of the first articles on electrically induced strain actuator appeared, in which a strain of 3 % was reported. At the time, this strain was an enormous improvement compared with piezoelectric ceramics. Later, it was realized that copolymerizing PVDF with trifluoroethylene, to produce poly(vinylideneflouride-trifluoroethylene) (P(VDF-TrFE)), would increase the output strain (4 %). Dielectric elastomers were investigated at the same time. DARPA-funded research in the 1990s at Stanford Research Institute International and led by Ron Pelrine developed an electroactive polymer using silicone and acrylic polymers; the technology was spun off into the company Artificial Muscle in 2003, with industrial production beginning in 2008. Usually, strains of DE actuators are in the order of 10–35 %; maximum values reach 300 % (the acrylic elastomer VHB 4910) [4].

In 1992, ionic polymer-metal composites (IPMC) were developed and shown to exhibit electroactive properties far superior to previous EAPs [5]. The major advantage of IPMCs was that they were able to show deformation at voltages as low as 1 or 2 V. These are orders of magnitude less than any previous EAP. Under a voltage, IPMCs often show a large bending deformation. Because IPMCs contain

water, they should work in a moist environment or under water, which is not suitable to develop an actuator device in air. Polyelectrolyte gel is a similar ionic EAP like IPMC. Then in the early 2000s, a few new ionic EAPs have been developed. Various ionic liquids (IL) used as solvents were introduced to ionic EAPs to take the place of water to prevent evaporation. IL-IPMC, conducting polymer actuator, and bucky-gel actuator were developed from this viewpoint completely or partly. Vast researches have been made to improve their actuation performances such as bending displacement, actuation force, and response speed in the last decade, and these researches are still going on.

Other flexible actuator such as shape-memory polymers (SMPs), light-driven actuators, and PH-sensitive gels are also very active in the last 20 years [6]. These technologies are at an early stage of research. They can convert thermal, optical, and chemical energy to mechanical energy. And the light-driven actuators even can be controlled remotely. However, compared with an electric source, a thermal source, an optical source, or a PH environment is not so convenient to provide, so to embed these actuators into a textile and drive them is not easy in contrast with EAPs.

Anyway, the flexible actuator technology is relatively new technologies which are currently in the stage of being established in different textile applications [7]. In contrast with the traditional actuators, flexible actuators are much easier to be embedded into a textile. The traditional processes of screen printing, and digital ink-jet printing, have taken on new importance in the rapidly developing field of printed electronics. Besides being sewed on a textile in the manner of patches, electroactive polymer layers can be printed onto flexible substrates in the manner of inks. It is also very convenient to be connected with digital components by flexible printed circuits.

Textiles of today are materials with applications in almost all our activities. Their most common uses are for clothing and containers such as bags and baskets. In the household, they are used in carpeting, upholstered furnishings, window shades, towels, covering for tables, beds, and other flat surfaces and in art. In the workplace, they are used in industrial and scientific processes and, chosen for characteristics other than their appearance, are commonly referred to as technical textiles. Currently, there are not many specific applications of flexible actuator technology in smart textiles. This technology is still at early stage in smart textiles. However, enormous potential applications can be imaged in this area. In the near future, the field of smart textile is sure to be affected significantly by the application of the flexible actuator technology.

Flexible Actuator Materials

For each class of flexible actuator materials, some typical flexible actuator materials are introduced, and their actuation mechanisms, actuation properties, and possible process integrated into a textile are discussed here. All of them would help us to explore their possible applications in smart textiles.

Dielectric EAPs

Dielectric Elastomer Actuator

Dielectric elastomer actuators consist of a polymer film sandwiched between two compliant electrodes. A voltage difference is applied between the compliant electrodes, causing compression in thickness and stretching in area of the polymer film.

Actuation Mechanism

In dielectric elastomers, the electric field-induced actuation response is initiated by the electrostatic attraction between oppositely charged conductive layers applied to the opposing surfaces of the polymer film [8]. This attraction induces a compressive stress, Maxwell stress (σ_M). The electromechanical response of dielectric EAPs is attributed to the development of the Maxwell stress, which is shown in Fig. 1. The stress acts normal to the film surface and thus serves to compress the film along its thickness (z) and stretch the film laterally (in x and y). According to Pelrine et al., the Maxwell stress acting along z can be expressed as [9]:

$$\sigma_M = \varepsilon_0 \varepsilon E^2 \tag{1}$$

where ε is the relative dielectric constant of the substrate polymer, ε_0 is the dielectric constant of free space, and E is the electric field. The magnitude of the stress is dictated by the magnitude of the electric field and the relative dielectric constant. The level of corresponding strain achieved upon actuation, on the other hand, depends on elastic modulus.

Actuation Properties

A wide variety of elastomers derived from chemically cross-linked homopolymers has been investigated as dielectric elastomer. Specific examples include acrylics, silicones (including fluorinated silicones), polyurethanes, fluoroelastomers, ethylene-propylene rubber (EPR), polybutadiene (PB), and polyisoprene (PI, natural rubber). The polymers are characterized by:

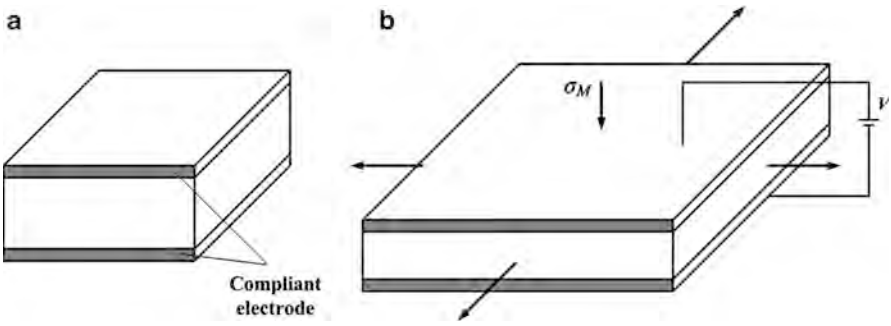

Fig. 1 A schematic illustration of the dielectric elastomer actuator: (**a**) at reference state and (**b**) under a voltage load (deformed state)

- Low stiffness (especially when large strains are required)
- High dielectric constant
- High electrical breakdown strength

Acrylic elastomers are one class of the most investigated DE substrate polymers. They show low elastic elastomer (1 ~ 3 MPa) and a dielectric constant of 4.8. This acrylic elastomer has been reported to exhibit an ultrahigh areal actuation strain of 158 % and transverse strains up to ca. 60–70 %, depending on the level of pre-strain applied in the in-plane direction. Usually this actuator requires a high driven voltage, which is ranged from 1 to 10,000 of volts. And the operating frequency ranges from 0 to tens of thousands Hz theoretically.

Compliant electrode material is also critical for the performance of DE actuator. Films of carbon powder or grease loaded with carbon black were early choices as electrodes for the DEAs. Such materials have poor reliability and are not available with established manufacturing techniques. Some new materials have been developed to improve, including sheets of graphene, coatings of carbon nanotubes, surface-implanted layers of metallic nanoclusters, and ionic gels, recently.

Most DE actuator applications expect large-dimensional change. To improve the extent of strain achieved upon actuation for a given voltage, these actuators must be flexible with a relatively low elastic modulus, possess a moderate-to-high dielectric constant, and be pre-strained biaxially or uniaxially to enhance the dielectric strength by promoting molecular alignment and reduce the effective compressive modulus of DE actuators (which enhances lateral actuation).

A severe drawback of DE actuators is that they need high driven voltage (>1 kV or ~150 MV/m) for actuation, which may be not safe for the human body. There is a need to convert line or battery voltages up to kilovolt potentials, which adds cost and consumes volume.

Polyvinylidene Fluoride-Based Actuator

Polyvinylidene fluoride (PVDF), as well as its copolymers and terpolymers, belongs to ferroelectric polymers. They are a group of crystalline polar polymers that are also ferroelectric, meaning that they maintain a permanent electric polarization that can be reversed, or switched, in an external electric field [8].

Actuation Mechanism

A ferroelectric polymer must contain permanent electrical polarization that can be reversed repeatedly, by an opposing electric field. In the polymer, dipoles can be randomly oriented, but application of an electric field will align the dipoles, leading to ferroelectric behavior. A molecular-level representation of field-induced actuation is provided for PVDF in Fig. 2 [10]. The electromechanical response of PVDF is attributed to a phase transformation from ferroelectric (all trans) to paraelectric (a mixture of T and gauche, g^+/g^-). It is evident from this figure that the transformation to a phase promotes a large change in the lattice constant. Then such a transition causes large molecular strains. Here the strain induced by an electric field is named piezoelectric effect. The polymer will generate an electric field when

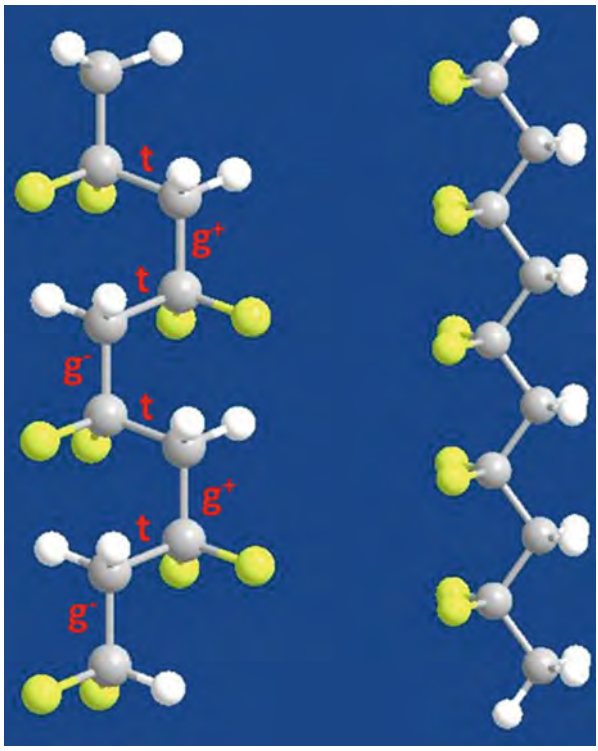

Fig. 2 Schematic description of two conformations of PVDF (*Left*: tg + tg. *Right*: all trans. *Yellow sphere*: fluorine atom. *White sphere*: hydrogen atom. *Gray sphere*: carbon atom)

stress is applied or change shape upon application of an electric field. This is viewed as shrinking, or changes in conformation of the polymer in an electric field, or by stretching and compressing the polymer, measure-generated electric fields.

Actuation Properties

The PVDF and its co/terpolymers may have low strains (~3 %) compared to DE actuator, but they output large actuation stress, on the order of 50 MPa at an electric field of 250 MV/m, compared to the 1 ~ 3 MPa record of DE actuator. The large molecular strains induced by a configuration transition are often accompanied by relatively large strain hysteresis.

This problem can be overcome by reducing the energy barrier associated with the conformational transition (polarization switching). High-energy electron radiation has been used to introduce defects into the crystalline structure of the PVDF-TrFE copolymer. Such radiation treatment breaks down domains of coherent polarization and transforms the polymer into a nanostructured material consisting of nanoscale polar regions (all trans phase) embedded in a nonpolar matrix (gauche g^+/g^- phase). Then PVDF-based actuator can achieve a thickness strain of 4.5 % with a coupling efficiency of 55 %. In another strategy, the dielectric constant of the PVDF-TrFE copolymer has been greatly improved through the physical addition of high dielectric constant organometallic filler [8].

Generally speaking, the advantage of PVDF-based actuator is that moderate strains (up to 7 %) can be achieved under low-frequency fields, but they can also be operated at frequencies in excess of 100 kHz. They can likewise generate high stresses (ca. 45 MPa) due to their high Young's modulus (>0.4 GPa) and thus produce higher energy densities relative to piezoelectric ceramics.

These actuators, like dielectric elastomers, require high fields (~150 MV/m and voltages >1 kV). Electrodes applied to the surface of the polymer fatigue due to the large strains imposed. Dissipation and the associated heating of the actuators often make the achievement of frequencies above 100 Hz impractical except in small samples or at small strains. Similar with DE actuator, the driven voltage of PVDF-based actuator is also very high for the smart textiles, and a key disadvantage of ferroelectric polymers is that there is substantial hysteresis.

Nonionic Gel Actuator

In contrast with the following ionic EAPs, nonionic gel actuator is composed of an electrically inactive material and a plasticizer (often a nonionic solvent), such as poly(vinyl alcohol) (PVA)-DMSO gel and poly(vinyl chloride) (PVC)-DMF gel [11]. In the case of PVC-DMF gel, PVC is versatile dielectric polymers because of its low electrical conduction. When PVC is mixed with DMF, it becomes a jellylike, soft, elastic, dielectric material. PVC gels are effective electrically active materials and have possible applications such as artificial muscles and actuators [12].

Actuation Mechanism

When PVC gel is placed between two parallel plate electrodes and an electric field is applied, the PVC gel deforms on the anode surface, and by turning off the electric field, the PVC gel quickly returns to its original state as shown in Fig. 3 [13]. The deformation of the PVC gel on the anode surface is unique and is analogous to the pseudopodial creeping deformation of amoeba.

Creep deformation is explained by the accumulation of injected negative charges from the cathode to the anode and the subsequent electrostatic repulsive forces among the accumulated charges. For a PVC gel, negative charges accumulated on the gel

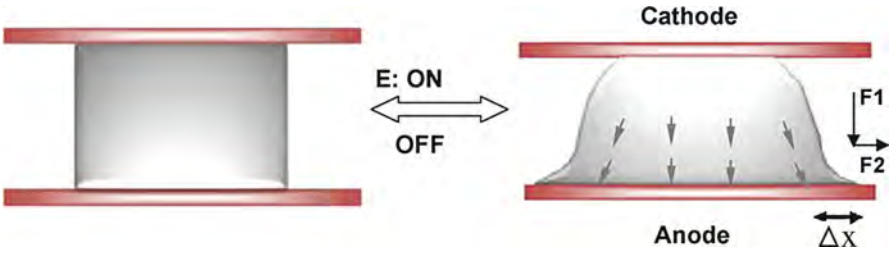

Fig. 3 Schematic diagram of creep deformation of PVC gel on applying a voltage (Reprinted from Sensors and Actuators A: Physical, 157, Hong Xia, Midori Takasaki, Toshihiro Hirai, Actuation mechanism of plasticized PVC by electric field, 307–312, Copyright (2010), with permission from Elsevier)

surface near the anode. It is expected that the accumulation of negative charges causes electrostatic adhesiveness between the PVC gel and the anode. And the adhesiveness increases with increasing electric field at the anode side, whereas at the cathode side, adhesiveness was not observed. Then the accumulation of negative charges near the anode and subsequent electrostatic repulsion cause creep deformation.

Actuation Properties

There is little experimental result on characterizing performance of the PVC gel actuator. The adhesive force between electrodes is about a few N/m^2. And the local creep displacement on the anode is in the range of hundreds microns.

The PVC gel requires a moderate driven voltage (1 ~ 10 hundreds volts) that is much lower than that of DE actuator, but it is still unsafe for application in smart textiles. And the PVC gel is too soft whose elastic modulus is no more than 1 MPa. It means very small output force (~mN).

Ionic EAPs

Polyelectrolyte Gels

A polymer gel consists of an elastic cross-linked network and a fluid filling the interstitial spaces of the network. The network of long polymer molecules holds the liquid in place to give the gel solidity. Gels are wet and soft and look like solid material but are capable of undergoing large deformation in response to environmental change. A polyelectrolyte gel is a charged polymer network with macro-ions fixed on the polymer chains, and micro-counter ions are localized in the network frame. They can exhibit a discontinuous volume phase transitions by small variations of external parameters such as electric and magnetic fields, temperature, solvent quality, or pH.

Actuation Mechanism

For the electro-responsive gel, a usual configuration is that it is immersed in salt solution with both electrodes placed far away from the sample. As illustrated in Fig. 4, an applied voltage causes water electrolysis and cations transport between the solution and the gel [14]. The gel shows bending deformation. There are a few actuation mechanisms proposed for it as follows:

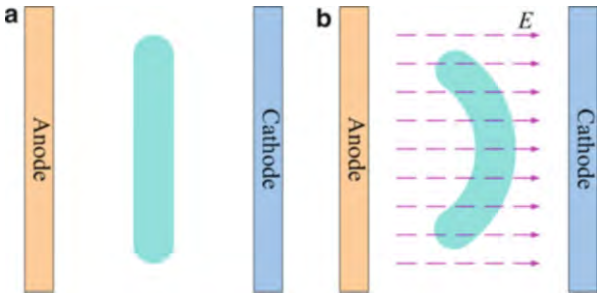

Fig. 4 Actuation of rodlike electro-responsive polyelectrolyte gel placed in salt solution. (**a**) Before and (**b**) after applying electric potential

Coulomb mechanism. Bending is attributed to the external electric field exerting a net force on mobile ions, causing a stationary current inside the gel, as well as on the charged groups attached to the polymer network. As a consequence, the gel is pulled toward one of the electrodes.

Electroosmosis mechanism. It relates electro-actuation to water transport associated with migration of the gel's counter ions. It is postulated that anisotropic contraction is governed by an electrophoretic migration of counterions that drags water along and causes the gel to locally contract or swell, leading to bending at larger scales.

Electrochemical mechanism. Actuation is attributed to changes in the gel's protonation state due to local pH changes near the electrodes.

Dynamic enrichment/depletion mechanism. Actuation is attributed to the dynamical accumulation (or depletion) of ions on both sides of the gel at the solution interface. Such changes in local ionic strength in turn change local swelling/shrinking near the gel faces, causing bending.

In practice, actuation is governed by a combination of the abovementioned mechanisms, and the polyelectrolyte gel shows a more complicate dynamic process of deformation.

Actuation Properties

There are a few electro-responsive gels that have been investigated such as ionic PVA gel, polyacrylamide (PAAm) gel, and poly(sodium acrylate) (PAANa) gel. PAANa gel is a typical negatively charged polyelectrolyte gel having ionizable $-COO^{-}Na^{+}$ groups. The PAANa gel ($70 \times 7 \times 7$ mm) bends semicircularly in 80 s in a 0.02 mol/L NaOH solution on the application of an electric field of 10 V/cm [15]. The maximum strain can reach to 12 %. In another way, the large volume change due to swelling/deswelling can be used to substance release such as drug delivery [16].

Electro-responsive gel exhibits a large bending deformation with a large response time (tens of seconds). The electrolysis of water plays an important role in the above-described shrinking and swelling of gels in electric fields. However, because it involves a disadvantage for designing smart devices, i.e., gas formation, the deformation of gels without the electrolysis of water (as following ionic EAPs) has been studied.

Ionic Polymer-Metal Composites

Ionic polymer-metal composites (IPMCs) consist of surface electrodes, such as thin metal (Pt, Pd, Ag, or Au) or carbon electrodes, and a water-swollen ion exchange membrane (IEM, such as commercial Nafion and Flemion membranes) substrate. The components and microstructure are shown in Fig. 5 [17]. When immersed in water, the fixed anionic groups at the ends of the side chains tend to aggregate to form tightly packed regions, referred to as clusters, which are saturated with cations and water and fully interconnected by nanoscale channels. Cations and water molecules can pass through these channels. In some new developed IPMCs, ionic liquids (IL) are used as solvents to take the place of water.

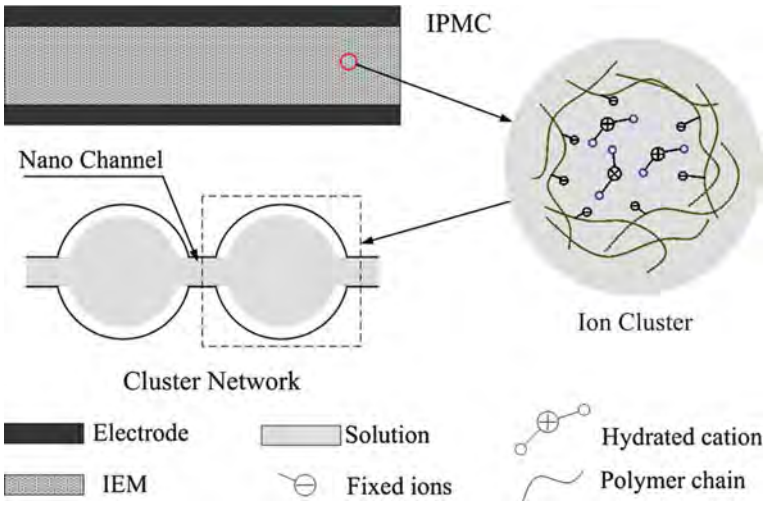

Fig. 5 Microstructure of IPMC

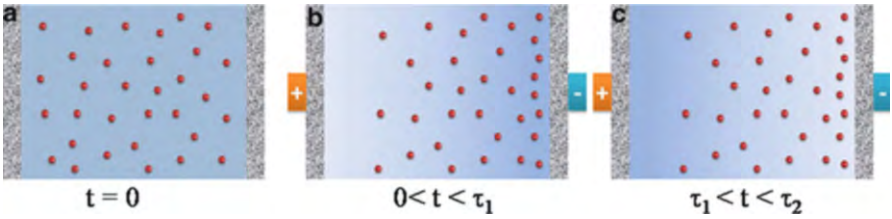

Fig. 6 Illustration of three actuation mechanisms of the IPMC. *Red particles*: dissociated cations. *Blue background*: water (distribution is indicated by the *shading*)

Actuation Mechanism

Under an applied voltage, Nafion-IPMC often shows a fast anode bending deformation followed with a back relaxation deformation. The deformation is the result of cation and water transport in the substrate membrane. And the water content in IPMC has great impact on the deformation properties, especially on the relaxation deformation. In general, the anode deformation is caused by fast motion of cations and water molecules carried by cations, and the relaxation deformation is due to the back diffusion of water in it. For the two deformation processes, they can be explained as:

Fast anode deformation. In Fig. 6, from (a) to (b) ($0 < t < \tau 1$), under an electric field, cations can be seen to migrate quickly to the cathode. The cations also carry water molecules to the cathode through hydration and pumping effects, which causes an imbalance in the distribution of water molecules. The swelling effect mainly induces the fast anode deformation. The characteristic time $\tau 1$ is about 0.1–1 s, because of the fast cation transport.

Relaxation deformation. In Fig. 6, from (b) to (c) ($\tau_1 < t < \tau_2$), under the action of a water concentration gradient and pressure gradient (elastic stress, osmotic pressure, and electrostatic stress) in the IPMCs, some of the free water is driven back to the anode and causes the relaxation deformation. The characteristic time τ_2 is approximately a few seconds because of the slow back diffusion of water.

With decreasing total water content, the effective dielectric constant (i.e., the capacity of stored charges) initially increases and then decreases. This causes the fast anode deformation to exhibit the same trend. And the relaxation deformation disappears quickly due to the increase in osmotic pressure and decrease in electrostatic stress induced by the evaporation of free water. Flemion-IPMC shows a third deformation process, a slow anode deformation. More details can refer to Ref. [18].

For ionic liquid-swollen IPMCs, there are two kinds of movable ions at least. The deformation can also be ascribed to cation migration under the combined action of electric field, concentration gradient and various eigen-stresses, and then the volume change by swelling.

The "piezoelectric effect" of IPMC is not based on the change of molecular configuration, but on the charge transport mainly. Applied an external mechanical load, pressure gradient induced by elastic stress also can cause a redistribution of ionic charges and then generate an electric potential between electrodes [19]. It means IPMC can also work as a mechanical sensor.

Actuation Properties

A typical water-swollen IPMC actuator is fabricated by depositing Pt or Pd electrode on the surface of a pretreated Nafion membrane. Its elastic modulus usually ranges from 100 to 500 MPa, which is dependent on the water content and the electrode properties. For a $0.2 \times 5 \times 30$ mm size beam, it can show almost a circle bending deformation without relaxation under a 2 ~ 3 V voltage, if the water content in it is optimized. The operation frequency is relative low, often in the range of 0 ~ 100 Hz. The actuation performance can be further enhanced by adjusting the composition and the interfacial structure [20].

Response speed. IPMC actuation is based on cation and water transport, so the response speed is decided by the transport speed. IPMC actuators with smaller cation and solvent molecule show a faster actuation.

Actuation deformation. There are mainly two ways to enhance the deformation, focusing on components and structure, respectively. Increasing the cation capacity of IEM substrate, doping the substrate with conductive particles, doping the electrode with RuO_2 and MnO_2, using conductive polymer electrode, and so on can increase the actuation performance. The other way is to improve the electrode-membrane interface structure. Increasing the specific ratio area of the interface can increase the amount of migrated cations, which also lead to a larger deformation.

IPMC shows relative low output force (~mN) as an actuator. It is better to be used as shape or position controller. And usually water-swollen IPMC should work in a moist environment or under water. To improve the stability, IL-based IPMCs are a new important direction. Recently, applications of carbon nanomaterials to electrochemical devices are very attractive in this area. It is very promising to use

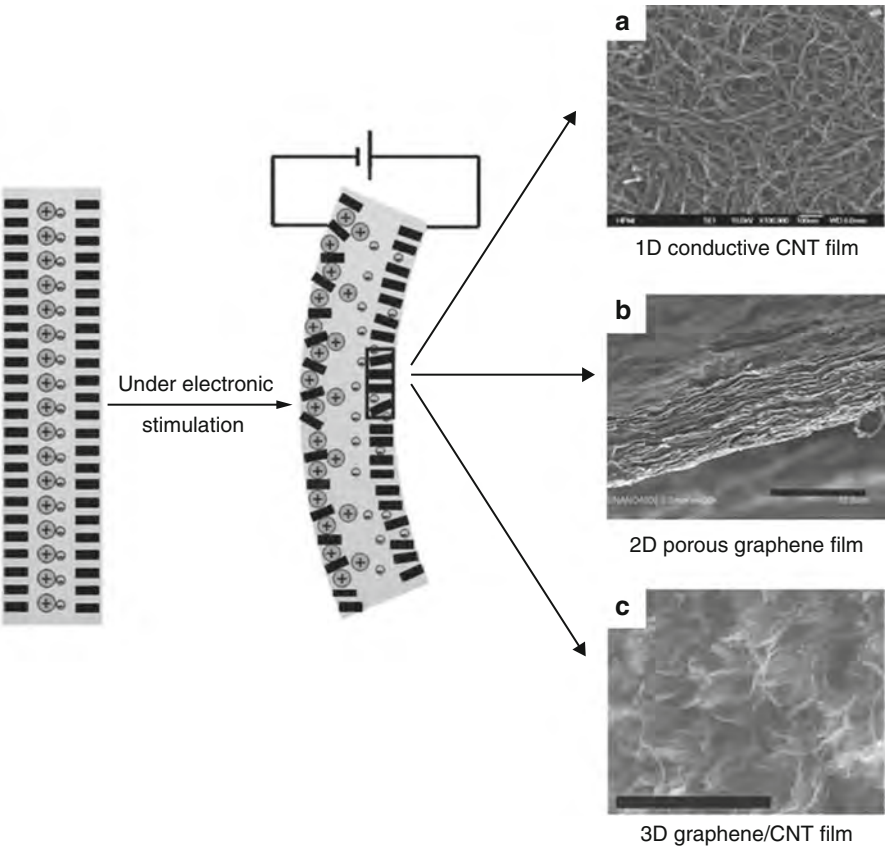

Fig. 7 Different carbon-based electrode materials for IPMC actuators (Lirong Kong and Wei Chen. Copyright © 2013 WILEY-VCH Verlag GmbH & Co. KGaA, Weinheim)

them as high conductive electrodes for the IPMC actuator. The development of carbon-based electrode materials has undergone the following sequence: from one-dimensional CNT to planar graphene and finally to graphene/CNT composite-based electrode materials as shown in Fig. 7 [21]. With unique one-dimensional (1D) CNT network nanostructure and highly anisotropic electrical conductivity, CNT films or bucky papers have proved to be a good replacement for traditional noble metal electrode. Their exceptional mechanical properties also facilitate the flexibility, electromechanical stability, and even high blocking force of the IPMC actuators. Moreover, with porous yet densely packed nanostructure and high-ion accessible surface area, two-dimensional (2D) graphene electrode films have exhibited promising foreground in the IPMC actuators. Due to its unique structure, the electrochemical strain is caused not only by the ion transfer at the interface between electrode and electrolyte layer but also by the ion insertion directly into the graphene electrode layer. As a result, the IPMC actuator performance could be greatly developed. By taking advantages of both 1D CNTs and 2D graphene materials, the novel

three-dimensional (3D) graphene/CNT films present significant improvement in electrical conductivity, electrochemical capacitance, and mechanical properties. As a result, the 3D electrode-based IPMC actuator exhibits attractive actuation response and durability and provides great possibility in interface design and optimization for higher actuation performance of next-generation IPMC actuators.

Conducting Polymer

Conducting polymer (CP) is arranged in two layers of conducting electrodes separated by a solid-state electrolyte that could function as actuators. The most common CPs presently available are polypyrrole (PPy) and polyaniline (PANi).

Actuation Mechanism

Conducting polymers are electronically conducting organic materials featuring conjugated structures. As shown in Fig. 8, electrochemically changing oxidation state of PPy leads to the addition or removal of charge from the polymer backbone and a flux of ions to balance charge [22]. Like in IPMC, this ion flux, which can be accompanied by solvent, is associated with swelling or contraction of the material. A number of things change including the length of C–C bonds on the polymer backbone, the angles between adjacent monomer units, and the interactions between polymer chains and solvent, backbone folding. However, the primary mechanism for volume change or actuation is insertion of ions between polymer chains.

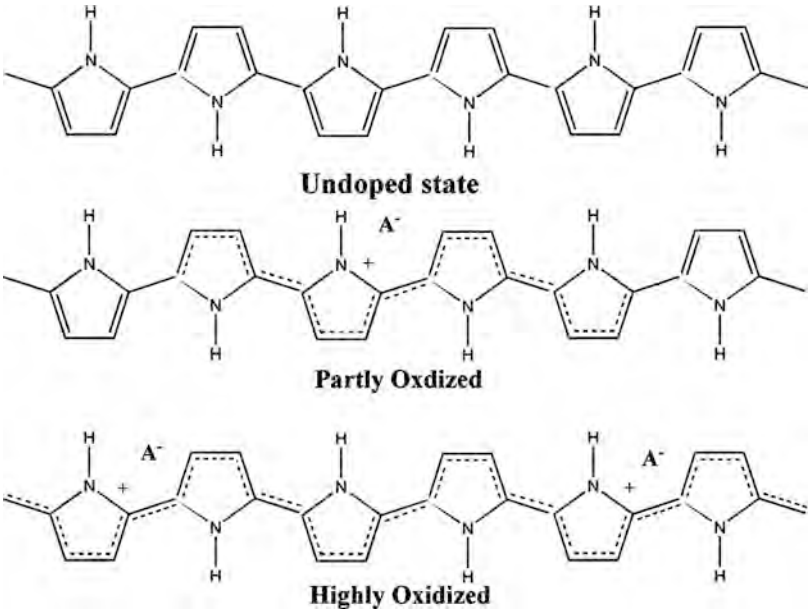

Fig. 8 PPy at different oxidation states. Anionic dopants (A^-) are incorporated to maintain charge neutrality in the oxidized state

Actuation Properties

Electrochemical reactions required to initiate this response commonly require low voltages (1–2 V), and resultant actuation strains range from 1 to ca. 40 %. A promising aspect of CP actuators is that their achievable force density, while measured up to ~100 MPa, is anticipated to be as high as 450 MPa [23]. In contrast with IPMC, CP actuator exhibits larger output force but slow response. The abovementioned methods to improve the actuation performance of IPMC are also applicable to CP actuators.

CP actuators suffer from several serious drawbacks. They exhibit low efficiencies (on the order of 1 %) and electromechanical coupling (<1 %). Actuation-strain rates (12 %/s max to date) are likewise slow due to the diffusion process required for ions to be absorbed in and expelled from the polymer, as well as internal resistance between the polymer and electrolyte solution.

Bucky-Gel Actuator

Bucky gel is a room-temperature gelatinous mixture of an ionic liquid and carbon nanotubes. Outstanding mechanical and electrical properties of carbon nanotube (CNT) and high conductivity and stability of ionic liquids made this mixture an attractive alternative in the field of smart materials and structures. Bucky-gel actuator (BGA) is a tri-layered bimorph nanocomposite system consisting of an electrolyte layer sandwiched between two identical electrode layers. The BGA electrode layer is composed of the bucky-gel mixture reinforced with a polymer matrix. The electrolyte layer is made of the same polymer matrix and ionic liquid utilized in the fabrication of the bucky gel. When a potential difference is applied to the electrodes, BGA bends toward the anode as shown in Fig. 9a.

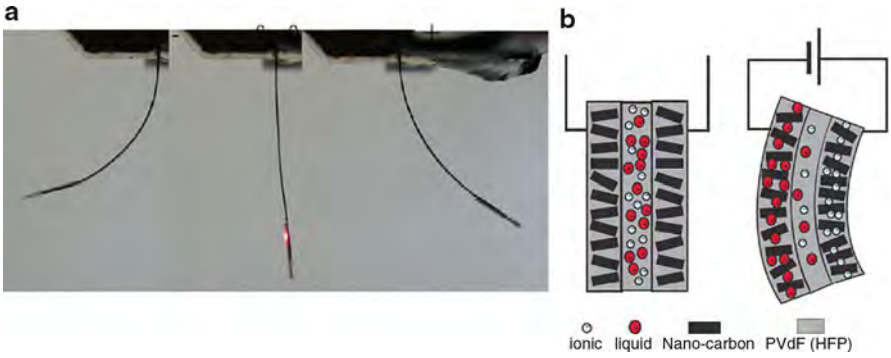

Fig. 9 (**a**) Bending motion of a bucky-gel actuator (15 mm in length, 1 mm in width, 0.095 mm in thickness) in response to alternating ±3.5 V square-wave voltages, (**b**) schematic drawing of actuation mechanism of the bucky-gel actuator (Reprinted from Electrochimica Acta, 53, Ken Mukai, Kinji Asaka, Kenji Kiyohara, Takushi Sugino, Ichiro Takeuchi, Takanori Fukushima, Takuzo Aida, High performance fully plastic actuator based on ionic-liquid based bucky gel, 5555–5562, Copyright (2008), with permission from Elsevier)

Actuation Mechanism

The reasons behind BGA bending motion are still not fully understood. There are mainly two superimposing mechanisms that explained the bending: charge injection and ion transfer [24].

Charge injection model states that when a voltage is applied to the electrodes, there will be a change in carbon-carbon bond length in carbon nanotubes that leads to the expansion and contraction of the opposite electrodes. Therefore, change in electrodes size causes the actuator to bend toward one side, since the layers are bound together.

Ion transfer mechanism states that the bending motion is the result of ion transfer between BGA layers, which is quite similar with that in IPMC, especially IL-swollen IPMC. According to this hypothesis, bending motion occurs when positive and negative ions are separately accumulated on the opposite electrodes. Unlike IPMC, BGA has porous electrodes. Those ions can not only be stored near the electrode-polymer boundary but also can penetrate into the electrodes in Fig. 9b [25]. Therefore, one electrode layer would swell, while the other one shrinks as a result of the size difference of the positive and negative ions. This change in the electrode size will cause BGA to bend toward the anode.

Actuation Properties

Besides working in air, actuation performance of BGA approximates to that of IPMC. It can be adjusted in three aspects mainly by changing the composition and proportion of the electrode layers: effective elastic modulus (30 ~ 600 MPa), effective electrode conductivity (0.1 ~ 2S/cm), and effective electrical capacitance (1 ~ 100 mF). Usually under a 2 ~ 3 V voltage, the maximum output force of BGA is in the order of 10 mN. The operation frequency is relative low, often in the range of 0 ~ 100 Hz.

The abovementioned methods to improve the actuation performance of IPMC are also applicable to BGA. Especially, the electrode properties largely influence the actuation performance. Carbon nanotubes and graphene have been widely used for BGA, which are almost unlimited resources and exhibit highly stable electrochemical and actuation performances. However, the chemical processing necessary for effective dispersion of carbon nanomaterials and large-scale actuator fabrication always results in an unavoidable loss of electrical conductivity and leads to poor frequency response performance. To overcome the low conductivity, Ag nanoparticles (AgNP) are introduced into the carbon electrode and wrapped by RGO in our recent work [26]. It shows much larger displacement and more stable deformation in air than Ag electrode-based actuator.

In general, BGA shows low output force (~mN) as IPMC actuator and narrow operation frequency range due to the diffusion process required for large ions to be absorbed in and expelled from the bucky-gel electrode. However, BGA exhibits very good deformation stability working in air.

Other Flexible Actuators

Thermal-Driven Actuator

Thermal expansion is one of basic properties of a material. Usually the volume of a material increases as its temperature increases. The expansion can be used as a way of force generation, and the material can be used as an actuator. Here the thermal-driven flexible actuators are also based on polymers.

Actuation Mechanism

When applying a heat load to a strip, it will elongate, contract, or bend due to thermal expansion. The heat can be loaded in various ways, such as thermal radiation, electrothermal effect and laser-induced thermal effect, etc. [27].

Actuation Properties

Figure 11 illustrates the electrical actuation of an electrothermal actuator, a 14 wt% MWNT/PDMS composite strip with two different actuation configurations. For the strip with two movable ends, when a dc voltage of 30 V was applied, the current quickly increased to 125 mA and the strip elongated along the direction of the electric field (Fig. 10a). Instead of elongation, the strip with two ends fixed arched upward under the 30 V voltage, as shown in Fig. 10b. From Fig. 10a, the actuator shows a strain of 7.5 % under the low driven voltage.

In contrast with ionic EAPs, thermal-driven actuator shows relative high output force. A coin that is 40 times heavier than the weight of the actuator can be easily

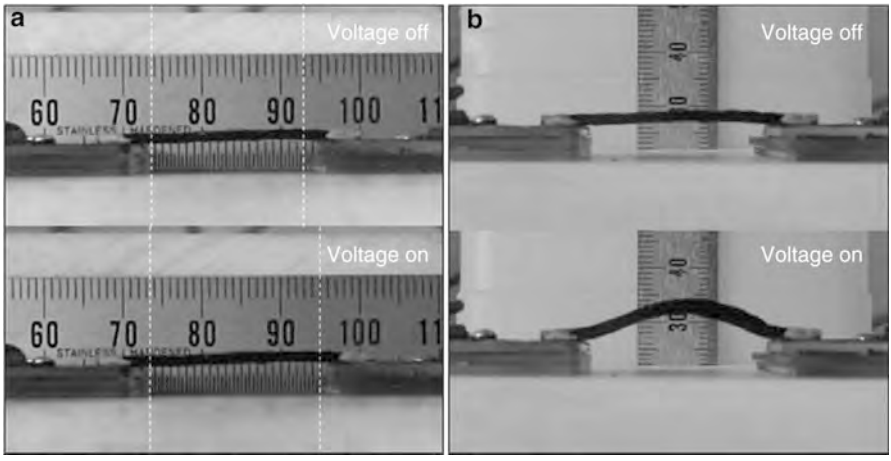

Fig. 10 Direct observation of the electrical actuation of the 14 wt % MWNT/PDMS composite strip under the applied 30 V dc voltage with two ends of the strip unfixed (**a**) and fixed (**b**) (Ying Hu, Guangfeng Wang, Xiaoming Tao, and Wei Chen. Copyright © 2013 WILEY-VCH Verlag GmbH & Co. KGaA, Weinheim)

lifted upward. However, the actuator shows much large response time (tens of seconds). And when the actuator works, the temperature rises up and can be much larger than the body temperature. It makes the actuator not suitable for the smart textiles that directly contact with the human body.

Shape-Memory Polymers

Shape-memory polymers (SMPs) can retain two or sometimes three shapes, and the transition between those is induced by temperature. In addition to temperature change, the shape change of SMPs can also be triggered by an electric or magnetic field, light, or solution [28]. Unlike other flexible actuators, the shape of SMP cannot be controlled continuously, but often transits from one state to another. Here only the heat-induced SMP is introduced; more can be referred to the review.

Actuation Mechanism

SMPs have both a current (temporary) form and a stored (permanent) form. The polymer maintains the temporary shape until the shape changes into the permanent form that is activated by an external heat stimulus. The secret behind these materials lies in their molecular network structure, which contains at least two separate phases. The phase showing the highest thermal transition, T_{perm}, is the temperature that must be exceeded to establish the physical cross-links responsible for the permanent shape. The switching segments, on the other hand, are the segments with the ability to soften past a certain transition temperature (T_{trans}) and are responsible for the temporary shape. In some cases, this is the glass transition temperature (T_g) and others the melting temperature (T_m). If T_g is chosen for programming the SMP, exceeding T_{trans} (while remaining below T_{perm}) activates the switching by softening these switching segments and thereby allowing the material to resume its original (permanent) form as shown in Fig. 11 [29]. Below T_{trans}, flexibility of the segments is at least partly limited. If T_m is chosen for programming the SMP, deformation and recovery can be trigged by cooling and heating based on a similar mechanism.

Actuation Properties

SMPs often have low elastic modulus, which is in the range of 1 ~ 100 MPa and dependent on temperature. The actuation deformation can be up to 800 %, and the transition temperature can be from −10 °C to 100 °C. The response speed of SMPs is slow, about 1 s ~ 1 min. And a heat source is needed for trigging the deformation.

Brief Performance Summary

In the following Table 1, the performance of different flexible actuators presented in this paper is summarized. Dielectric EAPs exhibit larger strain and wider operation frequency. They are suitable for force generation and audio devices,

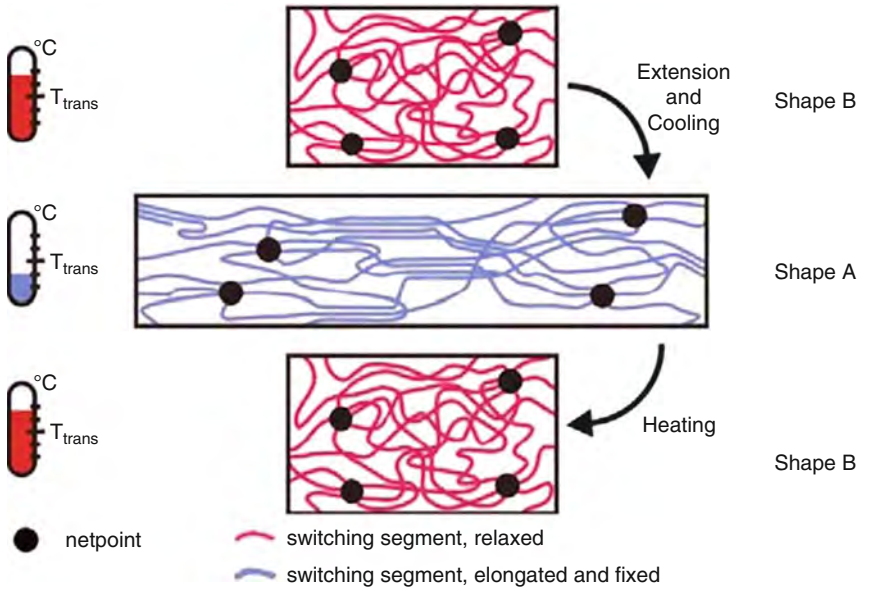

Fig. 11 Molecular mechanism of the thermally induced shape-memory effect Ttrans = thermal transition temperature related to the switching phase

Table 1 Comparison of various flexible actuators

Flexible actuators	Max strain	Operation frequency (Hz)	Elastic modulus	Stimulus	Generated stress
DEA	>100 %	0 ~ 10,000	1 ~ 3 MPa	1 ~ 10 KV	1 MPa
PVDF	3 ~ 7 %	0 ~ 100,000	1 ~ 2.5 GPa	1 ~ 10 KV	50 MPa
PVC gel	–	0 ~ 0.1	<1 MPa	0.1 ~ 1 KV	–
Electrolyte gel	2 ~ 11 %	0 ~ 0.1	<1 MPa	1 ~ 10 V	0.1 MPa
IPMC	2.3 ~ 2.6 %	0 ~ 100	100 ~ 500 MPa	1 ~ 3 V	5 MPa
CP	1 ~ 40 %	0 ~ 10	0.2 ~ 3 GPa	1 ~ 5 V	22 MPa
BGA	1 ~ 3 %	0 ~ 100	30 ~ 600 MPa	1 ~ 5 V	3 ~ 6 MPa
Thermal-driven actuator	7.5 %	0 ~ 0.1	1 ~ 10 MPa	1 ~ 30 V	0.1 ~ 1 MPa
SMP	>100 %	0 ~ 0.1	3 ~ 5 MPa	−10 ~ 100 °C	1 ~ 3 MPa

whereas ionic EAPs show large bending deformation under a relative lower driven voltage. Most of them possess both actuation and sensing functions, which can make more compact and smarter textiles. SMP can generate large strain but low stress under heat stimulus.

These flexible actuators are polymer substrate materials. It means they are good in processing performance and can be easily shaped. They can be incorporated into a textile in the following ways. First, these actuators with a sandwich structure are often fabricated in the form of film. They can be sewed into clothing as a patch directly and work as a film actuator. Second, most polymer substrates of these actuators can be formed by solution casting. For example, Nafion membrane, the substrate membrane of IPMC actuator, can be obtained by solvent evaporation of Nafion solution. By immersing a textile into those solutions, the substrate polymers can be deposited into the textile by evaporation. And then flexible electrodes can be printed onto flexible substrates in the manner of inks. In this way, the flexible actuator is inserted into a textile. Third, these actuators can be manufactured as the shape of stack and coil spring to enhance the force output. Then these actuators can be designed as external wearable aid devices.

Application of Flexible Actuator in Smart Textiles

Textiles have an assortment of uses in our normal life. The most common use of textiles is for clothing, which is directly in contact with the human body. Considering that there are many potential areas that can be developed for flexible actuators in textiles, only the uses in clothing are discussed here. Protection and aesthetics are the two fundamental functions for the conventional clothing [30]. And till now many new functions have been incorporated into clothing such as mechanical, optical, and chemical sensing, heating, communication, and so on [31].

Actuators' reaction may be in form of large deformation, movement, vibration, large force, and substance release. Conventional flexible actuator usually refers to pneumatic artificial muscles, which has been designed to assist devices for rehabilitation. These devices are large volume and not convenient for wearability, which are more close to mechanical devices, not textiles as shown in Fig. 12 [32]. Currently there is rare typical demonstration or product of smart textiles used for those abovementioned flexible actuators. It is mainly due to their poor actuation performance in contrast with pneumatic actuators. Enormous researches are carrying on improving their actuation performances. On the other hand, soft and filmlike actuators are quite suitable for processing into textiles.

Textiles in cooperation with those flexible actuators will produce real smart textiles with mechanical function, which can introduce some new fancy functions in clothing. First, large deformation or movement generated by these actuators can bring some unprecedented concepts such as dynamic art for fashion design. Second, flexible actuators produce force, bending moment as actuators and release substance, and can be used for some functions in medicine and healthcare. Finally, some function of those actuators such as force/tactile feedback, vibration, and sound production can be used for human-machine interface in a work suit.

Fig. 12 Wearable power assist devices for rehabilitation using pneumatic artificial rubber muscle (With permission from Elsevier)

Smart Fashion Design

Aesthetics is one of most important functions of clothing, especially fashion clothing. Now there are some new established companies focused in the development and commercialization of smart textile clothing. An interesting aspect in these efforts to commercialize smart textiles is the interdisciplinary collaboration between companies in fashion and electronics, respectively. Their clothing products are mainly on the optical and visual functions. LED technology and reflective materials are the most popular used in this field [1, 31]. For fashion design, besides color and style, pattern design is also a basic element. Shape change generated by flexible actuators can introduce dynamic design for clothing, and output force can bring new function for body shape control. A few fancy applications are proposed in the following.

Dynamic Decorations

Decorations are an object or act intended to increase beauty of a person, room, etc., which is of importance for fashion design. Patterns of various flowers and insects are often the main elements for decorations. Smart textiles with flexible actuator can be tailored to a belt, a patch, or a cloth with special pattern. They can be used to design textile decorations that can change their shape and pattern dynamically. For example, a flying butterfly brooch will be quite different from traditional static decorations and much more attractive in a banquet. Flexible actuators, especially the ionic EAPs, exhibit large bending deformation. The bending deformation can be

Fig. 13 Illustration of a stack DE-driven slimming belt (**a**) and stack DE actuator (**b**)

used to imitate the flying motion and create an active decoration. The same concept can be extended to other decorations, such as hair decorations and house decorations and so on.

Body Contouring Suit

Fashion is to increase beauty of a person. However, because of obesity problem, a number of people cannot enjoy it. For men, the beer belly often is a serious problem for their shape, whereas for women, much more areas should be paid attention to. Body contouring after massive weight loss refers to a series of procedures that eliminate and/or reduce excess skin and fat that remains after previously obese individuals have lost a significant amount of weight, in a variety of places including the torso, upper arms, chest, and thighs.

Smart textile incorporated with flexible actuator can be designed as body-shaping clothing. Flexible actuators are placed on those abovementioned critical parts of the body. An example of slimming clothing is illustrated in Fig. 13, in which stack flexible actuator is placed around the belly. Under an applied voltage, the clothing can change its shape as set and shape the body as required temporarily for fashion show or dinner party. In another hand, a vibration force activated on the body is helpful to reduce the excess fat effectively, which can be used for slimming. Dielectric EAPs show much higher output force and may have potential in this area.

Medicine and Healthcare

Rehabilitation Suit for Disabled Patients

In recent decades, the world's elderly population is growing steadily. The trends are the same both in developed and developing countries. Advancing age causes a general slowing of bodily functions. The increase in the number of elderly people and the growing need for rehabilitation therapies have sparked interest in the associated problems. In addition to aging problems, many people also suffer brain lesions that result from pathologies leading to cognitive and motor disabilities. The number of people in situations requiring special care, either for rehabilitation or for assistance, is very large.

Rehabilitation therapies mainly include two. One is continual exercise that prevents chronic patients' general condition from worsening; the other is prolonged exercise for trauma patients that may make it possible to regain total or partial muscle function. Rehabilitation therapies and systems can differ widely and must be personalized. It means high social costs. One possible answer is using robotized equipment to provide assistance and perform rehabilitation. Pneumatic actuators have been designed to assist people by means of a rigid structure such as an exoskeleton or by appropriately positioned straps. According to the natural movements or actuation functions accomplished by the pneumatic actuators, these rehabilitation devices are for [32]:

- Hand actuation: Pneumatic muscles are designed to accomplish finger bending, which are attached at the rear of the fingers. The muscles are supplied at 500 KPa to achieve approximately 20 N force required to produce movement and interact with objects.
- Elbow actuation: The muscles are designed to assist elbow movement or aid in recovering joint function.
- Upper limb actuation: There are a few different types of upper limb assist devices that have been investigated. The muscles are used to drive elbow joint movement.
- Trunk and waist actuation: The device developed to assist waist motion consists of two rigid sections connected by a hinge and attached to curved-type pneumatic muscles.
- Lower limb actuation: The muscles operating in parallel are used to power the knee joint in the active lower limb. The device's goal is to provide greater independence for an elderly or disabled person who can walk but has difficulty sitting and rising from a seated position.

The major issues involved in constructing wearable systems of this kind are weight, power, and deformability. For a wearable device, pneumatic muscles are still large volume and need a pressured gas source to drive. Satisfying those requirements calls for actuators that are safe, compact, lightweight, and agile. An ideal wearable rehabilitation device for the disabled patients should be as simple as normal clothes. A sheet-type flexible actuator such as those mentioned above will be the best choice. Usually dielectric EAPs have higher force density and are better used as force generator. To achieve the approximately 20 N, force is still difficult for dielectric EAPs actuators. A multi-rod or multilayer structure is needed to increase the driven force manifold. A wearable rehabilitation aid suit is illustrated in Fig. 14, in which DE stack actuators are distributed for different aid actuations.

Acupoint Massage Suit

Acupuncture points, also called acupoints, are specific points on the surface of the body located on a meridian (connected points across the anatomy which affect a specific organ or other part of the body) into which an acupuncture needle may be inserted for treatment. There are several hundred acupuncture points for one person

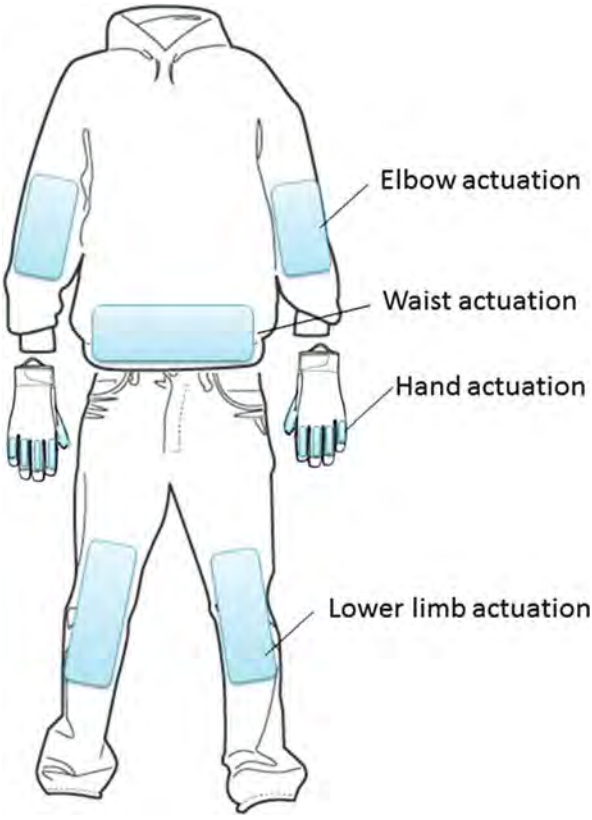

Fig. 14 Illustration of a stack DE-based wearable rehabilitation aid suit

in total. These point locations are frequently sites of Chi blockage and tension – especially in the points found in muscular areas. In traditional Chinese medicine, stimulating these points can treat a disease or release fatigue by acupuncture, acupressure, sonopuncture, and laser acupuncture treatment. Acupoint pressure therapy is implemented by applying firm, steady pressure to these points. If there is pain, it indicates that the muscles in that area are not relaxed. Through releasing or moving the Chi, the pain can be cured [33]. Acupoint pressure treatment has been developed to some healthcare devices in our normal life such as massage armchair and massage cushion.

Here flexible actuators are proposed to drive wearable massage clothing, which can be lightweight, compact, and portable. A similar wearable design, a massage sock named Acuwake, was proposed to wake up at a setting time. It is a pair of socks that buzzes you awake in a gentle fashion. As shown in Fig. 15, the socks come fitted with micro vibrators essentially, which massage your feet at the acupressure points resulting into a healthy heart, strong spine, and an efficient intestine [34]. Extended to a whole suit including a hat and shoes, flexible actuators are designed to an array or distributed form in a textile according to the acupoints distribution on the surface of the body.

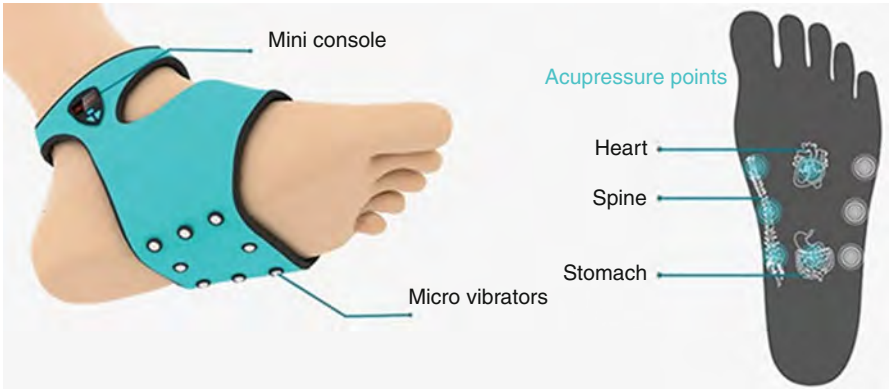

Fig. 15 Illustration of Acuwake massage sock

Drug Delivery Sleeve

Usually drug delivery methods like pills and injections will give no problems; nevertheless, situations can be thought of where other systems would be more preferable. In one case, in oral delivery systems like tablets, pills, and capsules, the drug is absorbed in the stomach or intestinal tract. Some drugs are metabolized; they might lose their activity before being able to fulfill their purpose, so relatively high doses are necessary to achieve the desired effect. Delivery through the skin bypasses the liver, making it possible to lower drug doses. In another case, prolonged drug treatment is necessary for some chronic diseases such as Parkinson's disease. Drugs like pills and capsules are needed to be taken two or more times every day for a long period of years [35]. A wearable textile drug delivery system has many advantages in safety and effectiveness over conventional drug delivery systems by reducing dosage and frequency of dosing.

There have been a few specific textile drug release systems in research. One of them, the way of ion exchange, can be triggered and controlled by electric filed. And polyelectrolyte gels are served as a reservoir and a means to control delivery rate. Many drugs are charged at physiological pH; therefore, they can act as mobile counterions, and this allows them to be used in ion-exchange delivery systems. At physiological pH, the human skin is negatively charged. As a result, cationic drugs permeate the skin more easily than anionic drugs. As shown in Fig. 16a, the positively charged chamber (the anode) will repel a positively charged chemical into the skin, whereas the negatively charged chamber (the cathode) will repel a negatively charged chemical into the skin [36]. And these polyelectrolyte gel chambers can be embedded into a textile in the form of fibers or patches in a sleeve as shown in Fig. 16b. The drug reserved in the patch is released by the microcontrol at a setting rate.

Astronaut Suit

In space exploration, the health of astronaut is critical for the space mission. NASA research has suggested that loss of bone mass can be minimized by vibrating

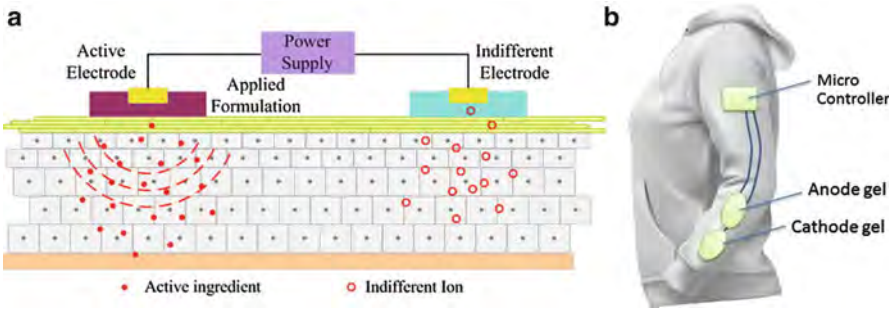

Fig. 16 Polyelectrolyte gel-based drug delivery sleeve. (**a**) Illustration of drug release mechanism, (**b**) a sleeve embedded with a drug delivery patch based on polyelectrolyte gel

body bones. A team of researchers discovered that normally active animals exposed to 10 min per day of low-magnitude (0.25 g), high-frequency (90 Hz) vibrations experienced increased bone formation when compared to the control group. A system providing such an oscillatory activation can be developed in various configurations using flexible actuation materials. These types of suits/devices – tightly worn around bone joints and backbone and neck areas – can be used while astronauts are working either inside or outside of spacecraft. Figure 17 shows a concept of a tightly worn suit with flexible actuator devices in it [37]. And the flexible actuators embedded in the suit are also helpful for anti-overload.

Emotional Care or Therapy

The high efficiency of society causes the fierce competitions. And the competitions are the exact reason of the fast-living pace in modern society. More and more people feel lonely due to lack of emotional communication. Touch (also called tactile perception) is considered one of the five traditional senses and has the psychological and physiological effects on one's health. Giving a touch or an embrace will make one feel much better, especially for the lone elders. Till now, a prototype (Hug Shirt) has been proposed by CuteCircuit company [1], which enables people to send hugs over distance. The shirt is embedded with sensors that feel the touch, the skin warmth, and the heartbeat rate of the sender and actuators the sensation of touch, warmth, and emotions of the hug to a shirt of another shirt. Such a suit embedded with flexible actuators can be used to transfer regards and cares and even can be used for emotional care or therapy.

Human-Machine Interface

The sense of touch is one of the most powerful learning tools that humans have. Whenever someone discovers something new, instinctively they want to hold it, poke at it, touch it, and feel it. So much can be conveyed by the haptic senses; integrating them into a virtual environment would yield great rewards [38].

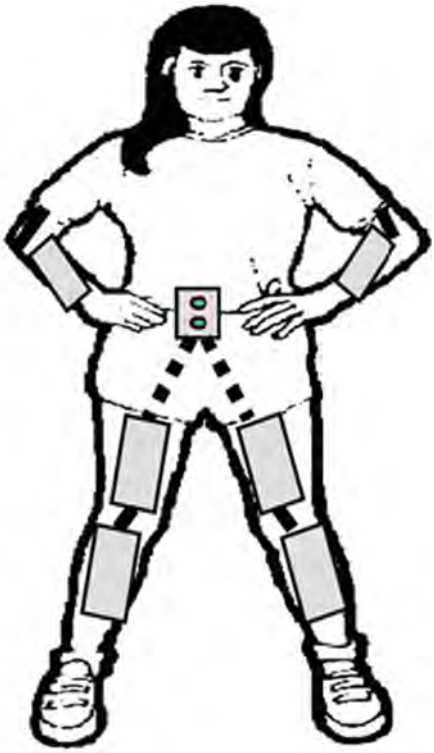

Fig. 17 Flexible actuators (the *gray* blocks) based astronaut suit (Reprinted from Acta Astronautica, 64, Kumar Krishen, Space applications for ionic polymer-metal composite sensors, actuators, and artificial muscles, 1160–1166, Copyright (2009), with permission from Elsevier)

Flexible actuators are good choices for creating touch stimuli, which is still a challenge. Since the touch stimuli devices should contact with skin directly, a textile would be a good carrier. Then the two trends, the use of flexible actuator and the use of textile, lead to a new application direction, force/tactile feedback clothing. It has enormous potential in the following fields.

Remote Control Gloves

Usually a remote control is a component of an electronics device, most commonly a television set, originally used for operating the device wirelessly from a short line-of-sight distance. Conventional way is an open-loop control. The control orders are sent to a remote machine such as a car, a plane, or a robot. The user cannot feel the real situation of the machine. For example, the user cannot feel the real manipulated force when picking up an egg by a remote controlled robotic hand. Sometimes the egg will be broken or dropped if the manipulated force is larger or smaller than that it is needed. Since the objects being manipulated do not exist in a physical sense, the forces are generated using haptic (force generating) operator controls. Data representing touch sensations may be saved or played back using such haptic technologies. When such devices are simulated using a computer (as they are in operator training devices), it is useful to provide the force feedback that would be

felt in actual operations. A medium output force is needed for this case, so the dielectric EAPs is more suitable than ionic actuators for this case. Haptic simulators are used in medical simulators and flight simulators for pilot training.

Silent Communication

Haptic and tactile feedback is best used to inform about narrow-bandwidth signals. The nature of the human touch perceptive system makes it difficult to convey large amounts of information through the touch channel; however, touch signals are very salient and have the potential to very easily draw attention. Haptic and tactile signals should thus be used mainly to represent variables that don't change very often but that require attention. For users with visual impairments, haptic feedback should be effective in many more cases than for normally sighted users; similarly, tactile feedback should be effective in difficult environments (e.g., outdoors, variable lighting, high glare, battlefield, etc.) [38]. This technology is suitable for specific work suits such as bunker clothing, space suit, diving suit, etc.

Force/Haptic Feedback Controller

Haptic feedback is commonly used in arcade games, especially racing video games. Simple haptic devices are common in the form of game controllers, joysticks, and steering wheels. Early implementations were provided through optional components, such as the Nintendo 64 controller's Rumble Pak in 1997. Many newer generation console controllers and joysticks feature built-in feedback devices too. In 2007, Novint released the Falcon, the first consumer 3D touch device with high-resolution three-dimensional force feedback; this allowed the haptic simulation of objects, textures, recoil, momentum, and the physical presence of objects in games. In 2013, Valve announced a line of Steam Machines microconsoles, including a new Steam Controller unit that uses weighted electromagnets capable of delivering a wide range of haptic feedback via the unit's trackpads.

In the future, wearable haptic feedback clothing will be developed for immersing games and virtual reality. The flexible actuators can make the whole body of the user feel the environment setting in the game. Especially, this technology is suitable for the acceleration and stall in the racing games and the flight games.

Summary

Several typical flexible actuators including their actuation mechanisms and properties are described in this chapter. They show large deformation with relative low driven force in general. Dielectric EAPs exhibit larger strain and wider operation frequency. They are suitable for force generation and audio devices. Considering that they work under a high voltage, a protective method should be taken into account when used in a textile. Ionic EAPs show large bending deformation under a few voltages. Most of them possess both actuation and sensing functions. And SMP can generate large strain but low stress under heat stimulus. These flexible actuators are is still at embryonic stage.

Currently, there is rare specific application of this actuator technology in the smart textiles. However, this area has tremendous potential. Some interesting concepts of flexible actuator applications have been proposed here. First, the flexible actuator can be used for smart fashion design. It can make the decorations more attractive and lively and shape body dynamically. Second, the flexible actuators can be used for wearable medicine and healthcare devices embedded in clothing. In these devices, they can help to provide clothing with capabilities that will prove invaluable for therapeutic massage techniques, rehabilitation, assistance, and drug delivery. And last, they can also used for human-machine interface design. They can help people to feel the object in a remote place or in a virtual world more real. Integrating these functions into a textile or clothing will make it smarter. And the flexible actuator technology is critical to make them come true, though there is still a long way to go, and the road ahead is challenging. It is believed that some of these flexible actuators can be comparable with natural muscles and have a great impact on the smart textiles in the future.

References

1. Berglin L (2013) Smart textiles and wearable technology – a study of smart textiles in fashion and clothing. The Swedish School of Textiles, University of Borås
2. Tao X (2001) Smart fibers, fabrics and clothing, fundamentals and applications. Woodhead, Cambridge
3. Mirfakhrai T, Madden JDW, Baughman RH (2007) Polymer artificial muscles. Mater Today 10:30–38
4. Kofod G (2001) Dielectric elastomer actuators. PhD thesis, Risø National Laboratory, The Technical University of Denmark
5. Oguro K, Kawami Y, Takenaka H (1992) Bending of an ion-conducting polymer film-electrode composite by an electric stimulus at low voltage. Trans J Micromach Soc 5:27–30
6. Mather PT, Luo X, Rousseau IA (2009) Shape memory polymer research. Annu Rev Mater Res 39:445–471
7. Black S (2007) Trends in smart medical textiles. In: Smart textiles for medicine and healthcare. Woodhead, Cambridge, pp 1–25
8. Shankar R, Ghoshcd TK, Spontak RJ (2007) Dielectric elastomers as next-generation polymeric actuators. Soft Matter 3:1116–1129
9. Pelrine R, Kornbluh R, Pei Q, Joseph J (2000) High-speed electrically actuated elastomers with strain greater than 100 %. Science 287:836–839
10. Lovinger AJ (1983) Ferroelectric polymers. Science 220:1115–1121
11. Hirai T, Zheng J, Watnabe M, Shirai H (2001) Electrically active polymer materials – application of nonionic polymer gel and elastomers for artificial muscles. In: Smart fibers, fabrics and clothing. Woodhead, Cambridge, pp 7–33
12. Hirai T, Ueki T, Takasaki M (2008) Electrical actuation of textile polymer materials. J Fiber Bioeng Inform 1:1–6
13. Xia H, Takasaki M, Hirai T (2010) Actuation mechanism of plasticized PVC by electric field. Sens Actuators A Phys 157:307–312
14. Glazer PJ, van Erp M, Embrechts A, Lemay SG, Mendes E (2012) Role of pH gradients in the actuation of electro-responsive polyelectrolyte gels. Soft Matter 8:4421–4426
15. Shiga T (1997) Deformation and viscoelastic behavior of polymer gels in electric fields. Adv Polym Sci 134:131–163

16. Wolgemuth CW, Mogilner A, Oster G (2004) The hydration dynamics of polyelectrolyte gels with applications to cell motility and drug delivery. Eur Biophys J 33:146–158
17. Zhu Z, Asaka K, Chang L, Takagi K, Chen H (2013) Multiphysics of ionic polymer–metal composite actuator. J Appl Phys 114:084902, 1–13
18. Zhu Z, Chang L, Asaka K, Wang Y, Chen H, Zhao H, Li D (2014) Comparative experimental investigation on the actuation mechanisms of ionic polymer–metal composites with different backbones and water contents. J Appl Phys 115:124903, 1–10
19. Griffiths DJ (2008) Development of ionic polymer metallic composites as sensors. Master thesis, Virginia Polytechnic Institute and State University
20. Chang L, Chen H, Zhu Z, Li B (2012) Manufacturing process and electrode properties of palladium-electroded ionic polymer–metal composite. Smart Mater Struct 21:1–14
21. Kong L, Chen W (2014) Carbon nanotube and graphene-based bioinspired electrochemical actuators. Adv Mater 26:1025–1043
22. Smela E (2003) Conjugated polymer actuators for biomedical applications. Adv Mater 15:481–494
23. Madden JD, Vandesteeg N, Madden PG, Takshi A, Zimet R, Anquetil PA, Lafontaine SR, Wierenga PA, Hunter IW (2003) Artificial muscle technology: physical principles and naval prospects. IEEE J Ocean Eng 29:706–728
24. Takeuchi I, Asaka K, Kiyohara K, Sugino T, Terasawa N, Mukai K, Fukushima T, Aida T (2009) Electromechanical behavior of fully plastic actuators based on bucky gel containing various internal ionic liquids. Electrochim Acta 54:1762–1768
25. Mukai K, Asaka K, Kiyohara K, Sugino T, Takeuchi I, Fukushima T, Aida T (2008) High performance fully plastic actuator based on ionic-liquid-based bucky gel. Electrochim Acta 53:5555–5562
26. Lu L, Liu J, Hu Y, Zhang Y, Chen W (2013) Graphene-stabilized silver nanoparticle electrochemical electrode for actuator design. Adv Mater 25:1270–1274
27. Hu Y, Wang G, Tao X, Chen W (2011) Low-voltage-driven sustainable weightlifting actuator based on polymer–nanotube composite. Macromol Chem Phys 212:1671–1676
28. Behl M, Lendlein A (2007) Shape-memory polymers. Mater Today 10:20–28
29. Lendlein A, Kelch S (2002) Shape-memory polymers. Angew Chem Int Ed 41:2034–2057
30. Park S, Jayaraman S (2003) Smart textiles: wearable electronic systems. MRS Bull 28:585–591
31. Schwarz A, Van Langenhove L, Guermonprez P, Deguillemont D (2010) A roadmap on smart textiles. Text Prog 42:99–180
32. Belforte G, Quaglia G, Testore F, Eula G, Appendino S (2007) Wearable textiles for rehabilitation of disabled patients using pneumatic systems. In: Smart textiles for medicine and healthcare. Woodhead, Cambridge, pp 221–252
33. Ernst E (2006) Acupuncture – a critical analysis. J Intern Med 259:125–137
34. Kulkarni V, Rajhans A, Sarda A (2014) Acuwake sock. Red point award: design concept 2014. http://www.red-dot.sg/en/online-exhibition
35. Nierstrasz VA (2007) Textile-based drug release systems. In: Smart textiles for medicine and healthcare. Woodhead, Cambridge, pp 50–70
36. Iontophoresis. http://www.electrotherapy.org/modality/iontophoresis
37. Krishen K (2009) Space applications for ionic polymer-metal composite sensors, actuators, and artificial muscles. Acta Astronaut 64:1160–1166
38. Subramanian S, Gutwin C, Sanchez MN, Power C, Liu J (2005) Haptic and tactile feedback in directed movements. In: Proceedings of guidelines on tactile and haptic interactions, University of Saskatchewan, Saskatchewan, Canada, pp 37–42

Development of Nanogenerators in Wearable Electronics

16

Chen Song, Xiaoming Tao, and Songming Shang

Contents

Introduction 412
Flexible and Soft Piezoelectric Energy Harvesting Devices 414
PENGs Based on Semiconducting Piezoelectric Materials 415
Flexible PENGs Made from Piezoelectric Ceramic Composites 416
Flexible PENGs Made from Polymeric Piezoelectric Materials 417
Enhancement in Charge Collection and Transfer 418
Summary of PENGs 420
Flexible Triboelectric Energy Harvesting Devices 420
Fundamentals and Influencing Factors of Triboelectrification 420
Flexible and Soft TENGs 423
Summary of TENGs 426
Conclusion 427
References 428

Abstract

This chapter reviews the progress of research development in soft and flexible electric generators for harvesting mechanical energy based on piezoelectric and triboelectric effects. In particular, it covers the operating principles, materials selection and synthesis, device structures, fabrication methods, and performance of two types of soft and flexible generators, that is, piezoelectric and triboelectric nanogenerators (PENGs and TENGs). Benchmark analysis is carried out for both

C. Song • S. Shang
Institute of Textiles and Clothing, The Hong Kong Polytechnic University, Kowloon, Hong Kong, SAR, China
e-mail: song.chen@connect.polyu.hk; shang.songmin@polyu.edu.hk

X. Tao (✉)
Institute of Textiles and Clothing, The Hong Kong Polytechnic University, Hung Hom, Hong Kong SAR
e-mail: xiao-ming.tao@polyu.edu.hk

© Springer Science+Business Media Singapore 2015

X. Tao (ed.), *Handbook of Smart Textiles*,
DOI 10.1007/978-981-4451-45-1_21

PENGs and TENGs. Various applications of the technology for powering wearable or portable electronics are demonstrated. Towards this end, critical issues and great challenges of soft and flexible TENGs and PENGs are discussed.

Keywords
Energy harvesting • Nanogenerator • Triboelectric • Piezoelectric

Introduction

Renewable, affordable, and green energy has attracted much attention in the last decades due to the increasing energy shortage and environment problems caused by fossil fuel. On the other hand, low-power electronics and wireless sensor networks, smaller batteries with more energy storage, as well as mechanical energy harvesting devices have become more and more attractive and thus have driven numerous research efforts both in industries and academia [1].

In the last decades, the development tendency of wearable electronics has been miniaturization, larger data handling capacity, data interaction and synchronization, and portability with much lower power consumption. Figure 1 shows the power available from various sources according to Texas Instruments [2]. The Internet of things has promised that in the future, wearable electronics integrated with

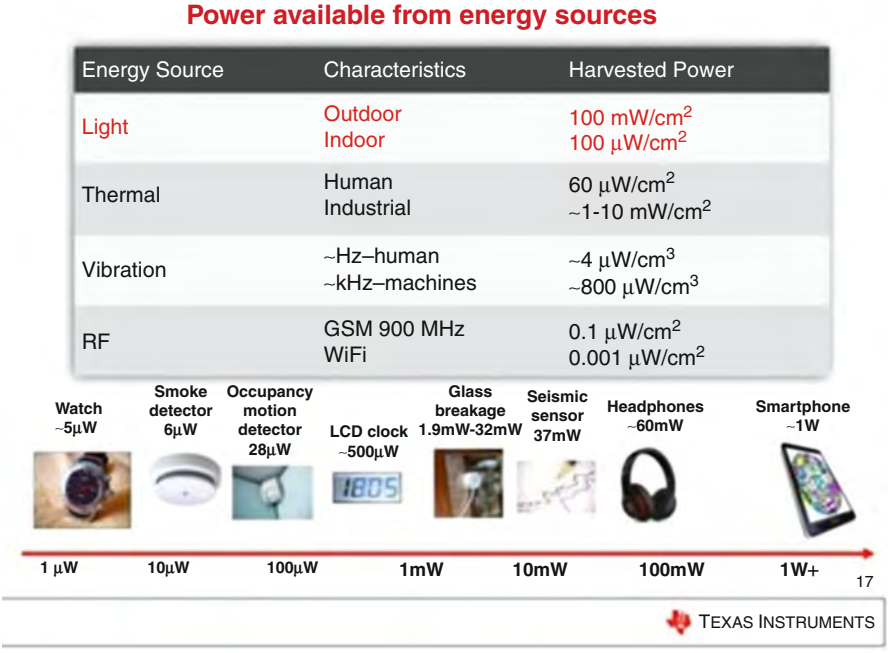

Fig. 1 Power available from various energy source and power consumption of common [2]

Fig. 2 Energy generated by human body [5]

thousands of tiny sensors can obtain various kinds of information from human and environment. The sensor networks should be wireless and placed everywhere in our mobile world, which must be powered at least for months. However, the major power supplies, batteries based on today's technology, are not sufficient. Hence, energy devices integrated in wearable electronics that harvest energy from ambient environment can provide an alternative power source. For instance, self-powered sensing network is a noticeably possible and attractive solution [3].

Because of the very low power consumed by miniaturized electronic devices, high-impedance sensors, and sensing arrays, it is feasible now to covert a portion of kinetic energy from a person's motion, such as walking, joint movement, muscle contraction, and heel strike, to drive the electronic devices [4]. For instance, a normal person generates substantial kinetic power in everyday activities, 67 W with foot motion and 60 W with arm motion [5]. At present, the flexible piezoelectric materials demonstrate a relatively small conversion efficiency (8–14 %); even so the converted kinetic energy is more than sufficient to drive many wearable systems if the generator devices can deliver the same level of conversion efficiency.

Energy harvesting from various sources such as solar, thermal, and mechanical energy (including vibration, human motion, air flow, etc.) has been increasingly regarded as a sustainable route [1b, 3]. Solar energy exhibits a high harvesting power density and stable power output, but it is limited to outdoor places with sufficient sunshine. On the contrary, mechanical energy from human motion such as muscle stretching or eye blinking, footfalls, and respiration [5], as illustrated in Fig. 2, is especially suitable for wearable electronics.

Recent work in the field of nanomaterials has provided new opportunities and directions in engineering effective materials for energy harvesters [3d, 6]. Much of research on energy harvesting has been based on nanomaterials and nanotechnology. Nanogenerators, nanotechnology-based energy harvesting technology, are attractive

emerging research topics in order to meet the energy requirement for widespread uses of wearable electronics and wireless sensor networks. According to the physical mechanisms of electric charge generation, two effects have been explored, that is, piezoelectric and triboelectric effects, for harvesting mechanical energy. Soft and flexible electric power generators are highly desirable for wearable electronics as they are light, deformable, and comfortable to wearers. The combination of nanotechnology and soft polymer materials aerates a wonderful opportunities for soft and wearable energy harvesters. Focusing on soft and wearable nanogenerators, this review chapter is aimed to provide an overview and review of soft and flexible materials and their resultant devices for harvesting mechanical energy from human movements. Furthermore, the review also attempts to present the principles and discuss influencing parameters identified from the previous published work [3b, c, 7].

Flexible and Soft Piezoelectric Energy Harvesting Devices

To utilize the direct piezoelectric effect, three major types of piezoelectric nanomaterials have been investigated: (1) nanoscale semiconductor piezoelectric materials, including Zinc oxide [8–14], cadmium sulfide, zinc sulfide (ZnS), gallium nitride (GaN) [15], and indium nitride [16]; (2) perovskite structured piezoelectric nanosized materials, such as lead zirconate titanate (PZT) [17], potassium niobate [18], sodium niobate [19], and barium titanate; [20] and (3) piezoelectric polymers, e.g., polyvinylidene fluoride (PVDF) [21]. Polymer composites or nanoscale thin films of such materials are normally employed to achieve softness and flexibility of the piezoelectric nanogenerators (PENGs). The fundamental principle of PENGs made from all the three types of materials is the same except that in semiconducting piezoelectric materials, the coupling of piezoelectric and semiconducting properties occurs [4]. In order to capitalize and transfer the mechanical energy to electric energy, semiconductor type of piezoelectric materials should possess a well-defined polar axis and crystal orientation, and the types of piezoelectric ceramics and polymers should have poling directions [22].

Softness and flexibility of wearable devices are comfortable thus much attractive. Reported by Shenck et al., piezoelectric generators utilizing PZT and PVDF films [23] were inflexible and difficult to be integrated in shoes as a wearable device. Furthermore, human motion normally involves mechanical actions at low frequency. Hence, an electric generator should harvest the mechanical energy at frequencies lower than 10 Hz [22]. At a low-frequency motion, the energy stored E_c can be expressed as follows [24]:

$$E_c = d_{ijk}\sigma_{jk} + \mu_{ijkl}\frac{\partial \varepsilon_{jk}}{\partial \chi_l}(i,j,k,l = 1,2,3)$$

The first term on the right-hand side refers to the piezoelectric effect, where σ_{jk} is the stress tensor and d_{ijk} the piezoelectric coefficient tensor, respectively. The second term on the right-hand side refers to the flexoelectric effect, i.e., the strain gradient ($\partial \varepsilon_{jk}/\partial \chi_l$) induced polarization and μ_{ijkl} is the flexoelectric coefficient

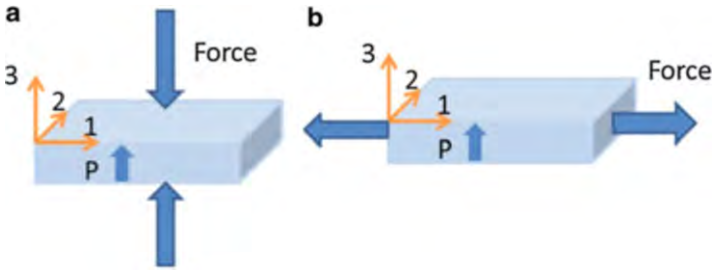

Fig. 3 (**a**) d_{33} mode and (**b**) d_{31} mode of piezoelectric nanogenerator

tensor. In many cases, the flexoelectric effect is small and thus can be ignored. However, in a flexible device, apart from piezoelectric materials, equal attention should be placed upon structural design of the wearable generators in which the significant flexoelectric effect can be utilized or eliminated [24, 25].

Two modes are commonly used for PENGs: d_{33} mode and d_{31} as shown in Fig. 3. The polar axis is defined as "3" direction. When a strain is applied in the direction of polar axis, it is d_{33} mode, and when the strain is applied in the vertical direction of polar axis, defined in "1" axis, it is d_{31} mode. When a strain is applied to a piezoelectric material, an electric potential occurs and electric charges are generated leading to a voltage between the electrodes. Hence the performance of electric generators depends on not only piezoelectric properties of the material, but also the applied strain and configuration mode.

The efficiency of the electric energy generated from the harvester comprises three components: (1) the intrinsic efficiency from the stressed piezoelectric materials; (2) the efficiency of the devices in collecting all the charges, which is related to the electrodes and conducting network within the piezoelectric materials; and (3) the efficiency of the device to output the energy, which is determined by the harvesting circuit. This article will concentrate on the first two aspects.

PENGs Based on Semiconducting Piezoelectric Materials

This group of piezoelectric materials is semiconducting and includes nanowires of zero- and one-dimensional nanosized inorganic materials like zinc oxide (ZnO) [8–14], GaN [15], and InN [16]. Nanosized ZnO has both semiconducting and piezoelectric properties, is easily synthesized and biocompatible [5], and thus is suitable for flexible PENGs. Most desirably, ZnO can convert mechanical energy to electric energy without poling due to its crystal structure. Large aspect ratio of one-dimensional nanostructures of ZnO also contributes to electric power generation. Much work has been devoted to study its physical and chemical properties [3b, c, 7]. Though single ZnO nanowires can convert mechanical energy [17] and serve as self-powered sensors, the low-power output is insufficient for many wearable electronic devices. To overcome this difficulty, various PENG structures were

investigated experimentally by using large arrays of ZnO nanorods or nanowires growing vertically on various substrates and with various electrodes [8].

References [9, 10] show PENGs made from vertical arrays of ZnO nanorods [9] and nanowires [10]. When a ZnO nanowire or nanorod deforms under an applied strain or stress caused by external force or vibration, an electric potential will occur and a voltage will appear between the bottom and top electrodes.

The measured current density of the PENG in Ref. [9] is 1 $\mu A/cm^2$, and power density of the piezoelectric nanogenerator in Ref. [10] is 10 mW/cm^2. The power output is too low to be used for realistic applications. Based on the understanding of the mechanism of potential generation, fine control of charge transfer has been adopted to enhance the electric performance of this type of generators. There is Schottky contact in the interface of ZnO and electrode [7a, b]. Another important factor is the appropriate density of free carriers. Since the electrode is directly placed on the surface of ZnO nanowires array, accordingly, a large density of free carriers will reduce the power output of the nanogenerator [7b]. A thin insulator layer of PMMA is utilized to reduce the Schottky contact and prevent the current leakage through the internal structure [7c, 11]. In Ref. [7c], a position-controlled vertical ZnO nanowire-based flexible PENG with its fabrication process was proposed. The Schottky contact was eliminated by spin-coating a thin layer of PMMA to cover the top of nanowire array. The nanowires were synthesized on the exposed seed surface by wet mechanical method. The electric performance is much improved with a maximum open-circuit voltage of 58 V and short-circuit current output of 134 μA, respectively. The maximum power density reaches 0.78 W/cm^3. Some other methods such as doping Li into ZnO to modify the density of free carriers [7d], pre-treatment of the ZnO nanowire array with oxygen plasma, and annealing in air [7c] can also achieve a better performance. Flexibilities are considered as an evaluation factor in the design of nanogenerator. Hence, a range of flexible substrates (polymer film [10, 12], paper [13], copper [8b], and textiles [8a, c]) have been studied to grow semiconductor piezoelectric nanowires, for example, p-type ZnO, GaN, and InN.

Flexible PENGs Made from Piezoelectric Ceramic Composites

The performance of PENGs depends on not only the piezoelectric coefficient but also the electromechanical coupling factor. Though semiconducting piezoelectric materials may vary in various nanostructures, their piezoelectric coefficient is low (approximately 20 pc/N). Piezoelectric ceramics with high piezoelectric coefficients (d_{33}, up to 600 pc/N) have been developed for decades. PZT is the most popular commercial material for many applications. In recent years, more and more lead-free piezoelectric ceramics have come into applications. Traditional piezoelectric ceramic material is rigid and brittle, hardly used as mechanical energy harvesting materials in wearable electronics. In order to overcome this limitation, nanostructured ceramic materials have been used in polymer composites. Alternatively, nanofibers of such ceramic materials were explored. Flexible PENGs were fabricated based on PZT

nanofibers on a flexible substrate or packaged with flexible polymers, such as polydimethylsiloxane (PDMS). In Ref. [17a], PZT nanofibers are deposited on pre-prepared interdigitized electrodes, which have arrays of fine platinum wires of diameter of 50 μm assembled on a silicon substrate. Then they are polarized by 4 V/μm electric field at a temperature of above 140 °C for about 24 h. The diameters of PZT nanofibers is around 60 nm and made from electrospinning using modified polyvinylpyrrolidone (PVP) sol–gel solution and annealed at 650 °C for about 25 min. The device was packaged by PDMS as the protecting layer. The fabrication process of flexible PENG in Ref. [26] is similar, and the PZT nanofibers are deposited on a textile substrate by electrospinning method and the diameters of PZT nanofibers about 370 nm after annealing. The nanofibers are polarized with a 4 kV/mm electric field at 130 °C for 15 min. The power output is not very high, and the maximum voltage output in Ref. [17a] is only 1.63 V, while the voltage and current output of the nanogenerators in Ref. [26] are only 6 V and 45 nA.

The fatigue life of such generators is short. Thus, soft polymeric composites containing ceramic nanomaterials have been explored to enhance fatigue resistance of such devices. As illustrated in Ref. [19], $NaNbO_3$ nanowires of <200 nm diameter are synthesized by hydrothermal method and dispersed in PDMS to form piezoelectric nanocomposite; Au/Cr-coated Kapton films act as top and bottom electrodes. The PENG was polarized under <80 kV/cm of electric field at room temperature. The power output of the first PENG prototype was not as high as the PENGs made from ZnO nanowires: only about 3 V voltage output and 80 nA current output. Nevertheless it represents a new route to design piezoelectric nanocomposites and PENG devices. Later on, the optimized flexible PENG based on vertical electrospun PZT nanowires/PDMS nanocomposite [17d] achieved excellent electric performance. The voltage and current reaches as high as 209 V and about 18 μA, respectively. However, owing to the lead component in PZT, it is not environmentally friendly and safe for human. Because of these issues, inorganic perovskite piezoelectric materials attract more and more attention in recent researches. Different nanostructures of lead-free piezoelectric ceramics, such as $KNbO_3$ nanorod [18], $BaTiO_3$ nanotube [20b], and nanowire [20c], have been investigated in order to obtain better performance of flexible PENGs.

Flexible PENGs Made from Polymeric Piezoelectric Materials

The third group of important piezoelectric materials is piezoelectric polymers, for instance, PVDF and its copolymers. The polymeric piezoelectric materials are naturally flexible, biocompatible, and lightweight [5]. Many piezoelectric devices have been developed based on PVDF film and nanofibers. PVDF nanofibers are normally electrospun by either near-field or far-field methods. The piezoelectric properties of PVDF depend on its phase state, as the piezoelectricity of PVDF comes from the β-phase crystalline structure which can convert mechanical energy to electric energy. Chang et al. utilized a direct-write technique to produce a PENG using near-field electrospinning polarized via in situ mechanical stretching

and high electrical field [21c]. Generally, both mechanical stretching and high electrical field are required to promote the formation of the β-phase [21c]. However, in some recent experiments, PVDF nanofibers without mechanical stretching or polarization under very high electrical field exhibit β-phase crystalline structure, which is achieved by other methods such as doping $NaNbO_3$ nanowires and electrospinning [21g].

Enhancement in Charge Collection and Transfer

Unlike PENGs from semiconductor ZnO nanowires, PDMS- and PVDF-based ones are insulating. Thus, free carriers are too few to transport the generated charges. Hence, the current output is low, only several μAs at maximum. In order to break this limitation, conductive materials were doped to improve charge transfer and thus power output. Multi-walled carbon nanotube (MW-CNT) has been considered as low-cost conductor which can enhance the conductivity of nanocomposites. Experiments were reported on the optimized concentration of carbon nanotube [32, 33] and piezoelectric nanocomposites [21g, 27] in PVDF. The schematic diagram of the fabrication process of flexible piezoelectric nanocomposites with multi-walled carbon nanotubes as an enhancer of charge transport is shown in Ref. [28]. $BaTiO_3$ and PZT particles serve as piezoelectric materials and energy generation source. After dispersing MW-CNTs and piezoelectric materials in PDMS matrix, the nanocomposites were spin-coated on 6-in. silicon (Si) wafer and then transferred to an indium tin oxide (ITO)-coated polyethylene terephthalate (PET) flexible substrates. The resultant PENGs were polarized at 140 °C by applying an electric field from 0.5 to 2 kV for 12 h. The doping MW-CNTs have led to significant improvement in performance: the 3 × 3 cm PENG from PZT particles can generate about 10 V and 1.3 μA, respectively, during regular mechanical bending and unbending cycles. Furthermore, a large-area PENG device (30 × 30 cm) fabricated by bar coating can generate about 100 V voltage and about 10 μA current and drive 12 LED arrays directly without external circuits.

Most of the reported PENGs have very poor fatigue resistance in cyclic loading, an essential requirement for wearable electronic devices. Even though the above-mentioned piezoelectric materials are flexible and soft, electrodes are made from conventional materials, such as metals or metal oxides, e.g., gold, silver, aluminum, and ITO. Apart from the brittleness, the materials used for electrodes have little compliance to deformation. During deformation, often large deformation in the wearable applications, the interfacial shear stress causes delamination of the sandwich layers because of mismatch of modulus and Poisson's ratio of the electrode and active layers. The devices lost mechanical integrity and electric connectivity and fail quickly in repeated large deformation, thus not suitable for such wearable applications.

In addition to the durability, the conductivity and contact area of electrodes are also crucial factors in the power generation [3, 5]. Two-dimensional flexible conductive materials are ideal candidates for electrodes in PENGs. Among them,

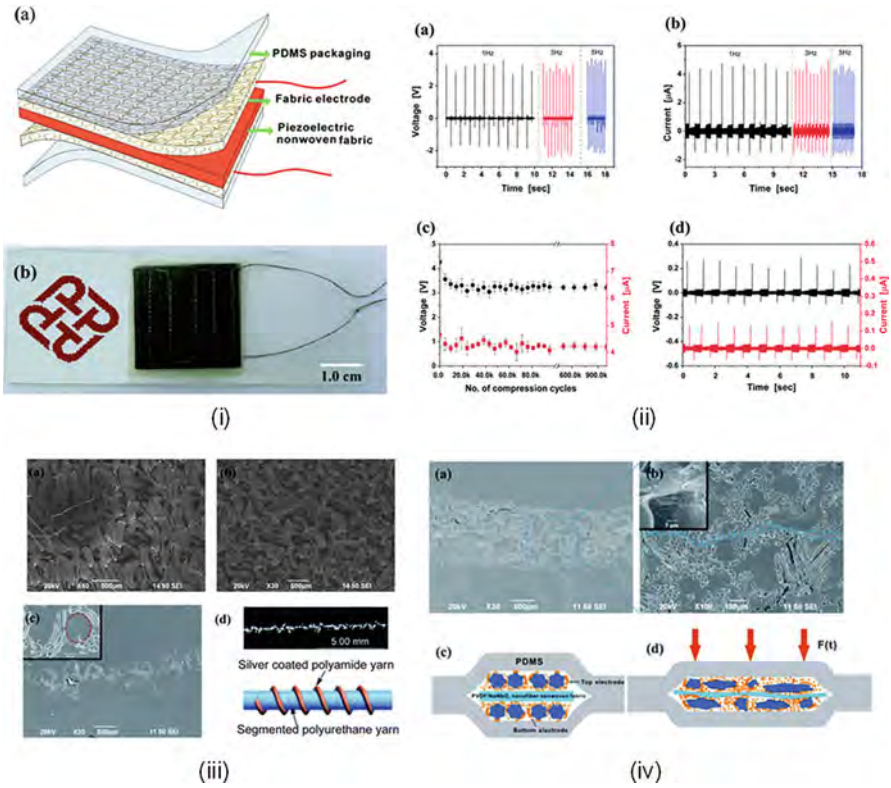

Fig. 4 Highly durable piezoelectric nanogenerator based on PVDF/$NaNbO_3$ nanocomposite and conductive fabric electrodes [21g]

soft and flexible conductive textile fabrics have shown some promises. Textile fabrics knitted from fine metal wires of 50 μm can retain their softness, stretch ability of over 100 %, and super fatigue resistance. The conductivity of conventional textiles, normally insulating, can be drastically increased to the level close to the bulk metals by surface coating via vapor- or solution-based treatments. A number of nanomaterials have been investigated for this purpose, including carbon nanotube [21d], graphene [21e], silver [21f], etc. PENGs with such electrodes are shown in Ref. [29] (graphene) and Fig. 4 (fabrics).

In Ref. [28], a stretchable and transparent PENG using poly(vinylidene fluoride tri-fluoroethylene) P(VDF-TrFE) sandwiched with mobility-modified CVD-grown graphene electrodes is demonstrated. The device was polarized by applying an electric field of 100 MV/m for 30 min between the electrodes. The observed output voltage is about 4 V with a current density of 0.8 $\mu A/cm^2$. A mechanism was proposed that the hole mobility of the graphene sheets will affect the carrier concentration because the dipole charge in P(VDF-TrFE) repel and attract holes in the p-type conducting graphene sheets. Figure 4 illustrates an all-fiber flexible,

soft, and wearable PENG consisting of a PVDF–$NaNbO_3$ nanofiber nonwoven fabric sandwiched structure by elastic conducting knitted fabrics electrodes made from segmented polyurethane and silver coated polyamide multifilament yarns. The fabric electrodes have as dual roles: (1) they work as a normal charge collection network as well as (2) a mechanical element that transfers the uniform compressive pressure on the device into localized deformation in the piezoelectric nanofiber nonwoven fabric. The front side of the fabric serves as contacting side with PVDF and can maximize the contact area of the fabric electrode. The thickness of the free-standing fabric electrodes are less than 1 mm indicated by the SEM in Fig. 4. (iii) and (iv). The loop structures in a plain knitted fabric structure promote a significant reduction of the fiber strain to less than 1 % even if the fabric is stretched over 60 %. Thus, the resistance of fatigue against cyclic deformation can be much enhanced. Remarkably, the all-fiber PENG retains its function after more than 1,000,000 loading cycles. Its open-circuit voltage and short-circuit current are 3.2 V and 4.2 μA, respectively. This flexible, soft, and wearable nanogenerator demonstrates great promise to covert low-frequency mechanical energy such as human walking into electricity.

Summary of PENGs

The materials, structures, and performances of various PENGs with semiconductor and inorganic piezoelectric materials are listed and compared in Table 1.

Since 2006, the accumulation of considerable research efforts has led to a quantum jump in 2012 with respect to the performance of soft and flexible PENGs. The levels for open-circuit voltage have increased from several mV to above 100 V and that for the short-circuit current from several nAs to over 100 μA, respectively. It is certain that the trend will continue, as evidently demonstrated in Fig. 5.

Flexible Triboelectric Energy Harvesting Devices

Fundamentals and Influencing Factors of Triboelectrification

Triboelectric effect, also known as contact electrification or triboelectric charging, is one of the oldest and ubiquitous physical effects in nature which owns far-reaching consequence [34]. It is a contact-induced electrification, and the surfaces will be charged electrically [3b] when two materials get in contact or rub against each other according to the triboelectric series with different relative polarity [92]. Adhesion is first formed due to the bonding between some areas of two contacting surfaces and then charges (electrons or ions or charged material) may transfer from one material to the other. Several kinds of contact electrification occur. The first is metal–metal contact where phenomenon can be clearly described

Table 1 Summary of various PENGs

Material	Open-circuit peak voltage (V)	Short-circuit peak current (μA)	Structure	Power or current density	Mode	References
ZnO	58	134	Nanowire	0.78 W/cm^3	d_{33}	[7c]
GaN	1.2	0.04	Nanowire	0.16 μA/cm^2	d_{33}	[15a]
$KNbO_3$	3.2	0.0675	Nanotube	9.3 nA/cm^2	d_{33}	[18]
$NaNbO_3$	3	0.08	Nanowire	0.6 mW/cm^3	d_{33}	[19]
PZT	1.63	na	Nanofiber	na	d_{33}	[17a]
PZT	209	18	Nanowire	23.5uA/cm^2	d_{33}	[17d]
BaTiO3	5.5	0.35	Nanotube	350 nA/cm^2	d_{33}	[20b]
BaTiO3	0.045	0.00015	Nanowire	6.27uW/cm^3	d_{33}	[20c]
$ZnSO_3$	0.1	0.03	Microbelt	na	d_{33}	[30]
PMN-PT	7.8	2.29	Nanowire	4.58 μA/cm^2	d_{33}	[31]
PVDF	0.03	0.003	Nanofiber	na	d_{31}	[21c]
PVDF	3.2	4.2	Nanofiber	na	d_{31}	[21g]
PVDF/CNT	6	na	Nanofiber	na	d_{31}	[32]
PVDF/CNT	1.35	na	Film	4 W/m^3	d_{33}	[33]
PVDF/Graphene	3	na	Film	0.37 μA/cm^2	d_{33}	[29]
PZT/CNT	100	10	Particle	na	d_{33}	[28b]
BaTiO3/CNT	3.2	0.3	Nanoparticle	na	d_{33}	[28a]

by charge. In this case, electrons transfer from the metal with higher Femi level or lower work function to the metal with lower Femi level or higher work function [3b, 35]. The amount of charges transferred is related with the difference between the work functions of the two contacting metals. The second case is insulator–insulator contact where the scientific understanding is very poor, regarding to who are the charge species, how the charges are transferred, etc. The third kind of contact electrification occurs between a metal and an insulator. Again, there are much more issues to be investigated and questioned to be answered. Furthermore, contacts between semiconductors or contacts between metal and semiconductor may shed light on charge transfer of conducting materials. In an excellent review article [35], the detailed discussions on four possible mechanisms behind the contact electrification are given for insulators. Table 2 gives the charge affinity and work functions of some commonly investigated materials for triboelectrification [36]. Less conductive materials or insulators exhibit stronger triboelectrific effect and can capture the transferred charges and retain them for an

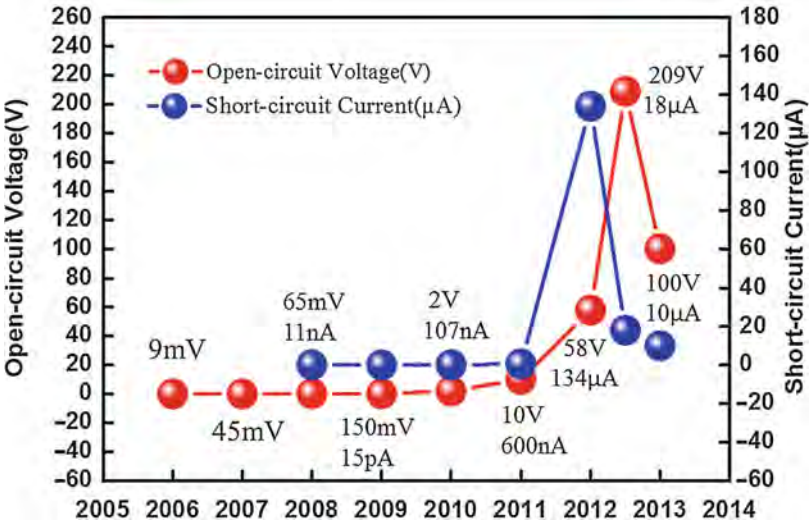

Fig. 5 A summary on the development of piezoelectric nanogenerators since 2006

Table 2 Triboelectricity and work function [36] of commonly used materials

Material name	Charge affinity (nC/J)	Metal effect	Work function(eV)
Hair, oily skin	+45	+N	na
Nylon, dry skin	+30	+N	na
PET	−40	+W	na
Silicones	−72	−N	na
Teflon	−190	−N	na
Aluminum	na	na	4.06–4.26
Copper	na	na	4.53–5.10
Gold	na	na	5.1–5.47

extended period of time, which are usually considered to be a negative effect such as in semiconductor manufacture process because it may cause static damage and reduce the yield.

Very recently, the contact electrification has been demonstrated as a promising way for harvesting mechanical energy from movement. The triboelectric nanogenerators (TENGs) are affordable, low cost, and easily fabricated with high power outputs. Their operating principle can be illustrated in an example given in Ref. [34].

In Ref. [34], when the surfaces of two materials with strong triboelectric effect, or large difference in the charge affinity, contact or rub with each other with an externally applied force, charges will transfer from one material to the other. They will be kept in the surface. While the external applied force is removed, the TENG starts to release and the two surfaces begin to separate to their original positions due

to the structure and substrate design. Once the two materials separate, an electric potential is then established in the two electrodes. The contact electrification is a non-equilibrium phenomenon, and these two separated surfaces should be neutral at equilibrium after contacting each other. However, the rate of charge transfer between the surfaces is negligible, allowing the non-equilibrium situation of charged surfaces to persist after the surfaces are separated and voltage to appear between the electrodes [34].

Though the triboelectric effect has been discovered for more than 2,500 years, the phenomenon of contact electrification remains elusive and the critical influencing factors and their effects are poorly described. The relative position of the two contacting materials in the triboelectric series [29, 36b], which is a list of materials depicting the tendency to gain or lose charges, plays the important role in the TENG design to enhance power output. It is well known that friction can enhance contact electrification, but the mechanisms of how the rubbing action increases charge generation or transfer are not clear, not to mention that even the list itself has different sequences, depending on the experimental conditions. Some researchers suggested that the rate of rubbing and roughness of surfaces should contribute to charge generation and transfer significantly. Some workers examined the effects of surface resistivity, pressure, humidity, surface properties of two materials [37], contact area and contact mode, as well as applied compression force. However, the studies were scattered not in a systematic manner, thus leading to inconsistent observations.

Flexible and Soft TENGs

In this section, various approaches for soft and flexible TENGs will be reviewed. The materials used, structural design, and performance of these TENGs will be described in both the contact and sliding mode. Benchmark analysis will be given. As described in last section, there are many types of contact electrification according to the conductive nature of the two interacting surfaces, that is, metal–metal, metal–semiconductor, metal–insulator, semiconductor–insulator, and insulator–insulator. Much work of reported soft and flexible TENGs has been focused on two types: insulator–insulator and metal–insulator nanogenerators.

TENG first reported by Wang's group in 2012 [34, 38] has a sandwich structure with two stacking insulator polymer sheets and two metal electrodes deposited on the top and bottom surface of the stacking sheets as demonstrated in Ref. [34]. Rectangular Kapton film (4.5 $\times$ 1.2 cm, 125 μm in thickness) and flexible PET film (220 μm in thickness) were utilized as the contact electrification materials to harvest energy caused by the friction between the surfaces with nanoscale roughness. The two edges of the nanogenerator are linked together by an adhesive tape to keep them in contact while applying external force. When the device is deformed by bending, a triboelectric potential is formed to attract electrons from external source leading to a voltage between the two electrodes. The electric power output was measured and is shown in Ref. [38]. The flexible TENG can generate 3.3 V

open-circuit voltage and 0.6 μA short-circuit current. The power density is 10.4 mW/cm^3 when the voltage is 3.3 V. PVC film and Kapton film were investigated. Low voltage and current output were observed owing to the relatively smaller charge affinity difference between the two materials in the triboelectric series [39].

The structure of TENG is simple; thus it is of low cost with readily scalable fabrication process. However, its power output is low. In order to increase the power output performance, materials with the largest difference in the charge affinity were used [36, 39b], modification of surface morphology was made, and a new device structure was adopted with a high separation and contacting rate were explored in an improved TENG from metal–insulator contact electrification. In Ref. [38], the arc-shaped structure with a steady gap between the plates at strain-free state, micro-patterned PDMS polymer, and fabrication process was proposed. In this device, flat Kapton film deposited with a 500 nm layer of SiO_2 film using plasma-enhanced chemical vapor deposition (PECVD) method served as a spacer. In the triboelectric series, PDMS and Al are almost at the two ends with a very large difference in the ability to attract and retain electrons. In the compression mode, to increase the friction area of the interaction surfaces, pyramid micro-pattern PDMS and cube micro-pattern Al layer were fabricated using a typical photolithography process and sealed together with a thin PDMS layer. The Al film is forced to bend and serves as one electrode, and the Kapton film is also bent in the opposite direction to form the arc-shaped structure. In the experimental demonstration, the arc-shaped TENG was able to generate 230 V open-circuit voltage and the peak 94 μA of the short-circuit current under 6 Hz repeated tests without noticeable performance degradation. From 2 to 10 Hz, the open-circuit voltage output is almost the same at different frequencies, while the short-circuit current increases from 35 μA at 2 Hz to 130 μA at 10 Hz due to the higher flow rate of charges. The area and volume power density of this flexible triboelectric device are 3.56 mW/cm^2 and 128 mW/cm^3, respectively.

In a later reported work [40], the same pyramid micro-pattern PDMS layer was used with a flat Al electrode film between the two arched PDMS layer. The power output of an arc-shaped-based triboelectric device which has two generators was enhanced. When an external periodic compressive force was applied on the devices, the Al and PDMS layers will rub twice in one cycle due to the sandwich-arc-shaped structure. In comparison with the nanogenerator in Ref. [40], the open-circuit voltage increases from 120 to 320 V due to external electrons flow in a shorter time as the frequency of external force increased from 1 to 5 Hz. The open-circuit voltage remains constant, while the frequency increases from 5 to 7 Hz. However, the open-circuit voltage decreases to 218 V at 10 Hz because the time was too short for the nanogenerator to recover to the original position before the next force impact. Connecting the two nanogenerators in series, the output is doubled with the highest peak voltage of 465 V, current of 107.5 μA, and power density of 53.4 mW/cm^3 mainly due to the double-layer structure and pyramid surface micro-pattern.

Triboelectric effect depends not only on the bulk materials, but also the upmost layer of the contact surface [35, 41]. A nanoparticle-enhanced TENG [41b] with surface modification and much simplified structure reaches the best performance about 1,200 V and 2 mA, respectively. It is composed of two flexible PMMA substrates, thin PDMS film, and gold electrodes. In the top substrate, gold is deposited on the surface of PMMA and coated with a thin PDMS film. In the lower PMMA substrate, the gold electrode is coated with gold nanoparticles to form a top layer on the surface (SEM image). This treatment has increased the contact area and surface charge density of the device, respectively. The open-circuit voltage of the TENG reaches a peak value of 200 V. The short-circuit current is from 160 to 175 μA at a small normal force of 10 N. It has demonstrated that the electric output is strongly related to the contacting force. When the normal force increases to 500 N such as when the device is triggered by footfall force which is about 500–600 N, the power output of the nanoparticle-enhanced TENG can drive and light up 600 commercial LEDs in real time with the estimated voltage about 1,200 V, and the maximum short-circuit current is about 2 mA, producing a power density of 313 W/m^2 with a conversion efficiency of 9.8 % conversion efficiency.

An interesting open setup of TENG is proposed in Ref. [42]. There are only three parts: an electrode, pyramid micro-pattern PDMS layer, and a reference copper electrode, which is earthed and separated physically from the connecting electrode and PDMS film. Some objects such as a finger or glove can act as the second friction surface in the friction pair. The device has a PET substrate (thickness: 125 μm) coated with a transparent ITO on the bottom as an electrode and a PDMS film with micro-patterned pyramids structure as one of the rubbing surface (SEM image). A 100 μm-thick grounded copper foil serves as the reference electrode surrounding the device. When a mobile object is in contact with the PDMS surface, either tapping or sliding, there will be charges on the surface of PDMS and voltage between the electrodes. The maximizing open-circuit voltage and short-circuit current are caused by tapping with a finger covered in a PE glove on the micro-patterned PDMS layer, about 250 V and 6 μA.

Apart from the compression mode, sliding mode of TENG is another important approach. As demonstrated in Ref. [43], two surfaces are fully coincided at original position with one sitting freely on the other. While applying a tangential force, there will be relative displacement in contact mode in lateral direction. Similar to contact mode triboelectric effect, there will be transferred charges in the surfaces, and after the two surfaces are fully separated, the charges and potential will disappear. Sliding-mode TENGs are normally less flexible due to relative sliding. As the required displacement of sliding-mode TENG is large to harvest sufficient energy, the applications in wearable electronic are perhaps limited for most cases.

According to the triboelectric series [39], PTFE owns remarkable ability to attract electrons and is much more triboelectrically negative during the contact with other materials. As demonstrated in Ref. [44], when sliding occurs between the

PTFE and Al, electrons will inject from Al to PTFE. The TENG has a simple structure that is easily fabricated. The single-electrode sliding-mode-based triboelectric nanogenerator has only two parts (Al and PTFE film). Its open-circuit voltage can reach to 1,100 V with a peak Isc of 6 mA/m^2 and drive 100 green LEDs directly. When the sliding displacement increases to 26 mm, the voltage on the PTFE surface can be up to 6,000 V. The maximum output power density reaches 350 mW/m^2 with a 100 MΩ resistance load. Linear-grating TENG can harvest more mechanical energy due to the unique structure. At a sliding velocity of 10 m/s, the TENG (6.4 × 3.8 cm) with 10 grating units is equivalent to a continuous current source of 0.44 mA (corresponding current density of 0.18 A/m^2) at an open-circuit voltage of 615 V.

Summary of TENGs

Working in either compression or sliding modes, various TENGs were developed and investigated in less than 2 years, including segmentally structured disk TENG [45], r-shaped hybrid TENG [46] combining triboelectric and piezoelectric effect, and TENGs integrated into clothes [47] and shoes [48]: serving as power source or self-powered sensors [49]. The materials, structures, and performances of these reported TENGs are summarized in Table 3.

Despite just over 1 year since the first TENG was reported, the progress has been remarkable with TENG's area power density jumping from 3.67 mW/m^2 to 313 W/m^2, as shown in Fig. 6, almost five orders of magnitude. The scalability of TENGs is very good because of their simple structure and robustness of the material systems. It is the hope of the authors that fundamental understanding

Table 3 Materials, structures, and performance of flexible TENGs

Material pairs	Open-circuit voltage(V)	Short-circuit current(uA)	Device structure	Power or current density	Operation mode	References
Kapton/PET	3	0.6	Flat	4 mW/cm^3	Compression	[35]
PDMS/Al	230	94	Pyramid patterned	128 mW/cm^3	Compression	[38]
PDMS/Al	465	107.5	Pyramid patterned	53.4 mW/cm^3	Compression	[40]
PDMS/Au	~1,200	1,200	Flat	313 W/m^2	Compression	[41a]
PDMS	250	6	Pyramid patterned	1uA/cm^2	Compression	[42]
PTFE/Al	615	440	Flat	50 mW/m^2	Sliding	[43]

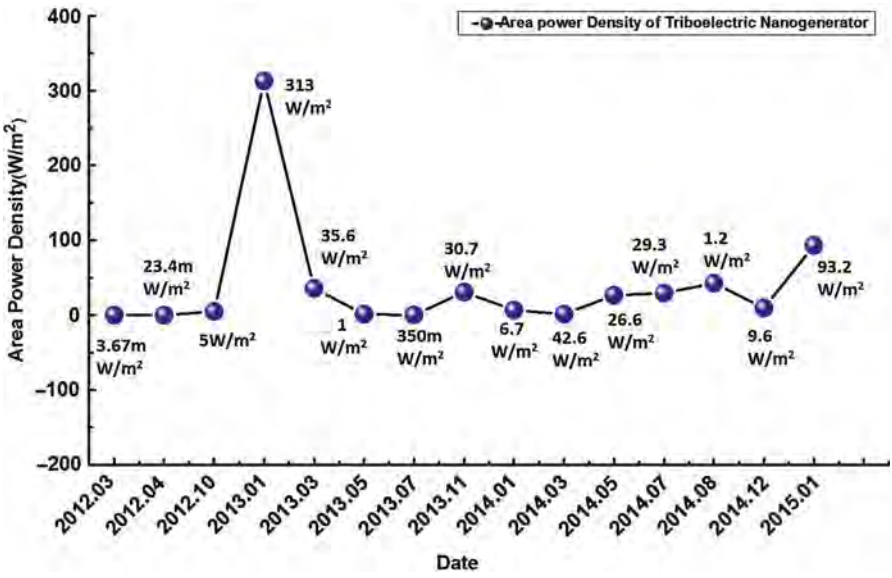

Fig. 6 A summary on the power density of various triboelectric nanogenerators

of the triboelectric phenomenon will shed new light on the material synthesis and structural design of wearable TENGs. The future of TENGs certainly looks very bright.

Conclusion

Starting from the fundamental concept to prototypes, this article has reviewed various approaches reported in the literature for harvesting mechanical energy based on piezoelectric and triboelectric effects, respectively. The operating principles, materials selection and synthesis, device structures, fabrication methods, and performance of soft and flexible piezoelectric and triboelectric nanogenerators (PENGs and TENGs) have been covered. Benchmark analysis has been carried out for both PENGs and TENGs. The prototypes and their power generating performance demonstrated so far have shown great promises for wearable applications in the not-so-distant future. The soft and flexible nanogenerator technology may soon impact our lives and supply power to wearable electronics. Various applications of using the technology for powering various wearable or portable electronics have also been demonstrated in this review. Towards this end, critical issues and great challenges of soft and flexible TENGs and PENGs are also discussed.

References

1. [a] Paradiso JA, Starner T (2005) Energy scavenging for mobile and wireless electronics. Pervasive Computing, IEEE, 4(1):18. [b] Mitcheson PD, Yeatman EM, Rao GK, Green TC (2008) Energy harvesting from human and machine motion for wireless electronic devices. Proc IEEE 96(9):1457. [c] Arunachalam VS, Fleischer EL (2008) The global energy landscape and materials innovation. MRS Bull 33:264
2. http://faster.sprint.com/2013/11/22/energy-harvesting-chips-the-next-big-thing-for-a-connected-world/
3. [a] Kumar B, Kim SW (2011) Recent advances in power generation through piezoelectric nanogenerators. J Mater Chem 21:18946. [b] Wang X (2012) Piezoelectric nanogenerators – harvesting ambient mechanical energy at the nanometer scale. Nano Energy 1:13. [c] Wang ZL (2013) Triboelectric nanogenerators as new energy technology for self-powered systems and as active mechanical and chemical sensors. ACS Nano 7(11):9533. [d] Xu S, Hansen BJ, Wang ZL (2010) Piezoelectric-nanowire-enabled power source for driving wireless microelectronics. Nat Commun 1:93
4. [a] Espinosa HD, Bernal RA, Jolandan MM (2012) Adv Mater 24:4656. [b] Wang ZL, Zhu G, Yang Y, Wang S, Pan C (2012) Mater Today 15:532
5. Qi Y, McAlpine MC (2010) Nanotechnology-enabled flexible and biocompatible energy harvesting. Energy Environ Sci 3:1275
6. [a] Jiang X, Huang W, Zhang S (2013) Flexoelectric nano-generator: Materials, structures and devices. Nano Energy 2:1079–1092. [b] Bowen CR, Kim HA, Weaver PM, Dunn S (2014) Piezoelectric and ferroelectric materials and structures for energy harvesting applications. Energy Environ Sci 7:25
7. [a] Liu J, Fei P, Zhou J, Tummala R, Wang ZL (2008) Toward high output-power nanogenerator. Appl Phys Lett 92:173105. [b] Liu J, Fei P, Song J, Wang X, Lao C, Tummala R, Wang ZL (2008) Carrier density and Schottky barrier on the performance of DC nanogenerator. Nano Lett 8:328. [c] Zhu G, Wang AC, Liu Y, Zhou Y, Wang ZL (2012) Functional electrical stimulation by nanogenerator with 58 V output voltage. Nano Lett 12:3086. [d] Sohn JI, Cha SN, Song BG, Lee S, Kim SM, Ku J, Kim HJ, Park YJ, Choi BL, Wang ZL, Kim JM. Kim K (2013) Engineering of efficiency limiting free carriers and an interfacial energy barrier for an enhancing piezoelectric generation. Energy Environ Sci 6:97. [e] Gao YF, Wang ZL (2009) Equilibrium potential of free charge carriers in a bent piezoelectric semiconductive nanowire. Nano Lett 9(3):1103
8. [a] Khan A, Abbasi MA, Hussain M, Ibupoto ZH, Wissting J, Nur O, Willander M (2012) Piezoelectric nanogenerator based on zinc oxide nanorods grown on textile cotton fabric. Appl Phys Lett 101:193506. [b] Sheikh N, Afzulpurkar N, Ashraf MW (2013) Robust nanogenerator based on vertically aligned ZnO nanorods using copper substrate. J Nanomater 2013:1. [c] Kim H, Kim SM, Son H, Park B, Ku J, Sohn JI, Im K, Jang JE, Park JJ, Kim O, Cha S, Park YJ (2012) Enhancement of piezoelectricity via electrostatic effects on a textile platform. Energy Environ Sci 5:8932
9. Wang ZL, Song JH (2006) Piezoelectric nanogenerators based on zinc oxide nanowire arrays. Science 312:242
10. Wang X, Song J, Liu J, Wang ZL (2007) Direct-current nanogenerator driven by ultrasonic waves. Science 316:102–105
11. Hu Y, Lin L, Zhang Y, Wang ZL (2012) Replacing a battery by a nanogenerator with 20 V output. Adv Mater 24:110
12. Choi MY, Choi D, Jin MJ, Kim I, Kim SH, Choi JY, Lee SY, Kim JM, Kim SW (2009) Mechanically powered transparent flexible charge-generating nanodevices with piezoelectric ZnO nanorods. Adv Mater 21:2185
13. Kim KH, Lee KY, Seo JS, Kumar B, Kim SW (2011) Paper-based piezoelectric nanogenerators with high thermal stability. Small 7:2577

14. [a] Gao PX, Song J, Liu J, Wang ZL (2007) Nanowire piezoelectric nanogenerators on plastic substrates as flexible power sources for nanodevices. Adv Mater 19:67. [b] Xu S, Qing Y, Xu C, Wei YG, Yang R, Wang ZL (2010) Self-powered nanowire devices. Nat Nanotechnol 5:366. [c] Lu MP, Song JH, Lu MY, Chen MT, Gao YF, Chen LJ, Wang ZL (2009) Piezoelectric nanogenerator using p-type ZnO nanowire arrays. Nano Lett 9(3):1223. [d] Yang R, Qing Y, Li C, Zhu G, Wang ZL (2009) Converting biomechanical energy into electricity by a muscle-movement-driven nanogenerator. Nano Lett 9(3):1201. [e] Xi Y, Song J, Xu S, Yang R, Gao Z, Hu C, Wang ZL (2009) Growth Of ZnO nanotube arrays and nanotube based piezoelectric nanogenerator. J Mater Chem 19:9260. [f] Liu Y, Hansen BJ, Yang R, Wang ZL (2010) Hybrid nanogenerator for concurrently harvesting biomechanical and biochemical energy. ACS Nano 4(7):3647. [g] Cha SN, Seo JS, Kim SM, Kim HJ, Park YJ, Kim SW, Kim JM (2010) Sound-driven piezoelectric nanowire-based nanogenerators. Adv Mater 22:4726. [h] Zhu G, Yang R, Wang S, Wang ZL (2010) Flexible high-output nanogenerator based on lateral ZnO nanowire array. Nano Lett 10:3151. [i] Li Z, Zhu G, Yang R, Wang AC, Wang ZL (2010) Muscle-driven in vivo nanogenerator. Adv Mater 22:2534. [j] Riaz M, Song J, Nur O, Wang ZL, Willander M (2011) Study of the piezoelectric power generation of ZnO nanowire arrays grown by different methods. Adv Funct Mater 21:628. [k] Voon LCLY, Willatzen M (2011) Electromechanical phenomena in semiconductor nanostructures. J Appl Phys 109:031101. [l] Qiu Y, Zhang H, Hu L, Yang D, Wang L, Wang B, Ji J, Liu G, Liu X, Lin J, Li F, Han S (2012) Flexible piezoelectric nanogenerators based on ZnO nanorods grown on common paper substrates. Nanoscale 4:6568. [m] Hsu CL, Chen KC (2012) Improving piezoelectric nanogenerator comprises ZnO nanowires by bending the flexible PET substrate at low vibration frequency. J Phys Chem C 116:9351. [n] Kumar B, Kim SW (2012) Energy harvesting based on semiconducting piezoelectric ZnO nanostructures. Nano Energy 1:342. [o] Lee M, Chen CY, Wang S, Cha SN, Park YJ, Kim JM, Chou LJ, Wang ZL (2012) A hybrid piezoelectric structure for wearable nanogenerators. Adv Mater 24:1759. [p] Lee S, Lee J, Ko W, Cha S, Sohn J, Kim J, Park JG, Parkd YJ, Hong JP (2013) Solution-processed Ag-doped ZnO nanowires grown on flexible polyester for nanogenerator applications. Nanoscale 5:9609. [q] Saravanakumar B, Mohan R, Thiyagarajan K, Kim SJ (2013) Fabrication of a ZnO nanogenerator for eco-friendly biomechanical energy harvesting. RSC Adv 3:16646. [r] Kim K, Sirbuly DJ (2012) Enhanced output of nanostructured piezoelectric arrays via controlled matrix/transducer interfacial interactions. Appl Phys Lett 101:213114
15. [a] Lin L, Lai CH, Hu Y, Zhang Y, Wang X, Xu C, Snyder RL, Chen LJ, Wang ZL (2011) High output nanogenerator based on assembly of GaN nanowires. Nanotechnology 22:475401. [b] Chen CY, Zhu G, Hu YF, Yu JW, Song JH, Cheng KY, Peng LH, Chou LJ, Wang ZL (2012) Gallium nitride nanowire based nanogenerators and light-emitting diodes. ACS Nano 6(6):5687
16. Ku NJ, Wang CH, Huang JH, Fang HC, Huang PC, Liu CP (2013) Energy harvesting from the obliquely aligned InN nanowire array with a surface electron-accumulation layer. Adv Mater 25:861
17. [a] Chen X, Xu S, Yao N, Shi Y (2010) 1.6 V nanogenerator for mechanical energy harvesting using PZT nanofibers. Nano Lett 10:2133. [b] Chen CY, Liu TH, Zhou Y, Zhang Y, Chueh YL, Chu YH, He JH, Wang ZL (2012) Electricity generation based on vertically aligned PbZr0.2Ti0.8O3 nanowire arrays. Nano Energy 1:424. [c] Qi Y, Kim J, Nguyen TD, Lisko B, Purohit PK, McAlpine MC (2011) Enhanced piezoelectricity and stretchability in energy harvesting devices fabricated from buckled PZT ribbons. Nano Letters 11:1331. [d] Gu L, Cui N, Cheng L, Xu Q, Bai S, Yuan M, Wu W, Liu J, Zhao Y, Ma F, Qin Y, Wang ZL (2013) Flexible fiber nanogenerator with 209 V output voltage directly powers a light-emitting diode. Nano Lett 13:91
18. Jung JH, Chen CY, Yun BK, Lee N, Zhou Y, Jo W, Chou LJ, Wang ZL (2012) Lead-free $KNbO_3$ ferroelectric nanorod based flexible nanogenerators and capacitors. Nanotechnology 23:375401

19. Jung JH, Lee M, Hong J, Ding Y, Chen CY, Chou LJ, Wang ZL (2011) Lead-free $NaNbO_3$ nanowires for a high output piezoelectric nanogenerator. ACS Nano 5(12):10041
20. [a] Park KI, Xu S, Liu Y, Hwang GT, Kang SJ, Wang ZL, Lee KJ (2010) Piezoelectric BaTiO(3) thin film nanogenerator on plastic substrates. Nano Lett 10(12):4939. [b] Lin ZH, Yang Y, Wu JM, Liu Y, Zhang F, Wang ZL (2012) $BaTiO_3$ nanotubes-based flexible and transparent nanogenerators. J Phys Chem Lett 3:3599. [c] Koka A, Zhou Z, Sodano HA (2014) Vertically aligned $BaTiO_3$ nanowire arrays for energy harvesting. Energy Environ Sci 7:288
21. [a] Sun C, Shi J, Wang X (2010) Fundamental study of mechanical energy harvesting using piezoelectric nanostructures. J Appl Phy 108:034309. [b] Hansen BJ, Liu Y, Yang R, Wang ZL (2010) Hybrid nanogenerator for concurrently harvesting biomechanical and biochemical energy. ACS Nano 4(7):3647. [c] Chang C, Tran VH, Wang J, Fuh YK, Lin L (2010) Direct-write piezoelectric polymeric nanogenerator with high energy conversion efficiency. Nano Lett 10:726. [d] Shang SM, Zeng W, Tao XM (2011) High stretchable MWNTs/polyurethane conductive nanocomposites. J Mater Chem 21(10):7274. [e] Yang XM, Li LA, Shang SM, Tao XM (2010) Synthesis and characterization of layer–aligned poly(vinyl alcohol)/graphene nanocomposites. Polymer 51(15):3431. [f] Wang RX, Tao XM, Wang Y, Wang GF, Shang SM (2010) Microstructures and electrical conductance of silver nanocrystalline thin films on flexible polymer substrates. Surf Coat Technol 204(8):1206. [g] Zeng W, Tao XM, Chen S, Shang S, Chan HLW, Choy SH (2013) Highly durable all-fiber nanogenerator for mechanical energy harvesting. Energy Environ Sci 6:2631
22. Chang J, Dommer M, Chang C, Lin L (2012) Piezoelectric nanofibers for energy scavenging applications. Nano Energy 1:356
23. Shenck NS, Paradiso JA (2001) Energy scavenging with shoe-mounted piezoelectrics. Micro IEEE 21(3):30
24. [a] Fouseka J, Crossa LE, Litvin DB (1999) Possible piezoelectric composites based on the flexoelectric effect. Mater Lett 39(5):287. [b] Zhu WY, Fu JY, Li N, Cross LE (2006) Piezoelectric composite based on the enhanced flexoelectric effects. Appl Phys Lett 89(19):192904
25. [a] Majdoub MS, Sharma P, Cagin T (2008) Enhanced size-dependent piezoelectricity and elasticity in nanostructures due to the flexoelectric effect. Phys Rev B 77:125424. [b] Eliseev EA, Morozovska AN, Glinchuk MD, Blinc R (2009) Spontaneous flexoelectric/flexomagnetic effect in nanoferroics. Phys Rev B 79:165433. [c] Majdoub MS, Sharma P, Çağin T (2008) Dramatic enhancement in energy harvesting for a narrow range of dimensions in piezoelectric nanostructures. Phys Rev B 78:121407
26. Wu WW, Bai S, Yuan MM, Qin Y, Wang ZL, Jing T (2012) Lead zirconate titanate nanowire textile nanogenerator for wearable energy-harvesting and self-powered devices. ACS Nano 6(7):6231
27. Pereira JN, Sencadas V, Correia V, Rocha JG, Méndez SL (2013) Energy harvesting performance of piezoelectric electrospun polymer fibers and polymer/ceramic composites. Sensors Actuators A Phys 96:55
28. [a] Park KI, Lee M, Liu Y, Moon S, Hwang GT, Zhu G, Kim JE, Kim SO, Kim do K, Wang ZL, Lee KJ (2012) Flexible nanocomposite generator made of BaTiO3 nanoparticles and graphitic carbons. Adv Mater 24:2999. [b] Park KI, Jeong CK, Ryu J, Hwang GT, Lee KJ (2013) Flexible and large – area nanocomposite generators based on lead zirconate titanate particles and carbon nanotubes. Adv Energy Mater 3(12):1539
29. Lee JH, Lee KY, Kumar B, Tien NT, Lee NE, Kim SW (2013) Highly sensitive stretchable transparent piezoelectric nanogenerators. Energy Environ Sci 6:169
30. Wu JM, Xu C, Zhang Y, Wang ZL (2012) Lead-free nanogenerator made from single $ZnSnO_3$ microbelt. ACS Nano 6(5):4335
31. Xu S, Yeh YW, Poirier G, McAlpine MC, Register RA, Yao N (2013) Flexible piezoelectric PMN-PT nanowire-based nanocomposite and device. Nano Lett 13:2393
32. Liu ZH, Pan CT, Lin LW, Lai HW (2013) Piezoelectric properties of PVDF/MWCNT nanofiber using near-field electrospinning. Sensors Actuators A Phys 193:13

33. Wu L, Yuan W, Nakamura T, Atobe S, Hu N, Fukunaga H, Chang C, Zemba Y, Li Y, Watanabe T, Liu Y, Alamusi, Ning H, Li J, Cui H, Zhang Y (2013) Enhancement of PVDF's piezoelectricity by VGCF and MWNT. Adv Compos Mater 22:49
34. Fan FR, Tian ZQ, Wang ZL (2012) Transparent triboelectric nanogenerators and self-powered pressure sensors based on micropatterned plastic films. Nano Energy 1:328
35. Lacks DJ, Mohan Sankaran R (2011) Contact electrification of insulating materials. J Phys D Appl Phys 44:453001
36. [a] http://en.wikipedia.org/wiki/Work_function. [b] http://www.trifield.com/content/tribo-electric-series/
37. [a] Nguyen V, Yang R (2013) Effect of humidity and pressure on the triboelectric nanogenerator. Nano Energy 2(5):604. [b] Baytekin HT, Baytekin B, Soh S, Grzybowski BA (2011) Is water necessary for contact electrification? Angew Chem Int Ed 50(30):6766. [c] Zhou YS, Liu Y, Zhu G, Lin ZH, Pan CF, Jing QS, Wang ZL (2013) Linear-grating triboelectric generator based on sliding electrification. Nano Lett 13:2771
38. Wang S, Lin L, Wang ZL (2012) Nanoscale triboelectric-effect-enabled energy conversion for sustainably powering portable electronics. Nano Lett 12:6339
39. Shaw PE (1917) Proc R Soc A Math Phys Eng Sci 94:16–33
40. Zhang XS, Han MD, Wang RX, Zhu FY, Li ZH, Wang W, Zhang HX (2013) Frequency-multiplication high-output triboelectric nanogenerator for sustainably powering biomedical microsystems. Nano Lett 13:1168
41. [a] Baytekin HT, Patashinski AZ, Branicki M, Baytekin B, Soh S, Grzybowski BA (2011) The mosaic of surface charge in contact electrification. Science 333:308. [b] Zhu G, Lin ZH, Jing Q, Bai P, Pan C, Yang Y, Zhou Y, Wang ZL (2013) Toward large-scale energy harvesting by a nanoparticle-enhanced triboelectric nanogenerator. Nano Lett 13:847
42. Meng B, Tang W, Too Z-h, Zhang X, Han M, Liu W, Zhang HX (2013) A transparent single-friction-surface triboelectric generator and self-powered touch sensor. Energy Environ Sci 6:3235
43. Yang Y, Zhang HL, Chen J, Jing QS, Zhou YS, Wen XN, Wang ZL (2013) Single-electrode-based sliding triboelectric nanogenerator for self-powered displacement vector sensor system. ACS Nano 7(8):7342
44. Zhu G, Chen J, Liu Y, Bai P, Zhou YS, Jing Q, Pan C, Wang ZL (2013) Linear-grating triboelectric generator based on sliding electrification. Nano Lett 13:2282
45. Hou TC, Yang Y, Zhang H, Chen J, Chen LJ, Lin Wang Z (2013) Triboelectric nanogenerator built inside shoe insole for harvesting walking energy. Nano Energy 2:856
46. Lin L, Wang S, Xie Y, Jing Q, Niu S, Hu Y, Wang ZL (2013) Segmentally structured disk triboelectric nanogenerator for harvesting rotational mechanical energy. Nano Lett 13:2916–2923
47. [a] Han MD, Zhang XS, Meng B, Liu W, Tang W, Sun XM, Wang W, Zhang HX (2013) r-Shaped hybrid nanogenerator with enhanced piezoelectricity. ACS Nano 7(10):8554. [b] Yang WQ, Chen J, Zhu G, Yang J, Bai P, Su YJ, Jing QS, Cao X, Wang ZL (2013) Harvesting energy from the natural vibration of human walking. ACS Nano 7(12):11317
48. [a] Bai P, Zhu G, Lin ZH, Jing QS, Chen J, Zhang G, Ma JS, Wang ZL (2013) Integrated multilayered triboelectric nanogenerator for harvesting biomechanical energy from human motions. ACS Nano 7(4):3713. [b] Zhang H, Yang Y, Hou TC, Su Y, Hu C, Wang ZL (2013) Triboelectric nanogenerator built inside clothes for self-powered glucose biosensors. Nano Energy 2:1019
49. Lin L, Xie YN, Wang SH, Wu WZ, Niu SM, Wen XN, Wang ZL (2013) Triboelectric active sensor array for self-powered static and dynamic pressure detection and tactile imaging. ACS Nano 7(9):8266

Textile Antenna Systems: Design, Fabrication, and Characterization

17

Hendrik Rogier

Contents

Introduction 434
Materials and Production Techniques 436
Antenna Topologies 439
Passive Textile Antennas 442
Some History 442
Active Textile Antennas 444
Active Antenna Circuit/Full-Wave Co-optimization 445
Integration of Energy Harvesters onto Wearable Antennas 447
A Complete Textile Wireless Node 449
Textile Multi-antenna Systems 451
MIMO Techniques for Textile Antenna Systems 451
Energy-Efficient Multi-antenna Processing Techniques 452
A Short Overview of Textile Antenna Applications 453
Summary 454
References 455

Abstract

Textile antennas are essential components in smart fabrics and interactive textile systems that implement sensing, localization, and wireless communication functionality while being unobtrusively and comfortably integrated inside garments. The implementation of such antennas in textile materials first requires dedicated material characterization techniques together with suitable fabrication procedures. Moreover, to ensure stable characteristics in proximity of the human body, a designer must also carefully select the right antenna topology. Subsequently, the antenna may be optimized to satisfy the requirements at hand, including some additional margins to accommodate adverse effects, such as

H. Rogier (✉)
Department of Information Technology, iMinds/Ghent University, Ghent, Belgium
e-mail: hendrik.rogier@ugent.be

© Springer Science+Business Media Singapore 2015

X. Tao (ed.), *Handbook of Smart Textiles*,
DOI 10.1007/978-981-4451-45-1_38

bending, changing environmental conditions, and body proximity. To make optimal use of the area consumed by the antenna, active electronic circuitry may be integrated directly onto the antenna feed plane, while energy harvesters can be positioned on top of the radiating patch. Moreover, the large area available in garments can be exploited to deploy multiple antennas, realizing diversity gain to combat fading and body shadowing. The methods proposed in this chapter leverage the development of highly efficient and robust body-centric communication systems for healthcare and rescue workers and military personnel.

Keywords
Wearable antennas • Smart textiles • Body-centric communication

Introduction

In the early nineties, the concept of smart textiles arose. It became quickly clear that wireless connectivity was one of the key features of such systems. Therefore, suitable antennas were required that are compatible with the textile integration platform. The new field of textile antennas was born.

One may wonder why there is a specific need for textile antennas and for smart textiles in general, given the wide range of portable wireless devices currently available. Yet, there exist clear benefits that motivate the extensive research efforts toward efficient textile antenna systems, seen in the past decade. The main drivers for off-the-self portable devices are cost, miniaturization, and multifunctionality. Therefore, the multitude of antennas, deployed in these devices, perform in a suboptimal manner, as compromises had to be made in terms of antenna gain and radiation efficiency to accommodate the different antennas in the portable hardware platform. In addition, the limited size of the wireless communication device's ground plane results in a significant performance reduction when the portable system operates in proximity of the human body, since an important fraction of the antenna radiation is absorbed by body tissues. Moreover, the presence of objects or body parts, such as the hand, on the device's casing may result in antenna detuning, reducing the wireless link quality even further. In addition, the device's orientation may deteriorate its wireless performance, because, for example, the antenna does not have a clear view toward the sky to receive satellite signals for localization. Textile antenna systems are able to overcome most of the aforementioned issues, mainly because they are able to exploit the large surface area that garments offer for the deployment of wireless systems. This enables the integration of one or more large but highly efficient antennas without causing discomfort to the wearer, provided that the antenna and its electronic circuit are flexible, breathable, and unobtrusively integrated into the piece of clothing. In particular at microwave frequencies, the antenna designer may rely on an electrically large antenna ground plane to avoid, or reduce, performance loss due to body proximity. In the

meanwhile, the ground plane lowers electromagnetic field absorption and specific absorption rate (SAR) levels inside body tissues. Moreover, textile antennas may be judiciously deployed in those areas of a garment where there is little chance that the antenna is detuned by direct contact with objects or body parts. In addition, by strategically distributing multiple antennas on well-chosen locations in a garment, one may ensure that at least one antenna is oriented such that optimal performance is obtained. The fact that the smart textile system forms an integral part of the garment also reduces the risk that the electronic module is forgotten or intentionally removed and, therefore, does not trigger an alarm in life-threatening situations, which may occur in home care, and search and rescue applications.

Of course, the design and fabrication of reliable, highly efficient, and comfortable textile antennas does not come without its own challenges. First, off-the-shelf textile fabrics serving as antenna substrate are not produced according to the same rigorous standards as typical antenna foams and high-frequency laminates. Therefore, the designer will have to cope with larger fabrication tolerances and higher material inhomogeneity. Moreover, electric material parameters are not readily available for common textile fabrics, and they may vary from batch to batch. Hence, dedicated dielectric characterization algorithms are in order to predict the textile material's permittivity and substrate losses. In addition, also the conductive parts that define the textile antenna's radiation patch and ground plane need to be characterized in terms of sheet resistance. Once a suitable characterization framework is in place, the textile antenna designer can start selecting the proper textile fabrics that ensure high antenna performance. Besides choosing low-loss materials, special care should be taken to guarantee stable antenna characteristics in varying environmental conditions. Suitably designed textile antennas serve as key components in high-performance smart textile systems for communication, localization, and sensing applications. However, when integrating the flexible textile modules inside the garments, the antenna will also be subject to deformation due to movements and physical activities by the wearer, causing bending, crumpling, stress, and strain. A dedicated design procedure is required to guarantee stable and reliable antenna performance under these conditions. In addition, soldered or glued connections between textile fabric and electronic circuitry may typically prove to be weak points that may also hamper the long-term reliability of the textile antenna. Furthermore, special measures should be taken to avoid additional long-term degradation due to maintenance procedures, such as washing or dry cleaning.

This chapter reviews all steps required to design, fabricate, and characterize high-performance textile antennas. In section "Materials and Production Techniques," the proper textile fabrics are selected, the different material characterization procedures are described, and an outline of the available fabrication techniques is given. Section "Antenna Topologies" provides an overview of the most common textile antenna topologies, depending on the operating frequency and the application at hand. Section "Passive Textile Antennas" covers some representative passive textile antenna designs, whereas section "Active Textile Antennas" summarizes the design and fabrication of active textile antennas, which have electronic circuitry and energy harvesters directly integrated onto the textile

antenna platform. Section "Textile Multi-antenna Systems" focuses on textile multi-antenna systems, including multiple-input multiple-output communication techniques to enhance the body-centric wireless communication channel. Some typical applications are discussed in section "A Short Overview of Textile Antenna Applications," whereas some future perspectives are given in section "Summary."

Materials and Production Techniques

In order to realize a textile antenna that provides both good radiation performance and high user comfort, the designer must select suitable materials [1, 2], both for the conductive and nonconductive parts, and rely on an appropriate fabrication technique to implement an antenna topology adapted to the garment and the body proximity. This should ensure that optimal performance in proximity of the human body is obtained by the textile antenna, which is invisibly and unobtrusively integrated inside a garment without hindering the wearer's activities. Special attention should be devoted to material selection and production techniques for textile antennas deployed in professional garments, such as firefighter suits and military uniforms, which are typically exposed to harsh operating conditions. For these scenarios, additional protection of the antenna module may be required by specific encapsulation techniques [3, 4] and thoughtful deployment of the textile antenna in the best protected areas of the garment.

Quite often, for the textile antenna's substrate, the designer will want to rely on those textile fabrics [1, 2] that are typically applied in the envisaged application, since those materials already exhibit some desired properties, such as ability to absorb shocks, to resist heat, and to repel water. Although these features are not directly related to antenna performance, they might be helpful in increasing antenna efficiency. Indeed, substrate losses will be lower for hydrophobic materials, while compressible materials tend to exhibit a permittivity close to that of air, which increases radiation efficiency. In a smart textile system, the antenna is typically one of the largest components. Therefore, it should be constructed by relying on textile fabrics that are sufficiently flexible, albeit not drapable, to avoid excessive permanent deformation caused by stress, compression, or crumpling and to guarantee stable antenna characteristics. This type of flexibility is also required for potential supporting structures, such as pouches, applied to protect the textile antenna. Moreover, materials with a compression set [5] smaller than 40 % should be adopted to limit the amount of permanent deformation after temporary compression. In most professional garments, the textile antenna should also be breathable, to avoid that excessive amounts of moisture or sweat are trapped by the antenna. Deploying the textile antenna in environments with different relative humidity conditions will cause a variation in the amount of water droplets that are absorbed by the different textile fabrics the antenna is composed of. This process will make the antenna performance dependent on the operating conditions. To limit the variation in antenna performance under different environmental conditions, one should preferably select hydrophobic textile fabrics, exhibiting a low moisture regain [6] smaller than 3 %.

Fig. 1 Textile microstrip patch antenna. Antenna patch and ground plane patterned in Zelt electro-textile. Fleece material used as antenna substrate

To pattern the conductive parts and to connect them to the nonconductive antenna parts, roughly three types of wearable antenna fabrication technologies are available. The simplest approach consists of integrating, knitting, or embroidering conducting wires, copper tape, or conductive yarns into a piece of clothing [7–9]. This approach is most often applied to construct antenna topologies without a ground plane. Another popular technique involves attaching e-textiles, which are typically copper- or copper-nickel-plated nonwoven fabrics to the textile fabric, e.g., by means of a thermally activated thermal sheet [1, 9]. This technique is well suited for the fabrication of microstrip and multilayered topologies, provided dedicated fixtures are used to guarantee proper alignment of the different layers. An example of a textile microstrip patch antenna, implemented by applying patterned Zelt electro-textile, for antenna patch and ground plane, on a fleece substrate, is shown in Fig. 1. Finally, additive techniques, such as screen or ink-jet printing, may be applied to pattern the antenna, reflector, and ground plane on the textile fabric [3, 10–12]. Quite recently, substrate waveguide technology, a well-established approach to realize waveguiding structures in (multilayered) high-frequency laminates, was applied to textile substrates. The technology is very suited to create cavities in a textile substrate by means of rows of tubelets or by embroidery. This approach offers promising perspectives for the design of a wide range of novel textile microwave circuits, including textile antennas with excellent isolation of the antenna radiation from the human body [13–15]. An example of a cavity-backed slot antenna implemented in SIW technology is shown in Fig. 2.

Since for off-the-shelf textile fabrics the dielectric properties of the materials composing or surrounding the wearable antenna are not readily available, dedicated characterization techniques must first be applied before the textile antenna design procedure can start. The characterization procedure is complicated by the fact that both the complex permittivity of the nonconductive fabrics and the sheet resistance of the conductive materials must be determined simultaneously. Indeed, a separate characterization method for the bulk conductive and nonconductive fabrics may

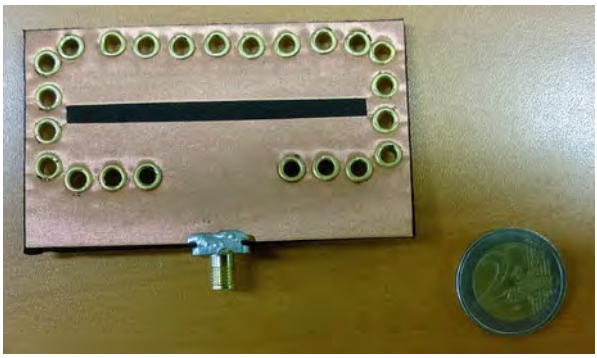

Fig. 2 Textile SIW cavity-backed slot antenna. Cavity implemented using brass tubelets and copper-plated Taffeta electro-textile. Protective foam applied as antenna substrate

result in electric properties that differ from those measured after the textile antenna is fully assembled [16]. This is due to the specific fabrication (knitting, weaving) and assembling (additional glues or adhesive sheets) processes applied during construction, as knitting and weave patterns, as well as glue penetrating the fabric, will alter the material's electric behavior. An accurate prediction of the wearable antenna performance might, therefore, require simultaneous characterization of all relevant conductive and nonconductive materials, through test structures that closely resemble the final textile antenna prototype [17]. In addition, textile production processes, such as knitting, weaving, and embroidering, may induce inhomogeneity, anisotropy, and instability (in terms of geometry and environmental conditions) of the fabric's material properties [18, 77]. Furthermore, a textile fabric exposed to its operating environment may be seen as a mixture of fibers and air and water molecules [17, 19], where the fraction of the three components may vary depending on the environmental conditions. The characterization procedure and subsequent wearable antenna design process must be able to account for these effects.

On the one hand, the bulk material properties of nonconductive textile fabrics, including anisotropy [75], may be characterized at one or a few discrete frequencies by resonance-based techniques [20], such as cavity-based and cavity perturbation algorithms. To determine the dielectric material properties over a wide frequency range, on the other hand, nonresonant approaches can be applied, based on reflection and/or transmission along transmission lines. As the test structures used in the latter procedures closely resemble the actual textile antenna [16], they often provide a better prediction of the material properties in the final textile antenna prototype. Indeed, it is found that knitting and weave patterns, as well as glue penetrating the fabric, may change the electric properties of the fabrics in the final assembled antenna prototype. However, nonresonant characterization procedures [76] typically only characterize the out-of-plane component of the electric field. Yet, when considering microstrip topologies and when neglecting fringing fields, this is the most important field component [21]. To fine-tune the wideband estimates of the material properties obtained by nonresonant methods, one may use these results as initial values in a second, more accurate, resonance-based procedure. The latter

technique is then based on narrowband patch antennas that are designed to resonate in proximity of the frequency band of interest [17, 22]. In addition, these test structures may be applied in a rapid characterization algorithm to quantify the effects on the textile antenna's resonance frequency of relativity humidity or moisture [6, 20, 23, 24], of compression or strain [25], and of repeated washing cycles on the material properties [3, 4, 26]. From the measured antenna resonance frequencies, the variation of permittivity, loss tangent, and sheet resistance may then be extracted.

When deriving the material properties of the conductive parts of the textile antenna, such as electro-textiles, conductive yarns, or inks, one should be careful to characterize the sheet resistivity or conductivity at the antenna's operating frequency, since, due to the typical surface roughness of the knitwear, the weave pattern or the material on which the conductive layer is plated or printed, the sheet resistivity at the antenna's operating frequency will be significantly larger than at DC [3, 27]. Similar to nonconductive fabrics, the conductivity or sheet resistance of the conductive layer will depend on the specific knitting or weave pattern [28]. A distinction is again made between resonant characterization procedures, based on resonant cavities [28], and nonresonant or mixed techniques relying on microstrip transmission lines [27, 29, 30] and antennas [17] as test structures. A dedicated de-embedding procedure is required to isolate the electro-textile's sheet resistance from all other antenna loss mechanisms. Of particular importance is the characterization of textile antenna performance degradation due to maintenance procedures, such as washing and dry cleaning. These operations may gradually decrease the conductivity of the wearable antenna's conductive parts. Therefore, a lot of research effort is currently invested to characterize this degradation over many maintenance cycles and to propose measures to avoid antenna performance reduction. One possible solution is to encapsulate the antenna with a breathable thermoplastic polyurethane (TPU) coating [3, 4, 12, 26]. As this coating alters the material properties of the textile antenna, it should be accounted for during the design process.

Antenna Topologies

The first challenge, the textile antenna designer is faced with, concerns the choice of a suitable antenna topology, as this requires reconciling a wide range of conflicting electrical and mechanical requirements. From the antenna performance's point of view, stable antenna characteristics and maximal radiation efficiency are desired, which requires that the effects of human body proximity are minimized. The latter also entails that body movements and equipment in the textile antenna's reactive near-field region do not significantly alter the antenna's operating characteristics. Therefore, as a general rule, antenna topologies with sufficiently large ground plane are preferred, as the latter directs the antenna radiation away from the human body and, therefore, acts as an electromagnetic shield that reduces electromagnetic field absorption in body tissues. Unfortunately, the use of a ground plane is only practical

in the microwave frequency range. At lower frequencies, the ground plane size will be too large to be practical for comfortable integration inside garments. Moreover, in order to obtain sufficient radiation bandwidth and radiation efficiency, a sufficiently large spacing between the ground plane and the antenna's radiating structures is required. In the lower frequency range, this requirement conflicts with the need for a low textile antenna profile, required to guarantee invisible and unobtrusive integration. As a general rule of thumb, for a practical and comfortable integration inside a garment, the antenna size should remain in the order of tens of centimeters, while its height should be limited to maximally a few centimeters. In case that size constraints prohibit the use of an antenna topology with a ground plane of sufficient size to guarantee sufficient isolation between the textile antenna's radiation and the human body, the body should be included in the design procedure. In that case, the high permittivity values of the body tissues lead to some size reduction. However, this miniaturization is limited, since one will typically apply a spacer of several tens of millimeters, to guarantee a sufficiently large antenna gain. After completing the design, the designer should verify whether the radiation performance remains satisfactory [31] when the textile antenna is deployed on people with different morphologies, for different postures and for varying operating conditions.

Wearable dipoles [32] or loop antennas [33], invisibly integrated into garments, may be applied to replace protruding whip antennas. In the lower frequency range, such as the VHF and UHF band, miniaturization techniques may be in order to limit the antenna size to acceptable proportions. Dipoles may be folded [34], meandered [35], and loaded to reduce the antenna size to well below half a wavelength. Asymmetric dipole arms [36] may be applied to excite additional modes, and one or both dipole arms may be flared to obtain antenna radiation over a broader frequency band. When (ultra-)wideband or multiband performance is desired, monopole topologies may also be applied [37]. Different monopole shapes have been optimized to increase the impedance bandwidth [38]. As an alternative, coplanar-waveguide-fed slot antenna topologies may be applied to obtain the required wide bandwidth [39]. Also the monopole's or the slot's ground plane may be optimized. Yet, since this ground plane does not act as a shield for the antenna radiation, the proximity of the wearer's body typically improves the impedance matching but reduces the antenna gain and radiation efficiency. This effect may be minimized by deploying the antenna on a spacer, to guarantee a minimal distance between the antenna and the human body. Moreover, this spacer may be backed by an artificial magnetic conductor (AMC) ground plane or an electronic bandgap structure [40], to better isolate the body from the antenna radiation [41].

The most popular antenna topology for textile antennas is definitely the microstrip patch textile antenna. Thanks to its ground plane, it provides sufficient shielding from the human body, such that the antenna's radiation characteristics nearly do not change in proximity of the human body, provided that a sufficiently large ground plane is used. In the lower frequency range, a large-size ground plane is not always practical, and a smaller ground plane will be applied, even though this

is nonideal in terms of body isolation. Often, the antenna patch topology will also be miniaturized. A very popular straightforward approach is to make use of the planar inverted-F topology, reducing the patch size to a quarter of a wavelength by means of a shorting wall. Even further reduction is possible by introducing slots in the patch [42] or by relying on a fractal pattern, such that the antenna currents follow a meandering pattern. Again, this approach may reduce the antenna bandwidth and its radiation efficiency. A typical drawback of the microstrip patch antenna topology is its inherent narrowband antenna characteristic. Besides choosing thick antenna substrates with permittivity close to that of air, special measures may be taken to increase the impedance bandwidth. Incorporating electronic bandgap structures in the substrate allows keeping the antenna low in profile, while realizing the required bandwidth and suppressing potential surface waves in the substrate. In addition, one may rely on multi-moding techniques where different modes are excited on the antenna patch at slightly different frequencies, to enlarge the operation bandwidth. In the process, circular polarization may be obtained in a limited frequency band, which is beneficial as the antenna performance becomes less dependent on its orientation. Moreover, a pure circular polarization may be required for satellite communication and localization. Also the feed structure may help to enlarge the bandwidth. On the one hand, the microstrip patch antenna topology offers a lot of flexibility to tune the antenna to the desired input impedance. On the other hand, the aperture-coupled feed topology enables to match the patch antenna over a broader bandwidth thanks to its inherent impedance transformation properties. Moreover, the latter feed mechanism avoids the use of vias, which are typically fragile connections in textile antennas and easily breaking at the solder points when pressure is exerted. Realizing broader impedance and circular polarization bandwidths may help to accommodate for detuning effects caused by bending or changing environmental conditions. As these effects are random in nature, a stochastic framework may be applied to quantify random detuning [43] and to adapt textile antenna specifications accordingly to ensure stable radiation performance.

When applying the microstrip antenna topology, it is required that the ground plane extends sufficiently far beyond the radiation patch, to shield the human body from the antenna radiation. If this is not the case, or when surface waves propagate in the microstrip substrate, the textile antenna will couple with the human body, and its characteristics will change when it is worn inside the garment. A new promising approach to avoid this problem consists in relying on a cavity-backed slot antenna topology, which realizes excellent isolation from the wearer's body. The cavity, which may be realized by substrate integrated waveguide technology, contains the electromagnetic fields, which only radiate away from the body through the slot. The designer must ensure that the vias implementing the cavity's vertical walls are spaced according to the rules of thumb derived for SIW technology [14] and that substrate compression by the tubelets or the stitches implementing the vias is taken into account [13, 14]. Multiband or ultra-wideband operation with excellent body isolation may be obtained by carefully exciting multiple eigenmodes in the cavity [44]. A similar technique may also be applied to implement ultra-wideband radiation characteristics using a microstrip topology [45].

For wireless body area networks, a particular challenge consists in proposing antenna topologies that are able to optimally radiate power tangential to the human body. In particular, the designer may want to construct compact low-profile textile antennas that are able to optimally couple electromagnetic fields into the Norton surface waves [46], which are able to transport energy over larger distances along the human body surface. Specific attention should be paid to the antenna polarization with respect to the human body surface: when excitation of the space wave is desired, one may want to apply horizontal antenna polarization, with respect to the body surface, whereas vertical polarization is wanted for optimal propagation along the body. A vertical dipole, however, may not be integrated unobtrusively into a garment, and therefore, one may want to use a low-profile higher-mode microstrip patch antenna [47] instead. As an alternative, array topologies, potentially relying on parasitic elements, may be optimized to launch surface waves [48]. Finally, Yagi-Uda antenna topologies may be applied to transmit electromagnetic fields along specific directions over the body surface [49].

Passive Textile Antennas

Some History

In the nineties, wearable computer systems emerged, being lightweight computers seamlessly integrated into garments worn by the user. This development paved the way toward electronic devices designed on textile fabrics. In 1999, Salonen et al. [50] proposed a dual-band planar inverted-F antenna (PIFA) designed for the 900 MHz GSM and 2.45 GHz ISM bands. Although the antenna was implemented on a standard printed circuit board, it was optimized for integration inside the sleeve of a garment. The first product combining electronics and textiles was the industrial clothing design (ICD+) line, launched in the late nineties by Philips and Levi Strauss & Co. The Levi's jacket was equipped with wearable electronics, being an MP3 player, a mobile phone, headphones, a microphone, and a remote control. All devices, such as mobile phone and MP3 player, were specifically designed in terms of size and weight to fit into a garment. Although all components had to be removed for washing, the prototype first proved the potential of wearable textile systems for, e.g., healthcare applications. During the design of the ICD+ line, Philips was confronted with the need for mobile phone antennas made of textile materials, suitable for unobtrusive integration into Levi's jacket. Starting from the idea of Salonen, they constructed the first mobile phone antenna based on textile materials. At Philips Research Laboratories, Massey [51] relied on electroless copper-plated ripstop nylon to fabricate the antenna patch and the ground plane of the 900 MHz GSM antenna. Both layers were separated by a 12.5-mm-thick foam sheet, while the patch was fed by a thin coaxial cable. In 2002, Salonen et al. [52] designed a flexible inverted-F antenna implemented on a 0.236-mm-thin flexible substrate, which makes the antenna more suitable for integration into the sleeve of a garment. The following year, Salonen constructed the first

textile antenna for operation in the 2.45 GHz ISM band [53], making use of a 3-mm-thick fleece substrate and a copper-knitted textile fabric to construct the rectangular patch and the ground plane. He obtained an antenna gain of 6.82 dBi and a radiation efficiency of 90 %. In 2004, he proposed three additional textile-based antennas, being a 1.575 GHz GPS antenna, a 1900 MHz and 2.45 GHz dual-band antenna, and a wearable electromagnetic bandgap antenna. A textile fabric was applied as antenna substrate, whereas the patch and ground planes were made of copper tape. In addition, the influence on the antenna performance was studied of the human body [54] and of the conducting material [55]. Also in 2004, the first 2.45 GHz circularly polarized textile antenna was introduced by Locher et al. A 6-mm-thick polyamide spacer fabric was applied as antenna substrate, while patch and ground plane are patterned in nickel-plated woven textile. In 2006, Hertleer et al. [56] introduced a robust microstrip textile antenna fabricated using a fleece substrate and a copper-plated nylon fabric antenna patch and ground plane, for wireless off-body communication in the 2.45 GHz ISM band. Robust antenna characteristics are achieved by applying the multi-moding technique to enlarge the impedance bandwidth. This, larger than required, bandwidth accommodates for shifts in resonance frequency due to bending and body proximity. In the meantime, linear polarization is avoided to ensure robust operation under different antenna orientations. In addition, it is discussed how antenna bending affects input matching and impedance bandwidth. Bending along the direction of the resonance has the most profound effect on input matching and impedance bandwidth. Around that time, [57] also proposed three additional purely textile-based antennas, two of which are linearly polarized. After testing all textile antennas in planar and bent state, it was observed that the polarization ellipse of the circularly polarized textile antennas is altered. Also in [58], it was found that the polarization ellipse transforms from circular to close to linear after bending a textile GPS antenna. In 2007, the first aperture-coupled patch antenna [59], entirely made of textile materials, was introduced, avoiding the fragile via feed which easily breaks under harsh operating conditions. Specifically for integration into protective garments, dedicated dual-polarized [60], circularly polarized [5], and GPS [61] textile antennas were proposed. Fig. 3 demonstrates the flexibility of a textile microstrip patch antenna implemented on a protective foam substrate, using copper-nickel-plated nylon as an electro-textile for patch and ground plane.

During the second half of the first decade of the twentieth century, more research groups developed an interest in textile antennas, and, as a consequence, research intensified. Without trying to be complete, a few interesting developments are summarized. Zhu and Langley developed a dual-band (2.45 and 5 GHz) wearable textile antenna on an EBG substrate [40], which was not only tested after bending but also after washing. A satisfactory performance was observed after washing and drying the felt/Zelt textile antenna. However, humidity affected the antenna performance, resulting in a downward shift of the resonance frequency and a decrease in the antenna gain in both frequency ranges. Bai and Langley [62] studied the effect of crumpling on antenna performance, which typically occurs when the textile antenna is worn near the joints. In addition, textile antennas were introduced

Fig. 3 Flexible circularly polarized textile microstrip antenna. Copper-nickel-plated nylon used for antenna patch and ground plane. Protective foam applied as antenna substrate

for other communication protocols, such as for FM reception (100 MHz) [32] and ultra-wideband (UWB) communication (3.1–10.6 GHz) [38].

In [34, 35, 63], NASA proposed textile antennas for integration in extravehicular activity (EVA) suits, mentioning as benefits their flexibility, lightweight, and robustness combined with high antenna gain and good coverage around the body in body-worn scenarios. Therefore, an eight-element e-textile antenna array was proposed, based on a Nomex felt substrate with the conductive parts implemented in silver-, copper-, and nickel-plated nylon fabric (Nora). In 2008, Salonen [64] further improved the flexibility and wearability of the textile antenna. It was found that the textile antenna's radiation pattern widens and its radiation efficiency decreases after bending [65].

Active Textile Antennas

To implement the functionality required in technical garments for rescue workers, healthcare professionals, and military, more than just a textile antenna is required. Wearable, robust, and autonomous wireless communication modules must be implemented. Therefore, a dedicated design strategy is discussed to optimize the textile antenna's radiation characteristics together with the performance of the active electronic circuits that are directly connected to and often integrated onto the textile antenna. In the process, one needs to convert the nominal application-specific design specifications into more stringent requirements to accommodate for the specific operating conditions, in which the active textile antennas operate. To cope with antenna bending, body presence, and environmental parameters, such as varying temperatures and relative humidity conditions, the textile antenna designer will add safety margins, by broadening the nominal frequency band of operation

and by tightening the matching requirement. In order to implement these dedicated design requirements, the choice of active textile antenna topology and materials is of prime importance. Next, a dedicated design procedure has to be set up to co-optimize the textile antenna together with its integrated active circuits. Two such formalisms are outlined in section "Active Antenna Circuit/Full-Wave Co-optimization." Section "Integration of Energy Harvesters onto Wearable Antennas" demonstrates that, besides integrating active electronics directly below the textile antenna's ground plane, the antenna patch may serve as a platform to deploy energy harvesters. It is shown that, by adopting a suitable antenna topology and by cleverly routing connections between the harvesters and the power management module, a compact, autonomous module may be built that exhibits identical radiation characteristics as the stand-alone antenna.

Active Antenna Circuit/Full-Wave Co-optimization

An active antenna has active electronic circuits directly integrated onto the antenna platform. The more intricate design process, involving the joint circuit/full-wave computer-aided design and optimization of active circuits together with the passive antenna, results in an active component with a reduced number of high-frequency connections and with shorter RF paths. In particular for textile antennas, this drastically increases the reliability of the smart textile system, by avoiding soldered or press-fitted connections on textile conductors. These fragile connections easily break under stress. Moreover, the length reduction of the high-frequency paths drastically improves the active textile antenna's performance, given the significant substrate and conductor losses experienced in textile materials. As the characterization and testing process of active antennas is much more involved, compared to designing and measuring the passive antenna separated from the active electronics, a highly reliable and comprehensive design formalism is required. The dedicated active textile antenna design process should be able to account for the specific challenges of designing active antennas on textile fabrics. Moreover, it should include a joint circuit/full-wave co-optimization step to yield global optimal performance for the combination of the textile antenna with the active circuitry. Thanks to this co-optimization procedure, the active textile antenna might outperform the cascade of an isolated passive textile antenna connected to the active electronic circuit.

The dedicated active textile antenna design formalism is now outlined, with particular focus on the joint circuit/full-wave optimization to simultaneously design the antenna and the active electronics, according to a set of desired specifications [22, 29]. This might include impedance matching and circular polarization over a certain frequency band, in terms of antenna characteristics, combined with specifications pertinent to the active circuits, such as a large available gain, input and output matching, as well as low-noise figure. For example, such requirements may be desired for a low-noise amplifier (LNA) circuit that is directly connected to the textile antenna's output port. It is immediately clear that the performance

requirements for both active and passive parts of the module result in a large number of design variables that must be optimized to satisfy a significant set of specifications. Therefore, two dedicated strategies [66, 67] are presented that keep the design process manageable and yield optimal designs in a reasonable time.

Active Textile Antenna Design for Optimal Noise Figure

This approach aims for a minimal noise figure at the LNA's output by tuning the passive textile antenna to a complex radiation impedance that is optimal for minimum noise operation of the LNA. This impedance is determined during the first step of the full-wave/circuit co-optimization procedure, where a preliminary optimal LNA design is performed by considering only the active electronic circuits without the antenna. In the process, the circuit's interconnections are represented by an N-port scattering matrix calculated by a full-wave electromagnetic field simulator. This scattering matrix is introduced in a circuit simulator together with the multi-port descriptions of the different active and passive lumped components composing the active circuit. The outcome of this analysis is the LNA's complex input impedance required for a minimal noise figure. Next, the designer will tune the passive textile antenna to this optimal impedance by a full-wave optimization of the antenna dimensions. Finally, the active circuits are combined with the passive textile antenna to form a complete integrated active textile antenna. In a final global optimization procedure, the complete module is co-optimized to yield optimal combined performance in terms of antenna and active electronic circuit requirements.

This design flow for optimal noise characteristics avoids the need for a matching network when connecting the antenna to the LNA. Therefore, the method results in short RF connections and avoids excess component losses. As this chapter deals with textile antennas, it is important that the most suited simulators are applied and combined in the design process for each part of the active textile antenna. Specifically, on the one hand, the passive antenna may be simulated by the 3D full-wave frequency domain simulator of CST microwave studio, such that the finite conductivity of antenna plane and ground plane, implemented in, for example, an electrotextile, can be taken into account. On the other hand, the flexible circuit and the interconnections of the LNA circuit may be modeled by means of the planar 3D full-wave simulator ADS Momentum. More details about this design procedure are found in [66].

Active Textile Antenna Design by Impedance Matching

Tuning the textile antenna to match the LNA's load impedance for minimal noise figure is only feasible when the textile antenna's output is directly connected the LNA's input. Often, this is undesired as a designer may want to filter the received antenna signal before amplification, to avoid intermodulation distortion leading to in-the-band leakage of undesired signals. To obtain a suitable filter characteristic with a compact filter, one will typically rely on a surface acoustic wave (SAW), bulk acoustic wave (BAW), or ceramic filter. These off-the-shelf discrete components are only available at well-defined impedance levels. Moreover, a designer

may also want to introduce other lumped microwave components, such as direction couplers, circulators, or diplexers between the antenna and the LNA, in order to realize the desired functionality. For example, to achieve wideband circular polarization, which for satellite communication typically means that the antenna's axial ratio must remain below 3 dB over a sufficiently large bandwidth, a designer may want to apply a quadrature hybrid instead of deforming the antenna patch and optimizing the feed structure. Since wearable microstrip implementations of directional couplers are typically too large at L-band frequencies (the 1–2 GHz band, in which GPS/Galileo/GLONASS positioning systems are located), a designer will resort to miniaturized off-the-shelf lumped couplers. Again, such components operate at fixed impedance levels, such as, for example, 50 Ω. Therefore, an adapted co-optimization strategy is needed.

First, to accommodate for the fixed impedance level of the discrete component, the antenna output and the LNA input are both separately tuned to 50 Ω. To safeguard optimal noise performance for the LNA, a matching network will therefore be designed. Next, the textile antenna is optimized, considering the requirements in terms of polarization (axial ratio) and input impedance, gain, and efficiency. Finally, a full-wave/circuit co-optimization is performed on the textile antenna with all its integrated active and passive components, to obtain the best possible performance. Again, the designer can choose from the wide range of available full-wave solvers and circuit simulators to apply the best simulation technique to every part of the active textile antenna. In the last step, all these simulators will be linked together, either based on commercially available software (such as, for example, the capabilities available in Agilent's Advanced Design System or in CST Studio Suite) or on the designer's own dedicated software tools. More details about this design methodology can be found in [67].

Integration of Energy Harvesters onto Wearable Antennas

In the previous section, it was explained how direct integration of active electronics may help to reduce the number of fragile connections between conductive textiles composing the antenna and the active electronic circuitry implementing the requested functionality. This, in turn, greatly improves the reliability of the smart textile system. Another important challenge for smart fabrics and interactive textiles consists of ensuring acceptable system autonomy without the use of excessively large and heavy batteries. A smart textile system running out of power may be the cause of life-threatening situations, since these systems are deployed in critical applications such as monitoring of patients and coordination of interventions of rescue workers and military forces. Therefore, the textile antenna designer must take the two following measures as to ensure a longer autonomy and a less frequent battery replacement or recharge: First, during the design, he/she must aim for the highest possible energy efficiency for his/her system. Therefore, he/she will resort to a low-power wireless communication protocol, whenever the application permits, in combination with high-efficiency textile antennas. As discussed in the

next section, more than one antenna will typically be deployed to overcome multipath fading and body shadowing, such that the reliability and power efficiency of the wireless channel is improved even further. Second, the designer may apply energy harvesting techniques to exploit the energy produced by the body and its environment. These scavenged energy sources may serve as a primary source, to power the system or, as a secondary source, to extend its lifetime. Specifically, solar energy is the most important readily available energy source in outdoor scenarios, whereas thermal and kinetic energy originating from body movement may be exploited in indoor conditions. Now, some techniques are discussed that reuse the area consumed by the textile antenna to serve as an energy harvesting platform. In addition, it is demonstrated how energy harvesters integrated directly on top of the wearable antenna module [67] may be connected to the power management system and deployed on the antenna's feed plane, without affecting the textile antenna's performance.

First, flexible solar cells may be directly deployed on the radiating patch of a planar inverted-F textile antenna. Since the quarter-wavelength antenna patch is short-circuited to the ground plane along one side, it also acts as a DC ground, to which the solar cell's cathode may be connected. Moreover, since the textile antenna does not radiate along this shorting wall, other connections, such as the solar cell's anode, may be routed along this edge, without disturbing the textile antenna's radiation mechanism. An example of such a shorted wearable solar patch antenna for communication in the 902–928 MHz UHF band is given in Fig. 4. The aperture-coupled feed topology applied to excite the antenna patch contributes to

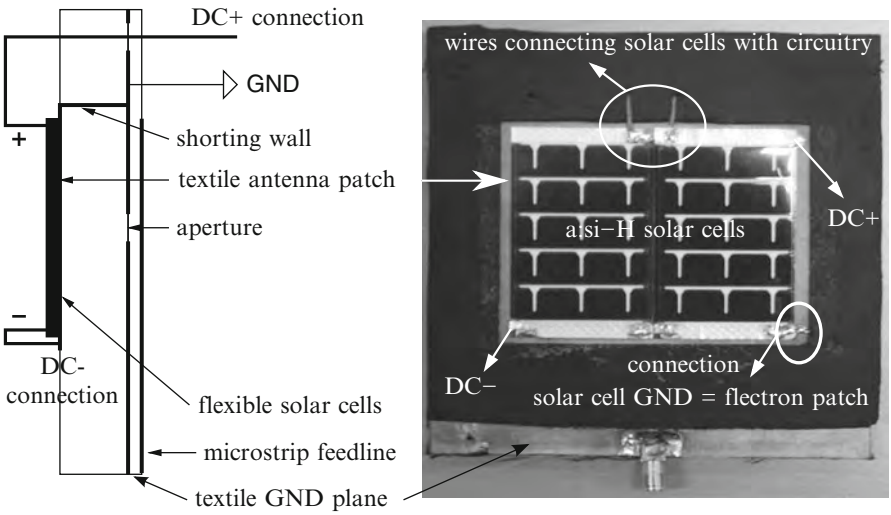

Fig. 4 Textile solar antenna. Flexible amorphous solar cells deployed on the antenna plane (Flectron electro-textile) of a planar inverted-F textile antenna. Protective foam applied as antenna substrate

the reliability of the textile antenna, by avoiding a via feed that might break when the antenna substrate gets compressed.

Cavity-backed slot antenna topologies also provide excellent opportunities to transform textile antennas into compact and efficient energy harvesting platforms. By combining SIW technology with textile materials, excellent user comfort is paired with optimal antenna performance in proximity of the human body. Moreover, the complete top plane of the antenna cavity may be exploited for harvesting solar energy, as long as the flexible solar cells do not cover any of the radiating slots. In addition, the power management module may be deployed on the bottom plane of the cavity. Connections between the solar cells and the electronic circuitry on the bottom plane may easily be routed through the tubelets that implement the vertical walls of the antenna cavity. As an example, Fig. 5 proposes an SIW textile solar antenna for the 2.45 GHz ISM band ([2.4–2.4835] GHz) and the 4G LTE band 7 ([2.50–2.57] GHz and [2.62–2.69] GHz). The SIW cavity is constructed by rows of tubelets that connect top and bottom planes, implemented in copper-plated Taffeta electro-textile sheets. The radiating slot in the top plane provides excellent isolation of the antenna's radiating fields from the human body. Two modes are excited inside the SIW cavity, implementing wideband matching to provide robust coverage of both the Wi-Fi and 4G bands, even with solar cells on the cavity's top plane and a power management system (PMS) on the bottom plane and when deploying this solar antenna on a human body. More details about this antenna can be found in [44].

A Complete Textile Wireless Node

The integration methodologies described in the previous subsections may be extended to an even more pervasive integration strategy, where all necessary functionality is implemented by complete electronic circuits on an ultrathin flexible polyimide substrate, which is directly positioned on the feed plane of the textile antenna platform. Such a wireless node will typically contain a transceiver chip, implementing the wireless communication protocol and potential fading and shadowing mitigation strategies, such as diversity techniques. Moreover, onboard flash memory may be incorporated together with sensors and a microcontroller that takes care of the node's operation. By combination of a suitable textile antenna platform with an ultraflexible circuit containing small discrete components that are well distributed over the flex substrate, the wearable node can be made fully flexible, while offering stable and reliable performance even for typical bending radii it might be exposed to. An example of such a wireless node is shown in Fig. 6. The textile node consists of an Analog Devices ADF7242 diversity transceiver (RTX), a 4 MB onboard flash memory, a compact low-power Silicon Laboratories C8051F921 microcontroller (MCU), and a three-axis accelerometer. These components are deployed on the feed plane of a dual-polarized textile antenna. For more details, the reader is referred to [68].

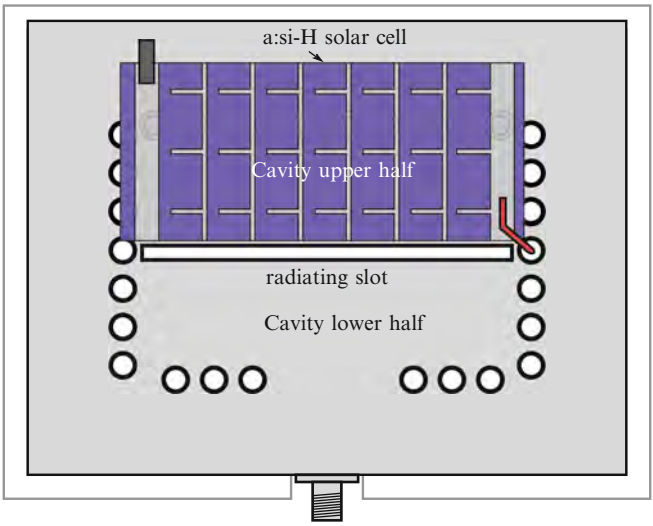

a Top view of SIW cavity-backed slot antenna with solar cell

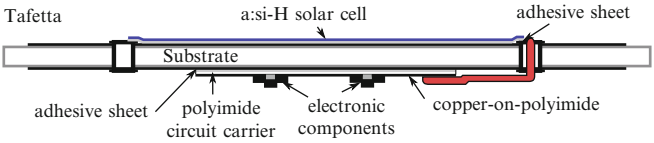

b Cross-section of textile/polyimide antenna

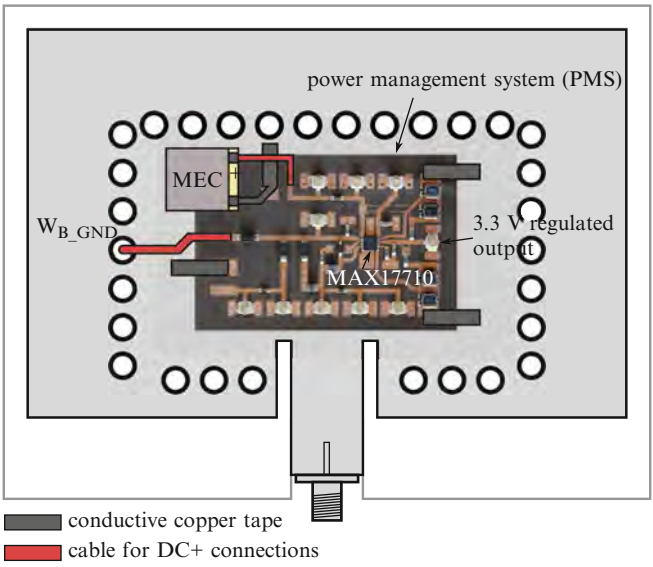

c Bottom view of SIW cavity with power management system

Fig. 5 Textile SIW cavity-backed solar slot antenna (2.45 GHz ISM band + 4G LTE band 7). Flexible solar cells integrated on top and power management system on the bottom of antenna cavity

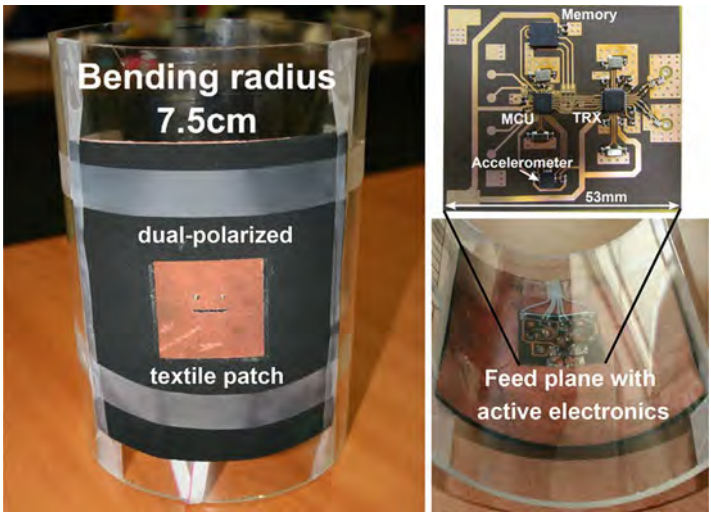

Fig. 6 Flexible dual-polarized textile microstrip patch antenna with integrated wireless node (transceiver, microcontroller, memory, and accelerometer) on an ultraflexible polyimide substrate

Textile Multi-antenna Systems

MIMO Techniques for Textile Antenna Systems

Body-centric communication channels suffer from different levels of signal variations that may drastically reduce the reliability of the wireless communication. At the smallest space and time scales, multipath fading occurs, which may be particularly important in indoor environments and may lead to signal level variations up to 40 dB. At the larger time and space scales, shadowing fluctuations take place, which in a body-centric setting are even more emphasized by body shadowing. Without specific measures to overcome shadowing and fading, higher transmit powers are typically required to achieve acceptable bit error rates (BERs), which seriously increases the weight of the system due to larger battery size and/or reduces the wearable system's autonomy. Fortunately, a wide range of diversity techniques exist, which are extremely efficient in overcoming fading and shadowing by setting up multiple, statistically independent, propagation paths. In this respect, the wearable wireless system can make beneficial use of the large real estate that a garment offers as an integration platform for the deployment of multiple wearable transmit/receive units, implementing these paths.

In terms of receive diversity systems, it is recommended to deploy at least one textile antenna in the front section and one in the rear section of the torso. Although the imbalance in average power on both antennas is undesired to counter multipath fading, this configuration is highly effective in mitigating body shadowing effects,

thanks to its inherent combined pattern/spatial diversity gain. Additional improvements in link reliability may be obtained by higher-order receive diversity schemes, either by adding additional textile antennas, integrated, for example, in the left and right sleeve sections, or by relying on polarization diversity, implemented by deploying dual-polarized antennas. The performance of the latter combined pattern/spatial/polarization receive diversity configuration is slightly worse than the former scheme, but the additional cost of deploying more textile antennas does not warrant the additional benefits in channel diversity gain.

To implement transmit diversity, the wireless wearable system designer may rely on the Alamouti code to achieve second-order diversity, or on higher-order space-time codes, which realize larger diversity gains at the cost of either being non-orthogonal or operating at a lower rate than the uncoded transmission. Again, at least one textile antenna should be positioned in the front part of the torso and one in the rear, to optimally counter body shadowing. By combining this configuration with a receive diversity system deployed at the fixed access point, complete multiple-input multiple-output (MIMO) diversity schemes [69] are obtained, which implement highly reliable wireless off-body links using low transmit power. In a realistic setup, it is, however, important to bear in mind that an increase in measured instantaneous signal levels not always automatically results in a reduction in the number of bit errors experienced in a wireless transmission. The reason is that, in an actual wireless transmission of data, the wireless channel state is unknown to both transmitter and receiver. To correctly decode and demodulate the received signal, the receiver will have to estimate the wireless channel state at each time instant. In very noisy channel conditions, occurring in case of low received signal levels, additional bit errors will be generated during decoding and demodulation of the data, due to imperfect channel estimation. In this case of erroneous channel estimation, the space-time codes do not provide the full diversity gain expected from theory. Note that, the more complex the MIMO coding scheme one applies, the more critical its performance will depend on the availability of reliable channel estimates. Indeed, a larger number of textile antennas, used in the MIMO scheme, lead to a rapidly growing complexity of the channel estimation algorithm. Moreover, a small increase of a few dB in received signal strength may allow the estimation algorithm to provide reliable channel state information. This, in turn, may lead to a reduction of the number of bit errors by several orders of magnitude, as the availability of correct channel state information then enables the MIMO scheme to fully exploit its diversity gain.

Energy-Efficient Multi-antenna Processing Techniques

Although multi-antenna processing techniques, such as diversity combining and space-time coding, offer large potential benefits in terms of channel reliability, the algorithms implementing these schemes incur an additional cost in terms of processing power to generate the codes at the transmit side and to accurately estimate channel state information and subsequently decode the data at the receive

side. Given the limited amount of available energy in a body-centric communication setup, it therefore pays off to study alternative approaches that, although less powerful in combating fading and body shadowing, make more efficient use of the wearable system's available battery power. A first technique that does not require any additional signal processing power consists of performing simple static beamforming to confine the transmitted beam in the vertical direction. This results in a larger received signal level and reduces the number of received multipath components and, therefore, the fading fluctuations. Before transmitting the actual data symbols, a quick calibration procedure may be performed, where the beam is scanned in the vertical direction, along the elevation angle, and the receiver feeds back the received signal levels, after which the transmitter selects the optimal beam for the wireless data transmission. Indoor measurements have proven that, in certain conditions, the beamforming scheme not only outperforms space-time coding in a line-of-sight scenario but also in non-line-of-sight situations, provided that the fixed access point implements receive diversity to cancel out remaining multipath fluctuations. More details are found in [70].

To obtain reliable channel estimates at the receiver, besides the data payload, the transmitter will have to include pilot symbols known to the receiver, introducing overhead as the pilot symbols serve no other purpose than estimating the channel state. To contain the reduction in useful data rate incurred by the pilot symbols, the receiver may track the channel state, after initial training based on the pilot symbols, by relying on data-driven channel estimation. Provided the wireless channel is sufficiently reliable, which may be guaranteed by implementing sufficient diversity gain, also the estimated data sequence may serve as pilot symbols. When the number of bit errors is sufficiently low, the use of estimated data to extract channel state information almost provides the same wireless link performance as channel estimation based on known symbols. An example of such an approach may be found in [71].

A Short Overview of Textile Antenna Applications

The main functionality implemented by electronic systems relying on textile antennas involves wireless communication, localization, and remote sensing. One of the earliest and still most important application domains concerns the wireless transfer of sensor data, voice signals, and/or images originating from rescue, military, or space exploration personnel during interventions or operations. In addition, such information may be collected by systems deployed on patients in eHealth applications. These wirelessly transmitted data are then shared between different team members and/or collected and interpreted by remote coordination and command centers, which may issue instructions and trigger alarms. Many different wireless communication standards may be applied, such as the Wi-Fi, Bluetooth, and ZigBee WLAN standards, as well as the GSM, UMTS, WiMAX, and LTE WMAN protocols.

A wide band of frequencies may be covered by textile antennas, starting from 30 to 80 MHz VHF-LB and 100 MHz FM antennas and extending up to 60 GHz antenna arrays.

Another particularly interesting application for textile antennas concerns Personal Locator Beacons (PLBs) for search and rescue (SAR) at sea, relying on, for example, the COSPAS/SARSAT system operating at 406 MHz. By integrating the antenna together with the PLB directly inside life jackets [72, 73], the PLB cannot be forgotten by the wearer and is always present when needed. Moreover, the antenna is well protected against the harmful effects of seawater, and its radiation pattern is nicely oriented toward the COSPAS/SARSAT satellites whenever the life jacket is deployed. Localization is another highly relevant functionality of wearable systems. Circularly polarized textile antennas have been designed for global navigation satellite systems (GNSS) [67], such as GPS, Galileo, and GLONASS. Several such textile antenna prototypes were developed, covering one or more of the civilian and military bands. Specific attention should be paid to the deployment of these antennas, since at least three satellites should be in the line of view to perform accurate localization. Hence, the best locations to integrate these antennas are the shoulder sections of a garment or the helmet. Of course, such satellite localization is only useful in outdoor scenarios. Therefore, the wearable system may be extended with functionality implementing indoor localization, making use of time-of-arrival or power-based techniques that rely on Wi-Fi or UWB textile antennas.

As a final application, the use of textile antennas as part of a wearable remote sensing system is discussed. As an example, textile antennas may be part of a wearable Doppler radar system for the detection of persons behind walls and closed doors or for finding victims under rubble. To ensure sufficient isolation between the transmit and receive parts of the radar, different transmit and receive antennas, with opposite circular polarization, may be applied. Moreover, an antenna array may be used to determine the direction in which the person is located. More details of such a system are found in [74].

Summary

Textile antennas have been extensively studied for more than a decade now. Most textile antenna designs up to now were performed by universities and research labs, with as main purpose to develop a proof of concept textile antenna prototype for a certain application, without having a specific commercial product in mind. Up to now, very few commercial products that contain textile antennas are on the market. The main reasons are reliability issues, where the soldered or glued connections between textile fabrics and electronic components form weak points that easily break under realistic deployment conditions, and problems concerning the maintenance of the smart fabric containing the electronic system. Indeed, up to now, repeated washing or dry cleaning cycles could deteriorate the wearable system performance to such an extent that the system stopped functioning after a few

maintenance cycles. At this moment, research is ongoing to solve these issues, and some promising more reliable systems that can withstand repeated cleaning have been proposed. Another important issue is cost and complexity of such systems. Efforts are ongoing to develop dedicated textile mass production techniques for the fabrication of textile antennas. In the meanwhile, designers are focusing on reducing system complexity by, for example, relying on a modular set of wirelessly interconnected wearable modules instead of one large smart textile system consisting of many distributed sensors that are all interconnected by wires integrated into the garment. Given all these recent steps, it is expected that textile antennas will be part of many new exciting wearable systems in the near future.

References

1. Hertleer C, Tronquo A, Rogier H, Van Langenhove L (2008) The use of textile materials to design wearable microstrip patch antennas. Text Res J 78(8):651–658
2. Salvado R, Loss C, Gonçalves R, Pinho P (2012) Textile materials for the design of wearable antennas: a survey. Sensors 12(11):15841–15857
3. Scarpello ML, Kazani I, Hertleer C, Rogier H, Vande Ginste D (2012) Stability and efficiency of screen-printed wearable and washable antennas. IEEE Antennas Wirel Propag Lett 11:838–841
4. Kellomäki T, Virkki J, Merilampi S, Ukkonen L (2012) Towards washable wearable antennas: a comparison of coating materials for screen-printed textile-based UHF RFID tags. Int J Antennas Propag. Article ID 476570, 11 pp
5. Hertleer C, Rogier H, Vallozzi L, Van Langenhove L (2009) A textile antenna for off-body communication integrated into protective clothing for firefighters. IEEE Trans Antennas Propag 57(4):919–925
6. Hertleer C, Van Laere A, Rogier H, Van Langenhove L (2010) Influence of relative humidity on textile antenna performance. Text Res J 2:177–183
7. Wang Z, Zhang L, Volakis J (2013) Textile antennas for wearable radio frequency applications. Text Light Ind Sci Technol 2(3):105–112
8. Wang J, Zhang L, Bayram Y, Volakis J (2012) Embroidered conductive fibers on polymer composite for conformal antennas. IEEE Trans Antennas Propag 60(9):4141–4147
9. Kaufmann T, Fumeaux I, Fumeaux C (2013) Comparison of fabric and embroidered dipole antennas. In: Antennas and propagation (EuCAP), 2013 7th European conference, Gothenburg, Denmark, pp 3252–3255
10. Chauraya A, Whittow W, Vardaxoglou J, Li Y, Torah R, Yang K, Beeby S, Tudor J (2013) Inkjet printed dipole antennas on textiles for wearable communications. IET Microwaves Antennas Propag 7(9):760–767
11. Whittow W, Chauraya A, Vardaxoglou J, Yi L, Torah R, Kai Y, Beeby S, Tudor J (2014) Inkjet-printed microstrip patch antennas realized on textile for wearable applications. IEEE Antennas Wirel Propag Lett 13:71–74
12. Kazani I, Scarpello ML, Hertleer C, Rogier H, De Mey G, Guxho G, Van Langenhove L (2012) Washable screen printed textile antennas, smart and interactive textiles, advances in science and technology. In: Symposium on smart and interactive textiles of CIMTEC/4th, international conference on smart materials, structures and systems, vol 80, Montecatini Terme, 10–14 June 2012, pp 118–122
13. Kaufmann T, Fumeaux C (2013) Wearable textile half-mode substrate-integrated cavity antenna using embroidered vias. IEEE Antennas Wirel Propag Lett 12:805–808
14. Moro R, Agneessens S, Rogier H, Bozzi M (2012) Wearable textile antenna in substrate integrated waveguide technology. IET Electron Lett 48(16):985–987

15. Agneessens S, Rogier H (2014) Compact half diamond dual-band textile HMSIW on body antenna. IEEE Trans Antennas Propag 62(4):2374–2381
16. Declercq F, Rogier H, Hertleer C (2008) Permittivity and loss tangent characterization for garment antennas based on a new matrix-pencil two-line method. IEEE Trans Antennas Propag 56(8):2548–2554
17. Declercq F, Couckuyt I, Rogier H, Dhaene T (2013) Environmental high frequency characterization of fabrics based on a novel surrogate modelling antenna technique. IEEE Trans Antennas Propag 61(10):5200–5213
18. Bal K, Kothari VK (2009) Measurement of dielectric properties of textile materials and their applications. Indian J Fibre Text Res 34:191–199
19. Bal K, Kothari VK (2010) Permittivity of woven fabrics: a comparison of dielectric formulas for air-fiber mixture. IEEE Trans Dielectr Electr Insul 17(3):881–889
20. Lilja J, Salonen P (2009) Textile material characterization for SoftWear antenna. In: Proceedings 28th IEEE conference on military communications, Piscataway, pp 628–634
21. Bouttout F, Benabdelaziz F, Benghalia A, Khedrouche D, Fortaki T (1999) Uniaxially anisotropic effects on resonance of rectangular microstrip patch antenna. IEE Electron Lett 35(4):255–256
22. Sankaralingam S, Gupta B (2010) Determination of dielectric constant of fabric materials and their use as substrates for design and development of antennas for wearable applications. IEEE Trans Instrum Meas 59(12):3122–3130
23. Lilja J, Salonen P, de Maagt P (2009) Environmental characterization of industrial fabric for SoftWear antenna. In: Proceedings IEEE Antennas and Propagation Society international symposium, Charleston, SC, USA, pp 1–4
24. Lilja J, Salonen P, Kaija T, de Maagt P (2012) Design and manufacturing of robust textile antennas for harsh environments. IEEE Trans Antennas Propag 60(9):4130–4140
25. Sanjari H, Merati A, Varkiani S, Tavakoli A (2014) A study on the effect of compressive strain on the resonance frequency of rectangular textile patch antenna: elastic and isotropic model. J Text Inst 105(2):156–162
26. Virkki J, Björninen T, Kellomäki T, Merilampi S, Shafiq I, Ukkonen L, Sydänheimo L, Chan YC (2014) Reliability of washable wearable screen printed UHF RFID tags. Microelectron Reliab 54(4):840–846
27. Shaw RK, Long BR, Werner DH, Gavrin A (2007) The characterization of conductive textile materials intended for radio frequency applications. IEEE Antennas Propag Mag 49(3):28–40
28. Yuehui O, Chappell W (2008) High frequency properties of electro-textiles for wearable antenna applications. IEEE Trans Antennas Propag 56(2):381–389
29. Lilja J, Salonen P, de Maagt P (2009) Characterization of conductive textile materials for SoftWear antenna. In: Proceedings IEEE Antennas and Propagation Society international symposium, Charleston, SC, USA, pp 1–4
30. Locher I, Klemm M, Kirstein T, Tröster G (2006) Design and characterization of purely textile patch antennas. IEEE Trans Adv Pack 29:777–788
31. King HE, Wong JL (1977) Effects of a human body on a dipole antenna at 450 and 900 MHz. IEEE Trans Antennas Propag 25(3):376–379
32. Kellomaki T, Heikkinen J, Kivikoski M (2006) Wearable antennas for FM reception. In: EuCAP 2006 European conference on antennas and propagation, Nice, pp 1–6
33. Winterhalter C, Teverovsky J, Wilson P, Slade J, Horowitz W, Tierney E, Sharma V (2005) Development of electronic textiles to support networks communications, and medical applications in future U.S. Military protective clothing systems. IEEE Trans Inf Technol Biomed 9 (3):402–406
34. Roh J-S, Chi Y-S, Lee J-H, Tak Y, Nam S, Kang TJ (2010) Embroidered wearable multiresonant folded dipole antenna for FM reception. IEEE Antennas Wirel Propag Lett 9:803–806
35. Psychoudakis D, Volakis JL (2009) Conformal asymmetric meandered flare (AMF) antenna for body-worn applications. IEEE Antennas Wirel Propag Lett 8:931–934

36. Lee GY, Psychoudakis D, Chen CC, Volakis JL (2011) Omnidirectional vest-mounted body-worn antenna system for UHF operation. IEEE Antennas Wirel Propag Lett 10:581–583
37. Paul DL, Giddens H, Paterson MG, Hilton GS, McGeehan JP (2013) Impact of body and clothing on a wearable textile dual band antenna at digital television and wireless communications bands. IEEE Trans Antennas Propag 61(4):2188–2194
38. Klemm M, Troester G (2006) Textile UWB antennas for wireless body area networks. IEEE Trans Antennas Propag 54(11):3192–3197
39. Lui K, Murphy O, Toumazou C (2013) A wearable wideband circularly polarized textile antenna for effective power transmission on a wirelessly-powered sensor platform. IEEE Trans Antennas Propag 61(7):3873–3876
40. Zhu S, Langley R (2009) Dual-band wearable textile antenna on an EBG substrate. IEEE Trans Antennas Propag 57(4):926–935
41. Raad HR, Abbosh AI, Al-Rizzo HM, Rucker DG (2013) Flexible and compact AMC based antenna for telemedicine applications. IEEE Trans Antennas Propag 61(2):524–531
42. Soh PJ, Vandenbosch GAE, Ooi SL, Rais NHM (2012) Design of a broadband all-textile slotted PIFA. IEEE Trans Antennas Propag 60(1):379–384
43. Boeykens F, Rogier H, Vallozzi L (2014) An efficient technique based on polynomial chaos to model the uncertainty in the resonance frequency of textile antennas due to bending. IEEE Trans Antennas Propag 62(3):1253–1260
44. Lemey S, Declercq F, Rogier H (2014) Dual-band substrate integrated waveguide textile antenna with integrated solar harvester. IEEE Antennas Wirel Propag Lett 13:269–272
45. Samal P, Soh P, Vandenbosch G (2014) UWB all-textile antenna with full ground plane for off-body WBAN communications. IEEE Trans Antennas Propag 62(1):102–108
46. Grimm M, Manteuffel D (2014) Norton surface waves in the scope of body area networks. IEEE Trans Antennas Propag 62(5):2616–2623
47. Conway GA, Scanlon WG (2009) Antennas for over-body-surface communication at 2.45 GHz. IEEE Trans Antennas Propag 57(4):844–855
48. Akhoondzadeh-Asl L, Nechayev Y, Hall PS, Constantinou CC (2013) Parasitic array antenna with enhanced surface wave launching for on-body communications. IEEE Trans Antennas Propag 61(4):1976–1985
49. Chahat N, Zhadobov M, Le Coq L, Sauleau R (2012) Wearable endfire textile antenna for on-body communications at 60 GHz. IEEE Antennas Wirel Propag Lett 11:799–802
50. Salonen P, Sydänheimo L, Keskilammi M, Kivikoski M (1999) A small planar inverted-F antenna for wearable applications. In: Third international symposium on wearable computers, San Francisco, CA, USA, pp 95–100
51. Massey PJ (2001) Mobile phone fabric antenna integrated within clothing. In: Eleventh international conference on antennas and propagation IEE conference publication N° 480, Manchester, pp 344–347
52. Salonen P, Sydädnheimo L (2002) Development of an S-band flexible antenna for smart clothing. IEEE Antennas Propag Soc Int Symp 3:6–9, San Antonio, TX, USA
53. Salonen P, Hurme L (2003) A novel fabric WLAN antenna for wearable applications. IEEE Antennas Propag Soc Int Symp 2:700–703, Columbus, OH, USA
54. Salonen P, Rahmat-Samii Y, Kivikoski M (2004) Wearable antennas in the vicinity of human body. In: IEEE antennas and propagation society international symposium, Monterey, pp 467–470
55. Salonen P, Rahmat-Samii Y, Hurme H, Kivikoski M (2004) Effect of conductive material on wearable antenna performance: a case study of WLAN antennas. In: IEEE antennas and propagation society international Symposium, vol 1, Monterey, pp 463–466
56. Tronquo A, Rogier H, Hertleer C, Van Langenhove L (2006) A robust planar textile antenna for wireless body LANs operating in the 2.45-GHz ISM band. IEE Electron Lett 42 (3):142–143
57. Locher I, Klemm M, Kirstein T, Tröster G (2006) Design and characterization of purely textile patch antennas. IEEE Trans Adv Packag 29(4):777–788

58. Kellomäkki T, Heikkinen JJ, Kivikoski MA (2006) Effects of bending GPS antennas. In: Proceedings of Asia-Pacific microwave conference, Yokohama, Japan, pp 1–4
59. Hertleer C, Tronquo A, Rogier H, Van Langenhove L (2007) An aperture-coupled patch antenna for integration into wearable textile systems. IEEE Antennas Wirel Propag Lett 6:392–395
60. Vallozzi L, Rogier H, Hertleer C (2008) Dual polarized textile patch antenna for integration into protective garments. IEEE Antennas Wirel Propag Lett 7:440–443
61. Vallozzi L, Rogier H, Hertleer C (2009) Design of a protective garment GPS antenna. Microw Opt Technol Lett 51:1504–1508
62. Bai Q, Langley R (2009) Crumpled textile antennas. IEE Electron Lett 45(9):436–438
63. Kennedy TF, Fink PW, Chu AW, Champagn NJ, Lin GY, Khayat M (2009) A body-worn E-textile antennas : the good, the low-mass, and the conformal. IEEE Trans Antennas Propag 57(4):910–918
64. Salonen P, Keskilammi M (2008) SoftWear antenna. In: Military communications conference, San Diego, CA, pp 1–6
65. Salonen P, Keskilammi M, Rahmat-Samii Y (2008) Textile antennas: effect of antenna bending on radiation pattern and efficiency. In: IEEE antennas and propagation society international symposium, San Diego, pp 1–4
66. Declercq F, Rogier H (2010) Active integrated wearable textile antenna with optimized noise characteristics. IEEE Trans Antennas Propag 58:3050–3054
67. Dierck A, Agneessens S, Declercq F, Spinnewyn B, Stockman G, Van Torre P, Vallozzi L, Vande Ginste D, Vanfleteren J, Vervust T, Rogier H (2014) Active textile antennas in professional garments for sensing, localisation and communication. Int J Microw Wirel Technol 6:331–341
68. Vanveerdeghem P, Van Torre P, Stevens C, Knockaert J, Rogier H (2014) Flexible dual-diversity wearable wireless node integrated on a dual-polarised textile patch antenna. IET Sci Meas Technol 8(6):452–458, doi:10.1049/iet-smt.2013.0224, Print ISSN 1751-8822, Online ISSN 1751–8830
69. Van Torre P, Vallozzi L, Rogier H, Moeneclaey M, Hertleer C, Verhaevert J (2011) Indoor off-body wireless MIMO communication with dual polarized textile antennas. IEEE Trans Antennas Propag 59(2):631–642
70. Van Torre P, Scarpello ML, Vallozzi L, Rogier H, Moeneclaey M, Vande Ginste D, Verhaevert J (2012) Indoor off-body wireless communication: static beamforming versus space-time coding. Int J Antennas Propag. Article ID 413683, 13 pp. doi:10.1155/2012/413683
71. Van Torre P, Vallozzi L, Rogier H, Moeneclaey M, Verhaevert J (2010) Channel characterization and robust tracking for diversity reception over time-variant off-body wireless communication channels. EURASIP J Adv Signal Process (Special Issue on Robust Processing of Nonstationary Signals). Article ID 978085, 13 pp. doi:10.1155/2010/978085
72. Serra A, Nepa P, Manara G (2012) A wearable two-antenna system on a life jacket for cospas-sarsat personal locator beacons. IEEE Trans Antennas Propag 60(2):1035–1042
73. Lilja J, Pynttari V, Kaija T, Makinen R, Halonen E, Sillanpaa H, Heikkinen J, Mantysalo M, Salonen P, de Maagt P (2013) Body-worn antennas making a splash: lifejacket-integrated antennas for global search and rescue satellite system. IEEE Antennas Propag Mag 55 (2):324–341
74. Agneessens S, Van Torre P, Declercq F, Spinnewyn B, Stockman G, Rogier H, Vande Ginste D (2012) Design of a wearable, low-cost, through-wall doppler radar system. Int J Antennas Propag. Article ID 840924, 9 pp. doi:10.1155/2012/840924
75. Chen LF, Ong CK, Neo CP, Varadan VV, Varadan VK (2004) Microwave electronics: measurements and materials characterization, 1st edn. Wiley, Chichester
76. Yue H, Virga KL, Prince JL (1998) Dielectric constant and loss tangent measurement using a stripline fixture. IEEE Trans Compon Packag Manuf Technol 21(4):441–446
77. Seager R, Zhang S, Chauraya A, Whittow W, Vardaxoglou Y, Acti T, Dias T (2013) Effect of the fabrication parameters on the performance of embroidered antennas. IET Microwaves Antennas Propag 7(14):1174–1181

Energy-Harvesting Fabric Antenna

18

Alessandra Costanzo and Diego Masotti

Contents

Introduction 460
Wearable Material Selection 461
Dielectric Fabrics 462
Conductive Fabrics 463
Electromagnetic Characterization of Wearable Materials 464
Textile Multiband Antenna Design 466
Integration of the Textile Antenna with a Rectifier Circuit 475
Power Management Unit Design 479
Summary 483
References 483

Abstract

The exploitation of novel fabrics, in place of standard substrates and metallizations, in the realization of radio-frequency energy-harvesting systems – commonly referred to as rectennas, rectifying antennas – for body area network applications is deeply discussed in this chapter. The use of these unconventional materials makes the design approach a delicate issue: firstly, the electromagnetic characterization of fabrics is needed; furthermore, the effects of bending of the whole system as well as the proximity to human tissue must be considered in the optimization procedure. The consequences of an approximate approach in the design of wearable rectennas could lead to significant deviations from the final prototype performance. For these reasons, we consider a computer-aided platform, which

A. Costanzo (✉)
DEI, University of Bologna, Cesena, Italy
e-mail: alessandra.costanzo@unibo.it

D. Masotti
DEI, University of Bologna, Bologna, Italy
e-mail: diego.masotti@unibo.it

© Springer Science+Business Media Singapore 2015

X. Tao (ed.), *Handbook of Smart Textiles*,
DOI 10.1007/978-981-4451-45-1_31

relies on the combination of full-wave solvers and nonlinear circuit-level tools, through the rigorous application of the electromagnetic theory: this way, the unavoidable electromagnetic couplings between different system sections and the dispersive/nonlinear behavior of the entire rectenna. In this way, the actual available power at the rectifier input port is accurately taken into account. The procedure is deeply described in this chapter through the stepwise analysis of the project of a fully wearable, fully autonomous tri-band rectenna. The experimental characterization of the prototype is used to provide a validation of the design procedure. The two-step procedure consists of the design of the rectenna with a fixed load in radio-frequency (RF) stationary conditions followed by the transient baseband design of the power management unit which acts as a dynamically variable load, depending on the actual incident RF power.

Keywords

Energy harvesting • Planar antenna • Wearable material • Body area network • Nonlinear circuits • Rectifier • Rectifying antenna • Electromagnetic simulation • Circuit simulation • Harmonic balance technique

Introduction

The need for pervasive distributed microsystems is progressively penetrating into human lives. This demands for a large number of small-size mobile devices to be distributed in different indoor and outdoor ambients to be exploited in many applications from agricultural monitoring to smart home appliances and smart clothing for monitoring environmental or vital parameters.

Such devices must be wireless, need to be integrated with antennas for communication, and must be of reduced cost and possibly energy autonomous with no need for maintenance. Operation with ultralow power requirements has been already successfully demonstrated [1] so that batteries are no longer required and energy can be harvested from the available energy in the ambient. Indeed the environment is an intrinsic source of low-density highly available energy [2] in either steady or intermittent and irregular forms such as vibrations [3], thermal gradients [4], indoor light [5], and electromagnetic radiation [6].

RF radiation is almost always available in many humanized environments, but it is available in a highly reduced amount and highly variable and intermittent. As an example, GSM or UMTS communication mobile terminals set their output power according to the directive imposed by the base station. WiFi spots are present in many ambient but with extremely reduced power densities. In this context, reliable models of RF energy sources have been developed to contribute in estimating the available power and the behavior of energy sources when subject to specific excitations [7–9].

One of the most promising applications of energy-harvesting fabric antennas is the implementation of body area network (BAN) which consists of a wireless network of wearable computing devices that may be either embedded inside the

body or surface mounted on the body in a fixed position. In the last case, people can carry these devices in different positions: distributed in clothes and pockets and handled by hand. This allows to implement communications for both health monitoring and entertainment for high rescue applications. In order to comply with the need for wearable, energy-aware, miniaturized wireless systems, fabrics already available in the market can be studied as possible substrates and conductors for the realization of the antenna part of the wireless systems in a flat printed-like configuration. Indeed, traditional rigid technological substrates adopted in current RF printed circuit technologies are not suitable to be embedded in garments. For this purpose, electrical models for fabrics with dielectric and conductive properties need to be exploited. Furthermore, techniques to effectively assemble such systems need to be carefully searched for, starting from the background of printed circuit to carrying out an extensive characterization of the system embedded in the proper ambient. This means that these system performances, especially the antenna parts, must be robust with respect to deformations, folds, and even temperature changes. Another issue is represented by the physical implementation of the nonlinear circuit, which is connected to the antenna port to provide DC power and voltages: component soldering to textile metallization layer is a delicate task, and its stability with respect to fabric deformation needs to be checked.

An overview of textile materials that may be suitable for realizing that planar antennas are easily embedded in garments is first provided in this chapter. Then their dielectric and conductive properties are discussed, and a procedure based on the rigorous characterization of the dispersive behavior of the transmission line technology is presented for a precise definition of the materials at the frequency bands of operation. The design of a textile-based multiband antenna and its rectifying circuits are then presented for RF harvesting from ambient available sources. First, the antenna design is described by electromagnetic theory, and then a numerical validation is presented to characterize both the near-field and the far-field behavior of the antenna in stand-alone conditions and in the vicinity of human tissues. A stepwise procedure to be adopted is detailed, which is based on the concurrent use of electromagnetic software tools and nonlinear circuit-level techniques, able to simultaneously predict the actual system behavior of an antenna system, consisting of the radiating and of the nonlinear blocks, at the component level.

Few representative applications are also discussed.

Wearable Material Selection

In the realization of wearable antenna, one of the biggest challenges is to choose materials from the textile industry suitable for being exploited for both substrates and metallic layers. Indeed such materials need to be fully integrated into everyday or technical clothes. In order to reach a successful design of the radiating parts, the electromagnetic characterization of these clothes is needed and usually is not available from the producer. Dispersive behavior of the electromagnetic

characteristic is also very important to predict the actual antenna performance in the frequency band of interest. Furthermore, effects of bending and stressing of the fabrics are also needed for a reliable design of antenna with wearable materials, which are entirely made out of flexible textile materials in order to integrate the antenna into clothes, thus making it mobile. The effects of antenna bending and human tissue on antenna characteristics are also of primary importance. In the following, a number of fabrics are analyzed with respect to their electrical characteristics.

Dielectric Fabrics

Ordinary fabrics have been already used as antenna substrate (e.g., fleece [10, 11], jeans [11], rubber [12]), demonstrating that either planar patch antennas can be realized on a wide variety of flexible supports, and the most delicate choice relies on the conductive material. Another interesting possibility is the flexible foam material [13], commonly used in protective clothing as additional protection for vulnerable body parts. An interesting aspect of this material is that it regains its original form after being exposed to compression so that the antenna characteristics remain stable in time.

Due to their intrinsic porosity, fabrics have quite low dielectric constant values, ranging from 1 to 2; in particular, flexible foam reaches values very close to unit. But, as previously stated, the exact knowledge of this electromagnetic characteristic of the selected material is mandatory in order to establish the value of the so-called guided-wavelength, roughly given by

$$\lambda_g = \frac{\lambda_0}{\sqrt{\varepsilon_r}} \tag{1}$$

where λ_0 is the free-space wavelength and ε_r is the (real) relative permittivity of the substrate. The guided-wavelength knowledge allows to establish the antenna dimension, typically being half-wavelength long. The porosity of these substrates adds another criticality in wearable antenna design, since the air humidity can change the substrate characteristics [14] and must then be controlled in practical applications.

However, the antenna performance strongly depends on the losses in the fabric material. Therefore, the complex permittivity value has to be known, $\varepsilon_r = \varepsilon_r' - j\varepsilon_r''$, or in alternative ε_r' and the loss tangent $\tan\delta = \varepsilon_r''/\varepsilon_r'$. The radiation efficiency of the antenna is strictly related to the loss-tangent value: the higher the losses, the lower the efficiency.

Moreover, the thickness of the fabric substrate is another important parameter to be taken under control in wearable solutions: in fact, thicker substrates typically guarantee (i) better antenna radiating performance, since the fringing effect of the electric field and consequently the radiation mechanism of the patch antenna are enhanced, and (ii) a larger bandwidth, antenna quality factor inversely related to

the thickness. Unfortunately, the thickness of extremely porous fabrics can change depending on the presence or not of attached conductive materials. For this reason, the actual thickness of the substrate should be measured after the conductive layer deposition.

For all these reasons, the electromagnetic characterization of wearable dielectrics, described in the following, is a challenging and mandatory issue.

However, for some commercialized materials, information on electromagnetic properties can be available. For instance, with decreasing values of losses, there are cotton with $\varepsilon_r' = 1.6$ and $\tan\delta = 0.04$, polyester (100 %) with $\varepsilon_r' = 1.9$ and $\tan\delta = 0.004$, and Quartzel with $\varepsilon_r' = 1.95$ and $\tan\delta = 0.0004$.

Conductive Fabrics

Conductive material for RF and microwave applications needs to be realized with minimum thickness (of the order of tens of microns, since the typical thickness of the metallic layers is 35 μm), with the lowest and most stable electrical resistance. These characteristics guarantee the use of conductive fabrics with minimum losses.

Furthermore, in order to make it possible to realize printed circuits and antennas, the conductive material sheets need to be flat and homogeneous to ensure constant resistance over a wide area. Indeed, for the realization in the UHF band, and the standard cell phone bands, printed antenna areas are of the order of few centimeters square so that the homogeneous requirement is essential for reliable wearable antennas. However, this is not easy to be reached since these materials are realized for nontechnical wearable applications. In other words, in order to exploit a material for the rectenna conductive part, the variance of the resistance must be small. Furthermore, the fabric should be flexible such that the antenna can be deformed, but its original area can be recovered.

There are three methods of creating conductive fibers: (i) filling of fibers with carbon or metal particles, (ii) coating of fibers with conductive polymers or metal, and (iii) the use of fibers that are completely made of conductive material. These processes may be adopted to realize either conductive threads or uniform electro-textiles, and these two may be chosen based on the selected antenna topology. Conductive threads are created from single or multiple strands of conductive and nonconductive fibers. Electro-textiles are mostly created by incorporating conductive threads into fabrics by means of weaving and knitting. These processes are shown in Fig. 1. In Fig. 2, few commercially available electro-textiles are shown. A possible solution is the Shieldit Super realized with a rugged plain weave nylon plated with nickel and copper, then coated on one side with conductive acrylic; an alternative is the Flectron, which is realized with high-quality copper-plated nylon ripstop fabric. Finally, Ni/Cu/Co fabric is characterized by high-conductivity, high-flexibility fabric tape with conductive adhesive nickel-, copper-, and cobalt-coated nylon ripstop fabric. The last material is extremely corrosion and tear resistant. Among these, a good choice can be the Flectron material, showing low surface resistivity (less than 0.1 Ω/sq) and able to tolerate a large temperature range

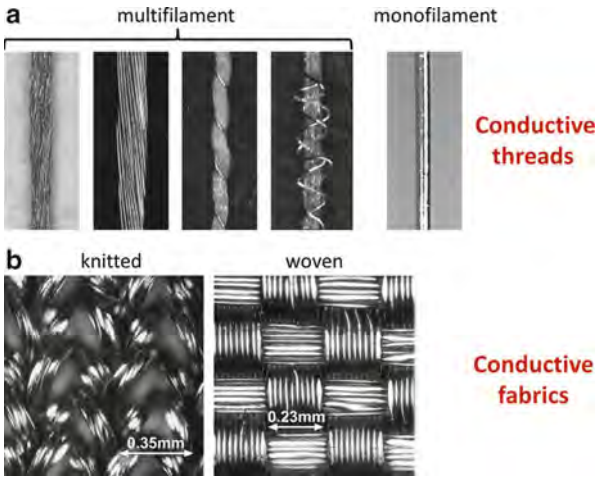

Fig. 1 Process for realizing conductive fabrics: (**a**) conductive threads; (**b**) electro-textile

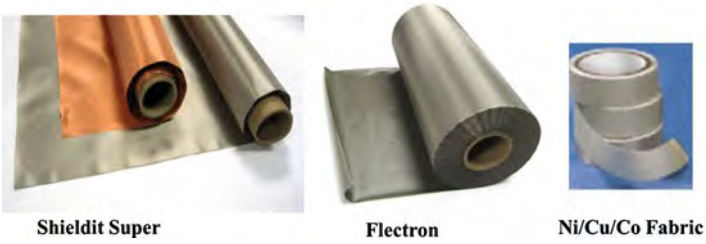

Fig. 2 Commercially available conductive fabrics

(−40° C to 180° C). These are characteristics of particular interest since the fabric enables the soldering of the connector without burning holes in the electro-textile.

Electromagnetic Characterization of Wearable Materials

The characterization of material properties is the first step to be completed before starting the rectenna design. Indeed, the effect of different substrates on the performance of a textile antenna in terms of return loss, bandwidth, and gain characteristics needs to be predicted. Traditional microwave methods of measuring the dielectric properties of a material can be adopted which can be divided into two main categories [15]: (1) nonresonant methods and (2) resonant methods. In both cases, anisotropy contributions, which can be present in textile materials, especially in those realized by multilayered sheets connected by a glue, are not usually accounted for due to their negligible effect.

Nonresonant methods are based on observation of transmission/reflection of electromagnetic waves through/from the material to be characterized and are not very accurate for frequency-dispersive materials. In [16], a very good example for

the adoption of transmission/reflection method for the characterization of fabric materials has been demonstrated for deriving both real and imaginary parts of permittivity. In that work, the well-known two-line method, which measures the propagation characteristics of microstrip lines, is combined with the matrix-pencil technique in order to reduce the perturbations in the transmission line parameters.

Resonant methods are used to get accurate knowledge of dielectric properties at a single frequency or several discrete frequencies. The most traditional ones are based on the characterization of a dielectric resonator whose quality factor and resonant frequency can be directly related to the permittivity and permeability of the material. They adopt a probe of the sample of known volume, which is inserted in predefined resonant cavity: from the perturbation of the measured resonant frequency and quality factor, the probe electromagnetic characteristics are derived. This technique has been widely experimented for rigid material and has the advantage of being narrowband and very accurate if very well-defined dimensions of the probes and its positioning inside the resonant cavity can be established. Resonant methods have been recently focused on the use of microstrip patch radiator, which also possesses the advantage of narrow bandwidth [15]. The most advantageous feature of this technique, which makes it distinct from other standard resonance methods, such as the cavity perturbation method, lies in sample preparation which requires the instruments needed for clothes cutting. Like the cavity resonance technique, this method also yields good measurement accuracy. The limitation of this approach is that it is not able to define the losses of the fabric, thus allowing only a conservative prediction of the wearable antenna performance.

An alternative approach based on resonant modes [17] has been successfully demonstrated in [18] where a simple two-port network in microstrip technology is used to account for the dispersive electromagnetic characteristic of these materials. A T-topology is considered where an open stub is connected to two branches of transmission line. This circuit has been realized by using only the textile materials described above, namely, the fleece for the substrate and the Flectron for the metallizations. The circuit behavior in terms of scattering parameters has been computed parametrically by full-wave electromagnetic simulation with parameters being the complex permittivity of the fleece and the conductivity of the Flectron, starting from estimated values of the quantities. This choice allows to define these parameters by exploiting redundant information due to the multiple resonant frequencies provided by the microstrip stub. The extraction procedure consists of the following three steps: (i) a starting guess of the relative permittivity (ε_r) value is chosen and the design of a T-resonator based on this estimation is carried out; (ii) a database containing the scattering parameters of the T-resonator is built by means of full-wave solvers [19], by changing the complex permittivity of the substrate (i.e., ε_r and the loss tangent) and the Flectron conductivity; and (iii) then the designed resonator is realized on a Flectron substrate 4 mm thick (see Fig. 3a), and the transmission coefficient between port 1 and port 2 (S_{21}) is measured up to 4 GHz: the prototype electromagnetic characteristics are derived from the S-parameter measurements both using [17] and by comparison with the full-wave

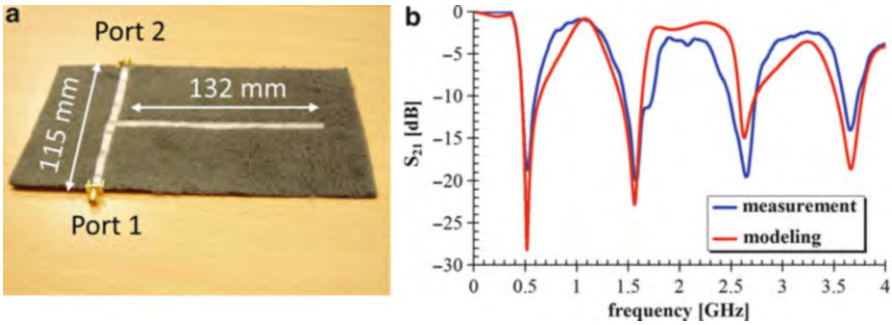

Fig. 3 (**a**) Wearable T-resonator prototype. (**b**) Measured and simulated transmission coefficient behavior versus frequency (**b**, Taken from our Ref. [18] (Conference EuCAP 2010))

database. In the example considered, the identical resulting relative permittivity and loss-tangent values provided by the two approaches are 1.23 and 0.0019, respectively, while the Flectron conductivity turns out to be 1e + 7 (S/m), thus revealing its excellent conductive properties.

In Fig. 3b, the comparison between the transmission coefficient S_{21} obtained from measurement and from the electromagnetic simulation of the T-resonator with the extracted material characteristics clearly demonstrates the effectiveness of the procedure.

Textile Multiband Antenna Design

In the design of a rectenna (wearable or not), a crucial role is played by the adopted architecture. In RF energy-harvesting applications, the choice is typically between the two rectenna solutions reported in Fig. 4: (i) a multi-element antenna with one rectifier for each antenna element and then a combiner acting in DC after conversion [20] and (ii) a single-element antenna with a single rectifier [21, 22]. The first solution does not act as an array because of the absence of the RF combining network. It is a space-consuming solution and forces each antenna to work in the presence of the other "parasitic" elements: this strongly affects the antennas' radiating properties. Moreover, the higher number of diodes is responsible for additional losses, thus justifying this kind of architecture in those scenarios where a sufficient amount of power is available. The second basic solution does not suffer from the previous drawbacks and is suitable for those applications where reduced space is needed and the available RF power is ultralow.

For these reasons, in the following, the attention is devoted to the design of single-antenna/rectifier energy harvesters, in particular for wearable applications. This simpler rectenna architecture is suggested, according to the researchers' experience, especially when multi-standard antennas are envisaged [21, 23, 24]: in fact, the design of such multi-resonant antennas is a demanding task for isolated antennas and could become cumbersome for a multi-antenna solutions, since the

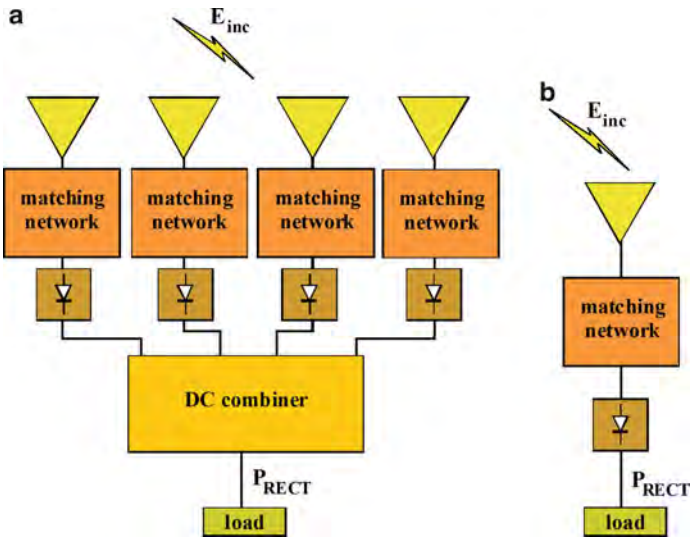

Fig. 4 RF energy harvester architectures: (**a**) multi-antenna multi-rectifier and (**b**) single-antenna single-rectifier solutions (Also used in chapter of book "Green RFID Systems" Cambridge University press, Editor Luca Roselli)

inter-element couplings influence each antenna impedance, thus increasing the difficulties in the design of matching networks.

In the following, the accurate design of a highly efficient, completely wearable tri-band rectenna, consisting of a compact multilayer structure resonating at the GSM 900, GSM 1800, and WiFi frequencies, is described [10, 25]. The frequency selection is recommended by the availability of these wireless standards in almost all the humanized environments and also to the experimental verification that the highest power density occurs in these bands (in particular, the GSM ones) [26]. Of course, dealing with wearable applications makes the rectenna design a more complicated task: in addition to the nontrivial material electromagnetic characterization, it is mandatory to take into account the presence of human body and the use of flexible materials while designing the whole subsystem.

This rectenna is envisaged for technical garments (see Fig. 5), thus exploiting wide areas such as the chest or the back: this is advantageous in the antenna design since wide antenna ground planes simultaneously provide better antenna radiating performance, reduce back radiation in the human body, and make the rectenna less sensible to the background material (body).

The single-antenna/rectifier harvester is arranged in a multilayer architecture, in order to favor a compact solution: in Fig. 2a, b, the adopted stack-up and the exploded view of the final rectenna layout are given. With respect to Fig. 6b, a larger fabric substrate and ground plane are used in the following ($250 \times 250\,\text{mm}^2$) due to the available areas shown in Fig. 5.

The antenna substrate consists of a 4 mm-thick fleece (or pile), whose relative permittivity and loss tangent have been derived in the way discussed in paragraph 3,

Fig. 5 Wearable rectenna placement on a technical garment (Taken from our Ref. [10] (Conference EuCAP 2011))

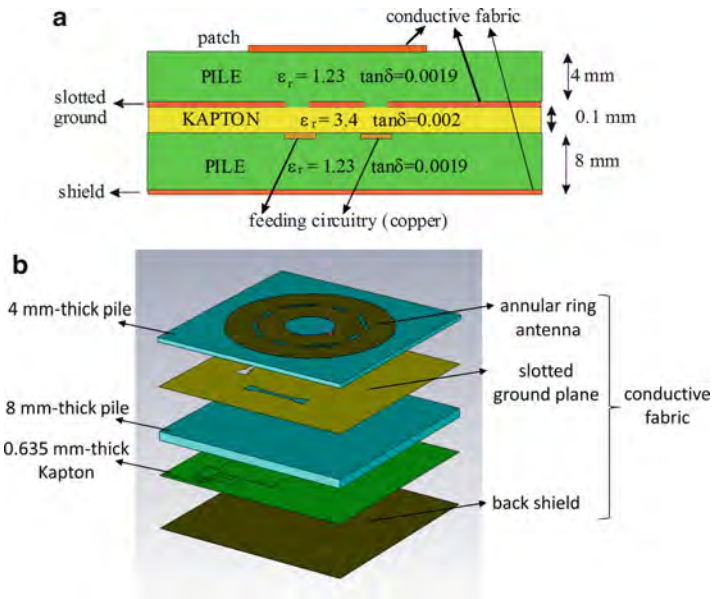

Fig. 6 (**a**) Wearable rectenna stack-up and (**b**) corresponding exploded view, with materials information

and result to be 1.23 and 0.0019, respectively. The Flectron fabric is chosen as the antenna conductive material for its good properties (e.g., conductivity = 1e + 7 (S/m) and its minimal fraying with respect to other fabrics). A thermo-adhesive is used at each pile-conductive fabric interface. An intermediate layer for the rectifying/feeding network is placed between the antenna and the ground plane: it is a flexible and light 0.1 mm-thick Kapton substrate (ε_r = 3.4, tanδ = 0.002) representing the only non-wearable portion of the subsystem; its area is limited to the sole antenna rectifier circuit (matching network, phase shifter, and power divider) for a more

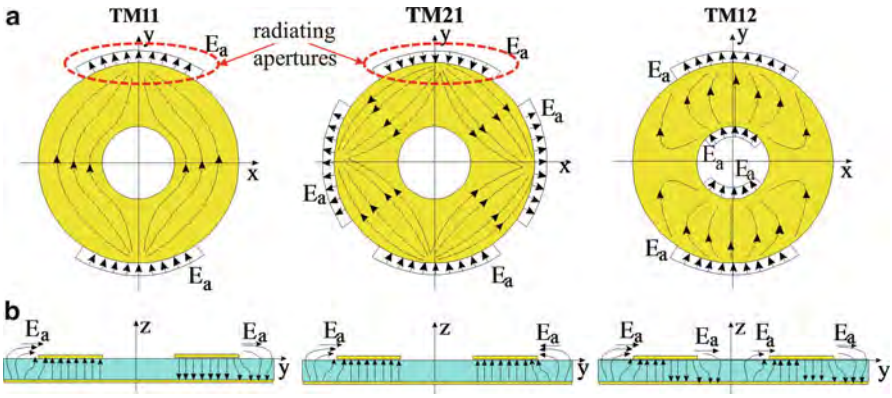

Fig. 7 (**a**) Theoretical electric current patterns for the ring antenna selected modes and corresponding radiating apertures due to (**b**) the electric field fringing effect

comfortable clothing. Note that the larger antenna ground plane is obtained by means of an additional conductive fabric attached to the Kapton layer with a conductive biadhesive frame, thus prolonging the Kapton ground to the desired area.

As rectenna radiator, an annular ring planar topology is chosen for a twofold reason: (i) due to the need to recover energy from 900 MHz, the antenna has to be large and traditional miniaturization strategies (e.g., shorting wall or shorting pins [27, 28]) do not fit with the wearable solution for mechanical reasons. With respect to a standard rectangular or circular patch, where the length or the diameter has to be half-wavelength long, in the annular case, the ring semicircumference mean path must obey to this rule, thus resulting in a smaller metallization. (ii) The annular ring offers both the fundamental and a higher mode with broadside (perpendicular to the antenna plane) radiation, which can be exploited for multiband harvesting purposes. According to the theoretical results given in [29], a suitable inner and outer radii choice could be 21 and 71 mm, respectively: this way, the ring modes selected to cover the two GSM and the WiFi standards are TM11 at 900 MHz, TM21 at 1,750 MHz, and TM12 at 2,450 MHz. In Fig. 7a, the theoretical surface current distributions on the patch metallization at all the frequencies are reported (dashed lines in xy-plane); in the yz-plane (Fig. 7b), the electric field fringing effect (solid lines) is emphasized to show the field on the radiating edge of the patch ("aperture" field $\mathbf{E_a}$), producing the radiating apertures in the xy-plane (not to scale), responsible for the field radiation. From figure inspection, it is easy to justify the broadside radiation of the first and third modes, where the apertures act as in-phase antennas for a two- and four-element array, respectively. The same cannot be said for the intermediate frequency, where the four symmetric apertures provide a null radiation in the broadside direction: but this is not a major concern in harvesting scenarios, where the incoming field direction is usually unknown.

By acting only on inner and outer radii of the patch, it is impossible to exactly place the three modes of the ring in correspondence of the desired frequencies. For this reason, some cuts in the metallization are introduced, as additional antenna

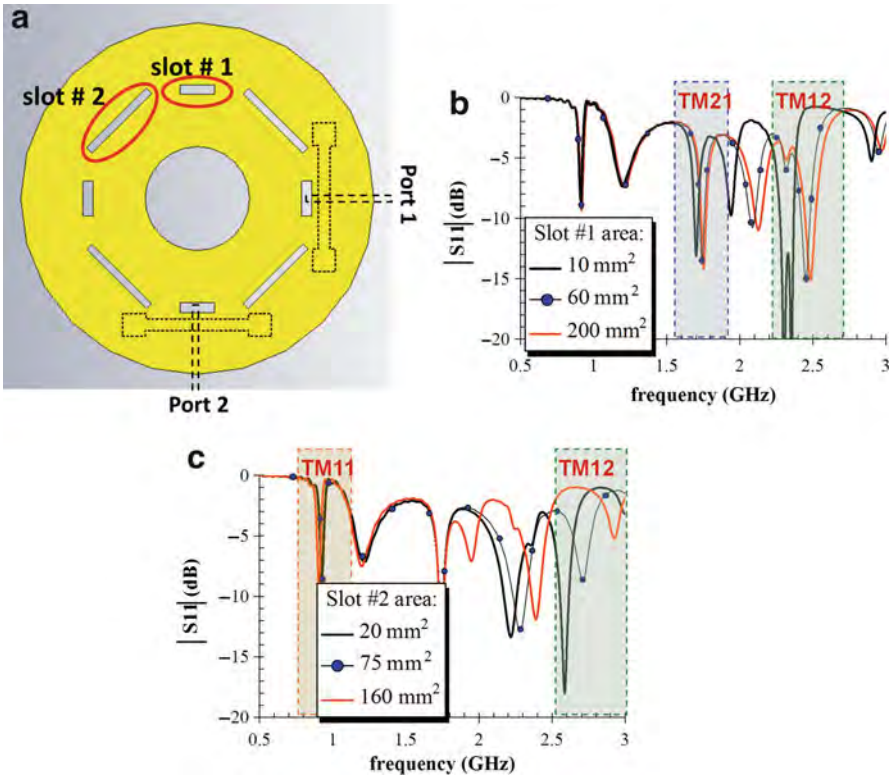

Fig. 8 (**a**) Final layout of the annular ring patch antenna with two microstrip feeding lines (*dashed lines*) and two ground apertures (*dotted lines*); (**b** and **c**) behavior of the reflection coefficient at port 1 as a function of slot 1 and slot 2 areas, respectively

design parameters: the role of these slots is to change the electrical length of the antenna by varying the corresponding mode current path and, as a consequence, to shift the mode resonant frequency. The final topology of the annular ring antenna is reported in Fig. 8a, while Fig. 8b, c demonstrate the effect of the slot area on the frequency tuning of the ring modes, in terms of magnitude of the reflection coefficient seen at port 1 of the back-side microstrip feeding line. The results of Fig. 8b, c indicate that the dimension of slot 1 mainly affects the resonant frequency of the first and third mode, while slot 2 influences the second and third frequencies. This behavior can be also inferred by the theoretical shape of the current paths of Fig. 7a. It has also been experimentally verified that the behavior of the slotted annular ring is not affected by the presence of the cuts in the metallization: as an example, in Fig. 9, the computed surface currents of the slotted ring, with excitation at port 2 only, are plotted for the three selected modes, resonating at the desired frequency; the current amplitude distribution is very similar to the predicted one for the standard ring antenna (Fig. 7a).

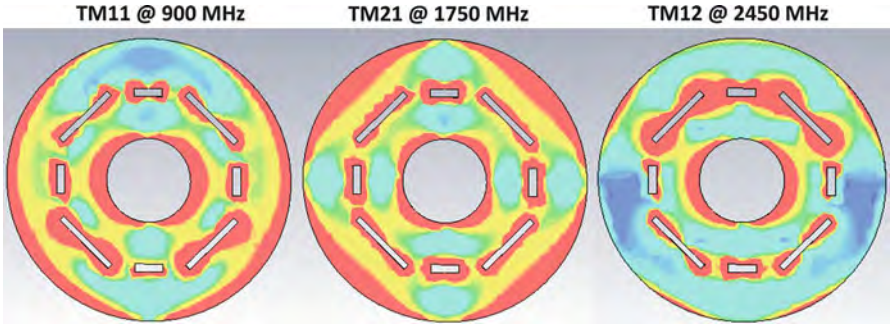

Fig. 9 Computed surface current amplitudes of the slotted annular ring at the three operating frequencies

The unknown reciprocal position of the harvester and of the transmitting antenna suggests a circular polarization at the receiving section: a simultaneous excitation of couples of orthogonal resonant modes at each frequency is then considered for this purpose. The antenna excitation is thus obtained through electromagnetic coupling with two feeding lines (dashed lines in Fig. 8a) located in the Kapton layer underneath the antenna, by means of two orthogonal apertures realized on the Kapton ground plane (dotted lines in Fig. 8a). Due to low RF power budget involved in typical harvesting scenarios, the design of the feeding network includes matching and port decoupling as final goals, for the need of maximizing antenna efficiency. The final "dog-bone" shape of the ground apertures represents the best trade-off between the conflicting requirements of port matching and port decoupling, all over the bands of interest. The two-port antenna scattering parameters are plotted in Fig. 10: the adopted ground apertures keep the maximum power transfer from port to port under −6 dB at the frequencies of interest, maintaining excellent performance in terms of reflection coefficient.

For circular polarization purposes, a wideband 90° phase shift between the two ports is needed, too. In Fig. 11, the computed radiation surfaces due to ideal orthogonal/in-quadrature mode excitation are reported, showing the foreseen broadside radiation for the TM11 and TM12 modes, while the intermediate TM21 mode has two main lobes slanted with respect to the broadside direction by about ±30°. Note that the total efficiencies (also including the ports matching/coupling) are always greater than 50 %. Figure 12 shows the results in terms of axial ratio (AR): an acceptable elliptical polarization with AR lower than 6 dB is guaranteed over a wide θ range for the two modes TM11 and TM12; the intermediate TM21 mode is not able to sustain the circular polarization because the two orthogonal modes are exactly superimposed in this case (see Fig. 7a).

As a final step of the electromagnetic design of the radiating section of the wearable harvester, a realistic, compact, broadband power divider/90° phase shifter [30] on flexible Kapton substrate has been first designed as a stand-alone component, with 50 Ω ports by means of a circuit simulator. Then the actual loads, taking into account the highly dispersive behaviors of the antenna ports, have been

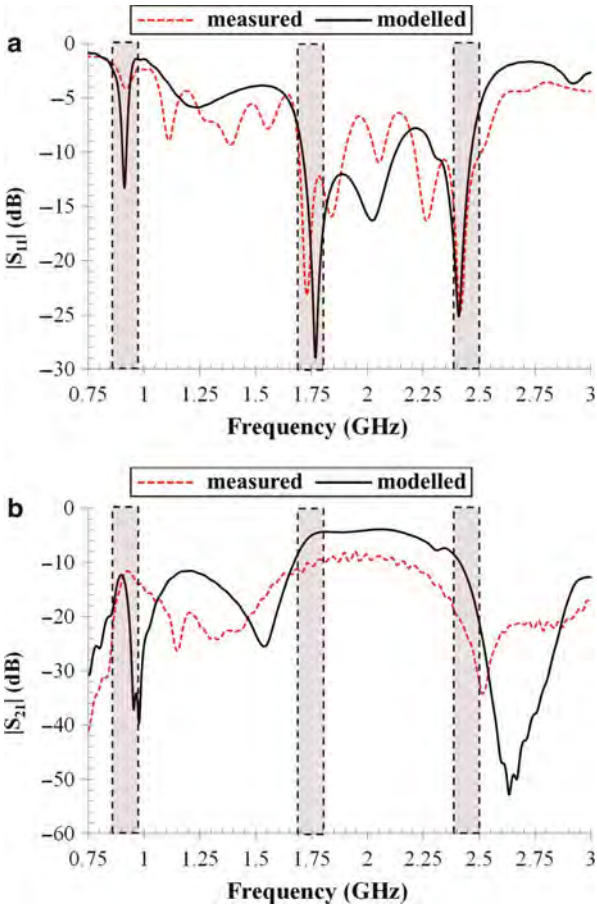

Fig. 10 Measured and simulated scattering parameters of the 2-port ring antenna versus frequency (Taken from our paper Costanzo et al. [42])

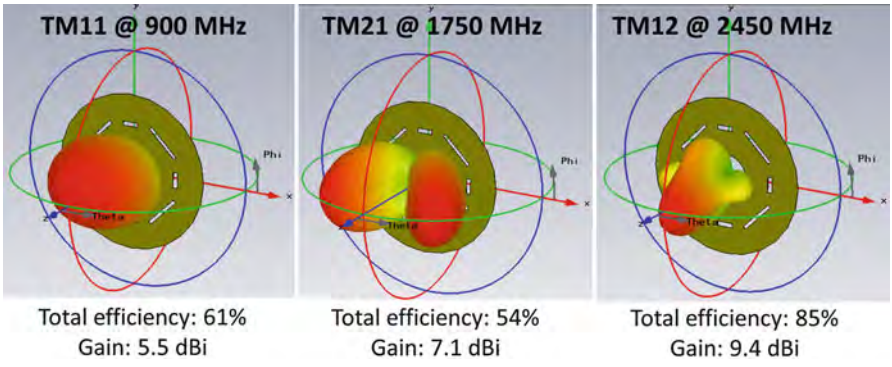

Fig. 11 Simulated radiation surfaces at the three operating frequencies (Taken from our Ref. [10] (Conference EuCAP 2011))

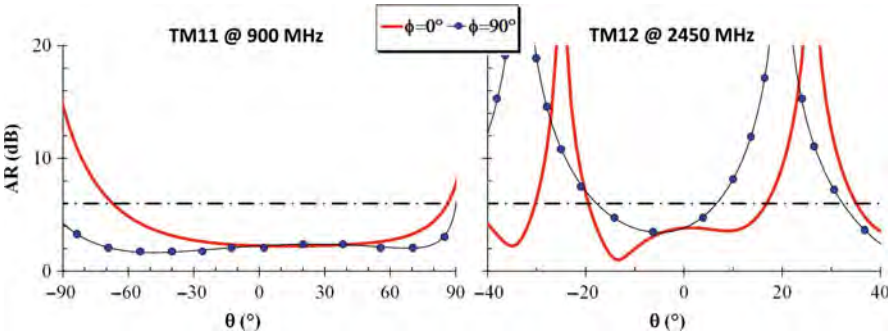

Fig. 12 Simulated axial ratios at two of the three operating frequencies (Taken from our Ref. [10] (Conference EuCAP 2011))

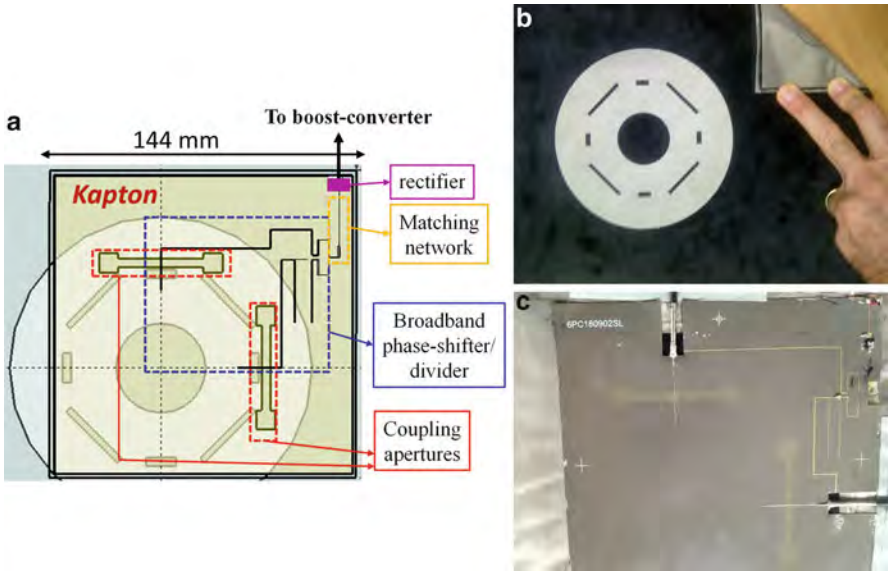

Fig. 13 (**a**) Final feeding network design of the tri-band wearable harvester; (**b**) antenna and (**c**) feeding network prototype layers (**a**, Taken from our Ref. [40] (Conference EuMC 2013))

considered: for this purpose, an accurate full-wave tuning of the phase-shifter topology is carried out, taking for granted the antenna one. The resulting final layout of the feeding network is given in Fig. 13, together with the photos of the prototype. The top antenna view (Fig. 13b) puts into evidence the compact multi-layer architecture. The feeding network of Fig. 13c shows the removal of two pieces of the Kapton layer in proximity of the ground apertures, for measurement purposes only: the measured two-port scattering parameters, superimposed to the numerical ones in Fig. 10, are obtained in this way and reveal very good agreement with simulation, despite of the complexity of the entire subsystem.

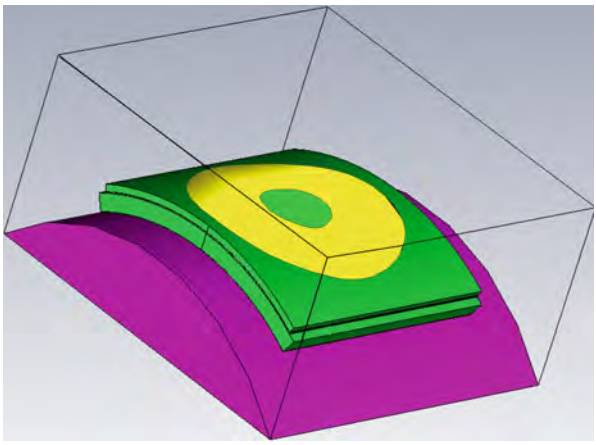

Fig. 14 Bent wearable rectenna numerical model in presence of human tissue

Table 1 Simulated maximum E field value (dBV/m)

	Flat	Bent	Bent with human tissue
900 MHz	12.7	11.2	13.5
1,750 MHz	11.8	12.9	15.0
2,450 MHz	13.2	14.6	13.9

Before starting with the entire rectenna nonlinear project, a fundamental step, when dealing with wearable and flexible structures, consists of verifying the effects of bending and human body on the linear performance [31–33]. For this purpose, two modeling setups are carried on addressing separately bending and human body effects. Firstly, the patch (in its original shape, without slots, since this experiment has been done during the initial antenna shape selection) and the feeding layers are bent around a vacuum cylinder with 150 mm diameter, corresponding to a typical rib cage. Secondly, the cylinder is filled with a human-body-like material ($\varepsilon_r = 53.3$ and $\sigma = 1.52$ S/m): Fig. 14 shows the entire model to be computed by electromagnetic simulation. The performances of both structures are checked with the flat ones and show acceptable discrepancies, as it is reported in Table 1.

Another important test in view of practical rectenna implementation consists of quantifying the effects of the misalignment between the reciprocal position of antenna and Kapton substrates: these positions can vary with respect to the symmetrical one depending on the manual precision in the bonding operation. In Fig. 15, the simulated reflection coefficient of the optimal solution in Fig. 10 is superimposed to the cases corresponding to a ± 3 mm shift due to positioning uncertainty: the results guarantee a sufficient robustness of the rectenna design with regard to unwanted asymmetries; the maximum resulting shift is about 4 % for the lower frequency, which is the most delicate band due to the sharpness of the negative peak of S_{11} magnitude.

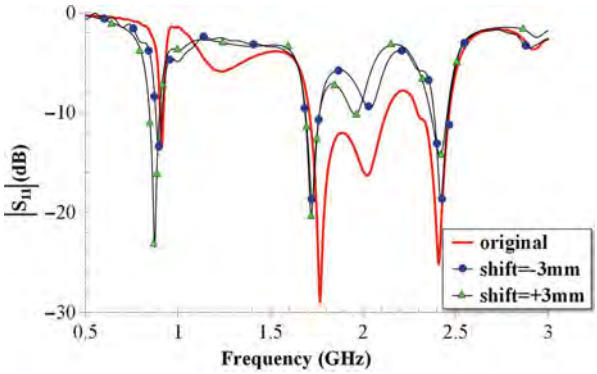

Fig. 15 Feeding network misalignment effects on antenna matching (Taken from our paper Costanzo et al. [42])

Integration of the Textile Antenna with a Rectifier Circuit

The feeding network layer of Fig. 13 also shows a matching network: it has the fundamental role to drastically reduce reflections between the subassembly antenna/feeding network and the nonlinear rectifier in the whole frequency band and for the incoming RF low power levels. For the optimization of this matching network, a circuit-level/full-wave co-simulation approach is needed: the full-wave description of the antenna/feeding network is exported in terms of wideband scattering matrix and then exploited within a nonlinear circuit simulator based on the harmonic balance (HB) technique [34]. This approach allows to rigorously take into account both the dispersive behavior of the radiating network and the dispersive and signal-level-dependent behavior of the nonlinear rectifier.

At this stage, a multiband nonlinear optimization of the whole rectenna is carried out by the HB technique: design specifications are simultaneously given at the three fundamental frequencies in terms of RF-to-DC conversion efficiency:

$$\eta_{RF-DC} = \frac{P_{RECT}}{P_{RF}} \tag{2}$$

where P_{RECT} is the rectified power at the rectenna output port, delivered to a fixed load, while P_{RF} is the available RF power on the antenna location. For any given RF source, we use the reciprocity theorem to effectively estimate the actual RF power available to the rectifier circuit [35, 36]. This is a fundamental step of the whole procedure, since, due to the extremely low power budget involved, an accurate estimation of the available power, to be used in the optimization, is a strategic issue. The most general formula for the evaluation of this contribution is the following [24]:

$$J_{eq}(\omega_{RF}) = \frac{1 + R_0 Y_H(\omega_{RF})}{U} \cdot \hat{\mathbf{n}} \bullet \int_{\sum} \left[\mathbf{E_i}\left(P_{\sum}\right) \times \mathbf{H_H}\left(P_{\sum}\right) - \mathbf{E_H}\left(P_{\sum}\right) \times \mathbf{H_i}\left(P_{\sum}\right) \right] d\sum \quad (3)$$

where J_{eq} is the equivalent Norton current generator at the receiving side, to be placed in parallel to the full-wave antenna/feeding network admittance ($\mathbf{Y_H}$) (see Fig. 16). It is given as a function of the incoming RF field ($\mathbf{E_i}$, $\mathbf{H_i}$) and the far-field radiated by the harvesting antenna when operating in the transmitting mode ($\mathbf{E_H}$, $\mathbf{H_H}$). These fields are numerically evaluated on a Σ plane (whose orthogonal unit vector is $\hat{\mathbf{n}}$), placed in between the two antennas. This formula has demonstrated to be very accurate, irrespective of the antenna orientations and transmitter-to-harvester distance, and eventually takes into account the nearby objects affecting the link (as the human body). It is worth mentioning that the possible polarization mismatching between the two fields is automatically considered by the vector products in Eq. 3.

Of course in the tri-band nonlinear optimization, the total available power to be used in the circuit simulator can be straightforwardly evaluated by

$$P_{AV} = \sum_{k=1}^{3} \frac{\left|J_{eq}\left(\omega_{RF,k}\right)\right|^2}{8\mathrm{Re}\left[Y_H\left(\omega_{RF,k}\right)\right]} \quad (4)$$

where $\omega_{RF,1} = 900$ MHz, $\omega_{RF,2} = 1{,}750$ MHz, and $\omega_{RF,3} = 2{,}450$ MHz.

At this stage, a first validation is performed: in a real office scenario, the available power at the rectifier input port (see Fig. 16) is measured and numerically evaluated according to Eqs. 3 and 4. The source is a horn antenna, with a gain of 10–12 dBi in the bands of interest, transmitting 17 dBm of power, placed at a distance d satisfying the Fraunhofer conditions:

$$\begin{aligned} d &\gg D \\ d &> 2\frac{D^2}{\lambda} \end{aligned} \quad (5)$$

where D is 142 mm, i.e., the maximum dimension of the receiving ring antenna.

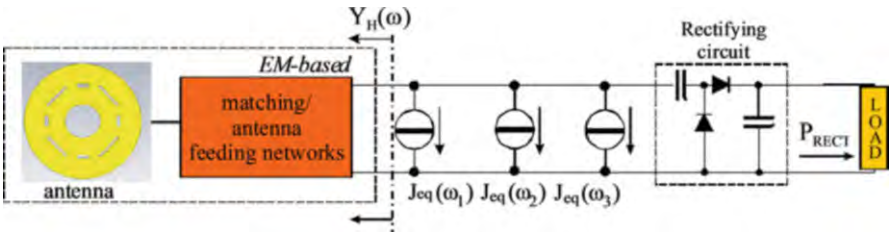

Fig. 16 Circuit-level description of the tri-band wearable harvester for numerical optimization purposes (Taken from our paper Costanzo et al. [43])

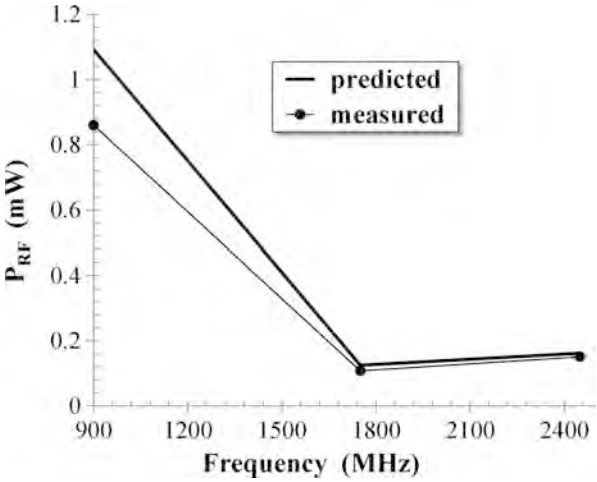

Fig. 17 Comparison between measured and simulated available powers at the rectifier port for all the frequencies of interest

The comparison shown in Fig. 17 supports the proposed approach: the small discrepancies are also due to the channel fading of the environment, which is not taken into account in the present case.

As regards the nonlinear rectifier, the preferred topology is a voltage doubler or single-stage full-wave peak-to-peak RF-DC converter, as shown in Fig. 16. This topology is simpler with respect to multistage rectifiers or voltage multipliers, typically employed in RFID applications: in fact, a higher number of stages are justified only when the incoming power level is medium high, while in ultralow power applications, the minimization of diode losses, thus the number of stages, has a priority role [24, 37]. The present solution employs low threshold-voltage diodes (Skyworks SMS7630). The inclusion, in the optimization process, of the model of the Skyworks SOT-23 diode package is of fundamental importance, because the package parasitics can influence the overall system performance: this has been experimentally verified, especially at higher frequencies.

The HB-based optimization is then carried out, referring to the circuit representation in Fig. 16. The design parameters are provided by the fixed load and the matching network layout, a simple microstrip impedance step, in this case: simultaneous design goals on the conversion efficiency Eq. 2 across the frequency bands of interest and for the actual power levels pertaining to the different wireless standards may be then directly accounted for with Eq. 3. It is worth noting that several crucial phenomena, such as power mismatch between antenna and receiver front end, polarization conflicts between incident and harvester electric fields, and the simultaneous presence of different RF sources, are automatically included in all the evaluations, in this way.

As a first result of the overall design procedure, the rectified power delivered to an optimum load is considered, with a sinusoidal signal of power P_{TX}, transmitted by an ideal dipole resonating each time at one of the three frequencies of interest, as RF source. The established link covers a distance of 30 cm, and maximum link

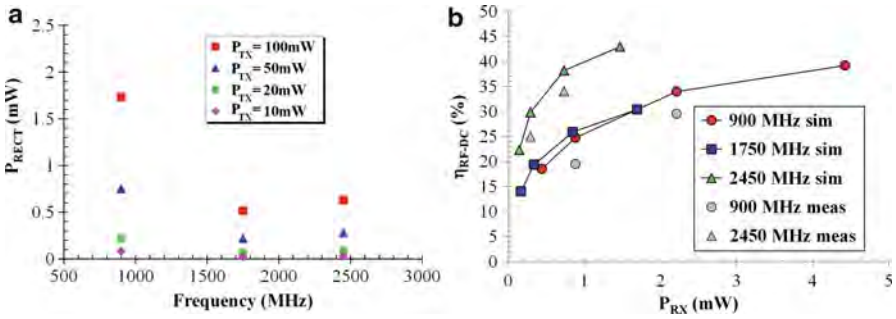

Fig. 18 (**a**) Rectified power and (**b**) RF-DC conversion efficiency due to a transmitting resonant dipole placed 30 cm apart (**a**, Taken from our Ref. [10] (Conference EuCAP 2011), also used in chapter of book "Green RFID Systems" Cambridge University press, Editor Luca Roselli)

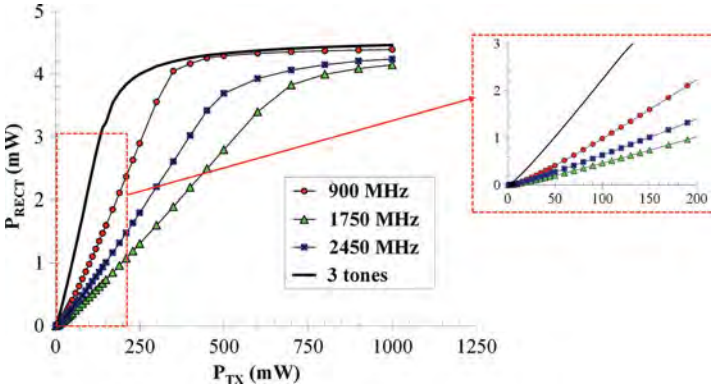

Fig. 19 Rectified output power at the three operating frequencies and in contemporaneous presence of the three tones

direction is adopted in the three evaluations (corresponding to $\theta = 0°$ at 900 and 2,450 MHz, $\theta = 30°$ at 1,750 MHz). In Fig. 18a, the rectified power at the operating frequencies, for different source levels P_{TX}, is reported, while Fig. 18b shows the three RF-DC conversion efficiencies as a function of the available RF powers, corresponding to the P_{TX} levels in Fig. 18a. The available measured efficiencies are also reported in the same figure: the small discrepancies from prediction agree with those in Fig. 17.

This procedure also allows to take into account the contemporaneous presence of all the three RF sources, as described in Fig. 16, by means of a multi-tone HB analysis, where three independent sources are placed at 900, 1,750, and 2,450 MHz and their intermodulation products up to the third order are used to describe the signal spectra. In Fig. 19, the rectenna rectified powers, on an optimum 900 Ω load, resulting from superposition of different sources (solid line) and from a single

source at a time, are compared, again as a function of the source dipole transmitted power. The transmitted power values of the figure are associated to one excitation in the single-tone analyses and are equally distributed among the different tones in the multi-tone case. Whereas at higher P_{TX} levels the intermodulation effect is negligible, at low levels typical of harvesting scenarios, the nonlinear behavior of the rectenna take advantage of the intermodulation distortion, as can be easily seen from the figure inset.

Power Management Unit Design

All the previous evaluations have been performed in RF stationary conditions, under the unrealistic assumption of a unique fixed load at the rectifier output port. In practical applications, the rectenna will have to provide energy to ultralow power external devices, which operate discontinuously, e.g., a wireless sensor that is normally quiet and only needs to be activated during short transmission bursts. In these cases, it is necessary to introduce an intermediate energy buffer, or power management unit (PMU), between the rectenna output port and a suitable energy storage device (typically a capacitor or a rechargeable battery). Thus, the fixed load must be replaced by a switching converter able to dynamically track the maximum power point (MPP) condition for any frequency and power level. The optimum power condition is approximately obtained when the rectified voltage (V_{RECT}) is about one half of the open-circuit voltage (V_{OPEN}) [24, 38], and this is irrespective of RF frequency. In order to properly define the converter components, a SPICE-like time-domain model of the dispersive rectenna [39] is used inside a time-domain optimization of the converter itself. During this design process, with switching elements, timings, and storage capacitor as design parameters, the entire system efficiency is taken under control to minimize the converter power consumption:

$$\eta_{TOT} = \eta_{RF-DC}\,\eta_{DC-DC} = \frac{P_{RECT}}{P_{RF}}\,\frac{P_{ST}}{P_{RECT}} \tag{6}$$

where P_{ST} is the DC power stored in the storage capacitor C_{ST}.

As a first example of a DC-DC converter, discrete-components design, the topology shown in Fig. 20, together with the antenna and the rectifying sections, is pursued [24]. The dynamic converter consists of two pairs of synchronous switches, an inductor, a diode, the storage capacitor C_{ST}, and a simple control circuit for driving the switches. To demonstrate the operation of the whole system in Fig. 20, an operation of RF harvesting "on-demand" is envisaged: when a phone call with a GSM 900 mobile at 1 m distance is performed, the corresponding instantaneous DC voltage at the rectenna output port (V_{RECT}) and the transient waveform of the stored voltage (V_{ST}) on the capacitor C_{ST} at the output port of the DC-DC converter are measured. These data are plotted in Fig. 21a, b, respectively. A stored DC voltage of ~600 mV is reached in 3 s and the average RF received

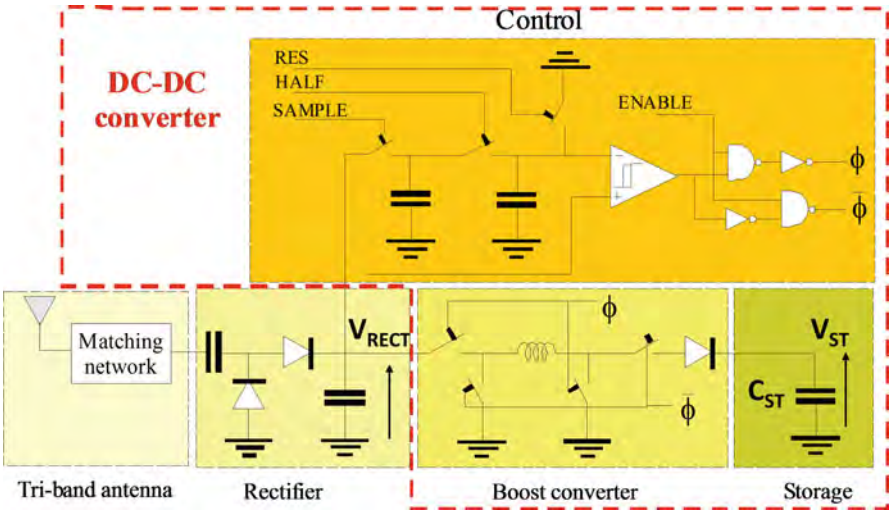

Fig. 20 Scheme of the proposed RF energy-harvesting system

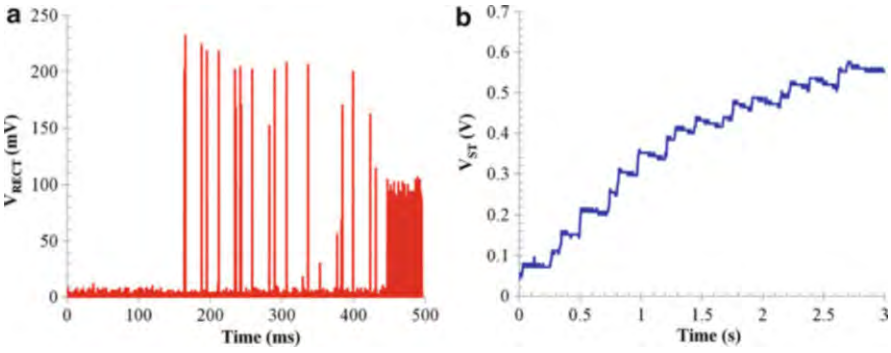

Fig. 21 (**a**) Measured rectenna output voltage (sampling rate = 0.2 ms) and (**b**) converter output voltage (sampling rate = 4 ms) during a GSM 900 phone call (Taken from our paper Costanzo et al. [42])

power is estimated as ~80 μW. From these plots, it is possible to conclude that the presented rectenna system implements the concept of batteryless wearable sensors and paves the way to the paradigm of smart clothes.

However, traditional MPP tracking solutions adopting state-of-the-art micro-power discrete components [24, 38] still suffer from too-high intrinsic consumptions to guarantee energy autonomy. In addition, although sufficient power may be available, the obtained voltages at the rectenna output (V_{RECT}) are usually too low to initially activate the power converters, which generally require values about 1.8 V. This is demonstrated in Fig. 22, where the rectified voltage, current, and power at the output port of the wearable rectenna previously described are plotted, at all the three

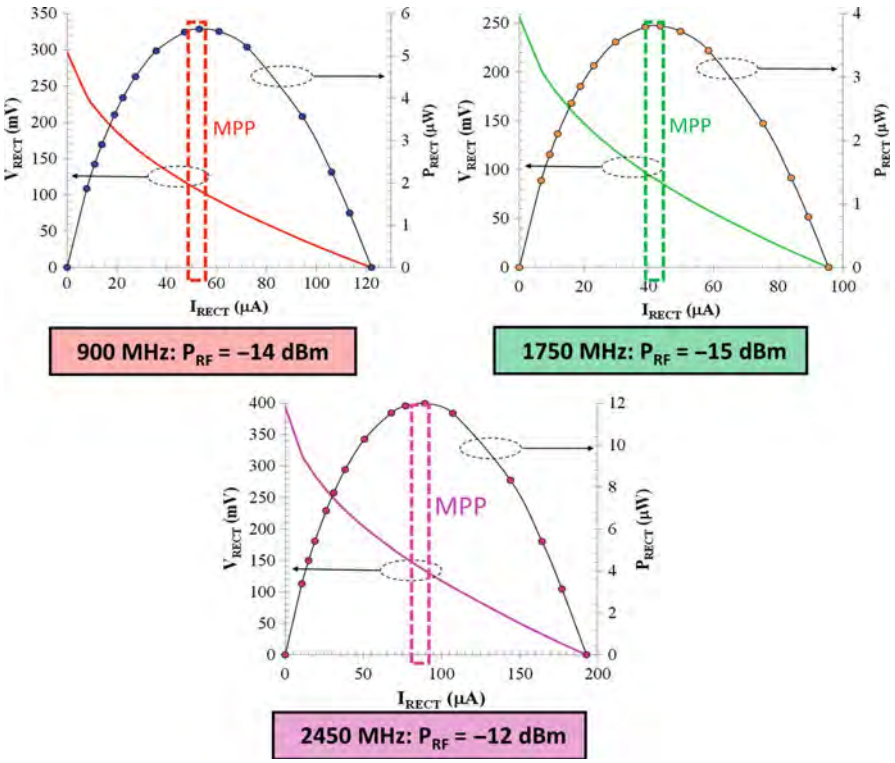

Fig. 22 P-I and V-I characteristics of the tri-band wearable rectenna for low available power levels (Taken from our Ref. [40] (Conference EuMC 2013))

operating frequencies, for values of received P_{RF} typical of realistic scavenging scenarios: according to the standard MPP strategy ($V_{RECT} \approx V_{OPEN}/2$), the rectenna output voltage reaches values below 150 mV in the present case. For this reason, a start-up strategy is needed.

The building blocks of the proposed autonomous system are shown in Fig. 23 [40]. The power source is the tri-band wearable rectenna previously designed; the PMU consists of a DC-DC power converter (PC) with MPP tracking capabilities, an additional start-up (SU) circuit, and the energy storage capacitor (C_{ST}). Differently from other implementations [41], this device does not require any external battery and can start autonomously from a fully discharged state. A microelectronic implementation of the whole baseband system is then carried out: this has demonstrated to be of strategic importance in order to solve the power consumption and voltage-level issues and also to reduce the overall dimensions. The power management IC here described is implemented in a STMicroelectronics 0.32 μm technology and has an overall die area of 4.6 mm^2.

The system obeys the following rules: when too-low energy is available in the storage capacitor C_{ST}, the DC-DC boost power converter (PC) is disabled. In such

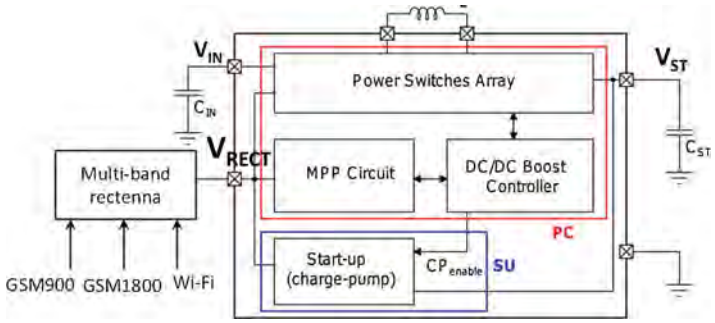

Fig. 23 Block diagram of the fully autonomous rectenna system (Taken from our Ref. [40] (Conference EuMC 2013))

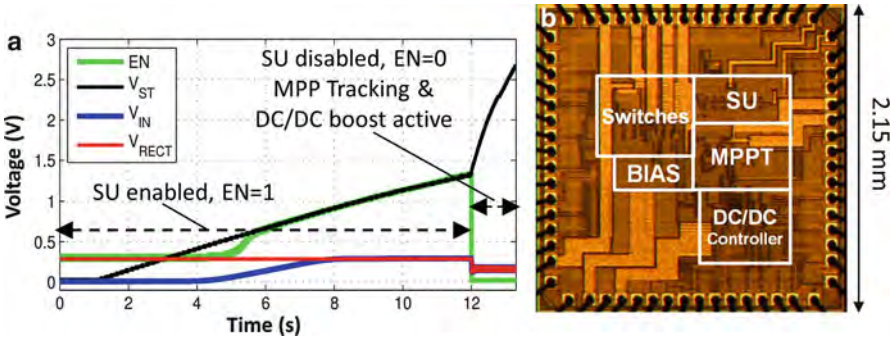

Fig. 24 (**a**) Transient waveforms of the SU and PC phases; (**b**) photo of the custom IC (die area of 4.6 mm^2)

conditions, the enable signal (EN) is high and the start-up (SU) circuit is used for charging the output capacitor to a voltage value which allows to safely activate the PC. The present SU block consists a ring oscillator and a 16-stage capacitive charge pump and is configured to charge C_{ST} from 0 V up to more than 1.4 V with a minimum input voltage of 250 mV coming from the rectenna output (V_{RECT}), slightly below the threshold voltage of MOSFETs. Once a minimum amount of energy is collected and a minimum voltage is reached, the SU is disabled through EN = 0 and PC is enabled, and standard power conversion with MPP tracking is carried out from this point onward ($V_{RECT} \approx V_{OPEN}/2$).

In Fig. 24a, experimental measured results of the final system are given for the rectenna operating at 900 MHz with an available RF power $P_{RF} = -13$ dBm, corresponding to an open-circuit voltage at the rectenna output equal to 320 mV: when the storage voltage V_{ST} reaches 1.4 V (minimum voltage required for DC-DC active operations of the PC), the SU is disabled. Fig. 24b shows the photo of the realized chip.

Summary

It has been demonstrated in the chapter that the use of rigorous CAD techniques allows the optimization of fully wearable energy harvesting and storage systems, designed to exploit electromagnetic sources available in the ambient. The small amount of environmental energy forces to proceed with extreme accuracy at each step of the procedure for a successful design. (i) An accurate prediction of the minimum received power is needed to ensure the rectifier turn-on and the start-up of the energy storage control circuit, and this can be done by resorting to rigorous electromagnetic theory. (ii) A robust procedure, deploying full-wave numerical analysis and measurements, has to be used for a precise characterization of dielectric and conductive fabrics realizing the system. (iii) Circuit-level/electromagnetic optimization of the rectenna nonlinear RF stationary regimes has to be carried out to determine reference values of the rectified signals. (iv) Time-domain optimization of the power management unit is finally needed to dynamically keep the rectenna at its optimum loading conditions. The effectiveness of the CAD platform is verified in the design of a textile multilayer multi-frequency rectenna, using fabric for both the substrates and the metallic layers, able to recover energy from GSM 900, GSM 1800, and WiFi sources: the realization of the system with off-the-shelf discrete components has shown to be suitable for "RF upon request" application, e.g., from mobile phones, thus paving the way toward the paradigm of "smart clothes." The further integration of the rectifying antenna with a microelectronic power management chip permits to drastically reduce the overall power consumption and the voltage levels needed for start-up operation, thus implementing a fully autonomous and batteryless system.

References

1. Paradiso J, Starner T (2005) Energy scavenging for mobile and wireless electronics. IEEE Pervasive Comput 4(1):18–27. doi:10.1109/MPRV.2005.9
2. Roundy S, Wright PK, Rabaey J (2003) A study of low-level vibrations as a power source for wireless sensor nodes. Comput Commun 26(11):1131–1144. doi:10.1016/S0140-3664(02)00248-7
3. Wang Z, Leonov V, Fiorini P, Van Hoof C (2009) Realization of a wearable miniaturized thermoelectric generator for human body applications. Sens Actuators A 156(1):95–102. doi:10.1016/j.sna.2009.02.028
4. Nasiri A, Zabalawi S, Mandic G (2009) Indoor power harvesting using photovoltaic cells for low-power applications. IEEE Trans Ind Electron 56(11):4502–4509. doi:10.1109/TIE.2009.2020703
5. Paing T, Shin J, Zane R, Popovic Z (2008) Resistor emulation approach to low-power RF energy harvesting. IEEE Trans Power Electron 23(3):1494–1501. doi:10.1109/TPEL.2008.921167
6. Chandrakasan A, Daly D, Kwong J, Ramadass Y (2008) Next generation micro-power systems. In: IEEE symposium on VLSI circuits, Honolulu, Hawaii, pp 2–5. doi:10.1109/VLSIC.2008.4585930
7. Rizzoli V, Costanzo A, Masotti D, Donzelli F (2010) Integration of numerical and field-theoretical techniques in the design of single- and multi-band rectennas for micro-power

generation. EuMA Int J Microw Wirel Technol 2(3–4):293–303. doi:10.1017/S1759078710000553
8. Boaventura AJS, Carvalho NB (2013) Extending reading range of commercial RFID readers. IEEE Trans Microw Theory Tech 61(1):633–640. doi:10.1109/TMTT.2012.2229288
9. Collado A, Georgiadis A (2012) Improving wireless power transmission efficiency using chaotic waveforms. In: 2012 I.E. MTT-S international microwave symposium digest, Montreal, Canada, pp 1–3. doi:10.1109/MWSYM.2012.6259595
10. Masotti D, Costanzo A, Adami S (2011) Design and realization of a wearable multi-frequency Rf energy harvesting system. In: 5th European conference on antennas and propagation (EuCAP), Rome, Italy, pp 517–520
11. Monti G, Corchia L, Tarricone L (2013) UHF wearable rectenna on textile materials. IEEE Trans Antennas Propag 61(7):3869–3873. doi:10.1109/TAP.2013.2254693
12. Kurian J, Rajan MNU, Sukumaran SK (2014) Flexible microstrip patch antenna using rubber substrate for WBAN applications. In: International conference on contemporary computing and informatics (IC3I), Mysore, India, pp 983–986. doi:10.1109/IC3I.2014.7019760
13. Hertleer C, Rogier H, Vallozzi L, Van Langenhove L (2009) A textile antenna for off-body communication integrated into protective clothing for firefighters. IEEE Trans Antennas Propag 57(4):919–925. doi:10.1109/TAP.2009.2014574
14. Hertleer C, Van Laere A, Rogier H, Van Langenhove L (2010) Influence of relative humidity on textile antenna performance. Text Res J 80:177–183. doi:10.1177/0040517509105696
15. Declercq F, Couckuyt I, Rogier H, Dhaene T (2013) Environmental high frequency characterization of fabrics based on a novel surrogate modelling antenna technique. IEEE Trans Antennas Propag 61:5200–5213. doi:10.1109/TAP.2013.2274031
16. Declercq F, Rogier H, Hertleer C (2008) Permittivity and loss tangent characterization for garment antennas based on a new matrix-pencil two-line method. IEEE Trans Antennas Propag 56(8):2548–2554. doi:10.1109/TAP.2008.927556
17. Rizzoli V (1977) Resonance measurement of single- and coupled-microstrip propagation constants. IEEE Trans Microw Theory Tech 25(2):113–120. doi:10.1109/TMTT.1977.1129050
18. Costanzo A, Donzelli F, Masotti D, Rizzoli V (2010) Rigorous design of RF multi-resonator power harvesters. In: Proceedings of the fourth European conference on antennas and propagation (EuCAP), Barcelona, Spain, pp 1–4
19. CST Microwave Studio (2012) http://www.cst.com
20. Hagerty JA, Helmbrecht FB, McCalpin WH, Zane R, Popovic ZB (2004) Recycling ambient microwave energy with broad-band rectenna arrays. IEEE Trans Microw Theory Tech 52(3):1014–1024. doi:10.1109/TMTT.2004.823585
21. Masotti D, Costanzo A, Del Prete M, Rizzoli V (2013) A genetic-based design of a tetra-band high-efficiency RF energy harvesting system. IET Microw Antennas Propag 7(15):1254–1263. doi:10.1049/iet-map.2013.0056
22. Collado A, Georgiadis A (2013) Conformal hybrid solar and electromagnetic (EM) energy harvesting rectenna. IEEE Trans Circuits Syst I Regul Pap 60(8):2225–2234. doi:10.1109/TCSI.2013.2239154
23. Rizzoli V, Costanzo A, Masotti D, Donzelli F, Bichicchi G (2009) CAD of Multi-resonator rectenna for micro-power generation. In: European microwave conference (EuMC), Rome. Italy, pp 1684–1687
24. Costanzo A, Romani A, Masotti D, Arbizzani N, Rizzoli V (2012) RF/baseband co-design of switching receivers for multiband microwave energy harvesting. Elsevier J Sens Actuators A Phys 179(1):158–168. doi:10.1016/j.sna.2012.02.005
25. Costanzo A, Masotti D, Donzelli F, Adami S (2012) Device to convert radiofrequency electromagnetic energy. Patent WO/2012/042348, PCT/IB2011/002253
26. Pinuela M, Mitcheson PD, Lucyszyn S (2013) Ambient RF energy harvesting in urban and semi-urban environments. IEEE Trans Microw Theory Tech 61(7):2715–2726. doi:10.1109/TMTT.2013.2262687

27. Mok WC, Chair R, Luk KM, Lee K-F (2003) Wideband quarter-wave patch antenna with shorting pin. IEE Proc Microw Antennas Propag 150(1):56–60. doi:10.1049/ip-map:20030439
28. Kan HK, Waterhouse RB (1999) Size reduction technique for shorted patches. Electron Lett 35 (12):948–949. doi:10.1049/el:19990703
29. Wu YS, Rosenbaum FJ (1973) Mode chart for microstrip ring resonators. IEEE Trans Microw Theory Tech 21(7):487–489. doi:10.1109/TMTT.1973.1128039
30. Tang X, Mouthaan K (2009) 180° and 90° phase shifting networks with and octave bandwidth and small phase errors. IEEE Microw Wirel Compon Lett 19(8):506–508. doi:10.1109/LMWC.2009.2024837
31. Boeykens F, Rogier H, Vallozzi L (2014) An efficient technique based on polynomial chaos to model the uncertainty in the resonance frequency of textile antennas due to bending. IEEE Trans Antennas Propag 62(3):1253–1260. doi:10.1109/TAP.2013.2294021
32. Lemey S, Rogier H (2014) SIW textile antennas as a novel technology for UWB RFID tags. In: 2014 I.E. RFID technology and applications conference (RFID-TA), Tampere, Finland, pp 256–260. doi:10.1109/RFID-TA.2014.6934239
33. Lilja J, Salonen P, Kaija T, de Maagt P (2012) Design and manufacturing of robust textile antennas for harsh environments. IEEE Trans Antennas Propag 60(9):4130–4140. doi:10.1109/TAP.2012.2207035
34. Rizzoli V, Masotti D, Mastri F, Montanari E (2011) System-oriented harmonic-balance algorithms for circuit-level simulation. IEEE Trans Comput Aided Des Integr Circuits Syst 30(2):256–269. doi:10.1109/TCAD.2010.2092250
35. Rizzoli V, Costanzo A, Monti G (2004) General electromagnetic compatibility analysis for nonlinear microwave integrated circuits. In: IEEE MTT-S international microwave symposium, Fort Worth, Texas, pp 953–956. doi:10.1109/MWSYM.2004.1339135
36. Georgiadis A, Andia G, Collado A (2010) Rectenna design and optimization using reciprocity theory and harmonic balance analysis for electromagnetic (EM) energy harvesting. IEEE Antennas Wirel Propag Lett 9:444–446. doi:10.1109/LAWP.2010.2050131
37. Essel J, Brenk D, Heidrich J, Weigel R (2009) A highly efficient UHF RFID frontend approach. In: IEEE MTT-S international microwave workshop on wireless sensing, local positioning, and RFID, pp 1–4. doi:10.1109/IMWS2.2009.5307866
38. Dolgov A, Zane R, Popovic Z (2010) Power management system for online low power RF energy harvesting optimization. IEEE Trans Circuits Syst I Regul Pap 7(7):1802–1811. doi:10.1109/TCSI.2009.2034891
39. Rizzoli V, Costanzo A, Mastri F, Neri A (2003) A general SPICE model for arbitrary linear dispersive multiport components described by frequency-domain data. In: IEEE MTT-S international microwave symposium digest, Philadelphia, Pennsylvania, pp 9–12. doi:10.1109/MWSYM.2003.1210871
40. Dini M, Filippi M, Costanzo A, Romani A, Tartagni M, Del Prete M, Masotti D (2013) A fully-autonomous integrated RF energy harvesting system for wearable applications. In: European microwave conference (EuMC), Nuremberg, Germany, pp 987–990
41. Paing T, Falkenstein EA, Zane R, Popovic Z (2011) Custom IC for ultralow power RF energy scavenging. IEEE Trans Power Electron 26(6):1620–1626. doi:10.1109/TPEL.2010.2096475
42. Costanzo A, Masotti D, Del Prete M (2013) Wireless power supplying flexible and wearable systems. In: Antennas and propagation (EuCAP), 7th European conference on, Gothenburg, Sweden, 8–12 Apr 2013, pp 2843, 2846
43. Costanzo A, Masotti D, Aldrigo M (2014) Compact, wearable antennas for battery-less systems exploiting fabrics and magneto-dielectric materials. Electronics 3(3):474–490

Mechanisms for Fiber-based Nanogenerators

19

Wei Zeng

Contents

Introduction 488
Fiber-Based Piezoelectric Nanogenerator 488
Basic Concepts of Piezoelectric Effect 488
Using the Piezoelectric Effect 490
Mechanism of Fiber-Based Piezoelectric Nanogenerator 491
Fiber-Based Triboelectric Nanogenerator 499
Basic Concepts of Triboelectric Effect 499
Using of the Triboelectric Effect 500
Mechanism of Fiber-Based Tribonanogenerator 501
Modeling and Theory 505
Factors of Triboelectric Nanogenerator 507
Summary 509
References 509

Abstract

Fiber-based nanogenerators for personal low-power electronics, the harvesting of energy from biomechanical motions, are believed to be the most reliable route because of efficient energy conversion performance, high durability, and comfort. In this section, the basic concepts and mechanism of fiber-based piezoelectric and triboelectric nanogenerators are summarized. To help understand the mechanism of the fiber-based nanogenerators, theoretical model and analytical theories having been established to calculate the output voltage, current, charges, and influencing factors depending on materials and environmental effects are described. Moreover, related significant applications and computer simulations are also involved in this section.

W. Zeng (✉)
Hong Kong Polytechnic University, Kowloon, Hong Kong, China
e-mail: tczengw@polyu.edu.hk

© Springer Science+Business Media Singapore 2015

X. Tao (ed.), *Handbook of Smart Textiles*,
DOI 10.1007/978-981-4451-45-1_19

Keywords
Fiber-based nanogenerator • Piezoelectric nanogenerator • Triboelectric nanogenerator • Mechanism • Modeling and theory

Introduction

Fiber-based structures hold great promises for wearable electronics that are expected to be flexible and conformable, long lasting, and lightweight. Many fibrous structures have been fabricated by well-established and cost-effective textile processing technologies, normally at ambient conditions [1]. Moreover, the advancement of nanotechnology has made it feasible to build individual components to the integrated system that can perform unique functions by integrating nanodevices with modern microelectronics technologies. The synergy between nanotechnology and textile processing technologies has yielded drastic advancements in wearable electronics such as self-powered nanogenerators which are mainly related to piezoelectric and triboelectric effects. Many fibrous nanogenerators have been fabricated by well-established and cost-effective textile processing technologies, normally at ambient conditions. As the size of the devices shrinks to the nanoscale, the power consumption also drops to a much lower level. It is entirely possible to drive the nanodevices by scavenging energy from the sources in the environment. Recent development of fiber-based nanogenerators has demonstrated a possibility for the design of a self-powered source that can directly harvest ambient mechanical energy [2, 3], which can be expected to realize wearable electronic systems, energy harvesting from human movement, and body-worn sensors.

Fiber-Based Piezoelectric Nanogenerator

Basic Concepts of Piezoelectric Effect

Harvesting ambient mechanical energy as sustainable self-sufficient micro/nano-power sources holds great promises for powering small electronics and achieving self-powered wearable electronic devices. Piezoelectric materials are promising candidates to be used for harvesting this energy for their unique characteristic of converting mechanical energy into useful electric energy. A piezoelectric material can generate an electric charge when applied to a mechanical stress on the piezoelectric material. This kind of effect was first reported in crystals that have no center of symmetry. Each individual molecule consisting the crystal has a polarization, where one side of the individual molecule can present as negatively charged and the other side as positively charged, which is also called a dipole. This is a result of the atoms that make up the molecule and the way the molecules are shaped. The polar axis is an imaginary line which should be considered throughout the center of both charges on the molecule. In a monocrystal, the polar axes of all of the dipoles lie in

one direction. Different from the monocrystal, there are different regions within the material that have a different polar axis in a polycrystal as shown in Fig. 1.

In order to produce the piezoelectric effect of polycrystal, the polycrystal will be heated and poling under the application of a strong electric field. The high temperature allows the molecules to move more freely and the electric field forces of all the dipoles in the crystal to line up and face in nearly the same direction, as shown in Fig. 2.

After the poling process, the piezoelectric effect can now be observed in the crystal. Figure 3 illustrates the piezoelectric effect. Figure 3a shows the piezoelectric

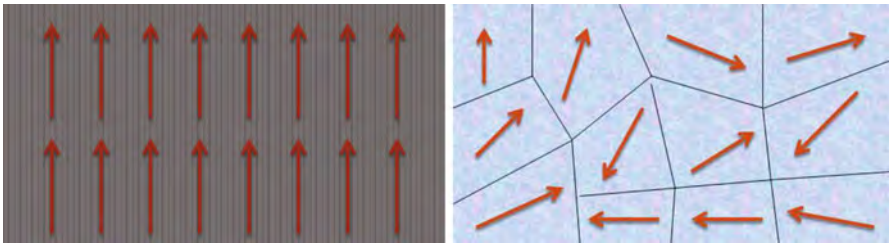

Fig. 1 The polar axis of monocrystal and polycrystal

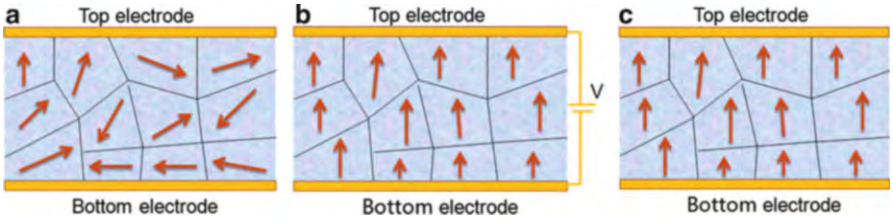

Fig. 2 Polarization of piezoelectric materials to generate piezoelectric effect. (**a**) Random polar axis. (**b**) Polarization. (**c**) Surviving polarity

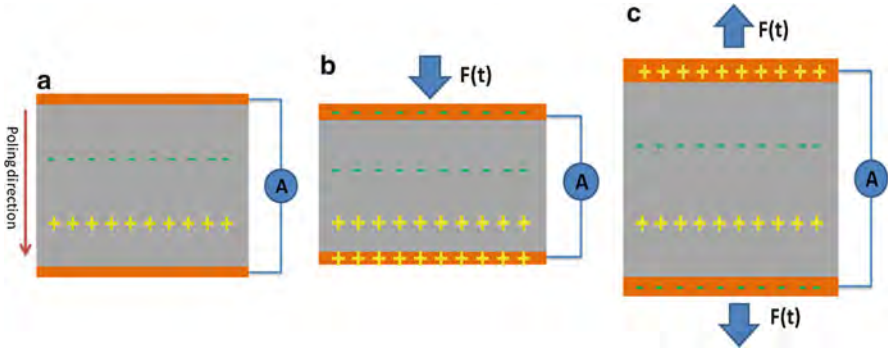

Fig. 3 Basic concepts of piezoelectric effect

material without a stress or charge. If the material is compressed, a piezoelectric potential of the same polarity as the poling voltage can be generated on the side surfaces due to the crystal lattice distortion (Fig. 3b). If stretched, a voltage of opposite polarity will appear between the two electrodes (Fig. 3c).

Using the Piezoelectric Effect

Piezoceramics, nanowires (ZnO, ZnS, InN, GaN, or CdS), and polymeric PVDF are typical piezoelectric materials which have been demonstrated as viable due to their piezoelectric effect for fiber-based piezoelectric nanogenerator. Piezoceramics have large electromechanical coupling constants which can provide a high energy conversion rate [4]. Currently, most of piezoceramics-based energy harvesters have film-based structures which are too brittle to use in a wearable piezoelectric nanogenerator. Compared with those film-based piezoceramics energy harvesters, the piezoceramics nanowires have higher energy conversion efficiency. The reason for piezoceramics nanowire to show higher potential is attributed to the higher piezoelectricity as well as semiconductor properties, and the piezopotential generated in nanowires has a strong effect on the carrier transport at the interface/junction. However, it is a key bottleneck for the applications of piezoceramics nanowire-based nanogenerators. Most of piezoceramics nanowire required high-temperature annealing processing to improve the piezoelectric property which has been described previously. Another kind of piezoelectric nanomaterials, such as zinc oxide (ZnO) nanowires and PVDF nanofibers, are highly flexible and easy to fabricate at room temperature for possible integration in wearable and flexible clothing. One of the earliest piezoelectric nanogenerators was based on ZnO nanowires, which can be utilized for possible energy scavenging applications from mechanical strain. By coupling their piezoelectric effect and semiconducting properties, mechanical strains applied on the ZnO nanowire can be converted into electricity. Further, nanogenerators with ZnO nanowires have demonstrated that peak open-circuit voltage and current can reach a record-high level of 58 V and 134 μA, respectively, with a maximum power density of 0.78 W/cm^3 [5]. PVDF nanofibers are another flexible piezoelectric materials, which have the unique good combination of material properties in lightweight, biocompatibility, high piezoelectric effect, and availability in various thicknesses and shapes and ultra-long lengths, making them an interesting candidate for energy harvesting applications in wearable and/or implantable devices.

Clearly, all of the piezoelectric nanofibers as reviewed in this section could be a particularly interesting candidate for energy scavenging applications and could take advantage of an energy harvesting and self-powering wearable device. For wearable applications, a proper experience and comfort to the wearer is required by the energy harvesting devices which should provide the right "feel" and comfort as well to the wearer. The current problems associated with flexible piezoelectric generators are (i) low output power densities, (ii) long and tedious processing techniques, and (iii) lack of integration techniques for wearable device [6]. Several groups have

demonstrated first prototypes of nanofiber-based nanogenerators for piezoelectric energy harvesting from mechanical energy. Beyond the scope of academic laboratories, further development of fiber-based nanogenerators should be necessary for practical applications.

Mechanism of Fiber-Based Piezoelectric Nanogenerator

Piezoelectricity is the ability of piezoelectric materials to generate a piezopotential in response to applied mechanical pressure. The groundbreaking work by Prof. Wang's group has obviously influenced the current research progress in the conversion of mechanical energy into electric energy using piezoelectric nanogenerators [7–9]. Because of the insulating properties of piezoelectric insulator, which cannot permit carrier transport from metal electrodes into the piezoelectric materials, as a result, the piezoelectric insulator material-based nanogenerators should generate alternating-current power. However, the piezoelectric nanogenerators fabricated from piezoelectric semiconductor materials can produce both direct-current and alternating-current power. Therefore, the coupled semiconducting and piezoelectric properties are the key issues for the direct-current and alternating-current power, respectively. Simply, the working mechanism of the fiber-based piezonanogenerator can be described as a directional flow of electrons driven by the piezopotential which is generated by piezoelectric effect. Firstly, an electric field is created inside the nanowire or nanofiber when the piezoelectric nanogenerator is subject to a compressive stress perpendicular to the nanowires which can deduce a deformation throughout the nanowire. Then, the accumulated inductive charges will accumulate on the top and bottom electrodes because of the electrostatic force. Analogously, the strained nanowires or nanofibers can be viewed as polarized dipole moments in a plate capacitor filled by a dielectric material. Finally, the disappearance of the piezopotential leads to a backflow of the electrons through the external circuit when the stress is released [3].

Energy Harvesting with Piezoceramics Nanowire

Piezoelectricity represents pressure electricity and is a property of certain crystalline materials such as piezoceramics nanowires that develop piezopotential when pressure is applied [4]. This is called the direct effect and may be defined as the electric polarization produced by mechanical strain in the certain classes of crystals. The piezoelectric polarization is proportional to the strain and changes sign with it. Generally, the piezoelectric output in piezoceramics nanowire is composed of intrinsic and extrinsic contributions. The former refers to linear piezoelectric effect of lattice displacement, and the latter generates mainly from movement of domain walls [10]. The mechanical properties of piezoceramics nanowires have been characterized in a number of previous experimental and modeling approaches. Physical constants of piezoelectric materials are generally discussed using conventional axis definition which identifies the property, crystallographic direction of applied stimuli, direction in which the property is being measured, and poling

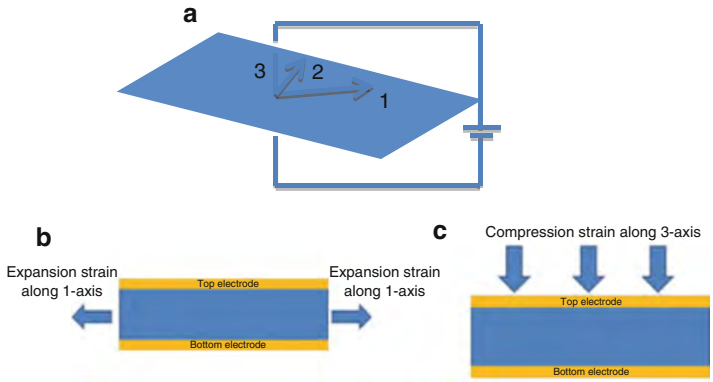

Fig. 4 (**a**) Conventional axis definition for a piezoelectric material, 3-axis is generally accepted as the polarization axis. (**b**) 31-mode and (**c**) 33-mode

direction. This takes the general form of notation as d_{ijk}; where i, j, and k represent different orientations. As shown in Fig. 4a, the indices 1, 2, and 3, respectively, are used to represent longitudinal tensile stress and strain along the x, y, and z axes, respectively. The piezoelectric nanogenerator was fabricated with top and bottom electrodes, after poling of the piezoelectric nanowire using a high voltage across the 3-axis electrodes at a higher temperature; the piezoelectric nanowire can produce a potential difference across the 3-axis in response to strain across axes 1, 2, or 3 [11]. For example, 31-mode operation signifies transverse mechanical strain along the 1-axis, inducing an electric field along the 3-axis, as shown in Fig. 4b. In the same way, the 33-mode (Fig. 4c) describes the polarization developed along the poling direction, when a tensile stress is applied in the same direction (or, equivalently, the tensile strain developed along the poling direction when an electric field is applied in the same direction).

Theoretical modeling of fiber-based piezoelectric nanogenerator should include not only the structure of piezoelectric materials but the piezoelectric coupling effect as well as the electrical behavior. Erturk and Inman proposed a theoretical calculation attempting to correct the oversimplified issues related to mathematical formulation like physical modeling, low-fidelity models, base motion modeling, and piezoelectric coupling effect [4, 12]. A comprehensive calculation was also reported to reveal the size–force–potential relationship for different piezoelectric nanomaterial morphologies. Numerical analysis was applied to $BaTiO_3$ nanowires which is a perovskite material and ideally has a rectangular cross-section, which would produce uniform potential on the two side surfaces [13]. Generally, the piezoelectricity of piezoceramics nanowires is a linear electromechanical coupling and can be modeled by two linearized constitutive equations [14]:

$$\text{Direct effect}: P_i = d_{ijk} \cdot \sigma jk$$

$$\text{Converse effect}: \varepsilon_{ij} = d_{ijk} \cdot E_k$$

where P is the polarization vector, σ is the stress tensor, ε is the strain tensor, E is the electric field vector, and d is the piezoelectric third-rank tensor. In a particular coordinate system, the third-rank tensor is given by a piezoelectric matrix having several independent constants, whose numerical values depend on the crystallographic structure of the material [14].

Based on the constitutive relations, Xudong Wang performed a numerical analysis to show that the $BaTiO_3$ nanowires have higher energy conversion efficiency and higher power-generating capability as compared to ZnO nanowires for the same size [13]. The theoretical reason for this higher power generation is due to the higher piezoelectric coupling coefficient of $BaTiO_3$ nanowires compared with ZnO nanowires. For the case, by using rectangular $BaTiO_3$ nanowires as a nanogenerator element, the rectangular nanowire can be assumed to a parallel capacitor with infinitesimally thick electrodes applied on the top and bottom of the $BaTiO_3$ nanowires for generating the electric energy due to an external force. Thus, the maximum piezoelectric potential of rectangular nanowire can be expressed by

$$\Delta V_{\max, rNW} = \frac{Q_p}{C_p} = \frac{f_y(1+v)b^3 e_{15}}{6I_{xx}\left[2(1+v)e_{15}^2 + k_{11}E\right]}$$

Henry A. Sodano et al. also reported a $BaTiO_3$ nanowire-based nanogenerator for energy harvesting as shown in Fig. 5a [15]. Compressive or tensile stress generated

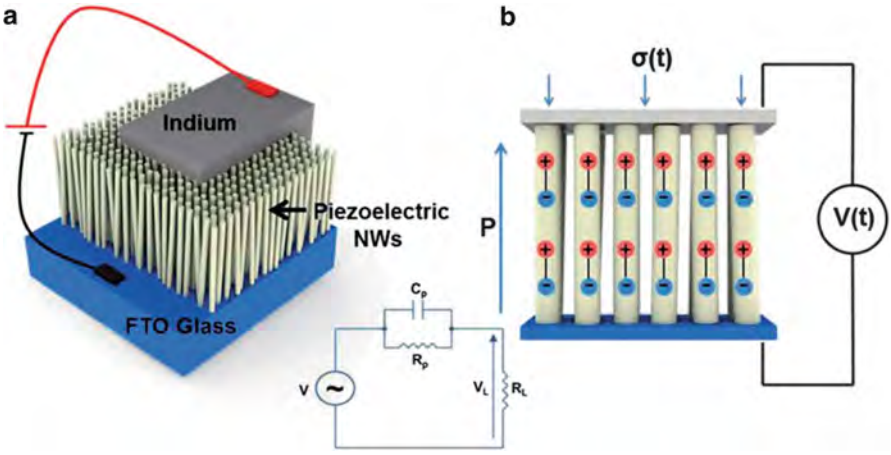

Fig. 5 Nano-electromechanical systems energy harvester configuration and characterization. (**a**) Schematic diagram of the NEMS energy harvester fabricated using piezoelectric NWarrays. (**b**) Schematic of voltage generation from the piezoelectric nano-electromechanical systems energy harvester [15] (All copyright reserved by RSC, 2013)

from the external force on the $BaTiO_3$ nanowire arrays will result in a piezoelectric charge due to the direct piezoelectric effect; as a result, an alternating potential difference can be developed between the two electrodes. The electrical equivalent circuit for the $BaTiO_3$ nanowire-based nanogenerator (also can be assumed to a parallel capacitor) is shown as an inset in Fig. 5 with the piezoelectric voltage, V, induced from the vibration acceleration in series with the inherent capacitance of the source, C_p, and piezoelectric leakage resistance, R_p, connected in parallel.

Energy Harvesting with ZnO Nanowires

Using ZnO nanowires grown on fibers, it is possible to fabricate flexible, foldable, and wearable power source in any shape (e.g., "power shirt"). The nanogenerator operates at <10 Hz in the range of conventional mechanical vibration, footsteps, and heartbeat, greatly expanding the application range of nanogenerators. To grow high-quality patterned ZnO nanowire arrays, the following two requirements should be meet. First, the ZnO nanowires should be grown following a designed pattern and direction, with a high degree of control in uniformity, orientation, dimensionality, and possibly shape. Second, the growth of ZnO nanofiber has to be at low temperature so that the nanowires can be integrated with fiber substrates. Patterned growth of ZnO nanowire arrays has been achieved by using patterned gold catalysts, seed layers, and self-assembled monolayer methods. In previous work, the researchers developed a simple catalyst-free process that could not only be used on flat polymer films but also on microfibers. Compared to the conventional piezoceramics nanowire-based nanogenerator, ZnO nanowire-based nanogenerators offer three distinct advantages: (1) enhanced piezoelectric effect (400–500 % enhancement of the piezoelectric effect), (2) superior mechanical properties (larger critical strain, higher flexibility, and longer operational lifetime), (3) high sensitivity to small forces (a force at the nanonewton or piconewton level), which has reported by Prof. Wang's group [16].

The nanogenerator based on ZnO nanowires can generate a potential as it is being dynamically strained under an extremely small force, and a transient flow of electrons in an external load as driven by the piezopotential to balance the Fermi levels at the two contacts is the fundamental mechanism of the nanogenetor [17]. The above conversion mechanism from mechanical energy into electrical power using vertically aligned ZnO nanowire arrays originally reported by Prof. Wang is based on the coupling of piezoelectric and semiconducting properties of ZnO nanowires, as well as Schottky barrier formed between the metal tip and the ZnO nanowires, which presumably rectifies the voltage generated by the piezoelectric effect at the mechanical excitation of ZnO nanowires. Accordingly, the mechanism for creating, separating, accumulating, and outputting the charges through a nanowire is presented in Fig. 6 [2]. For a vertical straight ZnO nanowire (Fig. 6a), the deflection of the ZnO nanowire by an atomic force microscope tip creates a strain field, with the outer side being stretched and inner side compressed. Because of the piezoelectricity of ZnO nanowire, a piezoelectric potential is produced across the nanowire, and the stretched side presents as positive and the compressed side presents as negative if the electrode at the bottom of the nanowire

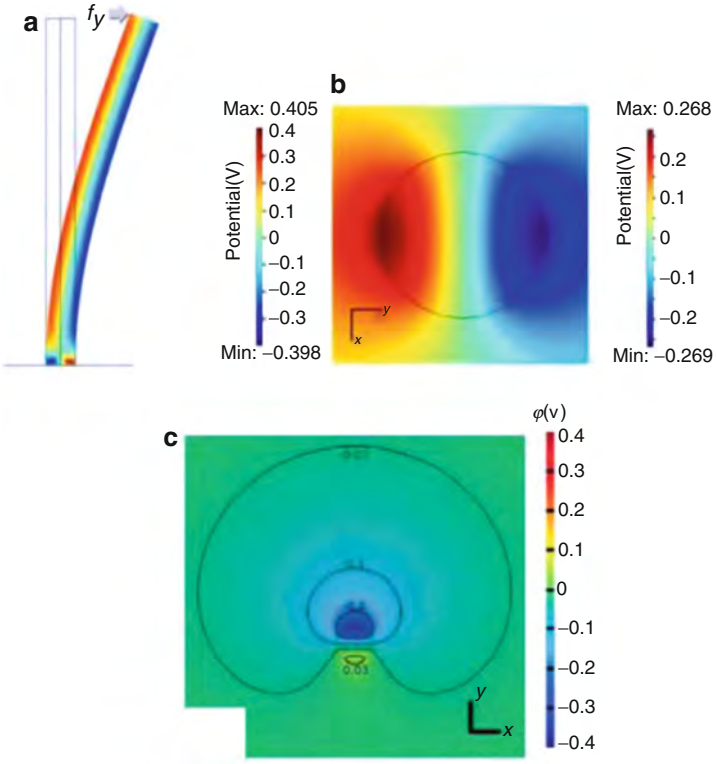

Fig. 6 Working principle of the ZnO nanowire-based nanogenerator [19] (All copyright reserved by ACS, 2007)

is grounded (Fig. 6b). The potential is created by the relative displacement of the Zn^{2+} cations with respect to the O^{2-} anions due to piezoelectric effect in the wurtzite crystal structure of the ZnO nanowire. Further, the ZnO nanowire can be regarded as an absolute insulator; these ionic charges cannot freely move and cannot recombine without releasing the strain [18]. The potential difference can be maintained as long as the deformation is in place and no foreign free charges (e.g., from the metal contacts) are injected in.

The ZnO textured film-based piezonanogenerator is also reported by Long Lin et al. [20]. The working mechanism of the piezonanogenerator is based on the piezoelectric property of the ZnO textured film. When the flexible piezonanogenerator device is deformed by an external force, a piezoelectric potential will be introduced in the ZnO textured film. As a result, a potential difference will be generated across the top and bottom electrodes due to induced charges, and it will drive the electrons flowing in the external load until equilibrium. When the external force is released and the piezoelectric nanogenerator recovers to its original shape, the piezopotential vanishes and the accumulated electrons will flow back in the opposite direction. Thus, an alternating-current output signal is expected from the

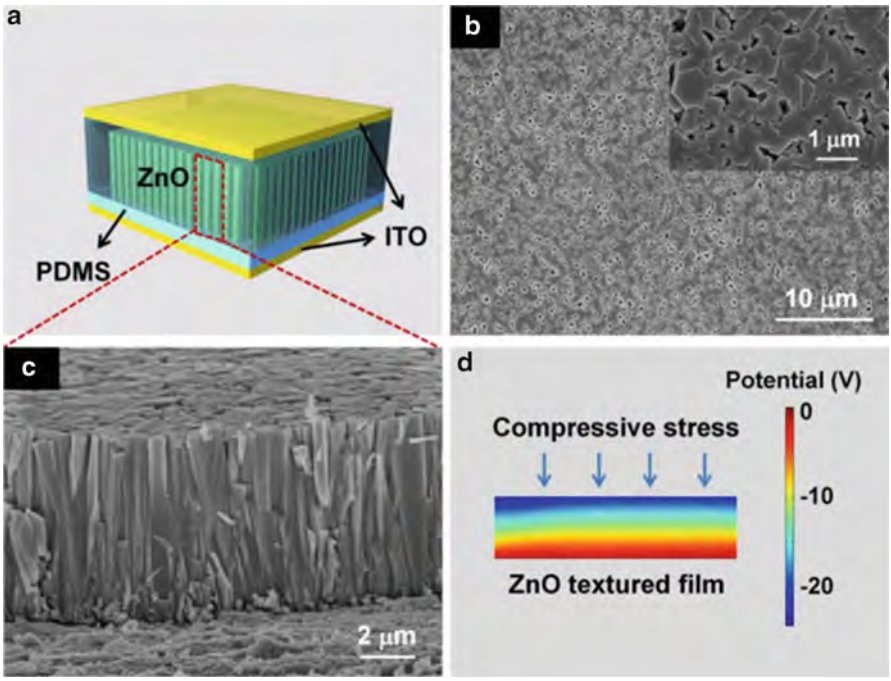

Fig. 7 Structure and working principle of the transparent flexible nanogenerator. (**a**) A schematic illustration of a typical composite structure of the flexible nanogenerator. (**b**) The *top*-view SEM image of the as-grown ZnO nanowire arrays. The inset is a high magnification of the image. (**c**) The cross-sectional SEM image of the as-grown ZnO nanowire arrays. (**d**) Demonstration of the working principle of the flexible nanogenerator from numerical calculation of the piezopotential in the ZnO textured film [20] (All copyright reserved by Elsevier Ltd, 2012)

electrical measurement. They used numerical calculation to theoretically estimate the generated piezopotential with an applied stress, as illustrated in Fig. 7d. For simplicity purposes, it was assumed that the textured film only experienced normal compressive stress during the deformation process. It was calculated that the piezopotential was 25 V with a compressive stress of 40 MPa. Since the piezoelectric nanogenerator was extraordinarily flexible owing to the unique characteristic of the PDMS substrate, the whole device could serve as an energy harvesting component in various working conditions, such as driven by wind blowing or body movement.

Energy Harvesting from Piezopolymer Nanofiber

Due to the low frequency of mechanical energy in human motion, an electric generator should possess the capability to harvest energy at low frequencies (<10 Hz). Earlier work reported by Shenck et al. presented a shoe-mounted piezoelectric generator using PZT and ZnO which is inflexible and difficult to be integrated in a wearable device. At a low-frequency motion, the energy stored E_c can be expressed as follows:

$$E_c = d_{ijk}\sigma_{jk} + \mu_{ijkl}\frac{\partial \varepsilon_{jk}}{\partial \chi_l}(i,j,k,l = 1,2,3)$$

The first term on the right-hand side refers to the piezoelectric effect, where σ_{jk} is the stress that is uniformly distributed across the material and d_{ijk} is the piezoelectric coefficient tensor. The second term on the right-hand side refers to the flexoelectric effect, i.e., the strain gradient ($\frac{\partial \varepsilon_{jk}}{\partial \chi_l}$) induced polarization and μ_{ijkl} is the flexoelectric coefficient tensor. In many cases, the flexoelectric effect is small and thus can be ignored. However, in a flexible device, apart from piezoelectric materials, equal attention should be placed upon the structural design of the wearable generators in which the significant flexoelectric effect can be utilized or eliminated.

Prof. X. M. Tao's research group has reported a highly durable all-fiber-based nanogenerator which can be worked in the low frequency of mechanical energy in human motion [21]. In the all-fiber generator, the piezoelectric nanofiber nonwoven fabric is physically sandwiched by two fabric electrodes. The interfacial stresses include pressure and friction without the presence of physical or chemical bonding. When subject to a uniform compressive pressure of 0.2 MPa on the top of the device, a complex nonuniform deformation filed is present, as shown in the cross-sectional SEM micrographs in Fig. 8a, b. Subject to compression on the top of the device, both the piezoelectric nonwoven fabric and electrode fabrics, which are flat and straight initially, are distorted to a large extent, bent, stretched, or compressed locally, which is contradictory to the earlier belief of uniform compression of the

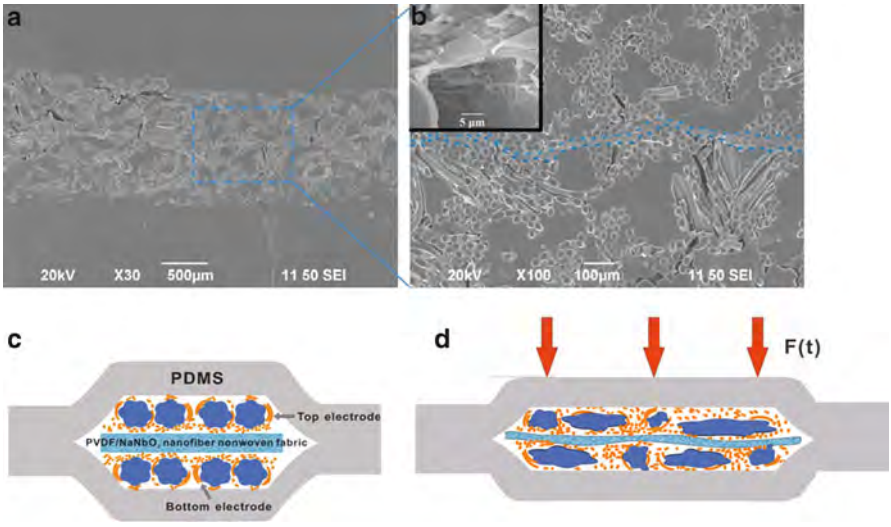

Fig. 8 The mechanism of the all-fiber nanogenerator with fabric electrodes [21] (All copyright reserved by RSC, 2013)

sandwich structure where all layers remain straight and deform only in the direction of thickness. This nonuniform deformation can be explained by the fabric structures. First, since the fabric electrode has a looped surface, the pressure distribution on the surface of PVDF/$NaNbO_3$ nanofiber nonwoven fabric is not uniform anymore. Secondly, the twisted composite yarns in the knitted loops are subject to lateral compression by adjacent yarns and the nonwoven fabric. Many other modes of deformation occur, including axial extension/compression, torsion, and bending of the yarn. It is evident that the cross-sections of the polyurethane core yarn are much distorted. Their cross-sectional areas become larger in some and in others flattened or reduced.

The working principle of the all-fiber-based nanogenerator is based on the insulating property of the PVDF/$NaNbO_3$ nanofiber and the creation of an inner piezoelectric field during applied tensile strain. Three working modes of the PVDF/$NaNbO_3$ nanofiber nonwoven fabric may take place simultaneously during the compression of the generator device, which lead to charge generation mainly due to the combination of out-of-plane compression strain (d_{33} mode) and in-plane tensile or compression strain (d_{31} mode) in the PVDF/$NaNbO_3$ nanofiber nonwoven fabric, as well as the flexoelectric effects as results of large strain gradient in the piezoelectric fibers. First, the thickness of PVDF/$NaNbO_3$ nonwoven fabric becomes ~20 μm from a free-standing one of 164 μm, which depicts the fact that the nanofiber fabric has a highly porous structure and relatively easy to compress. The thickness of a fabric electrode is also reduced from approximate 1 mm to 700 μm. Secondly, some polyurethane multifilament yarns exhibit a huge amount of cross-sectional deformation, either parallel or perpendicular to the direction of external pressure, which is much evident in the high-magnification image in Fig. 8b. Therefore, the surrounded silver-coated polyamide multifilament yarns were rearranged on the polyurethane core yarn, which will induce the localized in-plane membrane stretching or compression of the nonwoven fabric because of the internal friction between the silver-coated polyamide multifilament yarn and composite nanofibers. Some nanofiber stretching also occurs, as shown in the inset high-magnification image of Fig. 8b. Thirdly, since the measured Young's modulus of the nanofiber nonwoven fabric is 42 MPa, much smaller than 841 MPa of the silver-coated polyamide multifilament yarn, the nonwoven fabric is much easier to be deformed where it is not constrained by adjacent silver-coated polyamide yarns. Hence large strain gradients and significant flexoelectric effects are expected in these nonuniformly deformed areas of the piezoelectric nonwoven fabric. To summarize the discussions, the power generation mechanism of the all-fiber generator is illustrated in Fig. 8c, d, in which the PVDF/$NaNbO_3$ nanofiber nonwoven fabric is working in the localized longitudinal mode (d_{31}), and transverse mode (d_{33}) with significantly nonuniform strain field when a uniform external pressure is applied on the top surface of the generator device.

The fabric electrodes serve dual purposes: (1) it works as a normal charge collection network as well as (2) a mechanical element that transfers the uniform compressive pressure on the device into highly complex localized deformation in the piezoelectric nonwoven fabrics. Because of the semiconducting nature of the

PVDF/$NaNbO_3$ hybrid material, the generated charges have greater difficulties to flow through the PVDF/$NaNbO_3$ nanofiber nonwoven fabric, which results in a potential difference between the two fabric electrodes of the generator. In other words, the strained PVD all-fiber nanogenerator is analogous to a parallel-plate capacitor filled by a dielectric material. Hence the location and density of the electric contacts offered by the fabric electrodes may critically affect the total energy conversion performance of the devices. The second function of the fabric electrodes, the induction of nonuniform deformation fields in the piezoelectric nonwoven fabric and its associated charge generation mechanisms, is first revealed. Because of the complexity of the deformed fabric structure, a coupled mechanical and piezoelectric analysis of the nanogenerator is underway to determine the relationship between the fabric structures and the functions, together with full experimental investigations.

Fiber-Based Triboelectric Nanogenerator

Basic Concepts of Triboelectric Effect

The triboelectric effect can be attributed a type of contact charging effect in which certain materials become electrically charged after they contact with other materials. Simply, it can be described that an electric charge can transfer from one material to another when two different materials come into contact and separate, which is also called tribocharging. Actually, it is hard to classify the contacting process for charge transfer purposes into groups, such as vertical contact-separation, in-plane sliding and rolling, and thus the term of "triboelectric charging" is used in such a broad sense. The phenomenon of triboelectric charging between two difference materials have been studied for many years; however, there are still many unknowns, and in some cases, inconsistent results have been reported. This is because there are many factors, such as electrical, chemical, and physical properties of materials as well as environmental conditions, which can affect the triboelectric charging. Moreover, the distribution of the amount of charge on the surface also results in the difficulty to estimate the electrostatic charge and control the process. Figure 9 presents an ordering of materials based on their empirically derived direction of charge transfer. Generally, when two certain materials are contacted to each other, the material that is closer to the negative side of the triboelectric series will charge negatively while another material that is closer to the positive side will charge positively. For instance, the Teflon surface will charge negatively and the polyamide surface will charge positively when they are contacted to each other, because the Teflon is near the negative side and the polyamide is near the positive side of the series. The triboelectric series is not fully reproducible which has been reported in different research works, and these variations are likely due to small differences in the measurement technique, environment, or material structure. Owing to the coupling of contact charging and electrostatic induction, many triboelectric nanogenerators have been performed to

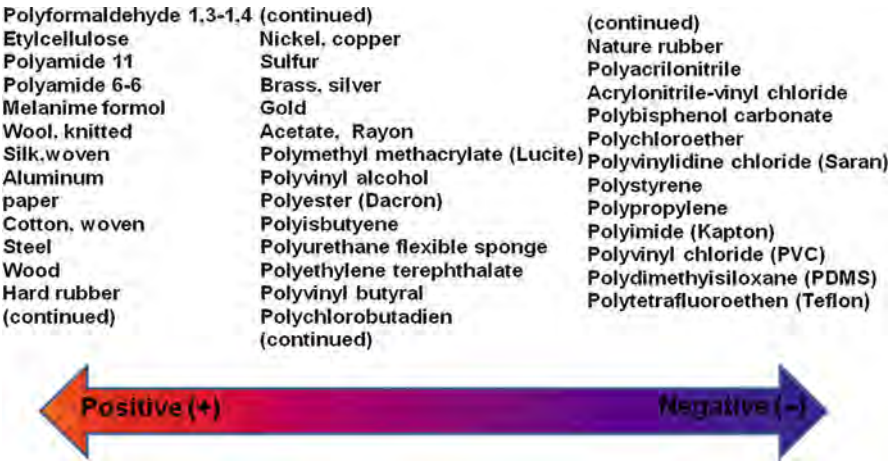

Fig. 9 Triboelectric series

some intrinsic property of the material, and electric generation was also achieved with repeating contact between the two polymer films that differ in polarity in triboelectric series. However, to analyze and control the triboelectric charging, it is still a very critical issue to measure the electrostatic charge and evaluate the electrostatic characteristics. Further, it is necessary to obtain an in-depth understanding based on theoretical analyses to improve existing processes and to develop new applications.

Using of the Triboelectric Effect

In recent years, triboelectric nanogenerators have attracted great attention in energy harvesting because they exhibited a high output power together with simple and flexible device structures. Typically, triboelectric nanogenerators are facilely prepared by closely separating two different triboelectric materials (e.g., polydimethylsiloxane (PDMS), polyester, Kapton, or aluminum) which are contacted to each electronic conductive layer as an electrode. When external mechanical forces are applied to triboelectric nanogenerators, electronic charges are generated by touching and rubbing the two triboelectric materials' surfaces together. Thus, the charge flow is repeatedly created under triboelectric potential by subsequent cycles of touching and separation between two materials. On the other hand, there have been many efforts to achieve high output power and efficiency in triboelectric nanogenerators by considering the effectiveness of (i) the triboelectric charge generation and (ii) the separation of two materials. The first one has been improved by employing microstructures of triboelectric materials. During the triboelectric process, energy conversion is achieved by the periodic contact between two

triboelectric materials that differ in the polarity of triboelectricity yields surface charge transfer, and the microstructures provide larger triboelectric charges at the surface. Further, it has been reported that micro-/nanostructured films produced large output power due to the increase in the contact area as compared with that of flat films. Moreover, the nano- or microstructures allow for an efficient separation between two triboelectric materials after friction because their morphology decreases the contact area of the surface. For more efficient separation, the use of a spacer or novel design of nanogenerators such as disk-like structures has been reported, which is useful for rapid operation. Unfortunately, these approaches require somewhat complicated sophisticated pattern design and a high degree of integration for high performance and have a limit for scalable production. Currently, various kinds of nanoparticles or nanowires are used to decorate triboelectric materials in order to increase the friction between two contact materials in the triboelectric nanogenerators. However, due to the soft and ductile behavior of nanoparticle/nanowires, the performance of triboelectric nanogenerators is generally degraded under a large applied force, and therefore power stability is essential. To utilize triboelectric nanogenerators in diverse and broad fields of our living environment, a simple and cost-effective fabrication process for efficient triboelectric nanogenerators is essential. Furthermore, the output performance of triboelectric nanogenerators is also drastically affected by the humidity; maintaining a stable performance in moisture atmosphere is currently a challenge. Therefore, the realization of triboelectric nanogenerators with high performance under a wide range of humid conditions is highly desirable because the abundance of water molecules in moisture atmospheres results in antistatic materials with a "sweat layer" function, which results in a huge reduction of the triboelectric charging capacity in all materials.

Mechanism of Fiber-Based Tribonanogenerator

The basic working principle for triboelectric nanogenerators is a combination of contact charging and electrostatic induction. Two classifications of the triboelectric nanogenerators could be obtained from the charge separation mechanism which are contact-mode and sliding-mode triboelectric nanogenerators, and the classifications are based on vertical charge polarization and in-plane charge polarization, respectively [22]. Both the modes of triboelectric nanogenerators have been demonstrated to many applications including self-powered system and wearable electronics. Generally, the mechanism of fiber-based tribogenerators can be described as follows. At the initial state, i.e., before the contact (friction) of the materials, there is no any electric potential. According to the triboelectric series, charges transfer though the friction (sliding) of the materials (at this stage, the triboelectric nanogenerators remain in electrostatic equilibrium state due to negligible dipole moment). As the triboelectric nanogenerator is laterally shifted, the electrostatic equilibrium is broken, and so electrons start to flow.

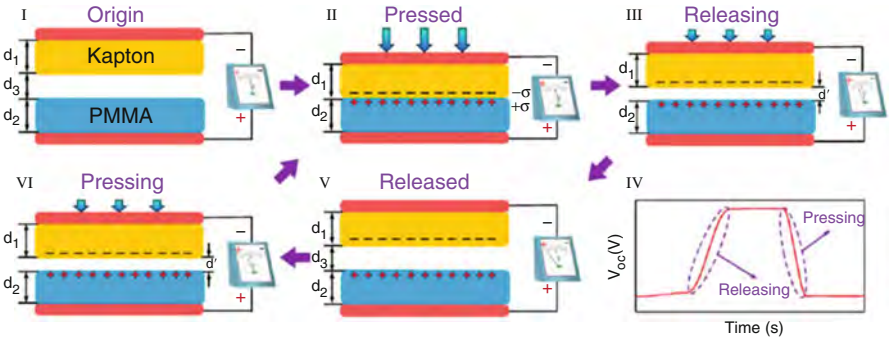

Fig. 10 The operating principle of the triboelectric nanogenerator worked open-circuit condition [23, 24] (All copyright reserved by ACS, 2012)

Vertical Contact-Separation Mode

The operating principle of the triboelectric nanogenerators for the case of dielectric-to-dielectric in contact-separation mode can be described by using contact charging and electrostatic induction which was reported by Prof. Wang [23]. Figure 10 describes the electric output mechanism of open-circuit voltage. Initially, no charge is generated on the surface of the two materials, with no electric potential difference between the two electrodes (Fig. 10, stage I). When applied an externally force on the triboelectric nanogenerator, surface charge transfer takes place at the contact area because of triboelectric effect. Suppose the triboelectric nanogenerator and the contacted materials are uncharged before, thus all of their surface static charges on the contact area are generated by the triboelectrification process. According to the triboelectric series, electrons are transfer from triboelectrically positive polymer (PMMA) into negative polymer (Kapton), resulting in net negative charges at the surface of triboelectrically negative material and net positive charges at the surface of triboelectrically positive material, respectively. It is interesting to notice that the insulation of the two polymers allows long-time retention of triboelectric charges for several hours or even days. Since the triboelectric charges with opposite signs are only confined on the contact surface, no electric potential difference will be generated between the two electrodes (Fig. 10, stage II). As one of the triboelectrically polymer (e.g., Kapton film) starts to move apart from the other, the Kapton film tends to revert back to the contact statute because of the electrostatic attraction between the triboelectric charges. Once the two polymer films are separated, an electric potential difference is produced between the two electrodes (Fig. 10, stage III). And the electric potential between the two electrodes can be calculated by [22]

$$V = -\frac{\sigma d'}{\varepsilon_0}$$

where σ is the triboelectric charge density, ε_0 is the vacuum permittivity, and d' is the interlayer distance at a given state.

When being released, the generator's open circuit of voltage (V_{oc}) increases until reaching the maximum distance (as shown in Fig. 10, stage IV and Fig. 10, stage V). Such a signal of maximum value (V_{oc}) will keep a constant value. If applied another externally force again, the electric potential difference starts decrease, and at the same time the distance of the two polymer layers become closer. Under this condition, when the two polymer layers make another full contact, V_{oc} drops to zero from the maximum value (Fig. 10, stage V, VI).

If the two electrodes are shorted, short-circuit current will be produced as shown in Fig. 11. When the polymer film separates from another one, the produced electric potential difference can drive electrons to flow from the bottom electrode to the top electrode through an external circuit in order to balance the generated triboelectric potential (Fig. 11 stage II). When the separation distance between the two polymer films is maximized, the flow of electrons stopped because an electrostatic equilibrium is reached (Fig. 11 stage III). Subsequently, the top polymer film is driving to contact with the bottom polymer again and could break the former electrostatic equilibrium. In consequence, electrons flow from top electrode back to bottom electrode, reducing the amount of induced charges (Fig. 11 stage IV). When the top polymer film and bottom polymer film contact with each other again, all of the induced charges are neutralized (Fig. 11 stage I). This process corresponds to an instantaneous negative current (Fig. 11, stage V). The induced charge density (σ_0) when the generator is fully released is given by [24]

$$\sigma' = \frac{\sigma d' \varepsilon_{rk} \varepsilon_{rp}}{d_1 \varepsilon_{rp} + d' \varepsilon_{rk} \varepsilon_{rp} + d_2 \varepsilon_{rk}}$$

where ε_{rk} and ε_{rp} are the relative permittivity of Kapton and PMMA, respectively, and d_1 and d_2 are the thicknesses of the Kapton film and the PMMA layer. The maximum value of $\sigma'_{\max}$ is obtained by substituting d_3 for d' in the equation above.

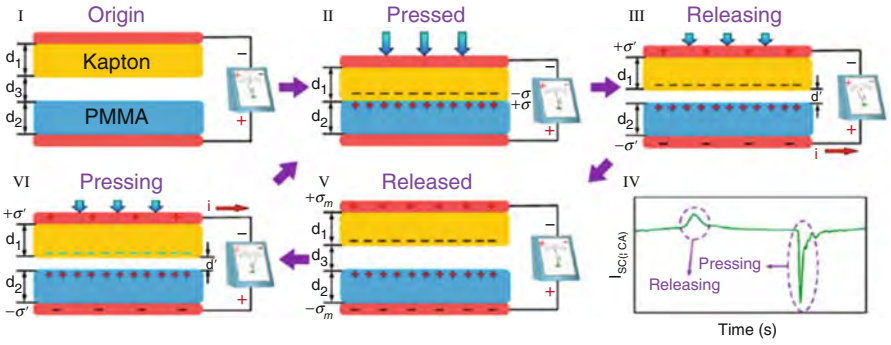

Fig. 11 The operating principle of the triboelectric nanogenerator worked short-circuit condition [23, 24] (All copyright reserved by ACS, 2012)

In-Plane Sliding Mode

Figure 12 schematically illustrated the sliding-induced electricity generation mechanism [25]. At initial position (Fig. 12, stage I), the two polymer films are fully overlapped and intimately contact with each other. Because PTFE is much more triboelectrically negative than nylon, electrons will transfer from PTFE film into the nylon film, leaving the Nylon surface and the PTFE surface with net positive charges and net negative charges with equal density, respectively. Since the tribocharges on the polymer film will only distribute in the surface of polymers and will not be leaked out for an extended period of time, the positive charges on nylon film and negative charge on PTFE film are fully compensated by each other, and thus there is no electric field in the surrounding space. As long as the top plate with the positively charged surface starts to slide outward (Fig. 12, stage II), the in-plane charge separation is initiated for the contact surface area decreasing. Following that, an electric potential difference is produced, which makes the electrons flow from top electrode to bottom electrode, for producing an electric potential drop that can cancel the tribocharge-induced potential. Compared with the lateral charge separation distance, since the vertical distance between the tribocharged polymeric surface and the electrode layer is negligible, an approximately equaled amount is achieved between the transferred charges on the electrodes and the separated charges at any sliding displacement (Fig. 12, stage II). The electrons stop flowing until the top plate fully slides out of the bottom plate and the tribocharged surfaces are entirely separated (Fig. 12, stage III). Subsequently, with a backward sliding of the top plate from an entirely separated statue to an overlapping statue, the separated charges begin to get in contact again, and the redundant transferred charges on the electrodes will flow back forming a reverse current in the load (Fig. 12, stage IV). As long as an overlapping position is achieved by the two plates, the charged surfaces get into another full contact. Under this condition, the electrode will own no residual transferred charges, and the flow of electrons will be stopped which is the end of one cycle (Fig. 12, stage I). In this entire cycle, since symmetric processes of sliding outward and inward occur, a pair of symmetric alternating-current peaks is expected to be obtained.

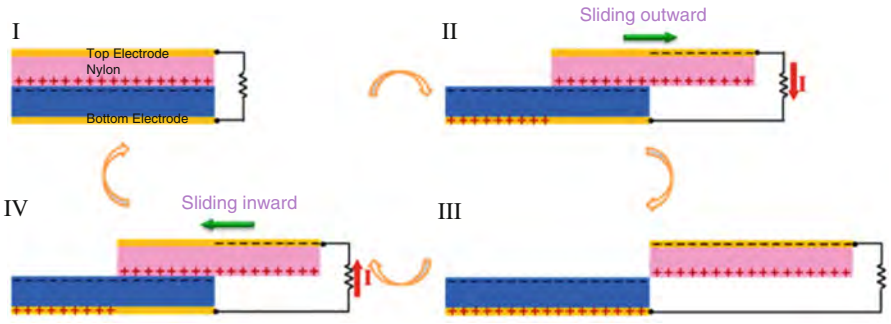

Fig. 12 Working mechanism and electric outputs of triboelectric nanogenerator worked on sliding mode [25] (All copyright reserved by ACS, 2013)

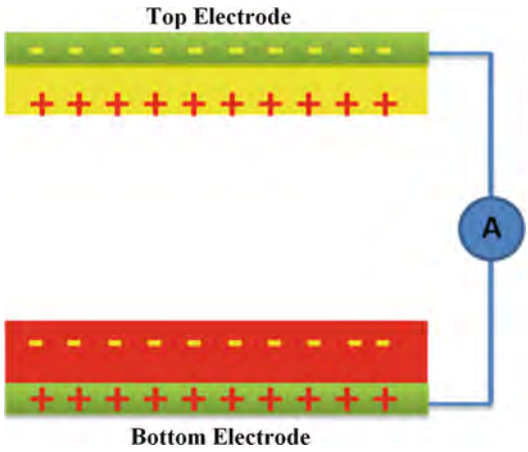

Fig. 13 Dielectric-to-dielectric contact-mode of triboelectric nanogenerator

Modeling and Theory

Vertical Contact-Separation Mode

The triboelectric nanogenerator can generate two kinds of output signals, which are open-circuit voltage attributed to the static information to be provided by the triboelectric nanogenerator, and short-circuit current depends on the rate at which the induced charge would flow [23]. Experimentally, it is known that the output power as provided by a triboelectric nanogenerator is a result of materials, separation distance, and contacting force. But a comprehensive theoretical model should be built for the triboelectric nanogenerator. Niu et al. constructed a theoretical model for contact-mode triboelectric nanogenerator recently, and the theory presented here is the first in-depth interpretation of the contact-mode triboelectric nanogenerator, which can be viewed as an important pioneer work for rational design of the triboelectric nanogenerator structure in specific applications [22]. According to the theoretical mode, three key parameters, including the output voltage (V), the amount of transferred charge (Q) between the two electrodes, and the separation distance (x) between the two triboelectric charged layers, were used to express the real-time power generation of a triboelectric nanogenerator, and the three parameters can be named the V–Q–x relationship. Firstly, the dielectric-to-dielectric contact-mode of triboelectric nanogenerator was shown in Fig. 13 [22]. The parameters of d_1 and d_2 are corresponding to the thicknesses of the two dielectric plates, and ε_{r1} and ε_{r2} are the relative dielectric constants of the two triboelectric layers, respectively. The separation distance (x) between the two triboelectric layers can be varied under the external mechanical force. The amount of transfer charges is defined as Q, which also represents the instantaneous amount of charges on each electrode (with opposite signs). When one triboelectric layer begins to separate from the other one, which corresponds to the increasing of the separation distance of x, an electric potential difference (V) between the two electrodes will be induced, which will drive the amount of transfer charges between

the two electrodes, and the amount of transfer charges is defined as Q, which also represents the instantaneous amount of charges on each electrode (with opposite signs).

Therefore, the V–Q–x relationship for the dielectric-to-dielectric triboelectric nanogenerator in contact-mode can be given by

$$V = -\frac{Q}{S\varepsilon_0}\left(\frac{d_1}{\varepsilon_{r1}} + \frac{d_2}{\varepsilon_{r2}} + x(t)\right) + \frac{\sigma x(t)}{\varepsilon_0}$$

Similarly, the model for the conductor-to-dielectric category can be built when $d_1 = 0$

$$V = -\frac{Q}{S\varepsilon_0}\left(\frac{d_2}{\varepsilon_{r2}} + x(t)\right) + \frac{\sigma x(t)}{\varepsilon_0}$$

The theory presented here is the first in-depth interpretation and analysis of the contact-mode triboelectric nanogenerator's working principle, clearly showing its unique operation characteristics, which will be able to serve as important guidance for rational design of the nanogenerator's structure in specific self-power applications.

In-Plane Sliding Mode

Compared to the vertical contact-separation mode of triboelectric nanogenerators, the V–Q–x relationship of triboelectric nanogenerators worked on sliding mode is highly complicated because of the nonuniform charge distribution on the metal electrode surface. Therefore, finite element method (FEM) has been used to calculate the distribution of electric potential, electric field, dielectrics, and charge on the electrodes which has been reported by Simiao Niu et al. [26]. In this case, the FEM calculation was carried out utilizing the COMSOL software under the open-circuit condition of the designed structure, and open-circuit boundary condition of the total surface charge density at each metal electrode was assigned as 0. The electric potential of the top electrode is positive while that of the bottom electrode is negative because of the electrostatic induction of the tribocharges [23]. From the experiment result, the open-circuit electric potential difference (V_{OC}) between these two electrodes was increased with increase the shift distance of x.

As a result, the V–Q–-x relationship for dielectric-to-dielectric sliding-mode triboelectric nanogenerators can be given by

$$V = -\frac{1}{\omega\varepsilon_0(l-x)}\left(\frac{d_1}{\varepsilon_{r1}} + \frac{d_2}{\varepsilon_{r2}}\right)Q + \frac{\sigma x}{\varepsilon_0(l-x)}\left(\frac{d_1}{\varepsilon_{r1}} + \frac{d_2}{\varepsilon_{r2}}\right)$$

Similarly, when d_1 is set to 0, the V–Q–x relationship for the metal-to-dielectric sliding mode of triboelectric nanogenerators can be given by

$$V = -\frac{1}{\omega\varepsilon_0(l-x)}\frac{d_2}{\varepsilon_{r2}}Q + \frac{\sigma x}{\varepsilon_0(l-x)}\frac{d_2}{\varepsilon_{r2}}$$

Furthermore, based on the analytical *V*–*Q*–*x* equation of triboelectric nanogenerator worked on contact and sliding mode, dynamic output performance of triboelectric nanogenerator was calculated with arbitrary load resistance, and good agreement with experimental data was reached. The theory presented in this section is not just only to demonstrate a milestone work for in-depth understanding of the working mechanism of the triboelectric nanogenerator but also to provide a theoretical basis for further enhancement of performance and to greatly broaden the application of energy-harvesters.

Factors of Triboelectric Nanogenerator

The Role of Surface Proprieties

The morphologies of the surfaces can be modified by currently micro-/nano-coating technologies, which are effective for enhancing the contact area and improvement energy conversion efficiency of the triboelectric nanogenerator. In order to enhance the triboelectrification effect, surface functionalization of polymer fiber can largely change the surface potential. For instance, the surfaces of the fiber-based nanogenerators can be functionalized chemically using various molecules, as well as nanowires or nanoparticles. For instance, the surfaces of the fiber-based nanogenerators can be functionalized chemically using various molecules, as well as nanowires or nanoparticles. Furthermore, the introduction of micro-/nanostructures onto the fiber surfaces can make a variation to local contact characteristics, which has the potential to improve the triboelectrification. However, the introduced micro-/nanostructure on the surface may increase the friction force, resulting in a reduction of the energy conversion efficiency. Therefore, an optimization structure should be designed to maximize the conversion efficiency, which involves a large amount of studies for testing a range of materials and a range of available nanostructures. Besides the surface functionalization of polymer fiber, the contact materials can be prepared by polymer composites, such as blending polymer systems, nanoparticles/polymer composites, and other polymer systems with unique structure. All the efforts may improve energy conversion efficiency of the triboelectric nanogenerator, which is due to not only the surface electrification but also the permittivity of the materials.

The Role of Humidity

In triboelectrics, the surface of the insulating material, such as PDMS, is electrically charged during contact, and it has the ability to hold charges for a longer time. However, the surface charge significantly depends on the ambient relative humidity and generally degrades with an increase of humidity in the atmosphere. It is generally accepted that humidity creates a layer of water on a surface, which allows charge to "leak away," thereby reducing the electrostatic charging effect. In fact, one type of

"anti-static" additive used to reduce the effects of contact charging works by this mechanism [27]. Here, hydroscopic surfactant molecules partition to the polymer surface and attract water and salts from the atmosphere to form a conducting layer on the surface. Until now, it is still a challenging task to maintain the electric charges and a stable and even electric output in a high-moisture atmosphere.

Prof. Kim's group has reported a new type of sponge structure-based triboelectric nanogenerator with stable power output performance under a wide range of humid conditions. The electric output performance of the triboelectric nanogenerators based on different pore size was measured and plotted under various relative humidity conditions [28]. It is clearly seen that the output voltage is maintained up to 70 % RH although the output voltage starts to decrease significantly from 80 % RH in the designed triboelectric nanogenerators. This may be ascribed to the dissipation of the charge buildup due to the formation of a water layer on the surface of the PDMS films, which is a well-known effect. It can believed that this work will serve as a stepping stone for high-performance and stable triboelectric nanogenerators studies and will also inspire major developments of triboelectric nanogenerators toward self-powered electronics in the near future.

The effect of the relative humidity on the performance of triboelectric nanogenerator also has been reported by Rusen Yang [29]. Triboelectric nanogenerator can work at different pressure from 50 Torr to an atmospheric pressure and at different relative humidity from 10 % to 90 %. This study also suggested that the ambient pressure at RH close to 0 % maximizes the triboelectric charge generation, and the optimal pressure drops to a pressure lower than the atmospheric pressure when the humidity is higher. The adsorbed water layer plays an important role in the charge generation. Although the water layer is necessary to distribute and separate the charge, the required layer should be thin, approximately below 2 nm, for the ion transfer. A thick water layer increases the surface conductivity and therefore discharges the surfaces.

The Role of Plasma Treatment on Triboelectric Nanogenerator

Some investigations suggest that the nature of the chemical species on the surface is the most important aspect for controlling the triboelectric charge of the triboelectric materials. One method for effecting chemical change on polymer surfaces is by using reactive gases or plasmas. For example, Hayes noted that brief exposure of polyethylene film to an air corona discharge or to ozone resulted in a change in the charging condition of the surface. J. Kodama reported that effect of plasma treatment on the triboelectric materials [30]. In this work, oxygen and/or nitrogen have been incorporated into the surface structure of polymer using a downstream microwave plasma reactor. The surfaces of PS and PMMA powders were modified by treating them with downstream nitrogen and oxygen plasmas. The surface charge density (Q/A) of nitrogen plasma-treated PS powder has shown a very rapid change toward a positive charge with small increases in N/C. It is believed that nitrogen atoms could act as a donor and increase the unoccupied surface states in the surface of PS. The variation of Q/A of PMMA has been much less than that of PS, perhaps because of the larger number of surface states in the band gap.

Summary

The widespread and relatively high-yield synthesis of fiber-based nanogenarator achieved in the past two decades offers great promise to their application in next-generation electronics and energy harvesting devices. However, a better understanding of mechanical and electromechanical behavior of these micro- or nanostructures is critical prior to their successful integration into optimized reliable nanogenerator.

With respect to piezoelectricity, several important physical effects have been reported in of the piezoelectric nanogenerator, including piezoelectricity, piezoelectric hysteresis and ferroelectric switching, stable and one-dimensional monodomain polarization, nonvolatile electric polarization, and size effect of nanowire. The current challenges should be resolved to improve the piezoelectricity, for example, to control the nanosize of nanowire below 100 nm in diameter, as well as current challenges in bridging experimental and computational studies. Even first-principle calculations are subject to variations depending on the piezoelectricity used, similar to what has been done for mechanical properties, is a critical need.

With respect to triboelectric nanogenerator, the analytical V–Q–x equation of triboelectric nanogenerator worked on contact-mode and sliding presented a milestone work for in-depth understanding of the working mechanism of the triboelectric nanogenerator, but all of the molds are base on the theory of parallel-plate capacitor. When consider the real structure of the inside surface, the effect of point discharge, the electric field direction and the size effect of micro or nanomaterials also should be reconsidered. Further, suitable materials and newly designed fabrication technology are urgently needed to achieve high performance that can match that of the current realistic configurations.

Overall, several challenges must be met before the realization of wearable fiber-based energy harvesting devices. Enhancement must be made for the overall power conversion efficiency for real applications, which has three components: (1) the internal conversion efficiency of the active materials; (2) the efficiency related to the device, that is, the ability to collect and transfer electric charges; and (3) the efficiency determined by the harvesting circuit and storage. One can further enhance the total power by using arrays or networks of nanogenerators, and durability is also a major issue in addition to comfort in wear.

References

1. Zeng W, Shu L, Li Q, Chen S, Wang F, Tao XM (2014) Fiber-based wearable electronics: a review of materials, fabrication, devices, and applications. Adv Mater 26:5310–5336
2. Wang XD (2012) Piezoelectric nanogenerators-harvesting ambient mechanical energy at the nanometer scale. Nano Energy 1:13–24
3. Wang ZL, Zhu G, Yang Y, Wang SH, Pan CF (2012) Progress in nanogenerators for portable electronics. Mater Today 15:532–543
4. Kim HS, Kim JH, Kim J (2011) A review of piezoelectric energy harvesting based on vibration. Int J Precis Eng Man 12:1129–1141

5. Zhu G, Wang AC, Liu Y, Zhou YS, Wang ZL (2012) Functional electrical stimulation by nanogenerator with 58 V output voltage. Nano Lett 12:3086–3090
6. Soin N, Shah TH, Anand SC, Geng JF, Pornwannachai W, Mandal P, Reid D, Sharma S, Hadimani RL, Bayramol DV, Siores E (2014) Novel "3-D spacer" all fibre piezoelectric textiles for energy harvesting applications. Energy Environ Sci 7:1670–1679
7. Jung JH, Lee M, Hong JI, Ding Y, Chen CY, Chou LJ, Wang ZL (2011) Lead-free NaNbO3 nanowires for a high output piezoelectric nanogenerator. ACS Nano 5:10041–10046
8. Park KI, Xu S, Liu Y, Hwang GT, Kang SJL, Wang ZL, Lee KJ (2010) Piezoelectric BaTiO3 thin film nanogenerator on plastic substrates. Nano Lett 10:4939–4943
9. Lin YF, Song J, Ding Y, Lu SY, Wang ZL (2008) Piezoelectric nanogenerator using CdS nanowires. Appl Phys Lett 92:0221051–0221053
10. Li JF, Wang K, Zhu FY, Cheng LQ, Yao FZ (2013) (K, Na) NbO3-based lead-free piezoceramics: fundamental aspects, processing technologies, and remaining challenges. J Am Ceram Soc 96:3677–3696
11. Shenck NS, Paradiso JA (2001) Energy scavenging with shoe-mounted piezoelectrics. IEEE Micro 21:30–42
12. Erturk A, Inman DJ (2008) Issues in mathematical modeling of piezoelectric energy harvesters. Smart Mater Struct 17:065016
13. Sun CL, Shi JA, Wang XD (2010) Fundamental study of mechanical energy harvesting using piezoelectric nanostructures. J Appl Phys 108:034309
14. Espinosa HD, Bernal RA, Minary-Jolandan M (2012) A review of mechanical and electromechanical properties of piezoelectric nanowires. Adv Mater 24:4656–4675
15. Koka A, Zhou Z, Sodano HA (2014) Vertically aligned $BaTiO_3$ nanowire arrays for energy harvesting. Energy Environ Sci 7:288–296
16. Action N, Albert C, Pearson L (2012) Piezoelectric energy harvesting devices: an alternative energy source for wireless sensors. Smart Mater Res 2012:1–13
17. Wang ZL (2001) Piezoelectric nanogenerators for self-powered nanosensors and nanosystems. In Wiley encyclopedia of electrical and electronics engineering. John Wiley, Sons, Inc. USA
18. Wang XD, Song JH, Wang ZL (2007) Nanowire and nanobelt arrays of zinc oxide from synthesis to properties and to novel devices. J Mater Chem 17:711–720
19. Gao Y, Wang ZL (2007) Electrostatic potential in a bent piezoelectric nanowire. The fundamental theory of nanogenerator and nanopiezotronics. Nano Lett 7:2499–2505
20. Lin L, Hu YF, Xu C, Zhang Y, Zhang R, Wen XN, Wang ZL (2013) Transparent flexible nanogenerator as self-powered sensor for transportation monitoring. Nano Energy 2:75–81
21. Zeng W, Tao XM, Chen S, Shang SM, Chan HLW, Choy SH (2013) Highly durable all-fiber nanogenerator for mechanical energy harvesting. Energy Environ Sci 6:2631–2638
22. Niu SM, Wang SH, Lin L, Liu Y, Zhou YS, Hu YF, Wang ZL (2013) Theoretical study of contact-mode triboelectric nanogenerators as an effective power source. Energy Environ Sci 6:3576–3583
23. Wang ZL (2013) Triboelectric nanogenerators as new energy technology for self-powered systems and as active mechanical and chemical sensors. ACS Nano 7:9533–9557
24. Zhu G, Pan CF, Guo WX, Chen CY, Zhou YS, Yu RM, Wang ZL (2012) Triboelectric-generator-driven pulse electrodeposition for micropatterning. Nano Lett 12:4960–4965
25. Wang SH, Lin L, Xie YN, Jing QS, Niu SM, Wang ZL (2013) Sliding-triboelectric nanogenerators based on in-plane charge-separation mechanism. Nano Lett 13:2226–2233
26. Niu SM, Liu Y, Wang SH, Lin L, Zhou YS, Hu YF, Wang ZL (2013) Theory of sliding-mode triboelectric nanogenerators. Adv Mater 25:6184–6193
27. Lacks DJ, Sankaran RM (2011) Contact electrification of insulating materials. J Phys D Appl Phys 44:453001

28. Lee KY, Chun J, Lee JH, Kim KN, Kang NR, Kim JY, Kim MH, Shin KS, Gupta MK, Baik JM, Kim SW (2014) Hydrophobic sponge structure-based triboelectric nanogenerator. Adv Mater 26:5037–5042
29. Nguyen V, Yang RS (2013) Effect of humidity and pressure on the triboelectric nanogenerator. Nano Energy 2:604–608
30. Kodama J, Foerch R, Mcintyre NS, Castle GSP (1993) Effect of plasma treatment on the triboelectric properties of polymer powders. J Appl Phys 74:4026–4033

Functional Nanofibers for Energy Storage 20

Yao Lu, Chen Chen, and Xiangwu Zhang

Contents

Introduction 514
Electrospinning of Nanofibers 516
Nanofiber Anodes 517
Carbon Nanofiber Anodes 518
Tin Antimony Alloy/CNF Anodes 521
Silicon/CNF Anodes 522
Manganese Oxide/CNF Anodes 526
Nanofiber Cathodes 528
$LiCoO_2$ Nanofiber Cathodes 529
$LiMn_2O_4$ Nanofiber Cathodes 531
$LiFePO_4$/CNF Cathodes 534
Li_2MnSiO_4/CNF Cathodes 535
Nanofiber Separators 539
Summary and Outlook 543
References 545

Abstract

Among a variety of current energy storage technologies, rechargeable lithium-ion batteries are considered to be an effective solution to the ever-growing demand for high-power and high-energy electrochemical power sources. Novel nanofiber preparation technologies, such as electrospinning, offer a great opportunity to design new materials for advanced lithium-ion batteries. This chapter addresses developing novel nanofiber-based anode, cathode, and separator materials for lithium-ion batteries. The discussion focuses on the preparation, structure, and performance of nanofiber-based anode materials such as carbon nanofibers (CNFs), tin antimony

Y. Lu • C. Chen • X. Zhang (✉)
Fiber and Polymer Science Program, Department of Textiles Engineering, Chemistry and Science, North Carolina State University, Raleigh, NC, USA
e-mail: ylu14@ncsu.edu; cchen20@ncsu.edu; xiangwu_zhang@ncsu.edu

© Springer Science+Business Media Singapore 2015

X. Tao (ed.), *Handbook of Smart Textiles*,
DOI 10.1007/978-981-4451-45-1_18

alloy/CNFs, silicon/CNFs, and manganese oxide/CNFs; cathode materials including lithium cobalt oxide nanofibers, lithium manganese oxide nanofibers, lithium iron phosphate/CNFs, lithium manganese silicate/CNFs, as well as separators such as lithium lanthanum titanate/polyacrylonitrile composite nanofiber separators. By employing the nanofiber structure, the nanofiber anodes and cathodes exhibit high capacity and stable cycling performance, while the nanofiber separators show improved electrolyte uptake, high ionic conductivity, low interfacial resistance, and enhanced capacity and cycling stability in lithium-ion batteries. These results suggest that electrospinning is a promising technology to fabricate nanofiber-based anode, cathode, and separator materials for rechargeable lithium-ion batteries.

Keywords

Nanofiber • Electrospinning • Lithium-ion battery • Cathode • Anode • Separator • Carbon nanofiber • Tin antimony alloy • Silicon • Manganese oxide • Lithium cobalt oxide • Lithium manganese oxide • Lithium iron phosphate • Lithium manganese silicate • Lithium lanthanum titanate • Polyacrylonitrile • Lithium aluminum titanium phosphate • Polyvinylidene fluoride

Introduction

Fossil fuels, including coal, oil, and natural gas, have been used at a dramatically increasing scale in the last decades, and associated global issues have come out, both economically and ecologically [1]. The constantly rising oil price and the long-term greenhouse effect due to massive emission of carbon dioxide generated from fossil fuels compose a battery of great challenges for the twenty-first century. Thus, there has been growing interest in renewable energy sources including wind, solar, tidal, and geothermal powers. However, these technologies are highly geo/weather dependent and are difficult to manage. It is therefore very urgent to advance energy storage technologies to effectively utilize these renewable energy sources in future smart grids and power delivery systems [2].

Among various energy storage technologies, rechargeable lithium-ion batteries draw extensive attention due to their high-energy densities and power densities: they can provide energy densities 2–3 times and power densities 5–6 times higher than traditional Ni-MH and Ni-Cd batteries [3, 4]. In addition to high power/energy densities, lithium-ion batteries also possess high coulombic efficiency, high operating voltage, low self-discharge, and no "memory effect" [5]. These advantages make lithium-ion batteries an effective solution to the ever-growing demand for high-energy electrochemical power sources and, consequently, they are currently accounted for 63 % share of the world's sales of portable batteries versus 37 % combined for Ni-MH and Ni-Cd batteries [3].

A typical lithium-ion battery is composed of an anode and a cathode, partitioned by an electrolyte-containing separator, as illustrated in Fig. 1. The electrolyte contains dissociated lithium salts and enables the lithium-ion transfer between

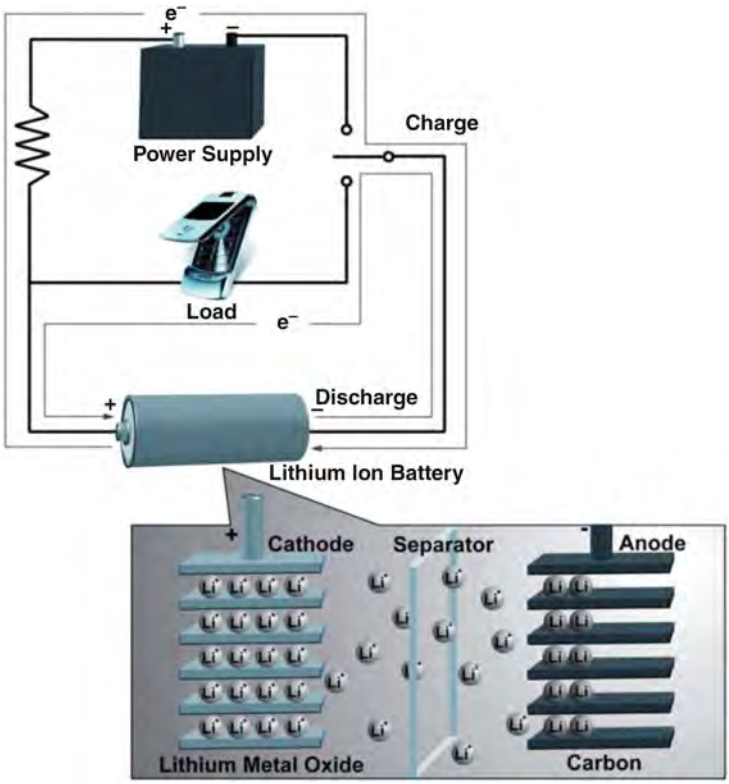

Fig. 1 Schematic of a lithium-ion battery. A typical lithium-ion battery consists of an anode, a cathode, and an electrolyte-containing separator (Reproduced from Ref. [7]. Copyright 2011, The Royal Society of Chemistry)

anode and cathode. The separator, typically a porous membrane, is used to prevent the physical contact between anode and cathode while allowing the ion transportation through the electrolyte it contains. When a lithium-ion battery is being charged, the cathode donates some of its lithium ions, which move to the anode through the electrolyte, while electrons are injected into the anode upon an external electrical power source. Then, electricity is stored in the lithium-ion battery in the form of chemical energy. When the battery is being discharged, lithium ions return to the cathode across the electrolyte; at the same time, electrons are released to the outer circuit to do the electrical work. As the battery is repeatedly charged and discharged, lithium ions shuttle between the anode and the cathode, and, hence, lithium-ion batteries are also known as "rocking chair" batteries. Currently, lithium-ion batteries are mainly developed for portable applications and electric vehicles, and the storage of energy relies on various active materials in the powder form, such as lithium cobalt oxide ($LiCoO_2$) powder for cathode and graphite powder for anode. However, powder materials usually exhibit long diffusion pathways for lithium ions and slow electrode kinetics, and, consequently, the performance

of current lithium-ion batteries have not yet reached their potential [6]. Hence, novel electrode materials for energy storage must be developed to construct superior lithium-ion batteries that can outperform current rivals and be applied in scaled-up systems.

Compared to conventional powder electrode materials, nanofiber-based materials are attractive electrode candidates for lithium-ion batteries because they exhibit shortened ion diffusion path, and their high area/mass ratio allows faster lithium intercalation kinetics. The high area/mass ratio also provides more sites for lithium-ion insertion, leading to reduced charge-transfer resistance at the interface between the electrode and the electrolyte. Therefore, nanofiber-based materials are advantageous to be used as electrode materials in lithium-ion batteries.

Electrode materials play a dominant role in deciding the performance of lithium-ion batteries; however, the separators are also important in batteries since they regulate cell kinetics, prevent electronic contact between anode and cathode, and sustain liquid electrolyte in batteries [8–11]. So far, most lithium-ion batteries utilize traditional microporous polyolefin membrane separators. Although polyolefin microporous membrane separators are chemically stable, suitable in thickness, and mechanically robust, they suffer from low porosity, low thermal stability, and poor wettability with polar liquid electrolytes, which result in high battery resistance, decreased energy density, and poor rate performance for lithium-ion batteries [8–13]. Recently, nanofiber-based materials were found to be appropriate separators [11–14], since their high porosity and small pore size facilitate high-rate charge/discharge of batteries.

Recent studies of nanofiber-based anode, cathode, and separator materials suggest that lithium-ion batteries employing these materials have excellent overall performance including large capacity, long cycle life, and high-rate charge/discharge capability. Electrospinning is currently the most widely used method in nanofiber preparation, and, therefore, this chapter begins with a review of electrospinning of nanofibers, followed by detailed discussions on representative nanofiber-based anode, cathode, and separator materials for lithium-ion batteries.

Electrospinning of Nanofibers

Electrospinning is a simple and versatile approach to fabricate large quantities of nanofibers from a variety of materials including polymers, ceramics, and composites [15, 16]. Figure 2 illustrates a schematic of a typical electrospinning setup, which is comprised of a syringe, a metal nozzle, a high-voltage power supply, and a metallic collector. Electrospinning solutions are firstly loaded into the syringe, and then a high voltage is applied between the syringe and the metallic collector, and this causes the electrically charged fluid to elongate and generate a conical droplet, known as “Taylor cone.” As the voltage reaches a critical value, where electrostatic force overcomes the surface tension of the polymer solution, a liquid jet is ejected from the nozzle tip and then undergoes a stretching-and-whipping process, accompanied by fast evaporation of solvent. During this process, the jet diameter reduces

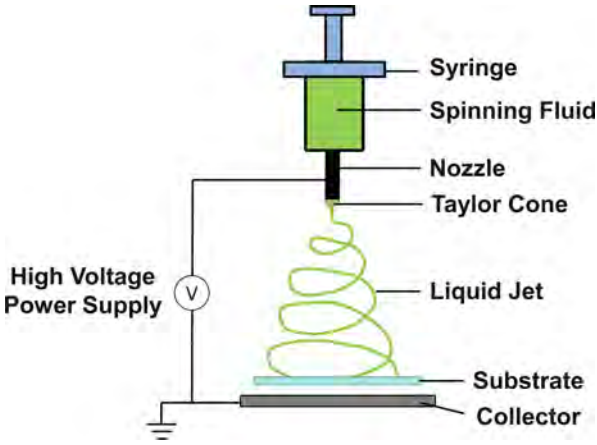

Fig. 2 Schematic of a typical electrospinning setup. During electrospinning, the electrically charged jet is stretched and whipped, and upon fast evaporation of solvent, the jet diameter reduces from hundreds of micrometers to as small as tens of nanometers

from hundreds of micrometers to as small as tens of nanometers, forming a long, thin thread. Dried nanofibers are accumulated on the surface of the metallic collectors, generating a nonwoven mat.

The morphology and diameter of electrospun nanofibers can be tuned by selectively adjusting (a) solution intrinsic properties including viscosity, electric conductivity, and surface tension and (b) operational conditions such as the applied voltage, the distance between the nozzle and the collector, and the feeding rate of the solution [15]. The thickness of the nanofiber mat can be controlled by varying the duration of the electrospinning process [17]. With careful design and control, it is also feasible to engineer electrospun nanofiber mats with a wide range of porosity values [18].

Most current electrospinning studies address the preparation of polymer nanofibers; however, carbon nanofibers (CNFs) can also be fabricated by carbonization of fibers electrospun from various precursor polymers including polyacrylonitrile (PAN), pitch, polyimide, polyvinylidene fluoride (PVDF), and polyvinyl alcohol (PVA) [19]. Among these precursor polymers, PAN is the most popular one mainly due to its high carbon yield and low cost. In addition to CNFs, ceramic nanofibers and composite nanofibers can also be synthesized by electrospinning of precursor solutions and subsequent calcination.

Nanofiber Anodes

Graphite, with a theoretical capacity of 372 mA h g^{-1}, is currently the dominant anode material for commercial lithium-ion batteries due to its low working potential, long working life, and low cost. However, with the rapidly increasing demand for superior energy storage systems, new anode materials with higher capacities need to be developed. Potential anode materials that can provide high capacities include tin dioxide (SnO_2), manganese oxide (MnO_x), and lithium alloys formed by metallic/semimetallic elements in groups IV and V such as Si, Ge, and Pb. Although the abovementioned materials are attractive due to their desirable capacities, there exist

challenges for their implementation in rechargeable lithium-ion batteries. For example, the poor electrical conductivity and huge volume expansion during lithium alloying/de-alloying remain a problem for many anode materials such as silicon.

Electrospinning is one of the most widely used techniques to produce CNFs. Similar to other carbonaceous materials, CNFs can be used as anode materials in lithium-ion batteries. In addition, the advantageous performance of electrospun CNFs can also help improve the performance of other anode materials including metal oxides and lithium-metal alloys. Firstly, the electrospun CNFs have high surface-to-volume ratios, which can shorten the path lengths for electron and lithium-ion transport. Additionally, the interlaced CNFs can form an electrically conductive structure to improve the performance of metal oxides as anode materials. Moreover, encapsulating metallic nanoparticles into CNFs is a good strategy to alleviate the volume change during lithium alloying/de-alloying processes.

Carbon Nanofiber Anodes

Many methods have been used to synthesize CNFs, such as chemical vapor deposition, arc discharge, template deposition, laser ablation, and electrospinning [20–23], among which, electrospinning is the most commonly used one due to its ease of operation and low cost. So far, it has been demonstrated that a rich variety of polymers such as PAN, PVA, polyimide, pitch, and PVDF can be used as precursors for electrospun CNFs. Generally, the conversion of polymer precursor nanofibers to CNFs involves stabilization in air under a temperature range between 220 °C and 280 °C, followed by a carbonization process under inert gas environment between 600 °C and 1,000 °C. For instance, if PAN is used in the production of CNFs, firstly the polymer nanofibers turn yellow from white during stabilization, and a ladder ring structure is formed. In the following carbonization step, the yellow nanofiber mat becomes a black, carbonized nanofiber mat [24]. Based on different carbonization temperatures, CNFs exhibit various lithium storage properties. For example, Jang-Kyo Kim et al. used various carbonization temperatures to explore the relationship between electrochemical performance and structure of PAN-based CNFs [24]. It is seen from Fig. 3 that the CNF electrodes prepared at carbonization temperatures of 550 °C and 650 °C delivered higher capacities compared to the rivals carbonized at other temperatures, especially those prepared at higher temperatures [24]. This is mainly because the higher carbonization temperatures eliminate more lattice and surface defects that exist along the CNFs and are able to promote fast lithium intercalation/deintercalation, and, hence, with increased carbonization temperatures, lower capacities are obtained [24].

In addition to solid CNFs derived from electrospun PAN nanofibers, porous CNFs can also be obtained through electrospinning and used as lithium-ion battery anodes. Recently, porous CNFs were prepared by Zhang et al. using PAN and zinc chloride ($ZnCl_2$) in *N*,*N*-dimethylformamide (DMF) solution as the precursor, followed by thermal treatment [25]. Firstly, PAN/$ZnCl_2$ precursor solution was electrospun into composite nanofibers. After the thermal treatment, the resultant

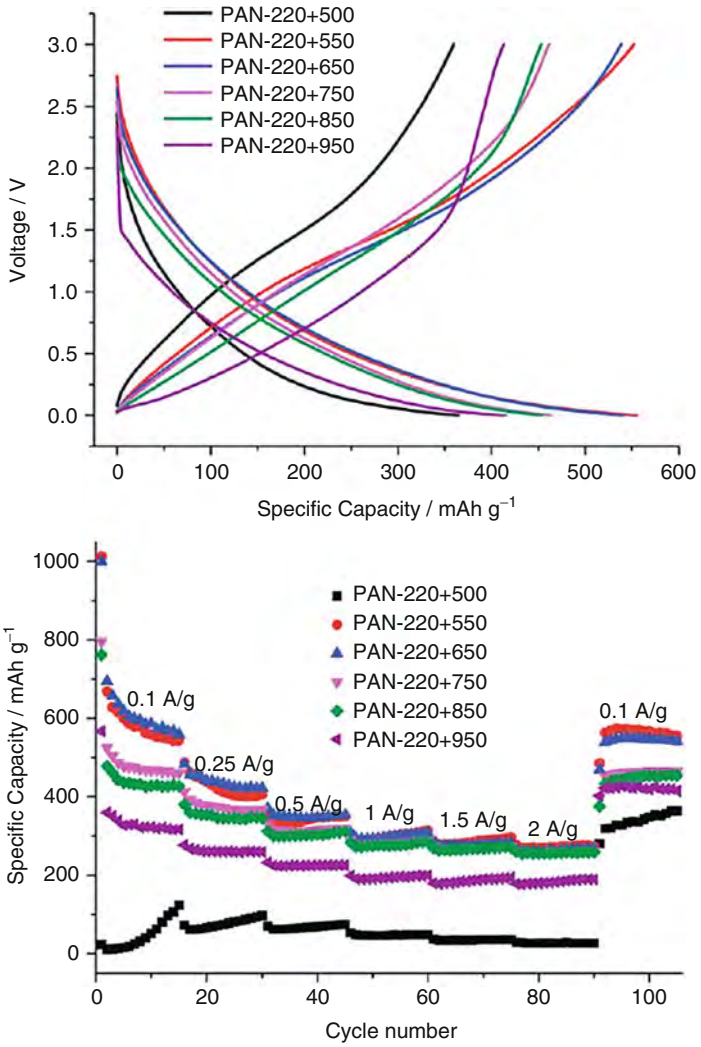

Fig. 3 (**a**) Charge/discharge curves of PAN-based electrospun CNFs prepared at various carbonization temperatures at the 105th cycle under a current density of 0.1 A g^{-1} and (**b**) rate performance of CNFs prepared at different carbonization temperatures (Reproduced from Ref. [24]. Copyright 2013, WILEY-VCH Verlag GmbH & Co. KGaA, Weinheim)

CNFs were washed with HCl acid and deionized water several times to remove the Zn-related compounds, resulting in the formation of porous structure. Figure 4 presents the SEM images of the porous CNFs prepared from precursor fibers with different amounts of $ZnCl_2$. The BET test confirms that large surface areas and small pores within the CNFs are generated. Compared with the nonporous CNFs, the porous CNFs exhibit larger specific surface area and higher pore volume. Figure 5 shows the cycling performance of porous and nonporous CNFs. It is

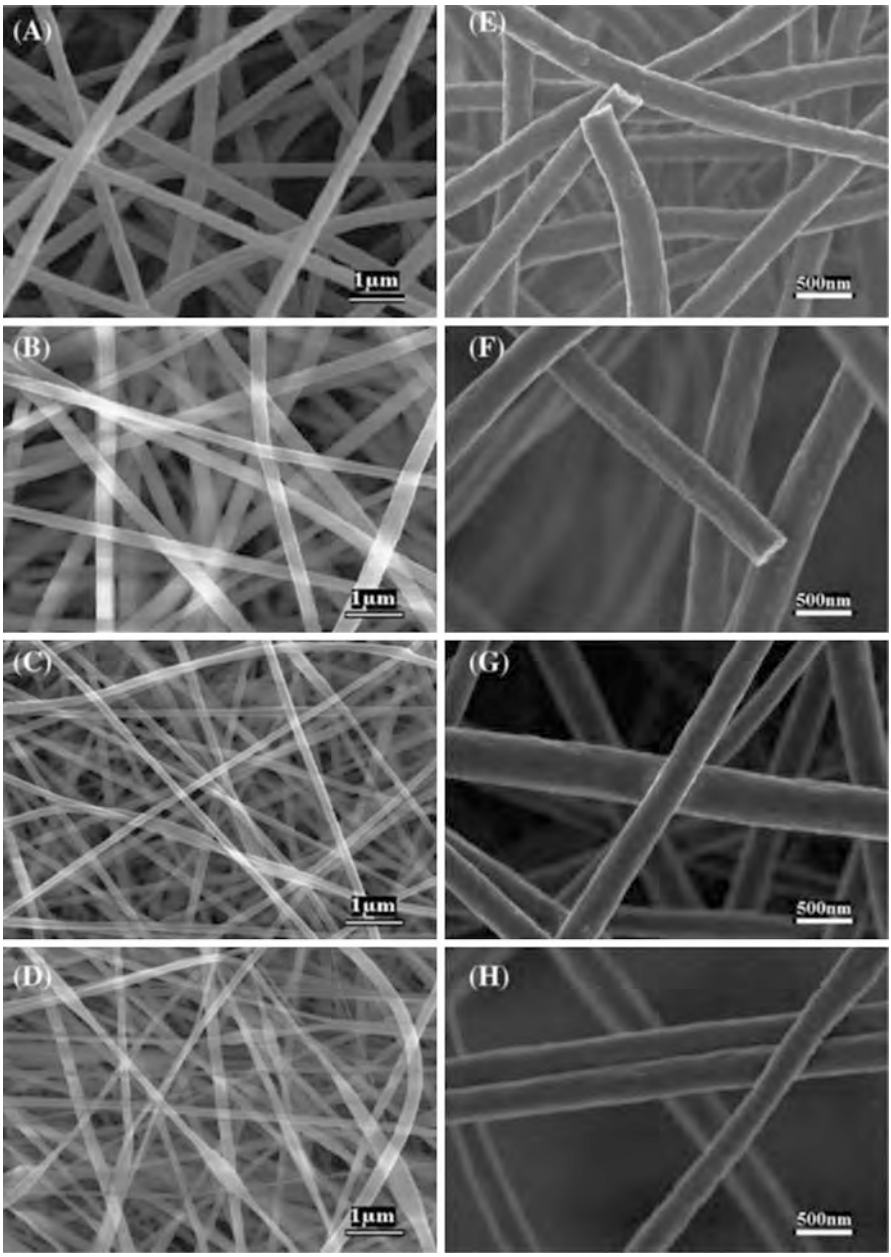

Fig. 4 SEM images of PAN/$ZnCl_2$ precursor nanofibers (**a**–**d**) and the resultant porous carbon nanofibers (**e**–**h**). $ZnCl_2$ contents in the PAN/$ZnCl_2$ precursors are (**a**, **e**) 0, (**b**, **f**) 5, (**c**, **g**) 10, and (**d**, **h**) 15 wt% (Reproduced from Ref. [25]. Copyright 2009, Elsevier)

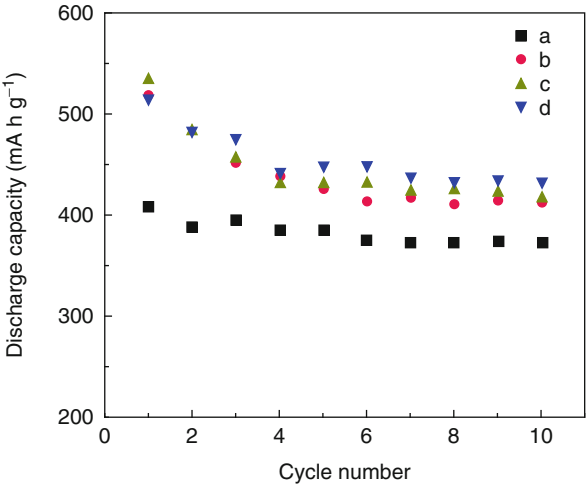

Fig. 5 Cycling performance of the porous carbon nanofibers at a current density of 50 mA g^{-1}. $ZnCl_2$ contents in the PAN/$ZnCl_2$ precursors are (*a*) 0, (*b*) 5, (*c*) 10, and (*d*) 15 wt% (Reproduced from Ref. [25]. Copyright 2009, Elsevier)

seen that the porous CNFs deliver higher reversible capacity (533 mA h g^{-1}) than nonporous CNFs (410 mA h g^{-1}) at the second cycle with a better cycling stability. Such enhanced electrochemical performance is resulted from the larger surface area, improved lithium-ion diffusion at the electrode–electrolyte interface, and the low resistance for electron conduction provided by the porous architecture. These results demonstrate that the unique porous CNFs are a promising anode candidate for lithium-ion batteries.

Tin Antimony Alloy/CNF Anodes

Among the alternative anode materials, Sn and Sb have attracted lots of attention due to their high theoretical capacity (993 mA h g^{-1} for Sn and 660 mA h g^{-1} for Sb). However, a major drawback of Sn and Sb is their significant volume change (300 % for Sn [26] and about 150 % for Sb [27]) during lithiation and delithiation processes, leading to pulverization of materials and electrical disconnection from the current collector. Therefore, such volume expansion greatly hampers the cycling life of these materials in lithium-ion batteries [28]. In order to make better use of these materials, studies have been done to alleviate the volume expansion and improve the electrochemical performance of Sn and Sb [29, 30]; however, the approaches adopted were typically complicated.

Recently, SnSb-encapsulated CNFs were prepared by Zhang's group [30] through electrospinning of a low-cost antimony tin oxide nanoparticles (<50 nm) as the precursor for SnSb alloy. In this approach, $Sn_{0.92}Sb_{0.08}O_{2.04}$ nanoparticles were added into the PAN solution prior to electrospinning. After mechanical stirring for 24 h, the homogeneous precursor solution was electrospun into nanofibers.

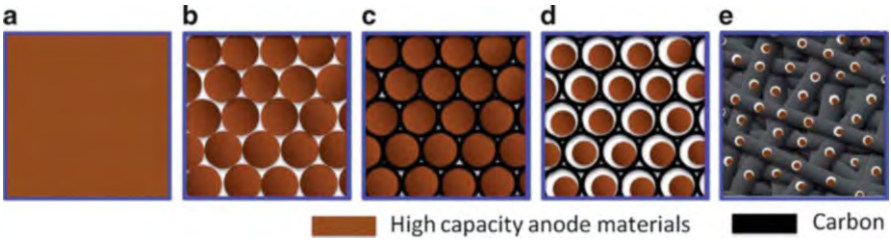

Fig. 6 Schematic of high-capacity lithium-ion battery anode materials with different morphologies: (**a**) bulk material, (**b**) nanoparticles, (**c**) carbon-coated nanoparticles, (**d**) carbon-coated hollow nanoparticles, and (**e**) nanoparticles with pores around and encapsulated in carbon nanofibers (Reproduced from Ref. [30]. Copyright 2013, The Royal Society of Chemistry)

The resultant precursor nanofibers were then stabilized and carbonized to obtain the SnSb/CNF composite. Figure 6 compares the high-capacity lithium-ion battery anode material with various morphologies. Figure 6a shows the bulk material while b to d show previous efforts in morphology design to address the volume expansion of the anode material. Figure 6e presents the morphology of the anode material prepared in this study. The hollow structure around SnSb nanoparticles can effectively buffer the volume expansion–contraction during the charge–discharge process. In addition, the use of nano-sized SnSb particles can increase the interfacial area, resulting in reduced pathways for lithium-ion transport and higher rate of charge–discharge [30]. Moreover, the CNF matrix maintains good electronic contacts between particles and avoids insulation of the anode material during the volume change. Benefiting from the unique structure, the SnSb-encapsulated CNFs exhibit excellent electrochemical performance. It is seen from Fig. 7a that the discharge capacity of the composite nanofibers decreases from 724 to 659 mA h g^{-1} for the first ten cycles and maintains excellent stability for the following cycles, resulting in a high-capacity retention of 88 % after 150 cycles. The rate capability of the composite nanofiber anode was also evaluated using different current densities of 50, 100, 200, 400, 800, and 1,600 mA g^{-1}. As shown in Fig. 7b, the SnSb/C composite delivers an initial capacity of 646 mA h g^{-1} at the current density of 50 mA g^{-1}; when the current density increases to 1,600 mA g^{-1}, a high capacity of 354 mA h g^{-1} is still retained, indicating a good rate capability. The good cycling performance and rate capability demonstrate that incorporating nanoparticles of anode materials into porous CNFs is an effective strategy to improve the cycling performance and rate capability for materials that suffer from huge volume change during repeated charge and discharge.

Silicon/CNF Anodes

Silicon is one of the most attractive anode material candidates for lithium-ion batteries due to its low discharge potential and highest known theoretical capacity of 4,200 mA h g^{-1}. However, the enormous volume change during lithium-ion

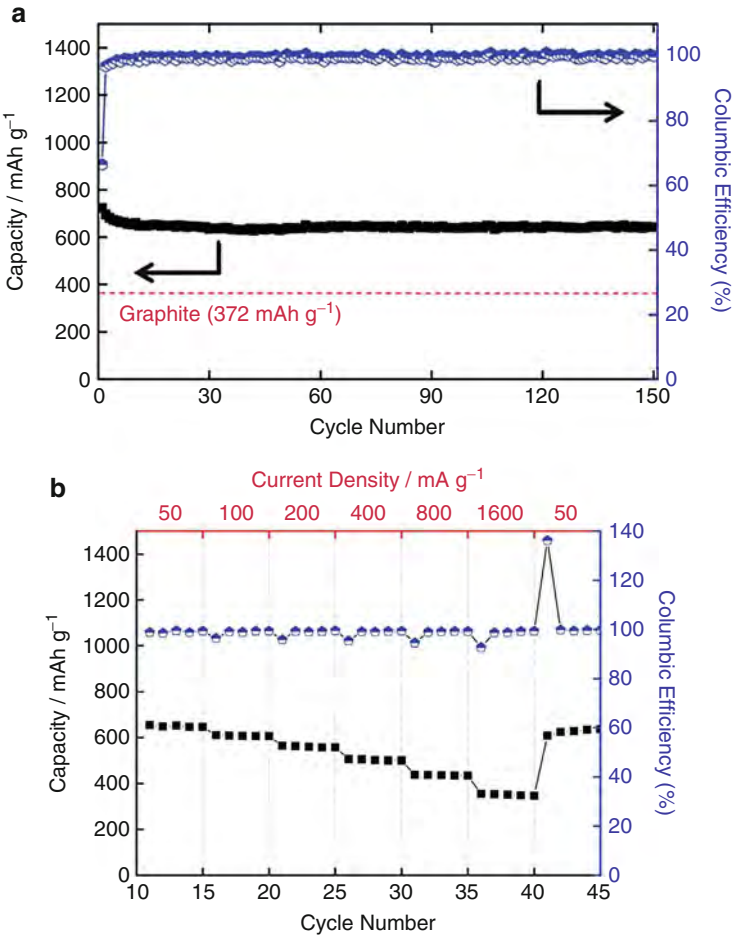

Fig. 7 (**a**) Cycling performance of porous SnSb/C composite nanofibers and (**b**) rate capability of porous SnSb/C composite nanofibers at various current rates from 50 to 1,600 mA g^{-1} (Reproduced from Ref. [30]. Copyright 2013, The Royal Society of Chemistry)

insertion–extraction process hampers the practical implementation of silicon in lithium-ion batteries. One widely adopted approach to address this problem is to introduce a carbon matrix on the surface of the silicon particles to buffer the volume change and provide good electrical contact during the charge–discharge process. Recently, the simple and environmentally friendly electrospinning method has been applied to modify the structure and performance of silicon-based anodes using electrospun CNFs [31, 32].

For instance, Zhang's group introduced porous structure into the traditional Si/CNF composite anodes to improve the performance of Si/C anode materials [33]. In this work, PLLA was used as a pore producer and was added into the PAN/DMF solution. Si nanoparticles were then dispersed in the as-prepared PAN/PLLA solution by

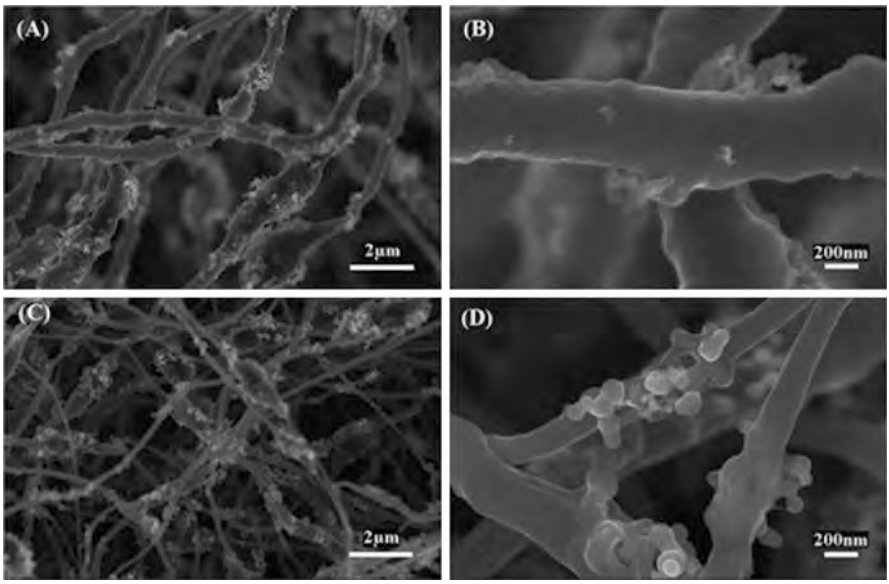

Fig. 8 SEM images of (**a**, **b**) Si/CNFs without PLLA-induced pores and (**c**, **d**) Si/CNFs with PLLA-induced pores (Reproduced from Ref. [33]. Copyright 2010, The Royal Society of Chemistry)

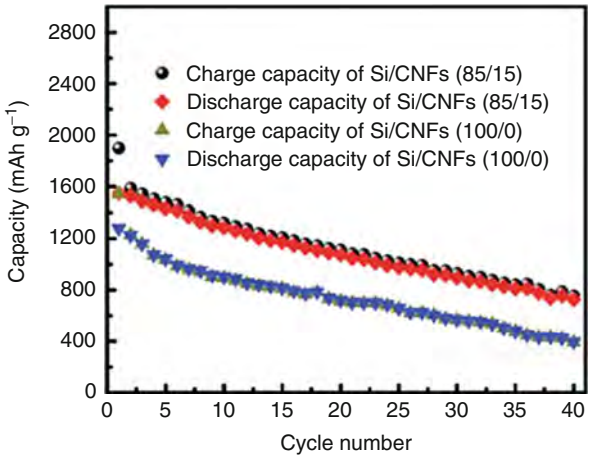

Fig. 9 Cycling performance of Si/CNFs and porous Si/CNFs prepared from PAN/PLLA weight ratios of 100/0 and 85/15, respectively. The current density is 50 mA g^{-1} (Reproduced from Ref. [33]. Copyright 2010, The Royal Society of Chemistry)

mechanical stirring and ultrasonic treatment. After carbonization, PLLA decomposed to create a pore structure in the resultant Si/CNFs. Figure 8 compares the SEM images of Si/CNFs with and without the porous structure introduced by PLLA.

Galvanostatic charge–discharge experiments were carried out for both porous and nonporous Si/CNFs. Figure 9 shows the cycling performance of the Si/CNFs and porous Si/CNFs. In this figure, Si/CNFs (100/0) stand for the nonporous

Si/CNF anode since it is prepared from PAN/PLLA precursor with a weight ratio of 100/0; similarly, Si/CNFs (85/15) represent the porous Si/CNFs prepared from PAN/PLLA precursor with a weight ratio of 85/15. It is seen from this figure that porous Si/CNFs show higher lithium storage capacities than the nonporous one. Specifically, the porous Si/CNFs maintain a capacity of 1,075 mA h g^{-1} after 20 cycles, while the capacity of the nonporous material fades to 726 mA h g^{-1} after 20 cycles. The improved electrochemical performance is attributed to the advantageous properties of both CNFs and the porous structure. Firstly, the carbon matrix plays a role of volume change buffer that can protect Si nanoparticles from pulverization. Moreover, the small pores around Si nanoparticles further help alleviate the volume expansion. In addition, the CNFs have small diameters and large surface area, leading to shortened lithium-ion transportation length. As a result, the porous Si/CNF composite anode exhibits superior electrochemical performance.

Research has also been done to investigate the processing–structure–performance relationships of Si/CNF composites [34]. For example, Si nanoparticles with different sizes (20–30, 30–50, and $\geq$70 nm) were employed as active material to fabricate Si/CNFs composite anodes. It is seen from Fig. 10 that the agglomeration of Si

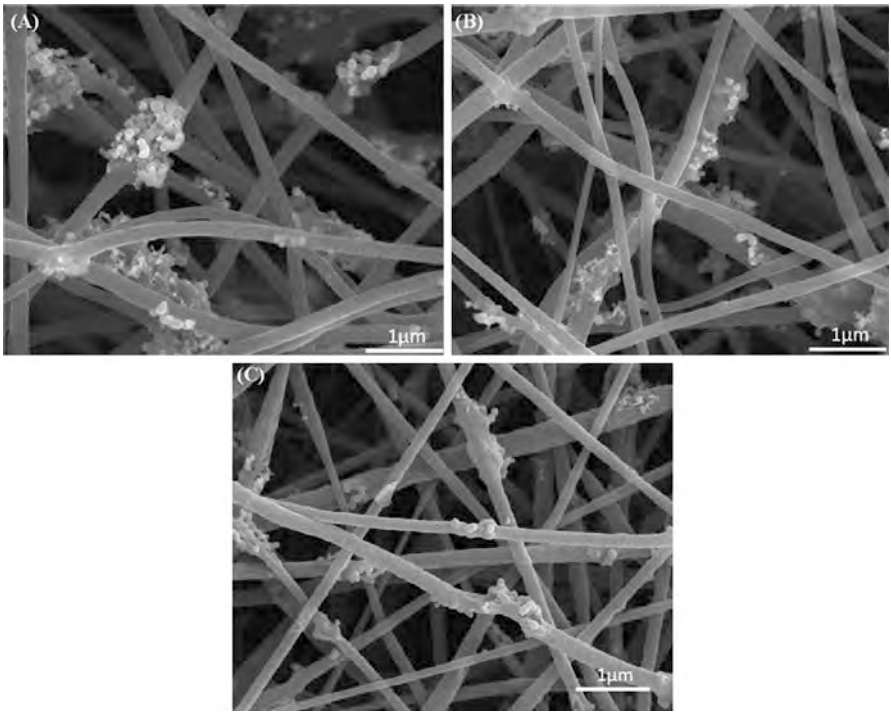

Fig. 10 SEM images of Si/C composite nanofibers with different Si nanoparticle sizes: (**a**) 20–30, (**b**) 30–50, and (**c**) $\geq$70 nm. Carbonization temperature: 700 °C (Reproduced from Ref. [34]. Copyright 2013, Elsevier)

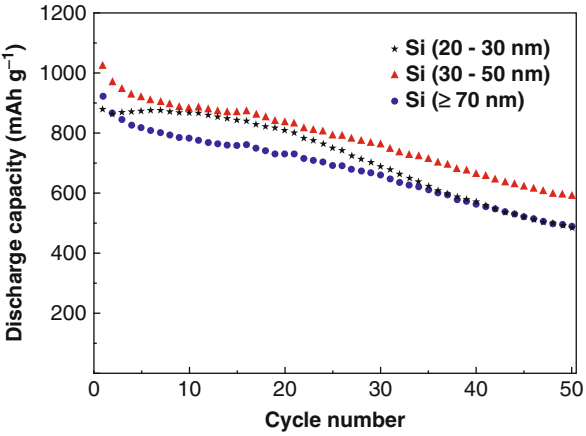

Fig. 11 Cycling performance of Si/C composite nanofibers made from Si/PAN with different Si nanoparticle sizes. Carbonization temperature: 700 °C (Reproduced from Ref. [34]. Copyright 2013, Elsevier)

nanoparticles is severe when the particle size is 20–30 nm due to the large surface area. The cycling performance of Si/CNF composite anodes with different Si nanoparticle sizes is shown in Fig. 11. It is seen that the composite anode containing 30–50 nm Si yields the highest capacity and the most stable cycling performance. Generally, smaller nanoparticles are expected to show better electrochemical performance when used as anode materials; however, when the nanoparticle size is as small as 20–30 nm, the severe agglomeration significantly retards the electrochemical performance.

Manganese Oxide/CNF Anodes

Various transition metal oxides, such as MnO_x, SnO_2, and FeO_x, have been studied as anode materials in lithium-ion batteries due to their low cost and high theoretical capacities. However, the volume change during lithiation/delithiation process and the poor electrical conductivity together limit their application as anode materials in practical lithium-ion batteries. Efforts made to solve the problem include introducing carbon coating and adding conductive agent [35]. CNFs combine the merits of both carbon coating and electrically conductive network and can significantly enhance the performance of transition metal oxides in lithium-ion batteries.

Recently, MnO_x/CNF composite was fabricated by electrodepositing MnO_x onto the CNF substrate. The CNFs were firstly synthesized by electrospinning of PAN followed by thermal treatment procedures. Then MnO_x was electrodeposited onto the CNF substrate using a three-electrode cell with a solution of 0.1 M Mn $(CH_3COO)_2$ and 0.1 M Na_2SO_4. It is seen from Figs. 12 and 13 that with various deposition durations, different amounts of MnO_x are introduced on the surface of the CNF substrates. The diameter of MnO_x particles on the surface of the CNFs increases with increased electrodeposition time, leading to higher active material loading.

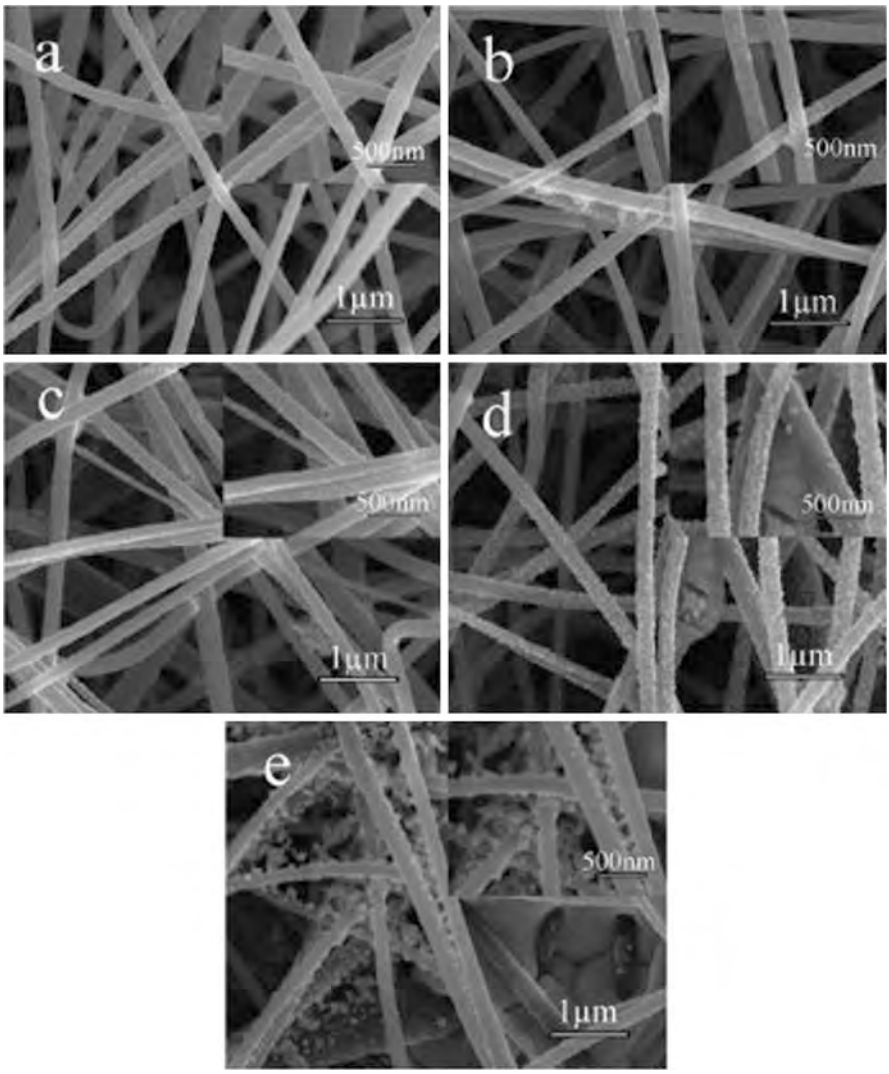

Fig. 12 SEM images of CNFs (**a**) and MnO_x/CNFs prepared with different deposition durations of 2.5 (**b**), 5 (**c**), 10 (**d**), and 20 h (**e**) (Reproduced from Ref. [35]. Copyright 2010, Elsevier)

The electrochemical performance was evaluated using the MnO_x/CNFs with a deposition time of 10 h. It is seen from Fig. 14 that the reversible capacity of the material in the second cycle is 558 mA h g^{-1}, corresponding to 90 % retention of the first cycle (618 mA h g^{-1}). Moreover, after cycling for 100 cycles, a capacity of 433 mA h g^{-1} is maintained, indicating a capacity retention of 70 % with respect to the initial capacity. The good cycling performance of MnO_x/CNFs composite can be attributed to the high electrical conductivity that resulted from the CNF network and the buffer effect of the CNF matrix.

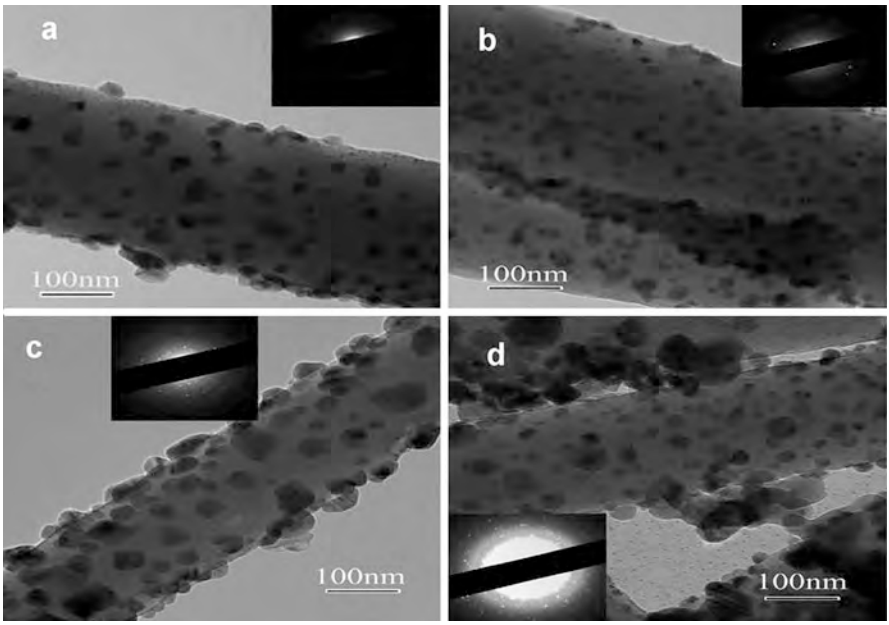

Fig. 13 TEM images of MnO_x/CNFs prepared with different deposition durations of 2.5 (**a**), 5 (**b**), 10 (**c**), and 20 h (**d**), respectively (Reproduced from Ref. [35]. Copyright 2010, Elsevier)

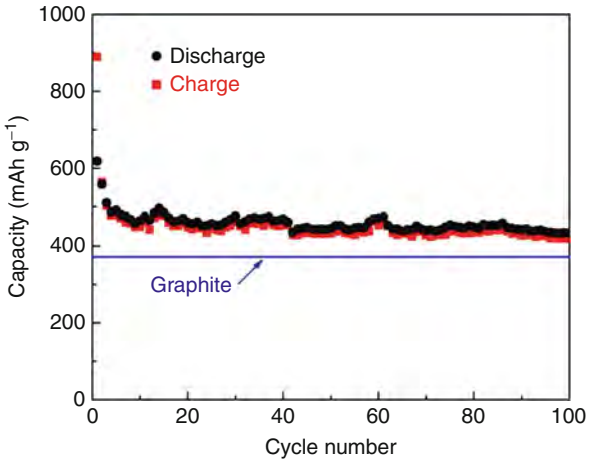

Fig. 14 Cycling performance of MnO_x/CNF composite anode at a constant current density of 50 mA g^{-1}. Deposition time: 10 h (Reproduced from Ref. [35]. Copyright 2010, Elsevier)

Nanofiber Cathodes

Recent advances in nanofiber-based cathode materials for lithium-ion batteries have mainly focused on layered oxides such as $LiCoO_2$, spinel oxides such as lithium manganese oxide ($LiMn_2O_4$), phospo-olivines including lithium iron

phosphate ($LiFePO_4$), and silicate such as lithium manganese silicate (Li_2MnSiO_4). As mentioned in previous sections, the nanofiber-based electrode materials exhibit shorter diffusion paths, fast intercalation/deintercalation kinetics, and more lithium host sites, making them more desirable electrode materials when compared to conventional powder electrode materials. In this section, representative studies on nanofiber-based cathode materials will be reviewed in terms of their preparation, structure, and electrochemical performance. Generally, these nanofiber cathodes were prepared by electrospinning of polymer solutions containing precursors for various active materials, followed by heat treatment at elevated temperatures. During heat treatment, the polymer component might be either completely removed, resulting in ceramic nanofibers (when thermally treated in air), or used as a source to produce carbon, making active material/carbon composite nanofibers (when thermally treated in inert gas).

$LiCoO_2$ Nanofiber Cathodes

$LiCoO_2$, discovered in 1980, is currently the most successful cathode material for rechargeable lithium-ion batteries in industry and has been used in commercial lithium-ion batteries since 1991, regardless of its high cost and toxicity of cobalt. $LiCoO_2$ is widely used as the lithium-ion battery cathode material mainly due to its high operating potential (3.75 V vs. graphite) and high theoretical capacity (274 mA h g^{-1}). However, only half of this theoretical capacity can be utilized and the relatively low capacity is attributed to its structural properties, the poor stability of the electrodes, and low reaction rates [36]. Efforts have been made to enhance the electrochemical performance of $LiCoO_2$ and most of the investigations focused on the preparation of $LiCoO_2$ particles with various particle sizes and shapes through traditional solid-state reaction route and solution-assisted approaches including sol–gel, hydrothermal, emulsion-drying methods, etc. [37].

Recently, $LiCoO_2$ nanofibers were prepared by Jiao's group [37], and the one-dimensional nanostructure offers attractive properties such as short ionic and electronic diffusion pathways, high specific surface area, and mechanical stability, which can improve the specific capacity and thus the overall battery performance. Typically, $LiCoO_2$ nanofibers were synthesized by a sol–gel-based electrospinning process using lithium acetate, cobalt acetate, and citric acid as the precursors. $LiCoO_2$ nanofibers were obtained after the calcination of the as-spun xerogel precursor fibers at elevated temperatures in air. The SEM and TEM images of $LiCoO_2$ nanofibers are illustrated in Fig. 15. It is seen that $LiCoO_2$ nanofibers show smooth surface and fiber diameter as small as 500 nm. The TEM images suggest that the $LiCoO_2$ nanofibers are comprised of uniform nanoparticles of 20–35 nm. Galvanostatic charge–discharge curves (Fig. 16a) show the first five cycles of the $LiCoO_2$ nanofiber cathode. The initial charge and discharge capacity for the nanofiber cathode is 216 and 182 mA h g^{-1}, respectively, with a potential plateau near 3.9–4.0 V. Figure 16b compares the cycling performance of the nanofiber cathode and a typical powder cathode. After 20 cycles, the discharge-specific

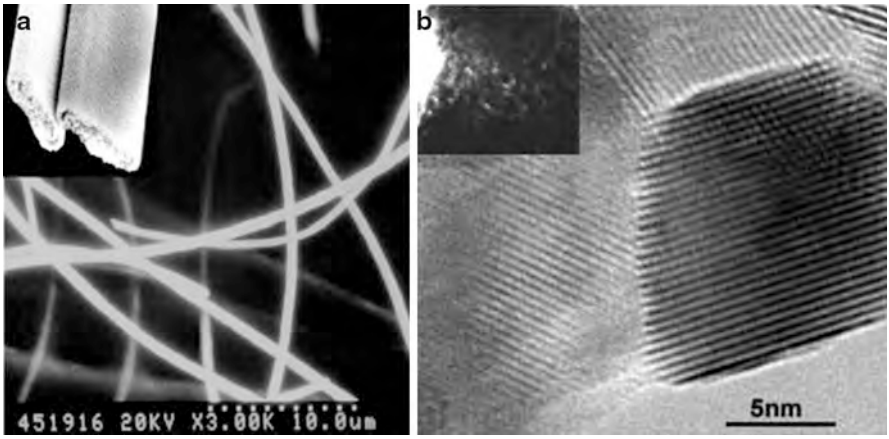

Fig. 15 SEM (**a**) and TEM (**b**) images of $LiCoO_2$ nanofibers (Reproduced from Ref. [37]. Copyright 2005, American Chemical Society)

capacity of $LiCoO_2$ nanofibers remains at 123 mA h g^{-1}, corresponding to 68 % of the initial discharge capacity. On the contrary, the $LiCoO_2$ powder electrode exhibits a lower initial discharge capacity of around 132 mA h g^{-1}; however, its capacity retention is nearly 82 %, which is in good agreement with the reported values.

In addition to preparing $LiCoO_2$ nanofiber cathode, Jiao's group also introduced metal oxide coating, such as MgO, onto $LiCoO_2$ nanofibers to enhance the structural stability during repeated cycling process by suppressing active materials from directly reacting with the electrolyte [38]. The $LiCoO_2$-MgO core-shell nanofibers were produced by coaxial electrospinning of lithium acetate, cobalt acetate, and citric acid as the precursors for the core, while magnesium acetate and citric acid as the precursors for the shell. After thermal treatment under appropriate conditions, morphologically stable $LiCoO_2$-MgO core-shell nanofibers were developed. Figure 17a, b illustrate the charge–discharge curves of the core-shell nanofiber cathode and bare $LiCoO_2$ nanofiber cathode for the initial five cycles. It is seen that the initial discharge capacity of the core-shell nanofibers is 181 mA h g^{-1} in the voltage window of 2.6–4.3 V, which is slightly lower than that of bare $LiCoO_2$ nanofibers. However, the core-shell nanofibers deliver significantly improved cycling performance: after 40 cycles, the core-shell nanofibers retain a discharge capacity of 163 mA h g^{-1}, corresponding to 90 % of the initial discharge capacity. As a comparison, the discharge capacity of the bare $LiCoO_2$ nanofibers decreases to 95 mA h g^{-1}, which is only 52 % of the initial value. Such greatly enhanced cycling performance of the core-shell nanofibers indicates that the MgO coating on the surface of $LiCoO_2$ nanofibers and the partial orientation of the nanocrystals composing the core together stabilize the cathode material.

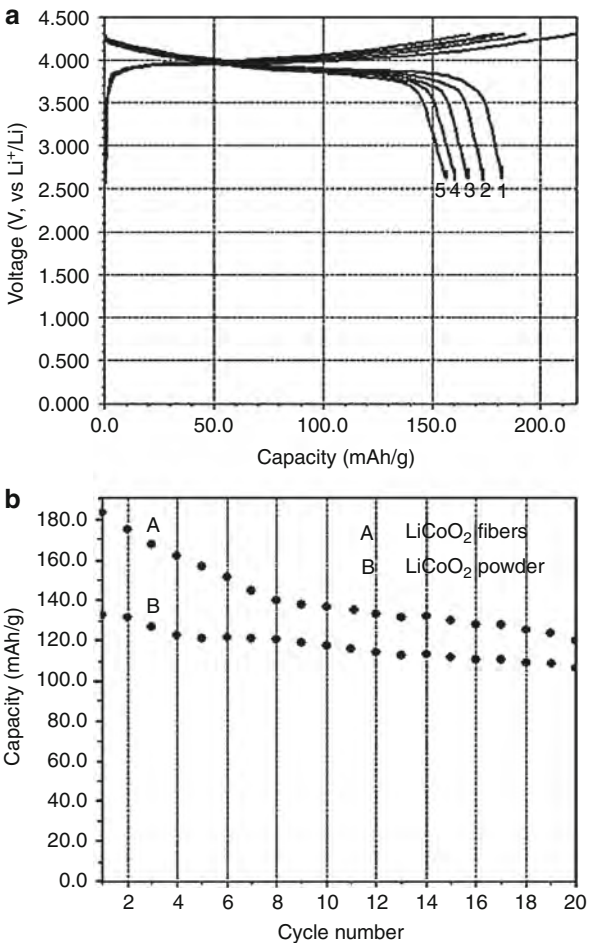

Fig. 16 First five cycles of charge–discharge curves for $LiCoO_2$ nanofibers (**a**) and the cycling performance of $LiCoO_2$ powder and $LiCoO_2$ nanofibers at a current density of 20 mA g^{-1} (**b**) (Reproduced from Ref. [37]. Copyright 2005, American Chemical Society)

$LiMn_2O_4$ Nanofiber Cathodes

Spinel $LiMn_2O_4$ material is one of the promising cathode candidates for lithium-ion batteries because of its high-power density, low cost, and nontoxicity. It also possesses a decent theoretical capacity of 148 mA h g^{-1}; however, $LiMn_2O_4$ powder electrodes suffer capacity degradation during repeated charge–discharge process due to the poor electronic/ionic conductivities and the Jahn–Teller effect caused by Mn^{3+} at the octahedral sites [36, 39]. Developing nanostructured $LiMn_2O_4$ can be a feasible approach to address the problem of low-capacity retention, because the high surface-to-volume ratio of the nanostructured materials, especially one-dimensional nanostructures including nanowires, nanotubes, nanorods, and nanofibers, offers short lithium diffusion pathways and facilitates

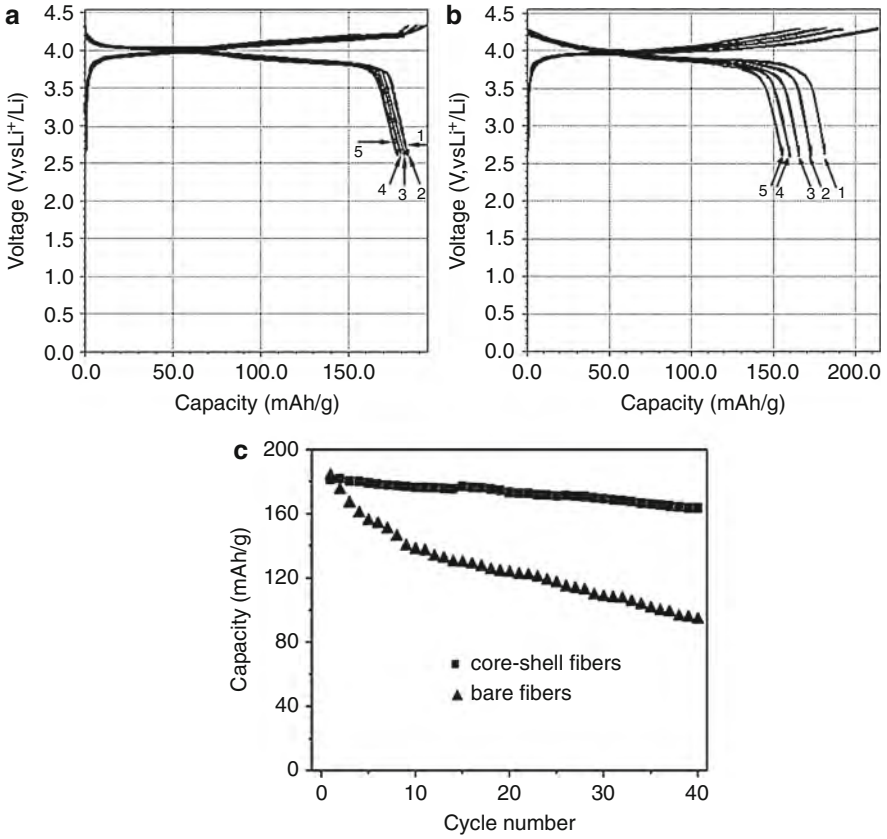

Fig. 17 Charge–discharge curves for the $LiCoO_2$-MgO core-shell nanofiber electrode (**a**), the bare $LiCoO_2$ nanofiber electrode (**b**), and their cycle performance (**c**) (Reproduced from Ref. [38]. Copyright 2007, The Royal Society of Chemistry)

the interaction between the electrode and the electrolyte, which are favorable to improve the overall electrochemical performance.

Recently, research has been performed to develop different one-dimensional nanostructures for $LiMn_2O_4$ to improve capacity retention; however, the study on fabricating $LiMn_2O_4$ nanofibers is limited. Recently, Zhou et al. prepared $LiMn_2O_4$ nanofibers by the electrospinning of polyvinylpyrrolidone (PVP) solution containing lithium nitrate and manganese acetate as the precursors for $LiMn_2O_4$. The electrospinning parameters used in the study included a flow rate of 0.5 mL h^{-1}, an applied voltage of 15 kV and a nozzle-collector distance of 12 cm. The as-spun precursor fibers were then calcinated at 700 °C in air to completely eliminate the PVP component and obtain the $LiMn_2O_4$ nanofibers. The SEM images of the as-spun $LiMn_2O_4$ precursor fibers and the $LiMn_2O_4$ nanofibers after calcination are shown in Fig. 18a, b. It is seen that the precursor fibers exhibit smooth surface with a fiber diameter of about 400 nm. After the calcination, the

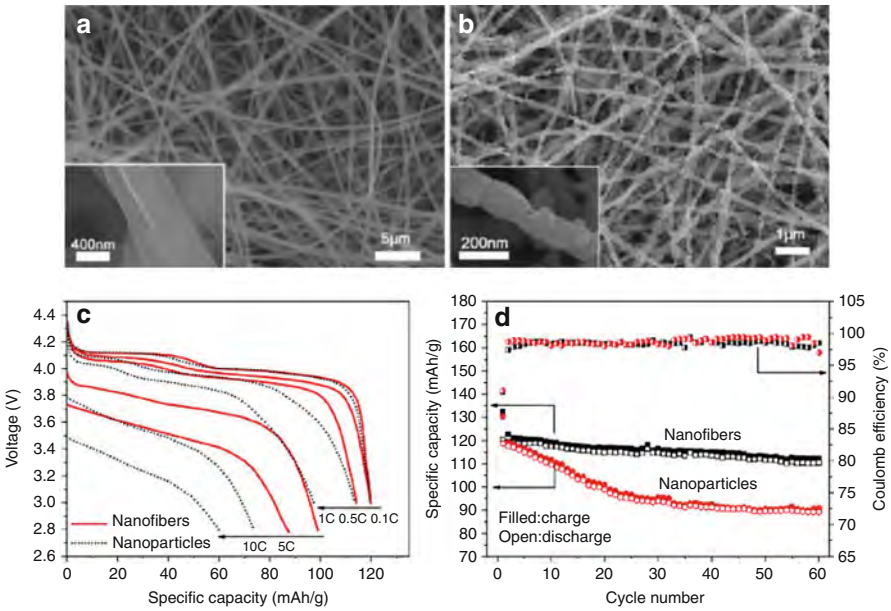

Fig. 18 SEM images of as-spun $LiMn_2O_4$ precursor fibers (**a**), $LiMn_2O_4$ nanofibers annealed at 700 °C (**b**), rate capability (**c**), and cycling performance (**d**) of $LiMn_2O_4$ nanoparticles and $LiMn_2O_4$ nanofibers at 0.5 C (Reproduced from Ref. [39]. Copyright 2014, Elsevier)

nanofibers are composed of interconnected $LiMn_2O_4$ nanoparticles and the fiber diameter shrinks to about 150 nm due to the complete removal of the polymer component. Such porous network structure provides short lithium diffusion paths and large specific surface area, which together contribute to fast charge–discharge feature and enhanced electrochemical performance.

Figure 18c compares the discharge curves of $LiMn_2O_4$ nanoparticles and $LiMn_2O_4$ nanofibers at different current densities. It is seen that the nanofiber cathode exhibits higher discharge capacity than the nanoparticle cathode and this can be ascribed to its larger surface area and shorter diffusion paths for lithium ions. In addition, the nanofiber structure also prevents the aggregation of nanoparticles, ensuring stable cycling performance. Figure 18d shows the comparison of the cycling performance of $LiMn_2O_4$ nanofiber and $LiMn_2O_4$ nanoparticle cathodes. It is seen that as the cycle number increases to 60, the discharge capacities of the nanofiber cathode and the nanoparticle cathode decrease to 110 and 89 mA h g^{-1}, respectively, corresponding to capacity retentions of 92 % and 75 %, respectively.

In addition to solid $LiMn_2O_4$ nanofibers, Jayaraman et al. also fabricated hollow $LiMn_2O_4$ nanofibers and evaluated their electrochemical performance [40]. The hollow $LiMn_2O_4$ nanofiber cathode exhibits a lithium storage capacity of 122 mA h g^{-1} in the voltage range of 3.5–4.3 V at a high current density of 150 mA g^{-1}. The hollow nanofiber cathode also shows outstanding capacity retention of 87 % after 1,250 cycles at a current density of 150 mA g^{-1}, possibly because the stable hollow

structure allows even faster lithium-ion diffusion at high current rates compared to the solid nanofiber cathode.

$LiFePO_4$/CNF Cathodes

Among a variety of cathode materials, $LiFePO_4$, first discovered by Goodenough in 1997, draws significant interests due to its relatively low cost, high discharge potential (3.4 V vs. Li/Li^+), high discharge capacity (170 mA h g^{-1}), excellent cycling performance, good thermal stability, safety, and low toxicity [41]. However, the low conductivity of $LiFePO_4$ (around 10^{-9} S cm^{-1}) leads to high impedance and low rate capability, which hinder its application in high-performance batteries. To overcome the low conductivity and make better utilization of the material, researchers employed different methods including reducing the particle size, doping metal ions, and coating conductive materials such as carbon.

$LiFePO_4$ is typically synthesized via solid-state reaction method and the carbon coating is introduced onto the particles afterwards. However, the synthesis of $LiFePO_4$ and the conductive carbon coating can be accomplished simultaneously using the simple electrospinning method followed with heat treatment. Recently, Zhang's group fabricated $LiFePO_4$/C nanofibers that have high conductivity and excellent electrochemical performance. The electrospinning solution is composed of PAN and $LiFePO_4$ precursors including lithium acetate, iron (II) acetate, and phosphoric acid. The electrospinning was conducted with an applied voltage of 15 kV and a nozzle-collector distance of 15 cm. In this study, PAN not only plays the role of spinning medium to offer good spinnability but also acts as the source to produce carbon. The as-spun precursor fibers were then stabilized at 200–280 °C in air and carbonized at 600–800 °C in argon. The resultant $LiFePO_4$/C nanofibers have nanoscale conductive carbon coating on $LiFePO_4$ particles, and the carbon-coated, interconnected $LiFePO_4$ particles have significantly improved conductivity and electrochemical performance.

The morphology of the precursor fibers and the $LiFePO_4$ nanofibers are shown in Fig. 19. Figure 19a, b display SEM images of the precursor fibers and the $LiFePO_4$/C nanofibers, respectively, while Fig. 19c illustrates a TEM image of the $LiFePO_4$/C nanofibers. It is seen that a network structure is obtained by the electrospinning of $LiFePO_4$ precursor/PAN solution. However, the fiber surface is not smooth and beads are generated, forming the "bead-on-string" structure. The average fiber diameter for the precursor fibers is about 125 nm. After stabilization and carbonization, the fibrous structure is maintained; however, more beads are observed. The fiber diameter undergoes a decrease from 125 to 90 nm, because some species, such as CO_2, NH_3, and HCN, are eliminated during the heat treatment. The TEM image of the $LiFePO_4$/C nanofibers (Fig. 19c) clearly indicates that $LiFePO_4$ nanoparticles are encapsulated into the CNFs, and the carbon coating is as thin as 8 nm.

Figure 20 shows the electrochemical performance of the $LiFePO_4$ nanofiber cathodes. In this figure, S1, S2, and S2 represent samples prepared from PAN and $LiFePO_4$ precursors with weight ratios of 1–1, 1–2, and 1–3, respectively.

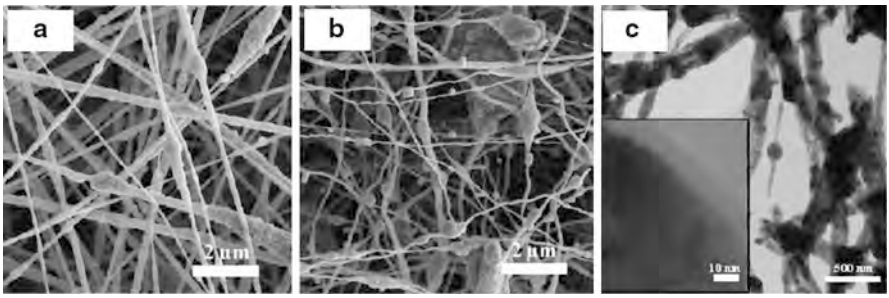

Fig. 19 SEM images of $LiFePO_4$ precursor fibers (**a**), SEM image of $LiFePO_4$/C nanofibers (**b**), and TEM image of $LiFePO_4$/C nanofibers (**c**) (Reproduced from Ref. [41]. Copyright 2011, Elsevier)

Taking sample S2 as an example, it is seen from Fig. 20a that there are two flat voltage plateaus at 3.35 V for the discharge process and at 3.55 V for the charge process, respectively. These two voltage plateaus in the charge–discharge curves are the main characteristic of the two-phase $LiFePO_4$ reaction. Additionally, the charge and discharge capacities are both greater than 140 mA h g^{-1} for the initial cycle. Figure 20b gives the cycling performance of the $LiFePO_4$/C nanofiber cathodes and no obvious capacity loss can be observed for sample S2 over 50 cycles. Figure 20c shows the rate capability of the material. At different charge rates from C/20 to 2C, the discharge capacities are from 162 to 37 mA h g^{-1}.

To further improve the electronic conductivities of the $LiFePO_4$/C nanofiber cathode, carbon nanotubes (CNTs) and graphene are incorporated into the composite nanofibers [42, 43]. For example, Zhang's group introduced a tiny amount of functionalized CNT (1.25 % with respect to the weight of $LiFePO_4$ precursors) into the electrospinning precursor solution. The resultant $LiFePO_4$/CNT/C nanofibers were obtained after heat treatment in the same conditions with those for preparing $LiFePO_4$/C nanofibers. The cycling performance, initial charge–discharge curves, and the rate capabilities of pristine $LiFePO_4$ powders, $LiFePO_4$/C nanofibers, and $LiFePO_4$/CNT/C nanofibers are compared in Fig. 21. It can be seen that higher capacity, more stable capacity retention, and better rate capability were resulted after the incorporation of CNTs, indicating the important influence of conductivity for $LiFePO_4$ materials.

Li_2MnSiO_4/CNF Cathodes

Compared to the widely studied $LiCoO_2$, $LiMn_2O_4$, and $LiFePO_4$ materials, Li_2MnSiO_4 is a relatively new cathode material for lithium-ion batteries. This material can theoretically deliver two lithium ions per formula unit, resulting in a specific capacity of 333 mA h g^{-1}. However, in most cases, only less than one lithium-ion per unit formula is able to intercalate/deintercalate from the material, and the material suffers significant capacity loss during cycling, probably because

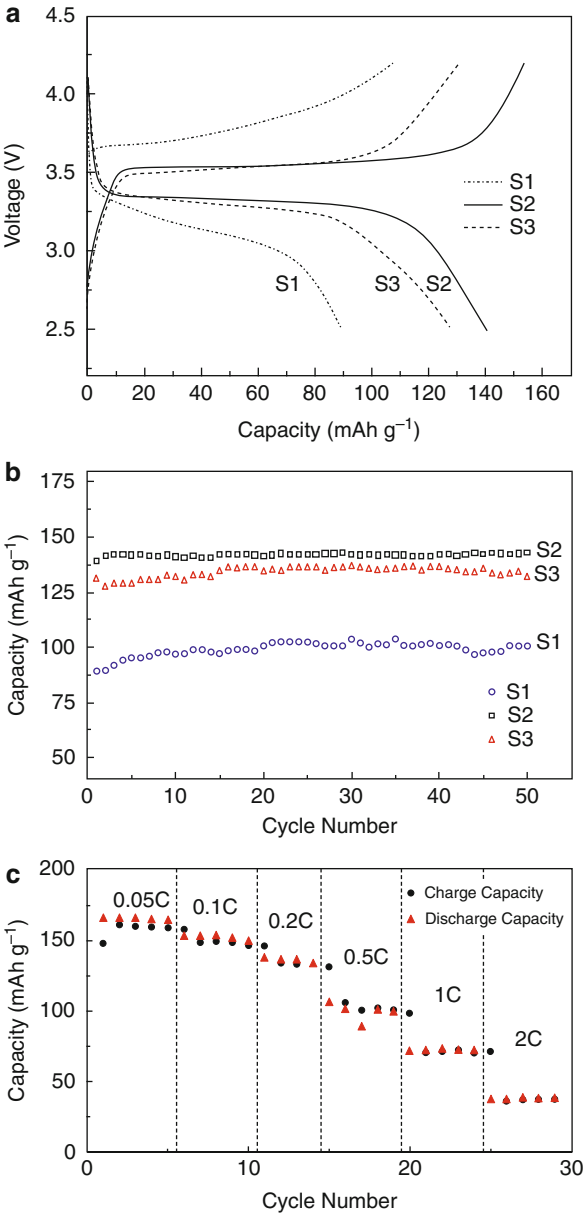

Fig. 20 Initial charge–discharge curves (**a**), cycling performance (**b**), and rate capability (**c**) of the $LiFePO_4$/C nanofiber cathodes (Reproduced from Ref. [41]. Copyright 2011, Elsevier)

the material has a poor conductivity of 5×10^{-16} S cm^{-1} and slow kinetics [44]. To improve the electronic conductivity and kinetics of the material, methods utilized in $LiFePO_4$ research, including reducing the particle size, coating with carbonaceous materials, and super-valent metal doping, can also be used. These approaches enhanced the electrochemical performance of Li_2MnSiO_4 to

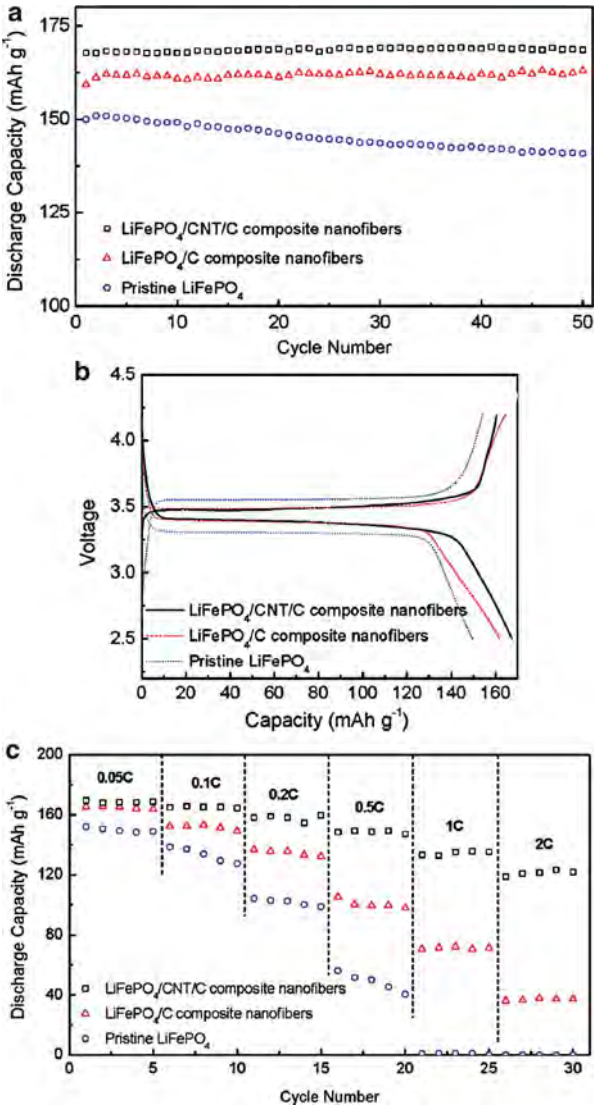

Fig. 21 (**a**) Cycling performance, (**b**) initial charge–discharge curves, and (**c**) rate capabilities of pristine $LiFePO_4$ powders, $LiFePO_4$/C nanofibers, and $LiFePO_4$/CNT/C nanofibers. Charge–discharge rate used in (**a**) and (**b**) was 0.05 C (Reproduced from Ref. [43]. Copyright 2012, American Chemical Society)

some extent; however, the performance is still insufficient for batteries in electric vehicles and hybrid electric vehicles.

Recently, Zhang et al. prepared Li_2MnSiO_4/C nanofibers by using lithium acetate, manganese acetate, and tetraethyl orthosilicate as precursors [44, 45]. Iron acetate and chromium nitrate were also added as precursors to conduct super-valent metal doping of iron (Fe) and chromium (Cr). The precursor gels were first calcinated in argon at 700 °C for 12 h, and the resultant powders were then added into PAN/DMF solutions for electrospinning. The electrospinning parameters include a feed rate of 1 mL h^{-1}, an applied voltage of 20 kV, and a

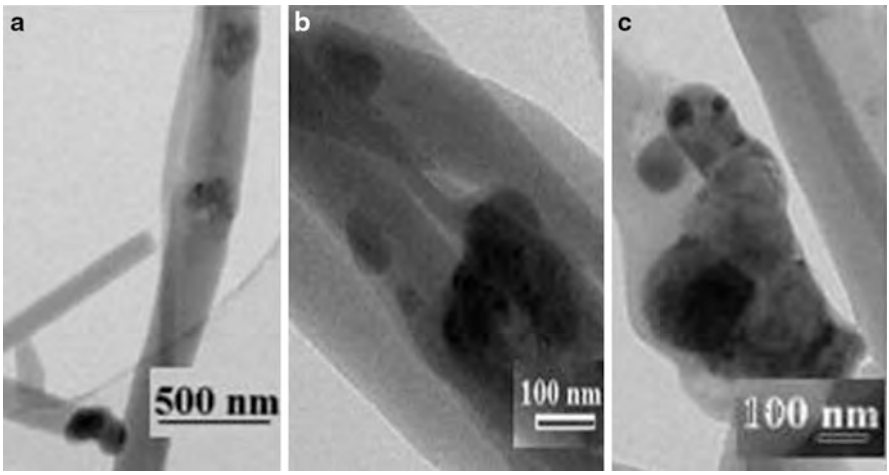

Fig. 22 TEM images of $Li_2Mn_{0.8}Fe_{0.2}SiO_4$/C nanofibers with different magnifications: (**a**) 10,000 and (**b**, **c**) 30,000 (Reproduced from Ref. [44]. Copyright 2012, Elsevier)

nozzle-collector distance of 15 cm. The flexible, free-standing nonwoven mat was then stabilized at 280 °C in air and carbonized at 700 °C in argon. The resultant products were Fe/Cr-doped Li_2MnSiO_4/C nanofibers, and the composite nanofibers were used directly as cathode materials in lithium-ion batteries without the addition of polymer binders and conductive agents.

Figure 22 shows the TEM images of $Li_2Mn_{0.8}Fe_{0.2}SiO_4$/C nanofibers at different magnifications. Figure 22a, b confirm that $Li_2Mn_{0.8}Fe_{0.2}SiO_4$ particles are dispersed inside the CNF matrix. It is also seen from Fig. 22c that the aggregated primary particles form the "bead-on-string" morphology. The charge–discharge curves and cycling performance of Li_2MnSiO_4 powders, $Li_2Mn_{0.8}Fe_{0.2}SiO_4$ powders, and $Li_2Mn_{0.8}Fe_{0.2}SiO_4$/C nanofibers are compared in Fig. 23. As shown in Fig. 23a, at a current density of 16.65 mA g^{-1} (C/20), the Li_2MnSiO_4 powder electrode presents a discharge capacity of 212 mA h g^{-1} for the initial cycle, corresponding to nearly 1.27 electron transfer per formula unit. The discharge capacity degrades rapidly to less than one electron exchange per formula unit for the following cycles. Such rapid capacity loss can be ascribed to the intrinsic structural instability of the cathode material. With 20 % iron doping, the $Li_2Mn_{0.8}Fe_{0.2}SiO_4$ powder electrode yields a higher discharge capacity of around 220 mA h g^{-1} for the initial cycle, corresponding to a 1.32 electron transfer per formula unit. It is seen from Fig. 23b that the reversible discharge capacity sustained at the 10th cycle is 170 mA h g^{-1}, suggesting that the electrode material is still able to retain more than one electron exchange per formula unit. By encapsulating $Li_2Mn_{0.8}Fe_{0.2}SiO_4$ powder into CNFs, a higher capacity is achieved along with enhanced capacity retention. It is seen from Fig. 23c that the composite nanofiber electrode presents a high discharge capacity of 224 mA h g^{-1}, which decreases to 171 mA h g^{-1} after 20 cycles. In a comparison, the discharge capacities at the 20th cycle for Li_2MnSiO_4 and $Li_2Mn_{0.8}Fe_{0.2}SiO_4$ powder

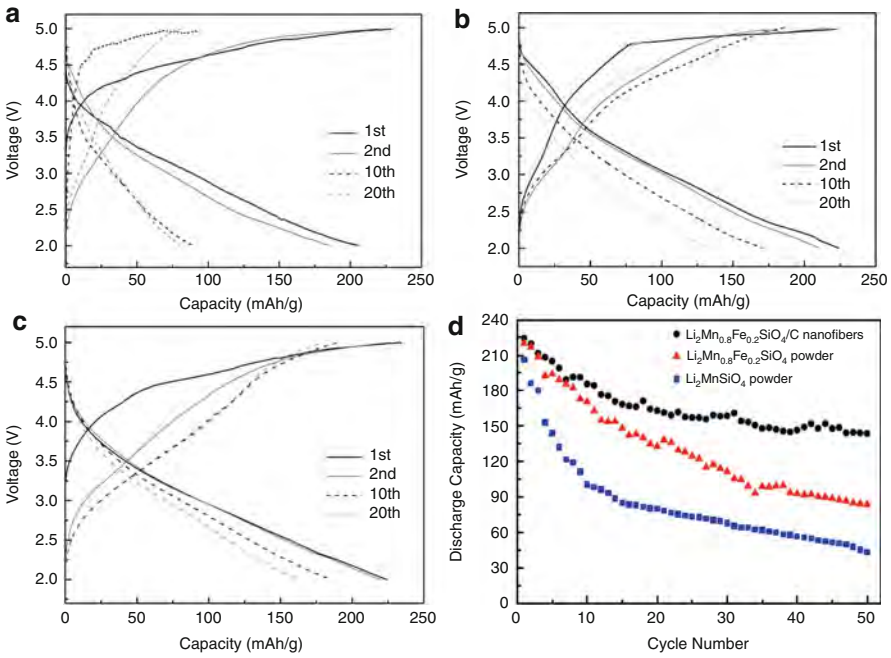

Fig. 23 Charge–discharge curves of Li_2MnSiO_4 powder (**a**), $Li_2Mn_{0.8}Fe_{0.2}SiO_4$ nanofibers (**b**), $Li_2Mn_{0.8}Fe_{0.2}SiO_4$/C nanofibers (**c**), and cycling performance of Li_2MnSiO_4 powder, $Li_2Mn_{0.8}Fe_{0.2}SiO_4$ nanofibers, and $Li_2Mn_{0.8}Fe_{0.2}SiO_4$/C nanofibers (**d**) (Reproduced from Ref. [44]. Copyright 2012, Elsevier)

electrodes are only 77 and 127 mA h g^{-1}, respectively. Figure 23d illustrates the cycling performance of the cathodes. Among the three materials, the $Li_2Mn_{0.8}Fe_{0.2}SiO_4$/C nanofibers exhibit the highest capacity retention of 63.8 % after 50 cycles, while the capacity retentions for the Li_2MnSiO_4 and $Li_2Mn_{0.8}Fe_{0.2}SiO_4$ powder electrodes are only 20.5 % and 41.3 %, respectively.

The composite nanofiber electrode shows the best electrochemical performance among the three electrodes, mainly because the super-valent ion doped Li_2MnSiO_4 materials have higher conductivity than the undoped one, and the CNF matrix not only prevents the particles from aggregation but also provides shorter diffusion pathways for both electrons and lithium ions. The advantageous characteristics of the super-valent metal doping and CNF matrix together contribute to a significantly improved electrochemical performance for $Li_2Mn_{0.8}Fe_{0.2}SiO_4$/C nanofibers.

Nanofiber Separators

Battery separators are porous membranes that are placed between anode and cathode. The major function of separators is to serve as the reservoir to hold the electrolyte and ensure ionic transport, while preventing the two electrodes from

physical contact. Most state-of-the-art lithium-ion batteries use traditional microporous polymer membranes as the separator. Although the conventional microporous separators possess good chemical stability, decent mechanical strength, and suitable thickness, their low porosity, poor thermal stability, and low wettability with polar liquid electrolytes lead to high electrochemical resistance, low energy density, and poor rate performance [8–13]. Recently, electrospinning method is adopted in the fabrication of novel nanofiber-based nonwoven membranes [46–50], which exhibit smaller pore size and larger porosity than conventional microporous membranes and can be directly used as separators in rechargeable lithium-ion batteries. The electrospun nanofiber-based separator materials allow high-rate charge and discharge for batteries due to their desirable ion transport paths and high porosity.

For instance, Liang and coworkers [48] introduced ionic-conducting ceramic particles into electrospun PAN nanofibers, and the resultant composite nanofibers not only obtained the basic functions of battery separators but also showed significantly enhanced ionic conductivity, which is favorable for fast battery kinetics. In this study, perovskite-type lithium lanthanum titanate, $Li_{3x}La_{2/3-x}TiO_3$ (LLTO), was prepared by a sol–gel method using $LiNO_3$, $La(NO_3)_3 \cdot 6H_2O$, and $Ti(OC_4H_8)_4$ as precursors. LLTO is an ionic-conducting ceramic that has a high bulk lithium-ion conductivity of around 10^{-3} S/cm at room temperature. Different amounts of LLTO particles were then added into PAN/DMF solutions for electrospinning. The solutions were electrospun into porous nonwoven membranes with an applied voltage of 18 kV, a flow rate of 0.5 mL h^{-1}, and a nozzle-collector distance of 18 cm. The as-spun nanofibers were then dried in air at 60 °C and were used directly as lithium-ion battery separators.

Figure 24 shows the SEM images of LLTO/PAN composite nanofibers containing different amounts of LLTO particles. As seen in Fig. 24a, the pure PAN nanofibers exhibit a smooth surface and are relatively taut and randomly oriented. The average fiber diameter for pure PAN nanofibers is about 250 nm. In comparison, 5 wt% LLTO/PAN composite nanofibers have a small amount of irregularities and the surface of the nanofibers are not as smooth and uniform as the pure PAN nanofibers (Fig. 24b). The average fiber diameter of the nanofibers with 5 wt% LLTO decreases slightly to 230 nm. It is seen from Fig. 24c, d that with further addition of LLTO particles to 10 and 15 wt%, the surface of the electrospun composite nanofibers becomes even rougher, accompanied by particle agglomeration and cluster formation. Moreover, the average fiber diameters of these two samples are smaller than 200 nm.

The as-spun LLTO/PAN composite nanofibers were used directly as separators without any post-treatment. Figure 25a illustrates the liquid electrolyte uptakes as a function of LLTO content. The electrolyte used in the study was 1 M lithium hexafluorophosphate in ethylene carbonate and ethyl methyl carbonate with a volume ratio of 1:1. Figure 25a suggests that as the LLTO content increases, the liquid electrolyte uptake increases slightly. The temperature dependence of the ionic conductivities of the electrolyte-immersed composite nanofiber separators is demonstrated in Fig. 25b. It is seen that all the four electrolyte-immersed separators show increased ionic conductivities when the temperature increases.

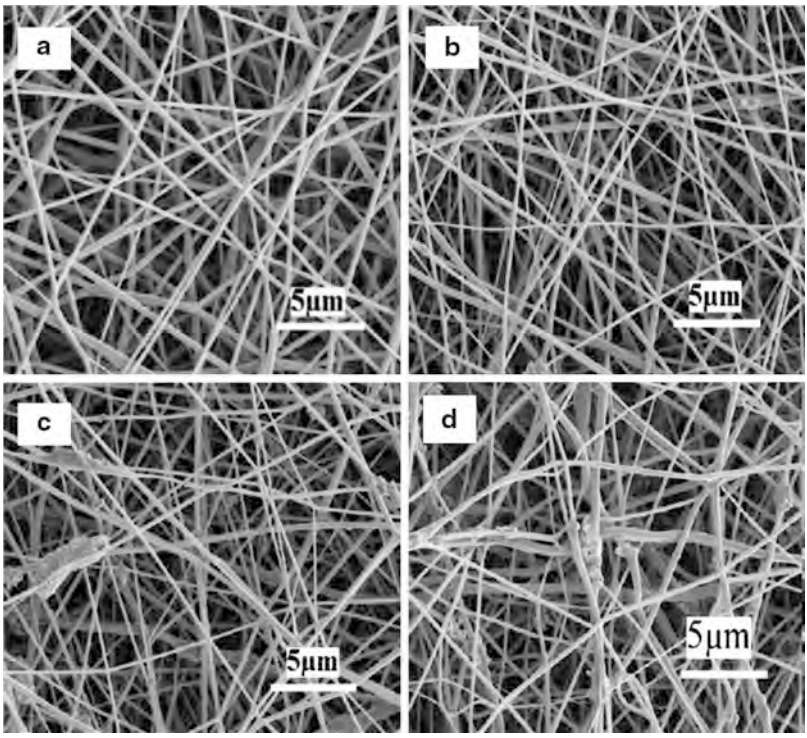

Fig. 24 SEM images of LLTO/PAN composite nanofibers with various LLTO contents: (**a**) 0, (**b**) 5, (**c**) 10, and (**d**) 15 wt% (Reproduced from Ref. [48]. Copyright 2011, Elsevier)

Furthermore, it is also seen that at each temperature, the ionic conductivity increases with higher LLTO content in the composite nanofibers. This is mainly because the addition of LLTO particles decreases the fiber diameter and gives larger specific surface area, making it easier to entrap more liquid electrolyte, i.e., resulting in higher electrolyte uptake (Fig. 25a). Moreover, the high bulk conductivity of LLTO also contributes to the improved conductivities of electrolyte-immersed composite nanofiber separators.

In addition to electrolyte uptake and ionic conductivity, other properties are also important in affecting the separator performance. For example, the interfacial resistance between the electrodes and the electrolyte-immersed separators is one of the important parameters for battery separators. To investigate the impedance, lithium cells were assembled and tested using LLTO/PAN composite nanofibers as the separator. The Nyquist plots of these cells are shown in Fig. 25c. It is seen that there is a semicircle at the intermediate frequency for each curve and the diameter of this semicircle indicates the interfacial resistance (R_i) between the electrode and the electrolyte. It is also seen that with more LLTO particles introduced into the PAN nanofibers, the diameter of the semicircle in the Nyquist plots becomes smaller, suggesting a smaller interfacial resistance. To further study the

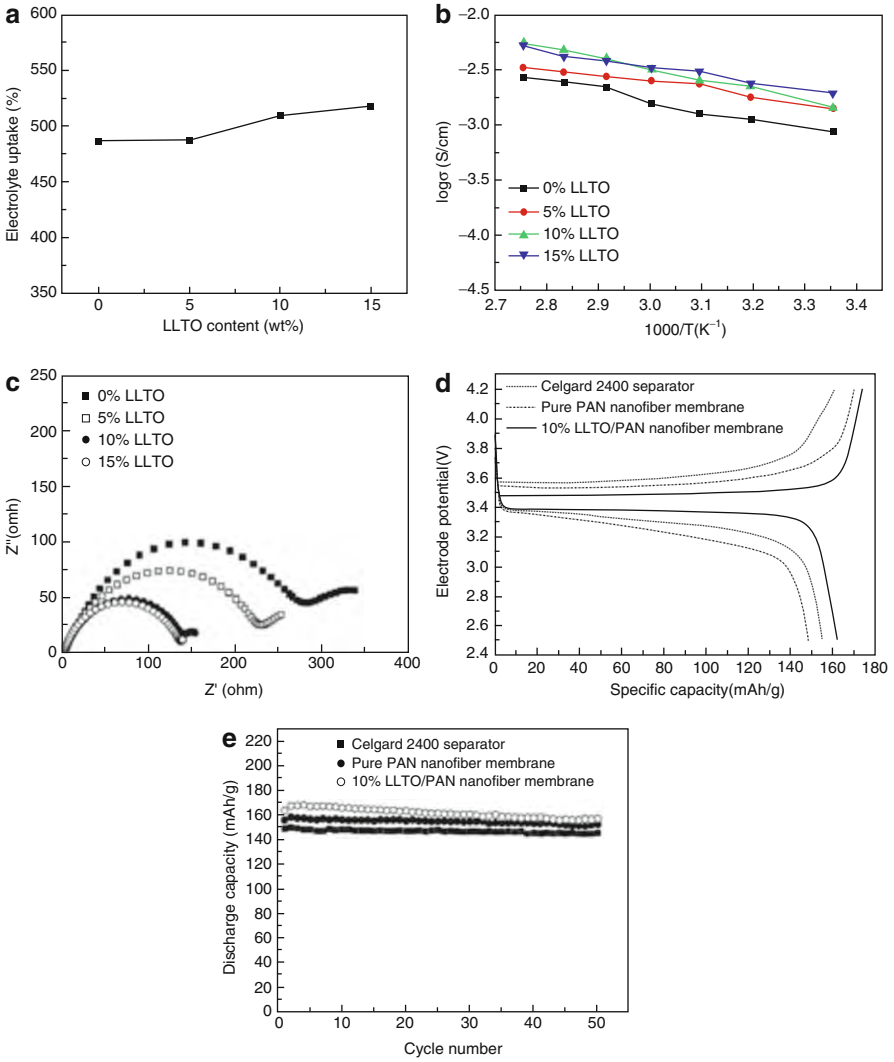

Fig. 25 (**a**) Electrolyte uptakes of electrospun LLTO/PAN composite fiber-based membranes; (**b**) ionic conductivities of liquid electrolyte-soaked electrospun LLTO/PAN composite fiber-based membranes; (**c**) Nyquist plots for liquid electrolyte-soaked LLTO/PAN composite fiber-based membranes; (**d**) initial charge and discharge curves of Li/$LiFePO_4$ cells containing liquid electrolyte-soaked Celgard 2400 separator, pure PAN fiber-based membrane, and LLTO/PAN composite fiber-based membrane at 0.2 C rate; and (**e**) cycle performance of Li/$LiFePO_4$ cells containing liquid electrolyte-soaked Celgard 2400 separator, PAN fiber-based membrane, and LLTO/PAN composite fiber-based membrane at 0.2 C rate (Reproduced from Ref. [48]. Copyright 2011, Elsevier)

performance using LLTO/PAN composite nanofiber separators in lithium-ion batteries, lithium half cells were assembled using $LiFePO_4$ as the cathode, lithium metal as the counter electrode, and 10 wt% LLTO/PAN composite nanofibers as the separator. Cells were also prepared using commercial separator, Celgard 2400, and pure PAN nanofiber separators as comparisons. The initial charge–discharge curves at room temperature are given in Fig. 25d. It is seen that all the three samples exhibit stable charge and discharge plateaus with the initial discharge capacities in the range of 140–162 mA h g^{-1}. However, the cell using PAN nanofiber separator shows higher charge and discharge capacities than that using Celgard 2400 separator. In addition, the cell using 10 wt% LLTO/PAN composite nanofiber separator exhibits higher capacities than the cells using PAN nanofibers or Celgard 2400 separators. The cycling behaviors of cells using different separators are compared in Fig. 25e. At the 50th cycle, the cell using LLTO/PAN composite nanofiber separator sustains the highest specific discharge capacity of 156 mA h g^{-1}, corresponding to 91.7 % of the theoretical capacity of LiFePO4 (170 mA h g^{-1}). It is confirmed that by introducing LLTO particles into PAN nanofiber separators, the efficiency of conducting lithium ions between the electrodes is improved. The results demonstrate that LLTO/PAN composite nanofibers are promising separator material for rechargeable lithium-ion batteries.

In addition to LLTO/PAN composite nanofibers, other nanofiber-based materials have also been studied as separators for rechargeable lithium-ion batteries. For instance, Liang and coworkers utilized another ceramic material, lithium aluminum titanium phosphate (LATP), to improve the ionic conductivity of PAN nanofiber separators [50]. By implementing a similar synthesis approach in the LLTO/PAN composite nanofiber separator study, they developed LATP/PAN composite nanofibers that present higher specific capacity and better capacity retention than pure PAN nanofiber separator and commercial microporous membrane separator. Another widely investigated nanofiber-based material for lithium-ion batteries is PVDF. Separators prepared by thermally treating PVDF at different temperatures [47], incorporating ionic conductive ceramics such as silica nanoparticles into PVDF nanofibers via combined electrospinning and electrospraying [49] and coating PVDF copolymers onto commercial polyolefin separators [46], show desirable electrolyte uptake, favorable ionic conductivity, and good mechanical strength and hence exhibit high capacities and good cycling performance in rechargeable lithium-ion batteries.

Summary and Outlook

Electrospun nanofiber-based materials are attractive electrode candidates due to their shorter diffusion pathways and more rapid lithium intercalation/deintercalation kinetics in comparison with conventional powder electrode materials. They also exhibit a large amount of lithium-accessible sites and hence show reduced charge-transfer

resistance at the electrode–electrolyte interface. Consequently, electrospun nanofibers are superior electrode materials in lithium-ion batteries. Nanofibers prepared by electrospinning can also be used as battery separators, and their high porosity and favorable pathways for lithium-ion transport ensure high-rate charge/discharge of lithium-ion batteries, making them more desirable compared to traditional microporous membrane separators.

In this chapter, novel nanofiber anodes, including CNFs, SnSb/CNFs, Si/CNFs, and MnO_x/CNFs; nanofiber cathodes, such as $LiCoO_2$ nanofibers, $LiMn_2O_4$ nanofibers, $LiFePO_4$/CNFs, and Li_2MnSiO_4/CNFs; and nanofiber separators including LLTO/PAN nanofiber separators, LATP/PAN nanofiber separators, and PVDF nanofiber separators, are reviewed. In lithium-ion batteries, carbonaceous materials are widely used as anodes. CNFs are adopted in nanofiber anodes not because they can contribute to the capacity, but also because they can provide excellent conductivity for less conductive materials and buffer the high volume change that is undergone by a lot of anode materials such as Si. Therefore, by encapsulating active materials with high lithium storage capacities into highly conductive CNF matrix, the composite nanofiber anodes can achieve high capacity and stable cycling performance. While for lithium-ion battery cathodes, nanofiber architecture is desirable since they provide shorter diffusion path, fast lithium intercalation/deintercalation kinetics, and more lithium host sites. Materials such as $LiCoO_2$ and $LiMn_2O_4$ have been made into nanofiber cathodes and they exhibit more advantageous performance compared to powder materials. Cathode candidates such as $LiFePO_4$ and Li_2MnSiO_4 have poor conductivity, and by fabricating $LiFePO_4$/C and Li_2MnSiO_4/C composite nanofibers, enhanced capacity and cycling stability are accomplished. In the case of nanofiber separators, the liquid electrolyte-immersed nanofiber separators such as LLTO/PAN nanofiber membranes show high electrolyte uptake; reduced interfacial resistance and the lithium-ion batteries using these nanofiber separators present high capacity and stable cycling performance. These results suggest that electrospinning is a promising method to fabricate nanofiber-based, high-performance anode, cathode, and separator materials for lithium-ion batteries.

However, the major obstacle that hinders the widespread implementation of nanofiber-based materials for lithium-ion batteries is the relatively low production rate and high cost of the electrospinning process. Currently, the industry is striving to improve the production rate and reduce the cost of electrospinning process. On one hand, companies such as MECC (Japan), Fuence (Japan), Toptec (Korea), Yflow (Spain), and Elmarco (Czech Republic) have developed and commercialized large-scale electrospinning instruments based on multi-nozzle or nozzle-less design. On the other hand, researchers are also developing novel spinning methods to replace electrospinning. For instance, a recently developed centrifugal spinning process is capable of producing nanofibers in a large-scale and low-cost fashion and can potentially substitute electrospinning in the future for producing nanofiber materials for lithium-ion batteries. The widespread implementation of nanofiber-based materials in commercial lithium-ion batteries also calls for research on thorough understanding of the processing–structure relationship and the possible routes for performance improvement of nanofiber-based anodes, cathodes, and separators.

References

1. Winter M, Brodd RJ (2004) What are batteries, fuel cells, and supercapacitors? Chem Rev 104:4245–4269
2. Padbury R, Zhang X (2011) Lithium–oxygen batteries – limiting factors that affect performance. J Power Sources 196:4436–4444
3. Tarascon JM, Armand M (2001) Issues and challenges facing rechargeable lithium batteries. Nature 414:359–367
4. Long JW, Dunn B, Rolison DR, White HS (2004) Three-dimensional battery architectures. Chem Rev 104:4463–4492
5. Guo YG, Hu JS, Wan LJ (2008) Nanostructured materials for electrochemical energy conversion and storage devices. Adv Mater 20:2878–2887
6. Manthiram A, Vadivel Murugan A, Sarkar A, Muraliganth T (2008) Nanostructured electrode materials for electrochemical energy storage and conversion. Energy Environ Sci 1:621–638
7. Ji L, Lin Z, Alcoutlabi M, Zhang X (2011) Recent developments in nanostructured anode materials for rechargeable lithium-ion batteries. Energy Environ Sci 4:2682–2699
8. Saunier J, Alloin F, Sanchez J, Caillon G (2003) Thin and flexible lithium-ion batteries: investigation of polymer electrolytes. J Power Sources 119–121:454–459
9. Lee YM, Kim JW, Choi NS, Lee JA, Seol WH, Park JK (2005) Novel porous separator based on PVdF and PE non-woven matrix for rechargeable lithium batteries. J Power Sources 139:235–241
10. Ooms FGB, Kelder EM, Schoonman J, Gerrits N, Smedinga J, Calis G (2001) Performance of Solupor® separator materials in lithium ion batteries. J Power Sources 97:598–601
11. Cho TH, Tanaka M, Onishi H, Kondo Y, Nakamura T, Yamazaki H, Tanase S, Sakai T (2008) Battery performances and thermal stability of polyacrylonitrile nano-fiber-based nonwoven separators for Li-ion battery. J Power Sources 181:155–160
12. Arora P, Zhang ZJ (2004) Battery separators. Chem Rev 104:4419–4462
13. Zhang SS (2007) A review on the separators of liquid electrolyte Li-ion batteries. J Power Sources 164:351–364
14. Bansal D, Meyer B, Salomon M (2008) Gelled membranes for Li and Li-ion batteries prepared by electrospinning. J Power Sources 178:848–851
15. Li D, Xia Y (2004) Electrospinning of nanofibers: reinventing the wheel? Adv Mater 16:1151–1170
16. McCann JT, Li D, Xia Y (2005) Electrospinning of nanofibers with core-sheath, hollow, or porous structures. J Mater Chem 15:735
17. Norris ID, Shaker MM, Ko FK, MacDiarmid AG (2000) Electrostatic fabrication of ultrafine conducting fibers: polyaniline/polyethylene oxide blends. Synth Met 114:109–114
18. Gibson P, Schreuder-Gibson H, Rivin D (2001) Transport properties of porous membranes based on electrospun nanofibers. Colloids Surf A Physicochem Eng Asp 187–188:469–481
19. Inagaki M, Yang Y, Kang F (2012) Carbon nanofibers prepared via electrospinning. Adv Mater 24:2547–2566
20. Zhang HL, Zhang Y, Zhang XG, Li F, Liu C, Tan J, Cheng HM (2006) Urchin-like nano/micro hybrid anode materials for lithium ion battery. Carbon 44:778–2784
21. Subramanian V, Zhu H, Wei B (2006) High rate reversibility anode materials of lithium batteries from vapor-grown carbon nanofibers. J Phys Chem B 110:7178–7183
22. Li C, Yin X, Chen L, Li Q, Wang T (2009) Porous carbon nanofibers derived from conducting polymer: synthesis and application in lithium-ion batteries with high-rate capability. J Phys Chem C 113:13438–13442
23. Ji L, Lin Z, Medford AJ, Zhang X (2009) In-situ encapsulation of nickel particles in electrospun carbon nanofibers and the resultant electrochemical performance. Chemistry 15:10718–22
24. Zhang B, Yu Y, Xu ZL, Abouali S, Akbari M, He YB, Kang F, Kim JK (2014) Correlation between atomic structure and electrochemical performance of anodes made from electrospun carbon nanofiber films. Adv Energy Mater 4:7

25. Ji L, Zhang X (2009) Generation of activated carbon nanofibers from electrospun polyacrylonitrile-zinc chloride composites for use as anodes in lithium-ion batteries. Electrochem Commun 11:684–687
26. Qin J, He C, Zhao N, Wang Z, Shi C, Liu EZ, Li J (2014) Graphene networks anchored with Sn@Graphene as lithium ion battery anode. ACS Nano 8:1728–1738
27. Besenhard JO, Hess M, Komenda P (1990) Anorganisch-Chemisches Institut, Universitiit Miinster, Wilhelm-Klernm-Strafle 8, D-400 Miinster, Federal Republic of Germany. 41:525–529
28. Yu Y, Gu L, Zhu C, Van Aken PA, Maier J (2009) Tin nanoparticles encapsulated in porous multichannel carbon microtubes: preparation by single-nozzle electrospinning and application as anode material for high-performance Li-based batteries. J Am Chem Soc 131:15984–15985
29. Derrien G, Hassoun J, Panero S, Scrosati B (2007) Nanostructured Sn–C composite as an advanced anode material in high-performance lithium-ion batteries. Adv Mater 19:2336–2340
30. Xue L, Xia X, Tucker T, Fu K, Zhang S, Li S, Zhang X (2013) A simple method to encapsulate SnSb nanoparticles into hollow carbon nanofibers with superior lithium-ion storage capability. J Mater Chem A 1:13807
31. Ji L, Saquing C, Khan SA, Zhang X (2008) Preparation and characterization of silica nanoparticulate-polyacrylonitrile composite and porous nanofibers. Nanotechnology 19:085605
32. Ji L, Zhang X (2008) Ultrafine polyacrylonitrile/silica composite fibers via electrospinning. Mater Lett 62:2161–2164
33. Ji L, Zhang X (2010) Evaluation of Si/carbon composite nanofiber-based insertion anodes for new-generation rechargeable lithium-ion batteries. Energy Environ Sci 3:124
34. Li Y, Guo B, Ji L, Lin Z, Xu G, Liang Y, Zhang S, Toprakci O, Hu Y, Acoutlabi M, Zhang X (2013) Structure control and performance improvement of carbon nanofibers containing a dispersion of silicon nanoparticles for energy storage. Carbon 51:185–194
35. Lin Z, Ji L, Woodroof MD, Zhang X (2010) Electrodeposited MnO_x/carbon nanofiber composites for use as anode materials in rechargeable lithium-ion batteries. J Power Sources 195:5025–5031
36. Kalluri S, Seng KH, Guo Z, Liu HK, Dou SX (2013) Electrospun lithium metal oxide cathode materials for lithium-ion batteries. RSC Adv 3:25576
37. Gu Y, Chen D, Jiao X (2005) Synthesis and electrochemical properties of nanostructured $LiCoO_2$ fibers as cathode materials for lithium-ion batteries. J Phys Chem B 109:17901–17906
38. Gu Y, Chen D, Jiao X, Liu F (2007) $LiCoO_2$/MgO coaxial fibers: co-electrospun fabrication, characterization and electrochemical properties. J Mater Chem 17:1769
39. Zhou H, Ding X, Yin Z, Xu G, Xue Q, Li J, Jiao S, Wang X (2014) Fabrication and electrochemical characteristics of electrospun $LiMn_2O_4$ nanofiber cathode for Li-ion batteries. Mater Lett 117:175–178
40. Jayaraman S, Aravindan V, Kumar PS, Ling WC, Ramakrishna S, Madhavi S (2013) Synthesis of porous $LiMn_2O_4$ hollow nanofibers by electrospinning with extraordinary lithium storage properties. Chem Commun 49:6677–9
41. Toprakci O, Ji L, Lin Z, Toprakci HAK, Zhang X (2011) Fabrication and electrochemical characteristics of electrospun $LiFePO_4$/carbon composite fibers for lithium-ion batteries. J Power Sources 196:7692–7699
42. Toprakci O, Toprakci HAK, Ji L, Lin Z, Gu R, Zhang X (2012) $LiFePO_4$ nanoparticles encapsulated in graphene-containing carbon nanofibers for use as energy storage materials. J Renew Sustain Energy 4:013121
43. Toprakci O, Toprakci HAK, Ji L, Xu G, Lin Z, Zhang X (2012) Carbon nanotube-loaded electrospun $LiFePO_4$/carbon composite nanofibers as stable and binder-free cathodes for rechargeable lithium-ion batteries. ACS Appl Mater Interfaces 4:1273–1280
44. Zhang S, Li Y, Xu G, Li S, Lu Y, Toprakci O, Zhang X (2012) High-capacity $Li_2Mn_{0.8}Fe_{0.2}SiO_4$/carbon composite nanofiber cathodes for lithium-ion batteries. J Power Sources 213:10–15

45. Zhang S, Lin Z, Ji L, Li Y, Xu G, Xue L, Li S, Lu Y, Toprakci O, Zhang X (2012) Cr-doped Li_2MnSiO_4/carbon composite nanofibers as high-energy cathodes for Li-ion batteries. J Mater Chem 22:14661–14666
46. Alcoutlabi M, Lee H, Watson JV, Zhang X (2012) Preparation and properties of nanofiber-coated composite membranes as battery separators via electrospinning. J Mater Sci 48:2690–2700
47. Liang Y, Cheng S, Zhao J, Zhang C, Sun S, Zhou N, Qiu Y, Zhang X (2013) Heat treatment of electrospun polyvinylidene fluoride fibrous membrane separators for rechargeable lithium-ion batteries. J Power Sources 240:204–211
48. Liang Y, Ji L, Guo B, Lin Z, Yao Y, Li Y, Acoutlabi M, Qiu Y, Zhang X (2011) Preparation and electrochemical characterization of ionic-conducting lithium lanthanum titanate oxide/polyacrylonitrile submicron composite fiber-based lithium-ion battery separators. J Power Sources 196:436–441
49. Yanilmaz M, Lu Y, Dirican M, Fu K, Zhang X (2014) Nanoparticle-on-nanofiber hybrid membrane separators for lithium-ion batteries via combining electrospraying and electrospinning techniques. J Membr Sci 456:57–65
50. Liang Y, Lin Z, Qiu Y, Zhang X (2011) Fabrication and characterization of LATP/PAN composite fiber-based lithium-ion battery separators. Electrochim Acta 56:6474–6480

Fabric Substrates and Interconnectors for Three-Dimensional Surfaces

21

Qiao Li and Xiaoming Tao

Contents

Introduction 550
Fabric Substrates 550
Structures 550
Materials 553
Geometrical Configurations 554
Mechanical Properties 558
Dimensional Stability 565
Breathability 566
Fabric Interconnectors 566
Fabric Interconnectors by Printing Technology 566
Fabric Interconnectors by Embroidering Technology 568
Woven Interconnectors by Weaving Technology 568
Knitted Interconnectors by Knitting Technology 569
Connection Technologies 572
Summary 573
References 574

Abstract

Human bodies are soft, stretchy, and curved. To enable electronics intimately wearable on curvilinear human bodies with various gestures and motions, it requires electronic devices to be breathable, foldable, elastic, reliable, and durable.

Q. Li (✉)
Institute of Textiles and Clothing, The Hong Kong Polytechnic University, Kowloon, Hong Kong SAR, China
e-mail: qiao.li@polyu.edu.hk

X. Tao
Institute of Textiles and Clothing, The Hong Kong Polytechnic University, Hung Hom, Hong Kong SAR
e-mail: xiao-ming.tao@polyu.edu.hk

© Springer Science+Business Media Singapore 2015

X. Tao (ed.), *Handbook of Smart Textiles*,
DOI 10.1007/978-981-4451-45-1_28

Electrical interconnectors play significant roles in conventional electronic devices and are indispensible in wearable electronics that work in repeatedly large deformation in tensile, bending, and shear modes and in three dimensions. This chapter conducts a systematic investigation into different types of (1) fabric substrates, including woven, knitted, and nonwoven, from aspects of structure, material, geometrical configuration, and mechanical performance, and (2) textile interconnectors, such as printed, embroidered, woven, and knitted ones, in terms of their structure, materials, and characteristics, for three-dimensional surfaces.

Keywords
Fabric substrate • Electrical interconnector • Wearable electronics • Three-dimensional surface

Introduction

Electrical interconnectors play significant roles in conventional electronic devices and are also indispensible in wearable electronics that work in a repeatedly large deformation in tensile, bending, and shear modes and in three dimensions [1]. Hence, electrical interconnectors should have low moduli comparable with those of human tissues like skin and muscles; they need to be permeable and comfortable to wearers [2]. Textile-based electrical interconnectors by integrating conductive materials into fabric substrates, therefore, have enormous potentials to fit for such a purpose. This chapter conducts a systematic investigation into (1) different types of fabric substrates, including woven, knitted, and nonwoven, in terms of structures, materials, geometrical configurations, as well as mechanical performances, and (2) textile interconnectors for three-dimensional surfaces, ranging from printed circuits to embroidered, woven, and knitted interconnectors from the aspects of conductive materials, fabrication, and characteristics.

Fabric Substrates

Fabrics that are thin, lightweight, soft, flexible, twistable, foldable, and even stretchable, as well as porous (or breathable) have attracted much attention as novel substrates for wearable electronics on soft, two-dimensional curvilinear and extensible human bodies [3]. Currently, three primary kinds of textiles, i.e., woven, knitted, and nonwoven, have been proposed and demonstrated as flexible substrates of electrical interconnectors with different characteristics for wearable applications. This section describes the three kinds of fabric substrates in terms of structures, materials, geometrical configurations, and mechanical properties.

Structures

Woven fabric is the assembly of two sets of threads, i.e., warp (along the length) and weft yarns (along the width of the fabric), through intersection at right angles to

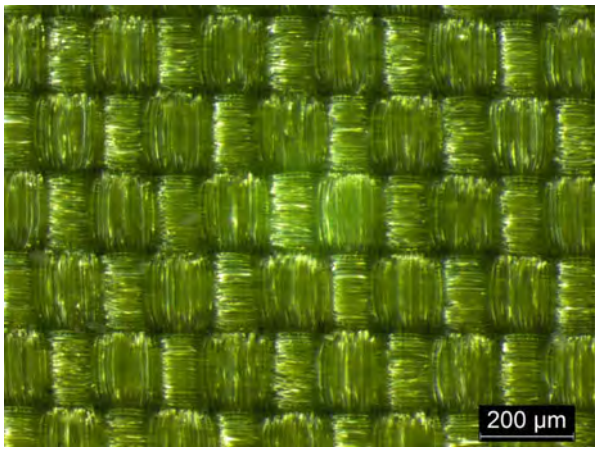

Fig. 1 Optical image of a plain weave fabric

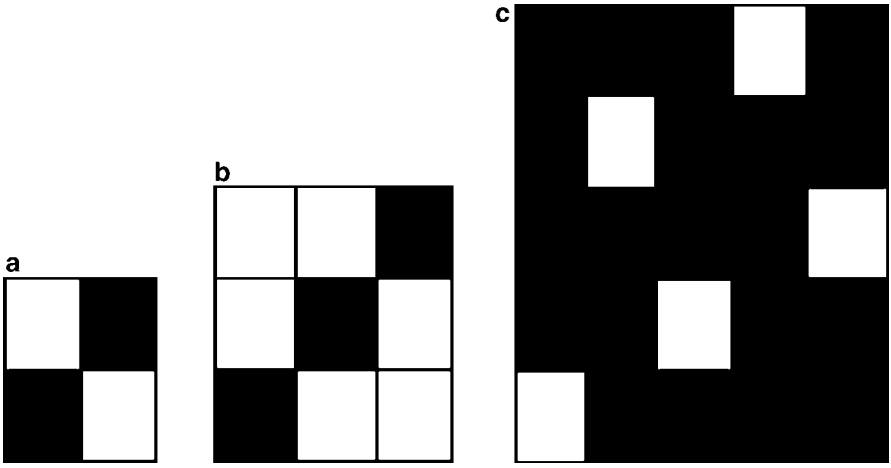

Fig. 2 Point paper diagram of the woven fabrics: (**a**) plain, (**b**) twill, and (**c**) satin

each other by inter-yarn frictions [4]. There are a number of weaves in woven fabrics, in which the most elementary ones are plain, twill, and satin. A plain weave, as the simplest repeating unit, is created by firstly inserting a weft yarn over and under one warp yarn and then passing it under and over the warp yarn, as illustrated in Fig. 1. A twill weave, producing diagonal patterns on the fabric surface, is made by passing one filling yarn over two warp yarns and under one warp yarn and then inserting the next filling yarn also over two warp yarns and under one with the pattern starting one warp yarn farther in. A satin weave is created by permitting warp or filling yarns to float over four or more warp or filling yarns [4]. Figure 2 illustrates the point paper diagram of the three elementary patterns. Currently, plain-woven fabrics are the most widely used in wearable electronics due to its simple structure, such as a pressure-sensing fabric consisting of weft and warp

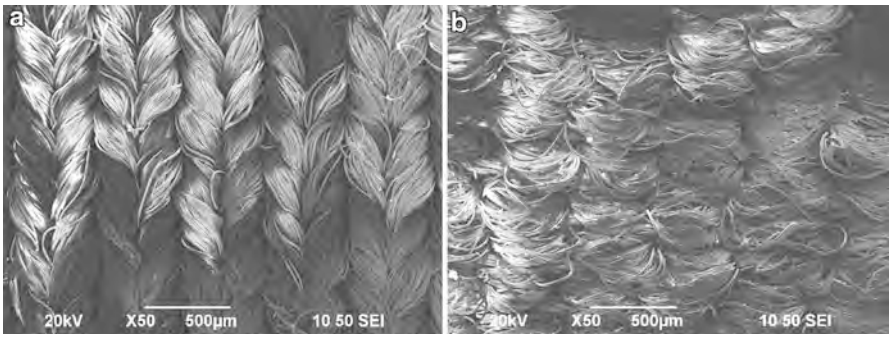

Fig. 3 Plain-knitted fabric: *front side* (*left*) and *back side* (*right*) [3] (Reproduced with permission)

conductive yarns [5] and printed/embroidered/woven circuits. However, a 2/2 matt pattern was employed for a soft fabric switch to improve the contact area between the warp and fill conductive yarns. It is believed that more complex fabric structure should be exploited for specific wearable applications.

Unlike woven fabric, knitted fabric is composed of interlaced yarns in a series of connected loops, where the column and row directions of the loop are referred to as wale and course, respectively. There are two categories of knitted structures: weft and warp knits, in which the former is made from a single yarn, with the loops traveling horizontally across the fabric; the latter is constructed of one or more sets of loops running vertically along the fabric. The elementary structures in the weft knits are plain (single jersey), rib, interlock, and purl knits. Single jersey has all knit stitches on the front and all purl stitches on the back, resulting in smooth front and more textured back with horizontal courses, as shown in Fig. 3. Unlike plain structure, which is made on a single-bed machine, the other three primary structures, i.e., rib, interlock, and purl, are created on double-bed machines with different arrangements of the needles. They possess different characteristics in terms of thickness, extensibility, laddering, and so on for specific applications. For instance, the plain-knitted fabric, as the thinnest one with about two yarn diameters, is broadly used as intimate apparels [6]. The basic element of warp-knitted fabrics includes pillar, tricot, atlas, double-loop, and tricot stitches based on rib stitches, where pillar and tricot stitches have been proposed and demonstrated for fabric sensors.

Nonwoven fabrics, as opposed to weave and knits, refer to textiles that are made directly from a set of fibers held together by bonding or entanglement by chemical, mechanical, heat, or solvent treatment. The main classes of nonwovens include stitch-bonded, adhesive-bonded, spun-bonded, spun-laced, and needle-bonded (or needle-punched) fabrics [7]. Few nonwoven samples, so far, have been demonstrated as flexible substrates of wearable electronics, except for some stretchable interconnects, since most of the nonwoven fabrics are not suitable for garments.

Table 1 Physical property of the dielectric supporting materials [3]

Properties	Polyester	Nylon	Spandex
Density (g/cm^3)	1.38	1.15	1.15–1.32
Elastic modulus (MPa)	2,800–3,100	2,100–3,400	
Poisson's ratio	0.38	0.4	0.862
Elongation (%)	50–150		400–700
Tensile strength (MPa)	55–75	75	
Thermal conductivity (W/(m.k))	0.15–0.24	0.25	
Melting point (°C)	250–300	190–350	250
Linear expansion coefficient (/k)	7×10^{-5}	4×10^{-5}	
Electrical conductivity (S/m)	Insulate	10^{-12}	Insulate
Dielectric constant	3.2	3.5	
Water absorption (%)	0.16	5–6	0.8–1.2

Materials

Regarding textile manufacturing technologies, any type of textile yarns with sufficient tenacity, such as natural (e.g., cotton, wool, and silk), natural blended chemical fibers, synthetic filaments (e.g., nylon, polyester, and spandex), as well as newly developed environmental-friendly filaments (like PLA or PHBV), could be used to make woven, knitted, and nonwoven fabrics. For the purpose of not affecting the electromechanical performance of the electrical interconnectors on textile substrates, however, synthetic filaments, like nylon, polyester, and spandex, are often selected as dielectric supporting materials by considering their physical, mechanical, and environmental characteristics. As summarized in Table 1, the synthetic filaments are (1) smooth on their surface, accommodating to a very large tensile strain and low hysteresis of the fabrics owing to less inter-friction; (2) available at low cost; and (3) currently employed in the field of flexible electronics in a broad range since they are resistive to most solvents such as water and sweat, resistant to high temperature, and highly isolative, without influencing the electrical behavior of the flexible interconnectors. The spandex filament, super extensible (up to 400–800 % strain) and recoverable of almost 100 % from 400 % strain attributed to the hard and soft segments in its molecular structure, could be incorporated under tension into the fabric, imparting more stretchability in both horizontal and vertical directions, hence imparting better form-fitting properties [3]. Such synthetic filaments could be integrated into textiles with any type of yarn forms, such as multi-ply twisted and single-/double-covered yarn types. Figure 4 illustrates a double-covered yarn, i.e., a highly elastic spandex filament yarn in the core (Dupont Lycra) and polyamide multifilaments wrapped around the core. Such type of yarns can improve the comfort of wearable electronics next to the skin.

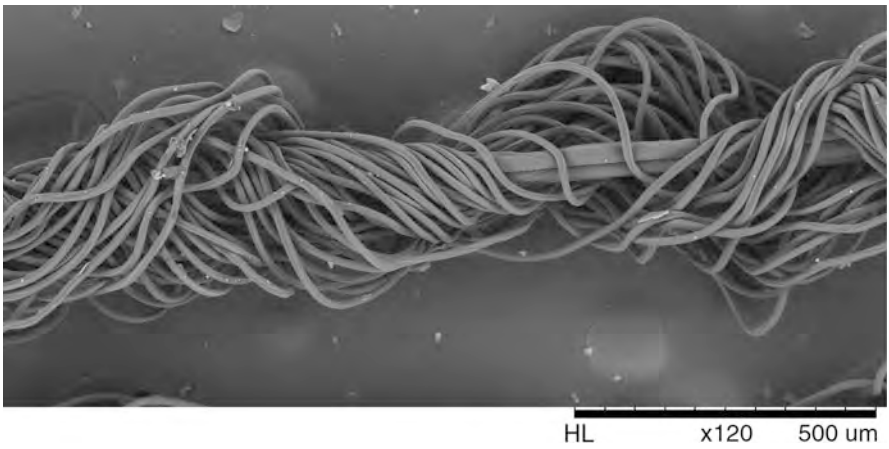

Fig. 4 SEM image of a double-covered yarn

Geometrical Configurations

Geometrical Configurations

The geometric structure of fabrics is extremely complicated since they are not regular in mathematical forms. Previous researchers, however, have idealized textile yarns as perfectly elastic, rigid, and isotropic materials with a circular cross section and established several simplified geometrical models of the woven and knitted fabrics, in which the most typical models of the plain-woven and single-jersey knitted fabrics were proposed by Peirce [8].

Figure 5 schematically presents Peirce's model of an ideal unit cell of a plain-woven fabric, in which the weft or warp yarns are composed of straight and curved segments. Such simple geometry established the relationship between different geometrical parameters, such as thread spacing, weave angle, crimp, and fabric thickness [4].

Figure 6 depicts a 3D looped configuration of a plain-knitted fabric based on Pierce's model [9, 10], which is applicable to the geometries of knitted fabrics with tight structure. The construction for a quarter portion of the 3D loop is divided into curved and straight sections. Hence, the generic point of its yarn axis was expressed by a piecewise function, i.e.,

1. For the curved part $(0 \le s < 1.5d(\pi - \theta))$

$$\left.\begin{aligned} x &= -R \sin\left[\{2d \cos\psi + 1.5d \cos\left(s/1.5d\right)\}/R\right] \\ y &= 1.5d \sin\left(s/1.5d\right) \\ z &= R \cos\left[\{2d \cos\psi + 1.5d \cos\left(s/1.5d\right)\}/R\right] \end{aligned}\right\} \tag{1}$$

2. For the straight part $(1.5d\,(\pi - \theta) < \mathrm{s} \le 1.5d(\pi - \theta) + 2d \sin\left(\theta - \psi\right))$

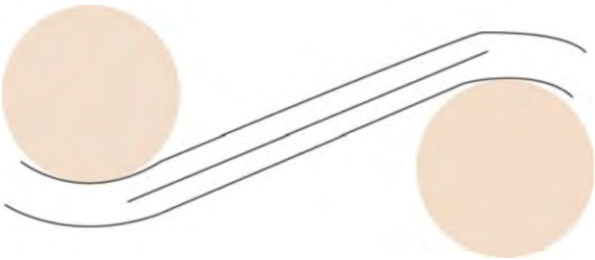

Fig. 5 Peirce's model of plain weave

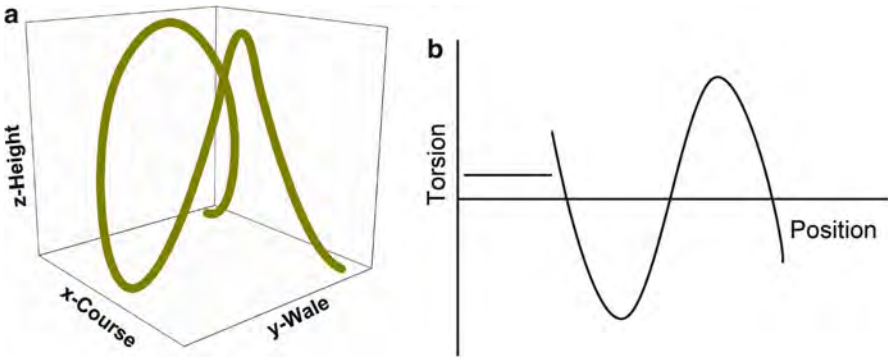

Fig. 6 Piece's model of a plain-knitted loop

$$\left.\begin{aligned} x &= -R\sin\{[2d\cos\psi - 1.5d\cos\theta - \{s - 1.5d(\pi-\theta)\}\sin\theta]/R\} \\ y &= 1.5d\sin\theta - \{s - 1.5d(\pi-\theta)\}\cos\theta \\ z &= R\cos\{[2d\cos\psi - 1.5d\cos\theta - \{\mathrm{s} - 1.5\mathrm{d}(\pi-\theta)\}\sin\theta]/R\} \end{aligned}\right\} \quad (2)$$

where $\theta = 1.2464$ (rad), $\psi = 0.5236$ (rad), $R = 4.172d$, and d is yarn diameter [3].

The limitation of Peirce's model of the plain-knitted loop is the torsion of the yarn axis is noncontinuous in a period. To overcome the disadvantage, Leaf proposed another 3D geometrical model of a plain-knitted fabric with loose structure [11, 12]. In his model, the knitted yarn was considered as a thin elastic rod, whose position was determined by joining the thin elastic rods end to end into a 2D knitted fabric and then placing the 2D model on a sine wavelike surface of a cylinder to create its 3D configuration. Thus, the 3D loop configuration of the yarn axis could be expressed by

$$\left.\begin{aligned} x &= b\{2E(\varphi,\varepsilon) - F(\varphi,\varepsilon)\} \\ y &= p\left(\frac{\pi}{2} - \psi\right) \\ z &= q(\sin\psi - 1) \end{aligned}\right\} \quad (3)$$

where $0 \le \varphi \le \pi/2$, $0 \le \psi \le \pi/2$, and ε is constant, i.e., $\varepsilon = 0.8090$, and $F(\varphi, \varepsilon)$ and $E(\varphi, \varepsilon)$ are incomplete elliptic integrals of the first and second kinds, respectively. The relationship of the parameters φ and ψ was established by

$$\cos\varphi = 1 - \frac{E(\psi, w)}{E(\pi/2, w)} \tag{4}$$

And the parameters p, q, b was determined by

$$\left.\begin{aligned} l &= 4bF\left(\frac{\pi}{2}, \varepsilon\right) \\ 2b\varepsilon &= \frac{q}{w}E\left(\frac{\pi}{2}, w\right) \\ w^2 &= \frac{q^2}{p^2 + q^2} \\ \cos\varphi &= 1 - \frac{E(\psi, w)}{E\left(\frac{\pi}{2}, w\right)} \end{aligned}\right\} \tag{5}$$

once the loop length l is obtained. Same to ε, w is constant, i.e., $w = 0.5766$. The loop length l was determined from Munden's observation about the experimental results [13], that is,

$$\left.\begin{aligned} C \times W &= K_1/l^2 \\ C &= K_2/l \\ W &= K_3/l \end{aligned}\right\} \tag{6}$$

where C and W are, respectively, the number of courses and wales per unit length, and K_1, K_2, and K_3 are constants. For dry-relaxed fabrics, they are $K_1 = 19.0$, $K_2 = 5.0$, and $K_3 = 3.8$. Based on the above equations, Leaf's model of a single-unit loop in the knitted fabric is presented in Fig. 7. It proved that the knitted yarn is bent simultaneously

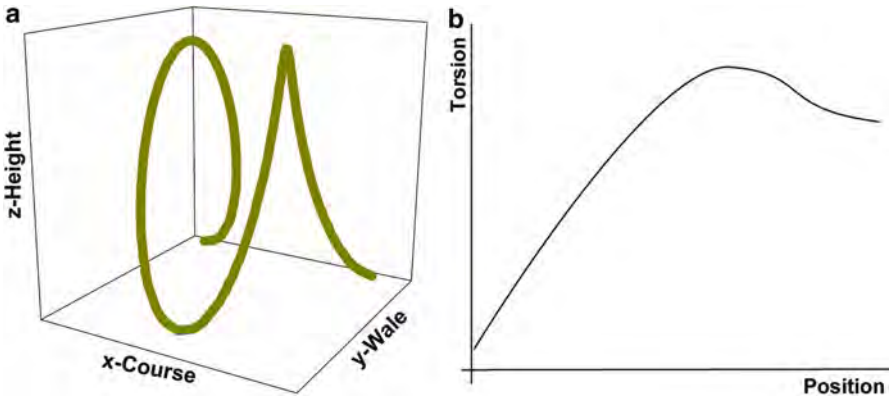

Fig. 7 Leaf's model of a plain-knitted fabric

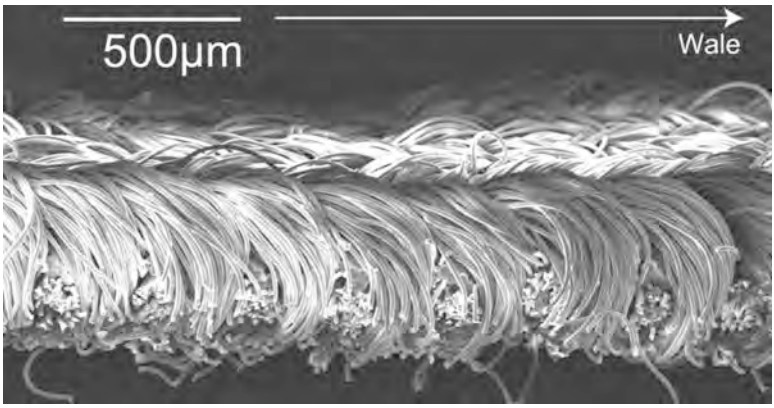

Fig. 8 Cross-sectional images of a single-jersey knitted fabric [3] (Reproduced with permission)

in two planes at an angle to one another, producing a degree of curvature and torsion. Obviously, the torsion is continuous in a period, as shown in Fig. 8 [3].

Surface Geometries

Different from plastic or elastomeric substrates, textiles are composed of multi-fibers so that their surface is neither flat nor smooth. As shown in Fig. 8, the cross-sectional images of a plain-knitted fabric demonstrate that the surface of the fabric substrates are rough due to yarn spacing, irregularity, fabric design, and other geometrical factors. Surface roughness of the textile substrates could contribute to the morphology of the printed electronics on textiles. Hence, it is of necessity to identify surface roughness of the fabrics before printing or depositing conductive materials on the fabric substrates.

Surface roughness of the fabrics, similar to the measurement of surface contours, could be observed by KES surface roughness instrument [14], which uses a sensor and smooth steel piano wire to detect variation of the fabric thickness under a normal load of 10 g on the probe over a 2 cm fabric length along the transverse and longitudinal directions by moving the fabric or sensor forward and backward [15], as shown in Fig. 9. The surface roughness chart, consisting of the trough and peak of the fabrics, was then obtained. It has been observed that the waves on the chart are not regular; the number of the waves, however, almost equals the sett (picks per inch) of the fabrics in their cross directions. The surface roughness *SMD* was finally derived by

$$SMD = \frac{1}{X}\int_0^x \left|T - \overline{T}\right| dx, \tag{7}$$

that is, the roughness is the average height of the area constructed by the average line and the zigzag curves.

Several models have been established to derive the surface geometries of the plain-woven and single-jersey knitted fabrics without considering the irregularity of

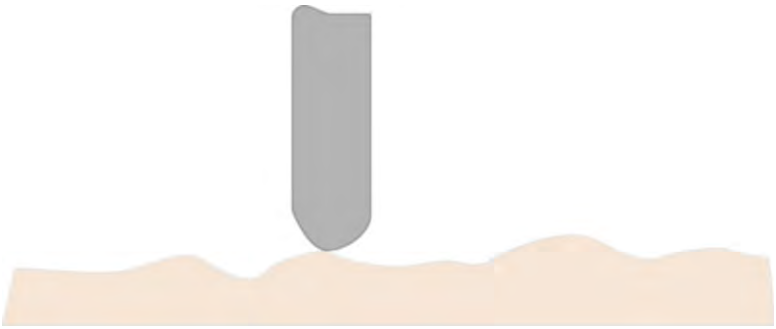

Fig. 9 Measurement of surface roughness by the KES instrument

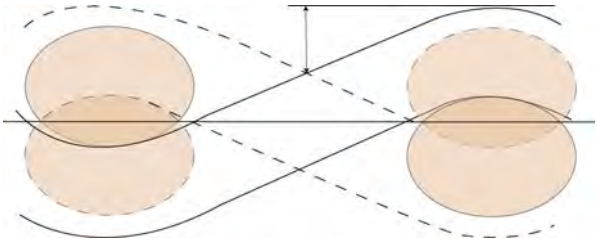

Fig. 10 Geometrical roughness of a plain-woven fabric

yarns and hairiness. Figure 10 presents a simplified model of the surface roughness of a plain-woven fabric, where the geometrical roughness was determined by the variation of the fabric thickness around a central line of the distance between the lowest and highest places on the fabric surface [15].

Figure 11 depicts the surface geometries of a plain-knitted fabric without consideration of the hairiness and multifilament structure of the yarn. The height profile (z) of the knitted fabric in its course (x) wise was approximated by

$$z = R\cos\left[\arcsin(-x/R)\right] \tag{8}$$

which is a sine wave function with the period of a half wale spacing of the knitted fabric. Alike, the height profile (z) in the wale (y) direction was estimated by

$$z = R\cos\left\{\left[2d\cos\psi - 1.5d\cos\theta - \left[(1.5d\sin\theta - y)/\cos\theta\right]\sin\theta\right]/R\right\} \tag{9}$$

It is also a sine wave function, whose period represents one course spacing of the knitted fabric [3].

Mechanical Properties

Fabrics are selected as substrates of wearable electronics mainly owing to their distinctive mechanical properties, such as extreme flexibility, large stretchability,

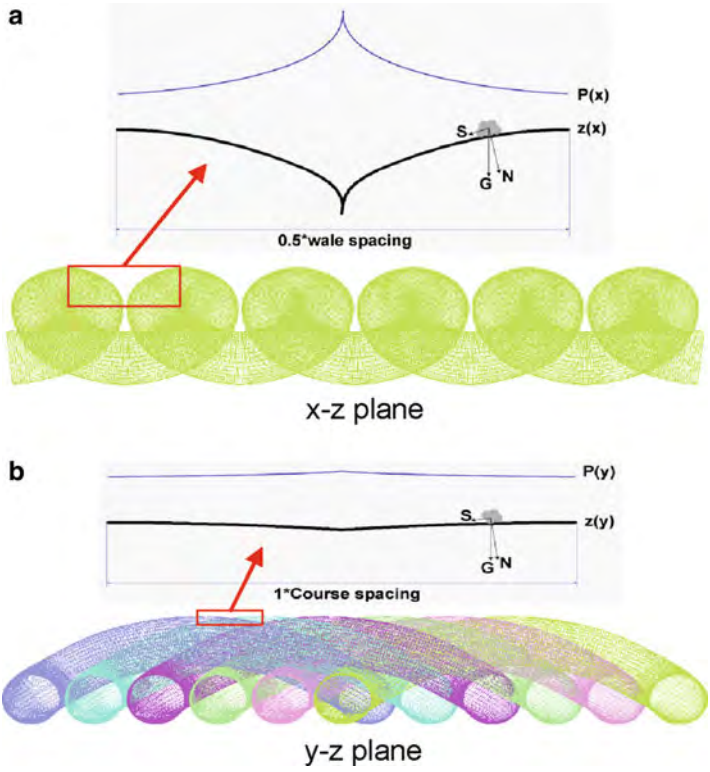

Fig. 11 Height profiles and applied pressure in the course (**a**) and wale (**b**) directions [3] (Reproduced with permission)

drapability, and so on. Also, some mechanical performance of the fabrics could affect the electromechanical properties of the wearable electronics. For instance, the fabrics will be compressed with a large deformation under a small pressure, which may be useful or harmful to the electromechanical properties of the wearable electronics. Therefore, it is of great importance to select proper fabrics before the use as flexible substrates of the electronics. This section describes the primary measurement systems and specific mechanical properties of different fabric substrates.

Measurement Systems

There are several primary test systems for the mechanical properties of the fabrics, i.e., KES, FAST, and Instron. The KES system is the first to test mechanical properties of the fabrics and has been broadly used all over the world due to high precision and reproducibility in the measurement. A complete KES system consists of precision instruments originally designed to measure the key mechanical properties, i.e., tensile, shear, pure bending, compression, as well as surface roughness and friction related to the hand, drape, and formability of fabrics [15].

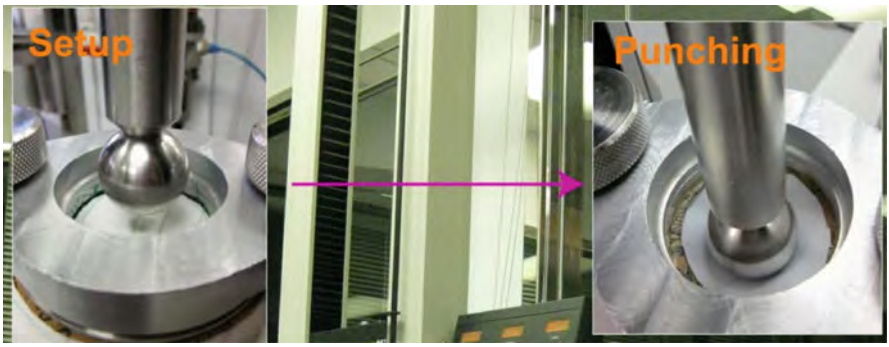

Fig. 12 Three-dimensional punching test

The FAST system is another set of test approaches developed by the CSIRO Division of Wool Technology (Australia) for measurement of the mechanical properties of the fabric. The system comprises compression, bending, extension meters, and dimensional stability tester.

Besides the above KES and FAST systems, several mechanical deformations, such as tensile, compression, shear, and three-dimensional punching modes, are often conducted on Instron. For instance, to investigate the 3D deformation when the fabrics are wrapped around the movable and curvilinear human bodies, a three-dimensional punching test could be carried out with a ball-burst test method on the Instron device. The ball-burst attachment consists of a clamping mechanism to hold the test specimen and a steel ball attached to the movable member of the tester. The polished steel ball has a diameter of 25.400 $\pm$ 0.005 mm and is spherical within 0.005 mm; the ring clamp has an internal diameter of 44.450 $\pm$ 0.025 mm. As depicted in Fig. 12, a specimen of the fabric substrate was securely fastened in the ring clamp without tension. The ball was then pushed into the central areas of the fabric at a constant speed [3].

The average strain of the fabric during the ball-punching test could be derived by the assumption of the fabric as membrane since the fabric is very thin in its thickness. The total length of the specimen in the punching process could be divided into two separate elements: L and S [3]. As illustrated in Fig. 13a, the right half part of the specimen is studied since the whole experimental setup is symmetrical. According to the principal properties of the right triangle, L can be expressed by

$$L = \sqrt{D^2 + R^2 - 2Dr} \tag{10}$$

where D presents vertical displacement of the bottom point of the stainless steel ball and R and r are radii of the ring clamp and the ball, respectively. S is arc length of the ball. When the displacement D is less than the radius r of the ball, the corresponding radian θ_1 of arc length S can be calculated by

$$\theta_1 = \arctan\left[R/(r - D)\right] - \arctan\left(L/r\right) \tag{11}$$

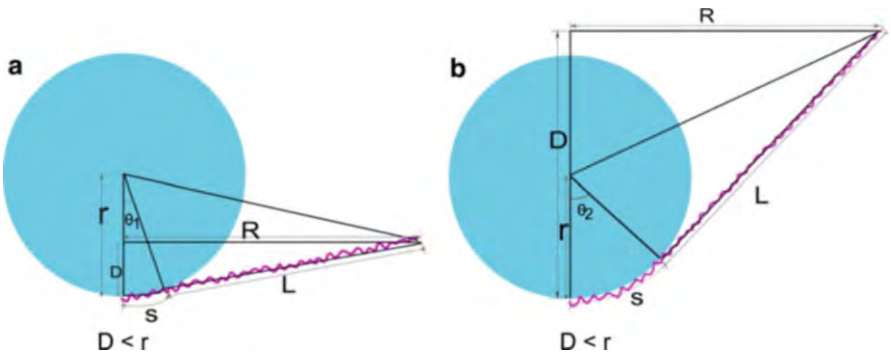

Fig. 13 Different states in the three-dimensional punching test [3] (Reproduced with permission)

When the displacement D of the ball is larger than the radius r of the ball (Fig. 13b), the corresponding radian θ_2 is expressed by

$$\theta_2 = \pi - \arctan\left[R/(D-r)\right] - \arctan\left(L/r\right) \tag{12}$$

The arc length S of the steel ball can be acquired by

$$S = r\theta_{1/2} \tag{13}$$

Hence, the average strain of the specimen $\overline{\varepsilon}$ during the ball-punch test can be obtained by

$$\overline{\varepsilon} = (L + S - R)/R \times 100\,\% \tag{14}$$

Mechanical Properties

The mechanical performance of the fabric substrates, such as stretching, bending, shear, and compression, is of considerable importance in determining how the fabrics will perform in the wearable electronics. This section describes the governing curves or properties of the woven and knitted fabrics in the above deformation modes.

Stretching Behavior

Figure 14 presents a typical nonlinear tensile strain–stress curve of a woven fabric. In the initial period, i.e., in the low-stress range, there is a low slope due to de-crimping and crimp interchange when the woven fabric is stretched; after a critical value, there is a drastic increment in the slope attributed to the extension of the fibers in the woven fabric [4, 15]. The cyclic loading behavior of the woven fabric demonstrates a residual strain is induced because of the viscoelastic property of the textile materials. Such phenomenon is called the hysteresis effect, denoting the energy lost during the loading and unloading cycle. Hence, a deformed fabric

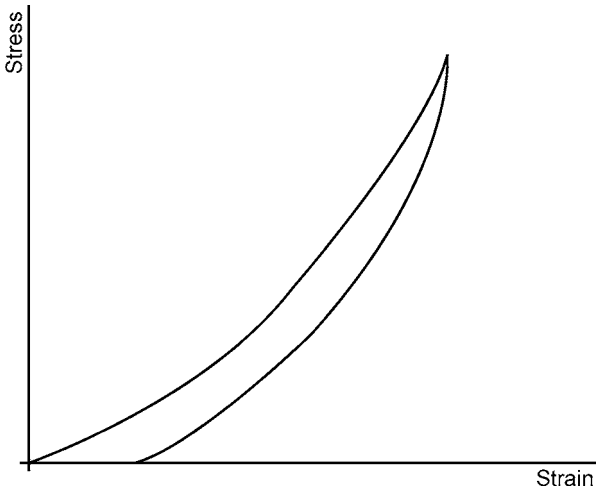

Fig. 14 Tensile *stress–strain curve* of the woven fabric

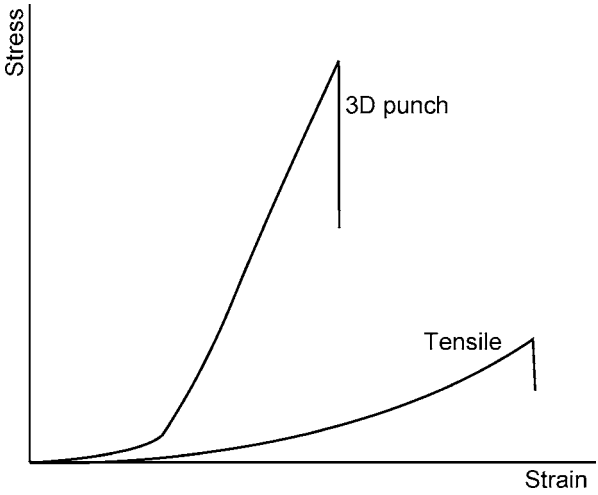

Fig. 15 Stretching properties of a knitted fabric

cannot recover to its original geometrical state [15]. If stress is applied at an angle to the warp or weft direction of the woven fabric, the mode of deformation will become a combination of extension and shear.

In contrast to woven fabrics whose accessible extension is usually less than 10 %, knitted fabrics are often capable of being stretched up to 100 % owing to their 3D looped configurations and the way in which neighboring loops fit together. As illustrated in Fig. 15 [3], a plain-knitted fabric with spandex filaments could be stretched over 500 % strain in both the horizontal and vertical directions. The same knitted fabric sample, however, exhibits a considerable reduction in its average membrane strain, i.e., ~300 % in a 3D punching test. The comparatively reduced stretchability in the 3D punch test may be attributed to the complex deformation

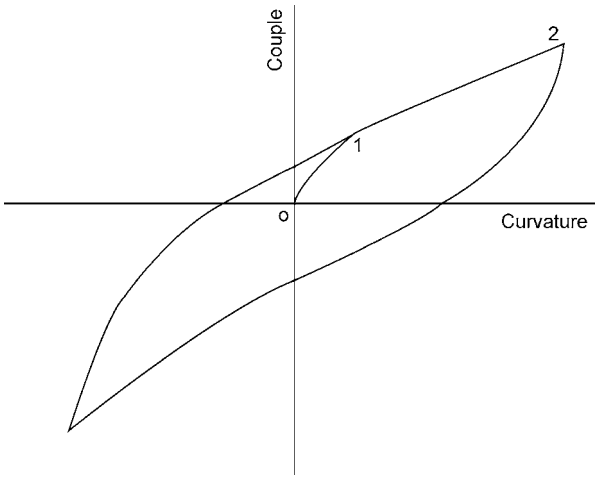

Fig. 16 Typical *bending curve–Font* of a fabric

modes, including fiber bending, lateral compression, torsion, and axial tension as well as compression and friction between the knitted fabric and the stainless steel ball [16].

Bending Behavior

Compared to the stretching behavior, fabrics are more susceptible to bending deformation, which could be determined by the weave or knitting structure, the yarn-bending behavior, and the finishing treatments applied on the fabrics.

Figure 16 illustrates a typical bending curve of a woven or knitted fabric. The couple–curvature curve shows that two stages exist in a hysteresis loop: (1) an initial nonlinear region, 0–1, in which the effective stiffness of the fabric decreases with the increment of curvature since more and more fibers start to move at the contact points, and (2) a near-linear region, 1–2, where the stiffness tends to be constant as all the contact points are in motion [4].

Shear Behavior

Shear deformation of the woven or knitted fabrics is very common during the wearing process since the fabrics are stretched or sheared to an extent as the body moves. Thus, the capability of shear deformation of the fabrics is a prerequisite to the fabrics on a 3D surface with motion, for instance, the human bodies.

A representative shear stress–strain curve of a fabric is shown in Fig. 17. It has three distinct zones: 0–1, the slope is large due to the frictional resistance of the yarns; 1–2, the slope gradually flattened with the swiveling of the yarns; and 2–3, the slope sharply increases at the jamming conditions [4].

Compression Behavior

Fabrics are compressible since they are composed of multifilament yarns and have numerous porosities in the fabrics themselves. The investigation into the compression behavior of the fabrics is very important for printed electronics, because the

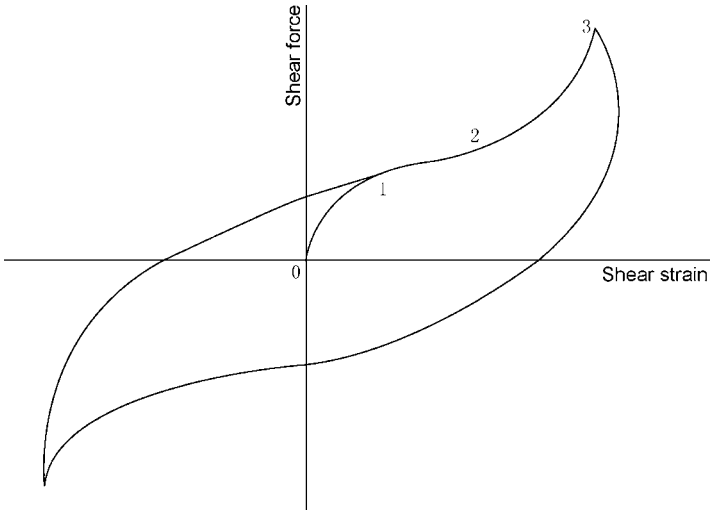

Fig. 17 Shear behavior of a fabric

applied pressure on the fabric from conductive materials may influence the thickness and surface geometries of the fabric substrates.

The thickness of a fabric is mostly affected by applied pressure. Considerable work has been reported on the thickness–pressure relationship of the fiber assemblies, either by an exponential or a hyperbolic function. Compared with woven fabrics, knitted fabrics are more easily compressed owing to their 3D looped configurations. This section describes the surface geometry of a plain-knitted fabric after the deposition of conductive materials on the knitted substrate based on Pierce's geometrical model and van Wyk's work on the compression properties of the fiber mass [3, 9, 17]. As shown in Fig. 12, the conductive material had a tendency toward the trough of the sine waves due to a produced shearing force when they slumped into the knitted fabric, inducing nonuniform compression. With the knowledge of dense conductive materials accumulating at the bottom, it was reasonable to suppose that the pressure distribution had an inverse relation in magnitude to the height profiles with the largest at the trough and the smallest at the crest. Thus, the pressure distributions in the course and wale directions were expressed by

$$\left.\begin{aligned} p(x) &\propto \frac{1}{z(x)} \\ p(y) &\propto \frac{1}{z(\mathrm{y})} \end{aligned}\right\} \tag{15}$$

Based on van Wyk's work on the compression properties of fiber mass, the loop yarns were limited to bending in the compression process; its volume (v)–pressure (P) relation was expressed by

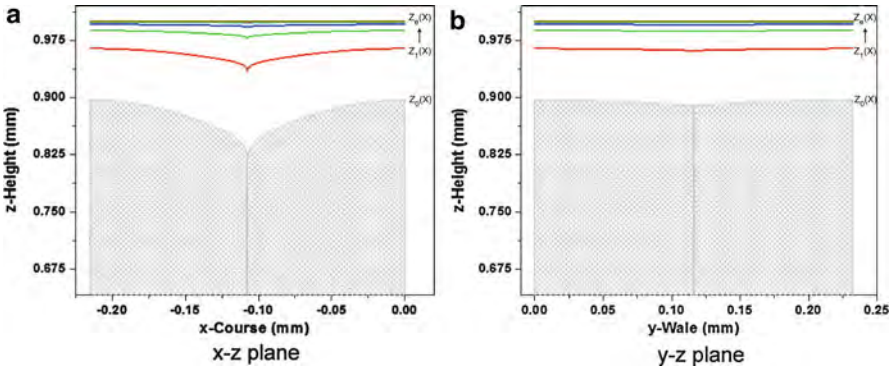

Fig. 18 Height profiles of the knitted fabric with applied pressure from conductive materials [3] (Reproduced with permission)

$$v \propto (P)^{-1/3} \tag{16}$$

Referring to such volume–pressure relation, the height–pressure relation of the knitted fabric printed by conductive materials was derived by

$$\left.\begin{aligned} z(x) \cdot 1 \cdot 1 &\propto (P)^{-1/3} \\ z(y) \cdot 1 \cdot 1 &\propto (P)^{-1/3} \end{aligned}\right\} \tag{17}$$

Thus, the height profiles of the plain-knitted fabric with applied pressure was derived, i.e.,

$$\left.\begin{aligned} z_m(x) &= \mathrm{k} z_{m-1}(x)^{1/3} \\ z_m(y) &= \mathrm{k} z_{m-1}(y)^{1/3} \end{aligned}\right\} \tag{18}$$

where m represented the number of the printing times; k was assumed to be constant. As observed from Fig. 18, the conductive materials could flatten the sine wavelike knitted fabric if with sufficient printing times [3].

Dimensional Stability

Fabrics are dimensionally stable if they resist permanent deformation during use, washing, and dry-cleaning. Compared to woven fabrics, knitted fabrics are poor in dimensional stability since they are prone to stretching, shrinking, and distortion. Appropriate finishing treatments such as shrinkage control, heat setting of synthetics, and resin finishes can improve the dimensional stability of the knitted fabrics. The fabrication process of wearable electronics demands the dimensional stability of the fabric substrates.

Breathability

One distinction of the fabrics from elastomeric or plastic substrate is they are porous, which is a vital concern for the comfort of the product next to the stratum corneum, the most superficial layer of the human skin [3].

Fabric Interconnectors

The human bodies are soft, stretchy, and curved. To enable electrical interconnectors intimately wearable on curvilinear human bodies with various gestures and motions, it requires the interconnectors on textile substrates to be breathable, foldable, elastic, reliable, and durable. A series of fabric interconnectors have been proposed and demonstrated through different conventional textile manufacturing technologies, ranging from printing to embroidering, weaving, and knitting technology. This section lists the current fabric interconnectors from the aspects of materials, structures, performance, as well as manufacturing processes.

Fabric Interconnectors by Printing Technology

Patterning conductive materials on fabric substrates to form electrical circuits and to achieve conductivity gradients has been reported. Processes that have been employed to form a patterned conductive path on fabric surfaces include deposition of polymeric or non-polymeric conducting materials and subsequent etching, reducing, or physical removal of the conductive materials from certain regions. Thus, the conductive material that is not removed forms a patterned electrical circuit or a region of higher conductivity. Other processes include in situ formation of conductive polymeric films on fabric substrates and subsequent patterning of the films using printing or depositing technologies. This section addresses screen printing technology, which could provide a large freedom in design of the fabric interconnectors since the printed layers can have any orientation on the fabric without necessarily following the yarn construction of the fabric substrates.

A broad range of conductive materials in a paste form have been screen printed on different fabrics through a pre-patterned mesh, creating a variety of wearable electronics, including sensorized gloves, antenna, electrodes, circuits, as well as supercapacitors. A typical process flow of the printed fabric interconnector is illustrated in Fig. 19. A fabric substrate is firstly prepared; conductive materials are then printed on the fabric substrate under the pressure applied by the squeegee; the fabric interconnectors are finally created after a curing process under a determined temperature.

Conductive materials used in printed interconnectors range in their electrical conductivities from insulating to highly conductive, i.e., 10^{-10}–10^{5} S cm^{-1}, where the later is preferable, thereby resulting in superior electrical current transmission between building blocks of the wearable electronic system. The most popular

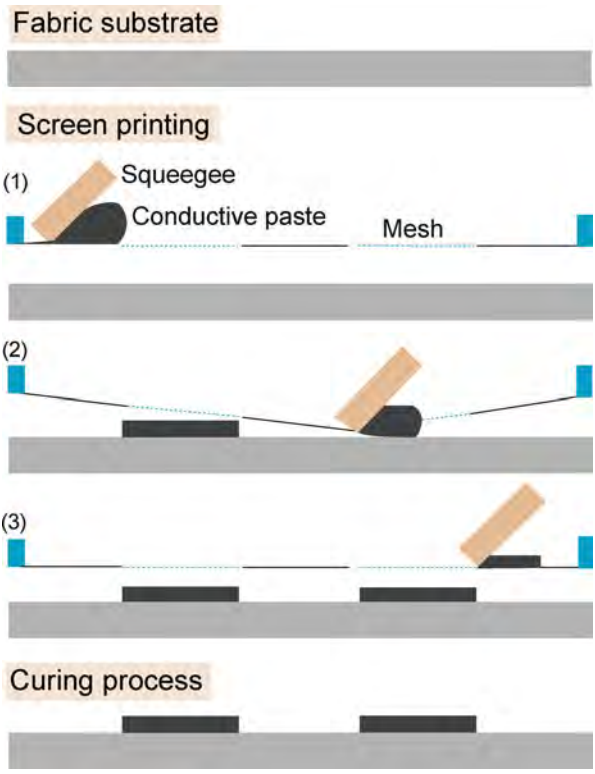

Fig. 19 Process flow of a typical screen printing technology

conductive materials are conductive inks, like carbon nanotube or AgNW, and metallic films, such as silver or copper nanoparticles, due to their high conductivity and comparatively lower curing temperature since fabrics could not withstand a high temperature (<150–200 °C). For instance, the silver ink that can be cured at 150 °C for 10 min is more compatible with fabric applications than other commercial inks which typically require higher temperatures (>200 °C) that often damage the fabric substrate. Additionally, a suitable paste size, viscosity, and surface tension should be controlled well for easy transfer of conductive paste from the screen meshes to the textile substrate.

Fabrics that were used for printing electronics included woven, knitted, and nonwoven fabrics composed of synthetic (like polyester, nylon, and spandex fibers) or natural fibers, such as cotton and wool. Several critical issues, however, exist when fabrics were used as substrates of the printed interconnectors. Firstly, a majority of textile materials cannot withstand curing temperatures above 150 °C. Hence, a sufficiently low curing temperature of the conductive materials is required. A preferable solution is to prolong the curing time at a comparatively low temperature. For instance, the standard 65/35 polyester cotton fabric can be thermally cured at 150 °C for 45 min, 175 °C for 15 min, 200 °C for 10 min, and 225 °C for 3 min without a noticeable degradation. Thus, a 150 °C curing

temperature with 45 min provides a suitable compromise between sufficient conductivity and compatibility with fabrics. Secondly, the fabric substrates have a notable surface roughness in the order of at least 10 μm, making it difficult to achieve a continuous and smooth track of the conductive materials on the fabric surfaces, hence often resulting in a large variation in both DC resistance and impedance characterization of the flexible interconnectors. To achieve a uniform coating, (1) multi-ply deposition of conductive materials on fabric substrates was proposed and proved to be effective [18]; (2) a UV curable polyurethane acrylate-based interface paste (Smart Fabric Inks Ltd., Fabink-UV-IF1) was used to reduce the surface roughness of the fabric, providing a flat and smooth surface for subsequent layer printing [19]. The surface of the screen printed interface layer (thickness, 200 μm) is relatively smooth with a surface roughness of less than 5 μm [20]; (3) the mesh count of the screen may be further reduced, but the results are still unknown. The third problem associated with printed interconnectors is the resilience of the conductive materials to different deformation modes of the textile substrates, like stretching, bending, shearing, and compression, since conductive inks or pastes with metallic particles are stiffer and more prone to cracking with applied deformation. The reason has been proved to be the weak adhesion between the conductive material and textile substrate. The conductivity of a coated fabric has decreased by approximately 26 % after an abrasion of 2,000 cycles. The other vital issue is low resolution of the printed interconnectors. Typically, the resolution of screen printing technology is 200 μm on fabric substrates.

Fabric Interconnectors by Embroidering Technology

Embroidery or sewing technology was one of the earliest to pattern electrical wires into textile substrates. The electrical wires, made by coating metallic particles, like silver, to textile yarns, such as nylon or polyester, are mechanically flexible and durable in the embroidery or sewing process. The embroidered/stitched electrical interconnectors, however, are less conductive and often failed mechanically and electrically within 20–30 % strain.

Woven Interconnectors by Weaving Technology

Weaving is the process of making woven fabrics by crossing two sets of threads over and under each other. Techniques derived from weaving could furnish new approaches to textile-based interconnectors [21].

A variety of woven interconnectors have been demonstrated, ranging from "wearable motherboard" to "wealthy system" and "PETEX." The wearable motherboard from Georgia Tech is the first integrated wearable system produced by weaving approach [22]. Rigid PCBs of size 5×5 cm^2 are attached to a woven shirt and are interconnected over an embedded bus structure of electrical and

optical fibers. Later, Virginia Tech [23], Infineon Technologies [24], and TITV Greiz [25] employed weaving technology to produce conductive fabrics. Dhawan et al. studied the bending rigidity of woven fabric-based electrical circuits [26]. In 2007, Locher et al. (Wearable Computing Laboratory, ETH Zurich) developed a hybrid fabric, i.e., PETEX, consisting of polyester yarns and coated copper wires with a diameter of ~53 μm. Since copper is stiffer and less ductile than the polyester yarn, it is a critical part for breaking. Copper with small diameter is better for durability of the PETEX. But the smaller the diameter is, the bigger the resistance becomes. They calculated the maximum diameter of the copper wire was 59 μm. Hence, the copper wire was determined as 40 μm in diameter, and it was coated by a polyurethane varnish with the thickness of 7 μm as electrical insulation [27]. The expected wire pitch between each coated copper wire was 0.5 mm in both warp and weft directions. However, the target of the wire pitch was 0.57 mm (the standard variation was 6.4 μm) in warp direction and 0.58 mm (the standard variation was 8.0 μm) in weft direction [28]. There are three reasons contributed to the variation of the wire pitch. Firstly, the ability to control the absolute position of wires in manufacturing is poor. The different tension control systems exist in warp and weft directions in manufacturing process; the conductive yarn is twisted, which is easy to move in manufacturing. Secondly, the actual wire pitch varied due to crimp structure of the woven fabric. Finally, as a textile material has viscoelastic behavior, inner tensions relieve over time and geometry may change [29].

Except from the above, it is noted that the conductive yarn is made by twisting metal wire to the polyester. The aim of this design is to endure mechanical stress. The twisted structure was also employed by the fabric electrodes of "wealthy system" consisting of two stainless steel wires twisted around a viscose textile yarn. But the copper wires still broke before the polyester yarn broke especially in the warp direction. The maximum mechanical elongation of the woven interconnectors is limited within 20–30 % strain due to their intrinsic geometrical configurations. And it is unknown that the copper wires broke at random locations within the fabric. Therefore, the electrical property of the PETEX fabric may not be satisfied under dynamic conditions. The copper wire can be expected to break with time and usage. Thus, the mechanical durability of the woven fabric circuit needs further improvement for daily activities of the wearers.

Knitted Interconnectors by Knitting Technology

As described, knitted fabric is formed by interlacing yarn in a series of connected loops. Hence, the knitted fabric, especially weft knitting, in comparison to woven and nonwoven textiles, is much more elastic (usually beyond 100 % strain) owing to its 3D looped configuration. Therefore, the efforts to develop knitted interconnectors may open doors to new applications in areas where woven and nonwoven electronic devices are not effective, such as intimately wearable electronics or next-to-skin health monitoring system.

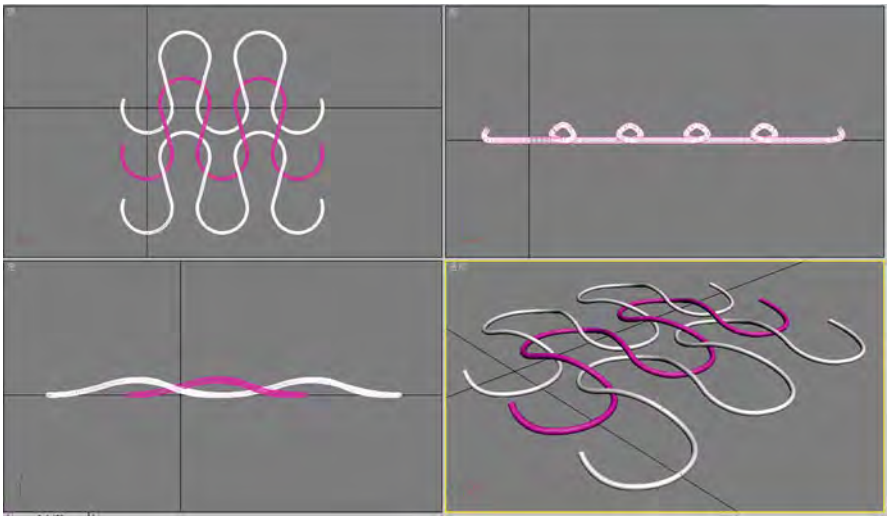

Fig. 20 Schematic diagram of a plain-knitted interconnector [3] (Reproduced with permission)

Figure 20 shows a schematic drawing of the knitted interconnector, created by integrating a conductive wire into a plain-knitted substrate, in which the conductive wire is interlaced with those nonconductive yarns in the form of three-dimensional looped configurations [3].

The conductive wire in the knitted interconnector is a fine metal fiber, with a core diameter of 20 μm, coated by polyurethane film with a thickness of 3 μm. It was chosen as conductive tracks due to their superior conductivity (the resistivity of copper fiber with 20 μm core diameter is ~0.55 Ω cm^{-1}) and current carrying capacity of 15 mA, satisfying to the standard IPC-9252A: the requirements for electrical testing of unpopulated printed boards. In addition, the metal fiber with a core diameter of 20 μm yields an elongation up to 7–8 % owing to the even coating of the polyurethane films; more importantly, the magnitude of the diameter is in the order of μm, endowing intrinsically brittle metal fiber flexible (rigidity, ~3.34×10^{-11}) to be bent into 3D looped configuration [3].

The elastic substrate is a plain-knitted fabric composed of polyester and spandex filaments. The dielectric constant of the polyester is 3.2, and it has been widely used in flexible circuit technology for a long period. Spandex is added for the enhancement of the elasticity of the substrate. Such knitted substrate is capable of undergoing large deformation before fracture (>300 % strain). Also, it is flexible and conformable to movable three-dimensional surfaces such as the curvilinear shapes of the human body. Besides, it is low cost with simple manufacturing technology [3].

The knitted electrical interconnectors were created by incorporating polyurethane-coated copper fibers, together with pre-stretched (~150 %), elastic filament yarns into a single-jersey knitted fabric in 3D hooked (or looped) configurations on a computerized knitting machine. Unlike woven circuit route with limitation into weft and warp directions, it was more feasible to "knit" stretchable

interconnectors with a more complex arbitrary route by intarsia or jacquard patterns, such as an array, matrix, network, and even any configuration [3].

The fabricated knitted interconnector consists of polyurethane-coated metal fibers (core diameter, ~50 μm; coating thickness, ~3 μm) with a series of connected 3D loops in which the circular portions at the two ends are out of planar (height of the loop, ~180 μm; period of the loop, ~800 μm), and the straight segments, penetrating into the knitted fabric, are interlaced with the elastic textile yarns. In the knitted interconnector, the metal fibers are completely covered by textile multifilaments from the front-side view owing to the pre-stretched spandex filaments, which then shrink to their original states when free of external force after the manufacturing process. Such porous fibrous structures can be worn directly on human bodies, without irritating the skin for a long-term use. Additionally, compression and friction during wear can be mitigated if the knitted interconnector with its front side toward the human body [3].

The electrical resistance of the coated metal fiber with 20 μm core diameter is observed within 24 h before and after integration into tight knitted fabrics (composed of spandex filaments). The resistance is in the range from 5.15 to 5.20 Ω, with a variation of 0.96 %, for the free-standing metal fibers with the length of 10 cm. The electrical resistance is in the range from 33.6 to 33.9 Ω, with a variation of 0.88 %, for the knitted interconnector with the length of 10 cm. The relationship of the electrical resistance before and after integration can also be expressed by

$$R_{\text{after}} = \frac{1}{N}\left(R_{\text{length}} + \Delta R_{\text{bending}}\right) \tag{19}$$

where R_{after} is the electrical resistance of the knitted interconnector, R_{length} is the electrical resistance of the metal fiber, and $\Delta R_{\text{bending}}$ is the resistance change due to the bending behavior of the metal fibers with 3D looped configuration in the knitted fabric [3].

To be deformable into curvilinear shapes and accommodate to the movement of the subject, knitted interconnectors have to be three-dimensional stretchable. Besides in-plane stretching test, a 3D tensile test, referred as the 3D punching test for textile fabrics, was proposed, too. In the experimental setup, a specimen of the knitted interconnector with 100 × 100 mm^2 was securely fastened in the ring clamp without tension. Before the test was conducted, the ball was made in contact with the knitted interconnector without tension. The metal conductor was connected to a digital multimeter (Keithley) interfaced with a personal computer. The electrical resistance was measured when the specimen was stretched by an Instron Universal Material Tester with the ball-burst attachment [2, 3, and 16].

Because of structural conversion in single-jersey knitted fabrics, the knitted interconnector could be stretched up to 300 % strain with a constant electrical resistance in either transverse (course) or longitudinal (wale) direction and 150 % strain without any considerable change in its electrical resistance in a 3D punching test. When the knitted interconnectors were stretched, the metal fiber loops slide and adjust their geometrical parameters, i.e., period and amplitude, by means of straightening in

the transverse case whereas bending to smaller radius of curvature in the longitudinal direction, hence accommodating the applied deformation. Unlike unidirectional tensile tests, the ball-punch test shows complex adjustments in the period and amplitude, hinting that much larger fiber strain might be induced [2, 3, and 16].

Wearable applications demand flexible and stretchable electronics to be mechanically and electrically robust with a sufficient fatigue life. Hence, the durability of the knitted interconnector was investigated in its unidirectional tensile test and 3D punching test. A cyclic tensile test for 1,000,000 cycles (equivalent to 3-month normal wear) at a set strain of 20 % was firstly conducted. The electrical resistance of the knitted interconnector remains unchanged $((R_{\max} - R_{\min})/R_{\min} \approx 0.65\%)$ over 1,000,000 cycles of 20 % applied strain in the transverse case, demonstrating the knitted interconnector could pass the test without electrical failure. A cyclic 3D punching test was then conducted at an equivalent strain of 78 %. The electrical resistance of the knitted interconnector maintains the same without any considerable variation within 8,000 cycles of 78 % applied strain in the 3D punching test. To estimate fatigue life of the knitted interconnectors, the Coffin–Manson law was used. The mean lifetime of the knitted interconnector is a function of fiber strain and can be estimated by

$$N = A{\varepsilon_{\text{fiber}}}^{B} \tag{20}$$

where $A = 1.025\text{e}(-20)$, $B = -11.92$, and $\varepsilon_{\text{fiber}}$ is the simulated peak strain of the metal fiber with practical elongation of the knitted interconnector. According to the equation, the knitted interconnector could withstand more than 10^7 cycles at 20 % peak strain, consistent with the average extension of the human skin [2, 3, and 16].

In summary, the knitted interconnector is porous, highly conductive, stretchable, as well as durable for three-dimensional surfaces. Hence, the electronics integrated into knitted fabrics is ideal for next-to-skin wearable applications, since it possesses high extensibility under low loading conditions (elongation, >300 % strain; Young's modulus, <1 MPa), which allows it to fit snugly (compared with the woven/printed/stitched electronics), and it is permeable, without the risk of irritating the human skin (in contrast to the rubber-/plastic-based electronics) [3].

Connection Technologies

Textile interconnectors or wirings are the base of the fabric electronics, which demands the interconnectors mechanically and electrically link building blocks through reliable connection on the fabric substrate. Hence, the connection between the interconnectors and electronic components or outer circuits is indispensible.

For insulated textile interconnectors, the process of the connection to electronic components or outer circuits involves three steps as follows: (1) coating removal, (2) electrical connection, and (3) encapsulation for chemical and mechanical protection. For woven interconnectors, "cut" or "disconnection" is needed to avoid short circuits, because of the nonarbitrary structure [28].

Laser was used in the *coating removal* step [24]. Laser treatment, however, may make serious damage to the neighboring area of the connection. For instance, nonconductive yarns in the woven-based interconnectors would be damaged by the laser, weakening their mechanical durability. Thus, *encapsulation* in the last step is extremely important to ensure the reliability of the connection [30]. However, some material used in the encapsulation may contribute to other problems, such as moisture absorption caused by epoxy encapsulation.

Connection is indispensible in the process flow. Many approaches have been proposed to achieve a reliable connection, including soldering, bonding (conductive adhesive), stapling, embroidering, and so on. For instance, a conductive yarn could be embroidered to a metalized contact area on a textile substrate. The pros and cons of each approach have been discussed a lot, but few of the exact examinations support their opinions. Until 2007, Locher measured the electrical property of the "textile via" (one connection in woven circuit) from DC resistance, line impedance, and scattering parameters and examined the mechanical stress of the connection [28].

Due to the perpendicular structure of woven interconnectors, mismatch pitch is a tough issue. To solve it, an adapted element, i.e., "interposer technology," was employed to redistribute the pads of the electronic component to the interconnectors on the fabric substrate. But the manufacture and calculation is complex; more critically, the interposer weakened the mechanical stress of the fabric interconnector since mechanical breakage easily occurred at the edges of the interposer.

Summary

To enable electronics intimately wearable on curvilinear human bodies with various gestures and motions, it requires electronic devices to be breathable, foldable, and elastic, as well as reliable and durable. To date, technologies based on in-plane or out-of-plane buckled thin films on compliant silicones or plastics, net-shaped integrated circuits, as well as organic stretchable conductors have all contributed to the development of flexible and stretchable electronics. Yet it is uncomfortable when elastic rubbers make an intimate contact with human skins for a long time. Also, the reliability and long-term durability of the stretchable electronics need to be investigated. Without relying on elastic rubbers, this chapter describes fabric-based interconnectors for three-dimensional surfaces. It firstly describes different fabric substrates, including woven, knitted, and nonwoven in terms of their structure, materials, and geometrical and mechanical properties, and then introduces the development of fabric interconnectors for three-dimensional surfaces with respect to different technologies, such as printing, embroidering, weaving, as well as knitting technologies. The primary characteristics of fabric interconnectors created by different technologies are discussed.

Fabrics are thin, lightweight, soft, flexible, twistable, foldable, and even stretchable, as well as porous (or breathable) so that they are ideal substrates for wearable

electronics on soft, two-dimensional curvilinear and extensible human bodies. Three main textile structures, i.e., woven, knitted, and nonwoven, were introduced from aspects of their most elementary patterns, geometrical and surface configurations, as well as their mechanical characteristics. The mechanical properties and surface geometries of the fabric substrates are the most important for flexible interconnectors for three-dimensional surfaces.

A series of fabric interconnectors have been proposed and demonstrated through different conventional textile manufacturing technologies, ranging from printing to embroidering, weaving, and knitting technology. Such fabric interconnectors were listed in terms of their materials, structures, performance, as well as manufacturing processes. Unlike woven/printed/embroidered interconnectors, the knitted interconnector is porous, highly conductive, stretchable, as well as durable for three-dimensional surfaces. Hence, the electronics integrated into knitted fabrics is ideal for next-to-skin wearable applications, since it possesses high extensibility under low loading conditions (elongation, >300 % strain; Young's modulus, <1 MPa), which allows it to fit snugly (compared with the woven/printed/stitched electronics), and it is permeable, without the risk of irritating the human skin (in contrast to the rubber-/plastic-based electronics).

To physically link the fabric interconnectors to other electronic components or outer circuits, different connection methods were summarized, in which one popular approach is divided into three steps: (1) coating removal, (2) electrical connection, and (3) encapsulation for chemical and mechanical protection.

References

1. Zeng W et al (2014) Fiber-based wearable electronics: a review of materials, fabrication, devices, and applications. Adv Mater 26:5310–5336
2. Li Q, Tao X-M (2014) Three-dimensionally deformable, highly stretchable, permeable, durable and washable fabric circuit boards. Proceedings of the Royal Society A: Mathematical, Physical and Engineering Sciences, 470(2171):2014472
3. Li Q (2014) Packaging of fabric sensing network with flexible and stretchable electronic components. PhD thesis, The Hong Kong Polytechnic Univerity
4. Behera BK, Hari BK (2010) Woven textile structure: theory and applications, Woodhead publishing series in textiles. Woodhead Publishing in association with The Textile Institute, Cambridge, xx, 450 p
5. Hui Z et al (2006) Pressure sensing fabric. In: Smart nanotextiles, San Francisco, California, U.S.A., vol 920. pp 113–119
6. Ray SC (2012) Fundamentals and advances in knitting technology, Woodhead Publishing India in textiles. Woodhead Publishing India Pvt., New Delhi
7. Nonwoven fabrics – raw materials, manufacture, applications, characteristics (2002) Wiley, Chichester, p 1, online resource
8. Peirce F (1937) The geometry of cloth structure. J Text Inst Trans 28(3):T45–T96
9. Peirce F (1947) Geometrical principles applicable to the design of functional fabrics. Text Res J 3:123–147
10. Leaf G (1955) The geometry of a plain knitted loop. J Text Inst 45:T587–T605
11. Leaf G (1960) Models of plain knitted loop. J Text Inst 51:T49–T58
12. Leaf G (1961) The stresses in a plain-knitted loop. J Text Inst Trans 52(8):T351–T365

13. Munden DL (1959) The geometry and dimensional properties of plain-knit fabrics. J Text Inst 50:T448–T471
14. Kawabata S (1980) Examination of effect of basic mechanical properties of fabric hand. In: Hearle JWS, Thwaites JJ, Amirbayat J (eds) Mechanics of flexible fibre assemblies. Sijthoff and Noordhoff, New York
15. Hu J (2004) Structure and mechanics of woven fabrics, Woodhead publishing in textiles. CRC Press/Woodhead Publishing, Boca Raton/Cambridge
16. Li Q, Tao XM (2011) A stretchable knitted interconnect for three-dimensional curvilinear surfaces. Text Res J 81(11):1171–1182
17. van Wyk C (1946) Note on the compressibility of wool. J Text Inst 37:T285–T292
18. Yi W (2012) Fabric strain sensor integrated with CNPECs for repeated large deformation. PhD thesis. The Hong Kong Polytechnic University, Hong Kong
19. Wei Y et al (2012) A novel fabrication process for capacitive cantilever structures for smart fabric applications. In: 2012 Symposium on Design, Test, Integration and Packaging of Mems/Moems (Dtip), Cannes, pp 136–139
20. Paul G et al (2014) An investigation into the durability of screen-printed conductive tracks on textiles. Meas Sci Technol 25(2):025006
21. Bonderover E, Wagner S (2004) A woven inverter circuit for e-textile applications. IEEE Electron Device Lett 25(5):295–297
22. Park S, Mackenzie K, Jayaraman S (2002) The wearable motherboard: a framework for personalized mobile information processing (PMIP). In: Proceedings of the 39th Design Automation Conference, 2002, New Orleans, LA, USA, pp 170–174
23. Jones M, Martin T, Nakad Z (2002) A service backplane for e-textile applications. In: Workshop on modeling, analysis, and middle-ware support for electronic textiles (MAMSET), 2002, San Jose, CA
24. Jung S et al (2003) Enabling technologies for disappearing electronics in smart textiles. In: 2003 I.E. International Solid-State Circuits Conference: Digest of Technical Papers, University of Pennsylvania, vol 46. pp 386–387
25. Gimpel S et al (2004) Textile-based electronic substrate technology. J Ind Text 33(3):179–189
26. Dhawan A (2007) Development of robust fiber optic sensors suitable for incorporation into textiles, and a mechanical analysis of electronic textile circuits. PhD thesis, North Carolina State University, Raleigh
27. Locher I, Troster G (2007) Fundamental building blocks for circuits on textiles. IEEE Trans Adv Packag 30(3):541–550
28. Locher I, Troster G (2008) Enabling technologies for electrical circuits on a woven monofilament hybrid fabric. Text Res J 78(7):583–594
29. Cottet D et al (2003) Electrical characterization of textile transmission lines. IEEE Trans Adv Packag 26(2):182–190
30. Linz T et al (2005) Embroidering electrical interconnects with conductive yarn for the integration of flexible electronic modules into fabric. In: Proceedings of the ninth IEEE international symposium on wearable computers, 2005. Osaka, Japan, pp 86–89

Photonic Fabric Devices for Phototherapy 22

Shen Jing

Contents

Introduction 578
Phototherapy 579
The Related Optical Parameters for Phototherapy 581
Wavelength 581
Fluence and Irradiance 581
Timing of Treatments Outcomes 581
Photonic Fabric Device 582
The Fabrication 582
Safety Evaluation of Photonic Fabric Device for Phototherapy 584
Photonic Fabric Device Prototype for Phototherapy 586
Fabrication 586
Properties Measurement 588
Safety Evaluation 590
Current and Promising Application of Photonic Fabric Device 590
Neonatal Jaundice 590
Photorejuvenation 591
Wound Healing 592
Sunburn Prevention 592
Seasonal Affective Disorder (SAD) 593
Summary 593
References 594

Abstract

Phototherapy is the use of light for the treatment and prevention of disease. Especially, low-level red and near-infrared light (600–950 nm) irradiation provides low-energy stimulation to tissues, which results in increased proliferation rate of

S. Jing (✉)
National Engineering Research Center for Ophthalmic Equipments, Beijing Institute of Ophthalmology, Beijing Province, China
e-mail: vivostar@126.com

© Springer Science+Business Media Singapore 2015

X. Tao (ed.), *Handbook of Smart Textiles*,
DOI 10.1007/978-981-4451-45-1_25

cells, as well as enhancement of growth factor synthesis and collagen production. Until now, only low-level laser and light-emitting diode (LED) are used for irradiation in low-level light therapy. Compared with the commercial laser or LED equipment, the photonic fabric device can provide a larger irradiation area with good flexibility, low weight, and low cost. In addition, it has no heating production, thus very promising for wearable phototherapy applications.

Based on a comprehensive review of phototherapy, this chapter introduces the photonic fabric device and includes the integration of POF into the textile structure, the manufacture of side-emitting POF, and then the connection with the light source. Besides, the safety of photonic fabric device is the most important thing because it is used for humans directly. In this chapter, the related safety evaluation standard is investigated, involving photobiological evaluation of light radiation and biological evaluation. It further provides a photonic fabric device prototype for photorejuvenation as an example and elaborates its fabrication and evaluation. This photonic fabric device prototype exhibits high performance and can be applied in phototherapy.

Keywords
Smart textiles • Photonic fabric device • Phototherapy • Polymer optical fiber • POF • Side-emitting optical fiber

Introduction

Smart textiles are defined as the textile materials that sense and respond to environmental conditions or external stimuli [1]. Optical fibers can carry light signal along their length and are immune to the electromagnetic interference. Specifically, POF can be woven or knitted into the fabric using conventional textile machines. Connected to an external light source, POFs incorporated in textile allow light transmission not only to selected locations but also on the whole textile surface. Today, applications of optical fibers in different textile technologies attract many attentions in various applications, for example, displays, communication devices, and sensing devices [1–4]. Several research on flexible displays and screens have been replaced over the past decades [5]. Different approaches have been developed involving new textile materials or using the optical fibers in the textile structures. Perpendicular-oriented fibers of warp and weft could present images and information on flexible wearable substrates to exhibit information or designs in cars, portable electronic devices, and buildings. Our group also developed a photonic fabric for display application, which can be used for exhibiting various patterns [6]. The screen matrix was created during weaving, using the texture of the fabric. A small electronics panel is integrated into the system to control the LEDs connected with groups of fiber. Each group is responsible to the lighting of one given area of the matrix. However, up to now, only some photonic fabric products have been explored for remedial purposes. Photonic fabric holds a huge market potential in therapy field.

Phototherapy is the use of light for the treatment and prevention of disease, which has a very long history. Sunlight benefits in treating skin diseases have been exploited for more than thousands of years in ancient Egypt, India, and China. Advances in laser technology have progressed so rapidly during the past decades that successful treatments have been developed and used for many cutaneous concerns and congenital defects, including vascular and pigmented lesions, tattoos, scars, and unwanted hair [7]. Along with the continuous emergence of artificial light sources, more and more devices are produced for clinical treatment. Meanwhile, light with a low-level intensity has been identified more effective in some clinical treatment of disorder, as wound healing, neonatal jaundice, photorejuvenation, anti-inflammation, and so on [8, 9].

Low-level red and near-infrared light irradiation (the wavelength range is about 600 ~ 950 nm, the power density is less than 50 mW/cm^2). The biological effects are directly caused by photomodulation for the tissue, not by heating in which the range of temperature increased is from 0.1 °C to 5 °C. Many previous studies have shown that low-level light irradiation provides low-energy stimulation to tissues, which results in increased cellular activity during wound healing, increased proliferation rate of fibroblasts and keratinocytes, as well as enhancement of growth factor synthesis, collagen production, and angiogenesis [10].

This chapter reviews the development of phototherapy and the effect of the related optical parameters. And the knowledge of photonic fabric device is also present, including the integration of POF into the textile structure, the manufacture of side-emitting POF, and then the connection with the light source. In addition, one photonic fabric device prototype for photorejuvenation is introduced, including the fabrication and safety evaluation. At the last, a brief review on the potential application field of the photonic fabric device in phototherapy is provided.

Phototherapy

Phototherapy or light therapy consists of exposure to daylight or to light of specific wavelengths generating by dichroic lamps, fluorescent lamps, lasers, LEDs, or very bright, full-spectrum light, usually controlled with various devices [11]. The light is administered for a prescribed duration of time and, in some cases, at a specific time of a day.

Light has been used as a therapeutic agent since ancient times. Dating to 1500 BC, medical literature in ancient India described a treatment of nonpigmented areas of skin by applying black seeds of the plant Bavachee of Vasuchika followed by exposure of the skin to sunlight. Similar records existed in old literatures from ancient China and Egypt. Then more effects of sunlight were shown, and the heliotherapy was founded. Downs and Blunt found that sunlight could kill bacteria. In 1890, Palm discovered that the sun could play a therapeutic role in rachitis. However, until the end of nineteenth century, heliotherapy was the only form of phototherapy because the only useful source of light was sun at that time. The era of controlled phototherapy started with the use of an artificial irradiation source until

Niels Finsen discovered that lupus vulgaris could be cured by short-wavelength light in the early twentieth century.

In 1917, Einstein proposed the theory of light amplification caused by the stimulated emission of radiation. The first laser was created according to Einstein's theory in 1960, which used a ruby crystal to produce light with 694 nm wavelength. Various laser systems were developed successively, for example, the neodymium: yttrium-aluminum-garnet (Nd: YAG) laser in 1961, the argon laser in 1962, and the CO_2 laser in 1964. Goldman pioneered the study on the effect of laser in dermatology by revealing the application of a ruby laser in the treatment of tattoos [12]; the Nd: YAG laser in the treatment of port-wine stains, tattoos, and cutaneous malignancies [13]; and the argon laser in the treatment of vascular lesions [14]. However, although early lasers, such as CO_2 and argon laser, were effective for the desired target, they kept the surrounding healthy tissue exposing in laser for prolonged time because of continuous-wave light emission. This collateral damage resulted in high rates of adverse effects, hypertrophic scarring, and pigment alteration.

In 1983, Anderson and Parrish proposed the theory of selective photothermolysis, which revolutionized the field of laser dermatology [15]. It was possible to achieve specific destruction of a target in the skin with minimal unwanted thermal injury by applying this theory. Subsequently, more kinds of laser, dye laser (577/585 nm), Q-switched Nd: YAG (1,064 nm) laser, and copper vapor laser (578 nm), were developed and used in dermatology. There were good therapeutic effects on various pigment lesion, vascular lesion, and hair removal.

In the last decade, laser technology has been developed, which can deliver selective light to a specific target and minimize unwanted adverse effects. In 2004, light-emitting diode (LED) photomodulation was also approved by US Food and Drug Administration (FDA) to be used in dermatology. LED photomodulation belongs to the category of low-level light therapy, which usually uses low-energy light irradiation and does not create thermal damage to the skin. This is achieved when the incident photons are absorbed by chromophores, for example, in the respiratory chain of the mitochondria for longer wavelength visible light and in cellular membranes for near-infrared light. Initial research of LED irradiation was developed by the National Aeronautics and Space Administration (NASA) to grow plants in space, but was found its therapeutic effects. LED therapy was used to reduce posttreatment erythema through anti-inflammatory effects. The application of LED therapy in wound healing also obtained positive results.

Phototherapy does not only make great progress in dermatology but also constantly opens up its application fields. Since a nurse accidentally discovered the efficacy of sunlight on improving jaundice in 1956, phototherapy has been broadly applied to neonatal jaundice. Phototherapy also has great development in treating various cancers by aid of photosensitizer, which is called photodynamic therapy (PDT).

The Related Optical Parameters for Phototherapy

Biological effects depend on the parameters of the irradiation such as wavelength, irradiation time (treatment time), intensity (irradiance), dose (fluence), continuous wave or pulsed mode, and for the latter, pulsing patterns. In addition, clinically, such factors as the frequency, intervals between treatments, and total number of treatments are to be considered. There are many factors related with a successful phototherapy.

Wavelength

Wavelength is not only a quite important parameter for light but also is of great significance for the phototherapy. Various chromophores or cells in the body have their own unique light absorption characteristics, each absorbing light at specific wavelengths. The wavelength determines not only the absorption behavior but also the penetration depth of the light in skin. In general, the longer the wavelength is, the deeper the penetration into tissue [16, 17]. For the best effects, the wavelength used should allow for optimal penetration of light in the targeted cells or tissue.

Fluence and Irradiance

Irradiance is the incident power per unit area (W/cm^2), which is the exposure dose rate at the tissue surface. Exposure dose is the total laser energy delivered per unit area and is properly referred to as fluence (J/cm^2). The terms irradiance should be used to describe the laser beam properties and surface exposure. Fluence describes the laser exposure within a cross-sectional area of tissue.

Approximately, the fluence is equal to the irradiance $\times$ time. Therefore, the same fluence should result from increasing duration and reducing light power, and vice versa. Experiments have shown that varying irradiance and exposure time to achieve a constant specified energy density affects LED therapy outcomes [18]. In practice, if light intensity is lower than the physiological threshold value for a given target, it does not produce photostimulatory effects even when irradiation time is extended. Moreover, photoinhibitory effects may occur at higher fluences.

Timing of Treatments Outcomes

There are some indications that cellular responses after light irradiation are time dependent. A recent study suggests that responses such as adenosine triphosphate (ATP) viability can be observed directly (1 h) after the irradiation, whereas other responses such as cell proliferation require at least 24 h before the true effect can be observed [19]. It is thus important to establish time-dependent responses to

adequately assess photomodulatory effects. Fibroblasts in culture show physiological cyclical patterns of procollagen type I upregulation and metalloproteinase-1 (MMP-1) downregulation that can be emphasized by LED treatments every 48 h [20].

Photonic Fabric Device

Photonic fabrics which integrate with polymer optical fiber (POF) in textiles have potentials to be used for phototherapy based on the mechanism of low-level light therapy. A large number of tightly intertwined POFs in POF fabrics enable efficient two-dimensional light emission in a large area, delivered by a laser or LEDs with an appropriate wavelength. Advantages of flexible POF fabrics are convenient and comfortable for the patient, easy to handle, light in weight, and not affected by electromagnetic interferences. However, in most medical applications, the POF fabrics are used to monitor human physiological parameters, like temperature, ECG, EEG, pulse, blood pressure, blood glucose, etc. Phototherapy devices made of POF fabrics are recent developments. Up to now, only a limited number of products of POF fabrics have been developed for phototherapy.

The Fabrication

Integration of POF into Textile Structures

POF Material

A POF is a flexible optical fiber made completely of polymer. POF normally consists of two parts: the core and the cladding. Most of the POFs integrated in textile structures comprise cores made of poly(methyl methacrylate) (PMMA), with fluoropolymers as cladding materials. Beside PMMA, other materials have been used as core material, such as polycarbonate (PC), polystyrole, and silicone. Most recently, there has been a trend toward new materials like polyethersulfone, polysulfone, and polyetherimide [21]. Heavier atoms like sulfur or bromine are included in the core material because they can improve refractive index of the polymer material [22].

Textile Processing

The POFs can be integrated into fabrics using different textile techniques, like weaving, knitting, and braiding.

Weaving

Woven fabrics involve interlacing two sets of yarns at right angles to each other. The lengthwise yarns are called warp yarns, while the widthwise yarns are known as weft yarns. The most important point for integrating POF into textile is that the size and mechanical properties of POF should be compatible with those of the warp

or weft yarns. POF can be integrated into any woven structure in the warp or weft directions. Various woven structures can be obtained by adjusting the weaving machines. In common woven structures, straight POFs are clamped between perpendicular lying textile yarns and parallel arranged in the fabrics. This woven structure allows exact fiber arrangement and position determination. This structure makes lower bending loss so that the light emission on the POF fabric surface should be achieved by a following POF surface treatment method mentioned above.

Knitting

Apart from woven structures, luminous knitted fabrics with integrated POFs have been developed. Knitting is a technique for producing a two-dimensional fabric made from a group of yarn. The yarn in knitted fabrics follows a meandering path, forming symmetric loops symmetrically above and below the mean path of the yarn. An advantage of knitted fabrics is the flexibility in creating three-dimensional shapes, compared to woven structure, which normally gives flat, inelastic fabrics. In a knitted fabric, the yarns and POFs are normally in the form of interloops that are exposed to severe bends at a very small radius of curvature. Hence the light emission happens because of macrobending.

Braiding

A braid is a complex structure or pattern formed by intertwining three or more strands of flexible material such as textile fibers, wires, or POFs. Compared with the process of weaving, a wide sheet of cloth from two separate, perpendicular groups of strands (warp and weft), a braid is usually long and narrow, with each component strand functionally equivalent in zigzagging forward through the overlapping mass of the others. However, compared with knitted structure, braiding does not induce serious macrobending during POF interlacing.

Surface Treatment of POF

In order to get photonic fabric, side-emitting POF should be manufactured first. Unlike the end-emitting POF, which transports light from one to another end of POF, side-emitting POF distributes the light from the light source along the length of the fiber. The fabrics being integrated with such POF have various applications in fabric display, two-dimensional lighting, and health monitoring sensors. The mechanism of side emitting is the change of waveguide structure of normal POF. Many methods can reach this goal.

Structural irregularity or imperfection at the core-cladding interface or in the core changes the propagation path of light and results in light leakage from side. To provoke light emission on the surface of POF, a surface mechanical or chemical treatment is added to make some imperfection on the POF [2]. Mechanical side notching allows simple figures of light dots. Surface mechanical abrasion, surface chemical etching, or sandblasting leads to a more even light distribution [23, 24]. Alternatively, writing Bragg gratings or adding scattering particles in the fiber core also can evoke light emission [25]. Another approach is to add fluorescent material into POF [26]. Photonic bandgap fibers with well-defined geometrical structure can

achieve controllable side emission [25, 27]. The mechanical or chemical methods to surface treat POF are easier and achieve better side emission than other methods. However, the physical damage weakens the POFs and renders them difficult to weave or knit. One solution is to apply the surface treatment of the POFs after integrating them into the fabric. In this case, it is important to design the fabric with a structure that exposes the POFs to the surface of the fabric in order to maximize the light-emitting efficiency.

Light Source and Its Connection with POF

Various light sources can be connected to optical fiber ends depending on the application of the POF fabrics. Bright LEDs or powerful light sources are usually used for illumination and decoration, while lasers with a suitable wavelength are used for medical treatment or sensing applications [28, 29]. When photonic fabrics are used for phototherapy, the type of the light source, as well as the wavelength and power used, should be considered.

The number of connected POFs can vary. Small groups of POFs were coupled to one LED; many, up to 100 POFs, were connected to a laser source; and 500 POFs were connected to a powerful lamp. For small batch sizes, connectors for defined bundles of POFs were made with polished surface at the POF endings. Efficient light transmission from the light source into the POFs is achieved when the area of delivering light overfills the numerical aperture of the fiber bundle. In order to improve the coupling efficiency, it is necessary to have a smooth end face of POF. Usually, by grinding/polishing or using a hot plate, a smooth end face of POF is obtained that can be cut with a razor blade.

Safety Evaluation of Photonic Fabric Device for Phototherapy

Photobiological Evaluation of Light Radiation

There is known radiation hazards for humans associated with some light sources, like single-wavelength laser system, fluorescent lamp, LED, incandescent lamp, and even sunlight. Light radiation can induce damage in biological tissue of the human body, mainly to the skin and to the eye, due to several mechanisms. Thermal effect of light radiation is one of damage mechanisms. When sufficient radiant energy has been absorbed by an organ in a relative short period of time, its component tissues experience a heating process. When the heating exceeds the critical point, thermal damage or burn occurs at radiation area where the denaturation of proteins is presented. Another mechanism is photochemical damage where the molecules in tissue absorb the given light energy and undergo a chemical reaction unique to their excited state [30]. By this mechanism, some tissues such as the skin, the lens of the eye, and in particular the retina show irreversible changes. Photochemical damage occurs mostly with short-wavelength (blue) and ultraviolet light and can be accumulated over the course of hours.

The pathological effects of the eye and skin caused by excessive exposure to light are summarized in Table 1. In the wavelength range from 400 to 1,400 nm, the

Table 1 The Pathological effects of excessive exposure to light on biological tissue

CIE spectral region	Skin	Eye
Ultraviolet C (180–280 nm)	Erythema (sunburn), accelerated skin ageing, increased pigmentation	Photo-keratitis (inflammation of the cornea, equivalent to sunburn)
Ultraviolet B (280–315 nm)		
Ultraviolet C (315–400 nm)	Pigment darkening, photosensitive reactions, skin burn	Photochemical cataract (clouding of the eye lens)
Visible (400–780 nm)		retinal injury caused by photochemical and thermal effects
Infrared A (780–1,400 nm)	Skin burn	Cataract, retinal burn
Infrared B (1.4–3.0 μm)		Aqueous flare (protein in the aqueous humour), cataract, corneal burn
Infrared C (3.0 μm to 1 mm)		Corneal burn

greatest hazard is retinal damage. The aqueous humor, cornea, vitreous humor, and lens are transparent for radiation in these wavelengths. The greatest hazard is damage to the lens or the cornea for the wavelengths of less than 400 nm or more than 1,400 nm. Depending on the wavelength, optical radiations can be absorbed preferentially or exclusively by the cornea (Table 1). UV light with wavelengths shorter than 400 nm can produce injuries at relatively low powers due to photochemical damage. IR light mainly causes thermal damage to the retina at near-infrared wavelengths and to more frontal parts of the eye at longer wavelengths.

The skin is usually much less sensitive to light radiation than the eye. However, excessive exposure to UV light from any source (laser or non-laser) can cause short- and long-term effects similar to sunburn. Visible and IR wavelengths are harmful mainly due to thermal damage. Extremely high irradiance may cause the pigmentation, ulceration, and scarring of the skin and damage to underlying organs.

International Electrotechnical Commision (IEC) specifies the corresponding exposure limits against different products in several standards to evaluate the photobiological safety of light source. In the IEC standard 62471: 2006 "Photobiological safety of lamps and lamp systems," the hazard exposure limits of eight conditions are proposed, for example, actinic UV hazard exposure limit for the skin and eye, retinal thermal hazard exposure limit, and thermal hazard exposure limit for the skin [31].

Biological Evaluation of Medical Device

Any medical device including any instrument, apparatus, appliance, material, or other article, including software, whether used alone or in combination, intended by the manufacturer to be used for human beings solely or principally, should first be provided the safety guarantee for human.

ISO 10993 is concerned with the safety in use of medical devices and materials. It is intended to assess the biological response of devices and materials as part of the

overall evaluation and development of devices and materials. ISO 10993 describes the general principles governing the biological evaluation of medical devices, the categorization of devices based on the nature and duration of their contact with the body, and the selection of appropriate tests. Hence on the basis of the guidance in ISO 10993-1:2003 "Biological evaluation of medical devices – Part 1: Evaluation and testing," suitable test can be selected to evaluate the safety of medical device [32].

Photonic Fabric Device Prototype for Phototherapy

Previous section provides complete specification about photonic fabric device for phototherapy, including fabrication and safety evaluation. This section presents the fabrication and evaluation of photonic fabric device prototype, which is developed for photorejuvenation.

Fabrication

POF Fabric

POFs (ESKATM, CK-10, supplied by Mitsubishi Rayon Co., Ltd, Japan) were step index optical fibers with a polymethyl methacrylate (PMMA) fiber core and a fluorinated PMMA derivative cladding, which were woven as weft yarn. Fiber diameter is 250 μm, NA = 0.5. High numerical aperture and large core of these POFs make it easy for light coupling. Moreover, small size of diameter makes the POFs more flexible and easy to handle and process in weaving.

In order to reduce the cover-up area of cotton yarns for POFs, finer cotton yarns, 80s/2, were selected for the warp simultaneously considering easy handling in weaving (Central Textile, Hong Kong).

POF fabrics were fabricated by conventional textile weaving process. An automatic sample loom (Jakob MÜller, Frick, Switzerland) was used to weave the POF fabrics. This sample loom is able to carry out small-scale weaving, and most of the weaving units are under manual control. Therefore, better handling and protection of the POF were achieved. During weaving, difficulties appeared including warping, POF tension control at weft insertion, POF breakage, and POF slippage. Hence the weaving machine was run at a low speed to avoid POF breakage and slippage. In addition, maintaining uniformity of POF tension during the weaving process was also critical. Figure 1 shows photos of the POF fabric. The inset illustrates the enlarged fabric structure where the POFs are arranged in the horizontal directions with good exposure of light-emitting spots and air permeability. The measured weft cover factor is 55.7 %, and the warp cover factor is 33 %. Large area of POFs was exposed because of the thin warp yarns and low warp density.

To guarantee that all the V-grooves were placed on the same face of the fabric, V-grooves were created on the POFs after weaving by a serrated tool shown in Fig. 2. The half angle of all teeth for the serrated tool was made as 33 °C according

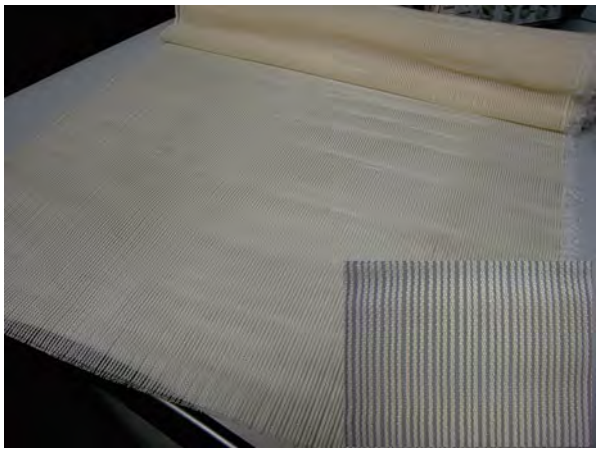

Fig. 1 Photo of woven fabrics produced from cotton yarns and POF with 250 μm diameter (*inset*: enlarged image)

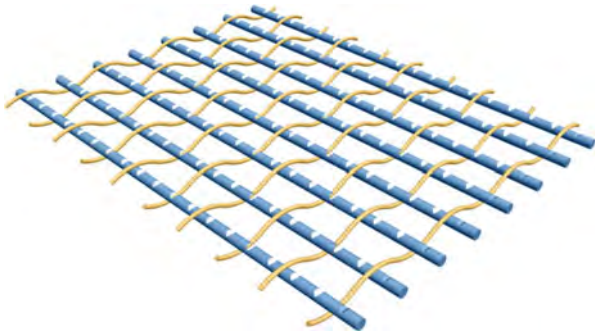

Fig. 2 Schematic of the POF fabric with V-grooves [33]

to calculation to obtain maximum side emission from the Y-X plane. The V-grooves were implemented on the POF by single-directional abrading on the surface using this tool, at the same time the tool was vertical to the fiber axis.

Light Source

Considering the effect of skin treatment, the wavelength and luminosity are of highest concern. The selection of an appropriate wavelength is essential for phototherapy because cellular reactions exhibit specificity to irradiation wavelengths. Proper dose of irradiation leads to a beneficial clinical effect, and excessive or deficient dose does not have positive effect for human.

Exposure to low-level red or near-infrared light might manipulate or regulate cell activity, achieving therapeutic effect. The most effective irradiation spectrum range is between 600 and 950 nm because the principal tissue chromophores (hemoglobin and melanin) have high absorption bands at wavelengths shorter than 600 nm and water begins to absorb significantly at wavelengths larger than 1,000 nm. Many previous studies have shown that low-level light irradiation at about 630 nm provides low-energy stimulation to tissues, which results in increased

Table 2 Technical specification of LEDs

Model number	Material	Wavelength λ_{peak}, $\lambda_{dominant}$ (nm)	V_f (V) Typ. (I_f = 400 mA)	Luminous flux Typ.	View angle	Dimensions (H × L × W) (mm)
6546417	AlGaInP	632,625	2.2	49 lm	120°	2 × 7.2 × 6.2

cellular activity during wound healing, increased proliferation rate of fibroblasts and keratinocytes, as well as enhancement of growth factor synthesis, collagen production, and angiogenesis. Hence in this case, enhanced thin film LED with 625 nm wavelength (Golden DRAGON®, Philips, USA) was selected for light source, whose technical specifications are given in Table 2. The other reason for this decision was its high luminosity to guarantee sufficient side emission.

Photonic Fabrics Device Prototype

185 POFs as a bundle were put together and connected with one LED by an optical adhesive, NOA 65 (Norland Products Inc., USA). The end of POF bundles was polished by sandpapers with various models (roughness, 220, 400, 600, 800, 1,000, 1,500, 2,000, 3 μm (particle diameter)) to improve the coupling efficiency. The LED has a Lambertian radiation pattern, in which the radiation angle is 120°, larger than the fiber acceptance angle. The fibers were double-end coupled with LEDs, and the coupling efficiency was 43.2 %. It was worth noting that the surface of POF and radiation zone LED would not contaminated by the adhesive. In order to guarantee the uniformity of irradiation of POF fabric, two layers of the same POF fabric were used. Figure 3 shows the scheme of luminous POF fabric device.

Properties Measurement

The prototype was evaluated for stability of power density and variations of temperature and humidity. The power density was measured every 30 min by optical meter (Optometer P9710, Gigahertz-Optik, Germany). Each data point was averaged by three locations. The power density of this phototherapy device prototype was almost constant for 9.59 h, as shown in Fig. 4. The average power density of this phototherapy device prototype is 0.1449 mW/cm^2.

The photomodulation effects are directly caused by very low light intensity irradiation on the tissue, not by heating. In order to avoid thermal effect during light irradiation, the temperature of cells must be keep constant. The whole device was placed in an environmental chamber (C7-600, VÖTSCH, Germany) set at 37 °C and 90 % humidity. The temperature and humidity sensor (SHT1x, Sensirion, Switzerland) was stuck on the surface of luminous POF fabric. Curves of temperature and humidity versus time are displayed in Fig. 5. The experimental results show that there is no significant temperature fluctuation in our device.

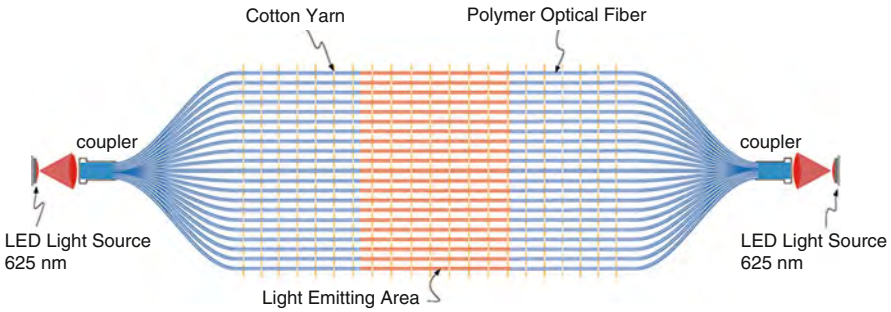

Fig. 3 Scheme of luminous POF fabric device [33]

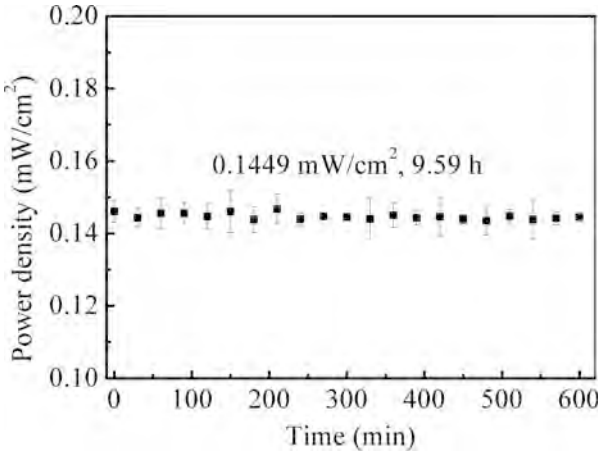

Fig. 4 Variation of power density of POF fabrics prototype for photorejuvenation

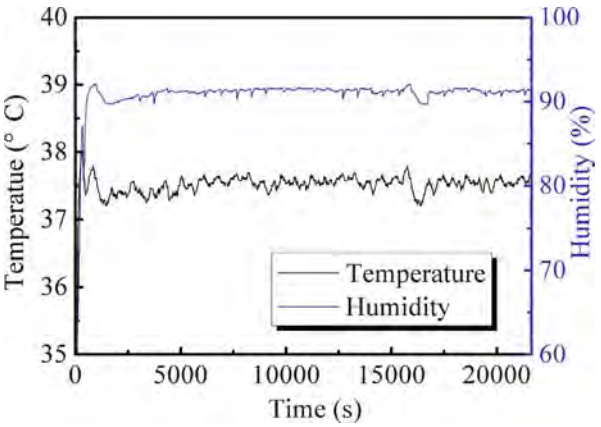

Fig. 5 Variations of temperature and humidity of POF fabrics prototype for photorejuvenation [33]

Safety Evaluation

As mentioned in the section "Fluence and Irradiance," light radiation can induce damage in biological tissue of the human body, mainly to the eye and to the skin. These damages of the eye or skin caused by excessive light radiation are different for light with different wavelengths. The light source of luminous POF fabric system is LED, the dominant wavelength of which is 625 nm. This visible light in wavelength range at 400 ~ 700 nm could cause retinal injury and skin burn. According to IEC 62471:2006 "Photobiological safety of lamps and lamp systems," POF fabric devices should fulfill the following limits: retinal blue light hazard exposure limit, retinal thermal hazard exposure limit, and thermal hazard exposure limit for the skin [31]. The calculated results have shown that the luminous POF fabrics with 625 nm are safe for human eye and skin.

The POF fabric device is intended to come in direct contact with the three-dimensional human body. Hence POF fabric was evaluated for its safety referred to the relevant standards from the International Organization for Standardization (ISO). According to ISO 10993-1:2003 Biological evaluation of medical devices – Part 1: Evaluation and testing [32], three kinds of evaluation test were conducted, in vitro cytotoxicity, skin sensitization, and skin irritation. The experiments completely followed the guidance of ISO 10993 standards [34, 35]. The experimental results indicated that the POF fabric was not considered cytotoxic and did not cause delayed dermal sensitization and skin irritation. Taken together, it is concluded that the POF fabric can be used in direct contact with human skin and does not pose risk to humans.

Current and Promising Application of Photonic Fabric Device

Neonatal Jaundice

Neonatal jaundice is one of the most common symptoms that require medical attention among newborns. About 60 % of term babies and 80 % of preterm babies develop jaundice in their first week of life. 10 % of breastfed babies are still jaundiced at 1 month of age [36]. Jaundice newborns have an apparent icteric sclera and yellowing of the skin and mucous membranes, which is the result of excessive bilirubin deposition, and the neonatal liver cannot clear bilirubin rapidly enough from the blood. Sufficiently elevated levels of bilirubin can cause bilirubin encephalopathy, subsequently kernicterus, permanent neurodevelopment handicaps, and even death in newborns [37].

Phototherapy is the most commonly used treatment for neonatal jaundice. In the 1950s, it was observed that infants exposed to sunlight had less jaundice at exposed areas, which opens the era of phototherapy for neonatal jaundice. Bilirubin has a strong absorption in the blue region of the spectrum between 430 and 490 nm. The light radiation associated to this spectral region can penetrate the epidermis, reaching the subcutaneous tissue and being, consequently, absorbed by the bilirubin

present in the blood. Absorption of light energy by bilirubin induces a photochemical reaction to convert it to molecules that can be easily excreted by liver and kidney. Two photochemical mechanisms have been proposed to explain the phototherapy action in the elimination of bilirubin. Photoisomerization is considered as the most important phototherapy mechanism of bilirubin degradation [38]. Photoisomerization is associated to the conversion of bilirubin in two isomers, which are known as configurational and structural isomers ("lumirubin"). The photoisomers are less lipophilic than the normal form of bilirubin and can be excreted unchanged in bile. Lumirubin isomers can also be excreted in urine. Photooxidation mechanism, in its time, consists in the oxidation of bilirubin molecules in aerobic environment to generate hydrosoluble pyrrolic derivatives, which are eliminated from organism through the urine. Commonly used phototherapy units include light boxes with special blue fluorescent lamps or LED lights, which have been found to be effective in clinical studies.

Lumitex Company developed a light emitting pad called Bili-Blanket to treat neonatal jaundice, which is a flexible woven fabric emitted blue light with the wavelength between 390 and 475 nm. The blanket consists of two layers of parallel POFs, which are woven together with polyester cross fibers. The ends of the POFs are gathered together at one side and plugged into a light source. This product is expected to be helpful for newborn babies with jaundice because they can receive the treatment by wrapping them in a light-emitting blanket while being cuddled and fed.

Photorejuvenation

Photorejuvenation is the process where light energy is used to reverse the process of photo- or sun-induced aging or environmental damage to the skin. Pulse CO_2 laser approved by FDA for skin resurfacing in 1991 and the erbium (Er): YAG laser (2940 nm) approved subsequently in 1996, which removed the epidermis and induced skin wounding to promote collagen biosynthesis and dermal matrix remodeling. These ablative lasers were greatly popular in the 1980s and 1990s. However, patients were dissatisfied with the prolonged downtime and long-lasting erythema, hyper- or hypopigmentation, infection, pain, bleedings, and sometimes scarring [39].

Nonablative treatments with significantly less adverse effects can also improve dyspigmentation, skin roughness, and fine and moderately deep facial wrinkles. Zelickson and Kilmer established the basis of all nonablative procedures [40]. This research showed that the pulsed dye laser (PDL) induced fibroblast proliferation and the production of new collagen in the papillary dermis at Grenz zone [40]. Subsequent studies have demonstrated that a variety of visible and infrared (IR) wavelengths can produce a similar effect, specifically stimulating the production of collagen, elastic fibers, and skin texture improvement, as long as low fluences are applied [41].

Results vary depending on the lasers or light sources used. The IR lasers improve texture in both photoaging and acne scarring, but because the wavelengths are not absorbed by either melanin or hemoglobin, no improvement is seen in skin color, redness or pigmentation, and vessels. The visible light lasers, such as PDL, improve

texture somewhat less than the IR lasers but are highly effective in reducing redness and telangiectasia and also in modulating hypertrophic scars. Intense pulsed light devices improve both red targets and brown discoloration and skin texture. Recently developed LEDs may improve redness and improve texture modestly. With all of these treatments, there is little downtime compared with the ablative laser resurfacing [42].

Thermal injury with subsequent wound healing is still believed to be the primary mechanism for most photorejuvenation using high-energy light source [43]. In contrast to these thermal mechanisms, there is another possible mechanism to alter cellular activity by light, which is also termed photomodulation [43]. This is the process where low-level light irradiation is used to modulate (activate or inhibit) the normal activities of a cell. It has been attributed to the absorption of monochromatic visible and near-infrared (NIR) radiation by mitochondria at the cellular level. Red visible and NIR light irradiation stimulates more ATP synthesis and low levels of reactive oxygen species (ROS), which stimulates cellular proliferation. Nitric oxide (NO) may be photo-released from its binding sites in the mitochondria and elsewhere, which helps to reverse the mitochondrial inhibition of respiration due to excessive NO binding. Low-level light therapy may activate transcription factors, upregulating protective proteins which are antiapoptotic, and generally promote cell survival. This mechanism still is not completely clear and need more exploration.

Wound Healing

Wound healing is a complex series of reactions and interactions which requires the performance of a well-orchestrated process of biological and molecular events. Many medical methods involve in enhancing wound healing including phototherapy, hyperbaric oxygen, negative pressure therapy, biological therapies, and reconstructive treatments.

Visible/NIR-LED light treatments at various wavelengths have been shown to increase significantly cell growth in a diversity of cell lines, including rat skeletal muscle cells, rat osteoblasts, murine fibroblasts, and normal human epithelial cells [44]. Reduction of wound size and acceleration of wound closure also have been demonstrated in various in vivo models, including rats, mice, swine, and guinea pigs [45]. Accelerated healing and greater amounts of epithelialization during skin grafts have been found in human studies [46]. The previous works also show that LED therapy is known to positively support and speed up healing of chronic leg ulcers: diabetic, venous, arterial, and pressure [10].

Sunburn Prevention

Beyond the repair of previous UV insults to the skin, visible to NIR light might offer protection against upcoming photodamage. It has been suggested that protective mechanisms against skin UV-induced damage may be activated by IR exposure

in a number of in vitro studies using primary culture human fibroblasts. Therefore, LED treatment could stimulate skin resistance to UV damage.

Study results suggest that LED 660 nm treatment before UV exposure provides significant protection against UV-B-induced erythema [46]. The induction of cellular resistance to UV insults may possibly be explained by the induction of a state a natural resistance to the skin without the drawbacks and limitations of traditional sunscreens. These results represent an encouraging step toward expanding the potential applications of low-level light therapy and could be useful in the treatment of patients with anomalous reactions to sunlight such as polymorphous light eruption or lupus.

Seasonal Affective Disorder (SAD)

Seasonal affective disorder (winter depression) is a well-recognized form of recurrent depressive disorder, characterized by typical and atypical (increased appetite, weight, sleep, and fatigue) depressive symptomatology and a distinct seasonal nature. SAD is thought to be related to natural seasonal variations in light levels. Bright light therapy – exposure of the patient each morning to bouts of artificially produced high intensity light – has been shown to produce amelioration of depressive symptoms. Recent data indicate that the human circadian rhythm system is most sensitive to light with wavelength in the range 450–480 nm [47].

Summary

Smart or intelligent textiles have been the trend of research and development in recent years. POF fabrics as one member of smart textile family have attracted great attentions because of their flexibility, low weight, immunity of EMI, easy handling, simple connection, and biocompatibility and so on. Although there are many POF textile products demonstrated for illumination, decoration, display and sensation, up to now, a limited number have been produced for medical application. Photonic fabric device for phototherapy opens a new application field for smart textiles. Compared to commercial phototherapy devices using LED or laser as light source, photonic fabric device has many advantages, for example, easy to handle, low weight, low cost. Especially, this flexible fabric can easily fit three-dimentional body surface of human. Effectiveness and safety for patients are the key factors for phototherapy device. From luminous POF fabric to phototherapy device, there are several key steps, precise control of side-emission of large-area POF fabric; fabrication of POF fabric device; stable performances including wavelength, light power density, temperature; safety evaluation of POF fabric device for human; effectiveness study of POF fabric device. Our research group studied the photonic fabric device for phototherapy and developed a prototype. However, some important issues still need to be further addressed in future including the improve the performance of the photonic fabric device, optimize the design to fulfill the practical demand and so on.

References

1. Tao XM (2001) Smart fibres, fabrics and clothing. Woodhead, Cambridge
2. Koncar V (2005) Optical fiber fabric displays. Opt Photonics News 16:40–44
3. Tao XM (2005) Wearable electronics and photonics. Woodhead, Cambridge
4. Rothmaier M, Luong MP, Clemens F (2008) Textile pressure sensor made of flexible plastic optical fibers. Sensors 8:4318–4329
5. Sayed I, Berzowska J, Skorobogatiy M (2010) Jacquard-woven photonic bandgap fiber displays. Res J Text Appar 14:97
6. Tao XM, Cheng XY, Yu JM, Liu LJ, Wong WK, Tam WK (2008) Photonic fabric display with controlled pattern, color, luminescence intensity, scattering intensity and light self-amplification. US Patent 7,466,896 B2
7. Tanzi EL, Lupton JR, Alster TS (2003) Lasers in dermatology: four decades of progress. J Am Acad Dermatol 49:1–31
8. Vladimirov YA, Osipov AN, Klebanov GI (2004) Photobiological principles of therapeutic applications of laser radiation. Biochemistry 69:81–90
9. Sebbe PF, Villaverde AB, Moreira LM, Barbosa AM, Veissid N (2009) Characterization of a novel LEDs device prototype for neonatal jaundice and its comparison with fluorescent lamps sources: phototherapy treatment of hyperbilirubinemia in Wistar rats. Spectroscopy 23:243–255
10. Whelan HT, Buchmann EV, Whelan NT, Turner SG, Cevenini V, Stinson H, Ignatius R, Martin T, Cwiklinski J, Meyer GA, Hodgson B, Gould L, Kane M, Chen G, Caviness J (2001) NASA light emitting diode medical applications from deep space to deep sea. Space Technol Appl Int Forum CP552:35–45
11. http://en.wikipedia.org/wiki/Phototherapy
12. Goldman L, Wilson R, Hornby P (1965) Radiation from a Q-switched ruby laser: effect of repeated impacts of power output of 10 megawatts on a tattoo of man. J Invest Dermatol 44:69–71
13. Goldman L, Nath G, Schindler G, Fidler J, Rockwell RJ Jr (1973) High-power neodymium-YAG laser surgery. Acta Derm Venereol 53:45–49
14. Goldman L, Dreffer R, Rockwell RJ Jr, Perry E (1976) Treatment of port-wine marks by an argon laser. J Dermatol Surg 2:385–388
15. Anderson RR, Parrish JA (1983) Selective photothermolysis: precise microsurgery by selective absorption of pulsed radiation. Science 220:524–527
16. Simpson CR, Kohl M, Essenpreis M, Cope M (1998) Near infrared optical properties of ex-vivo human skin and subcutaneous tissues measured using the Monte Carlo inversion technique. Phys Med Biol 43:2465–2478
17. Kalka K, Merk H, Mukhtar H (2000) Photodynamic therapy in dermatology. J Am Acad Dermatol 42:389–413
18. Lanzafame RJ, Stadler I, Kurtz AF, Connelly R, Peter TA Sr, Brondon P, Olson D (2007) Reciprocity of exposure time and irradiance on energy density during photoradiation on wound healing in a murine pressure ulcer model. Lasers Surg Med 39:534–542
19. Hawkins DH, Abrahamse H (2007) Time-dependent responses of wounded human skin fibroblasts following phototherapy. J Photochem Photobiol B 25:147–155
20. Barolet D, Roberge C, Germain L, Auger F (2004) Rhytid improvement by non-ablative, non-thermal LED photoinduction: in vitro and in vivo aspects. Lasers Surg Med 34:75
21. Abouraddy AF, Bayindir M, Benoit G, Hart SD, Kuriki K, Orf N, Shapira O, Sorin F, Temelkuran B, Fink Y (2007) Towards multimaterial multifunctional fibres that see, hear, sense communicate. Nat Mater 6:336–347
22. Lu CL, Yang B (2009) High refractive index organic–inorganic nanocomposites: design. J Mater Chem 19:2884–2901

23. Im MH, Park EJ, Kim CH, Lee MS (2007) Modification of plastic optical fiber for side-illumination. Hum Comput Interact Interact Platf Tech 4551:1123–1129
24. Endruweit A, Long AC, Johnson MS (2008) Textile composites with integrated optical fibres: quantification of the influence of single and multiple fibre bends on the light transmission using a Monte Carlo ray-tracing method. Smart Mater Struct 17:015004
25. Gauvreau B, Guo N, Schicker K, Stoeffler K, Boismenu F, Ajji A, Wingfield R, Dubois C, Skorobogatiy M (2008) Color-changing and color-tunable photonic bandgap fiber textiles. Opt Express 16:15677–15693
26. Daum W, Krauser J, Zamzow PE, Ziemann O (2002) POF polymer optical fibers for data communication. Springer, Berlin
27. Markov A, Reinhardt C, Ung B, Evlyukhin A, Cheng W, Chichkov B, Skorobogatiy M (2011) Photonic bandgap plasmonic waveguides. Opt Lett 36:2468–2470
28. Khan T, Unternährer M, Buchholz J, Kaser B, Selm B, Rothmaier R, Walt H (2006) Performance of a contact textile-based light diffuser for photodynamic therapy. Photodiagnosis Photodyn Ther 3:51–60
29. Rothmaier M, Selm B, Spichtig S, Haensse D, Wolf M (2008) Photonic textiles for pulse oximetry. Opt Express 16:12973–12986
30. International standard IEC 60825-1 (2007) Safety of laser products – part 1: equipment classification and requirements. International Electrotechnical Commission, Geneva
31. International standard IEC 62471 (2006) Photobiological safety of lamps and lamp systems. International Electrotechnical Commission, Geneva
32. International standard ISO 10993-1 (2009) Biological evaluation of medical devices – part 1: evaluation and testing. ISO, Geneva
33. Shen J, Chui CH, Tao XM (2013) Luminous fabric devices for wearable low-level light therapy. Biomed Opt Express 4:2925–2937
34. International standard ISO 10993-5 (2009) Biological evaluation of medical devices – part 5: test for in vitro cytotoxicity. ISO, Geneva
35. ISO 10993-10:2002/Amd. 1 (2006) Biological evaluation of medical device – part 10: test for irritation and delayed-type hypersensitivity. ISO, Geneva
36. American Academy of Pediatrics, Provisional Committee for Quality Improvement and Subcommittee on Hyperbilirubinemia (1994) Practice parameter: management of hyperbilirubinemia in the healthy term newborn. Pediatrics 94:558–562
37. Maisels MJ, McDonagh AF (2008) Phototherapy for neonatal jaundice. N Engl J Med 358:920–928
38. Steffensrud S (2004) Hyperbilirubinemia in term and near-term infants: Kernicterus on the rise? Newborn Infant Nurs Rev 4:191–200
39. Nanni CA, Alster TS (1998) Complications of carbon dioxide laser resurfacing: an evaluation of 500 patients. Dermatol Surg 24:315–320
40. Zelickson BD, Kilmer SL, Bernstein E, Chotzen VA, Dock J, Mehregan D, Coles C (1999) Pulsed dye laser therapy for sun damaged skin. Lasers Surg Med 25:229–236
41. Omi T, Kawana S, Sato S, Honda M (2003) Ultrastructural changes elicited by an non-ablative wrinkle reduction laser. Lasers Surg Med 32:46–49
42. Danielle MD, Jeffrey SD (2007) Nonablative tissue remodeling and photorejuvenation. Clin Dermatol 25:474–479
43. Robert AW, David HM, Roy GG (2003) Review of nonablative photorejuvenation: reversal of the aging effects of the sun and environmental damage using laser and light sources. Semin Cutan Med Surg 22:93–106
44. Hawkins-Evans D, Abrahamse H (2008) Efficacy of three different laser wavelengths for in vitro wound healing. Photodermatol Photoimmunol Photomed 24:199–210
45. Al-Watban FA (1997) Laser acceleration of open skin wound closure in rats and its dosimetric dependence. Lasers Life Sci 7:237–247

46. Conlan MJ, Rapley JW, Cobb CM (1996) Biostimulation of wound healing by low-energy laser irradiation. J Clin Periodontol 23:492–496
47. Barolet D, Boucher A (2008) LED photoprevention: reduced MED response following multiple LED exposures. Lasers Surg Med 40:106–112
48. Lockley SW, Brainard GC, Czeisler CA (2003) High sensitivity of the human circadian melatonin rhythm to resetting by short wavelength light. J Clin Endocrinol Metab 88:4502–4505

Polymer Optical Fiber Bragg Grating

23

Zhang Zhifeng

Contents

Introduction 598
Fabrication of Polymer Optical Fiber Bragg Gratings 598
Single-Mode POFs for POFBG Inscription 598
Methods of POFBG Inscription 600
Properties of Polymer Optical Fiber Bragg Gratings 604
Thermal Response 604
Humidity Response 606
Strain Response 607
Applications of Polymer Optical Fiber Bragg Gratings 608
Fiber Laser 608
Localized Strain Monitoring of Tapestries 608
In Situ Monitoring of Composite Material 608
Electrically Tunable Bragg Grating Filter 609
Sensing of Moisture in Fuel 609
Mechanical Sensor 609
Summary 610
References 610

Abstract

Polymer optical fiber Bragg gratings (POFBGs) are attracting increasingly more attention of researchers because of their potential sensing applications. This chapter presents the state of the art of the POFBG research, including its fabrication and properties and some typical applications. Two common grating inscription methods, the phase mask technique and the interferometric

Z. Zhifeng (✉)
The Hong Kong Polytechnic University, Hong Kong, China
e-mail: zhifeng.zhang@connect.polyu.hk

© Springer Science+Business Media Singapore 2015

X. Tao (ed.), *Handbook of Smart Textiles*,
DOI 10.1007/978-981-4451-45-1_27

technique, are compared. Properties of POFBGs including their thermal, humidity, and strain responses are reviewed. Finally a few typical applications of POFBGs are described.

Keywords
Polymer optical fiber • Polymer optical fiber Bragg grating • Fiber Bragg grating fabrication • Fiber optic sensor

Introduction

Polymer optical fiber Bragg gratings (POFBGs) are promising for sensing applications because they combine the superiorities of fiber Bragg gratings (FBGs) and polymer optical fibers (POFs). FBGs in silica fibers have been widely used in industry. As a supplement to silica FBGs, POFBG-based sensors provide advantages of FBGs like high sensitivity, small size, distributed sensing capability, etc., and also benefits of POFs like excellent ductility compared to silica counterparts. Specifically, POFs have an elastic deformation range that is almost one order of magnitude higher than silica fibers. Additionally, polymer surface can be readily functionalized to provide enormous opportunity to make POFBGs selectively sensitive to various chemical or biological measurands. Optical polymers like PMMA are biocompatible, making POFBGs suitable candidates for biological and even in vitro applications. As more types of transparent polymers are developed, more base materials are available for selection for particular situations. For example, traditional optical polymers like PMMA, PC, etc., are rigid, but recently-developed optical silicones are soft and much more thermally stable, which might provide more attractive properties of POFBGs. POFBGs are one of the enabling technologies for smart textiles because POFs are flexible enough to weave into fabrics. It's worthwhile to note here that Webb and coworkers had published a comprehensive and valuable book chapter on the POFBG in 2011 [1].

Fabrication of Polymer Optical Fiber Bragg Gratings

This section starts with a classification of single-mode POFs used for FBG inscription, followed by two methods for POFBG inscription.

Single-Mode POFs for POFBG Inscription

FBGs have been successfully written in various types of POFs, as tabulated in Table 1. In terms of fiber material, these POFs are based on two major optical polymers, PMMA and cyclic olefin copolymer (COC). They can also be classified into solid-core and microstructured ones according to the fiber structure.

Table 1 Classification of single-mode POFs inscribed FBGs in terms of material and fiber structure

Material		Fiber structure (solid/microstructured)	References
Matrix polymer	Dopant		
PMMA-based	–	Solid	[5–13]
	–	Microstructured	[14–18]
	Fluorescein	Solid	[2]
	trans-4-Stilbenemethano	Solid	[19, 20]
	Benzil dimethyl ketal	Solid	[21, 22]
	Benzil dimethyl ketal	Microstructured	[23]
COC	–	Microstructured	[15, 24–27]
CYTOP (slab)	–	Slab light guide	[4, 28]

Additionally, there are doped and undoped POFs in regard to presence of dyes in fibers, including fluorescein, *trans*-4-stilbenemethanol, and benzil dimethyl ketal (BDK).

PMMA-based fibers are firstly written in POFBGs [2]. The main reason is that single-mode POFs for Bragg grating inscription are not commercially available while PMMA fibers are relatively easy to fabricate. In addition, PMMA are highly transparent, and the refractive index difference between the fiber core and cladding of PMMA fibers can be readily controlled by copolymerizing the core with high-index monomers or by copolymerizing the cladding with low-index monomers. Furthermore, photosensitive dopants can be easily and homogeneously doped into the fiber core when mixing monomers for its polymerization. Even up to now, most research of POFBGs still uses PMMA fibers. COC is a newly developed polymer with excellent transparency, good thermal stability (compared to PMMA), and low water absorption. Due to the difficulty of its polymerization, researchers extrude rods from commercial COC granules, drill holes in rods and draw microstructured fibers, and finally write Bragg gratings. Compared to PMMA, POFBGs in COC is superior in the using temperature range and humidity insensitivity. However, writing FBGs in microstructure fiber is generally more difficult than the solid-core step-index type [3]. Bragg gratings are also fabricated into slabs of CYTOP (a commercial optical polymer developed by Asahi Glass), exhibiting better thermal stability than PMMA ones [4]. Molecular structures of PMMA, COC, and CYTOP are shown in Fig. 1. CYTOP has much lower loss at visible range due to high content of the fluorine. COC has higher Tg than PMMA and can be tuned over a wide range by adjusting the ratio of two monomers.

Fabrication of high-quality, single-mode, photosensitive POFs for grating inscription is one of the obstacles facing the POFBG research. There are commercial single-mode POFs used for grating inscription in literature, but the supply seems not stable. Consequently, POFBG researchers draw single-mode POFs by themselves. The commonly used method is the preform drawing. First, thick preforms with core/cladding structure are prepared by methods like Teflon thread

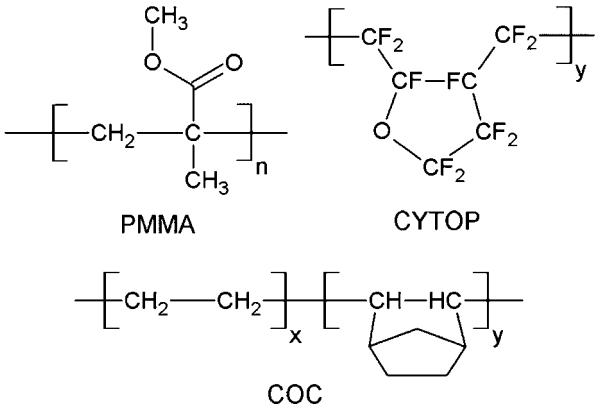

Fig. 1 Molecular structure of PMMA, COC, and CYTOP

method and then melt to draw down into fiber [14, 19, 29]. For microstructured ones, preforms are prepared by drilling holes in certain patterns in a polymer rod and then drawn to fiber [23, 26]. Drawing towers are customized, and normally the drawing tension is not precisely controlled, making the fabricated fibers differ significantly from lab to lab even for fibers with the same chemical composition.

Methods of POFBG Inscription

Phase Mask Technique

The phase mask technique is one of the most common methods to write FBGs. Figure 2 shows a typical setup. The UV laser beam is shaped and reflected to irradiate on a phase mask, beneath which the POF is placed. The phase mask is specially designed so that most incident light is diffracted into the +1 and −1 order diffraction, and two beams interfere immediately behind the phase mask forming an interference fringe that has the period of half of the phase mask pitch. Compared to the two-beam interference technique, the phase mask method is simple in alignment of optic components, and thus used by increasingly more research groups. By using the phase mask, long-length POFBGs can be easily inscribed by scanning the laser beam along the length of the fiber while the phase mask and the fiber are fixed, and the maximum length is only limited by the size of the grating on the phase mask. Most recently, it is found that reducing fiber diameter by etching can effectively enhance the reflectivity of the inscribed POFBGs in PMMA-based fibers due to the strong absorption of the UV laser beam by PMMA [30].

Normally, it is thought that the zeroth-order diffraction of the phase mask for FBG inscription should be less than 5 % or even lower [31]. Accordingly, the main quality factor of the phase mask for Bragg grating inscription is the diffraction ratio of the zeroth order. Creation of surface relief gratings in polymer optical preforms suggests that even 0.1 % zeroth-order diffraction would have substantial effects on the formation of gratings [31]. Nevertheless, there is a report that

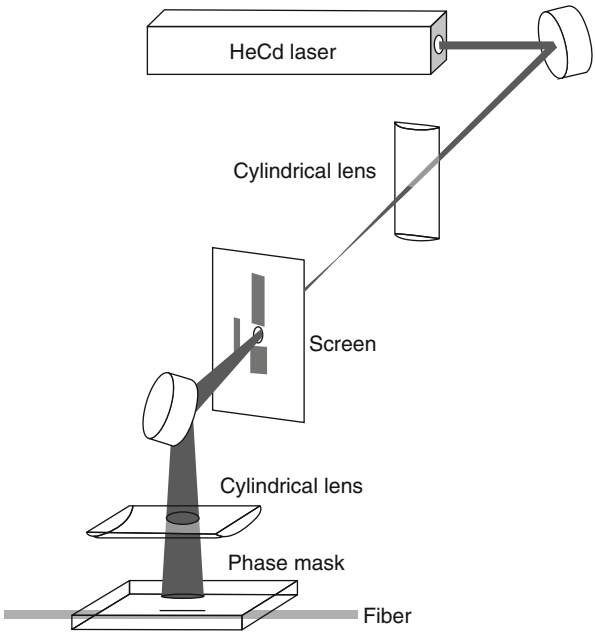

Fig. 2 Diagram of the writing system using the phase mask (Reprinted from Ref. [14] with permission from OSA)

uses phase masks with high zeroth-order diffraction to successfully write POFBGs. For example, a phase mask with 17 % zeroth-order diffraction has been used to write POFBGs around 962 nm in *trans*-4-stilbenemethanol-doped PMMA fibers [20].

One of the drawbacks of the phase mask technique is that a single phase mask can only write FBGs at a certain wavelength, especially for writing silica FBGs. However, by taking advantage of the large elastic range of POFs, it's possible to write FBGs with various peak wavelengths by a single phase mask [32]. That is, POFs are applied strain during grating inscription. Upon release of tension, the peak wavelength shifts toward shorter wavelength, and the final wavelength or the magnitude of shift depends on the applied strain. A series of POFBGs can be written in a single POF by repeating this method.

Interferometric Method

Using the interferometric method, Peng and coworkers inscribed and reported the first POFBG in 1999 [5, 33]. They inscribed gratings in fluorescein-doped PMMA-based fibers by using a modified Sagnac interferometer consisting of three quartz prisms, as shown in Fig. 3. The laser beam is split by a phase mask, and the +1 and −1 order diffraction beams are reflected by three prisms to form interference patterns where the POF is placed. The zeroth-order diffraction beam is blocked for aforementioned reasons. The intersecting point of the two reflected beams is in the same plane of the phase mask. By this configuration, the influence of the zeroth-order diffraction can be completely eliminated. The interference pattern is purely

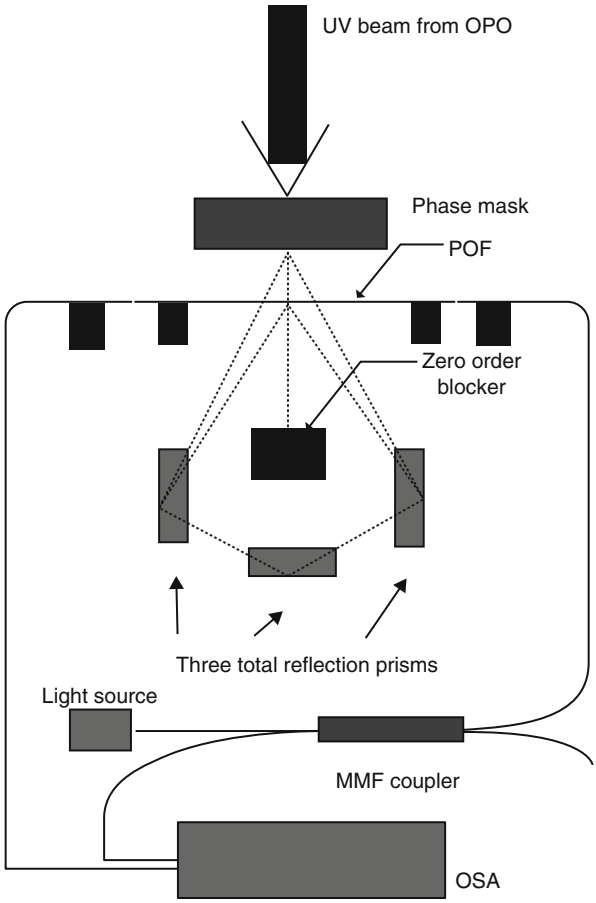

Fig. 3 Diagram of the grating writing system based on the Sagnac interferometer (Reprinted from Ref. [5] with permission from IEEE)

produced by +1 and −1 order diffraction. Additionally, this writing method allows writing POFBGs with different peak wavelengths by adjusting the intersecting angle of the two beams to change the period of the interference pattern. However, to write long-length POFBGs is troublesome by using this technique, and laser beams must be expanded to produce large area of interference patterns.

Grating Formation Mechanism

The formation mechanism of POFBGs depends on the chemical composition of the fiber core and also the wavelength of lasers for writing. Thus, POFBGs form through various mechanisms. Liu et al. closely examined the grating formation process in the PMMA-based POF with a PMMA cladding and a core of the copolymer of methyl methacrylate and benzyl methacrylate [6]. They identified two distinctive stages and accordingly named gratings at two stages as Type I and Type II following the nomenclature of silica FBGs. As shown in Fig. 4, the

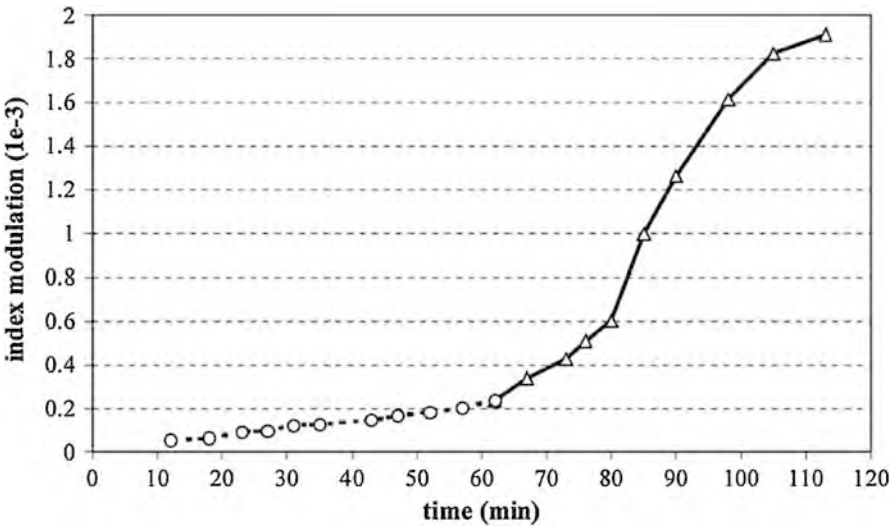

Fig. 4 Absolute refractive index decrease of the fiber core during grating inscription, calculated from Bragg peak shift. The used POF has a PMMA cladding and a copolymer (methyl methacrylate and benzyl methacrylate) core (Reprinted from Ref. [6] with permission from Elsevier)

refractive index of fiber core decreases slowly at the first stage. Beyond a certain irradiation threshold, the formation moves to the second stage, and the refractive index decreases dramatically. Though the reason for the refractive index at the first stage is not clear, the morphology study reveals that the fiber has been severely degraded at the second stage. Most likely, the grating formation process under UV irradiation is the combined result of photodegradation and photopolymerization [34]. The refractive index of PMMA increases upon irradiation by 325 nm laser due to photopolymerization of residual monomers [35]. Both processes depend on the irradiation wavelength, power density, and total energy. Interestingly, it has been found that stretching the PMMA fiber during grating inscription leads to an increased photosensitivity [34].

For dye-doped POFs, gratings are formed mainly due to the photo effects on dyes. For example, *trans*-4-stilbenemethanol-doped POFs are inscribed gratings due to its *trans-cis* isomerization under UV irradiation, as shown in Fig. 5 [19]. Its *trans* configuration has higher refractive index than the *cis* configuration. Under UV irradiation, molecules in *trans* configuration transfer to *cis*. One particular merit of the *trans-cis* isomerization of 4-stilbenemethanol is that its *cis* configuration is thermally dynamically stable. In contrast, most azo dyes, which have similar molecular structure and *trans-cis* isomerization, are not stable at *cis* configuration at room temperature. Their *cis* configuration spontaneously isomerizes to *trans* configuration even at room temperature. Benzil dimethyl ketal, another dye used to make POFs photosensitive for Bragg grating inscription, absorbs UV light, and the molecule splits to produce radicals, which leads to other reactions in the following to change the refractive index of the host material [21].

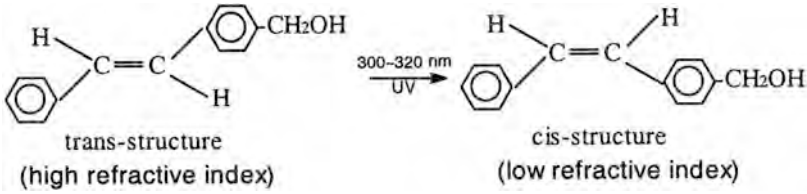

Fig. 5 Isomerization of 4-stilbenemethanol fromtrans tocisstructure upon UV irradiation (Reprinted from Ref. [19] with permission from OSA)

To write POFBGs at shorter wavelength is one of objectives that POFBG researchers are making efforts to accomplish. The transmission window of PMMA is mainly in the visible range of light, but most POFBGs are written around 1550 nm. The reason is that commercially available fiber-optic instruments like light sources and FBG interrogators are at this wavelength range for their wide use in fiber-optic communications. Additionally, single-mode POFs are manually connected (butt coupling) to silica fibers that connect to fiber-optic instruments via standard single-mode silica fiber connectors. Manual coupling is time consuming and leading to large variations in experiments. But the major problem of writing POFBGs around 1550 nm range is that POFs, especially PMMA-based ones, have high loss. Consequently only very short length of POFs, normally only a few centimeters, could be used. One solution to the problem is to write gratings at shorter wavelength where POFs have lower loss, like gratings at 962 nm in PMMA fibers [20], 870 nm in COC fibers [26], and 827 nm in multimode microstructured fibers [16]. The ideal wavelength range should be the visible range, and it has been realized recently as aforementioned [18]. Interestingly, It has been found that laser irradiation during grating inscription induces birefringence to POFs with increased polarization-dependent loss and differential group delay [30].

Properties of Polymer Optical Fiber Bragg Gratings

Thermal Response

Bragg wavelength of FBGs shifts due to temperature change following the equation

$$\frac{\Delta\lambda}{\lambda} = (\alpha_n + \alpha_\Lambda)\Delta T$$

where λ is Bragg wavelength, $\Delta\lambda$ is shift of Bragg wavelength due to temperature change ΔT, α_n is normalized thermo-optic coefficient $\left(\frac{dn}{dT}/n\right)$, and α_Λ is the linear coefficient of thermo expansion. For FBGs at 1550 nm in silica fibers, the temperature sensitivity ($\Delta\lambda/\Delta T$) is about 0.1 pm/°C, and a great number of methods have been reported to enhance temperature sensitivity of silica FBGs. POFBGs were

found having high temperature sensitivity, which is a decisive advantage for their application as temperature sensors. Therefore, thermal response of POFBGs is one of the mostly investigated properties.

Reported values of temperature sensitivities for POFBGs differ dramatically. The highest recorded value is 810 pm/°C, which is a POFBG at 1604 nm in a COC-based microstructured fiber with two rings of holes [15]. For PMMA-based FBGs, the highest reported sensitivity is a shift of −18 nm over a temperature increase of 50 °C, which is equivalent to a sensitivity of −360 pm/°C [36]. The negative temperature sensitivity originates from the negative thermal-optic coefficient of PMMA. Other values range from −10 to −149 pm/°C for different gratings and measurement methods [22, 37–40].

The high temperature sensitivity of Bragg gratings in PMMA fibers is endowed by the large negative thermo-optic coefficient, and its absolute value is larger than the linear coefficient of thermal expansion of PMMA. The thermo-optic coefficient for PMMA ranges from -0.85×10^{-4} to -1.23×10^{-4} °C^{-1} [41–43], which is roughly one order of magnitude higher than silica (8.86×10^{-6} °C^{-1} [44]). In comparison, its coefficient of thermal expansion is about 0.68×10^{-4} °C^{-1} [41].

Recent studies, however, suggest that the temperature sensitivities of POFBGs might not be as high as previously reported and believed, and even the magnitude of sensitivities is lower than that of silica FBGs. Habach and colleagues found that the temperature sensitivity of PMMA-based POFBGs depends on the humidity [45, 46]. They measured the temperature sensitivities of PMMA-based POFBGs at three conditions: dry (the grating is flushed with N_2), ambient, and wet (in water). Temperature sensitivities are −10, −138, and −35 pm/°C at dry, ambient, and wet conditions, respectively. Dependence of the temperature sensitivity on the humidity is evident though the humidity is not precisely controlled. Zhang and colleagues later systematically studied the Bragg wavelength shift of the PMMA-based POFBGs at various levels of temperature and humidity, as shown in Fig. 6 [47, 48]. They found that temperature and humidity have synergetic influence on the studied POFBG. That is, influences of temperature and humidity on the POFBG are mutually dependent. In other words, temperature sensitivity depends on humidity and vice versa. Most importantly, the intrinsic temperature sensitivity of the POFBG at absolute dry conditions (0 %RH) is measured from −20 °C and 60 °C. It was revealed that the dependence on the temperature is nonlinear and the magnitude of the sensitivity is extremely low compared to values measured at ambient conditions. Typically, the temperature sensitivity is only −1 pm/°C at 20 °C. At constant relative humidity above 0 %RH, the temperature sensitivity is also much lower than that at ambient conditions. Nevertheless, there is report of relatively high temperature sensitivity at constant relative humidity for POFBGs in microstructured PMMA fibers [49].

These conflicting results reflect the complexity of the thermal response of POFBGs. Superficially, the thermal response depends only on two parameters of the fiber material, that is, the thermo-optic coefficient and the coefficient of thermal expansion. But these two parameters are influenced by many other properties and even fabrication processes of POFs [50].

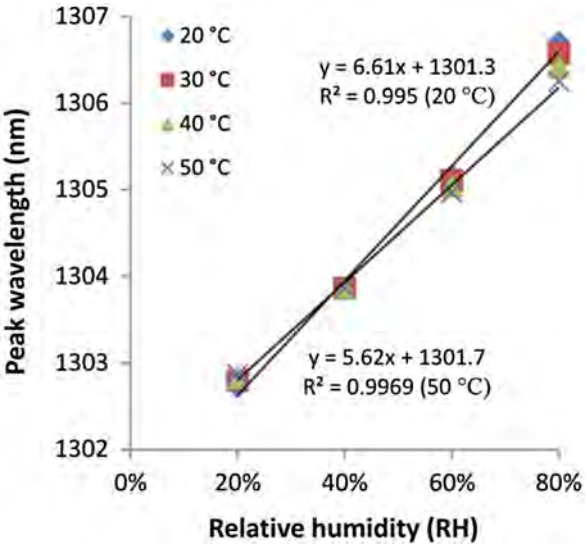

Fig. 6 Peak wavelength shift of a POFBG in PMMA-based fiber for the relative humidity 20–80 % at four temperature levels

One major obstacle in the thermal response study of POFBGs is the shrinkage of POFs after being heated to high temperature. Bragg peaks of POFBGs will permanently shift to short wavelength after a heating and cooling cycle [38]. Therefore, POFs must be annealed before thermal response measurements. Otherwise, the measured values are not meaningful. On the other hand, this permanent peak shift by heating provides a convenient way to write several gratings in a single fiber by using a single phase mask. For example, Johnson et al. find the gratings in PMMA-based fiber shift blue-shift 0–16 nm for 1550 nm gratings and 0–6 nm for 800 nm gratings depending on the heating temperature and duration, and they heat the gratings in as-drawn fibers to shift the Bragg wavelength and then write another grating at the original wavelength [17].

Humidity Response

PMMA-based POFBGs have been found humidity sensitive, making them promising humidity sensors. Figure 7 shows the humidity response of a POFBG in PMMA-based fiber over the whole range of relative humidity [47]. From 0 to 30 %RH, the Bragg peak shifts only 0.3 nm. In contrast, a total shift of 6.4 nm occurs from 30 to 100 %RH, equivalent to a shift of 0.091 nm per 1 %RH change.

High humidity sensitivity of POFBGs in PMMA-based fibers, on the other hand, becomes a problem for POFBGs in applications other than humidity sensing. One particular merit of COC-based POFBGs is their insensitivity to humidity. Yuan W. et al. demonstrated that a POFBG in a COC fiber with a Bragg peak at

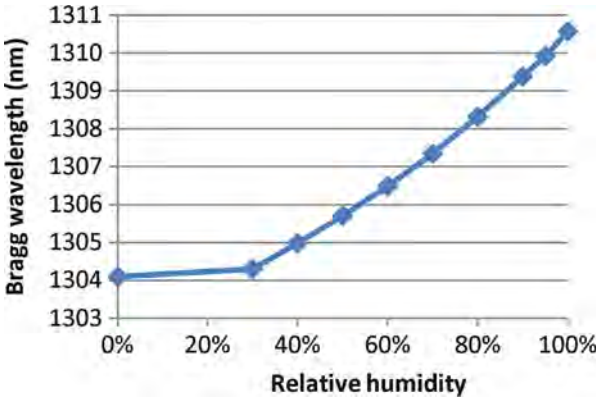

Fig. 7 Dependence of the POFBG in PMMA-based fibers on relative humidity from 0 % to 100 % at 25 °C [47]

849 nm does not shift as the humidity is continuously decreased from 90 % to 50 % within 4 hours [24]. It has also been discovered that prestretching a grating can eliminate the uncertainty of humidity response as well as reduce response time [51].

Equivalent to relative humidity, POFBGs are sensitive to concentration of various water solutions because of different equilibrium relative humidity or the water activity of solutions. It has been demonstrated that the Bragg wavelength of POFBGs in PMMA fibers depends on the concentration of saline solutions and sugar solutions [12, 52]. For the concentration from 0 % to 22 %, the Bragg wavelength of the POFBG in PMMA-based fibers shifts 0.9 nm, paving the way for POFBGs as biochemical concentration sensors. In essence, this dependence is due to the balanced water absorption/desorption between the fiber and the surrounding medium. That is, POFBGs in PMMA fibers can perform as an indicator of the water activity of the surrounding medium [52].

Strain Response

Most FBG sensors are based on their strain response following the equation

$$\frac{\Delta\lambda}{\lambda} = (1 - p_e)\epsilon$$

where p_e is the effective strain-optic coefficient and ϵ is the strain applied on the FBG. The strain sensitivity ($\Delta\lambda/\epsilon$) of PFBGs ranges from 0.64 to 1.48 pm/με [7, 11, 26, 39, 40, 53], depending on the material and the peak wavelength. Though the upper limit is a bit higher than strain sensitivity of silica FBGs (∼1 pm/με), the superiority is minimal.

Broad elastic range and large break strain of POFs make POFBGs attractive for strain sensors that require large strain range and high sensitivity. Therefore, strain

response is another extensively studied property of POFBGs. Bare POFBGs at 1536 nm in PMMA-based fibers can be tuned over 50 nm by applying a strain of 3.6 % with a sensitivity of 1.46 pm/με, while the intensity of the Bragg peak only decreases slightly; Most importantly, the wavelength shift is reversible [7]. It has been shown that the elongation to break for the PMMA fibers can be up to 30 % [54], though practically, such large strain measuring range is unreachable because the FBG interrogators or optical spectrum analyzer cannot cover such broad wavelength range.

Applications of Polymer Optical Fiber Bragg Gratings

Fiber Laser

Using a POFBG as a reflecting mirror, Liu et al. demonstrated a tunable fiber ring laser [8]. They used erbium-doped fiber (EDF) rings as the gain media, pumped by a semiconductor laser diode emitting at 980 nm. The POFBG is connected to one end of the circulator with the EDF, acting as the reflection mirror of the ring laser and also the wavelength selector. The emitting wavelength of the laser can be continuously tuned over a range of 35 nm by simply applying tension on the POFBG. The tunable laser has a strain sensitivity of 1.48 pm/με at 1534 nm.

Localized Strain Monitoring of Tapestries

Ye et al. attached two POFBGs and two silica FBGs to measure the localized strain at the position where the gratings are bonded [55]. By combing the response of FBGs and strain map obtained from a digital image correlation system, the strain transfer coefficient and reinforcement coefficient are calculated. It was found that the POFBGs provide improved strain transfer coefficients compared to silica FBGs and thus are more suitable for textile monitoring because of the lower Young's modulus of POF. This application represents the first attempt of utilizing the POFBG away from the optical bench.

In Situ Monitoring of Composite Material

FBGs have been embedded into materials to monitor inner stress, temperature, and curing process because of their small size [56]. Compared to silica FBGs that are suitable only for stiff-structure materials, POFBGs are usable for both stiff and soft materials for low modulus of POFs. For example, Rajan and coworkers embed a POFBG along with a silica FBG in composite materials to compare their performance upon thermal and mechanical loading on the composite [57]. The temperature sensitivity of the POFBG is close to that in free space,

while the embedded silica FBG shows higher temperature sensitivity. By using the POFBG, the localized temperature and thermal expansion of the composite can be obtained.

Electrically Tunable Bragg Grating Filter

FBGs have been successfully used as wavelength filters in wavelength-division multiplexing, and they are also made tunable by using various techniques [58]. Kalli et al. coated a palladium/copper (Pd/Cu) metallic layer via the photochemical deposition on a fiber written with a FBG [9, 38]. When the metallic layer is electrically connected, Joule heating leads to temperature increase and the thermal expansion of the fiber and thus Bragg wavelength red-shift of the POFBG. A wavelength shift of 2 nm is realized by an input power of 160 mW, making it suitable for filters. The average input power coefficient of the filter is 1.34 pm/mW with a time constant of 1.7 s^{-1}. This application demonstrates that POFBGs are useful not only for sensing applications but also for fiber communication.

Sensing of Moisture in Fuel

By exploiting their sensitivity to humidity or water activity, POFBGs are utilized to detect moistures in the jet fuel [49]. A wavelength shift of 1.6 nm is observed when the POFBG is moved from the dry fuel (15–20 ppm water) to wet fuel (120–150 ppm water) at room temperature. One major issue hampering the practical application of this technology is the long response time (tens of minutes). To address the issue of long response time because of slow diffusion of moisture through the fiber cladding to the fiber core, drawing fiber with smaller diameter or etching the fiber cladding are two effective methods experimentally proved [59].

Mechanical Sensor

FBGs are sensitive to strain and have been widely used to sense strain and pressure, etc. Various sensors based on POFBGs have been demonstrated. By etching a single-mode POFBG down to a diameter of 30 um, a force sensitivity of 643 nm/N is achieved, and a pressure sensor by attaching the etched grating to a vinyl diaphragm in a hard plastic tube provides sensitivity as high as 1.32 pm/Pa [60]. Chen et al. demonstrated a highly sensitive bending sensor by inscribing Bragg grating in an eccentric core polymer optical fiber, and the sensor has a bend sensitivity of 63 pm/m^{-1} in the curvature range of ± 22.7 m^{-1} [10, 61]. By embedding two POFBGs in a block of PDMS rubber (Fig. 8), Zhang et al. developed a soft fiber-optic sensor that can simultaneously measure the press and shear stress applied on the top surface of the block [62]. Due to low Young's modulus of POFs and proper sensor design, a pressure sensitivity of 0.8 pm/Pa and a stress sensitivity of 1.3 pm/Pa are realized.

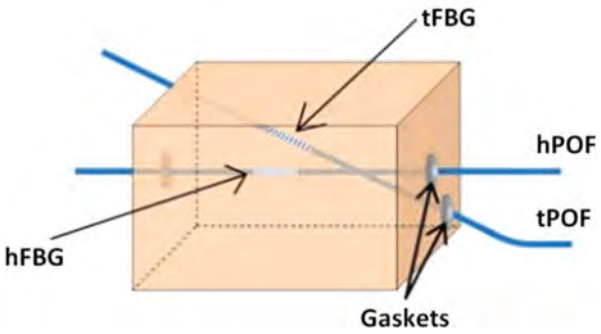

Fig. 8 Diagram of the sensor for pressure and shear measurement. Two POFBGs are embedded in a PDMS matrix. One is horizontal (*hFBG*) while the other is tilted (*tFBG*)

Summary

Inscription, properties, and applications of the POFBG are presented. POFBGs have been inscribed in both solid and microstructured types, doped and undoped POFs based on PMMA or COC polymers. Two widely used methods, the phase mask technique and the interference technique, are introduced. Lastly typical applications of POFBGs are described. POFBGs, as a supplement to silica FBGs, provide some unrivaled properties unattainable by silica counterparts. As the fabrication of single-mode POFs and grating writing processes improve, POFBGs will find more applications in future.

References

1. Webb DJ, Kalli K (2011) Polymer fiber Bragg gratings. In: Fiber bragg grating sensors: recent advancements, industrial applications and market exploitation, 1st edn. Bentham Science Publishers, United Arab Emirates, pp 292–312
2. Peng GD, Xiong Z, Chu PL (1999) Photosensitivity and gratings in dye-doped polymer optical fibers. Opt Fiber Technol 5:242–251
3. Berghmans F, Geernaert T, Baghdasaryan T, Thienpont H (2014) Challenges in the fabrication of fibre Bragg gratings in silica and polymer microstructured optical fibres: fabrication of Bragg gratings in microstructured fibers. Laser Photonics Rev 8:27–52. doi:10.1002/lpor.201200103
4. Liu HY, Peng GD, Chu PL (2002) Thermal stability of gratings in PMMA and CYTOP polymer fibers. Opt Commun 204:151–156
5. Xiong Z, Peng GD, Wu B, Chu PL (1999) Highly tunable Bragg gratings in single-mode polymer optical fibers. IEEE Photon Technol Lett 11:352–354. doi: 10.1109/68.748232
6. Liu H, Liu H, Peng G, Chu P (2003) Observation of type I and type II gratings behavior in polymer optical fiber. Opt Commun 220:337–343. doi: 10.1016/S0030-4018(03)01454-8
7. Liu HY, Liu HB, Peng GD (2005) Tensile strain characterization of polymer optical fibre Bragg gratings. Opt Commun 251:37–43. doi: 10.1016/j.optcom.2005.02.069
8. Liu H, Peng G, Liu H, and Chu PL (2006) Polymer fibre bragg gratings tunable laser. In: Optical fiber communication conference and exposition and the national fiber optic engineers conference. Anaheim, California, p OWM7

9. Kalli K, Dobb HL, Webb DJ et al (2007) Development of an electrically tuneable Bragg grating filter in polymer optical fibre operating at 1.55 μm. Meas Sci Technol 18:3155–3164. doi: 10.1088/0957-0233/18/10/S17
10. Chen X, Zhang C, Webb DJ et al (2010) Bragg grating in a polymer optical fibre for strain, bend and temperature sensing. Meas Sci Technol 21:094005. doi: 10.1088/0957-0233/21/9/094005
11. Luo Y, Yan B, Li M et al (2011) Analysis of multimode POF gratings in stress and strain sensing applications. Opt Fiber Technol 17:201–209. doi: 10.1016/j.yofte.2011.02.005
12. Zhang W, Webb D, Peng G (2012) Polymer optical fiber Bragg grating acting as an intrinsic biochemical concentration sensor. Opt Lett 37:1370–1372
13. Rajan G, Mohd Noor MY, Lovell NH et al (2013) Polymer micro-fiber Bragg grating. Opt Lett 38:3359. doi: 10.1364/OL.38.003359
14. Dobb H, Webb DJ, Kalli K et al (2005) Continuous wave ultraviolet light-induced fiber Bragg gratings in few- and single-mode microstructured polymer optical fibers. Opt Lett 30:3296–3298
15. Webb DJ, Kalli K, Zhang C et al (2008) Temperature sensitivity of Bragg gratings in PMMA and TOPAS microstructured polymer optical fibres. In: Proceedings of the SPIE 6990 photonic crystal. Fibers II. Strasbourg, France, p 69900L
16. Johnson IP, Kalli K, Webb DJ (2010) 827 nm Bragg grating sensor in multimode microstructured polymer optical fibre. Electron Lett 46:1217. doi: 10.1049/el.2010.1595
17. Johnson IP, Webb DJ, Kalli K (2011) Utilisation of thermal annealing to record multiplexed FBG sensors in multimode microstructured polymer optical fibre. In: Bock WJ, Albert J, Bao X (eds) Proceedings of the SPIE 7753 21st international conference on optical fiber sensors, Ottawa, p 77536T
18. Bundalo I-L, Nielsen K, Markos C, Bang O (2014) Bragg grating writing in PMMA microstructured polymer optical fibers in less than 7 minutes. Opt Express 22:5270. doi: 10.1364/OE.22.005270
19. Yu J, Tao X, Tam H (2004) *Trans*-4-stilbenemethanol-doped photosensitive polymer fibers and gratings. Opt Lett 29:156–158
20. Zhang ZF, Zhang C, Tao XM et al (2010) Inscription of polymer optical fiber Bragg grating at 962 nm and its potential in strain sensing. IEEE Photon Technol Lett 22:1562–1564. doi: 10.1109/LPT.2010.2069090
21. Luo Y, Zhang Q, Liu H, Peng G-D (2010) Gratings fabrication in benzildimethylketal doped photosensitive polymer optical fibers using 355 nm nanosecond pulsed laser. Opt Lett 35:751–753
22. Cheng XS, Qiu WW, Wu WX et al (2011) High-sensitivity temperature sensor based on Bragg grating in BDK-doped photosensitive polymer optical fiber. Chin Opt Lett 9:020602–020604. doi: 10.3788/COL201109.020602
23. Sáez-Rodríguez D, Nielsen K, Rasmussen HK et al (2013) Highly photosensitive polymethyl methacrylate microstructured polymer optical fiber with doped core. Opt Lett 38:3769. doi: 10.1364/OL.38.003769
24. Yuan W, Khan L, Webb DJ et al (2011) Humidity insensitive TOPAS polymer fiber Bragg grating sensor. Opt Express 19:19731–19739
25. Johnson IP, Yuan W, Stefani A et al (2011) Optical fibre Bragg grating recorded in TOPAS cyclic olefin copolymer. Electron Lett 47:271. doi: 10.1049/el.2010.7347
26. Yuan W, Webb DJ, Kalli K et al (2011) 870 nm Bragg grating in single mode TOPAS microstructured polymer optical fibre. In: Proceedings of the SPIE 7753, 21st international conference on optical fiber sensors. Ottawa, Canada, p 77538X
27. Johnson IP, Yuan W, Stefani A et al (2011) Humidity insensitive TOPAS polymer fiber Bragg grating sensor. Electron Lett 47:271–272
28. Oliveira R, Marques CAF, Bilro L, Nogueira RN (2014) Production and characterization of Bragg gratings in polymer optical fibers for sensors and optical communications. Procedia Technology 15:138–146

29. Peng GD, Chu PL, Xiong Z et al (1996) Dye-doped step-index polymer optical fiber for broadband optical amplification. Light Technol J 14:2215–2223
30. Hu X, Sáez-Rodríguez D, Bang O et al (2014) Investigations on birefringence effects in polymer optical fiber Bragg gratings. In: Proceedings of the SPIE 9128, micro-structured and specialty optical fibres III. Brussels, Belgium, p 91280Q
31. Xiong Z, Peng GD, Wu B, Chu PL (1999) Effects of the zeroth-order diffraction of a phase mask on Bragg gratings. Light Technol J 17:2361–2365. doi: 10.1109/50.803031
32. Rajan G, Mohd Noor MY, Ambikairajah E, Peng G-D (2014) Inscription of multiple Bragg gratings in a singlemode polymer optical fiber using a single phase mask and its analysis. IEEE Sens J 14:2384–2388. doi: 10.1109/JSEN.2014.2311121
33. Peng GD, Xiong Z, Chu PL (1999) Photosensitivity and gratings in dye-doped polymer optical fibers. Opt Fiber Technol 5:242–251. doi: 10.1006/ofte.1998.0298
34. Sáez-Rodríguez D, Nielsen K, Bang O, Webb DJ (2014) Photosensitivity mechanism of undoped poly(methyl methacrylate) under UV radiation at 325 nm and its spatial resolution limit. Opt Lett 39:3421. doi: 10.1364/OL.39.003421
35. Bowden MJ, Chandross EA, Kaminow IP (1974) Mechanism of the photoinduced refractive index increase in polymethyl methacrylate. Polym Eng Sci 14:494–497
36. Liu HY, Peng GD, Chu PL (2001) Thermal tuning of polymer optical fiber Bragg gratings. IEEE Photon Technol Lett 13:824–826. doi: 10.1109/68.935816
37. Zhang C, Zhang W, Webb DJ, Peng G-D (2010) Optical fibre temperature and humidity sensor. Electron Lett 46:643–644. doi: 10.1049/el.2010.0879
38. Carroll KE, Zhang C, Webb DJ et al (2007) Thermal response of Bragg gratings in PMMA microstructured optical fibers. Opt Express 15:8844–8850
39. Liu H, Liu H, Peng G, Chu P (2003) Strain and temperature sensor using a combination of polymer and silica fibre Bragg gratings. Opt Commun 219:139–142. doi: 10.1016/S0030-4018(03)01313-0
40. Yuan W, Stefani A, Bache M et al (2011) Improved thermal and strain performance of annealed polymer optical fiber Bragg gratings. Opt Commun 284:176–182. doi: 10.1016/j.optcom.2010.08.069
41. Waxler RM, Horowitz D, Feldman A (1979) Optical and physical parameters of Plexiglas 55 and Lexan. Appl Opt 18:101–104
42. Cariou J-M, Dugas J, Martin L, Michel P (1986) Refractive-index variations with temperature of PMMA and polycarbonate. Appl Opt 25:334–336
43. Moshrefzadeh RS, Radcliffe MD, Lee TC, Mohapatra SK (1992) Temperature dependence of index of refraction of polymeric waveguides. Light Technol J 10:420–425
44. Jewell JM (1991) Thermooptic coefficients of some standard reference material glasses. J Am Ceram Soc 74:1689–1691. doi: 10.1111/j.1151-2916.1991.tb07162.x
45. Harbach GN, Limberger HG, Salathé RP (2010) Influence of humidity and temperature on polymer optical fiber Bragg gratings. Bragg Gratings Photosensit. Poling Glass Waveguides. Optical Society of America, Karlsruhe Germany, p BTuB2
46. Harbach NG (2008) Fiber Bragg gratings in polymer optical fibers. PhD, Ecole Polytechnique Federale de Lausanne
47. Zhang ZF, Tao XM (2013) Intrinsic temperature sensitivity of fiber Bragg gratings in PMMA-based optical fibers. IEEE Photon Technol Lett 25:310–312. doi: 10.1109/LPT.2012.2235421
48. Zhang ZF, Tao XM (2012) Synergetic effects of humidity and temperature on PMMA based fiber Bragg gratings. Light Technol J 30:841–845. doi: 10.1109/JLT.2011.2182336
49. Zhang C, Chen X, Webb DJ, Peng G-D (2009) Water detection in jet fuel using a polymer optical fibre Bragg grating. In: Jones JDC (ed) Proceedings of the SPIE 7503 20th international conference on optical fibre sensors, p 750380
50. Zhang W, Webb DJ (2014) Factors influencing temperature sensitivity of PMMA based optical fiber Bragg gratings. In: Proceedings of the SPIE 9128, micro-structured and specialty optical fibres III. Brussels, Belgium, p 91280M

51. Zhang W, Webb DJ (2014) Humidity responsivity of poly(methyl methacrylate)-based optical fiber Bragg grating sensors. Opt Lett 39:3026. doi: 10.1364/OL.39.003026
52. Zhang W, Webb DJ (2014) Polymer optical fiber grating as water activity sensor. In: Proceedings of the SPIE 9128, micro-structured and specialty optical fibres III. Brussels, Belgium, p 91280F
53. Stefani A, Wu Y, Markos C, Bang O (2011) Narrow bandwidth 850-nm fiber Bragg gratings in few-mode polymer optical fibers. IEEE Photon Technol Lett 23:660–662. doi: 10.1109/LPT.2011.2125786
54. Jiang C, Kuzyk MG, Ding J-L et al (2002) Fabrication and mechanical behavior of dye-doped polymer optical fiber. J Appl Phys 92:4. doi: 10.1063/1.1481774
55. Ye CC, Dulieu-Barton JM, Webb DJ et al (2009) Applications of polymer optical fibre grating sensors to condition monitoring of textiles. J Phys Conf Ser 178:012020
56. Colpo F, Humbert L, Botsis J (2007) Characterisation of residual stresses in a single fibre composite with FBG sensor. Compos Sci Technol 67:1830–1841. doi: 10.1016/j.compscitech.2006.10.024
57. Rajan G, Ramakrishnan M, Semenova Y et al (2014) Experimental study and analysis of a polymer fiber Bragg grating embedded in a composite material. Light Technol J 32:1726–1733. doi: 10.1109/JLT.2014.2311441
58. Goh CS, Mokhtar MR, Butler SA et al (2003) Wavelength tuning of fiber Bragg gratings over 90 nm using a simple tuning package. IEEE Photon Technol Lett 15:557–559. doi: 10.1109/LPT.2003.809300
59. Zhang W, Webb DJ, Peng G-D (2012) Investigation into time response of polymer fiber Bragg grating based humidity sensors. Light Technol J 30:1090–1096. doi: 10.1109/JLT.2011.2169941
60. Rajan G, Liu B, Luo Y et al (2013) High sensitivity force and pressure measurements using etched singlemode polymer fiber Bragg gratings. IEEE Sens J 13:1794–1800. doi: 10.1109/JSEN.2013.2242883
61. Chen XF, Zhang C, Webb DJ et al (2010) Highly sensitive bend sensor based on Bragg grating in eccentric core polymer fiber. IEEE Photon Technol Lett 22:850–852
62. Zhang ZF, Tao XM, Zhang HP, Zhu B (2013) Soft fiber optic sensors for precision measurement of shear stress and pressure. IEEE Sens J 13:1478–1482. doi: 10.1109/JSEN.2012.2237393

Part III

Product Integration and Evaluation Technologies

Vladan Koncar and Xiaoming Tao

Applications of Electrospun Nanofibers for Electronic Devices

24

Jian Fang, Hao Shao, Haitao Niu, and Tong Lin

Contents

Introduction 618
Electrospun Nanofibers in Electronic Devices 619
Dye-Sensitized Solar Cells 619
Mechanical-to-Electric Energy Harvesters 622
Lithium-Ion Batteries 624
Supercapacitors 627
Sensors 629
Field-Effect Transistors 639
P–N Diodes 642
Light-Emitting Diodes 643
UV Photodetectors 645
Electrochromic Devices 648
Other Electronic Devices 650
Summary 650
References 650

Abstract

In recent decades, electrospinning of nanofibers has progressed very rapidly in both scientific and technological aspects, and electrospun nanofibers have shown enormous potential for various applications. In particular, electrospun nanofibers have significantly enhanced the application performance of many electronic devices, such as solar cells, mechanical-to-electric energy harvesters, rechargeable batteries, supercapacitors, sensors, field-effect transistors, diodes,

J. Fang • H. Shao • H. Niu • T. Lin (✉)
Institute for Frontier Materials, Deakin University, Geelong, VIC, Australia
e-mail: jian.fang@deakin.ed.au; ney@deakin.edu.au; haitao.niu@deakin.edu.au; tong.lin@deakin.edu.au

© Springer Science+Business Media Singapore 2015

X. Tao (ed.), *Handbook of Smart Textiles*,
DOI 10.1007/978-981-4451-45-1_32

photodetectors, and electrochromic devices. This chapter provides a comprehensive summary on the recent progress in the application of electrospun nanofibers in electronic devices.

Keywords
Electrospinning • Nanofibers • Nanofibrous materials • Electronic devices

Introduction

Electrospinning is a simple but efficient method to prepare continuous fibers with a diameter in the range of nano- to micrometer scale. In a typical electrospinning process, a polymer fluid, either solution or melt, is charged by a high-voltage electric field. Acted by the electric field, the polymer fluid at the spinneret deforms into a cone shape, which is so called "Taylor cone". Jet is ejected from the apex of the cone, when the electric force overcomes the surface tension of the polymer fluid. This charged jet through intensive interactions with the electric field undergoes a whipping instability to stretch it thinner. Meanwhile, charge repulsion within the jet assists in stretching the jet into finer filament. Further solidification of the polymer filament through solvent evaporation or cooling results in solid fibers, which deposit on the collector electrode forming a randomly orientated nonwoven web in most cases. From spinneret to collector electrode, electrospinning takes place very rapidly.

Electrospinning is versatile to process a wide choice of materials, including polymers, inorganic sol–gels, and biomaterials. Fiber diameter, morphology, and fibrous structure are controllable through adjusting the operating parameters and material properties. For example, uniform fibers, beads-on-string structure, porous fibers, hollow fibers, bicomponent fibers (e.g., side-by-side, core–sheath), aligned fiber webs, and three-dimensional fibrous architectures can be prepared by special spinning conditions or modified electrospinning setup. These advantages make electrospinning a key technology to prepare nanofibers with large-scale production potential.

Electrospun nanofibers often have large surface-to-weight (or volume) ratio. The continuous fiber structure makes electrospun fibers less likely to agglomerate into a dense structure. As a result, electrospun fibrous webs are highly porous with excellent pore interconnectivity. These unique features, together with the functionality from the fiber materials, have opened up many applications in areas such as energy generation and storage, environment protection, biomedical, functional clothing, and defense. The importance and ongoing research progress in the application development of electrospun nanofibers have been summarized in previous review articles [1–4]. Illustration 1 highlights the application of electrospun nanofibers in electronics. Electrospun nanofibers function like an active material or important part in electronic devices, and their use either enhances the device performance or adds novel feature. In this chapter, details on the novel applications of electrospun nanofibers in electronic devices are summarized.

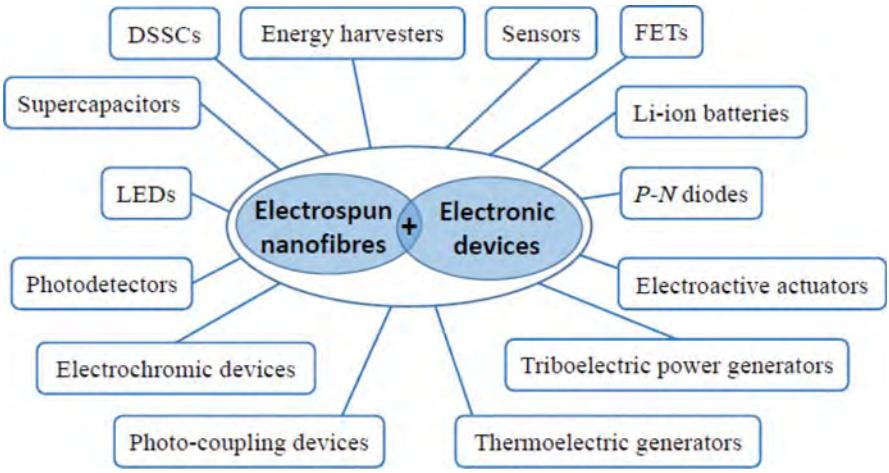

Illustration 1 Applications of electrospun nanofibers in electronic devices

Electrospun Nanofibers in Electronic Devices

Electrospun nanofibers have shown application potential in many types of electronic devices, such as solar cells, mechanical-to-electric energy harvesters, rechargeable batteries, supercapacitors, sensors, field-effect transistors, diodes, photodetectors, and electrochromic devices. Depending on the application requirements, electrospun nanofibers are used either in the form of single filament, fibrous web, or aligned fiber array. Their uses are based on the inherent property of nanofiber, the large surface area, the highly porous fibrous structure, or these combinations. The easy modification of nanofiber through modification of electrospinning solution is of great benefit to the applications of electrospun nanofibers in diverse electronic devices, especially in biosensors and electrodes for batteries. Detailed applications of electrospun nanofibers in each electronic device are described below.

Dye-Sensitized Solar Cells

Dye-sensitized solar cells (DSSCs) represent emerging solar energy devices. In comparison with silicon-based solar cells, DSSCs are advantageous in low production cost, simple cell structure, and high flexibility. In recent decades, DSSCs have attracted great attention in both scientific and industrial sectors.

Figure 1a depicts the structure of a typical DSSC device and its working principle. The device mainly consists of a working electrode made of inorganic semiconductor nanocrystal, a layer of dye sensitizer molecules covering the working electrode surface, a counter electrode, and electrolyte. Upon light

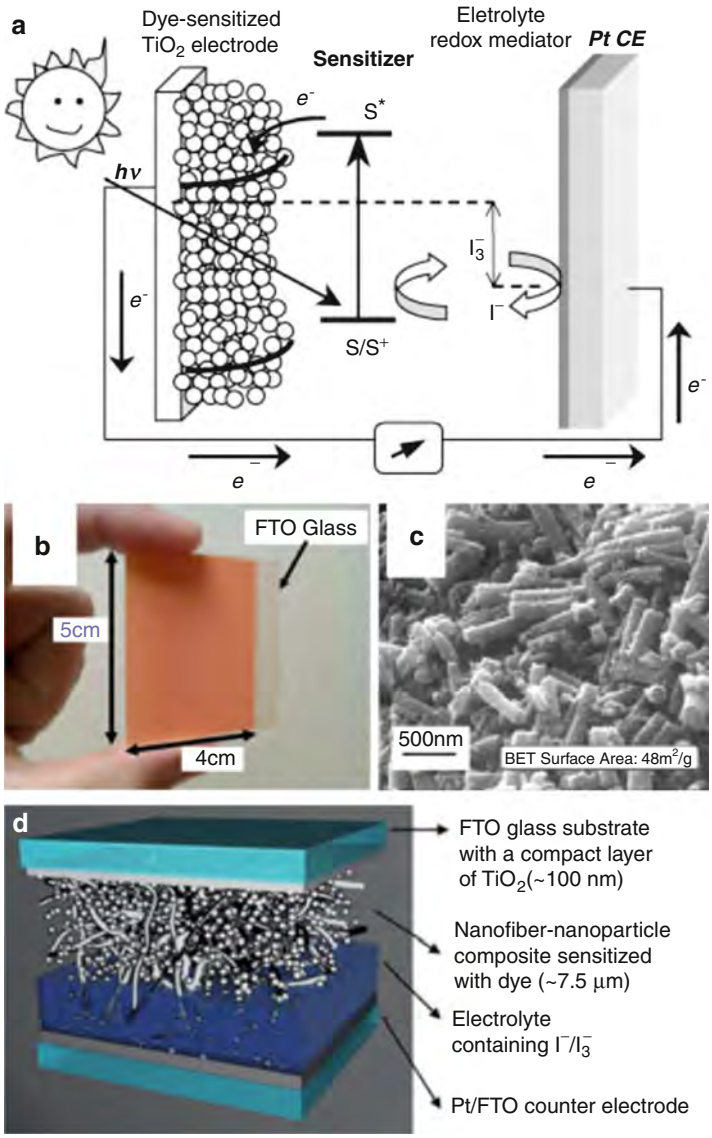

Fig. 1 (**a**) Schematic illustration of a typical DSSC device and its working principle, (**b**) digital and (**c**) SEM image of a working electrode made of shortened TiO_2 nanofibers, (**d**) an illustrated composite electrode with both TiO_2 nanofibers and nanoparticles (Reprinted with permission from Refs. [5–7])

irradiation, photons excite the sensitizer molecules, creating electron–hole pairs. The photo-generated electrons move to the conduct band of the working electrode and then flow to the counter electrode through the external load circuit. At the same time, the oxidized sensitizer molecules capture electrons from the electrolyte to

balance their charge for the next excitation. The electrolyte is regenerated by reduction at the counter electrode [8].

Working electrode forms the critical part of DSSC devices. For efficient photoelectron injection, the band gap of the semiconducting nanocrystal layer (normally made of TiO_2) is required to match well with the band structure of the dye sensitizer. To enhance light harvest and charge transport, the working electrode with a large surface area and good stability in electrolyte is highly desired. Conventionally, TiO_2 nanoparticles are used for making the DSSC working electrode because of the large surface area and high dye adsorption ability. However, the small grain size and a massive number of grain boundaries between TiO_2 nanoparticles often lead to high charge transfer resistance and lowenergy-conversion efficiency. It was expected that one-dimensional semiconductor nanomaterials have higher charge transfer efficiency than nanoparticles.

In early works reported on using electrospun nanofibers for making DSSC devices, newly electrospun TiO_2 precursor nanofibers were directly deposited onto conductive glass. After calcination and loading with dye sensitizer, the TiO_2 working electrode was assembled into DSSC devices. However, the resulting DSSC device showed worse photovoltaic property when compared to that made of TiO_2 nanoparticles [9]. The low solar cell performance was attributed to the lower surface area of TiO_2 nanofibers than TiO_2 nanoparticles, decreased TiO_2 material density, and poor adhesion with the substrate.

Several methods have been reported to improve the device performance of nanofiber-based DSSCs. TiO_2 nanofibers were ground mechanically into short length, and a slurry was then prepared by mixing the shortened nanofibers with a solvent. By spraying the slurry onto conductive glass, densely packed nanofiber electrode was finally prepared. Figure 1b and c illustrates the electrode prepared and the morphology of shortened TiO_2 nanofibers within the electrode [6]. The electrode prepared in this way showed significant increase in surface area and adhesion between the nanofiber and the underlying substrate. Consequently, the DSSC devices showed a comparable energy conversion efficiency to nanoparticle-based devices.

Increasing the light-harvesting ability is a practical approach to improving the energy efficiency of DSSCs. For this purpose, light-scattering layer is often integrated with DSSC devices. Three main strategies are often employed to enhance the light-scattering ability: (1) incorporation of large semiconducting particles into the electrode, (2) adding a separate light-scattering layer, and (3) synthesizing a special TiO_2 structure with both energy conversion and light-scattering ability. Electrospun nanofibers have been used in all the three strategies. For example, a composite working electrode was fabricated from electrospun TiO_2 nanofibers and TiO_2 nanoparticles, as illustrated in Fig. 1d [7]. By adding 15 % TiO_2 nanofibers into nanoparticle layer, the dye molecule loading on the electrode was reported to decrease by only 6.17 %. However, the energy conversion efficiency was increased significantly from 6.1 % (electrode made of pure nanoparticles) to 8.8 %. In comparison, the energy efficiency for the device made of pure nanofibers was only 2.9 %. Nanofibers in the composite electrode function like both light-harvesting layer and energy convertor.

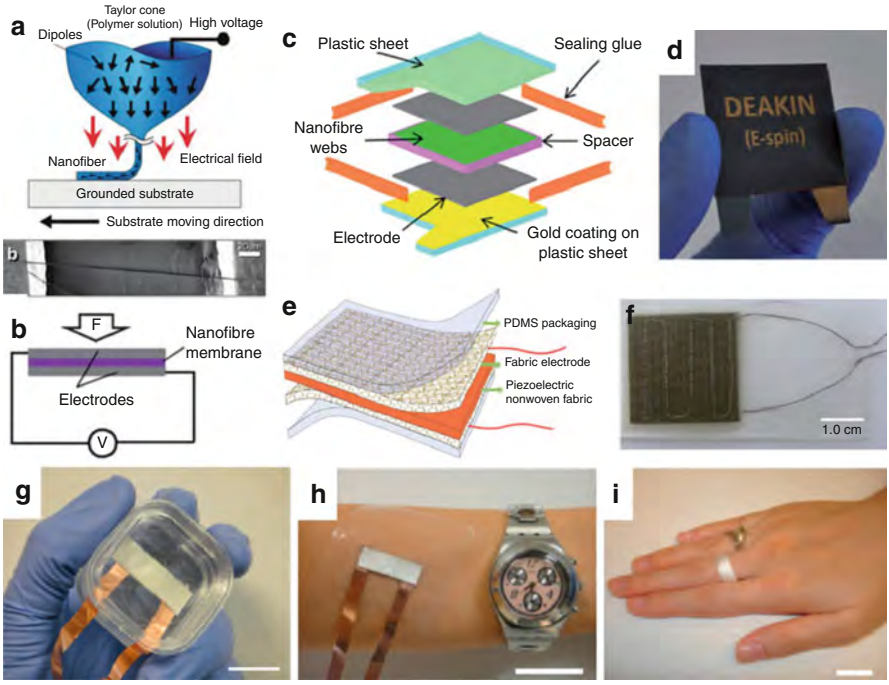

Fig. 2 Mechanical energy harvesters prepared from electrospun (**a~f**) PVDF and (**g~i**) PVDF-TrFE nanofibers (Reprinted with permission from Refs. [10–14])

Mechanical-to-Electric Energy Harvesters

Piezoelectric materials can convert a mechanical deformation into electricity. They have been used for making electrical transducers, mechanical sensors, and energy harvesters. Conventionally, piezoelectric materials are prepared either from inorganic compounds containing toxic elements or polymers which require a series of treatment including drawing at a high ratio and poling in a high electric field at an elevated temperature.

Electrospinning has shown advantages in processing piezoelectric polymers for energy harvesting applications. Using poly(vinylidene fluoride) (PVDF) or poly (vinylidene fluoride-co-trifluoroethylene) (PVDF-TrFE) as the models, several groups have reported the interesting piezoelectric property of electrospun nanofibers. Figure 2 summarizes energy harvesting devices prepared by electrospun nanofibers.

Nanofiber energy generators was reported by Chang et al. [10] who used a near-field electrospinning to prepare and deposited a single PVDF nanofiber between two metal electrodes. The near-field PVDF electrospinning technique and nanofiber device are illustrated in Fig. 2a. The device was able to convert small mechanical vibrations into an electric output around 30 mV and 3 nA. Hansen et al. [15] used a

normal electrospinning to prepare aligned PVDF nanofibers on a parallel electrode pair. The nanofibers were then subjected to an in-plane polarization treatment. The piezoelectric PVDF nanofibers were combined with an enzymatic biofuel cell device to harvest both mechanical and biochemical energies. This hybrid energy harvester was reported to be able to power a ZnO nanowire UV light sensor.

Later on, randomly-orientated PVDF nanofiber webs were reported to show large electric outputs. Using a needle electrospinning setup, Fang et al. [11] prepared PVDF nanofiber nonwoven mats. A simple energy harvesting device was prepared by sandwiching the nonwoven mat with two metal foils. When the device received a compressive impact, voltage output on the level of volts and current on the level of microamperes resulted (Fig. 2b). Although PVDF nanofibers have not undergone an extra stretching and electric poling treatment, they already contained a high content of β crystal phase. Mandal et al. [16] measured the CF_2 dipoles in PVDF-TrFE nanofiber webs using polarized FTIR spectroscopy and reported that PVDF-TrFE oriented during electrospinning to make CF_2 dipoles orientate along the web thickness.

It is known that PVDF has five molecular configurations which correspond to five different crystal phases, i.e., α, β, γ, δ, and ε in the solid state. The α phase is the most thermally stable state, while the β accounts for the piezoelectric property because of the largest dipole moment among the five crystal phases. Normally, raw PVDF is α phase-dominated with very low β phase content. However, when PVDF solution is subjected to an electrospinning process, the resulting nanofibers show unexpected high β crystal phase. This was explained by the electrospinning process. During electrospinning, the jet undergoes a high ratio mechanical stretching. Meanwhile, the existence of a high electric field allows the electric dipole in the PVDF chains to orientate along the spinning direction. Therefore, the inherent mechanical stretching and electric poling in electrospinning facilitate the formation of piezoelectric β crystal phase in the PVDF nanofibers.

To obtain an integrated device, an energy harvesting device consisting of a PVDF nanofiber layer, a space layer, two metal electrodes, and sealing materials was fabricated (Fig. 2c and d) [12]. A needleless electrospinning technique using a rotating disk fiber generator was used to prepare PVDF nanofibers on large scales. Since the use of a much higher applied voltage than conventional electrospinning, needleless electrospinning produced PVDF nanofibers with higher β crystal phase content, and the energy harvesting device made of needleless electrospinning showed better energy conversion performance as well.

In another study, elastic conducting fabrics were used as the top and bottom electrodes to fabricate all-fiber flexible energy harvesters (Fig. 2e and f) [13]. By using an electrospun PVDF-$NANbO_3$ nanofiber web as the active layer, the energy harvesters generated high peak voltage (3.4 V) and current (4.4 μA) when they were pressed repeatedly (0.2 MPa at 1 Hz). The device had excellent stability, even after 1,000,000 compression cycles.

In addition to harvesting compressive energy, electrospun PVDF nanofibers can also convert other mechanical energies (e.g., bending energy) into electricity. For example, aligned PVDF-TrFE nanofibers were prepared using a needle

electrospinning technique [14]. An energy device was prepared by placing two copper strips on the same side of the nanofiber web (Fig. 2g). By bending the energy harvesting device, electric outputs were generated. Such a device was reported to generate higher electric energy from bending than compressing. The same research group also demonstrated the potential use of aligned PVDF-TrFE nanofibers to detect mechanical vibration.

The usability of the electric energy generated by electrospun PVDF nanofiber devices has been demonstrated by several groups. In general, electric energy generated by PVDF nanofiber devices is AC nature. The electric outputs are often rectified into DC power and then stored in a capacitor. When the electric energy stored is sufficient, it drives various electronic devices, such as light-emitting diodes, electronic cooler, and wireless devices. Nanofibrous energy harvesters reported are summarized in Table 1.

Lithium-Ion Batteries

Lithium-ion (Li-ion) batteries are dominating the market for clean energy storage because of the high energy density, long lifetime, and low memory effect. Li-ion battery is comprised of a cathode, an anode, an electrode separator, and electrolyte (Fig. 3a). When Li-ion battery is recharged, Li^+ ions move from the cathode to the anode, while Li^+ ions move reversely during discharge.

The electrode separator functions like a physical barrier to prevent the anode and the cathode from contact with each other. It plays a critical role in maintaining the battery performance and lifetime. Ideally, the separator should have a minimum effect on the diffusion of Li^+ ions between two electrodes. Good mechanical strength and chemical stability are essential to ensure long battery lifetime. Large electrolyte absorption and low ion resistance are important for battery performance, which require that the separator have a large surface area and high porosity. Polymers reported for making nanofiber-based Li^+ ion battery separator mainly include PVDF, PVDF-HFP, polyacrylonitrile (PAN), poly(methyl methacrylate) (PMMA), polyvinyl chloride (PVC), thermoplastic polyurethane (TPU), polyimide (PI), and cellulose.

A coaxial electrospinning technique was reported to prepare core–sheath polyimide (PI)/PVDF-HFP nanofibers for battery separator application [17]. In comparison with the separator prepared by pure nanofibers, this core–sheath nanofiber separator was more stable in liquid electrolyte and had higher battery discharge capacity, better isotropic mechanical strength, and thermal stability (Fig. 3d and e).

Apart from separator, anode and cathode were also reported to be prepared by electrospun nanofibers. Similar to the separator, the electrodes are also required to have a large surface area for effective interaction with lithium ions. Graphite has been widely used for making Li-ion battery anode. However, graphite-based batteries typically have low theoretical capacity and lithium intercalation voltage. Metal oxides (e.g., TiO_2, WO_3, NiO, and Fe_2O_3) particularly for those with a

Table 1 Nanofibrous mechanical-to-electric energy harvesting devices

Fiber material	Electrospinning method	Fiber diameter/fibrous structure	Mechanical energy	Electric output
PVDF	Near-field	700 nm/single fiber	0.076 % strain	1.5 mV
PVDF	Near-field	500 nm ~ 6.5 μm/single fiber	0.085 % strain, 0.5 Hz	8 mV/3 nA
PVDF	Near-field	1.6 μm/nonwoven	0.05 % strain, 7 Hz	76 mV/39 nA
PVDF	Near-field	900 nm ~ 2.5 μm/500 rows of well-aligned PVDF microfibers	0.5 % strain, 15 Hz	1.7 V/300 nA
Poly(γ-benzyl-L-glutamate) (PBLG)	Near-field	7.5 ~ 46.8 μm/aligned fibers	31.5 Hz	66 mV
PVDF	Conventional needle	183 ± 37 nm/nonwoven	5 Hz	2.21 V/3.5 μA
PVDF	Conventional needle	84.6 ± 23.5 nm/nonwoven	100 Hz	0.7781 V
PVDF	Conventional needle	800 nm/aligned fibers	0.05 % strain	20 mV/0.3 nA
PVDF	Conventional needle	800 nm/nonwoven	0.05 N	3.9 V
PVDF	Conventional needle	120 nm/nonwoven	Thumb effect	1 V
PVDF	Conventional needle	80 ~ 150 nm/nonwoven	100 dB, 1 μW/cm^2, 100 Hz	0.3 V
PVDF-MWCNTs	Conventional needle	600 ~ 700 nm/nonwoven	0.8 Hz	6 V
PVDF-TrFE	Conventional needle	60 ~ 120 nm/nonwoven	5.3 Hz, 0.2 MPa pressure	0.3 V
$BaTiO_3$/PVDF-TrFE	Conventional needle	500 nm/nonwoven	Bending test with a finger	25 μW
PVD/nickel chloride hexahydrate	Conventional needle	100 nm/nonwoven	1,000 με	0.4 V
PVDF-HFP/Ag nanoparticles	Conventional needle	83 nm/nonwoven	2 Hz, 15 kPa	3 V
Lead zirconate titanate (PZT)	Conventional needle	60 nm/fibers	Finger tap	1.63 V
$0.5Ba(Zr_{0.2}Ti_{0.8})O_3$–$0.5(Ba_{0.7}Ca_{0.3})TiO_3$ (BZT–BCT)	Conventional needle	175 nm/nonwoven	–	3.25 V/55 nA
PVDF	Needleless	214 nm/nonwoven	5 Hz, 10 N	2.6 V/4.5 μA

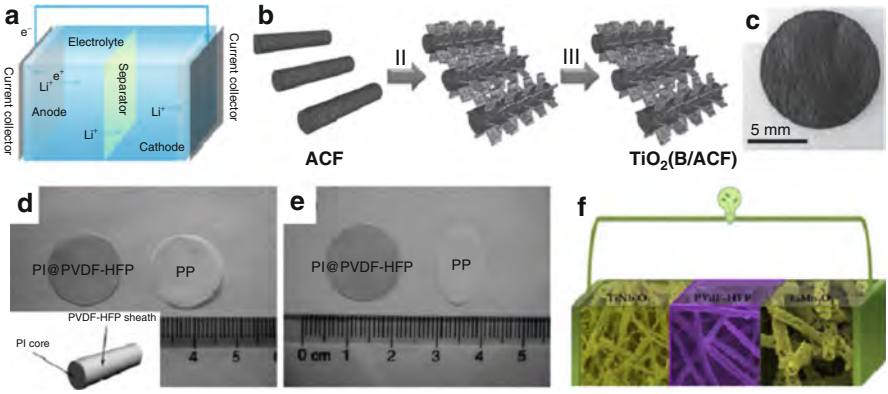

Fig. 3 (**a**) Illustration of Li-ion battery structure, (**b**) preparation of a composite anode with TiO_2 nanosheets on carbon nanofibers, (**c**) digital image of the composite anode, (**d**) comparison of PI@PVDF-HFP and PP separators before and after thermal treatment at 150 °C for 1 h, and (**e**) structure of an all-nanofiber Li-ion battery (Reprinted with permission from Refs. [17–20])

nanostructure have shown promising application as Li-ion battery anode. A hydrothermal technique was reported to grow TiO_2 nanosheets on carbon nanofibers which were prepared from electrospun PAN nanofibers (Fig. 3b and c) [19]. This TiO_2/carbon composite can form a free-standing film without using binder. The battery devices made of this TiO_2/carbon composite anode showed a high specific capacity of 90–220 mAh/g with excellent stability (cycling lifetime over 2,000). TiO_2 nanosheets on carbon nanofibers provide large surface and open pores, therefore reducing the length for lithium ions to diffuse and access to electrode.

Transition metal oxides such as $LiCoO_2$, $LiNiO_2$, and $LiFePO_4$ are often used as cathode materials for storing lithium ions. Among them, $LiCoO_2$ is the most used in commercial batteries because of the large theoretical capacity (140 mAh/g) and long charge–discharge cycle lifetime. However, the dissolution of lithium and cobalt ions during charging and discharging often leads to considerable reduction in capacity. This cathode dissolution issue can be effectively inhibited by covering $LiCoO_2$ nanofibers with a thin layer of MgO. $LiCoO_2$–MgO core–sheath nanofibers were prepared by a core–sheath electrospinning technique [21]. Battery made of the core–sheath nanofiber cathode can retain 90 % of the initial discharge capacity after 40 cycles of charge and discharge. For the device made of pure $LiCoO_2$ nanofiber cathode, only 52 % capacity was retained under the same testing condition.

Because of the versatility of using electrospun nanofiber as anode, cathode, and separator, an all-nanofiber battery was prepared using electrospun $TiNb_2O_7$ nanofibers as anode, electrospun $LiMn_2O_4$ as cathode, and a gelled PVDF-HFP nanofibrous web as the separator (Fig. 4f) [20]. The battery device had a working potential of 2.4 V with a reversible capacity of 116 mAh/g and an energy density of 280 Wh/kg.

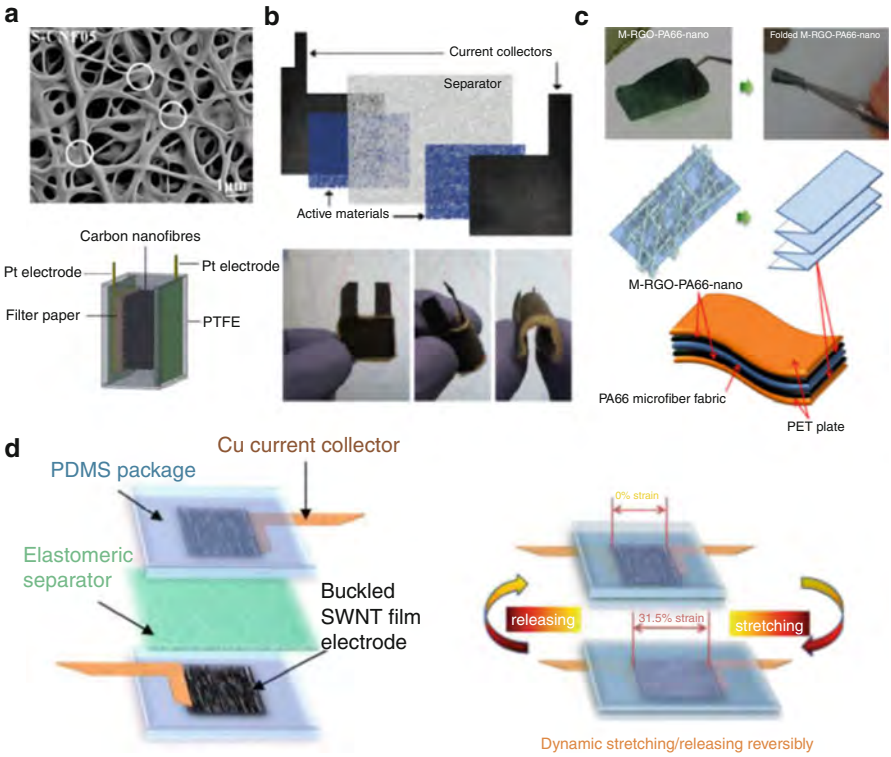

Fig. 4 Supercapacitors containing electrospun nanofibers (Reprinted with permission from Refs. [22–25])

Supercapacitors

Supercapacitors are high power density energy storage devices having wide applications in automobiles, consumer electronics, and backup power systems. Compared with secondary batteries, supercapacitors have higher charge–discharge rate and longer lifetime. Based on electrode materials used, supercapacitor devices can be classified into two categories: double-layer supercapacitor, which stores energy through the accumulation of electrostatic charges on the electrode/electrolyte interface, and pseudocapacitor, which stores energy based on redox reactions.

Porous carbons have been widely investigated as an electrode material in double-layer supercapacitors because of the large surface area, reasonable electrical conductivity, chemical/thermal stability, and low cost. Carbon nanofibers can be easily prepared by carbonization of electrospun polymer nanofibers. To this end, polyacrylonitrile (PAN) is often chosen as precursor polymer because of the soluble, but unmeltable feature. Double-layer supercapacitors made by carbonized PAN nanofiber electrode were reported to have a capacitance of 173 F/g [26].

Carbon nanofibers typically have an isolated fiber morphology with little inter-fiber connection. The lack of fibrous connection leads to low charge transfer within carbon nanofibers. It was reported that inter-fiber connection can be improved when side-by-side polyvinylpyrrolidone (PVP)/PAN bicomponent nanofibers were used as precursor [22]. During carbonization, PVP melted and tended to flow at the intersection areas of fibers, and it then carbonized at higher temperature to bond the two fibers together. In contrast, PAN did not melt, and it maintained the fibrous shape during the carbonization process. As a result, bonded carbon nanofibrous structure was formed through direct carbonization of side-by-side bicomponent PVP/PAN nanofibers (Fig. 4a). Compared with the carbon nanofibers prepared from the PAN only which show almost no inter-fiber connection, the inter-bonded carbon nanofibers show improved electrochemical capacitance because of their lower electrical resistivity.

Compared with electrical double-layer capacitors which have limited capacitance due to the limitation of surface charges accumulation, pseudocapacitors provide higher capacitance because of the fast and reversible faradic redox reaction of the electrode material. Transition metal oxides (such as V_2O_5, RuO_2, NiO_2, SnO_2, MnO_2, and TiO_2) are commonly used for making pseudocapacitor electrodes. For example, a supercapacitor with pseudocapacitor electrodes made of electrospun NiO nanofibers was reported to have a specific capacitance of 670 F/g. Conducting polymers were also investigated as the electrode material in pseudocapacitors. However the device stability is typically lower when compared with that of transition metal oxide-based devices.

Electrospun nanofibrous materials also contribute to the development of novel supercapacitor device structure. For example, a flexible supercapacitor was fabricated using layered fibrous materials (Fig. 4b) [23]. In this all-textile device, active layer was prepared by vapor-phase deposition of poly(3,4-ethylenedioxythiophene) (PEDOT) on electrospun nanofiber webs. Carbon cloth was used as outer layer to collect current, and a layer of electrospun PAN nanofibers was used as separator. The device used a solid electrolyte, PVDF-HFP containing $EMIBF_4$. The device showed a high cycling stability in ambient condition, and the performance was not affected by the bending of the device.

Recently, flexible supercapacitors were also fabricated using graphene-coated nylon nanofibers and microfibers as electrodes (Fig. 4c) [25]. All the prepared devices were highly flexible, and they functioned well even in folding state. The nanofibrous devices have a capacitance as high as 279.82 F/g, which are higher than the microfibrous devices.

Apart from bendable and foldable supercapacitors, stretchable supercapacitors were also reported. The stretchable device comprises carbon nanotube film electrodes, elastic electrospun polyurethane nanofiber separator, and solid electrolyte (Fig. 4d) [24]. The device showed stable performance under dynamic stretching/releasing and bending test. After 677 cycles of stretching/releasing at a strain rate of 1.11 %/s, 98.5 % of the capacitance was retained. After 2,511 test cycles at 4.46 %/s, the retention was 94.6 %.

Table 2 summarizes the material and capacitance of supercapacitor devices made of nanofibrous electrodes.

Table 2 Supercapacitor devices made of nanofibrous electrodes

Nanofiber type	Capacitance (F/g)
Carbon nanofibers (CNFs)	173
Nickel-CNFs	164
CNT-CNFs	310
V_2O_5	250
Pyrrole-CNFs	117
RuO_2-Pt	409.4
Fe_3O_4-CNFs	135
Interconnected CNFs	221
TiN-VN	247.5
PEDOT	85
V_2O_5/carbon	150
MnO_2/nickel	214
MnO_2/PPy@carbon	705
$LiCr_{0.15}Co_{0.85}O_2$	77.7
α-Fe_2O_3	256
Polyaniline	267
V–O–C composite	463
C-graphene	183
BN-CNFs	180
MnO_2	645
CNFs	256
Hollow polyaniline nanofibers	601
Graphene/CNFs	263.7
Nickel oxide/carbon	738
$LiNi_{0.4}Co_{0.6}O_2$	72.9
CNFs–Sn–ZrO_2	102.37
La-doped NiO	94.85
Si-CNFs	144.79
V_2O_5/α-Fe_2O_3	183
CuO	620
NiO	670
Co_3O_4	1,110
$ZnCo_2O_4$	770

Sensors

Sensors function to detect a physicochemical state or its change (e.g., gas, pH value, chemicals, or biochemical specie) and transduce it mostly into electric or optical output. Most sensors are required to have a large surface area and a highly porous structure to support fast access of the analyte and large signal-to-noise ratio. Nanofibrous materials match well with these features. In particular, electrospinning offers opportunities to process various sensing materials (e.g., functional polymers

and inorganic oxide) into nanofibers, and the fiber properties are easily modified through adding a dopant, functional chemical, or polymer into solution for electrospinning. Nanofibers with electrical conductive or semiconductive property can be prepared through either directly electrospinning or a surface coating technique. Considerable studies have been reported on using electrospun nanofibers to develop gas sensors, and these gas sensors were developed based on three main principles, such as acoustic wave, resistivity optics, and photoelectronics [27]. Table 3 lists sensor devices prepared by electrospun nanofibers.

In one research, NO_2 sensors were fabricated using electrospun nylon nanofibers which were coated with reduced graphene oxide on surface [28]. As shown in Fig. 5a, the nylon nanofibers were collected using a SiO_2/Pt substrate with platinum (Pt) interdigitated electrode arrays. The nanofiber webs were then functionalized using bovine serum albumin (BSA) to induce positive charges on fiber surface. Graphene oxide which had negative charges was assembled on nanofiber surface. After a chemical reduction, GO/nylon device was obtained (Fig. 5b). This nanofibrous sensor had a high sensitivity to detect NO_2 gas with a detection range of 0.25–4.5 ppm. A response value (7 %) was reported to 0.25 ppm NO_2 gas (Fig. 5c), which was considerably higher than that of a spin-coated sensor device without nanofibers (2 %). To demonstrate the advantage of nanofibrous structure, the fibrous web was heated to 300 °C and after heating the fibrous structure changed to a dense film (Fig. 5e). This led to dramatic reduction in sensing property, highlighting the importance of electrospun nanofibrous structure in gas sensing application.

In another paper [29], SnO_2 nanofibers which were prepared by calcination of electrospun nanofibers were used to prepare sensor device (Fig. 5f). At the operation temperatures between 100 °C and 450 °C, the device can detect H_2 and NO_2 gas of concentration ranging from 0.125 ppm to 2.5 ppm. The sensors showed different response to H_2 and NO_2. Because SnO_2 is an n-type semiconductor, its electrical resistance reduces when exposing to H_2 gas. The best sensing performance was found when 0.1 wt% Pt was present in the nanofibers. When the device was exposed to 2.5 ppm H_2 at 300 °C, the maximum response was 16.6. On the other hand, the nanofibers increased the resistance in an NO_2 environment. Sensor device prepared by pure SnO_2 nanofibers without Pt exhibited better NO_2 sensing performance than the Pt-containing one. The maximum response to 2.5 ppm NO_2 gas was 57.

The porous structure of nanofibrous webs makes them ideal for detecting biochemicals. As shown in Fig. 6a, poly(3,4-ethylenedioxythiophene) (PEDOT), a conducting polymer, was used to immobilize enzyme glucose oxidase (GOx) on commercial a microelectrode array to detect glucose [30]. For comparison, PEDOT was processed into dense films (Fig. 6b and c) and also coated on a fibrous structure (on poly(L-lactide) (PLLA) nanofibers; Fig. 6d and e). Both sensor devices had a linear response to glucose solution (concentration range 0.1–25 mM) (Fig. 6f and g), and PEDOT-coated PLLA nanofiber device exhibited much higher sensitivity, detection range, and stability compared to the film device.

Table 3 Summary of sensor devices prepared by electrospun nanofibers

Nanofibers	Sensor type	Analyte	Properties
ZnO	Gas sensor	C_2H_5OH	Operating temperature: 300 °C
			Response and recovery time: 3 and 8 s
Ag-doped In_2O_3	Gas sensor	HCHO	Operating temperature: 115 °C
			Sensitivity: 3 (5 ppm)
			Response and recovery time: 5 and 10 s
Polypyrrole (PPy)-coated TiO_2/ZnO	Gas sensor	NH_3	Operating temperature: room temperature (RT)
			Detection limit: 60 ppb (signal-to-noise ratio (S/N) = 3)
Cu(I) complex/polystyrene	Gas sensor	O_2	Operating temperature: RT
			Response and recovery time: 7 and 14 s
α-Fe_2O_3 ceramic	Gas sensor	C_2H_5OH	Operating temperature: 300 °C
			Response and recovery time: 3 and 5 s (100–5,000 ppm)
In_2O_3	Gas sensor	C_2H_5OH	Operating temperature: 300 °C
			Response and recovery time: 1 and 5 s (10–500 ppm)
Co-doped SnO_2	Gas sensor	H_2	Operating temperature: 330 °C
			Response and recovery time: 2 and 3 s
Porphyrinated polyimide (PPI)	Gas sensor	HCl	Operating temperature: RT
			Apparent binding affinity constant: $(1.05 \pm 0.23) \times 10^4$ L mol^{-1}
SnO_2–ZnO hybrid	Gas sensor	NO_2	Operating temperature: 200 °C
			Detection limit: 400 ppb
TiO_2	Gas sensor	CO	Operating temperature: 200 °C
			Response and recovery time: in the range of 32–86 and 84–109 s

(*continued*)

Table 3 (continued)

Nanofibers	Sensor type	Analyte	Properties
Cr_2O_3-sensitized ZnO	Gas sensor	Ethanol	Operating temperature: 300 °C
			Response: 3.6 (1 ppm)
			Response and recovery time: 1 and 5 s
			Detection limit: 1 ppm
Polyethyleneimine (PEI)/PVA	Gas sensor	Formaldehyde	Operating temperature: RT
			Linear response range: 10–255 ppm
In_2O_3	Gas sensor	H_2S	Operating temperature: RT
			Response: 167 (20 ppm)
			Linear response range: 1–100 ppm
In_2O_3/SnO_2	Gas sensor	CH_3OH	Operating temperature: 280 °C
			Response and recovery time: 8 and 5 s
PANi	Gas sensor	NH_3	Operating temperature: RT
			Detection sensitivity: 7 % versus 1 ppm of NH_3
$LaFeO_3$	Gas sensor	C_2H_5OH	Operating temperature: 200 °C
			Response and recovery time: 11 and 19 s
NiO/SnO_2	Gas sensor	Toluene	Operating temperature: 330 °C
			Response and recovery time: 11.2 and 4 s
Co/ZnO	Gas sensor	m-Xylene	Operating temperature: 320 °C
			Response: 14.8 (100 ppm)
			Response and recovery time: 4 and 6 s
Al-doped SnO_2	Gas sensor	H_2	Operating temperature: 340 °C
			Response and recovery time: 3 and less than 2 s
PEI modified polystyrene (PS)	Gas sensor	Formaldehyde	Operating temperature: RT
			Detection limit: 3 ppm

CuO-loaded SnO_2	Gas sensor	H_2S	Operating temperature: 300 °C
			Response: 1.98×10^4 (10 ppm)
			Response and recovery time: 1 and 10 s
SnO_2/In_2O_3	Gas sensor	Formaldehyde	Operating temperature: 375 °C
			Response:18.9 (50 ppm) and 2.2 (0.5 ppm)
2-Chloro-3,5-dinitrobenzotrifluoride (CDBF) loaded PAN nanofibers	Gas sensor	Fast ethylamine	Operating temperature: RT
			Response time: 0.4 s
La_xSr_{1-x} FeO_3	Gas sensor	C_2H_5OH	Operating temperature: 185 °C
			Response and recovery time: 11 and 21 s
$La_{0.67}Sr_{0.33}MnO_3$ (LSMO)	Gas sensor	O_2	Operating temperature: 800 °C
			Detection limit: 3.5 ppb (S/N = 3)
V_2O_5	Gas sensor	NH_3	Operating temperature: 200 °C
			Response and recovery time: 50 and 350 s
			Detection limit: 100 ppb
Catalytic Pt and IrO_2	Gas sensor	Acetone, H_2S	Operating temperature: 350 °C
Nanoparticles modified WO_3			Acetone response: $R_{air}/R_{gas} = 8.7$ (5 ppm)
			H_2S response: $R_{air}/R_{gas} = 166.8$ (5 ppm)
ZnO/In_2O_3	Gas sensor	C_2H_5OH	Operating temperature: 210 °C
			Response and recovery time: 2 and 1 s (100 ppm)
CuO/SnO_2	Gas sensor	H_2S	Operating temperature: 200 °C
			Response and recovery time: 23 and 15 s (1 ppm)
			Detection limit: <10 ppb
$La_{0.8}Sr_{0.2}MnO_3$	Gas sensor	CO	Operating temperature: 550 °C
			Response time: 85 s (200 ppm) and 65 s (500 ppm)

(*continued*)

Table 3 (continued)

Nanofibers	Sensor type	Analyte	Properties
CuO/SnO_2	Gas sensor	H_2S	Response: 650 (300 °C)
			Response and recovery time: 2 and 20 s (300 °C)
			Response: 3,000 (150 °C)
			Response and recovery time: 2 and 3,500 s (150 °C)
Pt-functionalized NiO composite nanotubes	Gas sensor	C_2H_5OH	Operating temperature: 200 °C
			Response: 20.85 (100 ppm)
$CaO–SnO_2$ nanocrystalline composite rods	Gas sensor	NOx	Operating temperature: RT
			Response: 6.63 (97 ppm) and 0.109 (9.7 ppb)
α-Fe_2O_3 nanorods/TiO_2	Gas sensor	Trimethylamine (TMA)	Operating temperature: 250 °C
			Response: 13.9 (50 ppm)
			Response and recovery time: 0.5 and 1.5 s
Polyacrylic acid (PAA) fibers and nanonets	Biosensor	Trimethylamine (TMA)	Operating temperature: RT
			Detection limit: 1 ppm
Porphyrinated polyimide	Gas sensor	2,4,6-trinitrotoluene (TNT)	Operating temperature: RT
			Apparent binding affinity constant: $(2.37 \pm 0.19) \times 10^7$ L/mol
$SnO_2–Fe_2O_3$ interconnected nanotubes	Gas sensor	Toluene	Operating temperature: 260 °C
			Detecting limit: 50 ppb
			Response and recovery time: 5 and 11 s (1 ppm)
Ni-doped ZnO	Gas sensor	C_2H_2	Operating temperature: 250 °C
			Sensitivity: 16.9
Ag nanoparticles (NPs) coated $ZnO–SnO_2$ nanotubes	Gas sensor	HCHO	Operating temperature: 210 °C
			Detection limit: 9 ppb

Al_2O_3/In_2O_3	Gas sensor	NOx	Operating temperature: RT
			Detection limit: 291 ppb
			Response: 100 (97 ppm)
Pd functionalized WO_3	Gas sensor	H_2S	Operating temperature: 350 °C
			Response: $R_{air}/R_{gas} = 1.36$ (1 ppm)
Ce-doped α-Fe_2O_3 nanotubes	Gas sensor	acetone	Operating temperature: 240 °C
			Sensitivity: 21.5–50 ppm
			Response and recovery time: 3 and 8 s
			Detecting limit: 1 ppm
SnO_2 nanoparticle-coated In_2O_3	Gas sensor	NH_3	Operating temperature: RT
			Response: 21 (1 ppm)
			Response and recovery time: 7 and 10 s (1 ppm)
			Detecting limit: 0.1 ppm
Single SnO_2 nanofiber	Gas sensor	Moisture and methanol	Response times: 108–150 s for moisture and 10–38 s for methanol gas
PEI functionalized polyamide 6 (PA 6) (PEI-PA 6) nanofiber/net (NFN)	Gas sensor	Formaldehyde	Detection limit: 50 ppb
ZnO/SnO_2 decorated hybrid carbon	Gas chemical sensor	Dimethyl methylphosphonate (DMMP)	Operating temperature: RT
			Detection limit: 0.1 ppb
			Response time: less than 1 s
LiCl-doped ZnO	Humidity sensor	Moisture	Response and recovery time: 3 and 6 s
Mg^{2+}/Na^+ doped rutile TiO_2	Humidity sensor	Moisture	Response and recovery time: 2 and 1 s
Barium titanate ($BaTiO_3$)	Humidity sensor	Moisture	Response and recovery time: 5 and 4 s (between 11 % and 95 % relative humidity)
Na^+ doped ZnO	Humidity sensor	Moisture	Response and recovery time: 3 and 6 s (between 11 % and 95 % relative humidity)

(*continued*)

Table 3 (continued)

Nanofibers	Sensor type	Analyte	Properties
TiO_2	Humidity sensor	Moisture	Response and recovery time: 1 and 4 s (between 40 % and 90 % relative humidity)
			Sensitivity: 150 MΩ/%RH (10 Hz) and 20 MΩ/%RH (100 Hz) (between 40 % and 90 % relative humidity)
Ethyl cellulose (EC)	Optical sensor	Ionic mercury	Linear response range: 1.0×10^{-10} to 1.0×10^{-4} mol L^{-1}
			Detection limit: 0.07 nM
Polystyrene (PS) doped with a fluorescent conjugated polymer fibers	Optical sensor	Hemoglobin (Hb), myoglobin (Mb), and cytochrome c (Cyt c)	Linear response range for Hb determination: 2.0×10^{-8} to 3.0×10^{-6} M
			Detection limit: 1.2×10^{-8} M
Polyamide-6/nitrocellulose (PA-6/NC) nanofibers/net	Optical sensor	Pb^{2+} ions	Detection limit: 0.2 μM
$Ru(bpy)_3^{2+}$-doped Nafion (ERDN)	Optical sensor	Phenol	Detection limit:1.0 nM (S/N >3)
Meso-2,6-dichlorophenyltripyrrinone (TPN-Cl_2)/poly(2-hydroxyethyl methacrylate) (poly HEMA)	Chemical sensor	Zn^{2+}	Detection limit: 10^{-6} M
			Time resolution: 5 min at 10^{-6} M and 1 min at 10^{-5} M
PVDF/poly(aminophenylboronic acid) (PAPBA)	Biosensor	Glucose	Linear response range: 1 ~ 15 mM
			Response time: less than 6 s
Ni nanoparticle-loaded carbon nanofibers	Biosensor	Nonenzymatic glucose	Detection limit: 1 M
			Linear response range: 2 M to 2.5 mM
Hemoglobin microbelts	Biosensor	Hydrogen peroxide and nitrite	Detection limit: 0.61 M for H_2O_2 and 0.47 M for nitrite (S/N = 3)
			Superior $K_{M,app}$ value: 0.093 mM for H_2O_2 and 0.713 mM for nitrite
Nickel oxide (NiO) microfibers	Biosensor	Nonenzymatic glucose	Sensitivity: 1785.41 μAmM^{-1} cm^{-2}
			Detection limit: 3.3×10^{-8} M (S/N = 3)

Mn_2O_3	Biosensor	Hydrazine	Response time:5 s
			Sensitivity: 474 μAmM^{-1} cm^{-2}
			Detection limit: 0.3 mM (S/N = 3)
PS	Biosensor	Chloramphenicol (CAP)	Linear response range: 5–100 ppb
			Response time: 2–3 s
			Detection limit: 5 ppb
Polyoxometalate hybrid nanofibers	Biosensor	Nitrite	Response time: 5 s
			Sensitivity: 10.95 μAmM^{-1} cm^{-2}
			Detection limit: 0.96 μM (S/N = 3)
NiO	Biosensor	Nonenzymatic glucose	Sensitivity: 1,100 μAmM^{-1} cm^{-2}
			Response time: less than 5 s
			Detection limit: 0.77 μM (S/N = 3)
Au-BSA/PEO	Biosensor	Hg^{2+}	Linear response range: 0.5–75 nM
			Detection limit: 57 pM
Polyurethane nanofibers doped with carbon nanotubes and silver NPs	Biosensor	H_2O_2	Sensitivity: 160.6 μAmM^{-1} cm^{-2}
			Linear response range: 0.5–30 mM
			Detection limit: 18.6 μM (S/N = 3)
$LaCoO_3$ poriferous	Biosensor	L-Tryptophane	Linear response range: 5.0×10^{-8} to 5.0×10^{-6} mol/L
			Detection limit: down to 1.0×10^{-8} mol/L
$MnCo_2O_4$	Biosensor	Nonenzymatic glucose	Linear response range: 0.05–800 μM
			Detection limit: 0.01 μM (S/N = 3)
AgNPs/CuO	Biosensor	Nonenzymatic glucose	Sensitivity: 1,347 μAmM^{-1} cm^{-2}
			Detection limit: 51.7 nM (S/N = 3)
CdSe QDs/polycaprolactone (PCL) composite porous fibers	Biosensor	Lactate dehydrogenase (LDH)	Linear response range: 200–2,400 UL^{-1}

(*continued*)

Table 3 (continued)

Nanofibers	Sensor type	Analyte	Properties
Carbon nanofibers	Electrochemical sensor	Dihydronicotinamide adenine dinucleotide (NADH)	Linear response range: up to 11.45 mM
			Detection limit: 20 nM
Rhodium nanoparticle-loaded carbon nanofibers	Electrochemical sensor	Hydrazine	Linear response range: 0.5–175 μM
			Sensitivity: 527 μA/mM
Au NPs-composite Nafion nanofibers	Electrochemical sensor	H_2O_2	Detection limit: 38 nM
$([Ru(bpy)3]^{2+})$/gold NPs/PAN nanofibers	Electrochemiluminescence sensor	Hydroquinone	Linear response range: 0.55–37 μM Detection limit: 80 nM (S/N = 3)
P(VDF-TrFE)	Mechanical sensor	Pressure	Sensitivity: 60.5 mV/N
PU/MWCNTs	Mechanical sensor	Strain	Good reversibility in electrical properties under large-strain deformation (up to 20 %)
PEDOT:PSS/PVP	Mechanical sensor	Strain	Linear elastic response to strain: up to 4 %
			Gauge factor: 360
Lead zirconate titanate (PZT)	Mechanical sensor	Acoustic emission	Output voltage: ~100 mV in response to the simulated acoustic emission
PVA/ZnO	UV sensor	UV	Dark current to photocurrent ratio (I_{ph}/I_d): 7.44
			Efficiency: 8.44
Poly(phenylquinoline)-block-polystyrene (PPQ-b-PS)/PS	pH sensor	pH value	pH-tunable photoluminescence
			Emission maximum varied range: 532–560 nm (pH value changed from 7 to 1)

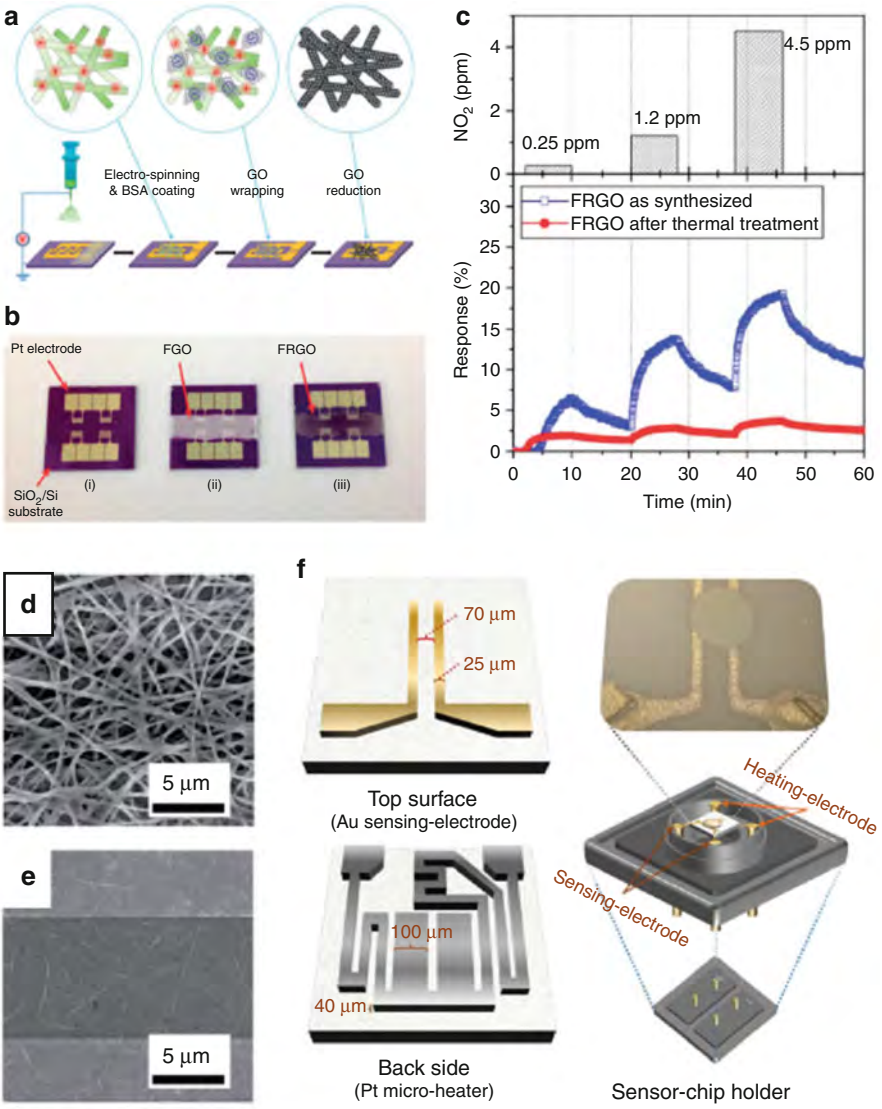

Fig. 5 Electrospun nanofibrous gas sensors (Reprinted with permission from Refs. [28, 29])

Field-Effect Transistors

Field-effect transistor (FET) is one of the most important electronic components in logic circuits and switches. Despite different device configurations, FETs share a very similar working principle which uses an electric field to control the conductivity between the drain and the source. To miniaturize FET devices, the semiconductive channel was fabricated using electrospun nanofibers from

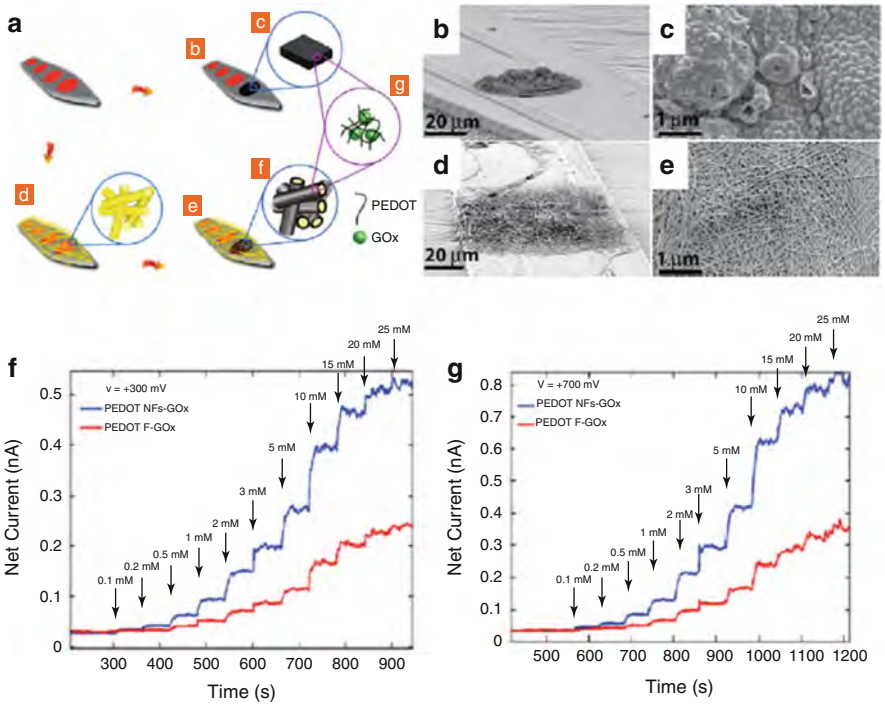

Fig. 6 Conducting polymer nanofiber biosensors and their glucose-sensing performance (Reprinted with permission from Ref. [30])

conducting polymers or metal oxides. A simple FET device was prepared by depositing a single poly(3-hexylthiophene) (P3HT) nanofiber onto prefabricated electrodes on SiO_2/Si substrate (Fig. 7a) [31]. The device had a field-effect mobility of 0.03 cm^2/V s and a current on/off ratio of 1,000. By using an array of aligned P3HT nanofibers and polyelectrolyte ion gel gate to prepare FET device (Fig. 7b), the field-effect mobility could be improved to 2 cm^2/V s with an on/off ratio of 100,000 [32].

Core–sheath poly(arylene ether ketone) (SPEAK)/polyaniline (PANi) nanofibers were used as active layer to prepare an organic FET (Fig. 7d) [33]. When positive charges were injected into the PANi layer, the sulfonic acid ($-SO_3H$) groups in the SPEAK core could move toward the PANi sheath (Fig. 7d), which increased PANi doping level and drain current. The FET device showed a field-effect mobility as high as 3 cm^2/V s. In addition, an organic FET device was prepared using single nanofiber from poly(3-dodecylthiophene) (P3DH)/P3HT composite (Fig. 7e), which was collected on a plastic substrate and sealed by a poly(methyl methacrylate) (PMMA) dielectric layer [34]. The device was flexible and able to work when being bent (Fig. 7f). Table 4 lists FET devices containing nanofibrous materials.

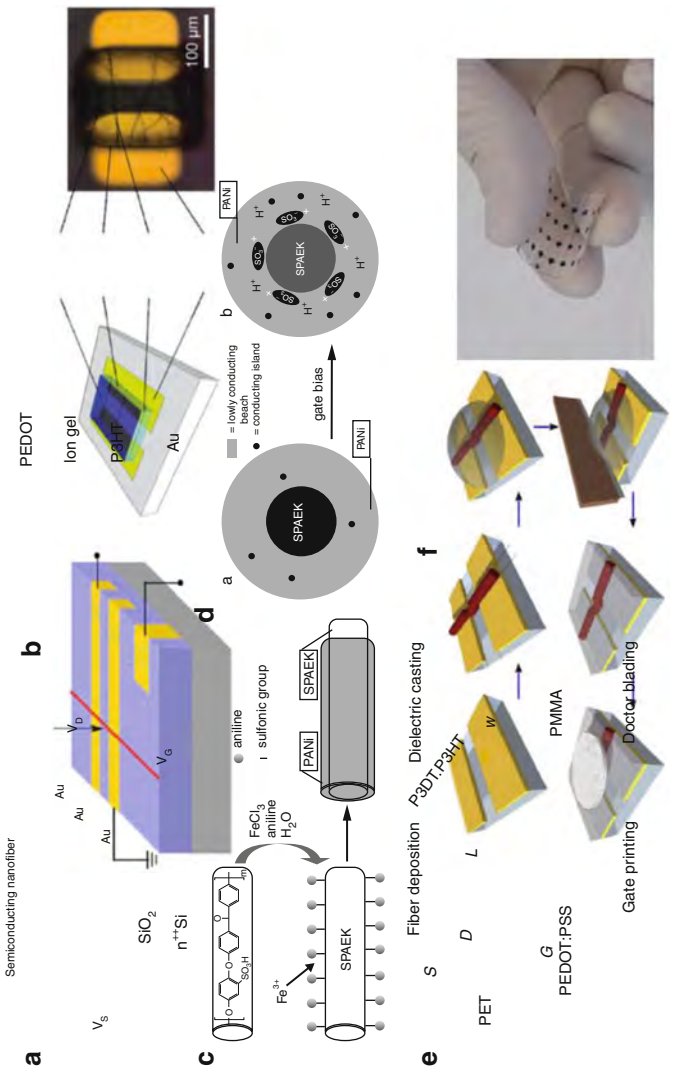

Fig. 7 Schematic illustration and digital photos of some nanofiber-based FET devices (Reprinted with permission from Refs. [31–34])

Table 4 FETs containing nanofibrous materials and their properties

Nanofiber type	Role			Properties
	Gate	Source	Drain	
Poly(3-hexylthiophene)	n-type Si	Au	Au	FET mobility: 0.03 cm^2/Vs
				On/off ratio: 10^3
Poly(3-hexylthiophene)	PEDOT:PSS	Au	Au	Operating voltage <2 V
				FET mobility: 2 cm^2/Vs
				On/off ratio: 10^5
Sulfonated poly(arylene ether ketone)/PANi	n^{++}-doped Si	Au	Au	FET mobility: 3 cm^2/Vs
				On/off ratio > 10^4
Poly(3-decylthiophene)/ poly(3-hexylthiophene)	PEDOT:PSS	Au	Au	FET mobility: 10^{-3} cm^2/Vs
Camphorsulfonic acid-doped PANi/PEO	Si	Au	Au	FET mobility: 1.4×10^{-4} cm^2/Vs
CuO	p-type Si	Silver	Silver	CuO nanofiber conductivity: 3×10^{-3} S/cm. Intrinsic p-type semiconductor
ZnO	p-type Si	Silver	Silver	Intrinsic n-type semiconductor
Poly(3-hexylthiophene)	Si	Cr	Au	FET mobility: 0.017 cm^2/Vs
SnO_2	Si	Au	Au	Intrinsic n-type semiconductor
				On/off ratio: 6,000
Poly(2-methoxy-5-(2-ethylhexoxy)-1,4-phenylenevinylene)	Si	Cr/Au	Cr/Au	FET mobility: 10^{-3} cm^2/Vs
				On/off ratio: 780
Au-doped PAN-PANi core–shell nanofibers	n^{++}-doped Si	Au	Au	FET mobility: up to 11.6 cm^2/Vs
Poly(3-hexylthiophene)	Si	Au	Au	FET mobility: 1.92×10^{-1} cm^2/Vs
				On/off ratio: 4.45×10^4
Poly(3-hexylthiophene)/ poly(stearyl acrylates)	n-type Si	Au	Au	FET mobility: 3.21×10^{-2} cm^2/Vs
				On/off ratio: 10^4
Poly(3-hexylthiophene)/ poly(n-lauryl acrylate)	n-type Si	Au	Au	FET mobility: 2.40×10^{-2} cm^2/Vs
ZnO	n-type Si	Ni	Au	Intrinsic n-type semiconductor
ZnO	n^{++}-doped Si	Au	Au	Intrinsic n-type semiconductor
Poly(9,9-dioctyl-fluorene-co-bithiophene) (F8T2)	n-type Si	Au	Au	FET mobility: $10^{-4} \sim 10^{-2}$ cm^2/Vs
				On/off ratio: 10^2–10^3
In_2O_3–ZnO–$ZnGa_2O_4$ composite fibers	Si	Al	Al	FET mobility: 7.04 cm^2/Vs
Poly(4-vinylpyridine) (P4VP)	Si	Au	Au	FET mobility: >1.50 cm^2/Vs
				On/off ratio: $>10^6$

P–N Diodes

Semiconducting nanofibers which show an electrical rectifying effect have been used to prepare *p–n* diodes. For example, *p*-type nanofibers were deposited onto an

n-type silicon to form a *p*–*n* junction [35, 36]. When the *p*-type nanofibers were prepared from polyaniline (Fig. 8a), the device showed a typical Schottky junction characteristic, and its rectifying behavior was dependent on fiber diameter and the doping level of polyaniline [36].

p–*n* junctions can also be formed between different types of electrospun nanofibers. For example, cross-connection of an electrospun P3HT nanofiber with an electrospun SnO_2 ribbon resulted in a *p*–*n* diode with a rectification ratio of 25 (Fig. 8b) [40]. In another work [41], a diode device was formed by twisting NiO and ZnO nanofibers (Fig. 8c). This *p*–*n* junction showed typical rectifying current–voltage behavior and was sensitive to UV irradiation.

In addition, a layered nanofibrous *p*–*n* junction was reported using a two-step electrospinning process [39]. A layer of SnO_2 nanofibers (*n*-type) was first prepared on an aluminum foil, followed by electrospinning a layer of PEDOT:PSS/PVP nanofibers (*p*-type) on the SnO_2 nanofiber layer. Au was finial sputter-coated on the surface of PEDOT:PSS/PVP nanofibrous layer (see the preparation process in Fig. 8d). Schottky barrier was formed between two nanofibrous layers, and the device showed rectifying effect on both forward and reverse biases. The thickness of the nanofiber layers had a considerable effect on the device resistance and rectifying performance. By reducing the PEDOT:PSS/PVP nanofiber layer thickness from 11.6 to 4.8 μm, the device increased the rectifying ratio from 35 to 48. Such a fibrous device is easy to prepare and could be used for the development of wearable electronics.

Light-Emitting Diodes

Light-emitting diodes (LEDs) are advantageous in less energy consumption, longer lifetime, less CO_2 emission, smaller size, and faster switching compared with incandescent light sources. Electrospun nanofibers can be used for making LED devices. For example, phosphor powder-based LEDs are often prepared using resins as binder, and powder agglomeration has been a serious issue during the device fabrication. This problem can be avoided by using electrospinning to process light-emitting materials into a nanofibrous layer. $CaSi_2O_2N_2$:Eu nanofibers was prepared by electrospinning a water–ethanol solution of $Ca(NO_3)_2$, $Eu(NO_3)_3$, and TEOS [42]. The as-spun nanofibers were then subjected to a multistep thermal treatment to gain a free-standing nanofibrous membrane (Fig. 9a and b). The nanofiber layer was more uniform and contained, less apt to crack than $CaSi_2O_2N_2$:Eu films. As a result, the nanofibrous $CaSi_2O_2N_2$:E had stronger light emission with broader emission spectrum. In addition, the $CaSi_2O_2N_2$:E nanofibers were easy to be handled during device fabrication. When a current of 20 mA was applied, the LED device made of a 70 μm thick nanofiber membrane radiated bluish light, while the device emitted near white light when the membrane thickness was 110 μm (Fig. 9c and d).

Broad-spectrum white light LED was prepared by using multiple electrospun nanofibrous layers which were prepared by different phosphor materials. Composite electrospun fibers from green fluorescent tris-(8-hydroxyquinoline) aluminum (Alq3)

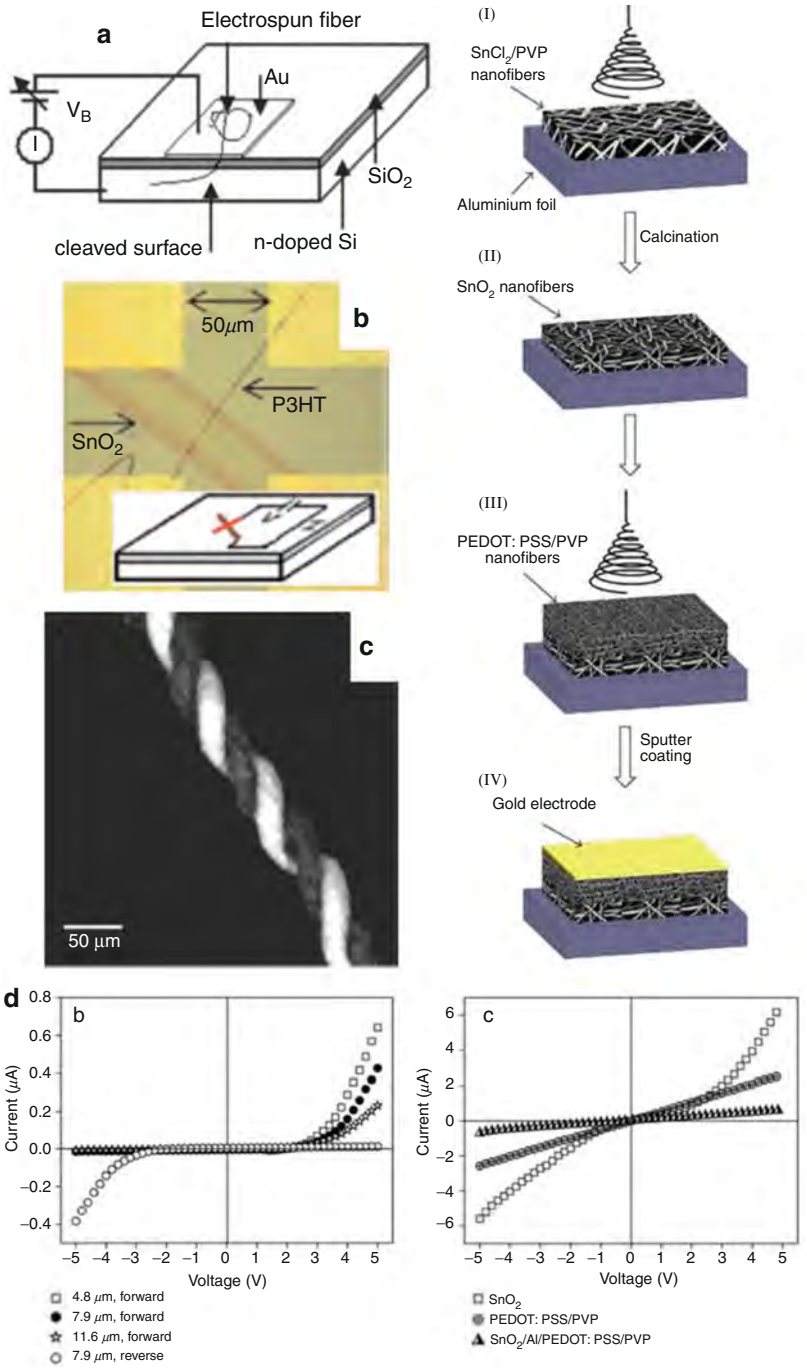

Fig. 8 *p–n* diode devices made of nanofibrous materials (Reprinted with permission from Refs. [36–39])

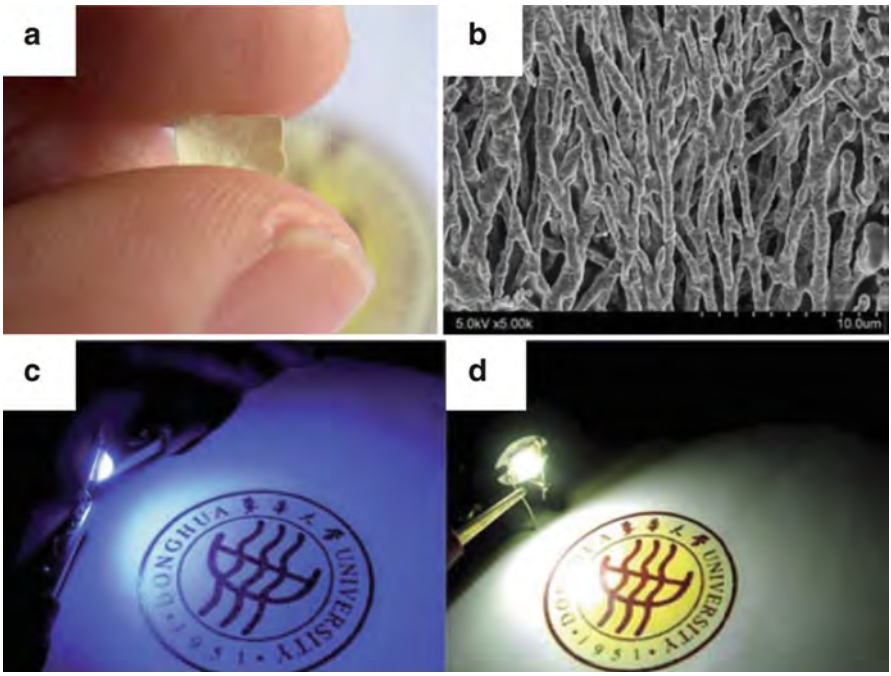

Fig. 9 (**a**) Digital photo and (**b**) SEM image of a free-standing $CaSi_2O_2N_2$:Eu nanofiber mat; effect of $CaSi_2O_2N_2$:Eu nanofiber layer thickness on light-emitting effect, (**c**) 70 μm, (**d**) 110 μm) (Reprinted with permission from Ref. [42])

and red fluorescent poly(3-butylthiophene) (P3BT) were directly deposited onto a blue LED [43]. Depending on the weight ratio of Alq3 and P3BT, the LED device emitted light of different colors. When the Alq3:P3BT ratio was 23:1, a white emission with the CIE color coordinate of (0.36, 0.37) resulted, which was very close to that of the perfect white light (CIE, 0.33, 0.33) (Fig. 10).

Many light-emitting materials have been processed into nanofibers through electrospinning, including organic dyes, quantum dots, conjugated polymers, inorganic compounds, metal oxides, and metal–organic frameworks. Table 5 summarizes LED devices prepared using nanofibrous materials.

In 2011, R&D 100 Award was granted to a company, RTI International, to recognize its successful development of "Nanofiber Light Improvement Technology" (NLITe^{TM}) [44]. Electrospun nanofibers functioned like a key element in this technology, and the LED devices often showed 20 % improvement in lighting performance.

UV Photodetectors

Many semiconducting materials can generate photocurrent under UV irradiation. This property has been used to develop UV photodetectors. A UV photodetector

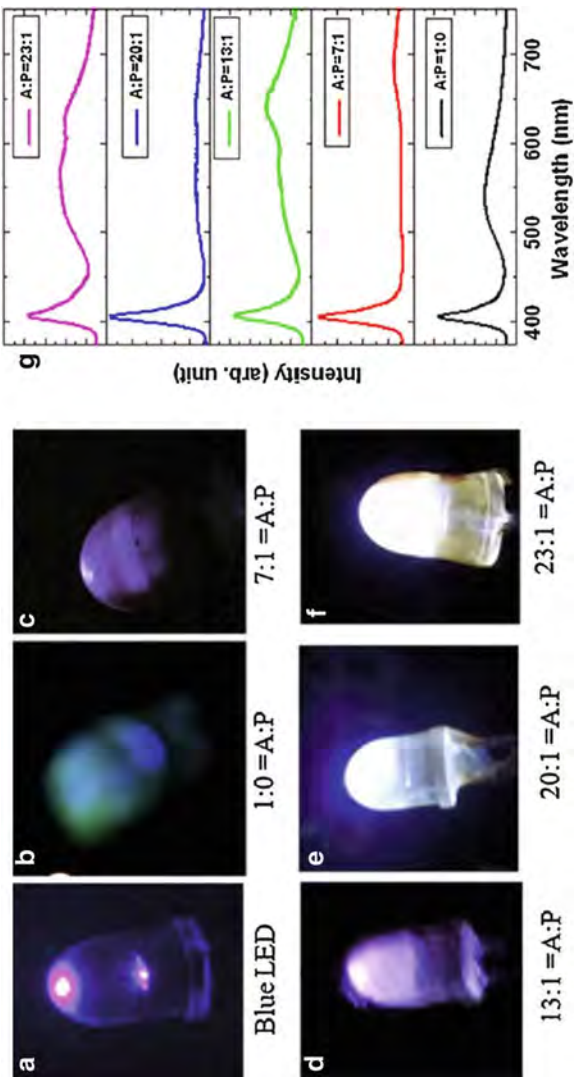

Fig. 10 Digital photos of a blue LED (**a**) without and (**b–f**) with electrospun Alq3/P3BT fibers; (**g**) corresponding emission spectra of the LED (Reprinted with permission from Ref. [43])

Table 5 Nanofibrous materials reported for making LEDs

Nanofibers	Emitting light
Polyvinyl alcohol/ZnO	White
$DiIC_1(5)$/PEO	Red
CdSe/ZnS/PEO	
$DiIC_1(5)$/PMMA	
Polymethine dye/PMMA	Near-infrared
TiO_2/poly(phenylene vinylene)	Yellow-green, green
CdS/polyethylene oxide	Blue, green
$Eu(TTA)_3(TPPO)_2$/PMMA, $Eu(TTA)_3(TPPO)_2$/PS, $Eu(TTA)_3(TPPO)_2$/PVP	White
DNA-CTMA	Red
$CaMoO_4$: Ln^{3+}(Ln = Eu, Tb, Dy)	Blue-green, yellow, orange-red
Y_2O_3: Eu^{3+}	Red
DB-PPV/PMMA	Green
$CaWO_4$ and $CaWO_4$:Tb^{3+}	Blue, green
CdTe NCs/PVA/PPV	White
Lu_2O_3:Eu^{3+}	Red
Dye-loaded zeolites/PFTPA/PEO	Blue
Cds/PVA/PPV	Blue
$CaSi_2O_2N_2$:Eu	Yellow and green
Polycrystalline-BCN and B_2O_3 crystal	Green and yellow
CdS/PMMA	Red
La_6MoO_{12}:$Eu^{3+/}$PVA	Red
MEH-PPV/PEO(HMW)/$LiCF_3SO_3$ and MEH-PPV/PEO(LMW)	Red
LnMOF/PVA	Green-yellow, yellow, orange
$KGdTa_2O_7$:Eu^{3+}	Red
PVK–CdSe/CdS/ZnS quantum dots	White
Alq3/P3BT	White

was reported using a single gallium nitrate (GaN) nanofiber which was prepared by electrospinning [45]. The device showed superior UV detection performance to the device made of a GaN nanowire which was prepared by a CVD method. The electrospun GaN nanofiber had rougher surface and larger surface area than the nanowire. The photocurrent (25 nA) of the nanofiber device was 830 times the dark current (0.03 nA), while this figure for the nanowire device was only 78. The nanofiber device also showed faster response and better reversibility than the nanowire one.

ZnO is another semiconductor commonly used for making UV photodetector. A randomly orientated electrospun ZnO nanofiber mat was used to prepare UV photodetector [46]. Under 260 nm UV light, the device generated 11.5 μA photocurrent with a sensitivity as high as 790 A/W. Figure 11 shows the structure of the photodetector device and the microscope images of three electrodes with different inter-electrode distances (20, 40 and 60 μm). Gold electrodes in the

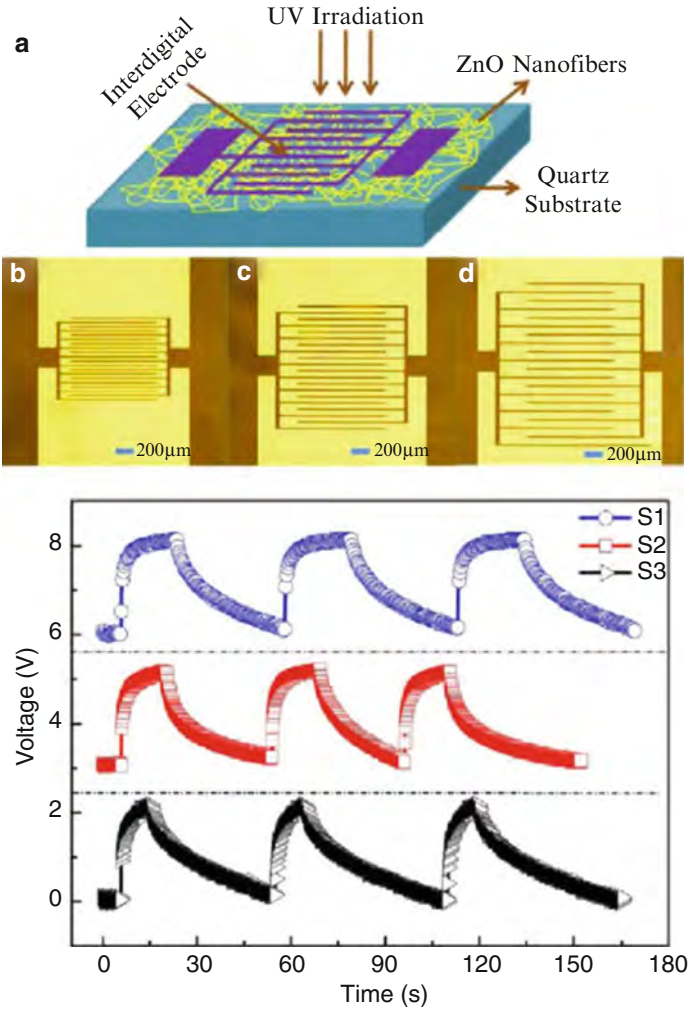

Fig. 11 ZnO nanofiber UV photodetectors with different inter-electrode spacing and their photoconduction responses (Reprinted with permission from Ref. [47])

photodetector device were found to affect photodetection [47]. Under the same experimental condition, the device with the shortest inter-electrode distance showed the highest sensitivity (287 A/W) and shortest response time.

Electrochromic Devices

Electrochromic materials change color reversibly in response to an external electrical stimulation. They show applications in smart windows, display panels, and

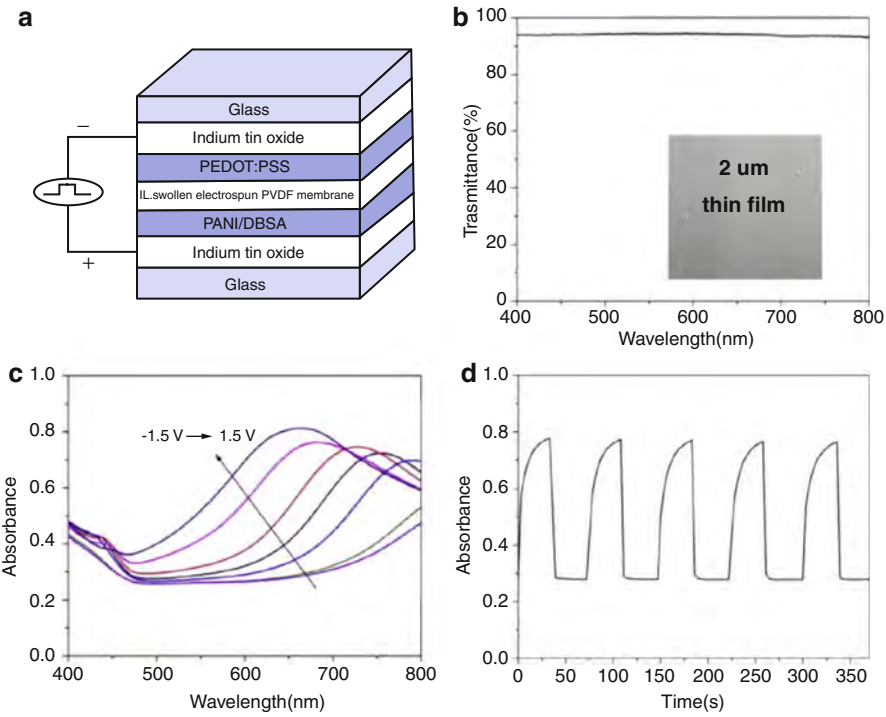

Fig. 12 (**a**) Configuration of a complementary electrochromic device; (**b**) visible transmission spectrum of electrospun PVDF-HFP/ionic liquid fibrous mat cross-linked by 1 wt% DAP; (**c**) visible absorbance spectra of the electrochromic device, under different external voltages (−1.5, −1, −0.5, 0, 0.5, 1 and 1.5 V); and (**d**) switching curve of the electrochromic device under square-wave potentials oscillating between +1.5 V and −1.5 V (Reprinted with permission from Ref. [49])

functional textiles. An electrochromic device was prepared by depositing aligned tungsten oxide (WO_3) nanofibers on an ITO-coated glass, and the device performance was compared with those made of WO_3 film through a sol–gel route [48]. The WO_3 nanofiber device had faster optical response (both coloration and decoloration) than the thin film. The coloration efficiency of the WO_3 nanofibers was 21 % higher than that of the film.

Recently, a multilayer electrochromic device (Fig. 12a) with high light transmittance (Fig. 12b) was prepared using PVDF-HFP/ionic liquid (1-butyl-3-methylimidazolium tetrafluoroborate) nanofibers as active layer [49]. Cross linking treatment of the PVDF-HFP by 1,3-diaminopropane (DAP) improved the mechanical stability of the nanofiber web of thickness as small as 2 μm could be easily handled. The electrochromic devices had a stable switch between yellowish green (reduced state) and blue (oxidized state) among an applied voltage range between +1.5 V and −1.5 V (Fig. 12c and d).

Other Electronic Devices

In addition to the abovementioned electronic devices, other nanofiber-involving electronic devices, such as field-emission cells, triboelectric power generators, thermoelectric generators, photo-coupling devices, and electroactive actuators, were also reported.

Summary

Electrospun nanofibers have shown great potential to be used for making various electronic devices. Their improvement in device performance can come from the one-dimensional feature, small fiber size, highly porous fibrous structure, controlled fiber size/morphology/structure, or tailored fiber properties. It is expected that wide use of nanofibers in electronic devices will lead to finding of more advanced performance. With further progress in electrospinning and fiber deposition techniques, nanofiber-based electronic devices will come into the market in not far future.

References

1. Li D, Xia Y (2004) Electrospinning of nanofibers: reinventing the wheel? Adv Mater 16(14): 1151–1170
2. Greiner A, Wendorff JH (2007) Electrospinning: a fascinating method for the preparation of ultrathin fibers. Angew Chem Int Ed 46(30):5670–5703
3. Fang J, Niu H, Lin T, Wang X (2008) Applications of electrospun nanofibers. Chin Sci Bull 53(15):2265–2286
4. Cavaliere S, Subianto S, Savych I, Jones DJ, Rozière J (2011) Electrospinning: designed architectures for energy conversion and storage devices. Energy Environ Sci 4(12):4761–4785
5. Longo C, De Paoli M-A (2003) Dye-sensitized solar cells: a successful combination of materials. J Braz Chem Soc 14:898–901
6. Fujihara K, Kumar A, Jose R, Ramakrishna S, Uchida S (2007) Spray deposition of electrospun TiO_2 nanorods for dye-sensitized solar cell. Nanotechnology 18(36):365709
7. Joshi P, Zhang L, Davoux D, Zhu Z, Galipeau D, Fong H, Qiao Q (2010) Composite of TiO_2 nanofibers and nanoparticles for dye-sensitized solar cells with significantly improved efficiency. Energy Environ Sci 3(10):1507–1510
8. Listorti A, O'Regan B, Durrant JR (2011) Electron transfer dynamics in dye-sensitized solar cells. Chem Mater 23(15):3381–3399
9. Mu Jo S, Yeon Song M, Rack Ahn Y, Rae Park C, Young Kim D (2005) Nanofibril formation of electrospun TiO_2 fibers and its application to dye-sensitized solar cells. J Macromol Sci A 42(11):1529–1540
10. Chang C, Tran VH, Wang J, Fuh YK, Lin L (2010) Direct-write piezoelectric polymeric nanogenerator with high energy conversion efficiency. Nano Lett 10(2):726–731
11. Fang J, Wang X, Lin T (2011) Electrical power generator from randomly oriented electrospun poly (vinylidene fluoride) nanofibre membranes. J Mater Chem 21(30):11088–11091
12. Fang J,Niu H, Wang H, Wang X, LinT (2013) Enhanced mechanical energy harvesting using needleless electrospun poly (vinylidene fluoride) nanofibre webs. Energy Environ Sci 6(7): 2196–2202

13. Zeng W, Tao X-M, Chen S, Shang S, Chan HLW, Choy SH (2013) Highly durable all-fiber nanogenerator for mechanical energy harvesting. Energy Environ Sci 6(9):2631–2638
14. Persano L, Dagdeviren C, Su Y, Zhang Y, Girardo S, Pisignano D, Huang Y, Rogers JA (2013) High performance piezoelectric devices based on aligned arrays of nanofibers of poly (vinylidenefluoride-co-trifluoroethylene). Nat Commun 4:1633
15. Hansen BJ, Liu Y, Yang R, Wang ZL (2010) Hybrid nanogenerator for concurrently harvesting biomechanical and biochemical energy. ACS Nano 4(7):3647–3652
16. Mandal D, Yoon S, Kim KJ (2011) Origin of piezoelectricity in an electrospun poly(vinylidene fluoride-trifluoroethylene) nanofiber web-based nanogenerator and nano-pressure sensor. Macromol Rapid Commun 32(11):831–837
17. Liu Z, Jiang W, Kong Q, Zhang C, Han P, Wang X, Yao J, Cui G (2013) A core@sheath nanofibrous separator for lithium ion batteries obtained by coaxial electrospinning. Macromol Mater Eng 298(7):806–813
18. Dong Z, Kennedy SJ, Wu Y (2011) Electrospinning materials for energy-related applications and devices. J Power Sources 196(11):4886–4904
19. Liu S, Wang Z, Yu C, Wu HB, Wang G, Dong Q, Qiu J, Eychmüller A, Lou XW (2013) A flexible TiO_2(B)-based battery electrode with superior power rate and ultralong cycle life. Adv Mater 25(25):3462–3467
20. Jayaraman S, Aravindan V, Suresh Kumar P, Chui Ling W, Ramakrishna S, Madhavi S (2014) Exceptional performance of TiNb2O7 anode in all one-dimensional architecture by electrospinning. ACS Appl Mater Interfaces 6(11):8660–8666
21. Gu Y, Chen D, Jiao X, Liu F (2007) LiCoO2-MgO coaxial fibers: co-electrospun fabrication, characterization and electrochemical properties. J Mater Chem 17(18):1769–1776
22. Niu H, Zhang J, Xie Z, Wang X, Lin T (2011) Preparation, structure and supercapacitance of bonded carbon nanofiber electrode materials. Carbon 49(7):2380–2388
23. Laforgue A (2011) All-textile flexible supercapacitors using electrospun poly (3,4-ethylenedioxythiophene) nanofibers. J Power Sources 196(1):559–564
24. Li X, Gu T, Wei B (2012) Dynamic and galvanic stability of stretchable supercapacitors. Nano Lett 12(12):6366–6371
25. Wang Y-S, Li S-M, Hsiao S-T, Liao W-H, Chen P-H, Yang S-Y, Tien H-W, Ma C-CM, Hu C-C (2014) Integration of tailored reduced graphene oxide nanosheets and electrospun polyamide-66 nanofabrics for a flexible supercapacitor with high-volume- and high-area-specific capacitance. Carbon 73:87–98
26. Kim C, Yang KS (2003) Electrochemical properties of carbon nanofiber web as an electrode for supercapacitor prepared by electrospinning. Appl Phys Lett 83(6):1216–1218
27. Ding B, Wang M, Yu J, Sun G (2009) Gas sensors based on electrospun nanofibers. Sensors 9(3):1609–1624
28. Yun YJ, Hong WG, Choi N-J, Park HJ, Moon SE, Kim BH, Song K-B, Jun Y, Lee H-K (2014) A 3D scaffold for ultra-sensitive reduced graphene oxide gas sensors. Nanoscale 6(12): 6511–6514
29. Jang B-H, Landau O, Choi S-J, Shin J, Rothschild A, Kim I-D (2013) Selectivity enhancement of SnO_2 nanofiber gas sensors by functionalization with Pt nanocatalysts and manipulation of the operation temperature. Sens Actuators B 188:156–168
30. Yang G, Kampstra KL, Abidian MR (2014) High performance conducting polymer nanofiber biosensors for detection of biomolecules. Adv Mater 26(29):4954–4960
31. Liu H, Reccius CH, Craighead HG (2005) Single electrospun regioregular poly (3-hexylthiophene) nanofiber field-effect transistor. Appl Phys Lett 87(25):1–3
32. Lee SW, Lee HJ, Choi JH, Koh WG, Myoung JM, Hur JH, Park JJ, Cho JH, Jeong U (2010) Periodic array of polyelectrolyte-gated organic transistors from electrospun poly (3-hexylthiophene) nanofibers. Nano Lett 10(1):347–351
33. Wang W, Lu X, Li Z, Lei J, Liu X, Wang Z, Zhang H, Wang C (2011) One-dimensional polyelectrolyte/polymeric semiconductor core/shell structure: sulfonated poly(arylene ether ketone)/polyaniline nanofibers for organic field-effect transistors. Adv Mater 23(43):5109–5112

34. Manuelli A, Persano L, Pisignano D (2014) Flexible organic field-effect transistors based on electrospun conjugated polymer nanofibers with high bending stability. Org Electron Phys Mater Appl 15(5):1056–1061
35. Parrag IC, Zandstra PW, Woodhouse KA (2012) Fiber alignment and coculture with fibroblasts improves the differentiated phenotype of murine embryonic stem cell-derived cardiomyocytes for cardiac tissue engineering. Biotechnol Bioeng 109(3):813–822
36. Rivera R, Pinto NJ (2009) Schottky diodes based on electrospun polyaniline nanofibers: effects of varying fiber diameter and doping level on device performance. Phys E Low Dimens Syst Nanostruct 41(3):423–426
37. Zhou Z, Wu X-F (2013) Graphene-beaded carbon nanofibers for use in supercapacitor electrodes: synthesis and electrochemical characterization. J Power Sources 222:410–416
38. Wu H, Hu L, Rowell MW, Kong D, Cha JJ, McDonough JR, Zhu J, Yang Y, McGehee MD, Cui Y (2010) Electrospun metal nanofiber webs as high-performance transparent electrode. Nano Lett 10(10):4242–4248
39. Fang J, Wang X, Lin T (2013) Nanofibrous p-n junction and its rectifying characteristics. J Nanomater 758395:1–7
40. Pinto NJ, Carrasquillo KV, Rodd CM, Agarwal R (2009) Rectifying junctions of tin oxide and poly(3-hexylthiophene) nanofibers fabricated via electrospinning. Appl Phys Lett 94(8): 083504
41. Lotus AF, Bhargava S, Bender ET, Evans EA, Ramsier RD, Reneker DH, Chase GG (2009) Electrospinning route for the fabrication of p-n junction using nanofiber yarns. J Appl Phys 106(1):14303
42. Gu Y, Zhang Q, Wang H, Li Y (2011) CaSi2O2N2: Eu nanofiber mat based on electrospinning: facile synthesis, uniform arrangement, and application in white LEDs. J Mater Chem 21(44):17790–17797
43. Dhakal KP, Lee H, Kim J (2014) White light-emitting LED using electrospun Alq3/P3BT composite microfibers. Synth Met 190:44–47
44. http://www.rti.org/page.cfm?obj=AA8E3EE5-5056-B100-318259D0069AA638
45. Wu H, Sun Y, Lin D, Zhang R, Zhang C, Pan W (2009) GaN nanofibers based on electrospinning: facile synthesis, controlled assembly, precise doping, and application as high performance UV photodetector. Adv Mater 21(2):227–231
46. Zhu L, Gu X, Qu F, Zhang J, Feng C, Zhou J, Ruan S, Kang B (2013) Electrospun ZnO nanofibers-based ultraviolet detector with high responsivity. J Am Ceram Soc 96 (10):3183–3187
47. Gu X, Zhang M, Meng F, Zhang X, Chen Y, Ruan S (2014) Influences of different interdigital spacing on the performance of UV photodetectors based on ZnO nanofibers. Appl Surf Sci 307:20–23
48. Shim HS, Kim JW, Sung YE, Kim WB (2009) Electrochromic properties of tungsten oxide nanowires fabricated by electrospinning method. Sol Energy Mater Sol Cells 93(12): 2062–2068
49. Zhou R, Liu W, Kong J, Zhou D, Ding G, Leong YW, Pallathadka PK, Lu X (2014) Chemically cross-linked ultrathin electrospun poly(vinylidene fluoride-co-hexafluoropropylene) nanofibrous mats as ionic liquid host in electrochromic devices. Polymer 55(6): 1520–1526

Printed Textile-Based Electronic Devices

25

R. Torah, Y. Wei, Y. Li, K. Yang, S. Beeby, and J. Tudor

Contents

Introduction 654
Printing Techniques for Smart Fabrics 656
  Screen Printing 657
  Inkjet Printing 658
Screen-Printed Conductors 659
  Antenna 660
  Biopotential Monitoring 660
Screen-Printed Dielectrics 660
  Capacitors 661
Screen-Printed Resistors 661
  Force Sensing 662
  Heater 663
Screen-Printed Semiconductors 664
  Thermoelectric Energy Harvesting 665
  Solar Energy Harvesting 666
Screen-Printed Piezoelectric Layers 666
  Piezoelectric Force Sensors 667
  Piezoelectric Energy Harvesters 667
Screen-Printed Chromic Layers 667
  Thermochromic 667
  Electrochromic 670
Screen-Printed Light-Emitting Layers 671
  Electroluminescent 671
Screen-Printed Sacrificial Layers 673
  Motion Sensing 676
  Printed Micropump 677
Inkjet-Printed Conductors 678
  Antennas 679

R. Torah • Y. Wei • Y. Li • K. Yang • S. Beeby • J. Tudor (✉)
Electronics and Computer Science, University of Southampton, Southampton, UK
e-mail: mjt@ecs.soton.ac.uk

© Springer Science+Business Media Singapore 2015

X. Tao (ed.), *Handbook of Smart Textiles*,
DOI 10.1007/978-981-4451-45-1_35

Inkjet-Printed Dielectrics 679
Capacitors 680
Inkjet-Printed Sensors 681
Durability 682
Summary 685
References 686

Abstract

Printed textile-based electronic devices are reviewed. The primary printing techniques utilized are screen and inkjet printing. Conductive tracks can be achieved by means of directly printing on the textile or via an interface priming layer which is first printed to smooth the textile. Conductive tracks can be used to fabricate simple electronic tracks for use as interconnects in a printed circuit board and a fabric antenna or for biopotential monitoring. Combining a dielectric and a conductive layer allows the formation of capacitors on textiles.

Force sensing can be achieved by means of printed resistors or piezoelectric materials. Printed resistors can also be used to produce a heater. Energy harvesting on fabric can be achieved by means of printed semiconductor layers based on thermoelectric harvesting and solar cells. Color variation on fabric can be achieved by printed chromic layers which change color in response to heat (thermochromic) or electrical stimulus (electrochromic). Light emission can be achieved by printed electroluminescent layers. Sacrificial layer technology allows the formation of three-dimensional structures on fabrics such as cantilevers which can be used for motion sensing.

Devices must be sufficiently robust to be suitable for daily use in particular in respect of bending, abrasion, and washing. The durability to bending can be tested by flexing the printed conductive layer around a mandrel. Abrasion durability is evaluated by rubbing the printed conductive textile against a 100 % wool textile with a specific force loading. Wash durability is the most critical function for everyday wearable electronics. Encapsulation, either by lamination or printing, is an effective method to improve the washing durability.

Keywords

Printing • Inkjet printing • Screen printing • Smart textiles • Smart fabrics • Sensors

Introduction

This chapter provides an overview of printed textile-based electronic devices. The textiles considered are limited to those textiles or fabrics which are wearable, that is, being suitable for clothing. Example textiles are those based on polyester yarns, everyday cotton, or specialist clothing materials such as Tyvek which is used in disposable coveralls. The terms textile and fabric are used synonymously throughout.

Printing has been used for many years to add entirely passive patterns to fabrics for the purpose of decoration. An example of this is the silk screen-printed T-shirt which enables custom-designed patterns to be achieved, at low cost, in a short timescale. The colored printed inks survive wearing and repeated laundering. Inkjet printing has been similarly used to produce colored T-shirts. Printing is therefore established in the textiles industry to add color designs to fabrics offering the attractions of:

- Design flexibility
- Suitability for small/medium or large-scale production
- Low materials usage
- Short development time

Printing is also established in the electronics industry for manufacturing hybrid circuits, flexible electronics, and photovoltaic devices and is emerging as a technique for the integration of heterogeneous smart electronic functions by means of a variety of functional nano-/microtechnology-based inks. This offers the capability of printing multiple, identical, or different devices from a wide range of materials. Typical substrates used for rigid-printed circuit boards are FR4 and alumina. Flexible circuits are typically fabricated using low-cost dielectric substrates such as polyester (Mylar®) or polyimide (Kapton®). The circuits typically involve the use of printed dielectric materials as an insulating layer and printed conductive tracks, although some passive components such as resistors can also be printed. Both active and passive surface mount components can be mounted on the flexible circuit. To ensure optimal performance under stress and for environmental protection, the circuits are typically encapsulated with a dielectric material.

The printing of electronic textile-based devices is developing as a method of producing functional electronic devices directly on the textile by printing electronically functional inks. The inks may be those already existing for the electronics industry or specially formulated. The inks must be compatible with the fabric but must also be capable of being combined with each other without degradation of performance or undesired interaction. The materials are deposited on the fabric in the desired pattern building up devices additively, layer by layer, on top the fabric without requiring subsequent photolithography or etching.

There are many challenging requirements in printing on fabrics beyond those of printed electronics or even flexible electronics:

1. The fabric is very rough (50–150 μm for polyester/cotton) when compared to the typical substrates used for flexible printed electronics (e.g., polyester/polyimide) which have nm scale roughness. This fabric roughness is acceptable for color inkjet printing on fabrics because the eye cannot detect a noncontinuous layer but it will stop an electronic layer functioning. To overcome this roughness, sufficient thickness of the primary printed layer must be printed, or a priming fabric interface layer can be printed to smooth the fabric surface allowing subsequent active electronic layers to be successfully printed.

2. The fabrics can only withstand low temperatures (<150 °C) which makes ink curing difficult. This compares with 1,000 °C which alumina can withstand in printed rigid electronics and 400 °C which polyimide can withstand in flexible electronics. However, for environmental considerations, the overall trend in ink development is toward lower temperature thermal curing; localized sintering using, for example, lasers; and the use of UV-curable inks.
3. The safety of the wearer must be ensured so biocompatibility is essential.
4. The printed fabric must be flexible, stretchable, breathable, durable, and washable offering similar characteristics to the unprinted fabric.

This often means, in the case of fabrics, that the ink system must be specially formulated and developed to suit their roughness, surface quality, flexibility, thermal behavior, and chemical compatibility. However, printing possesses the following attractions for smart fabric fabrication:

1. Printing of smart fabrics benefits by leveraging the enormous technology investment in inks and printer functionality in the color and rigid/flexible electronics printing industries. It also benefits from the growing 3D printing industry.
2. Printing allows the integration of multiple devices with differing functionality in a localized area from a wide range of materials with low materials wastage, since it is an additive process unlike current printed circuit board manufacturing.
3. The printed layers can be deposited anywhere on the fabric in any geometric layout and therefore printing offers almost complete design freedom. The printed layers do not need to contribute to the garment's form or functionality, as is a constraint with approaches using functionalized yarns.
4. The functional material is deposited only where required which also ensures that the overall fabric properties such as breathability and flexibility are not compromised by the printed layers.

In the next section of this chapter, the two most relevant printing techniques, screen and inkjet printing, are described. Each electronic function, corresponding to a printable ink, is then presented in turn describing the devices that are facilitated by that function. Screen-printed functions are presented first followed by inkjet-printed functions. The following functions are presented: conductive, dielectric, resistive, semiconductor, piezoelectric, chromic, light emitting, and sacrificial. The final section provides a description of the durability of printed electronic textile devices followed by conclusions.

Printing Techniques for Smart Fabrics

Digital printing or direct write is defined as printing from a digital-based image directly to a variety of media [1]. Printing is essentially instantaneous from the computer image since no physical media are required to define the printed pattern. Digital printing is ideally suited to the production of small quantities of

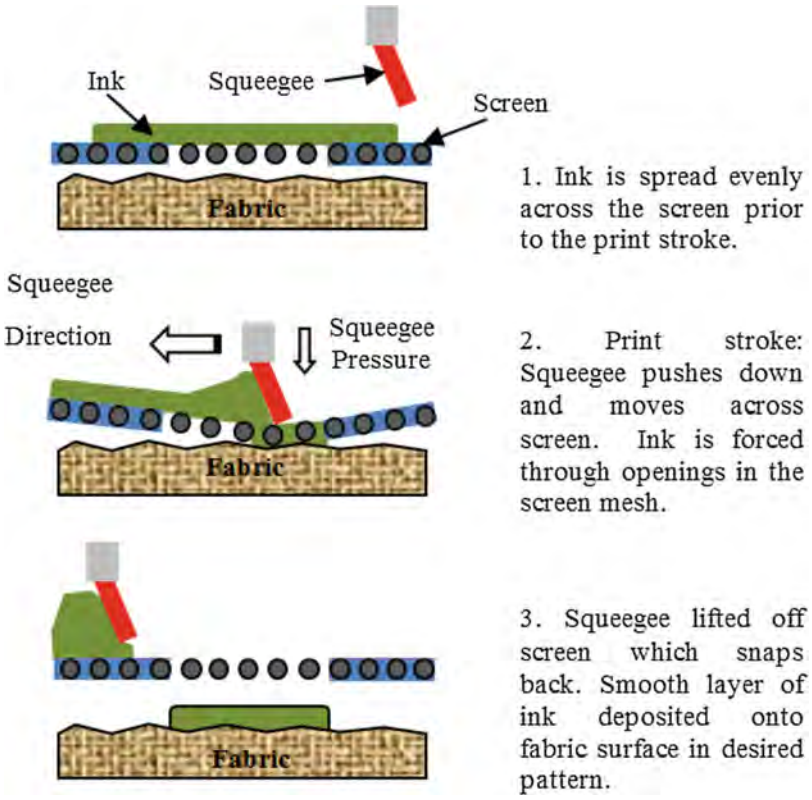

Fig. 1 Schematic of the screen-printing process

bespoke products but it can also be used for large production runs. Digital printing usually deposits a series of dots which can be built up in layers.

Screen Printing

Screen printing, illustrated in Fig. 1, is not a digital printing technique since it requires physical screens to be produced which define the geometry of each printed layer to build up a device. In the deposition process, a thixotropic ink is forced through a patterned screen onto a substrate below. Screen printing produces layers of ~25 μm per print pass and printed layers may be simply built up to produce layers of 100 μm thickness which can overcome the roughness of the fabric. Inks, often called pastes when screen printing, can have a high viscosity (~225 Pa s) and therefore high percentages of active materials can be used in the ink offering high functional activity. Screen printing is less well suited to one-off production compared to direct writing but can produce small-scale development batches and is highly suited to continuous roll-to-roll high-volume device production.

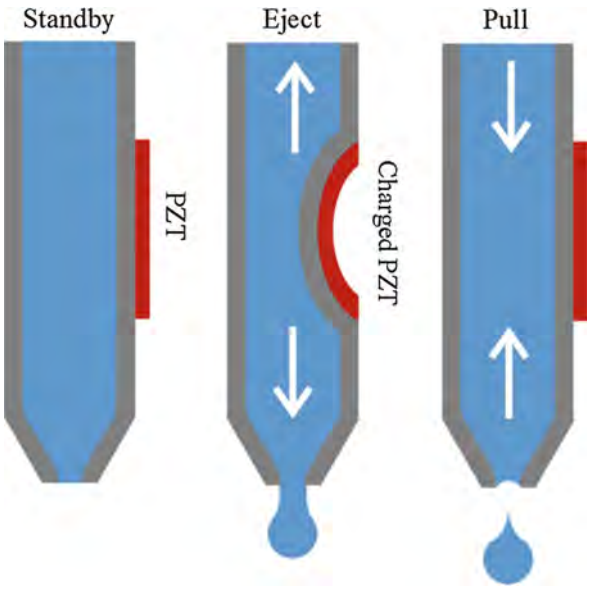

Fig. 2 Cross-sectional view of the droplet formation for a piezoelectric-controlled inkjet printer nozzle

Inkjet Printing

Inkjet printing, shown in Fig. 2, is familiar through its use with desktop PCs and has evolved into a manufacturing process for depositing small quantities of fluids (viscosity 20 mPa s, thickness ~1 μm) in electronic, optical, and bio-analysis applications.

Inkjet printers are now a ubiquitous printing method of which the resolution and speed have made it the natural choice at the low-cost end of the consumer PC market. In drop-on-demand inkjet printing, individual drops of ink are ejected in precise locations from the print head by a pressure pulse within a liquid-filled cavity. The droplets are normally from 10 to 60 pL in volume and exit the print head through a micromachined nozzle typically 20–100 μm in size. Film thicknesses can be built up by repeated multi-pass deposition at the same location. Inkjet printing is a promising technique for the deposition of smart and functional materials for the fabrication of polymer electronics and multicolor polymer light-emitting diode displays. The simple, low-cost process has the potential to achieve disposable electronic circuits for use in, for example, RFID tags. To date, research has mainly concentrated on those inkjet-printable materials required to realize basic electronic circuits on typical circuit boards. Studies have focused on low-resistance conductor materials, defect-free high dielectric strength insulators, and active organic semiconductor materials for use in printed transistors [2].

Inkjet printing has several key advantages. It is a simple noncontact technique that deposits the material in the desired pattern via a nozzle avoiding the use of screens, printing plates, or photolithography. It has good resolution being capable of depositing tracks with 50 μm width with the potential for significant future

improvement. The process is potentially compatible with many rigid and flexible substrates. It enables rapid development and manufacture and is a low waste, highly flexible process, especially suited to small development batches but it can also be used for mass production. However, there are disadvantages when the technology is specifically applied to achieving electronic functions on fabric surfaces:

1. The cured thickness of a material deposited by an inkjet printer is typically <1 μm. This makes it difficult to overcome the surface roughness of a fabric when attempting to print functional smart fabrics which require continuous electronic layers.
2. In addition fabrics are porous and absorb the liquid component of an inkjet ink, which is typically in the range of 70–90 %. This means there is less solid content, compared to screen-printing inks, to "fill in" the roughness of the fabric to provide a continuous film. Additionally the performance of a functional ink improves as the percentage of active material is increased.
3. The requirements for the physical properties of the ink are very strict (viscosity, surface tension, active particle size) with slight variations causing the printer head to malfunction and printing to stop. In addition, for the main commercial inkjet print heads (such as from Dimatix, Xaar, Epson, and Konica Minolta), many have different requirements for their inks to function correctly.

Screen-Printed Conductors

The screen printing of conductive layers onto fabrics typically follows one of two approaches:

1. The conductive layer(s) is printed directly on the fabric with sufficient thickness to overcome the fabric roughness and achieve good conductivity.
2. A surface primer or interface layer is first printed on the fabric and then the conductive layer is printed on the interface layer. The number of layers required to create a smooth surface is dependent on the interface material and on the surface roughness and pilosity of the fabric. Fabrics may also be selected which already incorporate a suitable additional surface primer.

The purpose of the interface layer is to smooth the surface of the fabric by removing the roughness and often additionally providing waterproofing and wash resistance and improving the durability of subsequent layers.

The interface layer-based approach is preferable when the conductive layer is more expensive than the interface layer since fewer conductive layers are needed to reach a given conductivity. This is often the case since conductive polymer pastes are typically silver loaded, although gold, nickel, carbon, and copper are also used. Silver is the most widely used because it offers high conductivity and good environmental stability. Copper is a lower cost alternative although it is less stable and oxidation results in a loss of conductivity. Carbon and nickel are the preferred

options in applications which can tolerate a higher resistance. Conductive polymer inks can be formed by using electroactive polymer materials, such as poly (3,4-ethylenedioxythiophene) (PEDOT) or polypyrrole, or by suspending metallic particles in a polymer matrix. Typical fabrics, on which printed conductors have been produced, are nonwoven fabrics, such as Evolon/Tyvek, which are essentially nonporous, and woven fabrics, such as cotton, polyester, polyester/cotton, and polyester viscose.

Antenna

The screen-printed conductor can form the basis of a screen-printed basic planar antenna structure, for example, a planar dipole and loop antenna, since it requires only one conductive layer for the radiating element. The most promising antenna geometries for printing include planar monopole, planar dipole, loop, patch, and inverted-F antenna. However, the vast majority of printed antennas are mainly on rigid and flexible substrates, e.g., glass slides and polyimide, with few examples on textile. Conductive silver is the most widely used conductive paste for screen printing onto textile substrates, as it provides high conductivity to organic materials and higher ambient stability than copper. A mixture of carbon and silver as the conductive paste can be used to screen print an antenna on Gore-Tex and cotton fabrics. These printed antennas have applications in the clothing industry for on-body communication between devices. There is also interest for these printed antennas in the automotive industry so that they can be embedded in the cabin interior to reduce the weight and manufacturing time compared to traditional antenna.

Biopotential Monitoring

Electrodes, printed on a fabric surface together with their associated wiring, can form a wearable monitoring system, for example, to measure electrocardiogram (ECG), electromyogram (EMG), or electroencephalogram (EEG) by means of the biopotentials at the skin surface. Such a technology, for example, based on printed silicone rubber on a vest can achieve printed sensors to measure respiration, heart rate, temperature, and humidity. A textile headband with printed electrooculography and electromyography can be used for computer control. In general thicker printed electrodes improve skin contact.

Screen-Printed Dielectrics

Screen-printable dielectric materials have existed for over half a century but have only recently been applied to fabrics. A screen-printable dielectric can simply be a pigment printed on the textile; the dielectric can be used as an insulator or an encapsulation layer. Such dielectrics can also act as a structural layer, such as a

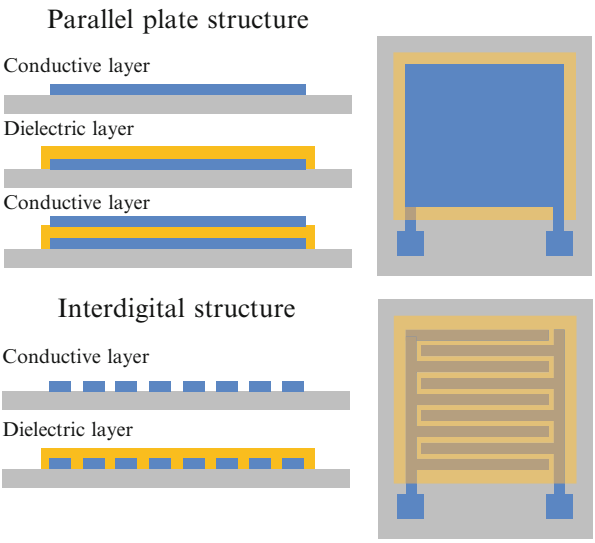

Fig. 3 The cross-sectional and planar view of both parallel plate and interdigital structure capacitor fabrication steps

cantilever, or as part of an electroluminescent device. In addition, a screen-printed dielectric on fabric can be used as an interface layer to support the subsequent printed functional layers. $BaTiO_3$ is a typical dielectric powder material used in paste composition. Alternative printable plastic materials are also used, such as acrylics, vinyls, and urethanes.

Capacitors

A basic printed capacitor structure on textile substrates requires two functional materials: a conductor and a dielectric. The structure can be either a parallel plate structure or an interdigital structure as shown in Fig. 3.

When fabricating a capacitor, the area and thickness of the dielectric layer in a parallel plate structure or the gap and length of the interdigital electrodes can be varied to achieve a range of target capacitance values. Comparing the two capacitor structures, it can be seen that three layers are required for the parallel plate structure and only two for the interdigital structure; it is therefore, in principle, easier to print the interdigital structured capacitor. The textile itself can also be used as the dielectric layer of a capacitor with conductors printed either side in the parallel plate structure or as the same layer in the interdigital structure.

Screen-Printed Resistors

Screen-printed resistors have been used for printed electronic circuits since the 1960s and are typically known as thick-film resistors. Initially the pastes were high-temperature curing (>850 °C), ceramic-based compositions used for printing on

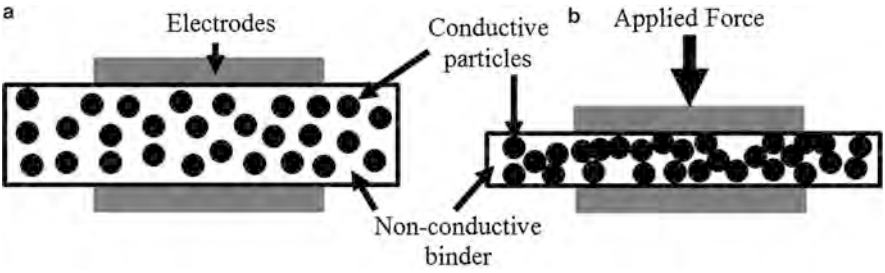

Fig. 4 Piezoresistive composite structure with (**a**) no pressure applied and (**b**) pressure applied resulting in increased conductive particle density

alumina substrates. These pastes use oxides of ruthenium, iridium, and rhenium and can achieve resistances from 1 to 100 MΩ [3]. More recently, polymer-based thick-film materials using different percentages of carbon loading have been used for flexible circuitry [4]. In each case, laser trimming is often used as a post-process to achieve high-accuracy resistance values for the final product.

Force Sensing

Resistors are commonly used to detect force, as strain or as a pressure, and therefore, their integration within textiles is a natural progression. One method uses a piezoresistive material which changes resistivity when subjected to a dimensional change [5]. An alternative, known as a force-sensitive resistor (FSR), uses a resistive layer suspended above a series of interdigital conductors so that when the resistor layer is pressed, it comes into contact with the conductors [6].

Piezoresistive materials are typically semiconductors such as single crystal silicon and polysilicon formed by the doping of silicon wafers [7]. However, such materials are difficult to print and still maintain their fundamental properties; therefore, alternatives have been developed whereby conductive particles are suspended in a flexible polymer such that when pressure is applied, the particles move closer together and the resistivity changes. This concept is shown in Fig. 4 where a piezoresistive composite is created using a combination of conductive and nonconductive materials. When the composite is compressed, the density of conductive particles increases causing a reduction in the resistivity of the material. This concept of piezoresistive composites has been applied to screen-printable pastes comprising carbon black particles with silicone rubber binders and inkjet-printed poly(3,4-ethylenedioxythiophene) polystyrene sulfonate (PEDOT:PSS) layers deposited directly onto yarns.

Tekscan [5] produces a range of screen-printed pressure sensors using piezoresistive materials, the two main examples being their T-Scan and F-Scan systems. Both systems use piezoresistive sensors that are screen printed onto polyimide or polyester plastic films along with printed conductive tracks and provide

a range of sensor arrays from a single force sensor up to 248 sensels per cm^2. The structure uses two separately printed structures with horizontal and vertical piezoresistive strips connected to the sensing electronics via printed conductive wires. This fabrication process is compatible with fabrics.

Interlink Electronics [6] are the leading commercial supplier of force-sensitive resistors. Their products use the more standard FSR layout where a spacer is used. This configuration is harder to replicate on fabric due to the requirement of the spacer layer. However, the principle of the structure can be combined with the piezoresistive paste printed over the top of the interdigital array so that when it is pressed, the particle density between specific fingers of the conductor layer is increased and the position can be determined along with the force.

There are many applications for force sensing using printed resistors and piezoresistors on fabric, especially when used in arrays to provide pressure mapping information. These applications include medical textiles for pressure mapping of the feet, body support in seats and beds, prosthetic limb rehabilitation, and dentistry. In addition they can be used to replace or complement existing systems which use yarn-based technology such as goniometers on the hands and limbs for the medical and entertainment industries, the automotive industry for tire tread analysis, seat comfort, and windscreen wiper performance.

Heater

A resistive heater can be achieved by supplying a current to a printed conductive track of the correct resistivity so that it will produce heat. Printed heaters are used in a wide range of applications such as heater elements for kettles, domestic irons, mirrors for cars, electronic displays, and battery testers. The majority of commercially available printed heated elements use either a single low-conductivity track meander structure or an array of resistive elements; two example designs are shown in Fig. 5.

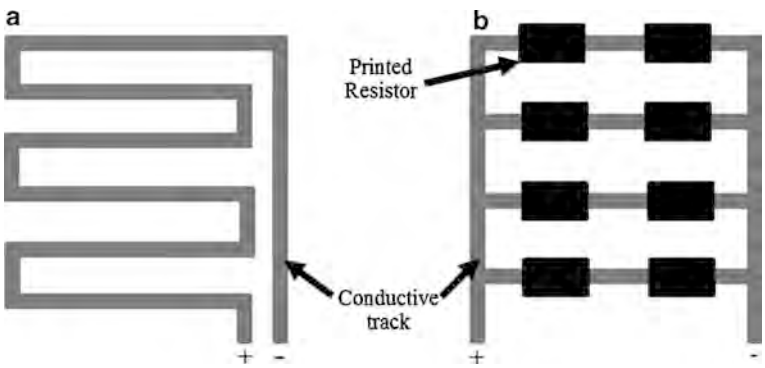

Fig. 5 Printed heater designs: (**a**) continuous meander-printed conductor, (**b**) parallel printed conductors with printed resistor-heating elements

Both of these configurations use printed pastes with specific resistivity properties to match the desired heating requirements of the application. These structures are used to distribute the heat around the substrate to reduce the need for complete coverage and therefore reduce costs. This method also allows the designer to have different heat concentrations in different segments of the heater, either by narrowing or widening the track in particular areas or using different value printed resistors [8].

There are a number of commercially available printed heaters from companies such as Minco, Heatron, Tempco, DeltaT, and Conductive Technologies. These companies currently focus on either ceramic-based pastes which require high curing temperatures unsuitable for printing on fabrics (>700 °C) or polymer-based pastes printed on plastic film substrates such as polyester, polyimide, or silicone rubber.

Currently, the majority of fabric-based heaters commercially available from companies such as SEFAR and WireKinetics use conductive yarns, either as a complete-heated fabric cloth or woven into an existing fabric, such as a car seat or jacket. Alternatively, companies, such as Eeonyx, coat the entire fabric with a conductive compound turning it into a heater. NEL technologies have used their Neltex fabric-based circuit technology [9] to create a heated jacket but the printing method is not defined. All of these approaches are viable for creating fabric-based heaters, but they all require the fabric to be altered at the initial construction stage, whereas printing is an additive process which could be performed on the final garment or fabric item allowing customization by the end user in their own facilities.

It is entirely possible to print a heater track onto fabric using polymer conductive pastes. However, printing directly onto fabric requires sufficient volume of conductive paste to overcome the surface roughness of the fabric which leads to nonuniform thicknesses of the conductive track. This nonuniformity will lead to hot spots within the track as it is heated, potentially causing breakage in the tracks and therefore reducing product lifetime. Therefore, the use of either a laminated film backing for the fabric or ideally a printed interface layer is required to homogenize the surface for the subsequently printed conductive track. This printed interface layer should have good thermal conductivity so that the heat generated from the track is transferred to the fabric as efficiently as possible. Figure 6 shows examples of a printed heater on polyester cotton fabric and elastic fabric and their associated infrared images produced when heated.

Screen-Printed Semiconductors

The electrical conductivity of semiconductor materials lies between conductors and insulators. The electrical current flow within a semiconductor material is due to the movement of holes and electrons. The behavior of holes and electrons is explained by quantum physics, and the properties of the material can be tuned by altering the composition of the material by doping with impurity atoms. Doping with donor

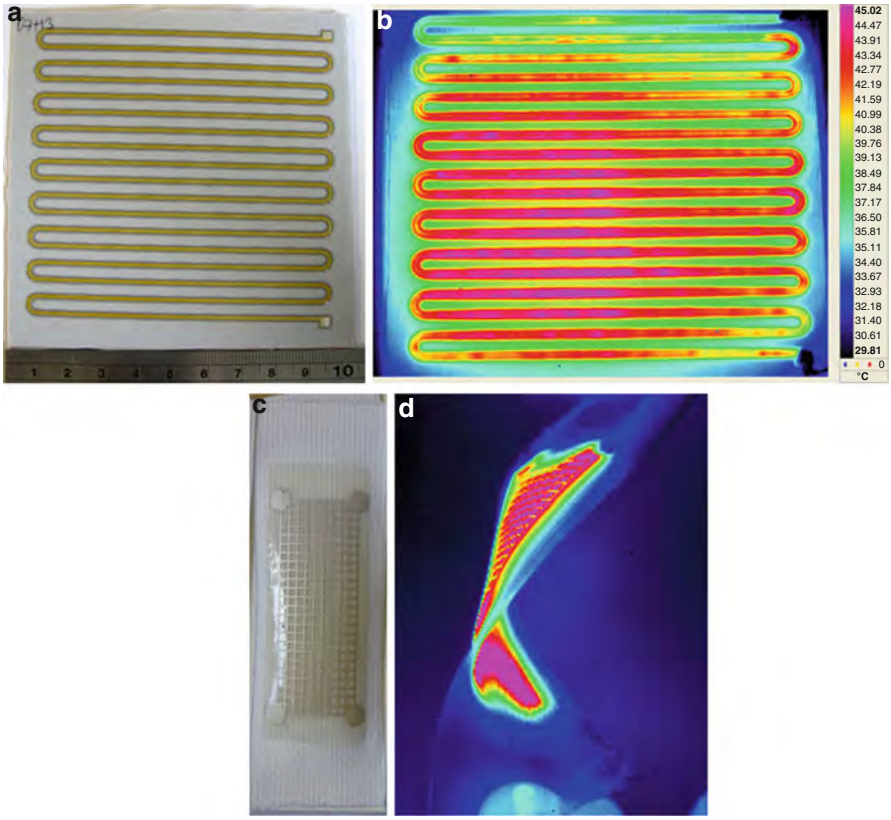

Fig. 6 Printed heaters on fabric and their respective infrared image showing heat distribution. (**a**), (**b**) is polyester cotton substrate from Klopman International, (**c**), (**d**) elastic knitted fabric from Elasta (Reproduced with permission from Torah et al. [10]. Copyright 2012)

impurities creates a majority of electrons and the material becomes n-type. Doping with acceptor atoms creates a majority of holes making the material p-type. Semiconductor properties are normally associated with single crystal materials (e.g., silicon wafers) but these can also be obtained in printable materials suitable for textile printing [11]. Two example applications of printable semiconductor materials on textile are thermoelectric devices for energy harvesting and inorganic solar cells for energy harvesting.

Thermoelectric Energy Harvesting

Thermoelectricity is the conversion of thermal energy into electrical energy (or vice versa). When a temperature gradient exists across a material, charge carriers will

flow from the hot side to the cool side. Thermoelectric devices consist of two dissimilar materials that contact each other forming a thermocouple. An array of thermocouples is linked electrically in series and parallel to generate the desired voltage and current from a given temperature gradient across them. The magnitude of the voltage generated is governed by the Seebeck coefficient of the materials. The largest thermoelectric effect occurs when p- and n-type semiconductor materials are paired. Common materials include bismuth telluride (Bi_2Te_3) and antimony telluride (Sb_2Te_3) which have high Seebeck coefficients at room temperature. The powder forms of these materials can be used to make screen-printable pastes by mixing them with a polymer binder [12]. This approach enables thermoelectric devices to be printed although device performance is at present limited by the temperature constraint imposed by the textile substrate that results in poor conductivity in the printed films.

Solar Energy Harvesting

Solar cells exploit the photovoltaic effect in materials whereby incident photons absorbed by the materials create electron-hole pairs. The majority of solar cells used today are based on silicon; both single crystal and polysilicon are used. Other semiconductor materials that can be used to fabricate solar cells include copper indium gallium selenide. This material is available in inkjet ink form and must be printed in a thin film (up to 4 μm thick) between two electrodes. Highest efficiencies are obtained on glass substrates and, while the inks can be printed onto textiles, again the temperature constraints imposed will reduce efficiency. Other processes such as electrospraying can be used to cover larger areas.

Screen-Printed Piezoelectric Layers

Credit for the discovery of the piezoelectric effect is given to Pierre and Jacques Curie who first reported the effect in 1880 [13]. They observed that certain crystalline materials became electrically polarized when subjected to a mechanical force. In addition, compression or tension on the crystal were shown to produce charges of opposite polarities, proportional to the applied force. Conversely, it was discovered that if a polarized crystal is subject to an electric field, a structural deformation occurs. These observations were defined as the piezoelectric effect and the inverse piezoelectric effect, respectively. Piezo is derived from the Greek word piezein, meaning to press or squeeze where piezoelectricity is “pressure electricity.” The most commonly used screen-printed piezoelectric materials are based on lead zirconate titanate (PZT) and polyvinylidene fluoride (PVDF) although for fabrics application, these are mostly still in the development stage by companies such as Solvay, Meggitt, and Smart Fabric Inks.

Piezoelectric Force Sensors

Piezoelectric materials have been used for detecting force and motion since the 1920s. A typical system uses a metallic diaphragm or membrane with the piezoelectric elements at the point of greatest stress. As stress is applied, the piezoelectric element generates charge in proportion to the stress and the magnitude of this charge is measured. Printed films of this type are currently only used in research applications or niche markets. Their piezoelectric performance is typically an order of magnitude lower than bulk or extruded film devices. However, printing allows greater design freedom and the piezoelectric material can be deposited alongside the other electronic materials to realize a device; existing bulk or film piezoelectric approaches need to be attached, for example, by gluing at the application location. Printing technology is therefore ideal for printing smart fabrics in a roll-to-roll process and could be used in applications such as motion-sensing clothing, haptic feedback devices, and pressure sensing.

Piezoelectric Energy Harvesters

Because piezoelectric materials are electromechanical transducers, they are suitable for kinetic energy-harvesting applications. As with the force sensors, there are a number of research institutions working on this concept and achieving incremental improvements in material performance, but none of these materials are currently used in commercially available harvesters. However, materials such as PZT can be incorporated into a polymer binder and PVDF is already a polymer and therefore both can be printed and cured at sufficiently low temperature to be combined with fabrics. Applications such as energy-harvesting shoes, backpacks, and clothing are being pursued in academia but are currently limited by the piezoelectric activity and the restrictions imposed by the level of energy that can be harvested from body movements before it becomes uncomfortable to the wearer.

Screen-Printed Chromic Layers

Chromism refers to a change in color of a material when triggered by an external stimulus. These color-changing phenomena have been defined by the stimulus causing the change. The common chromisms [14] are thermochromism, electrochromism, photochromism, mechanochromism, piezochromism, and magnetochromism. The vast majority of printing materials available are based on thermochromic screen-printing pastes.

Thermochromic

Thermochromism is the color change in a material triggered by a temperature change. The color change can be reversible or irreversible which is dependent on

the type of thermochromic material and the constituents of the thermochromic system. Temperature change may directly or indirectly stimulate the color changes in the thermochromic materials. For a direct stimulus, heat is the sole cause of color change, whereas in the form of an indirect stimulus, heat affects another property of the thermochromic system (e.g., pH level) which brings about a change in color. Thermochromic materials can be either organic or inorganic with most inorganic thermochromic compounds requiring higher temperatures to effect the change which is irreversible. Thermochromic pigments were invented in 1970 by Dr Suzuki of the Kirokusozai Company. There are two main types of organic thermochromic systems that can be applied to textiles: leuco dyes and liquid crystals [15].

Leuco dyes produce a reversible (or irreversible) color change from colored to colorless (or from colorless to colored) in response to the activation temperature. Leuco dye thermochromic systems are usually composed of a color former (i.e., pH-sensitive dye), a developer (i.e., proton donor), and a nonvolatile cosolvent, and those compounds are melted together and cooled to give the colored pigment [16]. The color of the thermochromic pigment is dependent on the color of the dye and the activation temperature is dependent on the melting temperature of the cosolvent. Below the melting point of the cosolvent, the color former and developer form complexes which cause the color former to form an open ring arrangement resulting in a colored state [17]. When the temperature exceeds the melting temperature of the cosolvent, the interaction between the color former and developer breaks down resulting in a colorless state.

The color change can, by mixing in traditional dyes, be altered to achieve a color change from one color to another. A range of colors is possible (e.g., red, green, and blue) as well as a range of activation temperatures (−15 °C up to 65 °C). The majority use three standard temperature ranges: cold (20 °C), human touch (31 °C), and warm (43 °C) [18]. The basic colors can be combined to create more shades and multiple activation temperatures are also possible offering multiple color changes. The temperature response of leuco dyes is not accurate; thus, a leuco dye system would not change color at a precise temperature. The color change is gradual over a range of temperatures.

Liquid crystals (i.e., thermotropic liquid crystals) are materials that exhibit properties in between those of solids and liquids. This means that the way the crystals are lined up changes with temperature. There are three subphases in the liquid crystalline phase, namely, nematic, smectic, and chiral. Since different subphases have different crystalline arrangements, they will reflect different wavelengths resulting in different colors being seen. Liquid crystals provide a continuously changing spectrum of colors by physical changes in the orientation of the liquid crystal. Liquid crystals can exhibit dramatic color changes over only a few degrees of temperature change. In addition, liquid crystals are more expensive than leuco dyes and are more challenging to print [19].

Thermochromic fabrics became available in 1980 through the Global Hypercolor brand. The entire shirt was made thermochromic by dying with pigment based on leuco dyes and which changes color due to the wearer's body temperature.

Fig. 7 Thermochromic-printed textiles before heating (*left*) and after heating with a hair dryer (*right*) (Reproduced with permission from Christie et al. [15]. Copyright 2012)

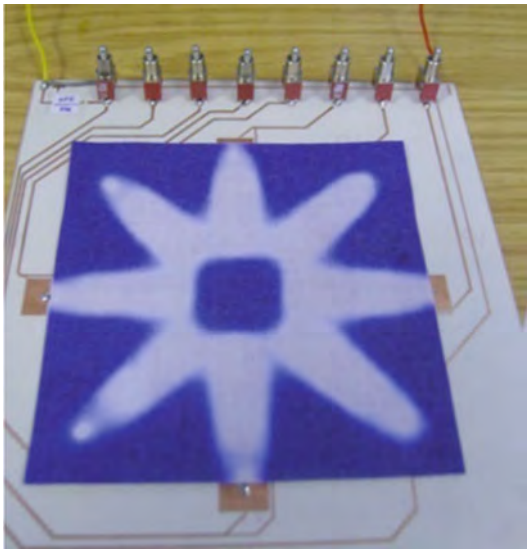

Fig. 8 Thermochromic fabric on rigid circuit board (Reproduced with permission from Robertson et al. [20]. Copyright 2008)

Thermochromic inks for printing on conventional substrates (paper, polyimide, polyester) are available from a range of suppliers such as Chromatic Technologies, Color Change Corporation, and Colour-Therm. These have been applied to make simple consumer products such as stick on thermometers and in product packaging.

To control the temperature of a thermochromic material, a heater may be integrated with the thermochromic textile. Such a heater may be achieved by means of a pre-patterned rigid-printed circuit board attached to the fabric. However, this compromises the fabric flexibility. A number of artists have used screen-printed thermochromic inks in artistic designs using externally applied or environmental heat to change color as shown in Figs. 7 and 8.

Alternative approaches are embroidered stainless steel-heating yarns with the thermochromic ink screen printed over the heating elements and the fabric changing color in response to heat produced along the yarns. The resistive heating element provides a relatively fast response to activate the thermochromic layer but deactivation takes longer due to the time required for air cooling. To achieve a fast response on both heating/cooling cycles, a Peltier device can be used as the activation element as it can increase and decrease the temperature by reversing the polarity of the supplied voltage. A rigid Peltier device can be attached to the fabric using a thermally conductive adhesive. To date approaches have focused on screen printing of thermochromic ink onto fabric with an external heating element to control the color change. The advantage of such an approach is to minimize the complexity of the entire fabrication process.

Electrochromic

The term electrochromism was first used in 1961 by Platt [21] who recognized that the absorption and emission spectra of certain dyes may be shifted by application of a strong electric field. Electrochromism is the change of color caused by a current passing through a material. The reversible color change is normally between a colorless state and a colored state or between two colored states.

Depending on their physical properties, electrochromic materials can be classified into three categories:

1. The coloring species are in a solution at all times.
2. The coloring species are in a solution before activation and solid after activation; thus forming a solid on the surface of the electrode whilst a current flows.
3. The coloring species are in a solid form at all times and no liquid form is involved.

Electrochromic materials can be either organic or inorganic. Organic electrochromic materials contain many aromatic ring systems, such as aniline and pyrroles. These polymers can be oxidized or reduced between a colorless state and a colored state, in the presence of a charge-balancing counterion [22]. The most widely used inorganic electrochromic materials are oxides from a wide range of metals, such as titanium (Ti) and tungsten (W). The color is formed by a charge transfer between metal centers in the solid-state lattice. Organic materials have the following advantages over inorganic materials: [14]:

1. Better coloration efficiency.
2. Faster switching ability.
3. Multiple colors can be achieved from a single material.

An electrochromic device consists of at least three layers, namely, two electrodes and one electrolyte layer. Electrochromic devices can be configured

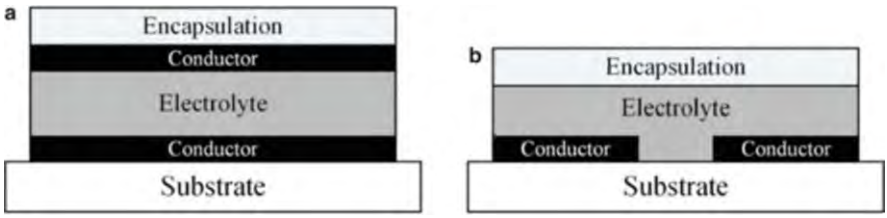

Fig. 9 Basic structures of an electrochromic device: (**a**) vertical and (**b**) lateral arrangement

into either a vertical or a lateral structure depending on the fabrication technique and applications, shown in Fig. 9.

The vertical structure commonly results in faster devices since switching between colored states is often limited by ion transfer between two electrodes; the electrolyte is normally thinner in the vertical configuration [23]. However, the lateral structure is simpler to print as both electrodes can be printed during a single printing stage. Inorganic electrochromic devices are mainly made on glass with the electrochromic layer sandwiched between two glass sheets with conductive layers on them. Screen printing is used to deposit the conductive pastes, such as carbon black or silver, onto the glass.

However, a fully screen-printed electrochromic device on textile has not been reported in the literature and there are several challenges limiting the use of printed electrochromic material on textiles:

- Screen-printable transparent electrode: Transparent conductive polymers have been developed such as indium tin oxide (ITO), antimony tin oxide (ATO), and PEDOT:PSS, but these materials are only semitransparent when screen printed.
- Screen-printable electrochromic material: A screen-printable inorganic electrochromic paste is not suitable for use on textiles due to its high curing temperature.
- Transparent encapsulation: The electrochromic device needs to be encapsulated to avoid material degradation in long-term operation. The encapsulation layer must be transparent or semitransparent to ensure the electrochromic layer is visible when activated.

Screen-Printed Light-Emitting Layers

Electroluminescent

Electroluminescence (EL) encompasses light-emitting capacitors, light-emitting diodes (LED), and organic light-emitting diodes (OLED); each of these technologies emits light due to external electrical stimuli [24]. However, in the context of printing, electroluminescence typically refers to light-emitting capacitors as this is the most common and established technological form for printed

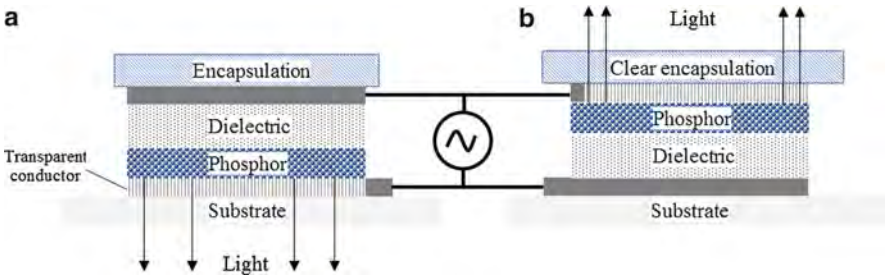

Fig. 10 Standard configurations for printed EL lamps: (**a**) light emitted through a transparent substrate, (**b**) light emitted through a printed transparent conductor

electroluminescent displays and the one most ideally suited for printing on fabric. Although there is significant fundamental research into all printed OLED and LED displays, these are not yet established as commercial products, and their sensitivity to active layer thickness and environmental conditions makes them currently impractical to print on fabrics.

The principle of EL lamps was discovered in 1936 by Georges Destriau, an associate of Marie Curie in her Paris laboratory, while working with zinc sulfide phosphor powders. However, they were not commercialized until the 1950s by companies such as General Electric and Sylvania Electric. Typical applications for this technology are in smart fabrics for display illumination, touch panels, advertising, warning work wear, architecture, furniture, automotive interiors, and fashion.

Light-emitting capacitors are more commonly known as EL lamps, and their fundamental structure consists of a light-emitting phosphor layer sandwiched between two electrode layers. To achieve light emission from this structure, one of the electrodes is required to be transparent. To provide a sufficiently high electric field, and therefore increase brightness and reliability, a dielectric layer is often included with the phosphor layer. The EL lamps are driven by an AC voltage of 100–400 V at a frequency of 300–600 Hz. A higher voltage produces greater brightness of the lamp, but the key advantage of EL lamps is that the current consumption is very low, typically <10 mA, and therefore, the power consumption and heating effect are very low compared to standard incandescent bulbs. Figure 10 shows two alternative configurations for printed EL lamps; lamp (a) is printed onto a transparent substrate coated with a transparent conductor with lamp (b) printed on top of a substrate in the reverse order with a printed transparent conductor on top.

Of these two types of printed EL lamps, option (b) is predominantly used for printing on fabric. Option (a) can be used, but because the substrate itself must be coated in a conductor which must be transparent, this excludes the majority of fabric materials. The base material for most EL lamp phosphors is zinc sulfide which is subsequently doped with copper, silver, or manganese to achieve green, blue, and red/orange colors, respectively; other colors are possible by combining these powders [25]. The conductor layers are typically carbon, copper, or silver

with PEDOT:PSS, ATO, or ITO used for the transparent conductor. The dielectric is ideally barium titanate to allow for a higher field strength, but any nonconductive polymer could potentially be used.

There are a number of screen-printed EL lamp displays on fabric which are commercially available, such as the T-Qualizer T-shirt [26]. However, these lamps are first printed onto a plastic backing film which is subsequently sewn onto the garment. EL lamps can be printed directly onto fabric if low-temperature (<150 °C) or ultraviolet (UV) curing polymer pastes are used. Examples include the "Puddle Jumper" raincoat which uses EL lamps screen printed onto a raincoat which is then combined with interwoven water sensors to produce an interactive display [27] and a watch display which was screen printed directly onto polyester cotton fabric [28].

Because they are less sensitive to changes in thickness compared to OLED/LED devices, they are more robust when printed onto an uneven fabric surface. However, nonuniformity in the printed layers will result in uneven light distribution across the EL lamp. Therefore, when printing directly onto fabric, the performance is improved by using an interface layer.

When using this approach, the interface layer is first printed onto the fabric followed by the layer sequence given in Fig. 10b. Typical print thicknesses are around 5–40 μm for each of the printed layers, producing a lamp with a total thickness around 150 μm which does not significantly impact on the flexibility, weight, or breathability of the fabric.

There are currently no commercially available EL lamps printed directly onto fabric as their durability has not yet reached a sufficiently high level to match those printed on plastic film. However, it is clear that as the printed materials improve, this technology could be applied to a number of applications with reduced manufacturing complexity when compared with printed EL films.

Screen-Printed Sacrificial Layers

Sacrificial technology exploits a selective layer removal process to fabricate free-standing structures [29]. The sacrificial layer acts as a temporary supporting platform for subsequent layer deposition and is removed at the final fabrication stage to leave a cavity or free space. Sacrificial technology has been developed over the last three decades in MicroElectroMechanical Systems (MEMS) [30]. Figure 11 shows a basic sacrificial process, in this case resulting in the formation of a cavity and a beam.

Sacrificial materials may be classified, by the type of removal mechanism, into three categories:

1. Water
2. Organic and inorganic solvent
3. Thermal

The water removal mechanism works by dissolving the sacrificial material, forming a solution. The solubility between the material and water is key to achieve this.

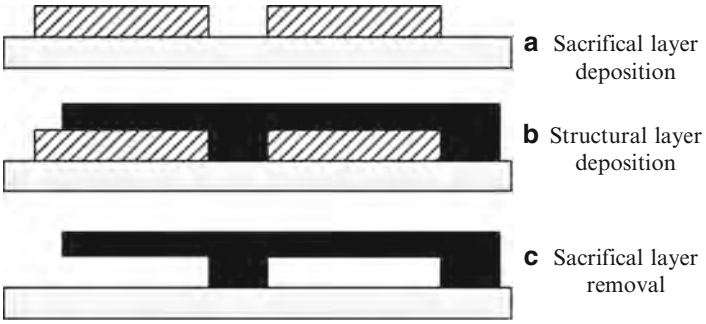

Fig. 11 Schematic diagram of the sacrificial deposition and removal process

Potential water-soluble sacrificial materials for surface micromachining are poly (acrylic acid) (PAA), poly(vinyl alcohol) (PVA), and dextran [31]. These materials are nontoxic, environmentally friendly, and insoluble in most organic solvents; solutions of these materials can be dried at temperatures below 150 °C in under 10 min. Once dried, the layers are strong enough to support the fabrication of subsequent layers and are compatible with a number of polymer materials.

The chemical reaction is key when inorganic materials are in contact with corresponding inorganic liquid removers, such as an acid or alkali. The inorganic removers used are chemicals which are corrosive, oxidizing, harmful, or flammable. The removal rate is dependent on the temperature and the concentration of the remover. As these removal mechanisms have high selectivity, high throughput, and are relatively inexpensive; they have been widely used in MEMS fabrication.

Unlike inorganic materials, organic materials do not require aggressive solvents, such as acids and alkalis, as the remover. Instead, a variety of organic solvents or solvent systems are used as the removers to dissolve them from the substrate. This reduces the probability of damage to structural or substrate materials. Inorganic materials typically focus on oxides and metals. The most common inorganic sacrificial material is silicon dioxide, as it can be preferentially etched in HF solution with high selectivity to silicon, and metallic materials, such as copper, which can also be removed with appropriate inorganic removers, such as a mixture of $FeCl_2$ and HCl [30].

Thermally removable sacrificial materials primarily transform the sacrificial material by a chemical or physical change caused by a change in temperature. The key factors for thermally removable mechanisms are the temperature and time required. The chemical changes of a material include decomposition and oxidation resulting in new substance(s). In contrast, physical transformation only changes the phase of the material without modifying the chemical composition and new substances are not produced. There are three physical phases, which are solid, liquid, and gas. Transformations between the three phases are possible by changing the temperature, as shown in Fig. 12.

Some materials sublime directly without a liquid phase due to their high vapor pressure at a lower temperature which is normally below its triple point (at which three phases of a substance coexist at the same time). The vapor pressure is only a

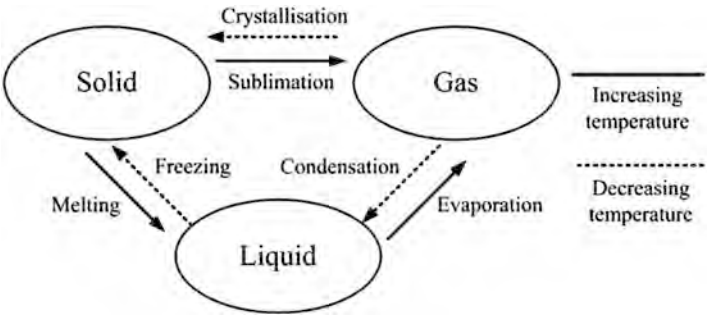

Fig. 12 Phase-changing diagram between solid, liquid, and gaseous phases

function of temperature and is independent of the volume of the system or the number of phases present [32]. In physical transformations only energy (e.g., from heating and cooling) is required. The decomposable materials polynorbornene and polycarbonate show a good compatibility with silicon dioxide, silicon nitride, and some polymers with high glass transition temperatures. However, the removal temperatures and deposition processes are not compatible with the majority of fabrics and the screen-printing process. Wax has a low removal temperature of 75 °C, which is compatible with most fabrics, but wax needs to be liquefied before deposition which is a significant challenge for screen printing. In addition, due to the brittle properties of the wax, printed wax layers cannot withstand the pressure used for screen printing resulting in damaged layers.

None of the sacrificial materials developed for MEMS are suitable for textile applications due to incompatible deposition processes or removal materials. Inorganic materials can be deposited onto most substrates but the deposition conditions are too harsh for fabrics. Further, the removal mechanisms would degrade or even destroy the fabrics and subsequent layers can also be damaged. Even though the removers of organic sacrificial materials are not as harmful to fabrics as those used in inorganic sacrificial materials, the deposition method is still not compatible with the surface topology of the textiles.

Unlike sacrificial materials in MEMS applications, screen-printable sacrificial materials have not been widely reported previously. The requirements for screen-printable sacrificial materials are as follows:

- The material should be of a suitable rheology for screen printing.
- When printed, the material must not react with other layers.
- The material should provide a solid foundation once it is dried or fired.
- The materials must be completely removed at the end of the process and the removal method should not damage other printed layers and the substrate.

Figure 13 shows a screen-printable sacrificial paste based on the plastic crystal [33] trimethylolethane which can be thermally removed at a relatively low temperature, 150 °C, leaving no residue without harming the fabric substrate.

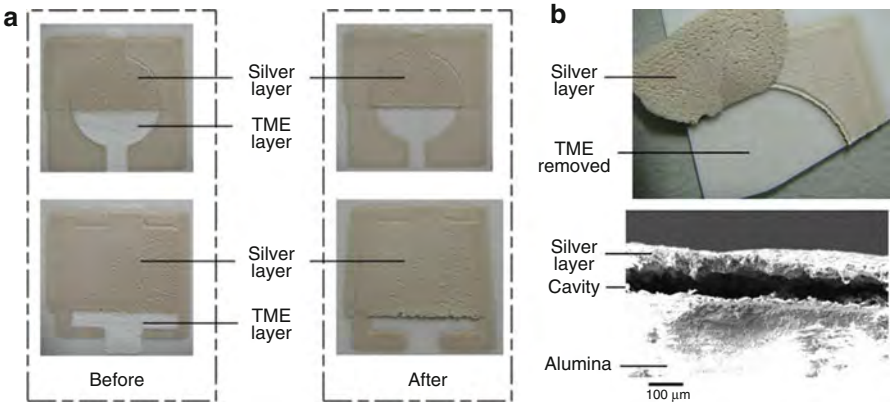

Fig. 13 (**a**) Initial removal of the sacrificial material; (**b**) free-standing silver layer peeled off from the alumina and a cross-sectional SEM micrograph of the printed sample (Reproduced with permission from Wei et al. [34]. Copyright 2012)

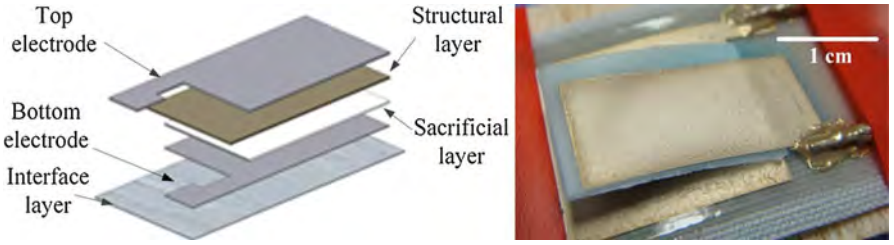

Fig. 14 Schematic diagram of printing sequence (*left*) and released results (*right*) for a capacitive cantilever on fabric (Reproduced with permission from Wei et al. [38]. Copyright 2013)

Motion Sensing

Smart fabric motion sensors have been reported in previous studies, and several sensing mechanisms and fabrication technologies have been used and developed to realize a motion sensor on fabrics. The most common transduction mechanisms for smart fabric applications are piezoelectric [35], piezoresistive fabricated by knitting and braiding [36], and capacitive [37].

Capacitance-Based Detection

A fully screen-printed capacitive-based motion sensor on a cantilever structure requires only conductive, structural, and sacrificial layers as shown in Fig. 14.

Piezoelectric-Based Detection

For the piezoelectric approach, a screen-printed free-standing cantilever structure with a piezoelectric layer on top can form a motion sensor as shown in Fig. 15.

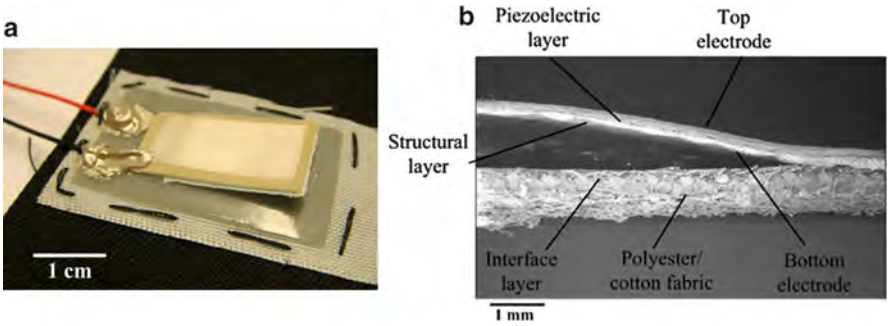

Fig. 15 (**a**) An example of a screen-printed piezoelectric cantilever after the removal process, (**b**) cross-sectional micrograph of a piezoelectric cantilever (Reproduced with permission from Wei et al. [39]. Copyright 2012)

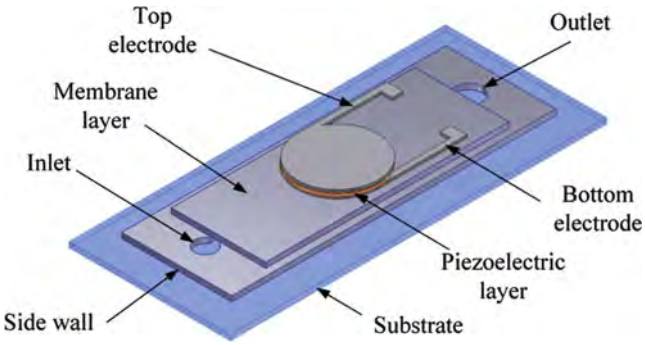

Fig. 16 Schematic diagram of a valveless micropump

To achieve a material with a low curing temperature and a higher piezoelectric coefficient, a screen-printable piezoelectric polymer composite is required. This composite combines the high piezoelectric coefficient of ceramic lead zirconium titanate (PZT) particles with the properties of a polymer (i.e., low curing temperature and flexibility). The printed layers are interface, sacrificial, structural, bottom electrode, piezoelectric, and top electrode. The curing requirements of these pastes are compatible with the sacrificial material and do not cause any significant mass loss of the sacrificial layer during the printing and curing of the subsequent layers.

Printed Micropump

There are two types of micropump: mechanical pumps use movable parts, such as valves and oscillating membranes, and nonmechanical pumps are based on direct transfer of energy into the fluid and do not require moving parts. Of the mechanical pumps, a valveless micropump can be screen printed on a flexible polyimide substrate as shown in Fig. 16.

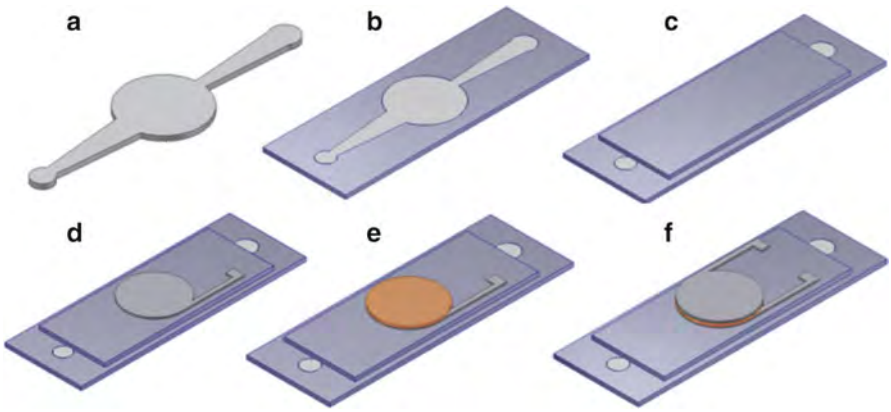

Fig. 17 Printing sequence of a valveless micropump with a piezoelectric layer: (**a**) sacrificial, (**b**) side wall, (**c**) membrane, (**d**) bottom electrode, (**e**) piezoelectric, (**f**) top electrode layers

The printing sequence, shown in Fig. 17, consists of:

1. The sacrificial layer which defines the dimensions of the pump chamber and channels, diffusers, and the reservoir
2. The side wall layer which is the same height as that of the sacrificial layer and ensures the membrane has a uniform thickness
3. The membrane which acts as the part of the actuation mechanism and forms the channels
4. The bottom electrode for the piezoelectric actuator
5. The piezoelectric layer which produces the actuation mechanism on the membrane
6. The top electrode for the piezoelectric actuator

Inkjet-Printed Conductors

Inkjet-printed electronics began with inkjet printing a conductive layer on a rigid substrate, such as a glass slide, then migrated to flexible substrates, such as paper and polyimide. Inkjet printing of conductors can consist of conductive silver or organic PEDOT layers on a yarn-based textile substrate (e.g., cotton). The inkjet-printed ink can be combined with a post-printing redox reaction to improve the final conductivity. As the inkjet-printable ink has a very high solvent content, it can penetrate through the whole thickness of the cloth and also distort the desired pattern beyond its original dimensions. Therefore, inkjet printing a conductive layer on a yarn-based woven textile is a significant challenge, which results in less successful results than screen printing.

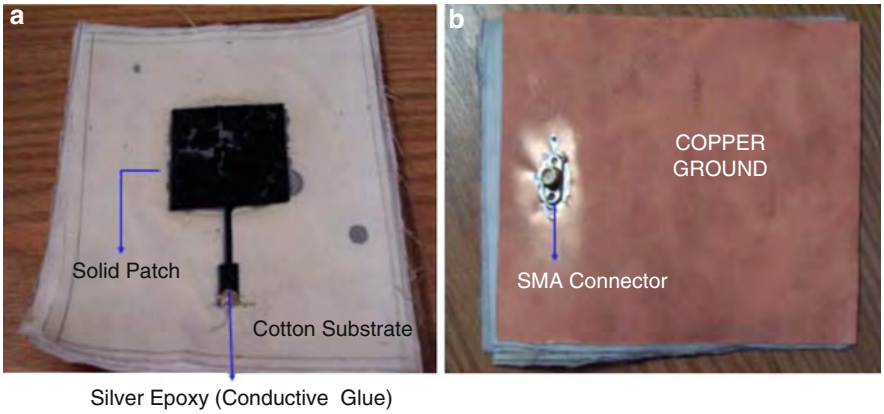

Fig. 18 Top view image of a microdroplet deposition-printed patch antenna by microdroplet deposition of PEDOT/PSS and (**b**) back view of the patch antenna back plane and connector (Reproduced with permission from Patra et al. [40]. Copyright 2007)

Antennas

A planar antenna structure is a straightforward application of an inkjet-printed conductor on a textile substrate. For smoother textiles, such as 100 % cotton mercerized twill, microdroplet deposition which is technically equivalent to inkjet printing can be used to realize a wearable textile patch antenna as shown in Fig. 18.

For rougher textile substrates, such as 65/35 polyester/cotton, an initial screen-printed flexible insulating interface prevents subsequently printed high solvent content inkjet-printable inks being absorbed by the yarns. This significantly increases the inkjet-printed silver conductivity, per deposit of the silver layer on textile substrate, reducing the manufacturing time and cost per device. This approach has been used to achieve an inkjet-printed textile dipole antenna, as shown in Fig. 19; an inkjet-printed textile patch antenna, as shown in Fig. 20; and an inkjet-printed textile frequency selective surface, as shown in Fig. 21.

Inkjet-Printed Dielectrics

An inkjet-printing dielectric is relatively straightforward in the printed electronics field; the majority of inkjet-printed dielectrics are used to encapsulate an active component or as an insulator layer on the metal insulator metal crossovers. In these applications, there are often no thickness or uniformity concerns in the final inkjet-printed dielectric layers. UV-curable inkjet-printable dielectric inks are in high demand in this area. Inkjet-printed dielectric layers can also be used as a functional layer in inkjet-printed devices such as inkjet-printed transistors and capacitors when thickness and uniformity are important.

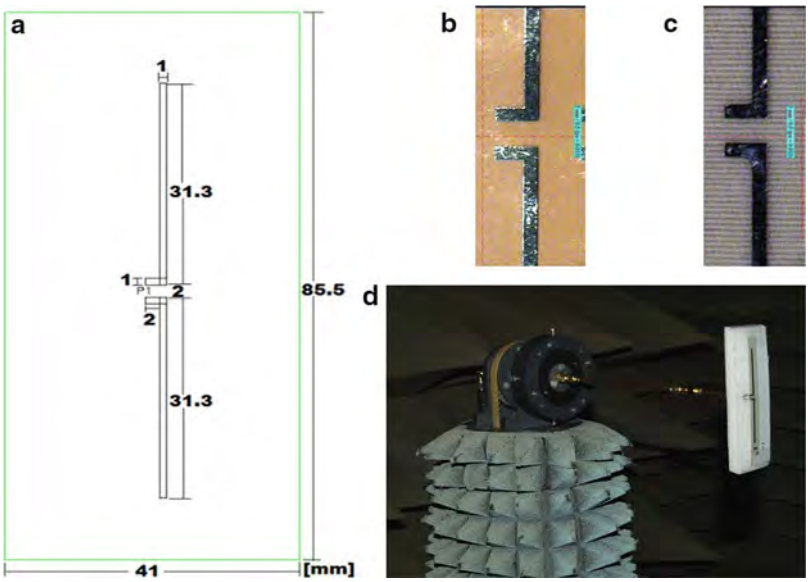

Fig. 19 (**a**) Geometry and dimensions: digital microscope image of dipole on (**b**) polyimide film, (**c**) interface-coated 65/35 polyester cotton fabric, (**d**) printed dipole antenna in an anechoic chamber (Reproduced with permission from Li et al. [41]. Copyright 2012)

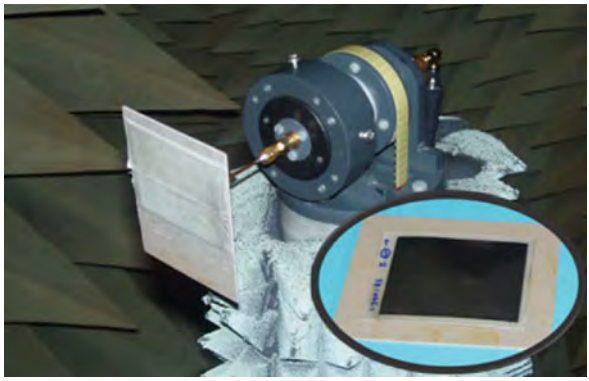

Fig. 20 Inkjet-printed patch antenna in an anechoic chamber. Inset: patch antenna before connection (Reproduced with permission from Li et al. [42]. Copyright 2013)

Capacitors

A capacitor is one of the fundamental passive electronic components in inkjet-printed smart fabric-based electronic circuits. However, fabrication is more challenging compared to an inkjet-printed antenna since two inks are required. The capacitor also typically requires a low-temperature processable, thin dielectric layer, adding a further challenge. The thickness, topology, and dielectric properties of the printed dielectric will significantly affect performance. Typically, two deposits of the dielectric ink for a single layer are required to avoid or minimize

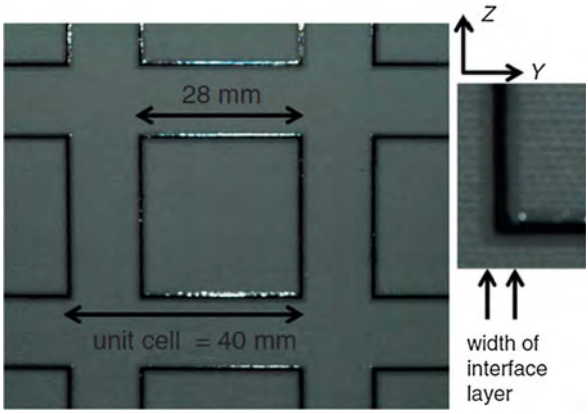

Fig. 21 Geometry of an inkjet-printed frequency selective surface on polyester cotton textile substrate (Reproduced with permission from Li et al. [43]. Copyright 2014)

the pinholes in the dielectric film; pinholes will cause short circuits or reduce performance. Pinholes can be caused by dirt on the surface, misfiring jets, or poor wetting between layers.

Solvent-based inkjet-printable dielectric inks can produce a thin dielectric layer in the micron or submicron range, but these typically require curing temperatures above the limit of most fabrics (>150 °C). An inkjet-printable UV-curable layer is typically thicker, of around 7 μm per layer, decreasing the capacitance. Therefore, an inkjet-printable UV-curable dielectric ink for thin layer deposition by inkjet printing at room temperature is of significant interest.

An all-polymer-printed capacitor can be fabricated on a rigid substrate by inkjet printing using PEDOT/PSS ink and a polyimide(amic acid solution)-based dielectric ink, with a low-temperature process (150 °C) potentially suitable for fabrics. Figure 22 shows an inkjet-printed smart fabric capacitor on a standard 65/35 polyester cotton textile substrate. It uses a screen-printed interface layer underneath the inkjet-printed silver layer and a UV-curable inkjet-printed thin dielectric film formulated using poly(4-vinylphenol) (PVP).

Inkjet-Printed Sensors

There are a further group of organic and inorganic materials which can be used for inkjet-printed sensors. Inorganic materials use chemical and physical property changes to react to external stimuli, such as force, temperature, or gas. Organic functional sensing materials incorporate sensing through their conjugated polymer chemical structure. Organic materials can be cataloged into four groups based on their sensing methods:

1. Conductivity
2. Electrochemical potential
3. Photovoltaic
4. Fluorescent

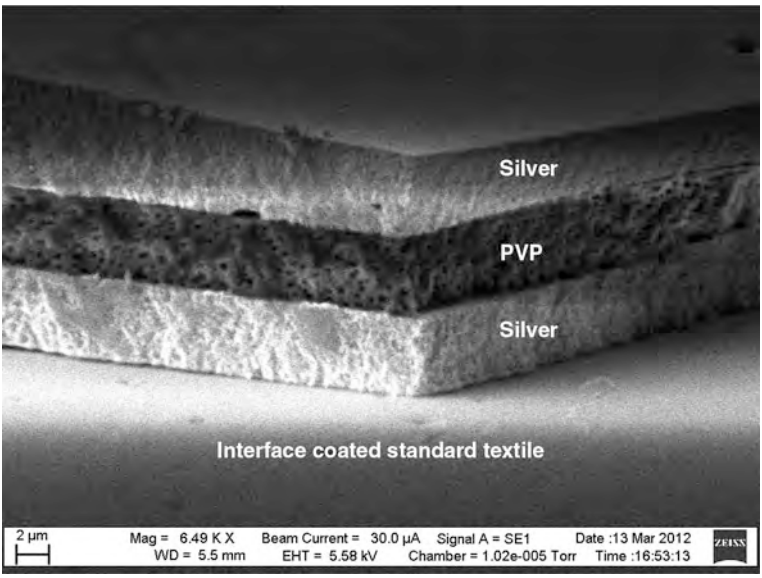

Fig. 22 SEM cross-sectional images for left, an inkjet-printed capacitor on textile (Reproduced with permission from Li et al. [44]. Copyright 2012)

Conductivity can be monitored to achieve inkjet-printed strain gauges on textile using multi-pass printing or a silver seed line may be printed and subsequently electroless plated. For the organic materials, the first three sensing methods are more likely to occur in conductive conjugated polymers. For example, polythiophene and polypyrrole have been used to detect metal vapor, gas, and other compounds. The fourth sensing method is commonly used by poly (phenylenevinylene) (PPV), polyparaphenylene (PPP), polyfluorene (PF), and poly(phenyleneethynylene) (PPE) to realize photoluminescence.

For inorganic material-based sensing applications, strain gauges, pressure and gas sensors have been developed in the last few decades. However, none of these organic or inorganic sensing applications have been realized on a textile substrate by either inkjet printing or screen printing to date.

Durability

Printing electronics on textile is a versatile fabrication method to integrate electronic functionality onto traditional textiles. The previous sections have presented various printed functions on textiles using screen printing and inkjet printing. However, these devices must be sufficiently robust to be suitable for daily use, in particular in respect of bending, abrasion, and washing. Evaluation of these properties initially focuses on the durability of the printed conductive tracks/pads which are a simple but fundamental element for printed electronic devices. The durability

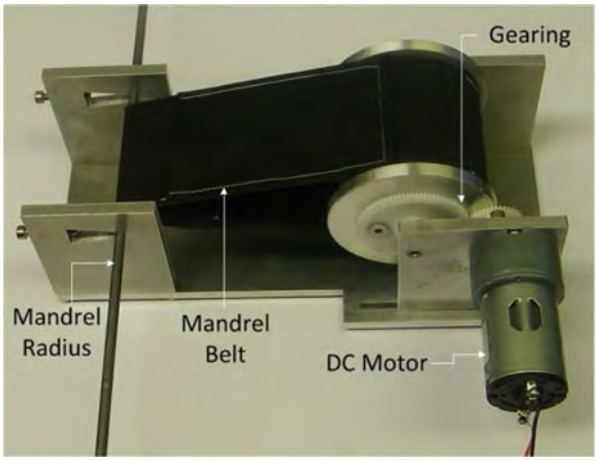

Fig. 23 The mandrel machine purpose built for testing conductive track-bending durability (Reproduced with permission from Paul et al. [45]. Copyright 2014)

of the printed electronic devices with more complicated structures (e.g., electroluminescent lamps, motion sensors) can then be investigated.

In order to achieve compatibility with textiles in terms of flexibility and low-temperature curing (110–130 °C for ~10 min), silver pastes are predominantly used on printed conductive textiles. The flexible silver not only maintains the inherent flexibility of the textile after printing/curing but also provides good conductivity while bending. The durability to bending can be tested by flexing the printed conductive layer around a mandrel such as that shown in Fig. 23. There are two orientations in which a conductive textile can be flexed around a radius, with the printed structure on the inside or outside of the bend and both should be tested as the results are different.

Abrasion resistance is an important property for the electronic textiles intended for wearable application since abrasion continuously occurs. Abrasion durability is evaluated by rubbing the printed conductive textile against a 100 % wool textile with a force loading, using the apparatus shown in Fig. 24. Abrasion cycles vary from 500 to 5,000 depending on the electronic textile tolerance and the application requirement.

Wash durability is the most critical function for everyday wearable electronics. Unencapsulated printed conductive tracks typically cannot survive machine washing due to the combined effects of mechanical stress, detergent, and water. Encapsulation, either by lamination or printing, is an effective method to improve the washing durability. There is no established standard for wash tests of printed electronics textile although ISO standards exist for the washing of everyday clothing. Most electronic textile wash tests are therefore carried out at 30–40 °C with a washing time from 10 to 60 min. The washing durability of conductors is determined using the resistance change after tens of washing cycles. Other device functions (e.g., electroluminescence brightness) can also be used to assess the wash resistance.

Fig. 24 Abrasion resistance test equipment (Reproduced with permission from Mathis et al. [46]. Copyright 2014)

The durability of the printed conductive textile is affected by a combination of the chosen textile, the conductive layer material, the printed pattern geometry, and the protective layer, if used. The following guidelines achieve a good initial performance and improve durability, in particular the washing resistance of the printed electronics:

1. Textile selection. For printing the electronics on fabric without using an interface layer, a fabric with a flat and smooth surface, high yarn density, low pilosity, and minimal pore size are recommended in order to reduce the penetration of the conductive paste into the yarns and achieve high conductivity. Nonwoven fabrics normally have better performance than woven fabric regarding printability. However, for everyday clothing, woven fabrics are more likely to be used because they are flexible, breathable, and comfortable. To improve the printability of these textiles, using an interface layer applied either by coating or printing is highly recommended. The interface layer not only reduces the usage of the subsequently printed conductive paste but also serves as a barrier layer to prevent damage, such as water penetration into the silver layer during washing.
2. Conductive material selection and pattern design. Silver paste is the most commonly used conductive paste due to its higher stability than copper paste and lower cost than gold paste. Most commercial silver pastes have good conductivity with a sheet resistance below 50 m Ω/□ at 25 μm thickness. A conductive material with high flexibility normally offers high durability with regard to bending and washing. However, it is typically not sufficiently robust to survive washing without a protective layer on top. The pattern geometry has a strong influence on the durability. Long and thin conductive tracks normally have lower durability than the short and wide tracks. Designs with curved patterns provide a more even stress/strain distribution compared to a 90° corner when the fabric is flexed and therefore have higher durability.

3. Protective layer. The most common protective material used for the protective layer is polyurethane due to its high flexibility and good adhesion. In lamination-based processing, a polyurethane film is used to cover the conductive pattern at elevated temperature under high pressure. In printing, a polyurethane paste is printed on top of the conductive tracks. Lamination is a faster processing fabrication method than printing; however, printing is a more versatile method as the encapsulation layer can be selectively printed only where necessary better maintaining the inherent properties of the textile.

Summary

The area of printed electronic textile devices has been presented in the context of those textiles that are suitable for clothing. This area is at the research stage and many of the devices are nascent. The primary printing techniques used are those of screen and inkjet printing. Screen printing offers the attraction of thicker layers, which are more suited to rough textiles, with high functional activity. Inkjet printing benefits by being a direct write technique producing printed layers directly from the computer image. Screen printing is the more successful technique when applied to textiles and, to date, has achieved a wider range of functions.

Screen-printed conductive textiles have been used to produce antenna and for biopotential monitoring. A low-cost surface primer interface layer may be first printed on the textile to minimize the thickness of the more expensive conductive ink required to achieve a given conductivity. Dielectrics can be used as this primer layer and, when combined with conductors, can form a capacitor on the textile. The capacitor structure can be either a parallel plate or interdigital structure. Three layers are required for the parallel plate structure and only two for the interdigital structure. Printed resistors or piezoelectric layers can be used to detect force on a textile. In addition a printed resistor or conductor can be used to achieve a heated textile.

In addition to the basic passive electronic components, printed semiconductors can be used to achieve energy harvesting by means of the thermoelectric effect or photovoltaic effect. Color change textiles can be achieved by means of the thermochromic effect, when combined with a printed heater, or directly, using the electrochromic effect. Light emission can be achieved by directly printing electroluminescent materials in combination with semitransparent conductors. Advanced three-dimensional free-standing devices, such as cantilevers or pumps, can be fabricated by utilizing a printed sacrificial material as a supporting material which is later removed to free the structure.

Printing is a powerful technique which allows the simultaneous fabrication of multiple devices on a fabric offering the potential to combine multiple functions in a small area. Since the printed devices do not contribute to the fabric structure (unlike yarn-based approaches), they can be printed in any design configuration and at any stage during the textile manufacturing process. Durability to washing, bending, and abrasion are important considerations for the adoption of printed textile electronic devices.

References

1. Whitbread D (2009) The design manual, 2nd edn. UNSW Press. ISBN: 978-1742230009
2. Magdassi S (2009) The chemistry of inkjet inks. World Scientific, Singapore. ISBN 978-9812818218
3. Panzini M (2011) Thick films: properties, technology and applications. Nova Science, New York. ISBN 978-1614703846
4. Gilleo K (1996) Polymer thick film. Springer, New York. ISBN 978-0442012205
5. Tekscan. http://www.tekscan.com/tekscan-technology#Sensor. Accessed 08 Jul 2014
6. Interlink Electronics. http://www.interlinkelectronics.com/products.php. Accessed 08 Jul 2014
7. Chang L (2006) Foundations of MEMS. Pearson Education Prentice Hall, New Jersey. ISBN 0-13-147286-0
8. ElectroScience Ltd. Application notes on thick-film heaters. http://www.electroscience.com/heaterappnotes.html. Accessed 09 Jul 2014
9. NEL Ltd. Neltex fabric-based circuit technology. http://www.nel-ltd.co.uk/neltex.php. Accessed 09 Jul 2014
10. Torah R, Yang K, Beeby S, Tudor J (2012) Screen-printed multilayer meander heater on polyester cotton. At 88th Textile Institute world conference, Shah Alam, May 2012, pp 15–17
11. Parker G (2004) Introductory semiconductor device physics. IOP Publishing, London. ISBN 978–0750310215
12. Beeby S, White N (2010) Energy harvesting for autonomous systems. Artech House, Norwood. ISBN 978-1596937185
13. Cady W (1964) Piezoelectricity: an introduction to the theory and applications of electromechanical phenomena in crystals, 1st edn. McGraw-Hill, New York
14. Bamfield P, Hutchings M (2010) Chromic phenomena – technological applications of colour chemistry, 2nd edn. RSC Publishing, Cambridge. ISBN 978-1847558688
15. Christie S, Robertson S, Taylor S (2007) Colour: design and creativity, design concepts for a temperature sensitive environment using thermochromic colour change. SDC issue 1
16. Aitken D, Burkinshaw SM, Griffiths J, Towns AD (1996) Textile applications of thermochromic systems. Rev Prog Color Relat Top 26:1–8. doi:10.1111/j.1478-4408.1996.tb00105.x
17. MacLaren D, White M (2003) Dye–developer interactions in the crystal violet lactone–lauryl gallate binary system: implications for thermochromism. J Mat Chem 13:1695–1700. doi:10.1039/B302249H
18. Kulcar R, Klanjšek G, Friškovec M (2010) Thermochromic inks – dynamic colour possibilities. In: CREATE conference, Gjøvik, Norway
19. Liquid crystals. http://www.colorchange.com/liquidcrystals. Accessed 01 May 2014
20. Robertson S, Taylor S, Christie R, Fletcher J, Rossini L (2008) Designing with a responsive colour palette: the development of colour and pattern changing products. Adv Science Technol 60:26–31. doi:10.4028/www.scientific.net/AST.60.26
21. Platt J (1961) Electrochromism, a possible change of colour producible in dyes by an electric field. J Chem Phys 34:862–863. doi:10.1063/1.1731686
22. Monk P, Mortimer R, Rosseinsky D (1995) Electrochromism: fundamentals and applications. VCH, Weinheim. ISBN 978-3527290635
23. Tehrani P, Isaksson J, Mammo W, Andersson N, Robinson N, Berggren M (2006) Evaluation of active materials designed for use in printable electrochromic polymer displays. Thin Solid Films 515:2485–2492. doi:10.1016/j.tsf.2006.07.149
24. Ono Y (1995) Electroluminescent displays, vol 1. World Scientific, Singapore
25. Vij D (ed) (2004) Handbook of electroluminescent materials. Institute of Physics, Bristol
26. T-equaliser Company. http://www.tqualizer.com/. Accessed 4 Jul 2014
27. Elise Co. Puddle jumper. http://www.organicui.org/?page_id=67. Accessed 4 Jul 2014

28. Torah R, Yang K, Wei Y, Li Y, de Vos M, Beeby S, Tudor J (2013) Screen and inkjet printed electronics on fabrics – the next generation of E-textiles. In: Plastic electronics conference, Dresden, Germany
29. Lee Y, Park K, Lee J, Lee C, Yoo H, Kim C, Yoon Y (1997) Dry release for surface micromachining with HF vapor-phase etching. J Microelectromech Syst 6:226–233. doi:10.1109/84.623111
30. Madou M (2011) Fundamentals of microfabrication and nanotechnology, 3rd edn. CRC Press, Boca Raton, Florida. ISBN 978-0849331800
31. Linder V, Gates B, Ryan D, Parviz B, Whitesides G (2005) Water-soluble sacrificial layers for surface micromachining. Small 1:730–736. doi:10.1002/smll.200400159
32. Dykyj J, Svoboda J, Wilhoit R, Frenkel M, Hall K (2000) Vapor pressure of chemicals: vapor pressure and antoine constants for oxygen containing organic compounds. Springer, New York/Berlin/Heidelberg. ISBN 978-3540649687
33. Humphrey LE (2012) Plastic crystals. Claud Press, Germany. ISBN: 9786201140219
34. Wei Y, Torah R, Kai Y, Beeby S, Tudor J (2012) A novel fabrication process for capacitive cantilever structures for smart fabric applications. Design, test, integration and packaging of MEMS/MOEMS
35. Edmison J, Jones M, Nakad Z, Martin T (2002) Using piezoelectric materials for wearable electronic textiles. In: Sixth international symposium on wearable computers, Seattle, Washington
36. Cho G, Jeong K, Paik MJ, Kwun Y, Sung M (2011) Performance evaluation of textile-based electrodes and motion sensors for smart clothing. IEEE Sensors 11:3183–3193. doi:10.1109/JSEN.2011.2167508
37. Merritt C, Nagle H (2009) Textile based capacitive sensors for respiration monitoring. IEEE Sensors 9:71–78. doi:10.1109/JSEN.2008.2010356
38. Wei Y, Torah R, Yang K, Beeby S, Tudor J (2013) Screen printing of a capacitive cantilever-based motion sensor on fabric using a novel sacrificial layer process for smart fabric applications. Meas Sci Technol 24:075104. doi:10.1088/0957–0233/24/7/075104
39. Wei Y, Torah R, Yang K, Beeby S, Tudor J (2013) A screen printable sacrificial fabrication process to realise a cantilever on fabric using a piezoelectric layer to detect motion for wearable applications. Sensors Actuators A Phys 203:241–248. doi:10.1016/j.sna.2013.08.041
40. Patra P, Calvert P, Warner S (2007) Textile based carbon nanostructured flexible antenna. National Textile Centre Annual Report, Project number: M06-MD01
41. Li Y, Torah R, Beeby S, Tudor J (2012) Inkjet printed flexible antenna on textile for wearable applications. In: 2012 Textile Institute world conference, Shah Alam, Malaysia
42. Whittow WG, Chauraya A, Vardaxoglou JC, Li Y, Torah R, Yang K, Beeby S, Tudor J (2014) inkjet printed microstrip patch antennas realized on textile for wearable applications. IEEE Antenna Wirel Propog Lett 13:71–74. doi:10.1109/LAWP.2013.2295942
43. Whittow WG, Li Y, Torah R, Yang K, Beeby S, Tudor J (2014) Printed frequency selective surface on textiles. Electron Lett 50(13):916–917. doi:10.1049/el.2014.0955
44. Li Y, Torah R, Beeby S, Tudor J (2012) An all-inkjet printed flexible capacitor on a textile using a new poly(4-vinylphenol) dielectric ink for wearable applications. IEEE Sensors 1–4. doi:10.1109/ICSENS.2012.6411117
45. Paul G, Torah R, Yang K, Beeby S, Tudor J (2014) An investigation into the durability of screen-printed conductive tracks on textiles. Meas Sci Technol 25:025006. doi:10.1088/0957-0233/25/2/025006 (11 p)
46. Mathis AG. http://www.mathisag.com. Accessed 05 Jul 2014

Thermal Regulation of Electrically Conducting Fabrics

26

Jiahui Tong and Li Li

Contents

Introduction 690
Thermal Garment 691
Resistive Property of Conductive Yarns 691
Temperature Control 694
Material Selection 710
Summary 718
References 718

Abstract

Most recently, thermal garment, one of the most popular topics in wearable electronic textiles, is on the rise in personal and business use. Ag (silver)/nylon yarns, which use nylon as the substrate with silver coated on it, are the most selected conductive yarns for a thermal garment in the market. In this chapter, the electromechanical property and electrothermal property of Ag/nylon yarns are fully discussed, and the resistive network model is proposed in resistance calculation of conductive fabrics. With knowledge of conductive yarns' properties and the thermal equilibrium of conductive fabrics, thermal control of conductive fabrics can be achieved. In the end, the selection of high-quality conductive Ag/nylon yarns and the testing methods are introduced.

Keywords

Wearable electronic textile • Functional fashion design • Resistance • Thermal regulation

J. Tong • L. Li (✉)
The Hong Kong Polytechnic University, Hong Kong, China
e-mail: joyway.tong@connect.polyu.hk; li.lilly@polyu.edu.hk

© Springer Science+Business Media Singapore 2015

X. Tao (ed.), *Handbook of Smart Textiles*,
DOI 10.1007/978-981-4451-45-1_36

Introduction

Wearable electronic textiles, also known as E-textiles, smart textiles, or smart fabrics, are fabrics that combine digital components and electronics to achieve various functions. It also covers intelligent clothing, smart clothing, wearable technology, and wearable computing projects. The field of wearable electronic textiles is related to both the field of clothing and advanced electronic technologies. The designs often incorporate practical functions and features that can bring great assistance and convenience to everyday life.

The history of wearable electronic textiles can go back to 1,000 years ago when artisans wrapped gold and silver foils around fabric threads, and many of Queen Elizabeth I's gowns are embroidered with gold-wrapped threads. At the end of the nineteenth century, when electric appliances are well developed and became mature, designers and engineers started to combine electricity with clothing and jewelry to develop illuminated and motorized necklaces, hats, and costumes, and this was the first time people achieved functional wearable electronics. Though wearable electronic textiles have a considerable long history, its transition from research labs to people's daily life is just ongoing recently.

Nowadays, wearable electronics is on the rise in personal and business use, especially in professional and patient settings in healthcare society. Wearable electronic textiles can integrate not only classical electronic devices such as resistors, integrated circuits, LEDs, and conventional batteries but also some active electronics such as transistors and solar cells into fabrics. Projects are pursued based on various different kinds of functionality. Some projects integrating sensors into fabrics to enable wearable electronics achieve health monitoring of vital signs of the wearer such as heart rate, respiration rate, temperature, and so on. Also some new projects start emerging, such as musical jacket, which uses MIDI and other technologies to provide garments that generate electronic music.

There is no doubt that wearable electronics is an industry with a great market and huge potential. However, there exist some issues that remain to be improved in today's wearable electronics industry. Firstly, it is still difficult for most consumers to accept wearable electronics which may be very different from the conventional wearable. The situation is that most of the wearable electronics today do not have a nice look, are not comfortable to wear, and sometimes need a big battery as the power supply. Consequently, a major number of consumers would have a bias against wearable electronics. The second issue is that the chain between the electronics industry and textile industry is not well integrated. The conventional electronics industry and textile industry are not familiar with each other and their technology and manufacturing process. Even for conventional textile industry, each link of the production chain from fiber to final garment is also not well integrated. Therefore, for the wearable electronic textiles industry, there is still a lot of room for progress and growth.

Thermal Garment

A thermal garment is one of the most popular projects in wearable electronics, which is widely used in body warming, physical therapy, and assisting drug delivery. Temperature control of thermal garments is achieved by arranging different conducting yarns and knitting structures and fulfilling the resistance requirement. Dr. L. Li's group starts the research on the resistive property of a thermal garment at the beginning of 2008. As most of the group members have a research background on engineering and industry, the methods used in the research are always based on application and practice.

Wearable electronic textiles have a variety of parameters including conventional textile parameters and electrical parameters, which are closely related to the property and functionality of wearable electronic textiles. With better understanding and insight of the relationship between these parameters and functionality, manufactures can make a better choice either in material selection or weaving/knitting method and achieve better performance and cost-efficiency of the products. A better knowledge of wearable electronics can not only accelerate the advancement of technology but also have a positive impact on human life.

Resistive Property of Conductive Yarns

As known to all, electrical resistance, a measure of the degree to which the conductor opposes an electrical current through that conductor, is the most fundamental concept in electricity. Electrical resistance is also one of the most fundamental and important parameters in wearable electronic textiles. The research of resistive property is considerably significant in wearable electronic textiles from the basic yarn and fabric stage to the final application. However, there exists a big difference between the field of electricity and wearable electronic textiles. It is found that the conventional knowledge and experience of electrical resistance cannot be applied to textile directly and many concepts and rules in electricity are not suitable in textiles any longer.

Take contact resistance as an example. Contact resistance is not very important in electricity but a vital concept in wearable electronic textiles, which should be fully considered. At first, it is better to give a brief tour of the structure of conducting yarns before discussing their resistive property. The most common conducting yarn in today's market is the Ag/nylon yarn which uses nylon as the substrate with silver coated on it (Fig. 1). Thus, the silver/nylon yarns become both conductive and flexible. As being silver coated on the surface makes the yarns conductive, the situation that the silver layers would contact with each other in overlapping yarns is inevitable which contributes to contact resistance. Thus, in wearable electronic textiles, it is necessary to consider both the length-related resistance and contact resistance to analyze the resistive property. As is known to

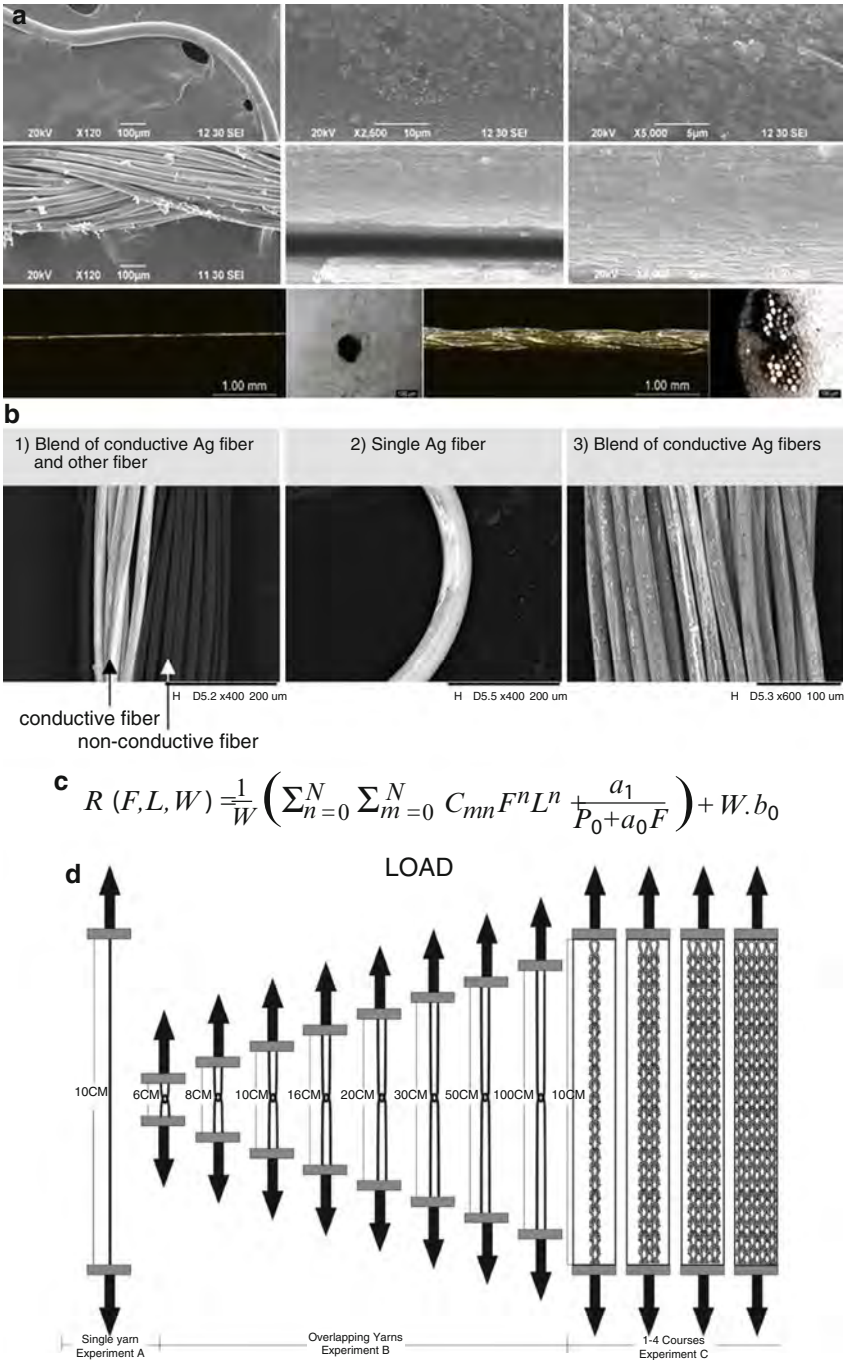

Fig. 1 (continued)

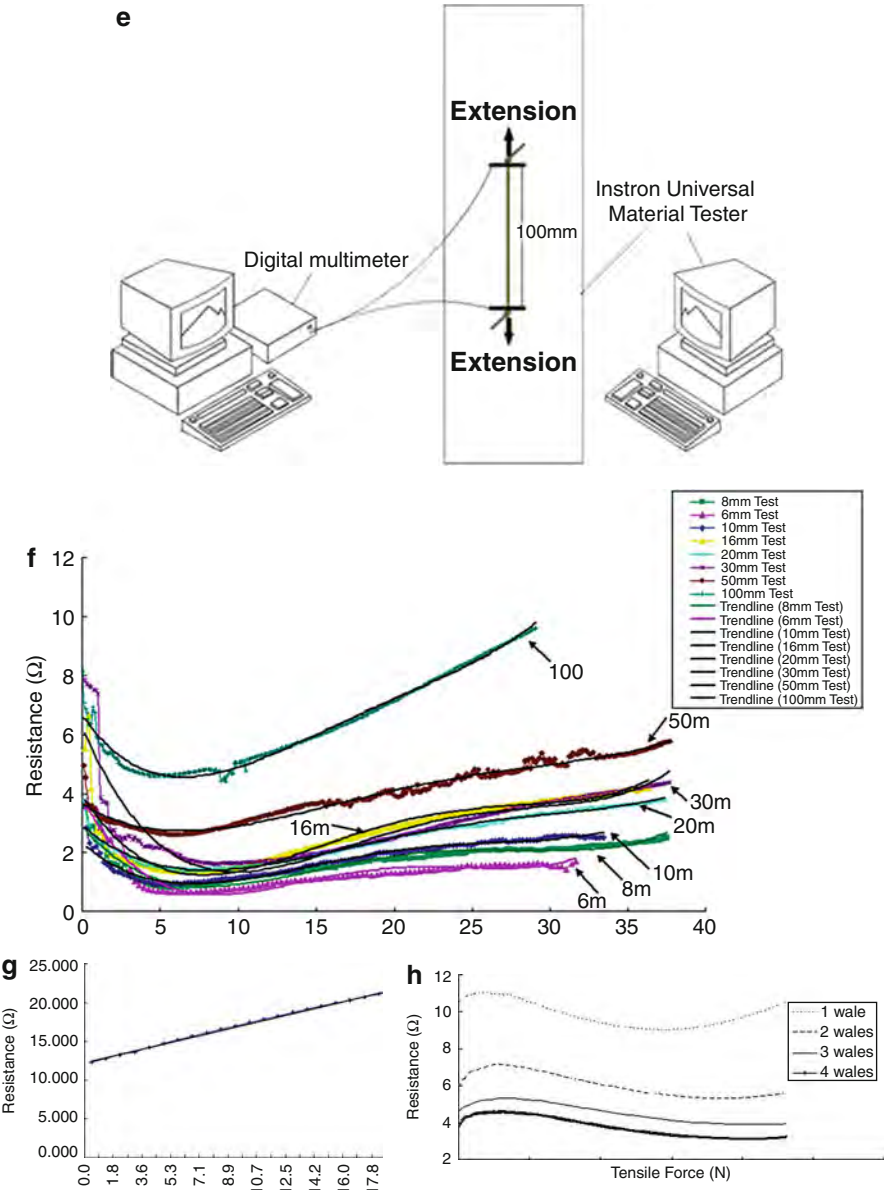

Fig. 1 (**a**) SEM image of the conductive fiber and its surface condition and cross section. (**b**) SEM image of three types of conductive yarns. (**c**) Relationship between resistance of conductive fabric and external force. (**d**) Experimental setup for electromechanical analysis of conductive yarn, overlapping yarns, and conductive knitted fabrics. (**e**) Data capture system that records the resistance change of conductive fabric in stretch. (**f**) Relationship between the resistance and extensile force of two overlapping conductive yarns. (**g**) Relationship between the resistance and extensile force of the single conductive yarn. (**h**) Comparison of relationship between the load and resistance of different wales of conductive fabrics [1]

all, length-related resistance of a conductor is directly proportional to its length and inversely proportional to the cross-section area. Consequently, with applied axial force, the conducting yarns would become longer and thinner, which will contribute to higher electrical resistance. On the contrary, higher force would result in better contact between the overlapping conducting yarns, which will contribute to lower electrical resistance. Therefore, these two factors, length-related resistance and contact resistance, would compete with each other when a conducting fabric is in the stretch process. Taking both of them into consideration, the total resistance of a conducting fabric would decrease at the initial stretch and increase later.

As mentioned above, an external applied force or stretch can make an effect on the electrical resistance, and this situation should be fully considered because people's movement would always lead to the deformation of wearable electronics. Another factor that also plays an important role in wearable electronics is the temperature (Fig. 2). It is known to all that the environmental condition, especially the temperature, may change when wearable electronics is in use. This effect may be undesired, causing the functionality of the product to deviate significantly from expectation. So an in-depth study of the temperature effect on the electrical resistance of conducting yarns is required. In electricity, the electrical resistivity of a material depends greatly on the temperature. For example, near room temperature, the resistivity of metals typically increases as temperature is increased, while the resistivity of semiconductors typically decreases as temperature is increased. As the conductor on the conducting yarns is silver, the temperature of a conducting yarn should increase as temperature is increased. However, things are different in wearable electronic textiles as in the case of that in conventional electricity. It is found that the resistances of either conducting yarns or conducting fabrics decrease as temperature is increased and then gradually return to initial resistance in the cooldown process. This unexpected phenomenon may result from the fact that the morphology of the conducting yarns is changed in the heating process. When temperature is increased, the conducting yarns can easily curl, which will lead to a local short circuit and contribute to resistance decrease. If coaxial extension is applied on the conductive yarn, the yarn curl in the heating process can be avoided and the conductive yarn would appear as a regular conductor, whose resistance increases as temperature is increased. However, it is inevitable that the conductive yarns are not stretched straightly and yarn curl is continuing in the heating fabric. To conclude, a temperature rise makes a negative effect on the resistance of a heating fabric woven/knitted by conductive yarns.

Temperature Control

Dr. L. Li's group aims to achieve temperature control of the thermal garment. As known to all, temperature of the thermal garment is determined by the balance between electrical power input and heat diffused from the garment into its environment (Fig. 3). When the electrical power input exceeds the heat lost, temperature of the thermal garment will continue rising. On the contrary, the temperature will go

down. For either situation, the heat diffusion rate will be adjusted by the temperature change continually until there exists a balanced between electrical power input and heat loss. Then the temperature of the thermal garment achieves a steady point. According to Ohm's law, the electrical power input into a conductor is determined by both the applied voltage of the battery and electrical resistance of the conductor. In addition, the heat diffused into the environment is related to thermal parameters of the thermal garment. Therefore, in order to gather a better insight of the mechanism and principle of thermal control, it is necessary to seek the resistance calculation method of heating fabrics made of conductive yarns and

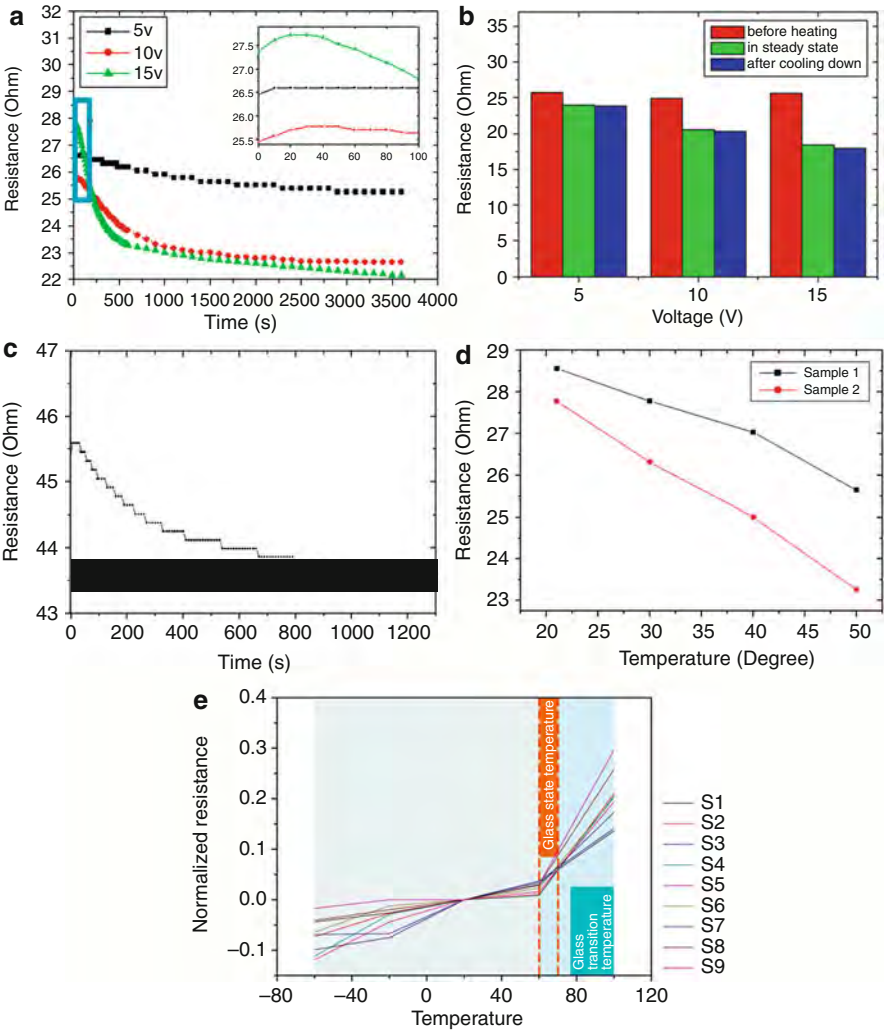

Fig. 2 (continued)

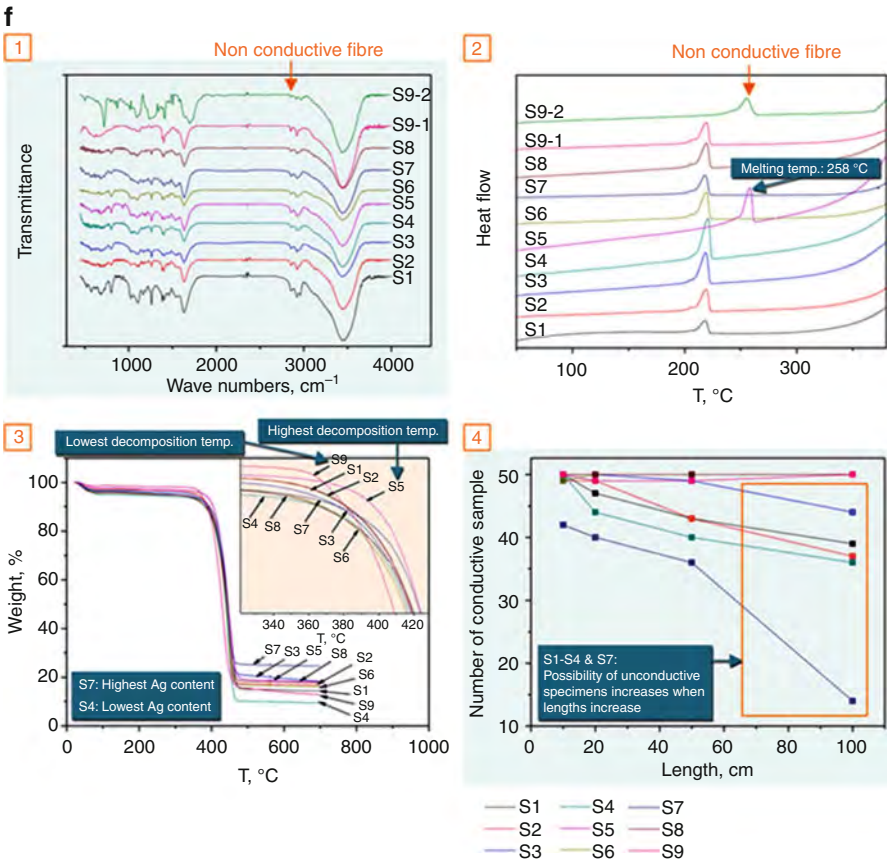

Fig. 2 (**a**) Electrical resistance change of heating fabric made of conductive yarns in heating process and (**b**) the comparison of its resistance before and after heating. (**c**) Electrical resistance change of conductive woven fabric in heating process. (**d**) The electrical resistance of conductive yarn varying with environmental temperature. (**e**) Conductive yarns with applied extensive force appear as regular conductors when temperature changes. (**f**) Chemical analysis of conductive yarns in different temperatures [2]

master their thermal properties at the same time. A detailed introduction of the resistance calculation will be conducted firstly.

The knitting structure is the most common structure in textile and can offer better flexibility, air permeability, and comfort. These good properties enable knitwear to become a good candidate for applications in sports, medicine, and other areas that incorporate electronic devices. A knitted fabric consists of a number of consecutive rows of loops/stitches, so a method of resistive network model is proposed to deal with this situation. The resistive network model regards the loop/stitch as a basic unit of knitting and makes the knitted fabric equivalent to a resistive network (Fig. 4). As mentioned before, contact resistance should be fully taken into consideration together with length-related resistance in conductive knitted fabrics. Thus, the resistance in the

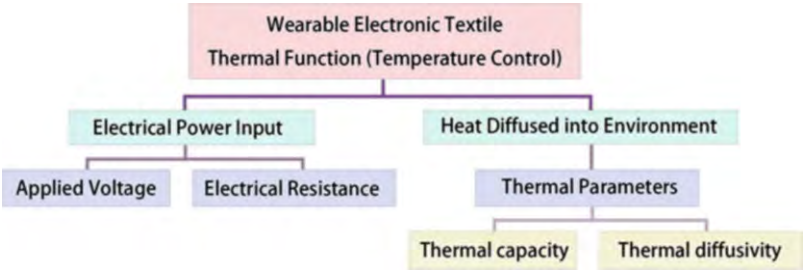

Fig. 3 Factors including electrical parameters and thermal parameters that are related to temperature control of thermal garment

heating fabric is divided into these two types, and the total resistance of the knitted fabric is a result from a series–parallel connection of length-related resistance and contact resistance. With the help of a Wheatstone bridge and some approximate methods, the electrical circuit of resistive network can be simplified successfully and the total resistance of a knitted fabric built with conductive yarns can be obtained finally. Knitting structures are not always limited to flat knitting, which was just analyzed; however, a similar method can still be applied to the calculation of electrical resistance. For woven fabrics, the topology is not that complex as knitting fabric. Unlike knitting fabrics, where a yarn follows a looped path all along, the strands of woven fabrics usually run straight horizontally and vertically. Generally, conductive yarns are embedded in parallel together with normal yarns in the weaving structure to make the weaving fabric conductive. So there is no contact resistance in weaving fabrics and what is needed to consider is only the length-related resistance. In addition, another approach was proposed to calculate the electrical resistance of many types of conductive fabrics from a macroscopic view (Fig. 5). Sheet resistance was proposed in this method, which is regardless of the size of the fabric. Therefore, the resistance of the conductive fabric with different sizes can be computed, once the sheet resistance and dimension is known. The last part of this section is a discussion of the suitable resistance of a conductive fabric for heating. Generally, the resistance of a conductive fabric can be adjusted to a large range by using different conductive yarns, changing yarn density, or arranging different structures. It is found that the conductive fabric can always achieve a wide range of electrical resistance, thanks to its broader adjusting range of yarn density. So what value of the electrical resistance is most suitable for a heating fabric? The answer strongly depends on the situation. On one side, the electrical resistance of a heating fabric should not be designed too high, because high resistance demands a higher voltage requirement from the battery and at the same time a higher voltage imposes more burdens on conductive yarns which may destroy them. On the other side, the electrical resistance of a heating fabric cannot be too low or the resistance distributed outside the heating fabric will get too much electrical power from the battery, and consequently, the heating fabric cannot easily warm up. In summary, a choice of the electrical resistance of thermal garment should be made on a case-by-case basis, which cannot be either too high or too low.

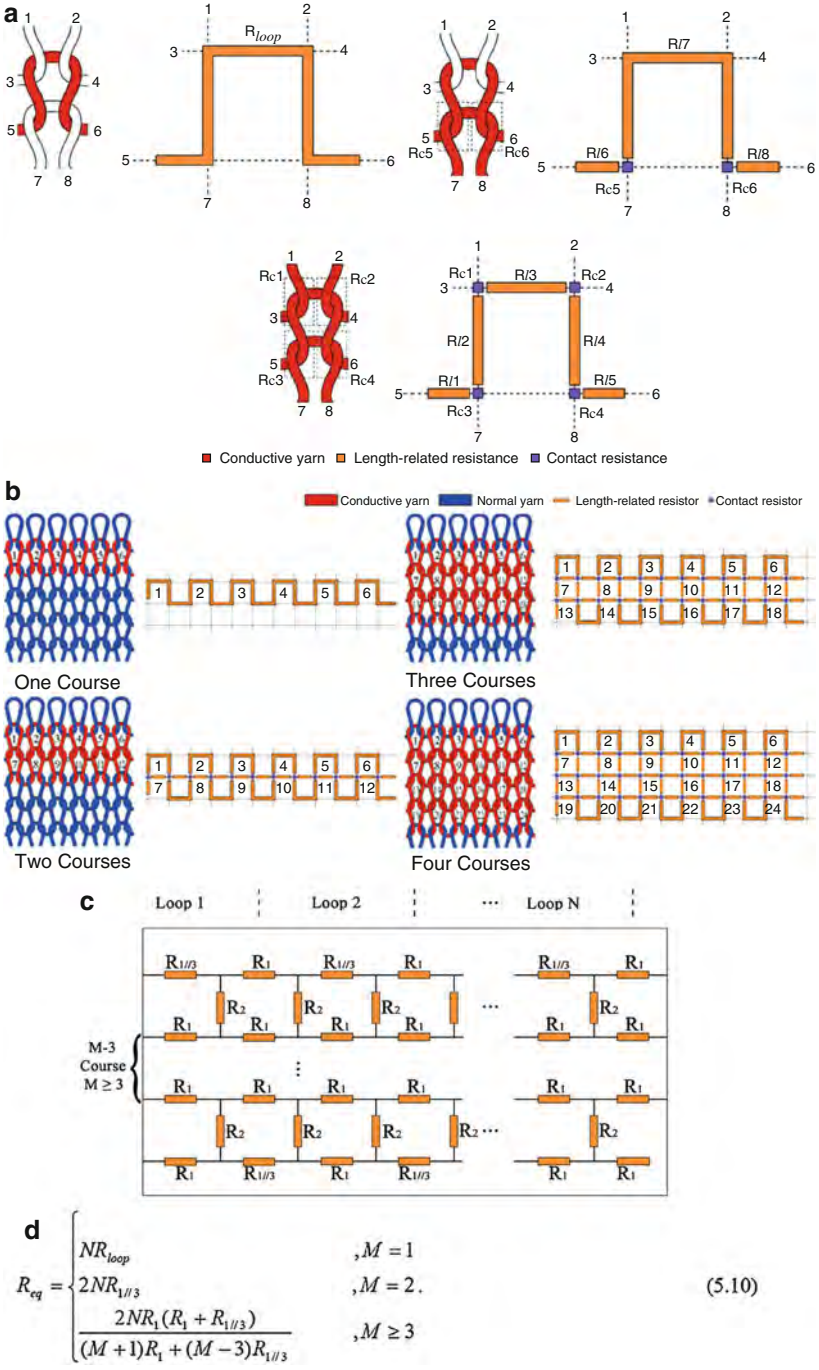

Fig. 4 (continued)

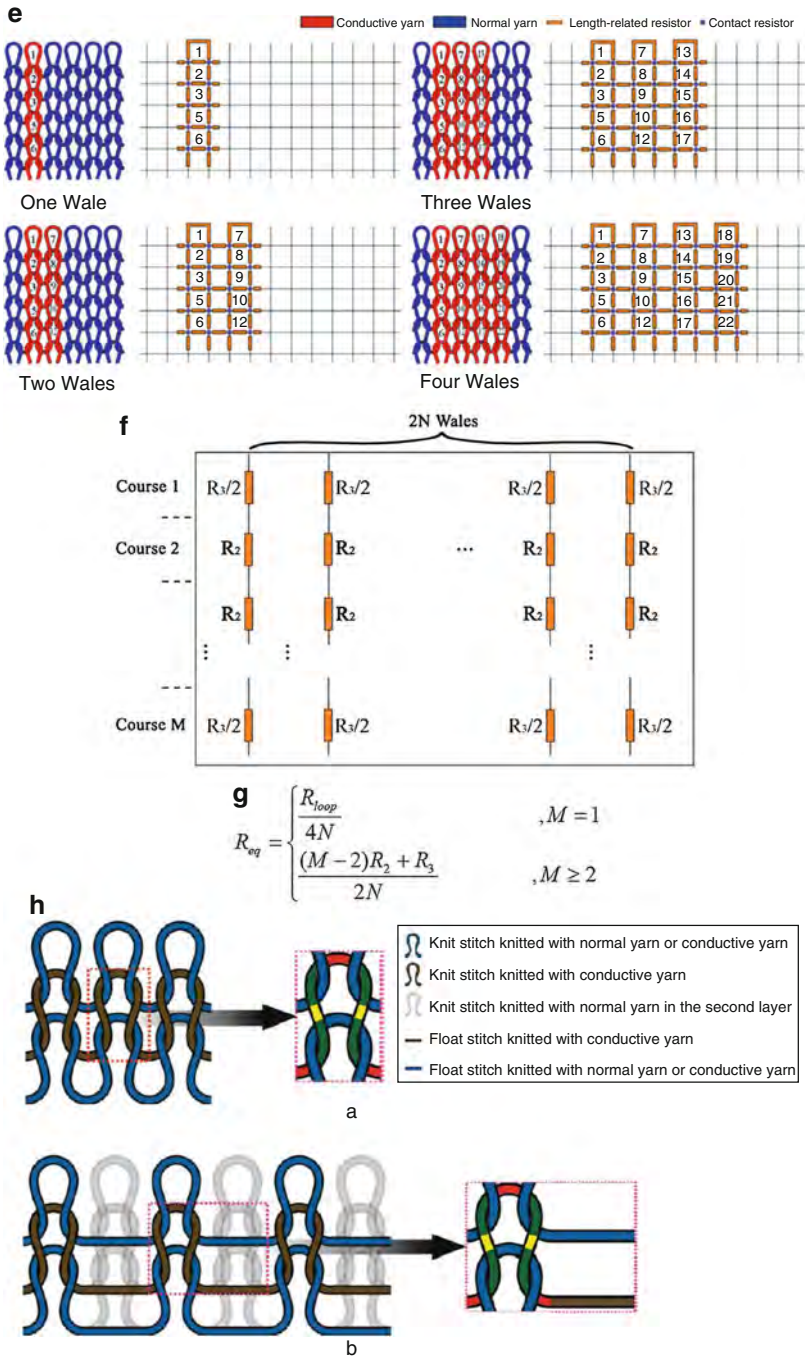

Fig. 4 (continued)

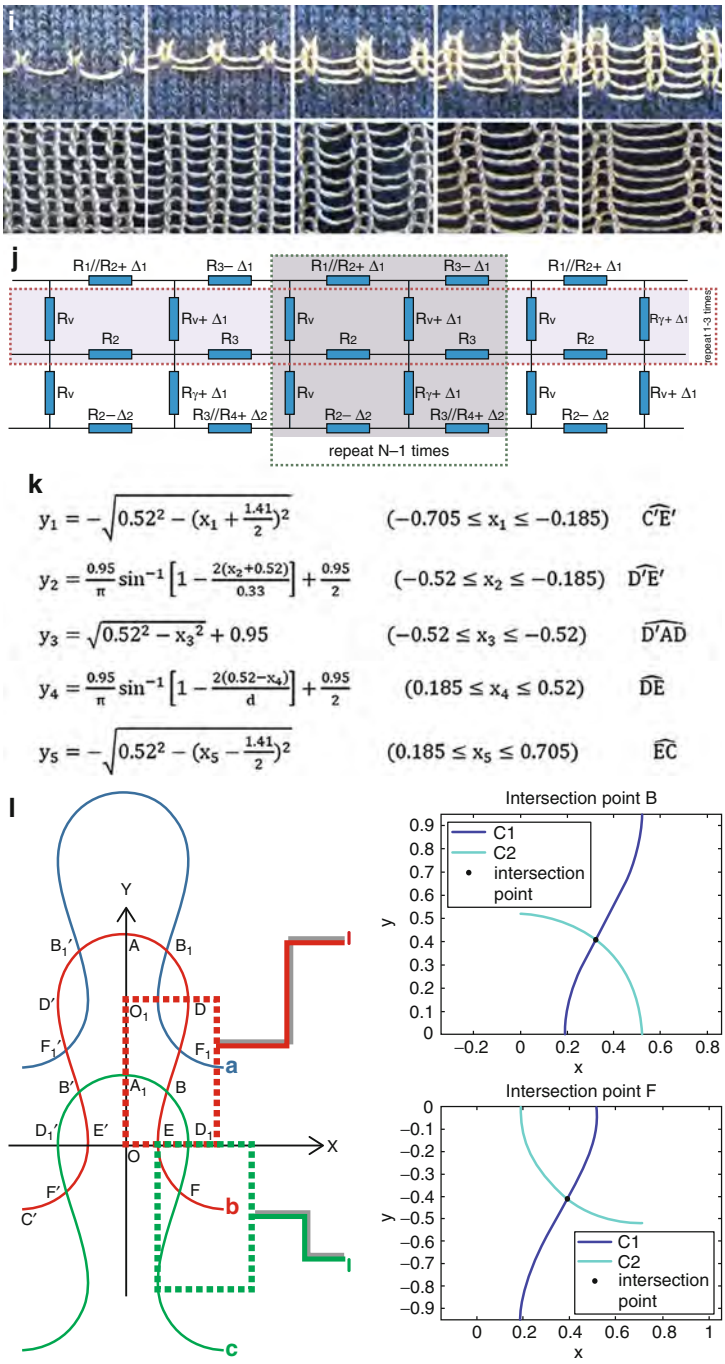

Fig. 4 (continued)

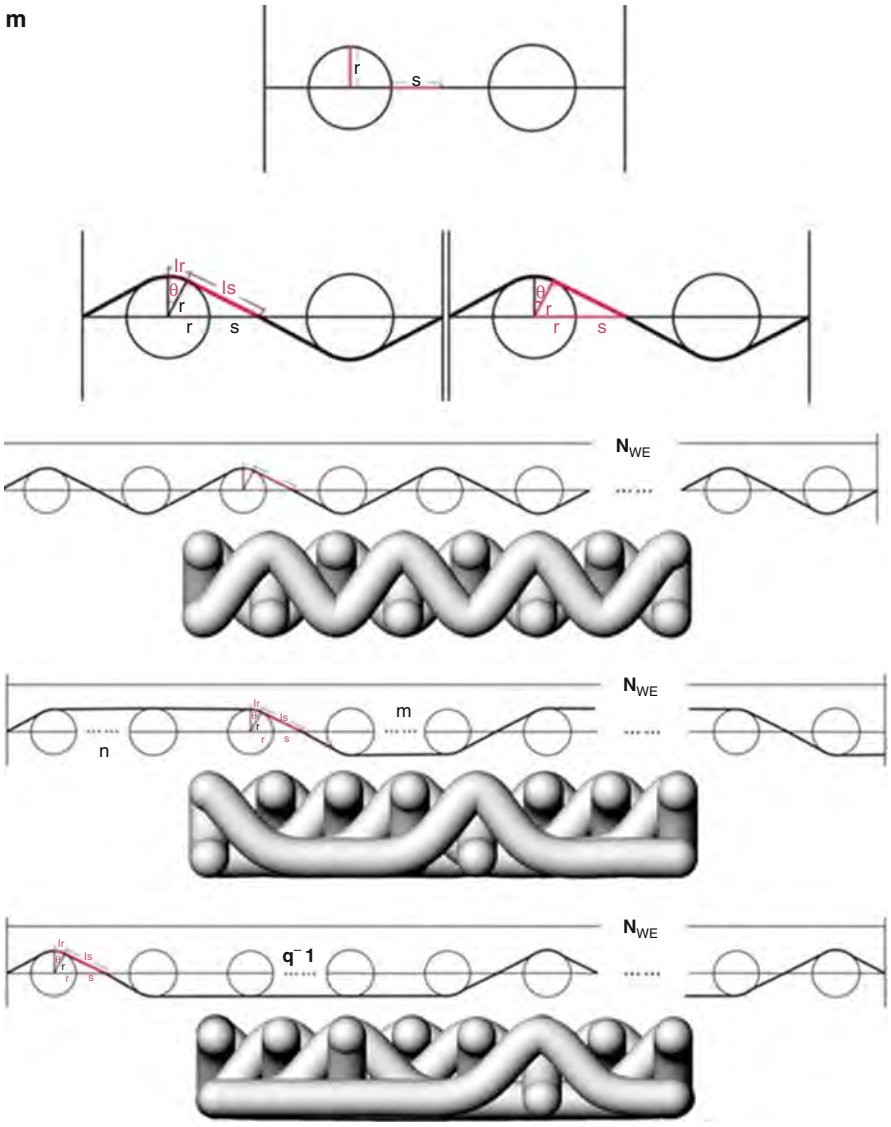

Fig. 4 (continued)

In this section, the thermal parameters of thermal garments or fabrics, which are directly related to the rate of their heat lost in the heating process, will be discussed. Thermal capacity and thermal diffusivity are two of the most important concepts in thermodynamics, which are also very significant to thermal garments. Thermal capacity, also known as heat capacity, is a measurable physical quantity equal to the ratio of the heat added to or subtracted from an object to the resulting temperature change. Thermal capacity reflects the ability of energy storage of an object.

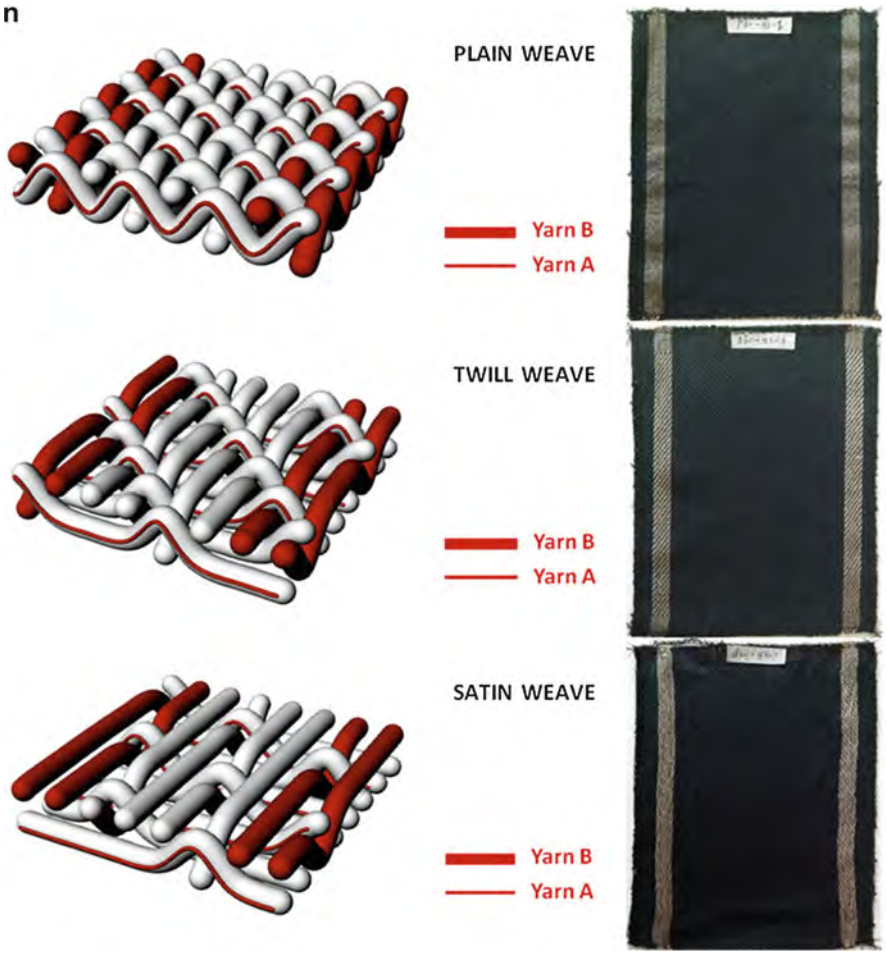

Fig. 4 (continued)

The object of higher thermal capacity can store more thermal energy when its temperature is increased to one degree. In other words, the temperature of object with higher thermal capacity is less sensitive to the thermal energy gain or loss. The experimental result shows that the thermal capacity of a heating fabric only affects the heating/cooldown rate and has no influence on the balance between electrical power input and heat loss. However, it does not mean that there is no need to consider the thermal capacity of the heating fabric. Higher thermal capacity is conducive to the stability of temperature control. A heating fabric with too low thermal capacity will have a great temperature fluctuation, which is against temperature control. Thermal diffusivity is another vital concept in heat transfer analysis, which measures the ability to conduct thermal energy relative to the

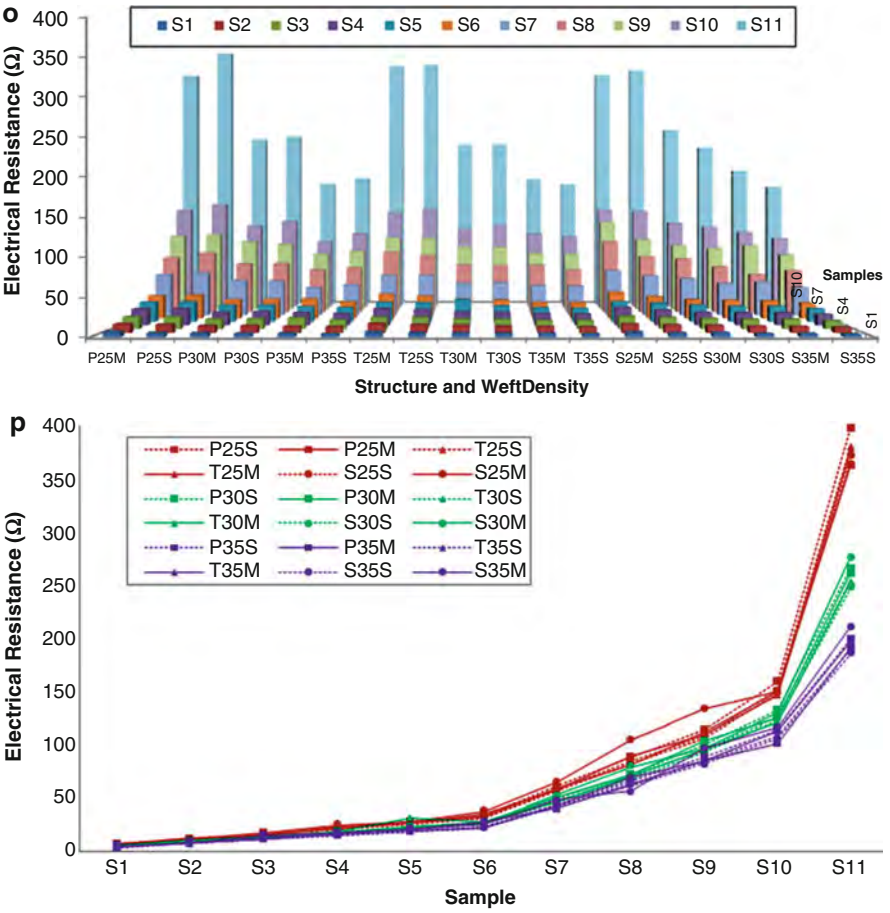

Fig. 4 (**a**) A lump resistor model represents the basic unit of stitch. (**b**) A resistive model for conductive knitted fabrics with different courses. (**c**) Equivalent electric circuit for fabrics with different courses. (**d**) The analytic equation of the equivalent resistance for a conductive knitted fabric along a course direction. (**e**) A resistive model for conductive knitted fabrics with different wales. (**f**) Equivalent electric circuit for fabrics with different wales. (**g**) The analytic equation of the equivalent resistance for a conductive knitted fabric along a wale direction to (**h**) a resistive model for conductive knitted fabrics with float stitches. (**i**) Conductive knitted fabrics with different float stitches. (**j**) Equivalent electric circuit for float stitches. (**k**) Calculation of the length of the loop on the fabric. (**l**) A model to represent the shape of the loop on the fabric. (**m**) 3D structure of woven fabric with its simulation model for resistance calculation. (**n**) Conductive woven fabrics with different structures. (**o**) Electrical resistance of measurement and simulation of plain, twill, and satin fabrics. (**p**) Comparisons between measured and simulated electrical resistance of conductive woven fabrics [3–5]

ability to store thermal energy. In a substance with high thermal diffusivity, heat moves rapidly through it. Thus, a thermal fabric with higher thermal diffusivity will have higher heat loss in the heat process and requires higher electrical power input, which means that thermal diffusivity is a parameter that is closely related to

temperature control of heating fabrics. Therefore, a heating fabric with higher thermal diffusivity is only able to achieve lower heating temperature. The experimental result shows that a heating fabric made of wool with higher loop density can achieve higher heating temperature than a fabric made of cotton and acrylic with lower loop density, as wool shows lower thermal diffusivity or better thermal resistance and higher loop density blocks heat conductivity (Fig. 6). Generally, the thermal diffusivity in a material is proportional to the cross section of the heat flow in heat transfer analysis. However, the situation becomes more complex when applied to heating fabrics. It was found that the thermal diffusivity of a heating fabric is not proportional to its area. The reason is that there exist two types of heat transfer in a heating fabric. The first type is that heat flows in the direction that is perpendicular to the fabric surface and thermal diffusivity of this type is proportional to area of the fabric. Another type of heat transfer occurs at the edge of the fabric which should be related to the perimeter of the fabric. In this section of discussion, the thermal capacity or thermal diffusivity of a heating fabric mentioned is not just limited to the yarns used but an integration of the yarns and the air soaked in the fabric and is also related to the structure of the fabric. In conclusion, the thermal capacity of a heating fabric is related to the stability of temperature control and the heating/cooldown rate, and its thermal diffusivity is directly related to the temperature control/temperature achievement.

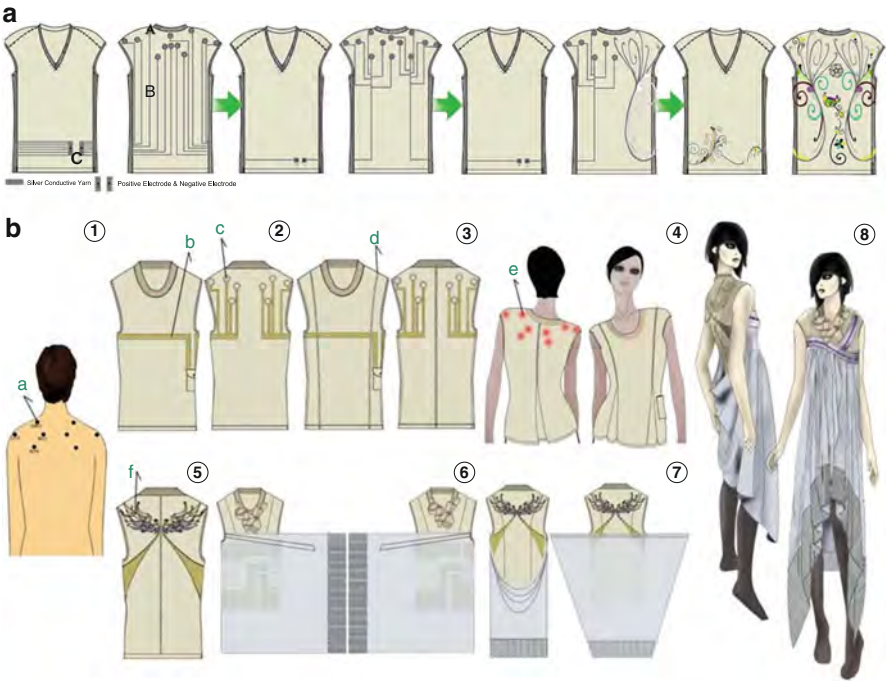

Fig. 5 (continued)

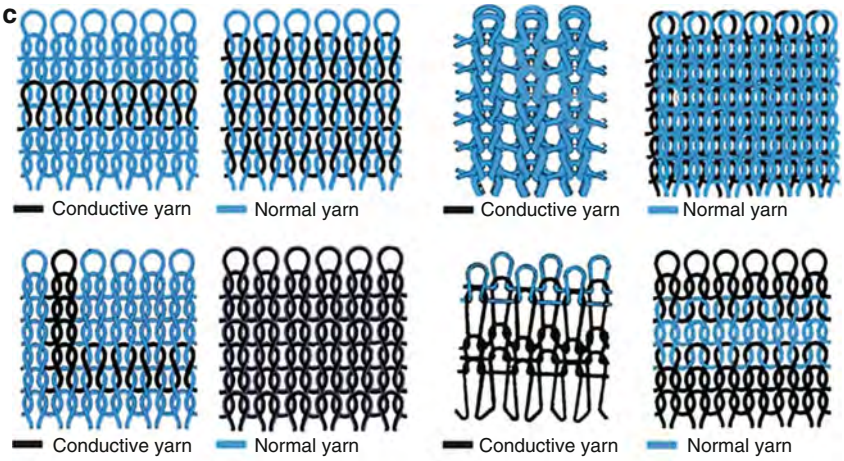

Sheet Resistance Method

$$R_f = \frac{1}{N}\sum_{i=1}^{N} R_i \left(\frac{W_i}{L_i}\right)$$

Ri: measure resistance of ith sample.
Li: fabric length of ith sample.
Wi: fabric width of ith sample.
N: total number of samples are used to average out the variations among different samples.

Fig. 5 (**a**) The electric circuit is redesigned to show a nice looking (**b**) design of an intelligent garment with specific function. (**c**) A model for sheet resistance method and its equation. (**d**) Design of an intelligent garment with transcutaneous electrical nerve simulation function [6–9]

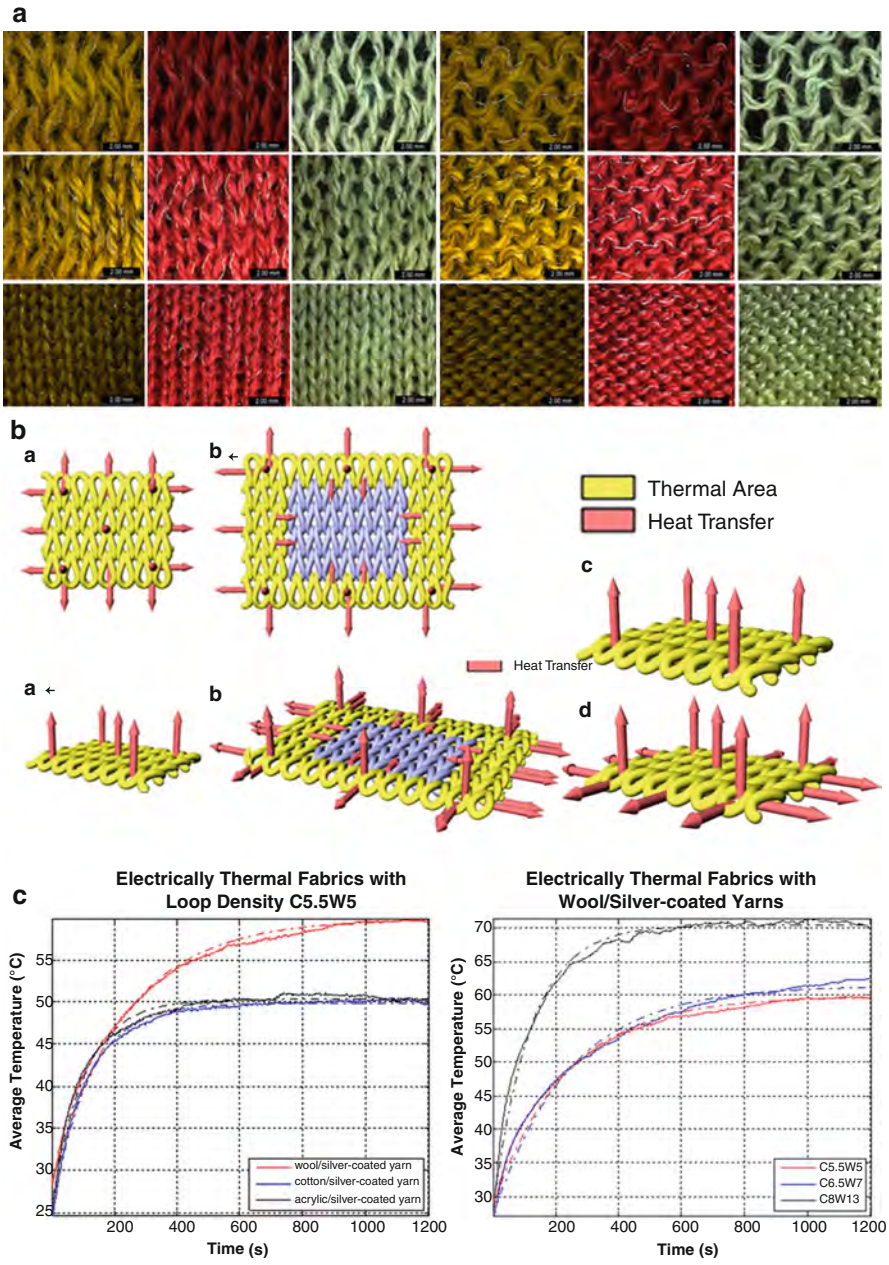

Fig. 6 (continued)

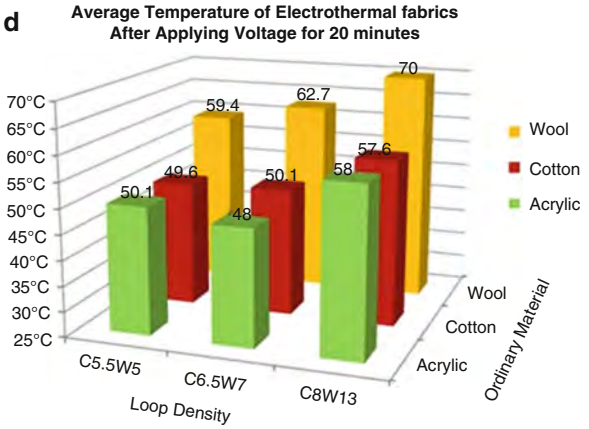

Fig. 6 (**a**) The thermal fabrics made of wool (*yellow*), cotton (*red*), and acrylic (*green*) with different loop density. (**b**) Two types of heat transfer in the heating fabric. (**c**) Temperature of fabric samples varying with time. (**d**) Temperature achievement of fabric with different loop densities made of different yarns [10]

In the previous section, the electrical resistance and thermal properties of the heating fabrics were discussed. Thus, the electrical power input and heat loss are both achieved, and the balance point between them can be easily found further. In the following section, the process method used in figuring out the relationship between heating temperature and each parameter of fabric and further achieving temperature control of heating fabric will be introduced. When an electrical current flows through a conductive heating fabric, heat is generated in the embedded conducting yarns in the fabric. According to Ohm's law, the electrical power provided by the power supply is proportional to the voltage squared and inversely proportional to the resistance of heating fabric. At the same time, the heat loss from the fabric to the surrounding environment is proportional to its thermal diffusivity and the temperature variation/temperature gradient. The temperature of the heating fabric will increase continuously with applied electrical power until a balance point between electrical power input and heat loss occurs and the heating fabric gets into stable state. The equation of this process can be written down as below:

$$\frac{U^2}{R} = \alpha * \ (T - T_0)$$

From the above equation, it is found that the heating temperature of a heating fabric is determined by the external applied voltage. With the obtained relationship between the heating temperature and applied voltage, it is possible to predict the temperature the heating fabric can achieve (Fig. 7). As mentioned before, the resistance of the knitted heating fabric is dependent on the temperature.

Fortunately, a good linear relation between the stable-state resistance of the conductive fabric and the applied voltage is achieved from the experiment results. In a further step, combining the equation above, the relationship between the stable-state resistance and temperature is derived. By substituting the formula of

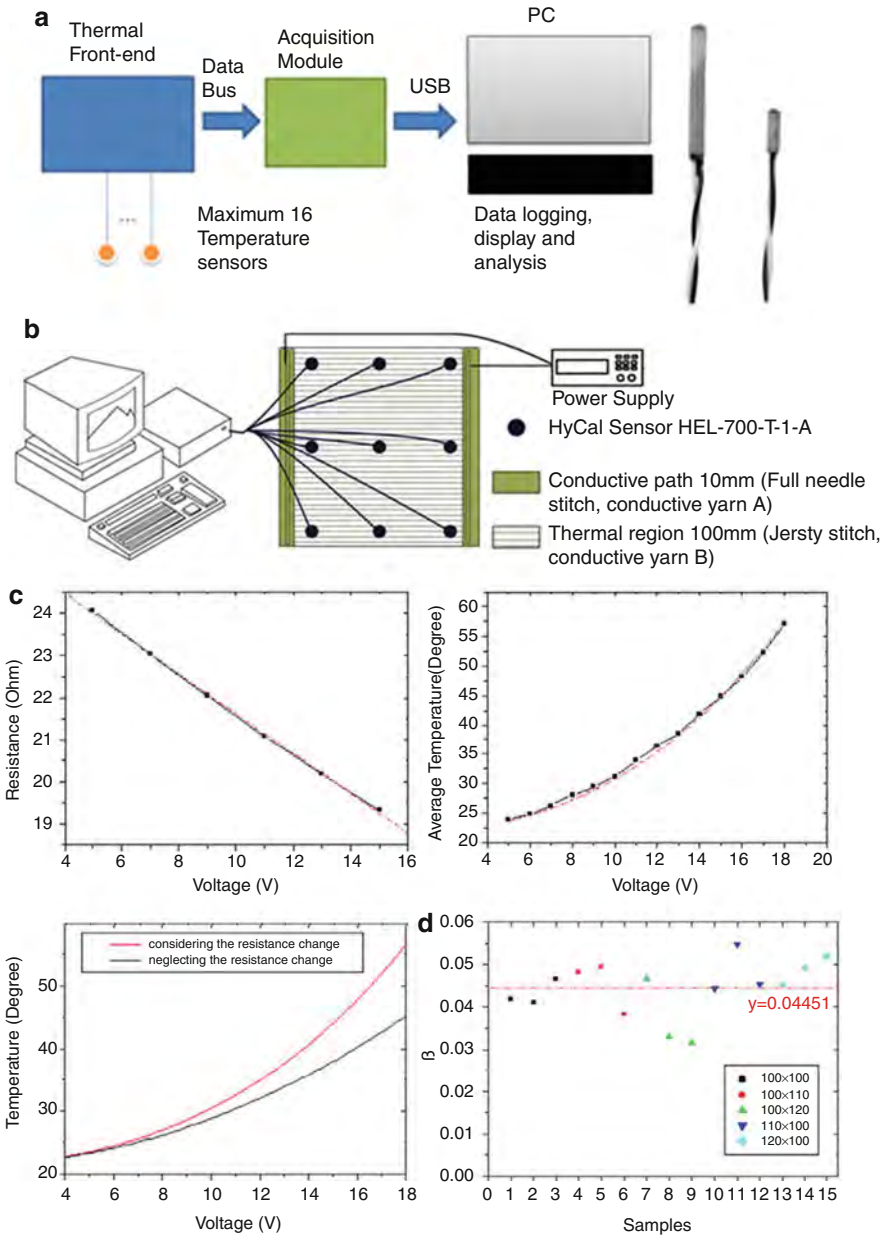

Fig. 7 (continued)

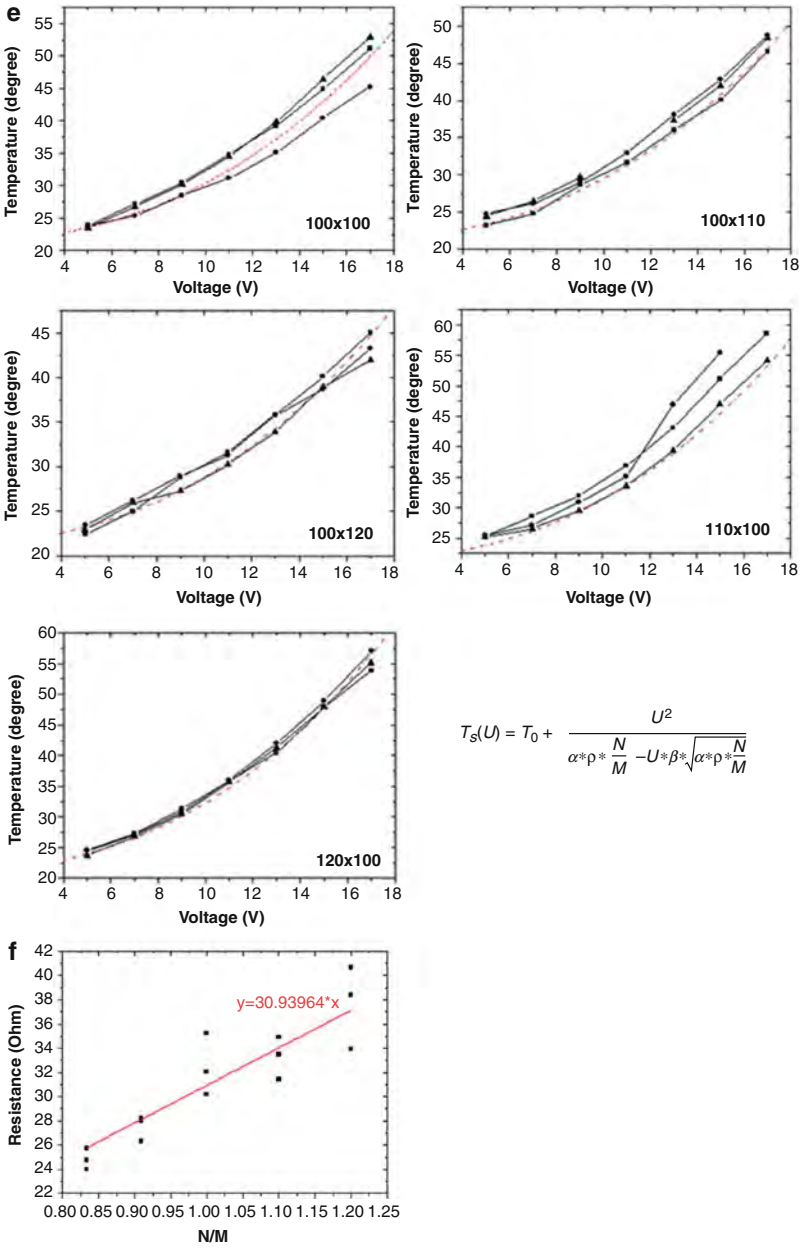

Fig. 7 (**a**) Temperature acquisition system and the temperature sensor. (**b**) Nine temperature sensors are attached on the fabrics and the temperature is recorded. (**c**) Temperature simulation process of a heating fabric. (**d**) Distribution of the β values of these 15 fabric samples. (**e**) Temperature simulation results of fabrics with different sizes. (**f**) The electrical resistance of fabrics with different sizes and their fitting results [2, 11]

stable-state resistance into the above equation and solving the equation, the heating temperature of the conductive fabric is obtained, which is shown as follows:

$$T_s(U) = T_0 + \frac{U^2}{\alpha * R_0 - U * \beta * \sqrt{\alpha * R_0}}$$

β is a constant, which is only related to the property of the conductive fabric and is independent on the initial resistance of the fabric or the size of the fabric. If the loop density, knitting structure, and selected materials of the conductive fabrics are fixed, their values of β are fixed. The parameter β reflects how the resistance changes in percentage corresponding to the temperature change. The above formula indicates that prediction of the heating temperature of a conductive fabric can be achieved with an external applied voltage and its parameters (initial resistance and thermal diffusivity). As discussed before, the initial resistance of the fabric can be achieved with the resistive network model, which is proportional to the wale number and inversely proportional to the course number. In addition, the thermal diffusivity of the heating fabric is proportional to the size of the fabric and can be also obtained after the adjustment of the edge effect. Finally, the temperature control of a series of conductive fabric with different sizes can be easily achieved. At the end of this section, the discussion is about the precision of the temperature control. In reality, it is hard to predict the heating temperature to a very precise degree for two main reasons. The first reason is that, even for the same heating fabric in different testing, because the conductive fabric cannot return to the initial state precisely, the initial state may be different and initial resistance can vary. The second reason is that obtaining inconsistent fabrics from the same machine and same fabrication method is inevitable in the textile industry. Therefore, in order to achieve high-precision temperature control, it is strongly recommended to measure the conductive heating fabrics on a one-to-one basis. Figures 8 and 9 show the design of thermal garments and the prototype of a functional thermal garment by Dr. L. Li's group.

Material Selection

In the final section of this chapter, some standards of conductive yarn selection will be discussed. Various materials will be needed in order to achieve different functions of wearable electronics. Thus, more attention should be paid to material selections. In thermal garment production, in order to achieve high-quality products, the selection of high-quality conductive yarns is a vital step. Nowadays, with the rapid development of materials science, the technology of conducting yarn is relatively mature from lab to market, and consumers can easily purchase it at market. As mentioned at the beginning of this chapter, Ag/nylon conductive yarns, as a kind of organic yarns instead of metal yarns and carbon yarns, due to its light weight, flexibleness, spinnability, and high mechanical stability, are the most selected material for the application of thermal garments. In addition, silver has inherent qualities that make it an ideal element to be used in applications as varied as medical wound

dressings, scent-free textiles, conductive tapes, and antimicrobial fabric wipes. Thus, this kind of Ag/nylon conducting yarns has been widely used in wearable electronic textile product design. Firstly, some characteristics of these conductive yarns will be introduced. There are three kinds of Ag/nylon conductive yarns in today's market: (1) the blend of conductive/nonconductive fibers, (2) single conductive fiber, and (3) the blend of numerous conductive fibers (Fig. 10). They have their own advantages over each other. The first kind of yarns is more resistant to laundry and corrosion with the protection of nonconductive fibers, and the third kind has better

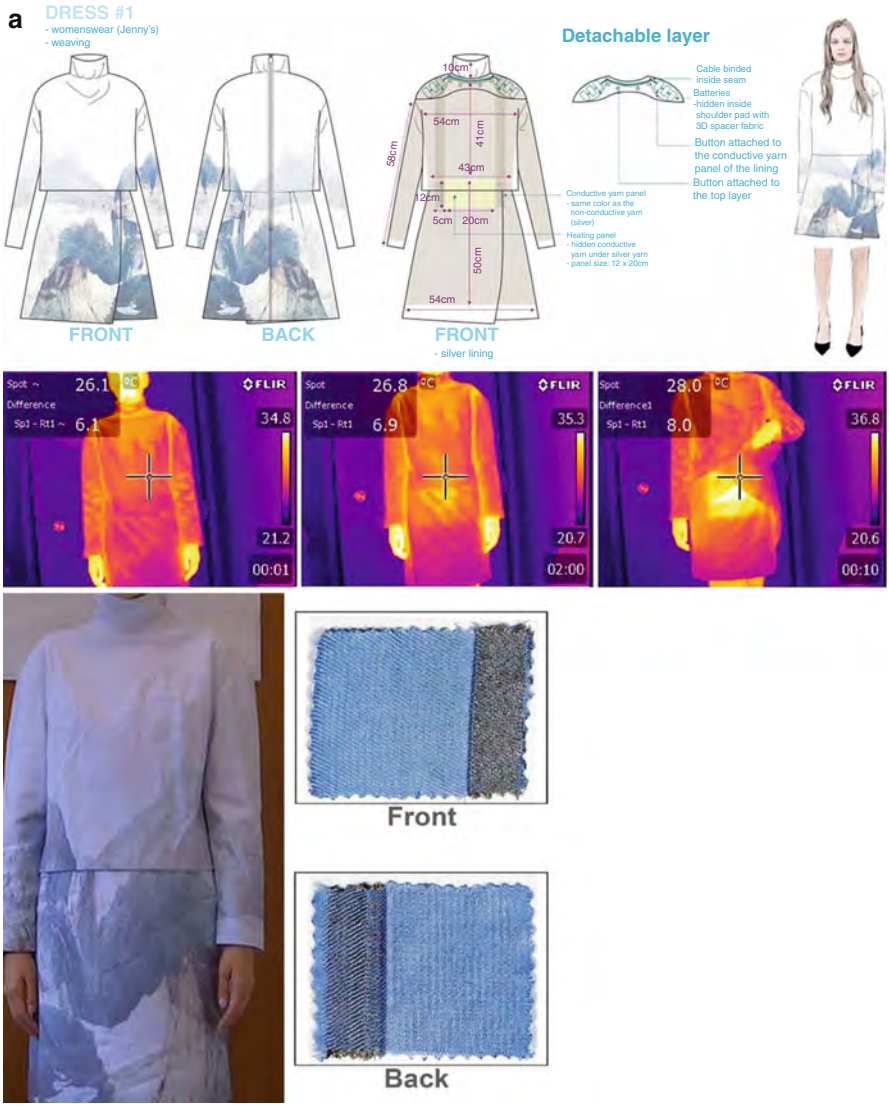

Fig. 8 (continued)

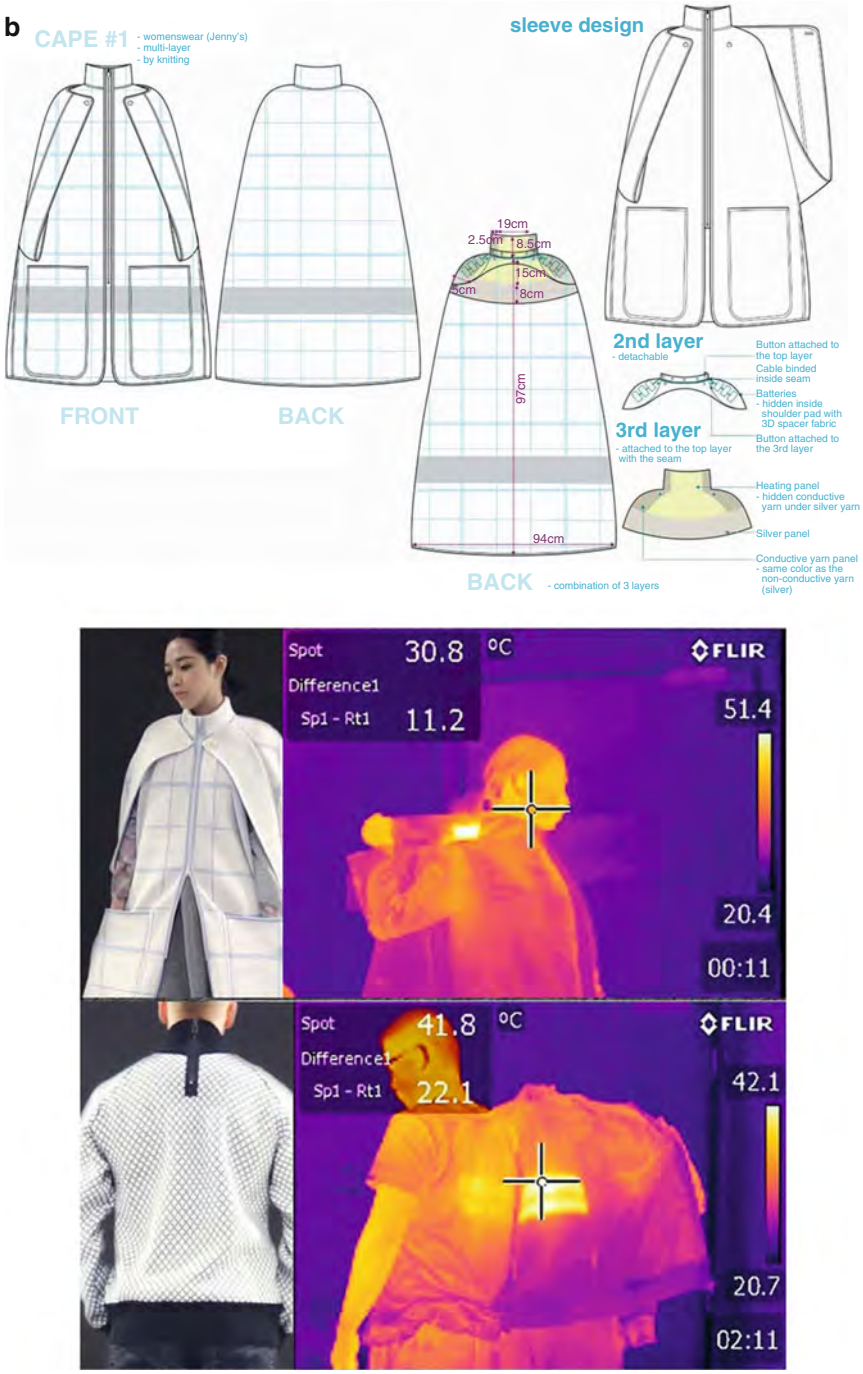

Fig. 8 (continued)

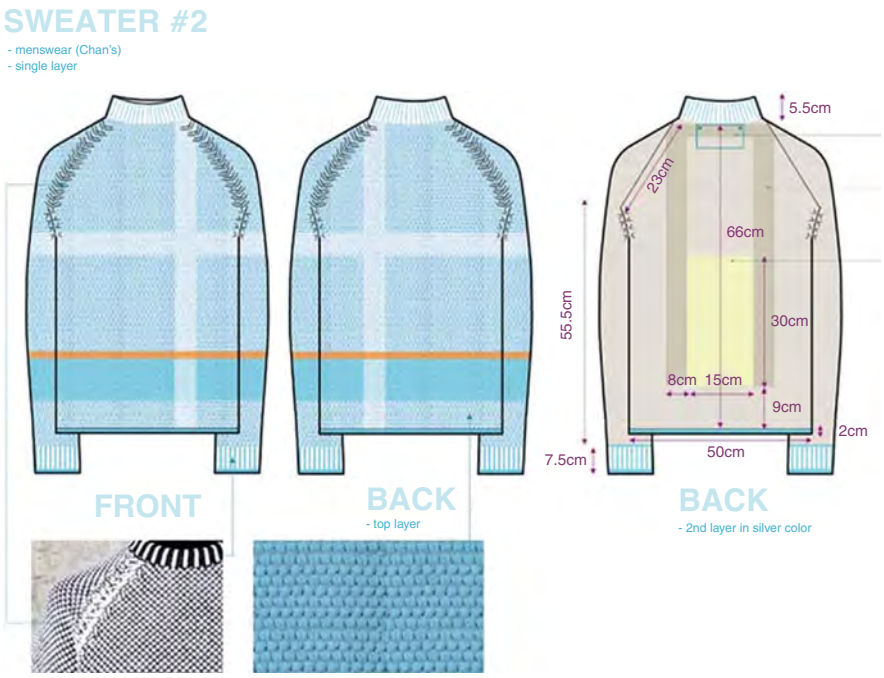

Fig. 8 The design of (**a**) the dress and (**b**) sweater with thermal function

conductivity. Also the second kind, the single Ag fiber, has the smallest diameter and size. These three kinds of yarns have their own unique features and could be applied in different functional wearable electronics. Thus, the manufacturer should select the right yarns in their first step.

As there exist massive kinds of conductive yarns with different qualities and properties in market, selecting high-quality conductive yarns is vitally important, which may directly affect the performance of the final products. Next, systematic assessment methods to test the stability and reliability of the conductive yarns according to the problems industrialists would experience with during every manufacturing process will be provided, and it aims to give guidance to industrialists in the selection of high-quality conductive yarns.

The optimal conductive yarns should be stable in property, resistant to various corrosions at each production stage, and outstanding in testing and examination. Thus, the assessment method would focus on the testing of stability and reliability. SEM imaging should be the most fundamental and direct method to identify the quality of the conducting yarns. As is known to all, the stability of conductive yarns not only depends on the structure of the yarns, which was mentioned before, but also the coating technique. With a good coating technique, the silver can be coated on the surface of the yarn uniformly and steadily. In other words, the surface morphology of conducting yarns has a close relationship with the coating quality, and it is convenient to make a preliminary judgment by detecting the surface morphology of

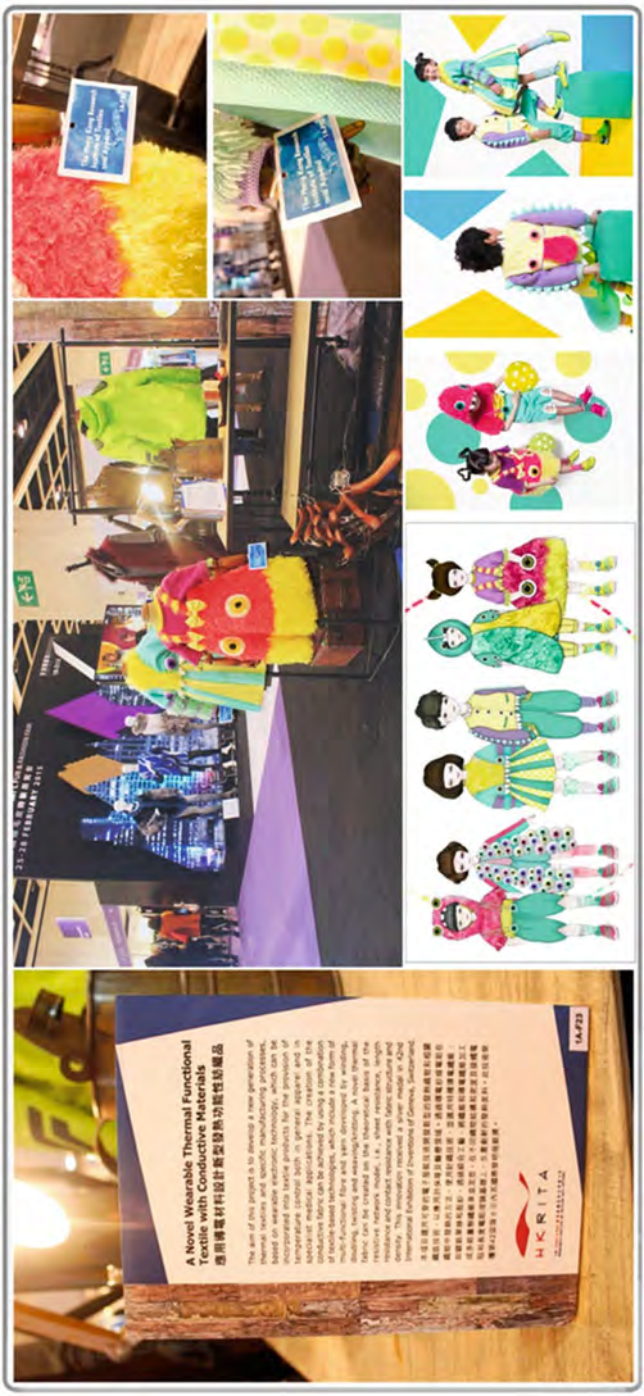

Fig. 9 Prototype of a functional thermal garment made by Dr. L. Li's group

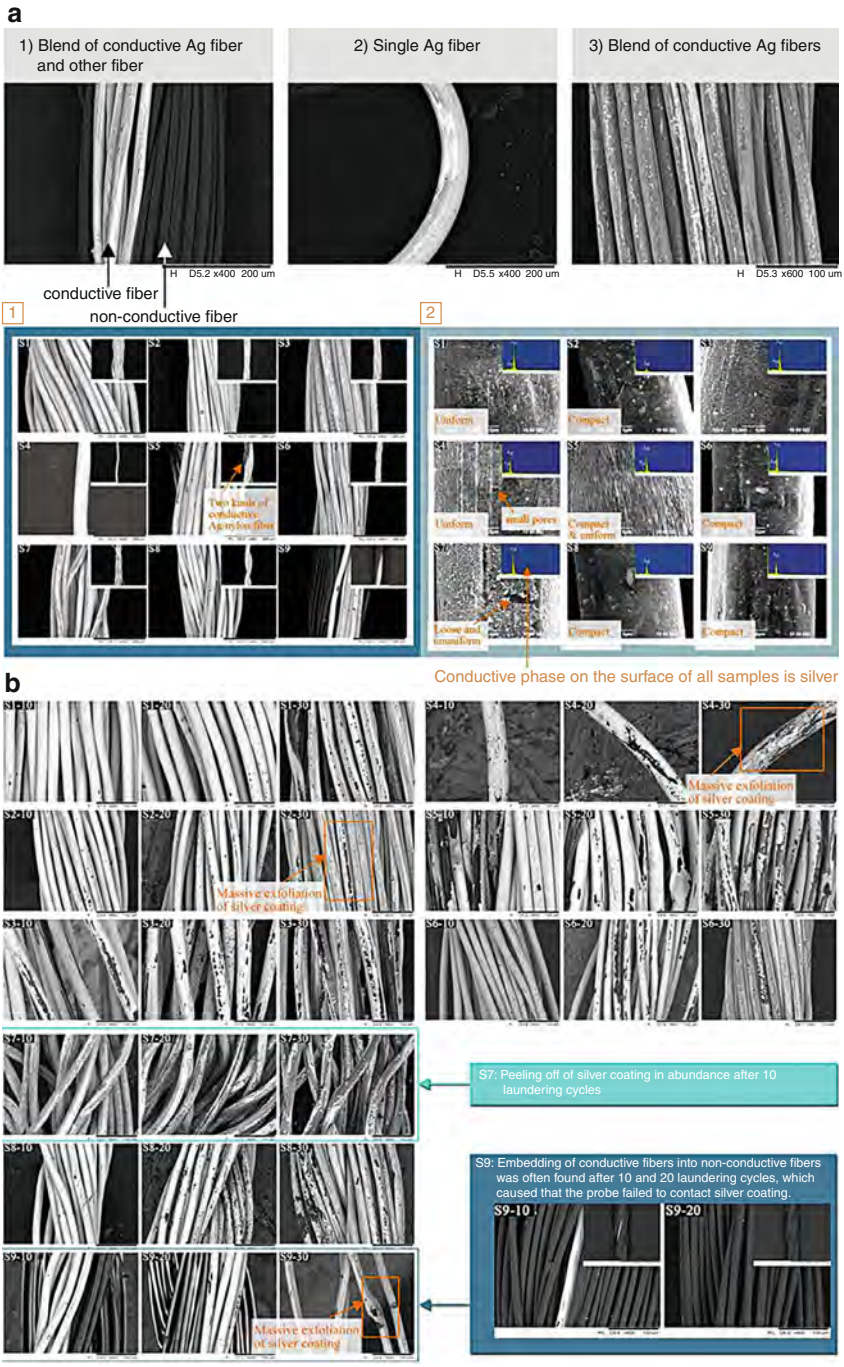

Fig. 10 (continued)

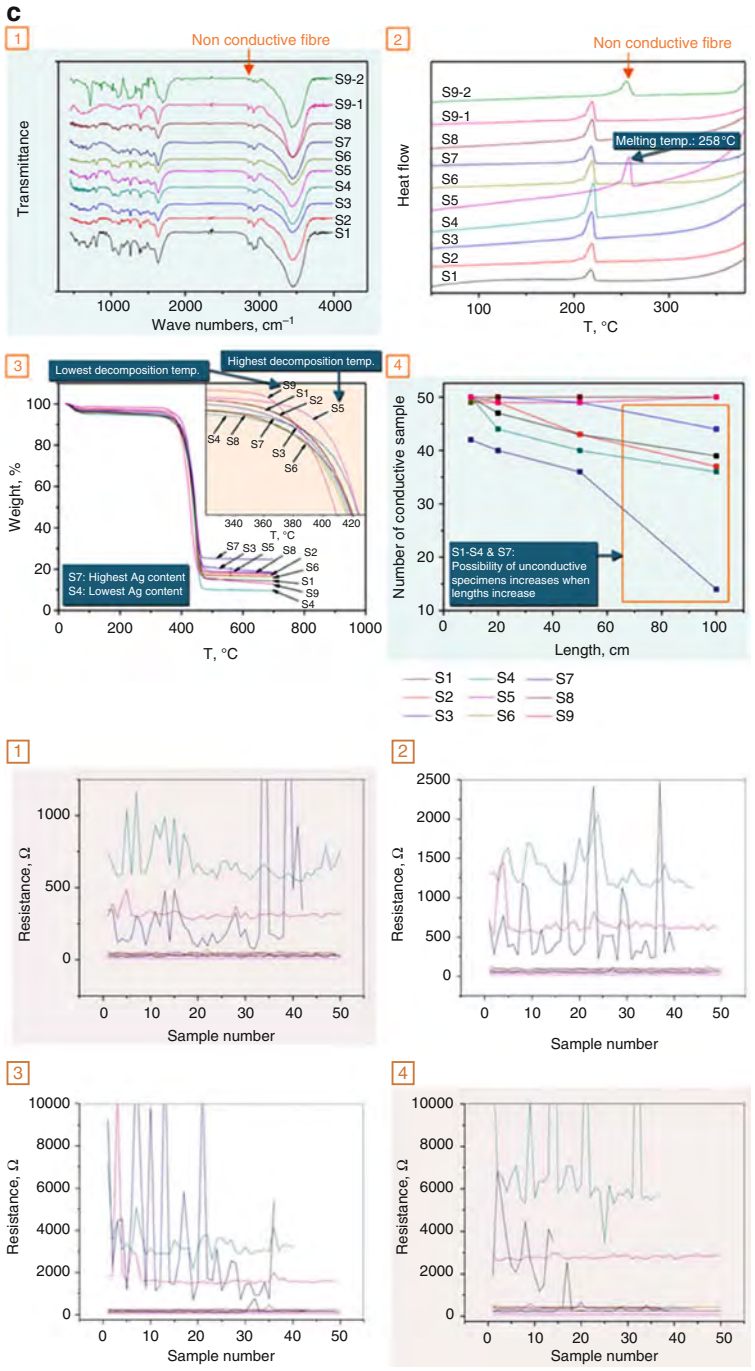

Fig. 10 (continued)

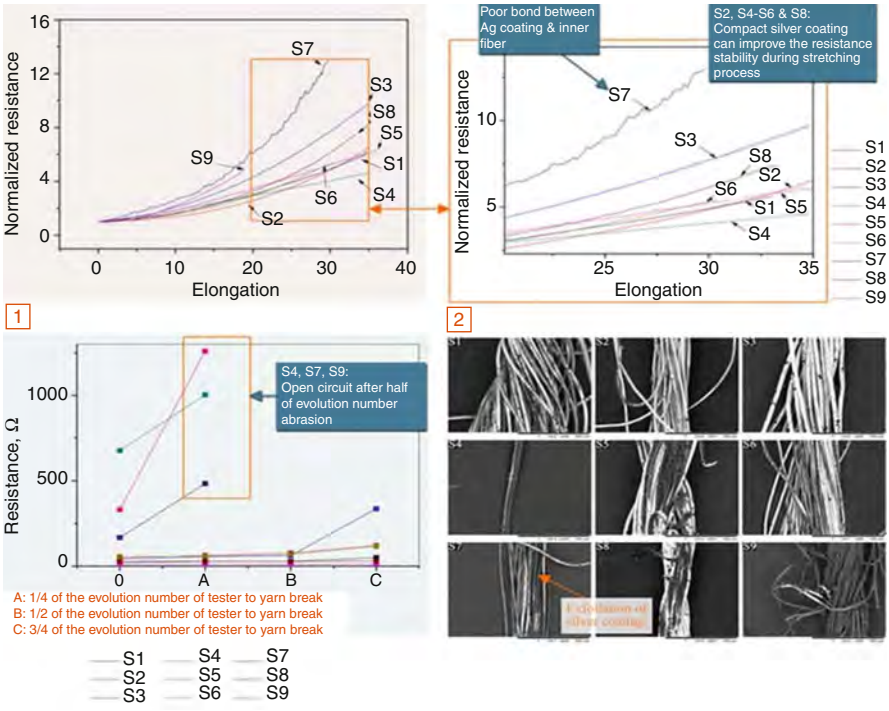

Fig. 10 (**a**) Three conventional structures of conductive yarns and the SEM inspection on their surface. (**b**) SEM images of conductive yarns after laundering. (**c**) Chemical analysis of conductive yarns. (**d**) Conformance testing of conductive yarns. (**e**) Resistance of conductive yarns during elongation and after abrasion

conductive yarns. The compact silver coating would contribute to the better stability of Ag/nylon conductive yarns under various conditions. The selected silver yarns should also be reliable in resistance distribution along the yarn. Significant resistance change should be avoided in high-quality conductive yarns. Conformance testing is required to confirm the consistency of yarns. In addition, mechanical property testing, abrasion testing, laundry testing, and corrosion resistance testing of conductive yarns are all required to ensure their resistance to elongation, abrasion, laundry in manufacturing, and corrosion of sweat in use. The testing results and SEM images together indicate that the stability and reliability of the conducting yarns depend greatly on the coating techniques. Conducting yarns with uniform silver coated on the surface in SEM images show better stability and properties in later testing.

In conclusion, when selecting Ag/nylon conductive yarns in the market, the industrialist should consider which structure of yarns is suitable to their products in their first step. Then they could give preliminary judgment of their quality by SEM analysis on the surface condition. It is found that different yarns may perform differently in different testing and it is almost impossible to simply use SEM analysis. Thus, it is strongly advised that the conductive yarn manufacturers can

give more testing results of yarns including abrasion testing, NaCl solution corrosion testing, and so on, so that the industrialists can obtain further information of their properties and quality, which can help them select what they need.

Summary

In this chapter, some discussion and advice on various properties, electrical design, testing, and material selection of thermal garments are provided for manufacturers' reference from the point of the view of the manufacturing process. The same way of thinking can be applied to other wearable electronics. As most wearable electronics projects are hybrids where electronic components are embedded into the textiles, the properties of them should be reconsidered. It is a great progress that the manufacturers and industrialists can make better decisions on material selection, have deeper insight into various properties of wearable electronics, have better designs, and do systematic testing, which can improve both the manufacturing efficiency and the quality of products and further promote the development of the wearable electronics industry.

References

1. Li L, Liu S, Feng D, Hua T, Au WM, Wong KS (2012) Electromechanical analysis of length-related resistance and contact resistance of conductive knitted fabrics. Text Res J 80(20):2062–2070
2. Tong JH, Ding F, Tao XM, Au WM, Li L (2014) Temperature effect on the conductivity of knitted fabrics embedded with conducting yarns. Text Res J. doi:10.1177/0040517514530026
3. Li L, Au WM, Wan KM, Wan SH, Chung WY, Wong KS (2009) A resistive network model for conductive knitting stitches. Text Res J 80(10):935–947
4. Liu S, Tong JH, Chan YF, Li L (2014) The resistive impacts of float stitches in conductive knitted structure. Text Res J
5. Zhao YF, Chan YF, Tong JH, Feng D, Wong KS, Li L (2013) A resistive simulation model for designing conductive weaving stitches. Text Res J
6. Li L, Au WM, Li Y, Wan KM, Wan SH, Wong KS (2009) Design of intelligent garment with transcutaneous electrical nerve stimulation function based on the intarsia knitting technique. Text Res J 80(3):279–286
7. Li L, Au WM, Li Y, Wan KM, Chung WY, Wong KS (2009) A novel design method for intelligent clothing embedded sensor system based on knitting technology and garment design. Text Res J 80(15):1670–1677
8. Li L, Au WM, Hua T, Ding F (2014) A design approach for electric stimulation textiles. Design J 17(1):137–154 (18)
9. Li L, Au WM, Hua T, Wong KS (2011) Design of conductive fabric network by sheet resistance method. Text Res J. doi:10.1177/0040517511410105
10. Li L, Au WM, Ding F, Hua T, Wong KS (2013) Wearable electronic design: electrothermal properties of conductive knitted fabrics. Text Res J. doi:10.1177/0040517513494254
11. Tong JH, Liu S, Yang CX, Li L (2014) Modelling of package-free flexible conductive fabric with thermal regulation where temperature can be customized. Text Res J. doi:10.1177/0040517514551470

Relationship Between Electromechanical Properties and Fabric Structures Made from Intrinsically Conductive Fibers

27

Zhang Hui

Contents

Introduction 720
Electromechanical Properties of Fabric Structure 721
Electromechanical Properties of Single Conductive Fiber 721
Electromechanical Properties of Continuous Filament Yarn 722
Electromechanical Properties of Short Fiber Stable Yarn 723
Electromechanical Properties of Fabrics 727
Summary 736
References 737

Abstract

With the development of science and technology, traditional textiles exhibit more functional, intelligent properties based on their structures' design such as sensors and electrodes. Smart textile is such a novel fields that provide more fantasy to our daily life. To be used as textile, sensor is a new application due to its advantages such as flexible, wearable, breathable, cheap, etc. Many research groups have been focusing on the applications of textile sensor based on the textile structure and material properties, because wearability is the trend of the next generation electronics.

The electromechanical properties of single fiber, fiber assembly, and fabric structure were analyzed theoretically by the circuit model and verified experimentally.

Used as strain or pressure sensor, electromechanical properties of textiles are of very important when designing the smart textiles. It is found from the research that the contact resistance between two contacting fibers in the yarn is the key

Z. Hui (✉)
School of Textiles, Zhejiang Fashion Institute of Technology, Jiangbei District, Ningbo, Zhejiang Province, China
e-mail: zhang_hui@mail.dhu.edu.cn

© Springer Science+Business Media Singapore 2015

X. Tao (ed.), *Handbook of Smart Textiles*,
DOI 10.1007/978-981-4451-45-1_30

factor governing the sensing mechanism. The fiber-fiber contacts in the yarns construct a complex resistance network, which will change the resistance according to the load applied. The yarn, based on fiber-fiber contacts, sets up a second-level resistance network which responses to the force applied on the fabric. How to design a suitable yarn and fabric structures that distribute the fiber contacts is the most important factor when designing a high-quality fabric strain/pressure sensor.

Keywords
Electromechanical • Smart/intelligent textiles • Textile sensor • Wearable electronics • Sensitivity • Resistance network • Fabric pressure sensor

Introduction

With the recent development of wearable electronics, textile-structured flexible sensors are in increasing demands. Such sensors should have the properties of elastic, wearable, washable, possibly extendable to cover a three-dimensional surface, robust to work in harsh environment, and reliable to supply accurate measurement. Meanwhile, they must be produced at low cost as to not affect the overall product cost.

Textiles, the traditional creation invented by the ancients to provide shelters for human body, are now taking fascinating roles in our modern society as smart materials [1]. Being used as sensors based on the configuration-induced electrical resistance change under external force are quite novel applications [2–7]. By far, some soft substrate or flexible strain sensors have been investigated and used. Glass optical fiber strain sensors can be used in high temperature but within small strain range [8, 9]; polymer optical fibers [10], piezoelectric polymer membranes, or other kinds of large strain gauges, on the other hand, can undergo larger strain but only under relatively low temperature. Most of these fabric gauges which can measure the strain or pressure exhibit poor environmental stability and cannot stand high temperature, limiting these gauges to be used under high-temperature, humid, or chemical-exiting environments with low accuracy and repeatability.

Textile structures with intrinsic electrical conductive fiber such as continuous stainless steel filament yarns have been demonstrated for these good sensing abilities. However, used as textile-structured sensor, low sensitivity, repeatability, and linearity are main problems need to be solved.

Sensors are devices that provide an interface between electronic equipment and the physical world and typically convert nonelectrical, physical, or chemical quantities into electrical signals. Of these, by far the most widely used in strain measurement are electrical resistance gauges, which first proposed by Lord Kelvin who, in 1856, discovered that the resistance of conductor changed when it was stretched [11]. However, due to electromechanical properties of the alloys, backing materials, and the adhesives used in these gauge systems, the maximum static strain

level that can be applied before failure is limited. Meanwhile, fatigue is also a problem in dynamic measurement because of the poor repeatability of alloys in extension and recovery cycles. Furthermore, limitation also exists in temperature and low stress measurement such as flexible materials because of the large rigidity of the gauges.

Electromechanical Properties of Fabric Structure

Electromechanical Properties of Single Conductive Fiber

Electromechanical properties are the relationships between electrical and mechanical properties [12]. It is the electrical response under the mechanical stimuli. In order to explore electromechanical properties of fabric structure, the fiber and yarn electromechanical properties should be investigated firstly as fabric structurally is composed by fiber and fiber assembly yarn.

Intrinsic electrical conductive fibers are conductive fibers such as metal, carbon fibers, which is different to conductive polymer fibers, structurally. In order to study the electromechanical properties of a single intrinsic conductive fiber, an idea of a fiber model with a diameter and length of A and L, respectively, is shown in Fig. 1.

Therefore, the total resistance of the fiber can be expressed in Eq. 1:

$$R = \rho \frac{L}{A}, \tag{1}$$

where ρ is resistivity of the fiber material,

when a force F is applied on the fiber shown in Fig. 2, the resistance of the fiber will change due to the change of cross-section area A and length L and resistivity ρ as expressed in Eq. 2:

$$\frac{dR}{R} = \frac{d\rho}{\rho} + \frac{dL}{L} - \frac{dA}{A}, \tag{2}$$

It can be seen from Eq. 2 that the change of the resistance comes from the relative change of resistivity, $\frac{d\rho}{\rho}$, and relative dimensional changes, $\frac{dL}{L} - \frac{dA}{A}$. For intrinsic

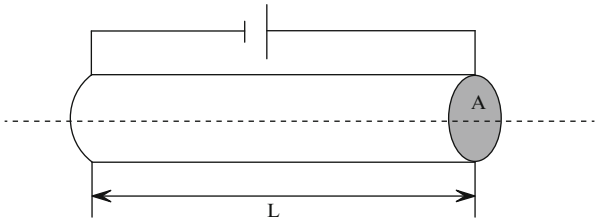

Fig. 1 Schematic model of single fiber

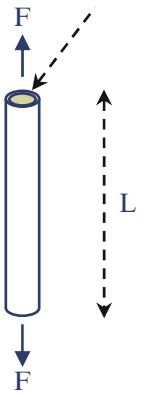

Fig. 2 Electromechanical properties of single fiber

conductive material, the relative change of resistivity can be ignored. Meanwhile, the changes of the fiber cross section and length are also very small when the fabric is under deformation, as most of changes come from structure deformation, instead of fiber deformation. Traditional strain gauge makes use of electromechanical properties of metals, similar to fiber deformation. It has the advantage of high accuracy but exhibits disadvantages of the following:

1. Small deformation range
2. Low sensitivity
3. Irreversible

Therefore, the electromechanical property of a single fiber is the change of resistance due to deformation of fiber and the change of resistivity of fiber material. Low deformation, low sensitivity, and irreversibility are the main disadvantages. It therefore needs more complex structures such as yarn and textiles.

Electromechanical Properties of Continuous Filament Yarn

Yarn is a fiber assembly which is controlled by manufacturing process. The electromechanical properties of yarn are different to fiber as the fiber-fiber physical contacts will create electrical contacts. It in turn introduces contact resistance in the system.

For continuous filament yarn shown in Fig. 3, it is different to stable yarn as there has not fiber-fiber contacts in longitudinal direction. When a current is applied on the yarn system, most of current will flow along the whole fibers instead of crossing adjacent fibers which will create large contact resistance.

Figure 4 shows the strain-resistance relationship of continuous stainless steel yarn; it can be seen that the resistance increases with the extension of the yarn. It is caused by the extension of fibers.

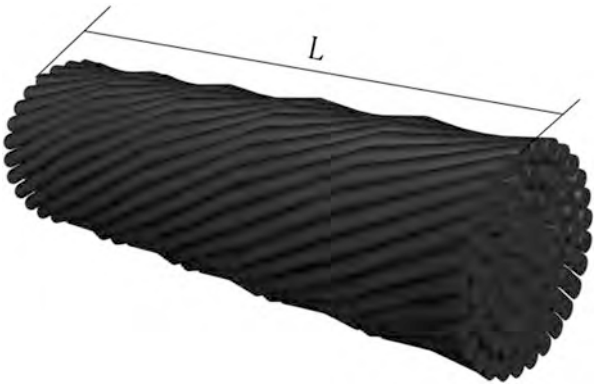

Fig. 3 Continuous filament yarn

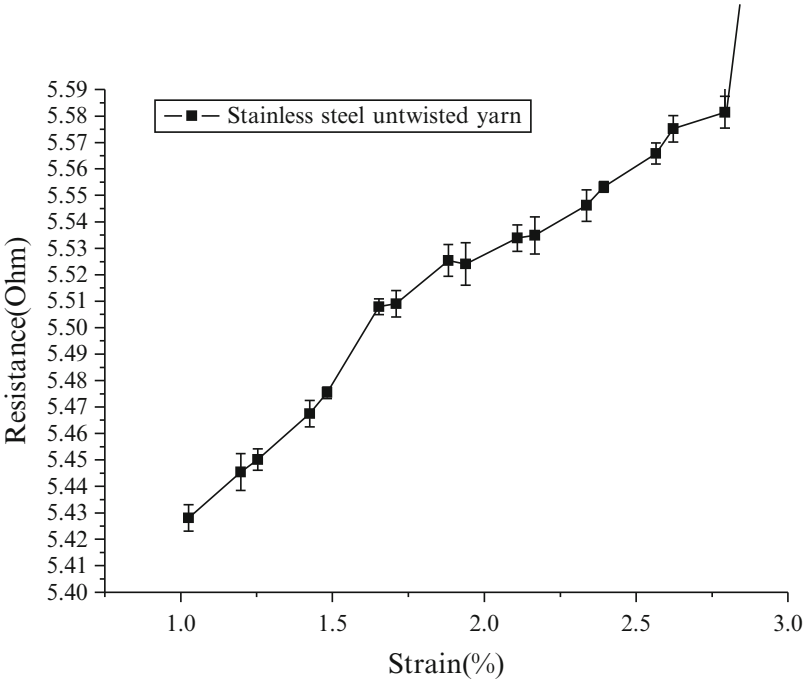

Fig. 4 Electromechanical properties of continuous stainless steel filament yarn

Electromechanical Properties of Short Fiber Stable Yarn

Fiber-Fiber Contacts and Contacting Resistance

Stable yarn is the twisting of short fibers to form a fiber assembly by weaving process. It therefore constructs mechanical contacts between fibers. These physical contacts will convert to electrical contacts when a voltage is applied on the fiber assembly. The current must flow through these fiber-fiber contacts to build up a

Fig. 5 Fiber-fiber contact resistance

Fig. 6 Model of stable yarn

circuit. This fiber-fiber conductive contacting resistance, called contact resistance, is the key factor which determines the electromechanical properties of stable yarn as shown in Fig. 5.

The contact resistance of two contacting objects as shown in Fig. 5 is indicated by Holm theory [11] that the contact resistance is inversely proportional to numbers of contacting points (contacting area). This means that a large contact force between two fibers creates a large contacting area between fibers, which in turn introduce small contact resistance.

Equivalent Circuit of Stable Yarn

In a stable yarn as shown in Fig. 6, the total resistance of the yarn can be expressed by the combination of contact resistance R_c between fibers and length resistance R_l of fibers.

For a given fiber in a stable yarn, it will build up a circuit shown in Fig. 7 which is composed by length resistance and contact resistance.

Based on the circuit of the single fiber in stable yarn analyze previously, the equivalent circuit of the whole stable yarn can be expressed by a complex resistance network as shown in Fig. 8. The nodes in the network represent the contact resistances, and the length resistances can be ignored compared to contact resistance (contact resistance is three order of magnitudes larger than length resistance by experiments).

Therefore, the circuit network will be determined by the minimum energy consumption theory expressed in Eq. 3:

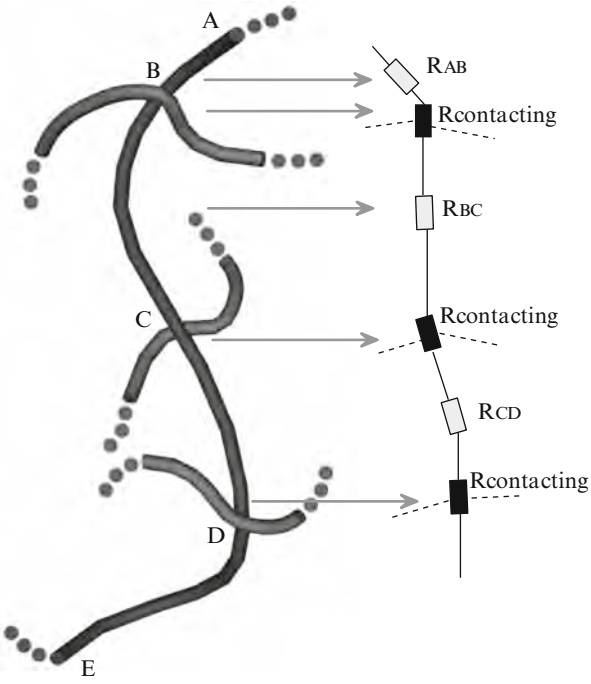

Fig. 7 Equivalent circuit of single fiber in stable yarn

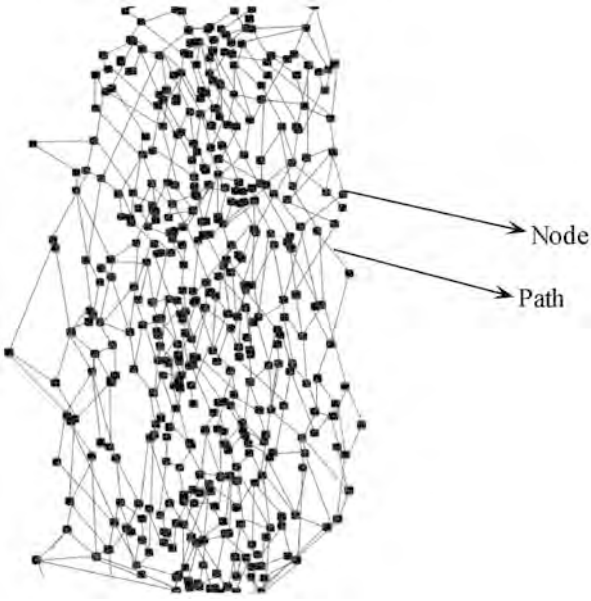

Fig. 8 Resistance network of stable filament yarn

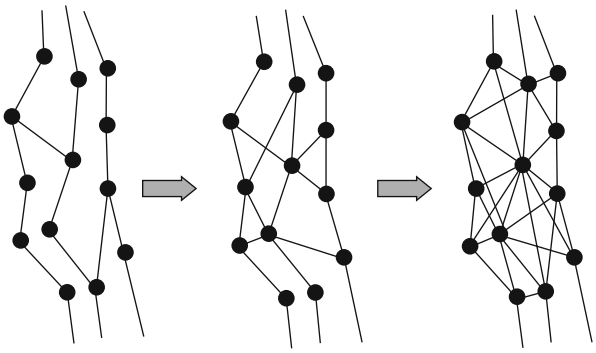

Fig. 9 Changes of the network of the stable yarn

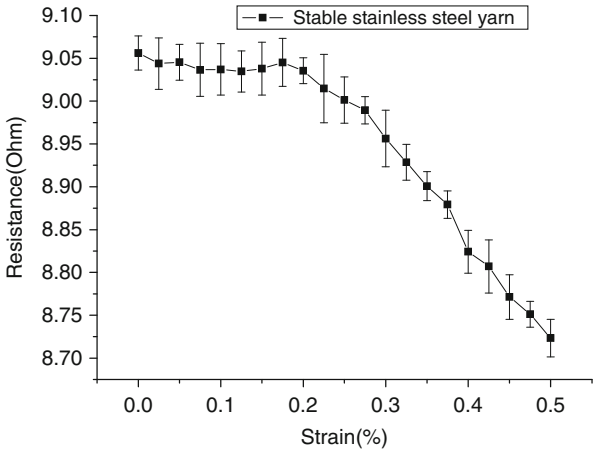

Fig. 10 Electromechanical properties of stable stainless steel yarn

$$\text{Min} \sum_{(i,j) \in A} R_{C(ij)} {i_{ij}}^2, \tag{3}$$

where R_c represents the contact resistance and stands for electrical current which flows along the fiber.

For a stable fiber, the nodes and path of the network shown in Fig. 8 will change when the fiber is under extension. The total resistance of the yarn will change accordingly as shown in Fig. 9.

Figure 10 shows the resistance-strain relationship of stable stainless steel yarn. It can be seen that the resistance decreases sharply when the strain reaches 0.2 %. This is because the change of the resistance is mainly caused by the increase of the conducting path and decrease of contact resistance between fibers. In the first stage smaller than 0.2 %, the resistance decreases moderately as the strain is mainly caused by the configuration change of yarns.

Compared with Fig. 4 of continuous filament yarn, it is obvious that electromechanically stable yarn exhibits different curves. This is because the electromechanical properties are differently analyzed previously.

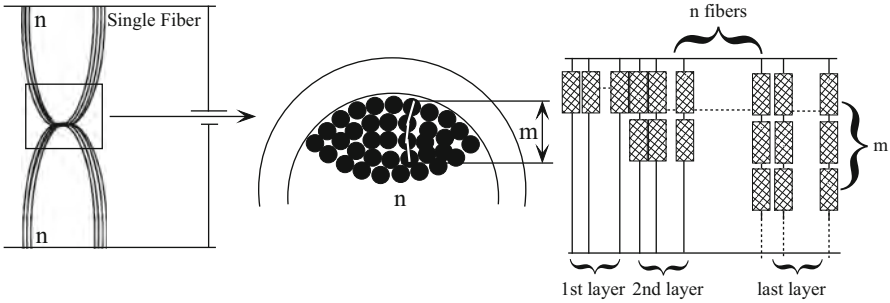

Fig. 11 Circuit of two contacting yarns

Electromechanical Properties of Fabrics

Yarn-Yarn Contacts

To demonstrate the conducting mechanism between two contacting yarns, an ideal orthogonal contact is sketched in Fig. 11. Each yarn contains n fibers.

When a voltage is applied on the two contacting yarns, the current reaches the surface fibers of the adjacent yarn by the directly contact fibers, i.e., the surface fibers at the contacting region. For a single fiber behind the surface fibers, suppose m contacts exist along the current path to the adjacent yarn's surface. Thus, m increases with the increase of the distance to that surface. Consequently, these m contacted fibers are in serial connections regarding the resistance, while the n fibers in a yarn within the contacting region are in parallel connections, as shown on the right of Fig. 11. Therefore, in the case of two contacting yarns being in a symmetric configuration, the conducting resistance can be calculated as follows:

$$R_{\text{contacting}} = 2\frac{1}{\sum_{i=1}^{n}\frac{1}{\sum_{j=1}^{m} R_{(i,j)\,\text{fiber contacting}}}}, \tag{4}$$

It is evident that, for a given fiber, the total contacting resistance in relation to the contacting surface increases with the number of the layers. As a result, most of the current will flow through the surface fibers, and accordingly the total contact resistance is mainly determined by the number of the surface fibers. The contacting circuit can be simplified by ignoring the large indirect contact resistance behind the surface layers, so that

$$R_{\text{contacting}} = 2\frac{1}{\sum_{i=1}^{k}\frac{1}{R_{(i)\ \text{surface fiber contacting}}}}, \tag{5}$$

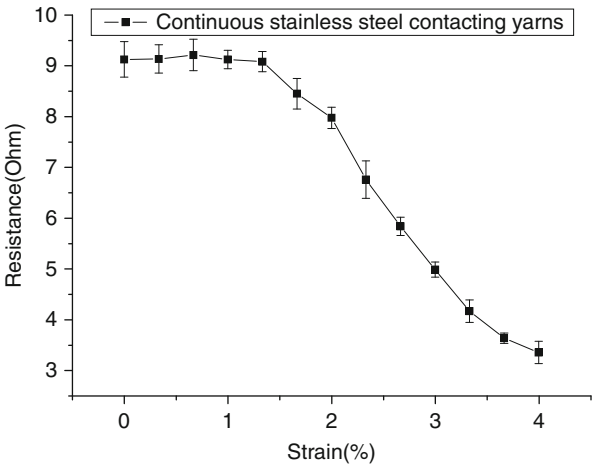

Fig. 12 Electromechanical properties of two continuous contacted yarn

where k denotes the number of the surface contact fibers.

When the two contacting yarns are stretched against each other, more fibers will be pushed onto the contact surfaces, leading to an increase in the number of the direct contact fibers, so as to reduce the total contact resistance. For two contacting stable yarn, the contacting mechanism will be more complex as there exist two networks shown in Fig. 8.

Figure 12 shows the strain-resistance relationship of two contacting continuous yarns. It can be seen that the resistance decreases with increase of extension. At the first stage, the resistance keeps small change and decreases sharply at the second stage. This is due to the configuration changes firstly and then fibers transferring.

Electrochemical Properties of Knitted Fabric

Fabric is a fiber assembly. The electromechanical properties of fabric are based on yarn and fiber [13]. Knit is a typical fabric structure which is more complex than woven one when analyzing the electromechanical properties due to their "loop-like" yarn-yarn contacts. Knitted fabrics have been used widely in clothing. Being used as sensors for measuring strain and temperature based on their loop configurations are quite novel applications. Elastic and extendable substrates of the fabrics give these sensors feasibility for measuring large strain.

Circuit Network of Knitted Fabric

A theoretical model to analyze electromechanical behavior of plain weft-knitted fabric made from conductive yarn was proposed. The fabric is made from stainless steel multifilament yarns.

Electrical conductive fabrics can be treated as a pure resistive circuit network. A unit loop is shown in Fig. 13 comprising two contacting resistances (R_c) and three length resistances (R_l), relating the contacting force of the overlapped yarns and the intrinsic resistance of the metallic yarns, respectively. When the fabric is subject to a load, the loops will change their configurations. Therefore, the contacting

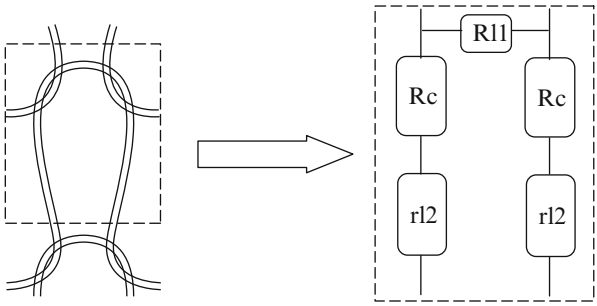

Fig. 13 A unit loop and representative unit of electrical network

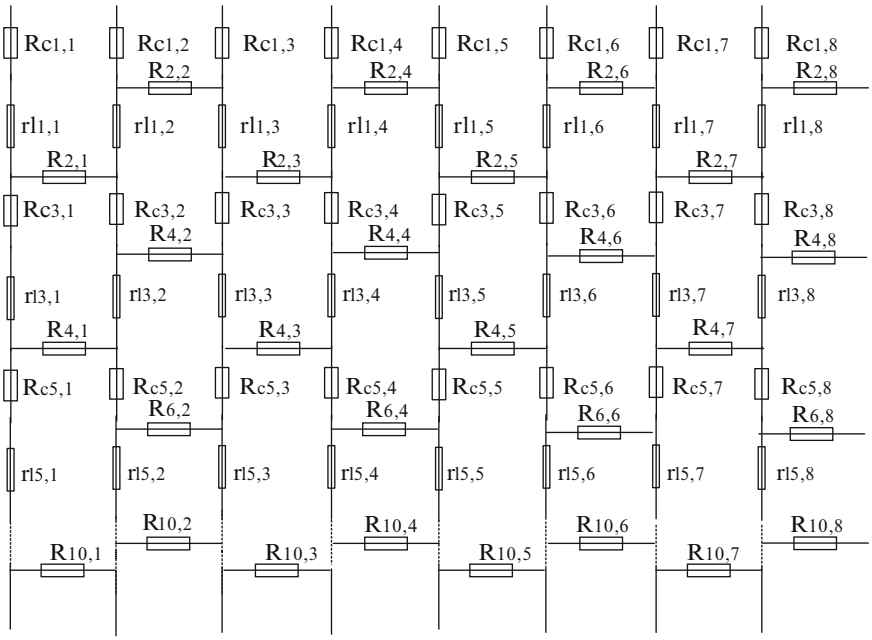

Fig. 14 Circuit simulating the plain knitted fabric

resistance R_c and the length-related resistance R_l will change according to the magnitude of the contacting force and the length of the yarn caused by the transferring of the yarns in the loops, respectively, during the extension of the fabric.

Therefore, the whole fabric circuit network can be obtained as shown in Fig. 14. A 4 × 5 unit loop fabric is chosen for investigations and simulations.

Each resistor in the circuit network is marked with subscript numbers to indicate the position in the fabric resistance network. Because the length resistance (0.029 Ω/mm) is much smaller than the contacting resistance (1 ~ 13 Ω) by experimental

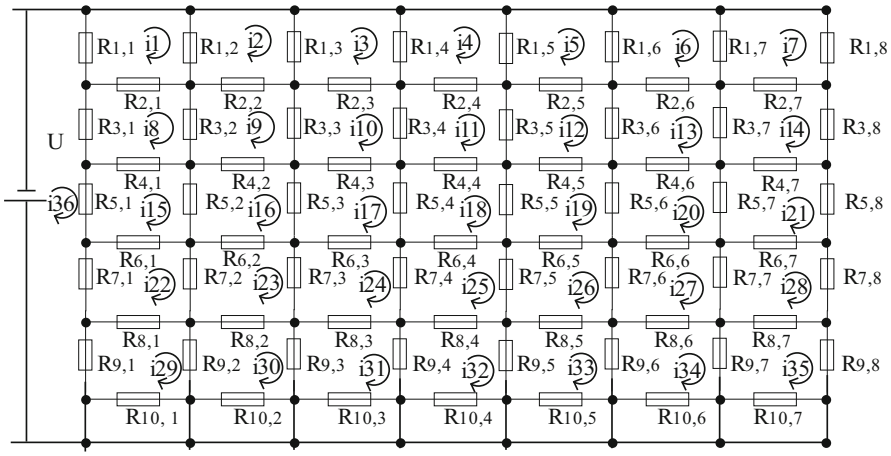

Fig. 15 Simplified network of circuit

results, hence, in order to simplify the circuit network, the length resistances in the wale direction are ignored and we let

$$R_c(i,j) = R(i,j)\,(= 1, 3, 5, 7, 9), \tag{6}$$

Thus, the circuit network can be simplified as illustrated in Fig. 15.

The fabric circuit network is connected by a number of electric "bridges." Each resistance value in the circuit is determined by the geometrical and electrical properties of the loops.

In order to calculate the equivalent resistance of the fabric, the circuit network equations should be established first. The equivalent resistance is defined as the ratio of the voltage U and the total current i_{total}:

$$R_{\text{eqivalent}} = \frac{U}{i_{\text{total}}}, \tag{7}$$

Kirchhoff's voltage law and electric circulation theories are employed to calculate i_{total} of the fabric circuit. Kirchhoff's voltage law states that in a closed circuit, the sum voltage of all components is zero. A hypothetic current i flows through every circulation of the circuit network; the real current I that flows through the branches of the circuit is the algebraic sum of the hypothetic current i. Thus, the circuit equations can be obtained, and the equivalent resistance of the fabric can be calculated by solving the equations.

A unit loop circuit shown in Fig. 16 is analyzed by the above method. The relationships between the hypothetic currents i and branch currents I can be expressed with Eq. 8. Equation 9 is obtained by Kirchhoff's voltage law:

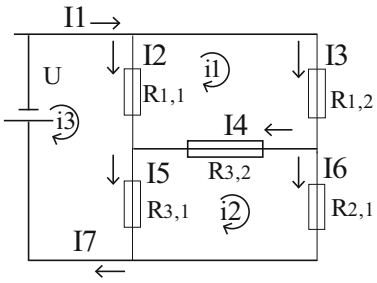

Fig. 16 A unit loop circuit

$$\begin{cases} I_1 = i_3 \\ I_2 = i_3 - i_1 \\ I_3 = i_1 \\ I_4 = i_1 - i_2 \\ I_5 = i_3 - i_2 \\ I_6 = i_2 \\ I_7 = i_3 \end{cases}, \tag{8}$$

$$\begin{cases} I_3R_{12} + I_4R_{21} - I_2R_{11} = 0 \\ -I_4R_{21} + I_6R_{32} - R_{31}I_5 = 0 \\ I_2R_{11} + I_5R_{31} = U \end{cases}, \tag{9}$$

Combining Eqs. 8 and 9, the equations can be obtained:

$$\left[R^*{}_{i,j}\right][i_i] \;=\; \left[U_j\right] \;(= 1, 2, 3, \quad = \quad 1, 2, 3), \tag{10}$$

where

$$\left[R^*{}_{i,j}\right] = \begin{bmatrix} R_{11} + R_{12} + R_{21} & -R_{21} & -R_{11} \\ -R_{21} & R_{21} + R_{32} + R_{31} & -R_{31} \\ -R_{11} & -R_{31} & R_{11} + R_{31} \end{bmatrix}$$

i_i is the hypothetic circulation current and U_j is the external voltages of the circulations.

i_3 can be obtained by solving Eq. 10, and the equivalent resistance of the fabric can be gained by Eq. 11:

$$R_{\text{eqivalent}} = \frac{U}{i_3}, \tag{11}$$

Similar to the unit loop circuit analysis above, the fabric circuit equations can be acquired and solved. The 36 independent circulations, shown in Fig. 15, are chosen for representing the fabric.

Figure 15 shows that the total current of the network is i_{36}. Hence, the equivalent resistance of the fabric can be expressed as:

$$R_{\text{eqivalent}} = \frac{U}{i_{36}}, \tag{12}$$

Similar to Eq. 10, the fabric circuit network equations can be express as:

$$\left[R^*_{i,j}\right]\left[i_i\right] = \left[U_j\right] (= 1, 2, 3, \ldots, 36 = 1, 2, 3, \ldots, 36), \tag{13}$$

where

$$\left[R^*_{i,j}\right] = \begin{bmatrix} R_{1,1}+R_{1,2}+R_{2,1} & -R_{1,2} & 0 & \ldots & -R_{1,1} \\ -R_{1,2} & R_{1,2}+R_{1,3}+R_{2,2} & -R_{1,3} & \ldots & 0 \\ 0 & -R_{1,3} & R_{1,3}+R_{1,4}+R_{2,3} & \ldots & 0 \\ \ldots & \ldots & \ldots & \ldots & \ldots \\ -R_{1,1} & 0 & 0 & \ldots & R_{1,1}+R_{3,1}+R_{5,1}+R_{7,1}+R_{9,1} \end{bmatrix}$$

$$\left[U_j\right] = \begin{bmatrix} 0 \\ 0 \\ \ldots \\ U \end{bmatrix}$$

The total current i_{36} can be gained by solving Eq. 13 if the components in $R_{i,j}$* are known.

Contacting Resistance R_c and Length Resistance R_l

R_l is the resistance that is in proportion to the length of the yarn, and R_c is determined by the contacting force of the two overlapped yarns. The resistance per unit length of the yarn can be acquired by measuring the resistance of different yarn lengths.

The relationship between the contacting resistance R_c and the contacting force on the overlapped yarns can be obtained by measuring the resistance of two hooked strands of yarns. The experimental setup is shown in Fig. 17.

The relationship between the normal force on the two hooked yarns and contacting resistance can be obtained by the following function:

$$R_c = f(N), \tag{14}$$

where N is the normal contacting force acting on the yarns. And the function f can be determined experimentally.

Mechanical and Geometrical Analysis of Loops

In order to simplify the loops, a two-dimensional hexagonal mechanics model, which was first proposed by Wu et al. [14], is used. This model ignores the 3D loop configuration and may represent the stretched fabric when all yarns are straightened. Figure 18 shows the hexagon model of the loops.

In order to analyze the contacting force, a unit loop is chosen as shown in Fig. 19.

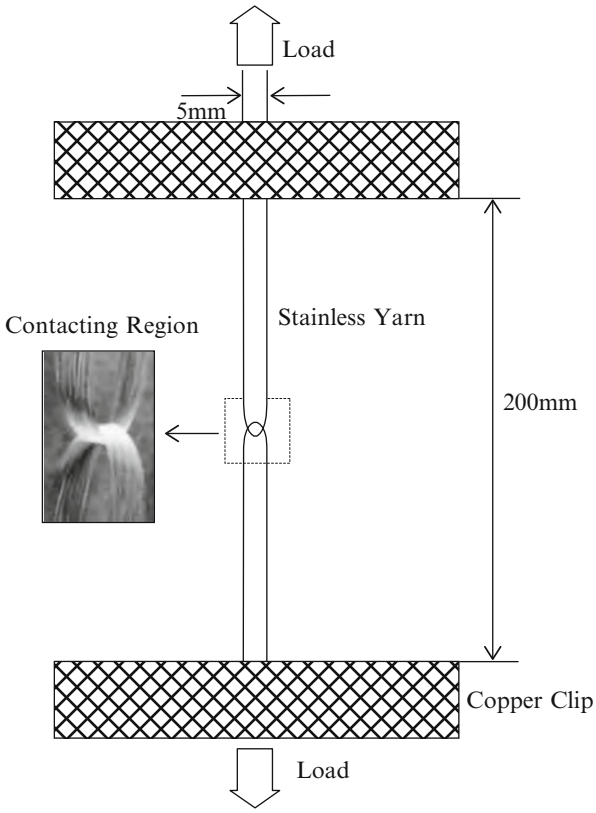

Fig. 17 Setup for yarn contacting resistance R_c

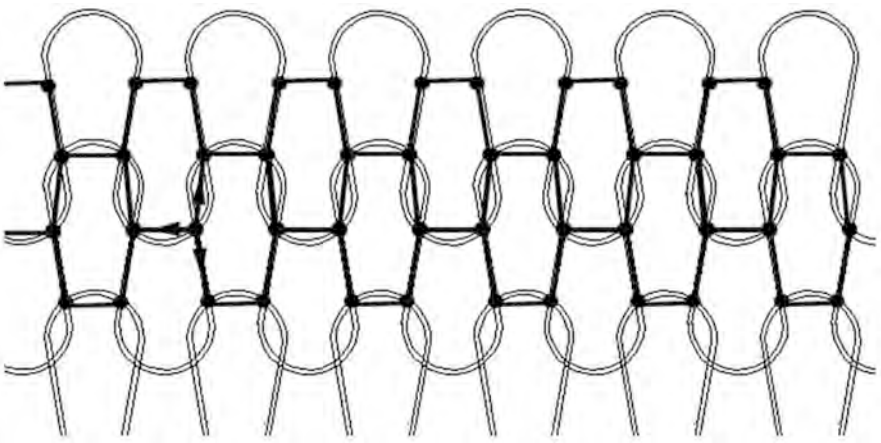

Fig. 18 Hexagon model of the knitted loops

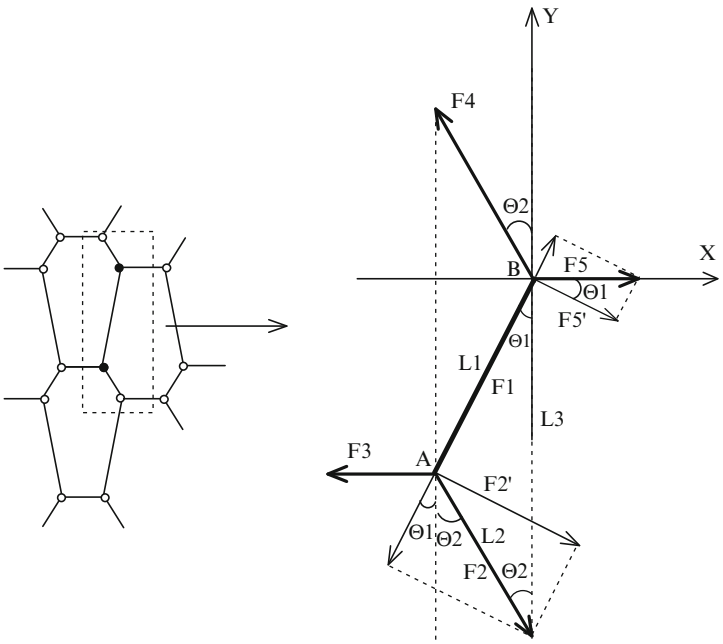

Fig. 19 Mechanic analysis of the hexagon model

Since the model has a symmetry, only half of the loop is analyzed. Rigid segment *AB* is considered.

The force equilibrium in directions *X* and *Y* and the moment equilibrium of point *A* lead to the following equations:

$$\begin{cases} F_4 \sin\theta_2 + F_2 \sin\theta_2 - F_5 + F_3 = 0 \\ F_4 \cos\theta_2 - F_2 \cos\theta_2 = 0 \\ F_4 \sin(\theta_1 + \theta_2) \times |AB| - F_5 \cos\theta_1 \times |AB| = 0 \end{cases}, \tag{15}$$

And the normal contacting forces on the loop are given by $F_2{}'$ and $F_5{}'$:

$$\begin{cases} F_2{}' = F_2 \sin(\theta_1 + \theta_2) \\ F_5{}' = F_5 \cos\theta_1 \end{cases}, \tag{16}$$

Hence, the total normal force N on the overlapped yarns can be expressed as:

$$N = F_2{}' + F_5{}' = F_2 \sin(\theta_1 + \theta_2) + F_5 \cos\theta_1, \tag{17}$$

σ_f is the fabric tensile force distributed uniformly on every yarn in the course direction in the fabric and expressed as:

$$\sigma_f = \frac{F}{N_w}, \tag{18}$$

where F is the load on the fabric and N_w is the yarn number in the wale direction.

By the force analysis, we have

$$F_2 = \frac{\sigma_f}{\cos\theta_2}, \tag{19}$$

From Eqs. 15, 16, 17, 18, and 19, the normal contacting force on the overlapped yarns can be given by

$$N = F_2' + F_5' = 2\frac{\delta_f \sin(\theta_1 + \theta_2)}{\cos\theta_2}, \tag{20}$$

By using the cosine laws, the contacting angles θ_1 and θ_2 can be calculated as the following:

$$\begin{aligned} \cos\theta_1 &= \frac{{l_1}^2 + {l_3}^2 - {l_2}^2}{2l_1l_3} \\ \cos\theta_2 &= \frac{{l_2}^2 + {l_3}^2 - {l_1}^2}{2l_2l_3}, \end{aligned} \tag{21}$$

Combining Eqs. 20 and 21, the normal contacting force on the loops can be obtained:

$$\begin{aligned} N &= F_2' + F_5' = 2\sigma_f \sin(\theta_1+\theta_2)/\cos\theta_2 \\ &= 2\frac{F}{N_w}\left(\frac{\sin\theta_1\cos\theta_2 + \cos\theta_1\sin\theta_2}{\cos\theta_2}\right) \\ &= 2\frac{F}{N_w}\left(\frac{\left(1-\left(\frac{{l_1}^2+{l_3}^2-{l_2}^2}{2l_1l_3}\right)^2\right)^{\frac{1}{2}}\left(\frac{{l_2}^2+{l_3}^2-{l_1}^2}{2l_2l_3}\right) + \left(\frac{{l_1}^2+{l_3}^2-{l_2}^2}{2l_1l_3}\right)\left(1-\left(\frac{{l_2}^2+{l_3}^2-{l_1}^2}{2l_2l_3}\right)^2\right)^{\frac{1}{2}}}{\frac{{l_2}^2+{l_3}^2-{l_1}^2}{2l_2l_3}}\right), \end{aligned} \tag{22}$$

Experimental Results

Substituting Eq. 22 with the load F and the length l of the loops, the contacting resistance matrix can be derived from Eq. 8. Together with the length resistance R_l (Eq. 14), the whole fabric equivalent resistance can be calculated by Eqs. 12 and 13. Figure 20 shows the simulated and experimental data.

Figure 20 illustrates that the resistances calculated by the model agree with those obtained by experiments to a reasonable extent. There seems to be a "shift" between the simulated and experimental results in Fig. 20. This may be due to the two-dimensional hexagon model that does not truly reflect the real contact between two yarns. Knitted fabric loops are of three-dimensional configurations, and the

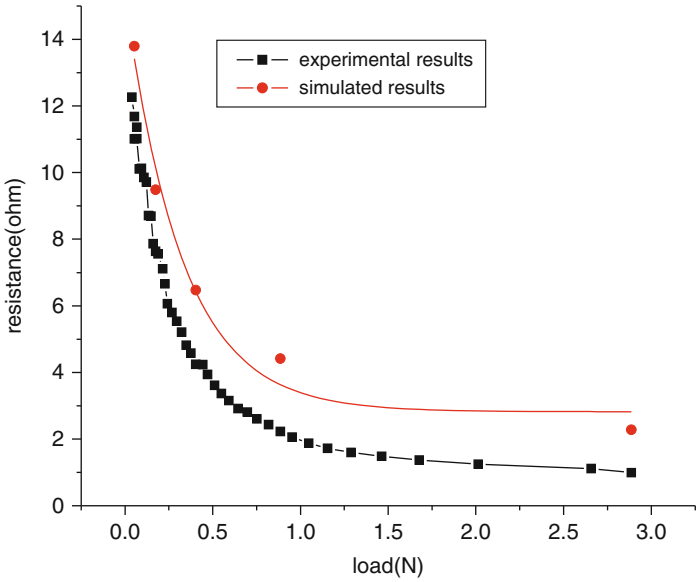

Fig. 20 Simulated and experimental values of the fabric resistance plotted

contacting forces acting on the contacting yarns are more complex than the two-dimensional model.

Summary

With the development of science and technology, traditional textiles exhibit more functional, intelligent properties based on their structures' design such as sensors and electrodes. To be used as textile, sensor is a kind of smart textile, and it has advantages such as flexible, wearable, breathable, thin and cheap, etc. Many research groups have been focusing on the applications of textile sensor based on the textile structure and material properties, because wearability is the trend of the next generation electronics.

Used as strain or pressure sensor, electromechanical properties of textiles are of very important when designing the smart textiles. It is found from the research that the contact resistance between two contacting fibers in the yarn is the key factor governing the sensing mechanism. The fiber-fiber contacts in the yarns construct a complex resistance network, which will change the resistance according to the load applied. The yarn, based on fiber-fiber contacts, sets up a second-level resistance network which responses to the force applied on the fabric. How to design a suitable yarn and fabric structures that distribute the fiber contacts is the most important factor when designing a high-quality fabric strain/pressure sensor.

References

1. De Rossi D, Santa A, Mazzoldi A (1999) Dressware: wearable hardware. Mater Sci Eng C 7:31–35
2. De Rossi D, Santa A, Mazzoldi A (1997) Dressware: wearable piezo- and thermoresistive fabrics for ergonomics and rehabilitation. In: XIX international conference of IEEE & EMBS, Chicago, p 30
3. Kincal D, Kumar A, Child AD, Reynolds JR (1998) Conductivity switching in polypyrrole-coated textile fabrics as gas sensors. Synth Met 92(1):53–56
4. Hepworth B, Leaf GAV (1970) Shape of the loops in an undeformed plain weft knit fabric, studies in modern fabrics: a report on the 1970 diamond jubilee conference of the textile institute, part 2, 1970. Text Inst Ind 8:209–213
5. Kuhn HH, Kimbrell WC, Worrell G, Chen CS (1991) Properties of polypyrrole treated textile for advanced applications. ANTEC, pp 760–764
6. Oh KW, Park HJ, Kim SH (2003) Stretchable conductive fabric for electrotherapy. J Appl Polym Sci 88:1225–1229
7. Xue P, Tao X, Leung MY (2005) Electromechanical properties of conductive fibres, yarns and fabrics. In: Tao X (ed) Wearable electronics and photonics. CRC Press, Boca Raton, pp 81–104
8. Munden DL (1959) The geometry and dimensional property of plain-knit fabrics. J Text Inst 50:448–471
9. Postle R, Munden DL (1967) Analysis of the dry-relaxed knitted loop configuration. J Text Inst 58:329–365
10. Gregory RV, Kimbrell WC, Kuhn HH (1989) Conductive textiles. Synth Met 28 (1–2):823–835
11. Holm R (1967) Electric contacts, 4th edn. Springer, New York/Berlin, pp 7–19
12. Zhang H, Tao XM, Wang SY (2006) Electromechanical properties of intrinsically conductive fiber assembles, its textile structure and applications as strain and pressure sensors. Doctoral dissertation, Dong Hua University
13. Zhang H, Tao X, Wang S, Yu T (2005) Electro-mechanical properties of knitted fabric made from conductive multi-filament yarn under unidirectional extension. Text Res J 75(8):598–606
14. Wu WL, Hiroyuki H, Zen-ichiro M (1994) Computer simulation of the deformation of weft-knitted fabrics for composite materials. J Text Inst 85:198

Fabrication of Organic Materials for Electronic Textiles

28

Tae Hwan Lim, Seong Hun Kim, and Kyung Wha Oh

Contents

Introduction 740
Preparation of Conductive Organic Materials 742
Origins of Organic Conducting Materials 742
Fabrication of Conducting Polymers 743
Fabrication of Carbon Materials 747
Fabrication Method for High-Performance Electronic Textiles 750
Textile Applications 755
Sensors 756
Textile Circuit for Smart Fashion 760
Actuator 761
Solar Cells 763
Supercapacitors 766
Battery 768
Summary 771
References 772

T.H. Lim
Technical Textile and Materials R&BD Group, Korea Institute of Industrial Technology, Ansan-si, Gyeonggi-do, South Korea

Department of Organic and Nano Engineering, Hanyang University, Sungdong-gu, Seoul, South Korea

S.H. Kim (✉)
Department of Organic and Nano Engineering, Hanyang University, Sungdong-gu, Seoul, South Korea
e-mail: kimsh@hanyang.ac.kr

K.W. Oh
Department of Fashion Design, Chung-Ang University, Anseong-si, Gyeonggi-do, South Korea

© Springer Science+Business Media Singapore 2015

X. Tao (ed.), *Handbook of Smart Textiles*,
DOI 10.1007/978-981-4451-45-1_13

Abstract

Recent years have witnessed the possibility of realizing wearable electronic textiles as well as performance advances in electrical devices for incorporating high technology into daily garments. In the development of wearable electrical devices, conductive organic materials such as conducting polymers and carbon have emerged as the optimum materials for substituting conventional inorganic materials or metals. In this chapter, the efforts toward the development of high-performance conductive organic materials from their initial stages to date are described chronologically. A variety of methods for inserting electrical devices into fabric and surface treatment methods for enhancing the electrical properties of conductive organic materials are also discussed. Finally, conductive organic material-based sensors, transistors, light-emitting devices, actuators, solar cells, supercapacitors, and batteries were introduced as implementable wearable devices for electronic textiles.

Keywords

Organic materials • Electronic textiles • Smart textiles • Conducting polymers • Carbon materials • Polyaniline • Polypyrrole • Polythiophene • Carbon nanotubes • Graphene • Coating • Laminating • Plasma treatment • Sensors • Organic light-emitting diodes • Transistor • Organic solar cells • Supercapacitors • Batteries

Introduction

Wearable electronic textiles realize the old dream of technologized textiles transforming clothes into communication devices. Wearable electronic devices could be achieved through multifunctional fabrics commonly called electronic textiles or smart textiles, which make daily life of people healthier, safer, and more comfortable. To realize the perfect smart textile, flexible and stretchable electrical devices should be developed that could be applied on general garments.

Flexible and stretchable electronics are emerging for consumer applications and are attracting interest for untraditional applications in which the mechanical flexibility of devices is preferred and required. To realize flexible electronics fully, organic materials are necessary for flexibility. Initially, scientists and engineers did not consider organic materials to have any electronic technological significance because of the lack of control on material purity and structural ordering compared to their inorganic counterparts such as Si or GaAs [1, 2].

In the past decade, organic electronic materials have received steady and increasing attention in optoelectronics. There have been many publications about flexible light emission, energy harvesting, and storage devices. There are three representative classes of organic electronic devices that can be classified according to their function. They are categorized into organic light-emitting diodes (OLEDs) and organic solar cells (OSCs), organic thin-film transistors (OTFTs), and organic

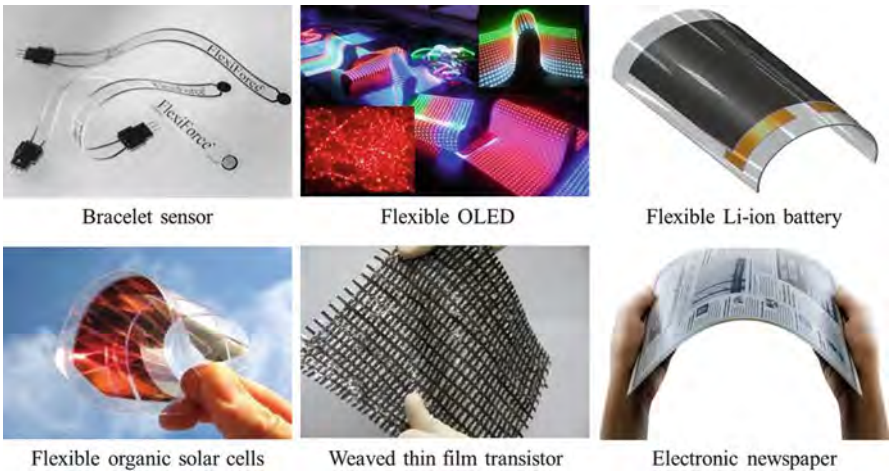

Fig. 1 Actual images of representative electronic devices (The images were permitted from Tekscan, Inc., National Physical Laboratory (Copyright from Crown Copyright), and Good E-Reader (Copyright from Oak Branch Media Inc.))

energy storage and harvesting devices such as capacitors and batteries [3–8]. The technology has sufficiently matured and commercial products are available, in particular, emissive flat-panel displays [9]. To the exclusion of the specific functions of each device, organic electronic materials generally have a sandwich structure of anode/organic material/cathode, and the entire device is a stack of thin films with a total thickness in the range of 50–200 nm. Representative electronic devices are shown in Fig. 1.

Inorganic-based electrical devices are intrinsically inflexible. In contrast, organic-based devices use organic materials that can be polycrystalline and amorphous. Therefore, they have several advantages over inorganic devices. First, organic materials, in particular amorphous ones, are mechanically flexible. Therefore, they can be used to cover plastic substrates to realize flexible electronic devices, for example, flexible and portable OSCs. The fabrication temperatures of organic devices are usually much lower than those of inorganic devices because of their weakly binding van der Waals forces [10]. Therefore, they can be fabricated through high-throughput low-temperature approaches that permit one of the several well-established printing techniques [11]. Furthermore, organic materials can be synthesized with a wide range of properties for device applications, such as molecular weight, molecular orbital energy levels, band gap, structural properties, wetting properties, and doping levels because of versatility in organic synthesis [12, 13].

Despite these advances, key challenges remain for these devices to become truly practical and commercialized. One outstanding challenge is increasing the environmental stability of organic materials. While the intrinsic van der Waals forces of organic materials give them their flexibility, it also means these materials have a

low melting point (T_m) and glass transition temperature (T_g). A typical T_g in "practical" materials can be lower than 100 °C; therefore, thin films prepared by organic materials are not thermally stable. As the temperature of the film reaches its T_g, the organic film tends to crystallize and delaminate from its adjacent contact electrode. These disadvantages induce incompatibility between fabrics and electrical devices or other organic films. Therefore, abundant effort has been made for designing thermally and environmentally durable organic materials [14–16].

In this chapter, the characteristics and efficiencies of organic material engineering applied in electronic textiles were discussed. The basic properties and synthetic histories of conducting organic materials are discussed in section "Preparation of Conductive Organic Materials." The fabrication methods of electrical devices and efficiency-enhancing techniques are covered in section "Fabrication Method for High-Performance Electronic Textiles," and the development trends in organic material-based electrical devices are described in section "Textile Applications." Finally, section "Summary" concludes.

Preparation of Conductive Organic Materials

Origins of Organic Conducting Materials

All the organic materials were not recognized as conducting forms before their electrical conductivity and other characteristics of interest were discovered. Although the electronic properties of some organic materials were known, they were not well characterized, and these properties were not of major interest compared with other properties such as thermal and mechanical behavior. For example, poly(*p*-phenylene sulfide) (PPS) was known as a thermal reinforcement since the early 1970s and is produced for thermoplastic applications under the commercial name Ryton by the Phillips Chemical Company.

The epoch of adapting conducting polymers for electronic applications has continued since the late 1970s when Heeger, MacDiarmid, and Shirakawa discovered a huge increase in the electrical conductivity of polyacetylene (PA) after treatment with I_2 [17, 18]. Theoretical studies on PA were conducted because it was the first time that a material was discovered with simple structure and high conductivity quite similar to metal; for this reason, they received the Nobel Prize in Chemistry in 2000. However, PA was excluded from research in electrical applications because of its poor processability and unstable doping state. Therefore, other polymers with high stability and electrical conductivity were studied for use in electronic applications. These structures are shown in Fig. 2.

Carbon is also known as an organic material with good electrical properties. The electrical properties of pyrolytic and polycrystalline graphite forms are superior to other carbon allotropes. Carbon materials have different characteristics according to its structure or dimensions. The carbon nanotube (CNT) is the representative carbon form composed of a tubular one-dimensional nanostructure. Tube-type carbon nanostructures were first observed in 1952 by

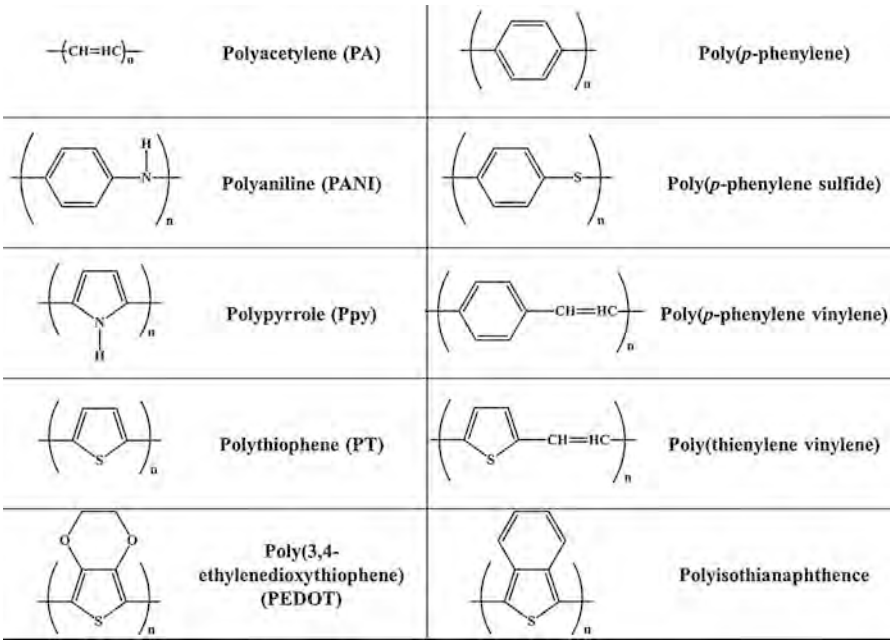

Fig. 2 The structure of representative conducting polymers

Radushkevich and Lukyanovich [9]. However, it was not an attractive material until Sumio Iijima reported the observation of CNTs in 1991 in *Nature*. This publication resulted in the development of the nanotube field. The discovery of CNTs has increased the variety of carbon-based materials. Recently, graphene, a two-dimensional flat hexagon ring network with open edges, opened a new realm of carbon materials with electrical applications. As the most basic form of the sp^2-hybridized carbon allotropes, Geim and Novoselov [19] successfully isolated graphene to one sheet from the stacked graphite in 2004. They subsequently won the Nobel Prize in Physics for this in 2010.

In this part, the fabrication methods of organic materials are presented in consecutive order and are divided into two parts, conducting polymers and carbon materials, to be described in more detail in the following sections.

Fabrication of Conducting Polymers

Polyaniline (PANI) is one of the earliest and most studied conducting polymers because of its high electrical conductivity, good environmental stability, low cost, easy preparation from common chemical materials, and excellent application potential. For these reasons, the mechanism and properties of PANI oxidation have been studied for more than four decades. In 1862, Letheby [10] discovered a blue substance produced by electrolysis of the sulfate of aniline, which he called PANI.

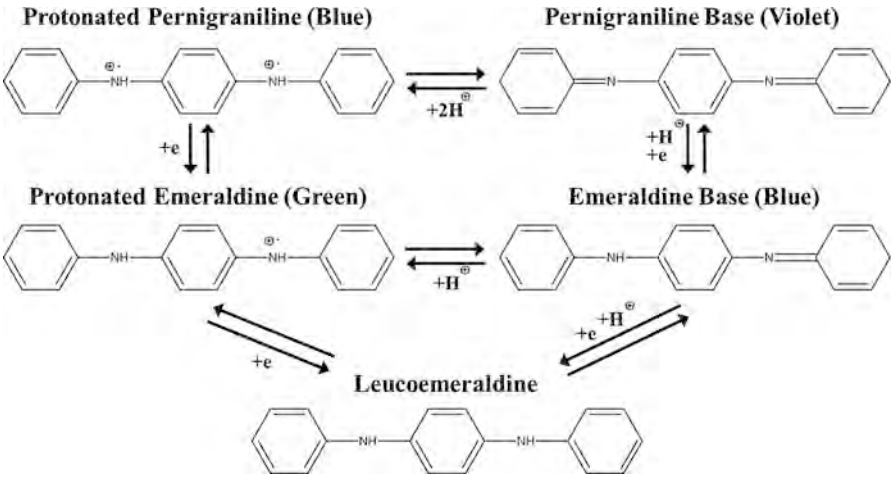

Fig. 3 Structures of PANI according to the oxidation state

This material received attention again in 1964 with the discovery of its electrical characteristic according to the pH state of aniline and high conductivity on the acidic state of aniline in 1980 by A. G. MacDiarmid.

The oxidation of aniline in acidic aqueous solution using the ammonium persulfate $(NH_4)_2S_2O_8$ as oxidant has become the most widely used chemical polymerization route and the typical synthesis method is described below. An amount of 10 mL of 2.5 M $(NH_4)_2S_2O_8$ is introduced with stirring into a 100 mL solution containing 0.55 M aniline monomer and 0.55 M trifluoromethanesulfonic acid as a dopant in an ice bath held at below 0 °C for 15 min [20].

PANI is obtained as the protonated emeraldine salt (PANI-ES), named after its green color. This state is deprotonated in alkali solution to the corresponding emeraldine base (PANI-EB), which is blue and nonconducting. Pernigraniline is the oxidized form of emeraldine and it also exists as a salt. The protonated pernigraniline is an important polymerization intermediate. Its blue color is similar to that of the emeraldine base; however, they show different maximum absorption peaks at 690 and 630 nm, respectively. Leucoemeraldine is a reduced form of emeraldine, which shows yellowish nonconducting form. These specific structures are shown in Fig. 3.

Aniline oxidation is represented by an intricate interplay of consecutive chemical redox reactions that are still far from being completely understood, although the preparation of PANI is a simple chemical polymerization from the theoretical point of view. The synthesis may yield products with a variety of properties and various supramolecular morphologies. Their conductivity ranges from 10^{-8} to 10^{2} S/cm according to their oxidation forms [21].

Electrochemical polymerization is employed less frequently for bulk PANI production [22]. However, it is used frequently to produce thin films for spectroelectrochemical or similar characterization. In a typical procedure, the

aniline monomer is dispersed in an aqueous sulfuric acid solution. A potential of less than +0.9 V (vs. Pt quasi-reference) is then applied to a suitable electrode on which the PANI film is desired. The polymerization is rapid and the thickness of the film is controlled by coulometric analysis.

Pyrrole was noted in 1916 to form a conductive "pyrrole black" matter. At first, polypyrrole (PPy) was obtained by spontaneous polymerization in air. Chemical polymerization by a chemical oxidant to generate a radical cation from monomers had been conducted until the 1950s. The typical chemical synthesis method is as follows. $FeCl_3$ and pyrrole monomer were added to a methanol solvent; the molar ratio of the monomers was 2.33:1 and the mixture was stirred at 0 °C for 20 min. The precipitate was washed thoroughly with methanol to remove non-polymerized pyrrole monomer and dried in a vacuum oven for 12 h. The conductivity of chemically polymerized PPy was reported to be approximately 10 ~ 100 S/cm, and these values were different from the solvents. In general, PPy polymerized in an alcohol solvent such as methanol, ethanol, pentanol, and octanol showed high conductivity, whereas PPy polymerized in organic solvents such as benzene, tetrahydrofuran, chloroform, and acetonitrile presented low conductivity below 20 S/cm [23].

In 1957, electrochemical polymerization was announced under various descriptions such as electrochemical oxidation and electroorganic preparation, which are now used widely as a major method for the synthesis of conducting polymers [24]. Due to a new polymerization method, in 1968, Dall'Ollio produced a conductive PPy by electrochemical synthesis. This synthesis is preferred over chemical polymerization because of its simplicity, high yield, and conductivity. In a typical electrochemical synthesis, a 0.01–1.0 M monomer is taken with 0.1–2.0 M dopant/electrolyte such as lithium perchlorate ($LiClO_4$) and tetraethylammonium toluene-4-sulfonate (Et_4NTOS) in acetonitrile solution. Stainless steel, graphite, and Pt are the most commonly used electrodes. Potentiostatic polymerization, at ca. +0.8 V (SCE), yields the best results, although potential sweeps are also employed routinely.

In the 1980s, poly(thiophene) (PT) was synthesized early as a conducting polymer; however, real interest in this class emerged with the discovery that three-substitution of the thiophene ring yielded a wide variety of practical and versatile conducting polymers. The most common chemical synthesis uses a Ni-catalyzed coupling of the di-Grignard derivative of thiophene, because it has a big advantage in giving 2,5-coupling linkages. Another method is Friedel–Crafts alkylation, which is a relatively simple direct oxidation with $FeCl_3$ or $MoCl_5$ as a dopant or oxidant in chloroform coupling of the dihalide using Ni catalysts and organic cuprate coupling. In 1987, the precipitation was obtained in MeOH after 15 h reaction. PT was also fabricated by electrochemical synthesis from a solution with dopant and monomer in organic electrolyte in the three-electrode mode. The common dopant electrolytes used include typically 0.5 M of Li or tetraalkyl ammonium tetrafluoroborate, hexafluorophosphate, and triflate. Acetonitrile, THF, and CH_2Cl_2 were the typical solvents used [25].

After these developments in the 1990s, highly conductive and high-performance conducting polymers were prepared by the new polymerization methods.

The various morphology types of PANI were obtained using a variety of experimental conditions for the aniline oxidation state. Starting from a granular morphology structure, which is the classical form, its one-dimensional structure produces interesting forms such as nanotubes and nanowires. First, polymerization at a low concentration of aniline (<0.01 mol/L) with a single oxidant produced the nanowire-type PANI with a diameter of tens of nanometers and a length of a few micrometers. This dilution method was performed using an ionic cluster template with oxidants such as peroxydisulfate, hydrogen peroxide, and silver nitrate. Polymerization at high aniline concentrations (>0.1 mol/L) with a weak organic acid using a soft template was tried, and PANI nanotubes were produced with external diameter of 50 ~ 500 nm and length up to 10 μm. Cylindrical micelles of low-solubility aniline salts with organic acids have been suggested as hypothetical micellar templates or a solid-phase template [26]. Interfacial polymerization between the organic material and the liquid is the most useful method.

Generally, the organic solvent phase contains the aniline monomer and the aqueous phase has oxidant and organic acids. Various structures could be obtained using this method such as nanorods, nanotubes, as well as two-dimensional, spherical, and hollow structures. The electrical conductivity of PANI is different according to its various factors such as morphology, polymerization temperature and time, kinds of dopant, and dopant amounts and feeding rates [27]. Some representative structures are shown in Fig. 4. Recently, a new synthetic method named "self-stabilized dispersion polymerization" for high-performance PANI was introduced. Compared with conventional homogeneous or dispersion polymerization methods, this method is performed at very low temperature in a heterogeneous interfacial system of organic and aqueous medium without any antifreezing stabilizers. This synthetic approach yields PANI with an ideal chemical nanostructure and a high conductivity (over 600 S/cm) in the thin-film state; in addition, it is advantageous in that the honeycomb-like porous structure with conducting nanoparticles might have good potential for improved processability of conducting polymers.

PPy is also a promising material because it shows good environmental stability and high conductivity compared with other conducting polymers. Recently, it was prepared by easy emulsion polymerization. The morphology and conductivity of PPy are determined by the types and concentrations of the dopants. Naphthalenesulfonic acid (NSA), dodecylbenzenesulfonic acid (DBSA), camphorsulfonic acid (CSA), and $FeCl_3$ are the representative dopant materials. For example, the shape of the PPy particles is determined by the pyrrole/TSA ratio and the TSA feeding rate. Different shapes such as rods, spheres, and grains exhibit different morphology, electrical properties, dispersity, miscibility, and thermal properties. In the PPy case, the highly ordered and high-crystallinity PPy rod type exhibits the best electrical conductivity, which was already confirmed with a variety of other conducting polymers [28] (see Fig. 5).

PT is practically used for derivatives of the PT form. Poly(3,4-ethylenedioxythiophene) (PEDOT) is the best commercial conducting polymer. PEDOT doped with poly(styrenesulfonate) (PEDOT:PSS) is extensively used as an interfacial layer to improve hole and electron injection in most organic devices.

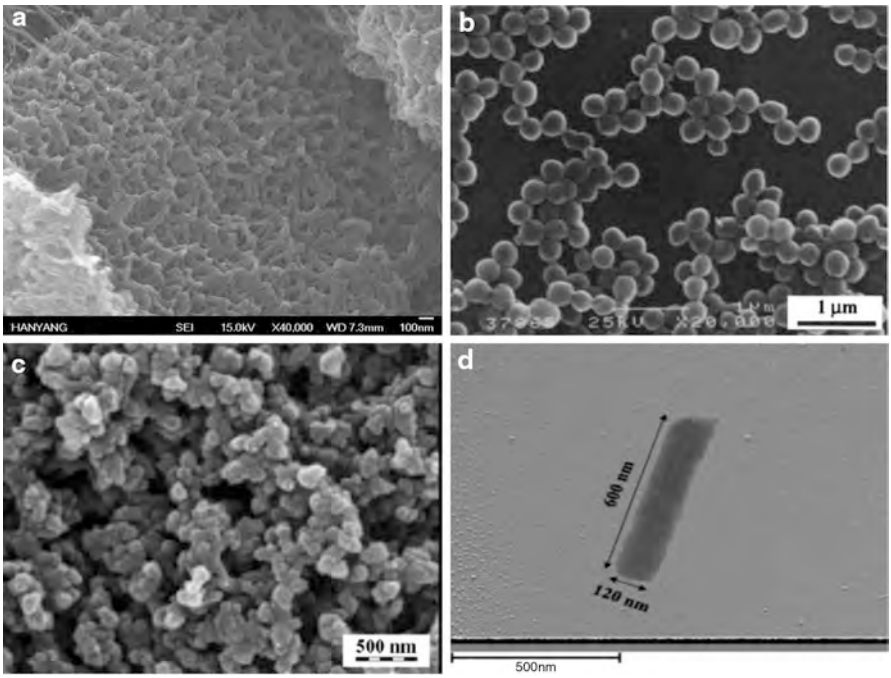

Fig. 4 Representative structures of PANI: (**a**) porous plain, (**b**) sphere, (**c**) grain, and (**d**) nanotube (The images were referenced from [22] and [44] (Copyright from John Wiley & Sons, Inc.), and [46] (Copyright from Elsevier B. V.))

Recently, a polar solvent with high boiling point such as dimethyl sulfoxide (DMSO), *N*-methylpyrrolidone (NMP), *N*,*N*-dimethylformamide (DMF), and ethylene glycol (EG) was added to the PEDOT:PSS solution to enhance electrical conductivity. These solvents induce a secondary doping effect by changing the morphology, which leads to larger grain sizes and lower intergrain hopping. This effect was not clearly verified. Therefore, further efforts are needed to explain the principles of this conductivity enhancement. A representative material having a high conductivity is PH1000, developed by Clevios™, showing a conductivity of approximately 1,000 S/cm. High-performance PEDOT:PSS was applied to the electrodes of organic devices in the film state to substitute inorganic or metal electrodes. Although there were serious problems with their low efficiency and environmental stability compared with inorganic tin oxide, polymer electrodes have the potential to be considered as a new electrode in a flexible display [29].

Fabrication of Carbon Materials

Since the "CNT fever" of the 1990s, a carbon material was found to be the most suitable material for typical alternative electrical materials such as metals and

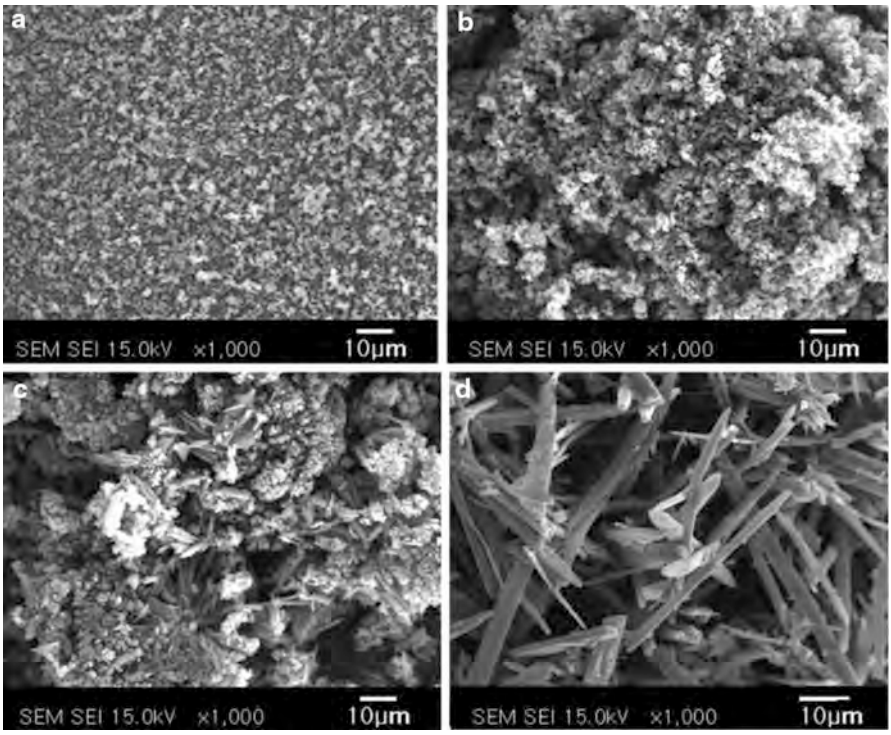

Fig. 5 Scanning electron microscopy images of PPy doped TSA according to different ratios. TSA/PPy is (**a**) 0.5/1, (**b**) 1/1, (**c**) 1.5/1, and (**d**) 2/1 (Referenced from [28], Copyright from John Wiley & Sons, Inc.)

inorganic oxides. CNTs show high intrinsic carrier mobility, conductivity, and mechanical flexibility and are lightweight; therefore, they are the most promising material for adapting to flexible and portable electrical devices.

One of the most widely used and effective methods to fabricate CNTs for electronic devices is chemical vapor deposition (CVD). In CVD growth, a substrate with catalyst particles is placed in a furnace generally at a temperature over 800 °C in a gas mixture containing C and H_2. The CNTs are consequently grown directly on the surface of the substrate. The main advantage of CVD-grown CNTs is that they have superior electrical performance compared with CNTs prepared by other methods such as solution fabrication.

There are two ways to deposit the catalyst on a substrate for the CVD growth of CNTs. To generate a random network of single-walled nanotube (SWNT) film, a catalyst solution consisting of metal oxides or ferritin is spin-cast onto a substrate Si wafer and subsequently reduced at elevated temperatures under H_2 gas. The density of the CNT film can be controlled by the concentration of the catalyst solution, the type of catalyst, and the duration of growth. One of the most important advantages of CVD-grown CNTs is the ease of aligning the CNTs. The alignment of CNTs

shows drastic enhancement of the electrical properties of the thin film by reducing the number of tube–tube junctions. Generally, well-aligned CNT film devices have higher mobility of approximately 10–40 times over a random network of CNT film devices [30].

To fabricate flexible electronics for adapted electronic textiles, the CNT films have to be deposited on flexible substrates as the latter are incompatible with the high-temperature processing of CVD. Typically used flexible substrates are poly (ethylene terephthalate) (PET), polycarbonate, polyethylene naphthalate (PEN), and polyimide (PI). There are a number of reported methods for transferring CVD-grown CNTs. Commonly, a metal layer is deposited on the CNT film and a "transfer substrate" such as polydimethylsiloxane (PDMS) or a heat-release tape is used to transfer the metal/CNT layer from the original to the receiving substrate. On the receiving substrate, the metal layer is removed using chemical etchants. Au, the representative metal used to transfer substrate, was subsequently removed using the KI/I_2 etchant. Other groups [9] have spin-coated polymethyl methacrylate (PMMA) or poly(vinyl alcohol) (PVA) directly onto the CNTs and used them as the transfer substrate. Separate from techniques using a transfer substrate, direct transferring techniques from the original to the receiving substrate have also been demonstrated using moderate-temperature annealing. Although CVD-grown CNTs show better electrical performance, their processing conditions are relatively laborious and difficult to implement in large-area fabrication. These problems are the limiting factor in the transition of CVD-grown CNT flexible electronics from laboratory to commercial applications. Solution processing of CNTs has relatively easy processing conditions and potential for low-cost and large-area fabrication; however, CNTs fabricated by this method show low electrical properties and it is difficult to control the alignment of the CNT chains. Therefore, CNT fabrication research is currently enthusiastically underway to overcome these drawbacks.

Graphene is a thin and planar nanostructure of carbon with exceptional properties, electronic in particular. Over the past few years, graphene has received enthusiastic attention as a hot research topic in nanotechnology that is intensively investigated by physicists, chemists, and materials scientists and engineers. The electronic field had shown early interest in its numerous possible applications ranging from nano- to microdevices. Graphene has a truly two-dimensional lattice called honeycomb-resembling hexagons. It is the basic structure for all carbon allotropes, including graphite, which consists of stacks of graphene layers bonded by van der Waals forces. The high strength of the covalent bonding among the layers and weak interlayer bonding allows them to slide quite easily. Graphene is surprisingly stable and withstands high temperatures. For instance, it shows no defects and no structural damage during annealing up to 250 °C within and without vapor-based synthesis approximately up to 1,000 °C, although its exact melting temperature is unknown. It exhibits an exceptionally high in-plane thermal conductivity up to approximately 5×10^3 W/mK, making it an adaptable material for efficient heat dissipation and thermal interface composites in computer chips [31].

Creating high-performance graphene in a scalable, economical process was the first step toward the practical application of graphene. Work on isolating graphene

Table 1 Properties of graphene fabricated by different methods

Fabricating method	Crystalline size (μm)	Sample size (mm)	Average charge-carrier mobility ($cm^2/V \cdot s$)
Mechanical exfoliation (Scotch tape method)	1,000	1	$10^5 \sim 10^6$ (at low temperature)
Chemical exfoliation	0.1	Infinite	100 (for a layer of overlapping flakes)
Chemical exfoliation from graphene oxide	100	Infinite	1 (for a layer of overlapping flakes)
SiC	1,000	1,000	10,000
CVD	50	100	10,000

has progressed over many decades of research. The structure of graphite, and essentially graphene as well, was known since the invention of X-ray diffraction (XRD) analysis. The solution-based exfoliation of graphite, for example, oxidation or graphite intercalation compounds (GICs), gave an early look at realizing the atomic planes of carbon. In the 1960s, Boehm predicted that reducing exfoliated graphite oxide would yield monolayers in solution, although the term "graphene" was not named until 1986 and accepted officially in 1994. A variety of early studies found monolayers of carbon in graphitic structures, formed on various carbide and transition metal surfaces as early as van Bommel in 1975 with SiC. Until 2004, two-dimensional surface science and chemistry studies did not explore any electronic properties, as the strongly bound metallic surfaces interrupted the perpendicular π-orbitals [32].

The first electronic measurements of ultrathin graphitic carbon in 2004 required samples that were sufficiently isolated from highly ordered pyrolytic graphite by the Scotch tape method and ignited an explosion of interest in the field. The synthesis techniques can be categorized into micromechanical exfoliation, solution-based and chemically assisted exfoliation, chemical synthesis, epitaxial growth through sublimation on SiC surfaces, and the pyrolysis of hydrocarbons on metal surfaces. Since the 2000s, the CVD method is one of the most promising techniques for the large-scale production of single-layer graphene films. Both single-crystal and polycrystalline transition metal surfaces are prepared at high temperature by pyrolysis of hydrocarbon precursors such as methane [33]. The properties of graphene fabricated by different methods are summarized in Table 1, and the various properties of carbon and other materials are presented in Table 2.

Fabrication Method for High-Performance Electronic Textiles

The electronic, mechanic, textile engineering, and fashion industries have developed electrical organic materials for smart textiles into wearable electronic devices. The term "electronic textiles" covers a broad range from conductive fiber to fabric-embedded or fabric-attached electrical devices. For example, in the electronic textile field, to enhance conductivity in antistatic finished fabric, a conductive

Table 2 Properties of graphene fabricated by different methods

Materials	Conductivity	Flexibility	Transparency	Cost	Processability	Stability
Inorganics	Good	Good	Poor	Normal	Normal	Normal
Metal oxides	Excellent	Good	Excellent	Good	Good	Good
Metal nanowires	Excellent	Good	Poor	Good	Good	Normal
Polymers	Good	Excellent	Good	Good	Excellent	Poor
CNTs	Good	Excellent	Good	Good	Normal	Excellent
Graphene	Excellent	Excellent	Excellent	Good	Normal	Excellent

particle is incorporated in the fiber-spinning process, textiles are modified with conductive metal coatings or by interweaving or stitching of metallic fibers, solar cells are attached to clothes, or batteries are included in the clothing. Numerous studies deal with improving performance of electronic textiles and progress has been made in various ways. One approach for highly conductive textiles is to use the intrinsically conductive organic materials that were discussed in the previous part. Another approach is to adapt dispersions or powders of conductive polymers or carbon materials as coatings. Another method is to treat the fabric surface with plasma.

In this part, various methods to fabricate conductive fiber and enhance electrical performance are described in more detail.

Coating is a textile finishing process prepared to add or improve function and to create a material with specific properties. A coating is a covering that is applied to the surface of a substrate such as fabric or plastic. Viscous polymers are commonly applied onto the fabric and cured.

Spin coating and ink-jet printing are representative coating techniques. The object of the spin-coating process is to deposit a uniform thin film onto a flat substrate. In the general spin-coating method, a small amount of coating material is added at the center of the substrate when the substrate is rotating at low speed or is at rest. The substrate is then rotated at high speed to spread the coating material by centrifugal force. Spinning continues until the coating material rotates off the edges of the substrate and the thickness objective of the film is reached.

There are many factors affecting the achievement of a thin film uniformly coated with the desired thickness. The major precondition for the spin-coating solvent is for it to be volatile and evaporate simultaneously. In addition, the thickness of the film depends on the solvent viscosity and concentration of the solution or solvent.

In a polymer case, the spinning time and speed and baking temperature after spin coating are significant factors that determine the properties of polymer film. For example, a highly crystalline conductive polymer shows high electrical conductivity. In practice, the polymer film prepared by the spin-coating method showed a lower electrical conductivity than the one prepared by solution casting; in other words, a nonspin-coating process is required for polymer film. As the rotation speed increased to fabricate a thinner film, the time of solvent evaporation is shortened,

thereby reducing the degree of crystallinity of the polymer film. In contrast, the solution-casting method enables polymer chains to have more relaxation time, which leads to better alignment of the polymer chains than the spin-coating method [34].

The annealing process is also a major factor because the crystallinity of the polymer film is controlled by the annealing temperature and time. It was confirmed that baking helps the alignment of the polymer chain; therefore, controlling the annealing temperature and time is important for increasing the conductivity of the polymer film.

To fabricate a conductive film by the spin-coating method, the optimum conditions should be selected. Recently, a new film-coating method for polymer electrodes was reported by Lee et al. using PANI doped with CSA dispersed in *m*-cresol solvent. It showed an optimum conductivity of 600 S/cm with 200 nm thickness by confirming the time of spin coating and annealing temperature [35]. By rigorously controlling the film formation parameters, the thin film could achieve high conductivity and transmittance. This film was able to adapt to a flexible substrate for using a polymer electrode; therefore, it is a useful fabrication method for a liquid polymeric conductive film.

Ultimately, ink-jet and aerosol printing are well-established conductive solution deposition methods that have industrially improved over the spin-casting method. These processes are promising in terms of enabling practical low-cost and high-throughput large-area fabrication onto a substrate. In 2006, numerous papers [19, 32] reported large-area patterning of carbon material on paper and polymer substrates using a commercially available desktop ink-jet printer. These methods were adaptable to maintain high electrical conductivity in a random deposition condition because these methods could not control the alignment of CNT and polymer chains. General CNT ink was prepared in deionized water with sodium dodecylbenzenesulfonate (SDBS) as a surfactant. The fabricated CNT film showed high conductivity on a variety of substrates. PEDOT:PSS in the solvent mixture was also adaptable in these processes because its conductivity determined the kind of solvent mixture that induced a secondary doping. Because of its usefulness, many studies have researched the expansion of applying materials and enhancing the electrical properties of the coated film.

Laminating is an important and easy technique for blowing an electrical value to techno-textiles. It extends the range of functional performance properties of common fabrics, and the use of this technique is growing rapidly as the applications for techno-textiles become more diverse. The basic structure of laminated smart textiles is composed of three or more parts: one part is electrical devices, such as the flexible solar cells, OLED, and battery, another is the fabric substrate, and the third is the adhesive material.

The simplest laminating method is using pressure-sensitive tape such as double-sided tape coated with adhesive on both sides of the polymeric film. It comprises an acrylic-based adhesive and a polyester thin carrier and is designed to join two surfaces in such a way as to be invisible in the end product. An aqueous- and solvent-based adhesive is also used to laminate two fabrics adapting a

pressure-sensitive method by knife-over-roller spreading or spray coating. An aqueous-based adhesive is spread on the bottom fabric and is then combined with other fabric or device substrates by bringing these into contact under heat and pressure to remove the water. Natural and synthetic rubber, PVA, acrylic polymer, and styrene butadiene resins (SBRs) are used as typical adhesive materials.

Hot-melt film laminating is the most preferred technique for using thermoplastic materials that can melt or soften under heat. Lamination of a film with another fabric could occur upon resolidification after the temperature cools down. Hot-melt materials for general use are polypropylene and PET, which have low cost and low T_m benefits. A variety of methods could be used with hot-melt adhesive. Slot-die extrusion allows high viscosity and low T_m material to be extruded as a continuous film directly on the various textiles. Powder- or chopped-fiber-type adhesive is applied from a hopper placed above a belt roller. Generally, these processes require two driven belts with a heating section in which the adhesive is melted and a cooling section in which the adhesive solidifies under pressure.

Based on these techniques, textiles embedded with electronic devices were developed and representative examples are shown below. Organic solar cells (OSCs) with an inverted structure are prepared by a thermal lamination method. General flexible OSCs were fabricated with a structure of flexible substrates such as PET, PEN, PES/transparent electrode/PEDOT:PSS hole transport layer (HTL)/poly (3-hexylthiophene) (P3HT)/6,6-phenyl C_{61} butyric acid methyl ester (PCBM) photoactive layer/LiF electron transport layer (ETL)/metal cathode material such as Au, Al, and Ag. Using a lamination process to introduce a Au electrode instead of conventional metal evaporation, the power-conversion efficiency (PCE) of an inverted structure OSC device with fabrics improved from 1.6 % to 2.6 %. It is suggested that the conventional vacuum-evaporation process could destroy the substrate and the photoactive layer, whereas the laminating process preserves the OSC device [36].

Tape casting is the traditional method for ceramic lamination. Aqueous tape casting was selected to obtain high-performance carbonaceous laminations with regular density and high strength. Research has focused on the rheological behavior of slurries that consist of solvent and additives such as a plasticizer, binder, and dispersant for the preparation of a regular slurry of mesocarbon microbeads. After three to five sheets of casting tape were laminated together at 85 °C under 40 MPa, the carbonized laminated materials were obtained after heating to 1,400 °C for 1 h. The basic properties were as follows. The average density was 1.66 g/cm^3, the bending strength was 82.76 MPa, and the electrical conductivity was 169.2 S/cm [37].

Laminating gives a powerful tool for progress of textile technology, and therefore numerous studies were conducted on the topic because it is an easy and powerful method to bond the electrical device to a fabric.

Surface treatment is a posttreatment process for enhancing the overall properties of materials. Plasma treatment is a very attractive and representative technique. It is possible to modify the surface properties while maintaining the bulk and transparency of substrate materials. In addition, it is a solvent-free, versatile, and fast

process compared with other chemical treatments. The plasma treatment is controlled by a variety of reactive factors such as electrons, ions, and radicals; therefore, many different reactions could occur during this treatment. As a result, the delicate chemical structure of the surface after exposure to the plasma is not precisely predictable. When a surface is exposed to plasma, two results are observed: one is modification and etching, and the other is plasma polymerization.

Although in several reports, plasma treatments were used to increase or maintain the electrical conductivity of conducting polymers, practically, the number of studies on plasma treatments of polymers with the objective of obtaining a conductive surface has decreased. It is difficult to avoid the aforementioned disadvantages when conducting polymers are used; however, there are some methods to overcome these disadvantages when plasma treatment is used as a means to transforming a polymer surface into a conductive surface layer.

A prerequisite condition is that the substrate material has all the desired properties for a specific application and only electrical conductivity is not satisfied. PI films were treated with air plasma at 50 MHz, which resulted in the formation of a negative charge on the surface by the injection of electrons. In a similar approach, N_2 plasma was used as an ion source for ion implantation in PI. An increase of six orders of magnitude in surface conductivity was measured up to 10^{-11} S, while the volume conductivity remained more or less constant. The reason could be known after analyzing the formation of a conductive surface layer. According to the Fourier-transform infrared spectroscopy (FT-IR) and X-ray photoelectron spectroscopy (XPS) measurements, it could be determined that the surface PI layer was converted into a carbon-rich layer by the ion beam.

Another experiment was conducted to clarify the result that a PP film was treated with different plasma gas (He, Ar, Ne, H_2, N_2, and O_2). As a result, the conductivity of the PP film treated with noble gases (He, Ne, and Ar) has increased. XPS measurements showed that graphite layers were formed at the surface when noble gases were injected. The approximated conductivity was calculated to be 10 S/cm; however, the ion penetration depth was wrongly assumed to be the thickness of the conductive layer. Helium appeared to be the most effective in increasing the conductivity. The reason was confirmed that the energy transfer from impinging ions to the surface is more effective when the ions are lighter. No effect on the resistance was found for treatment with plasmas of reactive gases (H_2, N_2, and O_2). Because of the incorporation of new chemical species, the formation of a graphite layer was prevented in these cases [38].

Plasma treatment also affected the higher polymerization yield of conducting polymers, which is an important reason for preparing high-performance conducting polymers. For example, the electrical conductivity of PANI polymerized on nylon 6 was increased by the effect of plasma treatment. Nylon fabric treated in O_2 plasma retained the highest PANI deposit site and the highest electrical conductivity compared with plasma treatments with other gases. The surface of the nylon 6 fibers was strongly etched by the O_2 plasma treatment and various functional groups such as COOH and CO double bond were produced on the nylon 6 fiber surface. In this case, O_2 was the most aggressive and effective plasma gas compared with NH_3 and

Ar gas plasma because other gases had a smaller effect on the doping level. In addition, the electrical conductivity of O_2 plasma-treated PANI–nylon 6 fabric was more stable with repeated washing and abrasion cycles than without plasma pretreatment. The electrical conductivity of nylon 6 fabric also increased with increase in the number of deposits added by plasma treatment. The conductivity of nylon 6-coated PANI fabric could be increased from −2.2 S/cm in a single deposit to −1.1 S/cm in three deposits [39].

Finally, plasma treatment had a beneficial influence on the electrical conductivity for controlling the molecular structure of polymers and the doping procedure. The deposition of thiophene and its derivatives by plasma polymerization was preceded by radical transfer that was generated via the most favorable energy dissipation path. In addition, a highly transparent conducting polymer surface with conductivity in the range of antistatic applications was obtained by plasma polymerization doped with I_2. A plasma polymerization layer of methylated thiophene after I_2 doping contained a higher amount of conjugated structures that induced higher conductivity. The plasma technique is a useful posttreatment method for enhancing the electrical conductivity of conductive fabrics.

Textile Applications

Materials considered for wearable devices in electronic textiles should be characterized by low cost and weight and ease of processing in various shapes, such as fiber form, for preserving the wearer's comfort. These properties are still far from perfect for commonly used sensors, optoelectronic devices, actuators, and power sources, despite the continuous effort toward their miniaturization. However, "all-organic" wearable devices help the complementary e-textiles satisfy the wearer's needs with very promising developments in organic materials technology, as well as in functional design. As will be discussed in the following sections, all the different functionalities required of interactive systems such as sensing, actuation, and energy generation or storage can now be performed by devices based on organic polymers. They offer several advantages compared with other inorganic counterparts because they are light and have high elasticity and resilience and are mechanically flexible, cost effective, and easy to process. Organic-based electrical devices can be manufactured into many shapes and forms such as printed, sewn, knitted into fabrics, and woven in fiber forms directly into textile structures. Additionally, the insulating, conducting, and semiconducting properties of different types of organic conducting materials provide special advantages for the realization of sensors, electronic components, actuators, and power supplies in comparison with conventional inorganic materials.

Electrically active organic materials could respond to an applied electrical stimulus with a change in shape or dimensions. These characteristics have enabled their use for polymer-based electrically driven actuation mechanisms for the development of artificial muscles. Additionally, several kinds of organic materials can also work as sensors, optoelectronic devices, and electrical power sources.

In the following sections, electrically active organic materials and devices with several smart functions that are currently under development will be described, with potential applicability to electronic textiles.

Sensors

The most useful devices for wearable sensor systems could be divided into active and passive sensors. Active sensors could intrinsically convert input energy into a useful electrical potential difference. Inversely, passive sensors are defined by the requirement of an external power source to convert the input into a usable output and by the fact that these sensors typically work according to a variation in their electrical resistance in response to an applied stimulus. The most-used organic and inorganic materials for sensors and the kinds of their activation stimuli are shown in Table 3. Wearable thermoelectric, thermoresistive, and pyroelectric sensors could

Table 3 Representative organic or inorganic materials for sensors according to the indicated types

		Materials	
Physical effects	Sensing devices	Organics	Inorganics
Piezoresistivity	Strain gauges	PVDF	PZT
	Piezoelectric sensors	PVDF complex	SiO_2
		PPy	ZnO
		PANI	$BaTiO_3$
		PT	$LiTaO_3$
		PA	
Thermoresistivity	Bolometers	PPV	Si
	Thermocouples		Ni
			Co
			Mg
			Metal oxides
			Titanate ceramics
Magnetoresistivity	Magnetoresistive sensors	PA	Ni–Fe alloys
		PVAc	Ni–Co alloys
Chemoresistivity	Chemoresistivity sensors	PPy	Pd
		PT	Metal oxides
		Ionic conducting polymers	Ti
			ZrO_2
Photoresistivity	Photoresistive sensors	Phthalocyanines	Si
	Photovoltaic cells	PT derivatives	Ge
		PPV	GaAs
			$CuInSe_2$
			InPCdTe
			InGaN

Table 4 Suitable or commercial sensor types for detecting human vital signs

Vital signs	Sensing devices	Product types
Electrocardiogram	Bioelectrodes	Woven or knitted metal electrodes
Electromyogram	Bioelectrodes	Woven or knitted metal electrodes
Carotid and radial artery pulse	Piezoelectric sensors	Conducting polymer using fiber
Ballistocardiogram	Piezoelectric sensors	Conducting polymer using fiber
Respiration	Piezoelectric sensors	Conducting polymer using fiber
Articulation segment position and movements	Piezoelectric sensors	Conducting polymer using fiber
Skin electrical impedance	Bioelectrodes	Woven metal electrodes
Blood oxygenation	Optical fibers	Optical fibers
Sound	Piezoelectric sensors	Conducting polymer using fiber
	Microphone	
Skin temperature	Thermoelectric sensors	Conducting polymer using fiber

perform continuous temperature measurements, whereas photoelectric sensors would be offered as a means of monitoring overexposure to electromagnetic radiation such as UV rays. Chemoresistive sensors integrated into fabrics could be useful for the wearer to avoid coming into contact with dangerous substances when helping chemistry professionals and soldiers. The detection of hazardous chemicals is certainly useful in various fields of application. This chapter focuses on devices that enable sensing of fundamental signals related to mechanical or physiological activities or vital signs of a human body (see Table 4). Their continuous monitoring system is recognized as one of the major tasks for the convenient use of e-textiles in biomedicine and the health-care system. Sensing devices and components are divided largely into two types: piezoresistive and piezoelectric sensors. In fact, the most common textile application for sensing devices is the piezocapacitive transducers that were used in the past. However, piezoresistivity and piezoelectricity represent very practical and efficient means of monitoring body signals and variables. Therefore, particular attention is paid to piezoresistive and piezoelectric sensors in this chapter.

Piezoresistive strain sensors could be advantageously used to endow garments with strain-sensing capabilities for monitoring body kinematics, such as movement or position, and for detecting some vital signs such as respiration. The principle of these sensors is their piezoresistive effect; their electrical resistance is modified by the imposed strain of the material [40]. Recently, a new technology for wearable organic material-based sensors has been developed to detect strain-sensing properties in fabrics. In particular, two types of piezoresistive organic materials have been

integrated into fabrics: π-electron-conjugated conducting polymers and carbon-added elastomers. Since the early 1970s, several conducting polymers such as PPy, PANI, and PT and its derivatives have been synthesized and their quality is improving continuously. These materials have been studied by numerous research groups for the development of organic piezoresistive sensors.

For example, conducting polymer sensors were prepared by epitaxial deposition of a thin layer of PPy on a nylon lycra/cotton fabric. These sensors showed both piezoresistive and thermoresistive properties and were used to sense a glove and a leotard. The Commonwealth Scientific and Industrial Research Organization (CSIRO, Canberra, Australia) and the University of Wollongong (Wollongong, Australia) have integrated this kind of fabric-based sensor into a knee sleeve. The quasi-static characterization of PPy-coated fabrics has measured an average gauge factor (GF) of −12 and a temperature coefficient of resistance (TCR) of approximately 0.018 $^{\circ}C^{-1}$. GF is defined as the ratio of fractional change in electrical resistance to the fractional change in length. PPy-coated fabric sensors show a high absolute value of GF, which is suitable for strain gauge implementations; however, two serious problems occurred. The first is its chemical instability with strong variation in time of their resistance, and the other is its high response time. Following the application of the sudden mechanical stimulus, the sensor resistance reaches the steady state in a few minutes and strictly limits the applicability of such devices [41].

A new generation of high-performance strain sensors has been prepared by coating fabrics with carbon-added elastomers that generally consist of a silicone matrix filled with carbon black powder. Sensors were fabricated on a nylon lycra/cotton fabric by smearing conducting ink. The GF of these sensors was evaluated at 2.5, a value that is quite similar to the GF of metals. Therefore, these materials are suitable for adapting a high-performance sensor that avoids the stiffness of conventional metal wires. Moreover, carbon-added elastomer sensors show high thermoresistive properties such as the PPy-based sensors. These devices have been used to demonstrate prototype sensorized garments such as gloves, leotards, and knee sleeves (Fig. 6). All these systems are smart wearable fabrics capable of recording body movement and position with no discomfort in wearing the garment. Carbon-loaded elastomer sensors integrated in the abdominal position of a shirt allowed the monitoring of respiratory activity with an accuracy comparative with that of conventional sensors in clinical use.

The embedding of piezoelectric material-based sensors into garments may also provide a useful tool for detecting human conditions and dangerous chemical gases. According to the well-known direct piezoelectric effect, the applications that stressed only one of the main axes of a piezoelectric material cause its polarization, which generates opposite charges on opposite surfaces. The electric potential difference induced by the opposite charge distribution could be detected by embedding materials between two electrodes. The mostly used piezoelectric inorganic materials for commercial applications are titanate ceramics such as lead zirconate titanate (PZT).

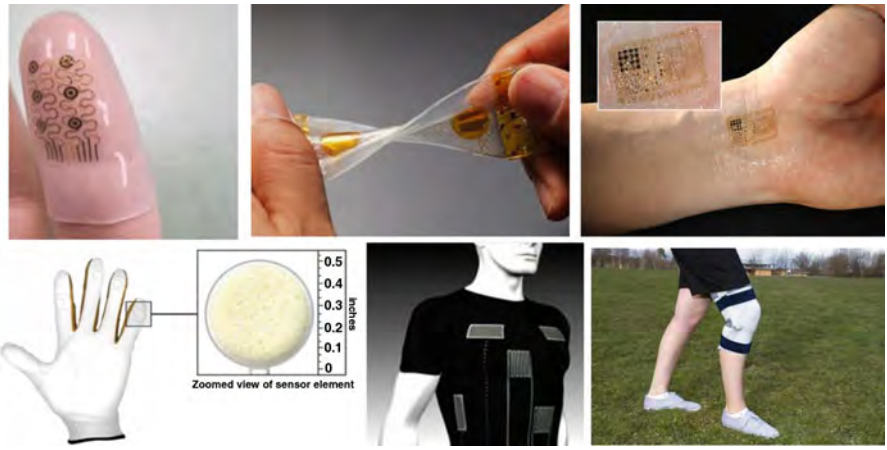

Fig. 6 A flexible sensor device and its commercial applications (The images were permitted from MC10 Inc., Fraunhofer-Gesellschaft Co., Sensor Products Inc., and www.crunchwear.com (Copyright from Evolve Media Group))

In the polymer case, polyvinylidene fluoride (PVDF) is the most commonly used piezoelectric material, with a typical piezoelectric coefficient of 24–27 pC/N [41]. These materials showed their possible use for electrical energy generation as wearable power sources. PVDF has been used for many years as a representative piezoelectric polymer for diverse sensing applications and might be applied in e-textiles in various fields, such as the detection of radial artery pulse, carotid pulse, heart apex pulse, and sound. In addition, PVDF-based transducers could be used as common-purpose contact sensors such as textile keyboards. Although PVDF could be rather immiscible with the fabric matrix, the textile embedding the PVDF piezoelectric fibers would be preferable from the research-and-development aspect because it ensures higher flexibility of the structure and shows higher comfort for the wearer.

This section discussed the requirements and challenges confronting researchers of recently developed wearable electronic sensors. In conclusion, the insights gained in the electrochemical technology and human science fields can be implemented to enable wearable electrical devices providing real-time sensing capabilities. However, various obstacles, such as the lack of appropriate methods to seamlessly integrate electronics and wireless transmitters into the sensor package, remain, which prevents the realization of practical wearable sensors suitable for routine use. Although there has been progress and significant developments in the wearable organic material-based sensors over the past several years, much effort is still required to further advance the capabilities of sensors in a broad range of health care, fitness, and military applications.

Textile Circuit for Smart Fashion

Organic semiconductors are forecast to be the material capable of carrying out most of the electronic functions required by electronic textiles. In addition, most of these flexible structures are endowed with electronic components. There are a few examples of possible fields of application of organic electronics such as flexible electronics for device control and data processing in electronic textiles, flexible displays providing different kinds of environmental and personal information, and flexible keyboards for active interaction with wearable devices. Conventional electronic devices are replaced with organic material-based devices because of the mechanical flexibility offered by several organic polymers overcoming the stiffness of inorganic crystals. Products integrating organic devices, such as displays, are already approaching the markets. However, further electronic performance as a perfect semiconductor is required.

Organic semiconductors have found applications as electronic and optoelectronic flexible devices such as field-effect transistors (FETs), light-emitting diodes (LEDs), solar cells, and matrix circuits for electronic paper. Besides, CNTs also represent a kind of organic material with macromolecular structures showing semiconducting properties that have enabled the implementation of high-performance FETs, data-storage memories, and infrared light emitters. The organic electroluminescent devices known as OLEDs could consist of several types of materials that depend on the selection of different emission wavelengths in the visible spectrum. They typically consist of multilayer structures where organic emitters are embedded between a vapor-deposited metal electrode and a conducting electrode coupled to a plastic or glass substrate. Indium tin oxide (ITO) thin films are widely used as transparent electrodes because of their low electrical resistivity and high transmittance for visible light. By applying a potential difference between the electrodes, charge transport layers are transported in the emission organic layer, and they recombine injecting when visible light is emitted. An additional conducting polymer layer such as PEDOT can be inserted to help hole conduction. These devices are gaining increasing industrial interest for multicolor flexible displays because of their high brightness enabled by low driving voltages.

Generally, CNTs are a promising nanomaterial for use in these devices as a representative material that is possible to realize. Primarily, the role of the CNT films in these devices has thus far been limited to their use as an electrode. However, more recently, many researchers have demonstrated an all-carbon LED device with SWNTs coated on PET substrates to fabricate flexible all-carbon field-emission displays using the spray-coating method as the electrode and a tetraethylorthosilicate–SWNT composite as the field emitter. However, adhesion problems between the CNTs and the substrates have been an issue that has limited the performance of LED devices. As a result, direct growth of CNTs on a PI substrate by using plasma-enhanced CVD and a microwave welding technique has been developed as well.

Several organic semiconductors have shown promising FET performance in terms of both charge-carrier mobility and on/off ratio. Room temperature values

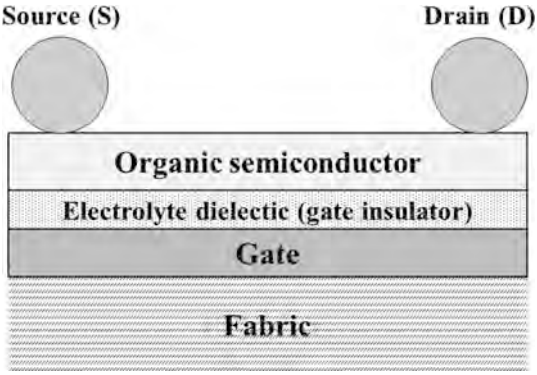

Fig. 7 The basic structure of an organic thin-film transistor (OTFT)

of 2.7 cm^2/Vs and 10^9 at 10 V, respectively, have been reported for pentacene-based devices, while CNT transistors have reached record mobility of 7.9×10^3 cm^2/Vs, exceeding that of Si (approximately 10^3 cm^2/Vs) [42]. Organic FETs are typically investigated in the form of thin films. The basic structure of a thin-film transistor (TFT) made of organic materials is reported in Fig. 7. The insulator consists of dielectric polymers, whereas graphite-based inks or conducting polymers can be used as flexible electrode materials. Transistors are typically fabricated onto substrates consisting of Si for inorganic devices. Fabrication techniques enabled by using soft substrate materials such as silicone rubbers have been introduced and the feasibility of substrateless TFTs has been reported recently. Because of their higher flexibility, they could be used for wearable applications.

There are two approaches in principle for embedding flexible organic TFTs in fabrics for electronic textiles. One is the direct application such as printing or sewing of these devices onto a textile substrate in a general method. The second technique is more challenging and aims at realizing textile fibers with endowed electronic functions such as fiber electronics. In the development of fiber-like flexible structures with semiconducting electronic properties, future results are expected from the use of high-performance organic semiconductors such as conducting polymers and carbon materials such as CNT and graphene in fiber form by extrusion, electrospinning, and wet or dry spinning. Although attempts to develop flexible electronic fibers with inorganic semiconductors have been reported [42], the definitely superior mechanical compliance and processability of semiconducting organic materials impose their prominent role in future flexible electronics and electronic textiles.

Actuator

Flexible actuating devices are needed to assign fabrics with motor functions. They share with sensors the necessity of overcoming several technological problems toward textile implementations. The most noticeable challenging issues include the identification of efficient principles of operation and suitable configurations,

selection of high-performance materials, and implementation of custom fabrication processes. Fabrics with shape-recovery capabilities have been developed integrating nitinol fibers, which is a shape memory alloy with thermal memory effect by D'Appolonia [43]. Despite this development, no substantial successes toward an effective and comfortable embedding of actuating functions into textiles have been reported to date. Organic material-based actuators may be used for such a purpose. Conducting polymer and inorganic dielectric elastomer actuators are representative materials to use as an actuator. In this section, the operation principles and benefits of a conducting polymer-based actuator are detailed because it is a perfect organic electrical material.

For many years, conducting polymers have been studied as materials for polymer actuation because their base structure includes two electrodes immersed in an electrolyte. For this purpose, they are used as components of electrochemical cells. In particular, the active conducting polymer material constitutes one of the two electrodes of the cell. By applying a potential difference between the electrodes, the conducting polymer shows a dimensional variation and works as an actuator.

The use of conducting polymers as actuators is typically limited by their short lifetimes and long response times. However, several attempts to overcome these limits are in progress. It has been demonstrated that lifetime and actuating performances can be enhanced to replace ordinary electrolytes with room-temperature ionic liquids, and this technique has also been applied to CNT actuators. In the achievable active deformations of conducting polymer actuators, expansion and contraction ratios higher than 12 % for one reduction–oxidation cycle have been recently announced. Highly active strains have also been reported with configurations exploiting smart electrodes.

In endowing fabrics with actuating functions, fiber-shaped actuators may be particularly useful. By the end of the 1990s, conducting polymer fiber actuators were presented in many reports [43]. PANI fiber fabricated by the extrusion process is coated with a thin layer of solid polymer electrolyte (SPE) such as ethylene carbonate (EC)/polyacrylonitrile (PAN)/sodium perchlorate ($NaClO_4$) and an outer layer of PPy acts as a counterelectrode, which consists of a metal wire twisted around the fiber. Actuators with such a fiber-like structure have shown strains of 0.3 % at an active stresses of 3 MPa, for a driving voltage lower than 1 V [43]. Such anisotropic deformations shown by conducting polymer fibers are not for practical use because applications frequently require high strains along the axial direction instead of the radial direction. This disadvantage may be overcome by using mechanisms capable of transforming radial strains into axial strains. Conducting polymer fibers have today become more readily available. For instance, Santa Fe Science and Technology Inc. produce PANI fibers under the trademark of Panion. They have been used to fabricate linear actuators: a bundle of Panion fibers operating as an actuating electrode is inserted into a Panion hollow fiber as a counterelectrode with a separator/electrolyte medium. This kind of actuator has reported a strain of 0.3 %, a stress of 1.8 MPa, and reduction–oxidation cycle lifetimes in excess of 10^4 cycles.

More recently, tubular conducting polymer actuators with improved actuating capabilities have been proposed by using smart electrical interconnects. The principle exploited by these actuators to achieve higher performance is substantially the same even though it is implemented differently. Its use as a working electrode has been proposed, within a typical electrochemical cell configuration of a conducting polymer hollow tube, by using a helical Pt wire embedded in the inner wall as an electrical interconnect. Because of its helical shape, this interconnect does not limit the deformation of the conducting polymer, while providing efficient electrical connection on the entire length of the tube. Similarly, the deposition of PPy on a W coil resulted in expansion–contraction ratios for one reduction–oxidation cycle of about 12 %. However, despite these new results, much more work has to be performed to endow textiles with efficient and reliable actuating functions.

In addition, to improve the performance of ion exchange polymer/metal composite actuators, PANI doped with *p*-toluene sulfonic acid was prepared with a template-free method. PANI showed different structure according to the TSA ratios; therefore, the optimum condition and structure with the highest electrical conductivity was selected by controlling the dopant-feeding rate. The conductivity of PANI in the rod structure was higher than that in the other structure. The actuator consisting of a three-layered membrane that was composed of PANI–Nafion/pure Nafion/PANI–Nafion layers had a higher angular distance and displacement than that of a pure Nafion membrane [44]. It appeared that the PANI–nanorods (NRs) may have reacted to the conductive pathway between the metal electrode and membrane when a voltage or current was applied resulting in the efficient attraction of Li cation clusters (see Table 5 for results). Consequently, PANI–NRs may be applied to conductive fillers for functional polymer blends with high conductivities.

Solar Cells

The photoelectric effect can be exploited for the development of photovoltaic cells able to produce electric energy from electromagnetic radiation. This effect consists of light-induced dislodging of electrons from atoms. In particular, light absorbed by a photoelectric material generates a pair of negative and positive electric charges named electrons and holes, respectively. They can be collected by each electrode and this effect induces an electric potential difference. The typical structure of an organic photovoltaic cell is reversed to that of an OLED (Fig. 8). A slightly different structure is presented by the so-called photoelectrochemical cells, which include an electrolyte layer coupled to the photoelectric polymer layer. Solar cells are a common example of photovoltaic cells employed to transduce solar energy into electricity.

The first photovoltaic cells fabricated onto flexible plastic supports have been developed already [29]. However, all photovoltaic generators based on several semiconductors such as conducting polymers and carbon materials require higher flexibility and bending stability. Nevertheless, because of their lower efficiency of charge-carrier photogeneration and higher electrical resistivity because of its lower

Table 5 Actuation performance of Nafion-based membrane actuator (Referenced from [44], Copyright from John Wiley & Sons, Inc.)

			Average actuation performance
Applied voltage (V)	+1.0	−1.0	±1.0
Bending angle (°)	41.4	45.6	43.5
Displacement (mm)	8	9	8.5
Displacement per second (mm/s)	0.8	1.2	1.0
Actuation performance	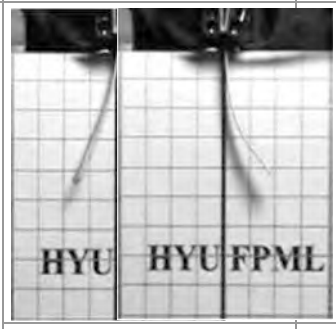		
	(+1.0 V)	(1.0 V)	

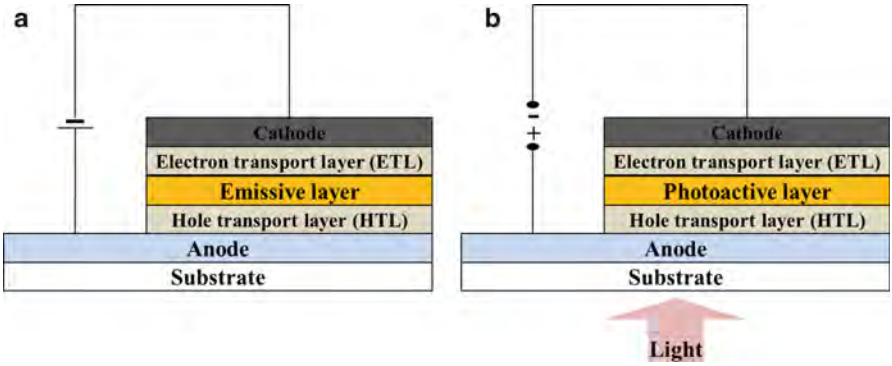

Fig. 8 The typical structures of (**a**) OLED and (**b**) OSCs

mobility of charge carriers, the PCE of organic photovoltaic devices is still lower than that of the best inorganic semiconductors. In particular, the highest reported PCE for organic cells is lower than 10 %, corresponding to about one fifth of the efficiency values enabled by the best solar cells made of inorganic semiconductors currently available. Increasing the PCE of OSCs is an effort shared by many research groups; it includes electron-acceptor material modifications or substitutions, introducing a novel photoacceptor in the photoactive layer and interposing a buffer layer between the photoactive layer and one or both of the electrodes. Therefore, a research focus became the need to increase the flexibility of

plastic-based solar cells so they could be adapted into fabrics and carried easily. There are several techniques to enhance the flexibility of OSCs.

One is conventional ITO substitutes with conducting polymers or carbon materials. A representative conducting polymer-applied electrode is PEDOT:PSS. Because of its high transparency in the visible light spectrum, easy aqueous solution processing and application for flexible substrates, PEDOT:PSS is definitely the predominant conducting polymer studied as an alternative to conventional ITO- and metal-based electrodes. PEDOT:PSS was developed and commercialized originally by Bayer AG under the trade name of Baytron, then by HC Starck GmbH, and currently by Heraeus Holding GmbH under the trade name of Clevios™. An exhaustive description of its synthesis, modifications, properties, and applications is reported by numerous sources [45].

Since the late 1990s, PEDOT:PSS has been the most widely used anode buffer layer in polymer solar cells. Before the development of high-conductivity PEDOT:PSS, low-conductivity grades of PEDOT:PSS were the subject of a few papers on ITO-free OSCs with polymeric anodes. The first attempt of using PEDOT:PSS for ITO-free polymer solar cells was reported in 1999 [45]. After that, a number of groups have devoted their research activity to improving the electrical properties of commercially available PEDOT:PSS formulations by secondary doping using a solvent mixture or to opening new roads by using in situ polymerization approaches. The main goal was, and still is, to obtain a good compromise between good conductivity and transparency, along with a high work function and good processability [45].

PANI is also reported as a polymer electrode different from PEDOT, though its low transmittance below 40 % at the 480 nm region could represent a limit when used as a transparent electrode. Through the thickness-controlled drop-casting method, CSA-doped PANI (PANI:CSA) in *m*-cresol with a conductivity of approximately 600 S/cm, high optical transmittance of approximately 85 % at 550 nm, and good performance preservation after 50 bending cycles has been demonstrated [46]. In addition, high-crystallinity PANI was fabricated by blending with self-assembly supramolecules prepared to prevent the recoiling of PANI chains in thin-film state. This film exhibited a high conductivity of approximately 850 S/cm and high optical transparency of over 80 % at 550 nm that was thinner than 200 nm of the film thickness. As a result, ITO-free OSCs including these PANI-based films as anodes exhibited a PCE of 2 % [46].

Carbon materials are regarded as the promising candidates for the replacement of ITO in the emerging field of plastic electronics because of their transparency in thin films, their excellent mechanical properties, high electrical conductivity, and the potential for easy fabrication processing. SWNTs and multiwalled CNTs (MWNTs) have been investigated as transparent anodes in OSCs. Graphene is also the rising star of material science; it exhibits remarkable mechanical and electronic properties and is recently attracting much attention as a novel transparent electrode material. Nevertheless, the performance of ITO-free polymer solar cells, including carbon material-based electrodes, is still rather poor and more work is required. CNT and graphene are a promising replacement of transparent conductive

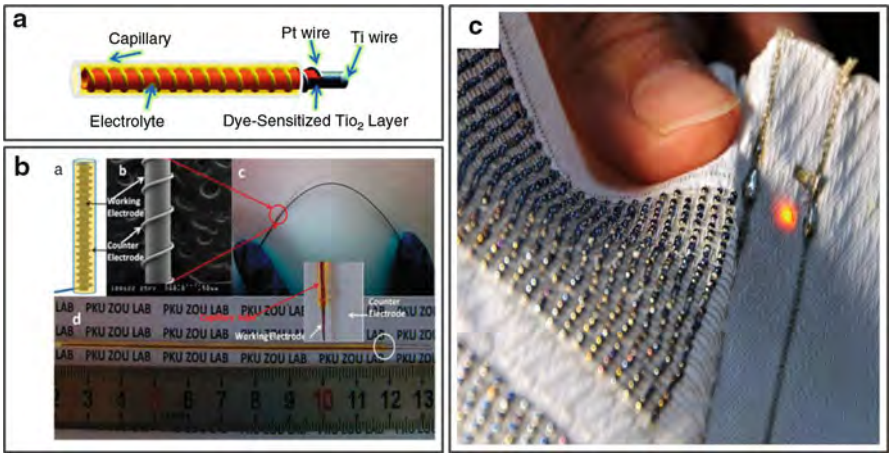

Fig. 9 (**a**) The schematic diagram of fiber-shaped DSSCs and (**b**) its images [47] (Copyright from Royal Society of Chemistry). (**c**) The optical image of fabric with solar cells generates electricity developed by Industrial Technology Center of Fukui Prefecture and Kyoto-based solar cell manufacture Sphelar Power Corp. (Copyright from The Asahi Shimbun Company)

oxides to replace other expensive materials (such as depletion and stiff and brittle ITO substrates).

Apart from these conventional approaches, high-efficiency, large-sized, fiber-shaped dye-sensitized solar cells (DSSCs) were developed recently [47]. In addition to three-dimensional photon collection, sufficient amounts of raw materials, easy fabrication, simple sealing, and the capability of scaling up and modulation, the special features of these cells might greatly facilitate the application of DSSCs. In the present work, the power efficiency of the cell is 5.4 % at 100 mW/cm^2 illumination in a 10 cm long fiber that is so far the longest and highest efficiency for a fiber-shaped solar cell. Pt wire was used as the counterelectrode, but it may be substituted by other metals with high catalytic activity such as Pt-coated Ti wire or carbon fibers because of their lower total fabrication cost. In addition, the completely flexible fiber-shaped solar cell can be fabricated by replacing glass-based technical fiber with transparent and flexible polymer-based technical fiber. This permits integration into smart fabrics, power suits, and solar modules through weaving technology. In present research, efforts to develop longer fiber-shaped solar cells are progressing because it is suitable for woven solar power textiles. These results and applied images were shown in Fig. 9.

Supercapacitors

Electrical energy storage is commonly operated by rechargeable batteries and capacitors. Because of the different means of energy storing, such as a static charge separation in capacitors or the electrochemical capacitance in batteries, capacitors

Table 6 List of several typical electrode and electrolyte materials used for rechargeable electrochemical cells (Referenced from [7], Copyright from Royal Society of Chemistry)

Organic materials		Inorganic materials		Hybrids	
Electrodes	Electrolytes	Electrodes	Electrolytes	Electrodes	Electrolytes
PA	$LiClO_4$/ propylene carbonate (PC)	Pb and PbO_2	H_2SO_4	Carbon and Li or MgO_2	$LiClO_4$/PC
PANI	Et_4NClO_4/PC	Fe and NiO	KOH	PA and Li	$LiClO_4$/PC
PANI/PPy	Et_4NClO_4/PC	Cd and NiO	KOH	PANI and Li	$LiClO_4$/PC
PT	Bu_4NBF_4/ acetonitrile	Metal hydride and NiO	KOH	PPy and Li	$LiClO_4$ or $LiBF_4$/PC
Poly (p-phenylene) (PP)	$LiColO_4$/THF			PT and Li	$LiClO_4$/PC
				PP and Li	$LiClO_4$/ THF

can typically store low energy densities and supply high power densities; on the other hand, batteries offer inverse performance: they store high energy densities and supply low power densities. Therefore, these two devices are frequently coupled in parallel for applications requiring both high energy and power. In general, a battery used as the primary energy source charges a capacitor used as a pulsed power supply. However, it could accumulate just small amounts of electrical energy density storage by capacitors; it reveals insufficiency whenever high pulsing energy is needed. Aimed at overcoming the intrinsic energy storage limitation of traditional capacitors and covering the gap between them and batteries, electrochemical supercapacitors are suggested as energy storage devices providing the typical high power properties of capacitors as well as high amounts of energy by means of a high capacitance per unit of electrode weight. The structure of a supercapacitor is close to that of batteries that comprise two electrodes in contact with an electrolyte separated by an ion-permeable separator. Their supercapacitance properties are enabled mainly by the particularity of the electrodes typically having a porous and high surface area. To reduce the resistivity of each electrode, the contact resistance among its constitutive elements, such as particles or fibers, is lowered by bonding each electrode to a metal current collector (Table 6).

The high values of capacitance can be caused by either double-layer capacitances or by redox pseudocapacitances. The former kind of capacitance originates from two separated layers of charges accumulated at the interface between the electrolyte and electrodes that have a highly porous area, such as activated carbons, CNTs, and carbon fibers. Differently, the redox pseudocapacitances arise with electrodes made of either conducting polymers, such as PANI, PPy, PT, and their derivatives, transition metal oxides such as RuO_2, Co_3O_4, and IrO_2, or both such materials operating with and within carbon-based structures. Supercapacitors with

carbon-based electrodes have shown values of capacitance per unit of electrode weight of 75 ~ 175 F/g with aqueous electrolytes and 40 ~ 100 F/g with organic electrolytes [48].

Organic solid-state electrolytes consisting of polymer matrices filled with ion conductors were studied for the development of all organic supercapacitors. Recently, Nafion has been most widely used as a SPE for supercapacitors and has allowed the achievement of a specific capacitance of 130 F/g with electrodes made of activated carbon and a surface area of 1,500 m^2/g. They also present lower charging or self-discharging times and extremely high lifetimes. Supercapacitors can be recharged and discharged millions of times without performance degradation and retain their capacitance even when unused for long periods. Recently, high-strength CNTs fibers were used to build fiber supercapacitors woven into the textile substrate for electronic textiles [30]. A fiber-shaped device was prepared by twisting together CNT fibers of approximately 100 μm diameter and dip coating with aqueous PVA/phosphoric acid electrolyte separately. Following the twisting, both fibers were recoated together with the electrolyte. Fiber-type supercapacitors have shown a specific capacitance of 5 F/g and an energy density of 0.6 Wh/kg at 1.0 V.

Flexible and stretchable CNT films were also incorporated in supercapacitors [49]. This film was fabricated by spray coating CNT on flexible PET film using both the electrodes and the charge collectors in conjunction with a printable gel electrolyte. These thin supercapacitors showed high performance with an energy density of 6.0 Wh/kg and a power density of 23 kW/kg. Another supercapacitor using a buckled CNT film on PDMS substrates was stretchable up to 30 % with well-maintained device performance. The devices were composed of two SWNT films: one was an organic electrolyte and the other a polymeric separator with excellent power and energy densities. The mechanical superiority of CNTs and their interactions in supercapacitors help design unique structures and enable cost reduction in charge-storage devices.

Battery

Electrochemical cells are ideal devices for the generation of electrical energy from chemical energy. Basic electrochemical cells are composed of two electrodes dipped into an electrolyte and separated by an ion-conducting separator generally called a salt bridge. Electrodes can be bonded to further conductors working as current collectors providing lower resistance. Typical lists of energy storage devices and their specific energies via specific power are plotted in Fig. 10. The electrochemical cells generate a voltage until the redox reactions among the two electrodes and the electrolyte reach chemical equilibrium. There are two types of electrochemical cells. One that does not permit recharging is defined as a primary cell, whereas a rechargeable one is called a secondary cell. “Battery” is the collective term that combines these two cells. Metals, transition metal oxides, carbon-based materials, or conducting polymers are used as battery electrode materials. Metals are typically used as anodes, metal oxides as cathodes, and

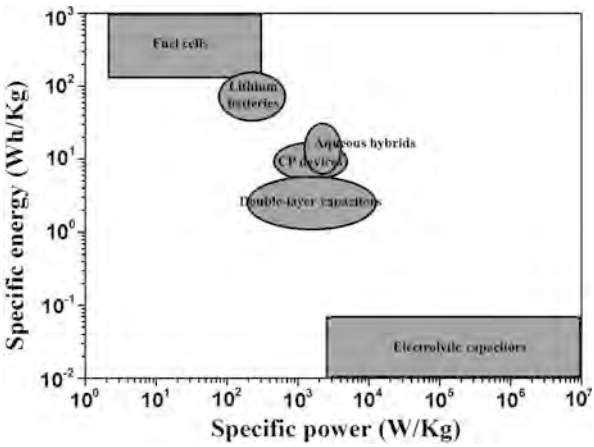

Fig. 10 Specific energy via specific power of energy storage devices (Referenced from [48] (Copyright from Elsevier B.V.))

carbon-based materials as cathodes or current collectors, while conducting polymers can act as both cathode and anode by controlling the work function level. Li is a frequently used material as an anode due to its high specific charge.

The most typical nonrechargeable Li-based battery is the Li–MnO_2 cell that generates 3 V, whereas the most common rechargeable one is the Li-ion cell that produces 3.6 V, which typically consists of a carbon anode, a MnO_2 cathode, and a solution of Li salts as the electrolyte. Most commercial batteries typically have inorganic electrodes such as metals and transition metal oxides. At present, hybrid structures composed of both inorganic and carbon-based electrodes are used as electrode materials. Similarly to other devices, several attempts were made to develop all-organic batteries for flexible devices. Conducting polymers were used as cathode materials in combination with a Li or Mg anode.

Electrolytes typically used for battery can be divided into the following four main classes: aqueous electrolytes, organic liquid electrolytes, SPEs, and ionic liquids. Common aqueous liquid electrolytes consist of acids such as H_2SO_4 or bases such as KOH. Several batteries use organic liquid electrolytes such as propylene carbonate, ethylene carbonate, dimethyl carbonate, and diethyl carbonate. To improve their electrochemical properties, innovative organic electrolytes can be introduced as solvents for metal salts such as $NaClO_4$, $LiClO_4$, and $LiPF_6$. Such electrochemical cells may require solid-state electrolytes that are more practical than the liquid ones. The materials that consist of ion-conducting polymers are called SPEs. A representative example is the ethylene carbonate/PAN/$NaClO_4$ composite, which has also been used to fabricate fiber-shaped all-polymer electrochemical cells [7]. A commercially available SPE is the perfluorosulfonate ionomer produced by DuPont under the name of Nafion, and this electrolyte has shown performance capabilities in other applications such as supercapacitors and ionic polymeric metal composite (IPMC) actuators. SPEs are particularly interesting parts of conducting polymers as they permit the realization of wearable solid-state batteries. The typical materials used as electrodes and electrolytes of

Table 7 List of several typical electrode and electrolyte materials used for supercapacitors and their electrochemical properties (Referenced from [48], Copyright from Elsevier B. V.)

Electrode material	Electrolyte	Specific capacitance (F/g)
PPy–SWNTs	Aqueous	144
PPy-gr-SWNTs	Aqueous	200
PEDOT-on-PPy	1 M $LiClO_4$ (aq)	230
PEDOT-on-PPy	1 M KCl (aq)	290
PPy–Fe_2O_3	$LiClO_4$ (aq)	420
PPy	PVDF–HFD gel electrolyte	78–137
PEDOT–MoO_3	Nonaqueous Li^+	300
Nonirradiated HCl-doped PANI	Gel polymer electrolyte	259
Nonirradiated HCl-doped PANI	Gel polymer electrolyte	210 (10,000 cycles)
Irradiated HCl-doped PANI	Gel polymer electrolyte	243
Irradiated HCl-doped PANI	Gel polymer electrolyte	220 (10,000 cycles)
RuOx-PEDOT-PSS		1,409
PPy-fast CV deposited	1 M KCl (aq)	480
Nontreated PEDOT	1 M H_2SO_4	72
Ultrasonicated synthesis of PEDOT	1 M H_2SO_4	100
MWNT/PANI 20/80 wt%		360
MWNT/PPy 20/80 wt%		190
PANI-coated CNF (20 nm)		264

supercapacitors and their electrochemical properties are listed in Table 7. Recently, novel ionic liquid materials were reported that use a particular class of electrolytes that can improve lifetimes and response speeds of various types of electrochemical devices, such as actuators, electrochromic devices, and flexible displays. Typical ionic liquids, such as ethylammonium nitrate ($EtNH_3$ NO_3), 1-butyl-3-methylimidazolium tetrafluoroborate (BMIM BF_4), and 1-butyl-3-methylimidazolium hexafluorophosphate (BMIM PF_6), are salts composed of organic cations and inorganic anions and exist in a fluid state at room temperature. Recently, to develop high-performance electrolytes for electrochemical devices, composite electrolytes that combine ionic liquids with the advantages of the solid-state matrices were developed by mixing ionic liquids with polymer.

The latest generations of Li cells are called Li-polymer cells that employ SPEs. The use of solid electrolytes has allowed the fabrication of thin flat batteries with major applications as flexible power sources. These devices are composed of a five-layer structure: a conducting layer working as current collector, an anode layer, an electrolyte and separator layer, a cathode layer, and an additional conducting collector layer. The basic Li-polymer batteries show capability for energy density higher than 100 Wh/kg by employing different SPEs, such as LiPF salts in ethylene carbonate/propylene carbonate organic liquid mixed with a matrix of PAN or poly (vinylidene fluoride-hexafluoropropylene) (P(VDF-HFP)).

Various companies and research groups have announced many applications for commercialized thin and flexible flat batteries. Power Paper Ltd. produces 1.5 V

batteries that can be printed by ink-type materials or pasted onto diverse substrates and have a thickness of 0.7 mm, and Zn and MnO_2 are used as anode and cathode materials, respectively. The thinner, more-flexible flat rechargeable batteries have a $LiCoO_2$ cathode, a Li anode, and lithium phosphorus oxynitride (LiPON) developed by Oak Ridge National Laboratories as a solid electrolyte. Thin-film flexible batteries fabricated directly onto textile substrates are important touchstones for future applications in electronic textiles. However, to ensure a superior grade of integration into textiles and a higher working surface in practice, the fiber shape of electrochemical cells is preferred to the flat structure. Since 2002, ITN Energy Systems Inc. has been developing fiber-shaped batteries fabricated by coating with thin-film layers on a fiber surface. The thin film consists of the same materials typically used in flat batteries, such as $LiCoO_2$ as the cathode, Li as the anode, and LiPON as solid electrolyte. In this way, textile applications using the structural and energy functions of this type of fiber battery were developed to supply power sources for wearable technology.

Summary

The main characteristics of all organic electronic devices are their low cost, easy portability, and flexibility. These advantages lead to perfect wearable electronic devices and such systems help realize our dream of wearing technology where all electronic devices are connected organically to each other. An essential element in enhancing their efficiency is to select optimum materials. In this chapter, the fundamental and synthesis methods of representative conducting polymers were described to be adapted into flexible electrical devices. The polymerization techniques for obtaining conducting polymers with high electrical performance are currently being developed and a variety of efforts has been made to adapt CNT and graphene into electronic devices. In addition, the fashion industry has explored this technology by continuously studying various coating and laminating techniques, which are important because high-performance flexible electrical devices can be embedded into daily clothes successfully. Numerous polymeric adhesives or surface plasma treatments will help the progress of textile technology; therefore, further studies should be conducted to develop adhesive strength and bending stability.

Based on these studies, various applications such as sensors, actuators, OLED, transistors, solar cells, supercapacitors, and batteries compatible with general textiles were realized in approaching the dream of wearable electronic textiles. The interplay among materials science, electrical and electronic engineering, and the fashion industry promises to be an exciting field for fundamental and applied research. Although significant developments have been reported in the wearable organic-based electronic devices over the past several years, the further development of these would bring functionalities that are even more sophisticated to applications in health care, fitness, and daily life.

References

1. Tiwari S, Rana F, Hanfi H, Hartstein A, Crabbe EF, Chan K (1996) A silicon nanocrystals-based memory. Appl Phys Lett 68:1377–1379
2. Look DC (1989) Electrical characterization of GaAs materials and devices. Wiley, New York
3. Zhang D, Ryu K, Liu X, Polikarpov E, Ly J, Tompson ME, Zhou C (2006) Transparent, conductive, and flexible carbon nanotube films and their application in organic light-emitting diodes. Nano Lett 9:1880–1886
4. Lee UJ, Lee SH, Yoon JJ, Oh SJ, Lee SH, Lee JK (2013) Surface interpenetration between conducting polymer and PET substrate for mechanically reinforced ITO-free flexible organic solar cells. Sol Energy Mater Sol Cells 108:50–56
5. Kim SH, Hong K, Xie W, Lee KH, Zhang S, Lodge TP, Frisbie D (2012) Electrolyte-gated transistors for organic and printed electronics. Adv Mater 25:1822–1846
6. Kim DK, Oh KW, Kim SH (2009) Synthesis of conducting composite of polyaniline and multiwall carbon nanotube grafted with sulfonated polystyrene. Mol Cryst Liq Cryst 510:51–59
7. Ji L, Lin Z, Alcoutlabi M, Zhang X (2011) Recent developments in nanostructured anode materials for rechargeable lithium-ion batteries. Energy Environ Sci 4:2682–2699
8. Ji X, Lee KT, Nazar LF (2009) A highly ordered nanostructured carbon-sulfur cathode for lithium-sulfur batteries. Nat Mater 8:500–506
9. Park S, Vosguerichian M, Bao Z (2013) A review of fabrication and applications of carbon nanotube film-based flexible electronics. Nanoscale 5:1727–1752
10. Heeger AJ (2010) Semiconducting polymers: the third generation. Chem Soc Rev 39:2354–2371
11. Jiang L, Wang X, Chi L (2011) Nanoscaled surface patterning of conducting polymers. Small 10:1309–1321
12. Brazovskii S, Kirova N (2010) Physical theory of excitons in conducting polymers. Chem Soc Rev 39:2453–2465
13. Otero TF, Martinez JG, Pardilla JA (2012) Biomimetic electrochemistry from conducting polymers. A review artificial muscles, smart membranes, smart drug delivery and computer/neuron interfaces. Electrochim Acta 84:112–128
14. Inzelt G, Pineri M, Schultze JW, Vorotyntsev MA (2000) Electron and proton conducting polymers: recent developments and prospects. Electrochim Acta 45:2403–2421
15. Tran HD, Li D, Kaner RB (2009) One-dimensional conducting polymer nanostructures: bulk synthesis and applications. Adv Mater 21:1487–1499
16. Liu YD, Choi HJ (2012) Electrorheological fluids: smart soft matter and characteristics. Soft Matter 8:11961–11978
17. Chiang CK, Fincher CR, Park YW, Heeger AJ, Shirakawa H, Louis EJ, Gau SC, MacDiarmid AG (1977) Electrical conductivity in doped polyacetylene. Phys Rev Lett 39:1098–1101
18. Genies EM, Bidan G, Diaz AF (1983) Spectroelectrochemical study of polypyrrole films. J Electroanal Chem 149:101–113
19. Novoselov KS, Geim AK, Morozov SV, Jiang D, Zhang Y, Dubonos SV, Grigorieva IV, Firsov AA (2004) Electric field effect in atomically thin carbon films. Science 306:666–669
20. Kim DK, Oh KW, Kim SH (2008) Synthesis of polyaniline/multiwall carbon nanotube composite via inverse emulsion polymerization. J Polym Sci Part B Polym Phys 46:2255–2266
21. Kim SH, Seong JH, Oh KW (2002) Effect of dopant mixture on the conductivity and thermal stability of polyaniline/nomex conductive fabric. J Appl Polym Sci 83:2245–2254
22. Sapurina I, Stejskal J (2008) The mechanism of the oxidative polymerization of aniline and the formation of supramolecular polyaniline structures. Polym Int 57:1295–1325
23. Xue P, Tao XM (2005) Morphological and electromechanical studies of fibers coated with electrically conductive polymer. J Appl Polym Sci 98:1844–1854
24. Sadki S, Schottland P, Brodie N, Sabouraud G (2000) The mechanisms of pyrrole electropolymerization. Chem Soc Rev 29:283–293
25. Liu RC, Liu ZP (2009) Polythiophene: synthesis in aqueous medium and controllable morphology. Chin Sci Bull 54:2028–2032

26. Bowman D, Mattes BR (2005) Conductive fibre prepared from ultra-high molecular weight polyaniline for smart fabric and interactive textile applications. Synth Met 154:29–32
27. Choi JH, Kim SH, Oh KW (2007) Conjugated polyaniline nanorod blends with cyanoresin. Mol Cryst Liq Cryst 464:281–289
28. Kim DK, Oh KW, Ahn HJ, Kim SH (2008) Synthesis and characterization of polypyrrole rod doped with *p*-toluenesulfonic acid via micelle formation. J Appl Polym Sci 107:3925–3932
29. Rahman MA, Rahim A, Maniruzzaman M, Yang K, Lee C, Nam H, Soh H, Lee J (2011) ITO-free low-cost organic solar cells with highly conductive poly(3,4 ethylenedioxythiophene): *p*-toluene sulfonate anodes. Sol Energy Mater Sol Cells 95:3573–3578
30. Hu L, Choi JW, Yang Y, Jeong S, Mantia FL, Cui LF, Cui Y (2009) Highly conductive paper for energy-storage devices. Proc Natl Acad Sci USA 106:21490–21494
31. Weiss NO, Zhou H, Liao L, Liu Y, Jiang S, Huang Y, Duan X (2012) Graphene: an emerging electronic material. Adv Mater 24:5782–5825
32. Novoselov KS, Fal'ko VI, Colombo L, Gellert PR, Schwab MG, Kim K (2012) A roadmap for graphene. Nature 490:192–200
33. Kim KS, Zhao Y, Jang H, Lee SY, Kim JM, Kim KS, Ahn JH, Kim P, Choi JY, Hong BH (2009) Large-scale pattern growth of graphene films for stretchable transparent electrodes. Nature 457:706–710
34. Lee BH, Park SH, Back H, Lee K (2011) Novel film-casting method for high-performance flexible polymer electrodes. Adv Funct Mater 21:487–493
35. Lee SH, Lee DH, Lee K, Lee CW (2005) High-performance polyaniline prepared via polymerization in a self-stabilized dispersion. Adv Funct Mater 15:1495–1500
36. Krebs FC (2009) Fabrication and processing of polymer solar cells: a review of printing and coating techniques. Sol Energy Mater Sol Cells 93:394–412
37. Lim VWL, Kang ET, Neoh KG, Tan KL (2001) Lamination of conductive polypyrrole films to poly(tetrafluoroethylene) films via interfacial graft copolymerization. J Appl Polym Sci 80:716–727
38. Chen FF (1974) Introduction to plasma physics and controlled fusion. Plenum Press, New York
39. Oh KW, Kim SH, Kim EA (2001) Improved surface characteristics and the conductivity of polyaniline-nylon 6 fabrics by plasma treatment. J Appl Polym Sci 81:684–694
40. Singha K (2012) A review on coating & lamination in textiles: processes and applications. Am J Polym Sci 2:39–49
41. Windmiller JR, Wang J (2013) Wearable electrochemical sensors and biosensors: a review. Electroanalysis 25:29–46
42. Ferreras LR, Pfattner R, Torrent MM, Laukhina E, Lopez L, Laukhin V, Rovira C, Veciana J (2011) Highly piezoresistive textiles based on a soft conducting charge transfer salt. J Mater Chem 21:637–640
43. Viry L, Mercader C, Miaudet P, Zakri C, Derre A, Kuhn A, Maugey M, Poulin P (2010) Nanotube fibers for electromechanical and shape memory actuators. J Mater Chem 20:3487–3495
44. Kim SH, Oh KW, Choi JH (2010) Preparation and self-assembly of polyaniline nanorods and their application as electroactive actuators. J Appl Polym Sci 116:2601–2609
45. Na SI, Kim SS, Jo J, Kim DY (2008) Efficient and flexible ITO-free organic solar cells using highly conductive polymer anodes. Adv Mater 20:4061–4067
46. Lim TH, Oh KW, Kim SH (2012) Self-assembly supramolecules to enhance electrical conductivity of polyaniline for a flexible organic solar cells anode. Sol Energy Mater Sol Cells 101:232–240
47. Lv Z, Fu Y, Hou S, Wang D, Wu H, Zhang C, Chu Z, Zou D (2011) Large size, high efficiency fiber-shaped dye-sensitized solar cells. Phys Chem Chem Phys 13:10076–10083
48. Snook GA, Kao P, Best AS (2011) Conducting-polymer-based supercapacitor devices and electrodes. J Power Sources 196:1–12
49. Lim TH, Oh KW, Kim SH (2012) Polypyrrole/MWCNT-gr-PSSA composite for flexible and highly conductive transparent film. J Appl Polym Sci 123:388–397

Evaluation Methods and Instruments of Dry Biopotential Electrodes

29

Liu Hao and Xiaoming Tao

Contents

Introduction 776
Behavior and Electrical Circuit Model of Electrodes/Electrolyte Interface 777
Evaluation Methods and Instruments 778
Description of Common and Special Evaluation Methods and Instruments for Dry Electrodes 778
Common Evaluation Methods and Instruments for Dry Electrodes 778
Open Circuit Potential and Response for Evaluating Performance of Dry Electrodes 788
Structure and Morphological Characterization for Evaluating Performance of Dry Electrodes 789
Several Special Evaluation Methods and Instruments for Dry Electrodes 789
Instruments and Methods in Static Measurement 789
Instruments and Methods in Dynamic Measurement 795
Summary 806
References 806

Abstract

Dry biopotential electrodes (DBPE) are suitable for measuring biopotential in long-term health monitoring systems due to simpler operation and less skin irritation than wet electrodes in the application process. So far, no uniform test standard and instrument was performed for evaluating the quality of dry electrodes. In this chapter, measurement methods and instruments for evaluating the quality of dry biopotential electrodes were reviewed systematically. These measurement methods

L. Hao (✉)
School of Textiles, Tianjin Polytechnic University, Tianjin, China
e-mail: liuhao@tjpu.edu.cn

X. Tao
Institute of Textiles and Clothing, The Hong Kong Polytechnic University, Hung Hom, Hong Kong SAR
e-mail: xiao-ming.tao@polyu.edu.hk

© Springer Science+Business Media Singapore 2015

X. Tao (ed.), *Handbook of Smart Textiles*,
DOI 10.1007/978-981-4451-45-1_33

and instruments were classified into two categories: (1) common methods and instruments and (2) special methods and instruments. Properties of dry biopotential electrodes were summed up in the following several aspects: electrical conductivity, electrochemical impedance spectra, contact impedance, appearance, crystal texture, open circuit potential (OCP), biopotential signal noise and dynamic open circuit potential (DOCP), and so on. With progress of materials and electronics technology, more and more novel dry electrodes will be developed, and corresponding evaluation methods and instruments will also be fabricated.

Keywords

Dry electrode • Textile-structured electrodes • Biopotential • Evaluation methods • Evaluation instruments • Motion artifact • Electrochemical impedance spectra • Equivalent circuit • Contact impedance • Dynamic measurement • Static measurement

Introduction

Biopotential electrodes (DBPE) play an important role for acquiring biopotential signal from the human body. The most used wet electrodes are not suitable for long-term bioelectricity monitoring because of skin preparation prior to application, and many cases of allergic contact dermatitis to the sites of electrocardiograph-monitoring electrodes are reported [1, 2]. Therefore, more and more researchers have focused on the development of DBPE in the last several decades. They tried to develop many methods and instruments for evaluating the stability and robustness of DBPE and then improve on them. For the different types and structures of DBPE, evaluation methods and instruments are different. So far, no uniform test standard and instrument was performed for evaluating the quality of dry electrodes. In this chapter, the measurement methods and instruments for evaluating the quality of dry biopotential electrodes were reviewed systematically in the last several decades. For convenience, these measurement methods and instruments were classified into two categories: (1) common methods and instruments and (2) special methods and instruments. Common evaluation methods mean that some commercial instruments are utilized for measuring one or more properties of electrodes, and measured data are analyzed by common software and conventional data process methods. However, special evaluation methods and instruments mean that a method or instrument is developed for a given task or object, that is, the performance of electrodes can't be evaluated by using conventional methods and instruments. Some properties for characterizing dry biopotential electrodes have been summed up from the following several aspects: electrical conductivity, electrochemical impedance spectra (EIS), contact impedance, appearance, crystal texture, open circuit potential (OCP), biopotential signal noise and dynamic open circuit potential (DOCP), and so on. In general, researchers will select one or several kinds of the above properties in terms of their research objects and characters of the electrodes.

Behavior and Electrical Circuit Model of Electrodes/Electrolyte Interface

Biopotential of the human body is actually an electrical signal source in certain range of frequency and amplitude. The task of electrode application is to transmit undistorted biopotential from the human body to electrical devices. The noise of measurement system and electrode/electrolyte interface and the response of electrode/electrolyte interface to signal are very important parameters to acquire the accurate biopotential signal. One discovered that charge transfer mode in the electrode/electrolyte interface is closely correlative with the material of the electrode. Actual charge such as electron etc can't pass cross the electrode/electrolyte interface for ideal polarization material, the double layer in the electrode/electrolyte interface plays a capacitor role, and charge transfer is achieved by charging and discharging approach. However, charge can pass freely across the electrode/electrolyte interface for ideal non-polarization electrode, and no energy is consumed in the electrode/electrolyte interface. However, polarization and non-polarization phenomena exist simultaneously in the electrode/electrolyte interface in the real world; the behavior of the real electrode/electrolyte interface can be illuminated by equivalent circuit (EC) that is in series and in parallel model of resistors and capacitors.

Figure 1 shows the ECs of the skin/electrolyte/electrode and electrode/electrolyte/artificial skin. The EC of the electrode/electrolyte interface is composed of C_D and R_D in parallel [3] and EC of the skin is composed of Cs and Rs in parallel [4]. C_D represents the capacitance of double layer, Uep represents the electrode potential, R_D represents charge transfer impedance and diffusion impedance, and R_L represents the resistance of electrolyte of interface. However, the human skin is composed of several layers (e.g., epidermis, dermis, subcutis), which can be regarded as a capacitance C_s. The numerous channels, perspiratory glands, and hair follicles within the skin which connect these layers can be regarded as the resistance R_s. The subcutis layer of skin may be represented as a

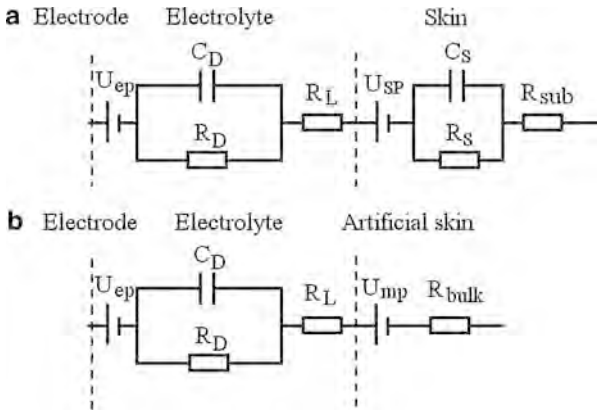

Fig. 1 (**a**) EC of electrode/electrolyte/skin and (**b**) EC of electrode/electrolyte/artificial skin

resistance R_{sub} due to supplied by blood. The layered structure of the stratum corneum leads to semipermeable membranes and differences in the ion concentration which result in a potential U_{sp}. U_{mp} represents the filter potential on membrane that is produced due to the ion concentration difference between two sides of the membrane.

Construction and analysis of equivalent circuit models can help us to better understand the electrical behavior difference between wet and dry electrodes, and equivalent circuit model is also in favor of designing a practical dry electrode which may perform similar to a gel electrode. Hence, many researchers have applied the equivalent circuit model for evaluating the performance of electrodes that were developed by themselves or were purchased from manufacturers. In brief, the equivalent circuit model is an important approach for exploring the interface charge transfer mechanism of the electrode/electrolyte and comparing quantificationally the performance of different types of electrodes.

Evaluation Methods and Instruments

Description of Common and Special Evaluation Methods and Instruments for Dry Electrodes

Dry electrodes [5] and textile-structured electrodes [6] have been well reviewed. Dry electrodes in references can be classified into several different types according to their characteristics, such as surface structure (with or without microneedle array), active or passive (with or without electrical elements), modulus of substrate, etc. (as shown in Fig. 2). Simultaneously, the dry electrodes in references can be also classified into several types according to the materials of the substrate (as shown in Fig. 3).

Many parameters, such as biopotential signals, resistance, impedance spectra, XRD maps, SEM images, open circuit potential (OCP), etc., may be utilized for characterizing the performance of dry biopotential electrodes.

Common Evaluation Methods and Instruments for Dry Electrodes

Impedance Spectra and Biopotential Signals for Evaluating the Performance of Dry Electrodes

Electrical conductivity is a fundamental property of resistive biopotential electrodes. DC resistance measurement is simple and the instruments are low cost. In most cases, the materials of biopotential electrodes have excellent electrical conductivity. However, real biopotential signal is in a frequency range. Impedance in the electrode/electrolyte interface depends on the frequency of signal due to the existence of double layer, and correlation between impedance and frequency is nonlinear. Therefore, electrical conductivity or resistance is not enough for characterizing dry electrodes.

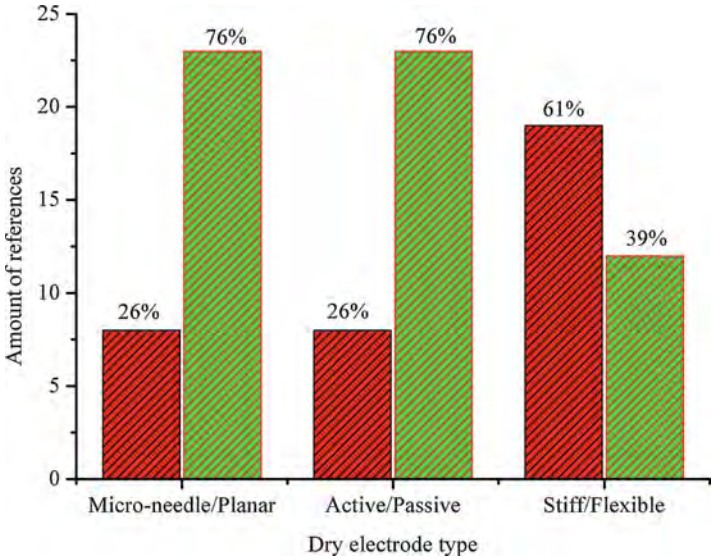

Fig. 2 Classification of dry electrodes according to surface structure, input impedance, or modulus

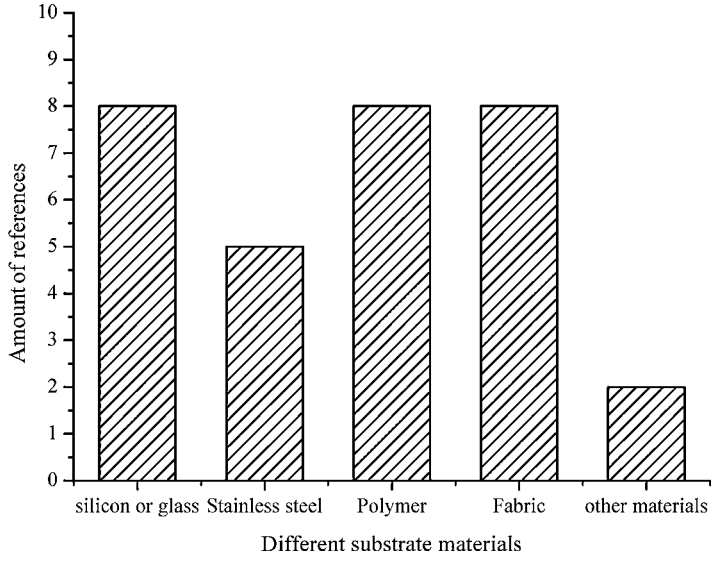

Fig. 3 Classification of dry electrodes according to materials of substrate

Impedance spectra can illuminate better the electrical properties in the electrode/electrolyte interface in frequency domain, because impedance spectrum measurement is similar to the biopotential measurement in charge transfer process of the electrode/electrolyte interface. Therefore, impedance measurement is a fit approach for analyzing the electrical properties of dry electrodes. In fact, impedance measurement is a popular method for evaluating the performance of dry electrodes in the last decades.

Impedance spectrum measurement of the electrode/electrolyte interface can obtain the curve of the impedance and phase angle at certain frequency domain which can reflect the real state of the biopotential through the electrode/electrolyte interface. Impedance spectra were utilized for characterizing the dry biopotential electrode by many researchers. Some researchers performed directly the impedance spectrum measurements on the skin of the human body for evaluating the performance of the dry electrode. However, in order to improve stability and reproducibility of measurement results, other researchers evaluated their dry electrode by measuring impedance on developed simulation devices.

Biopotential signal is also a favorite measured parameter for illuminating the performance of dry electrode, because biopotential measurement is the final application objective of dry electrodes. Some evaluation methods and instruments that were utilized for measuring biopotential signals and impedance spectra of dry electrodes were summarized in Table 1.

Silicon-Based Dry Electrode

Silicon wafer is a common material for fabricating the rigid planar and microneedle dry electrodes. Padmadinata et al. [7] fabricated an active dry skin electrode in which a buffer amplifier was integrated on a silicon chip; the substrate of the chip was designed as the input of the amplifier and as the sensitive unit of acquiring ECG from the skin. The ECG signals showed that the noise of the device can be reduced by using a metal layer evaporated on the substrate. Babak A. Taheri et al. [8] fabricated an active electrode that consisted of an interconnecting circuit substrate and silicon sensor substrate bonded together with a silver paste; the sensor substrate contained a planar array of four thin-film electrodes with silicon nitride on one side; biopotentials can capacitively couple to the electrodes. DC characteristics such as static power consumption and offset voltages were tested, and AC characteristics such as closed-loop gain of a channel (from input of the preamplifier to output of the chip), channel bandwidth, and noise were also tested. Biopotential signals, such as spontaneous EEG, sensory event-related potentials, brain-stem potentials, and cognitive event-related potentials, were measured on eight human subjects; the performance of the active dry electrode compared favorably with that of the standard wet Ag/AgCl electrode in all tests, with the additional advantages of no skin preparation, no electrolyte gel application, and higher signal-to-noise ratio. Wang Yu et al. [9] fabricated a microneedle array dry electrode that the microneedles on silicon wafer were obtained by performing dry etching and isotropic wet etching method, and then the Ti/Au was sputtered on the microneedles and the backside of the silicon wafer. The EEG signals from

Table 1 Summary of evaluation methods and instruments for dry electrodes using biopotential signals and impedance spectra

Reference	Measured parameters	Substrate and coating materials	Instruments	Comparison electrodes	Signal analysis method	Electrode type
[7]	ECG	Silicon and silver coating	An instrument amplifier and a digital memory oscilloscope	Stainless-steel and silver-foil electrodes	–	Active electrode
[8]	EEG	N-type (100) silicon with an 800 nm thickness silicon nitride layer	Commercial EEG instrument	Standard wet Ag/AgCl electrode	Frequency domain analysis	Active electrode
[9]	EEG, impedance spectra	N-type silicon (500 μm thickness) with Ti/Au coating	Commercial EEG instrument (for EEG); LCR meter (Agilent 4284A) (for impedance)	Commercial Ag/AgCl electrode	Frequency spectrum analysis	Passive electrode
[10]	Impedance spectra	Agx:TiN was deposited on glass and (100) silicon substrates	Gamry G300 equipment (Gamry instruments, USA) driven by the Gamry PHE200 software	Commercial Ag/AgCl electrodes	PSD	Passive electrode
[11]	EEG, impedance spectra	Silicon with Ag/AgCl-coating microneedles	Datex-Ohmeda S/5 anesthesia monitor (for EEG); a Solartron 1255 frequency-response analyzer coupled to a Solartron 1287 electrochemical interface (for impedance)	Commercial Zipprep electrodes	FFT, PSD	Passive electrode
[12]	EEG, impedance spectra	Silicon (500 μm thickness) and organic conductive polymer poly (3,4-ethylenedioxythiophene)	A commercial amplifier system (NeuroScan, SynAmps RT) (for EEG); a potentiostat/ galvanostat CHI 660D (for impedance)	Commercial wet electrode	Frequency spectrum analysis	Passive electrode
[13]	EOG	Silicon wafer with iridium oxide thin coating	An EEG acquisition system with 22-bit resolution	Commercial Ag/AgCl electrode	–	Passive electrode

(*continued*)

Table 1 (continued)

Reference	Measured parameters	Substrate and coating materials	Instruments	Comparison electrodes	Signal analysis method	Electrode type
[14]	EMG	Stainless-steel electrode with 10 mm diameter	Portable dual channel FFT analyzer CF-350, Ono Sokki Co. Ltd., 4 kHz A/D 16-bit resolution	Commercial Ag/AgCl electrode	Power spectra	Active electrode
[15]	EEG	Stainless-steel disk with a layer of 200 nm thick silicon nitride coating	Grass P511 amplifiers (spontaneous EEG and auditory long latencies); Cadwell system (VEPs, visual evoked potentials)	Standard wet Ag/AgCl electrode	FFT	Active electrode
[16]	EEG	316 L-grade stainless-steel disk with 6 mm diameter	Commercial EEG instrument	Commercial Ag/AgCl electrode	FFT, power spectra	Active electrode
[17]	Skin impedance	Dry silver, stainless-steel, and German-silver electrodes	Commercial instrument	–	–	Passive electrode
[18]	Impedance spectra	Stainless steel with Ti coating	A Solartron 1250 frequency-response analyzer connected to an EG&G, PAR 273 potentiostat	–	–	Passive electrode
[19]	ECG, EEG, impedance spectra	FullCure 720 (an insulating transparent biocompatible acrylic-based resin), titanium and gold coating	A lab-made device (for ECG); Micromed Brain Quick unit (for EEG); Agilent 33220A; and an oscilloscope (for impedance spectra)	Kendall™ ARBO (type H135SG, diameter 35 mm)	PSD (for ECG)	Passive electrode (for ECG), active electrode (for EEG)
[20]	EEG	PMMA solution are poured into PVA mold, Au-Pd and Au coating cover on surface	EEG amplifier, g.USBAmp, produced by g.tec GmbH, Graz (AU)	Wet commercial electrode	–	Passive electrode

[21]	EOG	Multiwalled carbon nanotube with Ag/AgCl coating	Commercial instrument	–	–	Passive electrode
[22]	Impedance spectra	Liquid silicone rubber (LSR)-based dry bioelectrodes without and with Ag coating	Solartron 1260 impedance/ gain-phase analyzer coupled to a Solartron 1287 electrochemical interface	–	–	Passive electrode
[23]	EEG	Two component thermoset polyurethane (PU) (48 % polyol and 52 % prepolymer)	Commercial instrument (for EEG); Agilent E4980A precision LCR meter (for impedance)	Commercial Ag/AgCl electrode	PSD	Passive electrode
[24]	ECG, impedance spectra	Flexible polydimethylsiloxane with Ti (100 nm) and Au (400 nm) coating	Developed device (microcontroller, Texas Instruments MSP430F149) (for ECG); Agilent E4980A precision LCR meter (for impedance)	Wet electrode	–	Passive electrode
[25]	ECG	Polymer substrate + Ag paste + dielectric paste + Ag paste	Commercial ECG instruments (Grass Technologies P511)	Rigid concentric ring electrode	Laplacian potential mapping	Active electrode
[26]	ECG, impedance spectra	Polydimethylsiloxane with Ti and Au coating	ECG amplifier (ECG 100C, BIOPAC System); commercial instrument (for impedance)	Commercial Ag/AgCl electrode	–	Passive electrode
[27]	ECG	Nonwoven fabric with Ag coating	Commercial ECG instruments	Commercial Ag/AgCl electrode, passive nonwoven electrode	FFT	Active electrode
[28]	ECG	Nonwoven fabric with Ag coating	Developed device (microcontroller, Texas Instruments MSP430F2274)	Commercial Ag/AgCl electrode, passive carbon electrode	PSD	Active electrode

(*continued*)

Table 1 (continued)

Reference	Measured parameters	Substrate and coating materials	Instruments	Comparison electrodes	Signal analysis method	Electrode type
[29]	ECG, impedance spectra	Nanofiber web textile substrate was fabricated by conductive poly (3,4-ethylenedioxythiophene)	Commercial ECG instruments; bioelectrical impedance spectroscopy (BIS) system for impedance	Commercial Ag/AgCl electrode	Power spectra	Passive electrode
[30, 31]	Impedance spectra	Textile-structured electrodes were composed of stainless-steel fibers	A potentiostat PGSTAT20 of ECO chemie and a frequency-response analyzer (FRA) module	Pd sheet	–	Passive electrode
[32]	Impedance spectra	Highly conductive fabric with Ag coating	High-precision LCR meter 4980A (Agilent Technologies, USA)	–	–	Passive electrode
[33]	Impedance spectra	Fabrics with coating of silver yarn	Commercial ECG instruments (MP36)	Commercial Ag/AgCl electrode, gold planar electrode	–	Passive electrode
[34]	ECG, impedance spectra	Fabrics with coating of silver yarn	Commercial ECG instruments	Commercial Ag/AgCl electrode, gold planar electrode	PSD	Passive electrode

microneedle array dry electrode and commercial electrode (Ag/AgCl) were very similar, the impedance of dry electrodes is lower than those of the Ag/AgCl commercial electrode. P. Pedrosa et al. [10, 35] fabricated silicon-based dry biopotential electrode; Ag and TiN coating were deposited by DC reactive sputtering. And SEM, XRD, and impedance spectra were utilized for evaluating the performance of dry electrodes. Patrick Griss et al. [11] characterized the microneedle dry biopotential electrode, and preliminary analysis of the calculated entropy of the recorded EEG didn't show any significant difference between microneedle electrode and commercial (Zipprep) electrode. YF Chen et al. [12] utilized the organic conductive polymer poly(3,4-ethylenedioxythiophene) (PEDOT) as the interface material for improving electrochemical performance of microneedle array dry electrode. Biopotential recording tests exhibited that the PEDOT electrode can acquire the perfect biopotential as wet electrode and had better signal-to-noise ratio than wet electrode. Dias et al. [13] presented a 4×4 microtip structure dry electrode for acquiring the biopotential and stimulating; the width and the height of microtips were, respectively, in the range of 150–200 μm and 100–200 μm, and the inter-microtip distance was 2 mm; and a thin layer conductive iridium oxide (IrO) on electrode is in favor of improving the contact with the skin. The EOG signals that were acquired by applied microneedle array dry electrode on the skin and Ag/AgCl electrode on a previous skin preparation were almost similar. Impedance spectrum measurement illuminated that the conductivity of IrO electrodes was higher than that of Ag/AgCl electrodes below 3 Hz frequency, and the phase angle of IrO electrodes was more negative than that of Ag/AgCl electrodes.

Stainless-Steel-Based Dry Electrodes

Stainless steel is also an important substrate material for constructing rigid biopotential dry electrode. Suzushi Nishimura et al. [14] presented an active dry electrode that is composed of a stainless-steel electrode terminal with 10 mm diameter and a voltage follower circuit of an FET-input operational amplifier. The performance of dry electrodes and conventional Ag/AgCl electrode was compared by two experiments: measurement and analysis of the surface EMG and the sensory nerve action potential which was evoked by an electric stimulus. Experimental results exhibited that the baselines derived from the active electrode were more stable than those derived from the conventional Ag/AgCl electrode, and EMG from the active electrode was little affected by the environmental noise such as humming noise. The power of the active electrode at 50 Hz was about 1 % of that of the passive electrode. The noise energy of the passive electrode from 100 Hz to 2 kHz is about 40 % of that of the active one. Despite the internal noise of the active electrode, the improvement of the stability of the baseline and the restraint from the interference of the environmental noise is effective. Since the amplitude of EMG signals is 1–100 mV, the author thinks that the active electrode is superior to the conventional passive electrode, at least, in the EMG measurement. Babak A. Taheri et al. [15] fabricated an active dry surface electrode for EEG recording; the electrode was composed of 3 mm diameter stainless-steel disk

and a 200 nm thickness silicon nitride (Si3N4) coating. A buffer amplifier (ICL7621 from Maxim) was utilized for raising the input impedance of dry electrode. The spontaneous EEG signals from 0.5 to 70 Hz bandwidth were measured by active dry electrode and wet Ag/AgCl electrode, the raw signal amplitudes of active dry electrode and wet Ag/AgCl electrode were comparable, and analysis results of fast Fourier transform (FFT) and power spectral density (PSD) also exhibited that there were no marked differences on frequency spectrum between active dry electrode and wet Ag/AgCl electrode. Fonseca et al. [16] fabricated dry active electrode that a stainless steel with 6 mm diameter and 2 mm thickness was utilized as the substrate of electrode and was covered by multilayers TiO_2 films using spin coating and anneal method; a square printed circuit board (PCB) with some electronic components and operational amplifier was mounted and assembled on the back of a stainless-steel disk. The EEG signals which were acquired in several healthy volunteers using dry active electrode and Ag/AgCl electrode at symmetric position were very similar, and the power spectra proved that the EEG signal from dry active electrode was less affected by the 50 Hz power-line noise.

Polymer-Based Dry Electrodes

Polymer was utilized for fabricating the microneedle array dry electrode due to easy molding and excellent plasticity. P. Salvo et al. [19] fabricated a 3D-printed dry electrode with conical needle array, the model of dry electrode was designed in AutoCAD software, each needle is 3 mm high with a base diameter of 600 μm and a top diameter of 100 μm, the inter-distance between needles is 250 μm, and then the electrodes were fabricated using 3D printer. The ECG signal of different electrodes was analyzed in frequency domain by power spectral densities (PSDs) that are calculated by Welch's method implemented in Matlab; results showed the difference of average power integral between dry and wet electrodes in the range from 4 to 12 Hz was extremely small (3.2×10^{-4} dB) which validated the reliability of 3D-printed dry electrodes. 3D-printed electrodes and Belek Ag/AgCl electrodes were placed on different positions for acquiring EEG during wakeful relaxation with closed eyes. The PSD of EEG showed the average powers calculated in 0–60 Hz band were 101 and 108 dB for dry and Ag/AgCl electrodes, respectively. M. Matteucci et al. [20] constructed a hollow microneedle array PMMA electrode substrate by a negative polyvinyl alcohol (PVA) mold. A few-nanometer-thick Au-Pd layer was coated on the surface of the substrate by pulsed laser deposition, and then a thicker (50 nm) Au layer was thermally evaporated on the microneedle surface. ECG signal from hollow microneedle electrodes had higher intensity than that from conventional electrodes. Both rhythms beta (eyes open) and alpha (eyes closed) were clearly detected in EEG recordings. Giulio Ruffini et al. [21] developed a microneedle dry electrode which a layer of carbon nanotubes array/forest was covered on the surface of the electrode by chemical vapor deposition (CVD), and the Ag and AgCl were deposited on the outside wall of CNTs. The TEM and SEM images were utilized to observing the appearance of CNTs and Ag on the surface of CNTs. A.R. Mota et al. [23] presented a

polyurethane-based quasi-dry electrode which can save 30 μl electrolyte in its reservoir, and the electrolyte can be released when the electrode deformed upon the application due to a specified adduction force. EEG signals and their power spectral density have similar signal characteristics for quasi-dry electrode and Ag/AgCl commercial electrode in the time domain and frequency domain. Chen CY et al. [24] fabricated flexible polydimethylsiloxane (PDMS) dry electrodes (FPDEs) which were composed of polydimethylsiloxane (PDMS) substrate, Ti (100 nm), and Au (400 nm) coating layers; ECG signals were acquired by front-end biopotential acquisition circuits and 16-bit MSP430F149 microcontroller, which illuminated the similar performance between FPDEs and wet commercial Ag/AgCl electrodes. The impedance value of FPDEs on five different subjects was also similar to that of wet commercial Ag/AgCl electrodes. G Prats-Boluda et al. [25] developed flexible and rigid concentric ring electrodes that were utilized for measuring the skin-electrode contact impedance and ECG on ten healthy volunteers at rest and in motion; experimental results showed that flexible concentric ring electrodes had lower skin-electrode impedance, lower baseline wander, less sensitive to interference, and less motion artifacts than rigid concentric ring electrode. Ju-Yeoul Baek et al. [26] investigated the performance of a flexible polymeric dry electrode for the long-term monitoring of ECG by impedance, ECG signal, and SEM. Elastomer polydimethylsiloxane, which is inexpensive, biocompatible, and amenable to micro-molding and with excellent gas and water permeability, was utilized as the substrate of dry electrode; Au (300 nm) and Ti (30 nm) layers were coated on the surface of substrate, respectively. Impedance of the dry electrode was much higher than that of the Ag/AgCl electrode at a frequency lower than 100 Hz, and the impedance differences became almost similar at a frequency higher than 100 Hz. However, the waveform of the ECG signal from dry electrodes was almost similar to that from the commercial Ag/AgCl electrode.

Textile-Based Dry Electrodes

In order to improve the comfortable of dry electrode and integral well dry electrodes into monitoring garments, many researchers try to utilize fabric as substrate of dry electrodes. For example, Tae-Ho Kang et al. [27] presented a nonwoven textile substrate active dry electrode in which the sensor area and routing of power and signal-transmission lines on nonwoven textile substrate can be achieved by hand- or screen-printing with Ag/AgCl ink, connection between two layers can be achieved by punching a hole and pouring Ag/AgCl ink, and conductive epoxy or silver paste can be used to fix the positions of electrical components and wires on nonwoven fabric. Experimental results showed the nonwoven fabric passive dry electrodes were similar to conventional Ag/AgCl gel electrodes by analyzing the ECG signal acquired in commercial ECG instruments. There was little difference between the ECG signals captured by the nonwoven fabric passive and active dry electrodes; however, ECG signals captured during jogging showed the nonwoven fabric active dry electrodes had better performance than the nonwoven fabric passive dry electrodes. Carey R Merritt et al. [28] developed two kinds of active fabric

dry electrodes: direct-attach active electrodes and interposer active electrodes. ECG signals of several kinds of electrodes were acquired during sitting and jogging, and PSDs of ECG signals indicated that active electrodes were similar to the commercial Ag/AgCl electrodes. Durability testing exhibited the direct-attach active electrodes did not work due to a crack of the line after five cycles of machine washing; however, the ECG signal of the interposer active electrode and the passive carbon electrodes had no major differences between before and after five cycles of machine washing and still had good clarity and visually compares well to the commercial Ag/AgCl electrodes. Tong In Oh et al. [29] fabricated two kinds of nanofiber web dry electrodes; then tested the contact impedance, step response, and noise and signal fidelity performance of two kinds of nanofiber web dry electrodes and three kinds of commercial metal-plated fabric electrodes; and compared these electrodes to conventional Ag/AgCl electrodes. They found that nanofiber web dry electrodes were more similar to conventional Ag/AgCl electrodes than metal-plated fabric electrodes; the contact resistance and capacitance of Ag-plated PVDF nanofiber web electrodes were the most similar to those of Ag/AgCl electrodes over the 10 Hz to 500 kHz frequency range. An agar object mimicking the human thorax was constructed for evaluating the waveform fidelity of ECG recording from five kinds of electrodes; results showed the waveform fidelity of nanofiber webdry electrodes was higher than that of metal-plated fabrics. Liu Hao et al. [33, 34] fabricated four different fabric electrodes (such terry structure with Ag/AgCl or Ag coating, plain structure with Ag/AgCl or Ag coating), and a pair of gold plate electrodes was utilized as reference electrode. Impedance spectra, open circuit potential deviation, and PSD difference exhibited the Ag/AgCl electrodes had less noise and could acquire better biopotential signals at static and, especially, at motion.

Other Substrate Materials

Ch. Gondran et al. [36, 37] proposed a NASCICON-type ceramic (high-sodium ion conductor) dry electrode; the principle of the measurements was based on a sodium ion exchange between the skin and the material. Impedance measurements in saline solution exhibited the electrode was slightly polarizable. The impedance between the skin and electrode decreased as a function of the time of application. The resistive component was the major source of the impedance change.

Open Circuit Potential and Response for Evaluating Performance of Dry Electrodes

Open circuit potential which should be the total of the potential between two measuring ends and other potential noise can be measured by electrochemical workstation or some high-precision voltage measurement modules or instruments. The OCP of the electrode/electrolyte interface was utilized for analyzing and evaluating the performance of dry electrodes by many researchers [10, 18, 23, 33] due to it being closely related with motion artifact of dry electrodes.

Structure and Morphological Characterization for Evaluating Performance of Dry Electrodes

Surface structure and material ingredient are important factors for application of dry electrode. In order to obtain the microneedle shape and size, the scanning electron microscope (SEM), transmission electron microscope (TEM), and optical microscope were utilized for observing the surface structure of dry electrodes [9, 11–13, 19–22]. The ingredient and crystal texture of materials of some novel electrodes can be analyzed by X-ray diffraction (XRD) maps [10, 35].

Several Special Evaluation Methods and Instruments for Dry Electrodes

To evaluate the performance of dry electrodes, impedance and biopotential of some electrodes were measured directly on human subjects [9, 11, 12, 17, 24, 37]. The advantage of this method is that measurement and application objects are identical, but the disadvantage of using human subjects is also obvious, because the human body is very complicated, and its parameters vary with time and individuals. Furthermore dry electrical properties of wearable electrodes are affected by many factors such as pressure, length of motion track and motion speed between the electrode and skin, temperature and concentration of electrolyte, humidity and mechanical properties of the skin, and so on. It is impossible to have controls over all the parameters by using human subjects. Hence, a standard measurement device is more stable and better for evaluating dry electrodes. These devices are classified into two categories: static simulation devices (no relative movement between electrode and simulation skin) and dynamic simulation devices. Static simulation devices have electrochemical cell for measuring electrochemical impedance spectra [30, 31], electrochemical cell with pressure-adjustable unit between the electrode [32, 33] and simulation skin and human body simulation device [22].

Instruments and Methods in Static Measurement

Static Measurement Device

A static measurement device shown in Fig. 4 was commonly utilized to analyze the electrochemical characteristic of dry electrodes, especially textile-structured electrodes. The electrodes were attached at the inner side of the PVC plates with rubber ring fittings. The distance between the electrodes can be adjusted by changing the length of the tube, and electrolyte solution was poured into this tube before testing; the above-described elements could be fixed by some screws.

Georgios Priniotakis et al. [30] had utilized this type of device to evaluate three different textile-structured electrodes such as woven, knitted, and nonwoven Textile-structured electrodes that were composed of stainless-steel fibers. Artificial

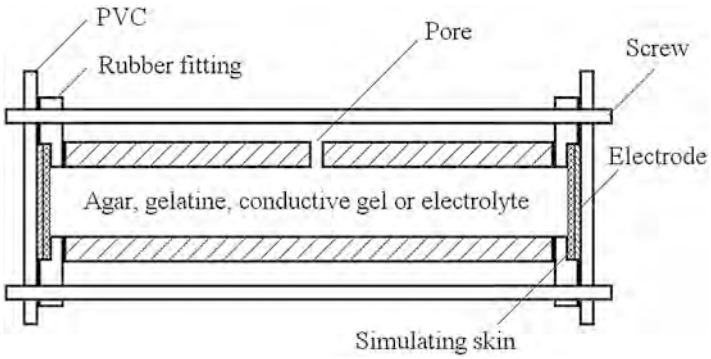

Fig. 4 Schematic diagram of static measurement device

sweat was composed of 20 g l^{-1} NaCl, 1 g l^{-1} urea, and 500 mg l^{-1} of other salts. The pH of the sweat was adjusted at a value of 5.8 by NaOH or HCl. Teflon membranes with 0.175 mm thickness, 35 % pore density, and 0.45 or 5 μm pore diameter were utilized as artificial skin. In this measurement system, a potentiostat PGSTAT20 of ECO chemie and a frequency-response analyzer (FRA) module were utilized for performing electrochemical and impedance measurements. The frequency of FRA could vary from 1 mHz to 1 MHz and maximum amplitude of FRA could reach 10 mV.

This study revealed some rules between resistance and other parameters such as concentration of electrolyte, area of electrode, and distance of electrodes by using three different types of intelligent textile structures, a knitted, woven, and nonwoven structure, made of stainless-steel fibers. The correlation between log R and log c is linear, and the slope of these curves is approximate -1 ± 0.05 which is in accordance with theoretical consideration. The slope of log R and log A is -0.65 ± 0.03 and the slope of log R and log d is 1 ± 0.04. In terms of the above conclusion, correlation between resistance and other parameters in this static simulation device can be expressed by Eq. 1 [31]:

$$R = k\frac{d^{0.98}}{cA^{0.65}} \tag{1}$$

where R is the resistance in V, k is a constant of 22.5 ± 1.0 at 298.0 K, d is the distance between the electrodes in mm, $A$is the surface area of the electrodes in mm^2, and c is the concentration of the electrolyte solution in mol l^{-1}.

To simulate the human skin, a layer of artificial skin membrane was assembled between the electrode and electrolyte. These membranes are positioned between the Textile-structured electrodes and the electrolyte and mimic the skin of the human body. However, Georgios Priniotakis also pointed out that the system is much more complicated due to joining of these membranes. The purpose of this type of experiments is to simulate the human body in rest (no sweat production) and during

Table 2 Electrical resistance of knitted, woven, or nonwoven stainless-steel electrodes in different NaCl concentrations and for different exposure times in artificial sweat

Concentration of electrolyte (mol l^{-1})	10^{-3}			0.5		
Electrode/time of exposure (hours)	$t = 0$	$t = 12$	$t = 24$	$t = 0$	$t = 12$	$t = 24$
Knitted	31,620	31,520	31,530	26.2	26.4	27.1
Woven	31,510	31,520	31,510	26.3	26.5	26.8
Nonwoven	31,520	31,510	31,520	26.5	32	57.1

sweating (electrolyte penetrating through the pores of the membrane or the skin) by using 0.45 and 0.5 μm diameter porous membranes. Experimental curves were obtained in a cell with an electrolyte solution concentration of 10^{-2} mol l^{-1}. The impedance spectrum using porous membrane with 5 μm diameter has two well-defined semicircles, but that using porous membrane with 0.45 μm diameter has only one well-defined semicircle.

Philippe Westbroek [32] investigated resistance change of textile-structured electrodes which were exposed to artificial sweat solutions for 24 h. The radius of electrodes is 5 mm and the distance of electrodes is 9.1 mm. Table 2 shows that only resistance of nonwoven electrode had obvious change when exposure time was 24 h and the concentration of artificial sweat was 0.5 mol l^{-1}; however, the resistances of woven- and knitted-structure electrodes almost had not changed, and resistance of nonwoven structure electrode almost had not changed when concentration of artificial sweat was lower or exposure time was shorter. Resistance change means the corrosion or adsorption appeared on the surface of electrodes; hence, it is necessary for developing a method as described above to control and evaluate the quality of Textile-structured electrodes.

Salla Kaitainen [22] fabricated dry microstructured electrodes based on electrically conductive liquid silicone rubber (LSR) and developed an impedance measurement setup for evaluating performance of electrodes (as shown in Fig. 5). Smooth LSR electrodes and micropillar-structure electrodes with inter-pillar distances of 20 and 100 μm that were coated or uncoated with Ag were measured in impedance spectra at 1, 10, 100, and 1,000 Hz. Table 3 showed that the impedance of electrode with Ag coating significantly decreases at low-frequency region (<1 kHz); however, the impedance of electrodes with micropillars decreased more obviously.

These devices for measuring static electrochemical impedance spectra of electrode/electrolyte interface will provide a standardized tool for evaluating the performance of DBPE. Moreover, the stability and reproducibility of measurement results will be better than the device that measurements were directly performed on human body.

Pressure-Adjustable Measurement Device

Static simulation devices described above can evaluate quantificationally the quality of textile-structured electrodes by the impedance spectra and resistance, and the distance between electrodes, concentration of the electrolyte, and area of the

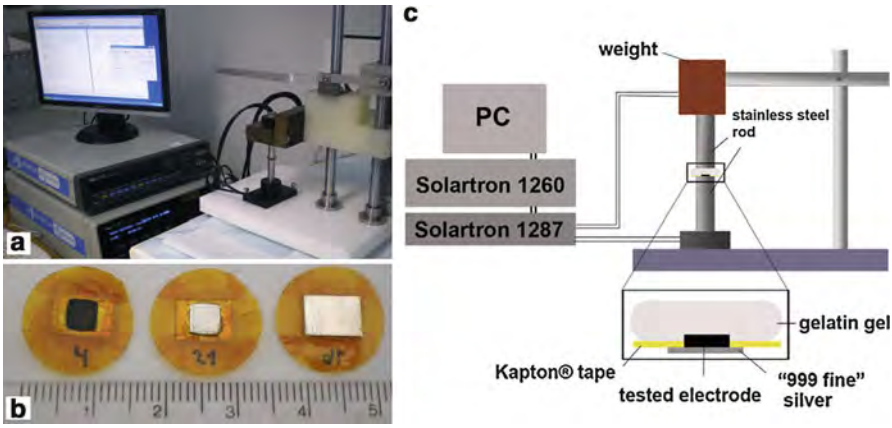

Fig. 5 (**a**) Setup used in EIS measurements and (**b**) electrodes ready for measurements (shown in centimeter scale). From *left* to *right*: smooth, 100 c, and underside of an electrode showing a larger area of fine silver piece glued to the LSR electrode. The *round-shaped* insulator around the electrode is Kapton tape. (**c**) Schematic representation of the setup. A small weight was applied to ensure constant contact pressure between the electrode and gelatin gel-based skin model [22]

Table 3 Contact impedance (mean ± std) of all electrodes [28]

1 Hz	|Z|kΩ		1,000 Hz	|Z|kΩ	
Type	Uncoated	Ag coated	Type	Uncoated	Ag coated
Smooth	135.0 ± 25.8	46.3 ± 7.4	Smooth	8.7 ± 1.3	12.8 ± 1.0
20	95.6 ± 33.9	9.0 ± 1.4	20	5.9 ± 1.7	2.5 ± 1.0
100	89.1 ± 17.8	10.7 ± 0.9	100	7.5 ± 1.8	2.7 ± 0.4

electrode were adjustable; however, other parameters such as pressure and relative motion between the electrode and artificial skin can't be achieved.

In order to simulate the contact state between electrodes and the skin, Beckmann L [32] developed a pressure-adjustable measurement device (PAMD) that is composed of three parts: the textile electrode to be characterized, a skin dummy, and a second electrode below the skin dummy covered with gold (as shown in Fig. 6). The dummy is made of agar, which is a gelatinous substance derived from seaweed, distilled water, disinfection agent, and salt, and the conductivity of distilled water was adjusted to 29.3 μS cm^{-1} by mixing into the salt and disinfection agent. Such conductivity is equivalent to the conductance of wet skin tissue at 10 kHz. The shape of the dummy can change in terms of simulating parts of the human body, for example, if the electrode contact on the arm is to be investigated, the shape of the skin dummy was changed into the cylindrical shape of an arm. Pressure between the electrode and dummy in this setup was adjustable by changing weight on top of weights. A two-point measurement was performed using the high-precision LCR meter 4980A (Agilent Technologies, USA) which was utilized for analyzing impedance of the electrode/skin dummy interface.

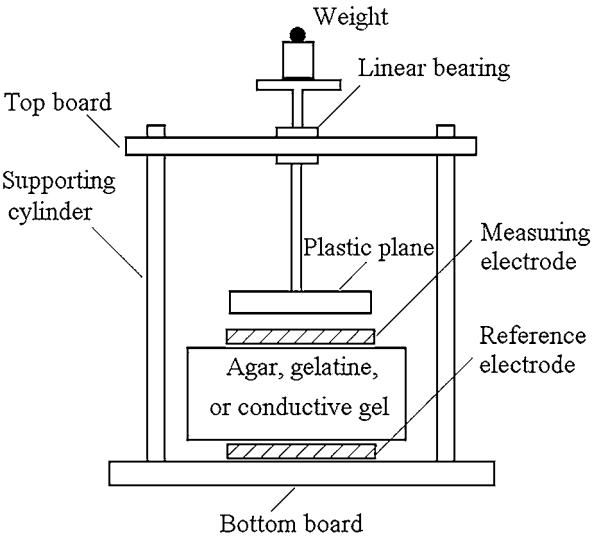

Fig. 6 Schematic diagram of pressure-adjustable measurement device

Human Body Simulation System

Oh Tong In [29] had evaluated two different nanofiber web dry electrodes and three metal-plated fabric electrodes; some parameters such as contact impedance, step response, and noise and signal fidelity were measured and analyzed.

Figure 7 showed the measurement method of contact impedance. First, three wire impedance measurements for each type of electrodes were performed according to the approach in Fig. 7a. Then four wire impedance measurements for each type of electrodes were performed at above each frequency according to the approach in Fig. 7b.

Contact impedances of electrodes can be characterized by impedance spectroscopy system with a frequency range of 10 Hz to 500 kHz. A parallel RC circuit was utilized to model the electrode/electrolyte contact impedance of each electrode, and impedances were measured at frequencies of 10, 50, 100, 1,000, 5,000, 10,000, 50,000, 100,000, 250,000, and 500,000 Hz. Results showed Ag-plated PVDF nanofiber electrodes and Ag/AgCl electrodes had minimum resistance about 110 Ω; averaged resistances and capacitances of the Ag/AgCl electrodes and Ag-plated PVDF nanofibers were very similar. The PEDOT-coated PVDF electrodes and PET-Cu-Ni-Au and PET-Cu-Ni-carbon fabrics had intermediate contact resistances of around 1 kΩ. Contact capacitances of three fabric electrodes were large; two kinds of nanofiber web dry electrodes had approximate capacitance values to those found in Ag/AgCl (about 2 nF). Moreover, averaged resistances and capacitances of the Ag/AgCl electrodes and Ag-plated PVDF nanofiber electrodes were very similar. After analyzing the measured data, the author concluded the impedance spectrum of both Ag-containing electrodes was similar, and dispersion range of impedance between 10 and 100 Hz was smaller than other electrodes.

An agar object mimicking the human body shown in Fig. 8 was constructed for evaluating the waveform fidelity of ECG. A pair of needle electrodes was inserted at

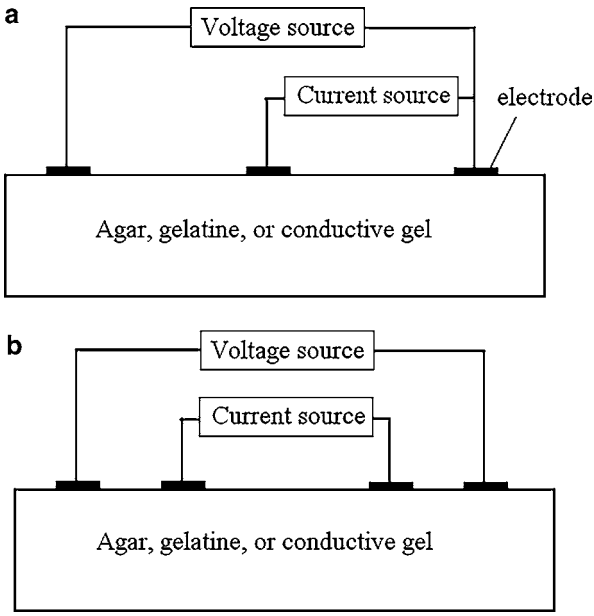

Fig. 7 Setups for (**a**) three-electrode contact impedance, (**b**) four-electrode contact impedance, and step response measurements

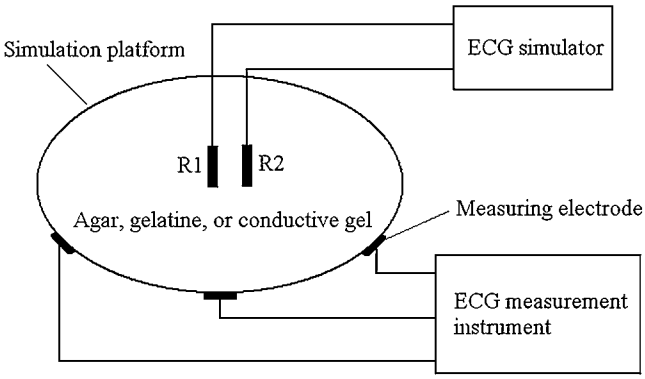

Fig. 8 Schematic diagram of human simulation platform

the center of the object; synthesized ECG voltage signals using a patient simulator (214A, Dynatech Nevada Inc., USA) was applied between two electrodes. Three electrodes of the same kind were placed at the anterior center and left and right sides of the simulation platform. The synthetic ECG signals over 800 cardiac cycles were measured, and an averaged ECG signal over one cardiac cycle for each electrode type was computed; the ECG signal using Ag/AgCl electrodes was utilized as the reference signal for ECG signals on all test electrodes. Results showed that the PEDOT-coated PVDF nanofiber web electrode had the highest waveform fidelity of 95 %. There was no significant difference for other Textile-structured electrodes.

Instruments and Methods in Dynamic Measurement

Dynamic measurement of dry electrodes is a more reasonable approach for revealing the mechanism of motion artifact and investigating quantificationally frequency and amplitude of motion artifact in different influence factors. Previous researches have been concentrated on ECG signal measurement on the skin of the human body and impedance spectrum measurement and measurement on static simulation devices. However, one paid a few attentions to correlations between the materials, structures of the electrodes, and motion artifact due to absence of dynamic measurement instrument. In this section, a dynamic measurement system (DMS) which can be used for assessment of the quality of dry biopotential surface electrodes (DBSE) is introduced. The DMS can simulate the interface state of the electrode/skin, especially the motion state which the previous presented measurement systems cannot reach. The electrical properties of electrodes can be acquired by measuring the EIS, and charge transfer process of interface can be analyzed by the dynamic open circuit potential (DOCP) variation and equivalent circuit (EC) parameters of EIS.

Structure and Principle of Dynamic Measurement System

Figure 9a, b shows the overall view and schematic diagram of DMS, respectively. DMS is composed of the skin simulator, the electrolyte regulator, the electrode holder, and the data acquisition and control module. The skin simulator and the electrolyte regulator were used for simulating the human body and skin. The electrode holders mount a pair of electrode samples, adjust the pressure between the electrode and artificial skin, and control the motion of the top electrode. The data acquisition and control module collects the monitoring signals, e.g., temperature and pressure, and the measuring signals, e.g., impedance, static OCP, and DOCP.

Cross-sectional view of the skin simulator of DMS is shown in Fig. 10. Two cover plates are installed on the two open ends of the PTFE barrel; two PTFE tori hold the macropore PVDF membrane (from Millipore) by six screws and are fixed on the holding plate by four screws. The tension of membrane can be controlled by adjusting the height of the inner torus. At the edges of the barrel and torus, sealing rings are used to prevent leakage of solution. Entry and exit for the solution is on the sidewall of the barrel.

Figure 11 shows the pressure controller comprises a linear bearing, a strain gauge, a buffer spring, an adjusted disk, two PTFE columns, and a contact button, supporting and hanging from the motion controller. An end of the linear bearing is connected to the strain gauge by a buffer spring. The contact button is enclosed by two PTFE columns for assembling the electrode, an electric wire connected with the button as a measuring port. Two pressure controllers and two motion controllers can be utilized for controlling the track and speed of the movement and the pressure between the electrode and skin. The motion controller is composed of two linear stages (Newport, USA) with 50 mm travel range, 0.1 μm resolution, and 100 mm/s maximum speed. The data acquisition and control module is composed of a

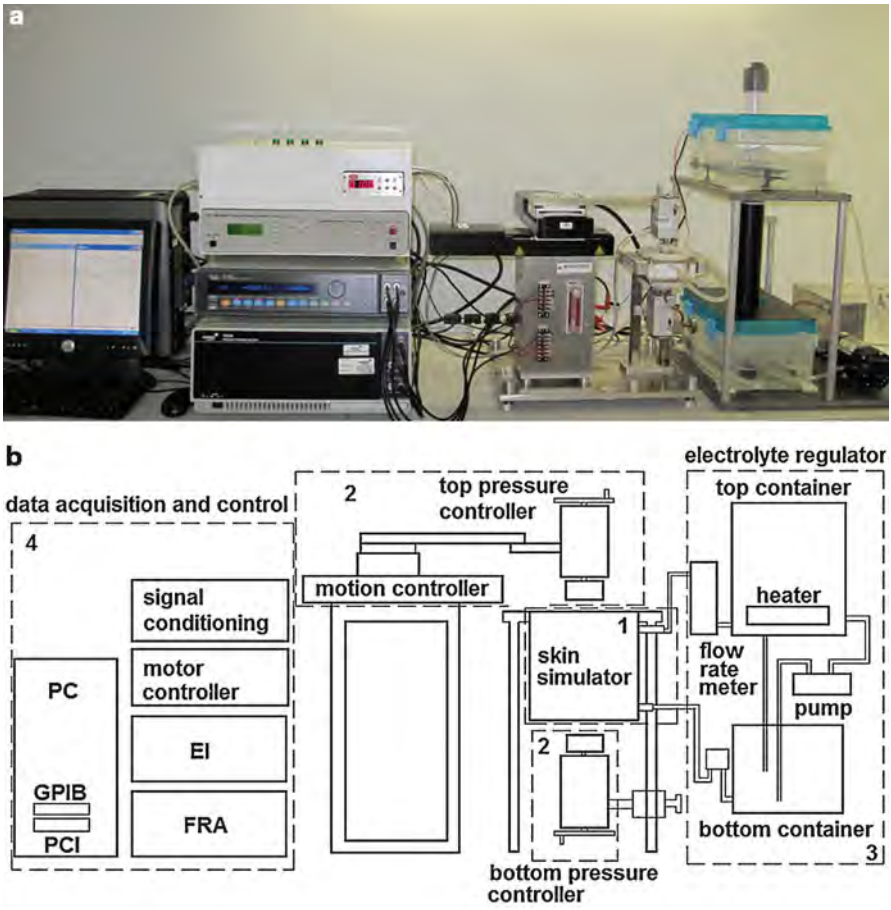

Fig. 9 (**a**) Overall view and (**b**) schematic diagram of dynamic evaluation system (DMS) [33]

computer, Electrochemical Interface 1252A (Solartron, UK) and Frequency Analyzer Response 1287 (Solartron, UK), a series of signal-conditioning devices, and sensors.

EIS Measurement

Four kinds of dry biopotential surface electrodes and gold button electrodes as shown in Fig. 12 were used for validating the DMS, terry coating silver chloride (TC), terry with silver yarn (TS), plain coating silver chloride (PC), and plain with silver yarn (PS) had 26 mm diameter, and the amount of four type electrodes was three pairs. The contact pressure between electrodes and artificial skin was at 1 kPa (deviation less 8 %).

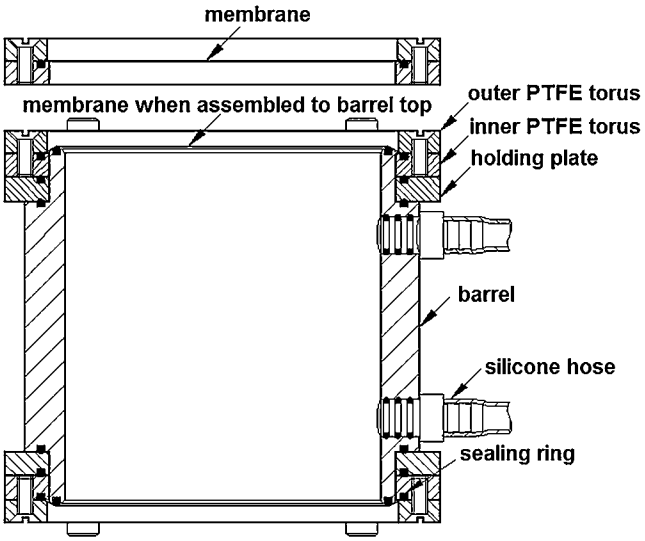

Fig. 10 Cross-sectional view of the skin simulator [33]

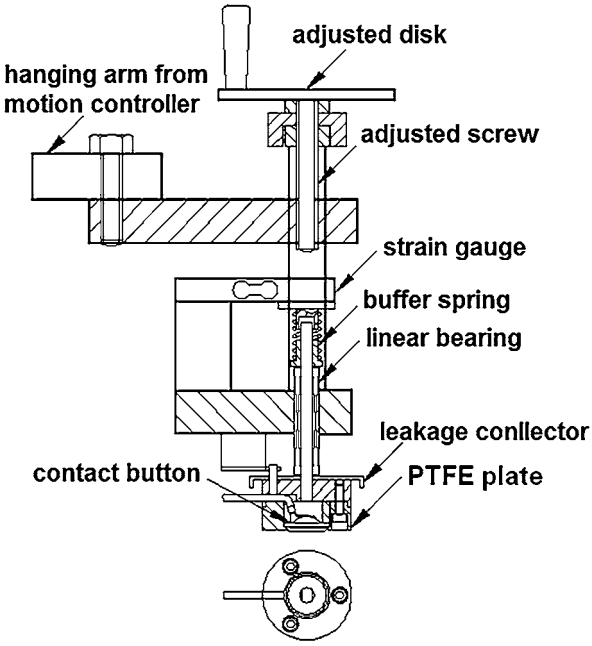

Fig. 11 Cross-sectional view of the pressure controller [33]

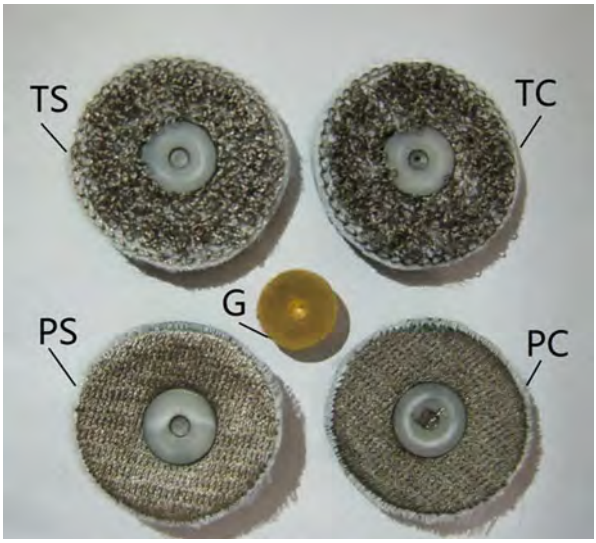

Fig. 12 Appearances of the five types of electrodes [33]

Figure 13 shows the Bode plot and EC model of EIS of gold electrode on simulator with or without artificial skin. A constant phase element (CPE) was often used in an EC model in place of a capacitance to compensate for inhomogeneity in a system; R_L is the total ohmic resistance of the electrochemical cell and contains contributions from the solution, cables, and other sources. R_d is considered to be the corrosion resistance of the gold, which is inversely proportional to the corrosion current density. The CPE is defined by two parameters, T and p, in the equation for impedance:

$$Z = \frac{1}{T(j\omega)^p} \tag{2}$$

where if p equals 1, then Eq. 2 is identical to that of a capacitance and T is identical to the value of capacitance. Figure 13 shows measured EIS and fitting EIS (using ZView software from Solartron, UK) of gold electrode, respectively, and the fitting data and measured data are highly consistent in frequency domain from 0.01 Hz to 100 kHz. Table 4 shows R_d of EIS on simulator with membrane is larger and T is less. The reason is probably due to the contacting area of the electrode/electrolyte on the simulator without membrane being bigger than that of the electrode/electrolyte on the simulator with membrane.

EIS of the five kinds of electrodes shown in Figs. 14 and 15 are measured on DMS, and Table 5 shows the EC parameters of EIS by fitting the EIS measurement data, R_d of polarization electrodes (G, PS, and TS) are far greater than that of less polarization electrodes (TC and PC), and T of TC and PC electrodes are an order of magnitude greater than that of G, PS, and TS. Accurate model construction and EC parameter fitting provide help for investigating the mechanism of motion artifact of electrode/electrolyte.

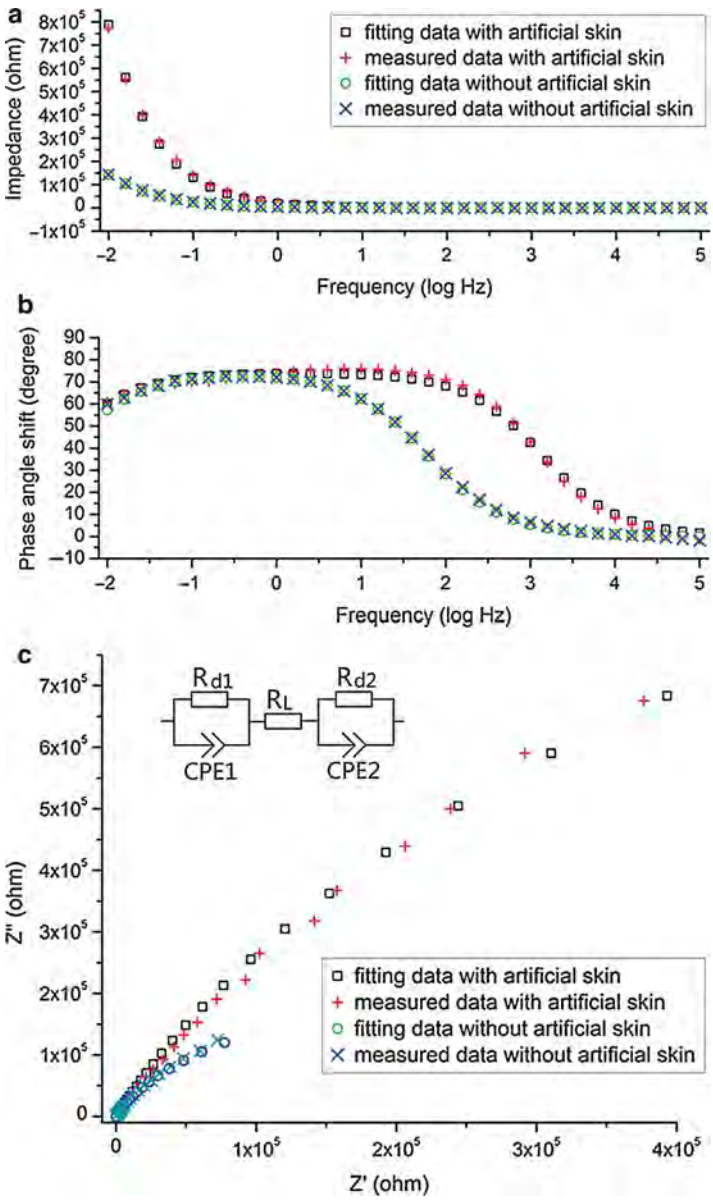

Fig. 13 (**a**) Bode plot, (**b**) equivalent circuit, and Nyquist plot of G electrode with or without membrane [33]

Table 4 Parameter of EC of gold electrode with or without membrane

Membrane	R_L (ohm)	R_{d1} (ohm)	T_1	p_1	R_{d2} (ohm)	T_2	p_2
Used	56	5E5	3.09E5	0.845	4.5E6	1.85E5	0.84
Unused	84	3.5E5	8E5	0.815	4.5E5	3E4	0.82

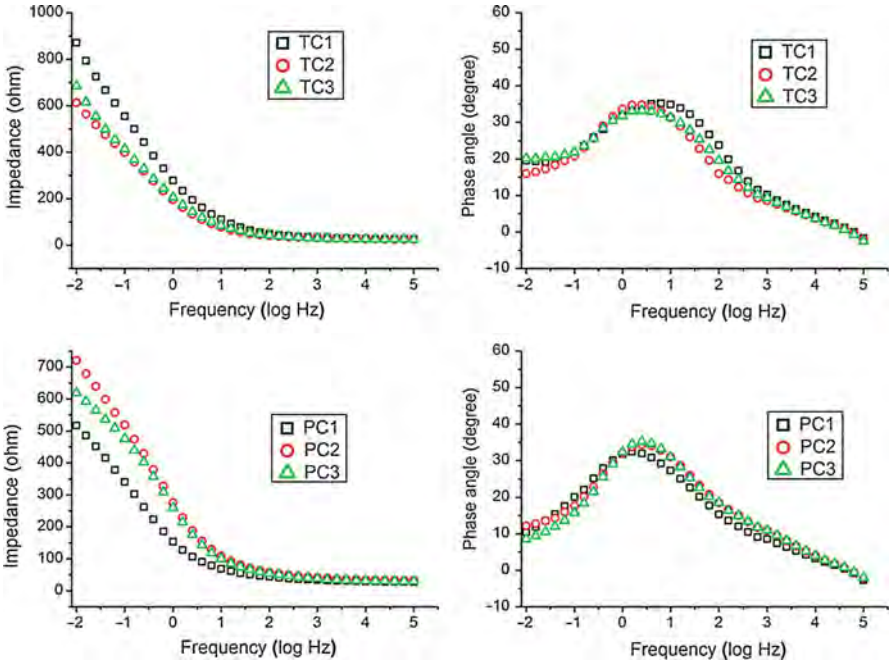

Fig. 14 Bode plots of TC and PC electrodes on DMS

DOCP Variation Measurement

DOCP variation which can be regarded as motion artifact is composed of several components and is affected by many factors, such as motion speed, pressure fluctuation, and lengths of motion track. In this section, correlation between DOCP variation and influence factors is introduced.

A pair of TC electrodes is measured with 2 mm radius and about 1 kPa pressure (fluctuation less than 6 %). The cycle of intermittent motion is 22 s. Figures 16 and 17 show the DOCP variations and pressure fluctuation in intermittent motion measurement (IMM) and continuous motion measurement (CMM), respectively. Figure 18 shows amplitudes of motion-induced potential variation of electrode decrease with increase of motion speed; the DOCP variation of IMM is larger than that of CMM in the same condition. Furthermore, Figure 19 shows the charging is slower than the discharging and rate of discharging depends on the motion speed.

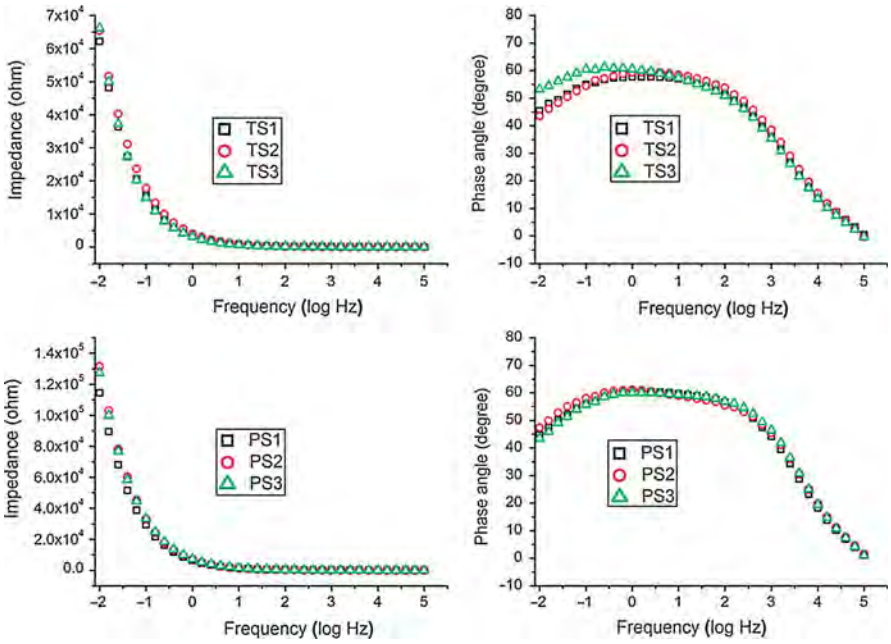

Fig. 15 Bode plots of TS and PS electrodes on DMS

Table 5 Parameters of EC of the five types of electrodes

Code	R_L (ohm)	R_{d1} (ohm)	T_1	p_1	R_{d2} (ohm)	T_2	p_2
G1	56	2.9E5	1.86E5	0.74	3.3E6	1.89E5	0.91
G2	56	2.9E5	1.86E5	0.74	3E6	1.89E5	0.91
G3	60	1.8E5	1.6E5	0.81	3E6	1.64E5	0.91
TC1	26	1,300	0.011	0.58	580	0.0011	0.57
TC2	25	970	0.019	0.51	460	0.0018	0.57
TC3	24	1,400	0.015	0.57	450	0.0016	0.545
TS1	25	1.2E5	1.65E4	0.65	1.2E5	1.65E4	0.65
TS2	26	1E5	1.6 E4	0.655	1.1E5	1.45E4	0.64
TS3	23	1.5E5	1.9 E4	0.72	2.9E5	1.75E4	0.61
PC1	28	1,000	0.045	0.4	500	0.0022	0.52
PC2	32	1,000	0.18	0.86	750	0.0012	0.51
PC3	29	680	0.03	0.45	500	0.001	0.62
PS1	27	1.2 E5	3E4	0.62	2.5 E5	5.3 E5	0.7
PS2	28	1.6 E5	2.3 E4	0.655	3.4 E5	5.1 E5	0.68
PS3	26	1 E5	2.7 E4	0.675	2.7 E5	4.5 E5	0.675

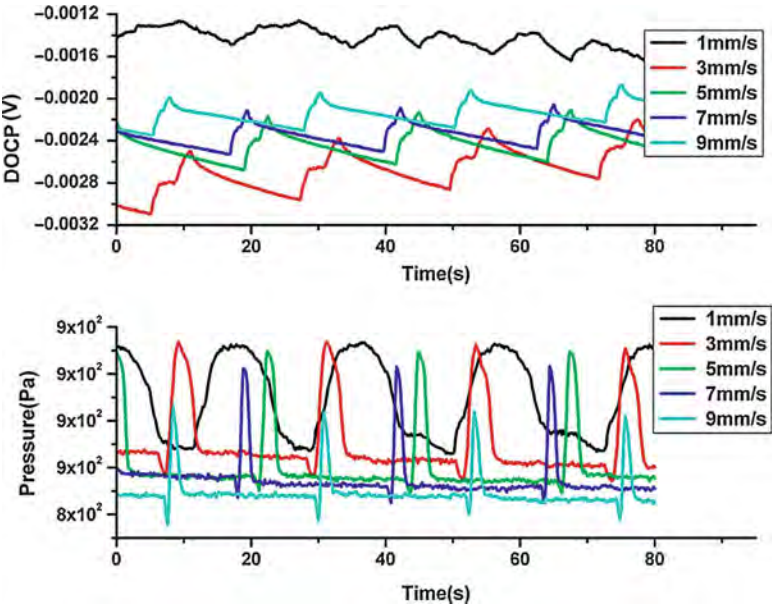

Fig. 16 DOCP and pressure of TC in intermittent motion measurement [33]

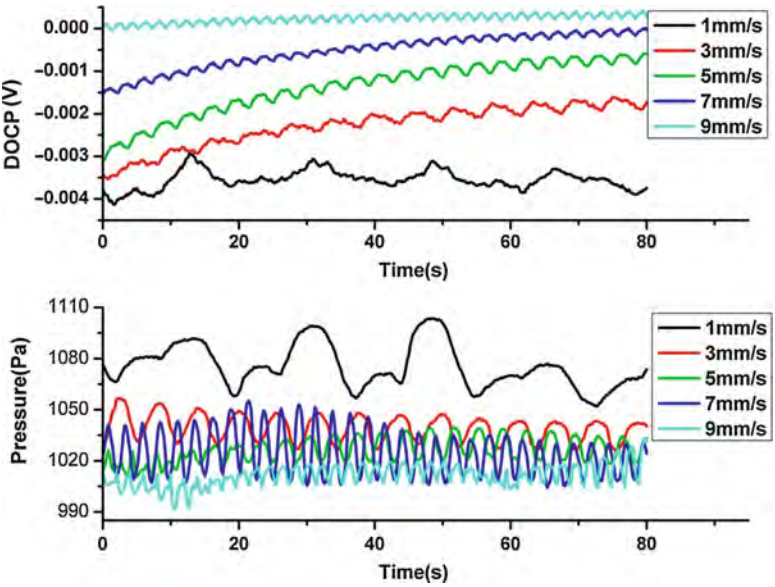

Fig. 17 DOCP and pressure of TC in continuous motion measurement [33]

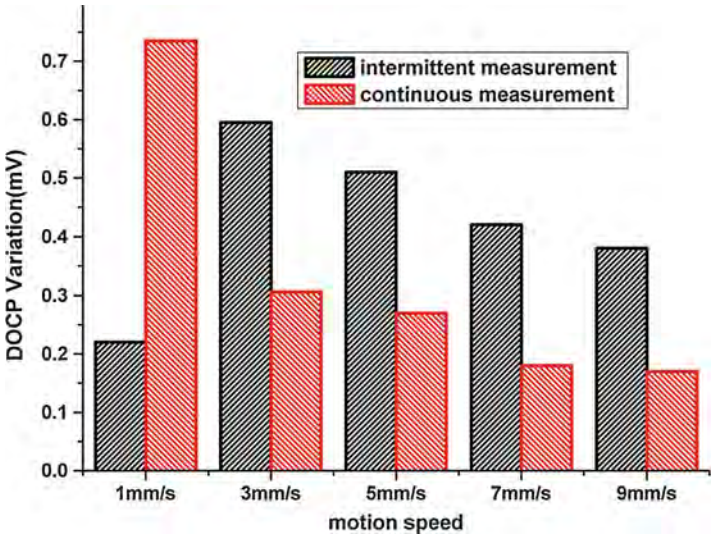

Fig. 18 Comparison of DOCP variations in continuous and intermittent motion measurement [33]

Obviously, in the IMM method, the charging and discharging processes can be corresponded easily with the static period and motion period of the electrode; hence, it is more convenient to analyze how the motion affects the potential of double layer than the CMM method. And Nernst-Planck equation and differential capacity of electrode can illustrate the mechanism of the electrode potential variation in the interface of the electrode/electrolyte. The Nernst-Planck equation blow relates the unidirectional x flux of a species j to diffusion, migration, and convection:

$$J_j(x) = -D_j \frac{\partial C_j(x)}{\partial x} - \frac{z_j F}{RT} D_j C_j \frac{\partial \phi(x)}{\partial x} + C_j v(x) \tag{3}$$

where $J_j(x)$ is a one-dimensional flux for species j at distance x from the electrode; D_j, z_j, and C_j are the diffusion coefficient, the charge, and the concentration for the species j, respectively; $v(x)$ is the rate with which a volume element moves in solution; $\partial C_j(x)/\partial x$ is the concentration gradient; and $\partial \phi(x)/\partial x$ is the potential gradient along the x-axis. Figure 19 shows schematic diagram of potential fluctuation with motion. Let ϕ_0 be the potential of zero charge of motion electrode and ϕ_1 be the equilibrium potential in static state; ϕ_A and ϕ_B are the peak and valley of potential of motion electrode, respectively; ϕ_n is the mean of potential, obviously, in period of t_n to t_{n+1}; relative motion-induced electrolyte convection dominates the mass transfer of interface electrolyte, residual charges of double layer of electrode/electrolyte interface which is stirred by contact friction between the electrode and membrane transfer into the bulk of electrolyte with mass transfer, hence the

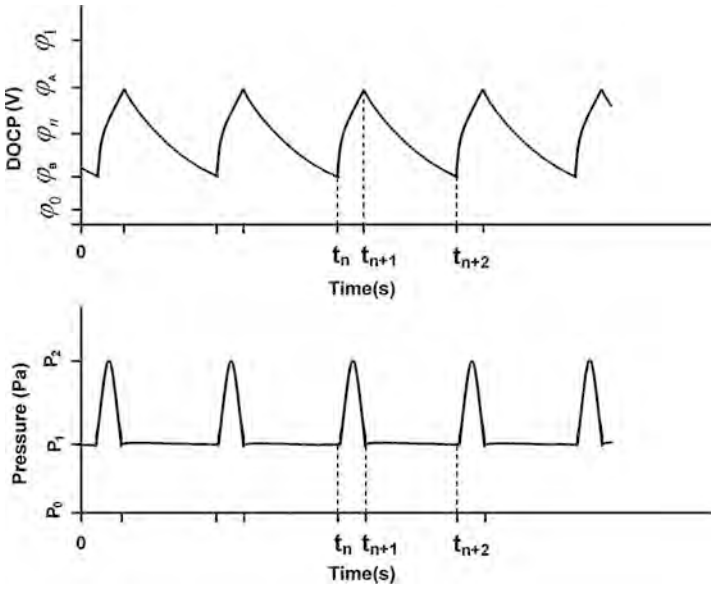

Fig. 19 Schematic of DOCP and pressure in intermittent motion measurement [33]

electrode potential drift toward the ϕ_0 due to decreasing of the charge density in double layer; this process can be regarded as discharging. In the period of t_{n+1} to t_{n+2}, the electrode is static, and the migration and diffusion dominate the mass transfer of interface electrolyte, the charged particles move along an electric field, and the species move against a concentration gradient, and the potential of the electrode drifts toward the ϕ_1 due to the increase of the charge density in double layer; this process can be regarded as charging. Hence, DOCP variation is actually closely correlative to residual charges and structure of electrode/electrolyte interface.

Figure 20 shows the lengths of motion track and DOCP variations are strongly linear correlative and correlation coefficients are over 0.92 from 3 to 9 mm/s. The motion radius was set at 1, 2, 3, or 4 mm, and the pressure was controlled about 1 kPa (fluctuation less 8 %), and the motion speed was set at 1, 3, 5, 7, or 9 mm/s. Subsequently, the motion radius was set at 2 mm, and the pressure was controlled at 0.3, 0.6, 0.9, or 1.2 kPa (fluctuation less 8 %), and the motion speed was set at 1, 3, 5, 7, or 9 mm/s; Fig. 21 shows the pressures and DOCP variations are also strongly linear correlative, and correlation coefficients are over 0.977 from 3 to 9 mm/s. The function between DOCP variation and pressure or length of motion track can be expressed in Eq. 4:

$$\begin{cases} y_p = a \cdot \overline{P} + b \\ y_s = c \cdot s + d \end{cases} \tag{4}$$

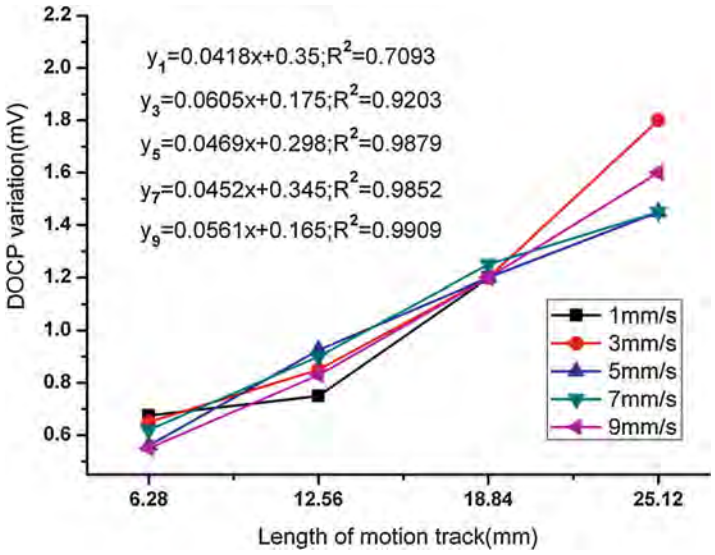

Fig. 20 Plot of DOCP variation and length of motion track [33]

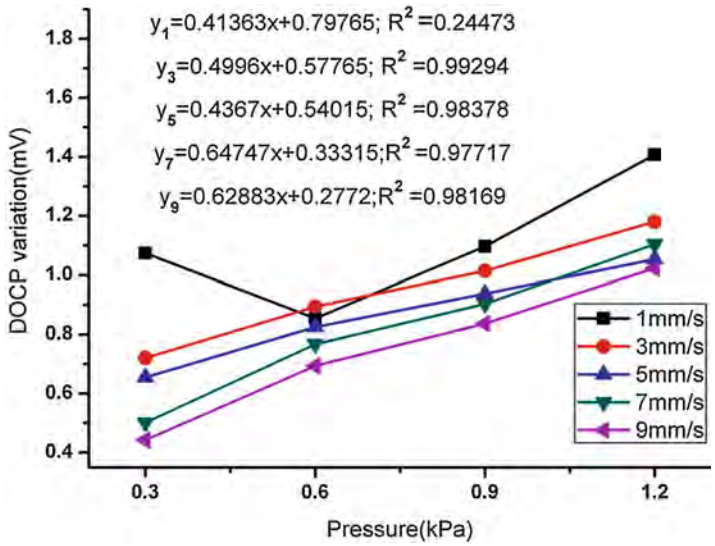

Fig. 21 Plot of DOCP variation and pressure [33]

where y_p and y_s represent the DOCP variation variance of pressure variation and length variation of motion track; in mV, $a = 0.0501 \pm 0.0094$ and $c = 0.5252 \pm 0.1169$ represent the slopes, and $c = 0.2646 \pm 0.09$ and $d = 0.5052 \pm 0.26$ represent the intercept.

Obviously, kinetic energy derived from relative motion between the electrode and membrane is the dominative factor for charge transfer and convection of species in the electrode/electrolyte interface. The function of the kinetic energy and controlled parameters can be expressed in Eq. 5.

$$W = \frac{\overline{P}}{A} \cdot \mu \cdot s \tag{5}$$

where W represents the kinetic energy, in J; $\overline{P}$ represents the mean of pressure, in Pa; μ represents the friction coefficient between electrode and membrane; and s represents the length of motion track, in mm.

Equations 4 and 5 show P or s is positive proportional to the W when the other variances are constant, and correlation of W and y_p and y_s can be expressed in Eq. 6:

$$W = \frac{\mu(y_p - b)(y_s - d)}{A \cdot \mathrm{a} \cdot c} \tag{6}$$

The DMS provides a powerful tool to construct models between motion artifact of electrode/electrolyte and some controlled parameters which can predict the motion artifact and help the design of the electrode and its integrated wearable garments.

Summary

In this chapter, these measurement methods and instruments were classified into two categories: (1) common methods and instruments and (2) special methods and instruments. Properties of dry biopotential electrodes were summed up from the following several aspects: electrical conductivity, electrochemical impedance spectra, contact impedance, appearance, crystal texture, open circuit potential (OCP), biopotential signal noise and dynamic open circuit potential (DOCP), and so on. Biopotential signals which directly were acquired and analyzed using DBPE on the human body or simulation devices were widely utilized for evaluating the performance of DBPE due to the consistency of measurement and terminal application. Impedance and equivalent circuit of electrode/electrolyte interface which can reveal the mechanism of biopotential transmission process are also popular methods for evaluating performance of dry biopotential electrode. With development of some microneedle array electrodes and new material electrodes, SEM images and XRD maps will be more and more utilized for characterizing the dry biopotential electrode in the future.

References

1. Coskey RJ (1977) Contact dermatitis caused by ECG electrode jelly. Arch Dermatol 113:839–840

2. Uter W, Schwanitz HJ (1996) Contact dermatitis from propylene glycol in ECG electrode gel. Contact Dermatitis 34:230–231
3. Webster JG (ed) (2010) Medical instrumentation: application and design, 4th edn. Wiley, Hoboken
4. Wiese SR, Anheier P, Connemara RD, Mollner AT, Neils TE, Kahn JA, Webster JG (2005) Electrocardiographic motion artifact versus electrode impedance. IEEE Trans Biomed Eng 1:136–139
5. Xu PJ, Zhang H, Tao XM (2008) Textile-structured electrodes for electrocardiogram. Text Prog 40:183–213
6. Meziane N, Webster JG, Attari M et al (2013) Dry electrodes for electrocardiography. Physiol Meas 34(9):R47–R69. doi:10.1088/0967-3334/34/9/R47
7. Padmadinata FZ, Veerhoek JJ, van Dijk GJA, Huijsing GH et al (1990) Microelectronic skin electrode. Sens Actuators B B1(1–6):491–494. doi:10.1016/0925-4005(90)80257-Z
8. Alizadeh-Taheri B, Smith RL, Knight RT (1996) An active, microfabricated, scalp electrode array for EEG recording. Sens Actuators A Phys A54(1–3):606–611. doi:10.1016/S0924-4247(97)80023-4
9. Wang Yu, Pei WeiHua, Guo Kai et al (2011) Dry electrode for the measurement of biopotential Signals. Sci China Inf Sci 54(11):2435–2442. doi: 10.1007/s11432-011-4354-0
10. Pedrosa P, Alves E, Barradas NP, Martin N, Fiedler P, Haueisen J, Vaz F, Fonseca C (2014) Electrochemical behaviour of nanocomposite Agx:TiN thin films for dry biopotential electrodes. Electrochimica Acta 125:48–57. http://dx.doi.org/10.1016/j.electacta.2014.01.082
11. Griss P, Tolvanen-Laakso HK, Merilainen P et al (2002) Characterization of micromachined spiked biopotential electrodes. IEEE Eng Med Biol Soc 49(6):597–604. doi:10.1109/TBME.2002.1001974
12. Yuanfang Chen, Weihua Pei, Sanyuan Chen, Xian Wu, Shanshan Zhao, Huan Wang, Hongda Chen (2013) Poly(3,4-ethylenedioxythiophene) (PEDOT) as interface material for improving electrochemical performance of microneedles array-based dry electrode. Sens Actuators B188:747–756
13. Dias NS, Carmo JP, da Ferreira SA et al (2010) New dry electrodes based on iridium oxide (IrO) For non-invasive biopotential recordings and stimulation. Sens Actuators A Phys 164(1–2):28–34. doi:10.1016/j.sna.2010.09.016
14. Nishimura S, Tomita Y, Horiuchi T (1992) Clinical application of an active electrode using an operational amplifier. IEEE Trans Biomed Eng 39(10):1096–1099. doi:10.1109/10.161342
15. Taheri BA, Knight RT, Smith RL (1994) A dry electrode for EEG recording. Electroencephalogr Clin Neurophysiol 90(5):376–383. doi:10.1016/0013-4694(94)90053-1
16. Fonseca C, Silva CJP, Martins RE et al (2007) A novel dry active electrode for EEG recording. IEEE Trans Biomed Eng 54(1):162–165. doi:10.1109/TBME.2006.884649
17. Geddes LA, Valentinuzzi ME (1973) Temporal changes in electrode impedance while recording the electrocardiogram with “dry” electrodes. Ann Biomed Eng 1(3):356–367. doi:10.1007/BF0240767
18. Fonseca C, Vaz F, Barbosa MA (2004) Electrochemical behaviour of titanium coated stainless steel by r.f. sputtering in synthetic sweat solutions for electrode applications. Corros Sci 46(12):3005–3018. doi:10.1016/j.corsci.2004.04.006
19. Salvo P, Raedt R, Carrette E (2012) A 3D printed dry electrode for ECG/EEG recording. Sens Actuators A Phys 174:96–102
20. Matteucci M, Carabalona R, Casella M, Di Fabrizio E, Gramatica F, Di Rienzo M, Snidero E, Gavioli L, Sancrotti M (2007) Micropatterned dry electrodes for brain–computer interface. Microelectronic Eng 84:1737–1740
21. Giulio R, Stephen D, Esteve F et al (2006) A dry electrophysiology electrode using CNT arrays. Sens Actuators A Phys 132(1):34–41. doi:10.1016/j.sna.2006.06.013
22. Salla K, Antti K, Mika S et al (2014) Liquid silicone rubber (LSR)-based dry bioelectrodes: the effect of surface micropillar structuring and silver coating on contact impedance. Sens Actuators A Phys 206:22–29. doi:10.1016/j.sna.2013.11.020

23. Mota AR, Duarte L, Rodrigues D et al (2013) Development of a quasi-dry electrode for EEG recording. Sens Actuators A Phys 199:310–317. doi:10.1016/j.sna.2013.06.013
24. Chen Chih-Yuan, Chang Chia-Lin, Chang Chih-Wei et al (2013) A low-power bio-potential acquisition system with flexible PDMS dry electrodes for portable ubiquitous health care applications. Sensors 13(3):3077–3091. doi: 10.3390/s130303077
25. Prats-Boluda G, Ye-Lin Y, Garcia-Breijo E, Ibanez J, Garcia-Casado J (2012) Active flexible concentric ring electrode for non-invasive surface bioelectrical recordings. Meas Sci Technol 23:125703. doi:10.1088/0957-0233/23/12/125703
26. Ju-Yeoul Baek, Jin-Hee An, Jong-Min Choi, Kwang-Suk Park, Sang-Hoon Lee (2008) Flexible polymeric dry electrodes for the long-term monitoring of ECG. Sens Actuators A 143:423–429. doi: 10.1016/j.sna.2007.11.019
27. Kang Tae-Ho, Merritt Carey R, Edward G et al (2008) Nonwoven fabric active electrodes for biopotential measurement during normal daily activity. IEEE Trans Biomed Eng 5 (1):188–195. doi: 10.1109/TBME.2007.910678
28. Merritt Carey R, Troy NH, Edward G (2009) Fabric-based active electrode design and fabrication for health monitoring clothing. IEEE Trans Inf Technol Biomed 13(2):274–280. doi:10.1109/TITB.2009.2012408
29. Oh Tong In, Yoon Sun, Kim ae Eui et al (2013) Nanofiber web textile dry electrodes for long-term bio potential recording. IEEE Trans Biomed Circuits Syst 7(2):204–211. doi: 10.1109/TBCAS.2012.2201154
30. Priniotakis G, Westbroek P, Van Langenhove L et al (2005) An experimental simulation of human body behaviour during sweat production measured at textile electrodes. Int J Cloth Sci Technol 17(3–4):232–241. doi:10.1108/09556220510590939
31. Westbroek P, Priniotakis G, Palovuori E, De Clerck K, Van Langenhove L, Kiekens P (2006) Quality control of textile electrodes by electrochemical impedance spectroscopy. Text Res J 2:152–159
32. Beckmann L, Neuhaus C, Medrano G, Jungbecher N, Walter M, Gries T, Leonhardt S (2010) Characterization of textile electrodes and conductors using standardized measurement setups. Physiol Meas 31:233–247
33. Hao Liu, Tao Xiaoming Xu Pengjun, Zhang Hui, Bai Ziqian (2013) A dynamic measurement system for evaluating dry bio-potential surface electrodes. Measurement 46(6):1903–1914
34. Liu Hao, Kang Weimin, Tao Xiaoming, Bai Ziqian, Xu Pengjun, Zhang Hui (2012) Performance evaluation of surface biopotential dry electrodes based on PSD and EIS. Int J Advancements Comput Technol (IJACT) 4(20):497–505
35. Pedrosa P, Machado D, Lopes C et al (2013) Nanocomposite Ag: TiN thin films for dry biopotential electrodes. Appl Surf Sci 285:40–48. doi:10.1016/j.apsusc.2013.07.154
36. Gondran C, Siebert E, Yacoub S, Novakov E (1996) Noise of surface bio-potential electrodes based on NASICON ceramic and Ag/AgCl. Med Biol Eng Comput 34(6):460–466. doi:10.1007/BF02523851
37. Gondran C, Siebert E, Fabry P (1995) Non-polarisable dry electrode based on NASICON ceramic. Med Biol Eng Comput 33(3):452–457. doi:10.1007/BF02510529

Applications of Terahertz Wave Technology in Smart Textiles

30

Dongxiao Yang

Contents

Introduction 810
Brief of Terahertz Wave Technology 811
Terahertz Wave Spectrum 811
Applications of Terahertz Wave Technology in Nature 813
Applications of Terahertz Wave Technology in Communication 813
Terahertz Spectroscopy Technique 814
Time-Domain Spectroscopy-Based Terahertz Pulsed System 815
Backward-Wave Oscillator-Based Continuous-Wave Terahertz System 816
Terahertz Spectroscopy for Textile Identification 817
Wool Textile Identification 818
Textile Fiber Identification 818
Spectra of Clothing Materials 821
Terahertz Spectroscopy for Textile Sensing 825
Terahertz Imaging Technique 827
Terahertz Imaging 828
Terahertz Tomography 830
Terahertz Imaging of Textiles 831
Textile Imaging 831
Textile Water Content 832
Terahertz Imaging Behind Textile Barriers 833
Target Detection Technique of Terahertz Textile Imaging 835
Target Detection Behind Textile Barriers 836
Terahertz Nondestructive Testing for Composites 837
Summary 839
References 840

D. Yang (✉)
Department of Information Science & Electronic Engineering, Zhejiang University, Hangzhou, China
e-mail: yangdx@zju.edu.cn

© Springer Science+Business Media Singapore 2015

X. Tao (ed.), *Handbook of Smart Textiles*,
DOI 10.1007/978-981-4451-45-1_41

Abstract

The terahertz radiation bridges the gap between microwave and infrared light, which consists of electromagnetic waves with frequencies ranging from 100 GHz to 1,000 GHz. There are approximately one-half of the total luminosity and most of the photons emitted since the Big Bang fall into the terahertz frequency region. Terahertz spectroscopy and imaging are two important techniques for the applications to textiles, which are described in this chapter. Some terahertz spectroscopy experimental systems were presented, such as time-domain spectroscopy-based terahertz pulsed system and backward-wave oscillator-based continuous-wave terahertz system. Several applications of the terahertz spectroscopy technique were reviewed to textile identification and sensing, such as textile fibers, textile materials, and wool textiles. Terahertz imaging of object behind textile barriers was demonstrated and the images were segmented for target detection. Terahertz imaging applications to textiles were also reviewed, such as measuring textile water content, detecting target behind textile barriers, and testing composites nondestructively.

Keywords

Terahertz wave • Textile • Composite • Material • Spectroscopy • Imaging • Identification • Sensing • Hidden object detecting • Nondestructive testing

Introduction

The microwave radiations are generally characterized by waves, because most microwave devices are comparable in size to the wavelength of the radiation. In contrast, the optical radiations are generally characterized by beams or rays, because the dimensions of the optical devices are much larger than the wavelength [1]. Science and technology are well-developed in both microwave spectral region including millimeter wave region, and optical spectral region as well as infrared spectral region, which are based on electronics and photonics, respectively. The terahertz radiation,whose frequencies ranging from 100 GHz to 1,000 GHz, bridges the gap between the microwave radiation and infrared radiation. Neither optical technique nor microwave technique is directly applicable in the terahertz frequency range since optical wavelengths and microwave wavelengths are too short and too long compared to terahertz field wavelengths, respectively. The terahertz spectral region is the gap of these technologically well-developed spectral regions. This "terahertz gap" is a relatively unexplored band of the electromagnetic spectrum. With the development of sufficiently terahertz sources and detectors, this gap has been filling, which will lead to unlock many new and potentially revolutionary technologies and applications to many areas of science and technology.

The principal application of terahertz techniques before 1990 was the research in astronomy, because astronomers can obtain a large amount of information of stars and intergalactic gases by detecting the terahertz radiations from outer space and

need not set up terahertz source system. Terahertz techniques were used for material characterization by physicists early in the 1990s, such as determining the carrier concentration and mobility of semiconductors. In the mid-1990s, some techniques for generation and detection of terahertz radiation had been accomplished with the help of different techniques, and corresponding terahertz sources and detectors had developed in the late 1990s.

Several commercial terahertz systems equipped with both source and detector were manufactured by electronic engineers in the beginning of the 21st century, such as terahertz time-domain spectroscopy based on terahertz generation and detection techniques which was developed using ultrafast laser pulses in the 1980s. The terahertz science and technology have been rapidly developed since 2000 with the help of commercial terahertz systems.The terahertz techniques have been used in many areas, such as spectrum analysis, imaging and tomography, wireless communication with high data rate, high-temperature superconductor characterization, protein folding measurement, molecular structure detection, cancer detection and genetic analysis, concealed object detection and target detection behind barriers, nondestructive testing and quality control, gas sensing and air pollution detection, and monitoring surrounding medium. But, unfortunately, the terahertz techniques are seldom used for textiles. Terahertz spectroscopy technique, terahertz imaging technique, and their applications to textiles were described in this chapter, which were developed by some research groups in the world.

Brief of Terahertz Wave Technology

Terahertz Wave Spectrum

The terahertz radiation bridges the gap between microwave and infrared light, which consists of electromagnetic waves with frequencies ranging from 0.1 to 10 THz (1 THz $= 10^{12}$ Hz) [2], as shown in Fig. 1.

This terahertz wavelength interval is the wavelength region between the top edge of the microwave to the boundary of the millimeter wave spectral region and the bottom edge of the optical spectrum corresponding to the boundary of the far-infrared spectral region [3]. The term terahertz is synonymous with the terms submillimeter and far infrared in the electromagnetic spectrum.

In order to get a better grasp of the terahertz frequency region, it is useful to mention that the frequency of 1 THz corresponds to a wavelength of 0.3 mm, to an electric field period of 1 ps, to a wave number of 33 cm^{-1} in common spectroscopic terms, to an equivalent blackbody temperature of 48 K, and to a photon energy of 4.1 meV (small energy compared to the thermal energy of 26 meV at room temperature).

The terahertz frequency region has drawn much attention because of the unique physical phenomena of the terahertz radiation. Two of these unique properties are listed below in brief.

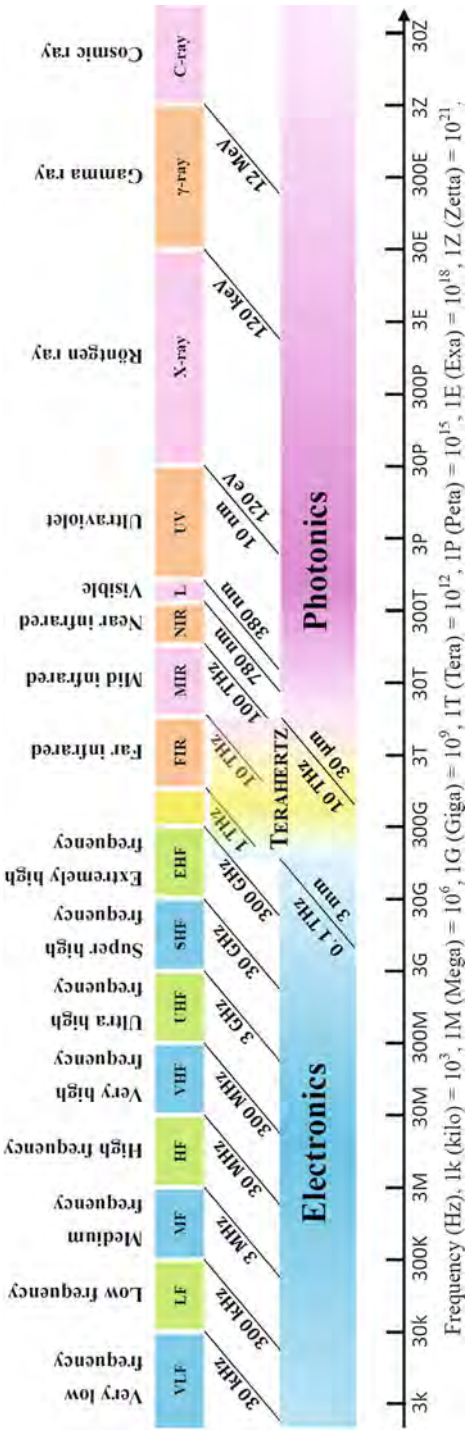

Fig. 1 Terahertz frequency region and the electromagnetic spectrum

Applications of Terahertz Wave Technology in Nature

The radiation in terahertz frequency region is a useful tool for discovery in cosmic astronomy on external platforms out of the Earth atmosphere [4]. According to the results from the NASA Cosmic Background Explorer Diffuse Infrared Background Experiment and the examination of the spectral energy distributions in observable galaxies, the corresponding frequencies of approximately one-half of the total luminosity and 98 % of the photons emitted since the Big Bang fall into the submillimeter wave and far-infrared light which lie in the terahertz frequency region [5]. The composition and origin of the solar system, the evolution of matter in our galaxy, and the star formation history of galaxies over cosmic timescales could be better to understand and easier to discover with the help of the diagnostic spectral signatures of ions, atoms, and molecules in the terahertz frequency region [6]. The second figure in Ref. [5] shows the radiated power spectra for interstellar dust, light, and heavy molecules, as well as a 30 K blackbody radiation curve and the 2.7 K cosmic background signature.

The relic radiations carry information about the cosmic space, galaxies, stars, and planet formation.

Terahertz fields interact strongly with the polar substances and penetrate the nonpolar substances. There are many distinct spectral peaks in the terahertz frequency region of the absorption spectra of many polar molecules [3]. The terahertz radiation is efficiently absorbed in air, except for some narrow windows, as shown in the fourth figure in Ref. [4].

This unique signature of molecules in the terahertz frequency region is very important in monitoring the surrounding medium, detecting air pollution, or gas sensing.

Applications of Terahertz Wave Technology in Communication

The demand for the ultrafast wireless communications is increasing due to more and more people using wireless networks. Nevertheless, it may be quite difficult to keep up with the needs of users without increasing the carrier frequencies for more spectral resources [7]. Since terahertz waves have huge bandwidth, terahertz wave technology has attracted a lot of attention in wireless communications for future with high data rates.

As shown in the fourth figure in Ref. [4], the Earth's atmosphere is an absorber of terahertz radiation in the water vapor strong absorption bands. Due to this limitation, the terahertz radiation is not suitable for long-distance terahertz transmission on the Earth. Notwithstanding, the long-distance terahertz transmission is less affected by adverse weather conditions like rain and fog in contrast to optical transmission [8]. Furthermore, terahertz waves are also suitable for high-altitude huge-data-capacity communications with high data rates, such as aircraft to satellite and between satellites. In spite of absorption in atmosphere, terahertz waves are suitable for short-distance huge-data-capacity communications with high data rates

on the Earth [7, 9]. There are some terahertz transmission windows with low atmospheric losses, such as the frequencies of 0.2–0.3 THz, as shown in the first figure and the fifth figure in Ref. [10]. The latter figure shows the specific attenuation from 0.001 to 0.35 THz at sea level for dry air and water vapor with a density of 7.5 g/m^3 [10].

A point-to-point terahertz wireless communication system with a carrier frequency of 0.2375 THz has been established for transmitting data over 20 m at a data rate of 100 Gb/s [8]. This data rate is much higher than those of the commercial wireless communication systems, such as 0.3 Gb/s for the fourth-generation (4G) wireless network over 3 km and uplink data rate of 1 Gb/s and downlink data rate of 10 Gb/s for the upcoming 5G wireless network. One of the applications for such a high-capacity terahertz wireless link will be the wireless link bridging a broad river in difficult-to-access terrain to provide high-speed internet access in remote and rural areas, as shown in the first figure in Ref. [8].

Because of considerable attenuation, terahertz waves are not very useful for long-distance communications. However, due to this strong absorption, the transmission spectra of many materials can provide information about the physical properties of the materials. In addition, an important feature of terahertz radiation is the ability to penetrate into nonmetallic materials and distinguish between them [4].

Terahertz Spectroscopy Technique

Terahertz spectroscopy is an important technique in terahertz science and technology, which is useful for both the fundamental research and the industrial application [11]. The former includes finding and understanding the mechanisms in physics, chemistry, and material science, and the latter includes imaging, sensing, material identification, safety-critical quality inspection, security scanning of concealed dangerous substances, contact-free testing, and nondestructive testing. Based on terahertz spectroscopy technique, simultaneously acquiring insight image of objects and identifying materials give terahertz technology a big advantage over other technologies. Terahertz radiation-related low-energy interactions can be studied by these waves in many materials to complement the knowledge of material behaviors obtained with far-infrared and Raman spectroscopy. One of the most attractive properties of terahertz waves is the ability to penetrate many materials, which can be used to analyze content through many types of packaging materials, such as paper, plastics, leather, and wood. Terahertz spectroscopy is a useful tool for characterizing vibrational modes, such as rotational, torsional, phonon, intramolecular, and intermolecular. Since the terahertz response is linked to the collective behavior of molecules in their environment and can distinguish polymorphism and chirality, terahertz spectroscopy has abilities different from conventional far-infrared spectroscopy.

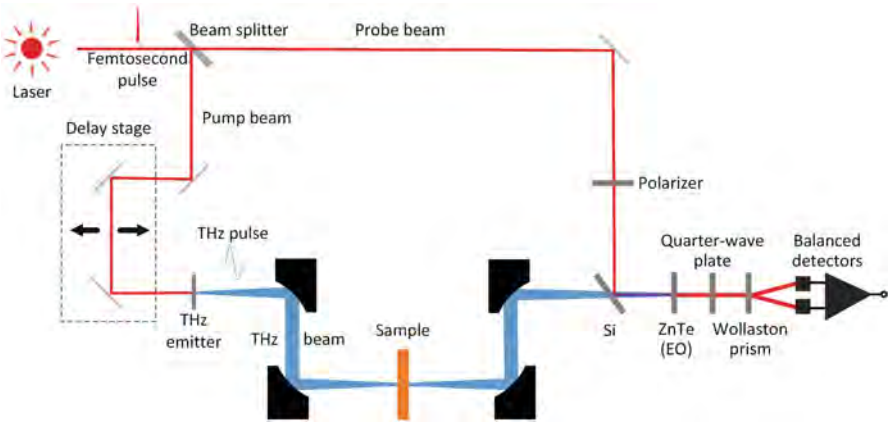

Fig. 2 Schematic diagram of a terahertz time-domain spectroscopy

Time-Domain Spectroscopy-Based Terahertz Pulsed System

Terahertz time-domain spectroscopy (THz-TDS) is a method for coherent generation and detection of broadband terahertz radiation using ultrafast laser pulse, as shown in Fig. 2.

A femtosecond pulse laser is used to generate ultrafast laser pulse beam at the wavelength around 1 μm. A beam splitter is used to split the laser beam of ultrafast pulse into a pump beam and a probe beam. The laser pump beam is used for generation of terahertz pulses. In order to generate terahertz pulses, a terahertz emitter is irradiated by the laser pump beam. The terahertz pulses are collimated and focused on the sample by a pair of 90° off-axis parabolic mirrors. A Si wafer is used to transmit the terahertz beam with low transmission loss and to reflect the laser probe beam with high reflectivity. The terahertz pulses carrying the sample information are collimated and focused on an electro-optic crystal (ZnTe) by another pair of 90° off-axis parabolic mirrors. Since the frequency in 10^{12} Hz of terahertz waves is much lower than that in 10^{15} Hz of the laser waves, the terahertz waves as a slow wave can modify the index ellipsoid of the electro-optic crystal for the laser wave transiently. The laser probe beam is used for detection of terahertz pulses and linearly polarized by a polarizer. The linearly polarized laser probe beam reflected by the Si wafer co-propagates with the terahertz pulse beam inside an electro-optic crystal where the diameter of the laser beam is smaller than that of the terahertz beam and is modulated by the refractive index change induced by the terahertz electric field as a slow wave. The phase change of the laser probe beam is converted to an intensity change by a quarter-wave plate and a Wollaston prism and detected by a pair of balanced photodiodes. A delay stage is used to scan optical delay line for offsetting the laser probe beam and the terahertz pulse beam excited by the laser pump beam. This allows the terahertz temporal profile to be iteratively sampled. This method for terahertz detection is called free-space electro-optic sampling.

Fig. 3 Photo of a terahertz time-domain spectroscopy experimental setup

Figure 3 is a photo of an experimental setup of a terahertz time-domain spectroscopy.

A polarization-sensitive terahertz time-domain spectroscopy can be used to measure anisotropic responses of materials and structures due to the applied factors, such as stress and magnetic fields [12]. A schematic diagram of a terahertz time-domain spectroscopic ellipsometry (THz-TDSE) is shown in the first figure in Ref. [13].

As shown in this figure, the terahertz time-domain system is similar as the terahertz time-domain system in Fig. 2. The differences between these two systems are that the terahertz time-domain spectroscopic ellipsometry is based on the photoconducting effect with photoconductive antennas for the generation and detection of terahertz pulses. Furthermore, the terahertz pulse beam is reflected from the sample, and a polarizer and an analyzer are placed in front of the sample and the detection antenna, respectively [12, 13].

The measurement of terahertz pulse with terahertz time-domain spectroscopy allows to extract some information, such as frequency-dependent amplitude and phase, which can be related to the physical properties of materials and devices [14]. Typical frequency resolution and output power of terahertz time-domain spectroscopy are several ten GHz and several μW [14, 15], respectively. Some terahertz time-domain spectroscopies have reached relatively high-frequency resolution of around 2 GHz [16, 17].

Backward-Wave Oscillator-Based Continuous-Wave Terahertz System

Backward-wave oscillator is a continuous-wave terahertz source [18] with highly monochromatic and powerful, spectrally bright and polarized, and finely frequency-tunable properties, such as a high-frequency resolution of 0.3 GHz [19] and high output power of 15 mW. Backward-wave oscillator-based continuous-wave terahertz system can be used to detect polarized spectra of physical properties of

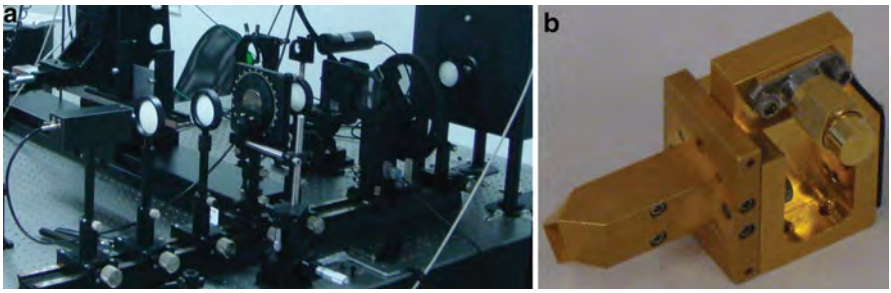

Fig. 4 Experimental setup for backward-wave oscillator-based continuous-wave terahertz system: (**a**) photo of continuous-wave terahertz system and (**b**) VDI detector equipped with antenna and amplifier

materials, such as real and imaginary refractive index, dielectric constant, and magnetic permeability. A backward-wave oscillator-based continuous-wave terahertz system is shown in Fig. 4a.

Monochromatic terahertz beam emitted from backward-wave oscillator with the frequency step of 0.3 GHz is attenuated to proper power for sample by a terahertz attenuator. After transmission through the attenuator, the terahertz beam is collimated or focused on the sample by two high-density polyethylene lenses. The transmitted beam from the sample is focused on a highly sensitive pyroelectric detector for detection by one or two high-density polyethylene lens. The response time of the pyroelectric detector is several milliseconds, which is a difficult-to-measure high-speed terahertz signal. One of the alternative terahertz detectors for high-speed signals is the VDI terahertz detector, as shown in Fig. 4b. When there is no electrostatic discharge (ESD) protection, the response rate of VDI terahertz detector can reach as high as 30 GHz. However, operating without ESD protection circuit is very risky. The VDI terahertz detector is composed of zero-bias terahertz detector with ESD protection circuit, terahertz coupling waveguide antenna, and output amplifier. Typical response rate of VDI terahertz detector is 250 kHz. The response rate of VDI terahertz detector with ESD protection can be raised to GHz by improving the ESD protection circuit, waveguide, and amplifier, such as the response rate of 3 GHz for VDI WR3.4ZBD zero biased detector equipped with MJ-LNA-0005-0300 amplifier and WR3.4DH antenna.

Terahertz Spectroscopy for Textile Identification

Because of the low attenuation of most textile materials in the terahertz frequency region, terahertz spectroscopy has some advantages in examining textiles, such as easy measurement, accurate determination, and effective identification. Since chemical additives in textile fibers, such as dyes, have multiple strong absorption peaks in near- and mid-infrared frequency region, the measured responses of textile materials by other spectroscopic techniques are obscure and disturbed in high levels [16].

Terahertz spectroscopy can be performed in real-time and in-line monitoring systems for textiles and can provide an effective, reliable, rapid, contact-free, and nondestructive testing for the textile identification and combating fraud.

Wool Textile Identification

According to different optical properties of the textile composed of wool of different animal origins, the type of wool can be identified and the textile counterfeiting can be combated. In order to accurately determine woolen textile composition, J. Molloy et al. [16, 20] have measured 15 wool fabric samples in two fabric orientations: with the warp parallel to the terahertz wave polarization (designated pa) and perpendicular to it (designated pe) with terahertz time-domain spectroscopy, as shown in the first figure in Ref. [16]. The second figure in this reference shows the transmission spectra of two samples in two fabric orientations.

Table 1 lists the wool fabrics, properties, and the distinct loss peaks and their frequencies and widths in the transmission spectra below the frequency of 2 THz for 15 wool fabric samples of different yarns with different compositions and structures [16].

Since the majority of the fabrics are dichroic, the transmission spectra are depended on the beam polarizations. The spectra of some woolen textile samples have different loss peaks with different peak frequency and profile for the two orientations, as listed in Table 1. The differences of measured loss peaks are to be ascribed to diffraction and scattering caused by the weave pattern, because the fiber thickness and the weave periodicity are both of the order of 50–1,000 μm which are comparable to terahertz wavelength.

According to the measurements, the terahertz transmission spectra have different spectral features for different types of woolen textile, which may be used for the textile identification. Fabrics with similar appearance and tactile texture have clearly distinct spectral features for different yarn compositions, which may be used for textile identification and fraud prevention.

Textile Fiber Identification

The terahertz spectral features of materials are mainly from both intramolecular and intermolecular forces. The material spectra in terahertz frequency region are sensitive to skeletal vibrations and weak intermolecular forces, such as hydrogen bond and van der Waals force. The remarkable loss peaks in the spectra of the interstellar dust, light, heavy molecules, and gas molecules in Earth atmosphere are shown in the second figure in Ref. [5] and the fourth figure in Ref. [4]. Remarkable peaks in the material spectra give the opportunity to fully investigate the internal vibration modes of textile fibers. In order to identify the ramie fiber and bamboo fiber with similar chemical composition, C. Yan et al. [15] have simulated and measured their terahertz spectra with terahertz time-domain spectroscopy.

Table 1 Wool fabrics, properties, distinct loss peak frequencies, and peak widths in two fabric orientations [16]

Fabric	Yarn	Composition	Weave	Threads (cm)	Peak (THz), in orientation		Peak width, FWHM (THz)	
				warp/weft	pe	pa	pe	pa
A1	8.0 Nm	LW/LB	Herringbone	12/12	/	1.37 ± 0.02	/	0.35 ± 0.04
A2	9.0 Nm	LW/NB	Herringbone	12/12	1.16 ± 0.02	1.33 ± 0.02	0.30 ± 0.03	0.42 ± 0.04
B1	3.6/2.0 Nm	100 % W	Herringbone	6/8	/	/	/	/
B2	3.6 Nm	100 % W	Herringbone	8/8	/	/	/	/
C1	3.8 Nm	100 % MW	Plain	7/7	/	/	/	/
C2	3.6 Nm	100 % W	Plain	7/7	1.095 ± 0.005	1.035 ± 0.005	0.15 ± 0.02	0.15 ± 0.02
D	3.6 Nm	100 % W	Plain	6/6	1.24 ± 0.02	0.845 ± 0.005	0.30 ± 0.03	0.13 ± 0.01
E	3.6 Nm	100 % W	Herringbone	7/7	1.025 ± 0.005	0.88 ± 0.02	0.12 ± 0.02	0.15 ± 0.02
F1	3.6 Nm	100 % W	2/2 twill	9/9	/	/	/	/
F2	Unknown	60 % WB	2/2 twill	9/9	/	1.35 ± 0.02	/	0.30 ± 0.03
G1	13.5 Nm	50 % C–50 % LN	Knit	12/12	1.46 ± 0.02	1.315 ± 0.005	0.35 ± 0.04	0.30 ± 0.03
G2	6 Nm 2-ply	68 % M–29 % C–3 % S	Knit	10/12	/	1.89 ± 0.02	/	0.35 ± 0.04
K1	14 Nm	100 % C	Knit	5/7	1.345 ± 0.005	1.280 ± 0.005	0.30 ± 0.03	0.30 ± 0.03
K2	8.5 Nm	70 % M–30 % C	Knit	7/9	1.56 ± 0.01	1.47 ± 0.01	0.35 ± 0.03	0.32 ± 0.03
L	3.4 Nm	70 % M–30 % C	Knit	3/5	/	1.135 ± 0.005	/	0.27 ± 0.02

Note: Nm = km/kg, *LW* lamb's wool, *LB* lycra blend, *NB* nylon blend, *W* wool, *MW* merino wool, *WB* wool blend, *C* cashmere, *LN* linen, *M* merino, *S* silk

Bamboo fiber is deemed to possess many advantages over other fibers, such as pleasant tactile sensations, ultraviolet protective ability, and antimicrobial activity. The bamboo fiber is easily counterfeited by ramie fiber on the market due to the similar physicochemical properties, which increases the complexity of discrimination [15]. Fourier transform infrared (FTIR) spectroscopy has the potential for providing rich information on molecular activities, such as vibrational and torsional modes arising from corresponding chemical bonds or functional groups. The FTIR spectra of ramie fiber and bamboo fiber in two wave number regimes of 4,000–400 cm^{-1} corresponding to the frequency regime of 12–120 THz and 200–30 cm^{-1} to 0.9–6.0 THz have almost the same features, such as the absorption features in terms of both attenuation and frequency, as shown in the third figure in Ref. [15].

Since the FTIR spectra of ramie fiber and bamboo fiber indicate that these two fibers consist of the same chemical constitution, it is a challenge to distinguish them from each other effectively by this approach. There are two remarkable peaks at the wave numbers of 175 and 125 cm^{-1} corresponding to the frequencies of 5.25 and 3.75 THz of both ramie fiber and bamboo fiber, which are defined as vibrations characterizing the crystalline structure of monosaccharides in cellulosic fibers.

The rich spectral information in the wave number regime below 100 cm^{-1} corresponding to the frequencies below 3 THz, which can be difficult to be obtained from the FTIR spectra, is useful to distinguish ramie fiber and bamboo fiber. Terahertz time-domain spectroscopy could provide this important spectral information of ramie fiber and bamboo fiber and can be used to identify them with relatively high resolution. The typical resolutions of Fourier transform infrared spectroscopy with the frequency regime of 12–120 THz, terahertz time-domain spectroscopy with 0.1–3.0 THz, and backward-wave oscillator-based continuous-wave terahertz system with 0.1–1.0 THz are 120, 40, and 0.3 GHz, respectively. The sixth figure to the eighth figure in Ref. [15] show the terahertz absorption spectra of ramie fiber and bamboo fiber measured with terahertz time-domain spectroscopy.

In contrast to the results obtained from FTIR spectroscopy, the distinct differences among terahertz absorption spectra of ramie fiber and bamboo fiber can be observed in these three figures in Ref. [15]. This indicates that terahertz spectroscopy is an acceptable tool to distinguish ramie fibers from bamboo fibers. According to the reference spectra in the sixth figure and the seventh figure in Ref. [15], the terahertz wave attenuation of ramie fiber or bamboo fiber is small. It is obvious that the intensity of terahertz wave above the frequency of 2.5 THz is very low; the effective terahertz absorption spectra should be below the frequency of 2.5 THz. The terahertz spectra of ramie fiber and bamboo fiber below the frequency of 1.0 THz present almost the same features. According to these three figures in Ref. [15], the considerable frequency range is 1.0–2.5 THz, where there are seven peaks and nine peaks in the terahertz absorption spectra of ramie fiber and bamboo fiber, respectively. The absorption peaks of ramie fiber are unambiguously observed at the frequencies of 1.09, 1.35, 1.5, 1.75, 1.94, 2.13, and 2.4 THz, especially the prominent spectral features at 1.94 and 2.4 THz. The absorption peaks of bamboo fiber are at the frequencies of 1.18, 1.31, 1.47, 1.62, 1.75, 1.92,

2.19, 2.35, and 2.5 THz. The strongest absorption of bamboo fibers is located at 1.92 THz. A gradual rise of the absorption baseline with increasing frequency results from nonresonant wave scattered at the samples. The ramie fiber and bamboo fiber can be readily distinguished according to the peak number and relative absorption level of their absorption spectra.

C. Yan et al. [15] have also simulated the ground-state structures and harmonic vibrational frequencies of the ramie fiber and bamboo fiber samples based on the density function theory. The experimental absorption peaks at 1.92 THz for bamboo fiber and 1.94 THz for ramie fiber may be attributed to the spectral feature of glucose at 1.95 THz obtained by the simulation, which originates from the torsional deformation of hexatomic ring of β-D-glucose. The spectral features observed at 2.19 THz for bamboo fiber and 2.13 THz for ramie fiber in experimental spectra are associated with the skeletal vibration. The spectral features at low frequencies in experimental spectra of ramie fiber and bamboo fiber may be attributed to the intermolecular hydrogen function.

Spectra of Clothing Materials

Terahertz radiation can easily penetrate through many clothing materials, such as typical household and military fabrics, and is nonionizing due to its relatively low frequencies. Terahertz active imaging is safe for humans compared to the ultraviolet radiation and X-ray and is suitable for security imaging, inspection, and nondestructive identification of contraband concealed beneath clothing, such as ceramic knife, plastic explosive, and illicit drug.

Several common clothing materials were measured by I. Dunayevskiy et al. [21]. Three independent systems, which are backward-wave oscillator-based continuous-wave terahertz system, Fourier transform infrared spectroscopy, and far-infrared gas laser, were used to measure the terahertz transmission spectra of 14 fabrics. The samples measured were the materials of heavy cotton shirt, denim shorts, knit sweater, wool jacket, polyester blouse, polyester-blend pants, rayon blouse, nylon jacket, suede shorts, silk blouse, Cordura (baggage material), canvas, Kevlar, and velvet, as listed in Table 2 [21].

All of the materials are regular clothing materials except ballistic Kevlar. The measured terahertz transmission spectra of 14 fabrics are shown in the first figure and the second figure in Ref. [21].

According to these two figures, the majority of the materials exhibit a single-layer transmission around 90 % in the frequency range from 130 to 170 GHz measured with backward-wave oscillator-based terahertz system. Nevertheless, the single-layer transmission measurements of Cordura and ballistic Kevlar are lower than 80 % in this frequency range. Most of the materials except Kevlar, Cordura, and knit materials have a transmission of higher than 50 % in the frequency range from 300 to 500 GHz measured with Fourier transform infrared spectroscopy. The transmission measurement results of silk, polyester, and nylon are higher than 50 % in the frequency range from 300 to 1,200 GHz. Nylon and

Table 2 Sample properties of 14 fabrics [21]

Sample description	Material composition	Thickness (mm)
Heavy cotton shirt	100 % cotton	1.50
Denim shorts	100 % cotton	0.90
Knit sweater	75 % cotton, 25 % acrylic	2.40
Wool jacket	100 % wool	0.65
Polyester blouse	100 % polyester	0.20
Polyester-blend pants	70 % polyester, 25 % rayon, 5 % spandex	1.00
Rayon blouse	100 % rayon	0.35
Nylon jacket	100 % nylon	0.12
Suede shorts	100 % pig suede	0.90
Silk blouse	100 % silk	0.30
Cordura (baggage material)	Nylon with rubberized backing	0.81
Canvas	100 % cotton	0.65
Kevlar	100 % ballistic Kevlar	0.65
Velvet	Velvet	1.20

polyester are the better transmission fabrics among these materials. The far-infrared gas laser used in the measurement irradiates terahertz waves at five frequencies of 566, 694, 715, 763, and 965 GHz, as shown in these two figures in Ref. [21].

The reflection spectra of knit, wool, rayon, nylon, Cordura, and velvet have been measured with Fourier transform infrared spectroscopy, as shown in the third figure in Ref. [21].

The reflectivities of the materials measured are low in the frequency region of 0.3–1.2 THz. Even if nylon and Cordura have higher reflectivity, the reflectivity around 10 % was measured for nylon and Cordura due to the very low level of the reflected signal.

J. E. Bjarnason et al. [22] have studied the terahertz wave transmission through cloth samples from eight types of fabrics used for garment and baggage, as listed in Table 3.

The transmission spectra through eight samples and the microphotographs of six samples are shown in the second figure and the third figure in Ref. [22], respectively. At the low-frequency end, all samples approach near-unity transmission in normalized terahertz transmission spectra, as shown on the left side of the second figure in Ref. [22]. As the frequency increases, each transmission decreases and is highly dependent on sample. The higher rate of increasing opacity occurs in the leather and wool samples, and the lower rate occurs in the nylon, rayon, and silk. There is a 9 dB discrepancy between wool and rayon at the frequency of 1 THz due to the different features of the samples in thickness and frequency-dependent absorption. The transmission spectra from 38 to 100 THz of the samples have been also measured with FTIR spectroscopy by J. E. Bjarnason et al. [22], as shown on the right side of the second figure in Ref. [22].

Transmission spectra and reflection spectra of fabrics are different for the same materials with different spinning and weaving structures due to wave scattering and

Table 3 Sample properties of eight fabrics [22]

Fabric	Morphology	Origin	Chemical basis	Thickness (mm)	Density (kg/m^3)	−3 dB frequency (THz)	Attenuation at 1 THz (dB)
Wool	Nap	Animal	Protein (α-keratin)	2.2	214	0.35	11.0
Linen	Woven	Plant (flax)	Structural polysaccharide (cellulose)	1.1	509	0.35	8.0
Leather	Compound polymer	Animal (mammal)	Fibrous protein (keratin)	0.75	813	0.40	10.0
Denim	Woven	Plant (cotton)	Structural polysaccharide (cellulose)	0.96	490	0.50	6.5
Naugahyde	Homogeneous polymer	Synthetic	Polyvinyl chloride	0.65	800	0.70	5.5
Silk	Woven	Animal (insect)	Polypeptide (fibroin)	0.36	256	1.0	3.0
Nylon	Knit	Synthetic	Polyamide	0.19	379	1.0	3.0
Rayon	Woven	Synthetic	Structural polysaccharide (cellulose)	0.15	733	>1.0	2.5

diffraction, such as shown in the first figure and the second figure in Ref. [16], respectively. É. Hérault et al. [23] have measured the influences of terahertz wave diffraction by the yarn network in common cloths with terahertz time-domain spectroscopy. The structure of most fabrics is an almost periodic network of interlaced yarns or threads with the periodicity around the terahertz wavelength, where the scattering and diffraction can be induced. The linen threads have a mean diameter of 375 μm (±30 %) that corresponds to the frequency of 0.8 THz, and the stitches are almost rectangular with an average size around 785 μm × 585 μm. The second figure and the third figure in Ref. [23] show the comparison between experimental (dots or triangles) and simulation (line) diffraction of linen threads along two orientations.

The linen fabric is described as a perfect two-dimensional periodic structure with the cell size of 800 μm × 645 μm and the thread diameter of 375 μm in simulation.

The second figure in Ref. [23] shows experimental (dots or triangles) and simulation (line) first-order diffraction angle of linen threads irradiated by terahertz wave with the polarization field oriented along the x-axis and y-axis, respectively. The measured result coincides with the simulated result. The normalized terahertz wave diffraction fields along two orientations obtained from measurement and simulation at three frequencies of 0.6, 0.75, and 1 THz in different detection angles are shown in the third figure in Ref. [23], respectively. The measured and simulated relations between the normalize terahertz wave diffraction field and the detection angle are shown in this figure, which is shifted vertically by one at each frequency in each orientation for the sake of legibility. É. Hérault et al. [23] have also observed the terahertz diffraction results of other fabrics, such as fleece, denim, and T-shirts, with different thread size and weaving tightness. The strength distribution of diffraction differs for each fabric and is concentrated at some specific angles. The additional diffracted signal could drastically disturb the signal detected or the image captured. A way to overcome the diffraction disturbance would be to perform experimental system with the terahertz wave having short coherent length or incoherent terahertz wave.

Besides diffraction effect in measuring spectra of clothing materials, isotropic scattering problem should be considered. The interaction of terahertz radiation with irregularly structured materials is an essential part of the design of terahertz sensing and imaging systems. Scattering within materials and structures, such as fibers in clothing and granules in powder, may produce false signatures in spectra or images. J. R. Fletcher et al. [24] have studied propagation of terahertz radiation through random structures and proposed a model describing the terahertz wave propagation through inhomogeneous materials. The optical properties of a randomly structured layer are analyzed with the help of a phase distribution function. The measured and simulated transmission losses of Harris tweed, fleece, and shirt are shown in the tenth figure in Ref. [24], respectively.

According to this figure, the agreement between the experimental data and the simulation predictions is satisfactory. This analytical approach can deliver predictions instantaneously and could be of great value for real surveillance systems operating at terahertz frequencies.

Terahertz Spectroscopy for Textile Sensing

Metamaterials are periodic artificial fabricated structures whose element is composed of a metallic resonator held together in a dielectric. Metamaterials have the ability to control the propagation of electromagnetic waves; in other words, they can tailor electromagnetic responses. Textiles are flexible, easily manufactured, and with similar structures to metamaterials. Moreover, the fabric periodicities are in the order of the terahertz wavelength. Textile metamaterials with metallic fibers allow strong coupling to terahertz radiation and tailor the wave responses which can be used to realize many applications, such as perfect absorbers and strain sensors. M. Ghebrebrhan et al. [25] have simulated and measured a textile metamaterial created by adding metal fibers directly into the polymer yarns. The microscope images and computational cells of woven and knitted fabrics are shown in the first figure in Ref. [25].

The yarn for producing the samples of woven fabrics and knitted fabrics consists of an iCon fiber with the resistance of 130 Ω/m twisted with a 72-filament polypropylene fiber at a rate of 0.5 twists per inch, as shown in this figure. Since the spacing of the iCon fibers is different in the warp direction corresponding to vertically oriented and weft direction corresponding to horizontally oriented, the spectra should be polarization dependent. The periodicities of the woven fabric sample in the warp and the weft directions are approximately 1.894 and 0.446 mm, respectively, as shown in this figure. As indicated in wool textile identification by J. Molloy et al. [16, 20] that the spectra of woolen textile samples have different frequencies of loss peaks for different polarizations due to the fabric orientations, fabrics with conducting fibers may increase this polarization dependence. Furthermore, the iCon conducting fibers within the fabric samples establish the periodic metallic resonators in the fabric metamaterials with the element of the split ring resonator. Strong response of resonant peaks can be induced by the textile metamaterials. The resonant frequencies can be tuned by varying the geometric parameters of the fabric samples. The inductance L of the resonator element increases with the crimp height due to the increasing area of the loop, and the capacitance C of the resonator element increases with decreasing the period of the weft fibers. The resonant frequency of $(LC)^{-1/2}$ can be directly controlled by the weft period. The longer the weft period is, the higher the resonant frequency becomes [25]. The tuning properties of the resonant frequencies of the textile metamaterial samples can be used to measure the strain in real time.

The response of fabrics can be attributed to resonances created by the iCon fibers. The periods of these fabric samples are roughly 0.5–1.5 mm with the polypropylene fiber diameter around 0.4 mm. The properties of the textile metamaterial samples have been measured by M. Ghebrebrhan et al., as shown in the fourth figure in Ref. [25].

As shown in this figure, the transmission spectra of a linearly polarized beam are measured for different polarization angles from 0° to 90° with the increment of 15° with respect to direction B in the first figure in Ref. [25]. Strong oscillations can be observed from the transmission spectrum of the woven fabric sample irradiated by the terahertz waves polarized along the warp fibers, while much weaker oscillations

for the orthogonal polarization, as shown in the left part of the fourth figure in Ref. [25]. The transmission spectra of the knitted fabric sample have been measured, as shown in the right part of the fourth figure in Ref. [25]. The oscillation properties of the woven fabric metamaterial sample depend more heavily on the polarization of the incident terahertz waves than those of the knitted fabric metamaterial sample.

H. Tao et al. [26] have fabricated and characterized metamaterial structures sprayed directly on the premade silk films with micro-fabricated stencils by a shadow mask evaporation technique. The responses of the metamaterial silk composites were measured with terahertz time-domain spectroscopy. The refractive index of the silk films was measured to be $n = 1.91 + i0.12$ with the spectroscopy. Three samples with different metamaterial element structures of the split ring resonators were measured at normal incidence of terahertz beam. The size of metamaterial elements of sample 1 is 50 μm × 50 μm, and sample 2 has the same size of metamaterial element as sample 3 which is 100 μm × 100 μm. The transmission spectra of 80-μm-thick pure silk film and these three samples are shown in the second figure in Ref. [26].

The black solid lines and the red dash lines show the experimentally measured and simulated transmission spectra, respectively. The resonant frequencies of the samples are 0.85, 0.7, and 0.4 THz, respectively.

According to the features of the resonant frequencies, such as the transmission spectra in the fourth figure in Ref. [25] and the second figure in Ref. [26], the textile metamaterials can be used to sense the properties of materials and structures. J. Li et al. have demonstrated a fourfold symmetric flexible metamaterial which can be used for dual-axis strain sensing, as shown in the second figure and the third figure in Ref. [27].

The metamaterial elements composed of 200-nm-thick gold layer with the structure shown in these figures are encapsulated between the 100 μm- and 10-μm-thick polymer substrate and superstrate. The resonant features of this flexible metamaterial are sensitive to strain along the polarization orientation of the incident terahertz waves and insensitive to strain perpendicular to the polarization orientation, as shown in the second figure in Ref. [27]. It can be used to measure large dual-axis strain of flexible materials and structures, such as textiles, as shown in the second figure and the third figure in Ref. [27].

S. Wietzke et al. have determined the dielectric spectra and the glass transition features of polymers with the terahertz time-domain spectroscopy, as shown in the fifth figure and the seventh figure in Ref. [28].

At room temperature, refractive index and extinction coefficient spectra of the nonpolar polymers of high-density polyethylene (HDPE) with the thickness at room temperature of 1,952 μm, cyclic olefin copolymer (COC) with 2,003 μm, linear low-density polyethylene (LLDPE) with 1,930 μm, low-density polyethylene (LDPE) with 3,981 μm, polypropylene (PP) with 2,062 μm, polymethylpentene (PMP) with 953 μm, and polytetrafluorethylene (PTFE) with 518 μm have been measured with the terahertz time-domain spectroscopy, as shown in the upper left part and the lower left part of the fifth figure in Ref. [28], respectively. Similar spectra of the polar polymers of polyamide 6 (PA6) with 501 μm,

polyoxymethylene (POM) with 965 μm, polyvinyl chloride (PVC) with 1,467 μm, polycarbonate (PC) with 517 μm, polymethyl methacrylate (PMMA) with 573 μm, and polyvinylidene fluoride (PVDF) with 511 μm have been also measured with the terahertz time-domain spectroscopy, as shown in the upper right part and the lower right part of the fifth figure in Ref. [28], respectively.

The glass transition temperatures T_g of the polymers of polypentylene heptanoate (PPH) with 462 μm, PA6, POM, PC, PVDF, PMMA, HDPE, and LLDPE have measured to be 220, 286, 203, 422, 222, 367, 231, and 218 K with the terahertz time-domain spectroscopy, respectively. The illustration for the concept of the free volume of the glass transition and the temperature-dependent refractive indexes of the polymers of PA6, POM, PPH, PC, PVDF, PMMA, HDPE, and LLDPE are shown in the seventh figure in Ref. [28].

H. Suzuki, et al. [29] have measured the terahertz spectra of nylon-6 in various solid states, and detected a phase transition (known as the "Brill transition") and a glass transition, in addition to a new anomaly in the amorphous phase. The measured absorption spectra of three kinds of nylon-6 samples are shown in the first figure in Ref. [29].

There are two broad peaks at 3 and 9 THz for spectrum of sample a in amorphous phase. Two of the broad peaks at 3 and 9 THz for spectrum of sample b containing the γ form are sharper than those of sample a. There are other three sharp peaks at 13.5, 15.5, and 17.5 THz corresponding to the formation of a crystalline phase in the spectrum of sample b. The peaks for the spectrum of sample c containing the α-form are sharper than those of sample a and sample b. Furthermore, there are two additional peaks at 2.0 and 6.5 THz in the spectrum of sample c.

The Brill transition of the α-form with $T_B \approx 160$ °C was investigated by monitoring the temperature variation heating from 26 °C to 202 °C of the terahertz spectra for sample c, as shown in the second figure in Ref. [29].

According to this figure, there are remarkable changes of both the absorbance peak and its second-derivative intensity for sample c at 6.6 THz, in which the absorbance decreases and its second-derivative intensity increases with the temperature increasing, respectively. According to the third figure in Ref. [29], there is an inflection point at the temperature of 160 °C for sample c at the frequency of 6.6 THz. This inflection point is caused by the Brill transition of the α-form. This temperature is called Brill transition temperature. For sample a, three inflection points can be observed at the temperatures of 60 °C, 110 °C, and 190 °C at the frequency of 6.6 THz. The inflection points at 60 °C and 190 °C correspond to the glass transition ($T_g \approx 54$ °C) and crystallization to the pseudohexagonal form, respectively.

Terahertz Imaging Technique

Due to the abilities to penetrate many materials and to characterize intramolecular and intermolecular vibrational modes, simultaneously acquiring insight image with terahertz imaging system and identifying materials with terahertz spectroscopy give terahertz technology a big advantage over other technologies. There are many

applications of the terahertz imaging technique, such as biological and biomedical imaging in life science and medical diagnosis, nondestructive and contact-free testing in industry, safety-critical quality inspection of food products, and security scanning of concealed dangerous substances in public life.

Terahertz Imaging

The terahertz imaging techniques were a natural development of terahertz spectroscopy techniques. Many terahertz imaging systems need external terahertz source, which are active imaging systems. Conventional terahertz spectroscopies can generate highly precise spectroscopic information at a single point of a sample. In a terahertz imaging system based on a terahertz time-domain spectroscopy, as shown in Fig. 2, the object is placed in the focal plane of the terahertz beam and is moved step by step in the x-y plane for image acquisition. The terahertz intensity can be recorded at each point by the scanning. Both spatial distribution of the object and the material spectra can be obtained with this terahertz imaging system. Nevertheless, the two-dimensional terahertz image is obtained pixel by pixel with long duration of time for completion. Backward-wave oscillator-based terahertz continuous-wave imaging system can be demonstrated by the terahertz continuous-wave spectroscopy with the similar scanning method. However, the material spectra cannot be obtained with this terahertz imaging system.

In order to reduce the time of image acquisition, two-dimensional terahertz field distribution is converted into a two-dimensional optical intensity by an electro-optic crystal, and a CCD camera is used to record two-dimensional optical intensity. M. Yamashita et al. have established a terahertz spectroscopic imaging system based on the two-dimensional electro-optic sampling technique, as shown in the first figure in Ref. [30].

This terahertz spectroscopic imaging system has the ability to shorten the data acquisition time dramatically in comparison with the scanning type of the imaging system based on the terahertz time-domain spectroscopy. There are some differences between the terahertz spectroscopic imaging system in this figure and the terahertz time-domain spectroscopy in Fig. 2. The laser pump beam is collimated and broadened to the diameter around the electrode gap of the photoconductive antenna by a pair of optical lenses. A high-voltage-biased large-aperture photoconductive antenna with the electrode gap of 25 mm is used as the terahertz emitter. The terahertz pulse beam irradiates the sample area to be imaged and is focused on an electro-optic crystal by a pair of polyethylene lenses. The diameter of terahertz pulse beam on the electro-optic crystal approximates the diameter of the polarized laser probe beam which is collimated and broadened by another pair of optical lenses. The polarized laser probe beam co-propagates with the terahertz pulse beam with the sample spatial distribution information inside the electro-optic crystal and is modulated by the refractive index change induced by the terahertz electric field with spatial distribution of the sample. An analyzer that is perpendicular to the polarizer is placed behind the electro-optic crystal to form the optical intensity with

the same spatial distribution as the sample. This spatial distribution of the optical intensity is recorded by a CCD camera (384 × 288 pixels, 20 frames/s). Terahertz images in the frequency domain with the frequency resolution of 22.5 GHz are obtained at each pixel in the terahertz time-domain images [30].

The spatial resolution of a conventional imaging system is diffraction limited to the scale of half a wavelength. The resolution can be improved with near-field approach, in which the resolution is no longer determined by the wavelength but by the aperture size [31]. However, the terahertz transmission energy through the aperture of size d decreases by d^3 due to much of the radiation reflected at the aperture plane. Significantly deteriorating the signal-to-noise ratio of the image for small apertures is the major limitation to aperture-based methods [32]. In order to break the diffraction limit and to enhance the spatial resolution of terahertz imaging system, H. T. Chen et al. [33] have demonstrated the application of scanning near-field microscopy techniques for terahertz imaging with aperture-based technique, tip-based technique, and focused beam method. A sharp metallic tip is placed above the structure, as shown in the first figure in Ref. [33].

The incident terahertz beam is focused onto the surface of the sample to the diffraction limit around the terahertz wavelength λ. The dipole moment is induced by the terahertz radiation in the tip and in the region below the sample surface and leads to scattering and absorption of part of the terahertz radiation. The terahertz transmission is detected. A spatial resolution of 150 nm has been achieved, which corresponds to about λ/1,000. The terahertz imaging and its spatial resolution can be achieved with the scanning tip in two dimensions.

J. H. Son [34] has reviewed the principle and applications of terahertz molecular imaging. S. J. Oh et al. [35] have achieved dramatically enhanced sensitivity compared with that of conventional terahertz imaging. The sample was located at the focus of the terahertz pulse beam from a reflection-mode terahertz time-domain spectroscopic system and was irradiated by a continuous-wave infrared laser beam with the wavelength of 800 nm, as shown in the second figure and the fourth figure in Ref. [35].

The sample temperature rose due to the hyperthermia effect induced by the surface plasmon resonance on the nanoparticle surface of gold nano-rods under infrared laser irradiation. The terahertz reflection signal increased with the sample temperature. Peak reflection changes of the terahertz signals from live cancer cells with and without nanoparticles of gold nano-rods under continuous-wave infrared laser irradiation are shown in the fourth figure in Ref. [35]. In the differential mode, the terahertz signal from the cancer cells with nanoparticles of gold nano-rods was 30 times higher than that from the cancer cells without nanoparticles of gold nano-rods [35].

Even though the terahertz radiation is nonionizing, it is important to consider the problems of the terahertz radiation on human body in ethical, legal, and other issues. With the help of the terahertz radiation from natural sources, such as humans, passive imaging systems can be developed. ThruVision company has produced commercially available passive terahertz imaging system which captures naturally occurring terahertz radiation and processes it to create images that can reveal objects beneath a person's clothing or in a bag, such as T4000 and T5000, as shown in the third figure and the fourth figure in Ref. [36].

The applications of passive terahertz imaging systems are security, anti-terrorism, and law enforcement. The passive terahertz imaging systems can detect concealed weapons and solid or liquid explosives at airports, public transport facilities, military installations, and other high-security sites. A. Svetlitza et al. [37] have presented a low-cost measurement setup for terahertz applications based on a blackbody source.

Terahertz Tomography

Terahertz tomography can be used to capture the internal inspection of any object transparent or translucent to terahertz waves. A series of reflected broadband terahertz pulses at refractive index discontinuities inside the object can be collected with time delay. The internal discontinuities of the object to a refractive index profile in the propagation direction could be mapped. A full three-dimensional map of the object can be obtained by raster scanning. If the received signals are line integrals along the direct paths, the Fourier-slice theorem can be applied [32].

Terahertz computed tomography (THz-CT) has the same principle as X-ray CT. A CT scan emits a plane wave and records a series of waves that are transmitted through or reflected from a target in two-dimensional plane, which is repeated at different angles around the object.

M. Jewariya et al. have demonstrated fast three-dimensional transmission terahertz computed tomography using real-time line projection of intense terahertz beam, as shown in the first figure in Ref. [38].

As shown in this figure, the sample is irradiated by the line-focused terahertz pulses along the y-axis and is scanned along the x-axis as well as rotated to capture the three-dimensional image. The three-dimensional reconstruction can be performed with a standard reconstruction algorithm [38, 39].

If the object inhomogeneities are comparable in size to the propagation wavelength, the diffractions along the path must be considered in terahertz tomography. Terahertz diffraction tomography (THz-DT) is used in this situation. The terahertz diffraction tomography is used to determine the spatial distribution of a sample's refractive index by the measurement of the diffracted terahertz field. In diffraction tomography, a terahertz probe beam interacts with a sample to capture the three-dimensional image of the sample with the waves scattered and diffracted inside the sample. This is the main difference with computed tomography which generally uses the amplitude signal transmitted through the sample. Terahertz diffraction tomography is a useful tool for capturing the complex samples with fine structures in which the diffraction effects dominate the measurements. S. Wang et al. have established terahertz diffraction tomography by using a femtosecond laser, generating terahertz radiation by optical rectification in a ZnTe crystal and detecting the signal with a CCD camera, as shown in the 11th figure in Ref. [40].

There are some differences between the terahertz diffraction tomography system in this figure and the terahertz time-domain spectroscopy in Fig. 2. The laser pump beam irradiated on the emitter of a ZnTe crystal is broadened by an optical lens.

The terahertz pulse beam from the emitter is collimated and broadened by a 90° off-axis parabolic mirrors and irradiates on the sample area to be image. A tin-doped indium dioxide (ITO) slab is used to transmit the laser probe beam with low transmission loss and to reflect the terahertz beam with high reflectivity. The diameter of terahertz pulse beam on the electro-optic crystal of another ZnTe approximates the diameter of the polarized laser probe beam which is collimated and broadened by another optical lens. The polarized laser probe beam co-propagates with the scattered terahertz pulse beam with the scattered sample spatial distribution information inside the electro-optic crystal is modulated by the refractive index change induced by the terahertz electric field spatial distribution. An analyzer that is perpendicular to the polarizer is placed behind the electro-optic crystal to form the optical intensity with the same spatial distribution as the sample. The third optical lens is used to focus the laser probe beam whose optical intensity has the same spatial distribution as the sample onto the CCD camera. The object can be rotated along the y-axis and moved along the x- or z-axes to scan three-dimensional terahertz image with the internal structure [40]. The application of terahertz diffraction tomography is able to provide the refractive index distribution inside the object. Terahertz diffraction tomography often provides poor reconstructed images due to the problem of reconstruction algorithms and signal interpretation. Nevertheless, the image acquisition speed of terahertz diffraction tomography is relatively faster than terahertz computed tomography.

Terahertz Imaging of Textiles

Textile Imaging

A. Redo-Sanchez et al. have reviewed terahertz technology readiness assessment and applications, such as to inspect defects in the thread of a textiles sample that cannot be seen optically, as shown as in the fifth figure in Ref. [41].

It is obvious from this figure that the invisible defects in the thread of textiles sample can be inspected with terahertz imaging technique.

Terahertz technology, including the terahertz imaging and terahertz spectroscopy, could become a complement to X-ray technique for the noninvasive investigation of relics, such as ancient mummies. X-ray technique is a useful tool to obtain the image with the internal features of the mummified body. The terahertz imaging and terahertz spectroscopy are noncontact, noninvasive, and nondestructive manners, which can be used to probe the layers of bandages constituting the mummy wrappings and to obtain the image and the material composition. Furthermore, terahertz radiation is safe for the operators and the objects measured. Due to the terahertz wave reflection by any discontinuity inside the materials, terahertz imaging can indicate the sequence of fabric layers and the eventual objects placed in between the bandages. Terahertz imaging can be used to probe the fabric layers surrounding Egyptian mummies. Terahertz waves can penetrate into nonmetallic materials and its reflection depends on the refractive index of materials at the interface, such as the interface textiles and the air and the interface between textiles.

K. Fukunaga et al. have measured the Kharushere mummy which lived during Egypt's 22nd dynasty (circa 945–712 BC) with terahertz time-domain reflection imaging, as shown as in the first figure in Ref. [42]. The upper left part of the second figure in Ref. [42] shows the terahertz image of the bandage layers and the mummy shroud penetrated of area 1 in the first figure in Ref. [42]. It is evident that the information of the bandage layers under the mummy shroud, such as the sequence and the number, can be obtained from the terahertz cross-sectional image scanned along the line of a-a', as shown in the lower left part of the second figure in Ref. [42].

The terahertz time-domain waveform along the middle point A of the line a-a' is shown in the right part of the second figure in Ref. [42]. According to this waveform, the first two peaks due to the reflections from the diagonal strap circling the mummy from the left shoulder to the right hip indicate that the diagonal strap consists of two fabric layers, and the two packets of four reflection peaks of the waveform are reflected from eight layers of the shroud. These two packets with four reflection peaks each are similar and indicate that the first four bandage layers are followed by another set of four layers with a gap in between. It is difficult to obtain the information of these eight bandage layers with the CT-scanning image, as shown in the right part of the first figure in Ref. [42].

According to the terahertz image in the c-c line, more than 10 layers of fabrics are observed in area 2 in the first figure in Ref. [42], as shown in the third figure in Ref. [42].

The terahertz images along the b-b' line and c-c' line of area 2 in the first figure in Ref. [42] indicate the intense reflections coming from the layers underneath the surface, such as reflected under the surface around 20 mm, as shown in the third figure in Ref. [42].

Textile Water Content

There several techniques of directly measuring the percentage of water incorporated in materials and structures, such as the Karl Fischer titration, chemometric method, and thermogravimetric analysis. But all of the above methods do not provide any spatially resolved information [43]. Furthermore, the samples for these destructive and time-consuming measurements should be specially prepared. The terahertz imaging and spectroscopy techniques are ideal tools for a nondestructive, contactless determination of the water content due to the sensitivity of terahertz radiation to water and the ability to penetrate many objects. C. Joerdens et al. [43] have used terahertz time-domain spectroscopy to study the sorption of water into polyamide and wood plastic composite. A model for the dielectric properties depending on the water content was developed and experimentally verified [43]. The dielectric properties of polyamide 6 and wood plastic composite samples are measured with a terahertz time-domain spectroscopy, as shown in the fifth figure and the sixth figure in Ref. [43], respectively.

The absorption coefficient of each sample linearly increases with water content, as shown in the right parts both the figures. The refractive index increases with

water content with a slightly nonlinear behavior, as shown in the left parts both the figures. The measured values coincide with the simulation results. C. Joerdens et al. [43] have also measured the sample image of wood plastic composite based on the terahertz time-domain spectroscopy. One-half of a piece of wood plastic composite filled with 60 wt% of wood fibers was immersed in distilled water for 4 days, as shown in the left part of the seventh figure in Ref. [43]. The water incorporated in wood plastic composite can be obviously seen in the terahertz image of the sample, as shown in the right part of the seventh figure in Ref. [43].

H. B. Zhang et al. [44] have proposed a quantitative method to obtain water content of thin materials with terahertz imaging. The fourth figure in Ref. [44] shows the visible image of a dry sample of cotton cloth [44]. The terahertz images of this piece of cotton cloth with different water contents and the corresponding water content images have been obtained and processed, as shown in the sixth figure and the tenth figure in Ref. [44], respectively. Both the water content and its spatial distribution can be measured with the terahertz time-domain spectroscopy.

Terahertz Imaging Behind Textile Barriers

D. Cleary [45] has reported brainstorming the way to an imaging revolution and a news focus on terahertz wave with the ability to see through clothes and paper in *Science* magazine, as shown in the news focus figure in Ref. [45].

Similar image of a metallic object hidden behind a paper, as shown in Fig. 5, can be captured by a simple terahertz continuous-wave imaging system based on backward-wave oscillator shown in Fig. 6.

K. B. Cooper et al. [46] have used NASA Jet Propulsion Laboratory's (JPL's) 675 GHz imaging radar with the ability to penetrate cloths to obtain the terahertz images of person-borne concealed objects. This terahertz imaging radar is an effective tool for rapidly searching targets from a long standoff range with high three-dimensional spatial resolution. Several images obtained by this terahertz imaging radar are shown in the eighth figure and the ninth figure in Ref. [46].

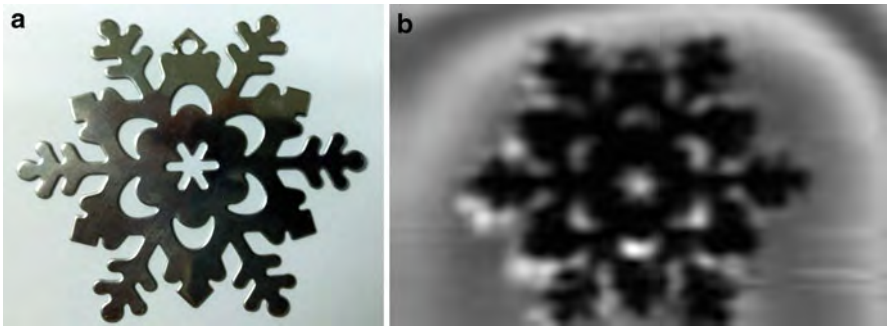

Fig. 5 Terahertz image of object hidden behind paper: (**a**) visible image of object and (**b**) terahertz image of hidden object

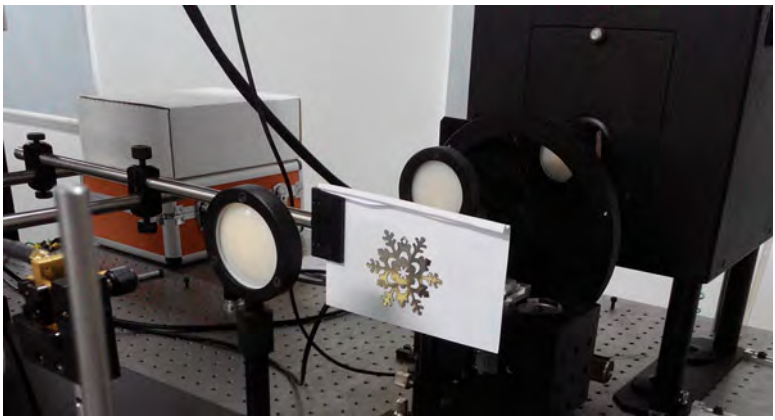

Fig. 6 Imaging system based on backward-wave oscillator

The terahertz radar images in the eighth figure in Ref. [46] were obtained with the frame rate of 5 s/frame. The upper left part of this figure shows the image of a back surface of a person who wore a jacket and stood in 25-m distance from the radar. The curves in the upper right part of this figure show the terahertz radar spectra around two selected points on the image in the upper left part of this figure, respectively. The images in the lower left part and lower right part of this figure show terahertz radar imagery revealing the hidden metallic handgun and mock bomb belt containing ceramic shrapnel and explosive stimulant. The ninth figure in Ref. [46] shows six images with 66×58 (azimuth $\times$ elevation) $= 3{,}828$ pixels of a 1 Hz frame rate video captured with the terahertz imaging radar. The person wore a cotton Polartec jacket and concealed three 1-in PVC pipes. There is no evidence of three 1-in PVC pipes concealed by a cotton Polartec jacket if the target is not in the terahertz field of view, as shown in the upper left part of this figure. The pipes can be seen when the subject moves into the radar field of view, as shown as in the upper right part of this figure. The image in the left-center part of this figure is the terahertz radar image for the back of the person without hidden objects detected. The person turned to face the terahertz radar again and moved his right arm to unzip his jacket. The right hand and the edge of the PVC pipes can be seen from the terahertz image, as shown in the right-center part of this figure. Both the terahertz image and optical image of PVC pipes without jacket for concealing can be seen, as shown in the lower left part and the lower right part of this figure, respectively.

J. C. Chen et al. have constructed a terahertz sensing system based on an interferometer, as shown in the first figure in Ref. [47].

Terahertz wave at the frequency of 0.6 THz was used to penetrate a barrier and to measure the vibrations behind the barrier. A white cotton T-shirt, a black wool vest, and a blue plastic recycling bin were used as barriers. A speaker behind a barrier was driven with only a single sine wave at the frequency of 100 Hz. The terahertz system was able to record the signal of 100 Hz tone with good fidelity, as shown in the fourth figure in Ref. [47].

Target Detection Technique of Terahertz Textile Imaging

There are terahertz image speckles due to the interference between different randomly wavelets scattered from the surface and the interface of the clothing layer. The fifth figure in Ref. [48] shows the speckles of several terahertz images through a layer of clothing using a broadband time-domain spectroscopy system with the frequency range from 200 GHz to 1 THz and a narrow terahertz wave with the frequency spectrum of 430 ± 3 GHz, respectively.

The speckles can be suppressed in the terahertz broadband image based on terahertz time-domain spectroscopy. Since the coherence length of the terahertz wave generated by terahertz time-domain spectroscopy is much shorter than that generated by backward-wave oscillator, the wavelets which travel paths of different length cannot interfere with one another.

In order to distinguish the target from the background, it is necessary to reduce the disturbance caused by irregular interference fringes. The disturbance of fringes can be reduced by measuring techniques, such as modulating the bias voltage of the supply for backward-wave oscillator. The frequency versus bias voltage of the backward-wave oscillator is shown in Fig. 7. The bias voltage of the backward-wave oscillator in Fig. 6 was modulated by the triangular voltage wave with the amplitude of several ten voltages at the frequency of 2.5 kHz. There is a fluctuation within 5 GHz due to the modulation at the terahertz frequency of 338 GHz from the backward-wave oscillator. This frequency fluctuation of the backward-wave oscillator can reduce the fringes in terahertz images, as shown in Fig. 8. However, this frequency of the backward-wave oscillator causes a fluctuation of terahertz irradiation power.

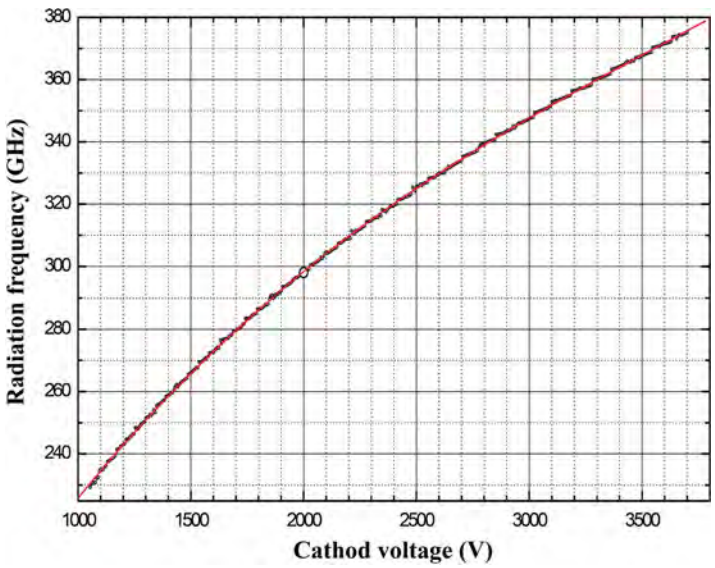

Fig. 7 Frequency versus bias voltage of the backward-wave oscillator in Fig. 6

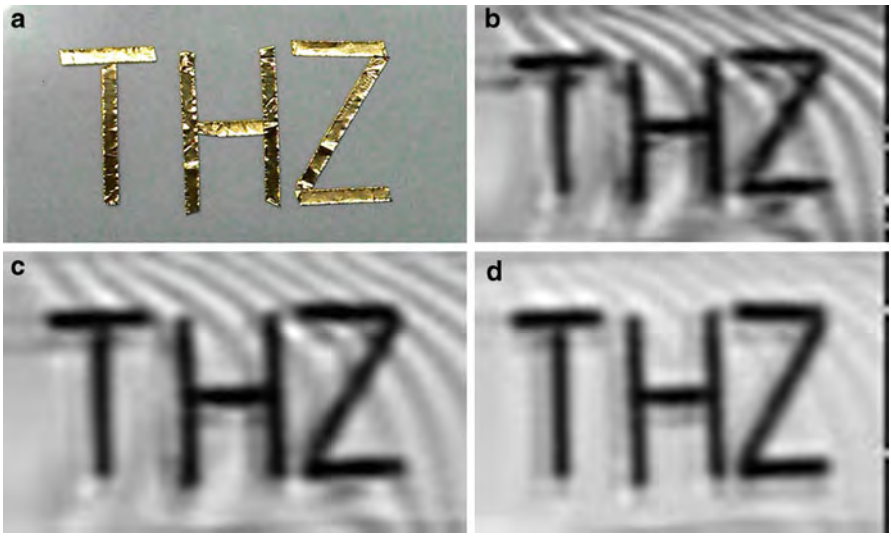

Fig. 8 Visible and terahertz images of word "THz" written with conducting glue with different modulations: (**a**) visible image, (**b**) without modulation, (**c**) modulation with 10 V, and (**d**) modulation with 20 V

According to Fig. 8b, there are interference fringes due to the coherence of the terahertz wave generated by the backward-wave oscillator. The fringes are obviously decreased through the frequency fluctuation of the terahertz wave induced by the modulation of the bias voltage for the backward-wave oscillator.

With the help of segmentation algorithms, the disturbance of fringes can also be drastically reduced. Fuzzy C-means is an efficient algorithm for data clustering. The clustering algorithm based on the fuzzy local information C-means (FLICM), with improved the membership function therein according to the properties of terahertz images, was used for the target detection from terahertz images, as shown in Fig. 9.

Target Detection Behind Textile Barriers

A simple experiment with a backward-wave oscillator-based terahertz continuous-wave imaging system is helpful in order to obtain a brief view on capturing image of an object hidden behind textile barriers and detecting the target from the image, as shown in Fig. 10a. Each sample was prepared in sandwich structure, which a surgical blade fixed on a paper is covered by a fabric, as shown in Fig. 10b, c.

The first sample is covered by 100 % cotton in the experiment, as shown in the left image in Fig. 11a. The terahertz image and the segmented image are shown in the center and right images in Fig. 11a, respectively. The fabrics of 100 % flax, blending fabric of 70 % cotton and 30 % flax, polyester, and polyurethane, were

Fig. 9 Segmentation of terahertz image of a blade hidden behind paper with improved FLICM algorithm: (**a**) visible image, (**b**) hidden terahertz image, and (**c**) after segmentation

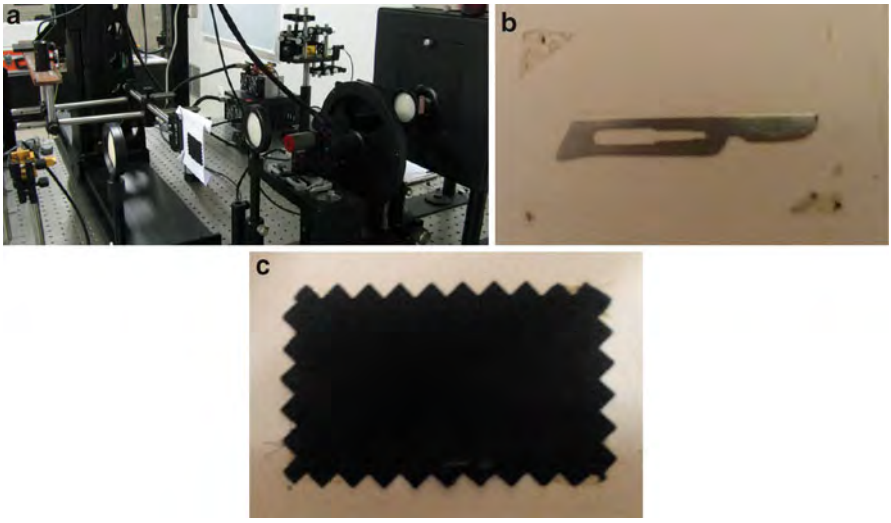

Fig. 10 Backward-wave oscillator-based terahertz imaging system and sample with sandwich structure: (**a**) experimentalsetup, (**b**) a surgical blade fixed on paper, and (**c**) covered by a fabric

used to prepare other four samples. The corresponding images are shown in Fig. 11b–e, respectively.

Terahertz imaging technique makes it possible to acquire images of dangerous substances concealed underneath clothing. X. L. Shen et al. have automatically detected and segmented concealed objects, as shown in the eighth figure and the 11th figure in Ref. [49].

Terahertz Nondestructive Testing for Composites

Because both the terahertz spectroscopy technique and the terahertz imaging can detect the properties inside many objects in a noncontact and noninvasive manner, terahertz nondestructive testing based on terahertz spectroscopy technique and terahertz imaging technique is a useful technique for structures and materials,

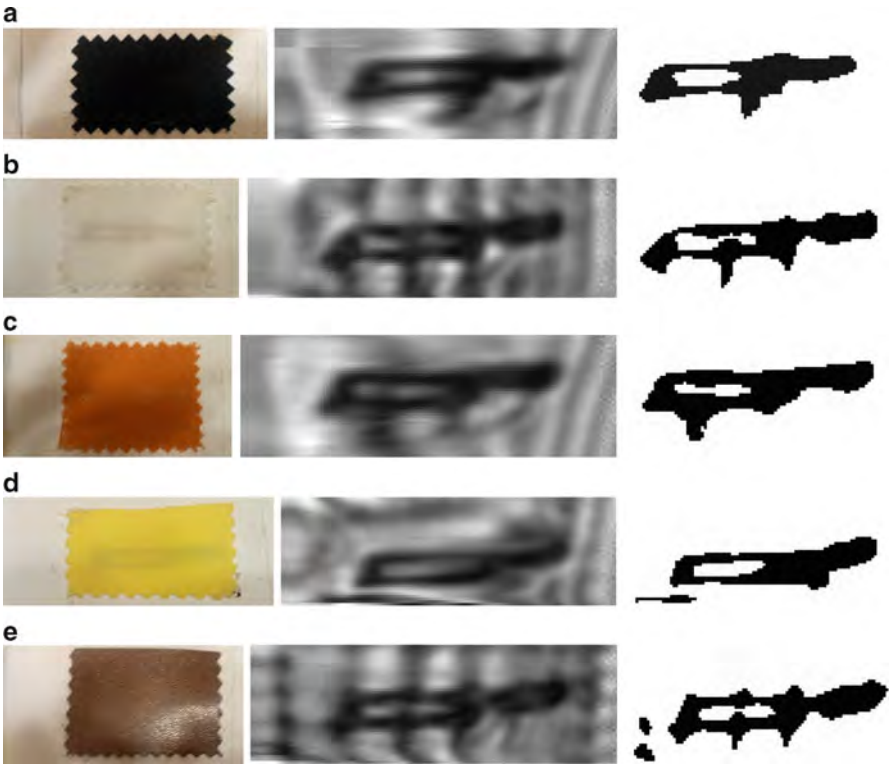

Fig. 11 Optical image of samples, terahertz images, and terahertz images after segmentation of target hidden behind five fabrics: (**a**) dark blue 100 % cotton with the thickness of 0.3 mm, (**b**) white 100 % flax with the thickness of 0.3 mm, (**c**) orange blending fabric of 70 % cotton and 30 % flax with the thickness of 0.4mm, (**d**) yellow polyester with the thickness of 0.3mm, and (**e**) brown polyurethane with the thickness of 0.7 mm

especially for composites. Besides, both the spectra and the images of objects can be obtained with one time-domain spectroscopy-based terahertz pulsed system.

The heat from jet engines, which may cause damage to the aircraft structures, should be considered in designing and maintaining aircraft. C. Stoik et al. [50] have used terahertz time-domain spectroscopy to measure the material properties of the aircraft composites in order to determine the changes of the properties and to find various damages of the composites according to terahertz images and terahertz spectra. Five composite samples with different features were used by C. Stoik et al., as shown in the third figure in Ref. [50].

Sample 1 is for thickness calibration in the measurement; sample 2 was burned at 440 °C for 4 min; sample 3 is another burn sample which was burned at 430 °C for 6 min in an area and at 425 °C for 20 min in another area; and samples 4 and 5 are mechanical stress sample and hidden defect sample, respectively. Terahertz images for one burned area on composite sample 2 and two burned areas on composite sample 3 are shown in the sixth figure in Ref. [50].

Terahertz images for the interesting areas on composite sample 4 and 5 are shown in the eighth figure and the ninth figure in Ref. [50], respectively.

It is obvious that the image properties of the burned areas, the area with mechanical stress, and the area with hidden defect are significantly different from other areas on the samples.

N. Palka et al. [51] have detected the internal structure of an ultrahigh-molecular-weight polyethylene composite material with a terahertz time-domain spectroscopy. Due to the very hard and resistant properties, this composite can used to manufacture personal armors. This multilayer composite structure was investigated and its properties were measured, as shown in the eighth figure and the ninth figure in Ref. [51].

A terahertz image of the structure indicates the regions with defects, as shown in the darker regions in the left part of the eighth figure in Ref. [51]. The terahertz time-domain pulse signal along the z-axis at point A in the defect regions was measured, as shown in the right part of the eighth figure in Ref. [51]. The first pulse and the third pulse in the waveform at point A are the reflected signals from the front surface and the back surface of the composite. The distance between the pulses corresponds to the composite thickness of 3.3 mm. The second pulse corresponds to the defect position along the z-axis.

The terahertz images of the horizontal and vertical B scans along the lines marked in left part of the eighth figure in Ref. [51] are shown in the images in the ninth figure in Ref. [51], respectively. The detailed three-dimensional terahertz images of the 3.3-mm-thick composite sample with all 74 layers and some defects inside the composite are clearly seen from the ninth figure in Ref. [51].

Summary

In this chapter, terahertz spectroscopy technique, terahertz imaging technique, and their applications to textiles were presented. First, a brief description of terahertz wave technology was given, including the properties of terahertz wave spectrum, applications of terahertz wave techniques to cosmic astronomy and wireless communication with high data rate. Then two important terahertz spectroscopy techniques, terahertz time-domain spectroscopy-based terahertz pulsed system and backward-wave oscillator-based continuous-wave terahertz system, were described. And then several applications of terahertz spectroscopy technique to textiles were reviewed, such as wool textile identification, textile fiber identification, and textile sensing. On the other hand, terahertz imaging technique was also described, including terahertz imaging based on two-dimensional electro-optic sampling technique, terahertz imaging based on near-field microscopy technique, terahertz computed tomography, and terahertz diffraction tomography. In the last section, several applications of terahertz imaging technique to textiles were reviewed, such as inspection of textile material for defects in the threads, detection of textile water content, imaging of object hidden behind textile barriers, target detection of textile imaging, and nondestructive testing for composites. With the

help of the abilities of terahertz wave techniques to penetrate many materials and to characterize intramolecular and intermolecular vibrational modes, simultaneously acquiring insight image with terahertz imaging system and identifying materials with terahertz spectroscopy give terahertz technology a big advantage over other technologies.

This work is supported by the National Natural Science Foundation of China under Grant No. 60971059. The author gratefully acknowledges all the authors of the cited references in this chapter for their research achievements, figures and tables. Without their information, this chapter would not have been possible.

References

1. Grischkowsky DR, Mittleman D (2003) Introduction. In: Mittleman D (ed) Sensing with terahertz radiation. Springer, Berlin, pp 1–7
2. Rao L, Yang DX, Zhang L et al (2012) Design and experimental verification of terahertz wideband filter based on double-layered metal hole arrays. Appl Optics 51:912–916
3. DragomanD DM (2004) Terahertz fields and applications. Prog Quantum Electron 28:1–66
4. Sizov F, Rogalski A (2010) THz detectors. Prog Quantum Electron 34:278–347
5. Siegel PH (2002) Terahertz technology. IEEE Trans Microwave Theory Tech 50:910–928
6. Kulesa C (2011) Terahertz spectroscopy for astronomy: from comets to cosmology. IEEE Trans Terahertz SciTechnol 1:232–240
7. Song H, Nagatsuma T (2011) Present and future of terahertz communications. IEEE Trans Terahertz Sci Technol 1:256–263
8. Koenig S, Lopez-Diaz D, Antes J et al (2013) Wireless sub-THz communication system with high data rate. Nat Photonics 7:977–981
9. Pawar AY, Sonawane DD, Erande KB et al (2013) Terahertz technology and its applications. Drug Invent Today 5:157–163
10. International Telecommunications Union (2013) Attenuation by atmospheric gases. Radiocommunication sector of ITU, Recommendation ITU-R P.676-10
11. Haddad J, Bousquet B, Canioni L et al (2013) Review in terahertz spectral analysis. Trends Anal Chem 44:98–105
12. Nagashima T, Tani M, Hangyo M (2013) Polarization-sensitive THz-TDS and its application to anisotropy sensing. J Infrared Millimeter Terahertz Waves 34:740–775
13. Nagashima T, Hangyo M (2001) Measurement of complex optical constants of a highly doped Si wafer using terahertz ellipsometry. Appl Phys Lett 79:3917–3919
14. Amenabar I, Lopez F, Mendikute A (2013) In introductory review to THz non-destructive testing of composite mater. J Infrared Millimeter Terahertz Waves 34:152–169
15. Yan C, Yang B, Yu Z (2013) Terahertz time domain spectroscopy for the identification of two cellulosic fibers with similar chemical composition. Anal Lett 46:946–958
16. Molloy J, Naftaly M (2014) Wool textile identification by terahertz spectroscopy. J Text Inst 105:794–798
17. Xia S, Yang DX, Li T et al (2014) Role of surface plasmon resonant modes in anomalous terahertz transmission through double-layer metal loop arrays. Opt Lett 39:1270–1273
18. Gorshunov B, Volkov A, Spektor I et al (2005) Terahertz BWO-spectroscopy. Int J Infrared Millimeter Waves 26:1217–1240
19. Rao L, Yang DX, Hong Z (2012) Guiding terahertz wave within a line defect of photonic crystal slab. Microw Opt Technol Lett 54:2856–2858
20. Naftaly M, Molloy JF, Lanskii GV et al (2013) Terahertz time-domain spectroscopy for textile identification. Appl Optics 52:4433–4437

21. Dunayevskiy I, Bortnik B, Geary K et al (2007) Millimeter- and submillimeter-wave characterization of various fabrics. Appl Optics 46:6161–6165
22. Bjarnason JE, Chan TLJ, Lee AWM et al (2004) Millimeter-wave, terahertz, and mid-infrared transmission through common clothing. Appl Phys Lett 85:519–521
23. Hérault É, Hofman M, Garet F et al (2013) Observation of terahertz beam diffraction by fabrics. Opt Lett 38:2708–2710
24. Fletcher JR, Swift GP, Dai DC et al (2007) Propagation of terahertz radiation through random structures: an alternative theoretical approach and experimental validation. J Appl Phys 101:013102
25. Ghebrebrhan M, Aranda FJ, Ziegler DP et al (2014) Tunable millimeter and sub-millimeter spectral response of textile metamaterial via resonant states. Opt Express 22:2853–2859
26. Tao H, Amsden JJ, Strikwerda AC et al (2010) Metamaterial silk composites at terahertz frequencies. Adv Mater 22:3527–3531
27. Li J, Shah CM, Withayachumnankul W et al (2013) Flexible terahertz metamaterials for dual-axis strain sensing. Opt Lett 38:2104–2106
28. Wietzke S, Jansen C, Reuter M et al (2011) Terahertz spectroscopy on polymers: a review of morphological studies. J Mol Struct 1006:41–51
29. Suzuki H, Ishii S, Sato H et al (2013) Brill transition of nylon-6 characterized by low-frequency vibration through terahertz absorption spectroscopy. Chem Phys Lett 21:36–39
30. Yamashita M, Usami M, Fukushima K et al (2005) Component spatial pattern analysis of chemicals by use of two-dimensional electro-optic terahertz imaging. Appl Optics 44:5198–5201
31. Knoll B, Keilmann F (1999) Near-field probing of vibrational absorption for chemical microscopy. Nature 399:134–137
32. Withayachumnankul W, Png GM, Yin X (2007) T-ray sensing and imaging. Proc IEEE 95:1528–1558
33. Chen HT, Kersting R, Cho GC (2003) Terahertz imaging with nanometer resolution. Appl Phys Lett 83:3009–3011
34. Son JH (2013) Principle and applications of terahertz molecular imaging. Nanotechnology 24:214001
35. Oh SJ, Kang JY, Maeng I et al (2009) Nanoparticle-enabled terahertz imaging for cancer diagnosis. Opt Express 17:3469–3475
36. Bogue R (2009) Terahertz imaging: a report on progress. Sens Rev 29:6–12
37. Svetlitza A, Slavenko AM, Blank T et al (2014) THz measurements and calibration based on a blackbody source. IEEE Trans Terahertz Sci Technol 4:347–359
38. Jewariya M, Abraham E, Kitaguchi T et al (2013) Fast three-dimensional terahertz computed tomography using real-time line projection of intense terahertz pulse. Opt Express 21:2423–2433
39. Guillet JP, Recur B, Frederique L et al (2014) Review of terahertz tomography techniques. J Infrared Millim Terahertz Waves 35:382–411
40. Wang S, Zhang XC (2004) Pulsed terahertz tomography. J Phys D Appl Phys 37:R1–R36
41. Redo-Sanchez A, Laman N, Schulkin B et al (2013) Review of terahertz technology readiness assessment and applications. J Infrared Millim Terahertz Waves 34:500–518
42. Fukunaga K, Cortes E, Cosentin A et al (2011) Investigating the use of terahertz pulsed time domain reflection imaging for the study of fabric layers of an Egyptian mummy. J Eur Opt Soc-Rapid Publ 6:11040
43. Joerdens C, Wietzke S, Scheller M et al (2010) Investigation of the water absorption in polyamide and wood plastic composite by terahertz time-domain spectroscopy. Polym Test 29:209–215
44. Zhang HB, Mitobe K, Yoshimura N (2008) Application of terahertz imaging to water content measurement. Jpn J Appl Phys 47:8065–8070
45. Cleary D (2002) Sensing: brainstorming their way to an imaging revolution. Science 297:761–763

46. Cooper KB, Dengler RJ, Llombart N et al (2011) THz imaging radar for standoff personnel screening. IEEE Trans Terahertz Sci Technol 1:169–182
47. Chen JC, Kaushik S (2007) Terahertz interferometer that senses vibrations behind barriers. IEEE Photonics Technol Lett 19:486–488
48. Chan WL, Deibel J, Mittleman DM (2007) Imaging with terahertz radiation. Rep Prog Phys 70:1325–1379
49. Shen XL, Dietlein CR, Grossman E et al (2008) Detection and segmentation of concealed objects in terahertz images. IEEE Trans Image Process 17:2465–2475
50. Stoik C, Bohn M, Blackshire J (2010) Nondestructive evaluation of aircraft composites using reflective terahertz time domain spectroscopy. NDT&E Int 43:106–115
51. Palka N, Miedzinska D (2014) Detailed non-destructive evaluation of UHMWPE composites in the terahertz range. Opt Quant Electron 46:515–525

Standards for Smart Textiles

31

Carla Hertleer and Lieva Van Langenhove

Contents

Introduction: What Is a Standard and Why Are They Important? 844
How Are CEN Standards Created? What Is the Process? 846
Standards and Smart Textiles 847
Are Textiles Smart or Intelligent? 848
Electrically Conductive Textiles: Determination of the Linear Electrical Resistance of Conductive Tracks 852
Textiles Containing Phase Change Materials (PCMs) Part 1: Determination of the Heat Storage and Release Capacity of Fibers, Yarns, and Fabrics 853
Summary 856
References 856

Abstract

Over the years, "smart textiles" have become a well-known term, not only in the textile community but also in other fields of technology. However, when looking at the retail trade, only few "smart textiles" are available for purchase by the consumer. The European project SysTEX focused on enhancing the breakthrough of smart textiles and concluded that, among others, lack of standardization slows down the commercialization of these high added value products.

In 2007, a working group was assembled to start setting up standardization of smart textiles. This was done in the framework of CEN, the European Committee of Standardization, within the Technical Committee 248 (CEN/TC 248 WG 31). The Belgian research institute Centexbel has the convenorship of this working group.

C. Hertleer (✉)
Department of Textiles, Ghent University, Zwijnaarde, Belgium
e-mail: carla.hertleer@ugent.be

L. Van Langenhove
Department of Textiles, Ghent University, Ghent, Belgium
e-mail: Lieva.vanlangenhove@ugent.be

© Springer Science+Business Media Singapore 2015

X. Tao (ed.), *Handbook of Smart Textiles*,
DOI 10.1007/978-981-4451-45-1_40

As a starting point for setting up smart textile related standards, some clear definitions were formulated. Three important groups of textiles were identified: functional textile materials, smart textile materials, and smart textile systems. They are defined and described in detail in the Technical Report 16298:2011, which was published in 2011.

Classifying smart textiles in such a way helped in revealing the standardization needs.

In January 2012, the WG 31 started working on two items that were selected as ready for standardization:

1. Electrically conductive textiles – Determination of the linear electrical resistance of conductive tracks
2. Textiles containing phase change materials (PCMs) – Determination of the heat storage and release capacity of fibers, yarns, and fabrics

In this way, Europe has taken the lead in starting up the standardization procedure for smart textiles. The first two standards are expected to be operational in 2015.

Keywords

Functional textile materials • Smart textiles • Smart textile materials • Smart textile systems • Electroconductive textile materials • Phase change materials • European standards • Technical report • Test procedure

Introduction: What Is a Standard and Why Are They Important?

A standard is formally defined as "a document that is established by consensus and approved by a recognized body that provides, for common and repeated use, rules, guidelines, or characteristics for activities or their results aimed at the achievement of the optimum degree of order in a given context" [1]. In other words, a standard is a written document that describes requirements, characteristics, and recommendations or test methods that are related to products, systems, processes, or services.

Standards are created to ensure reliability for materials, products, methods, and/or services used by people in everyday life. Although these every day consumers are rarely aware of the existence of standards, they would surely notice absence of them. This is nicely visualized in Fig. 1 – surrounded by standards.

Thanks to the existence of standards, the quality, safety, and reliability of the goods that consumers purchase are guaranteed. Standards describe universally understood and adopted specifications and procedures to ensure that products function properly, are compatible, or operate safely.

Furthermore, standards provide a technological language that is understood by the suppliers on the one hand and by their customers on the other.

Just imagine how the paper size standard for A4 paper simplified lives. Especially in this day and age that all of us have a private printer at home. Thanks to the

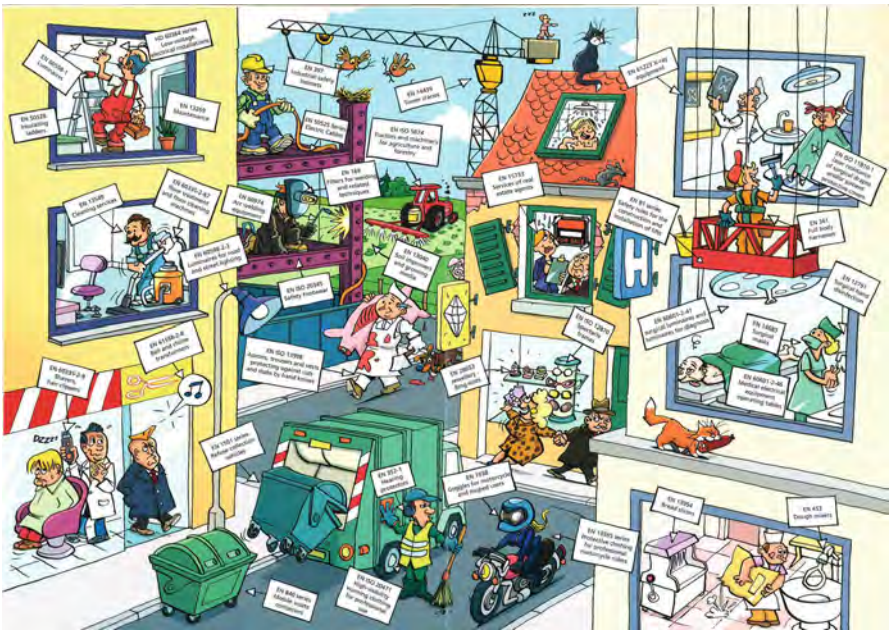

Fig. 1 Surrounded by standards in a work environment (© CEN, reproduced with permission; © CENELEC, reproduced with permission)

standard, one does not need to think about the size of paper to buy because in Europe, all printers use the same standard A4-size paper.

In the premises of a textile testing laboratory, standards are an essential working tool because they describe how the measurement on a piece of textile should be performed, e. g., the procedure on how to measure the tensile strength of a yarn is accurately described in the standard test method EN ISO 2062. When determining the tensile strength of a yarn in different laboratories according to that particular standard, all labs will test the yarn according to the same procedure, which makes their results comparable.

Besides others, a standard describes the technical details of how a test should be performed, what the specifications of the testing equipment are, and how the data has to be reported.

A textile-related example of a well-known standard is the care labeling code in garments. By virtue of these commonly known symbols, it is easy to find out how to correctly maintain clothes.

The worldwide largest developer of standards is ISO, the International Organization for Standardization. On the European level, there are three Standardization Organizations that are officially recognized to develop standards.

They are as follows:

- **CEN** – European Committee for Standardization [2]
- **CENELEC** – European Committee for Electrotechnical Standardization [3]
- **ETSI** – European Telecommunications Standards Institute [4]

Standards related to textiles and textile products are addressed by CEN; however, for smart textiles some overlap might be found with CENELEC or even ETSI.

The members of CEN are the National Standardization Bodies (NSBs) of the 28 European Union member states, the former Yugoslav Republic of Macedonia and Turkey, plus three countries of the European Free Trade Association (Iceland, Norway, and Switzerland). There is one member per country.

How Are CEN Standards Created? What Is the Process?

European standards are developed by teams of experts, people who have knowledge of the sector and the topic that is dealt with in the standard. When a need for a standard is identified, a Technical Committee (TC) is formed consisting of particular experts in the topic. Furthermore, this TC should take into account the interest of all related stakeholders such as research institutes, the industry, consumers, and other relevant organizations.

The TC proposes the development of a dedicated standard, and a preliminary work item (PWI) is requested to CEN. The working group can start its preparatory work when CEN has accepted the PWI. From that date on, the expert group has 3 years to prepare the full draft of the standard. This means that they have to write a coherent and understandable text that clearly describes the operation procedure for the test.

The structure of standards is fixed, and the following items (in the case of a standard for a test method) should be included in the document:

- Title
- Scope
- Normative references
- Terms and conditions
- Principle of the test
- Description of the test method
- Preparation of the test specimens
- Test procedure
- Calculations and presentations of the results
- Test report

When finalizing the draft text, the preliminary work item is activated and becomes a new work item (WI). From this moment on, a period of 3 years starts during which all stakeholders are consulted and standard is finalized. This is done in a number of consecutive steps. To start the procedure, the final draft text is publically launched by CEN. During a period of 5 months, the stakeholders from the CEN member countries can formulate comments to the text. This ensures that the standard is transparent and acceptable for all parties that will deal with the standard once it is operational. Finally, a comments resolution meeting (or meetings) is (are) organized to discuss and process the received remarks so

that the draft standard can be finalized. Within the following 2 months, the countries have to send their formal vote. The standard will be approved if a positive outcome of 71 % is achieved. Thereafter, the standard is officially published at CEN level and later on also at national level.

Standards and Smart Textiles

Over the years, "smart textiles" have become a well-known term, not only in the textile community but also in other fields of technology such as material science or electronics. They find applications in fields such as sports, health care, or medicine. However, when taking a closer look at the retail trade, only few smart textile products are available for purchase by the consumer. The European project SysTEX (May 2008–July 2011) [5] focused on enhancing the breakthrough of smart textile systems (e-textiles and wearable microsystems) and concluded that, among others, lack of standardization slows down the commercialization of these highly added value products. The consumer who purchases such a smart textile wants to be sure that the smart function works and that his safety is guaranteed when using the product. On the other hand, the textile manufacturer struggles with the challenge of proving this in an (internationally) accepted way.

During the European Framework Programs FP6 (2002–2006) and FP7 (2007–2013), a number of research projects dedicated to the development of smart textile materials and products were funded, such as ProeTex [6], a research project focusing on advanced e-textiles for firefighters and emergency workers or STELLA [7, 8], a project in which stretchable electronics for large-area application were developed or PROSPIE [8], a project working on protective responsive clothing for people working in an industrial environment. These are only a few examples of the many more. All projects aimed at developing smart textile products with high market potential. In several of them, the issue of standardization was tackled but not elaborately worked on. But the more prototypes that were developed, the more it became clear that the lack of standardization is an important drawback to get smart textile products out of the prototype stage and into the market. Then, in October 2012, the European FP7 project SUSTA-Smart [9] started. Its aim was to map, synthesize, and prioritize standardization needs in smart textiles. Also, the project partners worked out a standardization roadmap and presented input documents to the relevant European and international standardization committees. The projects ended in March 2014.

Europe has taken the lead the standardization procedure for smart textiles, by starting with the draft of two work items.

In 2007, the initiative was taken to start looking into standards for smart textiles under the convenorship of the Belgian research institute Centexbel. Therefore, Working Group 31 on *Smart Textiles* was established. This was done under the mandate of CEN, the European Committee of Standardization, within the Technical Committee 248 on *Textiles and Textile Products*, thus referred to as CEN/TC 248 WG 31. European experts and stakeholders in the field of smart textiles from all over Europe are involved in the work of this Technical Committee.

Due to the multidisciplinary nature of the smart textile product range, their standardization is not a straightforward process. It involves an overlap between the standardization of traditional textile products with that of functional properties of the *smart* product. This overlap may include national or European legislation (e.g., different EU directives), expertise, testing, as well as other synergies resulting from the combination of the different technologies that have contributed to the smart textile product. This becomes more clear if when imagining smart textiles often contain an electronic component. Information on the non-textile components should be gathered from other standardization bodies or committees such as CENELEC, operating in the electrotechnical domain or ETSI in the telecommunication domain. Standards already available in these fields might be useful for smart textiles and a good starting point to set up smart textile standards; however, they will rarely be applicable as such.

During the first discussions in CEN/TC 248 WG 31, it turned out that terminology related to smart textiles was not interpreted in the same way by all experts in the working group. Therefore, before starting the actual work of making standards, the members of CEN/TC 248 WG 31 decided to write a technical report (TR) comprising clear definitions related to the field of smart textiles. A technical report is an informative document that provides information on the technical content of standardization work [10]. In this case, the technical report identifies three important groups of textiles: *functional textile materials*, *smart textile materials*, and *smart textile systems*. They are extensively defined and described in detail in the Technical Report 16298:2011, and a short description is given here.

Are Textiles Smart or Intelligent?

In the English language, both terms *smart* and *intelligent* textiles are interchangeable and the two are used, however, with a preference for smart textiles. In some other languages, e.g., French and Dutch, the adjective “intelligent” is used. Therefore, it is stated in the TR 16298:2011 that the two terms smart and intelligent are equivalent, so you can talk about *smart textiles* or about *intelligent textiles*. They both have the same meaning and are interchangeable.

Then, the terms functional and smart textile materials and smart textile systems are distinguished and clarified.

Functional textile materials are defined as those materials that do not have any “smartness” as such, but in many cases form a basic component of a smart textile (system), e.g., electroconductive textiles or optical fibers.

Electroconductive textiles are often used to connect the different components in a smart textile system, e.g., the battery is connected to the data processing unit which in turn is connected to the sensors. They are essential in the field of smart textiles but on itself, electroconductivity cannot be considered as a “smart” property. Figure 2 shows screen-printed electro-conductive patches that can be used as textile electrodes.

Fig. 2 Screen-printed electro-conductive patches (UGent)

This also counts for optical fibers. Originally applied in the telecommunication industry where they are used as light source or for data transmission, they were introduced in textiles because of their compatibility with textile materials. Optical fibers by themselves are passive components but they are used in the field of smart textiles, e.g., for data transmission or for illumination (Fig. 3).

Apart from the ones mentioned above, other functional textiles can be relevant for the field of smart textiles such as thermally conductive, thermally emissive, fluorescent or phosphorescent textiles, and textile materials releasing substances.

Because of their specific role in the area of smart textiles, **functional textile materials** were separately described in the CEN Technical Report.

The next class of textile materials was defined as **smart textile materials**. They have a certain inherent degree of smartness by responding to an external stimulus. Depending on the physical stimulus that initiates the transformation, Table 1 gives an overview of a variety of response effects. The stimulus can be of optical, mechanical, chemical, electrical, or thermal nature, and depending on the physical outcome, the effect is named. Chromic materials, for instance, change color, which can be caused by a change in temperature, in light, or in pH. Other examples of smart textile materials are phase change materials or piezoelectric materials.

Fig. 3 Optical fibers for illumination (ENSAIT)

Table 1 Overview of stimulus–response effects (As reported by Clevertex [12])

	Response				
Stimulus	Optical	Mechanical	Chemical	Electrical	Thermal
Optical	Photochromism	Dilatant, auxetic	Controlled release	Photovoltaic	
Mechanical	Piezochromism	Shape memory, super-absorbing polymers	Controlled release	Piezoelectric	Friction
Chemical	Chemiluminescence, solvatochromism, halochromism	Inverse piezoelectric	Electrolysis		Exo/endotherm
Electrical	Electrochromism, electroluminescence				Joule heating Peltier effect
Thermal	Thermochromism	Shape memory		Seebeck effect	Phase change

The additional active property of the textile is something that is normally not expected from materials used in textiles, which are traditionally perceived as passive materials.

Finally, a **smart textile system** was defined as a textile comprising actuators, possibly also sensors and a data processing unit. A further distinction was made on whether the textile system either used energy (e.g., batteries) and/or external communication (e.g., antenna).

Apart from sorting out some definitions to create a common language among persons with scientific and commercial background, the technical report also gives some recommendations for standardization of smart textiles. One recommendation, e.g., is that consultation with other technical committees (TC) is required because

as mentioned before, smart textiles are an interdisciplinary research and development area. For example, when considering future firefighter garments to comprise integrated sensors and actuators as components of a smart textile system, the TC dealing with standards for protective clothing (CEN/TC 162) should be consulted when developing the new standards for smart textiles. In the case of, e.g., developing a T-shirt that enables heart and breathing rate monitoring, here, the CEN/TC 205 on medical devices will be involved in the standardization process.

The technical report on smart textiles was finished in the year 2011 and is since then available for purchase as *Technical Report CEN/TR 16298:2011 Textiles and textile products – Smart Textiles – Definitions, categorization, applications and standardization needs*.

Classifying smart textiles as shown above helped in revealing the real standardization needs. In the process of determining which standards should be established, priority was given to materials, products, or technologies that are already introduced into the market. The need for standards for these products is higher because of the bigger economic impact compared to materials, products, or technologies still in a research phase. Therefore, electroconductive textiles or electroconductive tracks and phase change materials were chosen as topics ready for standardization.

In January 2012, the discussion on two preliminary work items (PWI) was initiated by the working group CEN TC 248/WG 31. The standards to be developed are meant to be applied as test methods. Hence, they will define the procedure on how to perform the measurement. Because the title of a standard should reflect its scope, also special attention was given to the correct phrasing of the title of the PWI, and during the development process of the text, it was subject to progressive changes.

Finally, the titles of the PWIs (and later on the WIs) became:

1. Electrically conductive textiles – Determination of the linear electrical resistance of conductive tracks
2. Textiles containing phase change materials (PCMs)

Because PCMs have a dynamic action, the standard on textiles containing PCMs was split up into three parts:

– Part 1: Determination of the heat storage and release capacity of fibers, yarns, and fabrics
– Part 2: Determination of the heat transfer using a dynamic method
– Part 3: Determination of the heat transfer between the user and the product

The three parts will be dealt with consecutively; only Part 1 has been worked out at this stage.

The technical committee gradually worked on the measurement procedure for the above mentioned items to reach a final draft of the listed standards. As an important verification for the correctness of the written measurement procedures, interlaboratory comparative tests were performed. The purpose of this type of tests

is to verify whether the described method is not only repeatable within one lab but also reproducible in different labs. As a result, this gives rise to the fine-tuning of the draft text of the standards.

After that, the final draft of the standards was submitted to CEN in the summer of 2014.

In what follows, more information is given on the content of the two standards.

Electrically Conductive Textiles: Determination of the Linear Electrical Resistance of Conductive Tracks

In smart textiles, electrically conductive tracks (as shown in Fig. 4) are used to guide electrical current (besides others), for example, to connect different components such as sensors with a data processing unit. The conductive tracks are defined as the electrically conductive part of a textile with a length-to-width ratio of at least 10 to 1. Knowing the electrical behavior of these tracks is important. So far, the standard describes two methods for measuring the linear resistance (direct current (DC) resistance per unit of length) of these conductive tracks.

Two test methods are defined: a two-electrode four-wire and a four-electrode four-wire method. The outcome of the test is the linear resistance in Ohm per meter (Ω/m) under a direct current, not an alternating current (AC). The four-electrode method is the preferred method because it excludes contact resistance between the measurement clamps and the sample, and this results in a more accurate measurement outcome. To fulfill this measurement successfully, at least four places where contact can be made between the sample and the clamps are needed (see Fig. 6). However, in some cases, this is not possible, e.g., when electroconductive yarn is coated with an isolating layer that cannot be removed without damaging the yarn. In such a situation, a two-electrode setup needs to be used (see Fig. 5). Also this measurement setup is described in the standard.

The interlaboratory tests have shown that the test method was good and useful, but that the way it was described in the text was not always unambiguously apparent. So they have led to a restructuring of the text and here and there a reformulation for clarification. The resulting text was submitted to CEN for the activation of the work item, and it is this text that is available for evaluation by the different members.

Fig. 4 Examples of electro-conductive tracks made by Elasta and VDS Weaving (UGent)

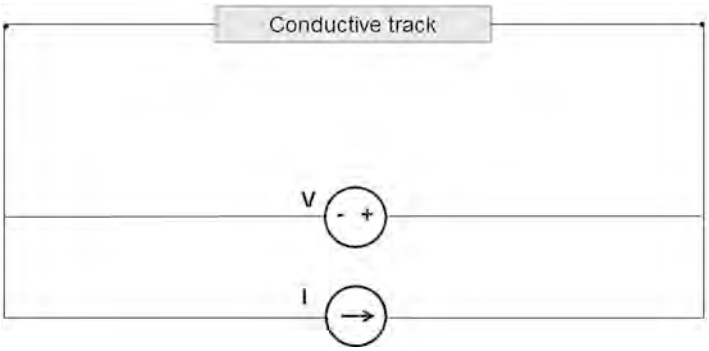

Fig. 5 Schematic of a two-electrode four-wire test setup (UGent)

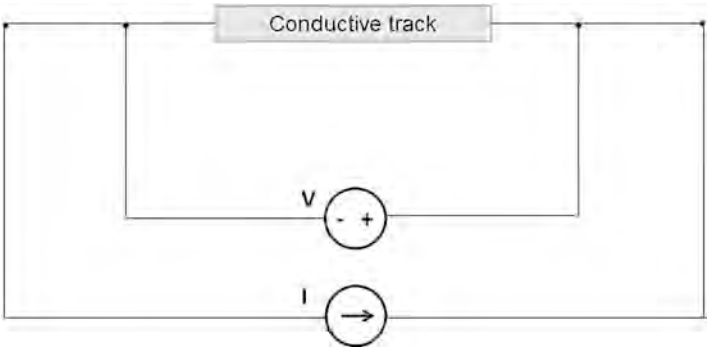

Fig. 6 Schematic of a four-electrode four-wire test setup (UGent)

Textiles Containing Phase Change Materials (PCMs) Part 1: Determination of the Heat Storage and Release Capacity of Fibers, Yarns, and Fabrics

Phase change materials are materials whose phase changes within a predetermined and restricted temperature interval. When a PCM melts or changes from a solid into a liquid form, three phases can be distinguished during this process:

- Energy is being supplied in order to start the heating up to the melting point of the PCM.
- This energy is absorbed and used to break the molecular bond in the solid structure. The material's temperature remains constant until the phase transformation is completely ended.
- The substance has become liquid. Next, the material's temperature starts to increase.

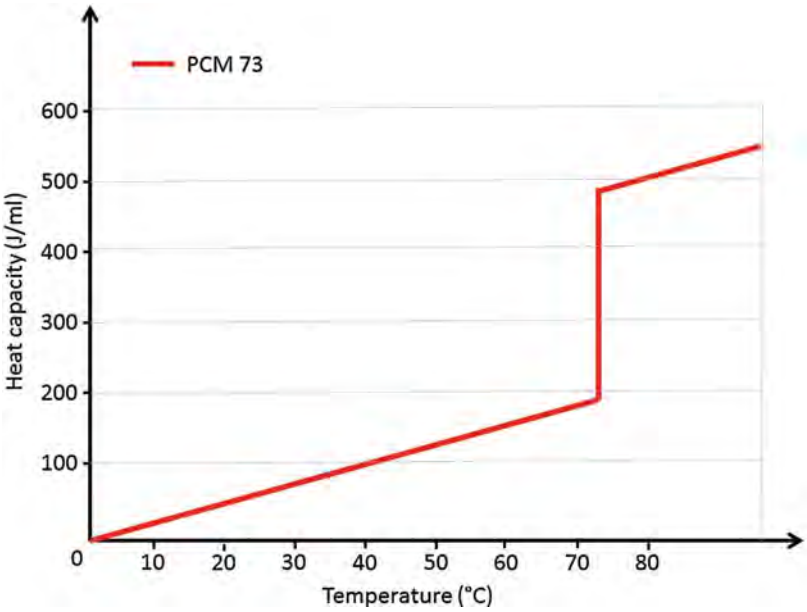

Fig. 7 Melting process of a PCM (UGent)

A high latent heat absorption and release occurs upon change of phase (from solid to liquid or from liquid to solid) with little attendant change in temperature (as shown in Fig. 7). Because of that remarkable melting/solidifying behavior, PCMs can be used as thermal control materials and can actively participate to the thermal comfort that textiles provide. The phase change materials used in the textile sector are usually paraffin waxes in solid or liquid state. These are hydrocarbons with a different chain length, such as heneicosane ($C_{21}H_{44}$), eicosane ($C_{20}H_{42}$), nonadecane ($C_{19}H_{40}$), and octadecane ($C_{18}H_{38}$). With these materials, the phase change occurs within a temperature range that lies in the vicinity of the body temperature. To prevent the substance in the liquid state from flooding, it is necessary that it is captured. PCMs are therefore microencapsulated in small particles with a solid membrane, as shown in Fig. 8. These microcapsules typically have a diameter between 1 and 10 μm. They are resistant to mechanical action, temperature, and a variety of chemicals. A textile material that contains PCMs assures a thermal regulation instead of a thermal insulation. This technique is already frequently used for ski suits, gloves, socks, sweaters, and shoes, and many products treated with PCMs have been on the market for many years. However, up to now no standard was available to really measure the effect of the presence of PCMs.

Textiles treated with PCMs claim to regulate a person's thermal balance because they store the thermal energy the body has produced (e.g., after physical effort) and release it when the body cools down. This way, thermal comfort improves.

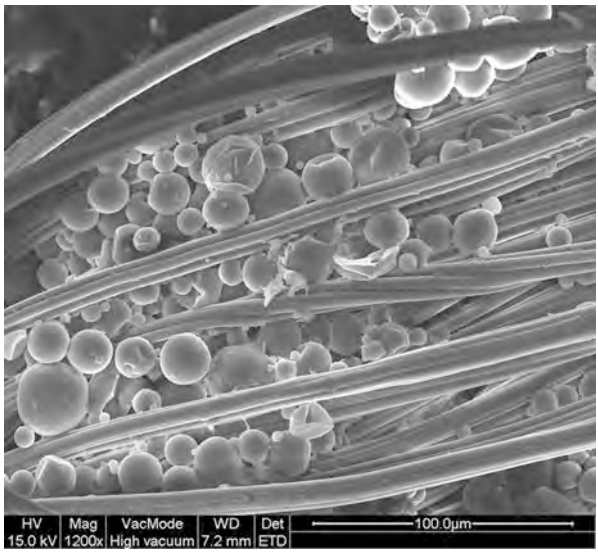

Fig. 8 SEM (scanning electron microscopy) picture of textile treated with microencapsulated PCMs (UGent)

But it is not easy to convince the customer of this effect and thus the benefits of the product. A standard that provides a test method to determine the heat storage and heat release capacity and the phase change temperature of the treated textiles was urgently required.

As mentioned above, the test method is split up into three parts.

The first part of the standard relates to the material itself, either the pure PCM or the textile treated with it. The equipment to be used in this measurement method is differential scanning calorimetry (DSC), and the outcome is the enthalpy of fusion (J/g) and the enthalpy of crystallization (J/g). The enthalpy of fusion indicates the change in enthalpy when a given quantity of a material changes its phase from solid to liquid, in other words when it melts. The temperature at which this occurs is the melting point. Similarly, the enthalpy of crystallization relates to the material's enthalpy when it is solidifying, thus changing phase from liquid to solid. The method how to perform this measurement is described in the first part of the standard.

The second part is a dynamic measurement and has the heat transfer as an outcome, while part three is a product-related measurement. In this part, a measurement procedure will be suggested to determine the transfer of heat between the user and the product, e.g., when a person is wearing a garment treated with PCMs.

Part 2 and part 3 of the standard are at this moment not yet under development; they have just been defined and will be worked out at a later stage.

Because the area of smart textiles is still in full development, it was suggested in 2014 to revise the Technical Report 16298:2011. The WG 31 suggested that it might be better to split it up into two new technical reports, also dealing with integrated electronics and ICT.

Summary

Smart textiles have been around for several years now, especially in research projects. On the other hand, smart textile products are coming but gradually into the market. As such, time has come to start the standardization process of smart textiles and that is what is ongoing in Europe. Two CEN standards, related to electrically conductive textiles and textiles containing phase change materials, are close to being adopted, and new work items for standardization are being proposed.

References

1. www.cencenelec.eu/standards/DefEN/Pages/default.aspx. CENELEC [Online]. [Consulted in Oct 2014]
2. www.cen.eu. CEN [Online]. [Consulted in Oct 2014]
3. www.cenelec.eu. [Online]. [Consulted in Oct 2014]
4. www.etsi.org. ETSI [Online]. [Consulted in Oct 2014]
5. www.systex.eu. [Online]. [Consulted in Oct 2014]
6. www.proetex.org. [Online]. [Consulted in Oct 2014]
7. www.cordis.europa.eu/project/rcn/80720_en.html. [Online]. [Consulted in Nov 2014]
8. www.stretchable-circuits.com/projects/healthcare/stella. [Online]. [Consulted in Oct 2014]
9. Chapman R (2013) Protective clothing for firefighters and rescue workers. In: Smart textiles for protection, Woodhead publishing series in textiles. Woodhead, Philadelphia, pp 357–358
10. www.susta-smart.eu. [Online]. Available: http://www.susta-smart.eu/. [Consulted in Oct 2014]
11. www.cen.eu/work/products/TR/Pages/default.aspx. [Online]. [Consulted in 10 Oct 2014]
12. www.clevertex.net. European FP6 project Clevertex, state-of-the-art, 2005. [Online]. [Consulted in Oct 2014]

Part IV

Applications of Smart Textiles

Vladan Koncar, Jinlian Hu, and Xiaoming Tao

Color-Changing Textiles and Electrochromism

32

Fern M. Kelly and Cédric Cochrane

Contents

Introduction 860
Chameleonic Textiles Using Chromic Technologies 863
Principals of Electrochromism 867
Electrochromic Materials 869
Inorganic Electrochromes 869
Organic Electrochromes 871
Flexible Electrochromic Devices (F-ECDs) 875
Challenges Concerning Flexible Electrochromic Displays 885
Summary 886
References 887

Abstract

Color plays a vital part in our lives, acting to warn (i.e., red is hot, blue is cold), to direct (i.e., red is stop, green is go), or to express (i.e., red is angry, blue is sad). As a powerful form of communication, color, and in particular a change in color, is irreplaceable. Textiles with the ability to change color provide the opportunity to act as a flexible communicative display. The display can be used to express emotions and opinions or can be used for identification and decoration or safety and camouflage purposes. In this chapter a range of pre-existing color-changing textiles that apply LED, optical fiber, and chromic (thermo-, photo-, halo-) technologies are considered. The possibilities of flexible

F.M. Kelly (✉)
ENSAIT, GEMTEX, Roubaix, France
e-mail: fern.kelly@ensait.fr; fernkelly@gmail.com

C. Cochrane
ENSAIT, GEMTEX, Roubaix, France

University of Lille Nord de France, Lille, France
e-mail: cedric.cochrane@ensait.fr

© Springer Science+Business Media Singapore 2015

X. Tao (ed.), *Handbook of Smart Textiles*,
DOI 10.1007/978-981-4451-45-1_16

communicative displays using electrochromic technologies are then explored in detail. The principals of electrochromism are discussed and electrochromic materials and their devices (ECDs) introduced. There is a great potential provided when electrochromism is applied to flexible textiles. A flexible color-changing display, visible in natural and ambient light, offers endless opportunities. A number of challenges for the optimization and commercialization of flexible electrochromic devices (F-ECDs) exist. However, with the persistent improvements, which are being made, the field as a whole will continue to see great success. A colorful future is ahead for flexible electrochromic devices.

Keywords

Flexible textile displays • Chromism • Electrochromism • ECD • Conducting polymer • Polythiophene • Polyaniline • Communication textiles • Smart textiles

Introduction

> Colour can help to facilitate and fulfil some very basic human needs. It can: identify and specify necessary objects (animal, vegetable or mineral) for survival and/or enjoyment; stimulate and work synergistically with all the senses – sight, smell, taste, hearing, and touch; mark territory and manage personal space; symbolize abstract concepts and thoughts; recall another time or space (create a mnemonic sensation); express fantasy and wish-fulfilment; create illusions and ambience; emphasize or camouflage figures or objects; enhance self-image and personal esteem; produce an aesthetic response. Most importantly, the use and arrangement of colour enables us to create beauty and harmony and express our personal taste, and by doing so, provides us with a sense of accomplishment.
> – in "Pantone Book of Color," Abrams, 1990

Color plays a vitally important role in the world in which we live. Color can sway thinking, change actions, and cause reactions. It can irritate or soothe, raise your blood pressure, or suppress your appetite. We are conditioned from birth to react to color in an emotional and psychological way. We are taught to obey certain colors – red means stop, green means go. In addition color is used to give warnings with blue meaning cold and red meaning hot. Color can also describe our moods – green with envy, feeling blue, seeing red, in the pink – or even our character. Within the textile domain, color has always been of importance. It is used for the expression of feelings and emotions and for identification, decoration, and camouflage. The apparel and textile industries exploit color in many ways to attract consumer's interest, project a message, and boost consumer sales.

As a powerful form of communication, color is irreplaceable. A change in color – whether from white to black, colorless to colored, or one color to another – can be easily detected by the human eye. Therefore, through visual signals, changes in color can be used to convey important information. Returning to the traffic light example above, the most obvious example of color change is the universal message when the change in light color to red means "stop" and the change to green means "go." Consequently, the application of color change to textiles has allowed for the

development of flexible communicative displays. Such textiles can be referred to as belonging to the domain of "smart textiles", a domain that is currently thriving in the following areas:

- Health (diagnosis, curing, heating or cooling, UV protection)
- Security (protection and safety, military camouflage)
- Communication (data exchanges, gaming, networking)
- Sport (measuring of performances, comparison with other sportsmen's performances)
- Fashion (aesthetic customization through color, form, or illumination)

"Smart textiles" can be defined as textiles that are able to sense and respond to changes in their environment [1]. They may be divided into two classes: (1) passive and (2) active communicative textiles. Passive communicative textiles have the ability to change their properties (optical, mechanical, thermal, electrical, or chemical characteristics) according to an environmental stimulation. Active communicative textiles are however fitted with sensors and actuators, in order to connect internal (e.g. personal temperature, heartbeat, breathing frequency) or external (e.g., environmental temperature, light, and sound levels) parameters to the transmitted message. The message can be displayed directly on the surface of the textile or can be transmitted to a distant control center. Color-changing textiles can principally be classified as passive communicative textiles; however, they can also act as the actuator in active communicative textiles.

Flexible color-changing communicative textiles are readily available in the commercial market today. LED, OLED, optical fiber, electroluminescent, and chromic technologies are the predominant technologies used to display the information. It should be noted that all, excluding chromics, are light-emitting technologies with power consumptions ranging from 60 to 120 W/m^2 [2, 3]. Examples in LED and optical fibers will be discussed briefly here, with a specific focus being placed on chromism and, in particular, electrochromism. LEDs, for instance, have been used by British company CUTECIRCUIT to create the T-Shirt-OS, the world's first wearable, shareable, and programmable t-shirt (Fig. 1a) [4]. The t-shirt has a 32 $\times$ 32 LED display incorporated on its front and is connected to different microelectronic equipment – including a camera, a microphone, a speaker, and an accelerometer. The t-shirt is controlled by bluetooth via a smart phone. The flexible display can show messages such as slogans or tweets and pictures and movies captured by the integrated camera. CUTECIRCUIT is also responsible for the world's largest wearable LED display, the Galaxy Dress (Fig. 1b), composed of 24,000 colored LED of 2 $\times$ 2 mm each hand embroidered on a white silk dress and connected to small batteries hidden in the hemline [5].

Woven optical fibers have been used by France Telecom R&D in 2002 to create a prototype flexible display capable of displaying static or animated graphics such as logos or texts (Fig. 2a) [6, 7]. Independent pixels may be formed and therefore can be turned on and off to create a changeable image. With this innovation, clothes became a graphical communication interface. Today, Italian company Luminex

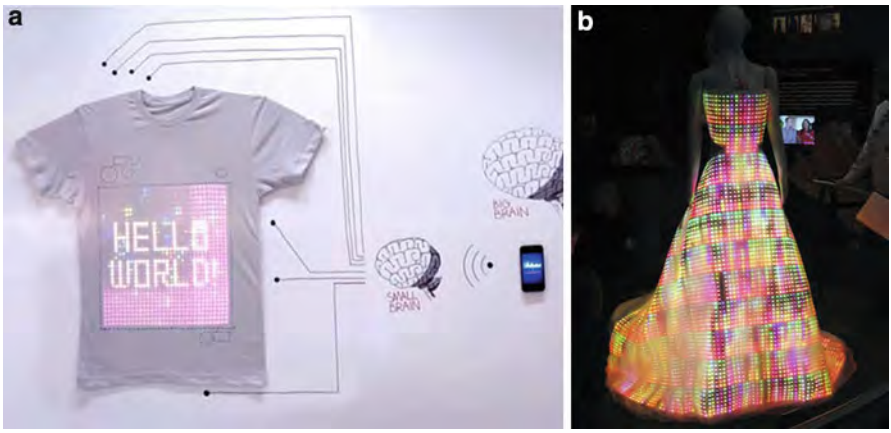

Fig. 1 CUTECIRCUIT's LED color-changing clothing: (**a**) The T-Shirt-OS [4] and (**b**) the Galaxy Dress [5] (Images reprinted with permission from CUTECIRCUIT http://cutecircuit.com/)

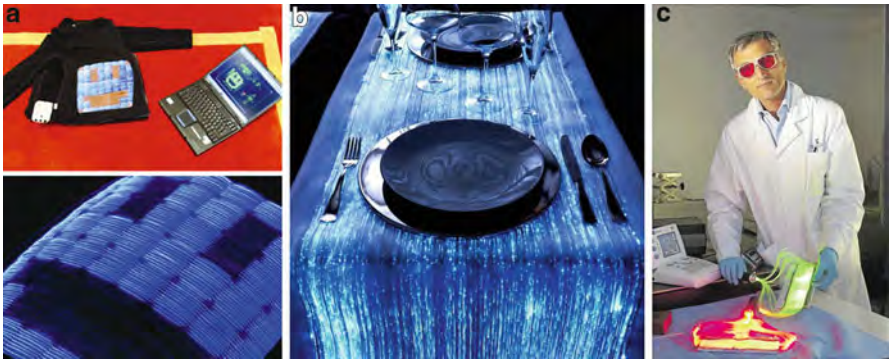

Fig. 2 Fiber-optic flexible displays: (**a**) flexible image-changing prototype by France Telecom R&D (Image reprinted from Cochrane et al. (2011) Indian Journal of Fibre & Textile Research 36:422) [2]; (**b**) flexible fiber-optic tablecloth by Luminex (Image reprinted with the permission of DreamLux, www.dreamlux.it) [8]; and (**c**) light-emitting fabric for photodynamic therapy (PDT) (Image reprinted from Mordon et al. (2011) Photodiagnosis and Photodynamic Therapy 8:142) [9]

commercializes optical fiber textiles [8]. Their focus is on products relating to fashion and design, such as illuminated dresses, pillows, bags, or tablecloths (Fig. 2b). However, unlike the France Telecom R&D prototype, these products are not able to broadcast messages or animation. Visually, the effect is purely aesthetic, that of a "starry sky". Additionally, the homogeneous distribution of light from optical fiber textiles with a plain weave provides the possible medical application in the field of photodynamic therapy (PDT) (Fig. 2c) [9]. PDT is a treatment that uses photosensitizing agents, along with light, to eradicate premalignant and early-stage cancer cells.

In comparison to the light-emitting textiles (LED, fiber optic, OLED, and electroluminescence) that require a darkened environment in order to observe the color change, chromic color changes are visible in daylight or ambient lighting. Chromism classifies a phenomenon of color change – materials that exhibit a reversible change in color upon the change of external conditions. Many materials express chromic properties, including inorganic and organic compounds. These electrochromic materials can be incorporated into textile products in the form of chromic dyes, pigments, or coatings. Chromic textiles can also be referred to as "chameleon textiles" given the fact that they can change their color with an external influence [10]. Chromism can result from many different mechanisms, and as such chromic materials are classified by the type of stimuli that induce their color change. The major kinds of chromism are as follows:

- *Thermochromism* – Materials' color change induced by a change in temperature of the immediate environment.
- *Photochromism* – Materials' color change induced by a change in exposure to electromagnetic (UV) radiation.
- *Halochromism* – Materials' color change is induced by a change in the pH of the solution.
- *Solvatochromism* – Materials' color change is induced by a change in the polarity of the solvents.
- *Cathodochromism* – Materials' color change is induced by a change in electron beam irradiation.
- *Electrochromism* – Materials' color change is induced by a change in the electrical potential due to the gain and loss of electrons.

The ability to change the color or motif "automatically," by a triggering through ambient light or temperature changes or by a simple flip of a switch, offers endless opportunities and possibilities when applied to textiles. Chameleonic textiles prepared using thermo-, photo- and halochromic materials will be discussed in further detail below. The major chapter focus will be particularly on electrochromic technologies. The principles of electrochromism will be considered and their application in flexible device structures discussed. The chapter will conclude by discussing the challenges and solutions pertaining to electrochromic devices and the future for flexible electrochromic devices (F-ECDs).

Chameleonic Textiles Using Chromic Technologies

Thermochromism is observed when there is a change in heat exposure to a thermochromic material. Thermochromic materials change their molecular or supramolecular structure and absorption spectrum as a result of the variation in environmental temperature. Application of inorganic thermochromic materials in textiles is limited due to the fact that a high temperature and/or a solvent is required to induce the color change. This explains why organic and thermochromic

Fig. 3 Thermochromic textiles: (**a**) Radiate Athletics' heat-sensitive sportswear (Image reprinted with the permission of Radiate Athletics http://www.radiateathletics.com/) [12] and (**b**) Shi Yuan's blossoming wallpaper (Image reprinted from Meunier et al. (2011) Indian Journal of Fibre & Textile Research 36:429) [49]

compounds are preferable for treating textiles because their color-changing temperatures are often between ambient and body temperatures. The structural changes of organic thermochromic compounds may include rearrangement of molecules (e.g. cleavage of covalent bonds or changes in the spatial configuration of a molecule) and changes in crystalline structures. Each of the technologies has been successfully used within the textile industry. In both cases, the dyes are entrapped in microcapsules and applied to fabric like a pigment in a resin binder.

The application of thermochromic dyes has predominately been used for decoration and fashion. In 1987, Toray Industries, Inc. commercially released a line of clothing made from temperature-sensitive chameleonic fabric, known by the name of "Sway" [11]. The change in color with temperature of these fabrics was designed to match the application, for example, ski wear 11–14 °C, women's clothing 13–22 °C, and "temperature shades" 24–32 °C. More recently, however, a US kick-starter company by the name of Radiate Athletics has applied thermochromic materials to sports clothes in order to monitor the body temperature of a person [12]. When a person is working out, their body heats up and consequently the fabric of the t-shirt, or other item of clothing, will change color (Fig. 3a). Certain parts of the shirt will change color before others, therefore making it possible to determine which parts of your body are being exercised the most. As a result, the color-changing function of the sports clothing offers the ability to monitor and maximize your workout. Thermochromic paints, applied to textiles, have also allowed a particular motif or pattern painted on them to change color or appearance. For example, London-based graphic designer Shi Yuan has created wallpaper painted with green vines printed in regular ink and flowers printed in thermochromic ink. When the heater turns on and the wallpaper starts to heat up, flowers are seen to blossom all over the wall, giving the effect that the vine is growing (Fig. 3b) [13, 49].

Fig. 4 Amy Winter's photochromic "rainforest" dress expressing the effects without (left) and with (right) UV exposure (Images reprinted with permission from Amy Winters, Rainbow Winters, www.rainbowwinters.com) [15]

Photochromism is observed when there is a change in sunlight (UV radiation) exposure to a photochromic material. The chemical structure of a photochromic material is temporarily altered as a result of UV irradiation. This change in chemical structure leads to a shift in the absorption of electromagnetic waves to the visible part of the spectrum, upon which the color changes from colorless to colored. A reverse change in its chemical structure, and consequently in its electromagnetic wave absorption spectrum, can take place in the absence of UV rays. As a result, the material returns to its original colorless state. Many photochromic compounds have been identified or developed for different applications. For example, they can be coated on spectacle lenses to have the lenses darken when exposed to strong sunlight, returning to colorless in dim light [14]. However, most of the inorganic photochromic substances, which are usually based on metals, are not suitable for treating textiles worn close to the skin. Therefore, organic photochromic dyes are commonly used to produce chromic textiles. Articles of clothing treated with photochromic materials were first introduced in the market in 1989, with the application intended for added fashion [11]. More recently, British designer Amy Winters has created a sun-reactive dress by printing photochromic inks directly onto the fabric. The "rainforest" dress is white indoors but becomes purple when exposed to sunlight (Fig. 4) [15]. Photochromic textiles have also been used for military purposes to provide protection by camouflage [16] and by monitoring UV radiation can be applied in solar protection [17, 18].

Halochromism is a color-changing phenomenon caused by a change in the pH of the environment surrounding a halochromic material. Halochromic dyes developed for textile use can be applied as pH sensors. For example, for burn patients

Fig. 5 Dahea Sun's halochromic textiles and designs expressing their effect to rainwater of different pHs (Images reprinted with the permission of Dahea Sun http://www.sundahea.com/) [20]

(whose skin pH values will vary during the healing process), the incorporation of halochromic molecules into a wound dressing allows the monitoring of the wound recovery process without causing disturbance to the wound bed [19]. Halochromic textiles can also be used in geotextiles or protective clothing that provides real-time changes in environmental pH values [16]. London designer Dahea Sun has recently created garments which act as pH indicators (Fig. 5). The halochromic ink applied to her fabrics is hypersensitive to pH, changing color in reaction to the pH levels of rainwater. Items of clothing are therefore able to provide an indication of atmospheric air quality [20].

Electrochromism is induced by a change in the electrical potential applied to an electrochromic material. Electrochromic materials experience a reversible change in color as a result of an electrochemical "redox" (i.e., oxidation and reduction) reaction. In order to affect the electrochromic color change, the passage of a weak electrical potential at a voltage no more than a few volts is required. In comparison to light-emitting displays (LED, OLED, optical fiber, electroluminescent), which

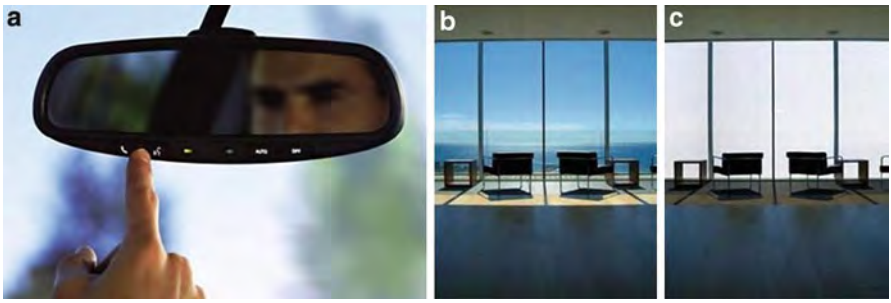

Fig. 6 Examples of electrochromic glass: (**a**) an auto-dimming electrochromic rear-view mirror [25] and (**b**) "smart glass" electrochromic windows in their clear-bleached (*left*) and fully opaque (*right*) states (Image reprinted with the permission from Decorating with Fabric http://www.dwfcontract.com/) [26]

require a continuous flow of electrical potential to display the color, electrochromic materials require only a short electrical pulse in order to effect the color change. Due to the "memory effect" of electrochromic color changes, little or no input of power is required to retain the new color [21]. Electrochromic displays are therefore far more economical in the consumption of power when compared to their light-emitting analogs. Additionally, there is no visual dependence on the viewing angle, and multiple colors, with high contrast, are available.

The first commercialized electrochromic devices have been auto-dimming antiglare car windows, including the sunroof and the rear-vision mirrors (Fig. 6a). Electrochromic technologies have also been used to produce "smart glass", glass windows which darken or become opaque reversibly at the flip of a switch. This can be to reduce the level of sunlight and heat and therefore reduce the requirement of air conditioning or to provide privacy (Fig. 6b). Other proposed applications include reusable price labels, devices for frozen-food monitoring, camouflage materials, and controllable light-reflective or light-transmissive displays for optical information and storage [22]. Developments are also being undertaken into electrochromically operated billboards, large-scale traffic direction boards, and rail and airport departure boards [23, 24].

Principals of Electrochromism

Electrochromic (EC) materials change their optical properties upon the loss or gain of electrons and/or ions. In a typical structure, the electrochromic device (ECD) consists of 7 layers (Fig. 7). An EC material is deposited on a conducting substrate (lower electrode) in the form of a thin film. The EC film is held in contact with an ionically conductive electrolyte. A second EC layer and second conducting substrate (secondary electrode + transparent substrate) complete the device. When a small voltage (1–5 V) is applied between the upper and lower electrodes, ions from the ionically conductive electrolyte are forced into the EC film. At the same time,

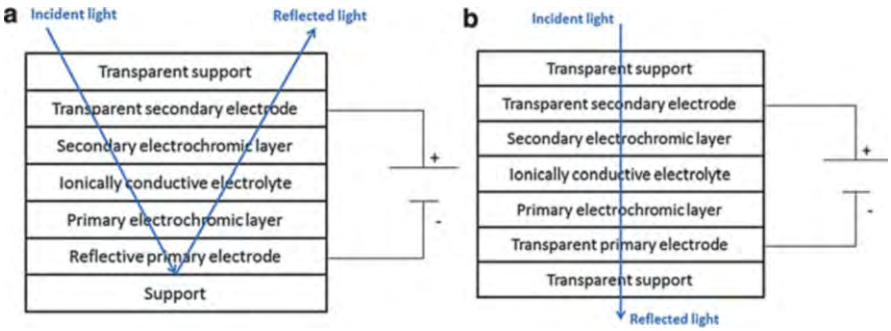

Fig. 7 Schematics of (**a**) reflective and (**b**) transmissive electrochromic devices

electrons are injected into the film from the substrate, so as to preserve the charge neutrality. The electrons are required to preserve the charge neutrality. The effect of the injected electrons is an altering of the electronic (redox) state and consequently the optical properties of the electrochrome. When the voltage is reversed, the ions are ejected out and return to the electrolyte. The electrons return to the substrate, and the electrochrome reverts to its original state.

Typically, ECDs have two modes of operation, reflective and transmissive. In reflective displays, the EC material is coated onto a reflective electrode or has a reflective counter electrode. Figure 7a provides a schematic for a common design for reflective displays. It consists of a thin film of the primary electrochrome on ITO glass, which is then placed upon a reflective counter electrode coated with a secondary EC layer, separated by an electrolytic gel. This device uses the absorption of light, which is reflected by a material such as platinum or rhodium alloy. The main advantage of the system is that, since the light passes through the layers twice, the EC material needs only to be half the thickness that it does in transmissive EC systems. This results in a faster EC system. An example of reflective EC systems is in the rear-vision mirrors of many current vehicles. In transmissive EC systems, the mirror (reflective counter electrode) is replaced with another glass substrate. Light is passed straight through the device to obtain the EC effect. Hence, EC devices of this kind often require a backlight to work. Figure 7b shows a schematic diagram of a transmittance EC device. An example of a transmissive display is "smart windows."

The electrolytes typically used within the above devices are either solids or high-viscosity liquids [27]. They function both as ionic conductors and as a supply/sink for ions moving into and out of the electrochromes. Electrolytes must also be compatible with the electrochromes used. Three types of electrolytes are most common: polymer electrolytes, polyelectrolytes, and solid inorganic electrolytes. Polymer electrolytes are neutral polymers such as poly(ethylene oxide) or poly (propylene glycol) with salts such as $LiClO_4$, CF_3SO_3H, or H_3PO_4 dissolved in them. The polymers are often made with an intermediate molecular weight as these are highly viscous liquids and are termed "semisolid solutions" [28]. Polyelectrolytes are polymers that contain ion-labile groups. Examples include poly

(2-acrylamido-2-methylpropanesulfonic acid), poly(ethylene sulfonic acid), poly (methyl methacrylate), poly(styrene sulfonic acid), and poly(vinyl alcohol). Solid inorganic salt electrolytes are often clear colorless inorganic solids and one or more small ions. Examples include hydrogen uranyl phosphate, Li_3N, Ta_2O_5, water glass, and ZrO_2.

An advantage of the polymer-based electrolytes is that they are easier to use in device fabrication, particularly polymer electrolytes. They are also flexible and can easily handle the stresses caused by the small expansion and contraction the solid electrochromes undergo during their redox processes. However, they are vulnerable to photolytic degradation, and so strict control of internal moisture level is often required. This is not a problem for solid inorganic electrolytes, which do not have this problem. However, they are brittle, and so cracks can form due to the expansion and contraction of the electrochromes. They also tend to have a high electrical resistance, which results in slower EC switching.

According to Pratt [29], the ideal EC will have a large contrast between its colors, have a very short switching time, maintain its color after the current has been switched off, and retain its electrochromism over a large number of switches. A number of electrochromes (electrochromic materials) exist and can be classified by their inorganic or organic nature. Inorganic electrochromes include transition metal oxides and the Prussian family (iron hexacyanoferrates). Organic electrochromes include viologens (bipyridinium salts), metallopolymers, and conducting polymers (polyaniline, polypyrrole, and polythiophene and its derivatives). Historically, inorganic transition metal oxide films have been the most commonly used electrochromes in ECD applications. Yet more recently, conducting polymers have gained a lot of attention due to their rapid response times when compared to their metal oxide analogs and their comparative ease of preparation. Each of the EC materials listed above will be discussed in brief as follows.

Electrochromic Materials

Inorganic Electrochromes

Transition Metal Oxides

Many transition metal oxides are capable of redox reactions that result in color change. Their electrochromism is derived from the color change associated with a change in the oxidation state of the metal anion, due to the double injection of ions and electrons (Fig. 8). This redox state has a strong EC absorption band due to charge transfer [30]. Metal oxide films are commonly prepared as thin layers of tungsten, titanium, vanadium, or other metal compounds. The most studied example of transition metal oxide EC is the WO_3 (tungsten trioxide) system. Tungsten trioxide, with all tungsten sites having the oxidation state + VI, is a transparent thin film. On electrochemical reduction, +V sites are generated to give the EC (blue coloration to the film) effect (Fig. 8). Table 1 below outlines a variety of other color changes of EC active transition metal oxides [31].

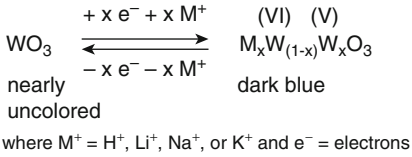

Fig. 8 Electrochemical reactions showing the different oxidation states of inorganic metal oxide, WO_3 (Image reprinted from Somani et al. (2003) Chemistry and Physics 77:117) [30]

Table 1 Examples of metal oxide films with electrochromic properties

Metal oxide	Reaction	Color change
Tungsten trioxide	$WO_3 + x(Li^+ + e^-) \rightarrow Li_xW^{VI}{}_{(1-x)}W^V{}_xO_3$	Very pale blue → blue
Cobalt oxide	$3CoO + 2OH \rightarrow Co_3O_4 + H_2O + 2e^-$	Green → brown
Indium tin oxide	$In_2O_3 + 2x(Li^+ + e^-) \rightarrow Li_2xIn^{III}{}_{(1-x)}In^I{}_xO_3$	Colorless → pale blue
Iridium oxide	$Ir(OH)_3 \rightarrow IrO_2.H_2O + H^+ + e^-$	Colorless → blue/gray
Molybdenum trioxide	$MoO_3 + x(Li^+ + e^-) \rightarrow Li_xMo^{VI}{}_{(1-x)}Mo^V{}_xO_3$	Colorless → blue
Nickel oxide	$NiO_xH_y \rightarrow \left[Ni^{II}{}_{1-z})Ni^{III}{}_z\right]O_xH_{(y-z)} + zH^+ + ze^-$	Colorless → brown/black
Vanadium pentoxide	$Li_xV_2O_5 \rightarrow V_2O_5 + x(Li^+ + e^-)$	Very pale blue → brown/yellow
Cerium oxide	$CeO_2 + x(Li^+ + e^-) \rightarrow Li_xCeO_2$	Yellow → very pale yellow
Manganese oxide	$MnO_2 + ze^- + zH^+ \rightarrow MnO_{(2-z)}(OH)$	Yellow → brown

Thin films of transition metal oxides are prepared by a number of techniques, including sol–gel electrochemical, d.c. or r.f. reactive sputtering techniques, electron beam evaporation, anodic or cathodic electrode position, or solution dipping of the EC metal compounds (or compounds that can be changed into these metal compounds) onto optically transparent electrodes (OTE). The behavior of EC transition metal oxide materials is dependent upon pH, moisture, and exposure to the atmosphere [32]. Generally, the switching rates of these films are somewhat slow, with typical switching times of about 15–60 s to achieve 100 % conversion to either colored or bleached state. An example of this includes nickel oxide, which changes from transparent (pale green) to brown/black in around 30 s [33]. Other examples include $[(NH_4)_5Ru]_2(pyrazine)^{5+}$ and $[(NH_4)_5Ru]_2(4,4'\text{-bipyridine})^{5+}$ whose electrochromism is significantly different due to the effect of the ligand [34].

Prussian Family

Prussian blue [PB, iron(III) hexacyanoferrate(II)] is the most common of the transition metal hexacyanometallates which forms an important class of insoluble

mixed valence compounds. They have the general formula M′k [M″(CN)6]l, where M′ and M′ are transition metals with different oxidation numbers. In these compounds, element exists in two oxidation states with the possibility of charge/electron transfer between them [30]. For PB, this element is iron (Fe). PB has been an important inorganic pigment and has been manufactured for many years on a large scale for use in paints, lacquers, printing inks, and other color uses. The use of PB as an EC however is relatively recent due to the technological possibility to synthesize PB as thin films [34]. These thin films are generally formed by electrochemical reduction of solutions containing iron(III) and hexacyanoferrate(III) ions. Reduction of the complex Prussian brown (iron(III) hexacyanoferrate(III), present in equilibrium with the iron(III) and hexacyanoferrate(III) ions) is the main electron transfer process in PB electrodeposition according to the following equation.

$$\left[\mathrm{Fe^{III}Fe^{III}(CN)_6}\right] + \mathrm{e^-} \rightarrow \left[\mathrm{Fe^{III}Fe^{II}(CN)_6}\right]^-$$

Organic Electrochromes

Viologens

Viologens are toxic bipyridinium derivatives of 4,4′-bipyridyl and salt of 4,4′-bipyridine. They are well known in biology and due to their strong herbicidal properties are manufactured on a large scale (Paraquat, trade name for N,N′-dimethyl-4,4′-bipyridinium dichloride). The nature of the quaternizing agent gives EC properties and is easy tunable. The exemplar viologen is 1,1′-dimethyl-4,4′-bipyridilium (methyl viologen). This molecule has three redox states, as is seen in Fig. 9.

The dication is the most stable form and is colorless. Electron transfer creates intensely colored radical cations. The precise color of the bipyridilium depends upon the substituents on the two nitrogen atoms. Alkyl-substituted bipyridilium radical cations are a blue/violet color, changing to crimson with longer chains, whereas aryl bipyridilium cations have a green hue. For soluble systems, the solvent

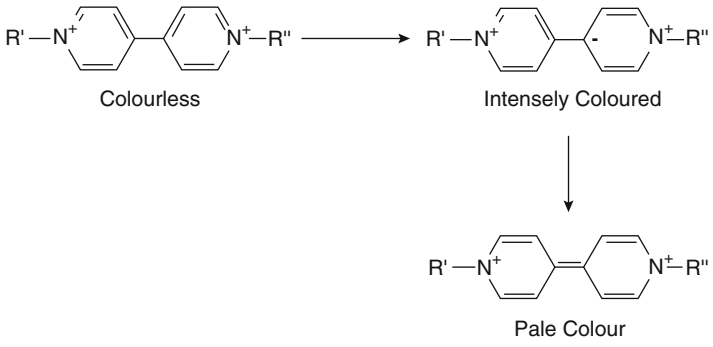

Fig. 9 Indicating the three redox states of viologen molecule

used can affect their color. The solubility of bipyridilium compounds decreases as the length of the substituents increases. Since the radical cation is less soluble than the dication, thin films of the radical cation can form upon reduction for some of the bipyridilium derivatives. The first EC display using viologens was reported in 1973 by Schoot et al. [35], but due to the competition of LCD displays, viologen displays have not been exploited further [22].

Metallopolymers (Transition Metal Coordination Complexes)

Transition metal coordination complexes consist of a metallic atom, surrounded by an array of organic molecules. Metallopolymers can contain a variety of metal centers from main group metals, such as tin and lead, to transition metals, such as iron, iridium, and platinum, to lanthanides such as europium. In addition, the metals can be located either in the polymer main chain (Fig. 10,1) or in the side group structure (Fig. 10,2). The arrays of molecules are called ligands and are generally bound to the central atom by a coordinate covalent bond.

The electronic configuration of the complexes gives them some important properties and color-change possibilities (intense redox reactivity). Chromophoric properties typically arise from a low-energy metal-to-ligand charge transfer, the intervalence charge transfer, the intra-ligand excitation, and the related visible-region electronic transitions. Because these transitions involve valence electrons, the color changes upon oxidation or reduction of the complex [22]. The color of metallopolymer films in the M(II) redox state may be selected by suitable choice of the metal – red if M is Fe, orange if M is Ru, and green if M is Os. Electrochromicity results from loss of the metal-to-ligand charge transfer absorption band on switching between the M(II) and the M(III) redox states.

Electrochemical polymerization is the typical method used to prepare EC polymer films on electrode surfaces. This technique allows the use of a wide variety of conducting substrates, and by controlling the electrochemical process (e.g., scan rate, potential range, polymerization time, monomer concentration, and electrolyte solution), the film thickness can be directly controlled. Thus, the reductive or oxidative electropolymerization of polypyridyl complexes offers potential ways to produce EC displays [22].

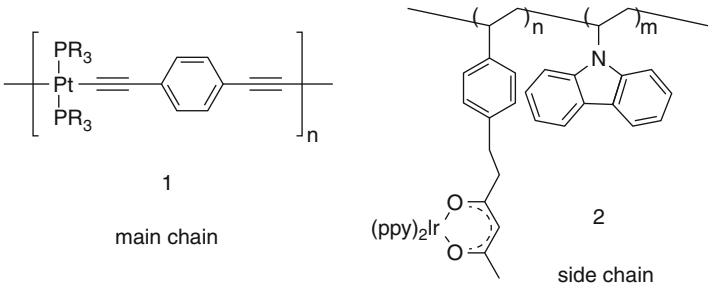

Fig. 10 Metal localization on polymer chain of metallopolymers (Image reprinted from Eloi et al. (2008) Materials today 11:28) [36]

Conducting Polymers

Conducting polymers are prepared through the chemical or electrochemical polymerization of various organic aromatic molecules such as thiophene, aniline, pyrrole, furan, carbazole, azulene, indole, and others. The most commonly used conducting polymers for EC display applications are polythiophene, polyaniline, and polypyrrole and their functionalized analogs. Several techniques are available for preparing thin films of these, including electrodeposition, vacuum deposition, chemical vapor deposition, sol–gel coating, and dip coating. In their oxidized forms, these polymers are "doped" with counter anions (p-doping) and possess a delocalized π-electron band structure. Reduction of the conducting polymer with a counter anion removes the electronic conjugation, to give the "undoped" form (neutral, electrically insulating). Conducting polymers can also have cathodic doping with cation insertion (n-doping). However, n-doped forms are less stable than p-doped forms.

The optical properties of conducting polymers are dependent on their band gaps. In general, conducting polymers with band gaps greater than 3 eV are colorless and transparent in their undoped form, and conducting polymers with band gaps less than 1.8 eV are absorbing in the undoped form [37]. Doping of the conducting polymers alters the observed colors. For example, in the neutral state, poly (3,4-(2,2-diethylpropylenedioxy)thiophene) (PProDOT-Et_2) has a band gap of 1.7 eV. In the UV-visible region, a strong absorption around 580 nm exists, and the polymer film shows a deep blue color. When it is oxidized and p-doped, the energy band gap becomes smaller. In turn, the absorption at 580 nm decreases, and a new absorption band appears in the near-IR region (~900 nm). The polymer film therefore becomes transparent. Reduction of the oxidized EC polymer will cause the polymer to switch back to the neutral state, returning the energy band gap and absorption back to the colored state.

Electrochromism in conductive polymers is due to the changes in the conjugated polymer's π-electronic character and the reversible insertion and extraction of ions through the polymer chains. This oxidation/reduction behavior is responsible for increased conductivity but also the color changes by "optical modulation." The speed of the color change is dependent on the speed at which the dopant ions can migrate in and out of the polymer matrix, with most systems taking about 100 ms to change color. In their thin-film form, all conducting polymers are potentially EC, with redox switching and the transfer of electrons/counterions giving rise to new optical absorption bands. For example, Figure 11 shows the color against oxidation states of polyaniline. The reason PAn is capable of this is because of the presence of the chemically flexible nitrogen in the polymer chain backbone. This nitrogen has free electron pairs and can consequently act as a Lewis base, donating electrons to either contribute to the aromatic π-system of the polymer or accept protons as dopants.

By manipulating the side chains of the conducting polymer monomer (e.g., thiophene) before polymerization, the observed color can be further tuned (Fig. 12) [39]. Additionally, it has also been shown that the polymer color can be

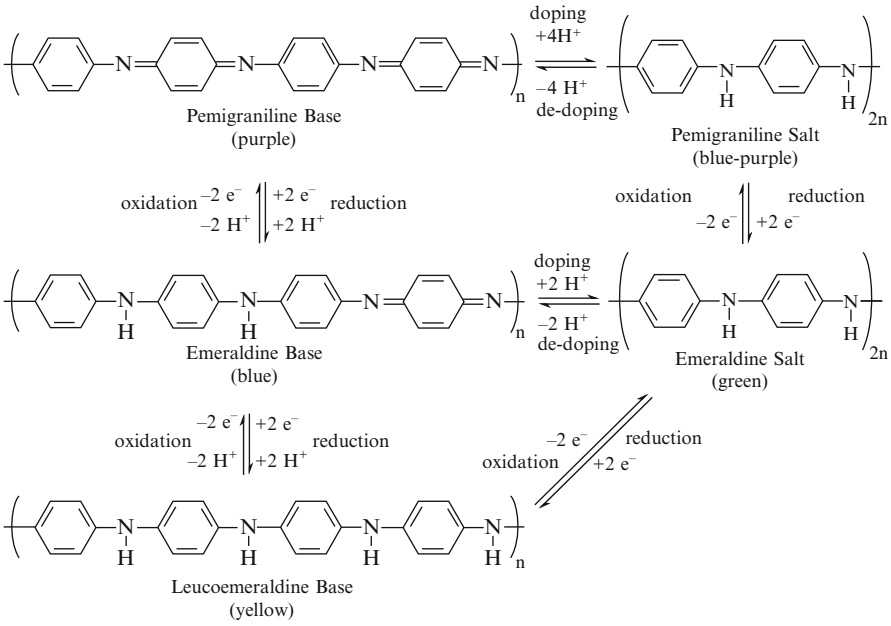

Fig. 11 The various redox states of polyaniline (Image reprinted with the permission of Fern Kelly) [38]

Monomer		Oxidised	Neutral
EDOT		Transparent Blue	Blue
ProDOT-Et2		Transparent Purple	Purple
5H-2,2′-BT	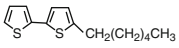	Transparent Green	Green
2,3′-BT		Grey/Green	Yellow
2,2′-BT, 2,2′-BT-3,2-T	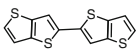	Green/Grey	Red
DT-3,2-2,3-T	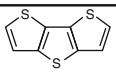	Blue/Grey	Red
2,2′ :5′2″-TT	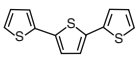	Dark grey	Orange/Yellow

Fig. 12 The color of thiophene electrochromics may be tuned by functionalizing the monomer unit before polymerization (Image reprinted with the permission of Fern Kelly) [41]

manipulated by controlling the ratios of two different monomers during electrochemical copolymerization [39, 40]. Guapp et al., for example, have combined different comonomer concentrations of EDOT and BEDOT-NMeCz, resulting in colors ranging from yellow to red to blue for the neutral polymer film, with each equally passing from a green intermediate state to a blue fully oxidized state (Fig. 13) [40].

Flexible Electrochromic Devices (F-ECDs)

Although chromism was not theoretically explained and understood until the 1960s, color-changing effects due to the gain or loss of electrons date back to the early nineteenth century. And in fact, the first documented account of a redox-active material used as a colorant was reported to be on a flexible textile-like support. The "cyanotype" process, developed in 1842, involved paper being impregnated with potassium ferrocyanide and ammonium ferric citrate to form Prussian brown ($Fe^{III}[Fe^{III}(CN)_6]$). When exposed to light (photochromic process), Prussian brown underwent a photoreduction of Fe^{III} to Fe^{II}in the complex, and Prussian blue ($KFe^{III}[Fe^{II}(CN)_6]$) was generated [31]. This process used for the production of "blueprints" became a method of mass production in the 1880s until the late twentieth century. The first documented F-ECD and *electrochromic* color change (based on the application of an electrical potential) on a flexible textile-like support, however, wasn't until 1942 when "electrolytic writing paper" was developed. The technology involved the pre-impregnation of paper with particulate MoO_3 and/or WO_3 [31]. A blue/gray image formed following an EC electron transfer reaction. The electrode, in effect, acted as a stylus, forming color wherever the electrode traversed the paper.

Since these early developments, success in the field of EC technologies has predominately been in rigid structures ("smart glass" and auto-dimming rear-vision mirrors). Therefore, since these first documentations, flexible EC devices have been limited. However, in more recent years, a number of academic and commercial research groups, including the engineering conglomerate Siemens, have been working toward the creation of ECDs that are flexible (Fig. 14a) [42]. Dublin-based start-up NTera Ltd. (founded in 1998) has also developed a flexible "next generation display technology" [43]. An image of the F-ECD technology which goes by the name of NanoChromics™ is shown in Fig. 14b.

NTera describe their F-ECD as a "paper quality" EC display (ECD of very high definition) that uses two metal oxide films – one at the negative electrode and, unusually, one at the positive electrode [44]. NTera have stated that their flexible display prototype can, in principle, be applied to all the product types: displays, windows, and mirrors. This could give rise to products such as "smart card" displays, dimmable window laminates, and applications in toys and games and ultimately flexible electronic paper displays. The company noted that signs using NanoChromics™ display technology would also be ideal for sports player substitution boards. It is thought that current LED boards can become bleached out and

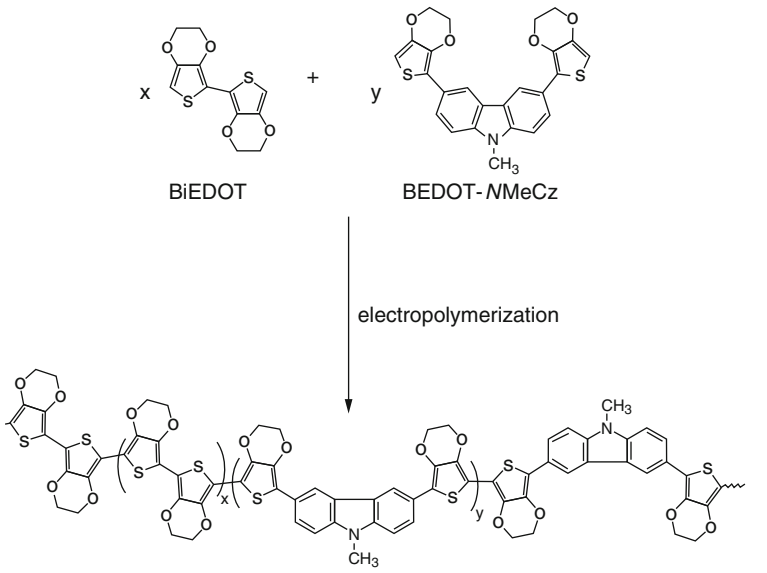

Comonomer Solution Composition	Neutral Polymer λ_{max} (nm)	Neutral Electrochromic Response (Photograph)
100% BiEDOT	577	
90:10	559	
80:20	530	
70:30	464	
50:50	434	
30:70	431	
20:80	429	
10:90	420	
100% BEDOT-*N*MeCz	420	

Fig. 13 Representative copolymer structure and electrochromic properties of electrochemically prepared copolymers of varied compositions (Images reprinted from Gaupp et al. (2003) Macromolecules 36:6305) [40].

difficult to read in bright daylight in sports stadia. Therefore, because NanoChromics™ display signs are easy to read in bright daylight, and at all angles, NTera has proposed that they would be perfect for this application. Interestingly,

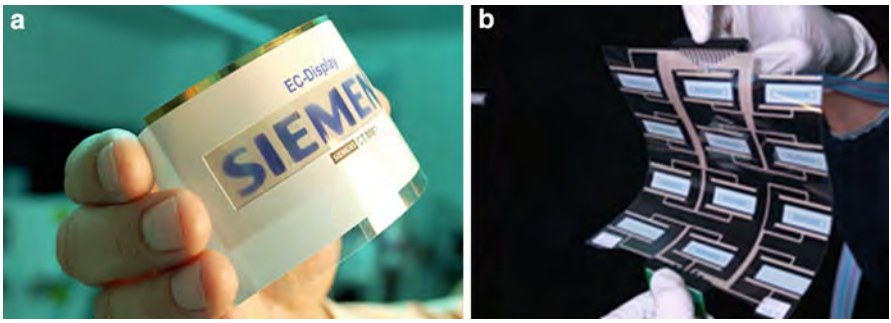

Fig. 14 A flexible electrochromic display, as developed by (**a**) Siemens (Image reprinted from Meunier et al. (2011) Indian Journal of Fibre & Textile Research 36:429) [49] and (**b**) NTera Ltd (Photo reprinted with the permission of Printed Electronics Now http://www.printedelectronicsnow.com/) [43]

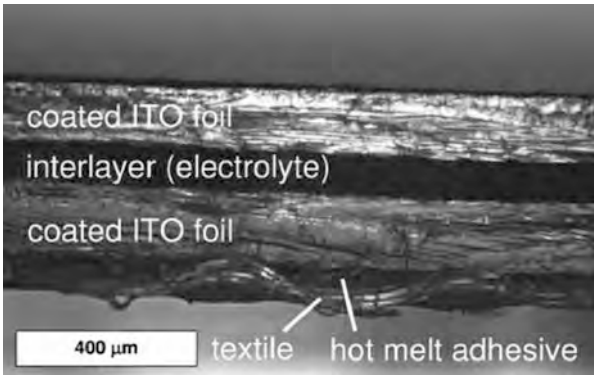

Fig. 15 Cross section of a flexible analog of "smart glass" indicating the structure of the device (Image reprinted from Schawaller D (First published online: 19 JUL 2013) Macromolecular Materials and Engineering) [45]

since their first announcement of the technology in 2010, the company has since closed.

Recently, Schawaller et al. have transferred the principles of electrochromism from rigid "smart glass" to a flexible structure [45]. "Smart glass" has proven successful for energy-efficient sun-protective applications but however suffers from high costs and high weight. Additionally, with any minor damage, replacement of the entire device is required. Hence, flexible EC materials, with their comparatively lower weights and preparation costs, represent an appealing alternative to their rigid analogs. They can be integrated in an easier approach to that of glass and can offer many more options with regard to interior design and repair. The structure used by Schawaller et al. to create their flexible, switchable EC textiles is offered in Fig. 15. Flexible ITO foils (special films made of PE, and sputtered with ITO) were coated via electrochemical deposition with the electrochromes polyaniline (PAni) and tungsten oxide (WO_3). An ion-conducting electrolyte interlayer based on lithium poly(styrene sulfonate) was applied to assist redox reactions allowing ion and electron movement between PAni- and WO_3-coated

ITO foils. A metallic fabric made of stainless steel was connected to the two EC parts of the element by a conductive adhesive and then fixed on a textile substrate using a hot-melt adhesive. The resulting structure can be reversibly switched from its dark-blue-colored state (sum of oxidized PAni- and reduced WO_3-coated ITO foils) to its decolored state (sum of reduced PAni- and oxidized WO_3-coated ITO foils) within 4 min and therefore shows good prospect for a future in flexible adaptable sun protection materials for both indoor and outdoor applications.

The EC materials applied in the Siemens, NTera, and flexible "smart glass" have typically been inorganic transition metal oxides. In addition to the lengthy preparation processes required, metal oxides exhibit slow response times. The flexible "smart glass" example above exhibited this fact showing a switching time of 4 min. Organic conducting polymers can be used as a valuable alternative. Like inorganic metal oxide materials, conducting polymers show high coloration over a wide range, good coloration efficiency, and low operating voltage, but, furthermore, they offer quick response times and ease of processing. In addition, a much larger color palette is available when using conducting polymers. Many conducting polymers express multi-chromism (more than two color states available), and the color transitions may be fine-tuned through chemical structure modification of the conjugated backbone. Due to the rapid response times, ease of processing, and tunable range of colors, conducting polymers are the electrochromes preferentially applied within textile-based F-ECDs.

Additionally, the Siemens, NTera, and flexible "smart glass" F-ECD examples are plastic in nature, and due to this they are limited in their flexibility and lack the intrinsic feel and drape of a textile fabric. Therefore, by treating *flexible textiles* with ECs, the application field of F-ECDs is greatly increased, and endless opportunities are offered for wearable displays, communicative advertising textiles, or adaptive camouflage. The change in color can be used for adding further interest or fashion to an item or for protection and safety. Due to the vast scope of textile-based F-ECDs, a number of research groups worldwide are working toward the creation and improvement of such devices.

In 2006, a plastic/textile hybrid F-ECD was developed by Leclerc et al. in the quest toward flexible, lightweight, and wearable adaptive camouflage [46]. The group applied a sandwich-type structure, whereby an electrochrome was spray coated onto one electrode and then sandwiched between the other. The anode was a transparent film of PET/ITO and the cathode, a commercially available conductive textile (Shieldit Super, Less EMF Inc.) (Fig. 16). Initial experiments used glass/ITO electrodes for proof of concept. The operating potentials for both the glass and the plastic/textile hybrid structures were between −1.1 and +2.2 V. One of the conducting polymers used was poly(thiophene-*b*-4-butyltriphenylamine) (PT(BuTPA)). PT(BuTPA) is multi-chromic showing three color states: yellow to green to black. For the purpose of their studies, however, they controlled the potential of the electrode to observe the neutral (yellow) and the intermediate (green) colors only (Fig. 17). It was noted that the conductive fabric could not handle any additional potential below −1.1 V and that the switching speeds were too slow for display applications. However, the coloring was very strong for a

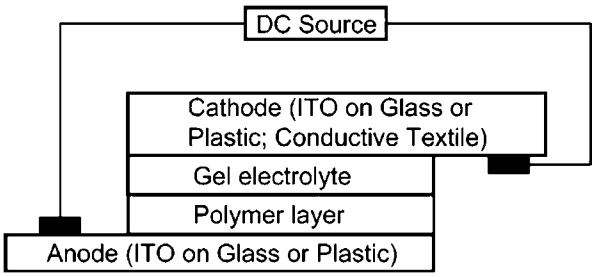

Fig. 16 Sandwich structure of plastic/textile hybrid F-ECD developed by Leclerc et al. (Images reprinted from Beaupré et al. (2006) Chemistry of Materials 18:4011) [46]

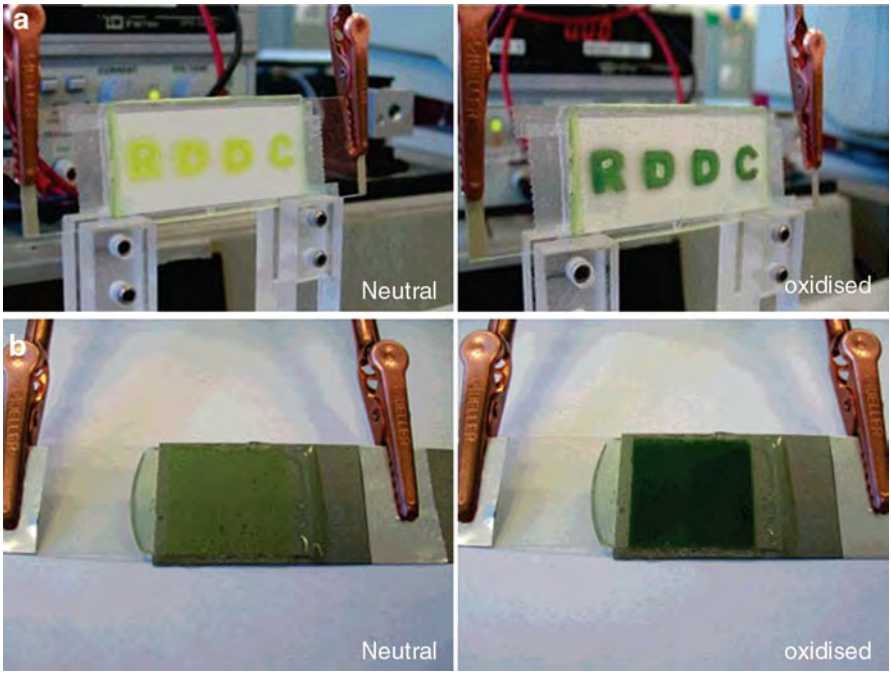

Fig. 17 Sandwich-type electrochromic cells using PT(BuTPA) as the electrochrome. Application of (**a**) two rigid glass/ITO electrodes and (**b**) one flexible PET/ITO film electrode and one conductive textile electrode (Images reprinted from Beaupré et al. (2006) Chemistry of Materials 18:4011) [46]

fabric-based device. More recently, in 2013, Xin et al. have created a hybrid F-ECD using PAni deposited on a PET/ITO film as one electrode and a copper-coated piece of fabric as the other [47]. By applying −1.0 to +1.0 V, the device could be switched between black and brown. Nevertheless, this structure showed a poor lifetime, with damaging effects on the change in color observed after 15 cycles.

A research group led by Fern M. Kelly at École Nationale Supérieure des Arts et Industries Textiles (ENSAIT), France, has also used PAni in a textile-based F-ECD in 2013 [48]. However, in comparison to Xin et al. whereby PAni has been

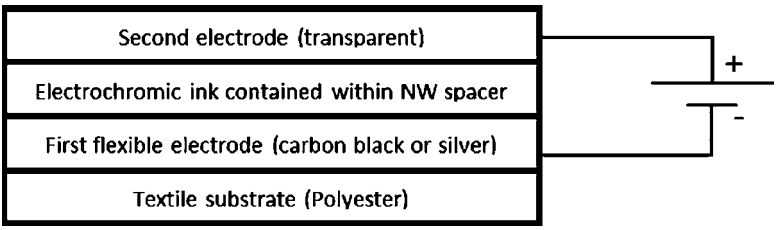

Fig. 18 Four-layer sandwich structure of the F-ECD prototype developed by Kelly et al. (Image reprinted from Kelly et al. (2013) Displays 34:1) [48]

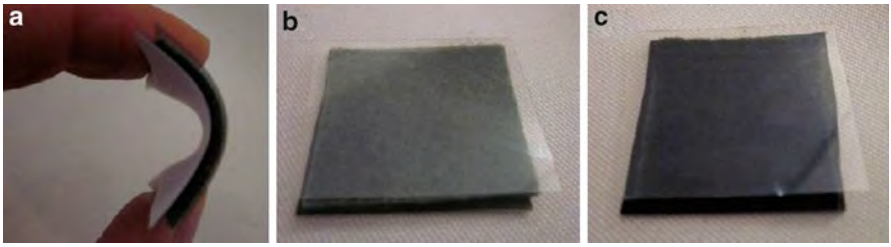

Fig. 19 F-ECD containing viscose–PAn composite (**a**), before (**b**) and after (**c**) the application of −3 V for 1 min (Image reprinted from Kelly et al. (2013) Displays 34:1) [48]

deposited as a film on a PET/ITO film, PAni has been chemically bound to PET or viscose nonwoven spacer fabrics. A nonwoven fabric (NW) is one that is neither knitted nor woven. The nonwoven, in this instance, was prepared by the hydroentanglement of discontinuous PET fibers in random directions. The preparation process of the nonwoven–PAni composite included the initial bonding of aniline monomer units to the spacer fabric, followed by a chemical polymerization. The resultant was a conductive electrochromically active fabric. When the nonwoven–PAni composite was inserted within the 4-layered sandwich structure, as is outlined in Fig. 18, the device was seen to switch color from green to blue/purple with the application of −3 V for 1 min (Fig. 19). This F-ECD device can be deemed as the second-generation device developed by Kelly et al. and sought to resolve challenges seen in the first-generation device which employed Prussian blue [49]. Unfortunately, however, as was seen in the Xin et al. example above, the switching times were slow, and the lifetime of the PAni-containing device was very short, reversibly changing color for no more than 10 cycles. The slow switching speed may be attributed to the solid nature of the PAni which reduces the speed of electron transfer and also the thickness of the nonwoven and hence the greater distance for electron transport between electrodes. The low cycle number is likely due to the disruption of electron transfer owing to the bonding of the polymer to the nonwoven spacer textile.

In an attempt to overcome the problems above – slow switching speeds and short lifetimes – Kelly et al. have employed liquid phase polythiophene electrochromes

as an alternative to the solid phase PAni in their third-generation F-ECD [39]. Due to the capillarity action of the nonwoven and the high viscosity of the electrolyte, retention of the liquid phase electrochrome within the prototype was achieved. Thiophene monomers were combined within a high-viscosity gel electrolyte and electrochemically polymerized in situ within the ECD device structure seen in Fig. 18 (however, using a woven PET fabric, rather than a nonwoven), by applying 3 V for 30 s. By varying the substitution of the thiophene monomer before polymerization, the color of the resulting polymers can be tuned, offering an interesting array of colors (Fig. 20). Due to the increased mobility of ions in the liquid state, the switching times of the polythiophene-containing ECD system were much faster than that of the PAni analogs, which took around 10 s. Additionally, the cycling between redox states was seen to be very good immediately after preparation, with polythiophene-containing devices displaying >>50 cycles of reversible color change without indication of color degradation. Figure 21 shows an F-ECD containing the polythiophene PProDOT-Me_2 cycled between its transparent-purple oxidized state (Fig. 21a) and its dark-purple reduced state (Fig. 21b).

Despite the potential offered by the above device, a number of challenges existed for the liquid phase polythiophene-containing F-ECD system. Included in these problems was sufficient sealing of the device. With tilting and flexing, the EC solution could be lost from the device, and with time (24–48 h), a drying of the electrochrome/electrolyte was noted, limiting the prolonged lifetime of the device. Additionally, the plastic nature of the PET/ITO film electrode reduced the flexibility, the fabric handle, and the textile nature of the device. In the most recent developments made by Kelly et al., the liquid phase polythiophenes have been replaced with their solid phase analogs and the PET/ITO film replaced with a conductive textile electrode (Fig. 22), giving rise to an all-textile, all-solid structure. In this fourth-generation F-ECD, the rapid switching times observed in the liquid phase polythiophene-containing device remain, yet the lifetime of the device has been seen to be extended to more than 3 weeks. This technology also allows for the creation of pixels or shapes in rectangular or fluid forms. Forthcoming generations of the devices prepared by Kelly et al. therefore express a lot of promise for the future.

Gregory A. Sotzing and his group at the University of Connecticut have been working on the development of an all-organic F-ECD using a stretchable spandex fabric soaked in PEDOT:PSS. The spandex itself becomes the electrode when it is soaked in a conductive polymer solution. A silane-containing precursor polymer was spray coated on the conductive PEDOT:PSS spandex textile and then oxidatively converted (electrochemically or chemically) to its EC counterpart [52–54]. A cross-sectional schematic of the fabric EC devices used in these studies is given in Fig. 23a. Devices were assembled with conductive steel fabrics as both electrodes, steel counter with spandex working electrode, and spandex as both electrodes. When a coating of EC polymers was applied to both upper and lower textile electrodes and two layers were sandwiched together over a film of gel electrolyte, a two-color reversible fabric was obtained. A different color, owing to the different oxidation state, was observed on each side (Fig. 23b). The EC polymers in their

a

Monomer	Structure	Neutral	Oxidised
EDOT	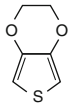	Dark Blue	Transparent Blue
ProDOT-Et_2	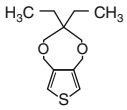	Dark Purple/Blue	Transparent Purple/Blue
ProDOT-Me_2	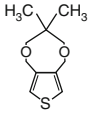	Dark Purple	Transparent Purple
ProDOT	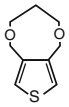	Dark Purple/Grey	Transparent Purple/Grey

b

Monomer	Structure	Neutral	Oxidised
3-PT	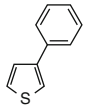	Yellow	Transparent Yellow
2,2'-BT	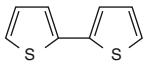	Green	Red
2,3'-BT	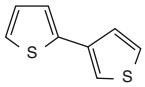	Grey/Green	Yellow
5-H-2,2'-BT	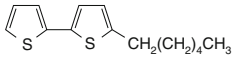	Green	Transparent Green

Fig. 20 Structures of substituted thiophene monomer units and the colors of their corresponding polymers in (**a**) oxidized and (**b**) neutral forms (Image reprinted from Kelly et al. (2013) Journal of Display Technology 9:626) [39]

solution phase may also be stenciled onto the flexible spandex fabric substrates (Fig. 24), with the color-changing properties remaining in relaxed and stretched forms. The color intensity of the EC spandex is modulated by the stretch of the

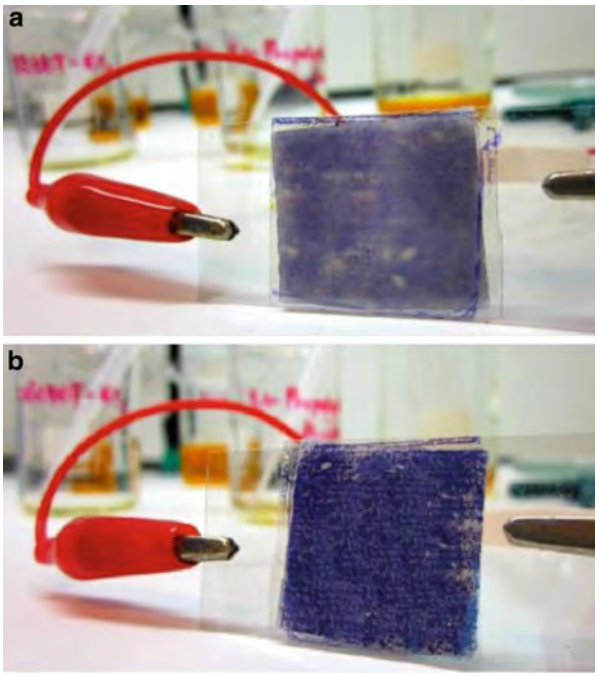

Fig. 21 F-ECD containing PProDOT-Me_2 in its (**a**) oxidized and (**b**) neutral (reduced) states [50]

Fig. 22 F-ECD containing PEDOT:PSS in its (**a**) oxidized and (**b**) neutral (reduced) states [51]

fabric. Sotzing's group is also working on EC threads and fibers for direct weaving into fabrics, therefore opening up a wide range of possibilities for the display and textile industries.

In addition, Sotzing et al. have extended the color effects of an electrochrome by applying them to fabrics of different colors [55]. Colored fabrics were firstly treated with a commercially available conducting polymer (PEDOT:PSS) to create a conductive fabric and were then coated with an EC conducting polymer precursor. The EC material was switched between their two colored states via reversible oxidation and reduction (Fig. 25). The combined color effects of the colored fabric and the electrochrome can create innumerable colored states that can be tailored for

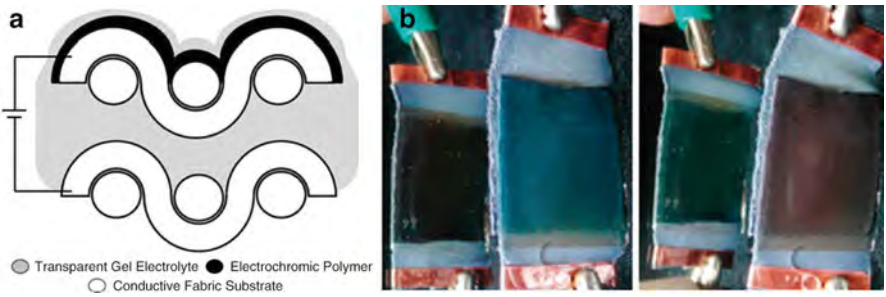

Fig. 23 (**a**) Cross section of the spandex electrochromic device for a typical reflective device used in this study; (**b**) a two-sided device has been placed in front of a mirror so that the color of each side of the fabric can be observed, device in its oxidized (*left*) and neutral (*right*) states (Images reprinted from M. A. Invernale et al. (2010) ACS Applied Materials and Interfaces 2:296, with permission of the American Chemical Society) [53]

Fig. 24 Stencil-patterned solid-state fabric ECD in its neutral (*top*) and oxidized (*bottom*) state (Image reprinted from Invernale et al. (2010) ACS Applied Materials and Interfaces 2:296, with permission of the American Chemical Society) [53]

Fig. 25 The effects of PEDOT:PSS in the (**a**) precursor, (**b**) oxidized, and (**c**) neutral states, on the color of dyed fabrics (Image reprinted from Invernale et al. (2011) Coloration Technology 127:167) [55]

the desired application. This information may be useful for the fabrication of a variety of wearable displays or fashion items.

Challenges Concerning Flexible Electrochromic Displays

The past decade, with the number of research groups participating in the field and multitude of publications published, has seen an exponential leap in the potential of F-ECDs. Numerous patents have been filed [54, 56–63], yet the commercial market continues to anticipate its first color-changing textile based on EC technologies. The most likely reasons for their delay are due to (1) fabrication techniques and stability of ECD structure with flexing, (2) switching times, and (3) operating lifetime.

The development and practical applications of F-ECDs are restricted by their methods of preparation and the EC material itself. Instability in EC devices can have at least four sources: mechanical, electrochemical, chemical, and photochemical [64]. Mechanical damage can occur from misuse or defects in the thin films during manufacturing. Traditional techniques for fabricating EC films include magnetron sputtering, plasma-enhanced chemical vapor deposition, electrodeposition, and lithography. These usually require expensive equipment, rigorous experimental conditions, and multiple processing steps. Conventional EC materials are liable to crack and detach from the substrate after repetitive bending or strain, owing to poor adhesion between materials and flexible substrate. ECs in their liquid phase pose the problem of leakage and/or drying if the device is not sealed sufficiently. Additionally, for the continuous functioning of F-ECDs, a robust intimate electrical contact must be maintained between all structural layers – electrodes, electrochromes, and electrolyte. Hence, the development of EC devices based on textiles, which are required to be inherently flexible, presents a substantial engineering challenge.

Another limitation with ECDs has been their relatively slow switching speeds from one color to another, preventing the ability to play moving images. The color-switching rate is limited by the diffusion rate of counterions into the film during the redox process. Hence, the simplest way to overcome slow switching rates would be to decrease the diffusion distance of ions, i.e., to reduce film thickness. However, it has been seen that thinner films alone are often too thin to have enough contrast to show good coloration. Sang Bok Lee and his team at the University of Maryland have been exploring nanotubes as a way to increase the switching times but also offer good color contrast [65, 66]. In the quest for paperlike displays (or so-called electronic paper), hollow nanotubes of EC polymers have been prepared and applied within ECDs. The nanotubes have walls 10–20 nm thick but several hundred nanometers in length. The thin nature of the nanotube walls offers a short ion diffusion distance, resulting in ultrafast switching rate (switching time less than 10 milliseconds), and the length of the nanotubes, in an array structure, produces a strong coloration for the display system. Since the initial developments, Lee et al. have further developed methods for increasing coloring by growing

hybrid nanotubes of several polymers [67]. Films of nanotubes that work in both reflective and transmissive modes have been prepared, showing great potential for rigid and flexible displays alike.

Finally, the operating lifetime poses a challenge for the successful commercialization of F-ECDs. In addition to the fabrication and structural challenges with flexing discussed above, the stability of the EC material can be considered as another key factor in determining the operating lifetime of the device. Electrochemical damage of the electrochrome can occur from an over polarization due to a nonuniformity of current across the surface [68]. Additionally, irreversible electrochemical processes include aggregation, dimerization, and non-electrochemical oxidation due to air and/or light. Modification and functionalization of conducting polymer monomer units have been studied as a method to improve the electrochemical stability. The mechanical and chemical stability of EC materials has also been seen to be improved by creating inorganic–organic composite hybrids. Chemically stable inorganic particles or matrixes such as SiO_2 or Al_2O_3 have been typically employed for this function with promising results. For example, Fu et al. have described that the direct interfacial reaction between the polymer and attacking electrolytes is reduced due to the strong interaction between surface groups of polyaniline and silica particles [69].

Summary

Color-changing textiles have an important place in the society. They can be used to express emotions and opinions, for identification and decoration, or for safety and camouflage purposes. Electrochromic displays have certain advantages over their light-emitting counterparts (LED, fiber optic, OLED, and electroluminescence). Their colors are visible in natural or ambient light, there is no visual dependence on the viewing angle, and multiple colors, with high contrast, are available. In comparison to light-emitting devices, which require a continuous flow of electricity for the color to be visible, ECDs only require a pulse of an electrical to effect the color change. Due to its optical memory, the color of the ECD remains until a pulse of the reverse potential is applied, therefore making it a highly economical technology for color-changing devices.

In terms of the range of flexible electrochromic device structures that have been reported and the novel applications proposed, the world of F-ECDs is steadily expanding. F-ECDs are multicomponent systems consisting of a combination of two electrodes, an electrolyte, and an electrochrome and include at least one flexible textile component. Due to the nature of such devices, challenges owing switching times, operating lifetime, and fabrication techniques and flexible structure stability exist. However, improvements in these areas are well underway, and enhancements in the synergy of all parts will see a great success in the field as a whole. The words of Roger Mortimer summarize very well the future of the EC domain, and transfer equally to the world of flexible textile ECD displays: "*The future is not only bright, but also high-contrast and colourful*" [67].

References

1. Tao X (2001) Smart fibres, fabrics and clothing: fundamentals and applications. Woodhead Publishing, Cambridge
2. Cochrane C, Meunier L, Kelly FM, Koncar V (2011) Flexible displays for smart clothing: part I—overview. Indian J Fibre Text Res 36:422–428
3. Flexmedia (08 Jan 2014) http://www.flexmedia.com/tWeb/images/pdf/FlexmediaOverview.pdf
4. Genz R, Rosella F (08 Jan 2014) http://cutecircuit.com/collections/t-shirt-os/
5. Genz R, Rosella F (08 Jan 2014) http://cutecircuit.com/collections/the-galaxy-dress/
6. Koncar V (2005) Optical fiber fabric displays - OFFD. Optics Photonics News 16:40–45
7. Deflin E, Koncar V, Weill A, Vinchon H (2001) Bright optical fiber fabric. GEMTEX Publication, Hong-Kong
8. Luminex (08 Jan 2014) http://www.luminex.it/
9. Mordon S, Cochrane C, Lesage JC, Koncar V (2011) Innovative engineering design of a textile light diffuser for photodynamic therapy. Photodiagnosis Photodyn Ther 8:142–143
10. Sudhakar P, Gobi N (10 Jan 2014) http://www.fibre2fashion.com/industry-article/technology-industry-article/chameleonic-textiles/chameleonic-textiles1.asp
11. Van Langenhove L (2007) Smart textiles for medicine and healthcare: materials, systems and applications. Woodhead Publishing, Cambridge
12. Radiate Athletics (10 Jan 2014) http://www.kickstarter.com/projects/radiate/radiate-athletics-the-future-of-sports-apparel?ref%E2=%E2popular and http://www.radiateathletics.com/
13. Chung K (10 Jan 2014) www.whodesignedit.net/design/heat-sensitive-paint-ideas-shi-yuan
14. Bamfield P (2010) Chromic phenomena: the technological applications of colour chemistry. The Royal Society of Chemistry, Cambridge
15. Winters R (11 Jan 2014) http://www.rainbowwinters.com/
16. Zhong W (2012) An introduction to healthcare and medical textiles. DEStech Publications, Pensylvania
17. Goudjil K (1996) Photochromic ultraviolet detector, US 5581090 A
18. Vikova M, Vik M (2011) Alternative UV sensors based on color-changeable pigments. Advance Chem Engineer Sci 1:224–230
19. Osti E (2008) Skin ph variations from the acute phase to re-epithelialization in burn patients treated with new materials (burnshield®, semipermeable adhesive film, dermasilk®, and hyalomatrix®). Non-invasive preliminary experimental clinical trial. Ann Burns Fire Disaster 21:73–77
20. Sun D (12 Jan 2014) http://www.sundahea.com/rain%20palette.html
21. Somania PR, Radhakrishnan S (2002) Electrochromic materials and devices: present and future. Mater Chem Phys 77:117–133
22. Mortimer RJ, Dyer AL, Reynolds JR (2006) Electrochromic organic and polymeric materials for display applications. Displays 27:2–18
23. Rosseinsky DR, Mortimer RJ (2001) Electrochromic systems and the prospects for devices. Adv Mater 13:783–793
24. Silver J (1989) Chemical chameleons for electronics
25. Bonsor K (12 Jan 2014) http://home.howstuffworks.com/home-improvement/construction/green/smart-window4.htm
26. Gordon N http://www.dwfcontract.com/Drapery–Window-Covering-Blog/bid/83137/Being-Green-with-Smart-Glass
27. Monk PMS, Mortimer RJ, Rosseinsky DR (1995) Electrochromism: fundamentals and applications. VCH, Weinheim
28. Hagenmuller P, Gool W (1978) Solid electrolytes. General principles, characterization, materials, applications. Academic, New York
29. Pratt C (2005) Chromism. homepage.ntlworld.com/colin.pratt/Chromism.pdf
30. Somani PR, Radhakrishnan S (2003) Electrochromic materials and devices: present and future. Mater Chem Phys 77:117–133

31. Monk P, Mortimer R, Rosseinsky D (2007) Electrochromism: fundamentals and applications. 504
32. Sapp SA, Sotzing GA, Reynolds JR (1998) High contrast ratio and fast-switching dual polymer electrochromic devices. Chem Mater 10:2101–2108
33. Scarminio J, Urbano A, Gardes BJ, Gorenstein A (1991) Electrochromism in nickel oxide films obtained by thermal decomposition. J Mater Sci Let 11:562–563
34. Oh DH, Boxer SG (2002) Electrochromism in the near-infrared absorption spectra of bridged ruthenium mixed-valence complexes. J Am Chem Soc 112:8161–8162
35. Schoot CJ, Ponjee JJ, van Dam HT, van Doorn RA, Bolwijn PJ (1973) New electrochromic memory display. Appl Phys Lett 23:64–65
36. Eloi J, Chabanne L, Whittell G, Manners I (2008) Metallopolymers with emerging applications. Mater Today 11:28–36
37. Patil A, Heeger AJ, Wudl F (1988) Optical properties of conducting polymers. Chem Rev 88:183–200
38. Kelly FM (2005) Hybrid materials of cellulose and protein with conducting polymers. Victoria University of Wellington, Wellington
39. Kelly FM, Cochrane C, Koncar V (2013) Evaluation of solid or liquid phase conducting polymers within a flexible textile electrochromic device. J Display Tech 9:626–631
40. Gaupp CL, Reynolds JR (2003) Multichromic copolymers based on 3,6-bis(2-(3,4-ethylenedioxythiophene))-N-alkyl carbazole derivatives. Macromolecules 36:6305–6315
41. Kelly FM (2013) Figure: the colour of thiophene electrochromics may be tuned by functionalising the monomer unit before polymerisation
42. Hanlon M (15 Jan 2014) http://www.gizmag.com/go/4821/
43. Savastano D http://www.printedelectronicsnow.com/articles/2009/10/nteras-innovations-partnerships-are-leading-to-exc
44. Mortimer RJ (2002) Electrochromic polymers. Wiley
45. Schawaller D (2013) Flexible, switchable electrochromic textiles. Macromol Mater Eng. Article first published online: 19 July 2013
46. Beaupré S, Dumas J, Leclerc M (2006) Toward the development of new textile/plastic electrochromic cells using triphenylamine-based copolymers. Chem Mater 18:4011–4018
47. Zhang Q, Xin B, Lin L (2013) Preparation and characterisation of electrochromic fabrics based on polyaniline. Adv Mater Res 651:77–82
48. Kelly FM, Cochrane C, Koncar V (2013) Polyaniline: application as solid state electrochromic in a flexible textile display. Displays 34:1–7
49. Meunier L, Kelly FM, Cochrane C, Koncar V (2011) Flexible displays for smart clothing : part II – electrochromic displays. Indian J Fibre Text Res 36:429–435
50. Kelly FM (2012) Photo: ECD containing PProDOT-Me2 in its oxidised and neutral states
51. Kelly FM (2013) Photos: F-ECD containing PEDOT:PSS in its oxidised and neutral (reduced) states, and showing its flexibility
52. Ding Y, Invernale MA, Mamangun DMD, Kumar A, Sotzing GA (2011) A simple, low waste and versatile procedure to make polymer electrochromic devices. J Mater Chem
53. Invernale MA, Ding Y, Sotzing GA (2010) All-organic electrochromic spandex. ACS Appl Mater Interfaces 2:296–300
54. Sotzing GA, Invernale MA (2012) Flexible electrochromic devices, electrodes therefor, and methods of manufacture US 8107153 B2
55. Invernale MA, Ding Y, Sotzing GA (2011) The effects of coloured base fabric on electrochromic textile. Color Technol 127:167–172
56. Nike Inc (2013) Article of footwear with color change portion and method of changing color US 8474146 B2
57. Sotzing GA, Mather PT (2012) Conjugated polymer fiber, preparation and use thereof US 8178629 B2
58. Orth M, Berzowska JM (2003) US Patent 200322415
59. Xu C, Ma C, Taya M (2010) Flexible panel based on electrochromic polymers US 7826124 B2

60. Chameleon Optics (2008) Adhesive ion-conducting layer for flexible electrochromic devices US 7414771 B2
61. Chameleon Optics (2002) Flexible Electrochromic Devices US 6456418 B1
62. Shim GH, Han MG, Foulger SH (2010) Electrochromic inks including conducting polymer colloidal nanocomposites, devices including the electrochromic inks and methods of forming same US 7785496 B1
63. Chameleon Optics (2009) Metal ferrocyanide-polymer composite layer within a flexible electrochromic device US 7586665 B1
64. Rauh R (1999) Electrochromic windows: an overview. Electrochim Acta 44:3165–3176
65. Cho SI, Lee SB (2008) Fast electrochemistry of conductive polymer nanotubes: synthesis, mechanism and application. Acc Chem Res 41:699–707
66. Cho SI, Xiao R, Kim S-H, Lee SB (2007) Electrochemical synthesis of Poly (3,4-ethylenedioxythiophene) nanotubes toward fast window-type electrochromic device. Nanotechnology 18:405705
67. Mortimer RJ (2013) Switching colors with electricity. Am Sci 101:38–45
68. Doblhofer K, Rajeshwar K, Skotheim T, Elsenbaumer RL, Reynolds JR (1998) Handbook of conducting polymers. Marcel Dekker, New York
69. Fu Y-b, Ma X-h, Yang Q-h, Zong X-f (2003) The effect of fumed silica on the interfacial stability in the polymer gel electrolyte. Mater Lett 57:1759–1764

Smart Nanofibrous Membranes with Controllable Porous Structure and Surface Wettability for High Efficient Separation Materials

33

Yang Si, Xiaomin Tang, Jianyong Yu, and Bin Ding

Contents

Introduction 892
Liquid-Proof Breathable Membranes 893
Basic Principles 893
Amphiphobic Waterproof Breathable Membranes 895
Superamphiphobic Liquid-Proof Breathable Membranes 900
Membranes for Oil Spill Cleanup 902
Backgrounds 902
Porous PS Nanofibers 904
PS–PU Core–Shell Nanofibers 909
Membranes for Emulsified Oil–Water Separation 911
Summary 915
References 916

Abstract

High-performance separation materials head one of the top materials facing the future environmental issues such as liquid–air separation, oil spill cleanup, and oil–water separation. Nanotechnology is responding to these challenges by designing and fabricating functional nanofibrous membranes optimized for separation applications. The route toward such nano-objects is based primarily on electrospinning, a highly versatile method that allows the fabrication of continuous fibers with diameters down to a few nanometers. This chapter focuses on the recent progress on the electrospun nanofibrous membranes for high efficient separation applications. Nanofibers with complex architectures,

Y. Si • X. Tang • J. Yu • B. Ding (✉)
State Key Laboratory for Modification of Chemical Fibers and Polymer Materials, College of Materials Science and Engineering, Donghua University, Shanghai, China

Nanomaterials Research Center, Modern Textile Institute, Donghua University, Shanghai, China
e-mail: siyang13@mail.dhu.edu.cn; mindytang@qq.com; yujy@dhu.edu.cn; binding@dhu.edu.cn

© Springer Science+Business Media Singapore 2015

X. Tao (ed.), *Handbook of Smart Textiles*,
DOI 10.1007/978-981-4451-45-1_1

such as adhesion structure, porous structure, core–shell structure, and bio-inspired structure, have been fabricated by special electrospinning methods. By the introduction of low surface energy materials such as fluorinated polyurethane and polybenzoxazine, the pristine nanofibers were endowed with promising superwettability, which significantly boosted the separation selectivity and efficiency. And nanoparticles such as SiO_2 and Al_2O_3 were used to create functional membranes with hierarchical structures, thus further improving the separation performance. Furthermore, the demonstration of electrospun nanofibers used for advanced separation applications has indicated that their impact has been realized well and is encouraging and will continually represent a key technology to ensure sustainable environment and human lives for the future.

Keywords
Electrospinning • Nanofibers • Porous structure • Wettability • Separation materials

Introduction

High-performance separation materials head one of the top materials facing the future environmental issues such as liquid–air separation, oil spill cleanup, oil–water separation, etc. [1, 2]. The two key factors of separation materials are porous structure and surface wettability, which are closely related to the separation efficiency and capacity [3]. Generally, the porous structure including the pore sizes and pore arrangements, as well as various magnitudes of the total porosity and thus of specific surface areas, has a significant effect on the separation performance [4]. On the other hand, the wettability of solid surfaces is controlled by the surface chemistry and the geometrical roughness. According to the Wenzel and the Cassie–Baxter model, the introduction of a proper multi-scale roughness could make a pristine hydrophobic surface to be more hydrophobic or even superhydrophobic owing to the air to be trapped underneath the water droplet as a cushion, whereas an oleophilic surface becomes more oleophilic or even superoleophilic owing to the capillary effect [5]. Thus, there is a chance to control the wettability of separation materials by the combination of low surface energy and proper rough topography.

Given the recognition to the relevant principles, the demands for high-performance separation materials have led to increasing attention in advanced functional nanosized materials [6]. Among those existed nanostructures, one-dimensional (1D) nanofibers are of current interest for their unique separation performance due to the small fiber diameter, large surface area, high porosity, and good connectivity [7]. Up to now, substantial strategies have been established to generate nanofibers including electron beam or focused ion beam writing; lithography; hydrothermal, chemical vapor deposition; template-directed, self-assembly, and interface synthesis technique; etc. [8]. However, most of these methods have limitations, such as material restrictions, high cost, and high process complexity.

Recently, the route toward such nano-objects is gradually focused on electrospinning, a highly versatile method that allows the fabrication of continuous fibers with diameters down to a few nanometers [9]. The mechanism responsible for the fiber formation mainly includes the Taylor cone theory and flight instability theories, which can be predicted theoretically and controlled experimentally [10]. The method can be applied to synthetic and natural polymers and polymer alloys, as well as metals and ceramics. Fibers with complex architectures, such as core–shell fibers, helix fibers, porous fibers, and hollow fibers, can be produced by special electrospinning methods [11]. Consequently, researchers are able to flexibly control the fiber component, morphology, and aggregate structure, which have provided much impetus to the dream of realizing the separation applications of electrospun nanofibers. This chapter focuses on the recent progress on the electrospun nanofibrous membranes applied in liquid–air separation, oil spill cleanup, and oil–water separation.

Liquid-Proof Breathable Membranes

Basic Principles

Liquid-proof and breathable membranes have been used in sports apparel, fashion rainwear, and protective workwear for more than 30 years, which were mainly applied in health care, agriculture production, military personnel, emergency responses, etc. [12]. Previously, the commonly used protective clothing materials are typically impermeable barriers to block penetration of any water or liquid contaminants. However, the achievement of such functionalities alters the wearing and comfort performance of clothing, including bulky materials, heavyweight, and high thermal burden to poor water vapor transmission (WVT) [12, 13]. Currently, technologies for incorporating membranes into fabrics and garments have evolved dramatically. Figure 1 shows various types of aesthetics for the liquid-proof and breathable fabrics, which provide the best possible compromise between comfort and protection, under the widest range of activities and climatic conditions [12, 14].

Nonwovens, which are used for protective clothing, have continued to grow due to relatively inexpensive, lightweight, and effective protection. A porous spunbond nonwoven with high air permeability exhibits low barrier performance, whereas a compact one provides high level of protection but low level of thermal transport [15]. In particular, microporous membranes and laminated fabrics, which are used as a barrier material for certain personal protective equipment applications, offer a higher level of protection. Generally, these membranes have a clearly visible system of holes as interconnected passage ways and hydrophobic surface, which enable them to discriminate between water droplets (liquid or other forms of atmospheric precipitation, diameters > 100 μm) and small-molecule gases (diameters < 1 nm), essentially on the basis of microporous structure and surface chemistry character [16].

The conventional fabrication strategies for microporous membranes, including mechanical fibrillation, wet coagulation, solvent extraction, radio frequency or

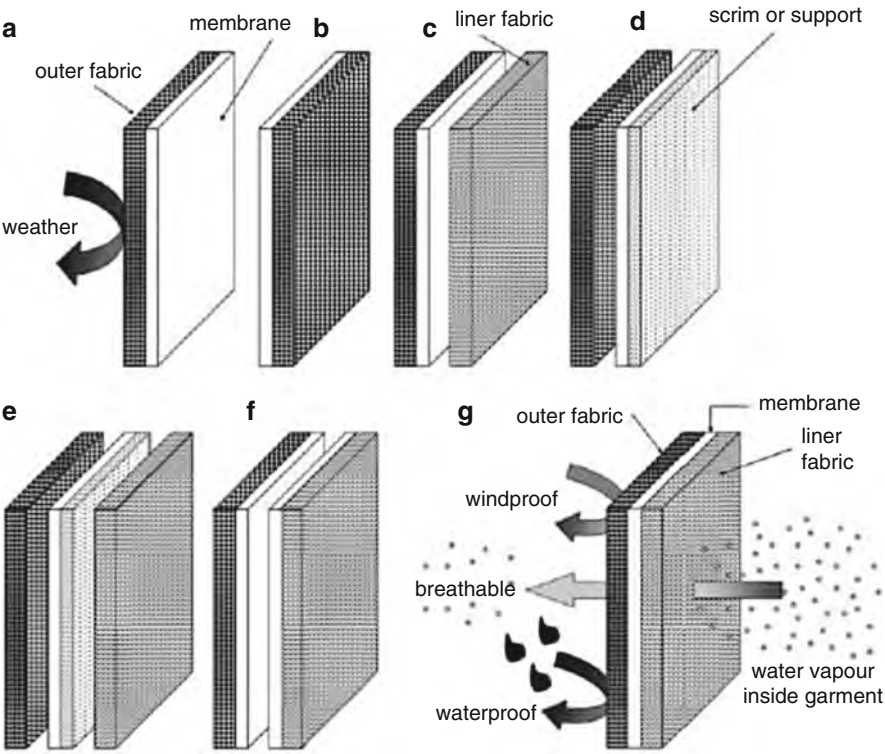

Fig. 1 Schematic showing the various types of aesthetics for the liquid-proof and breathable fabrics: (**a**) basic two-layer fabric with coating on inside, (**b**) two-layer, coating on outside, (**c**) two-layer plus loose liner fabric, (**d**) loose outer fabric plus scrim-supported membrane, (**e**) drop liner insert, (**f**) double-membrane system, (**g**) pictogram showing breathability and weatherproofness of a three-layer laminate (Reprinted with permission from Lomax [12], © 2007, Royal Society of Chemistry)

ultraviolet radiation, and melt blown, are known to be very complicated and costly, as well as unsuitable for the preparation of waterproof breathable membranes due to the limitation of raw materials and the difficulty in increasing porosity [17]. On the other hand, electrospinning has been shown to be a simple but powerful technique for the preparation of waterproof breathable fibrous membranes at the nano- and microscale levels. Polyurethane (PU) is mostly chosen as the starting polymer for the preparation of liquid-proof breathable membranes owing to a range of desirable properties such as elastomeric, resistant to abrasion, and excellent hydrolytic stability [18]. Also reported is the preparation of PU bicomponent electrospun membranes such as PU/polyacrylonitrile, PU/polysulfone, PU/polystyrene (PS), and PU/polyvinyl chloride [19]. However, the hydrophilic carbamate groups and ether groups in the main chain of PU lead to a relatively high surface energy ($>$40 mJ/m^2); thus, the waterproof property of relevant electrospun membranes was usually lower than 5 kPa, which limited the practical use of these membranes.

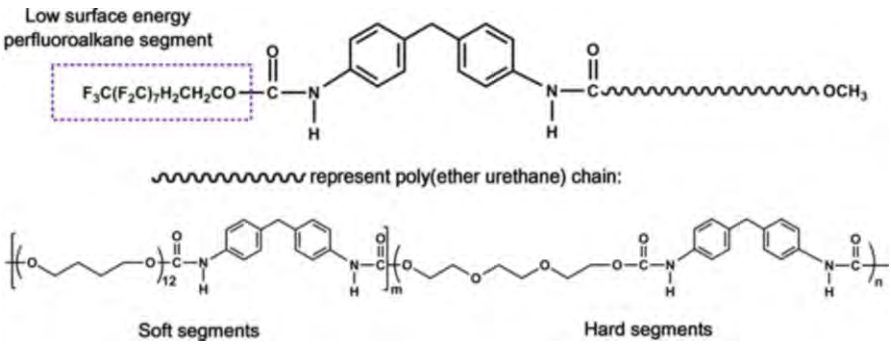

Fig. 2 Illustration showing the chemical structure of as-synthesized FPU [20] (Reproduced with permission from the Royal Society of Chemistry)

Table 1 Compositions and properties of various electrospinning solutions [20] (Reproduced with permission from the Royal Society of Chemistry)

Sample	PU (wt%)	FPU (wt%)	Viscosity (cps)	Conductivity (μS cm^{-1})
PUNF	4		155	3.80
F-NF1	4	0.1	170	3.07
F-NF2	4	0.25	165	2.23
F-NF3	4	0.5	168	2.18

Amphiphobic Waterproof Breathable Membranes

To overcome these problems, Ge et al. synthesized a novel fluorinated PU (FPU), as shown in Fig. 2, which contained low surface energy perfluoroalkane segment, thus endowed the pristine PU membranes with a promising amphiphobicity [20]. The concentration of PU in precursor solution was 4 wt%, and the concentration of as-synthesized FPU was 0, 0.1, 0.25, and 0.5 wt%, respectively. The detailed compositions were listed in Table 1, and the obtained nanofibers prepared from 0, 0.1, 0.25, and 0.5 wt% of FPU solution were denoted as PUNF, F-NF1, F-NF2, and F-NF3, respectively.

The representative FE-SEM image of PUNF shown in Fig. 3a revealed randomly oriented nonwoven membranes with an average fiber diameter of 468 nm. Obviously, adhesions (marked by dotted circle) could be observed among adjacent fibers, which were due to the incomplete solvent evaporation of DMF, as a good solvent for both hard and soft segments of PU. By the introduction of FPU, the morphology of the membranes greatly changed compared with PUNF, as shown in Fig. 3b–d. The average fiber diameters of relevant F-NF1, F-NF2, and F-NF3 were 691, 782, and 995 nm, respectively, indicating that the fiber diameters increased regularly with the increasing of FPU contents and the adhesion structure among fibers decreased gradually as well. A similar result has also been reported in a previous study; the utilization of solutions with high viscosity and low

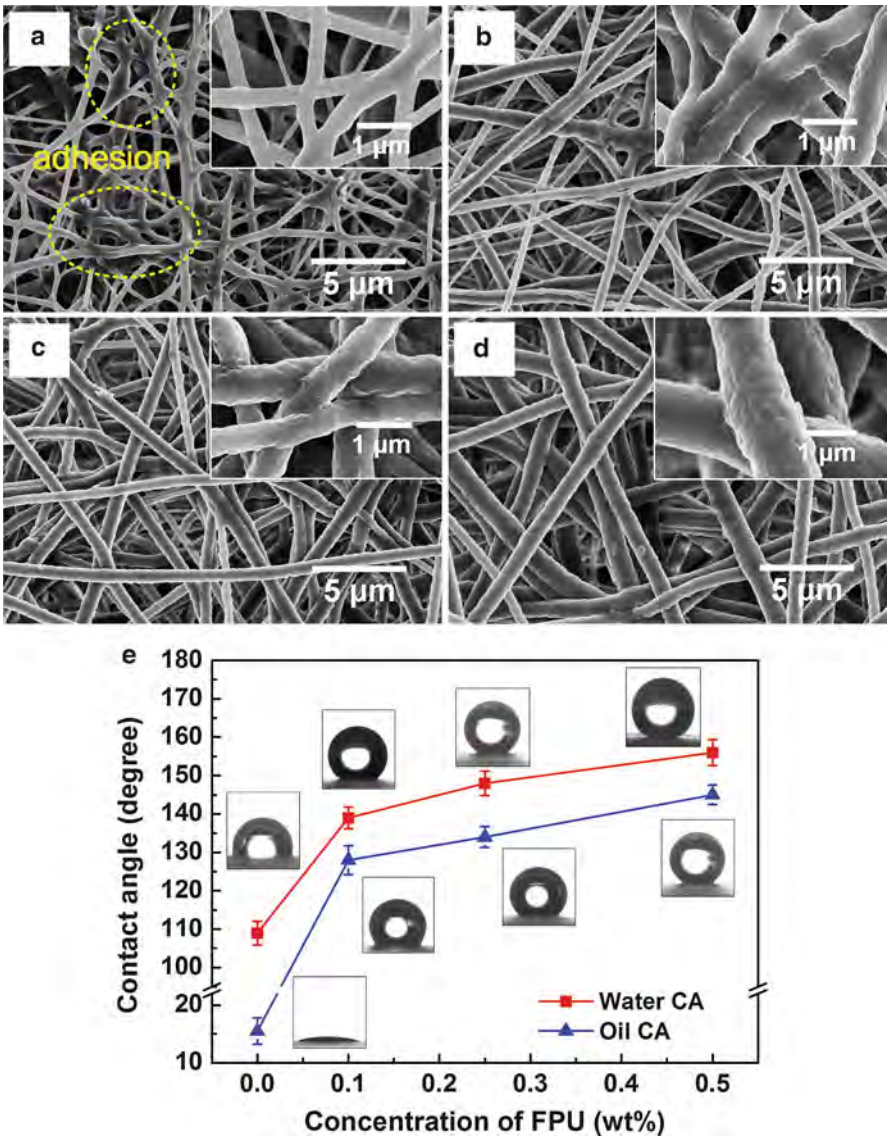

Fig. 3 FE-SEM images of (**a**) PUNF, (**b**) F-NF1, (**c**) F-NF2, and (**d**) F-NF3 membranes. (**e**) Water contact angle (*WCA*) and oil contact angle (*OCA*) of relevant of PUNF, F-NF1, F-NF2, and F-NF3 membranes. The insets show the corresponding optical profiles of water and oil droplets [20] (Reproduced with permission from the Royal Society of Chemistry)

conductivity in electrospinning contributed to the formation of this structure [21]. In addition, it was clearly showed that the gradually increased wrinkles were on the fiber surface toward the increasing of FPU contents, thus creating a hierarchical structure containing micro- and nanoroughness. This phenomenon could be

attributed to the generation of collapse on the fluid jet surface during fast phase separation, which was resulted from the decrease of jet stretch and electrical repulsion.

As mentioned above, the PU is a thermoplastic elastomer composed of hard diisocyanate segments and soft polyether segments, and the carbamate groups in hard segments and the ether groups in soft segments provide comparable hydrophilic structure, thus leading to a high surface energy of larger than 40 mJ/m^2 [22]. As a result, the PUNF membranes had a relatively low WCA of 109°, as shown in Fig. 3e. On the other hand, the as-synthesized FPU containing perfluoroalkane segments at the head of the polymer chain possessed an extremely low surface energy of 18.08 mJ/m^2; thus, the introduction of FPU greatly improved the hydrophobicity of resultant membranes. As shown in Fig. 3e, the WCA of F-NF1, F-NF2, and F-NF3 were 139°, 148°, and 156°, respectively, revealing that the WCA increased regularly with the increasing of FPU contents. These results could be explained by the reasons that the increasing of FPU contents not only decreased the surface energy of materials but also significantly enhanced the hierarchical rough structure of membranes, as demonstrated in FE-SEM observations [20].

Substantial studies have revealed that the mechanical behaviors of electrospun fibrous membranes were closely related to the geometric arrangement of the fibers and the bonding among fibers [23]. As demonstrated above, the as-prepared PUNF and F-NF membranes exhibited randomly oriented 3D nonwoven geometry; thus, the point-bonded structure would be the primary factor that affects the mechanical properties. Moreover, the FE-SEM images clearly showed that the relevant membranes had both bonding structure and nonbonding cross structure and thus could exhibit different structural transformations in the strain process [24]. The typical tensile stress–strain curves of relevant membranes were shown in Fig. 4a; all the membranes showed a nonlinear elastic behavior in the first region under a stress load, and then the stress–strain curves exhibited a typical linear increase until break. This interesting mechanical feature could be explained by the two-step break mechanism, as demonstrated in Fig. 4b. When a small external load was applied, the relatively weak nonbonded cross structures tended to break and slip apart, resulting in the first nonlinear elastic behavior. Thus, the membranes with higher FPU contents possessed more physically nonbonding points (less adhesion structure) and yielded larger slip strain (indicated by dotted line in Fig. 4a). Subsequently, the curves showed a linear elasticity as the intrinsic property of PU elastomer with the continually increasing of tensile stress, which was due to the elongation of individual fibers. Finally, the break of resultant membranes was resulted from the break of fibers between bonding points. Furthermore, the PUNF with the highest bonding structure showed the maximum tensile strength of 12.91 MPa, and all the F-NF membranes exhibited robust tensile strength (>10 MPa) and elongation at break (>600 %), thereby implying good mechanical properties for real applications [20, 25].

As expected, the as-prepared F-NF membranes with superhydrophobicity and good mechanical properties could have robust waterproof and breathable

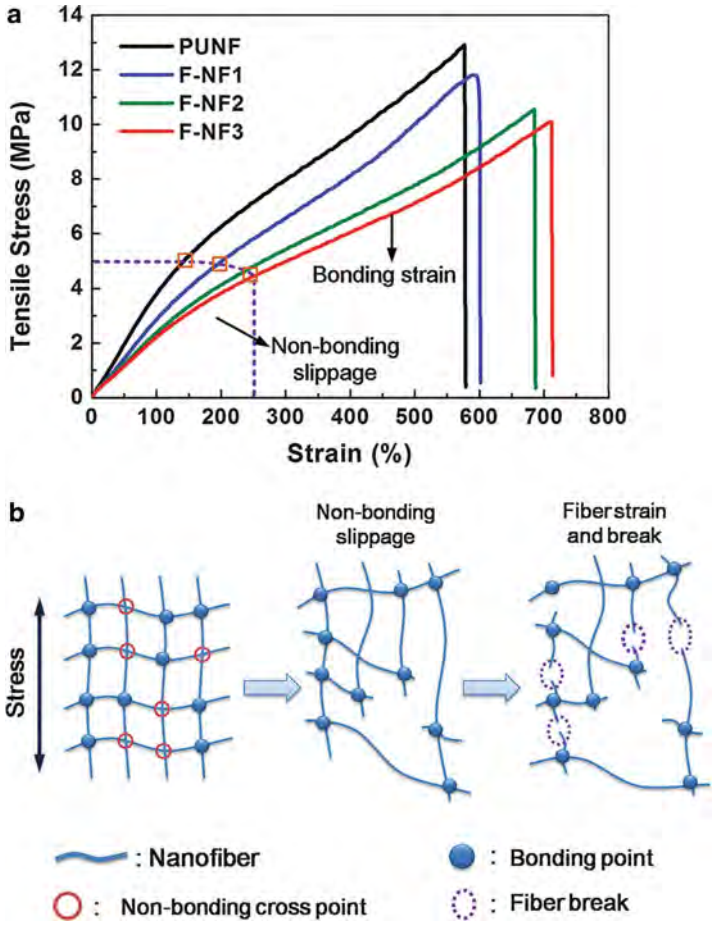

Fig. 4 (**a**) Stress–strain curves of relevant PUNF, F-NF1, F-NF2, and F-NF3 membranes. (**b**) Schematic showing the two-step break mechanism upon external stress [20] (Reproduced with permission from the Royal Society of Chemistry)

performances. Figure 5a showed the resistance to water penetration and water adsorption rate of relevant membranes. As shown in the curves, the pristine PUNF membranes exhibited a minimal hydrostatic pressure of 2.3 kPa due to the low hydrophobicity. Meanwhile, the hydrostatic pressures of F-NF1, F-NF2, and F-NF3 membranes were 19.2, 31.9, and 39.3 kPa, indicating an order of magnitude increase than that of PUNF. Similarly, the hydrostatic pressure increased regularly with the increasing of FPU contents [20].

The increasing of the waterproof performance could be attributed to the strong microporous capillary-repellent force. Generally, the randomly oriented 3D microfibrous structure of the as-prepared membranes provided numerous tortuous porous channels with a scale of several micrometers; on this condition, the

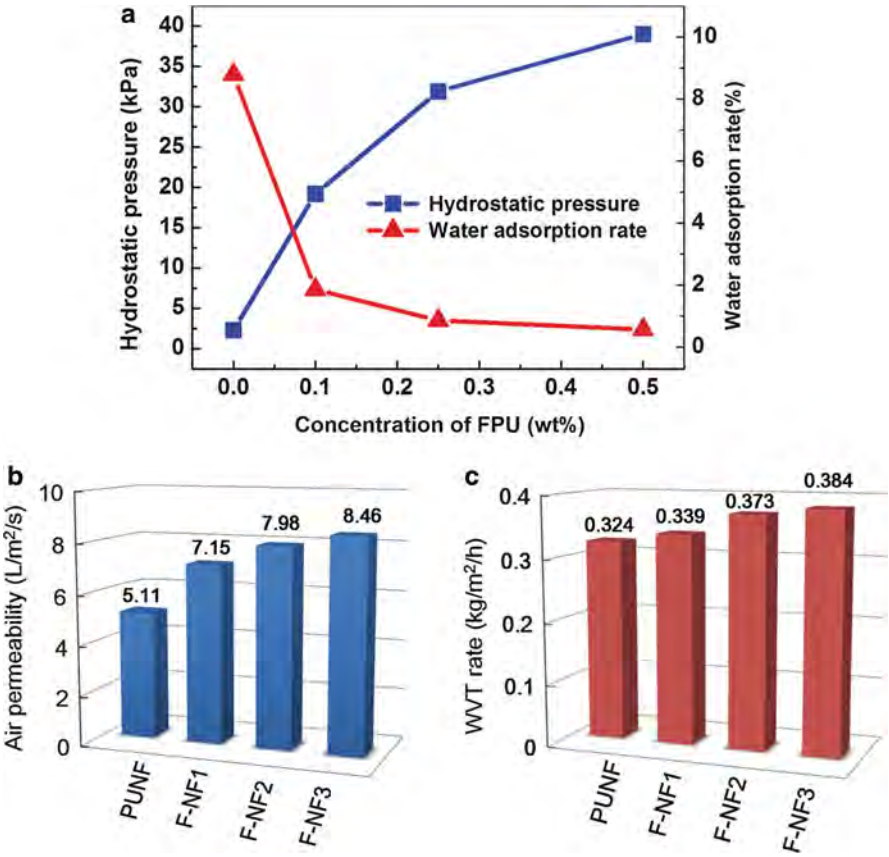

Fig. 5 (**a**) Hydrostatic pressure and water adsorption rate of PUNF, F-NF1, F-NF2, and F-NF3 membranes. (**b**) Air permeability results of relevant membranes. (**c**) WVT rate of relevant membranes [20] (Reproduced with permission from the Royal Society of Chemistry)

prevention of water penetration through these channels was mainly controlled by the capillary force. After adding FPU in membranes, the surface energy effectively decreased while the hierarchical rough structure enhanced significantly and thus finally increased the capillary force that leads to higher water resistance. Moreover, the water absorption rate of relevant membranes decreased with the increase of FPU contents as well, confirming the best waterproof performance of F-NF3 membranes [20].

On the other hand, breathable properties including the air permeability and water vapor transmittance (WVT) were also important for membranes, since they were directly related to the comfort property of relevant fabrics. Typically, the tiny gas molecules (such as air and water vapor) with a size less than 1 nm could facilely pass through the membranes via microporous channels, which were obviously different from the water droplets that would be prevented by the capillary force

[17]. As shown in Fig. 5b, c, the air permeability and WVT rate of relevant membranes increased with the increasing of FPU contents, which was due to the enhancement of the porous structure. Significantly, the as-prepared F-NF3 membranes exhibited the extremely high air permeability of 8.46 L/m^2/s and WVT rate of 0.384 kg/m^2/h, which were obviously higher than that of conventional commercial waterproof breathable membranes [20].

Superamphiphobic Liquid-Proof Breathable Membranes

The as-prepared membranes showed robust waterproof and breathable performance; however, these membranes could not repel to oily liquid. To further increase the liquid-proof performance, Ding et al. fabricated novel superamphiphobic nanofibrous membranes by the combination of FPU nanofibers and incorporated SiO_2 nanoparticles (SiO_2 NPs) [26]. Different from above FPU/PU composite membranes, the newly synthesized FPU with higher molecular weight could be directly used for electrospinning to obtain pure FPU nanofibers. Moreover, the using of SiO_2 NPs could create hierarchical roughness on the membrane surface, which enabled the membranes to show a promising superamphiphobicity. Typically, 18 wt% of FPU containing 0.1, 0.5, 1, 1.5, and 2 wt% of SiO_2 NPs was prepared as spinning solutions, and the corresponding electrospun membranes were denoted as FPU-18/SNP-x, where x was the concentration SiO_2 NPs.

Generally, the intrinsic hydrophobicity of a surface could be improved by being textured with multiple-scaled roughnesses, and nanoparticles owing to their accessibility are widely used to create functional membranes with hierarchical structures to improve the substrate properties [2]. As shown in Fig. 6, the relevant membranes had randomly oriented nonwoven membranes, indicating the typical fiber morphology with no bead-on-string structures, and the fiber diameter increased with the increasing of SiO_2 NPs. Moreover, gradually increased wrinkles and the nanoprotrusions in the range of 100–250 nm (indicated by dotted circle) were clearly visible on the fiber surface with the increasing of SiO_2 NPs contents, generating the hierarchical structures containing micro- and nanoscaled roughness, which could be ascribed to the fast evaporation of the solvent during electrospinning [26].

As expected, the protuberant structures on the surface of nanofibers could significantly boost the superhydrophobicity of the FPU-18/SNP membranes. Figure 7a showed that the WCAs of FPU-18/SNP-0.1, FPU-18/SNP-0.5, FPU-18/SNP-1, and FPU-18/SNP-2 were 159°, 161°, 165°, and 163°, respectively, indicating an obvious increase of WCAs toward the increasing of SiO_2 NPs content. Moreover, the SAs were determined by placing a 10 μL water droplet, which was then inclined at increasing angles until the drop started to roll, as shown in the inset of Fig. 7a. The hierarchical roughness of the fibers reduced the pinning of water droplet on the surface of the membranes (opposite to FPU membranes), thus leading to the low SAs in the range of 2–6°, which indicated the extremely low liquid–solid

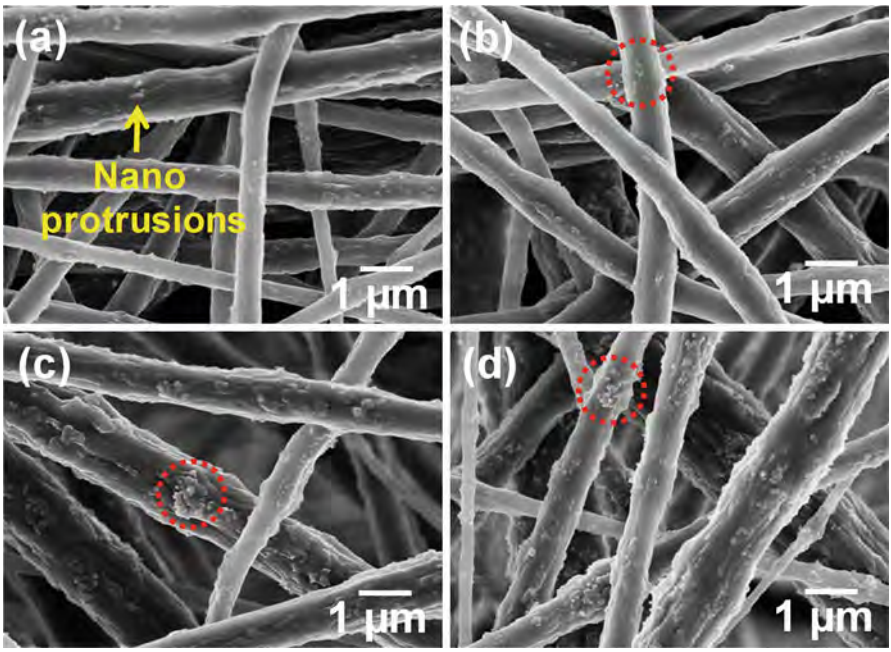

Fig. 6 FE-SEM images of (**a**) FPU-18/SNP-0.1, (**b**) FPU-18/SNP-0.5, (**c**) FPU-18/SNP-1, and (**d**) FPU-18/SNP-2 nanofibrous membranes [26] (Reproduced with permission from the Royal Society of Chemistry)

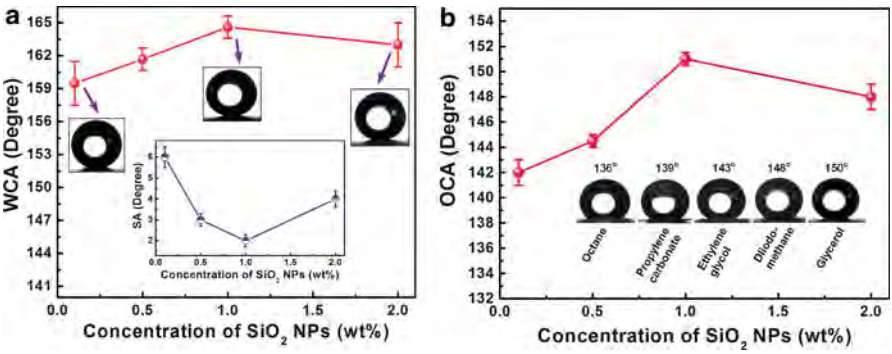

Fig. 7 (**a**) WCAs and (**b**) OCAs of water droplet of the FPU-18/SNP-0.1, FPU-18/SNP-0.5, FPU-18/SNP-1, and FPU-18/SNP-2 membranes. The inset in (**a**) shows the SAs of the relevant FPU-18/SNP membranes. The inset in (**b**) is the optical profiles of droplets and corresponding OCAs of various oily liquids on FPU-18/SNP-1 membranes [26] (Reproduced with permission from the Royal Society of Chemistry)

interface adhesion. Notably, the FPU-18/SNP-1 membrane with the maximum WCA of 165° showed the lowest SA of 2°. Furthermore, the changes in oleophobicity of FPU-18/SNP membranes were identical to that of the hydrophobicity toward the increasing of SiO2 NPs contents (Fig. 7b), and the FPU-18/SNP-1 membrane has shown the maximum oleophobicity with OCA of 151° as well, indicating the prominent superamphiphobicity. In addition, the FPU-18/SNP-1 membrane also exhibited robust oleophobicity toward various oily liquids over a wide range of surface tension, including octane (21.6 mN/m), propylene carbonate (41.1 mN/m), ethylene glycol (47.7 mN/m), diiodomethane (50.1 mN/m), and glycerol (64 mN/m), as shown in the inset of Fig. 7b [26].

To test the liquid-proof and breathable performance of as-prepared membranes, a designed rigorous but interesting experiment was performed as a proof of concept. As shown in Fig. 8, the FPU-18/SNP-1 membranes were fixed between an open tube and a closed tube with an air inlet (left panel in Fig. 8). Then, the membranes could load 1.5 kg water and oil (olive oil) at the same time maintain an extremely high air permeability of 2 L/min (middle panel in Fig. 8). More interestingly, close observation of the membranes (right panel in Fig. 8) showed that the numerous bubbles derived from permeated air continually generated on the surface of membranes, indicating the extremely high air permeability. Consequently, the above results showed that the FPU-18/SNP-1 membranes possessed excellent liquid-proof and breathable performances, which could be applied as promising materials for a wide range of potential applications in protective clothing, bioseparation, water purification, tissue engineering and microfluidic systems, etc. [3, 26].

Membranes for Oil Spill Cleanup

Backgrounds

Oil plays a very important role in the modern industrial world. It is a necessity for a great number of chemicals and synthetic polymers. Unfortunately, oil accidents occur as a result of its exploitation, transportation, utilization, storage, etc., resulting in not only energy loss but also threats to the environment [27]. Generally, oil spills would form an emulsion or floating film and could be toxic to various microorganisms. Moreover, sewers containing mineral oil or fuel carried from the streets by rain and water polluted with edible oils after continuous washing up in restaurants are also problems that must be dealt with [28]. Thus, efficient, cost-effective materials for oil spill cleanup are greatly desired. To date, various methods have been applied for oil spill cleanup, including physical methods (i.e., sorbents, booms, and skimmers), chemical methods (i.e., in situ burning and using of solidifiers), and bioremediation. However, most of these methods still suffer from complicated treatment procedures and high cost, as well as being unsuitable for practical applications because of harsh practical conditions, low stability, and poor selectivity.

Alternatively, mechanical recovery of oil by sorbents is attractive due to the possibility of collection and complete removal of the oil from the oil spill site.

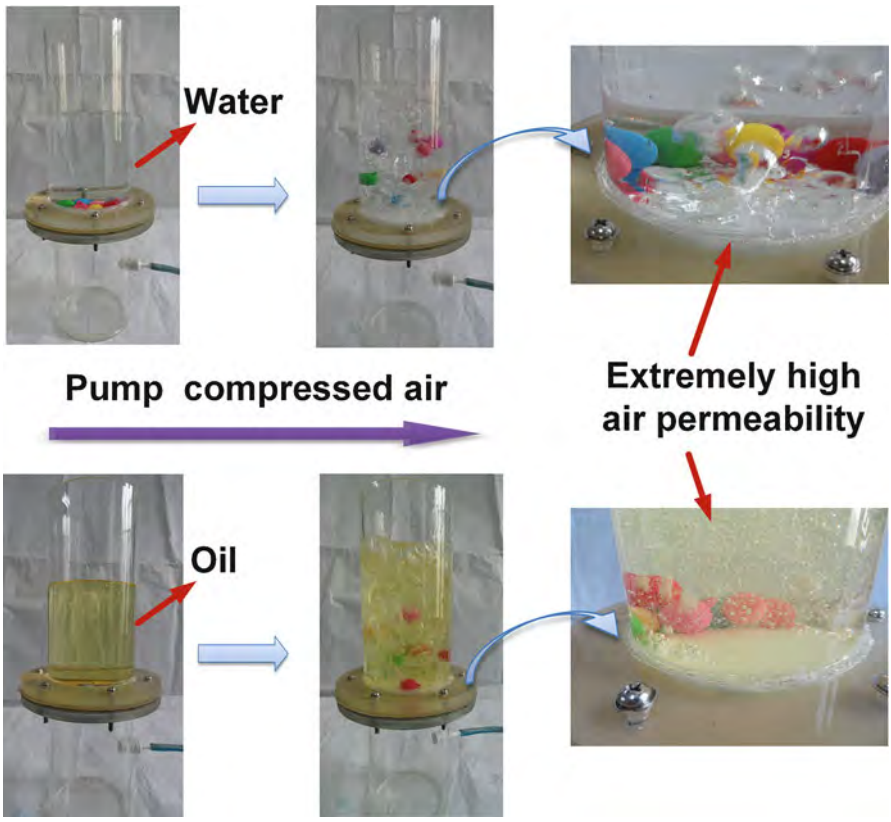

Fig. 8 A designed concept test shows the robust water-/oilproof and breathable performances of FPU-18/SNP-1 membranes, which could load 1.5 kg water/oil and at the same time maintain an extremely high air permeability of 2 L/min [26] (Reproduced with permission from the Royal Society of Chemistry)

Typically, good hydrophobicity–oleophilicity, a high uptake capacity, a high rate of uptake, and good buoyancy are required for an ideal sorbent material for oil spill cleanup [29]. Up to now, the sorbents used for oil sorption mainly included natural materials, inorganic mineral products, and organic synthetic fibers. Among various sorbent materials, synthetic nonwoven polypropylene (PP) fibers have been widely used as sorbents in oil cleanup due to their hydrophobic–oleophilic properties, good oil–water selectivity, high buoyancy, and scalable fabrication. However, they suffered from a low oil sorption capacity (15–30 g/g) because of their low porosity and solid fibers with large diameters [30].

In recent years, with continuous growth in the field of nanotechnology, various nanostructures including nanoparticles, nanofibers, nanowires, nanobelts, and nanotubes have been fabricated. In particular, an appropriate posttreatment through the use of a nonpolar material with low surface energy on these nanomaterials enables them to exhibit hydrophobicity–oleophilicity properties, which make them

a good candidate that suited for applications in oil spill cleanup [2, 4]. Moreover, electrospinning is becoming a simple but powerful technique for the preparation of functional fibrous membranes, and electrospun nanofibrous materials show many advantages compared to the conventional PP nonwovens. The oil sorption capacity will be increased if the fibrous sorbent has the capability of driving the oil not only into the voids among fibers but also into the interiors of fibers [31].

Porous PS Nanofibers

PS is a common thermoplastic polymer with low surface energy due to its CH and aromatic groups and has been widely used to fabricate artificially superhydrophobic surfaces via electrospinning [32]. To date, many efforts have been conducted on the variables in electrospun PS fibers, such as solvent type, solvent conductivity, processing parameters, and relative humidity, thus generating the electrospun PS fibers with typically fine morphologies such as flat and bead structures, porous structures, etc. [33]. Although porous PS fibers have been investigated by a number of researchers, only few efforts have been devoted to the fabrication of electrospun PS fibers with micro- and nanostructures via electrospinning directly, especially providing a full and intuitive observation of the porous structures within the resultant fibers, both interior and exterior. Recently, Ding et al. reported a new one-step method for the fabrication of highly porous PS nanofibers by the facile changing of solvent compositions and investigated the effect of porous structures and the specific surface area (SSA) on their oil sorption capacities [31, 33].

PS ($Mw = 208{,}000\ g\ mol^{-1}$) spinning solutions were prepared at concentrations of 20 %, by using THF–DMF mixtures with weight ratios of 100:0, 80:20, 60:40, 50:50, 40:60, 20:80, and 0:100, respectively. FE-SEM images of relevant PS electrospun fibers from relevant solvent compositions were shown in Fig. 9. In the case of pure highly volatile THF solvent, the pores with an average diameter of approximately 40 nm were densely packed on the fiber surfaces (Fig. 9a). Close observation indicated that the fiber comprised a porous sheath and a solid core. After adding the DMF with 20 %, the pores on fiber surfaces disappeared, but wrinkled surfaces emerged, as shown in Fig. 9b, and the porous core was clearer than that of the fiber electrospun from THF only. More interestingly, as shown in Fig. 9c, the fiber surfaces were coarsened with large pits and grooves with the increasing DMF percentage in the solvent mixtures. With further increasing the DMF content, the fiber surfaces showed the sea–island morphology (the nano-/microprotrusions resemble islands) with the nanopores on the surfaces, and the porous structure appeared to be throughout the cross sections of these fibers (Fig. 9d and e). For the pure DMF solvent, the structural features of porous surfaces became less clear with the fibers, as shown in Fig. 9f [31].

The difference in the porous structure of these resultant fibers could be attributed to the competition between the rapid phase separation and solidification resulting from the mutual diffusion of the solvent within the jet and the surrounding moisture due to the different solvent compositions utilized in electrospinning. The schematic

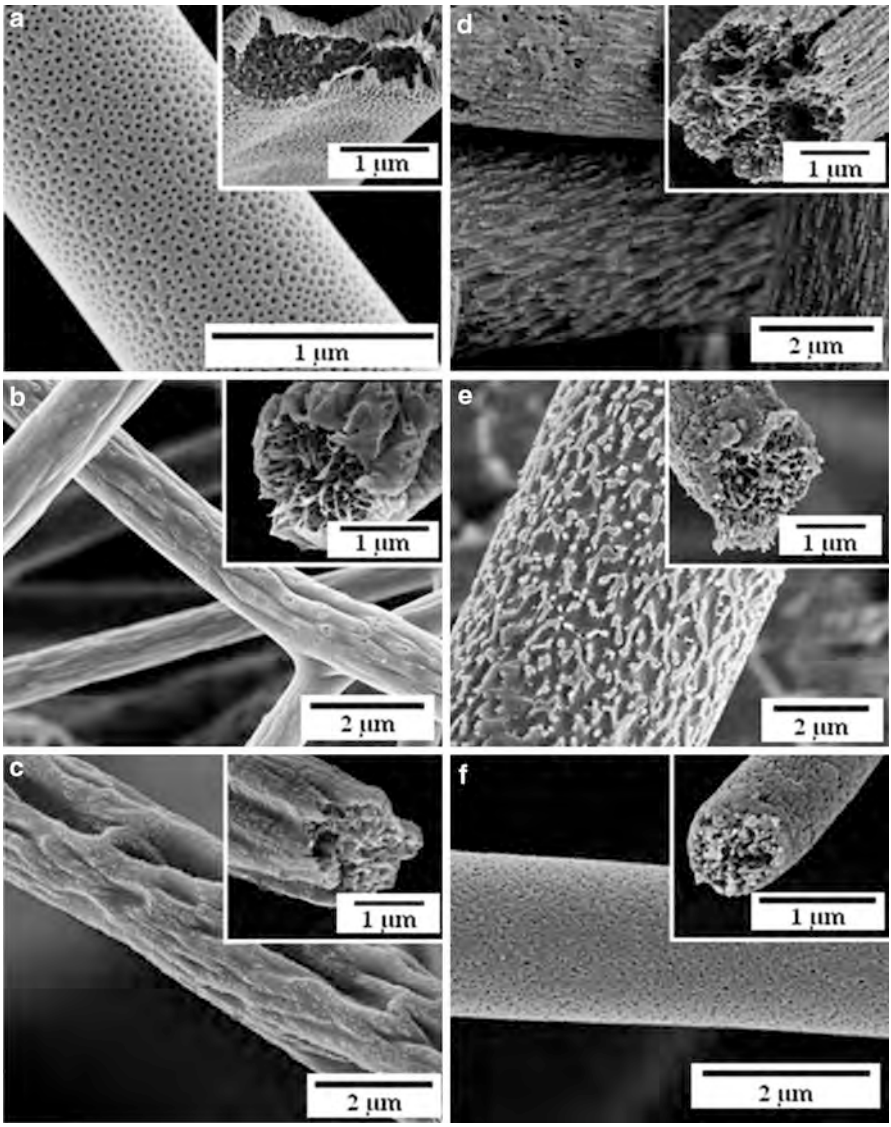

Fig. 9 FE-SEM images of the PS fibers formed from various weight ratios of THF–DMF in solvent: (**a**) 100:0, (**b**) 80:20, (**c**) 60:40, (**d**) 40:60, (**e**) 20:80, and (**f**) 0:100, respectively [31] (Reproduced with permission from the Royal Society of Chemistry)

diagram illustrating the formation process of porous fibers was shown in Fig. 10. Generally, when the charged fluid jet ejects from the Taylor cone contacting the air, a thin and elastic glassy shell is formed on the surface of the fluid jet rapidly due to solvent evaporation and solidification. Meanwhile, the non-solvent component (air and moisture) will penetrate into the fluid jet through the shell, and the solvent will

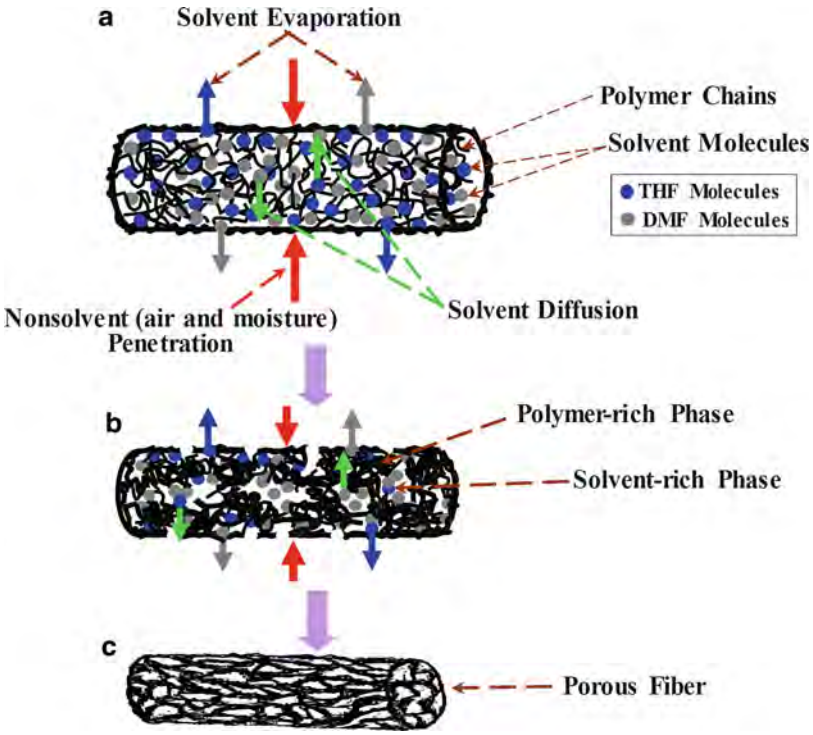

Fig. 10 Schematic diagram illustrating the formation process of porous fibers during electrospinning [31] (Reproduced with permission from the Royal Society of Chemistry)

diffuse out from the core of the jet, as shown in Fig. 10a. During this process, the deformation mismatch between the shell and the core will occur under the stretching of electrical force due to core shrinkage during solvent diffusion, and finally forming the wrinkled surfaces. On the other hand, the penetrating of the moisture would change the solution compositions; thus, the jet became thermodynamically unstable, and phase separation occurred within the fluid jet yielding a polymer-rich phase and a solvent-rich phase (Fig. 10b). Finally, the concentrated polymer-rich phase eventually solidified into the matrix, and the solvent-rich phase transformed into the pores, and the highly porous fibers were obtained (Fig. 10c) [31, 34].

Figure 11a–c showed the oleophilic and hydrophobic properties of relevant porous PS fibrous mats and commercial PP nonwoven fabric, respectively. It was clearly showed that water droplets were placed on the PS fibrous mats with a stable obtuse apparent water contact angle, whereas the oil droplets were immediately absorbed by the PS fibers (Fig. 11a). Although the commercial PP nonwoven fabric also showed oleophilic and hydrophobic properties, the selective wettability performance was weaker than that of PS fibrous mats (Fig. 11b), which was due to the large fiber diameters (about 15 ~ 20 μm, as shown in Fig. 11c) [31, 35].

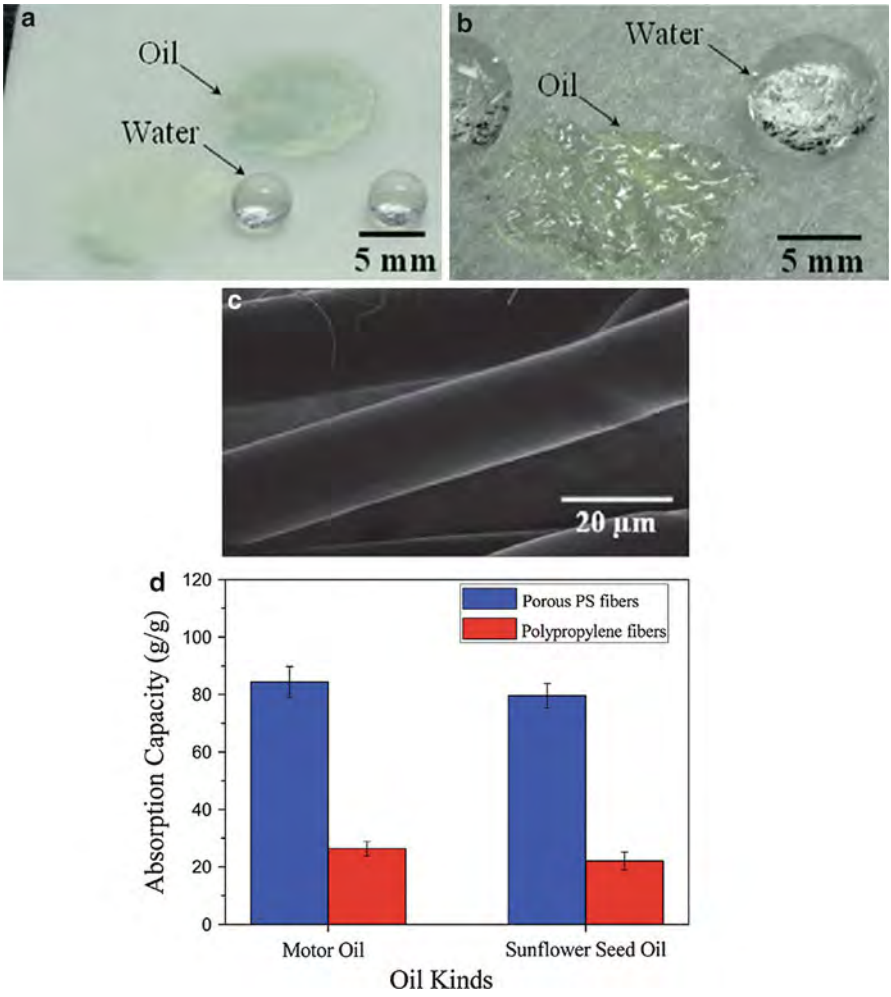

Fig. 11 Water and oil droplets placed on the (**a**) porous PS fibrous mats and (**b**) commercial PP nonwoven fabric. (**c**) FE-SEM image of the PP fibers. (**d**) Maximum absorption capacities of the porous PS fibrous mats and commercial PP nonwoven fibers for motor oil and sunflower seed oil [31] (Reproduced with permission from the Royal Society of Chemistry)

As expected, the porous PS fibers could have promising oil adsorption performance. Motor oil and sunflower seed oil were used to compare the oil sorption capacities for porous PS fibrous mats and commercial PP nonwoven fabrics. As can be seen from Fig. 11d, the porous PS fibrous mats showed much larger oil absorption capacities than that of commercial PP nonwoven fibers; the porous PS fibrous mats exhibited the robust absorption capacities of 84.41 and 79.62 g/g for motor oil and sunflower seed oil, respectively. These prominent absorption

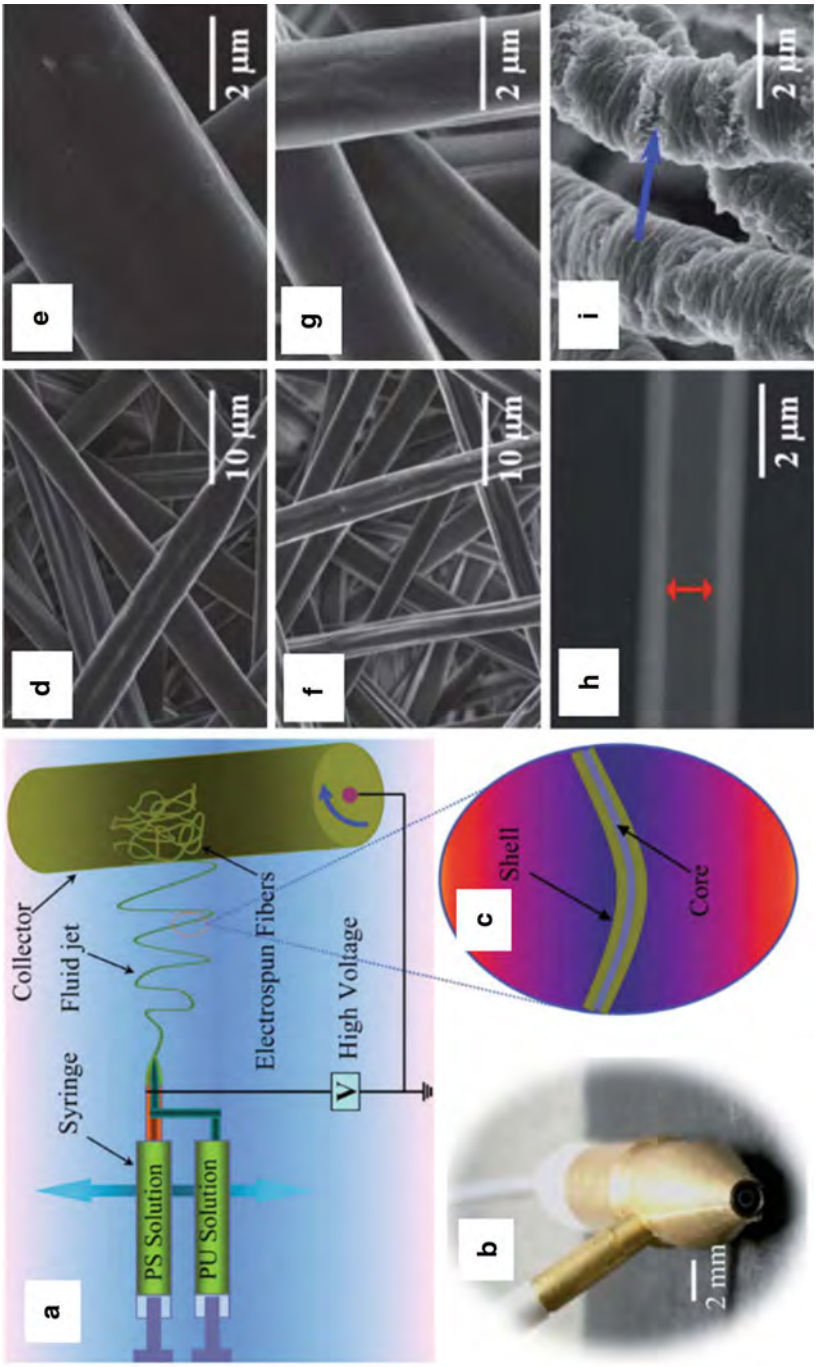

Fig. 12 (continued)

capacities of PS fibrous mats could be attributed to the enhanced porous structure of PS fibers and the high porosity of PS fibrous mats, which made them a good candidate toward real application for oil spill treatment [31, 36].

PS–PU Core–Shell Nanofibers

The reusability is a significant performance for the oil adsorption materials, especially for the practical applications. However, the electrospun fibers used as oil sorbents are the reduction in fiber strength and resiliency after oil sorption, which results in poor reusability. To solve this problem, Lin et al. used the core–shell configuration of fibers via coaxial electrospinning, which combined the both unique properties of each component [37, 38]. It is well known that electrospun polyurethane (PU) fibers have a good strength and elasticity. Thus, they fabricated composite PS–PU core–shell fiber with a high SSA prepared via coaxial electrospinning directly for oil adsorption. Typically, the 20 wt% PS solutions were prepared by dissolving PS in solvent mixtures of THF–DMF with weight ratios of 1:4. The PU resin was diluted to 75 and 50 wt%, respectively, in spinning solutions by adding DMF. The schematic of the coaxial electrospinning setup used in this study was shown in Fig. 12a–c; it could be seen from the figure that the solutions for the core and shell materials were separately fed into the coaxial nozzle from which they were ejected simultaneously by utilizing one syringe pump [38].

The FE-SEM images presented in Fig. 12d, f showed the morphologies of composite PS–PU fibers from PU solutions of 75 % and 50 %, respectively. It was clearly showed that the average fiber diameter decreased with the decreasing of core solution concentrations, and the fiber shape changed gradually from ribbonlike to circular as well. The phenomenon could be explained that the lower viscosity of core solutions could strengthen jet instability and change the competition between the solvent removal rate from jet surface and the solvent diffusion rate inside the jet. Moreover, close observation of the samples (Fig. 12e, g) revealed that there were no nanopores on fiber surfaces, which could be attributed to the increasing of PS within the composite fiber that could increase the thickness of the shell layer. Transmission electron microscope (TEM) measurement was used to further confirm the existence of the core–shell structure. As shown in Fig. 12h, the composite PS–PU fiber prepared with a 50 wt% PU resin exhibited the perfect core–shell structure, and the PU core fiber has a uniform average fiber diameter of 1.2 μm. Additionally, the

Fig. 12 (**a**) Schematic representation showing the core–shell electrospinning setup used in this study. (**b**) Photograph of the coaxial spinneret. (**c**) An illustration of the electrospun core–shell fiber. FE-SEM images of the composite PS–PU fibers formed with (**d**) 75 and (**f**) 50 wt% PU solutions as the core solutions. (**e**) and (**g**) show the high-magnification images of the samples shown in (**d**) and (**f**), respectively. (**h**) TEM image of as-spun fiber shown in (**f**). (**i**) FE-SEM image of fibers shown in (**f**) after stretching [38] (Reproduced with permission from the Royal Society of Chemistry)

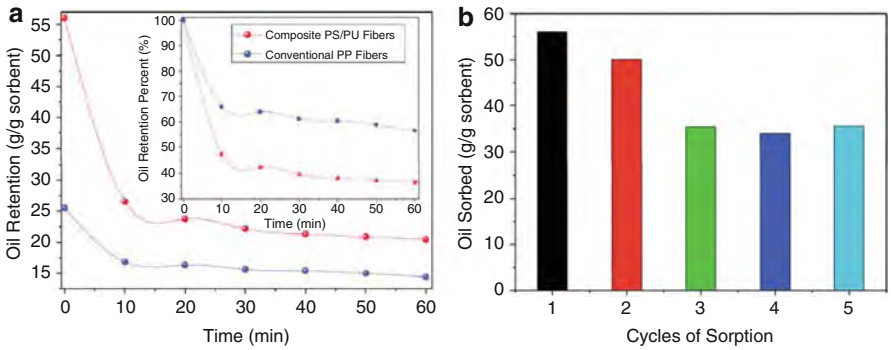

Fig. 13 (**a**) Plot of oil retention on the composite PS–PU fibrous mats during free draining. (**b**) Reusability of the composite PS–PU fibrous mat for motor oil [38] (Reproduced with permission from the Royal Society of Chemistry)

blue arrow marked in Fig. 12i showed that the fiber had a porous surface layer, indicating that the shell of the as-prepared fibers was also porous rather than solid [38].

For the practical application upon oil spill treatment, the oil sorbents are usually used to concentrate and transform a liquid oil to a semisolid phase or to a solid state, the oil-filled sorbent should be removed from the water and be handled in an appropriate manner without significant oil draining out; thus, the oil retention of sorbent is an important factor to be considered. The rate of motor oil desorption from the filled sorbent was tested by gravity over time. As shown in Fig. 13a, the two sorbents showed similar oil retention behaviors with the same trend. In the initial 10 min, the rate of oil release showed an obvious decrease during this period, and the oil amounts retained for PS–PU fibrous mats and PP fibers were 26.54 and 16.80 g/g, respectively, indicating the as-prepared PS–PU fibrous mats had better oil retention ability compared with PP fibers due to their high porosity [38, 39].

Figure 13b demonstrated the oil sorption capacities of the composite PS–PU fibrous mats after five cycles of the sorption process for motor oil, revealing that the oil sorption capacity decreased by approximately 10.70 % after the first cycle by squeezing it between two padding papers. Then, the oil sorption capacity decreased continuously and achieved the 63.09 % of its initial values after the second cycle, and the sorption capacity would be stable upon further cycle tests. Even after five sorption cycles, the fibrous mats still maintained the robust sorption capacity of larger than 60 % of the initial value with 35.54 g/g, which was three to five times larger than that of commercial nonwoven material. The decrease of oil sorption capacity could be attributed to the irrecoverable deformation and collapse of intra-fiber and/or inter-fiber pores during the process of mechanical squeezing [38, 31]. Consequently, it was believed that the composite PS–PU fibrous mats had a great potential application in wastewater treatment, oil accident remediation, and environmental protection.

Membranes for Emulsified Oil–Water Separation

With the ever-increasing industrial oily wastewater and the frequent oil spill accidents such as the Deepwater Horizon oil spill in the Gulf of Mexico, the treatment of oily wastewater has become a worldwide problem [40, 1]. Traditional techniques such as oil skimmers, centrifuges, depth filters, coalescers, and flotation technologies are useful for the separation of immiscible oil–water mixtures, but are not effective for emulsified oil–water mixtures, especially not for surfactant-stabilized microemulsions with a dispersed droplet size below 20 μm [41, 42]. Generally, the systematic design of membranes for oil–water separation requires the consideration of two important rules: selective wettability, the hydrophobic and oleophilic surface could lead to the breakthrough pressure difference across the membrane which prevents the permeation of the water phase, and porosity, which affects the rate of permeation of oil phase through the membrane [43, 44]. Owing to the different interfacial effects of oil and water, utilizing the superwetting behavior of solid surfaces to design an oil–water separation process has been considered effective. To date, a variety of superwetting materials have been fabricated by designing superhydrophobic or superoleophobic mesh films in combination with surface chemistry and roughness. However, most of these materials are still not applicable for emulsified oil–water separation because the pore sizes in these materials (>50 μm) are much larger than the droplet sizes of the emulsion (<20 μm) [44, 45].

Alternatively, electrospinning has been shown to be a simple but powerful technique for the preparation of functional fibrous with designed wettability and porous structure. Ding et al. fabricated a novel superhydrophobic–superoleophilic nanofibrous membranes by the combination of silica nanofibers and in situ polymerized fluorinated polybenzoxazine (F-PBZ), which could effectively separate micrometer-sized surfactant-stabilized water-in-oil emulsions solely driven by gravity, with high-separation efficiency [46, 47]. The overall fabrication procedure was schematically shown in Fig. 14. A novel fluorinated benzoxazine, namely, 3-(3-(trifluoromethyl)phenyl)-2H-benzoxazine-6-carbaldehyde (BAF-CHO), was used as a starting monomer, which was synthesized via a one-step Mannich reaction. Typically, the silica nanofibrous membranes (SNF) were first fabricated by calcination of electrospun tetraethyl orthosilicate/poly(vinyl alcohol) composite nanofibers. Subsequently, the silica membranes were dipped in dichloromethane solutions with BAF-CHO and well dispersed Al_2O_3 nanoparticles (Al_2O_3 NPs) and dried in the oven. Then, the in situ polymerization of BAF-CHO monomers was carried out at 200 °C in a vacuum for 1 h, leading to the formation of the Mannich bridge cross-linked structure and finally generating functional membranes (F-SNF/Al_2O_3) with cured thermosetting F-PBZ layer on the fiber surface. In addition, the membranes without Al_2O_3 NPs (F-SNF) were also prepared for comparison [47].

As shown in Fig. 15a, the pristine SNF nanofibers had a randomly oriented 3D nonwoven membranes with an average diameter of 225 nm. The as-calcined SNF had numerous hydrophilic silanol groups on fiber surfaces, leading to a high surface energy of larger than 40 mN m^{-1}. Thus, the SNF membranes showed

Fig. 14 Schematic for the strategy using the in situ polymerization approach to the synthesis of F-PBZ-/Al_2O_3 NPs-modified silica nanofibrous membranes [47] (Reproduced with permission from the Royal Society of Chemistry)

superhydrophilicity with the water WCA of 0° and oleophilicity with the oil contact angle (OCA) of 22° (Fig. 15a'). After curing at 200 °C, the fiber diameter increased to 262 nm, and the obvious adhesion could be observed (Fig. 15b), revealing the accomplishment of in situ polymerized BAF-CHO on the surface of silica fibers. On the other hand, the cross-linked F-PBZ containing fluorinated benzene ring possessed an extremely low surface energy of 16.4 mN m^{-1}; therefore, the modified silica nanofibrous membranes showed considerable transition in wetting behavior. As can be seen from the Fig. 15b', the F-SNF membranes showed the WCA of 140° and OCA of 13°, indicating the obvious selective wettability for oil and water [47].

By inclusion of Al_2O_3 NPs in the F-PBZ functional layer, the morphology of the resultant membranes was remarkably changed by creating nanoscaled rough structures on the surfaces of nanofibers (Fig. 15c). This unique hierarchical structure further increased the surface roughness and effective surface area and thus significantly reduced the water contact area, finally increasing the hydrophobicity of membranes. As shown in Fig. 15c', the F-SNF/Al_2O_3 membranes exhibited the robust superhydrophobicity with the WCA of 161° and superoleophilicity with OCA of 0°, indicating a significant enhancement of wetting performances [47]. It was worth to note that this prominent selective superwettability made the membranes a good candidate for the oil–water separation.

To further study the wetting behavior of as-prepared membranes, the contact angle hysteresis (i.e., the difference between the advancing and receding contact angles of a moving droplet) and sliding angle (i.e., the surface tilt required for droplet motion) were employed to directly characterize resistance to mobility, and

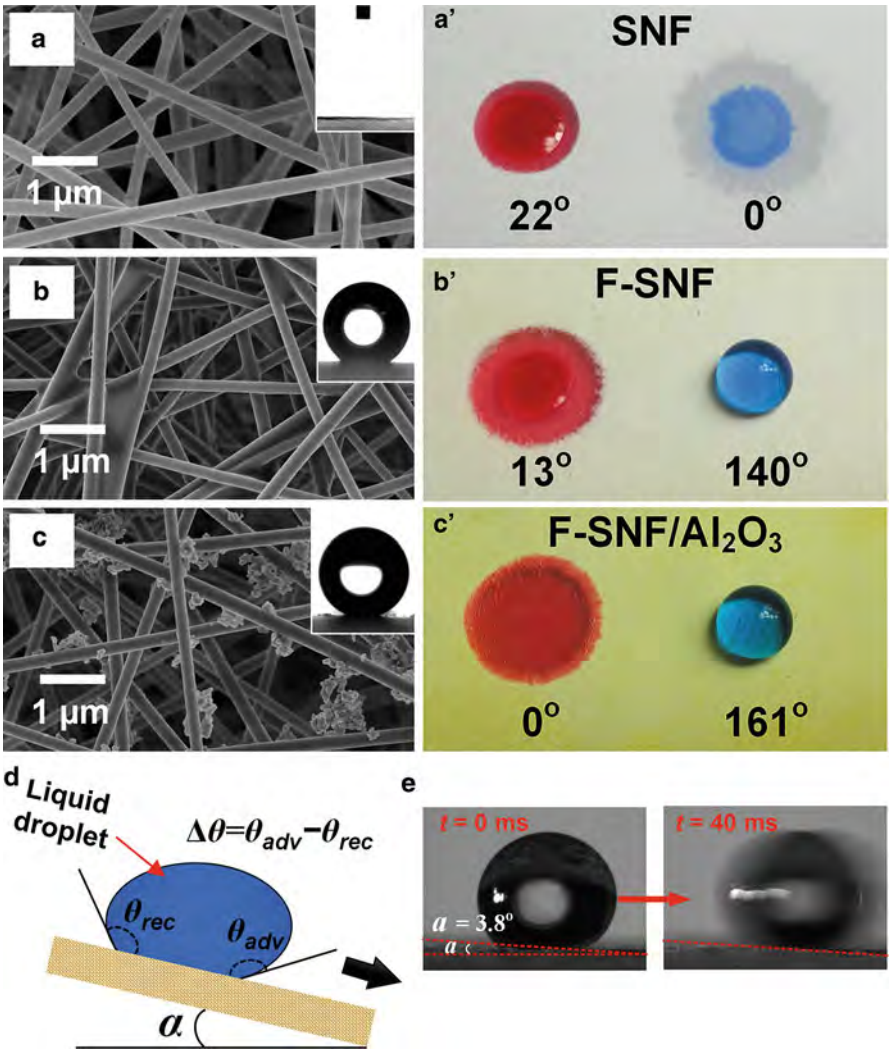

Fig. 15 FE-SEM images of (**a**) SNF, (**b**) F-SNF, and (**c**) F-SNF/Al_2O_3 membranes, respectively, the insets show the optical profiles of water droplet on the relevant membranes. Droplets of rapeseed oil (*dyed red*) and water (*dyed blue*) on the (**a'**) SNF, (**b'**) F-SNF, and (**c'**) F-SNF/Al_2O_3 membranes, respectively. (**d**) Schematic illustrating the contact angle hysteresis and sliding angle of a liquid droplet. (**e**) The water droplet (10 μL) sliding at a low angle of 3.8° on the as-prepared F-SNF/Al_2O_3 membranes [47] (Reproduced with permission from the Royal Society of Chemistry)

the low values therefore confirmed a lack of pinning, consistent with a nearly defect-free surface, as shown in Fig. 15d [48, 49]. The as-prepared F-SNF/Al_2O_3 membranes exhibited extreme water repellency as signified by very low contact angle hysteresis of 2.4°, which indicated that the water could not penetrate into the

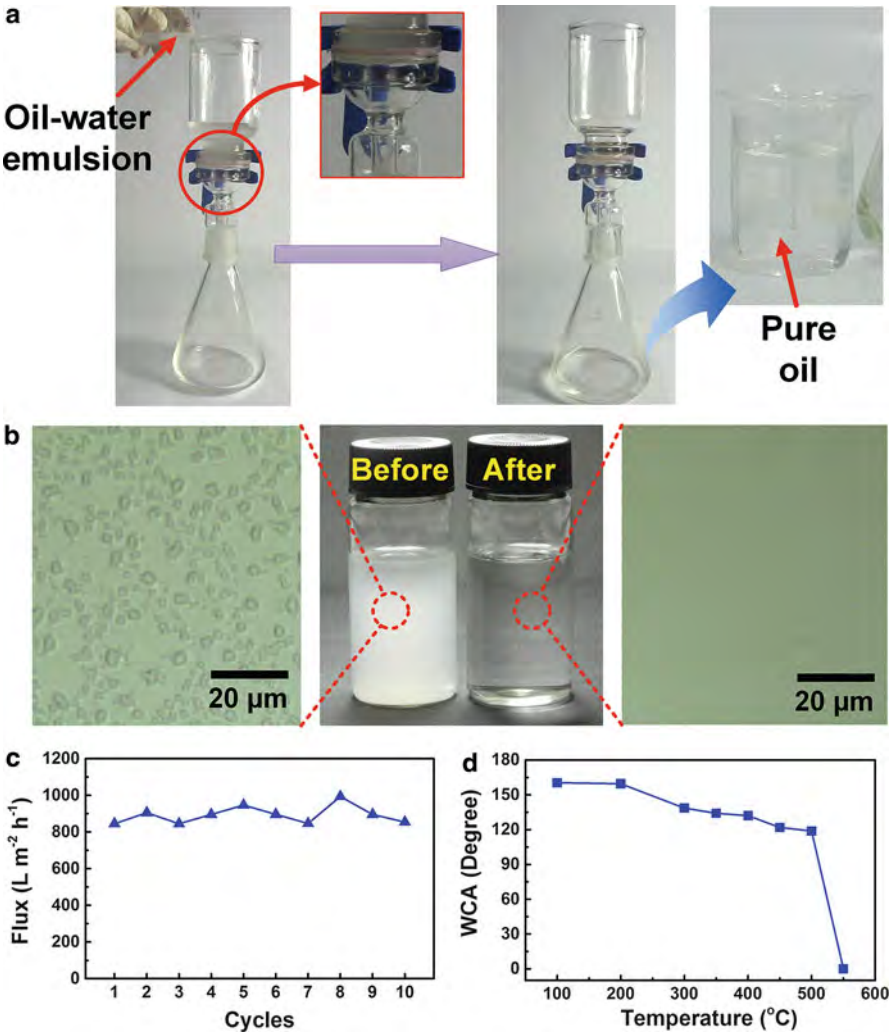

Fig. 16 (**a**) The solely gravity-driven separation for oil–water emulsion using F-SNF/Al_2O_3 membranes. (**b**) Photographs and optical micrographs of oil–water emulsion before and after separation. (**c**) Change of the flux with increasing cycle numbers using F-SNF/Al_2O_3 membranes. (**d**) WCAs of the F-SNF/Al_2O_3 membrane after calcined at different temperatures for 5 min [47] (Reproduced with permission from the Royal Society of Chemistry)

surface structures at large extent and sit on the asperities of the surface with the minimum liquid–solid adhesion. This low wetting hysteresis resulted in the minute sliding angle of 3.8°, as displayed in Fig. 15e. Accordingly, based on the measured contact angle hysteresis and droplet volume (10 μL), the estimated liquid retention force of the F-SNF/Al_2O_3 membranes was 1.63 μN, which was three times less than

the state-of-the-art lotus leaf-inspired omniphobic surfaces, whose liquid retention forces are of the order of 5 μN for water [47, 48].

The separation capability of the F-SNF/Al_2O_3 membranes was tested by using a surfactant-stabilized (span 80) water-in-oil (petroleum ether) emulsion with a droplet size at the micrometer scale. It could be seen from Fig. 16a that the milky white emulsions (100 mL) were poured onto the F-SNF/Al_2O_3 membrane, oil immediately permeated through the membrane and dropped into the below conical flask. Meanwhile, the emulsion droplets demulsified once touching the membrane and water were retained above. It was noted that no external driven force was used during the fast separation process (within 7 min); the separation was driven solely by the gravity [47]. In order to investigate the separation efficiency, the optical microscopic images of original emulsions and their corresponding collected filtrates were presented in Fig. 16b. It was clearly showed that no droplet was observed in the collected filtrate in the whole image shown, revealing the effectiveness of the F-SNF/Al_2O_3 membrane for separating water-in-oil microemulsion. Moreover, the membranes exhibited a promising flux of 892 $\pm$ 50 L m^{-2} h^{-1}, which was significantly higher than that of commercial UF filtration membranes. In addition, the antifouling performance presented in Fig. 16c, d indicated an outstanding reusability with nearly no flux decrease upon ten cycles and the robust thermal stability, which was an important parameter for practical application [47]. The above results indicated that the as-prepared membranes were a promising candidate to match with the requirements for treating the real emulsified wastewater on a mass scale.

Summary

In summary, electrospun nanofibrous membranes with controllable porous structure and surface wettability have exhibited great advantages over conventional media in separation applications, such as liquid-proof breathable materials, oil spill cleanup, and oil–water separation. One-dimensional nanostructured electrospun materials have significantly contributed to meeting the challenges in relevant fields as the control of the multi-scale structures. Moreover, various methods in structure manipulation, such as adhesion structure, porous nanofibers, core–shell structure, and modification of nanofiber surfaces, have been detailedly demonstrated. By the introduction of low surface energy materials such as FPU and F-PBZ, the pristine nanofibers were endowed with promising superwettability, which boosted the separation selectivity and efficiency. And nanoparticles such as SiO_2 and Al_2O_3 were used to create functional membranes with hierarchical structures, thus further improving the separation performance. Consequently, the convenient adaptability of the electrospun nanofibrous membranes to the conventional separation media allows functional nanofibers to become one of the most critical elements for the improvement of the existing conventional membranes.

References

1. Kwon G, Kota AK, Li Y, Sohani A, Mabry JM, Tuteja A (2012) On-demand separation of oil–water mixtures. Adv Mater 24(27):3666–3671. doi:10.1002/adma.201201364
2. Zhou X, Zhang Z, Xu X, Guo F, Zhu X, Men X, Ge B (2013) Robust and durable superhydrophobic cotton fabrics for oil/water separation. ACS Appl Mater Interfaces 5 (15):7208–7214. doi:10.1021/am4015346
3. Wang X, Ding B, Yu J, Wang M (2011) Engineering biomimetic superhydrophobic surfaces of electrospun nanomaterials. Nano Today 6(5):510–530. doi:10.1016/j.nantod.2011.08.004
4. Liang C, Li Z, Dai S (2008) Mesoporous carbon materials: synthesis and modification. Angew Chem Int Ed 47(20):3696–3717. doi:10.1002/anie.200702046
5. Wu J, Wang N, Wang L, Dong H, Zhao Y, Jiang L (2012) Unidirectional water-penetration composite fibrous film via electrospinning. Soft Matter 8(22):5996. doi:10.1039/c2sm25514f
6. Lee S, Obendorf SK (2007) Use of electrospun nanofiber web for protective textile materials as barriers to liquid penetration. Text Res J 77(9):696–702. doi:10.1177/0040517507080284
7. Ma H, Burger C, Hsiao BS, Chu B (2011) Ultra-fine cellulose nanofibers: new nano-scale materials for water purification. J Mater Chem 21(21):7507. doi:10.1039/c0jm04308g
8. Yuan J, Xu Y, Müller AHE (2011) One-dimensional magnetic inorganic–organic hybrid nanomaterials. Chem Soc Rev 40(2):640. doi:10.1039/c0cs00087f
9. Ramakrishna S (2005) An introduction to electrospinning and nanofibers. World Scientific, Singapore
10. Yarin AL, Koombhongse S, Reneker DH (2001) Taylor cone and jetting from liquid droplets in electrospinning of nanofibers. J Appl Phys 90(9):4836. doi:10.1063/1.1408260
11. Reneker D, Yarin A, Zussman E, Xu H (2007) Electrospinning of nanofibers from polymer solutions and melts. Adv Appl Mech 41:43–346. doi:10.1016/S0065-2156(07)41002-X
12. Lomax GR (2007) Breathable polyurethane membranes for textile and related industries. J Mater Chem 17(27):2775. doi:10.1039/b703447b
13. Yoon B, Lee S (2011) Designing waterproof breathable materials based on electrospun nanofibers and assessing the performance characteristics. Fibers Polym 12(1):57–64. doi:10.1007/s12221-011-0057-9
14. Bagherzadeh R, Latifi M, Najar SS, Tehran MA, Gorji M, Kong L (2011) Transport properties of multi-layer fabric based on electrospun nanofiber mats as a breathable barrier textile material. Text Res J 82(1):70–76. doi:10.1177/0040517511420766
15. Sambaer W, Zatloukal M, Kimmer D (2011) 3D modeling of filtration process via polyurethane nanofiber based nonwoven filters prepared by electrospinning process. Chem Eng Sci 66 (4):613–623. doi:10.1016/j.ces.2010.10.035
16. Mukhopadhyay A, Vinay Kumar M (2008) A review on designing the waterproof breathable fabrics part I: fundamental principles and designing aspects of breathable fabrics. J Ind Text 37 (3):225–262. doi:10.1177/1528083707082164
17. Hae Wook A, Chung Hee P, Seung Eun C (2011) Waterproof and breathable properties of nanoweb applied clothing. Text Res J 81(14):1438–1447. doi:10.1177/0040517510392462
18. Zhuo H, Hu J, Chen S, Yeung L (2008) Preparation of polyurethane nanofibers by electrospinning. J Appl Polym Sci 109(1):406–411. doi:10.1002/app.28067
19. Han J, Cao RW, Chen B, Ye L, Zhang AY, Zhang J, Feng ZG (2011) Electrospinning and biocompatibility evaluation of biodegradable polyurethanes based on L-lysine diisocyanate and L-lysine chain extender. J Biomed Mater Res A 96(4):705–714. doi:10.1002/jbm.a.33023
20. Ge J, Si Y, Fu F, Wang J, Yang J, Cui L, Ding B, Yu J, Sun G (2013) Amphiphobic fluorinated polyurethane composite microfibrous membranes with robust waterproof and breathable performances. RSC Adv 3(7):2248–2255. doi:10.1039/C2RA22111J
21. Ding B, Wang M, Wang X, Yu J, Sun G (2010) Electrospun nanomaterials for ultrasensitive sensors. Mater Today 13(11):16–27. doi:10.1016/s1369-7021(10)70200-5

22. Buruaga L, Sardon H, Irusta L, González A, Fernández-Berridi MJ, Iruin JJ (2010) Electrospinning of waterborne polyurethanes. J Appl Polym Sci 115(2):1176–1179. doi:10.1002/app.31219
23. Li XH, Ding B, Lin JY, Yu JY, Sun G (2009) Enhanced mechanical properties of superhydrophobic microfibrous polystyrene mats via polyamide 6 nanofibers. J Phys Chem C 113(47):20452–20457. doi:10.1021/jp9076933
24. Zhao F, Wang X, Ding B, Lin J, Hu J, Si Y, Yu J, Sun G (2011) Nanoparticle decorated fibrous silica membranes exhibiting biomimetic superhydrophobicity and highly flexible properties. RSC Adv 1(8):1482–1488. doi:10.1039/C1RA00605C
25. Cheng C, Chen J, Chen F, Hu P, Wu XF, Reneker DH, Hou H (2010) High-strength and high-toughness polyimide nanofibers: synthesis and characterization. J Appl Polym Sci 116 (3):1581–1586. doi:10.1002/app.31523
26. Wang J, Raza A, Si Y, Cui L, Ge J, Ding B, Yu J (2012) Synthesis of superamphiphobic breathable membranes utilizing SiO_2 nanoparticles decorated fluorinated polyurethane nanofibers. Nanoscale 4(23):7549–7556. doi:10.1039/C2NR32883F
27. Binner ER, Robinson JP, Kingman SW, Lester EH, Azzopardi BJ, Dimitrakis G, Briggs J (2013) Separation of oil/water emulsions in continuous flow using microwave heating. Energy Fuel 27(6):3173–3178. doi:10.1021/ef400634n
28. Kaombe DD, Lenes M, Toven K, Glomm WR (2013) Turbiscan as a tool for studying the phase separation tendency of pyrolysis oil. Energy Fuel 27(3):1446–1452. doi:10.1021/ef302121r
29. Kojima T, Takayama S (2013) Microscale determination of aqueous two phase system binodals by droplet dehydration in oil. Anal Chem 85(10):5213–5218. doi:10.1021/ac400628b
30. Zhai W, Li G, Yu P, Yang L, Mao L (2013) Silver phosphate/carbon nanotube-stabilized pickering emulsion for highly efficient photocatalysis. J Phys Chem C 117(29):15183–15191. doi:10.1021/jp404456a
31. Lin J, Ding B, Yang J, Yu J, Sun G (2012) Subtle regulation of the micro- and nanostructures of electrospun polystyrene fibers and their application in oil absorption. Nanoscale 4(1):176. doi:10.1039/c1nr10895f
32. Haberko J, Raczkowska J, Bernasik A, Rysz J, Budkowski A, Luzny W (2007) Pattern replication in polyaniline-polystyrene thin films. Synth Met 157(22–23):935–939. doi:10.1016/j.synthmet.2007.09.004
33. Ding B, Lin J, Wang X, Yu J, Yang J, Cai Y (2011) Investigation of silica nanoparticle distribution in nanoporous polystyrene fibers. Soft Matter 7(18):8376–8383. doi:10.1039/C1SM05791J
34. Lin J, Ding B, Yu J, Hsieh Y (2010) Direct fabrication of highly nanoporous polystyrene fibers via electrospinning. ACS Appl Mater Interfaces 2(2):521–528. doi:10.1021/am900736h
35. Lin J, Wang X, Ding B, Yu J, Sun G, Wang M (2012) Biomimicry via electrospinning. Crit Rev Solid State Mater Sci 37(2):94–114. doi:10.1080/10408436.2011.627096
36. Zhao Y, Qin M, Wang A, Kim D (2013) Bioinspired superhydrophobic carbonaceous hairy microstructures with strong water adhesion and high gas retaining capability. Adv Mater 25 (33):4561–4565. doi:10.1002/adma.201300858
37. Lin J, Tian F, Shang Y, Wang F, Ding B, Yu J (2012) Facile control of intra-fiber porosity and inter-fiber voids in electrospun fibers for selective adsorption. Nanoscale 4(17):5316–5320. doi:10.1039/C2NR31515G
38. Lin J, Tian F, Shang Y, Wang F, Ding B, Yu J, Guo Z (2013) Co-axial electrospun polystyrene/polyurethane fibres for oil collection from water surface. Nanoscale 5(7):2745–2755. doi:10.1039/C3NR34008B
39. Perles CE, Volpe PLO, Bombard AJF (2012) Study of the cation and salinity effect on electrocoalescence of water/crude oil emulsions. Energy Fuel 26(11):6914–6924. doi:10.1021/ef301433m
40. Peng J, Liu Q, Xu Z, Masliyah J (2012) Novel magnetic demulsifier for water removal from diluted bitumen emulsion. Energy Fuel 26(5):2705–2710. doi:10.1021/ef2014259

41. Zhang F, Zhang WB, Shi Z, Wang D, Jin J, Jiang L (2013) Nanowire-haired inorganic membranes with superhydrophilicity and underwater ultralow adhesive superoleophobicity for high-efficiency oil/water separation. Adv Mater 25(30):4192–4198. doi:10.1002/adma.201301480
42. Zhang W, Shi Z, Zhang F, Liu X, Jin J, Jiang L (2013) Superhydrophobic and superoleophilic PVDF membranes for effective separation of water-in-oil emulsions with high flux. Adv Mater 25(14):2071–2076. doi:10.1002/adma.201204520
43. Shang Y, Si Y, Raza A, Yang L, Mao X, Ding B, Yu J (2012) An in situ polymerization approach for the synthesis of superhydrophobic and superoleophilic nanofibrous membranes for oil–water separation. Nanoscale 4(24):7847–7854. doi:10.1039/C2NR33063F
44. Shi Z, Zhang W, Zhang F, Liu X, Wang D, Jin J, Jiang L (2013) Ultrafast separation of emulsified oil/water mixtures by ultrathin free-standing single-walled carbon nanotube network films. Adv Mater 25(17):2422–2427. doi:10.1002/adma.201204873
45. Osakai T, Yuguchi Y, Gohara E, Katano H (2010) Direct label-free electrochemical detection of proteins using the polarized oil/water interface. Langmuir 26(13):11530–11537. doi:10.1021/la100769q
46. Raza A, Si Y, Wang X, Ren T, Ding B, Yu J, Al-Deyab SS (2012) Novel fluorinated polybenzoxazine–silica films: chemical synthesis and superhydrophobicity. RSC Adv 2(33):12804–12811. doi:10.1039/C2RA21138F
47. Huang M, Si Y, Tang X, Zhu Z, Ding B, Liu L, Zheng G, Luo W, Yu J (2013) Gravity driven separation of emulsified oil–water mixtures utilizing in situ polymerized superhydrophobic and superoleophilic nanofibrous membranes. J Mater Chem A 1(45):14071–14074. doi:10.1039/C3TA13385K
48. Wong TS, Kang SH, Tang SKY, Smythe EJ, Hatton BD, Grinthal A, Aizenberg J (2011) Bioinspired self-repairing slippery surfaces with pressure-stable omniphobicity. Nature 477(7365):443–447. doi:10.1038/nature10447
49. Lafuma A, Quere D (2003) Superhydrophobic states. Nat Mater 2(7):457–460. doi:10.1038/nmat924

Thermo-responsive Textiles

34

Jiping Wang, Qi Zhong, Jindan Wu, and Tao Chen

Contents

Introduction 920
Thermo-responsive Polymers 921
Phase Separation of Thermo-responsive Polymers 921
Transition Behavior of Thermo-responsive Polymers 923
Effects Influencing Transition Behavior of Thermo-responsive Polymers 925
Classification of Thermo-responsive Polymers 928
Synthesis of Thermo-responsive Polymers 930
Thermo-responsive Textiles 934
The Application of Thermo-responsive Textile 935
The Requirements of Thermo-responsive Polymer for Textile Application 938
Immobilization of Thermo-responsive Polymers onto Textiles 939
The Characterization of Thermo-responsive Textiles 941
Challenges and Solutions of Thermo-responsive Textile 947
Summary 948
References 948

Abstract

Thermo-responsive polymers can switch their hydrophilic/hydrophobic state by varying the temperature below or above the lower critical solution temperature (LCST). This chapter systematically reviews the recent research on thermo-responsive polymers and their applications in the field of textiles. It mainly contains two aspects. The first aspect introduces the fundamental properties of the thermo-responsive polymers, including phase transition, transition

J. Wang (✉) • Q. Zhong • J. Wu • T. Chen
Key Laboratory of Advanced Textile Materials & Manufacturing Technology, Ministry of Education, National Base for International Science and Technology Cooperation in Textiles and Consumer-Goods Chemistry, Zhejiang Sci-Tech University, Hangzhou, China
e-mail: jipingwanghz@gmail.com; qizhonghz@gmail.com; wujd86@163.com; chentao930@gmail.com

© Springer Science+Business Media Singapore 2015

X. Tao (ed.), *Handbook of Smart Textiles*,
DOI 10.1007/978-981-4451-45-1_5

behaviors, and factors that influence the transition behaviors. After that, the main types of thermo-responsive polymers, such as polymers bearing amide groups, polymers bearing oxygen atoms in main or side chains, and polymers bearing phosphate groups, are discussed with their special properties. Then the synthesis of the thermo-responsive polymers and the characterization of their molecular structure, molecular weight, molecular weight distribution, morphology, and thermal properties are described. The second aspect mainly focuses on the textiles with thermo-responsive polymers. Some of the most promising applications of the thermo-responsive textile, such as moisture permeability-adaptive fabric, fabrics for medicine/perfume control release, and water storage, are reported first. After that, the requirements of the thermo-responsive polymers for textiles, including adjustable LCST, soft hand, and easy binding, are discussed. Then the diverse methods to immobilize thermo-responsive polymers onto textile and characterize the properties of the modified textile are introduced. The existing challenges and strategic solutions of the thermo-responsive textiles are also briefly summarized at the end.

Keywords
Thermo-responsive polymer • Smart textiles • Hydrogels • Phase transition

Introduction

Stimuli-responsive polymers are defined as polymers undergoing relatively large and abrupt, physical or chemical, reversible or irreversible changes in response to the small stimulus in external environments [1]. Various stimuli, such as temperature, pH, radiation, electric, magnetic, and so on, have been employed to trigger the changes mentioned above. These stimuli-responsive polymers can be in the form of solution, gel, nanoparticles, films, and bulk. Due to their potential applications in the fields of biology, medicine, and sensor technology [1], these unique polymers attract more and more attentions. Among stimuli-responsive polymers, as the temperature change is easy to realize in a practical way, thermo-responsive polymers are considerably investigated recently [2]. The recent research to the thermo-responsive polymers mainly focuses on two aspects: the fundamental research and application research. The basic research is designing novel thermo-responsive polymers, investigating the phase transition behavior, and understanding the structure and relevant interactions, such as hydrophilic–hydrophobic interaction, hydrogen bonding, and donor–acceptor relation, at molecular level, while application research is developing new devices or equipment according to their unique properties, such as drug delivery systems, valves to control liquid transfer, or optical devices.

Because the textile for human clothing is related to everyone in daily life, textile industry also shows a huge interest to introduce the thermo-responsive polymers into the textile to fulfill the specific technical and biomedical demands.

These modified textiles can both sense and respond to the external thermal stimulus, which is the great advantage over the conventional textile materials [3]. Therefore, these textiles are also called smart textiles.

Because the LCST of poly(N-isopropylacrylamide) (PNIPAAm) is 32 °C, which is close to the body temperature, it shows potential applications in the field of biomedicine and is extensively studied in the last few decades. Therefore, this chapter first reviews the fundamental properties of thermo-responsive polymers, which is mainly based on PNIPAAm. Then the immobilization methods of thermo-responsive polymers onto the textile and a selection of applications are discussed. The existing challenges of the smart textile and summary are given at the end of this chapter.

Thermo-responsive Polymers

Phase Separation of Thermo-responsive Polymers

When a neutral linear polymer is dissolved in a solvent, there are two forces to determine the swelling of the polymer [4]. One is the excluded volume interaction, and another is the elastic force. When the thermal energy K_BT of the repeating units in the polymer is very high, the excluded volume interaction dominates over the attraction between the repeating units. Therefore, the polymer can swell in the solvent.

When the temperature is cooling, the coil-to-globule transition of a single polymer chain in organic solvents can be described by the mean-field theory [5]. Because the thermal energy of repeating units becomes lower than the minimum of the potential related to the van der Waals interactions, the solvent switches from the thermodynamic favorable to thermodynamic unfavorable. Thus, the former swollen repeating units have the tendency to separate from the solvent, inducing the condensation of the solution.

Figure 1a shows a typical upper critical solution temperature (UCST) phase transition behavior, such as PS in cyclohexane. For the polymer possesses the UCST behavior, the polymer is miscible with the solvent when the temperature is above the critical solution temperature. The polymer solution obtained is homogeneous and transparent. When the temperature is below the critical solution temperature, the polymer and solvent are phase-separated. Thus the solution turns into turbid.

In contrast, Fig. 1b presents a totally different type of phase separation. When the temperature is below the critical solution temperature, it exhibits single phases in solution. However, increasing the temperature above the critical solution temperature, the polymer and solvent tend to separate from each other. The formerly transparent polymer solution comes to be turbid. This critical solution temperature is called lower critical solution temperature (LCST). A typical polymer with LCST behavior is poly(N-isopropylacrylamide) (PNIPAAm) which is popularly studied. When PNIPAAm is dissolved in water, hydrogen bonds are formed between the

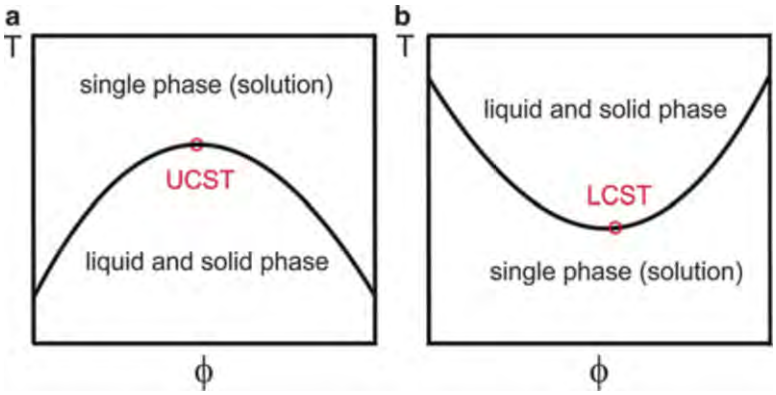

Fig. 1 Phase diagram for polymer solution with (**a**) upper critical solution temperature (*UCST*) behavior and (**b**) lower critical solution temperature (*LCST*) behavior

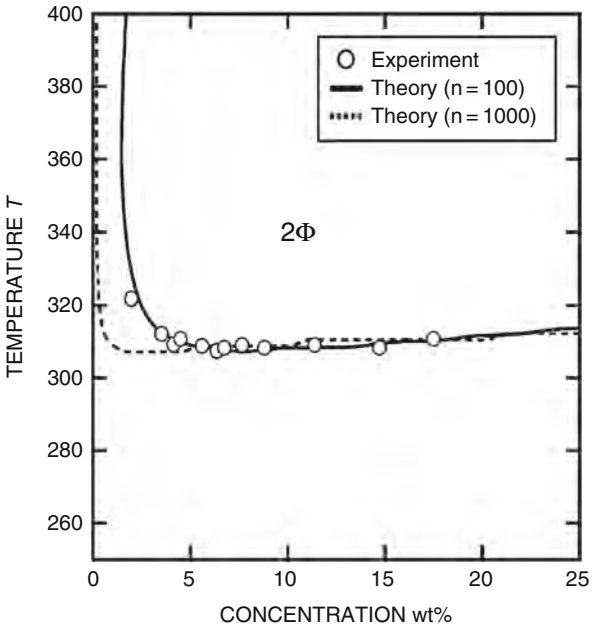

Fig. 2 Phase diagrams of aqueous PNIPAAm solution. Experimental data (O) is compared with theoretical calculation. The DP of the polymer is $n = 100$ (*solid line*) and $n = 1{,}000$ (*broken line*) (Reprinted with permission from Okada and Tanaka [6], Copyright (2005) American Chemical Society)

polymer chains and water. Moreover, as there are hydrophobic groups presented in PNIPAAm, hydrophobic interaction also exists in the system. When these interactions are dominant to the swelling of the polymer instead of the van der Waals interaction, the polymer will become immiscible to the solvent (water) and the phase separation sets in. Figure 2 presents a typical phase diagram of PNIPAAm in water [6]. The molecular weight of PNIPAAm is 6,15,500 g/mol. The circles are the experimental data, while the solid and broken lines are theoretical calculation with

different degrees of polymerization. It is obvious that when the concentration of aqueous solution is in the range of 5–20 %, PNIPAAm presents a flat transition behavior. The detail about the theory for swelling and transition process of the polymers with LCST behavior will be discussed later.

Transition Behavior of Thermo-responsive Polymers

As mentioned in the previous section, the LCST transition behavior is attributed to the favor of internal energy. When a water-soluble neutral polymer, containing both hydrophilic and hydrophobic groups, dissolves in water, the hydrophilic groups interact strongly with the water molecules and form hydrogen bonds. The formation of hydrogen bonds is the initial driving force for dissolution. Simultaneously, the hydrophobic groups do not intend to contact with water. Hence they hinder the association of the polymer with water. However, the attraction between the hydrophilic group and water is much stronger than the repulsion between the hydrophobic groups and water at lower temperature. Therefore, the polymer dissolves in water. Additionally, the water surrounding the hydrophobic groups organizes itself and forms an ordered hydration layer. This behavior is called "hydrophobic effect" [7], which helps to minimize the contact surface between the hydrophobes and water. However, this state is entropically unfavorable and unstable [8]. By increasing the temperature, the dominant force in the system is reversed and the solubility of the polymer is significantly reduced, leading to polymer precipitation.

Because PNIPAAm is a typical and the most investigated thermo-responsive polymer with LCST behavior, the transition behavior of PNIPAAm is discussed here as an example. N–H and C = O groups in PNIPAAm can form hydrogen bonds with water (C–O···H–O–H, N–H···OH_2). With infrared spectroscopy, it is observed that besides the intermolecular hydrogen bonds mentioned above, there are also the intramolecular hydrogen bonds formed between N–H and C = O groups (C–O···H–N) [9]. At lower temperature, the intermolecular hydrogen bonds are dominant ones; thus PNIPAAm is able to dissolve in water (see Fig. 3). However, the hydrophobic effect increases with temperature. When the temperature increases above the LCST, the intramolecular hydrogen bonds between hydrophobic parts of the polymer chains are more favored. Thus, the bound water is released and the polymer chains collapse. During the heating process, the negative change of the entropy is larger than the enthalpy of the hydrogen bonds. Therefore, the change in the free energy of the mixing is positive. This change results in the phase transition of the thermo-responsive polymer (see Fig. 1b).

Besides the hydrogen bonds discussed above, the cooperation of bound water also contributes to the transition of PNIPAAm [6]. The PNIPAAm chains are in the coiled state before being immersed in water. After being placed in water, the water molecules (blue circles in Fig. 4) start to connect with the amide groups or ether groups by hydrogen bonds. These water molecules forming direct interaction with polymers are called bound water. The other water molecules are called free water. The bound water causes a slight displacement of the isopropyl group on side chain.

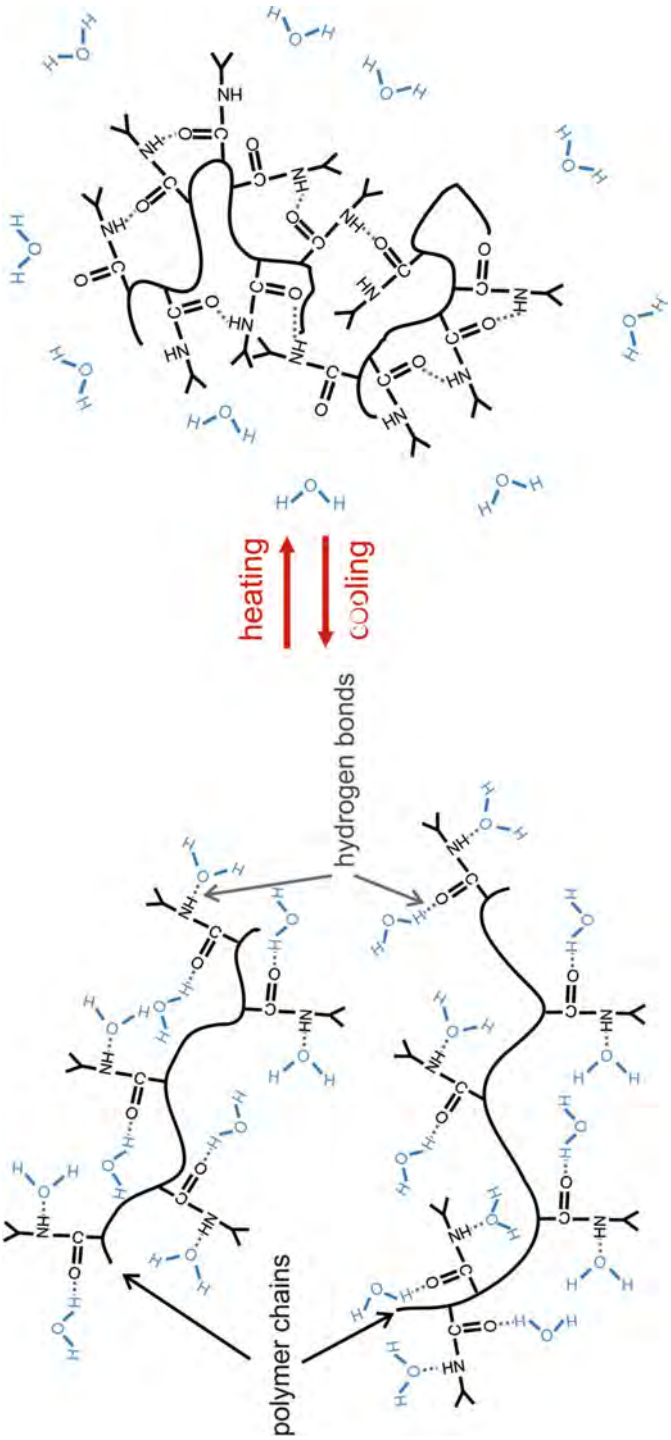

Fig. 3 Sketch of the swollen and collapsed thermo-responsive polymer chains below and above LCST

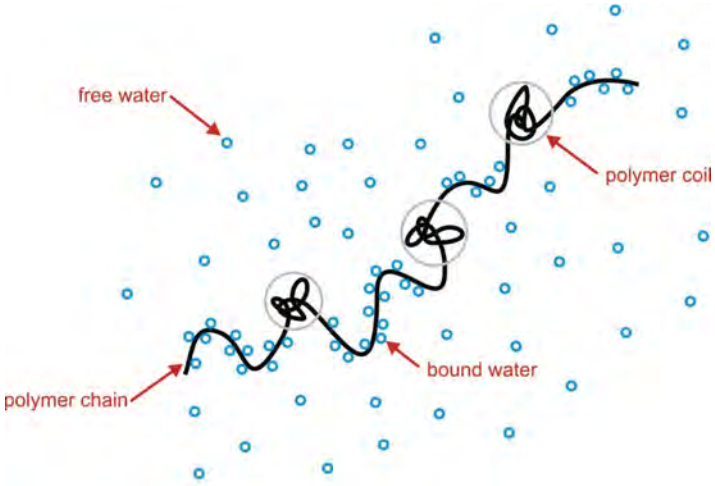

Fig. 4 Sketch for the cooperation of the bound water in PNIPAAm solution [(Reprinted with permission from Okada and Tanaka [6], Copyright (2005) American Chemical Society)

This displacement results in an easier formation of the second hydrogen bond on the neighboring position. Thus, a series of bound water is formed along the swollen chains. Simultaneously, the residual chains still stay in the coiled state, which is marked by gray circles in Fig. 4. When the temperature is heated up to the LCST, the detachment of one bound water molecule induces an easier detachment of the neighboring bound water molecule. Therefore, similar to a zip, a series of bound water molecules are released from the polymer chains. This cooperation results in the sharp transition behavior of PNIPAAm [6].

Effects Influencing Transition Behavior of Thermo-responsive Polymers

The transition behavior of thermo-responsive polymers can be influenced by several effects. As PNIPAAm is a well-investigated thermo-responsive polymer in the recent decades, it is taken as an example for discussing the effects that influence the transition behavior.

Molecular Weight

Many investigations have been done about the influence of molecular weight on the transition behavior of PNIPAAm. It was reported that the variation of molecular weight does not influence the transition temperature [10]. However, it was also observed that in some cases, the transition temperature showed a decreasing tendency when the molecular weight of PNIPAAm increases [11]. The reason for the contrary results may be attributed to the different end-group structures in PNIPAAm being presented in these investigations. When the molecular weight is

small, the effect of the end groups will be the dominant part and have an influence on the transition temperature. When the molecular weight is increased, the impact of the end group will be eliminated, causing the transition temperature to stay constant.

End Groups of Polymers

As mentioned above, due to the incorporation of specific end groups during the polymerization of PNIPAAm, these end groups influence the transition behavior of PNIPAAm. For instance, PNIPAAm ending with amide group exhibits an LCST of 45 °C (molecular weight 3,000 g/mol) [12]. However it should be noted that this end-group effect is most prominent for PNIPAAm when the molecular weight is very low. When the molecular weight is increased, as the relative concentration of the end group is reduced, the influence of the end group to the transition behavior is alleviated [11]. For example, when the molecular weight of PNIPAAm ending with amide group is 3,000 g/mol, the LCST is 45 °C. If the molecular weight increases to 16,300 g/mol, the LCST drops to 34 °C [12].

Tacticity of Polymers

The tacticity of PNIPAAm will not only influence the polymer dissolubility but also the transition temperature. For instance, the atactic PNIPAAm can be dissolved in water and is regarded as a hydrophilic polymer. However, the isotactic PNIPAAm is non-water-soluble. For the block copolymer consisting of the atactic and isotactic PNIPAAm, the transition temperature of aqueous solutions is strongly affected by the isotactic blocks. At a fixed concentration (5 mg/mL), an increase of the isotactic blocks in the block copolymers decreases the transition temperature [13]. Figure 5 represents the structure of isotactic (a), atactic (b), and block copolymers of atactic and isotactic (c) PNIPAAm.

Cosolvents

Because the LCST transition behavior is realized by the interaction of solvent with polymers and the hydrophobic–hydrophilic balance of polymers, there is no doubt that the additives to the thermo-responsive polymers solutions, such as the cosolvents and surfactants, will influence the transition behavior and transition temperature.

To the cosolvents, Fig. 6 shows the LCST variation of PNIPAAm in water–methanol mixtures [14]. It is obvious that LCST is varied when methanol is added into aqueous solution of PNIPAAm. The variation process can be divided into four regimes. In the first regime, when volume fraction of methanol is less than 0.05, LCST of PNIPAAm is not influenced by the addition of methanol. Because the methanol molecules can form water cages around themselves, they are kept away from each other at low concentration. When the amount of methanol is increased in the aqueous solution (volume fraction is increased from 0.05 to 0.35), the LCST drops from 31 °C to −7.5 °C (which is the minimum value observed in the measurement). Due to the fact that more and more methanol presented in the solution, the interaction of methanol with polymer chains becomes

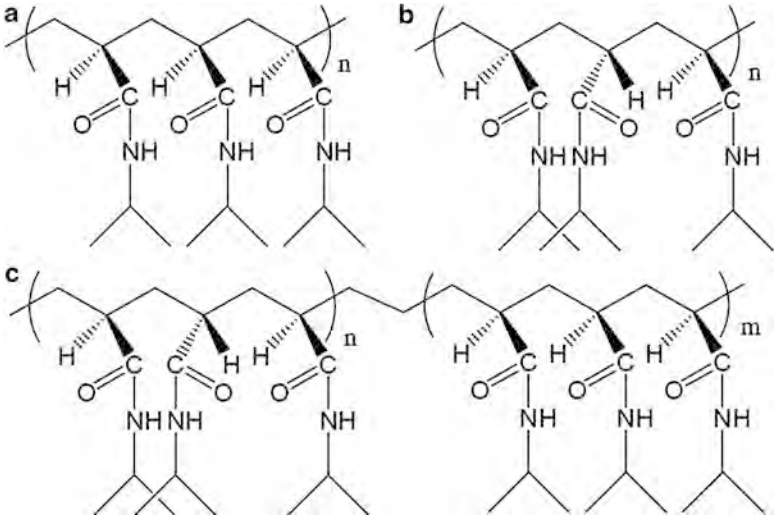

Fig. 5 The structure of isotactic (**a**), atactic (**b**), and block copolymers of atactic and isotactic (**c**) PNIPAAm

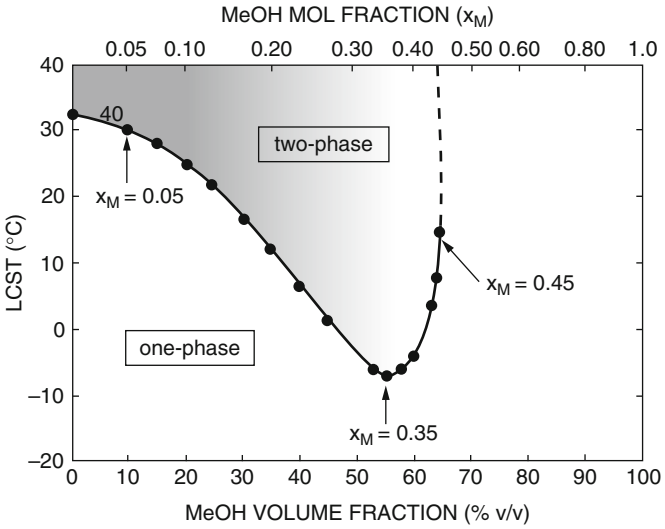

Fig. 6 Phase diagram of PNIPAAm in water–methanol mixtures (Reprinted with permission from Winnik et al. [14], Copyright (1990) American Chemical Society)

the dominant part, causing a decrease of LCST. Further increasing the amount of methanol, LCST dramatically increases. When the volume fraction of methanol is increased above 0.45, the formation of hydrogen bonds is hindered due to the fact that there is less and less water in the solution. Therefore, the PNIPAAm solution does not show the LCST transition behavior any longer.

Hydrophobic and Hydrophilic Modifications of Polymers

The transition behavior of PNIPAAm can be easily modified by introducing hydrophobic or hydrophilic groups into the PNIPAAm chains. For instance, when hydrophobic groups are introduced into PNIPAAm, the LCST drops [15]. As discussed in former section, the phase transition is realized by switching from the hydrophilic interaction to the hydrophobic interaction. The hydrophobicity of the copolymer is increased when the extra hydrophobic groups are introduced into the chains, and the LCST shifts to lower values. The higher the hydrophobic content in the copolymer, the lower is the LCST [15]. On the other hand, when hydrophilic groups are introduced into PNIPAAm, the result obtained is reversed. Due to the higher hydrophilic content in the copolymer, the switching from the hydrophilic interaction to hydrophobic interaction is hindered, inducing the LCST to shift to higher temperatures [16].

Furthermore, the position of the hydrophobic groups or the hydrophilic groups introduced in the polymer chain influences the LCST as well. For example, when only one end side of the PNIPAAm chain is copolymerized with hydrophobic groups, the copolymer will form core-shell micelles in water. The hydrophobic groups form the core, while the PNIPAAm chains form the shell with a brushlike corona structure [17]. If both ends of the PNIPAAm chain are copolymerized with hydrophobic groups, core-shell micelles are still obtained in water, but the shell part exhibits a flowerlike structure instead of the brushlike corona. Because the formation of the micelles increases the apparent molecular weight, the different kinds of micelles formed in the solution will further reduce the mixing entropy of the polymer chains. Thus, it favors the phase separation and shifts the LCST to lower value.

Classification of Thermo-responsive Polymers

The thermo-responsive polymer can be generally classified into three types according to their functional groups: (1) polymers bearing amide groups, (2) polymers bearing oxygen atom in main or side chains, and (3) polymers bearing phosphate groups. In the following section, these three types of thermo-responsive polymers are discussed with their basic properties and transition behaviors. Figure 7 shows the structure of the typical thermo-responsive polymers.

Polymers Bearing Amide Groups

This class of thermo-responsive polymers is polymers with acrylamide in the main chains. The most famous ones are the N-substituted poly(acrylamide)s and poly (methacrylamide)s (Fig. 7a and b), where R_1 can be H, CH_3, and C_2H_5 and R_2 can be CH_3, C_2H_5, and C_3H_7. In the case of R_2 is CH_3, while R_1 is H or CH_3, the obtained homopolymer does not present any LCST behavior in aqueous solution. However, if R_2 chain is increased to C_2H_5, no matter R_1 is H, CH_3, or C_2H_5, all the homopolymers obtained show LCST behavior in aqueous solutions. The transition temperature is in the range of 0–100 °C. Further increasing R_2 chain to C_3H_7, the homopolymers obtained only show LCST behavior in the case of R_1 is H [4].

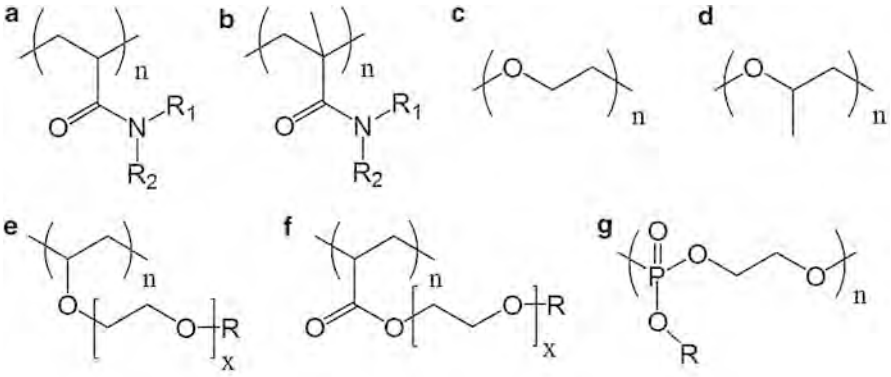

Fig. 7 The structure of the typical thermo-responsive polymers: (**a**) poly(acrylamide)s, (**b**) poly (methacrylamide)s, (**c**) poly(ethylene oxide), (**d**) poly(propylenoxide), (**e**) poly(vinyl ether)s, (**f**) poly(ethylacrylate)s, (**g**) poly(phosphoester)s

Among these homopolymers with R_1 = H and R_2 = C_3H_7, poly (N-isopropylacrylamide) is the well-investigated one due to the fact that the transition temperature is around 32 °C and the transition region is very sharp, which is suitable for the application in the field of biology and medicine [2].

Polymers Bearing Oxygen Atom in Main or Side Chains

Polymers with ether groups in the main or side chains are named polyethers. If the oxygen atom is in the main chain, the polymer is polyoxide, mainly consisting of poly(ethylene oxide) (PEO) and poly(propylenoxide) (PPO) [18]. Their structures are presented in Fig. 7c and d, respectively. The transition temperature of PEO and PPO are 96 °C and 35 °C, respectively. If the oxygen atom is in the side chain, they can be considered as the polymers containing PEO in the side chains. They are mainly consisting of poly(vinyl ether)s and poly(ethylacrylate)s (Fig. 7e and f) [19]. One prominent advantage of poly(ethylacrylate)s over the other thermo-responsive polymers is their transition temperature and transition behavior can be adjusted by varying the length of PEO chains. For instance, when poly (ethylmethacrylate)s contain two ethoxy side chains, the transition temperature is 26 °C. Further increasing the ethoxy side chains to three or eight to nine, the transition temperature dramatically increases to 52 °C and 90 °C, separately [19]. Therefore, the transition temperature can be easily tuned by changing the length of side chains according to the applications. In addition, poly(ethylacrylate)s present reversible transition behavior without any hysteresis. As a consequence, they can be promising candidates for the applications acquired through fast switching function, such as nanoswitch and nanosensor.

Polymers Bearing Phosphate Groups

Poly(phosphoester)s are polymers bearing phosphate groups (Fig. 7g) [20], which can be obtained by the ring-opening polymerization of cyclic phosphoesters. They

attracted more and more attentions in the field of biology and medicine due to their biocompatibility and biodegradability. In Fig. 7g, R can be C_2H_5 or C_3H_7 (isopropyl). When R = C_2H_5, the obtained poly(ethyl ethylene phosphate) shows a transition temperature of 38 °C. If R = C_3H_7 (isopropyl), the transition temperature of the obtained poly(isopropyl ethylene phosphate) is decreased to 5 °C. For both polymers, only small hysteresis of the reversible transition behavior is observed. Similar as the polyethers, the LCST of poly(phosphoester)s is also dependent on the molecular weights and composition [20].

Synthesis of Thermo-responsive Polymers

Methods to Prepare Thermo-responsive Polymers

Thermo-responsive polymers can be synthesized through conventional radical polymerization, ionic polymerization, or ring-opening polymerization. The choice of the polymerization method is dependent on the chemical structure and application of the resultant polymers. Of these polymerization methods, conventional radical polymerization methods, such as solution polymerization using AIBN or BPO as initiator, are widely adopted [21]. The advantages of conventional radical polymerization methods include mild reaction conditions, compatibility with water, and suitability for a wide variety of monomers. However, disadvantages, such as lack of control of the microstructure of the polymer, degree of polymerization, and polydispersity, also exist.

Emulsion polymerization, which is a type of radical polymerization, is one of the most popular synthetic routes to prepare vinyl-based thermo-responsive polymeric systems, where well-controlled particle size and size distribution can be readily attained [22]. During the course of polymerization, the molecular weight of the polymer can be increased without reducing the polymerization rate. Thus, both high molecular weight and high reaction rate can be attained simultaneously. However, one disadvantage of emulsion polymerization is that relatively large amounts of surfactant are required, and removal of these surfactants is difficult. Consequently, additional wastewater treatment is often required, and undesired contaminants may exist in the end product. To overcome this problem, surfactant-free emulsion polymerization (SFEP) has been developed, wherein a persulfate initiator is commonly used to generate a negatively charged surface [23].

Ring-opening polymerization, as a form of chain-growth polymerization, can be used to synthesize polyether kind of thermo-responsive polymers from cyclic ethers. Using this technique, polyethylene oxide (PEO), polypropylene oxide (PPO), and their triblock copolymers were synthesized [24]. Living anionic polymerization, a living polymerization technique involving an anionic propagating species, was also used to synthesize thermo-responsive polymers. Muller et al. synthesized poly(acrylic acid)$_{45}$-block-poly(N,N-diethylacrylamide)$_{360}$ by sequential anionic polymerization of tert-butyl acrylate (*t*BA) and N, N-diethylacrylamide (DEAAm) in the presence of Et_3Al and consequently hydrolysis [25]. Although these materials have been successfully prepared using living

polymerization techniques, they often require harsh reaction conditions and are restricted to a limited number of relatively nonfunctional monomers. Therefore, there is a need to develop novel techniques to synthesize well-defined stimuli-responsive copolymers.

In the 1990s, controlled/living radical polymerization was developed and used to prepare well-defined homo- or block copolymers under simple and mild reaction conditions. Through the introduction of dormant states in the propagating species, controlled/living radical polymerizations were achieved by minimizing normal bimolecular termination, thereby extending the lifetime of "living" polymers to much longer lifetimes. A number of controlled/living radical polymerization methods have been developed, including stable free-radical polymerization (SFRP), nitroxide-mediated polymerization (NMP), atom transfer radical polymerization (ATRP), and reversible addition fragmentation chain-transfer polymerization (RAFT). Recently, the scope of "living" radical polymerizations has expanded rapidly. A larger class of well-defined macromolecules can now be synthesized, resulting in the proliferation of research on thermo-responsive polymers [26].

Methods to Characterize Thermo-responsive Polymers

Molecular structure, molecular weight, molecular weight distribution, morphology, and thermal properties are several important aspects in thermo-responsive polymer characterization.

Molecular Structure

The properties of a polymer are closely associated with its molecular structure. Understanding how its structure affects its properties will help in the designing and synthesis of polymers with special functions. Many of the analytical techniques used to determine the molecular structure of unknown organic compounds are also used to characterize molecular structure of thermo-responsive polymers. Some common spectroscopic techniques, such as ultraviolet–visible spectroscopy (UV–vis), infrared spectroscopy (IR), Raman spectroscopy, nuclear magnetic resonance spectroscopy (NMR), electron spin resonance spectroscopy (ESR), and mass spectrometry (MS), can be used to collect information about the chemical structure of polymeric materials. For instance, Gao et al. synthesized an amphiphilic thermo-responsive ABA triblock copolymer, poly(methyl methacrylate)-b-poly(N-isopropylacrylamide-co-poly(ethylene glycol) methyl ether methacrylate)-b-poly(methyl methacrylate) (PMMA-b-P(NIPAM-co-PEGMEMA)-b-PMMA), via RAFT polymerization. Clearly, the existence of characteristic ^{1}H NMR signals at δ (ppm) 3.07, 1.57, and 1.38 for PMMA segments; δ 1.76, 2.01, 7.97, 3.95, and 1.08 for PNIAM segments; and δ 1.85 and 1.37 for PEGMEMA segments indicated the successful synthesis of the triblock copolymer. In FT-IR, the bends (cm^{-1}) at 3,443, 1,652, 1,555, and 1,384 for the absorbance of N–H, −OCHN-, N–C, and -CH $(CH_3)_2$ in PNIPAM segments, respectively, 2,975 and 1,149 for C–O–C in PEGMEMA units, and 1,728 for the absorbance of C = O stretch vibration of ester groups further confirmed the molecular structure of the copolymer (Fig. 8) [27].

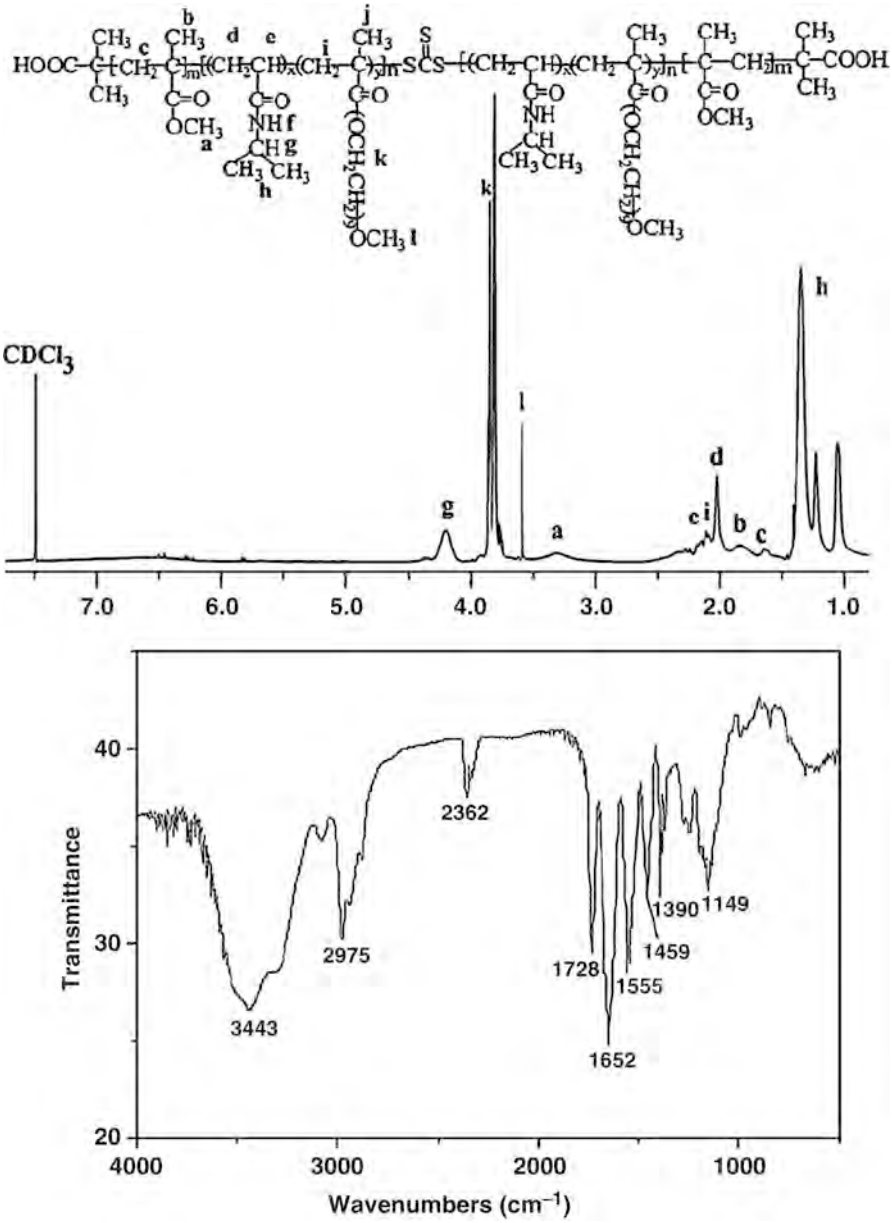

Fig. 8 ^{1}H NMR and FT-IR spectrum of PMMA-b-P(NIPAM-co-PEGMEMA)-b-PMMA triblock copolymer (Reprinted from Qu et al. [27], Copyright (2009) with permission from Elsevier)

Molecular Weight and Molecular Weight Distribution

The molecular weight of a polymer is important because it determines many physical properties, such as phase transition temperature and solubility, and mechanical properties, such as toughness and viscosity. Unlike small molecules, the molecular weight of a polymer is not one unique value. Rather, a given polymer will have a distribution of molecular weights. The distribution of molecular weights can be summarized by the number average molecular weight (M_n), weight average molecular weight (M_w), and polydispersity index (PDI). The most common methods for determining these parameters are colligative property measurements, light scattering techniques, viscometry of the dilute polymer solutions, ultracentrifugation, and size exclusion chromatography. Gel permeation chromatography (GPC), a type of size exclusion chromatography, is often used to determine the relative molecular weight as well as the molecular weight distribution of the polymer based on the size or hydrodynamic volume of the analytes. For example, Bergbreiter et al. studied the effects of end-group polarity and molecular weight on the LCST of PNIAAm, where the molecular weight of fractionated PNIPAAm samples was measured by light scattering and PDI were measured by GPC [11].

Morphology

The morphology of a polymer is a microscopic property. The molecular conformation and orientation of the polymer has a great effect on the macroscopic properties of the polymer. Microscopy techniques are especially useful in determining these microscopic properties, as the domains created by the polymer morphology are large enough to be viewed using modern microscopy instruments. Imaging methods are widely used for characterization of the polymer morphology. A great advantage of imaging methods is that the structure can be directly visualized at various parts of the polymer. Due to the versatility and utility of such methods, they have become an essential part of characterization of most materials, including thermo-responsive polymers. Scanning electron microscopy (SEM) is an important image analysis tool, which is widely used in the field of morphology. Chu et al. prepared a thermo-responsive core-shell microcapsule with a porous membrane and PNIPAAm gates. By SEM, the outer and inner surfaces of the microcapsules and cross-shell polyamide microcapsules were clearly displayed (Fig. 9) [28]. Other imaging methods include transmission electron microscopy (TEM) and atomic force microscopy (AFM). X-ray diffraction (XRD), which relies on the dual wave/particle nature of X-rays to obtain information about the structure of crystalline materials, is widely applied in thin film analysis, monitoring of crystalline phase and structure, investigation of sample stress and strain, etc.

Thermal Properties

Thermal analysis is another important aspect of characterization of polymers. Differential scanning calorimetry (DSC) is an analysis method that combines traditional equilibrium calorimetry with dynamic analysis of thermal processes. It offers possibilities to determine both thermodynamic parameters of substances and

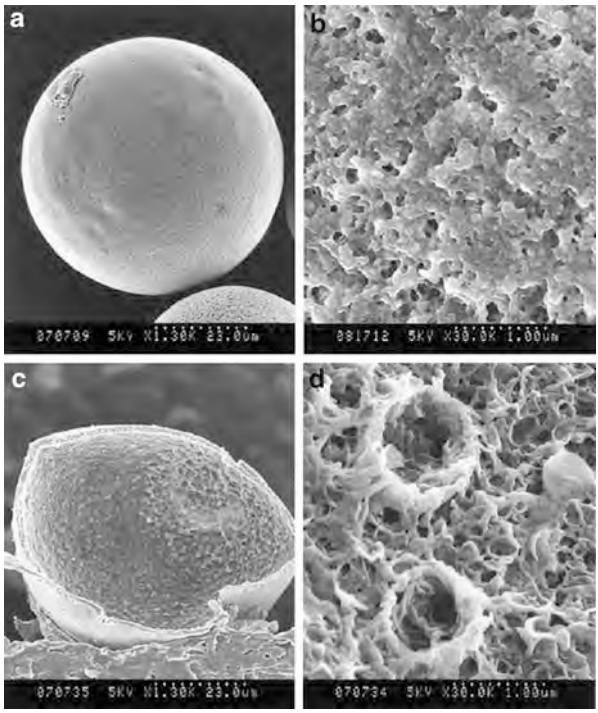

Fig. 9 FE-SEM micrographs of microcapsule with PNIPAAm gates. (**a**, **b**) Outer surface, (**c**) cross-section, and (**d**) inner surface (Reprinted from Chu et al. [28], Copyright (2001) with permission from Elsevier)

the kinetic characteristic of processes and relaxation transition under linear temperature change. Currently, DSC is widely used to test the phase transition temperature of thermo-responsive polymers [29]. Thermogravimetric analysis (TGA) is another thermal analysis technique used to characterize thermo-responsive polymers. TGA measures the amount and rate of change in the mass of a sample as a function of temperature or time in a controlled atmosphere. The measurements are used primarily to determine the thermal and/or oxidative stabilities of materials, as well as their compositional properties.

Thermo-responsive Textiles

With the development of material science, textiles are not only used for keeping human body warm but also enable for healthcare and safety protection. They are conceived as natural or synthetic materials with multifunctional characteristics and complex interface between humans and external environment. Now they are playing a more active role for adapting to the drastic changes of environment signals. Among all the stimuli-responsive textiles, thermo-responsive textiles are the most widely studied and hold great application potentials. They are playing an increasingly important role in the fields of daily life, industry, military, medicine, etc.

The Application of Thermo-responsive Textile

Here, the main focus is on the application of thermo-responsive polymers with LCST in the physiological range to the textiles. With the transition of polymers, textiles undergo swelling/de-swelling or hydration/dehydration behaviors, leading to switchable volume, wettability, and appearance. At lower temperature, hydrogen bonding between hydrophilic segments of the polymer chain and water molecules dominates and results in the swelling of polymers in water [9]. As the temperature increases, the hydrophobic interactions among hydrophobic segments become strengthened, which leads to the chain collapse. The formed dense and hydrophobic layer makes the surface transits from hydrophilic to hydrophobic.

Moisture Permeability-Adaptive Fabric

A new type of intelligent fabric with thermal and humidity managing ability was developed by combining with thermo-responsive polymers. When the ambient temperature is high, the formerly swollen polymer films on the fabric surface will switch to the collapsed state. Thus numerous pores form in the thermo-responsive polymer films, leading to the increased flushing of water and heat exchange (Fig. 10). Conversely, the water flow is blocked by the "off" state of the pores due to the swelling of the hydrogels. Lee and Shim grafted PNIPAAm and poly (acrylic acid) onto polyamide by copolymerization. The pore radius was 212.6 nm at 30 °C and 218.2 nm at 50 °C [3]. PNIPAAm grafted polypropylene, and cotton fabric also exhibited thermal controlled pore structure (size and porosity) and water permeability [30]. Usually, the water permeability is corresponding to the heat storage and loss. Therefore, the temperature-sensitive polymers on the textile are regarded as moisture and thermo-controlling system, which can be used to make high-performance apparel such as anti-soaking diving suits. Comparing to the conventional wet suit, it can protect the divers from cold hazards and keep warm in cold water. It has been reported the SmartSkin^{TM} produced by Midé Technology Corporation (USA) can reduce 70 % heat loss of human body [31]. Its outer layer is made of a close-cell Neoprene foam, and the inner layer contains a thermo-responsive hydrogel which enables thermoregulation in a certain range of environmental conditions.

Medicine/Perfume Control Release

A growing part of the textile materials are being used in the medical and healthcare applications, including medical bandages, wound dressing, surgical suture, artificial blood vessel, and so on. For these applications, thermo-sensitive polymeric hydrogels with phase transition temperature around 37 °C are grafted on the textiles. These hydrogels include cross-linked P(NIPAAm-co-BMA) hydrogels, interpenetrating polymer network of PNIPAAm and poly(tetramethylene ether glycol) (PTMEG), PNIPAAm/β-CD copolymer [4], and so on. Tiny shift in temperature may lead to the drastic volume change of the hydrogels which enable the loading and releasing of drugs conversely. The burst releasing of drugs at a certain

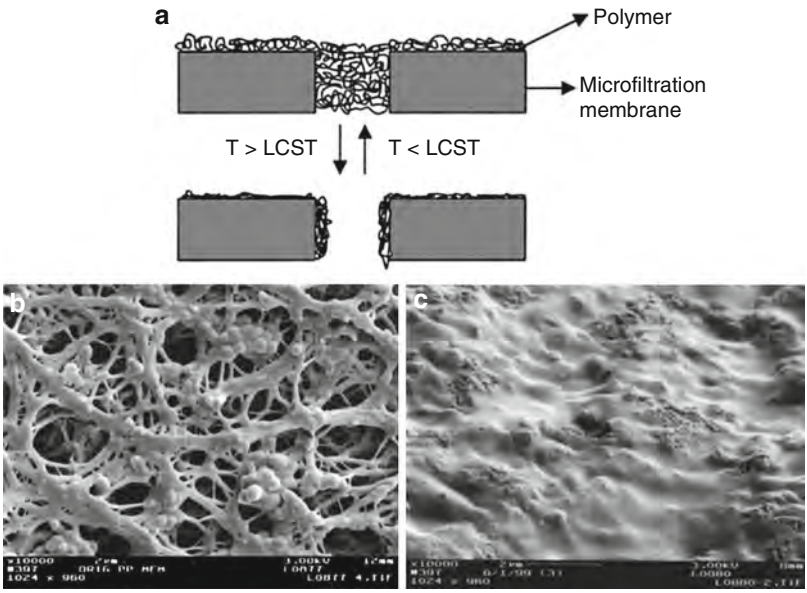

Fig. 10 (**a**) Temperature-dependent opening and closing of the pores of a polypropylene membrane filled with PNIPAAm. SEM photos of (**b**) the surface of the original polypropylene membrane and (**c**) the polypropylene membrane grafted with PNIPAAm (Reprinted from Liang et al. [30], Copyright (2000) with permission from Elsevier)

temperature should be precisely designed according to the medicine molecular weight. For example, vancomycin has a much slower releasing rate than caffeine because of bulky molecular size.

Wound dressing with thermo-sensitive hydrogels can provide a novel drug release system in response to temperature variations, which can aid in the fast healing of wounds [32]. Similarly, the temperature-responsive textiles with volume and shape changes may also be used for the controlled release of perfume, deodorant, essential oil, nutrient, and so on. Hu et al. developed a kind of smart fabric which can release deodorant agents and keep the body fragrant when the environment temperature is high [33]. By coating poly(N-isopropylacrylamide) hydrogels on the textile surface and further incorporating β-cyclodextrin (β-CD), the deodorant can be loaded and released in a more controlled manner. This kind of intelligent fabric also can be used for skin care by loading Vitamin C or other nutritious ingredients [33]. The releasing amount could be controlled by the changes in human skin temperature.

Water Storage

Smart materials with tunable wettability have been used in many fields, including water storage materials, self-cleaning surfaces, liquid–liquid separation membranes, and antifogging films [5]. When the thermo-responsive polymers are grafted onto surface, the structural changes lead to the reversible switching between

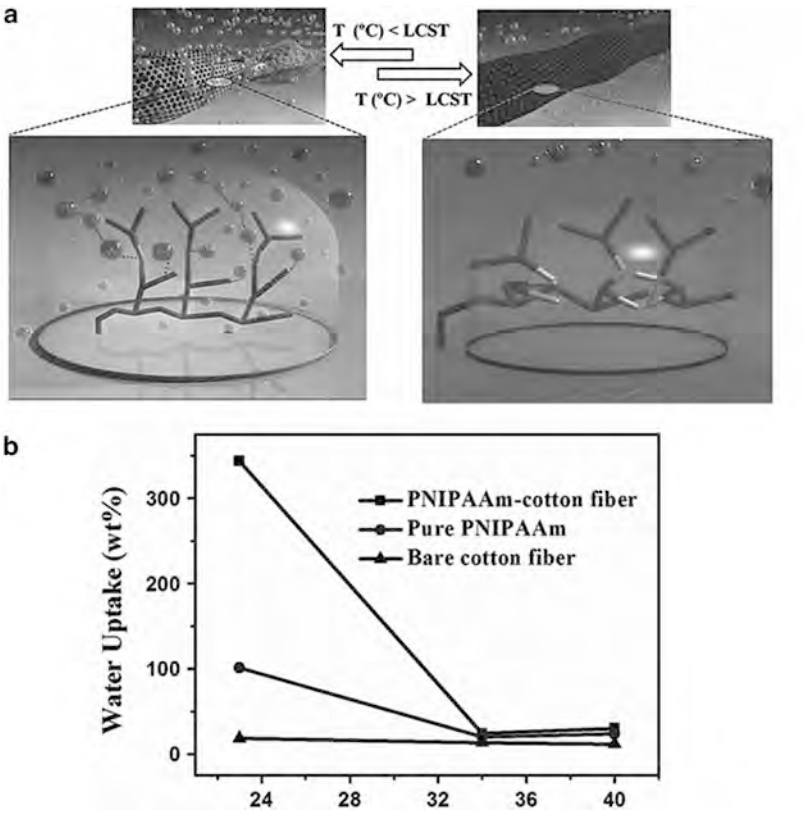

Fig. 11 (**a**) Water collection ("superhydrophilic state") by hydrogen bonding between PNIPAAm and water release ("superhydrophilic state") by the formation of PNIPAAm intermolecular bonds; (**b**) water uptake as a function of temperature for bare cotton, PNIPAAm-cotton, and pure PNIPAAm samples, exposed at high-humidity atmosphere (~96 %) at different temperatures and no direct contact with water [34]

wetting and unwetting states. It is much easier for textiles to achieve the superhydrophilic and superhydrophobic transition because of their high roughness with microscaled grooves and gaps [34]. One interesting application is water storage using cotton fabric composited with PNIPAAm layers on the surface. Water can be autonomously collected from a humid atmosphere and released at daytime, triggered by temperature variations within the day and night (Fig. 11) [34]. As much as three times the weight of water can be stored and released for many cycles. So, it is promising for the future of this water collection textiles used in parched area with water scarcity. This kind of smart textile also can be used for water purification. Due to the offshore oil spill accidents and increasing severe water pollution today, fabric with tunable wettability was utilized for water–oil separation [35]. The hydrophilic (water collecting) and lipophilic (oil collecting) profiles can be switched by changing temperature.

The Requirements of Thermo-responsive Polymer for Textile Application

Textile applications impose strict requirements on properties of polymers, such as high stability; nontoxic, noncorrosive, nonhazardous, reversible phase transformation; and so on. Fast response to thermal changes with no hysteresis is also preferred. Of course, from an economic point of view, low cost is also a very important aspect to consider. In addition, the following characters should be taken into consideration.

Adjustable LCST

The transition temperature should be tailored to specific application requirements. Since the temperature of human body is around 37 °C and the comfortable temperature for human body is around 33.4 °C, polymers should be designed accordingly. For the thermoregulating fabric used in cold weather, the LCST should be lower than that of textiles used in hot weather or in the case of large amount of exercise. LCST can be adjusted by varying either the repeat unit or the grafting ratio of copolymer. Through the copolymerization of 2-(2-methoxyethoxy)ethyl methacrylate (MEO_2MA) and oligo(ethylene glycol) methacrylate ($OEGMA_{475}$) with various commoner compositions, the LCST of the copolymer can be varied between 26 °C and 90 °C [19]. Liu et al. synthesize a series of copolymers consisting of PNIPAAm and poly(maleic anhydride-β-cyclodextrin) (poly(MAH-β-CD)) with different grafting ratios; the LCST changes from about 25 °C to 32 °C [4].

Soft Hand

Clothes are supposed to be soft and comfortable, although they may be coated with polymers to achieve a variety of additional functions. The softness of polymer modified textiles is mainly influenced by the polymer chain structure. The polymer chains should have a good flexibility. With a large content of C–O–C, Si–O, and C–C bonds, the chains can be flexible, whereas bulky aromatic groups can result to inflexible polymer chains. Additionally, the polymer glass transition temperature (Tg) also needs to be taken into consideration. The fabric grafted with polymers with high Tg will become rigid and stiff because these polymers are always in the glass state at the ambient temperature. So, polymers with flexible chains (e.g., polyolefin, polyether, and polysilane) and low Tg are a preferential choice for textile applications.

Easy Polymer–Textile Binding

It should be feasible for polymers binding to textiles with good durability. Usually, polymers are combined to textiles by chemical or physical ways, e.g., grafting, blending, capsulation, coating, or imbedded in the hollow fibers. These thermo-responsive polymers can be used in different forms, such as solution, emulsion, film, fiber, hydrogels, foam, and bulk for different cases [4]. They can be applied to textiles either by finishing or building in method. Therefore, there should be active groups in the polymer chains to enable the covalent binding to textiles.

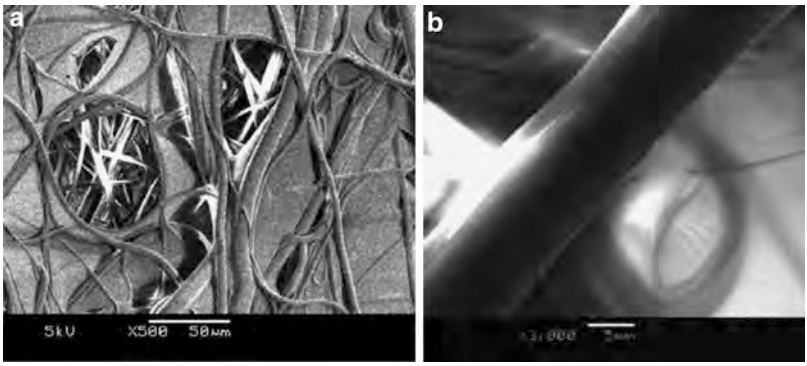

Fig. 12 (**a**) and (**b**) Scanning electron micrograph of the top surface of the PVA-NWF magnified × 500 and × 3,000, respectively (Reprinted from Zhang et al. [36], Copyright (2008) with permission from Elsevier)

Immobilization of Thermo-responsive Polymers onto Textiles

Immobilization of thermo-responsive polymers onto textiles is a viable strategy because the surface activity of the textiles can be altered to possess desirable properties, without any detrimental effect on the mechanical properties. Many techniques have been used to immobilize polymer onto textiles. These techniques include methods varying from physical adsorption to covalent attachment.

Physical Methods

The polymer can be non-covalently immobilized onto textiles using dip-coating and spraying coating techniques. These strategies require relatively simple equipment and handling and can be easily implemented in industrial processes. Currently, the most common method of hydrogel attachment to the textile surface is dip-coating, which is simple and practical. Textile is immersed into casting solution containing thermo-responsive polymer. When the textile is taken out, a thin solution layer adheres to the textile. The overcoats form after the solvent vaporizes and cross-link happens at certain temperature. Yang et al. modified nonwoven fabric (NWF) by polyvinyl alcohol (PVA) using dipping methods (Fig. 12) [36]. The results of measured water contact angle indicate that the hydrophilicity of the modified NWF was enhanced with PVA concentration increasing, and water static contact angles were decreased from 86 ± 1^{o} to $43 \pm 3^{\circ}$.

Another technique for producing a polymeric overcoat around textile is spray coating. This technique involves forcing the printing ink through a nozzle whereby a fine aerosol is formed. A carrier gas and electrostatic charging may be involved to aid in directing the aerosol at the surface of textile.

Usually, activating the textile substrate surface is required to improve adhesion of substrate surface in physical immobilization of polymer onto textiles. The simplest method that one can envisage for improving adhesion is to roughen a

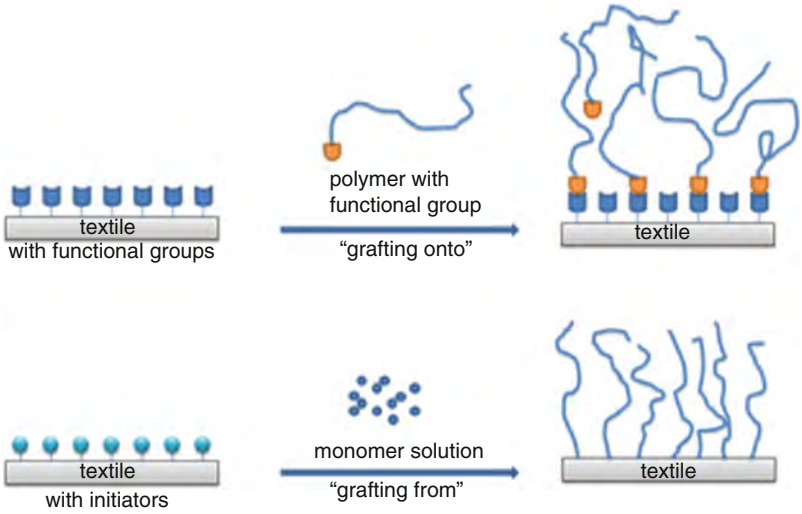

Fig. 13 "Grafting onto" and "grafting from" strategies

surface, thereby enhancing the total contact area and mechanical interlocking. Plasma treatment, as a feasible way to modify fiber surface, was widely used [37]. Although many measures can be taken to enforce the interactions between polymers and textiles, it consists mainly of electrostatic interactions or hydrogen bonding, which is still weak and reversible. This is the main drawback of physical immobilization methods.

Chemical Methods

The two most common types of chemical immobilization methods of thermo-responsive polymers onto textile are "grafting onto" and "grafting from" methods. As illustrated in Fig. 13, the former method is relatively easy and facile because the desired functionalized textiles can be obtained by simple reaction of the thermo-responsive polymer with the textile. Polymers possessing functional groups suitable for reaction with the target textiles and pretreatment of the textiles that make their surface present reactive functional group are two important aspects for "grafting onto" strategy. The advantage of such a method is that the molecular weight and the chain length of grafted polymer are well characterized, and the properties of thermo-responsive polymer in different states (in solution and in textile surface) can be consequently studied. However, with this approach, it is difficult to form thick (thicker than a few tens of nanometers) layers of coating, and the coating suffers from a low density of grafted chains due to the steric hindrance for the attachment of new polymer chains once a few initial chains have been grafted. Based on "grafting onto" stratagem, Save et al. immobilized the thermo-responsive copolymer poly(N-tert-butylacrylamide-ran-acrylamide, 27:73) onto cotton fabrics via a chemical reaction of the copolymer with the hydroxyl group of the cotton in

the presence of 1,2,3,4-butanetetracarboxylic acid as a cross-linker and sodium hypophosphite as a catalyst [38]. The thermo-responsive polymer was found to be efficiently grafted on the cotton surface. The coatings after integration to the cotton substrate retained thermo-responsive swelling behavior and showed a transition in the temperature range of 15–40 °C.

On the contrary, in "grafting from" approach, monomers are polymerized from surface-bound polymerization initiators, which overcome these crowding effects and increase the density of attached chains. Advantages of the "grafting from" method include the creation of relatively thick and dense coatings and polymerization of a wide variety of monomers since the monomer or polymer does not need to have any specific reactive functional groups. However, the molecular weight and chain length distributions of the resultant polymer chains cannot always be accurately controlled and measured. On the other hand, ATRP has been applied to a range of surfaces since it was first disclosed. The rapid development of the ARGET ATRP technique has made the "grafting from" technique more feasible and convenient. A recent example was reported by Xin et al. in 2012. The cotton fiber surface modification with thermo-responsive PNIPAAm was realized using a surface-initiated ATRP method as shown in Fig. 14 [39]. 2-bromoisobutyryl bromide reacted with the terminal amine groups, which is introduced by reaction of aminopropyl trimethoxysilane with hydroxyl group of cotton, to obtain the surface-grafted initiator (Cotton-ATMS-Br). Consequently, the initiator-containing cotton was immersed in a NIPAAm solution to initiate the surface polymerization of PNIPAAm brushes (cotton-PNIPAAm). The success of the polymer grafting was confirmed by FT-IR, XPS, SEM, and solid-state NMR experiments.

Furthermore, photo-induced grafting, gamma radiation grafting, and plasma grafting techniques are also applied to chemical immobilization of thermo-responsive polymer onto textiles. Chen et al. reported the photo-induced grafting polymerization of *N*-isopropylacrylamide (NIPAAm) gel onto polyethylene terephthalate (PET) film and polypropylene (PP) nonwoven fabric surface (Fig. 15) [40]. Plasma pretreatment was carried out before the grafting to provide peroxy groups at the surface of the fabric. The peroxy group formed is believed to favor the bond formation of the substrate and the monomer during the photo-induced grafting polymerization. The grafted gels were found to have the similar LCST (~32 °C) as a pure PNIPAAm hydrogel.

The Characterization of Thermo-responsive Textiles

As the temperature rises and falls, the thermo-responsive polymers change the conformations to give different textile profiles. For characterizing the thermo-responsibility of the smart textiles, the physicochemical properties including wettability and water/air permeability are measured. The assessment technologies of wear comfort are also overviewed considering their importance when applying the smart polymers for textile uses.

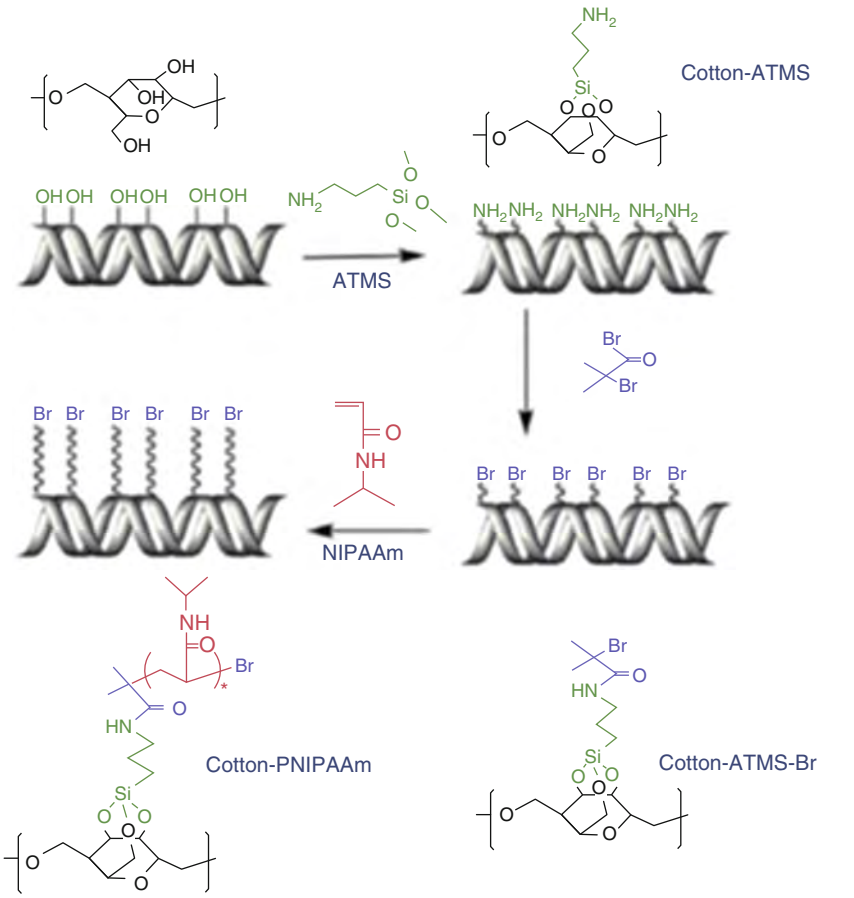

Fig. 14 Synthesis of cotton-PNIPAAm fabrics via a "grating from" approach (Reprinted from Yang et al. [39], Copyright (2012) with permission from Elsevier)

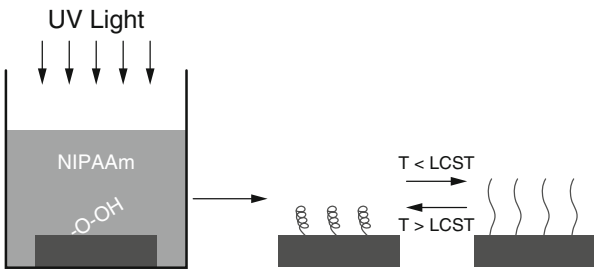

Fig. 15 Schematic of photo-induced grafting polymerization of NIPAAm (Reprinted from Chen et al. [40], Copyright (2002) with permission from Elsevier)

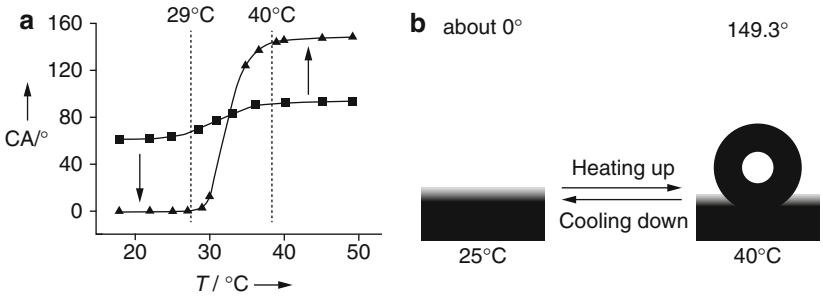

Fig. 16 (**a**) The temperature dependences of water CAs for PNIPAAm thin films on a rough substrate (*triangles*) and on flat substrate (*squares*). (**b**) The water profile for thermally responsive switching between superhydrophilicity and superhydrophobicity of a PNIPAAm-modified rough surface at 25 °C and 40 °C [41]

The Characterization of Thermo-responsibility

Wettability

Contact angle is the angle of liquid/vapor interface on a solid surface. Wettability of surfaces is influenced by two key parameters: the surface chemistry and roughness. The former one was characterized as an important indicator for the success of functionalization. With increasing temperature the contact angle of surface modified by polymers with LCST will have a sudden increase. On a smooth surface, the water contact angle (CA) increased about thirty degrees in an example [41]. This phenomenon can be explained by the switch between inter- and intramolecular hydrogen bonding. For textiles with rough surface, as demonstrated in the above, the thermo-responsive wettability is greatly enhanced (Fig. 16b) [41]. The value of CA reversely changes from 0° to 149.3° by heating up and cooling down. The CA curve also tells about the transition region of the thermo-responsive textiles. For example, as shown in Fig. 16a, the temperature transition region of PNIPAAm on rough surface (triangles) is 11°, which is much narrower than that of PNIPAAm on smooth surface (squares). That means the former one has a faster response. CA can be measured by a contact angle analyzer and dynamic surface tension tester equipped with a temperature control chamber. In some cases on the hydrophilic fabrics, the water drop will disappear in a very short time due to the wicking effect. To catch photos in a high speed (ms^{-1}), a high-speed camera is employed to videotape the instant process. Both the contact angle and the wicking time (the time it takes for a liquid to be drawn to fabric materials) can be calculated for wettability characterization.

Water Uptake

The specific volume change of thermo-responsive textiles is expected to control the water uptake. Thus, the liquid management ability is correlated to capability of responding to temperature signals. The relationship can be revealed by studying the swelling/de-swelling or hydration/dehydration kinetics [42]. Textiles are dual-scale

porous medium, and two modes of water permeation coexist during the performance. One is inter-tow macropore flow driven by the externally applied pressure, and the other is intra-tow micropore flow driven by the capillary effect. The latter one occurs because of intermolecular forces between water and the surrounding fiber surfaces, and it can be measured by thin layer wicking (TLW) method [42]. The rate of water wicking into fabric material can be described by Washburn equation for the horizontal capillary:

$$\frac{x^2}{t} = \frac{R}{2\eta}\Delta G$$

where x is the distance water climbs (cm), R is the apparent capillary radius of porous solid (m), t is the time to reach the distance x (s), η is the water viscosity (mPa·s), and ΔG is the Gibbs free energy change accompanying the liquid penetration process (mJ/m^2). Apparently, the water penetration rate (x^2/t) is a quantitative measure of the water transport ability of fabric. In order to assess the influence of temperature on this process, the measurement could be done with water at different temperatures. After grafting with microgels, polyester fabric shows a faster wicking, whereas the contact angle increased. It suggests that the capillarity is increased owing to increased fiber roughness [43].

Air/Moisture Permeability

Moisture permeability is an important criterion to evaluate the thermo-responsiveness capability. For thermo-responsive textiles, the moisture permeability is not present continuously, but it could be activated "on demand" by sensing the temperature change in the local environment. When the temperature is high, the smart fabric displays as normal cloth with open interspaces having good air and moisture permeability. As temperature falls under LCST, interspaces are sealed to resist moisture transmission. Water vapor transmission rate (WVTR) measurements can be performed according to the standard UNI 4818-26 or ASTM E96-80. In the former standard, a container with a round opening at the top to allow vapor exhaust was used for testing. Samples are mounted to cover the opening. And the container with the sample is then weighted and conditioned above and below the transition temperature at 80 % relative humidity for 24 h. The WVTR (g/m^{-2}day^{-1}) can be calculated according to following equation:

$$\mathrm{WVTR} = \frac{\Delta m \times 24}{S \times t}$$

Here, Δm is the change of mass (g) before and after conditioning, S is the testing area of the fabric sample (m^2), and t is the testing time (h) [44].

DSC

The temperature-responsive character of the fabric can be quantitatively verified by DSC measurement. In the diagram, the endothermic peak is attributed to the

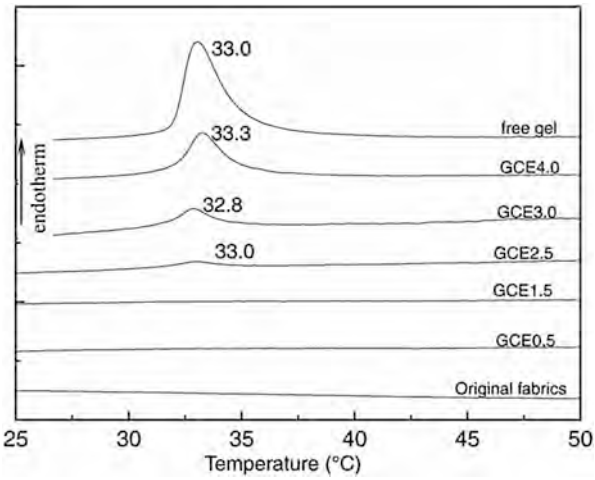

Fig. 17 DSC heating thermograms of the hydrated samples (GCE0.5, GCE1.5, GCE2.5, GCE3.0, and GCE4.0 indicated monomer concentrations 0.5%wt, 1.5% wt, 2.5%wt, 3.0%wt, and 4.0%wt, respectively) (Hu [45], copyright © 2007. Reprinted by Permission of SAGE)

dissociation of hydrogen bonds. After compositing with vinyl-capped polyurethane (VCPU) and NIPAAm by random copolymerization, the transition peak of the cotton nonwoven appeared in the range of 32.8 ~ 33.3 °C (Fig. 17) [45]. It is very close to the transition temperature of free VCPU-PNIPAAm gels.

Fabric Performance Evaluation

Since the thermo-responsive polymer functionalized fabric is aimed as consumer product, the characteristics of the material in production and use, such as comfort, safety, durability, and mechanical strength, are of vital importance.

Softness/Stiffness

The stiffness is defined as the ability to resist the bending of fabric. And the softness is used to evaluate the opposite characteristics, which is one of the most important properties of fabric. Generally speaking, the underwear clothes need to have good flexibility, whereas the coats should be stiff enough to be flat and keep the shape. The Kawabata Evaluation System (KES) and Fabric Assurance by Simple Testing (FAST) are the most important instrumental approaches to test fabric handing. It is worth to mention that FAST methods can also measure other properties such as drapability and smoothness. The evaluation of fabric hand can be also guided by AATCC protocols (AATCC Evaluation Procedure 5: Fabric Hand).

Strength

The strength of a fabric has much to do with its wearing quality and should meet the requirements for different applications. It is determined by several factors: weave, texture, yarn twist, and structure. But, for the thermo-responsive polymers modified textiles, the chemical process during the functionalization may bring some effect to the strength. The tensile strength is measured by drawing the piece of

fabric in two opposite directions until it breaks down. The tensile ratio and tensile strength are calculated from the results. The strength in wrap and weft directions is different because of the texture. The tear strength is a measure of how well a fabric can withstand the effects of tearing, which can be measured according to the ASTM D412 method. The bursting strength refers to the resistance to the pressure at which the fabric will burst. It is usually used to characterize the strength of knit fabrics.

Drapability

Drapability can be used to characterize the drape performance of fabric when it is allowed to hang under its own weight. It is an important factor in determining the aesthetic appearance and dynamic functionality. Fabric with good drapability is able to form a smooth surface modeling and fits properly with the human body. The drape coefficient means the percentage of the project area of draped fabric to its original area. It is the most popularly used parameter to quantify drape. A low drape coefficient indicates easy deformation of a fabric and vice versa. The measurement can be carried out by drapability tester. The modern instruments are equipped with digital image processing software for drape coefficient calculation and enable dynamical measurement.

Wrinkle Recovery

Wrinkle resistance is important considering the aesthetic and ease-of-care. It is defined as the ability of a fabric bounce back and keeps flat after it has been wrinkled in any way. Fabric with good resiliency is expected to eliminate wrinkles in a short time. The crease recovery angle tester can be used to determine the degree of a fabric recovery from wrinkling according to AATCC 66 and MS P22 methods. Samples were preconditioned at standard atmosphere (20 °C, 65%RH). The polyester fabric modified with microgels shows a 4 ~ 5 % decrease of crease recovery angle in both warp and weft directions as compared to the reference one [43]. It is a comprehensive concept defining the fabric wrinkling. For sufficiently describing the wrinkling, sometimes several other parameters are tested, including wrinkle density (the number of wrinkles per unit area), wrinkle profile (the height of the wrinkles or the extent to which the fabric distorted from a plane), and sharpness (the sharpness of the observed crease) [46].

Abrasion Resistance

Abrasion resistance is a property which resists the mechanical wearing and damage. It is mainly determined by the material of the fabric, but the polymeric coating also has some effect. In fact, different ways of abrasion happen at different parts of clothes. Plane abrasion, which takes place on the haunch and back, can be measured by Martindale pilling tester. The abrasion under pressure and bending often happens on the elbow and knee. The measurement can be carried out by curve abrasion tester. And the edge abrasion tester can be used to investigate the abrasion in the edge of folding fabric, which usually happens in the site of collars and cuffs.

Wash Fastness

Wash fastness is the ability of fabric holding the functional coating during washing. It is especially important for thermo-responsive textile application since it is related to the stability and durability of the functional layer during the use. The wash fastness can be characterized by measuring the properties of textiles (wettability, weight loss, thermo-responsibility) after washing under the standard condition for certain times. In detail, the fastness is tested according to the following laundering procedure: the fabric is washed by hand washing cycles according to AATCC Test Method 124-1996 using AATCC detergent. The temperature of water is set to 40 °C.

Challenges and Solutions of Thermo-responsive Textile

Generally speaking, the textile industry, especially in the developing country, is still a low value-added and single function. Intelligent textile research has made significant development since the 1990s. At present, the use of thermo-responsive polymers for textile applications remains largely unexplored. Main challenges lay in achieving efficient surface modification of the textile material for the durable incorporation of thermo-responsive polymers, retaining the soft handle of textiles after polymer combination, and building a system with fast responsiveness and high effectiveness:

1. The main challenge is the long-term stability and durability of the polymer coating on the textiles while undergoing ultraviolet irradiation, sweat vapor, washing, shaping, and wear abrasion [47]. It is still difficult to find a way to integrate the polymer layer into textiles with sufficient durability while still retain the effectiveness of the thermo-responsiveness. Obviously, chemical binding layers are more stable than physically coated ones. The covalent binding between the textile material surface and the polymer layer could be effectively tailored by the introduction of reactive functional groups to the substrate. Thermo-responsive polymers with end reactive functional group can be achieved by ATRP using functional initiators, and the reactive textile surface is readily achievable through chemical modification of textiles.
2. In most cases, the functional coatings should not have impact on the artistic appearance and soft handle of textiles. But textiles with high grafting ratio of polymers will became stiff and brittle, especially when the material is in the dry state. To solve this problem, thermo-responsive copolymers containing oligo (ethylene glycol) have been developed to substitute for PNIPAAm. Their LCST can be adjusted via molecular design. Copolymers of 2-(2-methoxyethoxy) ethyl methacrylate with oligo(ethylene ether methacrylate)s have both advantages of antifouling and thermo-responsive properties [48]. And what's more, the copolymer chains are more flexible than PNIPAAm, which is a solution for the reducing of fabric stiffness. Generally speaking, linear and unbranched polymers are preferred. The cross-linked polymers, although with a low coating thickness, may cause a negative effect on the fabric's original favorable properties.

3. The grafting ratio still needs to be very low, partly because of the high cost of the smart polymers. Another reason is that polymers can't expand fully in the over dense and thick layer. A minimum coat-thickness is needed for high response efficiency (swelling and de-swelling ability) [49]. Additionally, it is more challenging to develop complex systems that are sensitive to thermal signals with polymers in a low concentration range. The thermo-responsive macromolecules can be introduced onto the textiles as pore-filling materials. In this way, only a small amount of polymers is needed, which can efficiently control the pore-gate system. The change of polymer chain structure determines the "open" and "close" of pores. Besides, micro-sized hydrogels enable incorporation to textiles in a very thin layer and increase the surface area. Consequently, the response time is significantly improved in comparison to that of bulk hydrogels. The above strategies provide insights that would help maintain the advantageous conventional properties of initial textiles as well as produce an efficient thermo-responding system.

Overall, the thermo-responsive textiles allow for the introduction of artificial intelligence to the conventional textiles. Although only a few kinds of products have been commercialized so far, they are promising in many applications in the future.

Summary

This chapter briefly reviewed the fundamental and application research of the thermo-responsive polymers in the past few decades, especially the applications in the field of textile. Due to the unique ability to switch between hydrophilic and hydrophobic state by varying the temperature, thermo-responsive polymers are introduced into the textile by physical and chemical methods to meet the goal of "smart textile" and realize the smart control of permeability, medicine/perfume release, water storage, and so on. Although these applications of the smart textile have already been developed, they are still in the infancy stage and far from success. A large amount of problems needed to be solved, such as the following: the stability of the textile with thermo-responsive polymers is quite low, and the handle of the textile is very hard and brittle. Moreover, until now the achieved functions of the smart textile are mainly based on improving the conventional functions; novel ideas are acquired to achieve new functions of the smart textile. And these upgrades can make these regular textiles more attractive in the future.

References

1. Jeong B, Gutowska A (2002) Lessons from nature: stimuli-responsive polymers and their biomedical applications. Trends Biotechnol 20:360. doi:10.1016/S0167-7799(02)01962-5
2. Schild HG (1992) Poly(N-isopropylacrylamide): experiment, theory and application. Prog Polym Sci 17:163–249. doi:10.1016/0079-6700(92)90023-R

3. Lee YM, Shim JK (2003) Permeation controlled through stimuli-responsive polymer membrane prepared by plasma and radiation grafting techniques. In: Tao XM (ed) Smart fibers, fabrics and clothing. Woodhead Publishing, Abington, pp 109–123
4. Aseyev V, Tenhu H, Winnik FM (2011) Non-ionic thermoresponsive polymers in water. Adv Polym Sci 242:29–89. doi:10.1007/12_2010_57
5. Grosberg AY, Khokhlov AR (1994) Statistical physics of macromolecules. AIP Press, New York
6. Okada Y, Tanaka F (2005) Cooperative hydration, chain collapse, and flat LCST behavior in aqueous poly(N-isopropylacrylamide) solutions. Macromolecules 38:4465–4471. doi:10.1021/ma0502497
7. Klouda L, Mikos AG (2008) Thermoresponsive hydrogels in biomedical applications. Eur J Pharm Biopharm 68:34–45. doi:10.1016/j.ejpb.2007.02.025
8. Tanford C (1966) Physical chemistry of macromolecules. Wiley, New York
9. Maeda Y, Nakamura T, Ikeda I (2002) Changes in the hydration states of poly (Nalkylacrylamide)s during their phase transitions in water observed by FTIR spectroscopy. Macromolecules 34:1391–1399. doi:10.1021/ma020945w
10. Tiktopulo EI, Uversky VN, Lushchik VB, Klenin SI, Bychkova VE, Ptitsyn OB (1995) "Domain" coil-globule transition in homopolymers. Macromolecules 28:7519–7524. doi:10.1021/ma00126a032
11. Furyk S, Zhang YJ, Ortiz-Acosta D, Cremer PS, Bergbreiter DE (2006) Effects of end group polarity and molecular weight on the lower critical solution temperature of poly (N-isopropylacrylamide). J Polym Sci Part A Polym Chem 44:1492–1501. doi:10.1002/pola.21256
12. Xia Y, Burke NAD, Stover HDH (2006) End group effect on the thermal response of narrow-disperse poly(N-isopropylacrylamide) prepared by atom transfer radical polymerization. Macromolecules 39:2275–2283. doi:10.1021/ma0519617
13. Nuopponen M, Kalliomäki K, Laukkanen A, Hietala S, Tenhu H (2008) A-B-A Stereoblock copolymers of N-Isopropylacrylamide. J Polym Sci Part A Polym Chem 46:38–46. doi:10.1002/pola.22355
14. Winnik FM, Ringsdorf H, Venzmer J (1990) Methanol-water as a co-nonsolvent system for poly(N-isopropylacrylamide). Macromolecules 23:2415–2416. doi:10.1021/ma00210a048
15. Hellweg T, Dewhurst CD, Eimer W, Kratz K (2004) PNIPAAm-co-polystyrene core-shell microgels: structure, swelling behavior, and crystallization. Langmuir 20:4330–4335. doi:10.1021/la0354786
16. Feil H, Bae YH, Feijen J, Kim SW (1993) Effect of comonomer hydrophilicity and ionization on the lower critical solution temperature of N-isopropylacrylamide copolymers. Macromolecules 26:2496–2500. doi:10.1021/ma00062a016
17. Winnik FM, Davidson AR, Hamer GK, Kitano H (1992) Amphiphilic poly (N-isopropylacrylamides) prepared by using a lipophilic radical initiator – synthesis and solution properties in water. Macromolecules 25:1876–1880. doi:10.1021/ma00033a006
18. Molyneux P (1985) Water-soluble synthetic polymers: properties and behavior. CRC, Boca Raton
19. Lutz JF (2008) Polymerization of oligo(ethylene glycol) (Meth)Acrylates: toward new generations of smart biocompatible materials. J Polym Sci Part A Polym Chem 46:3459–3470
20. Yuan YY, Liu XQ, Wang YC, Wang J (2009) Gold nanoparticles stabilized by thermosensitive diblock copolymers of poly(ethylene glycol) and polyphosphoester. Langmuir 25: 10298–10304. doi:10.1021/la901120x
21. Chang JH, Kim KJ, Shin YK (2004) Sustained drug release on temperature-responsive polymer hybrid nanoporous silica composites. Bull Korean Chem Soc 25:1257–1260. doi:10.5012/bkcs.2004.25.8.1257
22. Chern CS (2006) Emulsion polymerization mechanisms and kinetics. Prog Polym Sci 31:443–486. doi:10.1016/j.progpolymsci.2006.02.001
23. Suzuki D, Yamagata T, Murai M (2013) Multilayered composite microgels synthesized by surfactant-free seeded polymerization. Langmuir 29:10579–10585. doi:10.1021/la4025537

24. Alexandridis P, Hatton TA (1995) Poly(ethylene oxide)-poly(propylene oxide)-poly(ethylene oxide) block copolymer surfactants in aqueous solutions and at interfaces: thermodynamics, structure, dynamics, and modeling. Colloids Surf A Physicochem Eng Asp 96:1–46. doi:10.1016/0927-7757(94)03028-X
25. Andre X, Zhang M, Muller AH (2005) Thermo- and pH-responsive micelles of poly(acrylic acid)-block-poly(N, N-diethylacrylamide). Macromol Rapid Commun 26:558–563. doi:10.1002/marc.200400510
26. Dai S, Ravi P, Tam KC (2009) Thermo- and photo-responsive polymeric systems. Soft Matter 5:2513–2533. doi:10.1039/B820044K
27. Qu T, Wang A, Yuan J, Shi J, Gao Q (2009) Preparation and characterization of thermo-responsive amphiphilic triblock copolymer and its self-assembled micelle for controlled drug release. Colloid Surf B 72:94–100. doi:10.1016/j.colsurfb.2009.03.020
28. Chu LY, Park SH, Yamaguchi T, Nakao SI (2001) Preparation of thermo-responsive core-shell microcapsules with a porous membrane and poly(N-isopropylacrylamide) gates. J Membr Sci 192:27–39. doi:10.1016/S0376-7388(01)00464-1
29. Topp MDC, Dijkstra PJ, Talsma H, Feijen J (1997) Thermosensitive micelle-forming block copolymers of poly(ethylene glycol) and poly(N-isopropylacrylamide). Macromolecules 30:8518–8520. doi:10.1021/ma9710803
30. Liang L, Shi M, Viswanathan VV, Peurrung LM, Young JS (2000) Temperature-sensitive polypropylene membranes prepared by plasma polymerization. J Membr Sci 177:97–108. doi:10.1016/S0376-7388(00)00453-1
31. Serra M (2002) Adaptable skin-hydrogel gives wetsuit protection. Smart Mater Bull 8:7–8. doi:10.1016/S1471-3918(02)00823-7
32. Cornelius VJ, Majcen N, Snowden MJ, Mitchell JC, Voncina B Preparation of smart wound dressing based on colloidal microgels and textile fibers. Proc SPIE 6413, Smart Materials IV, 64130X. doi:10.1117/12.712573
33. Hu JL, Meng H, Li GQ, Ibekwe SI (2012) A review of stimuli-responsive polymers for smart textile applications. Smart Mater Struct 21:053001. doi:10.1088/0964-1726/21/5/053001
34. Yang H, Zhu H, Hendrix MM, Lousberg NJ, de With G, Esteves ACC, Xin JH (2013) Temperature-triggered collection and release of water from fogs by a sponge-like cotton fabric. Adv Mater 25:1150–1154. doi:10.1002/adma.201204278
35. Xue B, Gao L, Hou Y, Hou ZW, Jiang L (2013) Temperature controlled water/oil wettability of a surface fabricated by a block copolymer: application as a dual water/oil on-off switch. Adv Mater 25:273–277. doi:10.1002/adma.201202799
36. Zhang CH, Yang FL, Wang WJ, Chen B (2008) Preparation and characterization of hydrophilic modification of polypropylene non-woven fabric by dip-coating PVA (polyvinyl alcohol). Sep Purif Technol 61:276–286. doi:10.1016/j.seppur.2007.10.019
37. Li R, Ye L, Mai YW (1997) Application of plasma technologies in fibre-reinforced polymer composites: a review of recent developments. Compos Part A 28A:73–86. doi:10.1016/s1359-835X(96)00097-8
38. Save NS, Jassal M, Agrawal AK (2005) Smart breathable fabric. J Ind Text 34:139–155. doi:10.1177/1528083705047905
39. Yang H, Esteves ACC, Zhu H, Wang D, Xin JH (2012) In-situ study of the structure and dynamics of thermo-responsive PNIPAAm grafted on a cotton fabric. Polymer 53:3577–3596. doi:10.1016/j.polymer.2012.05.053
40. Chen KS, Tsai JC, Chou CW, Yang MR, Yang JM (2002) Effects of additives on the photo-induced grafting polymerization of N-isopropylacrylamide gel onto PET film and PP nonwoven fabric surface. Mater Sci Eng C 20:203–208. doi:10.1016/S0928-4931(02)00034-6
41. Sun TL, Wang GJ, Feng L, Liu BQ, Ma YM, Jiang L, Zhu DB (2004) Reversible switching between superhydrophilicity and superhydrophobicity. Angew Chem Int Ed 43:357–360. doi:10.1002/anie.200352565

42. Lavrič PK, Tomšič B, Simončič B, Warmoeskerken MMCG, Jocić D (2012) Functionalization of cotton with poly-NiPAAm/chitosan microgel: Part II. Stimuli-responsive liquid management properties. Cellulose 19:273–287. doi:10.1007/s10570-011-9635-7
43. Glampedaki P (2010) Tunable wettability of polyester fabrics functionalized by chitosan/poly (N-isopropylacrylamide-co-acrylic acid) microgels. In: Dragan J (ed) Surface modification systems for creating stimuli responsiveness of textiles. University of Twente, Enschede, pp 61–76
44. Chung H (2004) Thermal properties and physiological responses of vapor-permeable water repellent fabrics treated with microcapsule-containing PCMs. Text Res J 74:571–575. doi:10.1177/004051750407400702
45. Hu JL, Liu BH, Liu WG (2007) Temperature/pH sensitive N-isopropylacrylamide/ polyurethane copolymer hydrogel-grafted fabrics. Text Res J 76:853–860. doi:10.1177/0040517507074625
46. Youngjoo N, Behnam P (1995) Assessing wrinkling using image analysis and replicate standards. Text Res J 65:149–157. doi:10.1177/004051759506500303
47. Stuart MAC, Huck WTS, Genzer J, Muller M, Ober C, Stamm M, Sukhorukov GB, Szleifer I, Tsukruk VV, Urban M, Winnik FM, Zauscher S, Luzinov I, Minko S (2010) Emerging applications of stimuli-responsive polymer materials. Nat Mater 9:101–113. doi:10.1038/nmat2614
48. Lutz JF (2011) Thermo-switchable materials prepared using the OEGMA-platform. Adv Mater 23:2237–2243. doi:10.1002/adma.201100597
49. Jocić D Functional finishing of textiles with responsive polymeric systems. pp 37–59

Novel Synthesis Pathways for PNIPAAm-Based Hydrogels and Their Application in Thermosensitive Textiles

35

Petar Jovancic, S. Petrusic, and R. Molina

Contents

Introduction 954
Poly(*N*-isopropylacrylamide): PNIPAAm 959
Basic Facts and Properties 959
Strategies for Synthesis of PNIPAAm-Based Hydrogels 960
PNIPAAm-Functionalized Smart Textiles 971
Systems PNIPAAm-Based Linear Polymers/Textiles 971
Systems PNIPAAm-Based Bulk Hydrogel Films/Textiles 974
Systems PNIPAAm-Based Microgels/Textiles 979
Summary 981
References 981

Abstract

The research focus is lately directed towards the development of the thermosensitive textiles with advanced functionalities. As sources of inspiration for a progress in the field of these innovative materials, stimuli-sensitive

P. Jovancic (✉)
Textile Engineering Department, Faculty of Technology and Metallurgy, University of Belgrade, Belgrade, Serbia
e-mail: pera@tmf.bg.ac.rs

S. Petrusic
Ecole Nationale Supérieure des Arts et Industries Textiles, ENSAIT, GEMTEX, Roubaix, France

Université Lille Nord de France, Lille, France
e-mail: stojanka.petrusic@ensait.fr

R. Molina
Plasma Chemistry Group, Department of Chemical and Surfactants Technology, Institute of Advanced Chemistry of Catalonia, Consejo Superior de Investigaciones Científicas, IQAC-CSIC, Barcelona, Spain
e-mail: ricardo.molina@iqac.csic.es

© Springer Science+Business Media Singapore 2015

X. Tao (ed.), *Handbook of Smart Textiles*,
DOI 10.1007/978-981-4451-45-1_12

polymer engineering, plasma surface engineering, and nanotechnology have been extensively explored. In this work, the polymerization methods for synthesis of Poly(N-isopropylacrylamide), PNIPAAm-based hydrogels, incorporating natural biopolymers (chitosan and β-cyclodextrin), for achieving dual temperature/pH sensitivity and improvement of relevant loading capacity towards specific guest molecules are outlined. These PNIPAAm-based hydrogels are of great interest for biomedical applications (transdermal drug delivery, cell encapsulation, wound dressing, tissue repair, etc.) and intelligent stimuli-sensitive textile coatings for moisture regain control, antimicrobial properties, water and/or oil repellency, and fragrance release. The strategies for synthesis of PNIPAAm-based hydrogels (macro and micro forms) and their proper integration onto textiles through the plasma surface modification, graft polymerization, and coatings are discussed. Novel possibilities for creating hydrogels based on atmospheric plasma polymerization of NIPAAm monomers in liquids have alos been reported. Plasma polymerization in liquids demonstrated a great technological potential given that it may be performed without the use of chemical initiators and even without cross-linking agents, offering multiple advantages over the conventional hydrothermal polymerization methods. Further research on adequate chemical and physical structures of PNIPAAm-based hydrogels and methods of their applications in textiles could boost a progress in the domain of smart textiles, implying novel performances and end uses.

Keywords

Poly(*N*-isopropylacrylamide) • Bulk hydrogel • Microgels • PNIPAAm-based IPNs • Comb-graft PNIPAAm-based hydrogels • Volume phase transition • Grafting • Hydrogel films • Liquid plasma polymerization • Thermosensitive textiles

Introduction

In recent times, an increasing amount of research has been done on smart functional finishing of textile materials (smart textiles) by incorporation of stimuli-sensitive polymers with ability to interact or respond to external conditions or stimulations [1]. The interaction with the surroundings is what attracts large and constantly growing interest of scientific public towards the smart textiles. Through this approach, the new added-value textile materials could be created containing fibers that maintain advantageous conventional properties (e.g., mechanical strength, flexibility, and wear comfort) but with advanced functionalities and/or environmental responsiveness implemented by the modification of a very thin surface layer of the material. Most of smart textiles are capable of both, sensing and responding to changes in the environment. The nature of stimulus and the manner of the textile response determine the classification of the smart textile materials into the following types: functional, electrical conductive, piezoelectric, thermal conductive, thermal emissive, optical, color change, shape memory, and textile

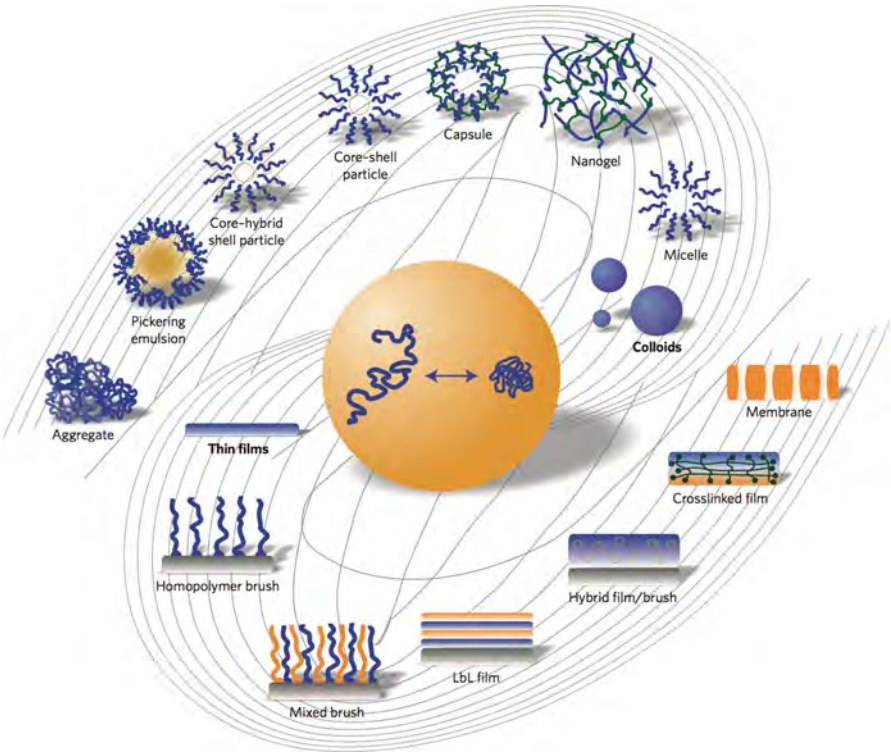

Fig. 1 Two-dimensional (films) and three-dimensional (particles and their assemblies) stimuli-sensitive systems (Reprinted from Cohen Stuart et al. [4] by permission from Macmillan Publishers Ltd)

material-releasing substances [2]. E-textiles that contain embedded computing, digital components, and electronics impart novel functions to garments far beyond cold resistance. Textiles with novel functions such as textile displays, self-cleaning textiles, temperature-regulated textiles, and self-moving textiles have been developed [3]. Stimuli-sensitive polymers can sense different environmental signals (change in temperature, pH, applied mechanical force, light irradiation, or electrical and magnetic field) responding to the respective signals by crystalline/amorphous transition, by conformational and chemical changes, changes in solubility, wettability, swelling capacity, and redox (reduction-oxidation) state. A number of reviews, including special journal issues, consider stimuli-sensitive polymers and hydrogels as well as the state of understanding on their application in textiles [3–5].

Different options for design of macro-, micro-, and nanoparticles and their assemblies and thin films of stimuli-sensitive polymeric materials and systems are summarized in Fig. 1 [4]. These materials rely on the phase behavior of macromolecule assemblies in thin films (polymer brushes, multilayered films made of different polymers, hybrid systems that combine polymers and particles, thin films of

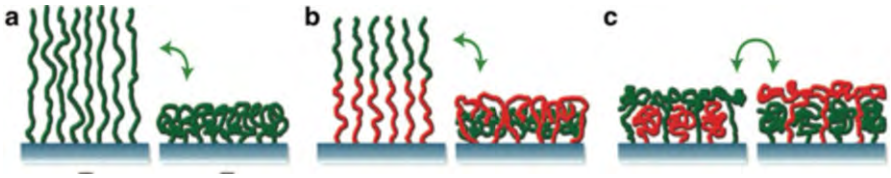

Fig. 2 Single-component (**a**), block copolymer (**b**), and mixed (**c**) polymer brushes (Reprinted from Cohen Stuart et al. [4] by permission from Macmillan Publishers Ltd)

polymer networks, and membranes being thin films with channels/pores) and nanoparticles (micelles, nanogels, capsules and vesicles, core–shell particles, hybrid particle-in-particle structures, and their assemblies in solutions and at interfaces in emulsions and foams).

Principal architectures and mechanisms of integration of stimuli-sensitive polymers onto specific surfaces fall into several categories: (1) polymer surfaces formed spontaneously in bulk polymer materials, (2) polymer brushes (grafted polymer thin films), (3) thin films of polymer networks, and (4) self-assembled multilayered thin films.

Stimuli-sensitive polymer brushes could contain macromolecules that are chemically grafted to a textile surface at sufficiently high grafting densities so that the polymer chains adopt a stretched conformation due to excluded volume repulsions (Fig. 2a–c). Polymer brushes are generally prepared either through the "grafting to" approach or the "grafting from" approach, offering exciting possibilities for the fabrication of adaptive and responsive interfaces [6]. Uniform, patterned, and gradient brushes (brushes in which grafting density and/or chemical composition gradually changes in one or two directions on the surface of the sample) have been used to generate responsive films on planar and curved nanoparticle surfaces. For single-component homopolymer brushes (Fig. 2a), responsive behavior originates from the properties of the grafted polymer chains and their grafting densities. The responsive behavior of block copolymer brushes (Fig. 2b) is based on the phase segregation of different blocks, specifically when solvent affinities of each of the blocks are significantly different. In mixed polymer brushes (Fig. 2c), at least two chemically different polymers are grafted to the same substrate. Phase segregation causes the switching of the spatial distribution of the functional groups present in the brush exterior so that the properties of materials are shifted in between the properties of two constituent polymers, similar to block copolymer brushes.

In spite of a great diversity in designing the stimuli-sensitive polymers and systems, a considerable attention has been drawn to the "smart" hydrogels not only because of their unique properties but also because of their potential for significant technological and biomedical applications. Among them, thermosensitive hydrogels have been the most widely studied for functional finishing of textiles. Thermosensitive hydrogels are three-dimensional macromolecular polymer networks containing a large fraction of water within their structures. Their degree of swelling is increased or decreased below or above their

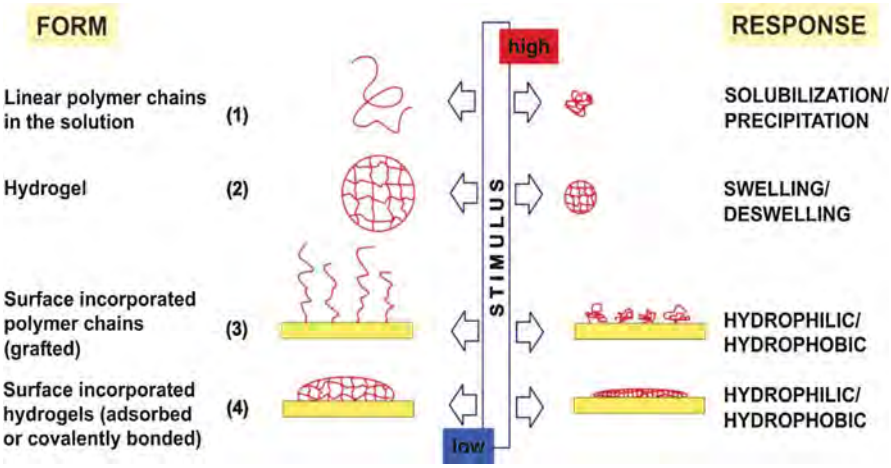

Fig. 3 The macroscopic response of different forms of stimuli-sensitive linear polymers and hydrogels (Reprinted from Jocic et al. [7] by permission from InTech and originally published under CC BY 3.0 licence)

volume phase transition temperature (VPTT). In case of thermosensitive hydrogels of thermo-shrinking type, at temperatures above their VPTT, hydrophobic interactions among hydrophobic segments of polymer chains are strong, while hydrogen bonding is weak. As a result, a volume phase transition manifested as shrinking of hydrogel occurs. By analogy, a macroscopic response of the surface with grafted stimuli-sensitive polymer chains is a particular change in its wettability and water permeability, due to alteration in hydrophilic/hydrophobic balance of the system (Fig. 3) [7].

Effective functional finishing of textiles with thermosensitive hydrogels depends on the choice of their adequate form (macro or bulk hydrogels, microgels, nanogels), the proper surface modification (surface pretreatment and/or activation of textiles), and, perhaps more important, the adequate integration of hydrogels into textile material structure with sufficient durability and without impairing the intrinsic property of a native textile material (Fig. 4). It is known that environmentally friendly physical activation of textiles enhances adhesion capabilities and binding efficiency towards hydrogel formulations [3, 5]. The choice of hydrogel form is closely related to the final application of thermosensitive system developed (thermosensitive hygroscopic fabrics for intelligent heat and moisture control, stimuli-sensitive nutrient delivery fabrics, environment-sensitive deodorant fibers, stimuli-sensitive drug release matrices, wound dressing products and fabrics for transdermal purposes, etc.). Generally, bulk hydrogels are often characterized by long response times (minutes to tens of hours), during which various polymer constituents either migrate to the surface from the bulk or rearrange locally and decrease the interfacial tension. This type of response is too slow for many applications. A rapid response with no corruption of the mechanical properties of

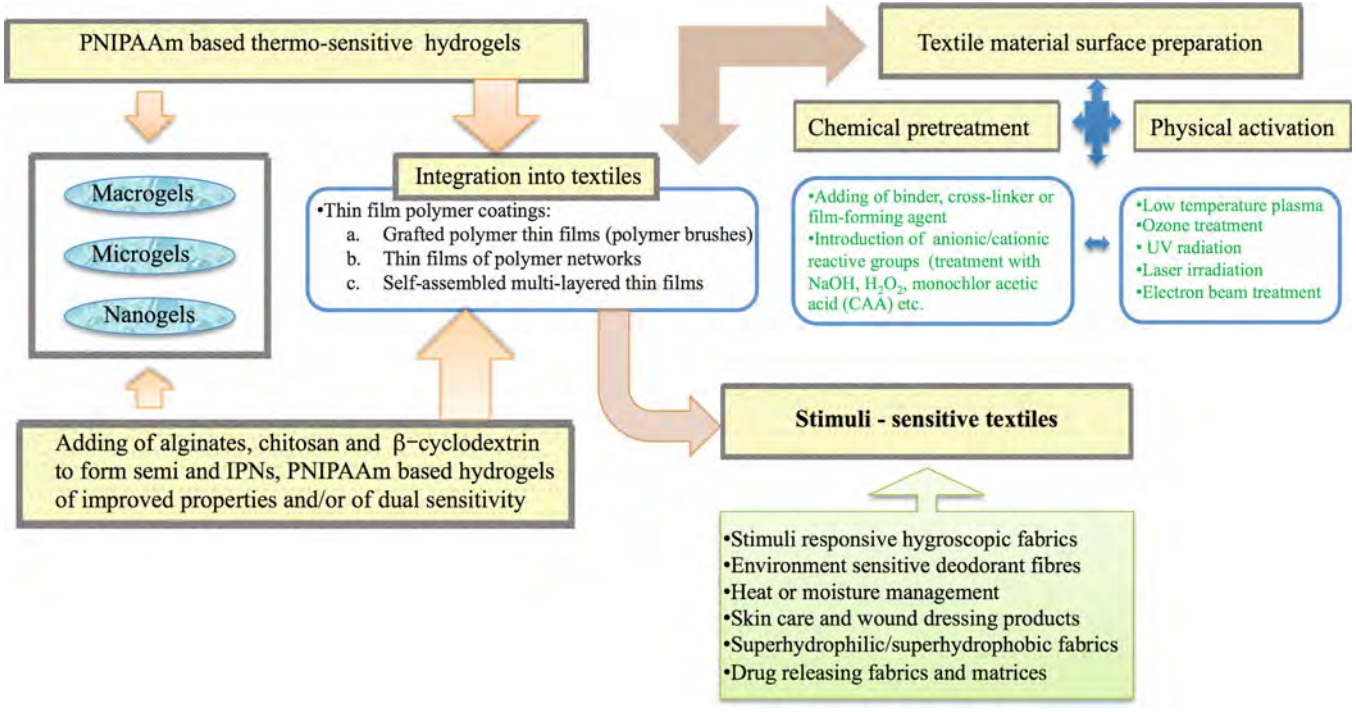

Fig. 4 Stimuli-sensitive textiles based on PNIPAAm hydrogels – general synthesis routes

the bulk material could be successfully achieved through a thin polymer-film coating. By using new design techniques, response times in thin films can now be tuned smoothly from hours to seconds. Therefore, bulk form of thermosensitive hydrogels could be a better choice for transdermal drug-releasing matrices and wound dressing products, whereas the microgels and nanogels are a preferred choice for heat or moisture management, deodorant fabrics, or reversible superhydrophilic/superhydrophobic fabrics. Thermosensitive hydrogel particles of submicron sizes could be incorporated to a textile material surface in a form of a very thin film, resulting in the increase of surface area per unit mass and in significant improvement of response time in comparison with bulk hydrogels.

A variety of end uses of thermosensitive smart textiles is the engine for high interest in the application of thermosensitive linear and cross-linked polymers on textile substrates. For instance, thermosensitive textiles could be used in the fabrication of diving suits in order to provide better thermal insulation in cold waters and great depths [8]. The important aspects of thermosensitive smart textile applications are advanced wound dressings with a layer of thermosensitive hydrogel [9] and thermosensitive textile patches with hydrogel finishing that are intended for transdermal drug delivery [10].

The most often studied thermosensitive hydrogel in textile use is poly(*N*-isopropylacrylamide) (PNIPAAm) hydrogel [1, 4, 5]. This chapter covers conventional as well as the novel strategies and synthesis pathways for PNIPAAm-based hydrogels. The incorporation of natural, pH-responsive biopolymer components for overcoming some disadvantageous properties of PNIPAAm and imparting pH sensitivity is described. The recent development of in situ liquid-phase plasma synthesis of PNIPAAm-based hydrogels with a great potential for the functional encapsulation of active biological ingredients and design of controlled drug release systems for transdermal applications is a outlined. The chapter also refers to the role of patterned plasma surface modification, graft polymerization, and coating techniques in the application of PNIPAAm-based formulations on textiles. Finally, up-to-date findings in the field of thermosensitive textiles functionalized with various forms of PNIPAAm-based hydrogels are summarized.

Poly(*N*-isopropylacrylamide): PNIPAAm

Basic Facts and Properties

PNIPAAm is a synthetic polymer sensitive to temperature changes in the range of physiologically interesting values. Temperature above which PNIPAAm becomes insoluble in an aqueous environment (around 32 °C) is known as lower critical solution temperature (LCST). When PNIPAAm is cross-linked or combined in linear form (whether as a homo- or copolymer) with another cross-linked polymer, it gives thermosensitive hydrogels of thermo-shrinking type. By adjusting the PNIPAAm copolymer composition and its quantity, the volume-phase transition temperature (VPTT) can be well controlled. The addition of hydrophilic monomer

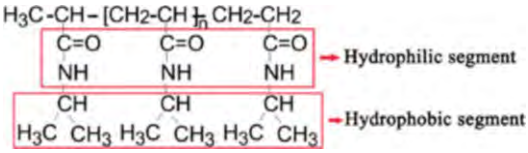

Fig. 5 Molecular structure of PNIPAAm (Reprinted from Xue and Hamley [11] with permission from Elsevier)

typically increases the VPTT, whereas the incorporation of more hydrophobic units has the opposite effect.

The temperature-induced phase transition of the hydrogels of thermo-shrinking type (PNIPAAm-based hydrogels) is analogous to the phase separation of polymer solutions with LCST or precipitation threshold. The specific dimensional change of PNIPAAm chains (swelling/deswelling cycle) that corresponds to coil-to-globule transition derives from the breakdown of the delicate hydrophilic/hydrophobic balance of the system, due to the presence of both hydrophilic amide groups and hydrophobic isopropyl groups in its side chains (Fig. 5).

Apart from the unique properties of PNIPAAm hydrogels related to their VPTT that is close to human body temperature and good swelling abilities, there are numerous possibilities of imparting an additional functionality to PNIPAAm hydrogels. The drawbacks of pure PNIPAAm hydrogels like slow response rate or weak mechanical properties could be overcome by combining PNIPAAm with a range of components, which is often achieved by formation of interpenetrating polymer networks (IPNs) [12].

Enormous versatility of linear/cross-linked PNIPAAm classifies it as the most widely used thermosensitive polymer/hydrogel testifying the importance of temperature as one of the most easily controlled environmental parameters. The convenient LCST, biocompatibility, and relative nontoxicity up to a certain concentration [13] give advantage to PNIPAAm in comparison with other thermosensitive polymers, particularly in the field of controlled drug delivery systems, biomedical engineering, and pharmaceutical formulations. PNIPAAm-based materials could be found in a myriad of fields ranging from microelectronics, medicine, pharmacy, microbiology, agriculture, bioengineering, and development of thermosensitive textiles [5, 6, 14].

Strategies for Synthesis of PNIPAAm-Based Hydrogels

PNIPAAm Bulk, Micro- and Nanogels

PNIPAAm bulk (macro) hydrogel, microgel, and nanogels can be successfully synthesized by conventional water-bath polymerization methods (emulsion polymerization, inverse microemulsion polymerization, dispersion polymerization, surfactant-free dispersion polymerization, inverse suspension polymerization, electrostatic extrusion, etc.). Afterwards, they can be chemically grafted on textile or other polymeric surfaces. Taking into consideration the requirement of maintaining the advantageous conventional properties of initial textile material, it can be suggested that the micro-sized hydrogels are preferred for textile finishing. It is

known that bulk hydrogels are monolithic polymer networks that typically range in size from millimeters or greater. Microgels, also referred to as hydrogel microbeads or hydrogel microspheres, are regarded as hydrogel particles of nanometer and even of micrometer sizes (from 100 nm to 1 μm). Since the universally accepted definition of microgels is still not well established [7], some authors even defined nanogels as the nano-sized particles (below 100 nm approximately) that possess similar internal network structure as microgels [15]. Microgels and nanogels have surface to volume ratios that are several orders of magnitude larger than those existing in bulk hydrogels, and they also exhibit much shorter response times in comparison with bulk hydrogel forms. Due to their submicron sizes, the incorporation of microgels and nanogels into textile material surface is achievable as a very thin film. An important attribute of microgel and/or nanogel thin films is their fast kinetics of swelling and shrinking compared with bulk hydrogels. According to the model of Tanaka and Fillmore [16], which shows that the characteristic time of the swelling transition is directly proportional to the square of the linear size of the hydrogel, the response times are less than 1 s for hydrogel films that are thinner than 10 μm.

The emulsion polymerization is a versatile technique that yields narrow particle size distributions. Conventional emulsion polymerization enables preparation of very small microgels (particle diameters even less than 100 nm), but its shortcoming lies in difficult removal of the residual surfactant. As opposed to this technique, surfactant-free dispersion polymerization (SFDP) does not suffer from residual surfactant contamination but it yields larger microgels, of 100–1.000 nm in diameter. The continuous phase must have a high dielectric constant (e.g., water) and ionic initiators are employed. Generally, the polymerization is conducted at 50–60 °C in order to generate free radicals by the decomposition of the initiator. Also, when thermosensitive polymer chains such as PNIPAAm chains are present in the system, elevated temperature is required to ensure that growing chains phase separate to form colloidal particles. The key feature of SFDP is that the particle nucleation period is very short (of the order of minutes), which ensures a narrow particle size distribution.

The preparation of colloidally stable PNIPAAm microgels cross-linked by *N, N′*-methylenebisacrylamide (MBAAm) was firstly reported by Pelton and Chibante [17] who applied an emulsifier-free emulsion polymerization process. The resultant microgels were thermosensitive, with VPTT of 31 °C and diameter in swollen state in the range of 200–700 nm. The microgels of PNIPAAm cross-linked with MBAAm, of hydrodynamic diameter less than 2.5 μm at 25 °C, were also obtained by suspension polymerization in or without the presence of ABA block (A, poly (hydroxyl stearic acid); B, poly(ethylene oxide), PEO copolymer as a stabilizer) [18]. Larger PNIPAAm microgels (0.25–2.8 mm) of the same composition could be synthesized by inversion suspension polymerization in a suitable organic medium since water cannot be used as the dispersion medium due to the significant solubility of NIPAAm in water (22.5 % w/w) [19].

The thermosensitive microgels with regular spherical shape of 20 μm in diameter were also synthesized by free-radical inverse suspension polymerization.

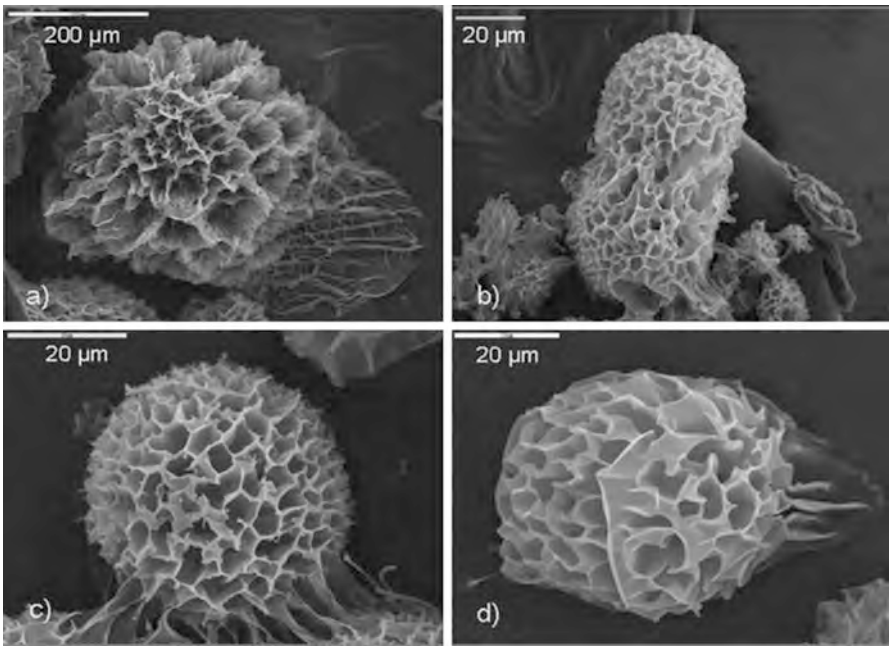

Fig. 6 SEM micrographs of PNIPAAm microgels with various amounts of emulsifier, volume ratio of oil to aqueous phase, and cross-linking degree (Adopted from Petrusic et al. [20] with permission from Springer Science + Business Media)

The polymerization reactions were conducted in the presence of an initiator, ammonium persulfate (APS), and a catalyst *N*,*N*,*N*′,*N*′-tetramethylethylenediamine (TEMED) at 25 °C, whereas the oil-to-aqueous phase volume ratio, the concentration of emulsifier, and the molar ratio of NIPAAm monomer to cross-linker (MBAAm) are changed to optimize optical, thermal, swelling, and morphological properties of prepared PNIPAAm microgels (Fig. 6).

A simple and effective approach for preparation of thermosensitive microgels and nanogels involves PNIPAAm–polysaccharide (graft) copolymers (Fig. 7a), which are soluble in cold water. These copolymers self-assemble into microgels and nanogels as a result of the temperature-triggered collapse of the PNIPAAm chains. By proper polymerization procedure, the specific stimuli-sensitive PNIPAAm-based microgels in the form of hybrid colloidal core–shell particles could be fabricated (Fig. 7b). The properties of the shell can be tuned by physicochemical means. Thus, the tendency of particles to aggregate and their affinity for liquid interfaces could be reversibly manipulated and find a great potential in biomedical and other applications.

Systems of PNIPAAm–polysaccharide or PNIPAAm-biopolymer (graft) copolymers are currently of great interest due to the a need for better biocompatibility and biodegradability of hydrogels and achieving their dual stimuli-sensitive behavior. Dual stimuli-sensitive hydrogels were successfully prepared by combining or

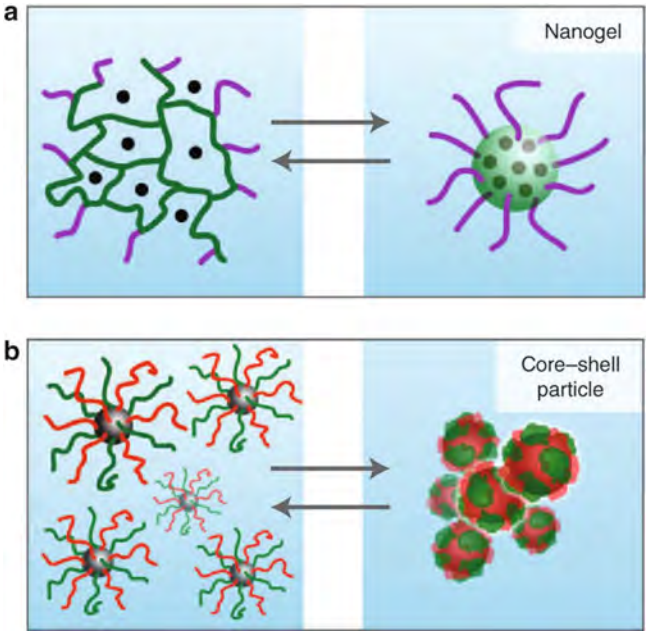

Fig. 7 Stimuli-responsive micro- and nanogels (**a**) and core–shell particles at interfaces (**b**) (Adopted from Cohen Stuart et al. [4] by permission from Macmillan Publishers Ltd)

copolymerizing a thermosensitive PNIPAAm with a chitosan, a natural pH-responsive polymer. Hydrogels responsive to temperature and pH have been the most widely studied stimuli-sensitive systems since these two parameters have a physiological significance. Chitosan is a typical pH-sensitive polymer ($pK_a = 6.3$) that responds to the changes in the pH of the surrounding medium by protonation/deprotonation that imparts charges on its amino groups and subsequently induces swelling/deswelling of the hydrogel. Also, chitosan is characterized by biodegradability, antibacterial activity, and biocompatibility. Due to these properties, chitosan currently attracts a great deal of interest for biomedical applications. Dually sensitive chitosan-g-NIPAAm copolymer was prepared by direct graft polymerization of NIPAAm onto chitosan using ceric ammonium nitrate (CAN) as an initiator (grafting agent) under the nitrogen atmosphere [21] by the surfactant-free dispersion copolymerization method. The grafting efficiency is dependent on NIPAAm concentration and exhibits the disadvantage of excessive PNIPAAm homopolymer formation. The specific homogeneous morphology of PNIPAAm-*co*-chitosan is obtained using an anionic APS initiator, whereas the core–shell morphology is demonstrated using a cationic azobis(2-methylpropionamidine) dihydrochloride (AIBA) initiator indicating the significant differences in polymerization mechanism regardless of the use of the same cross-linking agent (MBAAm) [22]. Chitosan acts as a surfactant preventing the coagulation of the PNIPAAm particles, lowering their diameter and enhancing the copolymerization efficiency.

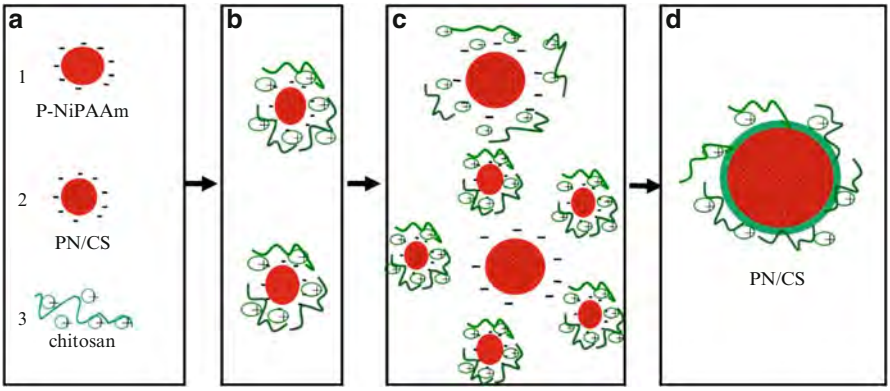

Fig. 8 Synthesis of PNIPAAm/chitosan microgel (SFDP mechanism) (Reprinted from Jocic et al. [7] by permission from InTech and originally published under CC BY 3.0 licence)

Interestingly, the swelling ratio of PNIPAAm-*co*-chitosan core–shell particles shows no dependence on temperature in contrast to the PNIPAAm-*co*-chitosan particles obtained using APS as the initiator. The copolymer particles synthesized using AIBA initiator have a core–shell morphology consisting of PNIPAAm as a core and chitosan as a shell. As a result, PNIPAAm core is not able to completely swell due to the chitosan poor sensitivity to temperature changes that affects the overall thermosensitive behavior of PNIPAAm-*co*-chitosan particles. However, the presence of chitosan leads to the significant pH sensitivity of the copolymer particles, no matter which type of initiator is used [23].

During dispersion copolymerization of NIPAAm and chitosan using APS as the initiator, the reaction occurs in three steps (Fig. 8). The first step refers to the polymerization of NIPAAm, initiated by APS, which forms negatively charged particles (Fig. 8a-1). The second step is the graft copolymerization of NIPAAm and chitosan, initiated by APS that forms PNIPAAm/chitosan complex particles with a negative surface charge (Fig. 8a-2). The last step presents the ionization of chitosan that results in positively charged chitosan molecules (Fig. 8a-3). These molecules might surround the negatively charged PNIPAAm or PNIPAAm/chitosan particles and behave like a surfactant to protect the polymer particles and thus prevent the coagulation (Fig. 8b). If chitosan molecules are not in the vicinity of the particles formed, the particles could coagulate and form larger positively charged particles, until the chitosan molecules are close enough to act like surfactants and prevent the coagulation (Fig. 8c–d). It was proven that chitosan might increase the polymerization rate by serving as a surfactant. On the other hand, the degraded chitosan chains can inhibit free radicals and slow down the polymerization reaction.

Another interesting comb-type graft hydrogel, composed of chitosan and PNIPAAm, was prepared to manifest rapid temperature and pH sensitivity. Initially, semitelechelic PNIPAAm with carboxylic end group was synthesized by radical polymerization using 3-mercaptopropionic acid (MPA) as a chain-transfer agent and azobisisobutyronitrile (AIBN) as an initiator. Afterwards, semitelechelic

PNIPAAm was grafted on chitosan film having amino groups (surface graft) or dissolved together with chitosan in acetic acid to form bulk graft [24]. Similar approach for synthesis of thermosensitive nanoparticles based on PNIPAAm core and chitosan shell was applied by Jung et al. [25]. PNIPAAm core nanoparticles containing carboxylic groups on their surface were synthesized by emulsion copolymerization between NIPAAm and acrylic acid (AAc) as a copolymer (PNIPAAm-*co*-AAc core) using MBAAm as a cross-linker. The carboxylic groups were conjugated with the amino groups of low-molecular-weight chitosan achieving the significant temperature responsiveness and also better biocompatibility than the PNIPAAm core itself.

Novel chitosan microgels coated with PNIPAAm-*co*-MAAc (poly(*N*-isopropylacrylamide-*co*-methacrylic acid) were prepared by free-radical polymerization using AIBN as an initiator, whereas the cross-linked chitosan microgels were obtained by cross-linking process in the presence of glutaraldehyde at different pHs. The maximum interaction between chitosan and PNIPAAm-*co*-MAAc was obtained at pH 6.0. The cross-linked chitosan core acts as a regulator for a pH-dependent release of FITC–dextran (fluorescein isothiocyanate–dextran), whereas the shell or coating layer of PNIPAAm-*co*-MAAc suppresses the release when the temperature is above the VPTT. This suppression of the release is significant in acidic environment where the thermosensitivity of the coating layer is highest [26].

Surfaces with switchable wetting behavior are of considerable interest due to their potential application in "intelligent" breath-active and water-repelling textiles. The switching wetting behavior of amphiphilic surfaces (self-adaptation) implies the increased hydrophilicity of the surface in water (polar environment) and increased oleophobicity in apolar solvents. The opposite and less natural response to the external stimuli could be desirable for many practical applications (systems with inversely switchable wetting behavior) where the system is able to become hydrophobic in water and hydrophilic in apolar media (so-called contraphilic wetting, where the dry surface is hydrophilic and the wetted surface is hydrophobic). One of the key approaches in design of contraphilic switchable systems relies on the synthesis of hydrogel particles with core–shell structure, i.e., hydrogel core covered with hydrophobic but elastic shells. These core–shell hydrogel particles (nano- and microgels) must be able to swell reversibly in water despite of the presence of hydrophobic shells. Also, the shells must be always hydrophobic regardless of the swelling degree. To this end, PNIPAAm-*co*-AAm core microgels are synthesized using the precipitation polymerization (MBAAm was used as a cross-linker, acrylamide (AAm) as a comonomer, and 2-2′-azobis (2-methylpropionamidine) dihydrochloride as an initiator). Hydrophobic polyisoprene (PI) shell patterned with polystyrene (PS) latex was synthesized by surface-initiated free-radical polymerization. The proper mixing of core and shell hydrogel particles was achieved ionically as the core particles were positively charged and shell particles were negatively charged. The PNIPAAm-polyisoprene-based core–shell microgels are covalently attached to the hydrophilic PAAc (polyacrylic acid) brushes grafted onto a hydrophilic substrate. The carboxylic groups present on

the hydrophilic substrate and amino groups of the microgels are used as a means for covalent attachment of the microgels to PAAc brushes [27].

Similarly, PNIPAAm microgel particles with hydrophobic corona were prepared by in water-in-oil emulsion polymerization using polyethylene oxide–polyisoprene block copolymer as a corona-forming agent [28]. Hydrophilic and thermosensitive PNIPAAm is chosen as a material for the preparation of the microparticle walls, whereas the PI is selected as the hydrophobic corona shell. The hollow morphology of the microcapsules is provided by the precipitation polymerization mechanism where water/oil interface of the emulsion acts as soft template and seed that induces selective precipitation of PNIPAAm above its LCST. PNIPAAm microparticles, 1–3 μm in diameter, appear in different microstructures and morphologies, depending on their mechanical properties of their walls in different solvents (cyclohexane, isooctane, anhydrous THF, and THF/water mixtures).

Smart responsive poly(*N*-isopropylacrylamide-*co*-benzo-18-crown-6-acrylamide) (P(NIPAAm-*co*-BCAm)) microgels as a membrane for selective recognition of barium(II) or lead(II) heavy metal ions were successfully prepared with oil-in-water-in-oil double emulsions as templates for polymerization. The stable BCAm/Ba^{2+} or BCAm/Pb^{2+} complexes in the P(NIPAAm-*co*-BCAm) membrane cause a positive shift of the VPTT of the P(NIPAAm-*co*-BCAm) microgels to a higher temperature and the repulsion among the charged BCAm/Ba^{2+} or BCAm/Pb^{2+} complexes. The osmotic pressure within the P(NIPAAm-*co*-BCAm) membranes induces the swelling of microgels. In the presence of barium(II) or lead(II) ions, the prepared microgels with P(NIPAAm-*co*-BCAm) membranes exhibit isothermal and significant dimensional changes not only in outer and inner diameters but also in the membrane thickness. The microgels developed in this study are highly attractive for developing smart sensors and/or carriers for detection and/or elimination of heavy metal ions [29].

PNIPAAm-Based IPNS and Semi-IPNs

PNIPAAm homopolymer hydrogels are rarely used due to their simple structure, low deswelling rate owing to the formation of a dense and thick skin layer that prevents water molecules from migrating out of the gel when the deswelling occurs and/or poor mechanical properties. Hence, NIPAAm monomer is frequently copolymerized with versatile components to give systems with higher functionality and required properties or to form full- and semi-interpenetrating polymer networks (IPNs and semi-IPNs, respectively). An IPN is an assembly of two cross-linked polymers, at least one of which is synthesized and cross-linked in the presence of the other. If only one component of the assembly is cross-linked leaving the other in linear form, the system is termed as semi-IPN. Besides these two structures, there are also homo-IPNs (as a subgroup of full-IPNs, where the same polymer is used in both networks), latex IPNs (formed by emulsion polymerization), and thermoplastic IPNs (which are moldable and made of at least one block copolymer). IPN structures could give stiffer and tougher hydrogel matrices in comparison with the conventional hydrogels and of more widely controllable physical properties.

There are a number of reports referring to linear alginate (sodium alginate) in combination with cross-linked PNIPAAm having structures of semi-IPNs, as well as to IPN hydrogels containing cross-linked PNIPAAm and cross-linked alginate, calcium alginate (CA) [30]. The combination of CA with cross-linked PNIPAAm results in hydrogel with a more regular structure, adequate mechanical properties, and swelling/deswelling rate when compared to the structure of each of its components [31]. The phenomenon is explained by the formation of a porous structure within the hydrogels in the presence of ionized alginate during the polymerization process. The deswelling rate is regulated by the alginate content in the hydrogel network. The higher the alginates content in the semi-IPN hydrogels, the higher the sensitivity of the semi-IPN hydrogel. Dumitriu et al. prepared a novel covalently cross-linked PNIPAAm/alginate "mixed-IPN" hydrogels [32]. Although ionic cross-linking of alginate is the most widely spread approach in the formation of alginate hydrogel, covalent cross-linking could be also applied. In this system, alginate is covalently bonded to PNIPAAm chains through MBAAm that also have a role of cross-linker for PNIPAAm chains. The obtained hydrogels show rapid response to temperature changes and enhanced swelling capacity with increase in alginate content. Also, PNIPAAm/CA semi-IPN and IPN microgels can be efficiently functionalized with maleic acid, resulting in denser hydrogel matrices and efficient drug loading [20, 33].

Verestiuc et al. prepared semi-IPNs by free-radical polymerization of NIPAAm onto chitosan using tetra-ethyleneglycoldiacrylate (TEGDA) as a cross-linking agent [34]. The proportion of chitosan that could be entrapped in the matrix was found to increase with the increase in cross-linking density of the network. As the chitosan content and cross-linking density rises, the phase transition temperature of the chitosan IPN hydrogels becomes less well defined and shifts towards lower values. The incorporation of chitosan into the structure induces significant pH sensitivity in addition to the thermosensitivity deriving from PNIPAAm. Semi-IPN microgels were also prepared by inverse suspension polymerization of NIPAAm using MBAAm as a cross-linker in the presence of chitosan. APS and TEMED were used to initiate and accelerate the reaction of NIPAAm polymerization. The swelling degrees of pH- and thermosensitive microgels are slightly decreased in comparison with pure PNIPAAm microgels due to the presence of chitosan, but the VPTT remains unaffected [35]. PNIPAAm-based IPN hydrogel was synthesized by the chemical combination of MBAAm cross-linked PNIPAAm network with formaldehyde cross-linked chitosan network [36]. It was demonstrated that the properties of IPN hydrogels such as the phase transition behavior, the swelling dynamics in aqueous phase, the swelling behavior in ethanol/water mixtures, and even the microstructure are quite different from those of the semi-IPN hydrogels. The VPTT of the IPN hydrogel is at least 4–5 °C greater than that of the corresponding semi-IPN hydrogel, which derives the difference in their microstructures. It was found that the semi-IPN hydrogels swell faster than the corresponding IPN hydrogels and that the swelling ratio for the semi-IPN hydrogels is almost independent of the temperature. Similarly, the specific polymer blends, i.e., IPN hydrogels of chitosan-g-NIPAAm copolymer were prepared in the

presence of CAN as a cross-linker for PNIPAAm network with glutaraldehyde as a cross-linking agent for chitosan. These IPN hydrogels demonstrate significant swelling at pH 4 due to the ionic repulsion of the protonated amino groups in chitosan. They collapse at high pH because of the influence of unprotonated amine groups. At temperatures above the VPTT of PNIPAAm, the swelling capacities of IPN hydrogels dramatically decrease comparing to those at 25 °C [21].

Novel Strategies for PNIPAAm-Based Hydrogel Synthesis

Although the polymerization of NIPAAm can be carried out with conventional polymerization methods previously mentioned, the use of the irradiation methods has been extensively used. Zhao et al. developed the method for fast synthesis of PNIPAAm hydrogels by microwave irradiation [37]. Thus, the reaction time required for synthesis of PNIPAAm hydrogels can be considerably shortened from several hours to several minutes in comparison with conventional polymerization methods. In addition, the swelling ratio of hydrogels below VPTT and above VPTT is improved. Similarly, 2-acrylamide-2-methylpropoanesylphonic acid (AMPS) and NIPAAm are successfully copolymerized by microwave low-temperature plasma to obtain P(AMPS/NIPAAm) hydrogel of both temperature and pH sensitivity [38]. Don and Chen reported synthesis of graft copolymers based on a maleilated chitosan and NIPAAm by UV radiation technique (Fig. 9) [39].

Maleilated chitosan was prepared by reaction of chitosan with maleic anhydride. The swelling ratio of maleilated chitosan-g-PNIPAAm depends on both pH and temperature of the aqueous solution due to the coexistence of amino and carboxylic acid groups in the maleilated chitosan chain and grafted PNIPAAm component, respectively.

Hydrogels based on PNIPAAm-grafted chitosan, alginate, and cellulose were prepared by gamma irradiation [40]. The swelling abilities of chitosan-g-PNIPAAm hydrogels improve with the increase of the grafting percentage. This dependence indicates that the swelling behavior of the hydrogels depends on the amount of the grafted chains. At higher pH values of buffer solution, the prepared hydrogels exhibit lower swelling ratio due to pH sensitivity of chitosan.

Novel possibilities for creating hydrogel systems based on glow discharge plasma polymerization of volatile monomers in gas phase [41], solid phase plasma polymerization [42], and plasma polymerization in liquids [43] have been reported. Among them, plasma polymerization in liquids and in contact with liquids demonstrates great technological potential given that it can be performed without using chemical initiators or/and even without cross-linking agents. These approaches offer multiple advantages over the conventional polymerization methods. An additional advantage of plasma polymerization in liquids lies in the fact that reactants or monomers with a high vapor pressure can also be used since no volatile compounds are needed in contrast to plasma polymerization in gas phase. Moreover, the monomer solution can be handled in a more safety manner.

Discharges in liquids and in contact with liquids generate UV radiation, shock waves, free radicals, and very active molecules or atoms (OH, O, H_2O_2, etc.) that

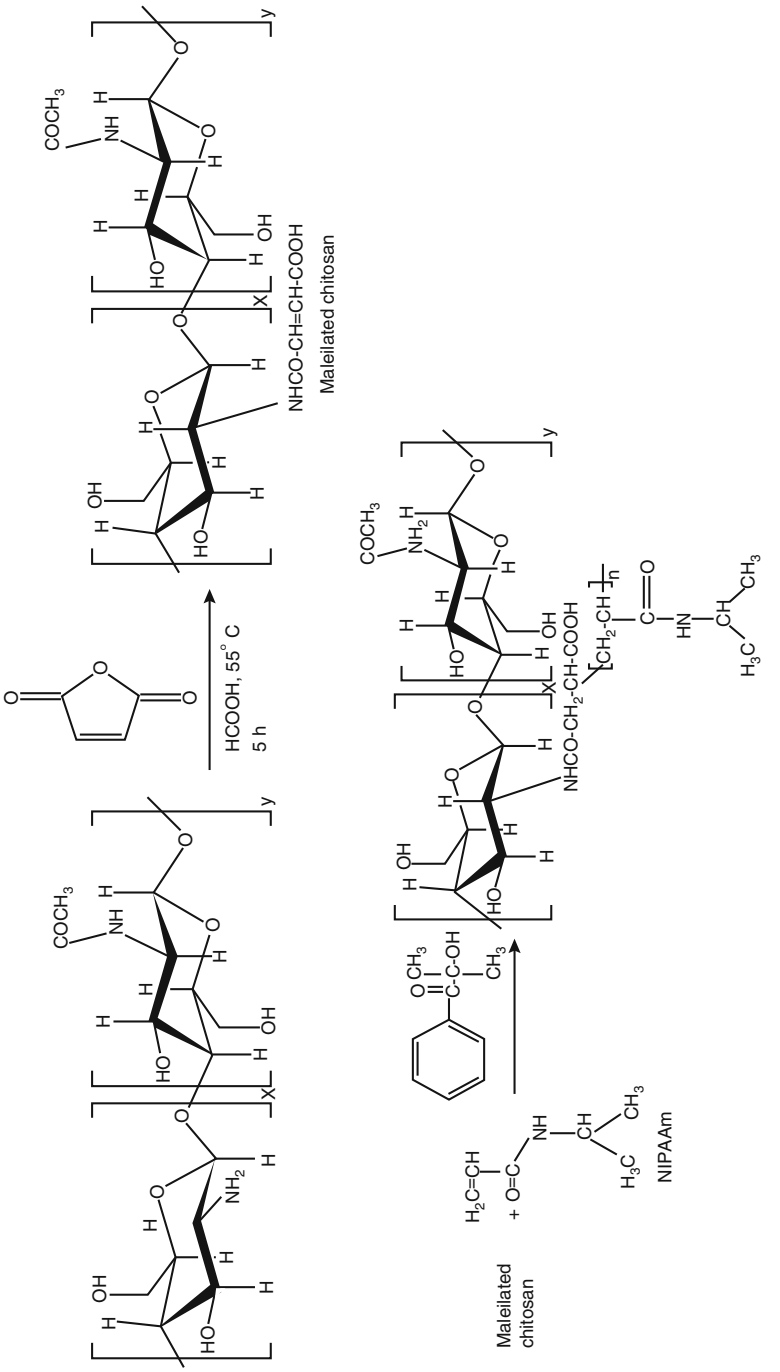

Fig. 9 Preparation of maleilated chitosan and maleated chitosan-g-PNIPAAm (Reprinted from Don and Chen [39] with permission from Elsevier)

can promote oxidation and degradation processes of pollutants and biological materials. Also, they are very effective in modifying the material surfaces or initiating the polymerization processes. Different experimental configurations are employed for the generation of nonthermal plasmas in liquid and/or in contact with liquids, e.g., direct liquid-phase discharges, discharges in the gas phase with liquid electrode(s), and discharges in bubbles in liquids [44]. Glow discharge electrolysis and liquid-phase capillary discharge have been used to obtain functionalized polymer surfaces with tailored chemical functionality such as carboxylic groups [45].

Molina et al. [46] employed a dielectric barrier discharge (DBD) between the two electrodes for generation of plasma in contact with the liquid surface as an innovative route for synthesis of a thermosensitive PNIPAAm. The VPTT of PNIPAAm obtained by liquid-phase plasma polymerization is quite similar to that obtained by conventional polymerization methods (around 32 °C). According to the simplified scheme of in situ plasma polymerization proposed, the surface layer of PNIPAAm films is predominantly cross-linked since the inner layers of films could be protected by the surface cross-linked layer itself as well as by low plasma penetration depth. The inner layers of PNIPAAm films are characterized by high content of PNIPAAm homopolymers and intact NIPAAm monomers. Nevertheless, the surface cross-linked layer also contains a certain quantity of PNIPAAm homopolymers and intact NIPAAm monomers, as demonstrated by ^{1}H NMR measurements (Fig. 10).

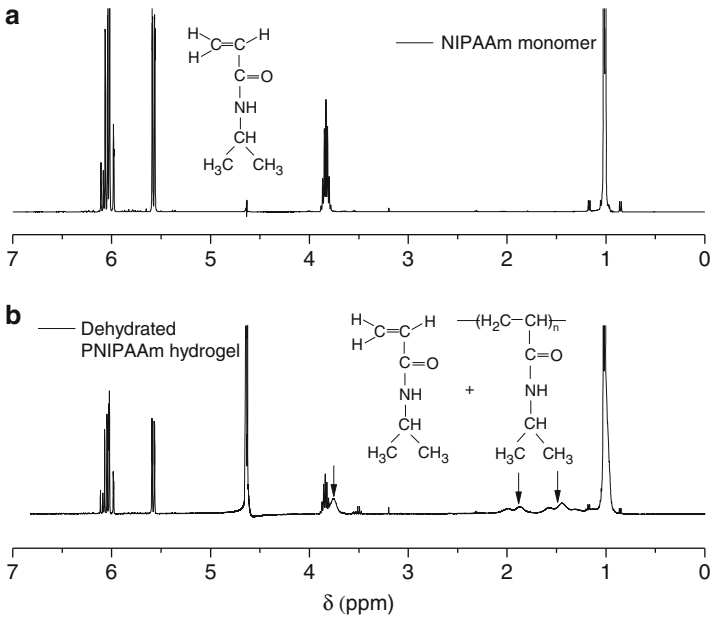

Fig. 10 ^{1}H NMR spectra of (**a**) NIPAAm monomer and (**b**) 20 % PNIPAAm film after dehydration above the VPPT (corresponding peaks of PNIPAAm homopolymer are *arrows* highlighted) (Reprinted from Molina et al. [46] with permission from John Wiley and Sons)

The results of the cross-linking efficiency, morphology, and thermosensitive properties of PNIPAAm obtained by in situ polymerization of aqueous solutions of NIPAAm initiated by atmospheric plasma offer novel perspectives for preparation of stimuli-sensitive textile coatings, with great potential for a variety of applications.

PNIPAAm-Functionalized Smart Textiles

Development of thermosensitive textiles is in a vast proportion related to linear or cross-linked PNIPAAm, mainly copolymerized with a range of various components [1, 5]. A rough classification of PNIPAAm forms applied in smart textiles could be made into three categories: PNIPAAm-based linear polymers, PNIPAAm-based bulk hydrogel films, and PNIPAAm-based microgels (Fig. 11).

Accordingly, the following three chapter sections summarize the achievements in development of smart thermosensitive textiles functionalized with linear polymers, bulk hydrogel films, and microgels based on PNIPAAm. The review will center on methods of fabrications, thermosensitive properties, and potential applications of PNIPAAm-functionalized textiles.

Systems PNIPAAm-Based Linear Polymers/Textiles

One of the simplest ways of imparting thermosensitivity to textiles could be achieved using solutions of thermosensitive polymers. Advantages and potentials of grafting, as one of the most popular methods used to modify chemical and physical properties of polymer surfaces, is well documented in review by Bhattacharaya et al. [47]. Among the various techniques of grafting, like those initiated by chemical treatment, radiation, and plasma, in the development of thermosensitive textiles, graft-radiation techniques take the leading place.

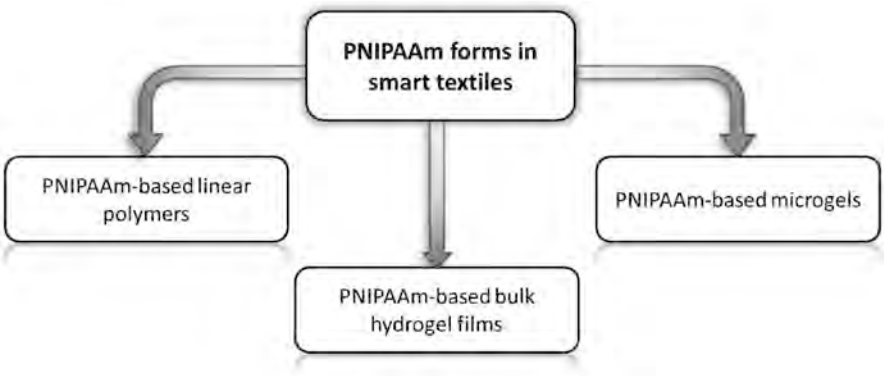

Fig. 11 General forms of PNIPAAm application in smart textiles

Kim et al. prepared thermosensitive polypropylene (PP) membranes grafted with linear PNIPAAm by plasma-induced polymerization [48]. Nonwoven PP membranes of various pore sizes are treated with argon radio-frequency (RF) plasma (10 W, 60 s at 10 Pa) and afterwards graft-polymerized with different NIPAAm monomer solutions at 60 °C. Plasma treatment generates different plasma constituents like electrons, ions, free radicals, metastables, and UV photons that contribute to the introduction of reactive groups and free radicals onto the surface of PP membranes and thus improve the interactions with NIPAAm monomer solutions. In addition, plasma could increase the surface roughness of cotton fibers that can enhance the incorporation of PNIPAAm onto the surface of PP membranes, facilitating the graft polymerization process. PP-g-PNIPAAm membranes demonstrated the temperature-dependent water permeability that was notably higher comparing to the original PP membranes. Adopting similar approach, Wang at al. [49] obtained thermosensitive polyethylene (PE) membranes of improved water permeability. Among a wide range of organic/water solvent systems used as a reaction media for grafting polymerization, water yields the highest polymerization rate.

Jianqin et al. grafted linear PNIPAAm on cotton cellulose fabric [50]. The pre-irradiation of the textile substrate was performed in air by ^{60}Co gamma rays. It was followed by the immersion of the treated fabric in an aqueous NIPAAm grafting solution. The main active particles initiating reaction were the trapped radicals located in the interphase between the crystal and amorphous regions of cotton cellulose. Measured LCST was 35.4 °C, close to that of pure PNIPAAm, which testifies thermosensitive behavior of the functionalized fabric.

The research group of Gupta et al. [51] applied a similar principle of preparation to obtain a thermosensitive textile material. They grafted poly(NIPAAm-*co*-acrylic acid) (P(NIPAAm-*co*-AAc)) on the woven polyester fabric in two steps. Initially, polyester backbone was submitted to the radiation activation (by ^{60}Co gamma source). Thus, formation of hydroperoxide groups along the polymer chains was induced. These groups have a role in the subsequent initiation of the polymerization of monomer mixture onto the textile substrate. The degree of grafting is strongly influenced by the radiation dose, additives, and monomer composition, whereas the LCST of the thermosensitive treated fabric is controlled by fraction of NIPAAm in the initial grafting mixture. The LCST of the fabric reaches 37.5 °C for the NIPAAm fraction of 0.35 within the grafted copolymer. The grafted polyester fabric is intended for use as a thermosensitive textile patch for transdermal drug delivery. It shows higher cumulative release of an antibiotic drug tetracycline hydrochloride at higher temperature as a result of polymer chains collapse that acts as the driving force for the drug expulsion. The functionalized polyester fabric could serve as an efficient system for thermoregulated drug delivery via the skin.

Parameters of the radiation-induced graft copolymerization of NIPAAm and AAc mixture on PP nonwoven fabric were investigated by Ikram et al. [52]. The authors reported the fabrication of smart thermosensitive PP nonwoven fabric intended for transdermal drug delivery systems where the drug release takes place

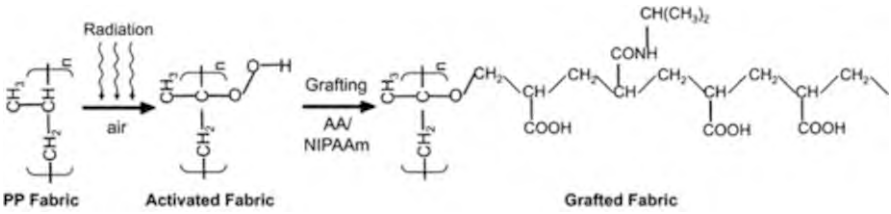

Fig. 12 Schematic representation of the PP grafting using NIPAAm/AAc mixture (Reprinted from Ikram et al. [52] with permission from Elsevier)

above 37 °C in contact with the human body. PP fabric was initially activated by pre-irradiation (by ^{60}Co gamma source) prior to immersion into the reaction mixture of NIPAAm and AAc solution. The grafting process occurred due to rapid and uniform formation of the active sites by high-energy irradiation of the substrate. The structure of the grafted copolymer on the PP surface is displayed in Fig. 12. The highest grafting degree was obtained at temperatures below 30 °C, as a result of polymer chain conformation that facilitated diffusion of monomers from the grafting solution towards the surface of the fabric.

More recent publication of the same group of authors refers to a detailed analysis of the surface of NIPAAm/AAc-grafted PP fabric elaborated in the previous work [53]. It is proved that PNIPAAm/PAAc exists on the textile substrate as the hydrophilic component since the contact angles of the grafted fabric decrease with an increase in degree of grafting. Variation of the NIPAAm/AAc composition in the feed monomer mixture induces distinct changes in the surface morphology of the functionalized fabric (Fig. 13).

An interesting study conducted by Erencia et al. shed a light on another aspect of PNIPAAm-based smart textile fabrication [54]. The approach used in this work does not imply treatment of the textile surface but the textile fibers (lyocell) that were grafted with PNIPAAm. Mechanism of grafting included treatment with ceric ammonium nitrate (CAN) and initiation of the reaction with NIPAAm monomer forming new radicals. The resulting lyocell/PNIPAAm copolymer is characterized by increased water absorption capacity at temperature below the LCST of PNIPAAm when the degree of grafting is above 60 %. At high temperature (45 °C), the dehydration and collapse of the PNIPAAm-grafted chains induces a decrease in water absorption capacity of the system.

The cited studies indicate an importance of optimizing the conditions of PNIPAAm grafting onto the textile surfaces. The concentration of the feeding monomer mixture, ratio of NIPAAm and comonomer(s), temperature of grafting, and methods of grafting initiation are parameters that regulate the thermosensitive behavior of the textiles functionalized with PNIPAAm-based polymers, whereas the adequate pre-activation of textile surface could enhance the PNIPAAm film deposition. Deeper understanding of these aspects of textile functionalization would open new perspectives in smart textile design.

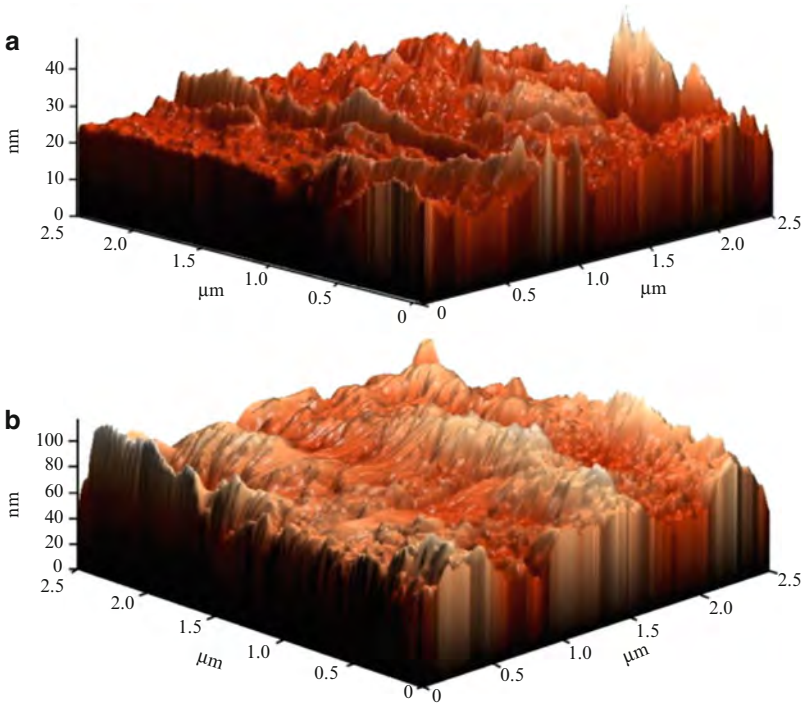

Fig. 13 AFM micrographs of PP fiber surfaces: untreated (**a**) and 9.5 % grafted with PNIPAAm/PAAc (**b**) (Reprinted from Kumari et al. [53] with permission from Elsevier)

Systems PNIPAAm-Based Bulk Hydrogel Films/Textiles

Apart from the development of thermosensitive textiles grafted with PNIPAAm-based linear polymers, a research interest has been focused on fabrication of textiles functionalized with three-dimensional PNIPAAm-based hydrogels. This research field implies complexity of fabrication due to the fact that cross-linking of polymer chains should be additionally achieved in comparison with the previously described systems. On the other hand, hydrogels show advantages particularly in immobilization of active agents (controlled drug release applications), diversity in structures, and multifunctionality in comparison with linear polymers.

In addition to radiation processes, a number of studies refer to the chemical grafting of PNIPAAm-based hydrogels on textiles. Hu et al. investigated free-radical graft copolymerization of NIPAAm and vinyl-capped polyurethane anionmer on nonwoven fabric (70 % cellulose fiber, 30 % polyester), initiated by ammonium persulfate [55]. The functionalized nonwoven fabric was characterized by pH and temperature sensitivity (VPTT around 33 °C). It is regarded as potentially applicable in fabrication of smart wound dressings and skin care cosmetic materials.

Another thermosensitive PNIPAAm textile was realized by Xie et al. who used ceric ions as effective chemical initiators for the graft polymerization of vinyl monomers on the cellulose fabric surface [56]. Hydroentangled nonwoven cotton was pretreated by immersion in CAN solution; NIPAAm/MBAAm mixture was added. It was established that a 15-min exposure to the 20 mM CAN solution is optimal for initiating the graft copolymerization/cross-linking of NIPAAm on the textile substrate. The grafting was realized either on a glass surface (method I) or in the presence of an additional monomer/cross-linker (NIPAAm/MBAAm) solution (method II). The impact of the preparation method as well as a degree of grafting of the hydrogel could be observed in SEM micrographs in Fig. 14. In the case of the method I, morphologies of the systems ranged from hydrogel-covered fibers to hydrogel-filled fibrous substrates (Fig. 14a–d). Nevertheless, the application of the method II resulted in cellulose substrates completely imbedded within the hydrogels formed (Fig. 14e). Overall swelling of the functionalized textiles decreases with increasing the cross-linker concentrations. Developed thermosensitive textiles exhibit notable change in swelling degree between 28 °C and 40 °C. They could find their application as smart wound dressing materials and controlled drug release devices.

Chen et al. performed photo-induced graft polymerization to prepare thermosensitive hydrogel-functionalized nonwoven fabric [57]. Pure PNIPAAm hydrogel was grafted on argon plasma-activated PP nonwoven fabric surface (and polyethylene terephthalate (PET) film), under 50 W for 10 min. It is assumed that peroxy groups formed during the fabric surface activation directly enhance the bonding between PNIPAAm hydrogel and PP surface (PET film) and increase the grafting density with no effect on thermosensitivity and the VPTT of hydrogel formed. Pretreated substrates were immersed in the grafting solution, containing monomer NIPAAm, cross-linker MBAAm, initiator APS, and catalyst TEMED, and photo-induced graft polymerization was carried out at room temperature using a high-pressure mercury lamp (1.000 W). Functionalized nonwoven PP (as well as PET film) exhibited thermosensitive behavior with VPTT around 32 °C and is hence qualified for the use as smart fabric with moisture or heat management.

PNIPAAm/polyurethane (PNIPAAm/PU) hydrogel-coated nonwoven cellulose fabric with and without chitosan was reported by Liu et al. [58]. The developed fabric could find application in medical and cosmetics fields. The leading idea of the researchers was to develop a smart textile functionalized with PNIPAAm hydrogel of improved mechanical strength at high temperatures. In addition, they imparted antibacterial property via surface modification of PNIPAAm/PU hydrogel-grafted nonwoven fabrics using biodegradable, biocompatible, and antimicrobial chitosan. Initial functionalization of the fabric was performed using solution of vinyl-capped polyurethane anionmer (VPUA) and NIPAAm, in addition to APS and TEMED. The surface modification of PNIPAAm/PU hydrogel-grafted nonwoven fabrics with chitosan was performed using 1-ethyl-3-(3-dimethylaminopropyl) carbodiimide (EDC) as a coupling agent. It is proved that chitosan surface modification adds the antimicrobial property to the PNIPAAm/PU hydrogel-grafted nonwoven fabric, which was confirmed using the bacteria

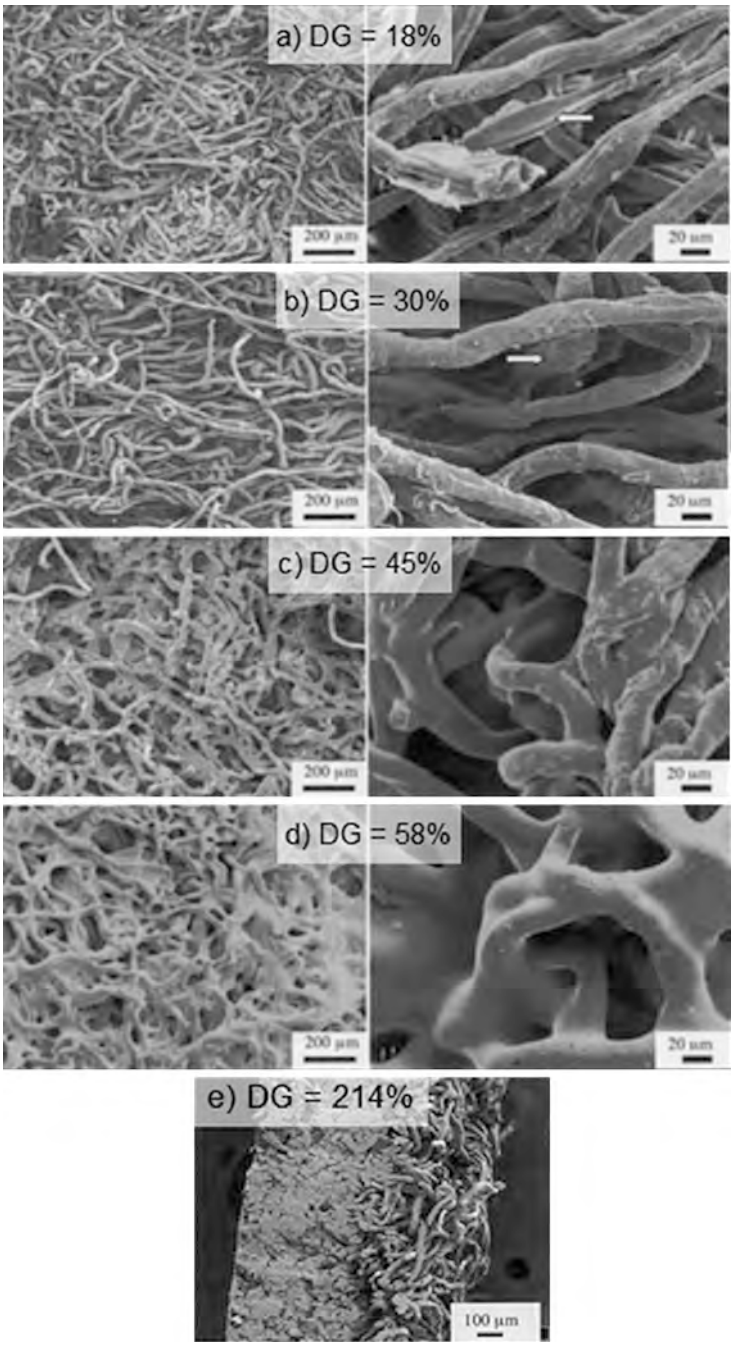

Fig. 14 SEM micrographs of cellulose-supported PNIPAAm hydrogels prepared by method I at different degrees of grafting (*DG*) (%) (**a**–**d**) and method II (cross section) (**e**) (Reprinted from Xie and Hsieh [56] with permission from John Wiley and Sons)

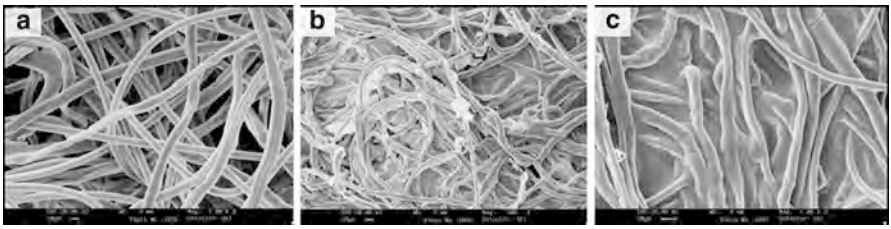

Fig. 15 SEM micrographs of original cellulose nonwoven fabric (**a**), hydrogel-grafted nonwoven PNIPAAm/PU prepared at 3.5 % monomer concentration (NIPAAm/PU5/1) with (**b**) and without chitosan (**c**) (Adopted from Liu et al. [58] with permission from John Wiley and Sons)

Staphylococcus aureus (Gram positive) and *Escherichia coli* (Gram negative). The authors assumed that functionalization of the surface of cellulose nonwoven fabric is guided not only by free-radical graft copolymerization of NIPAAm and PU with chitosan initiated by APS but also by the physical entrapment and anchoring. Differences in the surface morphology of untreated and functionalized fabrics are displayed in Fig. 15. Thermosensitivity of the functionalized fabrics deriving from PNIPAAm is not impeded neither by PU nor chitosan and the final VPTTs are around 33 °C.

Although a PNIPAAm-*co*-maleic anhydride-β-cyclodextrin hydrogel with pH and temperature sensitivity was synthesized by free-radical polymerization in an aqueous solution 10 years ago [5], the first compelling study on grafting of PNIPAAm hydrogel with and without unmodified β-cyclodextrin (β-CD) on nonwoven PP fabric was reported recently [59]. Developed thermosensitive textile is intended for hosting the guest molecules such as fragrances and antibacterial molecules owing to the specific cone-shaped molecule structure of β-CD with a hydrophobic interior cavity and a hydrophilic external surface. The grafting of previously argon plasma-activated fabric was done using an aqueous solution of NIPAAm and MBAAm (and β-CD in the second test), with APS as an initiator and TEMED as a catalyst. Both PNIPAAm-g-PP and PNIPAAm/β-CD-g-PP exhibited thermosensitivity with VPTTs of 31.9 °C and 33.2 °C, respectively. Differences in the morphology of nonwoven PP materials before and after grafting with PNIPAAm and PNIPAAm/β-CD can be observed in Fig. 16. Although the addition of β-CD does not have a considerable impact on thermosensitive properties of treated fabric, it affects the roughness of hydrogel layers on PNIPAAm/β-CD-g-PP sample in comparison with the one without β-CD. It is proven that PNIPAAm/β-CD-g-PP samples have the ability to form an inclusion complex 8-anilino-1-naphthalenesulfonic acid ammonium salt (ANS) as a guest molecule. Moreover, the functionalization of PP fabric resulted in improved wicking ability at lower temperatures and the hydrophilic properties.

Similarly, PNIPAAm/β-CD-g-wool smart textiles were developed by grafting of PNIPAAm and/or β-CD hydrogels on wool surface applying UV-induced graft polymerization. The wool fabric was previously activated by O_2 RF plasma that results in better hydrophilicity of the substrate with novel active sites for posterior

Fig. 16 SEM micrographs of unmodified nonwoven PP fabrics (**a**), PNIPAAm-g-PP (grafting yield = 15.7 %) (**b**), and PNIPAAm/β-CD-g-PP (grafting yield = 6.92 %) (**c**) (Reprinted from Amiri et al. [59] with permission from SAGE Publications)

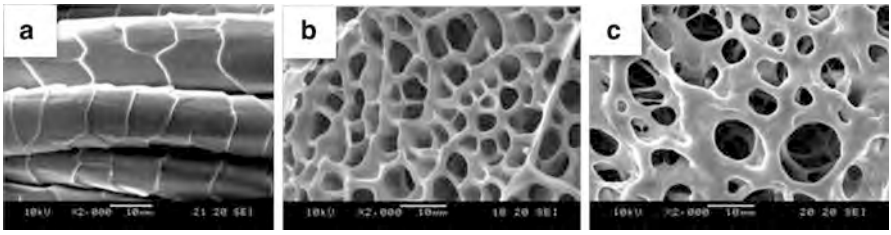

Fig. 17 The SEM micrographs of untreated wool fabric (**a**), PNIPAAm-g-wool (**b**), and PNIPAAm/β-CD-g-wool (**c**) [60]

hydrogel grafting by UV light [60]. SEM micrographs clearly demonstrate differences in the morphology of wool material before and after grafting with PNIPAAm and PNIPAAm/β-CD hydrogels (Fig. 17). The presence of β-CD in the reaction mixtures has changed the contact angle of the system PNIPAAm/β-CD-g-wool in comparison with the PNIPAAm-g-wool. The addition of 1 owf % (percentage on weight of fabric) of β-CD into the PNIPAAm hydrogel results in the pore size increase from 8 to 10 μm that affects the inclusion/release of possible guest molecules.

In certain studies referring to the grafting of PNIPAAm to textile substrates, investigation of the resulting thermosensitive properties was not a dominant subject, although it has an important role in the final application of functionalized textiles. For instance, Lin et al. [61] reported novel method of preparation of easily stripped-off wound dressing material composed of nonwoven PE fabric grafted with NIPAAm and gelatin. The NIPAAm is grafted onto plasma-activated PE nonwoven fabric by gamma irradiation, and finally a layer of a bovine gelation containing glycosaminoglycans is grafted by UV light to form a tri-layer wound dressing assembly. Chen et al. [62] grafted PNIPAAm onto the PP nonwoven substrate by UV light-induced graft polymerization as an easy stripped-off interlayer of wound dressing composite material. To improve the grafting yield, the PP nonwoven substrate was previously treated by argon RF plasma. Finally, chitosan was immobilized on the PNIPAm-g-PP material by cross-linking reaction with glutaraldehyde, as the outer layer of wound dressing assembly in intimate contact with the target skin defect.

It is worthwhile mentioning the work of Haining et al. even if it does not belong to the domain of smart textiles [63]. However, their PNIPAAm hydrogel-based products have a potential application in all-weather waterproof garments. These authors fabricated thermosensitive microporous membranes of PU/PNIPAAm semi-IPN structure. The VPTT of the synthesized membranes ranged from around 34 °C to 40 °C, depending on PNIPAAm and its cross-linker (MBAAm) concentration. These membranes can be regarded as hydrogel films of linear PU and cross-linked PNIPAAm. They exhibited lowered water vapor permeability at temperatures below the VPTT as a consequence of the PNIPAAm swelling, i.e., the reduction of micropore sizes and vice versa. Similarly, Crespy and Rossi [1] introduced applications of thermal-responsive hydrogels in textiles for the purpose of thermal and humidity management of the human body.

Systems PNIPAAm-Based Microgels/Textiles

PNIPAAm microgels, as the first thermosensitive microgels synthesized in 1986, have been a topic of research in a number of studies [64]. The importance, versatility in properties, vast potential, and applications of stimuli-sensitive microgels are documented in details in relatively recent review article [65]. Research interests up to date tend to center on the application of macro forms of PNIPAAm-based hydrogels rather than PNIPAAm-based microgels on textiles. Taking into consideration the fact that pioneering studies in the development of microgel-functionalized smart textiles date just several years ago, a systematic review on this topic still cannot be found in the literature.

Microgel-functionalized cotton fabric that responds to pH and temperature changes was reported by Kulkarni et al. [66]. Microgels based on PNIPAAm and chitosan (PNCS microgels) were prepared by precipitation polymerization. The microgels of around 200 nm in diameter were covalently bonded to the woven plain cotton fabric using 1,2,3,4-butanetetracarboxylicacid (BTCA) as a cross-linking agent, by pad-dry-cure method. The modified fabric shows strong change in the swelling degree at around 30 °C due to the volume-phase transition phenomenon of PNIPAAm-based hydrogels that are swollen at lower temperature and collapsed at elevated temperatures (Fig. 18). A significant contribution of this study is good durability of the microgel-based coating on the cotton fabric. Around 80 % of the surface-modifying system remains incorporated to the fabric cotton even after five washing cycles, indicating a strong chemical bonding between the microgel and textile substrate.

The primary aim of this innovative strategy for developing PNCS microgel-functionalized textiles was the improvement of the thermal comfort of a wearer, which is directly linked to water vapor and liquid management properties [67, 68]. The incorporation of PNCS microgels changes the visual aspect of the cotton fiber surface, as demonstrated by SEM micrographs in Fig. 19.

Due to the thermosensitivity of PNIPAAm and pH sensitivity of chitosan, the functionalized fabric changes its water vapor permeability and water content in

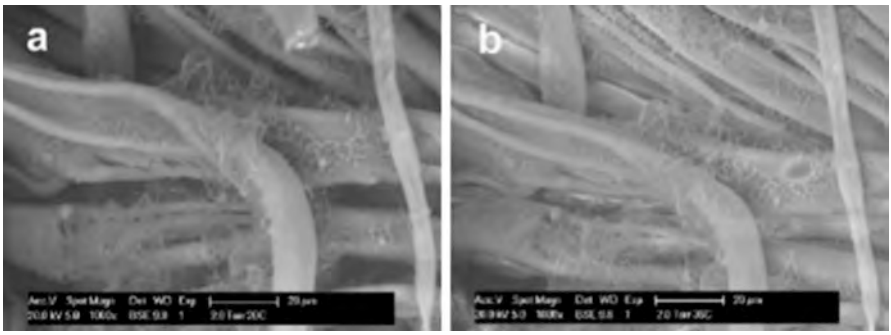

Fig. 18 ESEM micrographs of cotton with incorporated PNCS microgels at 20 °C (**a**) and 36 °C (**b**) (Reprinted from Kulkarni et al. [66] with permission from Elsevier)

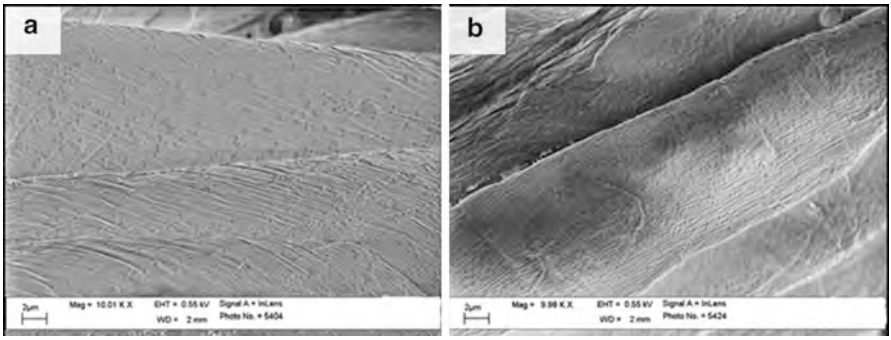

Fig. 19 SEM micrographs of cotton with incorporated 1 % owf (**a**) and 3 % owf (**b**) of PNCS microgel [67]

aqueous environments of different temperature and pH. At temperatures above the VPTT of PNCS microgels, the treated fabric exhibits higher water vapor permeability as a result of microgel deswelling [67]. It is shown that water uptake as well as water retention capacity of the functionalized fabric can be modified depending on the temperature and pH of the environment [68]. The presence of the microgels at the fiber surfaces impedes the water penetration as a consequence of microgel water absorption ability, whereas the drying capability is improved, at least in the initial stage of drying.

A progress in the synthesis of PNIPAAm-based microgels of an adequate VPTT, mechanical strength, and response rate or dimensions directly determines the advancement in the field of thermosensitive textiles. Further studies in the area of thermosensitive microgel-functionalized textiles might also include the upgrading of PNIPAAm-based microgel incorporation on textile substrates of different structure and chemical compositions. For instance, an interesting approach to achieve antimicrobial composite materials incorporating zinc oxide nanoparticles into biocompatible PNIPAAm hydrogel layer is recently reported [69].

Summary

The literature suggests that among a variety of novel multifunctional polymeric materials, thermosensitive hydrogels based on PNIPAAm are worthy candidates for the development of novel types of smart textiles. Different approaches in preparation of macro-, micro-, and nanoparticles and their assemblies and thin films of PNIPAAm thermosensitive polymeric materials are described in this chapter. The novel strategies and synthesis pathways for PNIPAAm-based hydrogels that are of potential for designing the novel thermosensitive textiles are also underlined. The recent development of in situ liquid-phase plasma synthesis of PNIPAAm-based hydrogels with a great potential for the functional encapsulation of active biological ingredients and design of controlled drug release systems for transdermal applications is reported. The use of macro forms of PNIPAAm hydrogels in smart textiles usually implies simultaneous processes of hydrogel formation and application on the textile material, which is favorable from the industrial point of view. Application of micro-scaled PNIPAAm-based hydrogels to textiles is more time and energy consuming since it requires initially their synthesis and the subsequent textile finishing. Nevertheless, benefits of micro forms of thermosensitive hydrogels over macro forms lie in their faster response to temperature changes and a weaker impact on the ultimate textile properties. Regrettably, there has been relatively little research on fabrication of textiles functionalized with PNIPAAm-based microgels that could satisfy high standards, particularly in a medical field. Further studies on the applicability of various physical forms of PNIPAAm hydrogels in the domain of smart textiles will permit exploitation of the full potential of the most widely used thermosensitive hydrogels. Thus, development and growth of the PNIPAAm-functionalized smart textiles market could be anticipated in the upcoming years.

References

1. Crespy D, Rossi RM (2007) Temperature-responsive polymers with LCST in the physiological range and their applications in textiles. Polym Int 56:1461–1468
2. CEN/TR 16298 (2011) Textiles and textile products – smart textiles – definitions, categorizations, applications and standardization needs
3. Hu J, Meng H, Li G, Ibekwe SI (2012) A review of stimuli-responsive polymers for smart textile applications. Smart Mater Struct 21(8):053001, 23 pp
4. Cohen Stuart AM, Huck TSW, Genzer J, Müller M, Ober C, Stamm M, Sukhorukov BG, Szleifer I, Tsukruk VV, Urban M, Winnik F, Zauscher S, Luzinov I, Minko S (2010) Emerging applications of stimuli-responsive polymer materials. Nat Mater 9:101–113
5. Liu B, Hu J (2005) Application of temperature-sensitive hydrogels to textiles: a review of Chinese and Japanese investigations. Fibres Text East Eur 13:45–49
6. Yu B, Zheng Z, Li Y, Zhou F (2009) Surface grafted polymer brushes: potential applications in textile engineering. J Fiber Bioeng Inf 1:249–259
7. Jocic D, Tourrette A, Krizman Lavric P (2010) Biopolymer-based stimuli-responsive polymeric systems for functional finishing of textiles. In: Elnashar M (ed) Biopolymers. ISBN: 978-953- 307-109-1, InTech. Available from http://www.intechopen.com/books/biopolymers/biopolymer-based-stimuli-responsive-polymeric-systems-for-functional-finishing-of-textiles

8. Serra M (2002) Adaptable skin: hydrogel gives wetsuit protection. Smart Mater Bull Volume 2002, Issue 8:7–8
9. Petrulyte S (2008) Advanced textile materials and biopolymers in wound management. Dan Med Bull 55:72–77
10. Lee TW, Kim JC, Hwang SJ (2003) Hydrogel patches containing triclosan for acne treatment. Eur J Pharm Biopharm 56:407–412
11. Xue W, Hamley IW (2002) Thermoreversible swelling behaviour of hydrogels based on *N*-isopropylacrylamide with a hydrophobic comonomer. Polymer 43:3069–3077
12. Zhang XZ, Wu DQ, Chu CC (2004) Synthesis, characterization and controlled drug release of thermo-sensitive IPN-PNIPAAm hydrogels. Biomaterials 25:3793–3805
13. Malonne H, Eeckman F, Fontaine D, Otto A, De Vos L, Moës A, Fontaine J, Amighi K (2005) Preparation of poly(*N*-isopropylacrylamide) copolymers and preliminary assessment of their acute and subacute toxicity in mice. Eur J Pharm Biopharm 61:188–194
14. Roy D, Cambre JN, Sumerlin BS (2011) Biological- and field-responsive polymers: expanding potential in smart materials. In: Urban MW (ed) Handbook of stimuli-responsive materials. Wiley-VCH, Weinheim, pp 27–57
15. Oh JK, Drumright R, Siegwart DJ, Matyjaszewski K (2008) The development of microgels/nanogels for drug delivery applications. Prog Polym Sci 33:448–477
16. Tanaka T, Fillmore DJ (1979) Kinetics of swelling of gels. J Chem Phys 70:1214–1218
17. Pelton RH, Chibante P (1986) Preparation of aqueous latices with *N*-isopropylacrylamide. Colloids Surf 20:247–256
18. Dowding PJ, Vincent B, Williams E (2000) Preparation and swelling properties of poly (NIPAM) "minigel" particles prepared by inverse suspension polymerization. J Colloid Interface Sci 221:268–272
19. Hirose Y, Amiya T, Hirokawa Y, Tanaka T (1987) Phase transition of submicron gel beads. Macromolecules 20:1342–1344
20. Petrusic S, Jovancic P, Lewandowski M, Giraud S, Bugarski B, Djonlagic J, Koncar V (2012) Synthesis, characterization and drug release properties of thermo-sensitive poly(*N*-isopropylacrylamide) microgels. J Polym Res 19:9979. doi:10.1007/s10965-012-9979-1
21. Kim SY, Cho SM, Lee YM, Kim SJ (2000) Thermo- and pH-responsive behavior of graft copolymer and blend based on chitosan and *N*-isopropylacrylamide. J Appl Polym Sci 78:1381–1391
22. Lee C, Wen C, Chiu W (2003) Synthesis of poly(chitosan-*N*-isopropylacrylamide) complex particles with the method of soapless dispersion polymerization. J Polym Sci A Polym Chem 41:2053–2063
23. Lee C, Wen C, Lin C, Chiu W (2004) Morphology and temperature responsiveness– swelling relationship of poly(*N*-isopropylamide–chitosan) copolymers and their application to drug release. J Polym Sci A Polym Chem 42:3029–3037
24. Lee SB, Ha DI, Cho SK, Kim SJ, Lee YM (2004) Temperature/pH-sensitive comb-type graft hydrogels composed of chitosan and poly(*N*-isopropylacrylamide. J Appl Polym Sci 92:2612–2620
25. Jung H, Jang MK, Nan JW, Kim YB (2009) Synthesis and characterization of thermo-sensitive nanoparticles based on PNIPAAm core and chitosan shell structure. Macromol Res 17:265–270
26. Kang MK, Kim JC (2010) FITC-dextran release from chitosan microgel coated with poly(*N*-isopropylacrylamide-*co*-methacrylic acid. Polym Test 29:784–792
27. Horecha M, Senkovsky V, Schneider K, Kiriy A, Stamm M (2011) Swelling behavior of PNIPAAm-polyisoprene core-shell micro-gels at surface. Colloid Polym Sci 289:603–612
28. Horecha M, Senkovsky V, Stamm M, Kiriy A (2009) One-pot synthesis of thermoresponsive PNIPAM hydrogel microcapsules designed to function in apolar media. Macromolecules 42:5811–5817
29. Pi SW, Ju XJ, Wu HG, Xie R, Chu LY (2010) Smart responsive microcapsules capable of recognizing heavy metal ions. J Colloid Interface Sci 349:512–518

30. Prabaharan M, Mano JF (2006) Stimuli-responsive hydrogels based on polysaccharides incorporated with thermo-responsive polymers as novel biomaterials. Macromol Biosci 6:991–1008
31. Petrusic S, Lewandowski M, Giraud S, Jovancic P, Bugarski B, Ostojic S, Koncar V (2012) Development and characterization of thermo-sensitive hydrogel based on poly(*N*-isopropylacrylamide) and calcium alginate. J Appl Polym Sci 124:890–903
32. Dumitriu RP, Mitchell GR, Vasile C (2011) Multi-responsive hydrogels based on *N*-isopropylacrylamide and sodium alginate. Polym Int 60:222–233
33. Petrusic S, Jovancic P, Lewandowski M, Giraud S, Grujic S, Ostojic S, Bugarski B, Koncar V (2013) Properties and drug release profile of poly(*N*-isopropylacrylamide) microgels functionalized with maleic anhydride and alginate. J Mater Sci 48:7935–7948
34. Verestiuc L, Ivanov C, Barbu E, Tsibouklis J (2004) Dual-stimuli-responsive hydrogels based on poly(*N*-isopropylacrylamide)/chitosan semi-interpenetrating networks. Int J Pharm 269:185–194
35. Chen X, Song H, Fang T, Bai J, Xiong J, Ying H (2010) Preparation, characterization and drug-release properties of pH/temperature-responsive poly(*N*-isopropylacrylamide)/chitosan semi-IPN hydrogel particles. J Appl Polym Sci 116:1342–1347
36. Wang M, Fang Y, Hu D (2001) Preparation and properties of chitosan-poly(*N*-isopropylacrylamide) full-IPN hydrogels. React Funct Polym 48:215–221
37. Zhao Z, Li Z, Xia Q, Xi H, Lin Y (2008) Fast synthesis of temperature-sensitive PNIPAAm hydrogels by microwave irradiation. Eur Polym J 44:1217–1224
38. Ma X, Cui G, Dong S (2007) Synthesis of a new intelligent hydrogel initiated by microwave low temperature plasma. J Appl Polym Sci 106:1368–1374
39. Don TM, Chen HR (2005) Synthesis and characterization of AB-crosslinked graft copolymers based on maleilated chitosan and *N*-isopropylacrylamide. Carbohydr Polym 61:334–347
40. Lee SB, Seo SM, Lim JM, Cho SK, Lee JM, Nho J (2004) Preparation of alginate/poly(*N*-isopropylacrylamide) hydrogels using gamma irradiation grafting. Macromol Res 12:269–275
41. Cheng X, Canavan HE, Stein MJ, Hull JR, Kweskin SJ, Wagner MS, Somorjai GA, Castner DG, Ratner BD (2005) Surface chemical and mechanical properties of plasma polymerized *N*-isopropylacrylamide. Langmuir 21:7833–7841
42. Unver A, Akovali G (2010) Plasma-induced, solid-state polymerization of *N*-isopropylacrylamide. J Appl Polym Sci 115:3311–3320
43. Gao J, Wang A, Li Y, Fu Y, Wu J, Wang Y, Wang Y (2008) Synthesis and characterization of superabsorbent composite by using glow discharge electrolysis plasma. React Funct Polym 68:1377–1383
44. Bruggeman P, Leys C (2009) Non-thermal plasmas in and in contact with liquids. J Phys D Appl Phys 42:053001
45. Joshi R, Schulze RD, Meyer-Plath A, Wagner MH, Friedrich JF (2009) Selective surface modification of polypropylene using underwater plasma technique or underwater capillary discharge. Plasma Process Polym 6:S218–S222
46. Molina R, Ligero C, Jovančić P, Bertran E (2013) In situ polymerization of aqueous solutions of NIPAAm initiated by atmospheric plasma treatment. Plasma Process Polym 10:506–516
47. Bhattacharya A, Misra BN (2004) Grafting: a versatile means to modify polymers techniques, factors and applications. Prog Polym Sci 29:767–814
48. Kim S-Y, Kanamori T, Shinbo T (2002) Preparation of thermal-responsive poly(propylene) membranes grafted with *N*-isopropylacrylamide by plasma-induced polymerization and their water permeation. J Appl Polym Sci 84:1168–1177
49. Wang X-L, Huang J, Chen X-Z, Yu X-H (2002) Graft polymerization of *N*-isopropylacrylamide into a microporous polyethylene membrane by the plasma method: technique and morphology. Desalination 146:337–343
50. Jianquin L, Maolin Z, Hongfei H (1999) Pre-irradiation grafting of temperature sensitive hydrogel on cotton cellulose fabric. Radiat Phys Chem 5:55–59
51. Gupta B, Mishra S, Saxena S (2008) Preparation of thermo-sensitive membranes by radiation grafting of acrylic acid/*N*-isopropyl acrylamide binary mixture on PET fabric. Radiat Phys Chem 77:553–560

52. Ikram S, Kumari M, Gupta B (2011) Thermo-sensitive membranes by radiation-induced graft polymerization of *N*-isopropyl acrylamide/acrylic acid on polypropylene nonwoven fabric. Radiat Phys Chem 80:50–56
53. Kumari M, Gupta B, Ikram S (2012) Characterization of *N*-isopropyl acrylamide/acrylic acid grafted polypropylene nonwoven fabric developed by radiation-induced graft polymerization. Radiat Phys Chem 81:1729–1735
54. Erencia M, Lopez-Mesas M, Carrillo-Navarretea F (2013) Thermo-sensitive fibres of lyocell/poly(*N*-isopropylacrylamide): multiparametric analysis for studying the graft copolymerization. Polym Int 62:1316–1323
55. Hu JL, Liu BH, Liu WG (2006) Temperature/pH dual sensitive *N*-isopropylacrylamide/polyurethane copolymer hydrogel-grafted fabrics. Text Res J 76:853–860
56. Xie JB, Hsieh YL (2003) Thermo-sensitive poly(*N*-isopropylacrylamide) hydrogels bonded on cellulose supports. J Appl Polym Sci 89:999–1006
57. Chen KS, Tsai JC, Chou CW, Yang MR, Yang JM (2002) Effects of additives on the photo-induced grafting polymerization of *N*-isopropylacrylamide gel onto PET film and PP nonwoven fabric surface. Mater Sci Eng C 20:203–208
58. Liu B, Hu J, Meng Q (2008) Nonwoven supported temperature-sensitive poly(*N*-isopropylacrylamide)/polyurethane copolymer hydrogel with antibacterial activity. J Biomed Mater Res B Appl Biomater 89:1–8
59. Amiri S, Zadhoush A, Mallakpour S, Lambertsen Larsen K, Duroux L (2012) Preparation and characterization of thermal-responsive non-woven poly (propylene) materials grafted with *N*-isopropylacrylamide/β-cyclodextrin. J Ind Text 43:116–131
60. Chen KS, Liao SC, Guo CY, Lin HY, Chen WY (2013) Post treatments of plasma polymers for creating functional surface on fibers. In: International symposium on advanced fiber/textile science and technology (ISAF), University of Fukui, Fukui, 18 Mar 2013, Book of Abstracts, pp 1–5
61. Lin FH, Chen TM, Chen KS, Wu TH, Chen CC (2000) An animal study of a novel tri-layer wound dressing material – non-woven fabric grafted with *N*-isopropylacrylamide and gelatin. Mater Chem Phys 64:189–195
62. Chen KS, Ku YA, Lee CH, Chen TM (2005) Immobilization of chitosan gel with crosslinking reagent on PNIPAm gel/PP nonwoven composite structure. Mater Sci Eng C 25:472–478
63. Haining L, Yuan X, Zaisheng C, Jie S (2012) Microporous membrane with temperature-sensitive breathability based on PU/PNIPAAm semi-IPN. J Appl Polym Sci 124:E2–E8
64. Cheng H, Zhang G (2012) Thermally sensitive microgels: from basic science to applications. In: Lyon LA, Serpe MJ (eds) Hydrogel micro and nanoparticles, 1st edn. Wiley-VCH, Weinheim, pp 1–32
65. Motornov M, Roiter Y, Tokarev I, Minko S (2010) Stimuli-responsive nanoparticles, nanogels and capsules for integrated multifunctional intelligent systems. Prog Polym Sci 35:174–211
66. Kulkarni A, Tourrette A, Warmoeskerken MMCG, Jocic D (2010) Microgel-based surface modifying system for stimuli-responsive functional finishing of cotton. Carbohydr Polym 82:1306–1314
67. Krizman Lavric P, Warmoeskerken MMCG, Jocic D (2012) Functionalization of cotton with poly-NiPAAm/chitosan microgel. Part I. Stimuli-responsive moisture management properties. Cellulose 19:257–271
68. Krizman Lavric P, Tomsic B, Warmoeskerken MMCG, Simoncic B, Jocic D (2012) Functionalization of cotton with poly-NiPAAm/chitosan microgel. Part II. Stimuli-responsive liquid management properties. Cellulose 19:273–287
69. Schwartz VB, Thétiot F, Ritz S, Pütz S, Choritz L, Lappas A, Förch R, Landfester K, Jonas U (2012) Antibacterial surface coatings from zinc oxide nanoparticles embedded in poly(*N*-isopropylacrylamide) hydrogel surface layers. Adv Funct Mater 22:2376–2386

Textile-Based Body Sensor Networks and Biomedical Computing for Healthcare Applications

36

Yong Kim and Honggang Wang

Contents

Introduction 986
Wearable Biomedical Sensors for Electronic Textiles 987
Biomedical Sensors and Measurement 988
Textile Biosensors and Electronic Textiles 990
Wearable Body Sensor Networks and Wireless Data Acquisition 992
Network Architecture 993
Energy Minimization Techniques 994
Energy-Harvesting Techniques 995
Security Design for Wearable Body Sensor Networks 996
Wireless Biomedical Computing and Applications 999
Wireless Biomedical Computing 1000
An Example for Infant Monitoring 1001
Future Trends 1002
Summary 1002
References 1003

Abstract

Integrating body sensors with electronic textiles will be a great solution to realize the ubiquitous noninvasive health monitoring in people's daily life. However, developing textile-based body sensor networks poses significant challenges for the sensor and senor network design such as miniaturization of

Y. Kim (✉)
Department of Bioengineering, University of Massachusetts Dartmouth, North Dartmouth, MA, USA
e-mail: ykim@umassd.edu

H. Wang
Department of Electrical and Computer Engineering, University of Massachusetts Dartmouth, North Dartmouth, MA, USA
e-mail: hwang1@umassd.edu

© Springer Science+Business Media Singapore 2015

X. Tao (ed.), *Handbook of Smart Textiles*,
DOI 10.1007/978-981-4451-45-1_17

sensors, integration of radio integrated circuits (ICs) and modules with body-worn antennas, energy consumption minimization, and so on. In the chapter, the challenges of designing electronic textile-based body sensor networks are discussed, and strategies and solutions to overcome the problems are proposed. To demonstrate the applicability of textile-based body sensor networks, the infant monitoring system will be illustrated.

Keywords
Electronic textiles (ETex) • Wearable body sensor networks (WBSN) • Biosensors • Energy harvesting

Introduction

Textile-based wearable body sensor networks (WBSN) for noninvasive healthcare monitoring will be the most desirable development required for preventive medicine, early diagnosis, and timely treatment of chronic diseases [1]. Healthcare and health delivery system evolve around progress in material science, wireless network technology, and biomedical technology. A close interdisciplinary collaboration between biomedical sensor technology, electronic textiles (ETex), and advanced wireless network technology is needed to provide personalized healthcare and noninvasive health monitoring by means of easy-to-use wearable interfaces between devices and humans. Moreover, all economically developed countries are undergoing social changes such as aging population, further integration of people with disabilities, and increase in chronic diseases. These changes will accelerate further development and market growth of WBSN.

The body sensor network (BSN) systems embedded in ETex can provide healthcare services such as medical monitoring of physiological signals and ambulatory communication. This WBSN application is growing rapidly. In the near future, noninvasive WBSN with multiple types of body sensors will be deployed to collect and communicate wearer's health status anytime and anywhere. The medical offices and doctors to do early diagnosis and/or early intervention could use the collected information from the sensors. However, deploying an increased number of traditional body sensors could make users uncomfortable because of their sizes and weights. A potential but very important solution is to integrate the increased number of sensors with smart textile structures or ETex without sacrificing the user's comfort and awareness [2]. However, the integration requires drastic changes in the design of biosensors and sensor networks. Firstly, the size of body sensors must be minimized which necessitates the miniaturization of all the hardware components [3, 4]. Among them, especially the antenna for wireless transmission and the battery for the power supply need to be reduced in size. Secondly, the sensor network should be able to accommodate the relatively short-distance communications among body sensors and from sensors to the sink nodes (e.g., computer, PDA, smartphone, tablet etc.) Thirdly, the energy-efficient body sensor network techniques must be developed. For example, how to reduce the energy

consumption while meeting the network requirement for the body sensor networks is a critical factor. The last but not the least, the security and privacy of wearable body sensor networks remain a major concern. Many applications of body sensor networks are life critical. The information collected must be secure and also the users' privacy should be protected. In such a body sensor network, the integrity and confidentiality of sensitive medical data among sensor nodes must be protected against modification or other malicious attacks of the wirelessly transmitted packets. Other similar attacks include deliberation of health data leading to wrong diagnosis and treatment and falsification of alarms or suppression of real alarms in emergency. However, because the biomedical sensors used in WBSN applications must be small in form factor, light in weight, and low in complexity, they are very resource constrained in terms of power, computation capability, and transmission capability. This makes it a more challenging task to secure the transmission of sensitive medical data over those tiny and resource-constrained wearable biomedical sensors in WBSN.

In this chapter, biomedical sensors for electronic textiles including their measurand and measured parameters are discussed, and then the available techniques for the textile-based body sensor network design are considered. In order to demonstrate the potential benefits of the textile-based wireless body sensor networks, a case study on the infant monitoring system will be illustrated.

Wearable Biomedical Sensors for Electronic Textiles

The sensors employed in wearable body sensor network systems can be divided into active sensors and passive sensors. There is ambiguity in the classification, and many authors are using the other way around. In biomedical measurement field, however, the definition of sensor type follows the convention of other electronic instrumentation fields; the active sensors are those sensors that require an external power source to convert the input into a usable output signal, while passive sensors are those that intrinsically provide its own energy or derive energy from the phenomenon being measured into a useful electrical potential or current. An example of active sensor is the resistive strain gauge blood pressure sensor where external voltage supply is needed, while a thermocouple is a passive sensor, which is often used to measure body temperature or others in research setting.

Electronic textiles combine textile technology and advanced smart sensor materials, which will open new frontier for intelligent textile structures in healthcare monitoring. Integration of body sensor networks (BSN) into a garment enables wearable systems of making interfaces between humans and computers disappear. The wearable body sensor networks will be able to detect patients' vital signs and retransmit them to the sinking nodes. In this section the characteristics of biosensors for collecting vital physiological signals, textile biosensors, and integration strategy into smart garments are discussed.

Biomedical Sensors and Measurement

Physiological vital signs are measures of various physiological statistics to be acquired by WBSN in order to assess the most basic body functions of patients. The vital sign taking normally involves recording body temperature, heart rate, blood pressure, and respiratory rate but may also include other measurements such as posture and motion, pulse oximetry, and electrocardiography (ECG). For biomedical signal measurements such as pressure, flow, and temperature, various sensors were adopted from industry to meet the common medical measurand characteristics, which are listed in Table 1.

Only a few medical signals such as body temperature are constant or varying very slowly. These biosensors are converting biosignals that are function of time, that is, biosignals are dynamic not static in nature. Thus, bio measurement systems together with sensors should be considered from the standpoint of dynamic instrument characteristics. Instruments are described by a linear differential equation relating output signal to input signal in time domain.

Depending on the order of the differential equation, they can be classified as zero-order, first-order, and second-order instrument. A linear potentiometric displacement sensor is a good example of the zero-order instrument, where output signal voltage is directly proportional to the input displacement. The first-order system consists of one energy storage element and the system equation contains the first-order derivative of output signal. An RC low-pass filter found in biosensor input circuit is an example of a first-order instrument. A first-order system will respond to static input as if it is a zero-order system, which shows that static outputs are equal to static inputs. For sinusoidal input signals, the magnitude of first-order output (gain) decreases as the frequency increases, i.e., low frequency passes. Many medical instruments are second order or higher. However, many higher-order instruments can be approximated to second-order system by assumptions and described by three constants: K = static sensitivity, ω_n = undamped natural frequency, and ζ = damping ratio. An RLC low-pass filter employed in bioinstrumentation is a good example of second-order system. Only for damping ratio $\zeta < 1$ (underdamped) the step response overshoots the final value. For sinusoidal input,

Table 1 Biomedical measurand characteristics [5]

Measurement	Range of parameter	Frequency, Hz	Sensor or method
Blood flow	1–300 mL/s	0–20	Flow meter
Blood pressure	0–400 mmHg	0–50	Strain gauge or cuff
Electrocardiography	0.5–5 mV	0.05–150	Skin electrodes
Electroencephalography	5–300 μV	0.5–150	Scalp electrodes
Electromyography	0.1–5 mV	0–10,000	Needle electrode
pH	3–13	0–1	pH electrode
Respiratory rate	2–50 breaths/min	0–10	Impedance
Temperature	32–40 °C	0–0.1	Thermistor

a low-pass frequency response results in with twice-fast attenuation rate as frequency increases compared with the first-order system [6].

Physiological sensors mainly used for biomedical measurement are surface electrodes, pressure sensors, thermistors, and photodiodes. For certain kinetic movement detection, sensors are based on strain gauges, accelerometers, and GPS.

A surface electrode is a transducer that coverts ionic current in the body to electrical current [7]. Medical surface electrodes are placed in contact with the skin of the subject to monitor biopotential generated by tissues and organs. The biopotential originated from the electrical brain activity is called electroencephalogram (EEG). The biopotential generated from the muscle action potential can be recorded with skin electrodes, which is called electromyogram (EMG). Electrocardiogram (ECG) is recording of cardiac action potential originated from the sinoatrial node of the heart with silver/silver chloride skin electrodes. Blood circulation is effected by a chain of events involved in electrical activation of the ventricle. This activation sequence generates closed-line ionic currents that flow in the thoracic volume conductor. For ECG measurement, two skin electrodes are placed at defined locations on the body called leads to convert the potential difference between the two electrode positions. Currently used Ag/AgCl electrodes are coated with gels to minimize skin impedance, which causes skin irritation or uncomfortable feeling to the subject. Thus, there is need for noncontact textile ECG electrodes for WBSN based on ETex.

Pressure and displacement sensors are needed for measuring the size, shape, and position of the organs and tissues of the body. Common types of displacement sensors are changes in resistance, inductance, capacitance, and piezoelectricity. Resistive displacement sensors are potentiometers and strain gauges. For direct blood pressure measurement, a wire strain gauge mounted on a diaphragm with Wheatstone bridge interface circuit can be used. Bridge circuits are used to detect strain or forces. They can be configured in half-bridge or full-bridge circuit and give voltage output $V_0 = -V_{EX}\,(GF/2)\,\varepsilon$ and $V_0 = -V_{EX}\,(GF)\,\varepsilon$, respectively. Here $\varepsilon =$ strain and $V_{EX} =$ bridge excitation voltage. Gauge factor is defined as $GF = (\Delta R/R)/\Delta L/L = (\Delta R/R)/\varepsilon$.

Inductive sensors for displacement measurement are based on the fact that inductance of a coil, $L = n^2\,G\mu$, where $n =$ number of turns of coil, $G =$ form factor, and $\mu =$ effective permeability of the medium. Each of these three parameters can be changed by mechanical displacement. Linear variable differential transformer (LVDT) inductive sensors show good linearity over a large range of displacement, high resolution, and better sensitivity compared with strain gauge [6].

Capacitive sensors can be used to detect displacement from capacitance between two parallel metal plates, $C = \varepsilon_0\varepsilon_r\,A/x$, where $\varepsilon_0 =$ dielectric constant of free space, and $\varepsilon_r =$ relative dielectric constant of media. Displacement can be measured by changing all these three parameters. A good example is the capacitance microphone that is responding to displacement by sound pressure. Piezoelectric sensors are used to measure physiological displacement and record heart sounds. These sensors are fabricated from piezoelectric ceramics and piezoelectric polymers. For flexible

wearable sensors, fiber or film form of polymer piezoelectric materials such as PVDF is desirable.

For patient's body temperature monitoring, thermocouples and thermistors are used. Thermocouples are based on Seebeck electromotive force (emf) across a junction of two dissimilar metals. Typical empirical calibration data can be fit by curvilinear regression equation: $E = a_1T + a_2T^2 + \ldots$, where E is Seebeck emf in mV, T is in degree Celsius, and reference junction is maintained at 0 °C. Thermistors are ceramic semiconductors that are thermal resistors with high negative temperature coefficient. For biomedical applications, the resistivity of thermistors used is between 0.1 and 100 Ωm [6]. For core body temperature measurement, radiation thermometry instrumentation is used to determine the internal body temperature by measuring infrared radiation emitted from tympanic membrane and surrounding ear canal. Ear infrared thermometry provides clinical advantages such as short response time (0.1 s) and accuracy (approximately 0.1 °C) over oral or rectal temperature measurement [6]. Photodiodes are light sensors and LEDs are used as inexpensive light sources in biomedical instrumentation. A good example is a pulse oximetry for detecting blood oxygen saturation.

Biomeasurement system consists of biosensor, amplifier/detector, analog signal conditioner, analog-to-digital converter (ADC), digital signal processor (DSP), and display and data storage. The measured data can be transmitted via Bluetooth, ZigBee, and Wi-Fi to the data server in the doctor's office or hospital for further interpretation and intervention. Recent development in application-specific integrated circuit (ASIC) and field-programmable gate array (FPGA) not only consolidated all these functional components into a miniature energy-efficient single chip but also integrated microcontroller and radio system together. The noninvasive healthcare monitoring system can be reconfigured effectively in ETex platform with the help of wearable body sensor networks connected via ASICs and FPGAs.

Textile Biosensors and Electronic Textiles

Biomedical sensors embedded in WBSN may need to be modified to accommodate the user's comfort and reliability. In addition, the integrated fabric sensors should be small in size, flexible, and adaptable to ETex connectivity.

To monitor cardiac health, several initiatives were developed to integrate cardiac sensors in ETex. The "smart shirt" wearable motherboards [8] Wealthy [9] and Lifeshirt [10] are the results of these initiatives to name a few. All of these WBSN ETex products are equipped with ECG and respiratory sensors. All these shirts are based on several textile sensor technologies to acquire ECG signals instead of traditional Ag/AgCl wet electrodes. The flexible textile electrodes are fabricated with: (a) metallic conductive fibers by forming a patch by weaving or knitting or (b) organic conductive polymers or electroactive polymers (EAPs). The conductive yarns for patch electrodes are formed either by wrapping/twisting stainless steel (SS) filaments with textile yarns or by laying SS filament and regular textile yarns side by side. Then the conductive yarns are knitted or woven to form noncontact dry textile electrodes, which can be integrated into WBSN garments.

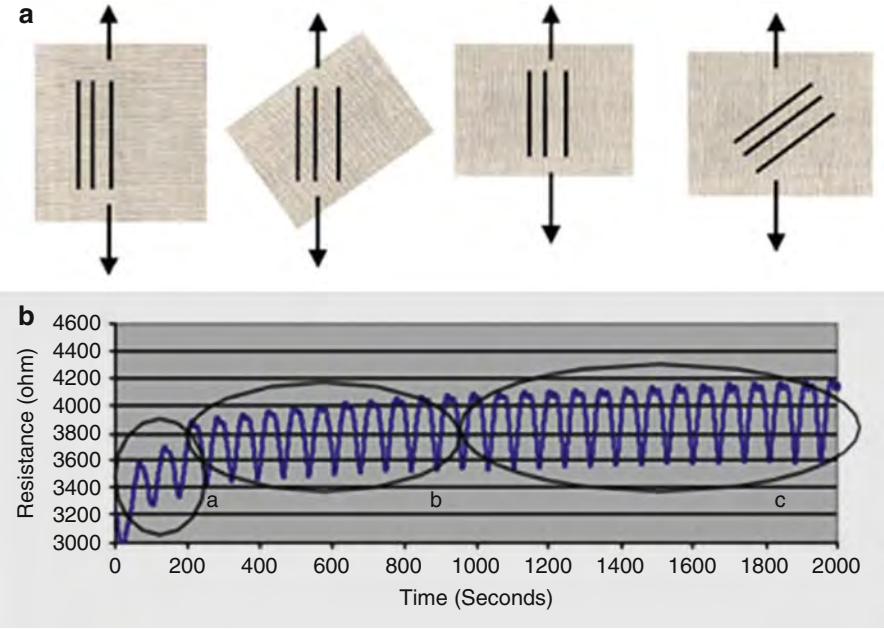

Fig. 1 PEDOT strain sensors (**a**) and a response to respiration of a typical sensor (**b**)

Conductive polymer-based ECG electrodes can be obtained by either composite film strips or direct depositing conductive polymer ink on textile fabric by digital printing or other coating methods. Patra et al. have successfully printed organic conductor, poly-3,4-ethylenedioxythiophene (PEDOT) strain sensors, and silver connecting lines onto the fabrics [11]. The printed conductors are partly embedded in the fabric and partly on the surface, with the embedded component providing durable sensing. Their preliminary analysis has shown that these biosensors can be effectively used to monitor body motions, such as respiration. A typical printed sensor and its response to respiration are shown in Fig. 1.

This type of piezoresistive sensor patterns on a flexible fabric substrate can form miniature respiratory sensor arrays for wearable health monitoring systems. Moreover, using the same technique, in situ capacitor arrays can be printed to form noncontact ECG sensors.

Respiratory rate is measured by means of either based on techniques that measure thoracic expansion or based on measurement of changes in skin impedance. For the former technique, most systems use strain gauges made from piezoresistive material combined with textile structures. Hertleer et al. reported a fabric sensor made of SS yarn knitted in spandex belt [12]. For the latter technique, noninvasive skin electrodes are placed on the thorax, and the variation of the electrical impedance can be detected during respiration cycles.

Body temperature can be monitored by embedding thermocouples or thermistors in conductive textile structures. Plastic optical fiber (POF) loops are temperature

Table 2 Flexible textile biosensors for WBSN application

Biosignal	Sensor type	Textile biosensor
Electrocardiogram (ECG)	Surface electrodes	Woven/knitted metal electrodes
Electromyogram (EMG)	Surface electrodes	Woven/knitted metal electrodes
Respiration	Piezoresistive sensor	Electroactive polymeric (EAP) fiber
Blood oxygenation	LED/Opto Diode	Woven/knitted plastic optical fibers
Skin temperature	Thermistor	POF or EAP textiles
Skin electrical impedance	Surface electrodes	Woven/knitted metal electrodes
Heart sound	Piezoelectric microphone	PVDF film or woven patch

sensitive and used to detect body temperature in 0.3 °C resolutions [13]. Optical sensors are immune to external electromagnetic interference and signal-to-noise ratio is very high compared with thermocouples and thermistors. The POF sensor is also easy to integrate into smart textile structures easily.

Pulse oximetry can be integrated into wearable structure with woven or embroidered POF textile structures such as glove or patch for LED/photodiode sensor together with microcontroller connection. The blood oxygen saturation (SaO_2) data can be interfaced to the WBSN and transferred to the data sink in medical offices for further interpretation and timely intervention. Textile biosensors considered above for WBSN based on ETex are summarized in Table 2. These textile sensors are flexible and good connectivity for integration of ETex and body sensor networks.

Wearable Body Sensor Networks and Wireless Data Acquisition

Integrating the wearable body sensors into textiles such as smart clothes can make users more comfortable with the long-term noninvasive monitoring systems. It also makes the sensor deployment more flexible when the sensors can be embedded in the garment. However, there are significant challenges of designing such a system. Firstly, the management of the number of these types of sensors on different locations is not a trivial task. These sensors will generate huge amount of data through variable contacts with the skin and these data may not be robust and accurate due to the body motion and signal interference. Secondly, the size of sensors must be minimized in order to provide the users' comfort. The monitoring system based on wearable body sensor networks has advantages over the traditional monitoring system. For example, it has better sensor placement and increase number of sensors that also make users more comfortable. Since the sensors are integrated in the fabric structures, the physiological signals are acquired in an unobtrusive manner. In addition, the collected physiological signals must be made available to the users and medical professionals, and so the feedback and assistance could be provided when needed. From technical perspective, the signal quality also should be enhanced in order to receive the robust data reliably. Wearable body sensor networks (WBSN) will be the infrastructure platform for the future ubiquitous healthcare system. The system must be able to deliver the data

reliably to the data center for the further processing. Currently, the wearable body sensor network technology is still at its primitive stage and is receiving extensive research attentions. The technology, once accepted and adopted, is expected to be a breakthrough invention in healthcare, leading to concepts like telemedicine and m-health becoming real. However, before the wearable body sensor networks can be widely used in monitoring human health, a critical question has to be answered: can the health and medical information provided by the WBSN be trusted? This problem is largely due to the lack of *security* in the operation and communication of resource-constrained medical sensor nodes. To answer this question, the authenticity and data integrity of the security requirements must be satisfied for wireless medical data transmissions over WBSN. The authenticity is to guarantee that the received information by the receiver is from trusted sources. In addition, one patient's data are only sensed and derived from that patient's dedicated WBSN system and should not be mixed with other patients' data. In the section, the network architecture for wearable body sensor networks and some key techniques such as energy consumption minimization and harvesting that can enable the data acquisition based on WBSN are discussed.

Network Architecture

A typical wearable body sensor network consists of multiple types of biomedical sensors and gateway (e.g., smartphone or other mobile devices), which can aggregate the data from the sensors and transmit them to remote control servers or cloud. Especially, for the textile-based wearable sensors, the sensors might have limited wireless communication capability; thus, the data routing and aggregation are necessary. In order to accommodate the network architecture, energy-efficient communication protocol must be designed to support the data communications among wearable sensors and between sensors and gateway.

As shown in Fig. 2, all the textile-based sensors will be connected via textile data bus and power grid to a mobile phone which has an Internet connection through either Wi-Fi or 3G/4G wireless. The collected data from these textile sensors will be finally delivered to remote servers. In the previous studies [14], a secure and resource-aware BSN architecture is developed to enable real-time healthcare monitoring. In particular, a communication protocol is designed for a secure wireless ECG data streaming platform and monitoring system. The system is tested with existing small and low-power wireless three-lead ECG sensors and obtained a reliable signal transmission with graphic user interface (GUI)-based software. The recent formation of the IEEE 802.15's TG6 (BSN) has stimulated great interest in the development and application of wireless technology in biomedical applications. Although these textile-based sensors are placed on the human body or hidden in the user's clothing, it will be challenging to apply general body sensor networks for human health monitoring. There is a strong need to consider both the energy efficiency and real-time performance. Therefore, the development of the channel models, efficient protocol that will make wearable sensor networks reliable as well

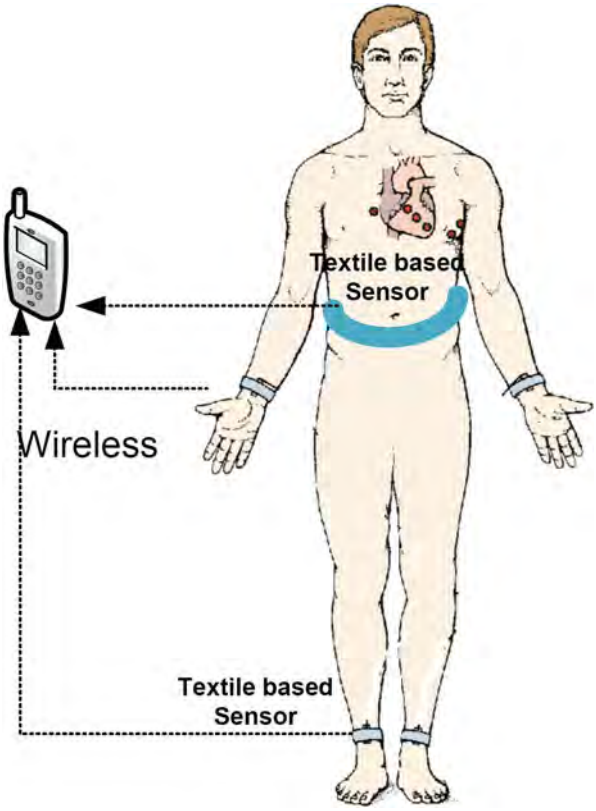

Fig. 2 A typical wearable body sensor network architecture

as effective, must be designed. The future important work includes the development and evaluation of improved channel models that will capture the manner in which signal fading and link reliability and provide a solid foundation for the development of: (1) more efficient antennas, (2) more realistic device deployment guidelines, and (3) more effective fade mitigation strategies at the physical layer.

Energy Minimization Techniques

In the wearable textile-based wireless body sensor network, the small-size sensors usually should be supported by the battery power. Therefore, it is critical to investigate the energy minimization techniques for these sensors. There have been numerous studies in the area of the energy minimization techniques. In body sensor networks, wireless channel is varied with time and significantly impacts the per hour energy consumption. The energy efficiency is always suboptimized without including the communication channel quality. It is critical to consider the channel condition measurement and delay study in the power optimization of textile-based sensor networks. Although several ongoing studies have conducted

on power management based on the sensor networks, they are limited to duty-cycle optimization. For energy optimization, the PHY (physical layer), MAC (medium access control), and routing layer protocols must be designed together based on available sustainable power. There is a strong need to optimize the values of the PHY layer parameters such as the bit error rate, sleep/wake-up scheduling at MAC/link layer, and routing selection at network layer to achieve overall performance. In addition, the routing and power management techniques are also needed for textile-based wearable body sensor networks. For example, when small-size sensors usually have limited communication range, the multi-hop routing techniques are needed for the sensors to deliver the data to the gateway (e.g., smartphone). In addition, a cross layer approach to optimize the PHY, sleep/wake-up scheduling, and routing design will be a major solution for the energy minimization. In this solution, at the physical layer, the transmission rate and power control are interactively adapted based on wireless channel condition in order to find an optimal strategy for data transmission. Based on the remaining energy amount and application requirements, the optimal sleep/wake-up optimization can be performed. At the network layer, a delay-ware routing should be developed based on the lower layer service. In this design, the system couples several layers and their functionality and thus overall forms a cross layer optimization problem.

Energy-Harvesting Techniques

For textile-based wearable body sensor networks, the energy-harvesting technology such as solar power and piezoelectric fiber generator/nano-generator might be adopted. It is reported that the piezoelectric fiber transducers are efficient and robust in creating electric power. When a body motion stresses piezoelectric fiber structures configured in nano-generator, a charge appears on the surface of electrodes attached to the piezoelectric structures to counteract the imposed strain. This charge could be collected, stored, and delivered to power electrical circuits (e.g., sensors) or processors.

The energy-harvesting technique can provide sustainable energy resource to sensors to execute the specific tasks in many applications. Based on these possible energy sources, new power management techniques would be significantly different from the ones in traditional wireless body sensor networks (WBSN). In the literature, instead of minimizing total energy consumption, energy neutrality [15] is considered as a better desirable design objective. In energy neutral mode, the sensor node consumes only as much as harvested, with a sustained but peak-limited energy harvesting. Vigorito et al. [16] improved their work and proposed a duty-cycle optimization without an energy source modeling requirement. These approaches are to optimize the duty cycle in the sensor network to save energy but not breaking the energy neutrality rules. However, these research works ignore two important factors in their optimization. One is the delay requirement, which is critical in event-based sensor networks. For example, the long delay in many applications such as body sensor networks might not be tolerable. In the literature, energy-aware

tasking protocols for various applications have been studied extensively in recent years. However, these proposed approaches are only based on the existing battery level and ignored the potential of energy harvesting that can supplement battery supply. Although other recent works have been explored in integrating energy-harvesting techniques into wireless sensor networks [17, 18], these works have been simply utilizing the extra energy provided by the harvesting system as an overall enhancement of the lifetime and performance. Two research works in [18] incorporate the energy harvesting component into a tasking algorithm in order to improve performance and lifetime. Recent studies in [18] introduced and explained the concept of "energy neutrality," which approximately states a condition that the energy each sensor consumes over a long period of time is less than or equal to the energy harvested from the environment. In those schemes, the energy neutrality is ascertained by adaptively controlling the duty cycle at MAC protocol layer. However, they provide only heuristic techniques for using the harvested energy efficiently; other critical factors such as delay and channel condition have not been ignored. Obviously, the energy-harvesting hardware has offered promising potentials to eliminate the energy sustainability limitations. The traditional batteries' limitation does not exist when the harvesting transducers on a sensor node continuously harvest instantaneous available power.

The traditional optimized designs targeted at energy efficiency fall in the suboptimal with the availability of energy-harvesting functionality. However, existing energy-aware techniques based on nonrenewable energy source may not work efficiently in the next-generation energy-harvesting wearable body sensor networks. The best energy efficiency could not be achieved if the network protocol design does not include energy neutrality. There is a lack of a cross layer-based framework that can fully utilize the harvesting energy to improve the sensor network performance. There is a strong need to develop efficient power utilization techniques for next-generation communication wireless body sensor network system. The work could be in two directions: first, a cross layer framework that includes routing and sleep/wake-up control needs to be developed to achieve the best energy efficiency; second, the delay constraints and channel condition factors should be considered in the sensor wake-up optimization, which can guarantee the strict real-time performance in wireless body sensor networks.

Security Design for Wearable Body Sensor Networks

The wearable medical sensors worn in WBSN are severely resource constrained. In addition, these sensors should allow remote storage and access to external processing and analysis tools. Due to these special features of medical sensors, security still remains a major concern in WBSN despite many projects such as CodeBlue, MobiHealth, and iSIM conducted in the last several years. In [19], a system framework was proposed to provide real-time feedback to the user and deliver the user's information to a telemedicine server. In [20], a system called UbiMon aiming to develop a smart and affordable healthcare system was

developed. MIThril developed by MIT Media Lab aimed to provide a complete insight of human-machine interface [21]. The MIT lab studied interfaces and wearable computers and devices [22]. A wearable physiological monitoring system called LifeGuard was developed for astronauts in [23]. IEEE organizations such as 802.15.6 [24] and 1,073 [25] are working toward the solution and standards of low-power in-body and on-body wireless communications for medical and nonmedical applications.

Those efforts in the development of wearable body sensor networks are imperative for modern telemedicine and *m*-health. However, the security remains a formidable challenge yet to be resolved. Especially, the security system over wearable body sensor must be implemented with low computational complexity and high power efficiency. As nodes of textile-based body sensor networks are expected to be interconnected on or in the human body, the body itself can form an inherently secure communication pathway that is unavailable to other bodies. Multiple body sensors placed at different body parts of the same individual share a secure circulation media or a trust zone, i.e., the human body, which is unavailable in any other kind of networks. The biometric information collected from these trusted zones can uniquely represent an individual and unambiguously differentiate multiple individuals, which lay foundations for biometric-based entity authentication in wearable body sensor networks. Using these biometric values provides strong security and data integrity while eliminating costly key distribution. It may serve as a substitution of public key infrastructure-based authentication, which is too expensive in terms of computation and energy consumption in resource-constrained wearable body sensor networks. The focus is on the problem of how sensors within a body sensor network can utilize the biometric authentication and differentiate whether they belong to the same person or not. Since the inborn secure circulation media in a human body naturally forms a communication trust zone, the integrity of data packets coming from the same individual can therefore be protected.

Limited researches have been reported in literature regarding secure communications in WBSN utilizing biometric information. Venkatasubramanian et al. provided an overview of security solutions in pervasive healthcare systems, where biomedical information was utilized for securing data collected by medical sensors and for controlling access to health information managed by pervasive healthcare systems. Cherukuri et al. proposed a biometric-based key distribution scheme to secure the inter-sensor communications on the same human body. A pseudorandom number was generated through error-correction code using biomedical properties of the human body recorded simultaneously at different locations, and this same random number was used to encrypt, decrypt, and securely distribute the symmetric key. They argued that the traditional public key cryptography (i.e., asymmetric cryptosystems) involved heavy exponentiation making it orders of magnitude more expensive than private key cryptography, and it was unsuitable for resource-constrained medical sensors. Poon et al. furthered this idea and proposed a similar key-exchange scheme for symmetric cryptosystem in WBSN using IPI as the biometric trait. The secret key was committed at the sender side using its

own local IPI signals and de-committed using receiver-side IPI signals recorded at the same time. In [26], a fuzzy key commitment scheme was applied to correct the errors in the recovered encryption key due to the slight IPI signal variations in different body locations. The committed key was used for further encryption. Other similar researches regarding biometric security in WBSN were found in [27, 28], where biometric signals such as IPI and heart rate variation (HRV) were encoded into a 128-bit sequence and the dissimilarities were measured by hamming distances.

However, all above research studies have focused on secret key distribution issues, while the specific and unique challenge in biometric authentication, i.e., how to merge the payload with the biometric information while preserving the statistical uniqueness of the biometric information, has not been addressed. Furthermore, all abovementioned biometric-based key-exchange schemes need critical time synchronization because they need to record biometric information simultaneously at different positions of the same human body, which incurs considerably extra communication overheads in extremely resource-constrained wearable body sensor networks. In addition, one of the biometric features may not be unique, and accidental faulted measures (e.g., due to hardware or software failures) may malfunction the traditional biometric-based security system.

The future work in wearable body sensor networks will be in several directions: (1) provide an accurate and low-cost biometric-based multiple model selection method to select the best biometric features and modes for data authentication, (2) develop a key agreement scheme that uses multiple collected dynamic biometric features as a key and share it among communication partners with low communication and computational cost, and (3) develop a biometric-based authentication system for textile-based body sensor networks under the low-cost key agreement scheme.

There will be a strong need to develop a multiple biometric feature-based cognitive method to select the best classification model and biometric features for accurate and low-cost biometrical data authentication. The biometric-based authentication system should be able to secure data communication channel over body sensor networks. It has two major components: (1) a cognitive multi-model biometric-based authentication approach using a set of statistics of biometric features extracted from vital signs and (2) criteria for model selection to support low-cost and secure communications. Wang et al. [29] showed that the GMM/HMM approaches could be potential candidates for modeling the statistic characteristics of biometric information such as ECG features to secure data transmission. However, a multi-model selection strategy is a more reasonable solution to real-time data modeling. This strategy can facilitate a comparative effectiveness analysis of a suite of potential model candidates under real-time scenarios. Moreover, it may lead to potential calibration or development of a new model. Using biometric signals (e.g., IPI, PR interval, BP, and ST segment) will be a potential solution for securing inter-sensor communication within WBSN. The security design should not be confined to these biometric signals. Any of the unique biometric signals measured from the body can be considered in the proposed framework when they can be utilized with low complexity.

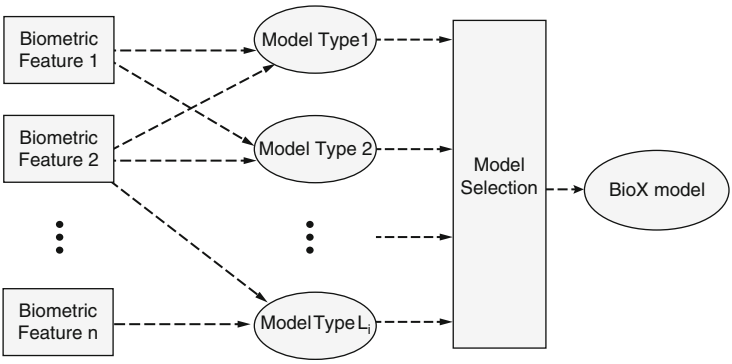

Fig. 3 Security design through model selection

As shown in Fig. 3, a multi-model selection approach is designed to choose the most appropriate model for the authentication. The criteria of model selection include accuracy and low cost. Based on multi-features (e.g., IPI, PR interval, BP, and STsegment), the PIs propose to evaluate multiple models and select an appropriate model for low-cost and highly accurate data authentication. As shown in Fig. 3, there is a set of L_i candidate models $\{M_{il} : l = 1, \ldots, L_i\}$ for each class C_i; each model M_{il} is regarded as the combination of the model structure T_{il} (or topology) and the parameter of the model θ_{il}. Also, for each class C_i, assume a representative data set X_i. The model selection is to select a single topology T_{il} as the sole representative of the class C_i. This is implemented by devising a selection criterion $C()$ such that for each class C_i, choose T_{il} if $T_{il} = argmaxC\left(T_{i,k}\right)$. A common practice in Bayesian model selection is to ignore the prior over the structure $P(T_{il})$ and use the evidence $P(X_i|T_{il})$ as the criterion for model selection. The criteria of model selection are to achieve optimal model fit with low misclassification rate and time cost. Classical criteria for model selection assess the fit of a model rather than its ability to produce a low classification error rate. Typical classification model selection criteria in pattern recognition literature include Akaike information criterion (AIC, the smaller the better), Bayesian information criterion (BIC, the smaller the better), and adjusted BIC (the smaller the better). Bayesian entropy criterion (BEC, the smaller the better) was recently proposed by Bouchard and Celeux, which takes into account both model fit and classification rate. It was shown that BEC is not only an alternative to the cross validated error rate which is computationally expensive but also outperforms AIC and BIC. Although we assume BEC provides more credible model selection results, the four criteria can be conservatively used for model selection.

Wireless Biomedical Computing and Applications

Reliable and continuous collection via wireless communications of patient vital signs such as blood pressure and flow, ECG (electrocardiography), EEG (electroencephalography), and SaO_2 is crucial for making real-time triage decisions.

Multiple types of sensors collecting vital signs are connected to central control nodes (e.g., smartphone and PDA) wirelessly. At a given time, a combination of multiple vital signs (biometric features) is unique to each patient. These features are important indicators to a clinician about the patients' health states. They are correlated: if any parameter is missing or appears abnormal, the rest could be informative. Acute changes in these features over time and in response to varying circumstances provide a clinician with important insights to what happens in an individual patient at a specific time and then over time, such that these patients could be more intensively monitored and changes could be made to their lifestyle practices or medication regimen. The integrations of ubiquitous communication, wireless biomedical computing, and wearable sensing will enable many wireless biomedical applications. The data generated by the sensors deployed in big populations could be huge and raise the significant challenges of data processing, storage, and transmissions. The problem could also be defined as the one of the BIG DATA problem. Employing emerging BIG DATA techniques for traditional biomedical computing applications will open a new vista for future wireless health services. In the following section, the challenging problems of future wireless biomedical computing and an example application that employs the wearable body sensor networks are discussed.

Wireless Biomedical Computing

The collections of biomedical data from wearable sensors involve the processing of the data such as compression in sensors/gateway and data fusion in the gateway or remote servers. Many available data compression techniques could be applied as long as the computation power of sensors could be enough for the compression. For most of the wearable sensors, it might be a good strategy to off-load the data processing tasks to the gateway. However, there is a trade-off between the communication overhead and computational complexity. At the gateway of wearable sensor networks, intelligent data processing techniques such as the data fusion could be applied. For example, in some cases, there might be redundant deployment of biomedical sensors. The redundant data could be coded using the difference coding techniques or not transmitted to the remote servers. In addition, the gateway of wearable body sensor networks may make some intelligent decision based on the collected data. For example, in the application of health monitoring alerting system, the gateway can apply some data mining techniques to determine whether the health status of a monitored person is normal or abnormal. If it is normal, it might not be necessary to report the collected health data to remote servers. Further, the existing intelligent techniques such as data mining, fuzzy modeling, and data fusion can also be applied to improve the capability of self-configuration and management in wearable wireless body sensor networks.

Further, there is a new technology trend of integrating the wireless body sensor networks with smartphones for many biomedical applications. Smartphone itself has numerous types of sensors such as GPS, accelerometer, gyroscope,

magnetometer, microphone, and proximity sensor. It can support many biomedical computing applications such as falling detection of elders and health recommendations through phone apps. The integration of biomedical body sensors and smartphones can support many great mobile biomedical applications in the future.

In addition, off-loading the computing tasks of collected data to the cloud is becoming an important research direction of future wireless biomedical computing. The cloud could provide unlimited storage and computational capability. There are several changeling issues related to the cloud-supported wearable body sensor networks. Firstly, the quality of service (QoS) between the wearable body sensor networks and the cloud should be satisfied. The QoS involves with the communication, computation, and cloud server response; secondly, the security and privacy should be preserved between the users and cloud servers. Especially, the monitored data are private data and should not be disclosed to unauthorized users. Also, the persons who are monitored should also be able to control the access of his/her personal health data from body sensors. Thirdly, the efficient decision support algorithms should be realized in the cloud and help the medical doctor to make appropriate treatment decision.

An Example for Infant Monitoring

One of the important WBSN applications is the preterm infant monitoring. The infants could pause in their breathing if they are born prematurely; this event is called apneas (pauses in their breathing). If it lasts longer than 20 s, it can cause damage to the heart, lungs, and brain of the infants. In addition, bradycardia (slowness of heart rate) and hypoxia (tissue-level oxygen desaturation) often follow the apnea episode in these preterm infants. Apnea has serious consequence and can cause apparent life-threatening events in neonatal intensive care units (NICU) and sudden infant death syndrome (SIDS) at home. However, it is not easy to monitor these preterm infants whose body masses are very small and their skins are underdeveloped and very sensitive to common biosensors. Therefore, integrating noncontact wireless body sensors with fabric material could be very helpful for this application. The existing system for monitoring the physiology of neonates has relatively large sensors that are with wires. It is hard to employ multiple wired sensors along with the data acquisition system for the purpose of home monitoring. The existing system is also difficult for medical staffs to define pathological states requiring treatment for preterm infants, as there is no method available to translate these signals into validated indices to define pathology. Textile-based body sensor networks consisting of multiple wearable wireless sensors attached to the human body have been widely used to monitor physiological as well as behavioral signals in adults, which can be used for monitoring the physiological signals of neonates in NICU or at home. The challenges involved in developing textile-based body sensor networks for this application are the system size and how to customize the system to the environment. In addition, how to choose multiple types of sensors and fuse their information together for the infant monitoring could be another challenging issue,

for example, an apnea is detected on the respiration signal followed by a bradycardia observed in ECG and oxygen desaturation in SpO_2. Textile-based wireless body sensor network can provide reliable and continuous monitoring of these physiological signals that can be used for assessing the physiological states of the infants. Processing these signals requires signal processing framework for the assessment of risks of infants and provides appropriate alert signal to the nurses and doctors. In the future work, integrating multiple noncontact wearable body sensors for infant monitoring and developing efficient signal processing algorithm will be the direction of the application. In addition, the smartphone-based applications could also be developed for the nurses or doctors to check the infant health situation regularly.

Future Trends

The textile-based wearable body sensor networks will significantly advance the understanding in the emerging fields of biosensor design, BSN, and biomedical computing, which will play a key role in the modem society to meet the broad goals of applications in both the hospital and home environment. Specifically, a comprehensive system framework including communication and computation is needed to be developed, involving three important components: wireless biosensors that can be attached to infants who are very small and vulnerable, efficient communication protocols that can transmit the physiological signals from the sensors to remote servers, and efficient signal processing algorithms than can extract useful information from the sensor data for medical doctors to make decisions. Textile-based wearable body sensor networks will be a technology platform of future smart and connected health system, especially for ubiquitous health monitoring and computing. Novel algorithms, theoretical models, and guidelines for practical implementation should be established to enable lightweight and efficient health monitoring. The future research in this area will involve with signal processing and data processing, sensor design, wireless healthcare, modeling, simulation, and performance analysis. Wearable body sensor networks will have a significant impact on nonintrusive ambulatory health monitoring by integrating lightweight sensor solutions into the sensing, communication, and computing.

Summary

In this chapter, the technology trends of wearable body sensor networks and some key techniques that can realize the future ubiquitous wireless healthcare services based on WBSN are discussed. There will be a strong need to have a close interdisciplinary collaboration between biomedical sensor technology, intelligent textiles, and advanced wireless network technology. The collaboration needs to involve the experts from multidisciplinary fields such as medical, information technology, and computing fields. It was also demonstrated that application of wearable BSN-based technology in preterm infant monitoring is a very promising

example of the significant WBSN technology. It is believed that the growing biomedical applications based on the WBSN technology will significantly improve health and well-being of human beings in the future.

References

1. Yamakhoshi K (2011) Current status of noninvasive bioinstrumentation for healthcare. Sens Mater 23:1–20
2. http://www.wearaban.com Website of EU project 242473, Wear-a-BAN, for unobtrusive wearable human-to-machine interfaces
3. Boehme C, Vieroth R, Hirvonen M (2012) A novel packaging concept for electronics in textile UHF antennas. In: Proceedings of 45th international symposium on microelectronics, San Diego, California, USA, pp 425–432
4. Manic D, Severac D, Le Roux E, Peiris V (2011) Cost-effective and miniaturized system-on-chip based solutions for portable medical & BAN applications. In: Proceedings of 5th international symposium on medical information and communication technology, Montreux, Switzerland, pp 15–19. doi:10.1109/ISMICT.2011.5759787
5. Hugo K (2004) Measurement systems. In: Webste JG (ed) Bioinstrumentation. Wiley, New York
6. Olson WH (2010) Basic concept of medical instrumentation. In: Webster JG (ed) Medical instrumentation: application and design, 4th edn. Wiley, New York
7. Baura GD (2012) Medical device technologies. Elsevier, Amsterdam
8. Park S, Jayaraman S (2003) Enhancing the quality of life through wearable technology. IEEE Eng Med Biol Mag 22(3):41–48
9. Pardiso R, Wolter K (2005) Wealthy- a wearable healthcare system: new frontier on E-textiles. Int News Lett Micro Nano Integ 2(5):10–11
10. Vivononetics (2014) http://vivonoetics.com/products/sensors/lifeshirt/. Accessed 25 Mar 2014
11. Patra PK, Calvert PD, Warner SB, Kim YK, Chen CH (2006) Quantum tunneling nano-composite textile soft structure sensors and actuators, National Textile Center Annual Report, Project No: NTC M04-MD07
12. Hertleer C, Van Longenhove L et al (2002) Intelligent textiles for children in a hospital environment. In: Proceedings of 2nd AUTEX conference, Bruges
13. Moraleda AT, García CV, Zaballa JZ, Arrue J (2013) A temperature sensor based on a polymer optical fiber macro-bend. Sensors 13:13076–13089
14. Wang H, Peng D, Wang W, Sharif H, Chen HH, Khoynezhad A (2010) Resource-aware secure ECG healthcare monitoring through body sensor networks. IEEE Wirel Commun Mag 17(1):12–19
15. Penella MT, Gasulla M (2007) A review of commercial energy harvesters for autonomous sensors. In: Instrumentation and measurement technology conference proceedings, 2007 IEEE, 1–3 May 2007, Warsaw, Poland, pp 1–5
16. Vigorito CM, Ganesan D, Barto AG (2007) Adaptive control of duty cycling in energy-harvesting wireless sensor networks. In: Sensor, mesh and ad hoc communications and networks, 2007. SECON '07. 4th annual IEEE communications society conference on, 18–21 June 2007, pp 21–30
17. Kansal A, Hsu J, Zahedi S, Srivastava MB (2007) Power management in energy harvesting sensor networks. ACM Trans Embed Comput Syst 6(4). Article No. 32
18. Kansal A, Srivastava M (2003) An environmental energy harvesting framework for sensor networks. In: ACM joint international conference on measurement and modeling of computer systems (SIG-METRICS) San Diego, CA, USA
19. Jovanov E, Milenkovic A, Otto C, de Groen P (2005) A wireless body area network of intelligent motion sensors for computer assisted physical rehabilitation. J Neuroeng Rehabil 2(6):1–10

20. http://www.ubimon.net. Date visited, 16 Mar 2014
21. http://www.media.mit.edu/wearables/mithril. Date visited, 9 Mar 2014
22. http://www.hitl.washington.edu. Date visited, 25 Mar 2014
23. http://lifeguard.stanford.edu. Date visited, 11 Mar 2014
24. http://www.ieee802.org/15/pub/TG6.html. Date visited, 16 Mar 2014
25. IEEE P1073.0.1.1/D01J (2006) "Draft guide for health informatics- point-of-care medical device," communication technical report-guidelines for the use of RF wireless technology. Institute of Electrical and Electronics Engineers, New York
26. Juels A, Wattenberg M (1999) A fuzzy commitment scheme. In: Proceedings of 6th conference on computer and communications security, Nov 1999, Hong Kong, China, pp 28–36
27. Bao S, Zhang Y, Shen L (2005) Physiological signal based entity authentication for body area sensor networks and mobile healthcare systems. In: Proceedings of IEEE engineering in medicine and biology, Sept 2005, Shanghai, China, pp 2455–2458
28. Zhang Z, Wang H et al (2012) ECG-cryptography and authentication in body area networks. IEEE Trans Inf Technol BioMed 16(6):1070–1078
29. Wang W, Wang H, Hempel M, Peng D, Sharif H, Chen HH (2011) Study of stochastic ECG signal security via gaussian mixture model in wireless healthcare. IEEE Syst J 5(4):564–573

Photonic Fabrics for Fashion and Interior 37

Jeanne Tan

Contents

Introduction 1006
Photonic Textiles 1007
Laser Engraving 1008
LED Light Sources 1010
Ultraviolet Bonding Technique 1010
Cable Gland Technique 1012
Sensors and Remote Controls 1012
Motherboard 1013
Power Sources 1014
Case Studies 1014
Case Study: *Totem* 1015
Case Study: *Urban Glow* 1019
Case Study: Ephemeral 1024
Interdisciplinary Approach for Designing Photonic Textile Products 1027
Design Challenges 1029
Visual Appearance of Photonic Textiles 1029
Construction of Prototypes 1030
Installation of Technology 1030
Summary 1031
References 1032

Abstract

The evanescent nature of design trends creates demand for fashion and interior textiles that can adapt to the user's evolving needs. Interactive photonic textiles that can emit customizable patterns of illumination have great potential for application in the fields of fashion and interior textiles. Conventional textiles

J. Tan (✉)
Institute of Textiles and Clothing, The Hong Kong Polytechnic University, Hung Hom, Hong Kong
e-mail: Jeanne.tan@polyu.edu.hk

© Springer Science+Business Media Singapore 2015

X. Tao (ed.), *Handbook of Smart Textiles*,
DOI 10.1007/978-981-4451-45-1_29

are passive and inadaptable, whereas photonic textiles that incorporate polymeric optical fibers (POFs), light-emitting diodes (LEDs), and sensors and controls enable users to interactively personalize their garments and environment by changing the colors, patterns, and emission frequency of the emitted light. Continuous research into the development of minute components and methods of incorporating them into lightweight fabrics has enabled the development of portable and accessible products that are relevant to current lifestyles. Such textiles offer an innovative and effective platform for communication between users, viewers, and their surroundings. The juxtaposition of solid components with pliable textiles presents a challenge within the design process. The development of smart textiles for fashion and interior use requires the seamless integration of technology as the textiles come into close contact with the body. This chapter explores the design process and prototyping techniques for photonic textiles, considering both aesthetic design and functional technology. Based on the author's and her research team's design practice, this chapter discusses three case studies that illustrate the interdisciplinary approaches and design challenges. The case studies are derived from the development of two fashion design and one interior textile prototypes. The chapter aims to address a gap in literature, which has predominantly focused on the technological perspective.

Keywords

Interactive photonic textiles • Interdisciplinary design process • GYRO sensor • Motherboard • Remote control • Android mobile phone

Introduction

Contemporary lifestyles are fluid and transient, breaking down the traditional perceptions of fashion design and interior spaces. There is a need for textiles that can adapt to users' fast-evolving needs. Dynamic photonic textiles can be actively adapted and remotely controlled using convenient information technology devices. Such textiles enable users to customize their clothing and interiors by emitting different colors, patterns, and frequencies of light. The emotive power of color affects people across different regions [1] and influences individuals' cognitive and affective functioning [2]. In contrast to conventional textiles, which remain inert, photonic textiles provide contemporary users with an alternative communication platform.

In recent years, illuminative textiles have emerged as an innovative and effective fabric for fashion and interior design. Fashion designers have used light-emitting clothing to create costumes for international performers. The use of lights and colors enables performers to create a visual spectacle and enhance the dynamic effect of their performance [3]. In addition to appealing to the visual sense of the audience, light-emitting costumes also serve a highly functional purpose by

increasing the visibility of the artist when performing in a large arena. There is also a potential market to develop color- and pattern-adaptive garments for the fast-moving trends of the fashion market. As the production costs of components continue to fall, adaptive photonic textile fashions may offer a sustainable option for the fickle mass market.

Changes in lifestyles and demographics have led users to desire homes that can adapt and allow them to manage their space efficiently as their needs evolve [4]. There is a pressing need for sustainable products that enable people to modify their living spaces according to their evolving lifestyles. The ability to customize and adapt existing living environs is particularly applicable to cities with limited and compact living spaces. Interactive photonic textiles allow users to create flexible living spaces via the illumination of different colors and patterns and to create atmospheric moods without incurring the wasteful disposal of construction wastes whenever there is a need to adapt the interior environment.

Various materials and technologies have been applied to create light-emitting textiles for fashion and interior purposes, including LEDs applied on the surface or embedded under the base fabric of smart products [5–7] and integrated electroluminescent materials [8] and the use of photonic textiles [9, 10]. Although light-emitting textiles that directly apply LEDs and electroluminescent materials are effective, the superficially applied light sources and components are obtrusive and are generally used for products that are meant for display or have limited contact with the body. In contrast, photonic textiles are woven with POFs and textile-based yarns to create pliable textiles with good tactile quality. LEDs are connected to the fiber ends to serve as a light source, allowing the electronic components to be discreetly placed on different areas of the product with little contact with the user's body. Photonic textile products provide users with a familiar sense of touch that is highly similar to conventional textiles and can be effectively developed into invaluable commonplace products.

Photonic Textiles

Photonic textiles are created by weaving POFs to create a fabric. POFs are often used in the application of optical fibers because they are more resistant to textile manufacturing processes and are more flexible than glass fibers [11]. Due to the brittle and fragile nature of POFs, they are often woven with textile yarns to achieve a flexible and high-quality hand feel. Experiments conducted by the researcher and her team indicated that 0.25 mm polymethyl methacrylate (PMMA) optical fibers yielded positive results in terms of tactility and flexibility. Although contemporary POFs are highly flexible and thin, they are still susceptible to breaking when bent. The loop structures in knitted fabrics can cause the POFs to break and disrupt the emission of light. Photonic textiles can be effectively made using techniques such as plain weaving, jacquard weaving, and needle felting [12], which allow the POFs to lie flat during the textile process.

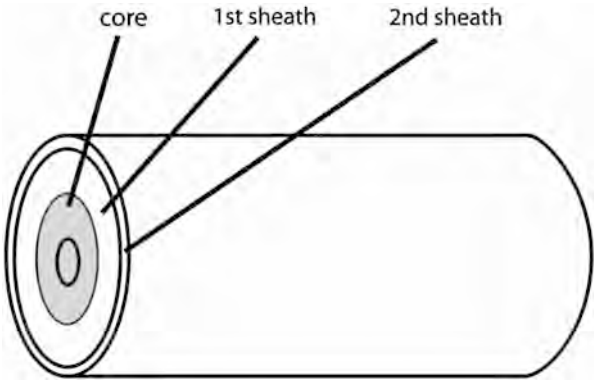

Fig. 1 Cross section of a POF, illustrating the core and the cladding layers

Weaving is a conventional textile production technique and is the most common way to construct photonic fabrics [13]. According to Abouraddy et al., the fiber grid in a woven textile allows POFs to be placed in specific arrangements and positions [14]. The woven construction of the textile depends on a number of features, including the textile-based threads and the POFs, which should be small in diameter and flexible, the pattern in which the textile is woven, and the distance between each parallel fiber. The proximity of the woven POFs and other fibers affects the tactile and tensile quality. When thicker POFs are used, the illumination is dimmer because less light is delivered to the POFs across the fabric. Weave patterns that are too tight can also cause the POFs to bend into awkward positions, which may break them. Warp yarns are threaded under tension through the loom, but POFs that are introduced via the warp may be susceptible to breaking [15]. Research on the luminosity of woven textiles based on the assimilation direction of POFS implies that better illumination results are achieved when the fibers are woven in through the weft [16–18]. By varying the weave structure and incorporating the photonic luminescence generated by the integrated photonic fibers, different surface patterns, textures, colors, and lusters can be created.

Laser Engraving

Conventionally, POFs possess three layers and are designed to transmit light from one end to the other (Fig. 1). Light escapes from the POFs when the cladding on the external surface of the fiber is damaged by thermal, physical, or chemical treatments, thus creating the lateral illumination of the fibers (Fig. 2). Although these treatments are effective, they can only produce simple patterns with little definition as they are imprecise and difficult to control.

Laser engraving can be applied to photonic textiles to create precise patterns of surface damage. The illumination pattern can be predesigned using computer software and engraved in a highly controlled manner. The laser engraving is carried out using a GFK Marcatex Flex-150 CO_2 laser coupled to an Easymark® 2009 laser

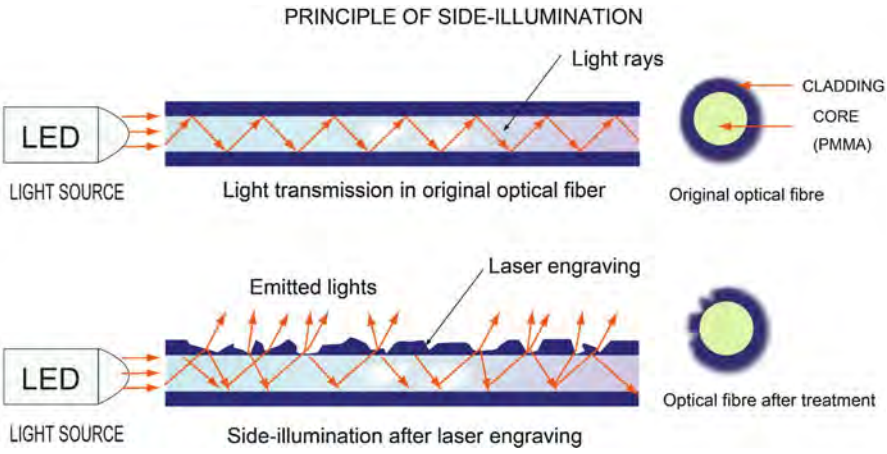

Fig. 2 Creating damage on the surface of the POF enables light to be emitted from the lateral surface

system. This is a type of gas laser that emits light at a wavelength of 10.6 μm in the far infrared region of the electromagnetic spectrum. Laser engraving is used to remove part of the POF's cladding, allowing light to seep out from the fiber's core [13].

The photonic fabric is placed on a platform and a laser is directed onto the fabric's surface. The laser is repeatedly applied according to the predesigned pattern via a computer linked to the laser machine. By altering the resolution (in dpi) of the designed pattern and the pixel time (in μs) of the laser radiation, different engraving parameters can be achieved across the fabric and the photonic fibers can be damaged to varying extents to achieve different side-lighting effects. The engraving process is accurately controlled by a computer program.

It is imperative that the laser engraving is carefully controlled to ensure a specific amount of damage is applied. If the POFs are not sufficiently damaged, only a small amount of light will be emitted and the intensity of the illumination will be reduced. Too much damage will immediately cause light to leak from the treated area; thus, there will be insufficient light to travel through the entire length of the fiber, affecting the lateral illumination of the fabric. To ensure the illumination is even and intense, it is important to execute the laser treatment with the appropriate resolution, pixel time, and number of engraving repetitions.

A series of laser engraving experiments with different resolutions, pixel times, and engraving repeats were conducted. To examine the effect of engraving on the POFs in treated fabrics, the treated POFs were observed with a field emission scanning electron microscope (FE-SEM). The experiments indicated that POF fabric engraved with a resolution of 20 dpi, a pixel time of 140 μs, and 7–9 engraving repeats achieved satisfactory removal of the POF cladding and therefore accomplished a satisfactory illuminating effect (Fig. 3).

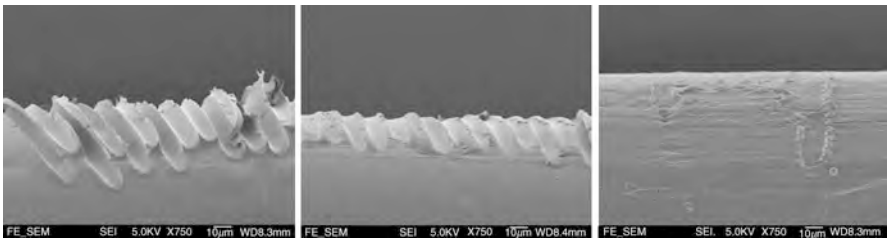

Fig. 3 FE-SEM images of a POF exposed to too much damage (*left*), appropriate damage (*center*), and insufficient damage (*right*)

LED Light Sources

The color and intensity of the light emitted from the photonic textiles rely on the coupled LEDs that serve as the light sources. Bright LEDs [19] have been used for illuminating applications because they produce a cool light and the light source can be remotely located. For radiometric purposes, lasers with a suitable wavelength have been used for medical treatment [20] or sensory applications [21, 22]. The usability of the final product needs to be considered when designing photonic textiles. It is very important that the electronic components, including light sources and control devices, are unobtrusive. With advancements in technology, LEDs and relevant electronic components have become smaller and lighter and can be seamlessly integrated into photonic textile products. As most interior products need to be lightweight, durable and mobile, powerful laser light sources are not suitable for this kind of application. In the studies reported here, red, green, and blue LEDs were used as the light source. An extensive range of colors can be achieved by mixing these primary colors. The colors of photonic textiles can be changed and tuned by a predetermined program. All of the electronics for controlling the LEDs are docked in a motherboard (Fig. 4). Touch and movement sensors are integrated to enable users to interact with the products and their surroundings.

The POFs can be coupled to the LEDs via ultraviolet bonding or the use of cable glands. The former technique is frequently seen in photonic textiles research, whereas the latter requires customized parts developed by the author and her team. To prepare the photonic textiles for connection with the LEDs, the textile-based yarns that were woven with the POFs are removed from the two lateral ends of the fabric (Fig. 5). This helps to reduce unnecessary bulk when the POFs are bundled together for coupling with the light source.

Ultraviolet Bonding Technique

The ultraviolet bonding technique involves bundling the POFs together with a plastic tube at the fiber ends. The fiber ends are attached to an LED, using

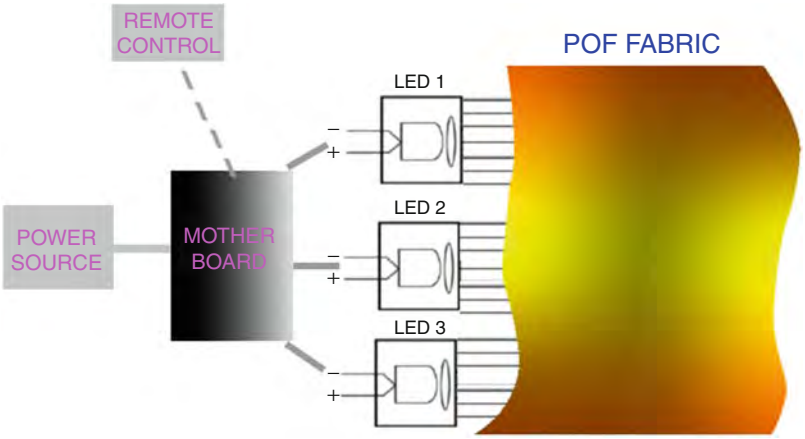

Fig. 4 Schematic drawing of the photonic textile connected to the LEDs, motherboard, power source, and remote control

Fig. 5 Preparation of the photonic textile for POF bundling and connection to the light source and components

Norland 65 optical adhesive as the coupling agent. To solidify the optical glue, the assembly (including fiber ends, optical glue, and LED) is exposed to ultraviolet radiation for several minutes, after which the fiber ends are fixed to the LEDs. This technique can maximize the light efficiency and reduce the coupling loss to ensure

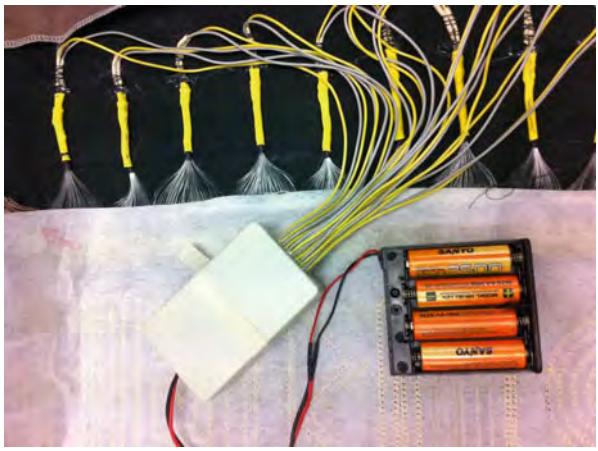

Fig. 6 POFs in a photonic textile connected to a motherboard using the ultraviolet bonding technique. Conventional batteries were used in this prototype

the intense illumination of the photonic textile. However, as a photonic textile comprises many bundles of POFs, this technique is laborious and very time consuming as each bundle has to be individually glued and exposed to ultraviolet light (Fig. 6).

Cable Gland Technique

According to experiments conducted by the author's research group, the use of cable glands significantly reduces the time required for POF coupling compared to the ultraviolet bonding technique. This technique involves the use of a customized coupler based on a cable gland (Fig. 7). A tricolor LED is fixed inside the coupler and connected to the motherboard via wires. A bundle of POFs is inserted into the coupler and then fastened by the cable gland, thus eliminating the fussy gluing and curing process. This technique is labor efficient and produces bright illumination.

Sensors and Remote Controls

Generally, the exploration of illumination in photonic products has only resulted in alternative passive types of light sources. To create value-added products that can be customized and serve as a communicative platform, it is important to consider the integration of sensors and remote control functions.

According to Norstebo [23], sensors transform physical phenomena into processable electrical sensors. Biometric and environmental data can be measured by sensors to translate the information from the physical environment into a specific command for the interactive textile. Temperature, motion, sound, weight and gyro

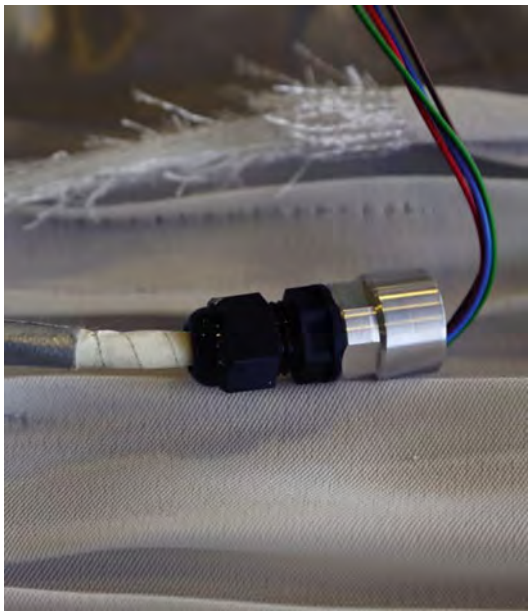

Fig. 7 Customized coupler based on a cable gland. The POFs are simply inserted into the coupler without the need for optical glue

sensors, and remote controls using Bluetooth functions are all viable for application. The sensor and remote control functions are available in minute components that allow them to be installed on a motherboard without adding bulk to the product design. Each of these sensors enables the photonic textile to react immediately to the user and the environment, thus creating a highly adaptable and communicative product.

In recent years, the smartphone has emerged as an indispensable gadget in daily life. It is portable and can be connected wirelessly using Bluetooth technology. For convenience and accessibility, it is highly feasible to consider the smartphone as a means of remotely controlling photonic textile products to facilitate interactions between a product, its user, and the environment.

Motherboard

A motherboard, also referred to as a printed circuit board (PCB), contains all of the electronic components needed to facilitate the use of a photonic textile product. Current developments have seen the emergence of very compact motherboards with components that are the size of small fingernails (Fig. 8). The prototypes cited below contain motherboards that are similar in size to a typical credit card, thus allowing complex and intelligent systems to be concealed within the products.

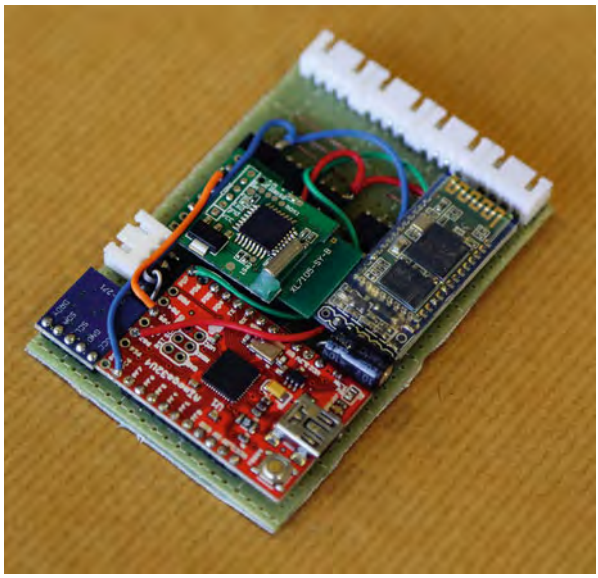

Fig. 8 Compact motherboard with relevant electronic components

Power Sources

Conventional products that require a power supply are typically connected to an AC supply via a plug or via the use of conventional batteries, which are bulky. LEDs are power-saving light sources that require only a small amount of electricity; thus, it is viable to consider using mobile power sources for small-scale prototypes. The motherboard that controls the sensors and light emission from the photonic textile is compact, slim, and smaller than a typical credit card. Corresponding to the miniature size of the components, slim mobile phone chargers and compact batteries, which are readily available in the consumer market, are used in place of cumbersome lithium batteries (Fig. 9). The miniaturization of these components enables the unobtrusive integration of technology and provides ease of use.

Case Studies

As the majority of studies emphasize the technological aspects of photonic textiles, the integral design process and considerations have tended to be neglected. To develop user-friendly products that are relevant to contemporary lifestyles, it is important to consider the creative and functional aspects of the product in tandem. To gain a better understanding of the interdisciplinary design process when developing interactive photonic textile products, case studies based on the author's development of three prototypes are discussed in the following sections. Each of the prototypes was developed for various purposes and was implemented with different technology to suit its end use.

Fig. 9 A compact battery and a typical mobile phone charger, which can serve as power sources for photonic textile products

Case Study: *Totem*

Totem is a photonic dress prototype. The prototype was developed to be showcased on a model and in an exhibition at the *Connect: Expand* + exhibition at the National Gallery, Bangkok, Thailand, in November 2013 [24, 25].

Design Inspiration and Development Process

The inspiration for the design was taken from the symbolic meaning of totemic myths (Fig. 10). The design attempts to interpret ancient tribal symbols in a contemporary manner. In addition to the photonic textiles, the key design feature is the white synthetic leather paneling, which features an abstract totem graphic of a hybrid animal-human face. Many print, color, and fabric combinations were experimented with to create a raised textured effect (Figs. 11 and 12). The graduated digital print of the organza was selected to represent the diverse symbols of totemic culture, while the photonic textile in the side panels of the dress symbolizes the advancement of technology, which enriches the future of humanity.

Before creating the final garment, numerous experiments using actual fabrics and digital simulation were performed to test different fabrics and print effects. It was important to design an aesthetically pleasing fashion garment that would have "hanger appeal" even when the photonic textiles were not lit.

Simple cotton toiles of the initial prototypes were created to assess the viability of the component placements. A loose fitting trapeze silhouette was chosen for the dress to allow sufficient space to discreetly position the electronic components. Although the components are small in size, they are made of materials with hard edges which may create obvious bulges against the fabrics.

Fig. 10 Design inspiration board for *Totem*

Fig. 11 Initial sketches experimenting with color combinations

Fig. 12 Experiments with fabrics of different colors and textures and paper pattern designs for the garment paneling

Placement of Electronic Components

The placement of the electronic components was carefully considered because the organza fabric panels are translucent and incorrect placement would reveal the unsightly electronic components – a motherboard and six LEDs, three illuminating each dress panel. As the visual focus is primarily on the front of the outfit, there are two LEDs at the front and one at the back. The motherboard and the batteries are in a box placed at the center of the back panel, as indicated in Fig. 13. The components are strategically placed beneath the synthetic leather panels so that they cannot be seen by the viewer. That part of the body does not need to bend; thus, the components do not hinder the wearer's movement.

Due to the static nature of the prototype display, an interactive remote control was included in the *Totem* dress to encourage interactivity between the viewer and the prototype (Fig. 14). This wireless remote control will also work effectively on a moving model within a restricted space to allow the detection of the technology. Bluetooth technology was adopted to achieve the wireless communication between the dress and mobile phone. Users can download and install the application onto a typical Android mobile phone to control the color of the dress. The user interface is shown in Fig. 15. The screen shows several buttons that can be used to turn the LEDs on and off and change their color or illumination level and to change the speed at which the LEDs change. To ensure the design would be highly accessible and not restricted to users who are technically savvy, a simple

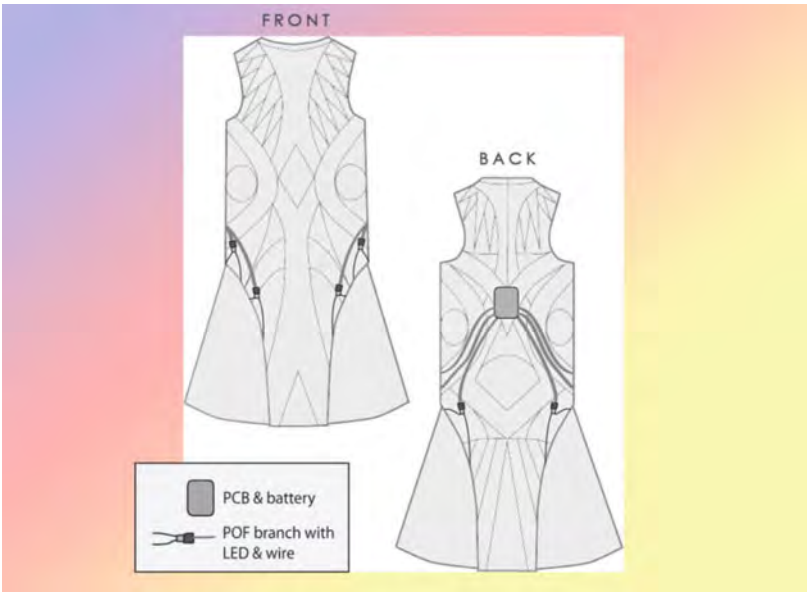

Fig. 13 Placement of LEDs, motherboard, and battery for *Totem*. The *gray lines* indicate the bundles of POFs

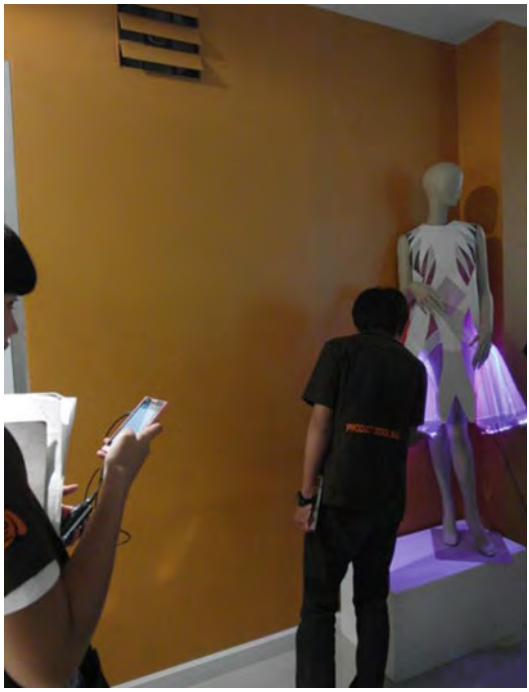

Fig. 14 *Totem* can be remotely controlled by an application installed in a typical Android phone

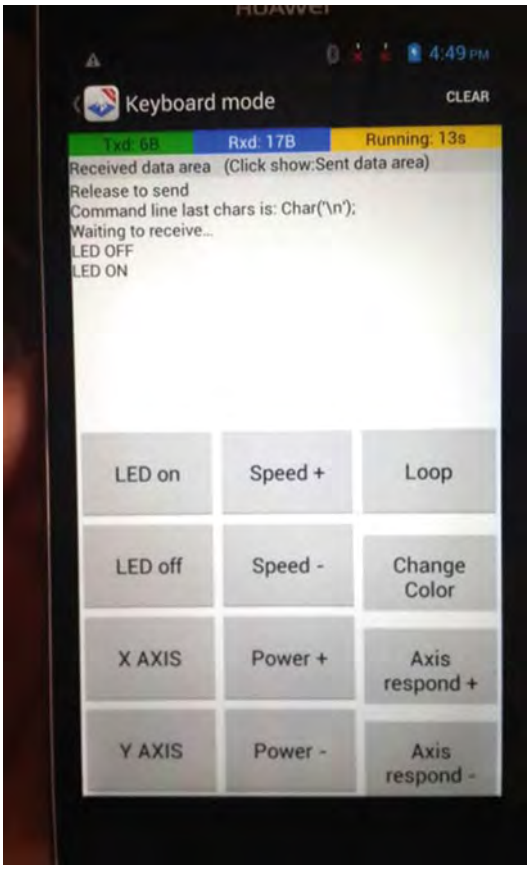

Fig. 15 User interface for *Totem* on an Android mobile phone

design was adopted for the interface. The viewer can effectively communicate with the wearer of the dress via the color illumination without the need for verbal language.

Case Study: *Urban Glow*

This case study involves two photonic textile fashion outfits entitled *Urban Glow*. The outfits were designed for the Hong Kong Museum of History for an exhibition of contemporary cheongsams in Hong Kong. The two outfits were exhibited simultaneously in Hong Kong and showcased in a fashion show in Taipei, Taiwan, for Hong Kong Week in November 2013 [26].

Design Inspiration and Development Process

The creative aim of the designs was to reinterpret the traditional cheongsams into contemporary designs incorporating illuminating technology. Traditional

Fig. 16 Inspiration board for *Urban Glow*

cheongsam elements such as the stand collar, Chinese knot buttons, slim-fitting silhouettes with tapered hemlines, and side slits were retained, in keeping with the cheongsam style. Photonic textiles are innovative and visually exciting; however, they primarily serve a decorative purpose in dark or dim environments. To ensure the photonic textile design possessed aesthetic purpose in both lit and unlit environments, all elements of the design, such as the fabric design, style lines, and materials, were carefully considered to produce a high-quality design. The surface design of the non-photonic textiles was inspired by Hong Kong's history and the *Bauhinia Blakeana*, a symbolic flower of Hong Kong. Influenced by Hong Kong's history, the creative concept was derived from the geographical characteristics of an antique map of Hong Kong's Victoria Harbour (Fig. 16). The historical map represents the city's evolving journey from a rural village to a contemporary cosmopolitan city. The textile design was digitally printed with a symmetrical duplication of the *Bauhinia* flower, and details from the maps were used as the basis of a graphic, which was screen printed in metallic foil (Fig. 17). The vibrancy of the digital print combined with the opulence of the foil print represents Hong Kong's dynamism (Fig. 18). The photonic fabric at the bottom of the side panels glows in lights of various colors, symbolizing the advance of technology enriching the future of humanity.

To ensure the technology would sit well with the textile elements of the design, the POFs were woven with a Lurex metallic yarn to create a gray photonic textile matching the base color of the printed fabric. The engineered textile prints were designed to be placed in precise areas of the garment, with consideration of the form

Fig. 17 Digital print development for *Urban Glow*. The digital prints were engineered and placed at specific positions on the fabric. The engineered prints were designed to work with the body contours and the style lines of the garment

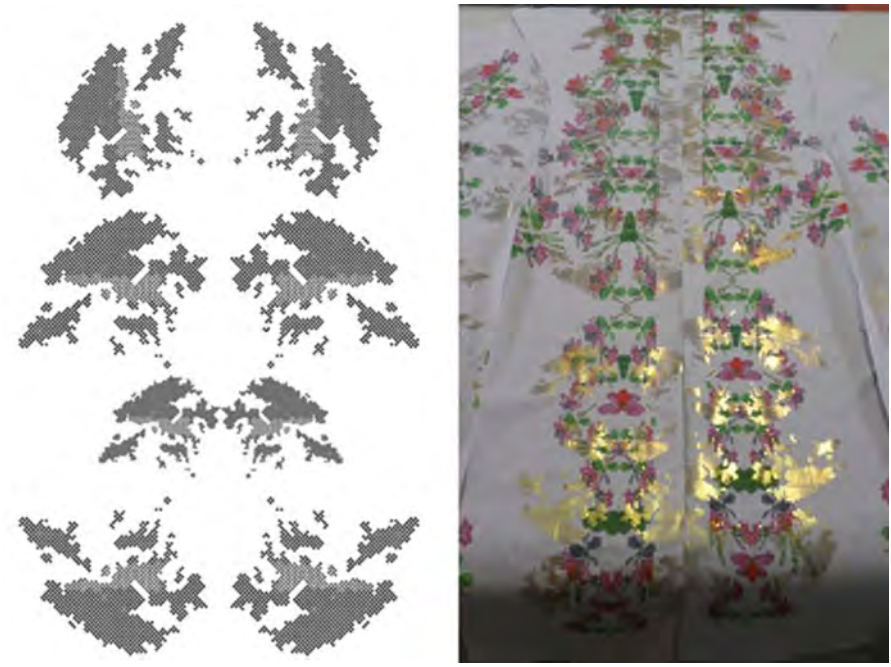

Fig. 18 Metallic foil was screen printed on *top* of the digital print to create texture and additional decorative effect

and style lines. The placement of conventional all-over prints may cause the patterns to stop abruptly at seams which will disrupt the continuous flow of the pattern, while engineered prints, although more labor intensive, will ensure the prints to flow without disruption, thus creating a visually pleasing aesthetic.

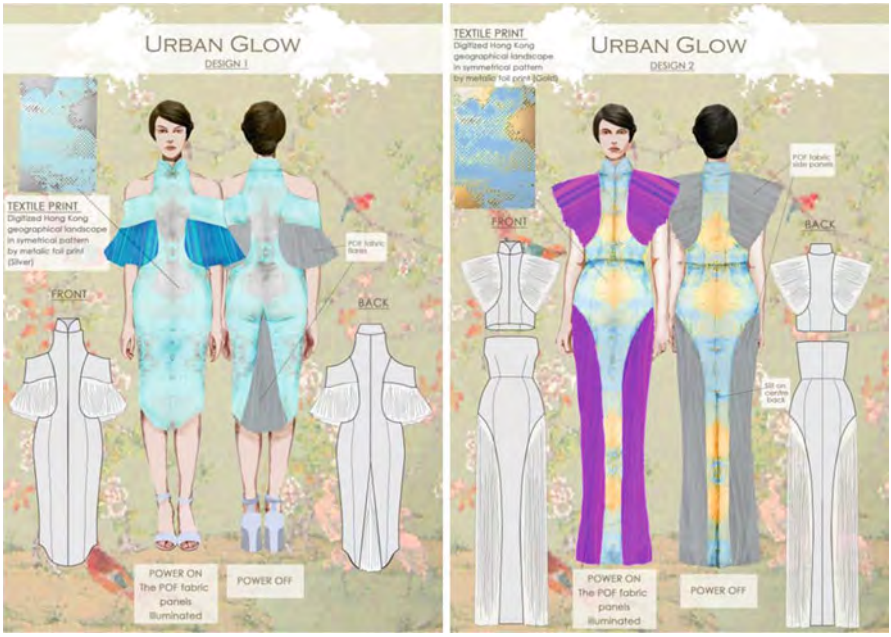

Fig. 19 Final design illustrations with production drawings of *Urban Glow* mini collection

Due to the brittle nature of POFs, photonic textiles cannot be bent or folded along the POFs' shafts; otherwise, they may break, causing light to escape and resulting in an uneven light display. It is vital for the photonic textiles to be placed on areas of the body that do not need to bend. Once the initial design sketches were completed, sample toiles of the cheongsams were created with cotton fabric to assess the viability of the design and to experiment with the placement of the components. The toiling process is vital in the fashion design process, as it allows the designer to gauge the feasibility of a design and technology and consider the dimensions of the fabrics and the fit of the garment with the integration of the technology (Fig. 19). After repeated experiments with the toiles, photonic textiles were placed on the sleeves and skirt panels of the cheongsams. These positions were selected because these areas of the body bend less, thus reducing the possibility of the POFs breaking and affecting the illumination. The photonic textiles were integrated with sensors to enable the fabrics to change color in tandem with the wearer's movement.

Each design requires different electronic components depending on the number and size of the photonic textiles involved. The first design comprises a one-piece dress that requires a motherboard, a battery, and five LEDs with coupler cable glands and wires. All of these components are placed inside the garment and cannot be seen by the viewer (see Fig. 20 for an illustration of the component placements). As the main focus of the first design is the sleeves, two LEDs are placed on each sleeve and one at the apex of the photonic skirt panel. A slim and compact mobile

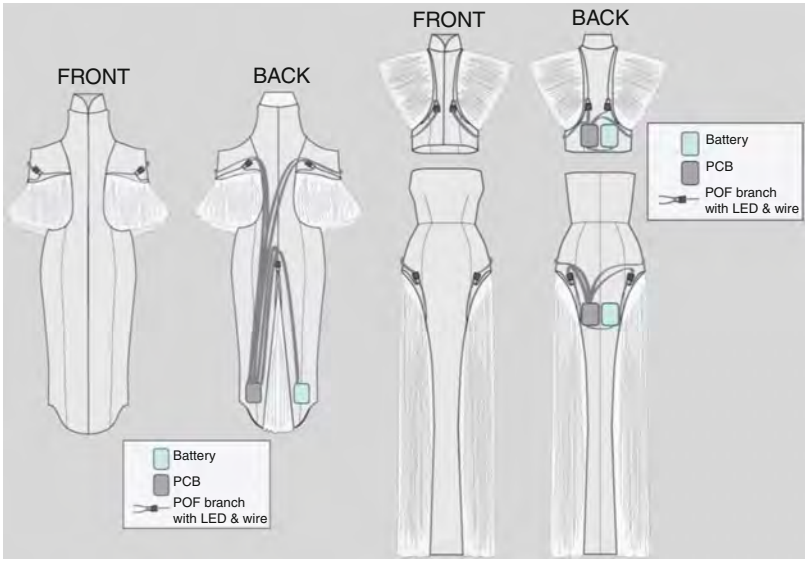

Fig. 20 Placement of LEDs, motherboard, and battery for the *Urban Glow* mini collection. The *gray lines* indicate the bundles of POFs

phone-type battery is used in place of conventional batteries. The compact power source is lightweight and non-bulky, allowing it to be discreetly placed within the garment. To evenly distribute the weight of the electronic components so that they do not affect the silhouette of the cheongsam, the motherboard and the power source are separately positioned in the back panels near the hem of the dress.

The second design comprises two separate pieces. The top has two photonic textile sleeves, while the dress has two photonic textile side panels. This design requires a motherboard, a battery, and eight LEDs with coupler cable glands and wires. This design requires more LEDs as it comprises separate, wider photonic textile panels. For the top, each sleeve is illuminated by two LEDs placed under the lining. The motherboard and compact battery are placed in the center panels at the back of the waist, an ideal position as the body has a subtle hollow that enables the components to be positioned unobtrusively. Each side panel of the dress is illuminated with two LEDs, with the battery and motherboard placed in the center back panel beneath the curve of the wearer's buttocks. All of the components are placed so that the wearer can gain access to them without needing to remove the entire garment. It is also convenient for the wearer to change power sources if the need arises.

In contrast to interior photonic textile products, which are intended for static display, this mini collection was showcased in a fashion show. Because the models would be wearing the designs and displaying them on the catwalk, it was viable to explore the interactivity between the wearer and the garment. Inspired by the elegant movements of a model on a catwalk, a gyro sensor was selected for these

Fig. 21 Fashion photo of *Urban Glow* (Photo from Tan [31])

two cheongsams. Gyro sensors, also known as angular rate sensors or angular velocity sensors, are devices that sense angular velocity and are usually applied in mobile games, digital cameras, car navigation devices, etc. [27]. In this research, a gyro sensor was embedded in the motherboard to detect the motion of the wearer's body. The colors of the LEDs were predetermined according to the changing angle of the gyro sensor. Therefore, the color of the garment changes as the wearer moves.

The wearer can actively change and control the emitted colors of the garment by simply changing her movements (Fig. 21).

Case Study: Ephemeral

Ephemeral comprises a collection of three framed photonic textiles designed to be installed on a wall for interior design purposes. Different colors and patterns are illuminated from the textiles as users interact with the installation, creating different ambiences within the room (Fig. 22). This body of work was exhibited at the Neophotonics Exhibition at the Hong Kong Museum of Medical Science in July 2013 [28]. The design motivation for *Ephemeral* was to explore the synthesis of

Fig. 22 User interacting with *Ephemeral*

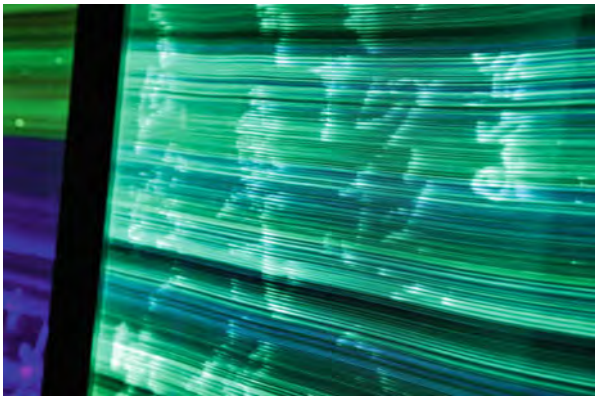

Fig. 23 Closeup view of the laser engraved patterns on *Ephemeral*

traditional Chinese art with innovative technology. Traditional Chinese calligraphy patterns and landscape motifs were engraved onto the photonic textiles (Fig. 23). As traditional Chinese paintings are conventionally explored with muted inks, this body of work attempted to create a contrasting contemporary perspective with the use of bright neon colors.

The design process for a framed photonic textile is much simpler than that for a photonic textile dress. Emphasis was placed on the integration of the technology within the frame and the selection on an appropriate interactive sensor suitable for the design and purpose of this creation.

The first phase of the process involved designing the graphic pattern to be engraved on the photonic textile. Then, a mounting device in the form of a frame

Fig. 24 Cable glands were fixed onto the frames to ensure the POFs fibers did not shift and affect the illumination

was specifically designed to conceal the raw edges of the fabric and the electronic components. After laser engraving, the photonic textile was mounted onto the frame. The cable glands and couplers were installed on the frames to ensure the LED coupling was fixed and thus ensure stable light illumination.

Placement of the Electronic Components

The photonic textiles were mounted onto metal frames with POFs coupled to the cable glands attached to the frame, as shown in Fig. 24. As it was intended to be installed in an interior environment, *Ephemeral* was not connected to a battery power source but was designed with a conventional power plug to draw power from a typical alternating current (AC) power supply.

A motion sensor was incorporated as the frames were intended to be installed in a fixed position; thus, the technology relies on the environment and users to realize the interactive platform. As illustrated in Fig. 25, red, green, and blue LEDs are coupled with optical fiber bundles to create the light source, which are controlled by an MPU (microprocessor union) on the motherboard. Radar and ultrasonic sensors are placed on the frames to explore how sensors can be embedded into interior textiles to detect and respond to stimuli from the user, thus promoting interaction between the textile and user. The function of the radar is to detect when a person enters the area and then send a signal to the control board to light up the corresponding LEDs. The function of the ultrasonic sensor is to accurately detect the distance of the person.

Three interactive modes were designed to examine the interactive function of *Ephemeral*: mode 1, up and down; mode 2, individual; and mode 3, dynamic. In the up and down mode (Fig. 26), when the ultrasonic sensor detects the movement of people within 2 m, the upper part of the three frames lights up, and then the illuminated Chinese calligraphy appears; when people are detected within 1 m, the lower part of the three frames lights up, and then the illuminated Chinese motifs appear. The colors of the lights change sequentially. In the individual mode, all of the lights on an individual frame light up once it senses movement within 2 m. In the dynamic mode, once the radar detects movement within 4 m, all three frames

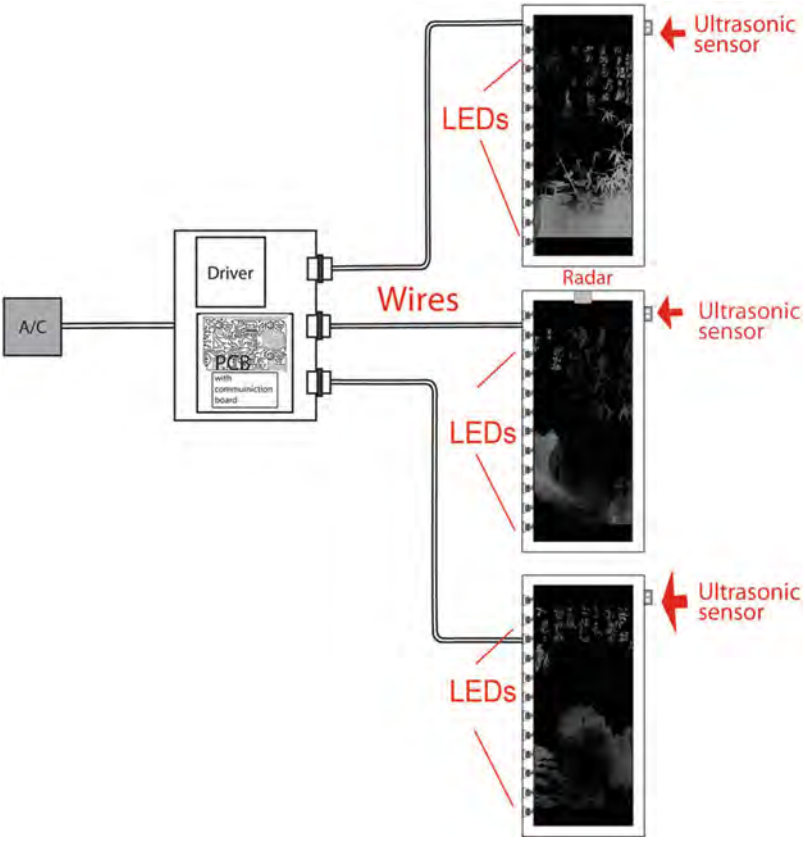

Fig. 25 Sensor and electronic placement for *Ephemeral*

show the illuminating patterns with alternating colors. The glowing images can appear and disappear in just a second. Viewers can enjoy a whole new experience with the dynamic illuminating images.

Interdisciplinary Approach for Designing Photonic Textile Products

As the above case studies illustrate, design development methods and textile technology are used in combination throughout the entire prototyping process. The aesthetic and functional technological aspects of the design must be considered in tandem: each aspect is integral to the design process and simultaneously supports the other. The process is highly reflective and experimental, whereby the product evolves simultaneously with the considerations and development of design, function, materials, and form. It is a continuous and evolutionary process that allows the product to be further "refined and defined" [29].

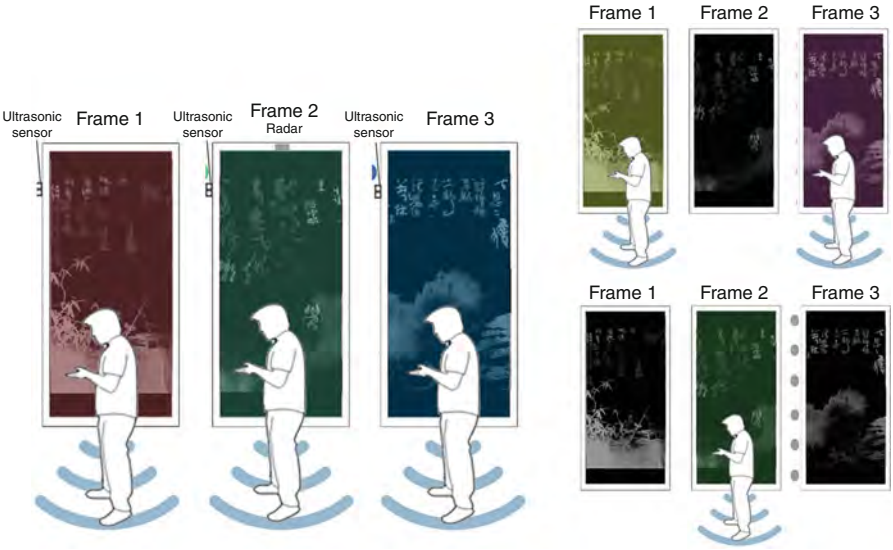

Fig. 26 Different parts of the pattern are illuminated depending on the user's distance from the prototype

The design process adopted by the author begins with inspiration and concept development, where initial ideas are sketched out. These are explored via a series of experiments on different materials and design forms and the integration of different technologies and electronic placements. Viable materials, designs, and technologies are combined to create development samples. The experimental process continues until a final prototype is developed that meets the aesthetic, functional, and comfort requirements. Considering the nature and complexity of the design process, a mixed-method approach is adopted, involving quantitative research techniques in the form of experiments and qualitative research techniques in the form of user experience analysis.

The design process is unique to every design practitioner. Designs need to be continuously revised in accordance with experiments on the prototypes. The process is also reflective and iterative, as illustrated in the design framework developed by the author and her team (Fig. 27) [30]. Continuous and evolving experiments with technology, aesthetic form, and materials are integral to the design process, and the development of each process is reflected in the others. The whole process involves a continuous cycle of improvement until the final prototype meets all predetermined requirements in aesthetics, functionality, and practicality.

The roles of design and technology are closely integrated to create products with both aesthetic appeal and innovative technological functionality. The simplistic integration of technology at the final stage of the development process results in poorly designed products with obtrusive technology. The implementation of components should be considered in tandem with the design to ensure a well-rounded product. Although the advancement of technology has made smaller electronic

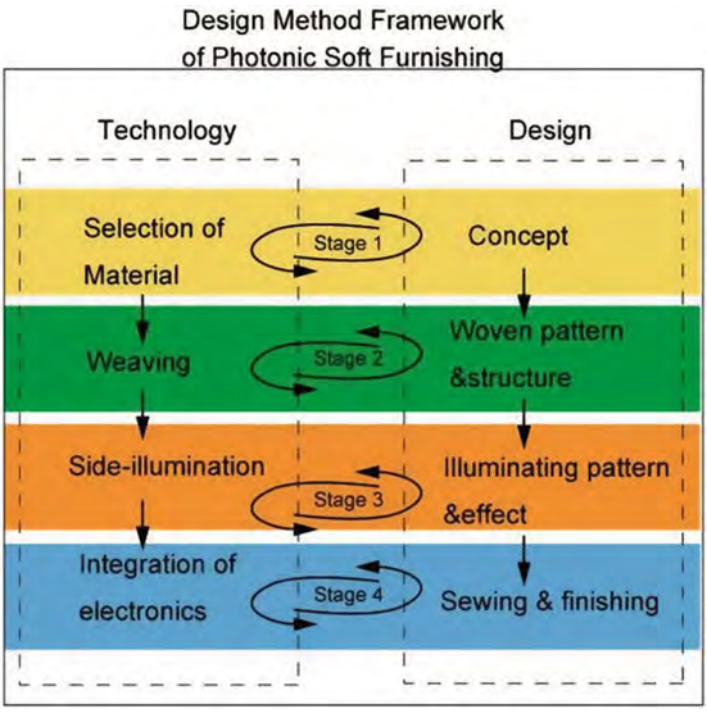

Fig. 27 Design method framework

components readily available, innovative finishing methods needed to be developed to enable the electronics to be embedded into the products. The unobtrusive positioning of electronic parts enables the seamless integration of innovative technology into value-added everyday products.

Design Challenges

The synthesis of the opposing qualities of design and technology presents some unique challenges to the design process. This section discusses the three main challenges that the author and her team faced during the research and prototyping process.

Visual Appearance of Photonic Textiles

Photonic textiles look just like normal fabrics when they are not emitting light; therefore, it is important to ensure that the visual appearance of the photonic textile matches the overall design aesthetic of the product. During the fundamental phase

of the design process, when the concept is explored in the initial sketches, it is also important to consider the required tactile quality and design of the photonic textiles. In the above case studies, matching colored textile yarns were woven with the POFs to create a fabric matching the colors and textures of the other materials used in the design. This ensured that the photonic textiles retained the design integrity of the final prototypes.

Construction of Prototypes

Although photonic textiles are pliable and highly tactile, the POFs within the textile are brittle and susceptible to breaking when bent. To prevent the uneven emittance of light, it is important to ensure that the POFs are not damaged during the prototype construction process. For the three prototypes cited in this chapter, POFs were woven into the fabric via the weft for optimum illumination. In a typical garment construction process, the warp of the fabric is placed parallel to the center front of the garment so that the weft yarns lie across the body. As POFs are stiff and do not conform to the contours of the body when placed across it, it was more viable to place the weft parallel to the center front of the garment to allow the fabric to lie flat against the body.

The photonic textiles must be specifically placed in areas where the body does not need to bend at acute angles. For example, photonic textiles are not usually applied across the waist, elbows, or knees, as these body parts need to bend when the wearer moves.

POFs are susceptible to breaking when subjected to a high impact. The construction of a garment using a sewing machine exposes the fabric to repetitive piercing by the needle. The speed of the sewing process must be reduced to allow the needle to penetrate the fabric between the POFs and to ensure that the impact of the sewing machine's footer and needle does not accidentally break the fibers. The speed reduction of the sewing machine does not affect the construction of the prototype.

Installation of Technology

The installation of appropriate technology is critical to the success of an interactive photonic textile product. The integrated technology should enhance the overall design and be suitable for the end purpose of the product.

For photonic clothing to be accepted as an enhanced fashion design that can be worn in everyday situations, it must possess the same characteristics as typical clothing in terms of comfort, ease of use, and mobility. Clothing and products which require wired attachment to power sources are cumbersome; it is practical to consider mobile power sources and wireless remote controls. Although the electronic components and power sources are highly compact, their physical state is hard and in direct contrast to the soft and pliable nature of fabrics. Inappropriate placement of

the components may be obtrusive and uncomfortable to the wearer. There are limitations to the materials that can be used with the components; for example, stretch materials will conform to the exterior shape of the components and will be highly visible; thus, it is better to use woven textiles. Appropriate amount of ease should be incorporated into the pattern construction of the garment to allow space between the component and the body as a tight fit will cause the fabric to mold against the components and reveal the technology placement.

The placement of the components is particularly challenging as there are three major considerations. First, the components must be placed discreetly so that they cannot be seen; second, they must be placed somewhere comfortable and easily accessible by the wearer; and third, their placement should not affect the practical execution of the technology. For example, the fiber ends are connected to the LEDs via the cable glands, but if the design does not make it viable to make the connection at the immediate site, a special route will need to be found that does not require the POFs to bend acutely.

Although POFs and the relevant technology have attained a level of sophistication, recent research indicates that there are still two notable areas for improvement. First, the compact power source generates a low level of heat when used for a sustained period of time, which may be uncomfortable for the wearer. Currently, this challenge is overcome by creating an additional fabric cover for the power source to prevent direct contact with the skin; however, this increases the bulk of the components and does not provide a sustainable solution for the seamless integration of technology. Second, although photonic textiles are resistant to environmental changes, the electronic components may become unstable with high atmospheric humidity or when in contact with moisture. This restricts the use of photonic textiles to specific conditions, which is highly impractical.

Summary

Interactive photonic textiles have the potential for application in value-added lifestyle products that possess the necessary characteristics to meet the fast-changing needs of contemporary lifestyles. Advancements in POF coupling and the miniaturization of components heighten the sophistication of the technology and contribute to the aesthetic design of interactive photonic fashions and interior textiles. Existing photonic textiles tend to be applied in static displays that offer a simplistic alternative light source. However, it is important to exploit the use of sensors to create products that increase the interactivity between the product, its users, and the environment. This will increase the functionality of conventionally passive products.

Research that focuses solely on the technological aspects of smart textiles often results in highly functional products that may not have aesthetic appeal. The use of an interdisciplinary approach that combines both aesthetic and technological considerations will contribute to the development of products with user appeal. The case studies cited here illustrate a cyclical design process that requires the

investment of time and labor to continuously refine both the functionality and design of the product. It is essential for design teams to possess a wide range of expertise in research, design, materials, and technology to execute a covetable smart textile product. The design process requires greater flexibility, as amendments are made to incorporate new findings from a wide range of experiments.

Everyday activities should be enhanced and not inhibited by the addition of interactive technological products. Further research should be conducted to improve the performance stability of photonic products in different environments. Even smaller components and coupling techniques will facilitate the development of products that can have more intimate contact with the body. It is also critical to develop POFs with greater flexibility so that photonic textile products can be exposed to realistic everyday use. Photonic textiles are sustainable because they are adaptable and can be mixed and matched with different sensors and controls to accommodate different end users. Advanced sourcing and development of non-heat-emitting and extremely compact power sources would also contribute to higher quality designs. The continuous research and design development of the technology and products will ensure their longevity within the market place.

References

1. Xin JH, Cheng KM, Taylor G, Sato T, Hansuebsai A (2004) A cross-regional comparison of colour emotions. Part I. Quantitative analysis. Colour Res Appl 29:451–457
2. Kwallek N, Soon K, Lewis CM (2007) Work week productivity, visual complexity, and individual environmental sensitivity in three offices of different colour interiors. Colour Res Appl 32:130–143
3. Cute Circuit. http://www.cutecircuit.com. Retrieved 28 June 2014
4. Marshall-Johnson R (2009) Thinktank consumer attitudes: new homes. WGSN. Accessed 19 Mar 2009, from WGSN database
5. Black S (2010) Reconciling electronics and fashion: Cute Circuit's Francesca Rosella and Ryan Genz in conversation with Sandy Black. Fash Pract 2(1):105–120
6. Harold P (2006) Creating a magic light lighting experience with textiles. Password Philips Res Technol Mag 28:7–11
7. http://www.red-dot.sg/ko/online-exhibition/concept/?code=816&y=2013&c=19&a=0. Retrieved 2 July 2014
8. http://loop.ph/portfolio/digital-dawn. Retrieved 25 June 2014
9. Hashimoto S, Suzuki R, Kamiyama Y, Inami M, Igarashi T (2013) LightCloth: senseable illuminating optical fibre cloth for creating interactive surfaces. In: Proceedings of the SIGCHI conference on human factors in computing systems. ACM, Paris
10. Bai ZQ, Tan J, Tao XM (2011a) Chinois Photonics, 'Future Photonics' Exhibition. Hong Kong Innovation Centre, Aug 2011. Reviewed by Prof. Robert Young, Professor of Polymer Science and Technology. School of Materials, University of Manchester
11. Kuzyk MG (2006) Polymer fibre optics: materials, physics, and applications. Taylor & Francis, Boca Raton
12. Tao XM, Tan J, Song LN (2008) Haley's night. In: Exhibition catalogue, From Lusanne to Beijing, 2008 International Fibre Art Biennale. Tsing Hua University, Beijing
13. Bai ZQ, Tan J (2012) Innovative design of polymeric photonic fibre fabric for interior textiles. Res J Text Appar 17:10–15

14. Abouraddy AF, Bayindir M, Benoit G, Hart SD, Kuriki K, Orf N, Shapira O, Sorin F, Temelkuran B, Fink Y (2007) Towards multimaterial multifunctional fibres that see, hear, sense communicate. Nat Mater 6:336–347
15. Bai ZQ, Tan J, Tao XM (2011b) 'Future Photonics' exhibited at the Innocentre, Hong Kong, 22 Aug–2 Sept
16. Koncar V (2005) Optical fibre fabric displays. Opt Photonics News 16:40–44
17. Harlin A, Mailis M, Vuorivirta A (2003) Development of polymeric optical fibre fabrics as illumination elements and textile displays. AUTEX Res J 3:1–8
18. Masuda A, Murakami T, Honda K, Yamaguchi S (2006) Optical properties of woven fabrics by plastic optical fiber. J Text Eng 52:93–97
19. Graham-Rowe D (2007) Photonic fabrics take shape. Nat Photonics 1:6–7
20. Khana TT, Unternahrer M, Buchholza J, Kaser-Hotz B, Selm B, Rothmaier M, Walt H (2006) Performance of a contact textile-based light diffuser for photodynamic therapy. Photodiagn Photodyn Ther 3:51–60
21. Rothmaier M, Luong MP, Clemens F (2008) Textile pressure sensor made of flexible plastic optical fibres. Sensors 8:4318–4329
22. Rothmaier M, Selm B, Spichtig S, Haensse D, Wolf M (2008) Photonic textiles for pulse oximetry. Opt Express 16:12973–12986
23. Norstebo CA (2003) Intelligent textiles, soft products. J Future Mater
24. Tan J, Bai ZQ, Fan S (2013) Totem exhibited at the 'Connect: Expand + Exhibition'. The National Gallery, Bangkok, 6–28 Nov 2013
25. Zhao CC, Tan J, Bai ZQ, Hua T (2014). Innovative fashion design via the integration of interactive photonic textile technology. In: Proceedings of fashion in fiction: style stories and transglobal narratives 2014, City University of Hong Kong, Hong Kong, p 29
26. Tan J (2013) Urban Glow showcased at the 'Legacies & Innovations: Cheongsam Fashion Show'. Organised by the Hong Kong Museum of History. Eslite, Taipei, Taiwan, 29 Nov 2013
27. http://www5.epsondevice.com/cn/sensing_device/gyroportal/about.html. Retrieved 5 July 2014
28. Tan J (2013) Neophotonics exhibited at the Hong Kong Museum of Medical Science, July 2013. Reviewed by Prof Alison Harley, Head of School, Textiles and Design. Heriot-Watt University, Edinburgh
29. Tan J (2005) Intuition vs rationale: an investigation into the fashion practitioner's process. Shih Chien Univ Des J 1:9–29
30. Bai ZQ, Tan J, Johnston C, Tao XM (2012) Enhancing the functionality of traditional interior textiles by integration of optical fibres. Res J Text Appar 16(4):31–38
31. Tan J (2014) Urban Glow at Legacies & Innovations: Cheongsam Fashion Show Catalogue. Organised by Hong Kong Museum of History, The Hong Kong Polytechnic University, the Institute of Textiles of Clothing, in collaboration for Hong Kong Week 2013. Presented by Hong Kong-Taiwan Cultural Co-operation Committee, Hong Kong, pp 50–51

Smart Textiles: Past, Present, and Future

38

Lieva Van Langenhove

Contents

Introduction 1036
The Past 1036
Present 1038
The Technology Perspective 1038
The Market Perspective 1047
The Future: Potential and Actions Needed 1049
Potential 1049
The PPE Submarket 1050
Health-Care Market 1052
Consumer Market 1052
Challenges 1053
Summary 1056
References 1056

Abstract

Smart textiles have been around for 15 years now. After the hype, reality has come. In spite of huge investments in research and obvious potential of applications, only few products have made it to the market. This presentation will describe the evolution so far and further perspectives as well as actions needed to proceed. Challenges and opportunities will be highlighted using specific cases.

Keywords

Smart textiles • Markets • Challenges • Technologies

L. Van Langenhove (✉)
Department of Textiles, Ghent University, Ghent, Belgium
e-mail: Lieva.vanlangenhove@ugent.be

© Springer Science+Business Media Singapore 2015

X. Tao (ed.), *Handbook of Smart Textiles*,
DOI 10.1007/978-981-4451-45-1_15

Introduction

The concept "smart material" was for the first time defined in Japan in 1989. The first textile material that, in retroaction, was labeled as a "smart textile" was silk thread having a shape memory. The discovery of shape-memory materials in the 1960s and intelligent polymeric gels in the 1970s were however generally accepted as the birth of real smart materials. It was not before the late 1990s that intelligent materials were introduced in textiles. It is a new type of products that offers the same potential and interest as technical textiles.

The definition of smart textiles is not an obvious topic. One can distinguish between functional and smart materials, smart materials and smart textiles, and smart textile systems and electronic textiles. Typical functions of smart textiles are at least sensing and reacting, possibly also data processing, communication, and energy supply. This makes the textile passive, active, or very smart. A working group within the CEN committee on textiles (TC248 WG31) has published a technical paper with the terms and definitions of smart textiles.

Regardless of the definition, smart textiles have become a multidisciplinary and promising research subject for many research groups all over the world.

The Past

The first generation of intelligent clothing uses conventional materials and components and tries to adapt the textile design in order to fit in the external elements. They can be considered as e-apparel, where electronics are added to the textile. A first successful step toward wearability was the ICD+ line at the end of the 1990s, which was the result of the cooperation between Levi's and Philips. This line's coat architecture was adapted in such a way that existing apparatuses could be put away in the coat: a microphone, an earphone, a remote control, a mobile phone, and an MP3 player. The coat construction at that time did require that all these components, including the wiring, were carefully removed from the coat before it went into the washing machine. The limitation as to maintenance caused a strong need for further integration.

Further evolution has included three trends:

- Search for new concepts and technologies for a wide range of applications
- Making electronic components compatible with the textile substrate
- Transforming electronic components into true textile structures

At the beginning of the new millennium, three research labs were pioneering in the field of developing real smart textile products: Georgia Tech (wearable motherboard), University of Pisa (Wealthy (IST-2001-37778)), and Ghent University (Intellitex baby suit [1]). The three of them were targeting textile electrodes for monitoring heart and respiration rate, for different applications: military, sports and health, and babies, respectively. Optical and electrical carriers were used.

Fig. 1 Intellitex baby suit

At UGent, for instance, this resulted into a stand-alone baby suit for monitoring sudden infant death syndrome, as illustrated in Fig. 1.

The Intellitex Textrodes consist of stainless steel fabrics; respiration is measured via piezoresistive stainless steel staple fiber yarns. A coil of stainless steel yarn is embroidered on the baby suit. It creates an inductive link with a second coil, which is embedded in the mattress. The latter can be connected to external power supply, data processing units, further communication devices, and response devices such as an alarm. The conductive link thus provides the baby suit with energy while at the same time transferring the data. The baby pajama only contains a small processor and no battery. This approach overcomes some major challenges in terms of washability of the textile product.

The first generation of projects demonstrated the potential and the strengths of smart textile products. Many other universities and research centers initiated projects on a wide variety of smart textile topics. Materials were based mainly on stainless steel fibers and optical fibers. As such fibers are not very compatible with regular textile fibers from the point of view of processing (abrasion), product properties (hardness, stiffness), and behavior during normal use (separation of materials); soon it became clear that new conductive materials and structures had to be developed. In response new types of conductive materials were achieved by adding nanoparticles into the polymer, by combining elastic filaments with nonelastic conductive fibers [2], and by coating fibers with metallic layers [3].

Some of the new materials even turned out to have sensor properties [4].

So overall, these projects have led to developing improved materials, sensors, and actuators.

Unfortunately some problems showed to be more difficult to solve than foreseen: integration, interconnections, and washability. The wearable motherboard already used the textile product in itself as platform for interconnecting the active components. Further progress was achieved by ETH Zurich [5]. Other suggested solutions for integration and washability include packaging and stretchable electronics [6]. In addition full textile-compatible conductive materials are lacking.

Most of the projects target applications in the area of health care or protection. In such domains the added value of smart textiles is obvious: it can detect threatening conditions in an early stage and thus send out a warning to seek for help or protection.

From the beginning Europe has started investing money in research on smart textiles. Several networks have been set up for coordinating the efforts and for identifying needs and opportunities. As a result Europe is currently in the lead.

Present

The Technology Perspective

An Overview

As stated before, smart textiles have basically five functions that have to be integrated and interconnected in a cost-effective way.

In each of these areas, R&D has been carried out and results are available to a certain extent.

Some of the examples given hereafter illustrate the impressive achievements today. A detailed overview is given in 7.

Sensors

A lot of work has been done on sensors. A wide range of sensors is already available, with variable levels of textile transformation and at least at the prototype stage.

The first sensors were based on electromagnetic measurements. Conductive textiles were and still are used for monitoring heart rate. This was a major aspect of the EU project MyHeart (www.hitech-projects.com/euprojects/myheart). Within the European project ConText (www.hitech-projects.com/euprojects/context), a contactless sensor has been developed. The consortium uses embroidery and lamination technology to produce EMG sensors for monitoring stress in professional situations. Piezoresistive strain sensors indicate respiration rate [8] or motion [9]. Optical systems are used as well. They use direct methods through optical fibers with Bragg grating (www.ofseth.org).

Pressure can be measured using contact, piezoresistivity, or capacitors. Contact-based pressure sensors include a variety of mechanisms. Conductivity of textile structures is determined by a range of mechanisms such as:

- Conductivity of the material itself
- Its sensitivity to deformation

- Contact resistance
- Number of contacts between fibers and yarns

Material properties and structure of yarns and fabrics determine these effects. Pressure will obviously affect contact resistance leading to qualitative and quantitative effects. Intrinsic piezoresistive materials can be based on the quantum tunneling effect, such as QTC materials from Eleksen [10].

Detection of chemicals has been studied in the European project Inteltex, using change in conductivity by swelling of CNT charged fibers as a basic mechanism (www.inteltex.eu).

Color-changing dyes indicate pH, which is a useful tool for monitoring proper healing of burning wounds [11]. Many other color-changing dyes have been reported.

Detection and analysis of sweat has been the topic of the EU project BioTex [NMP-2004-IST-NMP-2, 16789].

Actuators

Actuators can be considered as reverse sensors: sensors are expected to transform an impulse into a readable signal (mostly electrical), whereas actuators should respond upon a signal that will be mostly electrical. Actuators should respond as expected, consistently, fast, and energy efficient. Today this is still an important challenge.

Optical actuators emit light.

Initial developments have focused on the integration of optical fibers [12]. LEDs light optical fibers. The light is released in areas where the cladding layer has been damaged. By integrating such fibers in a woven or knitted structure, lighting areas can be achieved. The color of the LED determines the color of the emitted light, so this can be altered. The location is fixed by the location of the optical fibers as well as the damaged areas. In addition the system is rather complex, as many parameters have to be right: LED, power supply, interconnections, optical fibers, and lighting areas. Therefore, direct emission of light seems more appealing.

The Philips program Lumalive has intended the integration of LEDs in combination with textiles, such as clothes and furniture [13]. Further work has targeted miniaturization and textile integration (www.stella-project.de). One step further is making the textile itself light emitting [14]. Challenges at this moment are that organic active layers are not very efficient yet, so the yield is still low, and that the material is very sensitive to oxidation.

Nowadays, ribbons containing LEDs are available on the market [15]. They can be integrated easily in a textile product.

Another approach is using electrochromic dyes [16].

Electrical actuators use textile electrodes for electrostimulation. Stimulation can range from tactile impulses over electrochemical reactions up to active contraction of muscles.

They consist of two electrodes between which an electrical field is applied. The conditions of current depend on the targeted effect.

Some reported applications are:

- Fitness, wellness, and pain relief: standard devices for home use are available on the market.
- For training purposes and physiotherapy.
  - For treating pain and/or swelling, this treatment is sometimes referred to as TENS or transcutaneous electrical neuromuscular stimulation.
  - It stimulates weaker muscles to contract during exercise to improve strength more quickly. Consequently neuromuscular electrical stimulation (NMES) can significantly improve recovery times.
- For the treatment of specific neurological problems such as anxiety, depression, and insomnia [17].
- For enhancing wound healing [18].

Two major challenges arise:

- There is not always much clinical proof of the positive effects of electrostimulation and the precise conditions at which these effects can be achieved.
- At higher levels of stimulation, current concentration at the edges may occur, leading to hot spots. Appropriate design can overcome this problem [19]. In addition user appreciation for the same type of electrodes and conditions of stimulation may range from "pleasant" to "painful" [20]. The textile must be properly designed for ensuring proper placement and tight contact with the body.

In few applications today textile electrodes are being used. Nevertheless textile products offer the advantages of being recyclable and easy to use and ensuring proper positioning of the electrodes.

Thermal actuators can provide heating or cooling.

Heating is fairly simple in principle: it only takes a conductive material and a DC current.

One of the first examples of heating textiles is the E-CT fabric from Gorix [www.gorix.com]. Other commercially available active heating garments are Polartec® Heat® panels by Malden Mills [www.polartec.com], the Bekinox® heating elements by Bekaert, and the Novonic Heat System by Zimmerman.

Although basically very simple, the main issue of heating through conductive textile materials is current distribution leading to local overheating, as has already been mentioned in the previous paragraph. In heating applications, the current will concentrate in order to minimize resistance. It will follow the shortest path and pass by areas with lower resistance, thereby avoiding high resistances such as transfer between yarns. Considering the inhomogeneity of textile materials and the complexity of their structure, current distribution is pretty unpredictable.

Figure 2 illustrates how such effects determine the path of current and thus heating. Temperature is recorded by an IR camera [19].

As a result conductive yarns are integrated in a very simple pattern, being either a parrallel set of yarns of equal length or one yarn that reciprocates over the heating

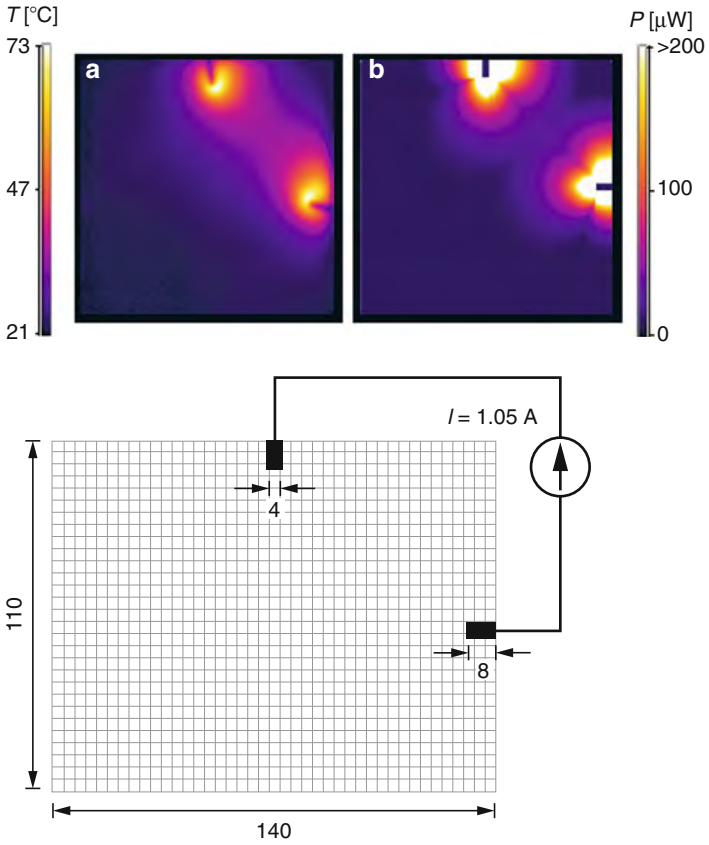

Fig. 2 Inhomogeneous heating effect in a polypyrrole-coated fabric due to current distribution; *left*: temperature recorded with IR camera, *right*: simulated profile

area. So there is currently no easy and flexible manufacturing process for heating elements.

Cooling is a very challenging issue. Passive cooling systems use endothermic processes such as evaporation of water, recrystallization, melting, etc. (www.prospie.com). They work well, but their capacity is limited.

The Italian company Grado Zero has embedded ultrathin tubes in textile structures through which a cooling liquid can be circulated. An F1 pilot racer suit has been manufactured [21]. The liquid is cooled by a small Peltier element that is fixed at the backside of the suit.

Chemical actuators release chemicals in a controlled way. Several concepts are available such as microcapsules [22], cyclodextrins [23], hydrogels [24], and nanofiber structures [25],

Mechanical actuators do exist, but all of them have major drawbacks. They are either slow, require high voltage, cannot exhibit high forces, or are not reversible.

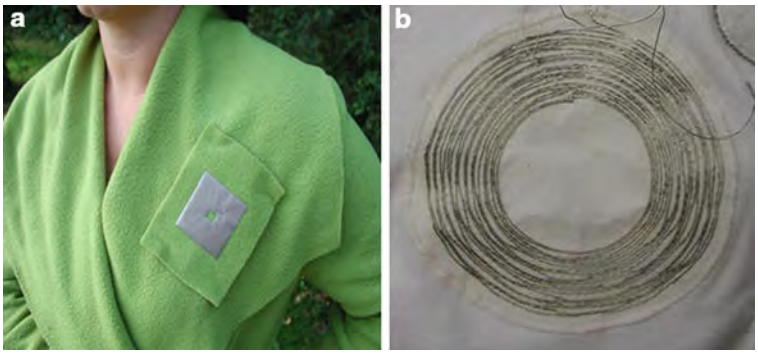

Fig. 3 Wireless textile link (**a**) Antenna operating in the ISM band (**b**). Inductive link

They include shape-memory materials [26], multilayer structures [27], electrostrictive materials [28], or diffusion-based electroactive polymers. Proper design enables a variety of movements.

Communication

BAN (body area network) communication is fairly easy and electroconductive, and optical fibers and yarns can be used to this end. Wireless communication is the main challenge. Two approaches have been studied, for medium and short distances, as illustrated in Fig. 3. The microstrip patch antenna (left picture) is active in the SIM band, which also includes Bluetooth [29]. This allows communication with, for instance, a smart phone or laptop. Further data processing and wide area communication do not need to be handled by the textile in this way. The antenna is screen-printed. The picture on the right illustrates an inductive link [1, 30]. It is embroidered on the textile substrate. Such a connection only works well when the second antenna is nearby and parallel. The electrical field decreases exponentially with distance and should not exceed a few millimeters. This is an appropriate solution, for instance, for monitoring a person during sleep, where the second antenna can be integrated in the mattress.

In the ProeTEX project, a GPS system embedded in a rescue suit allows to determine the location of a person.

Energy Supply

Energy supply can be achieved through two approaches: energy storage and energy scavenging.

Energy storage can be achieved through batteries. Capacitive or electrochemical batteries are currently in use. The disadvantage of capacitors is that the voltage supplied is not constant. For both, density of storage is limited, so capacity requires volume. For flat batteries, volume means surface.

Flexible batteries are commercially available. Although they are flexible, they are not breathable, so comfort is limited. Research is going on concerning textile-based batteries, but they are far from being commercial [31]. An example of such a battery is illustrated in Fig. 4.

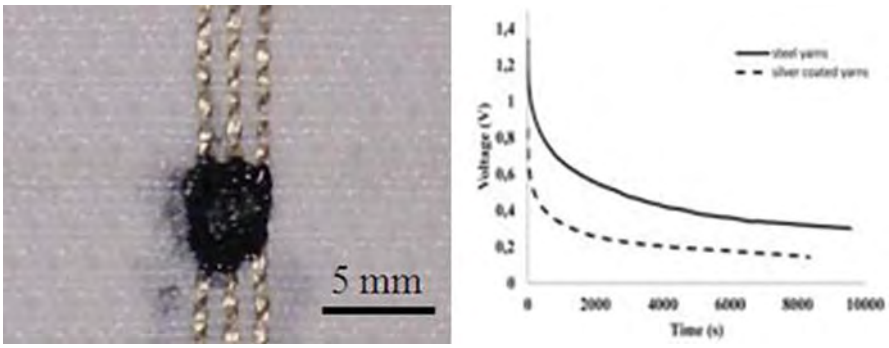

Fig. 4 Textile battery based on PDOT-PSS

Energy is available in the environment under the form of heat, light, and motion. Several mechanisms are known to harvest them.

Infineon has developed a device that harvests electricity from body heat. It was one of the first washable smart textile components. The demonstrator developed by Infineon has the dimensions of a euro coin and produces enough energy for a small sensor. This means that a stand-alone sensor can be achieved by integrating a local thermogenerator together with the sensor.

Scavenging nergy from light is a technology that is commonly used in photovoltaics (PV). Today flexible PV foils become commercially available. It is one of the highlights of the European network on organic large area electronics COLAE (www.colae.eu). The application of PV cells on textile substrates is the subject of the European projects DEPHOTEX (www.dephotex.com) and Powerweave (www.powerweave.eu).

Energy from motion can be captured in two ways, namely, using piezoelectric materials [32] and by EM induction [33].

Data Processing

Data processing requires electronic components. Initial research targeted miniaturization and encapsulation. Later on, flexible boards have been developed. A major step forward is the development of stretchable and washable electronics (www.stella-project.de). This has largely increased the textile compatibility.

Follow-up projects are further elaborating on this (e.g., FP7 projects PASTA [www.place-it-project.eu] and PLACE IT [projects.imec.be/pasta/node/1]).

The ultimate challenge is to develop fiber-based electronics. Several studies target fiber transistors [34, 35].

Interconnections

The last challenge is integrating and interconnecting all active components. All components need to be integrated seamlessly in the textile structure. The Wearable Motherboard that has been discussed previously is the first development in this respect. It consists of a grid of optical fibers embedded in a woven or knitted structure; at several connectors, active components such as sensors can be attached.

Based on the work of ETH Zurich [5], the Swiss company SEFAR has designed a woven textile structure with a grid of electroconductive yarns onto which electronic components can be attached so that the appropriate connections are achieved with a good level of durability.

Embroidery is considered as a textile technology suitable for interconnecting electronics to textiles. T. Linz [36] explored the potential and limitations in his PhD study "Analysis of failure mechanisms of machine embroidered electrical contacts and solutions for improved reliability."

Failure happens due to breakage at the transition zone from soft to hard materials and due to relaxation of the materials causing the contact to become loose.

The first problem will become less important as active elements are being transformed into true textile structures, such as with smart fibers (transistor fibers) or smart yarns [37]. However, electrical contacts remain a major challenge, particularly in view of rearrangement of fibers causing the structure to relax.

A Practical Case: The Smart Firefighter Suit

The firefighter suit is an excellent case for illustrating the status of smart textile products. It is a piece of high-tech textiles with many active components, offering a good platform for further exploitation in other applications.

Today's firefighter suit offers an extreme level of thermal protection. This level of protection is so high that the firefighter loses perception of the real danger in and around the fire. By the time he (or she) feels the heat or excessive body stress, it may be too late to get out and take off the equipment and clothes. So monitoring of vital signs and effective intervention are needed.

In addition heat and water cannot get into the suit, but they cannot get out either. This leads to dangerous conditions such as overheating by own body heat and sweat being converted into steam.

The European Commission has funded a number of research projects on smart thermal protection for professional use. Most of them target monitoring of vital signs and endangering ambient conditions, as well as communication tools. In addition each project approaches specific challenges in their own way:

- I-Protect (www.ciop.pl/21160.html) targets protection of firefighters and chemical and mine rescue workers. The selected solution will be based on fiber-optic sensors integrated in underwear.
- ProFiTex (www.project-profitex.eu) follows a user-centered design approach. To mitigate the notorious problem of unreliable wireless communication in building structures, ProFiTex will explore the approach of integrating into the lifelines used by many firefighting services, an innovative system for data transmission and tactical navigation.
- The PROSPIE project (www.prospie.eu) targets active cooling technologies, using phase change materials, cooling salts, and adequate design.
- SAFEPROTEX (www.safeprotex.org) addresses specific risky operations such as extreme weather conditions, wild land fires, and aid to medical staff.

Fig. 5 ProeTEX underwear

- Safe@sea (www.safeatsea-project.eu) targets advanced protective clothing for the fishing industry; it includes outerwear, gloves, and head protection.

The most advanced project is the ProeTEX (protective e-textiles) (www.proetex.org). This European FP6 funded project targeted research and development on materials for smart textiles for improved performance, on textile sensors, on communication through textiles, on the development of prototypes including the electronic platform, and on feasibility studies of fiber-based smart textiles such as piezoelectric textiles for energy scavenging and fiber transistors. Three generations of prototypes have been built (Fig. 5), consisting of an inner garment (underwear) containing sensors that have to be in direct contact or near to the body:

- Temperature of the skin
- Heart and respiration rate
- The composition of sweat (detection of dehydration)

The outer jacket includes (Fig. 5):

- Accelerometers that provide information on the activities and position of the wearer (standing still, walking, running; upright or lying down)
- Thermosensors to indicate the risk of breakthrough of heat through the jacket
- A GPS device to provide information on the location (in open field, for instance, when fighting fires in the forest)
- Two textile antennae that operate in the ISM band, enabling communication with a base station within a range of 10–100 m
- An electronic box for data collection and processing, a flexible battery, and a LED that turns red when a person is in trouble
- Flexible battery for power supply (Fig. 6)

Fig. 6 ProeTEX outer jacket

Fig. 7 ProeTEX victim patch

Some sensors have been built upon the results of previous EU projects such as MyHeart (textile sensors for measuring heart and respiration rate) and BioTex (www.biotex-eu.com) (sensors for sweat analysis).

Gas sensors are integrated in the boots.

A spin-off product is the victim patch (Fig. 7). This patch is to be put on the arm of the victims in case of major disasters, enabling fast evaluation of urgent need for care. It uses a combination of components integrated in the underwear and outer jacket: heart and respiration rate and body temperature.

It is compatible with the rest of the system, so data interpretation and organization of help can be organized smoothly.

A non-technological aspect of the firefighter application is the specific situation of acquisition. Public authorities often pay acquisition, be it directly or indirectly. Procurement procedures need to be followed. Often procurement procedures cannot cope with innovative and complex systems such as smart firefighter suits. Within the EU project Smart@fire, novel procurement procedures are being established to this end (www.smartatfire.eu).

The Market Perspective

Products on the Market

Today, a limited number of products are on the market. Their complexity varies from simple to complex. This offers a good range of cases with different specifications and requirements.

The price of the products has been studied in the SYSTEX project. The price depends on the complexity of the system. Simple monitoring products can be as cheap as some tens of euros. When advanced and centralized data processing tools are needed, prices increase to hundreds of euros. High-end products for protection against harsh conditions may cost more than 1,000€. Some examples are:

- Adidas-Polar smart shirt [38] for monitoring heart rate for sports applications can cost approximately 25€; this price includes only the shirt with electrodes, not the data processing unit; the latter can cost from 40€ (small processor just indicating heart rate) up to 200€ (full connection to smart phone with apps).
- Twirkle shirt is a T-shirt from the London designers CuteCircuit (www.cutecircuit.com). It blinks as a function of the wearer's movements. The LEDs are integrated in the textile, whereas the sensors (accelerometers), electronics, and battery are embedded in a small pack that is attached to the T-shirt. Its price starts from 150€.
- Smart carpet tiles SensFloor [39] from Future Shape follow a person's behavior in a house. From this a series of conclusions can be drawn such as whether a person has fallen, where a person is, presence of a burglar, etc. The price consists of the tiles, the central data processing unit, and communication devices. The tiles are the cheaper part. The data processing unit is more expensive, but it can serve up to 10 rooms. Prices start at 600–700€.
- Smart firefighter suits are high-end complex systems which must be totally reliable even in extreme conditions; all of its functions are demanding. Prices of around 1,500€ per suit have been mentioned.

Prices are expected to evolve in time. They will drop as market grows. On the other hand, new technologies will bring additional features, causing the price to rise again.

This information and understanding allow companies to adequately estimate expected prices for products and applications.

The Hype of Smart Textiles

Smart textiles are a typical example of what one could call hype. After the first projects had presented their prototypes, smart textiles attracted a lot of attention from research and industry. The potential being quite obvious, it immediately creates a lot of interest from all stakeholders. It does not need a lot of imagination to think of appealing applications for each individual. So it became a popular theme at conferences and workshops and a source of inspiration for many research projects. It soon became the hope for rescuing the textile industry that has been in decline for many years. This technology-driven positive hype has created extremely high expectations.

Several initiatives were set up in Europe in which industry and academia got together for mapping the potential of smart textiles (*SYSTEX* [www.systex.eu], ETP [40], Prometei [41]). In these initiatives, studies have been made on market potential, research and industry players, ongoing RTD, gaps and needs, etc. Information was collected from research projects, literature, surveys, and workshops. It was concluded that in spite of the huge market potential and significant research investments, no commercial breakthrough has been achieved yet. In other words, many applications remain very niche and have not enabled a mainstream market yet. Major reasons mentioned for this are:

- Complementary technologies need further development (smart materials, integration and interconnection technologies, large-scale production, design models, data processing tools, etc.).
- Business models need to be developed which are complementary to existing products in each of the applications.
- Established companies need to invest into adjacent markets, which might need a change in the dominant logic within the company.

The initial positive hype was technology driven, and thousands of ideas were launched. Unfortunately, other aspects such as business models and market approach, as described above, have been ignored. This has led smart textiles into the next phase: after the climb, the fall.

Today smart textiles have become a community, but at the same time, prototypes have shown the real challenges and difficulties, and this has severely damped the initial enthusiasm, particularly of industry. This is a negative hype, which leads to the trough of disillusionment. From now on, the few products that do make it to the market will restore confidence.

This typical evolution is illustrated in Fig. 8:

The message today is: the potential is clear, but challenges need to be addressed for achieving real breakthrough.

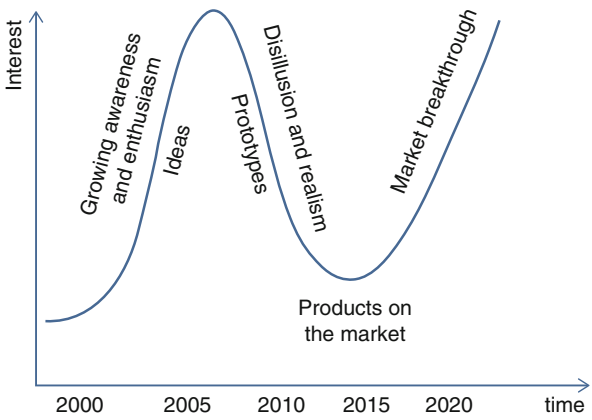

Fig. 8 Evolution of interest in products that have become hype

The Future: Potential and Actions Needed

Potential

The world annual market for smart textiles is estimated around 1,000 M$ [42].

The market for smart textiles is relatively small for now, but it is growing quickly, according to Smart and Interactive Textiles. In August 2007, a report was published by US-based research firm BCC Research. In 2007, the US market for smart textiles was worth about $79 m (€53.7 m), says BCC, but sales of conductive fabric products are expected to more than double each year through 2012, when the market is expected to reach $392 m – a compound annual growth rate of 38 %.

The smart fabrics and interactive textiles (SFIT) market is estimated to reach US $1.8 billion by 2015, according to new report by the Global Industry Analysts, Inc., consulting firm published in 2011.

When looking at the evolution of market forecasts, one can conclude that the estimated market potential is growing, but market breakthrough is slower than originally expected.

Despite slow adoption rates in several markets, the demand for SFIT technology should be driven by emergence of advanced products and new application areas with significant potential.

Axes that drive smart textiles market toward growth are:

- Development in nanotechnology, chemistry, and biochemistry will help further the potential of intelligent textiles.
- Defense, health care, followed by the consumer sector will emerge into important markets for intelligent textiles.

- Continued miniaturization of non-textile technologies especially from the field of information and communication technologies and growing commoditization of computing systems will help to enable easy integration of the same into textiles and clothing for superior functions and features; miniaturization of capacitive fabric sensors enables easy integration into substrate fabrics.

Some products will replace existing non-textile products. If the added value of the textile solution is obvious, the product can be taken to the market fairly easy because the market is already there. This is the case for sensors for heart monitoring, for instance, for sports.

In other applications, smart textiles are adding new functions, such as for the smart firefighter suit.

A third category is totally new markets. These are most promising but challenging too.

The PPE Submarket

The European Commission has identified protective textiles as a lead market [43]. The Lead Market Initiative (LMI) is the European policy for six important sectors that are supported by actions to lower barriers to bring new products or services onto the market. Protective textiles are one of them, next to eHealth, sustainable construction, recycling, bio-based products, and renewable energies. These markets have been chosen because they are highly innovative; provide an answer to broader strategic, societal, environmental, and economic challenges; and have a strong technological and industrial base in Europe. Also they depend on the creation of favorable framework conditions through public policy measures more than other markets.

Let us have another look at the market for smart firefighter suits. This market consists of two subgroups: volunteers and professional brigades. The market as such is mature, so the only possible expansion for a company is increasing market share. The overall market potential for both groups is illustrated in Fig. 9. These graphs, based on the total, take into account the evolution of the number of potential users, the fraction using the product, and the product price. The latter is estimated based on the composition of the smart firefighter suit combined with the value of components and systems used in smart textiles. Volunteers are likely going to use a more basic version of the suit, whereas professional brigades will use the advanced version.

Of course market implementation will only happen if technology is ready. Within the SYSTEX project, the following technology forecast has been established:

- ***Phase 1, The Basic Smart Firefighter Jacket***
  - EN469 compatible; measurement of temperature inside and outside, including basic warning to the firefighter; gas detection; radio control button on jacket; one device per function (no “double” devices); one standard interface protocol

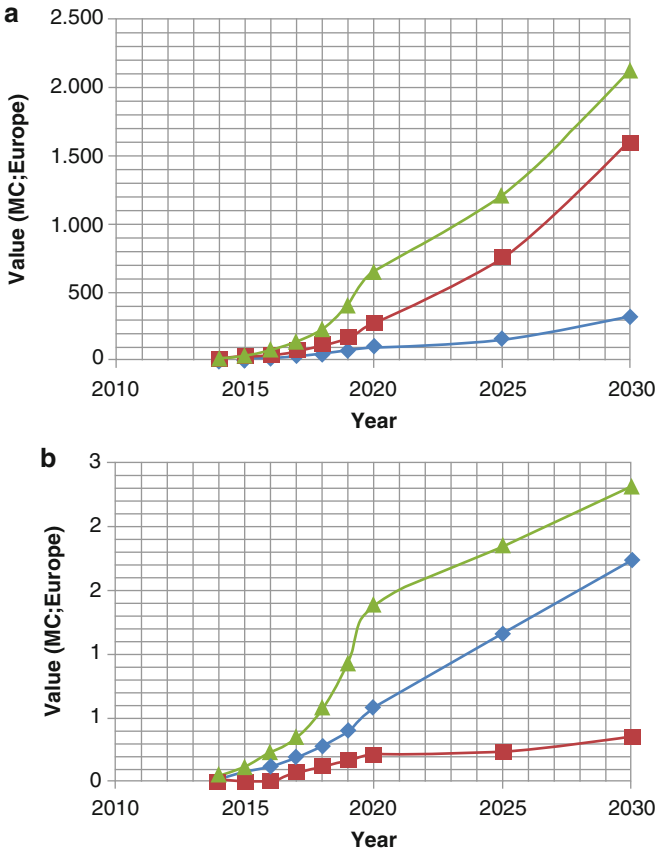

Fig. 9 Firefighter markets for volunteers (*left*) and professional brigades (*right*)

- ***Phase 2, Monitored Smart Firefighter Jacket***
  - *Phase 1 product extended with external monitoring*
- ***Phase 3, Heat Stress Monitoring Firefighter Jacket***
  - *Phase 2 product including below features:*
  - Detection of man down; detection of air left; simple heat stress monitoring (not person specific); position management
- ***Phase 4, Smart Heat Stress Monitoring Firefighter Jacket***
  - *Phase 3 product including below features:*
  - Self-learning on heat stress
  - Thermoregulation

It can be expected that phase 4 will only be reached after 5–7 years.

This example should be carefully looked at. Indeed one should not wait till the ultimate product is technically feasible. One should envisage taking basic versions within reach to the market and learn from customer feedback.

Health-Care Market

A smart textile system could perform a wide range of tasks. In its simplest form, it provides information on a person and the environment of the textile itself. Adequate analysis of such data may allow identifying health risks in the earliest possible phase. This is particularly important for health care and protection, as it provides a chance of preventing incidents and accidents from happening. When a smart textile system detects a person is at risk, it could send out an alert preventing injuries. After an incident did happen, it could analyze the situation and provide instant aid or call for help. Last but not least, it could support and follow up the rehabilitation process or even take over body functions that may have failed.

This clearly shows the huge potential of smart textiles for health care. Many projects address medical markets.

The ageing population brings along an increase of age-related diseases such as neurological disorders, epilepsy, Parkinson's disease, Alzheimer's disease, cardiovascular and cerebrovascular diseases, obesity, diabetes, cancers, wounds, ulcers, and sores.

Generally speaking, people's interest in health and safety is increasing continuously. Follow-up of pregnancy is a first important market; neonates and children are important target groups in this respect.

One can think of many roles textile products could fulfill for patients but also for caretakers. Not only clothes could become active but also bedding, floor and wall covering, furniture, and many more.

Cost-effectiveness has become an important issue in health care. Smart textiles are expected to bring more benefits than costs, considering its role in prevention, remote monitoring, and support.

These are important drivers that are beneficial for smart textiles.

Many studies do address the medical market. It turns out to be a very difficult market. There are lots of regulations and extensive clinical trials that have to be met. Cost calculations have to be made. Products need to be sterile. Medical staff needs to be convinced about the added value. After many years of research, the smart textile community is now convinced that medical applications will not be the first big success stories.

Consumer Market

The consumer market is huge. As explained before, textiles can replace conventional active components in an existing application. A good example of this is heating blankets. They exist for many years, but the heating elements consist of conductive wires. Such wires adversely affect comfort and cause risk of overheating as discussed before. Conductive textile structures are an interesting alternative.

Market potential for heating blankets (simulations resulting from market studies and discussions with companies) is illustrated in Fig. 10:

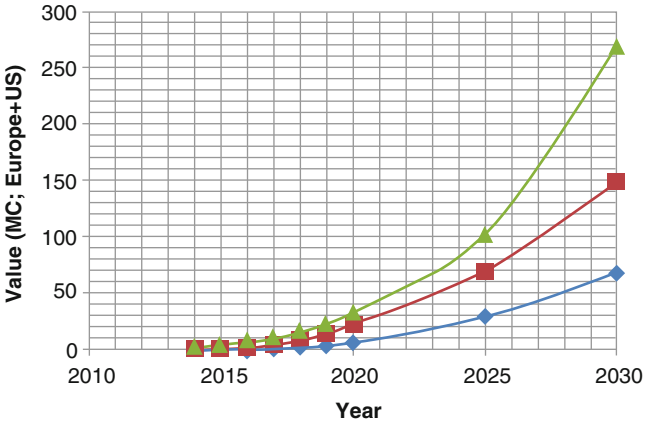

Fig. 10 Market forecasts for heating blankets in Europe and USA

Other markets, which have not been fully explored, are gaming, cosmetotextiles, and even fashion.

Consumer markets are heavily underexplored. Products do not have to be high-end and gadget-like products can be sold as well. Such products are not very demanding, but are rather cheap and have limited life cycle. New business models are typically needed for such markets.

Challenges

Why Textiles?

Intelligence is currently embedded in daily objects like watches. However, textiles show several advantages, as clothes are unique in several aspects.

They are extremely versatile in products as well as processes. The building stones of the textile material are *fibers* or *filaments*. Innumerable combinations of these source materials result into a whole range of textile materials. Fibers are available in a very broad range of materials: single or combined, natural or synthetic, strong, elastic, biocompatible, biodegradable, solid or porous, and optical or electroconductive. After treatments allow the creation of very special properties such as hydrophilic/hydrophobic nature, antimicrobial, selective permeability, etc., textile materials are able to combine advanced multifunctionality with traditional textile properties.

Textiles are all around: clothes, decoration, furniture, bed, and so many more.

Clothes are our own personal houses. They can be customised, with a perfect fit and high level of comfort. Clothes make contact with a considerable part of the body. They are a common material to everyone, in nearly all activities. They look nice and attractive and their design and look are being adapted to the actual consumer group. We all know how to use them. Maintaining textile is a daily practice: house as well as industrial laundry is well developed.

And last but not least, textiles and clothes can be produced on fast and productive machinery at reasonable cost.

These characteristics open up a number of applications that were not possible before, especially in the area of monitoring and treatment, such as:

- Long-term or permanent contact without skin irritation.
- Home applications.
- Applications for children, in a discrete and careless way.
- Applications for the elderly; discretion, comfort, and aesthetics are important.

However, textile products bring along disadvantages too. Generally speaking, they perform less than conventional components: more noise, higher energy consumption, etc. In addition requirements for textile compatibility are challenging: repeated stretch, compression and extension during use, and resistance to water and chemicals during laundry.

Any product will only become a commercial success when the textile solution has a clear added value.

Technological Issues

Applications in technical textiles will be built upon all components and materials of smart textiles. For other applications, the materials and technologies needed are variable.

Conductive and lighting materials, electronics, and advanced polymers will play a major role in nearly all applications.

Conductive materials are expected to be available around 2016. Electronic components and energy harvesting materials are expected to be available a bit earlier but with bigger spread.

Advanced polymers will be available as from 2013 with a very big spread (until 2021).

Health applications have a lesser need for energy generation or storage systems. For clothing, in general, there is less interest in smart functionalities, but aspects like comfort and usability are more important, so there is less interest in incompatible elements like electronics, metallic, or ceramic materials.

From this in combination with market perspectives and technology needs, it can be concluded that research should be intensified on conductive materials and advanced polymers, whereas developments on electronic components and energy harvesting should be continued.

Technical obstacles are cost, compatibility with production equipment, and ease of use and durability, but also integration, performance, and safety and health issues. Opposite to what is generally accepted, not many true textile components are available. Even sensors that are assumed to be readily available such as ECG electrodes are not fully understood yet. In addition their robustness is rather limited.

The system approach (needed for active smart materials) is a bigger challenge than the individual elements (passive smart materials). Integration technologies in particular have to be developed further. Participants expect that all factors will be challenging, but cost and health and safety are particular concerns.

The EU is considered ahead for active and very smart but less for passive smart materials. This might be due to the fact that projects concentrate on the application and on the more complex systems. There should be more research on basic materials; the research interest is there.

Production can be targeting integration of textile-compatible components such as stretchable circuits or miniaturized sensors or the production of true textile components.

Apart from the production itself, correct positioning and interconnections are needed.

All production technologies require further progress in all aspects. Knitting, embroidery, and braiding and laminating are mostly used, being the most flexible technologies. Therefore, they are considered as more developed. Functional performance of printing is critical. Sewing is costly, automation has to be improved, and the research interest is weak. Nonwoven is mentioned as an unsatisfactory technology, probably because of its limited flexibility. No specific processes have been designed for smart textiles, and on the other side, existing processes are being modified.

Regarding feasibility, extrusion is very challenging.

The Business Perspective

From the business point of view, the challenge of "smart textiles" lies in the fact that the technology is positioned on the cross border between different industries. Although the technology is an extension of textiles, its extensions enter into different industries such as electronics, sports, medical, etc. Hence, the typical business model of a textile company cannot be copied into the new industry without adjustment. Indeed, taking the sports industry as an example, it is unlikely that, for instance, the application of a heart monitor in a typical T-shirt will have most benefits for a sports textile company like Adidas, Nike, or Brooks. Instead, electronics producers such as Garmin or Polar, which already commercialize complementary products such as smart watches, might benefit more from the value created. If the value then needs to be split between a textile producer and an electronics company, the chances are high that the electronics company, which sells its watch at 300–400 euro rather than the textile company selling a regular T-shirt for 20–30 euro, will capture the value. Hence, it is necessary to go beyond the boundaries of the textile industry to achieve the full commercialization potential of smart textiles. The *smart camp* [44] and *lead user method* [45], for instance, provide adequate alternatives to traditional business models.

In terms of business model, one will have to accept that the source of value creation, be it "novelty," "efficiency," "lock-in," or "complementary" as in the sports example, will most probably be different for each application.

The Wide Environment

A smart textile product is a stand-alone system, but at the same time, it is part of a bigger system.

As mentioned before, a specific market may impose quite some extremely strict rules of usage. Therefore, it is also important to meet such regulations and specifications.

Proving proper functioning and reliability is the first challenge as standards are lacking or not suited for textile materials. Standardization of smart textiles is the topic of a CEN working group [CEN TC 248 WG31].

The next challenge is the procedure of acquisition. For medical applications, doctors are often the ones who prescribe a solution to a patient. The medical staff is generally reluctant to change their procedures.

Reimbursement by health insurance can be a decisive factor.

For other markets such as firefighters, acquisition takes place at governmental level or according to procedures prescribed by public authorities. Appropriate procedures for public procurement, for instance, are essential in this respect. Innovative procurement is the subject of the EU project Smart@fire (www.smartatfire.eu).

Environmental aspects should be considered as well. Pioneering work on ecodesign for smart textiles has been done by A. Köhler [46].

Ethical aspects include accessibility to technology for everyone and privacy issues.

Last but not least, user acceptance can be mentioned. For some user groups such as children and the elderly, this can be a major factor.

Summary

There are huge potential markets for smart textiles, such as health care and PPE, but not for every product. The added value of the textile solution has to be demonstrated and competitive non-smart textile solutions need to be assessed.

High-performance products do not always result into a commercial success, because many non-technological aspects need to be addressed as well, such as directives and standards, societal drivers, marketing, and sales.

Many technologies are available at prototype stage. They have to be taken one step further in terms of robustness and large-scale manufacturing.

New business models need to be addressed too.

References

1. Catrysse M, Puers R, Hertleer C et al (2004) Towards the integration of textile sensors in a wireless monitoring suit. Sens Actuators A Phys 114(2–3):302–311
2. Schwarz A, Kazani I, Cuny L, Hertleer C, Ghekiere F, De Clercq G, De Mey G, Van Langenhove L. (2011) Electro-conductive and elastic hybrid yarns – The effects of stretching, cyclic straining and washing on their electro-conductive properties. Mater Des (formerly Int J Eng Appl) 32(8–9):4247–4256. Available online 10.1016/j.matdes.2011.04.021
3. Schwarz A, Hakuzimana J, Kaczynska A, Banaszczyk J, Westbroek P, McAdams E, Moody G, Chronis Y, Priniotakis G, De Mey G, Tseles D, Van Langenhove L (2010) Gold coated para-aramid yarns through electroless deposition. Surf Coat Technol 204(9–10):1412–1418

4. Cochrane C, Koncar V, Lewandowski M, Dufour C. (2007) Design and development of a flexible strain sensor adapted to textiles based on a conductive polymer composite. In: First international workshop, DOAJ, Sensors (Impact Factor: 2.05). 7(4):473–492. DOI: 10.3390/s7040473
5. Loecher I (2006) System-on-textile integration, PhD thesis ETH Zuerich
6. http://www.stretchable-circuits.com/projects/healthcare/stella
7. Castano LM, Flatau AB (2014) Smart fabric sensors and e-textile technologies: a review. Smart Mater Struct 23(5). doi: 10.1088/0964-726/23/5/053001
8. Van Langenhove L, Hertleer C, Lanfer B (2006) Long term behaviour of textile sensors. Trans Inst Meas Contr 29(3–4):271–281
9. Tognetti A, Carpi F, Lorussi F, Mazzoldi A, Orsini P, Scilingo EP, Tesconi M, De Rossi D (2003) Wearable sensory-motor orthoses for tele-rehabilitation. In: Proceedings of the 25th annual international conference of the IEEE engineering in medicine and biology society, Cancun
10. Bloor D, Graham A, Williams EJ, Laughlin PJ, Lussey D (2006) Metal–polymer composite with nanostructured filler particles and amplified physical properties. Appl Phys Lett 88:102103. doi:10.1063/1.2183359
11. Vanderschueren L, De Clerck K (2013) Halochromic textile materials as innovative pH sensors. Adv Sci Technol 80:47–52
12. Harlin A, Mäkinen M, Vuorivirta A (2003) Development of polymeric optical fibre fabrics as illumination elements and textile displays. Autex Res J 3(1)
13. http://www.lighting.philips.com/main/projects/index.wpd?ProdId=luminous%20textile
14. Meunier L (2012) Création et realization d'afficheurs électrochromes textiles flexibles, PhD study, (ENSAIT 2012)
15. http://www.zdalighting.com/en/8-led-flexible-light-strips?gclid=CKinuIn1hb8CFcoBwwodCwYAVQ
16. Meunier L, Fern M, Kelly CC, Koncar V (2011) Flexible displays for smart clothing: part II – electrochromic displays. Indian J Fibre Text Res 36:429–435
17. Gilula MF, Kirsch DL (2005) Cranial electrotherapy stimulation review: a safer alternative to psychopharmaceuticals in the treatment of depression. J Neurotherapy 9(2). doi: 10.1300/J184v09n02_02
18. Clark M (2013) Electrical stimulation and wound healing. Wound Healing Int 4(eSuppl):4–6. Available at http://www.woundsinternational.com/pdf/content_10799.pdf
19. Banaszczyk J, De Mey G, Schwarz A, Van Langenhove L (2009) Current distribution modelling in electroconductive fabrics. Fibres Text East Eur 73:28–33
20. Anne S (2011) Electro-conductive yarns: their development, characterisation and applications. PhD at Ghent University. ISBN 978-90-8578-430-2
21. www.gzespace.com/gzenew/learn_more/RACING_Gze_En.pdf?PHPSESSID=bc3318fb77a5b8595fe811f991d67ae5
22. Abbaspourrad A, Carroll NJ, Kim S-H, Weitz DA (2013) Polymer microcapsules with programmable active release. J Am Chem Soc 135(20):7744–7750
23. Hirayama F, Uekama K (1999) Cyclodextrin-based controlled drug release system. Adv Drug Deliv Rev 36:125–141
24. Laftah WA, Hashim S, Ibrahim AN (2011) Polymer hydrogels: a review. Polym Plast Technol Eng 50:1475–1486
25. Han D, Steckl AJ (2013) Triaxial electrospun nanofiber membranes for controlled dual release of functional molecules. ACS Appl Mater Interfaces 5(16):8241–8245
26. Vasile S, Ciesielska-Wróbel IL, Van Langenhove L (2012) Wrinkle recovery of flax fabrics with embedded superelastic shape memory alloys wires. Fibres Text East Eur 20, 4(93):56–61
27. http://www.reading.ac.uk/web/FILES/tsbe/Ogwezi_TSBE_Conference_Poster_2013.pdf
28. Pelrine RE, Kornbluh RD, Joseph JP (1998) Electrostriction of polymer dielectrics with compliant electrodes as a means of actuation. Sens Actuators A 64:77–85
29. Tronquo A, Rogier H, Hertleer C, Van Langenhove L (2006) A robust planar textile antenna for wireless body LANs operating in the 2.45-GHz ISM band. Electro Lett 42(3):142–143

30. Tronquo A, Rogier H, Hertleer C, Van Langenhove L (2006) A robust planar textile antenna for wireless body LANs operating in the 2.45-GHz ISM band. Electron Lett 42(3):142–143
31. Textile energy storage device, Odhiambo S, De Mey G, Schwarz A, Van Langenhove L (2012) In: 7th Central European conference on fibre-grade polymers, chemical fibres and special textiles, proceedings. pp 85–89
32. Krucinska I, Cybula M, Rambausek L, van Langenhove L (2010) Piezoelectric textiles: state of the art. Mater Technol 25(2):93–100
33. Terlecka G, Vilumsone A, Blums J, Gornevs I (2011) The structure of the electromechanical converter and its integration in apparel, Scientific Journal of Riga Technical University, Material Science. Textile and Clothing Technology, pp 123–129
34. Tao X, Koncar V, Dufour C (2011) Novel geometry for the wire organic electrochemical textile transistor. J Electrochem Soc 158(5):H572–H577
35. Rambausek L, Van Genabet B, Schwarz A, Bruneel E, Van Driessche I, Van Langenhove L (2013) Essential building blocks of fibrous transistors, Part I: gate layer. Adv Sci Technol 80:83–89
36. Linz T (2011) Analysis of failure mechanisms of machine embroidered electrical contacts and solutions for improved reliability, PhD thesis, UGent. search.ugent.be/meercat/x/all-view?q=author%3A"Vanfleteren%2C+Jan+"&start=50&filter=&count=5&sort=&rec=rug01:001670699
37. Dias T, Cork CR, Ratnayaka A, Anastasopoulos I (2013) Electronically functional yarns for smart textiles, Nano. Nano 1757–2517. IoN Publishing
38. http://www.crunchwear.com/adidas-polar-fusion-apparel-for-runner/
39. http://www.future-shape.com/en/technologies/23/sensfloor
40. Thematic expert group on smart textiles of the European Technology Platform for Textiles and Clothing. http://www.future-shape.com/en/technologies/23/sensfloor
41. A European roadmap for PPE (personal protective equipment)
42. Venture Development Corporation (2007) Smart fabrics, interactive textiles and related enabling technologies – market opportunities and required analysis, 3rd edn. http://www.vdcresearch.com/_Documents/proposal/pro-attachment-2126.pdf
43. http://ec.europa.eu/enterprise/policies/innovation/policy/lead-market-initiative/
44. Clarysse B, Kiefer S (2011) The smart entrepreneur: a roadmap to success. http://eur-lex.europa.eu/LexUriServ/LexUriServ.do?uri=COM:2007:0860:FIN:en:PDF
45. von Hippel E (1986) Lead users: a source of novel product concepts. Manage Sci 32:791–805
46. Köhler A (2013) Anticipatory eco-design strategies for smart textiles, PhD thesis, TU Delft. ISBN 97890-6562-335-5

Index

A
Actuator(s)
  chemical, 1041
  contractile, 15
  dielectric polymer, 25
  elastomer, 9
  electrical, 1039
  mechanical, 1041
  optical, 1039
  thermal, 1040
Adidas-Polar Smart shirt, 1047
Android mobile phone, 1019
Anode, 517–528
Artificial muscle, 14
Artificial skin, 322, 352

B
Backward-wave oscillator, 816–817
BAN. *See* Body area network (BAN)
Batteries, 768–771
Beltron 9R1, 371
Binders, 235–236
Biomedical textiles, 202, 205
Bio-potential, 775–806
Biosensors 990
Body area network (BAN), 460, 1042
Body-centric communication, 451
Bucky gel actuator (BGA), 395–396
Bulk hydrogels, 957, 961

C
Capacitive sensors, 359–362
Carbon materials, 742, 747–750, 752, 761, 763, 765
Carbon nanofiber, 518–521
Carbon nanotubes (CNTs), 44, 46, 49, 51, 742, 748–749, 760, 767
Cathode, 528–539
Chemical-biochemical sensors, 367–368
Chromism, 863
Circuit simulation, 475
Coating, 234–236, 239, 242, 244, 248, 249, 751–752, 758, 768, 771
Comb-graft PNIPAAm based hydrogels, 964
Communication, 1042
Communication textiles, 861
Conducting polymer(s), 31–60, 65, 742–743, 754, 758, 761–763, 765, 769, 873–875
Consumer market, 1052–1053
Contact impedance, 787, 788, 792, 793

D
Data processing, 1043
Dielectric constant, 5, 17–22
Dielectric elastomer (DE), 385–386
Dielectric polymer, 6–8
Differential shape memory fiber, 192–198
Doping, 73–74
Dry electrode, 775–806
Dry spinning, 184, 187
Dynamic measurement, 795–806

E
Electrical conductivity, 32–34, 42–43, 45, 47, 49–50, 53, 56, 59
Electrical interconnector, 550
Electro-active polymer (EAP), 385–396
Electrochemical impedance spectra, 780–784, 789
Electrochromic device (ECD), 879–885
Electroconductive textile materials, 848
Electrolyte gel, 389–390
Electromagnetic simulation, 465–466, 474
Electro-mechanical functions, 4

© Springer Science+Business Media Singapore 2015

X. Tao (ed.), *Handbook of Smart Textiles*,
DOI 10.1007/978-981-4451-45-1

Electromechanical properties
continuous filament yarn, 722–723
fabrics, 727–736
short fiber stable yarn, 723–727
single conductive fiber 721–722
Electronic devices
dye-sensitized solar cells, 619–621
electrochromic devices, 648–649
field-effect transistors, 639–642
light emitting diodes, 643–645
lithium-ion batteries, 624–627
mechanical-to-electric energy harvesters, 622–624
P-N diodes, 642–643
sensors, 629–630
supercapacitors, 627–629
UV photodetectors, 645–648
Electronic skin, 321
Electronic spinning, 184, 187, 198–201, 204
Electronic textiles (ETex), 739–771, 987
research in, 358
Electrooptical function, 22
Electrospinning, 71–73, 516–517, 618, 893–894, 900, 904, 909, 911
Energy conversion, 6, 8
Energy harvesting, 413, 995–996
body area network implementation, 460
RF, 466, 480
Energy supply, 1042–1043
Equivalent circuit, 777, 778, 795, 799
European standards, 846
Evaluation instruments, 775–806
Evaluation methods, 775–806

F
Fabric pressure sensor, 736
Fabric strain sensor
conductive elastomeric composites, 303–306
conductive nano-materials, 299–302
conductive yarns, 298–299
inductive sensor, 307–311
intrinsically conductive polymer, 295–297
polymer optical fiber, 311–312
resistive type, 307
Fiber based circuitry, 259–267
Fiber-based nanogenerator, 488–499
Fiber Bragg grating fabrication, 598
Fiber optic sensor, 609
Fiber spinning, 31–60, 236–238
Fiber transistor, 257–259
Fire fighter suit, 1044–1047
Flexible actuators
dielectric EAPs, 385–389
ionic EAPs, 389–396
in smart textiles, 400–408
SMPs, 398
thermal driven actuator, 397–398
Flexible electronic, 329, 343, 347
Flexible pressure sensors, 327, 337
Flexible textile displays, 861, 885–886
Force/haptic feedback, 408
Functional fashion design, 691, 694, 710, 713, 714
Functional textile materials, 848

G
Grafting, 971
Graphene, 743, 749–750, 761, 765
Gyro sensor, 1012–1013, 1024

H
Harmonic balance (HB) technique, 475, 477
Health care market, 1052
Heartbeat, 69–70
Human-machine interaction, 319
Human-machine interface, 406–408
Hydrogel(s), 935, 938–939
Hydrogel films, 974–979

I
Impact sensor, 23
Inductive sensor, 307–311, 362–363
Inkjet printing, 658–659
Intelligent footwear system, 257, 267–276
Intellitex textrodes, 1037
Interactive photonic textiles, 1007, 1031
Interconnections, 1043–1044
Inter-disciplinary design process, 1014, 1027–1029
Ionic polymer-metal composites (IPMCs), 390, 394

K
Kapton, 360

L
Laminating method, 238, 752–753
Light-intensity, 114
Liquid plasma polymerization, 968

Lithium aluminum titanium phosphate (LATP), 543
Lithium cobalt oxide (LiCoO2), 515, 528–530
Lithium-ion battery, 514–515, 518, 522, 529, 544
Lithium iron phosphate (LiFePO4), 529, 534–535
Lithium lanthanum titanate, 540
Lithium manganese oxide (LiMn2O4), 528, 531–534
Lithium manganese silicate (Li2MnSiO4), 529, 535–538

M
Manganese oxide, 526–528
Mechanical property(ies), 36, 41–45, 48, 49, 52–54, 56, 187–191, 194, 195, 201, 203
Mechanism, fiber-based piezoelectric nanogenerator, 491–499
Medicine and healthcare, 402–406
Melt spinning, 184, 187, 191–193, 196
Melting point, 231
Microcapsulation technology, 239
Microcapsules, 234–244, 248
Micro-encapsulation, 238
Micro-fiber, 26
Microgels, 961, 979–980
Modeling and theory, 505–507
Motherboard, 1011, 1013
Motion artifact, 788, 795, 798, 800, 806

N
Nanofiber, 25–26, 70–72, 618, 892, 895, 900
  anodes, 517–518, 527
  cathodes, 528–539
  electrospinning, 516–517
  materials, 628, 630
  P3HT, 73
  separators, 539–543
Nanogenerator, 415–417, 420
Nonlinear circuits, 461, 475

O
Optical fibres
  polymer, 81
  sensors, 95–103
Optical sensors, 365–367
Organic light-emitting diodes, 740, 752, 760
Organic materials, 739–771
Organic solar cells, 740, 753, 765

P
P3HT. *See* Poly(3-alkylthiophene)s (P3HTs)
Paraffin, 238
Phase change materials (PCMs), 226–234, 236–239, 243, 245–249, 853–855
PEDOT:PSS. *See* Polyaniline and poly (3,4-ethylenedioxythiophene):poly (styrene sulfonate) (PEDOT:PSS)
Phase transition, of thermo-responsive polymers, 921–928
Photonic crystals (PCs) structure, 130–131
Photonic fabric device, 582–590
Photonic textiles, 104
Photo-switchable magnetic devices, 159, 169
Phototherapy
  description, 579–580
  optical parameters, 581–582
  photonic fabric device, 582–590
Piezoelectric
  ceramic composites, 416–417
  flexible and soft, 414–415
  nanogenerator, 488–499
  PENGs, semiconducting materials, 415–416
  polymeric materials, 417–418
  sensors, 363–365
Piezoresistive
  effect, 295, 303, 305
  sensors, 369–375
Planar antenna, 461
Planter pressure monitoring, 272, 274–275
Plasma treatment, 753–755
PNIPAAm-based IPN, 967
POF fabric, 117–122
POF sensor
  advantages, 114
  applications, 117–122
  coupling fiber, 115–116
  evanescent field, 116–117
  macro-bending, 115
  micro-bending, 114–115
POF. *See* Polymer optical fiber (POF)
Poly(3-alkylthiophene)s (P3HTs), 71–74
Polyacrylonitrile (PAN), 517–518, 521, 523, 534, 540–541, 543
Polyaniline and poly (3,4-ethylenedioxythiophene)\:poly (styrene sulfonate) (PEDOT:PSS), 65–69

Polyaniline (PANI), 743–744, 746, 754, 758, 763, 765, 767, 873–874
Polyimide strips (Kapton), 360
Polymer optical fiber Bragg gratings (POFBGs)
  applications, 608–610
  fabrication, 598–600
  properties, 604–608
Polymer optical fiber (POF), 81, 311, 598
  fabrics, 586–587
  light sources, 584
  materials, 582
  surface treatment, 583–58
Poly(N-isopropylacrylamide), 959
Polypyrrole (PPy), 745–746, 758, 762, 767
Polythiophene (PT), 745–746, 758, 767, 880
Polyvinylidene fluoride (PVDF), 363, 386, 388, 518, 543–544
Poly(vinylidenefluoride-trifluoroethylene) (PVDF-TrFE), 363
Porous structure, 892–915
Post-treatment, 190–191, 193
PPE submarket, 1050
Printing
  challenges, 655
  inkjet, 658–659
  screen, 657–658
  sequence, 678
  uses, 655
PROETEX (protective e-textiles), 1045–1046

R
Readout approach, 288
Rectifier, 467, 475–479
Rectifying antenna, 468, 479
Refractive index, 82–83, 85
Remote control, 1012–1013
Resistance, 691, 694–697, 717
Resistance network, 724

S
Screen printing, 164, 657
Self-healing, 204
Sensitivity, 295, 298, 301, 311, 722
Sensor(s), 756–759, 761, 1038–1039
  array, 261–267
  inkjet printed, 681–682
  piezoelectric force, 667
Separation material, 892
Separator, 515–516, 539–543
Shape memory fibers, 184
  for textiles, 200–204
Shape memory polymers (SMPs), 398
Side-emitting optical fiber, 583
Silicon, 522–526
Sitting pressure monitoring, 280–288
Smart carpet tiles SenseFloor, 1047
Smart cushion cover, 277–288
Smart fabrics, 656–659
Smart fashion, 401–402
Smart material, 1036
Smart textile(s), 110, 156, 294–295, 304, 311, 436, 447, 578, 656, 659, 847–848, 861, 921, 937, 948
  challenges, 1053–1056
  consumer market, 1052–1053
  health care market, 1052
  hype of, 1048 (*see also* Electronic textiles)
  materials, 849
  systems, 850
Smart/intelligent textiles, 720, 736
Soft pressure sensors, 337, 340, 348
Solid–liquid PCM, 227, 239
Solid-solid PCM, 227, 231, 233
Spider silk, 210
Standards
  CEN, 846–847
  definition, 844
  smart textiles, 847–848
Static measurement, 789–794
Stretchable electronics, 324, 336
Stretchable pressure sensors, 336
Structural color, 130–131
  study of 130
Styrene-Ethylene-Butylene-Styreneblock copolymer, 371
Supercapacitors, 766–768

T
Tactile sensor(s), 74–75
  capacitive tactile sensors, 323–330
  conductive liquid tactile sensors, 348–351
  flexibility, 322
  hysteresis, 321
  optical tactile sensors, 344–348
  piezoelectric tactile sensors, 330–334
  resistive tactile sensors, 334–344
  response time, 322
  sensitivity, 321
  spatial resolution, 322
  stretchability, 322–323
Technical report, 848, 851
Temperature-regulating, 234

Terahertz imaging techniques, 828–830
behind textile barriers, 833–834
non-destructive testing for composites, 837–839
target detection behind textile barriers, 836–837
target detection technique, 835–836
textile imaging, 831–832
textile water content, 832–833
Terahertz non-destructive testing for composites, 837–839
Terahertz spectroscopy technique backward-wave oscillator, 816
for clothing materials, 821–824
imaging, 828–830
terahertz time-domain spectroscopy, 815–816
textile fiber identification, 818–820
for textile sensing, 825–827
tomography, 830–831
wool textile identification, 818
Terahertz time-domain spectroscopy (THz-TDS), 815–816
Terahertz tomography, 830–831
Terahertz wave technology applications in communication, 813–814
in nature, 813
imaging behind textile barriers, 833–834, 836–837
non-destructive testing for composites, 837–839
target detection technique, 835–836
textile imaging, 831–832
textile water content, 832–833
spectroscopy technique (*See* Terahertz spectroscopy technique) spectrum, 811–812
Test procedure, 846
Textile electrode, 69, 778, 787–788
Textile fiber identification, 818–820
Textile polymers, 5
electric characteristics, 5
weaving technology, 23–25
Textile sensor(s), 270, 272, 274–275, 720, 736
capacitive sensors, 359–362
chemical-biochemical sensors, 367–368
classification, 359
inductive sensors, 362–363
mechanism of sensors, 359
optical sensors, 365–367
piezoelectric sensors, 363–365
piezoresistive sensors, 369–375
Thermal regulation, 691, 701, 704, 710
Thermo-responsive polymer
classification of, 928–930
effects influencing transition behavior of, 925–928
phase separation of, 921–923
synthesis of, 930–934
for textile application, 938–941
transition behavior of, 923–925
Thermo-sensitive textiles, 953–981
Three-dimensional surface, 563, 570, 572–573
Tin antimony alloy, 521–522
Transistors, 760–761
Triboelectric energy, 420–423
Triboelectric nanogenerator, 499–508
Twirkle shirt, 1047

V
Volume phase transition, 957

W
Washability, 1038
Wearable antennas, 447–449
Wearable body sensor networks (WBSN), 992
Wearable electronics, 256–257, 261, 289, 550–551, 558–559, 565–566, 569, 720
textiles, 691, 711
Wearable materials
conductive fabrics, 463–464
dielectric fabrics, 462–463
electromagnetic characterization, 464–466
Wearable sensor, 294–295, 299–300
Wet spinning, 41, 45, 47, 49, 52–53, 66–69, 186–187, 189–190, 238
Wettability, 892, 906, 912
Woven fabric based fiber optic sensor, 366
Wool textile identification, 818